Fracture Mechanics

Twenty-Third Symposium

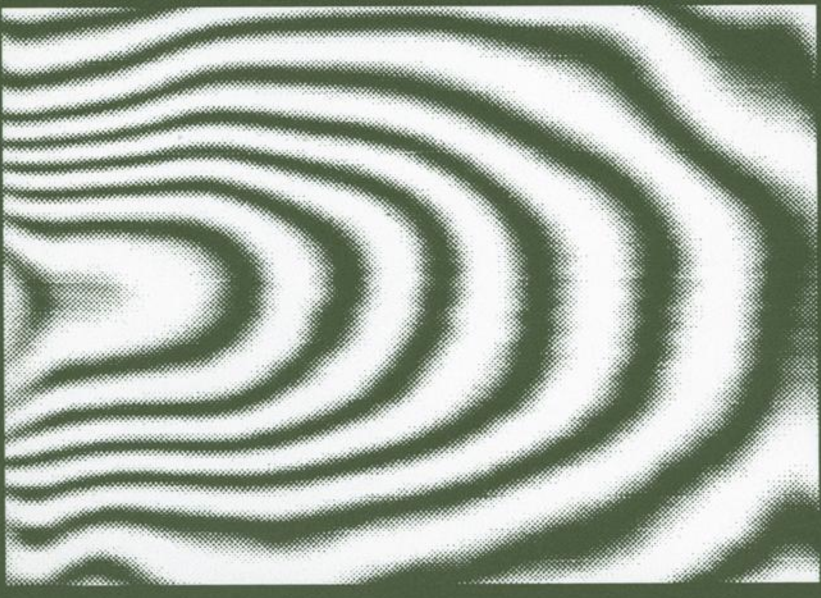

Ravinder Chona, editor

STP 1189

STP 1189

Fracture Mechanics: Twenty-Third Symposium

Ravinder Chona, editor

ASTM Publication Code Number (PCN)
04-011890-30

ASTM
1916 Race Street
Philadelphia, PA 19103

ASTM Publication Code Number (PCN) 04-011890-30
ISBN: 0-8031-1867-8
ISSN: 1040-3094

Peer Review Policy

Each paper published in this volume was evaluated by three peer reviewers. The authors addressed all of the reviewers' comments to the satisfaction of both the technical editor(s) and the ASTM Committee on Publications.

The quality of the papers in this publication reflects not only the obvious efforts of the authors and the technical editor(s), but also the work of these peer reviewers. The ASTM Committee on Publications acknowledges with appreciation their dedication and contribution to time and effort on behalf of ASTM.

Printed in Baltimore, MD
September 1993

Foreword

The Twenty-Third National Symposium on Fracture Mechanics was held on 18–20 June 1991 in College Station, Texas. ASTM Committee E24 on Fracture Testing was the sponsor. Ravinder Chona, Texas A&M University, presided as symposium chairman and is the editor of this publication.

Contents

Elastic-Plastic Fracture Mechanics—Applications

Linear-Elastic Fracture Mechanics—Analyses

Linear-Elastic Fracture Mechanics—Applications

FATIGUE AND NONDESTRUCTIVE EVALUATION

COMPOSITES AND NONMETALS

Overview

The National Symposium on Fracture Mechanics has evolved, since its beginnings in 1965, into an annual forum for the exchange of ideas related to the fracture of engineering materials. The Twenty-Third National Symposium carried on this tradition and was held in College Station,Texas, on 18–20 June 1991. The symposium was sponsored by ASTM Committee E24 on Fracture Testing, with the cooperation and support of the Department of Mechanical Engineering at Texas A&M University.

The diversity of interests and the wide range of problem areas in which fracture mechanics can play a role in ensuring structural integrity was reflected in the topic areas that were addressed in the 63 papers that were presented at the symposium. The symposium drew 110 attendees from 18 countries around the world, highlighting the strong international flavor that the National Symposium and ASTM's fracture-related activities have acquired over the years.

The efforts of the authors of the manuscripts submitted for publication and the diligence of the persons entrusted with the task of peer-reviewing these submittals have resulted in the compilation of papers that appear in this volume. These papers represent a broad overview of the current state of the art in fracture mechanics research and should serve as a timely recording of advances in basic understanding, as a compilation of the latest test procedures and results, as the basis of new insights and approaches that would be of value to designers and practitioners, and as a stimulus to future research.

The volume opens with the paper by Dr. John M. Barsom, who delivered the Second Annual Jerry L. Swedlow Memorial Lecture at this symposium. Barsom's presentation addressed the need for a better understanding of the basic issues involved in several different structural applications of fracture mechanics technology. As such, it serves as a road map for future directions and is a highly appropriate tribute to the memory of the individual who played a very important role in shaping the National Symposium into the forum that it is today.

Following the Swedlow Lecture are forty-five papers that have been broadly grouped into seven topical areas, based on the main theme of each paper. These groupings are, however, only intended as an aid to the reader, since no classification can ever be absolute. Topics of interest to a particular reader will therefore be found throughout this volume, and the reader is encouraged to consult the Index for the location of topics of specific interest.

The groupings that have been adopted are detailed next and are similar to the broad categories that were used to divide the presentations into coherent topical sessions at the symposium itself. The first group of nine papers addresses analytical and constraint-related issues in elastic-plastic fracture mechanics, with much of the emphasis being on topics related to transition range behavior. The next section of seven papers also deals with elastic-plastic fracture, but emphasizes applications. Following this are two sections that both address linear-elastic fracture mechanics, with a group of three papers emphasizing analytical aspects, and a group of four papers that are more applications oriented. Subcritical crack growth and nondestructive evaluation methods are the joint themes of the next group of eight papers. Following this are eleven papers addressing the fracture of composites and nonmetals, a topic area that is receiving increasing attention from the fracture community and which had significant representation at a National Symposium for the first time. Finally, a grouping of three papers dealing with probabilistic and dynamic issues closes out this volume.

In addition to the technical program, a highlight of the symposium was the presentation by Dr. George R. Irwin of the 1991 medal named in his honor to Dr. Hugo A. Ernst of the Georgia Institute of Technology, and the presentation by Dr. C. Michael Hudson, Chairman of Committee E24, of the 1991 Award of Merit and designation of Fellow of ASTM to Dr. Richard P. Gangloff of the University of Virginia.

The Symposium Organizing Committee consisting of Prof. T. L. Anderson, Prof. R. Chona, Dr. J. P. Gudas, Dr. W. S. Johnson, Jr., Prof. V. K. Kinra, Prof. J. D. Landes, Mr. J. G. Merkle, Prof. R. J. Sanford, and Mr. E. T. Wessel are pleased to have been a part of this very significant technical activity. The committee and the symposium chairman in particular would like to express their appreciation of the support received from the authors of the various papers presented at the symposium; of the thoroughness of the peer-reviewers who have played a major role in ensuring the technical quality and archival nature of the contents of this publication; of the efforts by various ASTM staff to help make the symposium and this volume a success, particularly Mr. P. J. Barr, Ms. L. Hanson, Ms. H. M. Hoersch, Ms. M. T. Pravitz, Ms. D. Savini, and Ms. N. Sharkey; and of the support, encouragement, and assistance extended by Prof. W. L. Bradley, Head of the Department of Mechanical Engineering at Texas A&M University. Finally, the symposium chairman would like to especially thank Ms. Katherine A. Bedford, Staff Assistant at Texas A&M University, for all her contributions during the planning of the symposium and the preparation of this volume.

Ravinder Chona

Department of Mechanical Engineering, Texas A&M University,College Station, Texas; symposium chairman and editor.

Jerry L. Swedlow Memorial Lecture

John M. Barsom[1]

Structural Problems in Search of Fracture Mechanics Solutions*

REFERENCE: Barsom, J. M., "**Structural Problems in Search of Fracture Mechanics Solutions,**" *Fracture Mechanics: Twenty-Third Symposium, ASTM STP 1189*, Ravinder Chona, Ed., American Society for Testing and Materials, Philadelphia, 1993, pp. 5–34.

ABSTRACT: This second Jerry L. Swedlow Memorial Lecture presents a few significant developments in fracture mechanics that occurred over the past 25 years and some unresolved problems relating to materials and design and to technology transfer and education. Examples of some accomplishments and problems needing solutions are presented in areas of fracture toughness, including elastic, elastic-plastic and short cracks, and of environmental effects.

Professor Jerry L. Swedlow was an educator and a researcher who devoted his career to the transfer of technology to his students and to scientists and engineers. Thus, the lecture appropriately concludes with a few observations, needs, and recommendations concerning technology transfer.

KEY WORDS: fracture mechanics, fatigue (materials)

It is an honor and a privilege to present the second Swedlow Memorial Lecture. Jerry was a colleague with whom I worked closely on several projects. He was a neighbor whose children and mine spent several years playing and growing up together. Above all, Jerry was a friend whom I think of frequently and I miss terribly. I thank the National Symposium Committee for inviting me to make this presentation.

Although Jerry Swedlow's publications were concentrated in the analytical aspect of fracture mechanics, his interests spanned all facets of the technology. He was very interested in applying fracture mechanics to practical problems and toiled hard as a professor and as chairman of the National Symposium on Fracture Mechanics to transfer the available knowledge to others. Jerry and others' contributions to the analytical aspects of fracture and some of the unresolved analytical problems have been presented by M. L. Williams [*1*] in the first Jerry L. Swedlow Memorial Lecture. This second lecture presents a few significant fracture mechanics developments that occurred over the past 25 years and some unresolved problems relating to materials and design and to technology transfer and education.

Materials and Design Considerations

The application of national and international specifications results in safe and reliable engineering structures. These specifications are continually being updated and should reflect the most current knowledge in a given field. Incorrect use and violation of the requirements of the specifications may result in failure of a component or an entire structure. Also, because specifications present minimum requirements, the need for additional requirements must be

[1] Senior consultant, Metallurgical Services, U.S. Steel, Pittsburgh, PA 15219-4776.

* Second Annual Jerry L. Swedlow Memorial Lecture.

investigated for new and improved designs, for use of new materials, for use of common materials in new and unique applications, and for any other nontraditional situation. Such an investigation should occur early in the design process, at which time the responsible engineer should obtain and incorporate the needed additional requirements.

Technical developments during the past 20 years resulted in significantly improved characterization of the behavior and performance of steel structures. These developments include understanding and prediction of the effects of temperature and rate of loading on fracture toughness, the fatigue crack initiation and propagation behavior of fabricated components under constant and variable amplitude loading, and corrosion fatigue crack initiation and propagation behavior of constructional steels in aqueous environments [*2*]. Some of these developments have been incorporated in specifications for bridges [*2,3*].

Although significant progress has occurred during the past 25 years, further technical accomplishments are needed to improve the safety, reliability, and economy of steel structures. Predictive models are needed to identify fatigue-crack initiation sites and unstable crack extension in weldments where large variations in mechanical properties and microstructure occur in neighboring small regions. Analytical and experimental procedures are needed to characterize the fatigue and fracture behavior of short cracks where traditional fracture mechanics analyses for deep cracks are not valid. Plant-life extension methodologies should be developed to predict the remaining life of plant components. Other problems exist for which solutions are needed and where fracture mechanics technology can contribute significantly. The following sections present some accomplishments and problems needing solutions in the areas of fracture toughness, including elastic, elastic-plastic, and short cracks and of environmental effects.

Linear Elastic Fracture-Toughness Characterization

Most constructional steels can fracture either in a ductile or in a brittle manner. The mode of fracture is governed by the temperature at fracture, the rate at which the load is applied, and the magnitude of the constraints that prevent plastic deformation. The effects of these parameters on the mode of fracture are reflected in the fracture-toughness behavior of the material. In general, the fracture toughness increases with increasing temperature, decreasing load rate and decreasing constraint. Furthermore there is no single unique fracture-toughness value for a given steel even at a fixed temperature and loading rate.

The increase of fracture toughness with temperature is shown in Fig. 1 for Charpy V-notch (CVN) specimens and in Fig. 2 for plane-strain critical stress intensity factor, K_{Ic}, specimens [*2,4*]. The data in Fig. 2 also show the shift of the fracture-toughness transition curve to higher temperature as the rate of loading increases.

From a failure analysis point of view, the fracture-toughness value for the material may be used to calculate the critical crack size at fracture under a given applied stress, or the magnitude of the stress at fracture for a given critical crack size. However, it is essential that the fracture-toughness value be determined at the fracture temperature and at the appropriate loading rate for the structural component of interest. A low dynamic fracture toughness [7 J for example, (5 ft·lbf)] at the fracture temperature does not necessarily mean that the steel did not possess adequate fracture toughness under slow loading conditions. Similarly, cleavage features at a short distance from the initiation site do not necessarily mean that the steel was brittle under slow loading conditions. Unfortunately, misunderstanding these simple and basic observations has resulted in erroneous analyses of fractures.

The Charpy V-notch impact specimen continues to be the most widely used specimen for characterizing the fracture-toughness behavior of steels. These specimens are routinely tested for many failures regardless of the relevance of the test results to the particular investigation.

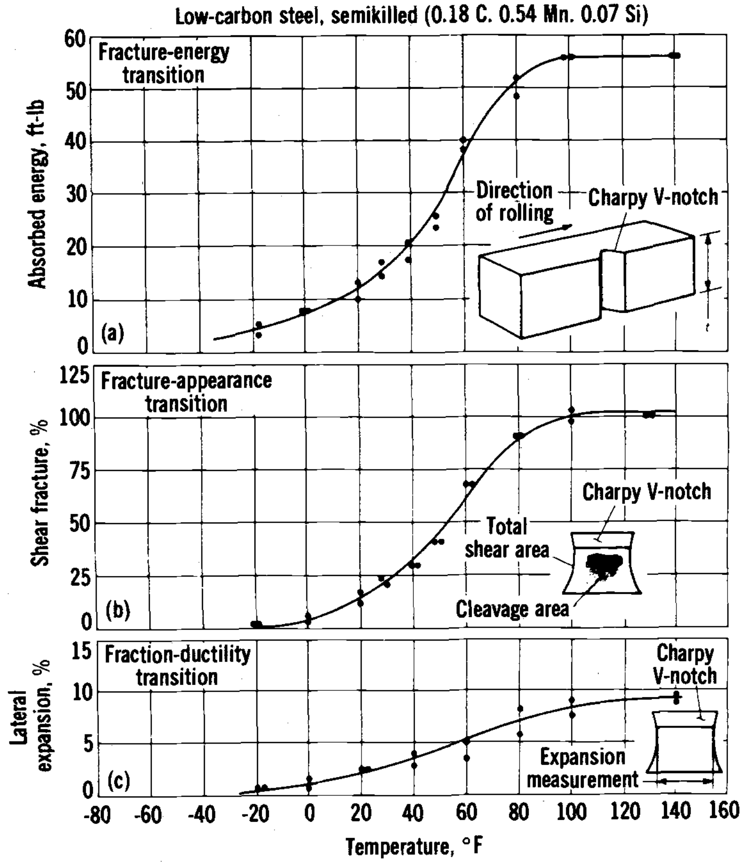

FIG. 1—*Charpy V-notch test results for a low-carbon steel.*

Furthermore, the steel is usually characterized as brittle and not having sufficient fracture toughness for its intended application if it exhibits Charpy V-notch values below about 20 J (15 ft·lbf) at the fracture temperature. The characterization is made without regard for the difference in loading rate between the test and the structure.

The static and dynamic (impact) fracture-toughness behavior for constructional steels can be understood by considering the fracture toughness transition curves, Fig. 3 [*2,4,5*]. The shift (that is, distance along the temperature axis) between the static and impact fracture-toughness transition curves depends on the yield strength of the steel, Fig. 4 [*2,4,5*]. Thus, the static and impact fracture-toughness transition curves are represented by a single curve for steels having yield strengths higher than about 897 MPa (130 ksi). On the other hand, the shift between these curves is about 71°C (160°F) for a 248 MPa (36 ksi) yield strength steel.

The fracture-toughness curve for either static or dynamic loading can be divided into three regions as shown in Fig. 3. In Regions I_s and I_d for the static and dynamic curves, respectively, the steel exhibits a low fracture-toughness value.

In Regions II_s and II_d, the fracture toughness to initiate unstable crack propagation under static and dynamic loading, respectively, increases with increasing temperature. In Regions III_s and III_d, the static and dynamic fracture toughness, respectively, reach a constant upper-shelf value.

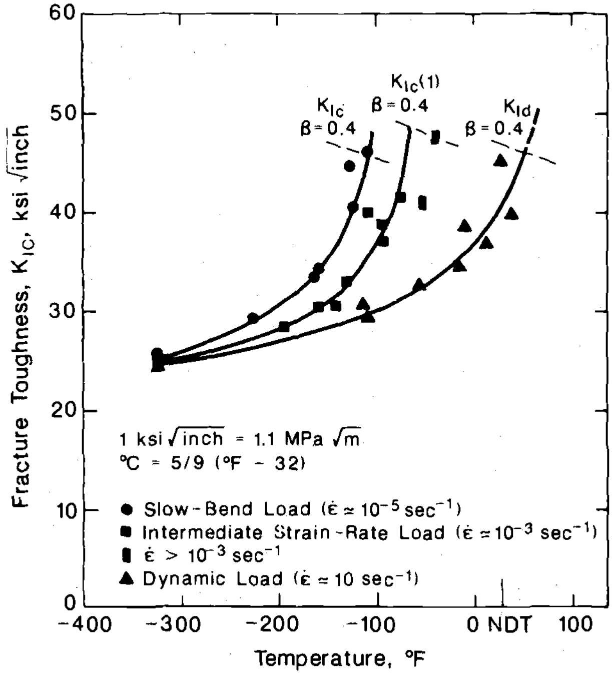

FIG. 2—*Effect of temperature and loading rate on plane-strain fracture toughness of an A36 steel plate.*

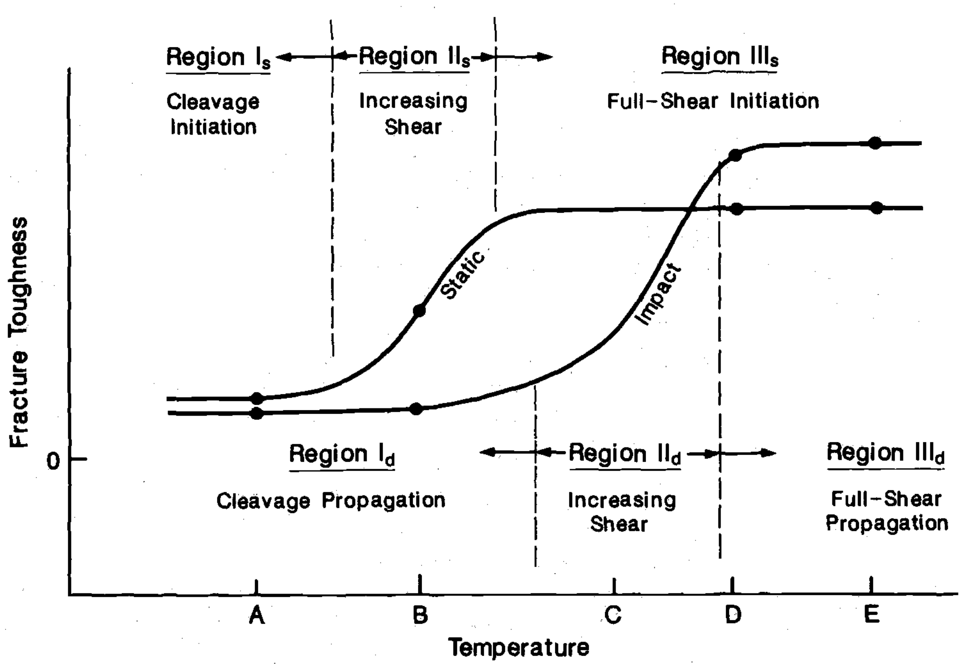

FIG. 3—*Fracture-toughness transition behavior of steels under static and impact loading.*

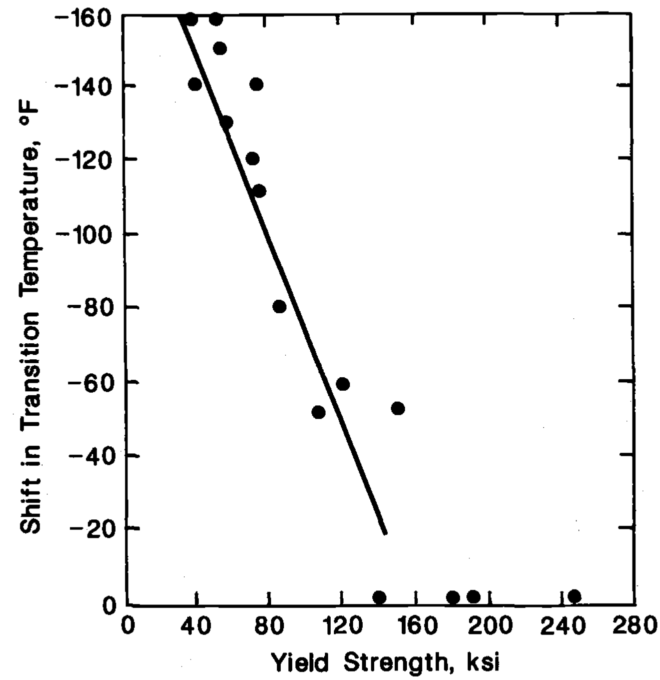

FIG. 4—*Effect of yield strength on shift in transition temperature between impact and static plane-strain fracture-toughness curves.*

In Region I_s, the static and the dynamic fracture-toughness values are essentially identical. Thus, the same low fracture-toughness values would be expected regardless of the loading rate used to fracture the specimens. In Regions II_s, the static fracture toughness increases to an upper-shelf value while the dynamic fracture toughness remains low. Therefore, the specimen may exhibit a high fracture-toughness value under static loading but a low fracture-toughness value under impact loading. Depending on the yield strength of the steel and the corresponding shift between the static and impact curve, this behavior may extend well into Region III_s. Within this temperature zone, the steel may have a high fracture-toughness value under static and intermediate loading rates yet exhibit a 7 J (5 ft·lbf) impact Charpy V-notch fracture-toughness value. Many constructional steels in actual engineering structures operate within this temperature zone. Consequently, a 7 J (5 ft·lbf) Charpy V-notch value at the fracture temperature does not necessarily mean that the steel did not possess sufficient fracture toughness for its use in a slowly loaded structure. This mistake has been made often in failure analyses despite the various documents that have been published on this subject.

In Region III_d, the static and dynamic fracture toughnesses are on the upper shelf. In this region, the mode of fracture is shear deformation that is governed by the yield strength and strain-hardening characteristics of the material. Because the dynamic yield strength for steels is about 172 MPa (25 ksi) higher than the static yield strength [*2*], the dynamic fracture toughness in Region III_d is higher than the static fracture toughness.

Fracture Surface Characteristics

Another error frequently made in failure analyses of steel components is caused by misinterpretation of the visual and fractographic observations on the fracture surface. Fractures of constructional steels usually exhibit flat cleavage surfaces in the crack-propagation zone. In many cases, this fracture surface feature is incorrectly assumed to reflect low fracture-toughness characteristics for the steel without regard for the crack-initiation behavior for the material, the temperature at the time of fracture, or the loading rate under which the fracture initiated.

The features of fracture surfaces for steels can be understood by reexamining the fracture-toughness transition behavior under static and impact loading, Fig. 3. The static fracture-toughness transition curve depicts the mode of crack initiation and the features of the fracture surface at the crack tip. The dynamic fracture-toughness transition curve depicts the mode of crack initiation under impact loading and the features of the crack propagation region under static or impact loading.

In Region I_s, for the static curve, Fig. 3, the crack initiates in a cleavage mode from the tip of the fatigue crack. Figure 5 is a scanning electron micrograph of an ABS-C steel specimen statically loaded to fracture in Region I_s.

In Region II_s, the fracture toughness to initiate unstable crack propagation increases with increasing temperature. This increase in crack-initiation toughness corresponds to an increase in the size of the plastic zone and in the zone of ductile tearing (shear) at the crack tip prior to unstable crack extension. In this region, the ductile-tearing zone is usually very small and dif-

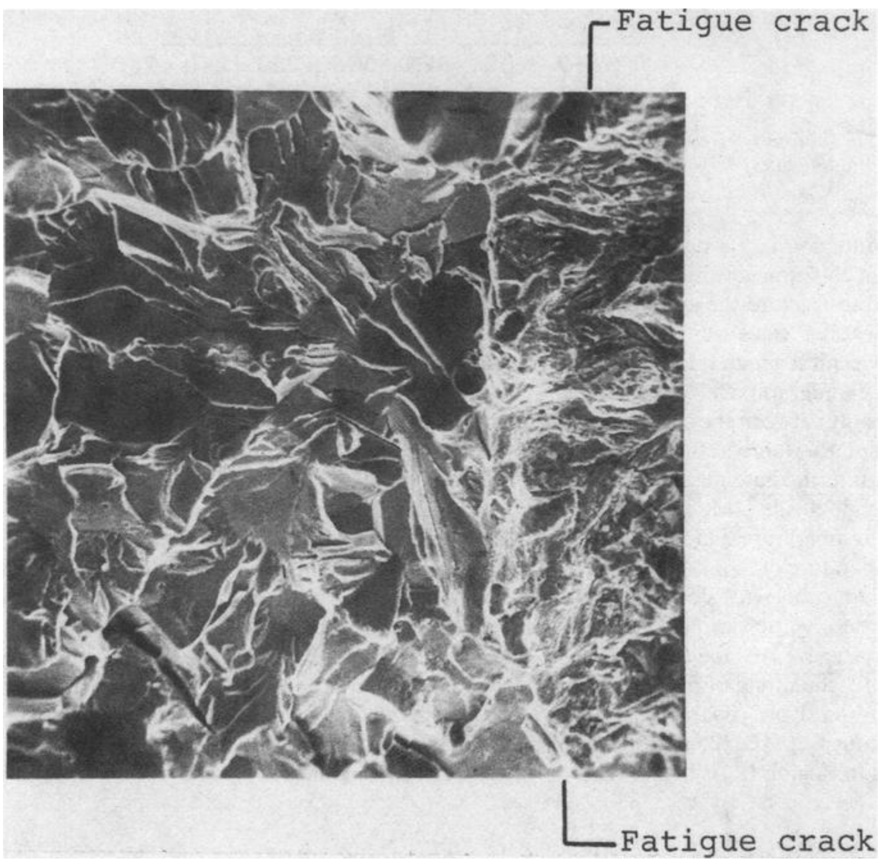

FIG. 5—*Scanning-electron micrograph of static fracture initiation Region I_s.*

ficult to delineate visually. In Region III_s, the static fracture toughness is quite high and somewhat difficult to define, but the fracture initiates by ductile tearing (shear).

Once a crack initiates under static load, the features (cleavage or shear) of the fracture surface for the propagating crack are determined by the dynamic behavior and degree of plane strain at the temperature. Regions I_d, II_d, and III_d in Fig. 3 correspond to cleavage, increasing ductile tearing (shear), and full-shear crack propagation, respectively. Thus, at Temperature A, the crack initiates and propagates in cleavage. At Temperatures B and C, the crack exhibits ductile initiation but propagates in cleavage at Temperature B and in a mixed mode (cleavage plus ductile dimples) at Temperature C. The only difference between the crack initiation behaviors at Temperatures B and C is the size of the ductile-tearing zone, which is larger at Temperature C than at Temperature B. At Temperature D, cracks initiate and propagate in full shear.

Figure 6 presents a light micrograph of a fracture profile and scanning electron micrographs of static fracture initiation and subsequent propagation for an ABS-C steel specimen tested at a temperature between Points B and C in Fig. 3. Figure 7 presents similar micrographs for an identical specimen of the same ABS-C steel plate tested dynamically at the same temperature as the one presented in Fig. 6. A comparison of Figs. 6*a* and 7*a* shows more plastic deformation in the vicinity of the fatigue crack front under static loading conditions than under dynamic loading. Figure 6*b* shows a region of ductile dimpling crack-initiation zone at the tip of the fatigue crack front followed by cleavage propagation. The metallographic features for the initiation and the propagation regions of this statically loaded specimen are shown at higher magnification in Figs. 6*c* and 6*d*, respectively. Figure 7*b* shows that the crack initiation and propagation for this dynamically fractured specimen were by cleavage. Thus, under identical test conditions, the ABS-C steel exhibited high fracture toughness and ductile crack initiation under static loading, but low fracture toughness and cleavage initiation under dynamic loading. However, both specimens exhibited cleavage crack propagation. These examples demonstrate that a cleavage crack initiation may occur either because the steel has low static fracture toughness at the fracture temperature or because the steel was subjected to dynamic loading. Moreover, cleavage crack propagation can occur even for a material having a high crack-initiation fracture toughness sufficient for a structure that is loaded slowly or at an intermediate loading rate.

Figure 8 [*2,4*] shows the fracture surfaces and fracture-toughness values (CVN and K_c) for an A572 Grade 50 steel. The specimen tested at −41.1°C (−42°F) exhibited a small amount of shear initiation at a temperature slightly below B in Fig. 3. The specimen tested at 3.33°C (38°F) exhibited increasing shear initiation (between B and C). The specimen tested at 22°C (72°F) exhibited full shear initiation (Temperature C) and, despite the high fracture toughness [67 J (49 ft·lbf) and 490 MPa $\sqrt{m}$ (445 ksi $\sqrt{in.}$)], still exhibited a large region of cleavage propagation. Thus, ductile crack propagation should only be expected at Temperature D, which is essentially dynamic upper-shelf, Charpy V-notch impact behavior.

Most constructional steels exhibit adequate initiation fracture toughness at the temperature and loading rates for common engineering structures. However, once this fracture-toughness level is exceeded, the crack may propagate unstably exhibiting a flat, cleavage, brittle fracture surface.

Elastic-Plastic Fracture Toughness

A thorough understanding of material and structural performance awaits further developments in elastic-plastic fracture mechanics. Despite the excellent progress that has occurred over the past several years [*6–9*], better understanding of testing, interpreting, and applying

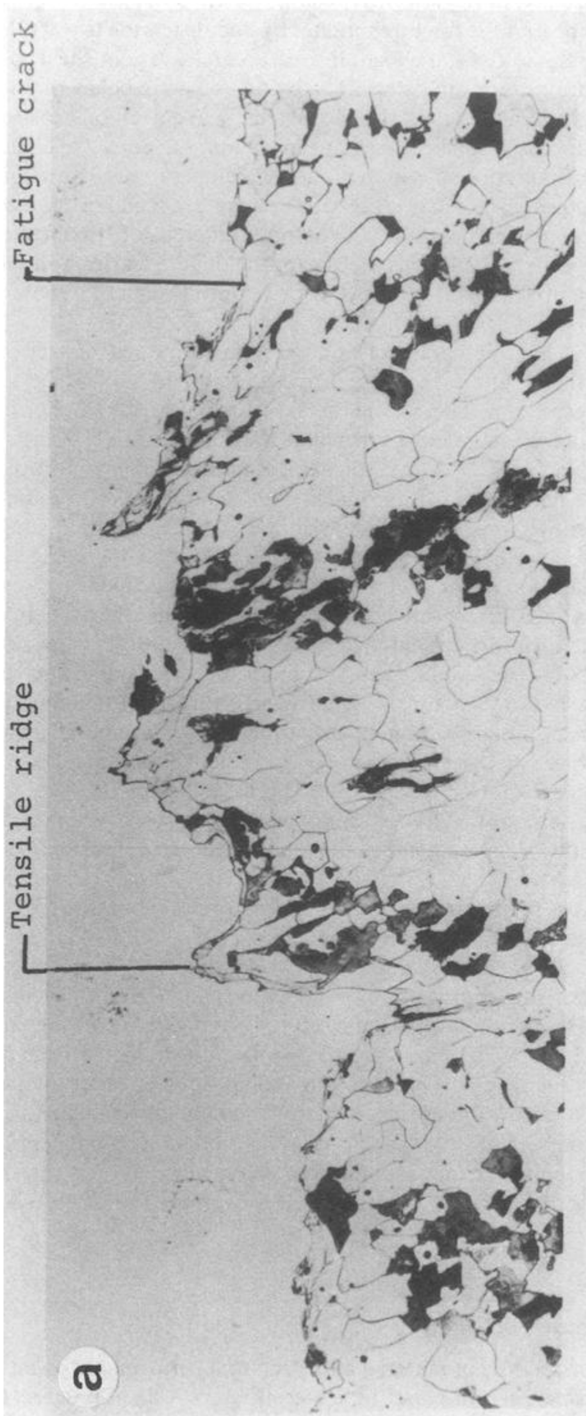

FIG. 6—*Light micrograph of fracture profile and scanning-electron micrographs of static fracture initiation in Region II. Fig. 6a*—×250.

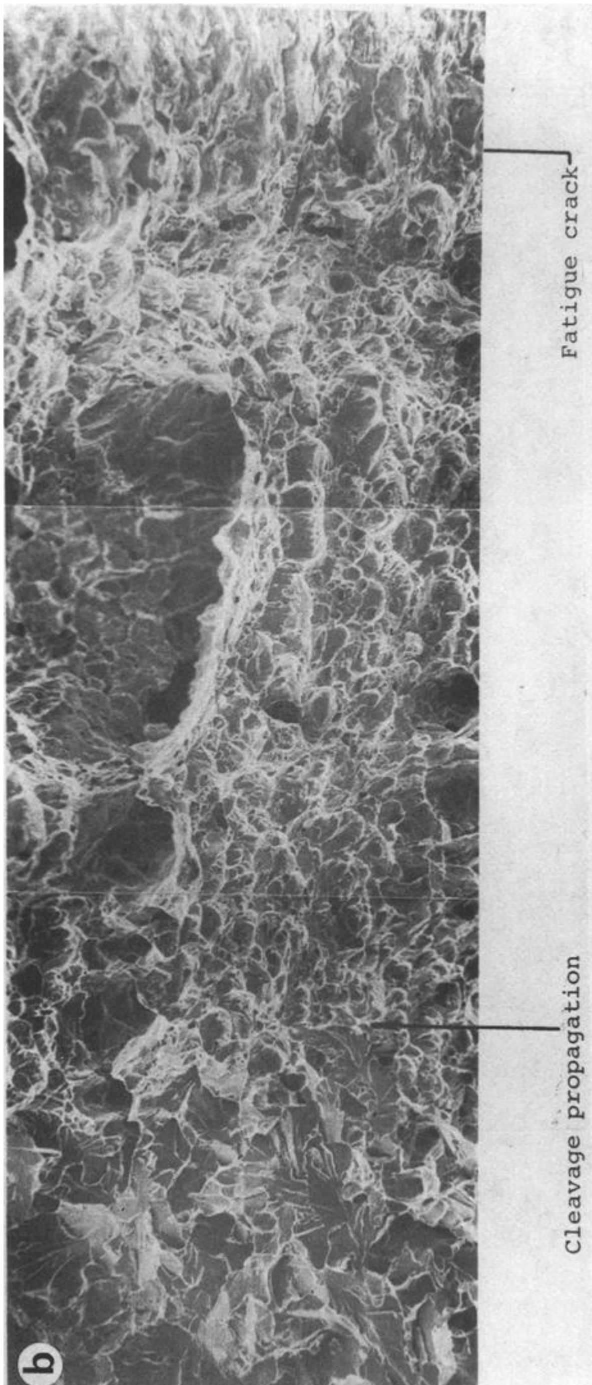
Fatigue crack
Cleavage propagation
b

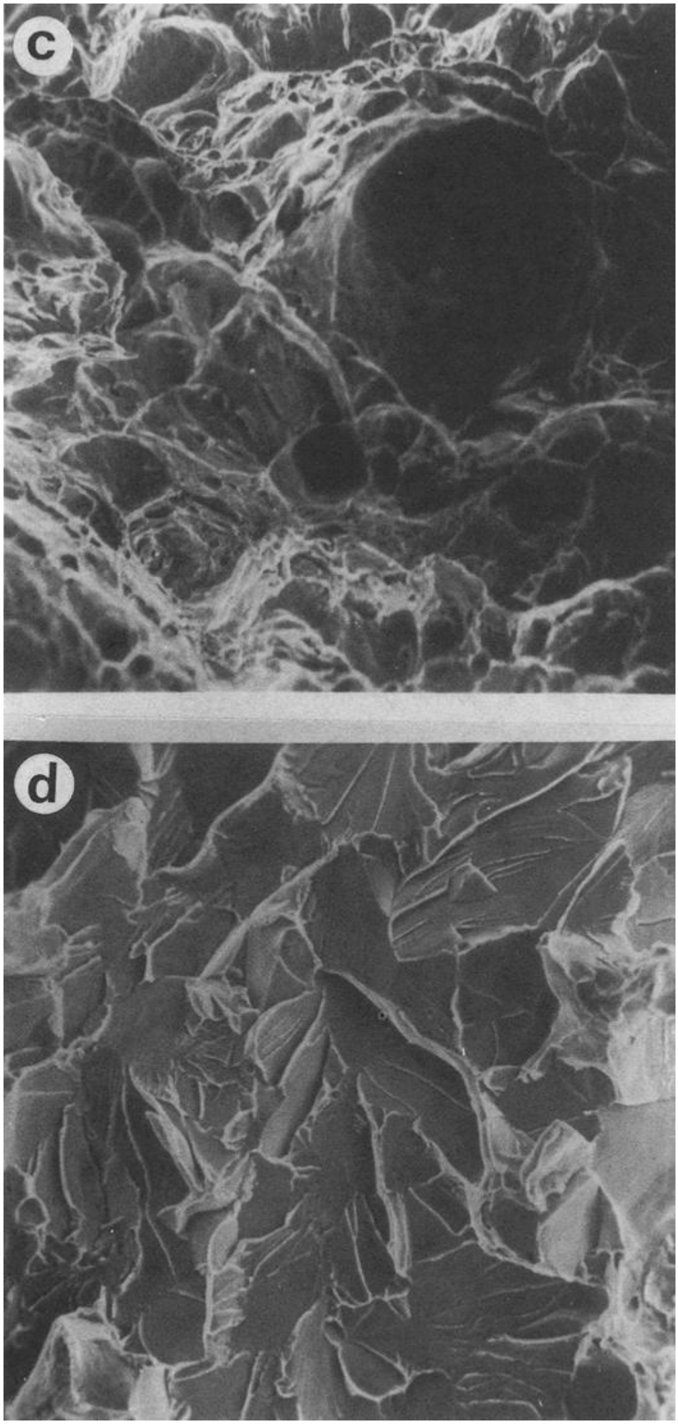

FIG. 6*c* and *d*—×*625.*

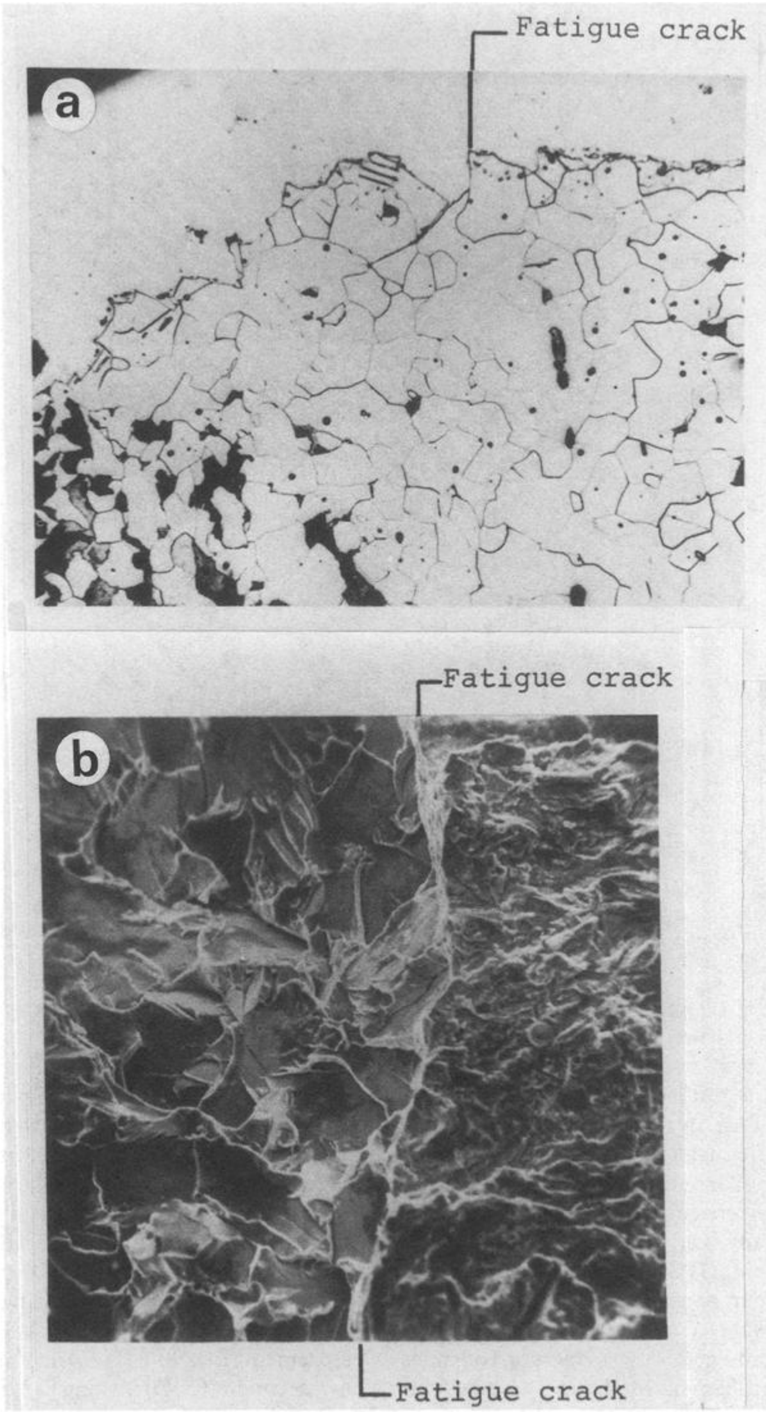

FIG. 7—*Light micrograph of fracture profile and scanning-electron micrographs of dynamic fracture initiation in Region* II_s (a) *×250 and* (b) *×625.*

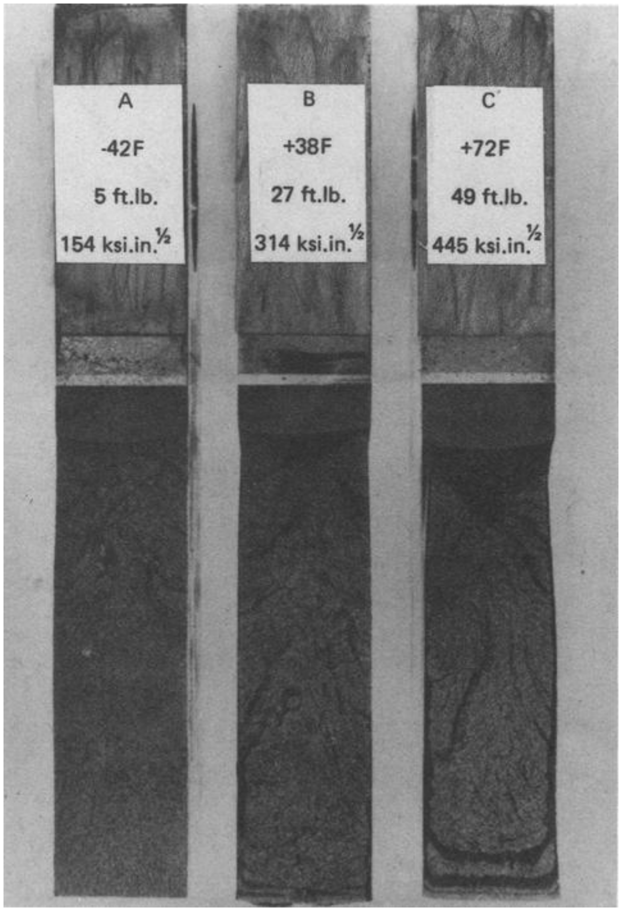

FIG. 8—*Fracture surfaces of 38 mm (1.5-in.)-thick compact-tension specimens of A572 Grade 50 steel.*

elastic-plastic fracture toughness is urgently needed. A few of the several areas that should be investigated are presented in the following discussion.

Most low- and medium-strength constructional steels have insufficient thickness to maintain plane strain conditions under slow and intermediate loading at normal service temperatures. Thus, for many structural applications, the linear-elastic analyses used to calculate K_{Ic} values are invalidated by the formation of a large plastic zone along the crack front prior to fracture. Consequently, test methods and fracture-toughness parameters have been developed to characterize the elastic-plastic and plastic fracture-toughness behavior of metals. The most commonly used elastic-plastic fracture-toughness parameters are the crack-tip opening displacement (CTOD) and the J-integral. The CTOD parameter is a measure of the critical displacement, or strain, at the tip of a crack. Standard test methods for determining the critical CTOD value at a fracture have been published in ASTM Test Method for Crack-Tip Opening Displacement (CTOD) Fracture Toughness Measurement (E 1290-89) [*10*] and in the British Standard BS5762 Method for Crack Opening Displacement (COD) Testing [*11*].

In general, the CTOD value for structural steels, like CVN test results, increases with increasing test temperature. Beyond a given test temperature, the rate of increase in CTOD values accelerates until the CTOD values reach a constant value resulting in an upper-shelf behavior similar to CVN test results. An example of this behavior is shown in Fig. 9 [*2,12*]. The significant increase in CTOD values with an increase in the amount of visually observable ductile (fibrous) stable-crack extension is seen prior to fracture. The behavior at temperatures corresponding to the CTOD upper-shelf is an indication of the ability of the material to exhibit ductile crack extension prior to fracture rather than the inherent resistance to crack initiation.

The CTOD fracture-toughness curve in Fig. 9 may be divided into four regions as shown schematically in Fig. 10 [*2,13*]. The four regions have been designated lower-shelf, lower-transition, upper-transition, and upper-shelf fracture-toughness behavior. The load-displacement records for each of these regions is shown in Fig. 11 [*12*].

The lower-shelf region is characterized by linear-elastic fracture mechanics where fracture toughness is represented by K_{Ic}. The plastic zone along the crack tip is extremely small and, visually, the fracture surface exhibits brittle cleavage features with no visible ductile fracture zone in the vicinity of the crack tip.

Visual observation of the fracture surface of specimens tested in the lower-transition region shows negligible, if any, ductile (fibrous) fracture zones at the crack tip. However, the plastic-zone size at the crack tip becomes larger than permitted by ASTM Test Method for Plane-Strain Toughness of Metallic Materials (E 399-83) for linear-elastic analyses to be applicable. This deviation from linearity is usually reflected in the load-displacement curve, Fig. 11. Finite-element analysis [*14*] shows that in this region a plastic hinge develops in a three-point

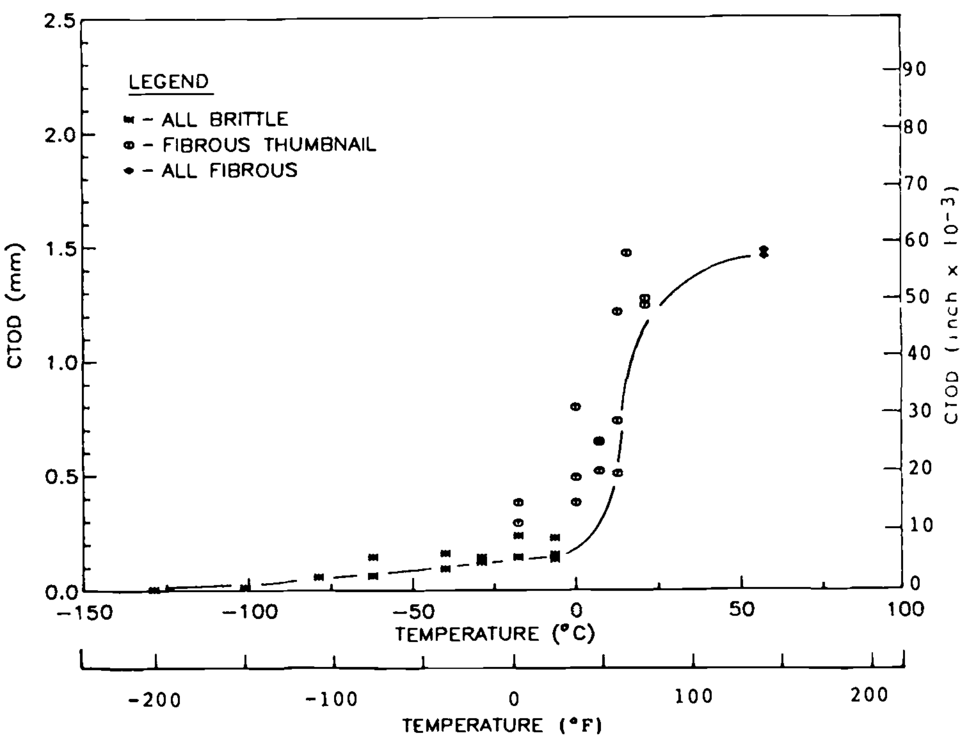

FIG. 9—*CTOD-temperature transition curve for an A36 steel plate.*

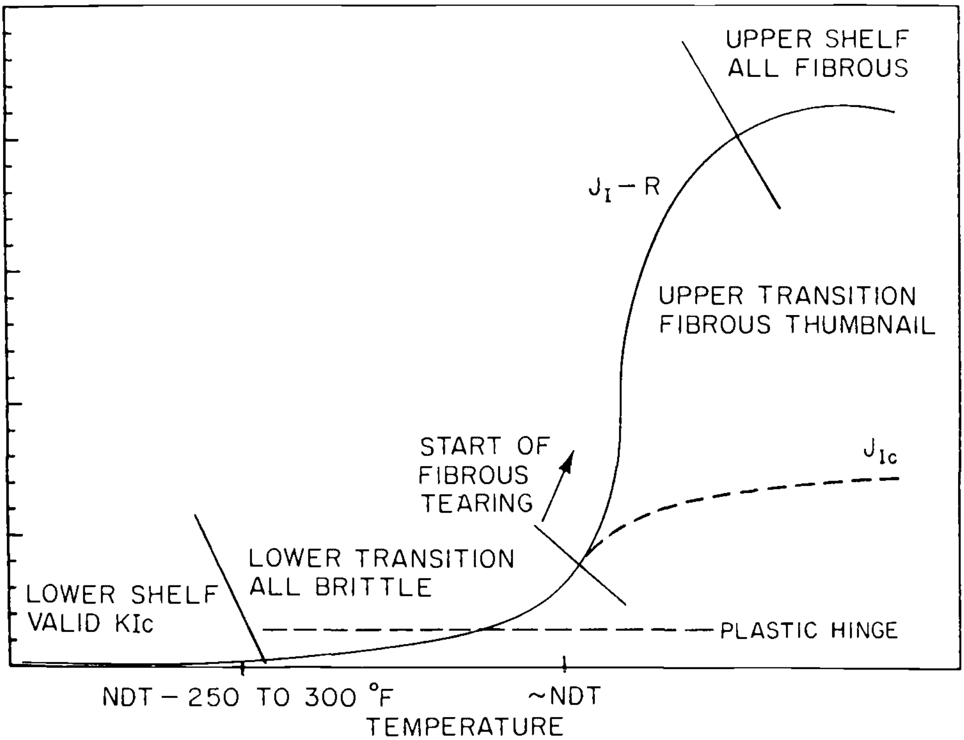

FIG. 10—*Schematic CTOD-temperature transition curve showing the four regions of behavior.*

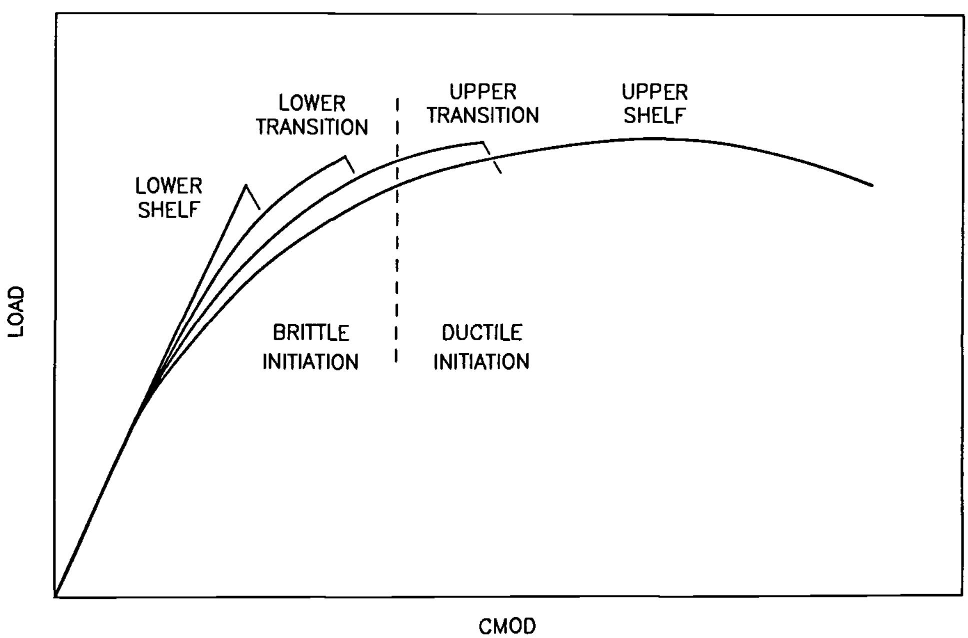

FIG. 11—*Load-displacement curves corresponding to the four regions of behavior.*

bend test specimen that demonstrates that the lower transition region is definitely a region of elastic-plastic fracture behavior. Consequently, elastic-plastic fracture-mechanics analysis is required to characterize the fracture-toughness behavior in this region.

The upper-transition region is characterized by ductile crack initiation followed by ductile stable-crack extension prior to unstable crack extension in a brittle manner. The ductile stable-crack extension is recognized by a fibrous "thumbnail" that is detectable by unaided visual observation of the fracture surface. The load-displacement curves exhibit significant plasticity (deviation from linearity) prior to unstable-crack extension, Fig. 11.

The upper-shelf region is characterized by ductile crack initiation and ductile crack propagation. The entire fracture surface is often fibrous, and the load-displacement record is a round-house curve, Fig. 11.

CTOD values measured at elevated test temperatures where the steel behaves plastically are at least an order of magnitude larger than the values measured at low temperatures. Thus, a CTOD-versus-temperature plot for a steel tested at low temperatures, where the crack propagates brittlely [CTOD $\leq$ 0.025 mm (1 mil)] and at elevated temperatures, where the crack propagates partially or fully in a ductile mode [CTOD $\geq$ 0.25 mm (10 mil)], masks the plane-strain K_{Ic} fracture-toughness transition behavior [CTOD $\leq$ 0.25 mm (1 mil)] discussed earlier. Consequently, a better understanding of the fracture toughness transition behavior for steels from low temperatures to high temperatures may be obtained by studying the change in the critical stress intensity factor at various temperatures. This study is presented in a later section.

Variability

Elastic-plastic fracture-toughness data in the temperature transition zone exhibit large scatter, Fig. 12 [*13*]. A systematic investigation and a thorough understanding of the cause of data scatter has been hindered by conveniently relegating the scatter to material inhomogeneities. Most materials including steels are not homogeneous or isotropic, and therefore, do contribute

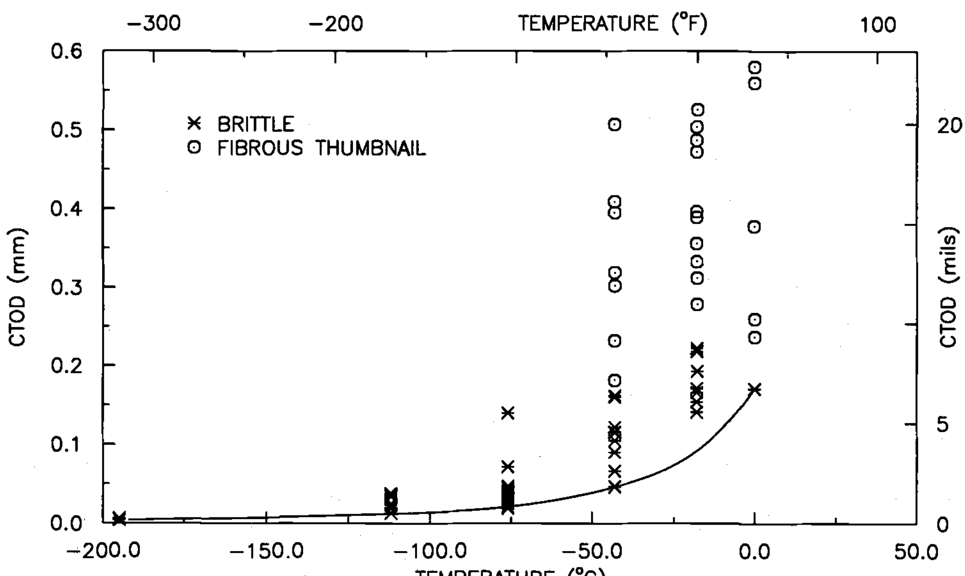

FIG. 12—*CTOD versus temperature test results for the rectangular A36 steel specimens.*

partially to the observed fracture-toughness data scatter. However, fracture-toughness test results even for a homogeneous isotropic steel would exhibit large data scatter in the transition zone. This behavior is inherent in the change in the microscopic fracture processes at the crack tip as a function of temperature. Thus, at very low temperatures, the crack initiates and propagates in cleavage and the steel exhibits low fracture toughness values with small data scatter. At very high temperatures, the crack initiates and propagates by ductile tearing and the steel exhibits high fracture toughness values with small data scatter. Thus, the transition zone is bound at the low temperature end by cleavage crack initiation and propagation and at the high temperature end by ductile crack initiation and propagation. In the hypothetical case, where the fracture toughness transition occurs in a very small temperature zone, half the specimen would exhibit cleavage crack initiation and propagation and the other half would exhibit ductile crack initiation and propagation. This hypothetical example suggests that a significant portion of data scatter in the transition zone may be caused by the unstable equilibrium characteristic of the crack-tip fracture mechanisms. The magnitude of variability is a function of the rate of change of the fracture mechanisms as a function of temperature with the narrower transition zones producing larger data scatter.

It has long been known that fracture toughness transition is influenced by the constraint at the crack tip. For example, plane stress, K_c, test results exhibit transitions at lower temperatures than K_{Ic} test results for the same material. Consequently, a better understanding of the causes of fracture toughness variability in the transition zone and the effects of constraint on variability may help explain the increased scatter in the elastic-plastic fracture-toughness values as the specimen size and crack size change, Fig. 13 [*13,14*].

Correlations of Various Fracture-Toughness Parameters—Several theoretical and empirical relationships have been developed to correlate various fracture-toughness parameters. The following are useful relationships that are available for analyzing material behavior and structural performance.

Relationships for K, J, *and CTOD* [2]—The equations used to estimate K from J are

$$K = \sqrt{JE} \text{ plane stress} \tag{1}$$

The equation used to estimate K from CTOD is

$$K = \sqrt{mE\sigma_{ys}\,\delta} \tag{2}$$

where m is a constant factor that varies from 1 to 2 depending on the degree of through-thickness constraint, that is, plane strain or plain stress.

Equations 1 and 2 indicate that J can be related to CTOD by the following relationship

$$J = M\sigma_{ys}\,\delta \tag{3}$$

Finite-element analysis [*15*] of three-point bend specimens having different sizes and from five materials indicated that J and CTOD are linearly related over the entire range of behavior from linear elasticity to the limit load. In addition, for the range of material and specimen sizes investigated, the finite-element analysis provided a consistent correlation of J with CTOD using the flow stress, σ_{flow}, instead of the yield stress and using $m = 1.6$ for the plane strain and $m = 1.2$ for plane stress. The flow stress is the algebraic average of the yield strength and the tensile strength of the material. However, the best correlation between J and CTOD for both plane-strain and plane-stress test results is given by the equation

$$J = 1.7\sigma_{flow}\,\delta \tag{4}$$

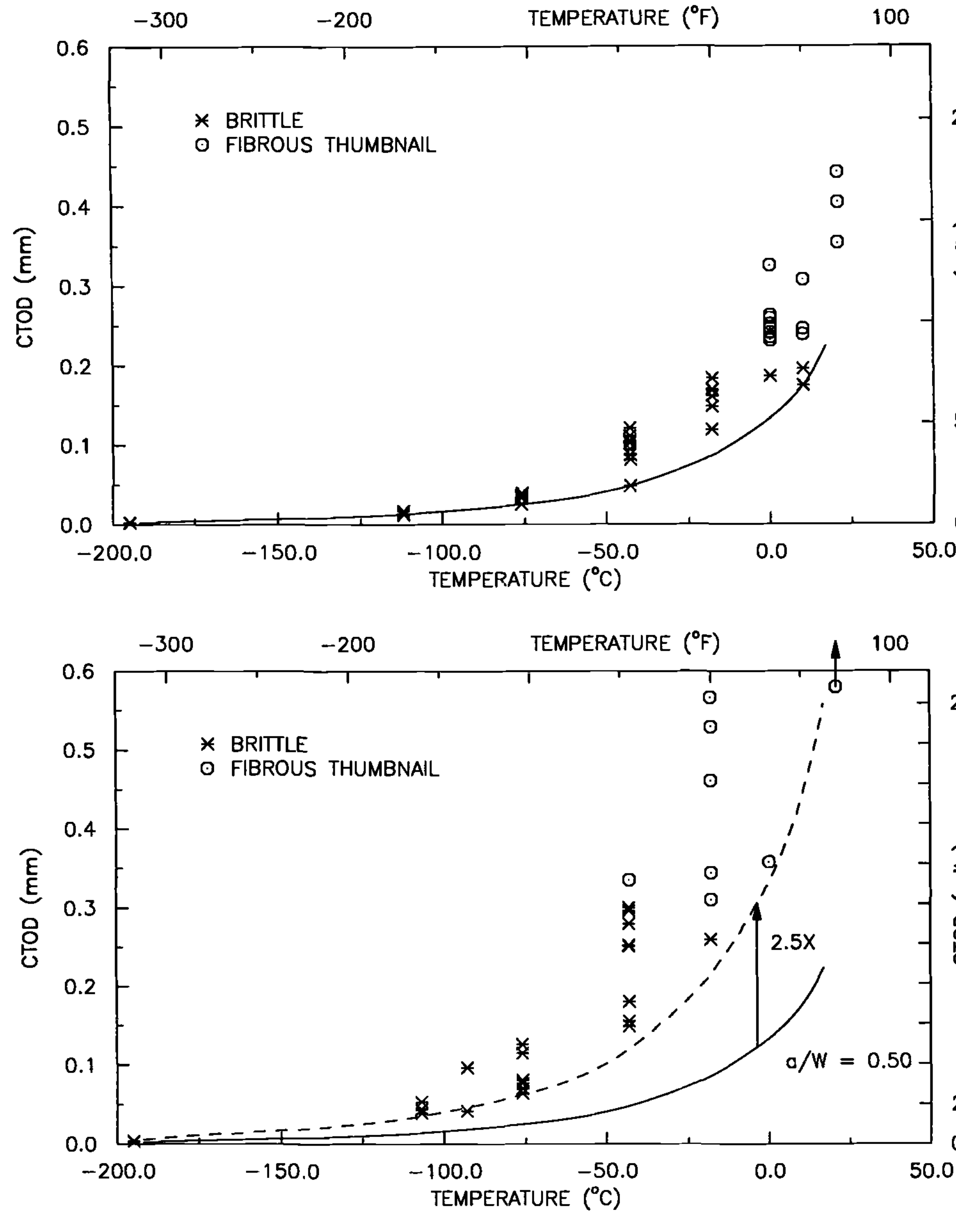

FIG. 13—*CTOD versus temperature test results for square A36 steel specimens.*

This equation is based on extensive data obtained by testing 13 steel grades having yield strengths of 228 to 924 MPa (33 to 134 ksi), Fig. 14 [*16*], and three-point bend specimens having different sizes and crack-length to specimen-width ratios, Fig. 15 [*15*].

Correlation of K_{Id}, K_{Ic}, *and Charpy V-Notch (CVN) Impact Energy Absorption*—The Charpy V-notch impact specimen is the most widely used specimen for material development, specifications, and quality control. Moreover, because the Charpy V-notch impact energy

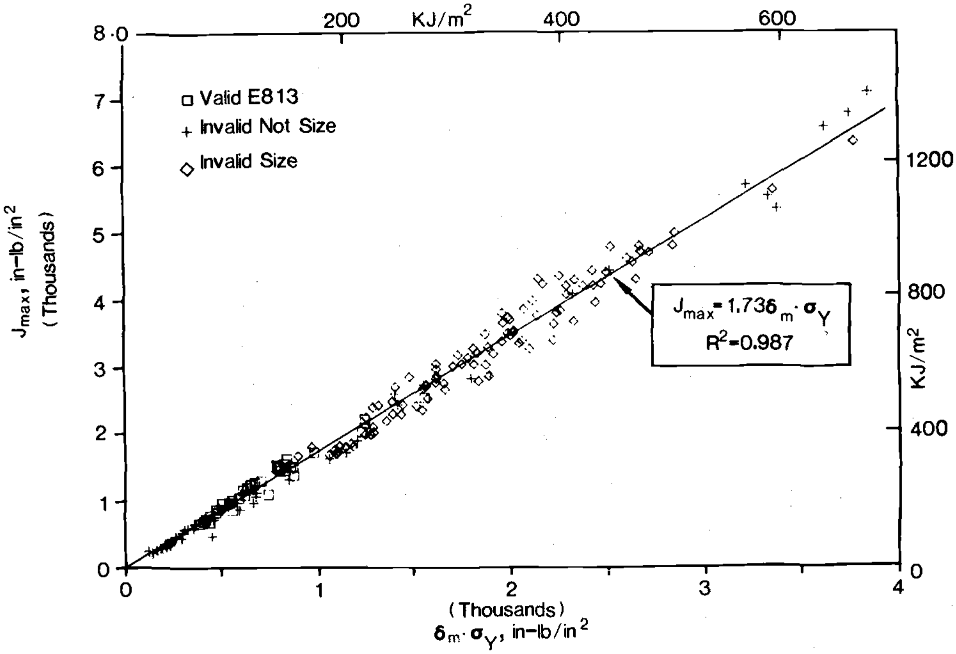

FIG. 14—*Correlation of* J*-integral determined at maximum load and CTOD at maximum load times the flow stress for 13 steels.*

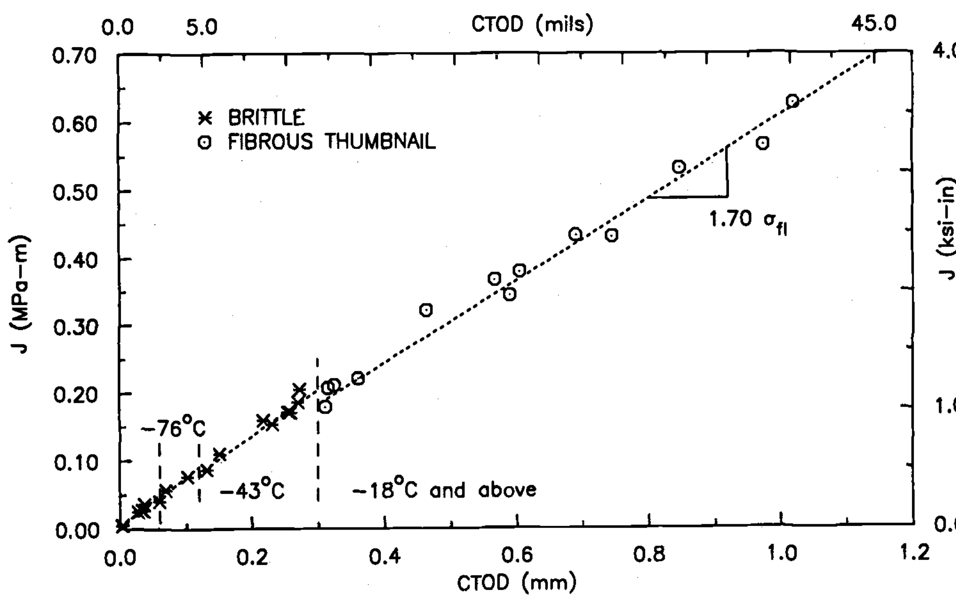

FIG. 15—*Correlation of* J*-integral and CTOD test results for different specimen geometries.*

absorption curve for constructional steels undergoes a transition in the same temperature zone as the impact plane-strain fracture toughness (K_{Id}), a correlation between these test results has been developed for the transition region and is given by the equation [2,4]

$$\frac{(K_{Id})^2}{E} = 5(\mathrm{CVN}) \tag{5}$$

where K_{Id} is in psi/in.$^{1/2}$, E is in psi, and CVN is in ft·lbf. The validity of this correlation is apparent from the data presented in Fig. 16 [4,17] for various grades of steel ranging in yield strength from about 248 (36) to about 966 (140) MPa (ksi) and in Fig. 17 [4,17] for eight heats of SA 533B, Class 1 steel. Consequently, a given value of CVN impact energy absorption corresponds to a given K_{Id} value (Eq 5), which in turn corresponds to a given toughness behavior at lower rates of loading. The behavior for rates of loading less than impact are established by shifting the K_{Id} value to lower temperatures by using the data presented in Fig. 4 that show that the shift between static and impact plane-strain fracture toughness curves is given by the relationship

$$T_{\text{shift}} = 215 - 1.5\sigma_{ys}$$

for

$$248 \text{ MPa (36 ksi)} < \sigma_{ys} \leq 130 \text{ ksi}$$

and

$$T_{\text{shift}} = 0$$

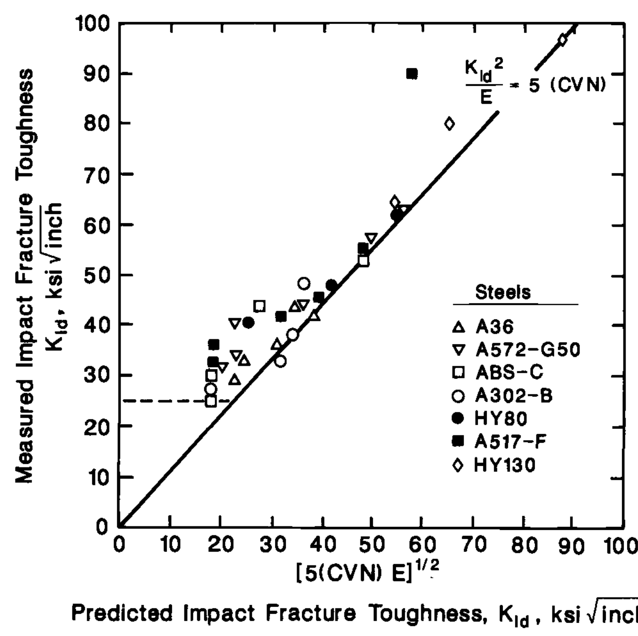

FIG. 16—*Correlation of plane-strain impact fracture toughness and impact Charpy V-notch energy absorption for various grades of steel.*

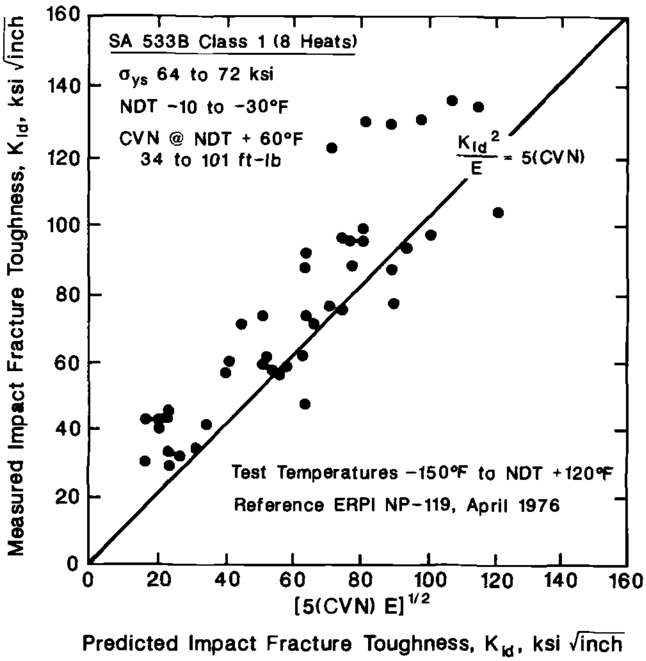

FIG. 17—*Correlation of plane-strain impact fracture toughness and impact Charpy V-notch energy absorption for eight heats of SA533B Class 1 steel.*

for

$$\sigma_{ys} > 896 \text{ MPa (130 ksi)}$$

where T is temperature in °F and σ_{ys} is room-temperature yield strength. The temperature shift between static and any intermediate or impact plane-strain fracture-toughness curves is given by [2]

$$T_{\text{shift}} = (150 - \sigma_{ys})\dot{\epsilon}^{0.17} \tag{6}$$

where

T = temperature, °F;
σ_{ys} = room temperature yield strength, ksi; and
$\dot{\epsilon}$ = strain rate, s^{-1}.

The strain rate is calculated for a point on the elastic-plastic boundary for the crack tip according to

$$\dot{\epsilon} = \frac{2\sigma_{ys}}{tE} \tag{7}$$

where t is the loading time and E is the elastic modulus for the material.

For a desired behavior at a minimum operating temperature and a maximum in-service rate of loading, the corresponding behavior under impact loading can be established by using Eq 6 and the equivalent Charpy V-notch impact value can be established by using Eq 5.

Barsom and Rolfe [2] suggested a relationship between K_{Ic} and upper-shelf Charpy V-notch impact energy absorption. This upper-shelf correlation was developed empirically for steels having room temperature yield strength, σ_{ys}, higher than about 759 MPa (110 ksi) and is given by the equation

$$\left(\frac{K_{Ic}}{\sigma_{ys}}\right)^2 = \frac{5}{\sigma_{ys}}\left(\text{CVN} - \frac{\sigma_{ys}}{20}\right) \tag{8}$$

where K_{Ic} is in ksi/in.$^{1/2}$, σ_{ys} is in ksi, and CVN is energy absorption in ft·lbf, for a Charpy V-notch impact specimen tested in the upper-shelf (100% shear fracture) region.

The K_{Ic} calculated by using the upper-shelf correlation with CVN appears to correspond closely to the maximum critical K-value for crack initiation prior to stable ductile crack extension. Thus, the upper-shelf correlation appears to define the critical stress intensity factor at the boundary between the lower transition and the upper transition behavior.

Fracture-Toughness Transitions—Elastic Through Plastic Behavior—Fracture toughness characterization by using CTOD masks the elastic plane-strain fracture-toughness transition for constructional steels, Fig. 9 [2,12]. This masking occurs because the CTOD value corresponding to the upper limit of plane-strain elastic fracture-toughness behavior is less than about 0.025 mm (1.0×10^{-3} in.), which is between 1 and 5% the CTOD value at the upper-shelf plastic behavior. One may overcome this masking first by recognizing the existence of and testing for the plane-strain fracture-toughness transition then by plotting the data on a scale that shows this behavior. The use of the critical stress intensity factor presents an interesting insight into the various fracture toughness transition regions for steels.

Figure 18 [2,12] presents the critical stress intensity factor for A36 steel throughout the fracture toughness behavior regions. This figure includes critical K-values calculated by using the J, CTOD, and CVN correlations that were presented in the preceding section.

Region S_I, Fig. 18, represents the plane-strain fracture-toughness transition under slow loading. For most steels, this transition occurs at very low temperatures, less than 43°C (110°F), where the yield strength decreases significantly with increasing temperature [2] and the fracture toughness increases by about 100% from a low value of 27.5 MPa $\sqrt{\text{m}}$ (25 ksi $\sqrt{\text{in.}}$) to over 55 MPa $\sqrt{\text{m}}$ (50 ksi $\sqrt{\text{in.}}$).

The increase in fracture toughness is characterized by an increase in the crack-tip strain at fracture manifested by an increase in the stretch zone, plastic zone, and a ductile dimpling zone at the crack tip. Once the crack initiates, it extends unstably in a brittle manner across the entire specimen cross section.

in Region S_{II}, Fig. 18, the crack initiates ductilely and the fracture occurs at essentially constant critical crack-tip strain. This critical strain may increase slowly as the test temperature increases depending on the rate of change of the yield strength and the strain hardening. In this region, the crack tip exhibits a negligible, if any, visible subcritical ductile crack extension and the stored energy at fracture is sufficient to propagate the initiated crack brittlely across the specimen. The fracture toughness in this region appears to correspond closely to the value obtained from J_{Ic}.

In Region S_{III}, the fracture toughness increases significantly principally due to increasing stable ductile crack extension with increasing test temperature. Thus, in this region, cracks initiate ductilely and exhibit increasing amounts of stable crack extension with increasing temperature. Also, this transition seems to occur in the same temperature zone as the impact Charpy V-notch fracture toughness transition that is also related to increasing amounts of ductile crack extension measured as percent fibrous fracture on the specimen fracture surface.

In Region S_{IV}, the crack initiates and propagates ductilely.

Short Cracks—Most engineering structures contain small stress raisers and crack-like imperfections that are either material related or fabrication induced. Various codes and stan-

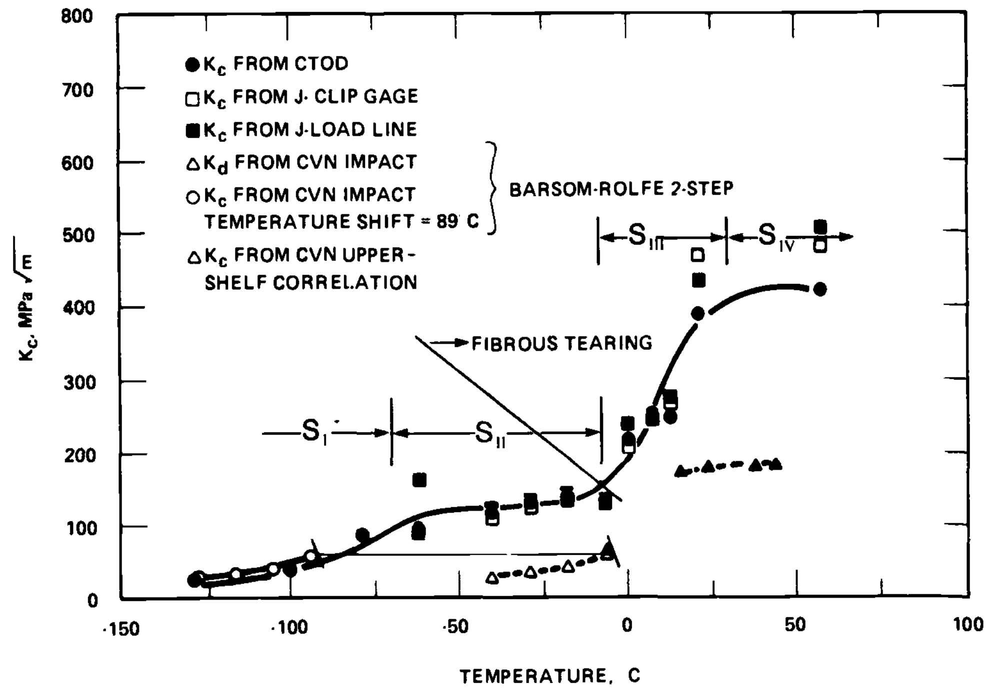

FIG. 18—K_c-*CVN-CTOD-J correlations for an A36 steel.*

dards impose limits on the size of allowable imperfections. Fracture mechanics analyses of these imperfections invariably assume them to be planner discontinuities whose fracture behavior is similar to large cracks. In most applications this assumption is unrealistically conservative and, based on the available data, technically unjustified. Thus, one of the most significant anticipated technical developments is understanding and characterizing the behavior of short cracks and the application of this knowledge to engineering structures.

The plastically deformed zone in the vicinity of a short crack is larger than for a deep crack when both cracks are subjected to identical, elastically calculated, stress intensity factors. Increased plastic deformation increases metal damage under fluctuating loads and increases the metal's resistance to fracture under static loads. Consequently, fatigue crack growth rates for short cracks differ from those for deep cracks subjected to the same, elastically calculated, stress intensity factor range. Similarly, the fracture toughness of short cracks is higher than for deep cracks at the same test temperature, Fig. 13*b*.

The data in Fig. 19 [*18*] show the increase in CTOD at a given temperature with decreasing a/W. The data correspond to the transition behavior between Regions S_{II} and S_{III} where an appreciable amount of plasticity occurs prior to fracture. These differences are the result of change in constraint and plastic deformation and would not occur in an ideal elastic brittle material. The available data suggest that the fracture toughness value is governed by yield strength, strain hardening, and inherent fracture toughness of the material and by the absolute value of the crack length and the specimen dimensions.

The data in Fig. 19 [*18*] indicate that the CTOD for the material tested increased by 2.5 times when a/W increased from 0.5 to 0.15. This increase is significant when analyzing the safety and reliability of actual structures with shallow cracks. Until recently, most investiga-

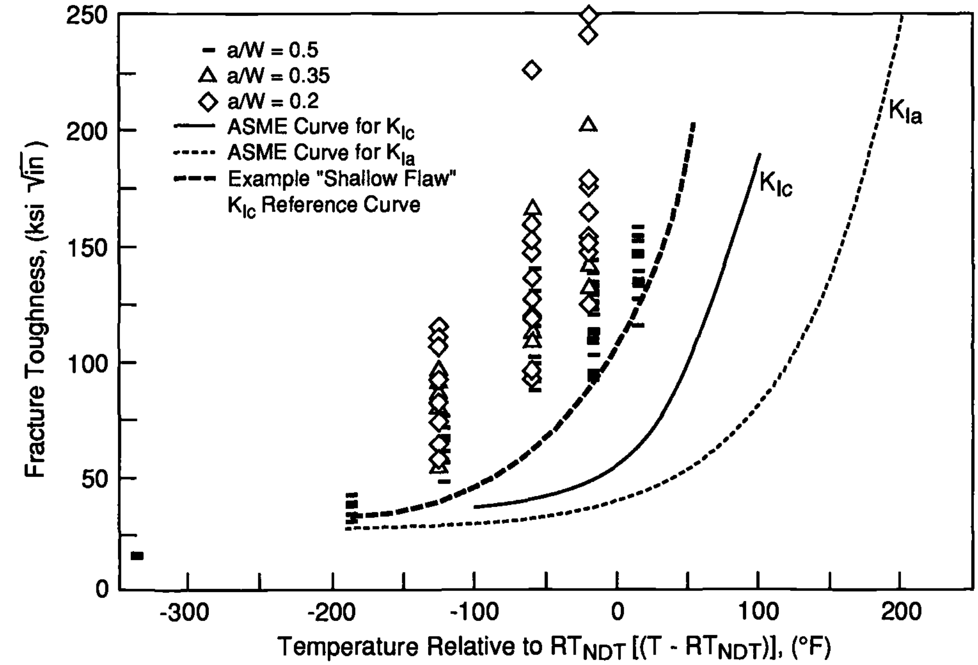

FIG. 19—*Comparison of A36 steel test results for specimens having different* a/W *ratios and the ASME Section XI reference curves.*

tions into the fracture behavior of shallow cracks concentrated on deriving the behavior of highly constrained deep cracks from the behavior of less-constrained shallow cracks. Fortunately, the recognition of the importance of predicting short crack behavior from deep crack data is increasing. Such information should lead to a better understanding of structural performance and failure analyses, and to safe and economical designs.

Analytical and experimental investigations [*12–15,19–25*] carried out over the past few years have increased our understanding of the behavior of short cracks. However, numerous investigations are needed to better characterize short cracks. Further analytical solutions are needed to relate the fracture behavior of short cracks to material properties and constraint. Also, simple standardized test methods should be developed to measure the fracture toughness that is characteristic of short cracks. The simple adoption or adaptation of present test methods for deep cracks may not be adequate to properly characterize short crack behavior. Finally, the application of this knowledge to material selection and to design and analysis of engineering structures and equipment is essential.

Environmental Effects

Research is urgently needed to increase fundamental knowledge of environmental effects on the behavior of steels under static loads and under constant- and variable-amplitude fluctuating loads. A primary objective of such an effort should be the prediction of the behavior of any material-environment system from basic properties and characteristics of the material and the environment, or from short-duration tests, or both.

Figure 20 [*2*] presents corrosion-fatigue crack-initiation data for four steels (A36, A588

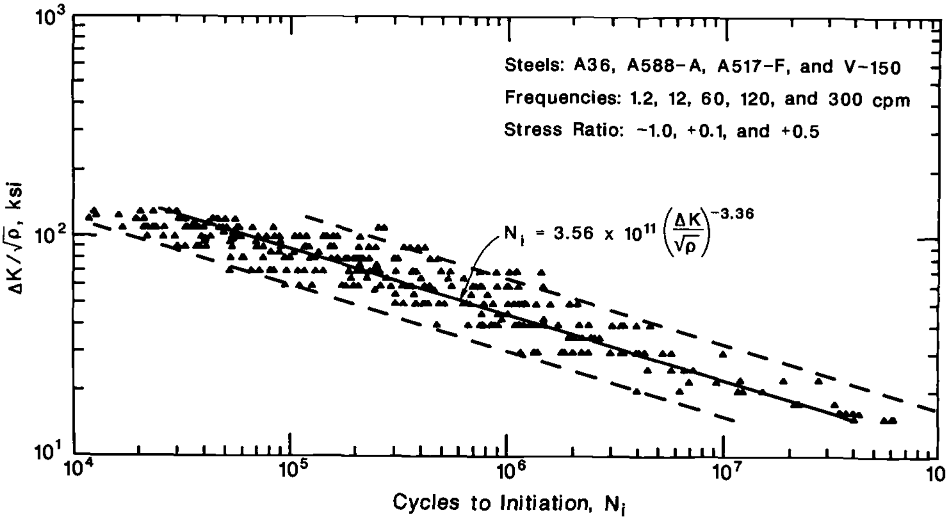

FIG. 20—*Summary of corrosion fatigue crack initiation behavior for various steels.*

Grade A, A517 Grade F, and V150) under full-immersion conditions in a room-temperature 3.5% solution of sodium chloride in distilled water. These steels represent large variations in chemical composition, thermo-mechanical processing, microstructure, and mechanical properties (tensile strength, yield strength, elongation, strain hardening, fracture toughness, etc.). The combined data encompass frequencies of 1.2 to 300 cycles per minute (cpm) and stress ratios from -1.0 to 0.5 and span four orders of magnitude in corrosion-fatigue crack-initiation life between about 10^4 and 10^8 cycles.

Considering the large variation in materials and test conditions, the data fall within a surprisingly narrow scatter band. The data show significant environmental effects well below the fatigue limits in air for steels tested. Also, the data indicate that a corrosion-fatigue crack-initiation limit does not exist for steels even in a mild aqueous environment. The data and the correlating equation presented in Fig. 20 are very important for equipment and structural design. However, the same data generate more questions than answers. For example, what is the corrosion-fatigue crack-initiation mechanism that is essentially independent of steel composition, microstructure, physical properties, cyclic frequency, and immersion time? What are the synergistic mechanisms that occur below the fatigue limit in air between cyclic stress fluctuation and the environment resulting in the initiation of corrosion-fatigue cracks even when the localized stresses are elastic? Finally, are the observations and conclusions derived from this set of data applicable to other material-environment systems? Answers to these and other questions can lead to better designs in various materials and environments and can save extensive time and money needed to generate corrosion-fatigue crack-initiation data, especially at low frequencies and stress fluctuations. Some of the test results in Fig. 20 required a machine dedicated for one year to obtain a single datum point at 120 cpm. Time and expense for low-frequency tests that better simulate actual structures are prohibitive.

Observations and conclusions derived from corrosion-fatigue crack-initiation test results cannot be extended to corrosion-fatigue crack-propagation behavior. Once a corrosion-fatigue crack initiates and becomes a propagating crack, whose plane is perpendicular to the applied stress, the significance of the various test parameters changes. For example, unlike corrosion-fatigue crack initiation, test frequency, Fig. 21 [*2,26*], stress ratio, Fig. 22 [*2,27*], and load path

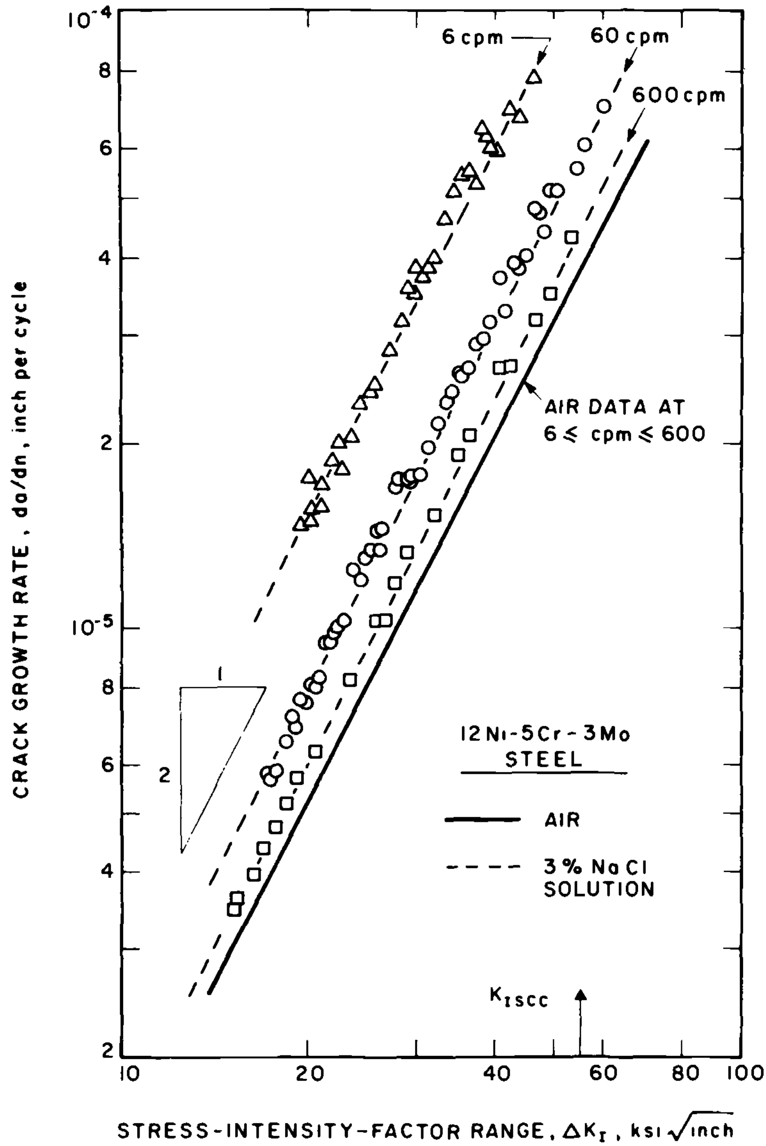

FIG. 21—*Corrosion fatigue crack growth data as a function of test frequency.*

in a cycle, Fig. 23 [*2,28*], can have significant influences on the corrosion–fatigue crack propagation behavior. Also, compressive stress fluctuations are as damaging as tensile stress fluctuations for corrosion-fatigue crack initiation where they have negligible effect on the rate of corrosion-fatigue crack propagation.

Corrosion-fatigue crack-propagation data show that the environment at the tip of the crack is different from the bulk environment, that the environmental damage does occur below the stress-corrosion-cracking threshold under static loading, and that this damage occurs only during transient deformation that increases the crack-tip opening. The data indicate the existence

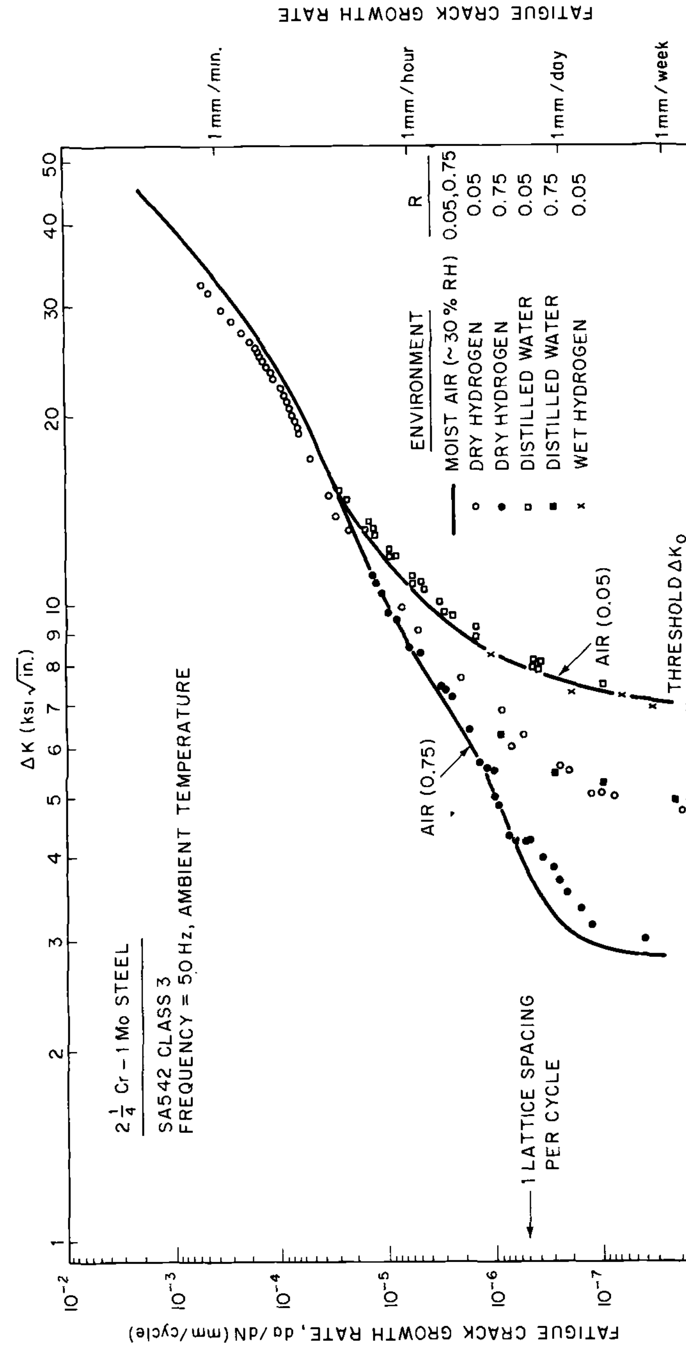

FIG. 22—Influence of environment on near-threshold fatigue crack growth in SA542 Class 3 steel.

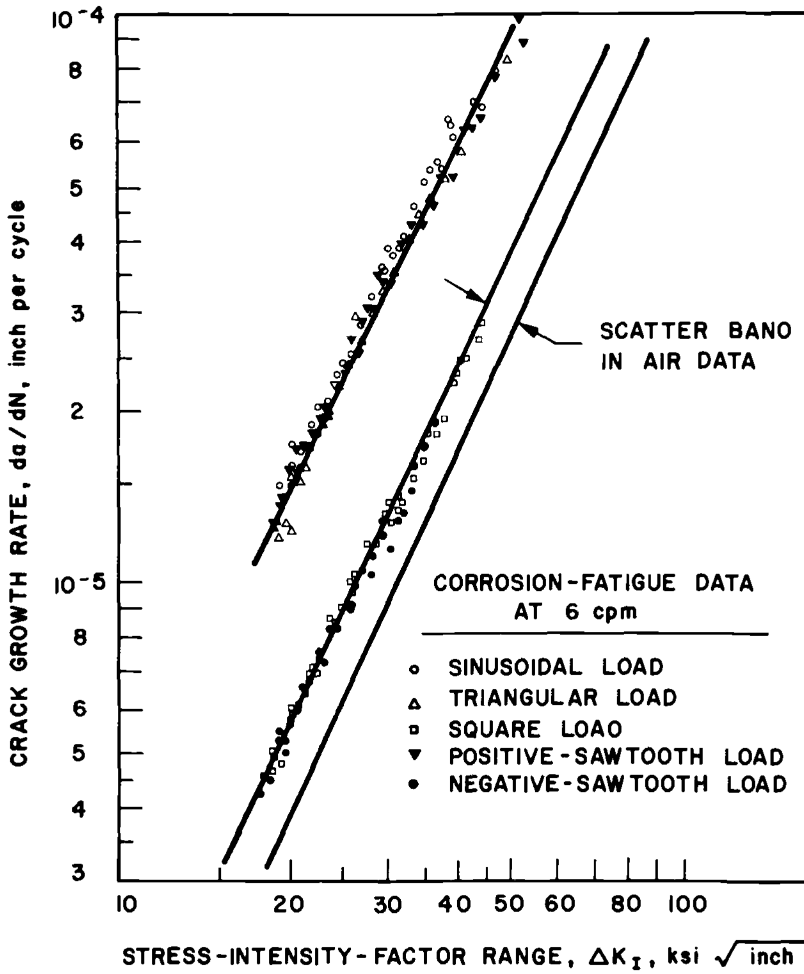

FIG. 23—*Corrosion fatigue crack growth rates in 12Ni-5Cr-3Mo steel in 3% solution of sodium chloride under various cyclic stress fluctuations with different stress-time profiles.*

of a cyclic frequency that is unique for the material-environment system at which the combined mechanical fatigue damage and the environmental damage are at a maximum. Corrosion-fatigue crack extension occurs less at frequencies above or below this unique cyclic frequency. Based on the available information, a schematic representation of the corrosion-fatigue crack-propagation behavior for steels subjected to different sinusoidal cyclic-load frequencies has been constructed, Fig. 24 [*2*]. This figure is an oversimplification of a very complex phenomenon.

At this point in time, there are no procedures or models available to predict a priori the corrosion-fatigue crack-propagation behavior of any material-environment system. The only available tool is to conduct tests on the material in the environment of interest under conditions that simulate the actual structure. Tests at low cyclic-load frequencies are difficult, time consuming, and very costly in the propagation region and are prohibitive for the threshold behavior. Fundamental understanding of the corrosion-fatigue mechanisms are urgently

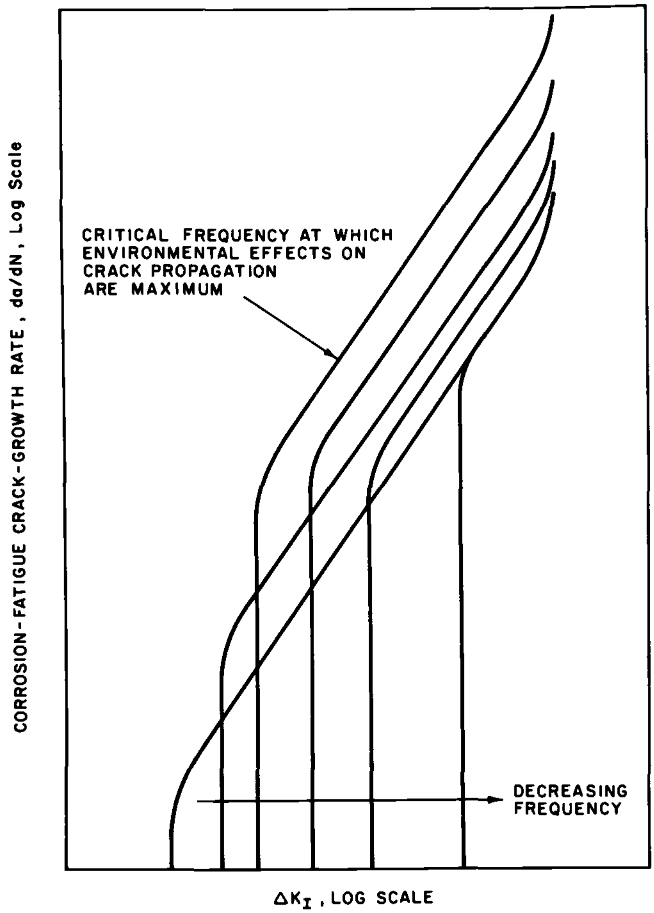

FIG. 24—*Schematic of idealized corrosion fatigue behavior as a function of cyclic load frequency.*

needed. Predictive models that are based on basic characteristics of the material and the environment are badly needed for various material-environment systems.

Technology Transfer and Education

Professor Jerry Swedlow was an educator and a researcher who devoted his career to the transfer of technology to his students and to scientists and engineers. Consequently, it is appropriate to end this presentation with a few comments concerning technology transfer.

Historically, safety, reliability, and economy of engineering structures have been accomplished by pursuing fundamental scientific and engineering knowledge and from extensive field experience. Although further improvements can be achieved by conducting research on specific topics, immediate improvements can be achieved by transferring existing knowledge to present and future scientists and engineers.

The transfer of fracture mechanics technology should occur in different environments and at various levels. The transfer is needed in classrooms, within the fracture mechanics community, and to other scientists and engineers. Each of these environments involves conditions and requirements that are unique. Despite the significant technological development during the past 25 years in understanding material behavior under complex loading conditions, a negligible number of institutions of higher learning have incorporated them into their curriculum and very few material scientists, engineers, and designers are aware of these developments.

There is an urgent need to transfer available technologies to present and future scientists and engineers. For the future generations in science and engineering, this technology transfer should be addressed in the classroom and formally incorporated in the curriculum. Given the over-crowded nature of the present four-year curriculum, this will require imaginative rethinking of the courses in mechanical behavior of materials and design of structural components and equipment.

Very few material scientists, engineers, and designers are aware of the available technical developments. Consequently, the need for additional requirements beyond the minimums dictated by the applicable codes may not be recognized by designers and practicing engineers. Material scientists rarely appreciate the design and fabrication requirements that materials must satisfy to be fit for their intended application.

Technology transfer among the material scientists and engineers and the design engineers suffers from lack of understanding of each other's capabilities and needs. At times, they appear to exist as distinct cultures who, for all practical purposes, have ceased to communicate. Technology transfer for current practitioners can be accomplished by conducting short courses and seminars and by publications aimed at the uninitiated rather than at peers. Technology transfer between scientists, engineers, and practitioners can be accomplished only by breaking the cultural barriers separating them and by a sincere desire to communicate and understand each other's technical strengths and needs.

References

[*1*] Williams, M. L., "Thick-Plate Fracture, Elasto-Plasticity, and Some Unresolved Problems," *Fracture Mechanics: Twenty-Second Symposium (Volume I), ASTM STP 1131,* H. A. Ernst, A. Saxena, and D. L. McDowell, Eds., American Society for Testing and Materials, Philadelphia, 1992, pp. 5–33.

[*2*] Barsom, J. M. and Rolfe, S. T., *Fracture and Fatigue Control in Structures—Applications of Fracture Mechanics,* 2nd ed., Prentice-Hall, Englewood Cliffs, NJ, 1987.

[*3*] *Standard Specifications for Highway Bridges,* American Association of State Highway and Transportation Officials, Washington, DC, 1989.

[*4*] Barsom, J. M., "Fracture Mechanics—Fatigue and Fracture," *Metals Handbook—Desk Edition,* H. E. Boyer and T. L. Gall, Eds., American Society of Metals, Metals Park, OH, 1984, pp. 32.2–32.8.

[*5*] Barsom, J. M., "Fracture," *Constructional Steel Design—An International Guide,* Elsevier Applied Science Publishers, Ltd., UK, to be published.

[*6*] *Elastic-Plastic Fracture: Second Symposium, Volumes I and II, ASTM STP 803,* C. F. Shih and J. P. Gudas, Eds., American Society for Testing and Materials, Philadelphia, 1983.

[*7*] *Elastic-Plastic Fracture Test Methods: The User's Experience, ASTM STP 856,* E. T. Wessel and F. J. Loss, Eds., American Society for Testing and Materials, Philadelphia, 1985.

[*8*] *Nonlinear Fracture Mechanics: Volumes I and II, ASTM STP 995,* J. D. Landes, A. Saxena, and J. G. Merkle, Eds., American Society for Testing and Materials, Philadelphia, 1989.

[*9*] *Elastic-Plastic Fracture Test Methods: The User's Experience, ASTM STP 1114,* J. A. Joyce, Ed., American Society for Testing and Materials, Philadelphia, 1991.

[*10*] *Annual Book of ASTM Standards,* Volume 3.01, American Society for Testing and Materials, Philadelphia, 1989.

[*11*] Methods for Crack Opening Displacement (COD) Testing, BS5762: 1979, British Standards Institute, London, 1979.

[*12*] Wellman, G. W. and Rolfe, S. T., "Engineering Aspects of CTOD Fracture Toughness Testing," *Welding Research Council Bulletin,* No. 299, Welding Research Council, New York, Nov. 1984.

[*13*] Sorem, W. A., Dodds, R. H., and Rolfe, S. T., "An Analytical and Experimental Comparison of Rectangular and Square Crack-Tip Opening Displacement Specimens of an A36 Steel," *Nonlinear Fracture Mechanics: Volume II: Elastic-Plastic Fracture, ASTM STP 995,* J. D. Landes, A. Saxena,

and J. G. Merkle, Eds., American Society for Testing and Materials, Philadelphia, 1989, pp. 470–494.

[14] Sorem, W. A., Dodds, R. H., and Rolfe, S. T., "An Analytical Comparison of Short Crack and Deep Crack CTOD Fracture Specimens of an A36 Steel," *Fracture Mechanics: 21st Symposium, ASTM STP 1074*, J. P. Gudas, J. A. Joyce, and E. Hackett, Eds., American Society for Testing and Materials, Philadelphia, 1990, pp. 3–23.

[15] Sorem, W. A., Dodds, R. H., and Rolfe, S. T., "An Analytical and Experimental Comparison of the J-Integral and CTOD Fracture Parameters for Short Crack Specimens," *Welding Research Council Bulletin*, No. 351, Welding Research Council, New York, March 1990.

[16] Wilson, A. D. and Donald, K., "Evaluating Steel Toughness Using Various Elastic-Plastic Fracture Toughness Parameters," *Nonlinear Fracture Mechanics: Volume II: Elastic-Plastic Fracture, ASTM STP 995*, J. D. Landes, A. Saxena, and J. G. Merkle, Eds., American Society for Testing and Materials, Philadelphia, 1989, pp. 144–168.

[17] Barsom, J. M., "Material Considerations in Structural Steel Design," *Engineering Journal*, Vol. 24, No. 3, American Institute of Steel Construction, Chicago, 1987.

[18] Rolfe, S. T., Whorley, R., and Holcomb, R., "PVRC Progress Report," Pressure Vessel Research Council, New York, 4 June 1991.

[19] Merkle, J. G., "An Approximate Method of Elastic-Plastic Fracture Analysis for Nozzle Corner Cracks," *Elastic-Plastic Fracture, ASTM STP 668*, J. D. Landes, J. A. Begley, and G. A. Clarke, Eds., American Society for Testing and Materials, Philadelphia, 1979, pp. 674–702.

[20] Merkle, J. H., "An Examination of the Size Effects and Data Scatter Observed in Small-Specimen Cleavage Fracture Toughness Testing," U.S. Nuclear Regulatory Commission, NU-REG/CR-3672, Oak Ridge, TN, 1984.

[21] Dodds, R. H., Anderson, T. L., and Kirk, M. T., "A Framework to Correlate a/W Ratio Effects on Elastic-Plastic Fracture Toughness (J_c)," *International Journal of Fracture*, Vol. 48, 1991.

[22] Kirk, M. T., Koppenhoefer, K. C., and Shih, C. F., "Effect of Constraint on Specimen Dimensions Needed to Obtain Structurally Relevant Toughness Measures," presented at the ASTM Symposium on Constraint Effects in Fracture, Indianapolis, 8 and 9 May 1991, to be published.

[23] Parks, D. M., "Engineering Methodologies for Assessing Crack Front Constraint," *Proceedings*, Spring Meeting, Society of Experimental Mechanics, Milwaukee, 10 and 11 June 1991, to be published.

[24] Theiss, T. J. and Bryson, J. W., "Influence of Crack Depth on Reactor Pressure Vessel Steel," presented at the ASTM Symposium on Constraint Effects in Fracture, Indianapolis, 8 and 9 May 1991, to be published.

[25] "An International Project to Develop Shallow Crack Fracture Mechanics Tests," EWI Project J6098/TWI Project 5574, Edison Welding Institute, Columbus, OH, and The Welding Institute, Abington, UK, 1992.

[26] Barsom, J. M., "Corrosion-Fatigue Crack Propagation Below K_{Iscc}," *Journal of Engineering Fracture Mechanics*, Vol. 3, No. 1, July 1971.

[27] Suresh, S. and Ritchie, R. O., "Closure Mechanisms for the Influence of Load Ratio on Fatigue Crack Propagation in Steels," Materials Science Division, U.S. Department of Energy, Report Contract No. DE-AC03-76SF00098, Washington, DC, April 1982.

[28] Barsom, J. M., "Effect of Cyclic-Stress Form on Corrosion-Fatigue Crack Propagation Below K_{Iscc} in a High-Yield-Strength Steel," *Corrosion Fatigue: Chemistry, Mechanics, and Microstructure*, International Corrosion Conference Series, Vol. NACE-2, National Association of Corrosion Engineers, Houston, 1972.

Elastic-Plastic Fracture Mechanics—Analyses and Constraint Issues

David K. M. Shum[1] *and John G. Merkle*[1]

Crack Initiation Under Generalized Plane-Strain Conditions

REFERENCE: Shum, D. K. M. and Merkle, J. G., "**Crack Initiation Under Generalized Plane-Strain Conditions,**" *Fracture Mechanics: Twenty-Third Symposium, ASTM STP 1189,* Ravinder Chona, Ed., American Society for Testing and Materials, Philadelphia, 1993, pp. 37–54.

ABSTRACT: A method for estimating the decrease in crack-initiation toughness, from a reference plane-strain value, due to positive straining along the crack front of a circumferential flaw in a reactor pressure vessel, is presented in this study. This method relates crack initiation under generalized plane-strain conditions with material failure at points within a distance of a few crack-tip-opening displacements ahead of a crack front, and involves the formulation of a micromechanical crack-initiation model. While this study is intended to address concerns regarding the effects of positive out-of-plane straining on ductile crack initiation, the approach adopted in this work can be extended in a straightforward fashion to examine conditions of macroscopic cleavage crack initiation. Provided single-parameter dominance of near-tip fields exists in the flawed structure, results from this study could be used to examine the appropriateness of applying plane-strain fracture toughness to the evaluation of circumferential flaws, in particular to those in ring-forged vessels that have no longitudinal welds. In addition, results from this study could also be applied toward the analysis of the effects of thermal streaming on the fracture resistance of circumferentially oriented flaws in a pressure vessel.

KEY WORDS: crack-initiation toughness, generalized plane strain, fracture toughness, micromechanics, slip-line theory, reactor pressure vessel, ring-forged vessels, thermal streaming, circumferential flaw, fracture mechanics, fatigue (materials)

For U.S. pressurized-water reactor (PWRs), use of plane-strain fracture toughness data to evaluate the potential for initiation of longitudinal flaws in the reactor pressure vessel (RPV) is appropriate when the RPV is subject to loading situations in which the total axial strain is close to zero. However, this approach may not be appropriate for circumferential flaws. In the case of a circumferential crack, the strain parallel to the crack front produced by the pressure-induced hoop stress is positive (Fig. 1). It is well-known from small-specimen testing that a loss of plane-strain constraint results in a ligament contraction along the crack front and an associated increase in resistance to crack initiation [*1,2*]. For some structural materials, the elevated toughness can be on the order of two to five times the plane-strain value. Because a negative strain parallel to the crack front has been demonstrated to be associated with a greater resistance to crack initiation, it is reasonable to suppose that a positive strain parallel to the crack front may be associated with an enhanced tendency toward crack initiation.

The point to be made is that transverse strain is not necessarily a cause of toughness deviation from a reference plane strain value. Rather, available experimental data suggest the possibility of correlating the magnitude of the crack-initiation toughness with the magnitude of the transverse strain. Issues thus arise relative to the application of plane-strain fracture toughness to the evaluation of circumferential flaws, particularly to those in ring-forged vessels that

[1] Research specialists, Oak Ridge National Laboratory, Oak Ridge, TN 37831.

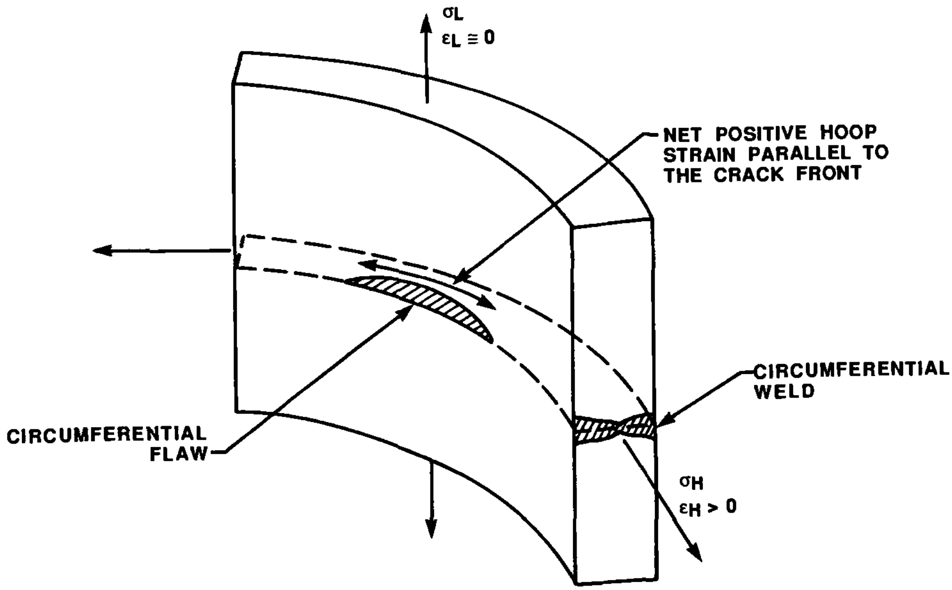

FIG. 1—*Configuration of circumferential flaw in weld of ring-forged reactor vessel showing positive tensile hoop strains parallel to the crack front.*

have no longitudinal welds [*3*]. The need for early resolution of these issues is accentuated by the fact that four out of five reactor vessels that currently violate the minimum Charpy upper-shelf requirement given in Ref *4* are of ring-forged construction [*5*].

Current fracture analysis methods do not provide a straightforward procedure to estimate the effects of positive out-of-plane straining on crack-initiation toughness by extrapolating existing plane stress to plane strain crack-initiation data. Current capability to estimate crack-initiation toughness under conditions of minor relaxation from plane strain is empirical, and methods such as Irwin's β_{Ic} approach [*6, 7*] are physically plausible only for limited deviations from plane-strain toward plane-stress conditions. Without a better understanding of the correlation between a critical value of K or J at crack initiation and the associated through-thickness straining conditions in the vicinity of a crack front, it is difficult to justify the use of an extrapolation scheme to estimate effects of positive out-of-plane straining on crack initiation.

Objective and Scope

The objective of this paper is to describe the development of a method for estimating the decrease in crack-initiation toughness, from a reference plane-strain value, due to positive straining along the crack front of a circumferential flaw in a reactor pressure vessel (RPV). This paper will present the first phase of this work, which focuses on the development of a slip-line description of the near-tip region based on a generalized plane-strain version of the Rice-Johnson model of a blunting crack under plane-strain conditions. In addition, the scope of the investigation is limited to crack front constraint conditions that can be described in terms of the conventional one-parameter in-plane K-fields and the transverse strain. Preliminary estimates on the change in crack-initiation toughness associated with either negative or positive straining along a crack front will be presented. It is anticipated that results from the slip-line analysis will be used to guide the development of a finite-element description of the near-tip region in the next phase of this study, at which time the effects of the higher order T-stress on crack initiation under generalized plane-strain conditions will also be examined.

While this study is intended to address concerns regarding the effects of positive out-of-plane straining on ductile crack initiation, the approach adopted in this work can be extended in a straightforward fashion to examine conditions of macroscopic cleavage crack initiation. Provided single-parameter dominance of near-tip fields exists in the flawed structure, results from this study could be used to examine the appropriateness of applying plane-strain fracture toughness to the evaluation of circumferential flaws, in particular, to those in ring-forged vessels that have no longitudinal welds. In addition, results from this study could also be applied toward the analysis of the effects of thermal streaming on the fracture resistance of circumferentially oriented flaws in a pressure vessel [*8–10*].

Micromechanical Approach to Crack-Initiation Prediction

The crack-initiation prediction adopted in this study relates crack initiation under generalized plane-strain conditions with material failure at points in the vicinity of a crack front and involves the formulation of a micromechanical crack-initiation model. A micromechanical or near-tip approach to crack-initiation prediction involves not only a proper description of the near-tip stresses and strains at the onset of crack initiation but also considers the microscopic mechanisms through which a macroscopically sharp crack initiates from its original position. While a comprehensive understanding of these aspects of crack initiation is not yet available, qualitative understandings of crack initiation have been available for some time. Examples of crack-initiation models using a micromechanical approach can be found in the literature [*11–19*]. In principle, the micromechanical approach can be validated using plane-strain to plane-stress crack-initiation data so reasonable confidence in its validity can be established.

The starting point of the micromechanical crack-initiation model involves a description of the stress and strain distributions within a distance of two to three crack-tip-opening displacements (δ_t) directly ahead of a two-dimensional crack front. The essential difference between this formulation and traditional small-geometry-change (SGC) linear-elastic and elastic-plastic fracture mechanics formulations [*20–22*] is that large-geometry-change (LGC) effects in the vicinity of the crack tip are considered. Consideration of LGC effect means that the traditional mathematically sharp crack is now replaced with a blunted notch under load, which is the physically more meaningful crack-tip representation when one is interested in events within a distance of a few δ_t from the deforming crack tip.

The near-tip model of a blunted notch employed in this study is a modified version of the Rice-Johnson (RJ) model of a blunted notch under plane-strain conditions [*12,23,24*]. The modified RJ model presented here is formulated to analyze a blunted notch under generalized plane-strain conditions and is identical to the RJ model under plane-strain conditions. Both the RJ and the modified RJ models investigate LGC effects by examining the near-tip stress and strain fields using slip-line theory. Use of slip-line theory is properly limited to a rigid, perfectly plastic material. However, methodologies exist within the context of both the RJ and the modified RJ models to take into account elastic-plastic and strain-hardening material response in an approximate fashion. Note that the near-tip analysis could be carried out using a finite-element description of the near-tip region, and such a description is planned for the next phase of this work. The simplicity and "analytic" nature of the slip-line near-tip formulation, as opposed to the "numerical" nature of a finite-element description make the slip-line formulation well suited to revealing qualitatively the effects of generalized plane strain on crack initiation. Essential features of the problem can be highlighted readily and trends in results established. For the purpose of providing preliminary estimates of the effects of transverse straining on fracture toughness, the present methodology is deemed to be adequate for the first phase of this work. Nevertheless, the probable limitations of one-parameter approaches are recognized.

Generalized Plane-Strain Rice-Johnson (RJ) Model

The modified or generalized plane-strain RJ model follows closely the development of the RJ model. However, instead of using plane-strain slip-line theory, a generalized plane-strain description of the slip-lines has been employed. A general derivation of the slip-line equations, for arbitrary values of the uniform out-of-plane strain component, ε_z, is a formidable task. Fortunately, in considering the effects of positive out-of-plane straining on crack initiation of circumferential flaws in RPVs, one is interested in values of ε_z that are usually less than, and at most on the order of a few times, the yield strain. Within a region of dimensions comparable in magnitude to a few δ_t ahead of a blunted notch and over the range of values of ε_z of interest in this study, it is anticipated that the out-of-plane stress component, σ_z, analogous to its plane-strain counterpart, will remain the intermediate principal stress component. This is because, near the crack tip, the value of ε_z is small compared to ε_x and ε_y. Development of the governing equations for generalized plane-strain slip-line theory, subject to the stipulation that σ_z remains the intermediate principal stress component, is much more tractable and is presented in Ref *25*. While the generalized plane-strain equations given in Ref *25* reduce to their plane-strain counterparts when $\varepsilon_z = 0$, they cannot be used to analyze plane-stress problems where $\sigma_z = 0$ for reasons already stated. Associated with the class of generalized plane-strain problems examined in Ref *25* are limitations on the forms of the generalized plane-strain equations, and these limitations have been made explicit in Ref *25*. Let the degree of out-of-plane straining at a material point be characterized by the value of the function, ζ, that takes the form

$$\zeta = \sqrt{1 - \left(\frac{\varepsilon_z}{\varepsilon_e}\right)^2} \tag{1}$$

In Eq 1, ε_e is the Mises effective plastic strain defined by the relationship

$$\varepsilon_e = \sqrt{\tfrac{2}{3}\varepsilon_{ij}\varepsilon_{ij}} \tag{2}$$

where ε_{ij} is the strain tensor. The stipulation that σ_z remains the intermediate principal stress imposes limitations on the allowable range of values for $\varepsilon_z/\varepsilon_e$. Specifically, $\varepsilon_z/\varepsilon_e$ must obey the inequality

$$\left|\frac{\varepsilon_z}{\varepsilon_e}\right| < \frac{1}{2} \tag{3}$$

such that the ζ function assumes values in the range

$$1 \geq \zeta \geq \frac{\sqrt{3}}{2} \tag{4}$$

A state of plane strain exists when the ζ function takes on the value of unity. The generalized plane-strain, slip-line relationships appropriate to both the sharp crack and the blunted notch problems are developed in Ref *25* and summarized in the following sections.

Small-Geometry-Change Solution

Under generalized plane-strain conditions, the plane-strain Prandtl stress field indicated in Fig. 2*a* is modified as follows. Within Regions A and B, the slip-lines gradually deviate from the indicated 45° and 135° inclination with respect to the crack plane as one moves away from the plane of symmetry. This deviation is dependent on the degree of out-of-plane straining, ζ. This deviation from "straightness" also applies to the radial slip-lines within the centered fan, *C*. However, the asymptotic nature of the present problem (that is, the small size of the crack-tip zone being analyzed as compared to δ_t) permits one to regard the sharp-crack slip-lines as "straight."

Following Ref *12*, a deformation theory of plasticity is used to describe the strains, so that the path independent *J*-integral [*23*] can be used to obtain simple relationships between *J*,

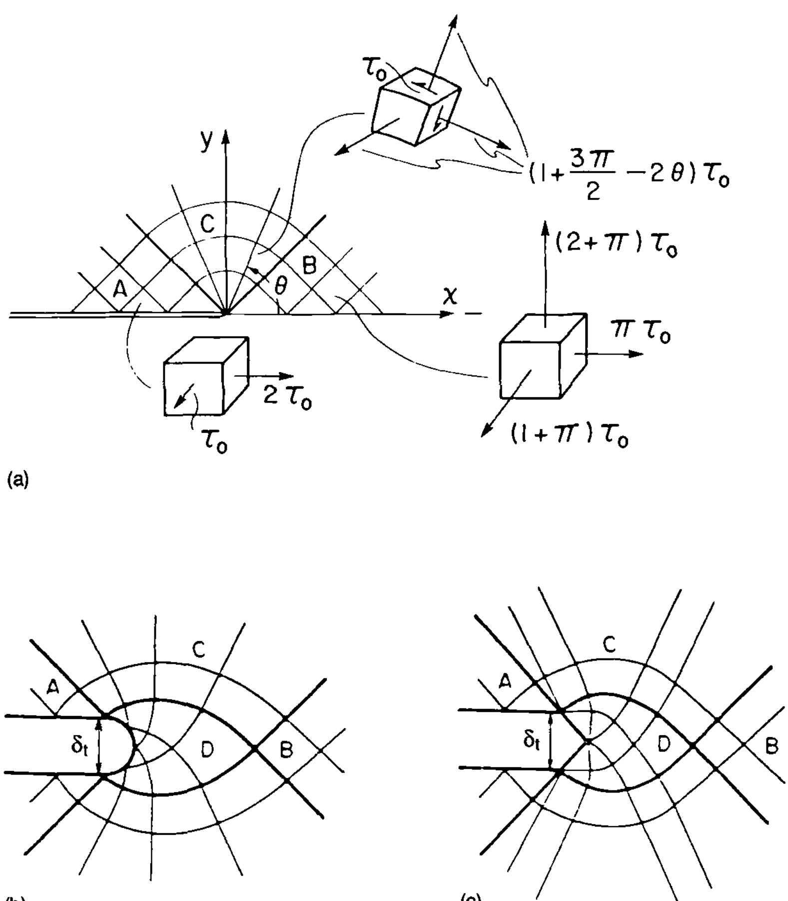

FIG. 2—(a) *Prandtl slip-line construction of near-crack-tip stress state for contained yielding of an ideally plastic material. This slip-line field corresponds to singular strains in the fan region and results in a nonzero value of the crack-tip-opening displacement.* (b) *Slip-line construction for the blunted notch region assuming a smooth blunted notch tip profile.* (c) *Slip-line construction for the blunted notch region assuming sharp vertices exist along the notch tip.*

R_{max}, and δ_t. Specifically, these relationships subject to plane-strain, small-scale-yielding conditions are given in Ref *12* and take the form

$$R_{max} = \frac{3(1-\nu)}{4\sqrt{2}\,(2+\pi)}\left(\frac{K}{\tau_0}\right)^2 = 0.217\left(\frac{K}{\sigma_0}\right)^2 \quad (5a)$$

$$\delta_t = \frac{2(1-\nu^2)}{2+\pi}\frac{K^2}{E\tau_0} = 0.613\frac{K^2}{E\sigma_0} = 2.8\frac{\sigma_0}{E}R_{max} \quad (5b)$$

where τ_0 is the yield stress in shear. The quantity, R_{max}, may be regarded as a very approximate measure of the maximum distance to the elastic-plastic boundary along a radial line within the fan. In Eqs 5*a* and *b*, Poisson's ratio is taken to be $\nu = 0.3$. In addition, the Mises shear-tension yield relationship is used such that $\sigma_0 = \tau_0\sqrt{3}$, where σ_0 is the yield stress in tension. The coefficients in Eqs 5*a* and *b* are probably slightly large, and discussions concerning more refined elements can be found elsewhere [*12,16,26–29*]. For the purpose of this study Eqs 5*a* and *b* are entirely adequate because it is the functional form of these relationships that is of interest.

An important approximation in the RJ model concerns the manner in which the sharp crack SGC solution provides the appropriate boundary conditions for evaluating the near-tip fields of the blunted notch LGC problem. According to slip-line theory, it is known that straight slip-lines transmit a uniform velocity parallel to themselves. From Eq 5*b*, it is seen that δ_t is of the order σ_0/E times the maximum extent, R_{max}, of the plastic zone. Therefore, Region D in Fig. 2*b* is typically 2 orders of magnitude smaller than R_{max} such that when viewed on the larger size scale of the plastic zone in Fig. 2*a*, Region D still appears as a point. It is therefore argued in Ref *12* that the velocities on the boundary of Region D are known in terms of velocities in the fan far away from the boundary, and these velocities are then assumed to be given by the velocities in the centered fan of the SGC solution.

The crack-tip-opening displacement, when viewed on the scale of Fig. 2*b*, is the relevant measure of loading that determines the stress and strain distributions within Region D. Conceptually, this is equivalent to taking δ_t as a measure of "time," so the velocities mentioned in the previous paragraph are defined as the rate of change of displacement quantities with δ_t. From Ref *12*, the radial velocity, V_r, within the centered-fan region takes the form

$$V_r(\theta) = \frac{1}{2\sqrt{2}}\left[\cos\left(\theta - \frac{\pi}{4}\right) - \cos\left(2\theta - \frac{\pi}{2}\right)\right] \quad (6)$$

Large-Geometry-Change Solution

Introduce a set of characteristic α,β coordinates into Region D as indicated in Fig. 3 [*12*], where lines of β = constant and α = constant are the first and second principal shear directions, respectively. The coordinate origin is located at the apex of Region D and is defined such that $\alpha = 0$ and $\beta = \phi - \pi/4$ on the upper boundary of Region D and $\beta = 0$ and $\alpha = \phi - \pi/4$ on the lower boundary. The first principal shear angle is denoted as ϕ. The scaling arguments presented in the last section imply that the constant displacement rate, V_α, along each straight α line of the LGC noncentered fan, can be approximated by the radial displacement rate, V_r, of the SGC centered fan, with the shear angle, ϕ, of the noncentered α lines replacing the polar coordinate, θ (which coincides with the shear angle), for the radial or α lines of the centered fan. Consequently, the velocity normal to the boundary of Region *D*, V_α, now takes the form [*12*]

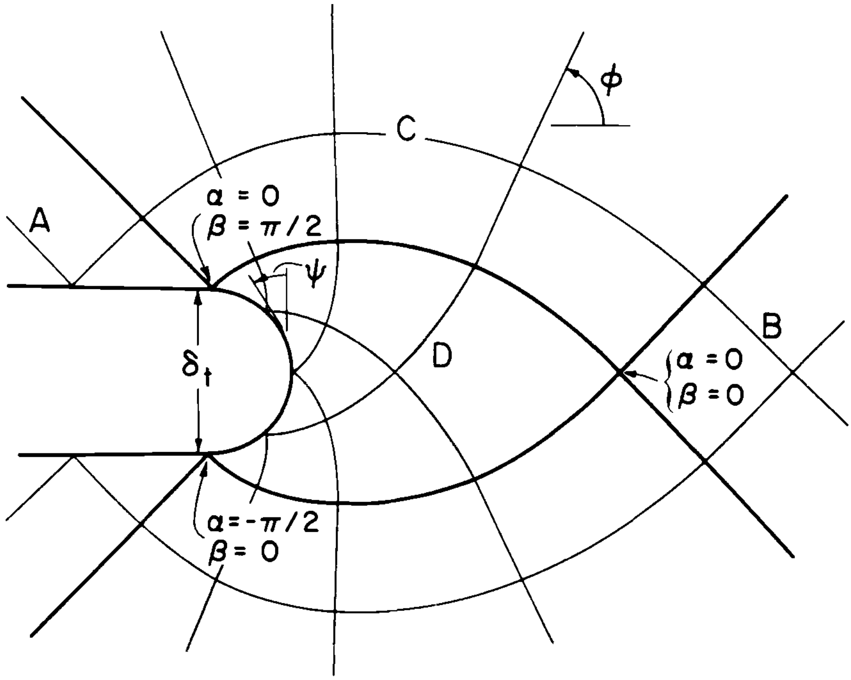

FIG. 3—*Schematic illustrating the definition of the slip-line coordinate system (α,β) in the neighborhood of the blunted notch. The first principal shear angle is denoted as ϕ.*

$$V_\alpha(\phi) = \frac{1}{2\sqrt{2}}\left[\cos\left(\phi - \frac{\pi}{4}\right) - \cos\left(2\phi - \frac{\pi}{2}\right)\right] \tag{7}$$

Evaluation of the stress and strain distributions within Region D is thus formulated in terms of a boundary value problem with the velocities as unknowns.

The present generalized plane-strain study also assumes the validity of a single-parameter description of the near-tip stress and strain fields. Consequently, relationships of the type shown in Eqs 5*a* and *b* also hold in the present case. However, it is not known if the numerical coefficients under generalized plane strain are the same as those in Eqs 5*a* and *b*. For the purpose of comparing crack-initiation toughness values under varying degrees of out-of-plane straining, the plane-strain relationship, Eq 5*b*, is assumed to hold under generalized plane-strain conditions.

Finite-element results in Ref *25* indicate that generalized plane-strain loading introduces modifications to the plane-strain velocity fields (Eq 6) within the centered fan. A rigorous finite-element treatment of the present problem, for an elastic-plastic material, would entail a Poisson's effect correction of the "remote" boundary conditions in Eq 7, and the effects of this correction were examined for the SGC problem in Ref *30*. However, it is unclear how this correction could be incorporated into the present slip-line model.

In addition, the stipulation of remote elastic *K*-fields in Eqs 5*a* and *b* properly limits the allowable range of the out-of-plane strain to less than the yield strain. Within the framework of a slip-line approach and the intent of this study, it is necessary to consider values of the out-of-plane strain that are on the order of a few times the yield strain.

As discussed in Ref *25*, the perturbations to Eq 7 due to nonzero values of ε_z are accounted for in this study using an empirical relationship. The velocity normal to the boundary of Region *D*, V_α, under generalized plane-strain conditions now takes the form

$$\hat{V}_\alpha(\phi) = \frac{(1 - 2\varepsilon_z)}{2\sqrt{2}} \left[\cos\left(\phi - \frac{\pi}{4}\right) - \cos\left(2\theta - \frac{\pi}{2}\right) \right] \tag{8}$$

The in-plane velocities within Region D, along the characteristic directions, are determined by the solutions to the equations

$$\frac{\partial V_\alpha}{\partial \alpha} + V_\beta = -\frac{\dot{\varepsilon}_z}{2} \frac{\partial S_\alpha}{\partial \alpha} \tag{9a}$$

and

$$\frac{\partial V_\beta}{\partial \beta} + V_\alpha = -\frac{\dot{\varepsilon}_z}{2} \frac{\partial S_\beta}{\partial \beta} \tag{9b}$$

where $\dot{\varepsilon}_z$ is the uniform "strain rate" along the out-of-plane direction, and S_α and S_β are dimensional distances along the characteristic coordinate directions. Because δ_t serves as a measure of "time" in this problem, the uniform strain rate, $\dot{\varepsilon}_z$, is defined according to the relationship

$$\dot{\varepsilon}_z = \frac{d\varepsilon_z}{d\delta_t} = \frac{\varepsilon_z}{\delta_t} \tag{10}$$

An interpretation of Eq 10 is that the magnitude of the out-of-plane strain component, ε_z, is reached when the crack-tip-opening displacement attains the reference steady-state value, δ_t, such that the generalized plane-strain loading situations examined in this study can be considered proportional in nature. Therefore, the quantity, ε_z/δ_t, in Eq 10 should be regarded as "constant" during an analysis. Because the derivatives, $\partial S_\alpha/\partial\alpha$ and $\partial S_\beta/\partial\beta$, in Eqs 9*a* and *b* are unknowns themselves, Eqs 9*a* and *b* need to be evaluated in an iterative manner for the unknown velocities within Region D. For the range of ε_z values considered in this study, an efficient iterative scheme is found by using the logarithmic spiral solution associated with a semicircular notch profile as an initial guess for evaluating the derivatives, $\partial S_\alpha/\partial\alpha$ and $\partial S_\beta/\partial\beta$. In all cases considered, less than ten iterations of Eqs 9*a* and *b* were required to achieve a convergent solution.

Strain Distribution Directly Ahead of a Blunted Notch

Following Ref *12*, solution for the strain distribution directly ahead of the blunted notch tip begins by associating all quantities along the *x*-axis, directly ahead of the notch tip, parametrically in terms of the tangent angle, ψ, of the point on the notch tip intersected by the β slip-line drawn from the point of interest on the *x*-axis, as schematically shown in Fig. 4. Hence, $\psi = \pi/2$ represents the point on the *x*-axis at the outer extremity or apex of Region D. The point at the deformed notch tip on the *x*-axis corresponds to $\psi = 0$. From the velocity solution, the dimensionless *x*-direction velocity component directly ahead of the blunted notch, V_x, is known and can be expressed via ψ in the form

$$V_x(x,y)|_{y=0} = V(\psi) \tag{11}$$

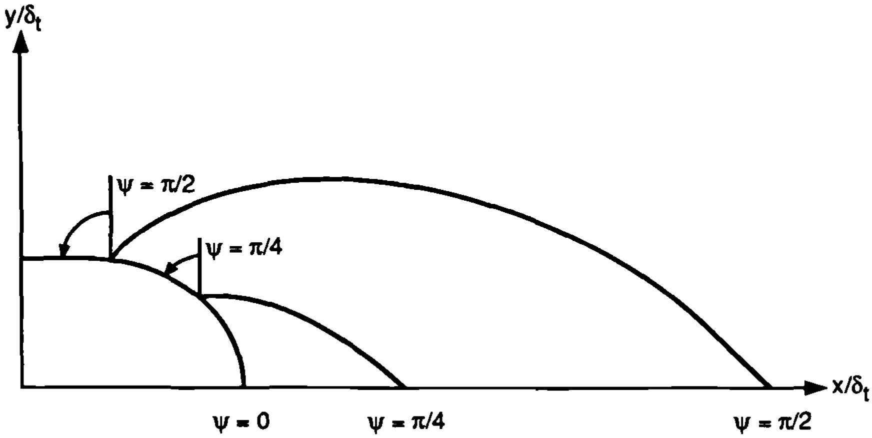

FIG. 4—*Schematic illustrating the definition of the tangent angle, ψ, associated with location along the* x-*axis directly ahead of the blunted notch tip. The point at the deformed notch tip on the* x-*axis corresponds to ψ = 0.*

Let the deformed x-coordinate of a material point corresponding to Angle ψ be written in terms of the nondimensional function, $F(\psi)$, defined by the relationship

$$x = \delta_t F(\psi) \tag{12}$$

In the RJ model, the distortions occurring ahead of Region D, in the neighborhood of the apex, are considered small. As a result, the y-direction or "opening" strain, ε_y^n, ahead of the blunted notch takes the form

$$\varepsilon_y(\psi) = -\int_{\psi}^{\pi/2} \frac{V'(\eta)}{F(\eta) - V(\eta)} d\eta \tag{13}$$

A significant difference between the plane-strain RJ model and the modified RJ model used in this study arises from the assumption concerning the state of strain at the apex. The magnitudes of the strains in the constant stress regions, A and B, in Fig. 2*a* are on the order of the yield strain, and hence the state of strain at the apex in Fig. 3 can be expected to be of similar magnitude. Let $\varepsilon_{\alpha\beta}$ denote the shear strain components along the characteristic directions ahead of the blunted notch. In the plane-strain RJ formulation, $\varepsilon_{\alpha\beta} = \varepsilon_y$ along the crack plane, so that use of Eq 13 within Region D implies zero strain at the apex. Evidently, this assumption was deemed acceptable in view of the large strain that develops adjacent to the blunted notch tip. However, it is clear from Eq 3 that the state of strain must have nonzero values of the in-plane strain components for a state of generalized plane strain to exist at the apex (and throughout Region D). Therefore, inclusion of the small, but nonzero, state of strain at the apex is crucial toward a proper consideration of generalized plane-strain effects. For the purpose of comparing the difference in initiation toughness due to nonzero values of the out-of-plane strain, ε_z, the assumption is made that a nonzero value of $\varepsilon_{\alpha\beta} = \varepsilon_a$ exists at the apex and that the magnitude of this shear-strain component at the apex is independent of the magnitude of ε_z. The condition governing $\varepsilon_{\alpha\beta}$ at the apex employed in this study is admittedly arbitrary. However, within the context of both the RJ and the modified RJ models, the state of strain at the apex is not quantitatively defined.

Associated with the assumption of $\varepsilon_{\alpha\beta} = \varepsilon_a$ at the apex, Eq 3 provides the "reality condition" governing the admissible values of ε_z as a function of the assumed state of strain at the apex of the form

$$\left|\frac{\varepsilon_z}{\varepsilon_a}\right| < \frac{2}{3} \tag{14}$$

The y-direction strain at the apex, ε_{ya}, is related to ε_a via the relationship

$$\varepsilon_{ya} = \varepsilon_a - \frac{\varepsilon_z}{2} \tag{15}$$

The x-direction strain at the apex, ε_{xa}, can then be found via the condition of plastic strain incompressibility. The y-direction strain directly ahead of the blunted notch takes the form

$$\varepsilon_y(\psi) = \varepsilon_{ya} - \int_{\psi}^{\pi/2} \frac{V'(\eta)}{F(\eta) - V(\eta)}\, d\eta \tag{16}$$

By formally setting the apex shear strain, $\varepsilon_a = 0$, the modified RJ relationship Eq 16 can be reduced to its plane-strain RJ counterpart Eq 13.

In presenting numerical results, both the magnitude of the out-of-plane strain, ε_z, and the apex shear strain, ε_a, are normalized with respect to the uniaxial yield strain, ε_0. The strain distribution normal to the crack plane within Region D of Fig. 3 is shown in Figs. 5*a* and *b* as a function of the normalized undeformed distance, X/δ_t, for $\varepsilon_a/\varepsilon_0 = 4$ and three values of $\varepsilon_z/\varepsilon_0 = -2, 0, 2$. Figures 5*a* and *b* represent the same strain distribution drawn to two different strain scales for clarity. For the values of $\varepsilon_a/\varepsilon_0$ and $\varepsilon_z/\varepsilon_0$ indicated in Fig. 5, the strain distribution is fairly insensitive to the input parameters except in the immediate neighborhood of the apex.

As first demonstrated by the plane-strain RJ model [*12*], large strains are predicted directly ahead of the blunted notch when LGC effects near the blunted notch tip are considered in a consistent near-tip formulation. However, these large strains exist only within a distance of less than three δ_t from the blunted tip. A consequence of the limited extent of the large strain region is that in situations where crack initiation involves ductile mechanisms requiring large strains, the opening displacement at initiation must be such that Region D incorporates characteristic microstructural dimensions relevant to the fracture process [*12*].

Note that a strain singularity is predicted as X approaches zero in the present analysis due to the assumption of a smoothly blunted notch. Plane-strain finite-element calculations based on a blunted notch profile (Fig. 2*c*) that has included vertices suggest that the magnitude of the opening strain is large but finite as the tip is approached [*31*].

Stress Distribution Directly Ahead of a Blunted Notch

Solution for the stress distribution directly ahead of the blunted notch tip in Fig. 3 follows closely the procedures employed in the plane-strain RJ model, and therefore only the key steps will be discussed here. Following Ref *12*, the uniaxial true stress-strain relationship is assumed to take the form

$$\sigma = f(\varepsilon^{tr}) \tag{17}$$

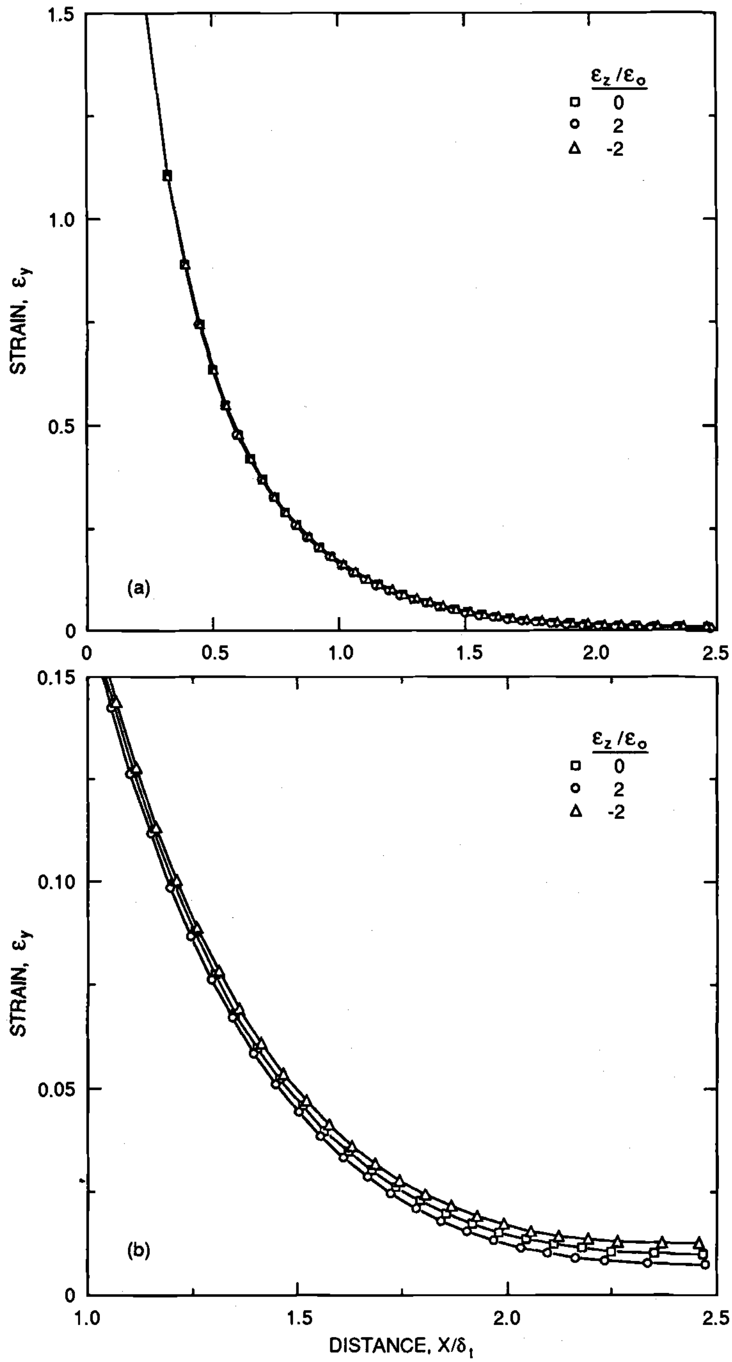

FIG. 5—(a) *Distribution of the "opening" strain, ε_y, normal to the crack plane as a function of normalized undeformed distance, X/δ_t. Note that large strains are predicted ahead of the blunted notch.* (b) *Distribution of the "opening" strain, ε_y, normal to the crack plane redrawn on a different scale along the strain axis. Note that for values of the out-of-plane strain component, ε_z, up to two times the yield strain, ε_0, the effect on the ε_y strain distribution is minimal.*

where $f(\varepsilon^{tr})$ is the uniaxial hardening relationship. The equation for the y-direction "opening" stress directly ahead of the blunted notch, within the intense strain Region D in Fig. 2*b*, then takes the form

$$\sigma_y = \frac{2}{\sqrt{3}} M(\psi) f\left(\frac{2}{\sqrt{3}} \varepsilon_e\right) + \frac{2}{\sqrt{3}} \int_0^{\psi} M(\eta) f\left(\frac{2}{\sqrt{3}} \varepsilon_e\right) d\eta \tag{18}$$

where

$$M(\psi) = 1 - \frac{1}{3}\left(\frac{\varepsilon_z}{\varepsilon_e}\right)^2 \tag{19a}$$

$$\varepsilon_e(\psi) = \sqrt{\varepsilon_y^2 + \varepsilon_z^2 + \varepsilon_y \varepsilon_z} \tag{19b}$$

and ε_y is given by Eq 16. Under plane-strain conditions such that $\varepsilon_z = 0$, $M(\psi) = 1$, and $\varepsilon_e(\psi) = \varepsilon_y$ and the corresponding RJ expression is recovered. Numerical evaluation of Eq 19 is based on a uniaxial power-law stress-strain relationship of the form

$$\frac{\sigma}{\sigma_0} = \left(\frac{\varepsilon^{tr}}{\varepsilon_0}\right)^N = \left(\frac{E\varepsilon^{tr}}{\sigma_0}\right)^N \tag{20}$$

In Fig. 6, the effect of the magnitude of the apex shear strain on the opening-stress distribution is indicated for input parameter values $N = 0.2$, $\sigma_0/E = \varepsilon_0 = 0.0025$, $\varepsilon_z/\varepsilon_0 = 0$, and five values of the apex shear strain $\varepsilon_a/\varepsilon_0 = 0, 1, 2, 3$, and 4. The RJ prediction [12] assumes $\varepsilon_{\alpha\beta} = 0$ within Region D (Fig. 3) and corresponds to the case $\varepsilon_a/\varepsilon_0 = 0$. Detailed finite-element near-crack-tip results obtained by assuming K-dominated far-field conditions [16] and from various compact-tension specimen geometries [32] indicate that the apex shear strain, ε_a, is on the order of a few times the yield strain, ε_0.

Note that there is actually a stress singularity predicted in the hardening cases at $X = 0$, although the singularity is weak and dominates over a very small distance relative to δ_t as shown in Fig. 6. Physically, this upturn in stress as X approaches zero can be disregarded for two reasons: (1) this upturn in stress is a consequence of the continuously hardening stress-strain relationship adopted in Eq 20, and the stress would saturate if a limiting flow stress is imposed on Eq 20; and (2) the region of dominance of the singular stress is much less than one δ_t so that its physical relevance can be questioned.

Disregarding the stress singularity, it is seen that a stress maximum is predicted at a finite distance ahead of the blunted notch tip when LGC effects are considered, in contrast to SGC sharp crack analyses. This stress maximum occurs either within the large-strain region, or at the location where the large-strain stress solution intersects the small-strain solution. Note that both the value and the location of the stress maximum are strongly dependent on the assumed apex strain state. The concept of a maximum achievable stress suggests the possibility of abrupt toughness transitions with temperature or loading rate in materials susceptible to stress-controlled cleavage failure [12]. This observation has important consequences with regard to the application of conventional cleavage failure models, which consider cleavage failure to be possible when the maximum achievable stress exceeds a material failure stress over a microscopically significant distance, generally on the order of a few grain diameters.

In Fig. 7, the effect of out-of-plane straining on the opening stress distribution is indicated for input parameter values $N = 0.2$, $\sigma_0/E = 0.0025$, $\varepsilon_a/\varepsilon_0 = 4$, and three values of the out-of-

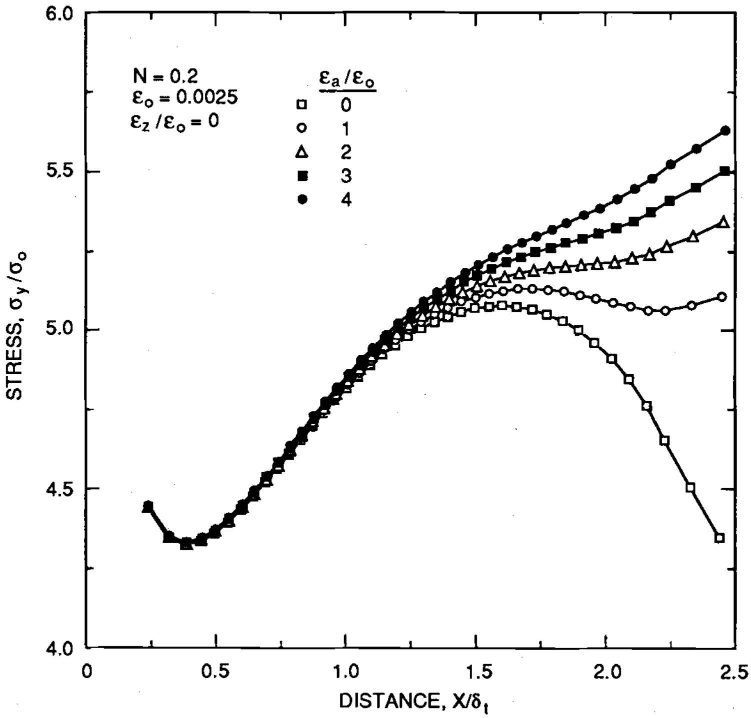

FIG. 6—*Distribution of the "opening" stress, σ_y, normal to the crack plane as a function of normalized undeformed distance, X/δ_t. Disregarding the spurious stress singularity, it is seen that a stress maximum that is strongly dependent on the value of the apex shear strain, ε_a, is predicted at a finite distance ahead of the blunted notch tip.*

plane strain $\varepsilon_z/\varepsilon_0 = -2, 0$, and 2. It is seen that deviation from plane-strain constraint results in either minimal change or a decrease in the value of the opening stress ahead of the blunted notch. While a decrease in σ_y under less than plane-strain conditions appears consistent with observed cleavage toughness trends, the rather pronounced reduction in σ_y due to positive out-of-plane straining is counter-intuitive. Discussions on the observed trends for σ_y can be found in Ref *25*. Implications of the present results regarding (ductile) toughness predictions under generalized plane-strain conditions are presented in the next section.

Material Failure Criteria and Crack-Initiation Toughness Prediction

A number of material failure criteria exist in the literature, all of which seek to correlate the attainment of a critical value of the macroscopic fracture parameter, such as K or J, with more fundamental material properties such as limiting stresses and strains. Because fracture parameters involve a length dimension, an empirical microscopic length parameter—such as mean grain size or mean void spacing—is usually associated with these material failure criteria. In situations where the material failure process is ductile in nature, it is commonly accepted that the failure strains are sensitive to the associated stress state.

A simple ductile failure criterion is adopted in this study to estimate the decrease in crack-initiation toughness, from a reference plane-strain value, due to positive straining along the crack front. This material failure criterion assumes that crack initiation can be expressed in

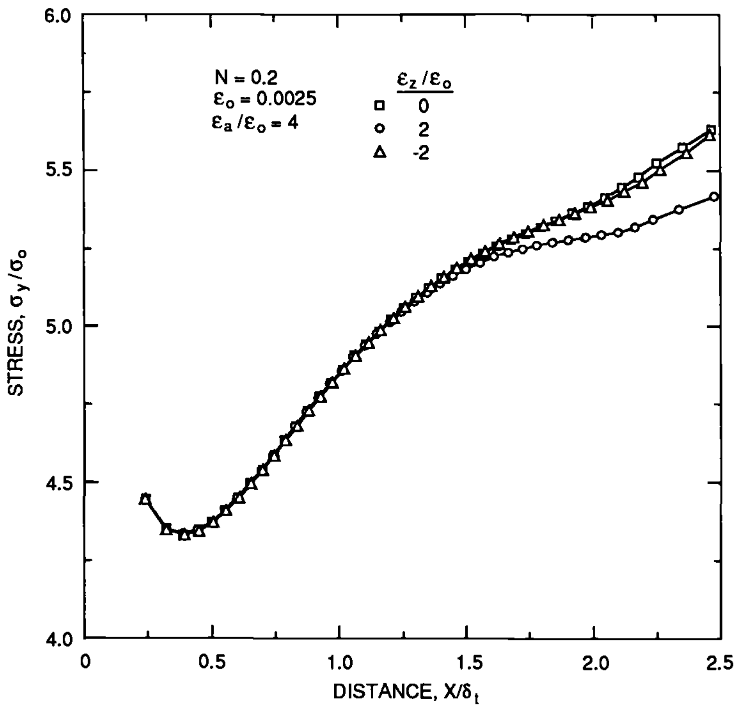

FIG. 7—*Distribution of the "opening" stress, σ_y, normal to the crack plane as a function of normalized undeformed distance, X/δ_t. Note that deviation from plane-strain constraint results in either minimal change or a decrease in the value of σ_y ahead of the blunted notch.*

terms of critical values of global or macroscopic stress and strain parameters and is similar to the simpler of the two failure criteria used in Ref *12*. Specifically, the Mises effective strain directly ahead of the blunted notch is assumed to be the limiting strain parameter, and the critical value of this strain parameter at failure is assumed to be a function of the associated triaxial stress rate at the material point. Following Refs *14* and *15*, the material failure criterion is assumed to take the simple form

$$\varepsilon_e^f = \alpha e^{\left(-\frac{3}{2}\frac{\sigma_m}{\sigma_e}\right)} \tag{21}$$

where σ_m is the mean stress, ε_e and σ_e are the Mises effective stress and strain, and α is the value of the failure strain as the triaxial stress ratio, σ_m/σ_e, approaches zero. Motivation for the functional form of Eq 21 comes from various theoretical analyses [*11,33*] that suggest that the growth of voids is strongly dependent on the state of triaxial stress in the vicinity of these voids. In Fig. 8 (taken from Ref *15*), the experimentally determined material failure curves are shown for a wide variety of materials. The failure curves are strong functions of the materials of interest, and thus application of Eq 21 to toughness prediction requires the generation of a failure curve appropriate to the material under investigation. Two curves corresponding to $\alpha = 1$ and $\alpha = 2$ have been included in Fig. 8 for comparison with other experimentally generated failure curves.

In the first phase of this work, a hypothetical failure curve corresponding to $\alpha = 1$ in Eq 21 is used to examine the influence of out-of-plane straining on the deviation from plane-strain

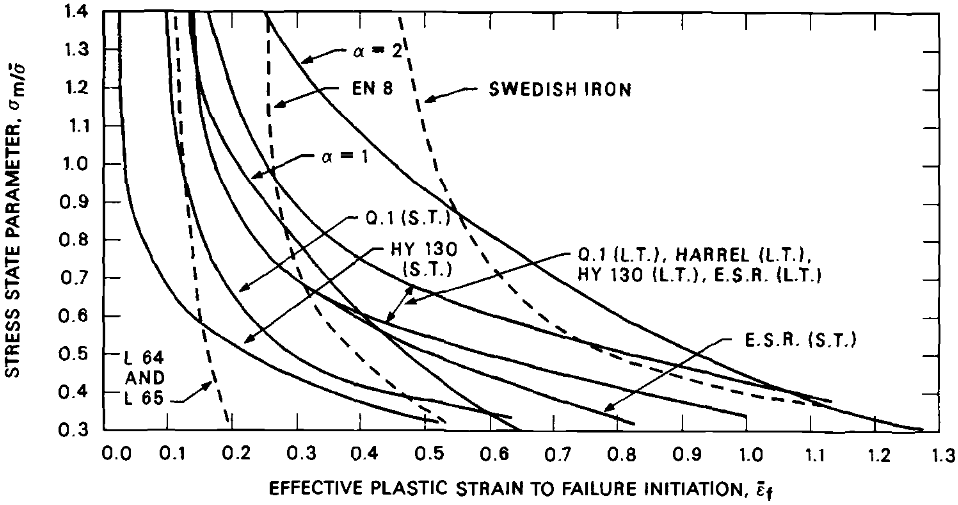

FIG. 8—*Material failure curves for a variety of structural materials. It is seen that the shapes of these failure curves are strongly dependent on the material of interest. Material failure curves corresponding to* $\alpha = 1$ *and* $\alpha = 2$ *in Eq 21 are indicated for comparison.*

crack-initiation toughness. Note that, in general, the results to be presented based on $\alpha = 1$ will not be quantitatively correct for RPV grade materials such as A533-B at a given temperature. The limiting values of ε_e associated with the $\alpha = 1$ curve and various values of ε_z are determined as the intersection of the $\alpha = 1$ curve with the calculated stress-strain distributions. The corresponding critical values of the normalized distance parameter, X/δ_t, ahead of the blunted notch tip can be related to a critical value of the fracture parameters, K or J, via relationships of the type indicated in Eq 5*b*. Prediction of the absolute magnitude of the fracture parameter at initiation ($K = K_c$) requires that a definite value of the characteristic distance variable, $X = X_c$, be available. Previous attempts at fracture toughness predictions based on definite values of X_c can be found in Refs *12* and *14*. In determining the relative change in initiation toughness due to ε_z, it is only necessary to assume X_c is independent of ε_z. With the further assumption that the numerical coefficient in Eq 5*b* is also independent of ε_z, an assumption that appears to be well supported by the finite element results [*25*], the relative change in initiation toughness can be determined from the relationship

$$\frac{K_c}{K_{Ic}} = \sqrt{\frac{\delta_{Ic}}{\delta_c}} \tag{22}$$

where (K_c, δ_c) are the critical values of K and δ_t associated with a nonzero value of ε_z, and (K_{Ic}, δ_{Ic}) are the critical values of K and δ_t associated with the plane-strain conditions corresponding to $\varepsilon_z = 0$. Toughness predictions based on this procedure are summarized in Table 1 for input parameters $\sigma_0/E = 0.0025$, $\varepsilon_a/\varepsilon_0 = 4$, $N = 0, 0.1$ and three values of $\varepsilon_z/\varepsilon_0 = -2, 0$, and 2.

Results in Table 1 indicate minimal change in the initiation toughness for the given choice of input parameters. It should be reemphasized that the material failure curve associated with $\alpha = 1$ is chosen merely to illustrate the manner in which the present analysis method could be used to predict crack-initiation toughness. In addition, the results in Table 1 are strongly dependent on the assumed form of the material failure criterion. The implication of these calculations is that the decrease in crack-initiation toughness from a reference plane-strain value

TABLE 1—*Toughness predictions based on yield strain* σ_0/E = 0.0025 *and apex strain* $\varepsilon_a/\varepsilon_0 = 4$ *as a function of the degree of strain hardening*, N, *and the degree of out-of-plane straining*, $\varepsilon_z/\varepsilon_0$.

N	$\varepsilon_z/\varepsilon_0$	ε_e^f	X/δ_t	K_c/K_{Ic}
0	−2	0.108	1.232	1.011
0	0	0.101	1.260	1
0	2	0.092	1.292	0.988
0.1	−2	0.059	1.465	1.026
0.1	0	0.049	1.542	1
0.1	2	0.040	1.625	0.974

due to a moderate degree of out-of-plane straining is minimal, provided the stress and strain states in the vicinity of the crack tip can be characterized by a one-parameter K field. Obviously, this observation must be considered tentative, and much more work remains to validate the assumptions and to improve the approximations used in the present analysis.

Discussion

Limited biaxial studies on part-through, surface-cracked plates [*34,35*] indicate that the crack-initiation toughness expressed in terms of the stress intensity factor, K, is rather insensitive to the range of biaxial loading examined in those studies under "cleavage" crack-initiation conditions. However, it is significant that the implications from the present near-tip analysis stand in contrast with wide-plate results presented in Refs *36* and *37*. As discussed in Ref *25*, it is believed that a two-parameter approach is needed to characterize crack initiation in some of the wide-plate tests. Use of the present approach to predict crack initiation under positive out-of-plane straining conditions for a circumferential flaw awaits the determination of the near-tip stress and strain fields appropriate to pressure vessel applications.

Acknowledgment

Research was sponsored by the Office of Nuclear Regulatory Research, U.S. Nuclear Regulatory Commission under Interagency Agreement 1886-8011-9B with the U.S. Department of Energy under Contract DE-AC05-84OR21400 with Martin Marietta Energy Systems, Inc.

References

[*1*] Rolfe, S. T. and Barsom, J. M., *Fracture and Fatigue Control in Structures: Applications of Fracture Mechanics*, Prentice-Hall Inc., Englewood, NJ, 1977.
[*2*] Kanninen, M. F. and Popelar, C. H., *Advanced Fracture Mechanics*, Oxford University Press, New York, 1985.
[*3*] Pennell, W. E., "Heavy Section Steel Technology Program Fracture Issues," *Proceedings*, USNRC Seventeenth Water Reactor Safety Information Meeting, USNRC Conference Proceedings NUREG/CP-0105, Vol. 3, March, 1990, pp. 1–26.
[*4*] *Code of Federal Regulations*, Title 10, Part 50, Section 50.61 and Appendix G, USNRC, 1988.
[*5*] Merkle, J. G., "An Overview of the Low-Upper-Shelf Toughness Safety Margin Issue," USNRC Report NUREG/CR-5552 (ORNL/TM-11314), Aug. 1990.
[*6*] Irwin, G. R., "Fracture Mode Transition for a Crack Traversing a Plate," *Journal of Basic Engineering*, Vol. 82, No. 2, 1960, pp. 417–425.
[*7*] Merkle, J. G., "An Examination of the Size Effects and Data Scatter Observed in Small-Specimen

Cleavage Fracture Toughness Testing," USNRC Report NUREG/CR-3672 (ORNL/TM-9088), Aug. 1984.
[8] Theofanous, T. G. and Iyer, K., "Mixing Phenomena of Interest to SBLOCAs," *Nuclear Engineering and Design*, Vol. 102, 1987, pp. 91–103.
[9] Kussmaul, K., et al., "Cyclic and Transient Thermal Loading of the HDR Reactor Pressure Vessel with Respect to Crack Initiation and Crack Propagation," *Proceedings*, Sixth International Seminar on Assuring Structural Integrity of Steel Reactor Pressure Boundary Components: SMIRT-10 Post Conference Seminar No. 2, 1989.
[10] Kuna, M., Kordisch, H., and Ockewitz, A., "Thermoelastic-Plastic FEM-Analysis of a Semi-Elliptical Surface Crack in a Cylinder Under Non-Axial Symmetric Cooling," *Proceedings*, European Symposium on Elastic-Plastic Fracture Mechanics: Elements of Defect Assessment, 9–12 Oct. 1989, Freiburg, Germany, to be published.
[11] McClintock, F. A., "A Criterion for Ductile Fracture by the Growth of Holes," *Journal of Applied Mechanics*, Vol. 35, 1968, pp. 363–371.
[12] Rice, J. R. and Johnson, M. A., "The Role of Large Crack Tip Geometry Changes in Plane Strain Fracture," *Inelastic Behavior of Solids*, McGraw-Hill, New York, 1977, pp. 641–672.
[13] Ritchie, R. O., Knott, J. F., and Rice, J. R., "On the Relationship Between Critical Tensile Stress and Fracture Toughness in Mild Steel," *Journal of the Mechanics and Physics of Solids*, Vol. 21, 1973, p. 395.
[14] Hancock, J. W. and MacKenzie, A. C., "On the Mechanisms of Ductile Failure in High-Strength Steels Subjected to Multi-Axial Stress-States," *Journal of the Mechanics and Physics of Solids*, Vol. 24, 1976, pp. 147–169.
[15] MacKenzie, A. C., Hancock, J. W., and Brown, D. K., "On the Influence of State of Stress on Ductile Failure Initiation in High Strength Steels," *Engineering Fracture Mechanics*, Vol. 9, 1985, pp. 167–188.
[16] McMeeking, R. M., "Finite Deformation Analysis of Crack-Tip Opening in Elastic-Plastic Materials and Implications for Fracture," *Journal of the Mechanics and Physics of Solids*, Vol. 25, 1977, pp. 357–381.
[17] Aravas, N. and McMeeking, R. M., "Finite-Element Analysis of Void Growth Near a Blunting Crack-Tip," *Journal of the Mechanics and Physics of Solids*, Vol. 33, 1985, pp. 25–49.
[18] Needleman, A. and Tvergaard, V., "An Analysis of Ductile Rupture Modes at a Crack Tip," *Journal of the Mechanics and Physics of Solids*, Vol. 35, 1987, pp. 151–183.
[19] Teirlinck, D., et al., "Fracture Mechanism Maps in Stress Space," *Acta Metallurgica*, Vol. 36, No. 5, 1988, pp. 1213–1228.
[20] Irwin, G. R., "Fracture Mechanics," *Structural Mechanics*, Pergamon Press, New York, 1960, pp. 557–594.
[21] Hutchinson, J. W., "Singular Behavior at the End of a Tensile Crack in a Hardening Material," *Journal of the Mechanics and Physics of Solids*, Vol. 16, 1968, pp. 13–31.
[22] Rice, J. R. and Rosengren, G. F., "Plane Strain Deformation Near a Crack Tip in a Power-Law Hardening Material," *Journal of the Mechanics and Physics of Solids*, Vol. 16, 1968, pp. 1–12.
[23] Rice, J. R., "A Path Independent Integral and the Approximate Analysis of Strain Concentration by Notches and Cracks," *Journal of Applied Mechanics*, Vol. 35, 1968, pp. 379–386.
[24] Rice, J. R., "Mathematical Analysis in the Mechanics of Fracture," *Fracture: An Advanced Treatise*, H. Liebowitz, Ed., Vol. II, Academic Press, New York, 1968, pp. 191–311.
[25] Shum, D. K. M., et al., "Analytical Studies of Traverse Strain Effects on Fracture Toughness for Circumferentially Oriented Cracks," USNRC Report NUREG/CR-5592 (ORNL/TM-11581), Feb. 1991.
[26] Levy, N., et al., "Small Scale Yielding Near a Crack in Plane Strain: A Finite Element Analysis," *International Journal of Fracture Mechanics*, Vol. 7, No. 2, June 1971, pp. 143–156.
[27] Rice, J. R. and Tracey, D. M., "Computational Fracture Mechanics," *Numerical and Computer Methods in Structural Mechanics*, Academic Press, New York, 1973, pp. 585–623.
[28] Rice, J. R., "Elastic-Plastic Fracture Mechanics," *The Mechanics of Fracture, Applied Mechanics Division*, Vol. 19, 1976, pp. 23–53.
[29] Tracey, D. M., "Finite Element Solutions for Crack-Tip Behavior in Small-Scale Yielding," *Journal of Engineering Material and Technology*, April 1976, pp. 146–151.
[30] Parks, D. M. and Wang, Y. Y., "Three-Dimensional Crack Front Constraint," presented at the Constraint Working Group Meeting, University of Illinois, Champaign-Urbana, IL, 27 Feb. 1990.
[31] McMeeking, R. M., "Blunting of a Plane Strain Crack Tip into a Shape with Vertices," *Journal of Engineering Material and Technology*, Vol. 99, 1977, pp. 290–297.
[32] Aurich, D. and Sommer, E., "The Effect of Constraint on Elastic-Plastic Fracture," *Steel Research*, Vol. 8, 1988, pp. 358–367.

[33] Rice, J. R. and Tracey, D. M. "On the Ductile Enlargement of Voids in Triaxial Stress Fields," *Journal of the Mechanics and Physics of Solids*, Vol. 17, 1969, pp. 201–217.

[34] Garwood, S. J. and Davey, T. G., "Behavior of A533B under Biaxial Loading at +70°C," *International Journal of Pressure Vessel and Piping*, Vol. 36, 1989, pp. 199–224.

[35] Garwood, S. J., Davey, T. G., and Wong, Y. C., "The Effect of Biaxial Loading on A533B in the Ductile/Brittle Transition," *Fracture Mechanics: Twenty-First Symposium, ASTM STP 1074*, J. D. Gudas, J. A. Joyce, and E. M. Hackett, Eds., American Society for Testing and Materials, 1990, pp. 195–214.

[36] Naus, D. J., et al., "High-Temperature Crack-Arrest Behavior in 152-mm-Thick SEN Wide Plates of Quenched and Tempered A 533 Grade B Class I Steel," USNRC Report NUREG/CR-5330 (ORNL/TM-11083), April 1989.

[37] Naus, D. J., et al., "High-Temperature Crack-Arrest Tests Using 152-mm-Thick SEN Wide Plates of Low-Upper-Shelf Base Material: Tests WP-2.2 and WP-2.6," USNRC Report NUREG/CR-5450 (ORNL/TM-11352), Feb. 1990.

Walter G. Reuter,[1] Wilson R. Lloyd,[1] Richard L. Williamson,[1] James A. Smith,[2] and Jonathan S. Epstein[1]

Experimental Relationship Between Equivalent Plastic Strain and Constraint for Crack Initiation

REFERENCE: Reuter, W. G., Lloyd, W. R., Williamson, R. L., Smith, J. A., and Epstein, J. S., **"Experimental Relationship Between Equivalent Plastic Strain and Constraint for Crack Initiation,"** *Fracture Mechanics: Twenty-Third Symposium, ASTM STP 1189,* Ravinder Chona, Ed., American Society for Testing and Materials, Philadelphia, 1993, pp. 55–79.

ABSTRACT: The applicability of fracture mechanics data generated from standard fracture toughness specimens in predicting structural integrity is often a concern. For elastic-plastic conditions, a second parameter identified as "constraint" (hydrostatic stress divided by the equivalent stress) is being used to link different specimen/flaw configurations, thus providing a mechanism for using data generated from standard fracture toughness specimens to predict structural integrity. Much of the literature is concerned with the difference in constraint between specimens and a structure, while little effort is being given to investigating the sensitivity of the crack initiation process to constraint for a given material. This paper presents experimental results relating crack initiation processes to constraint for a ferritic steel and an aluminum-based alloy.

KEY WORDS: tension tests, equivalent plastic strain, constraint, crack initiation, fracture mechanics

This paper addresses one of the concerns associated with using small, standard fracture toughness specimens to accurately predict structural integrity. The concern is the effect on fracture of the difference in constraint between the fracture toughness specimen and the structural component that arises from their different configurations. A major part of this concern is the material's fracture sensitivity to constraint, which has not been quantified. Previous work [*1*] used specimens containing surface cracks to simulate structural components for comparison with crack-tip opening displacement (CTOD) measurements associated with initiation of crack growth in single-edge notch bend, SE(B); compact tension, C(T); and middle crack tension panels M(T). These specimens exhibited different values of constraint.

These results [*1*] established that the apparent correlation between constraint and CTOD associated with crack growth initiation depends on the definition of crack growth initiation. Constraint was defined as the hydrostatic stress divided by the equivalent stress, where the latter is based on the von Mises yielding criterion. The variation in the correlations between constraint and CTOD was due to the substantial ranges observed in the slopes of the CTOD versus crack growth (Δa) plots for the different specimen geometries tested. Hancock et al. [*2*] concluded that crack growth initiation in the A710 steel used in this work is sensitive to constraint. This conclusion is based on defining crack initiation as crack growth of 200 μm.

[1] Principal engineer, engineering specialist, and senior engineering specialists, respectively, Idaho National Engineering Laboratory, P.O. Box 1625, Idaho Falls, ID 83415.
[2] Graduate student, Texas A&M University, College Station, TX 77843.

Because crack initiation was a dimple rupture event, tension specimens were tested to quantify the sensitivity to constraint of crack initiation. Given the uncertainty of the relationship between constraint and initiation of cracking for A710 steel, a second material (6061-T6 aluminum) was studied to examine possible differences in crack initiation sensitivity to constraint. Sensitivity to constraint is related to microstructural features associated with initiation of holes (voids) and their subsequent coalescence. The significant difference in the volume fraction of second-phase particles, as well as the particle sizes, between the two materials was expected to produce differences in sensitivity of the crack initiation process to constraint.

Metallurgical factors associated with particle size and shape, as well as the strength of the particle and of the bond between the particle and matrix, will affect the sensitivity of crack initiation to constraint. For example, Cox and Low [*3*] suggested that stress triaxiality does not have a significant effect on void formation. In their work, the AISI 4340 contained manganese sulfide (MnS) inclusions and the 18-Ni, 200 grade, maraging steel contained titanium carbonitride inclusions. They concluded that the degree of triaxiality had no discernible effect on fracture, and that void nucleation was dependent on the level of applied tensile stress.

These conclusions contrast with observations of Hirth and Froes [*4*] who suggested that triaxiality primarily influenced hole nucleation by particle/matrix decohesion. Recent work by Harvey and Jolles [*5*] showed differences in microvoid density as a function of constraint. These observations suggest that it is necessary to quantify how a specific material's fracture behavior is affected by constraint. This may be done by testing different fracture toughness specimens that include surface cracks or tension specimens with varying degrees of constraint. The tension specimens used in this study were similar to those used by Hancock and MacKenzie [*6*].

Experimental Procedures

Tests were conducted at 20°C on specimens fabricated from as-rolled ASTM A710 steel and from 6061-T6 aluminum. Their chemistry and mechanical physical properties are presented in Table 1.

Specimen Configuration and Constraint

Three axisymmetric tension specimen configurations (Fig. 1) were used to measure the critical strain for initiation of dimple rupture as a function of constraint. Finite-element models were developed to predict the stress and strain fields during tensile loading of these specimens. Figure 2 shows the initial computational mesh for a sample notch configuration. Because of symmetry, only a portion of each specimen was modeled. Axisymmetric quadratic elements were employed, with the mesh refined in the notch region where large stress and strain gradients were observed. Geometric nonlinearity effects were included in the analyses. Loading

TABLE 1—*Chemistry and mechanical and physical properties.*

A710
0.05 C, 0.47 Mn, 0.010 P, 0.004 S, 0.25 Si, 0.74 Cr, 0.85 Ni, 0.21 Mo, 1.20 Cu, 0.038 Cb, and balance Fe
σ_{ys} = 470 MPa, σ_{ut} = 636 MPa, E = 208.4 GPa, ν = 0.256
6061-T6 ALUMINUM
0.64 Si, 0.6 Fe, 0.33 Cu, 0.13 Mn, 1.1 Mg, 0.23 Cr, 0.23 Zn, 0.10 Ti, and balance Al
σ_{ys} = 228 MPa, σ_{ut} = 290 MPa, E = 69 GPa, ν = 0.33

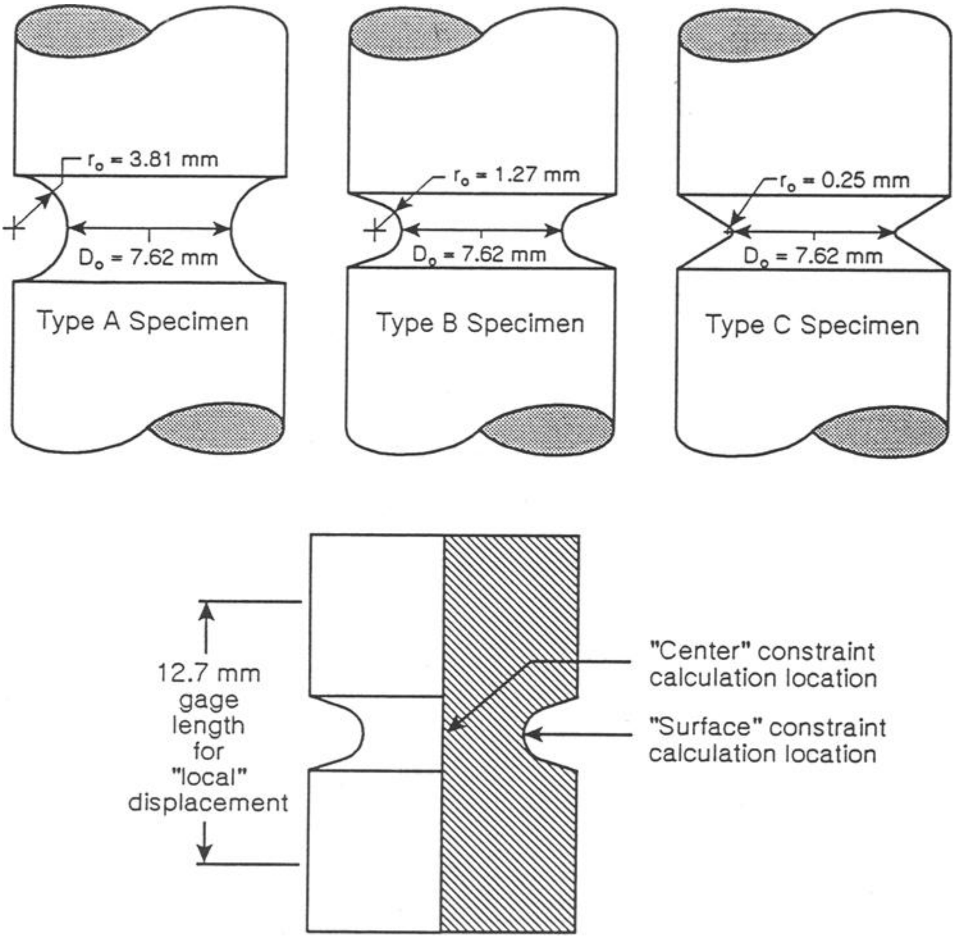

FIG. 1—*Schematic of notched tension specimens. Four integration points were used in each element for which solutions were calculated.*

resulted from the application of a uniform displacement along the top boundary of the specimen. Material response was simulated assuming elastic-plastic behavior based on a von Mises yielding condition and isotropic hardening. The true stress-true strain plots for both the steel and aluminum materials, provided in Fig. 3, were used for these calculations.

Constraint is defined as the hydrostatic stress ($\sigma' = \frac{1}{3}\sigma_{kk}$) divided by the von Mises equivalent stress

$$\bar{\sigma} = \sqrt{\frac{3}{2} S_{ij} S_{ij}} \tag{1}$$

where

σ_{kk} = the trace of the stress tensor, and
S_{ij} = the components of the stress deviator tensor.

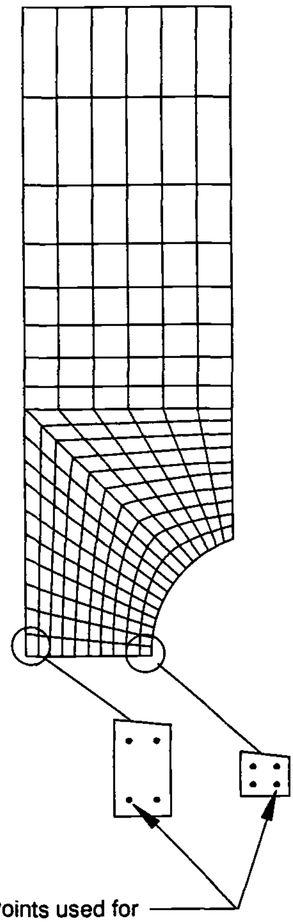

FIG. 2—*Mesh plot for notched tension specimens.*

The constraint was quantified at the center of the small diameter (D_0) and at the surface of the notch root, see Fig. 2. The ABAQUS finite-element computer code [7] was used to quantify the constraint, the local stress, and the equivalent plastic strain

$$\bar{\epsilon}_p = \sqrt{\frac{2}{3}\epsilon_{ij}^p\epsilon_{ij}^p} \tag{2}$$

where ϵ_{ij}^p are the components of the plastic strain tensor, as a function of applied strain as measured by the ratio of the original small diameter (D_0) to the instantaneous small diameter (D). All stress results reported from ABAQUS are in terms of the Cauchy stress definition. Figure 4 shows plots of the equivalent plastic strain and constraint versus D_0/D for the three A710 specimen geometries. Changes in notch root radii were included in the calculations of constraint as a function of plastic flow.

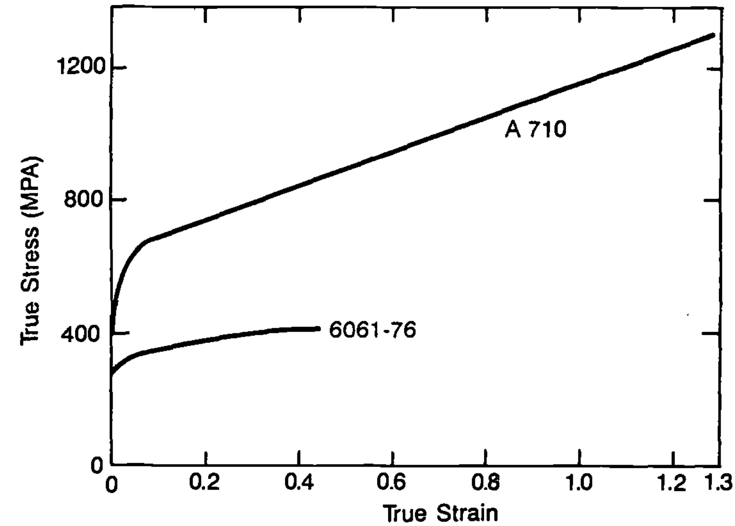

FIG. 3—*True stress-true strain plots for A710 steel and 6061-T6 aluminum.*

Techniques Used to Locate Cracks

Measurements of void size, shape, and location were made using both metallographic and microtopographic techniques. In the metallographic examinations, a longitudinal section through the gage region of the tension specimen was examined using light microscopy; material was removed from the sample in nominally 0.64-mm (0.025-in.) increments between examinations. The microtopographic technique was used on specimens tested to failure. The topography of the fracture surface was measured and various software was used to reconstruct the void initiation and growth process. The magnitude and location of dimple formation was measured by each technique as a function of applied strain (D_0/D) to estimate the local plastic strain required for void initiation as a function of constraint. These two techniques provided complementary results. Crack initiation was arbitrarily defined as the local stress, strain, and constraint associated with a crack having a length of nominally 0.05 mm, which is about two grain diameters for A710 and one grain diameter for 6061-T6 aluminum.

Reconstruction of Crack Growth Process

Microtopography allows reconstruction of the crack growth process. This provides a basis for identifying the crack initiation location and determining the relative crack growth (given at least a small amount of plasticity) in test specimens loaded to failure. The microtopographic data collection system is analogous to systems used to develop topographic land maps. The area of interest on the two mating fracture surfaces must be exposed completely to give access to the high-resolution laser range finder. Then, local height measurements over the area of interest on the two mating fracture surfaces are made. By maintaining registration between the two surfaces and using a common height reference plane, mathematical operations can be performed on the raw data that result in a "topographic map" of the height difference, that is, the void volume, at the instant of fracture. Various aspects of the fracture process can be investigated by using this technique with selective specimen loading schemes, including periods of fatigue, monotonic loading, and cleavage.

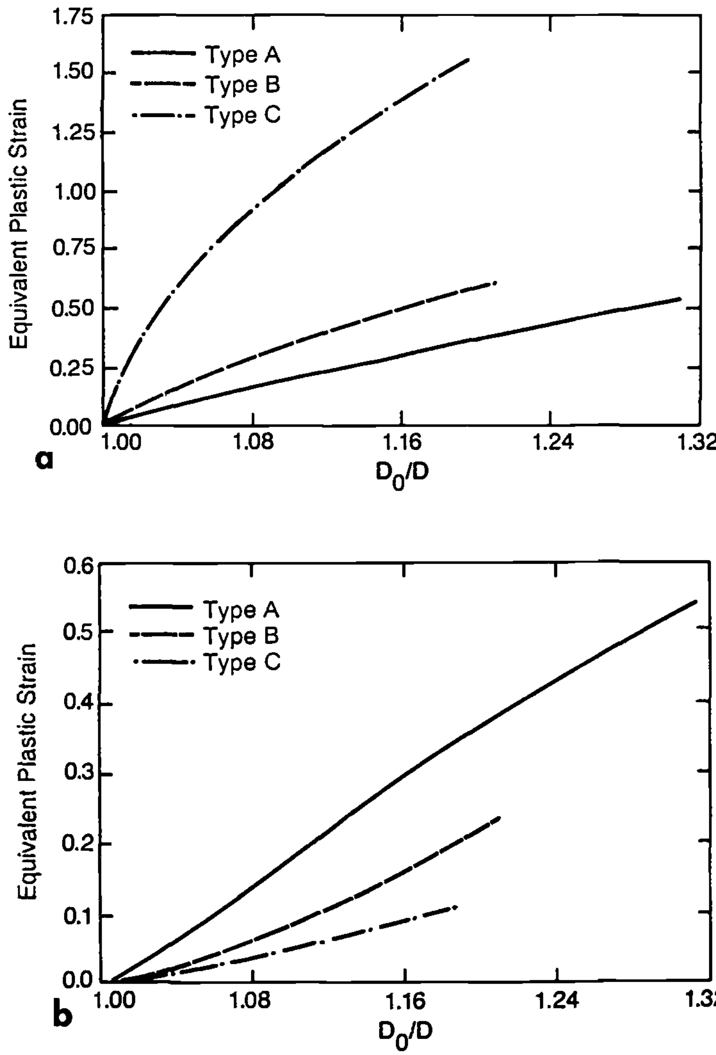

(*a*) Equivalent plastic strain at the notch surface.
(*b*) Equivalent plastic strain at center.

FIG. 4—*Numerical results for equivalent plastic strain and constraint versus* D_0/D.

From the void volume map generated by the microtopography system, three things can be determined. First, the areas of crack initiation can be identified. Second, the direction and (qualitatively) relative amount of crack extension from initiation sites can be determined; and third, the degree of plastic deformation associated with onset of crack growth can be assessed. These determinations are based on the fact that as a ductile crack grows, the fracture surfaces in the wake have continuously increasing separation as a function of crack growth. The actual amount of separation is dependent upon, at a minimum, the von Mises stress in the crack-tip process zone, the material's constitutive behavior (amount of hardening), and the instantaneous crack shape, both locally and globally. The general premise is that the fracture surface

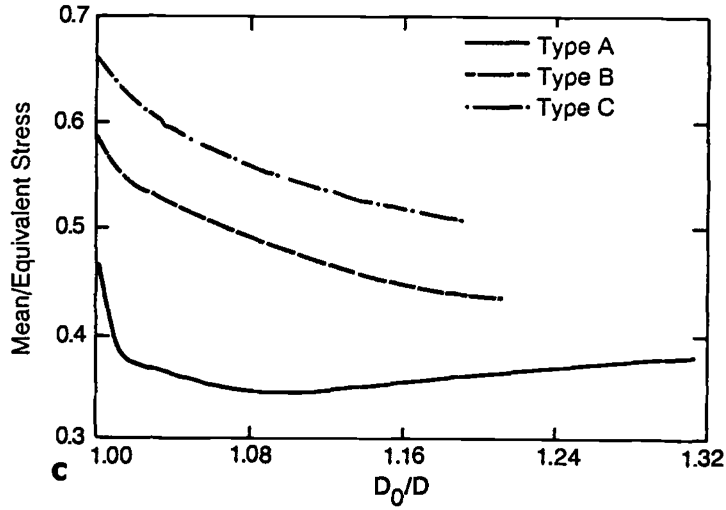

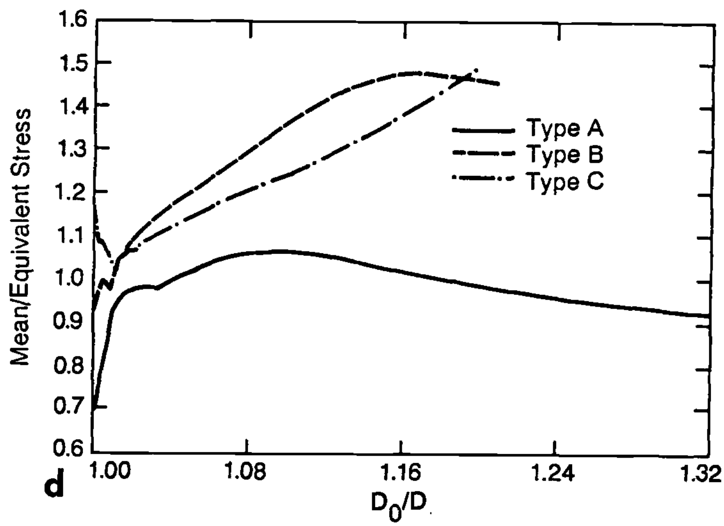

(*c*) Constraint at the notch surface.
(*d*) Constraint at center.
FIG. 4—*Continued.*

coinciding with larger separations (void "height") at the instant of failure actually separated earlier in the fracture process than points with less separation at failure. Constant void height contour lines thus show the initiation sites and subsequent growth when successive contours are viewed in sequence. Potential errors of this process and the methodology used to manage these errors are presented in the Appendix.

As noted in Fig. 1, a "local" specimen displacement (extension) was measured over a 12.7-mm gage length, axially spanning the entire reduced (notch) section of the test specimens. As a first approximation, it was assumed that this displacement had a 1:1 correlation with instantaneous crack opening, that is, an increment of remote displacement corresponds to an equal

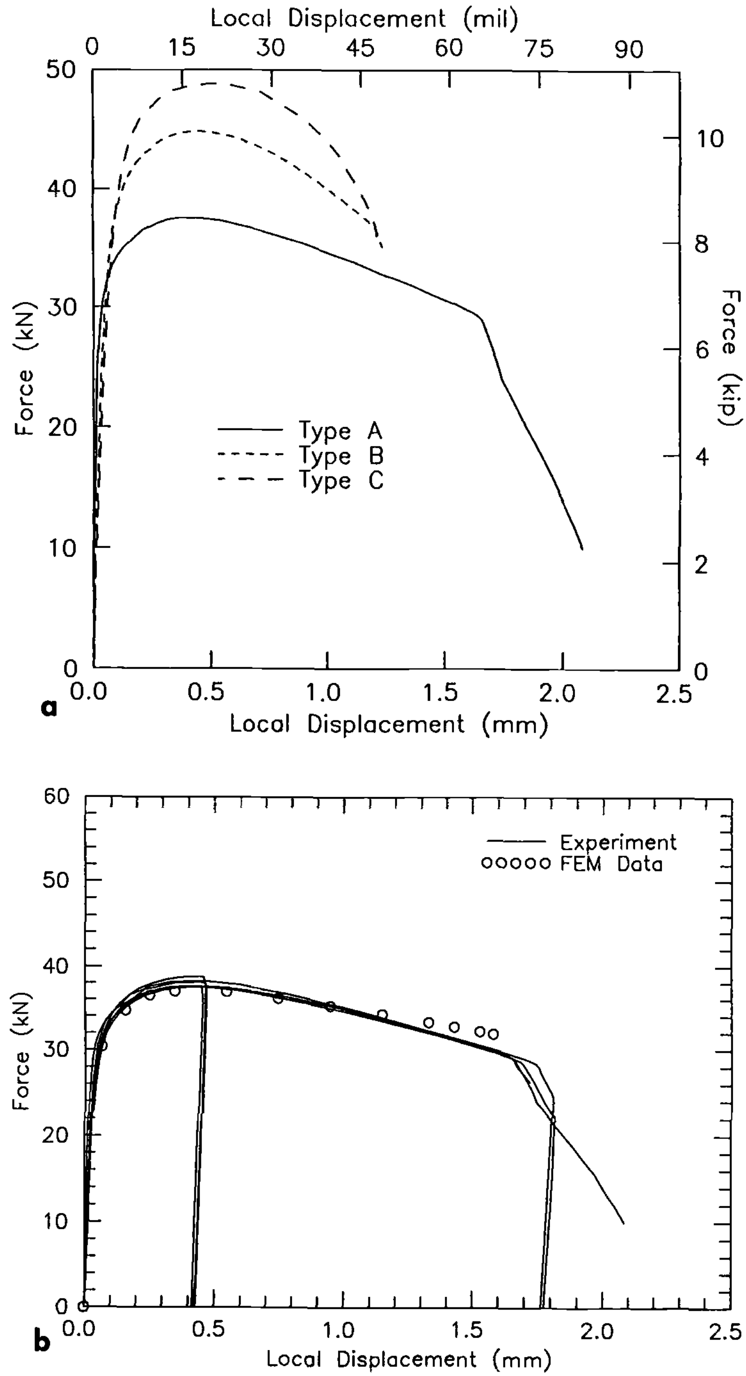

(*a*) Representative curves for specimen Types A, B, and C.
(*b*) Type A specimens.

FIG. 5—*Force versus local displacement.*

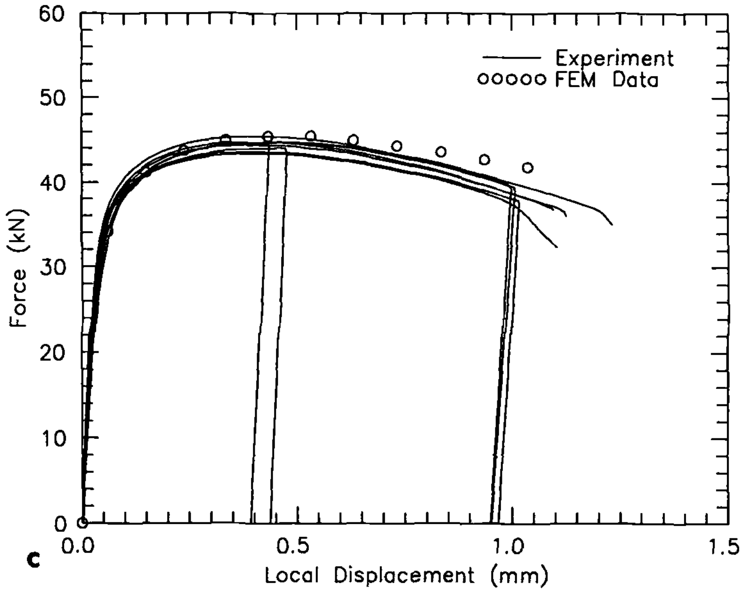

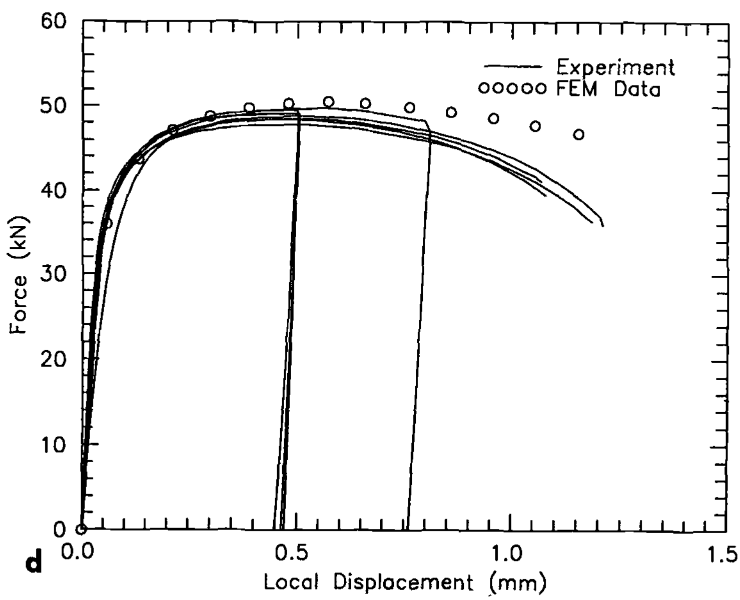

(*c*) Type B specimens.
(*d*) Type C specimens.

FIG. 5—*Continued.*

increment of crack opening at the initiation point or points. For the later stages of crack growth, just before final specimen failure, this is probably not unreasonable. However, there are errors in this approach when extrapolating back to the point of crack initiation from the displacement at failure. Some of these are discussed later.

Results

Tension Tests

For the three different specimen configurations and two materials, there was good agreement between load-load point displacement plots for replicate specimens.

A710—Figure 5*a* shows representative load-load point displacement plots for notched tension specimens tested at 20°C. Figures 5*b*, *c*, and *d* show variations in load-load point displacement plots for specimen Types A, B, and C, respectively. Also included are predictions based on numerical analysis techniques. Many of the specimens that were loaded and then unloaded weer examined metallographically. Some of the specimens that failed during the test were examined by microtopography. All of the Type A specimens failed by dimple rupture. All of the Type B and C specimens failed by cleavage after experiencing some ductile (dimple) rupture. Figure 6 shows the fracture surface of Type B and C specimens where ductile fracture initiated on the central region and at the perimeter, respectively.

6061-T6—Specimen test results were similar to those shown in Fig. 5. Some of the specimens that were loaded and then unloaded were examined metallographically, and some of the specimens that failed during the test were examined by microtopography.

Metallography

A710 Steel—The specimens that were tested are listed in Table 2 with a summary of the results. Those specimens designated "microscopy," for posttest examination, were mounted and examined at each of several polishing steps, as explained earlier, to locate the source of cracking and identify the nominal values of D_0/D associated with crack initiation. For this evaluation, cracks/holes of nominally 0.05 mm long were defined as initiation. Figure 7 is a summary plot of the equivalent plastic strain versus constraint. Closed symbols denote where cracking was detected and the open symbols designate results where cracking was not detected. A substantial trend of decreasing equivalent plastic strain with increasing constraint for crack initiation is evident. The microstructural features associated with this trend were not identified. Figures 8, 9, and 10 show the extent of cracking in Specimens A-2, B-1, and C-4, respectively. For Type A specimens, cracking initiated in the central region and continued in a dimple rupture process until final fracture by shear. For Type B specimens, the crack generally initiated in the central region. Cracking was just starting to initiate at the surface for Specimen B-5, but the extent of cracking at the surface was nominally 0.008 to 0.030 mm at only a few locations, well short of the 0.05 mm defined as initiation. This specimen configuration experienced some dimple rupture followed by cleavage fracture. For Type C specimens, the cracking initiated next to the tip of the notch. This specimen configuration experienced dimple rupture around the perimeter before failing by cleavage.

6061-T6—Similar to the approach used for A710, cracks/holes nominally 0.05 mm long were defined as crack initiation. Figure 11 is a summary plot of the equivalent plastic strain versus constraint; again, closed symbols denote cracking. Here also a trend of decreasing equivalent plastic strain with increasing constraint for crack initiation is evident. Figures 12

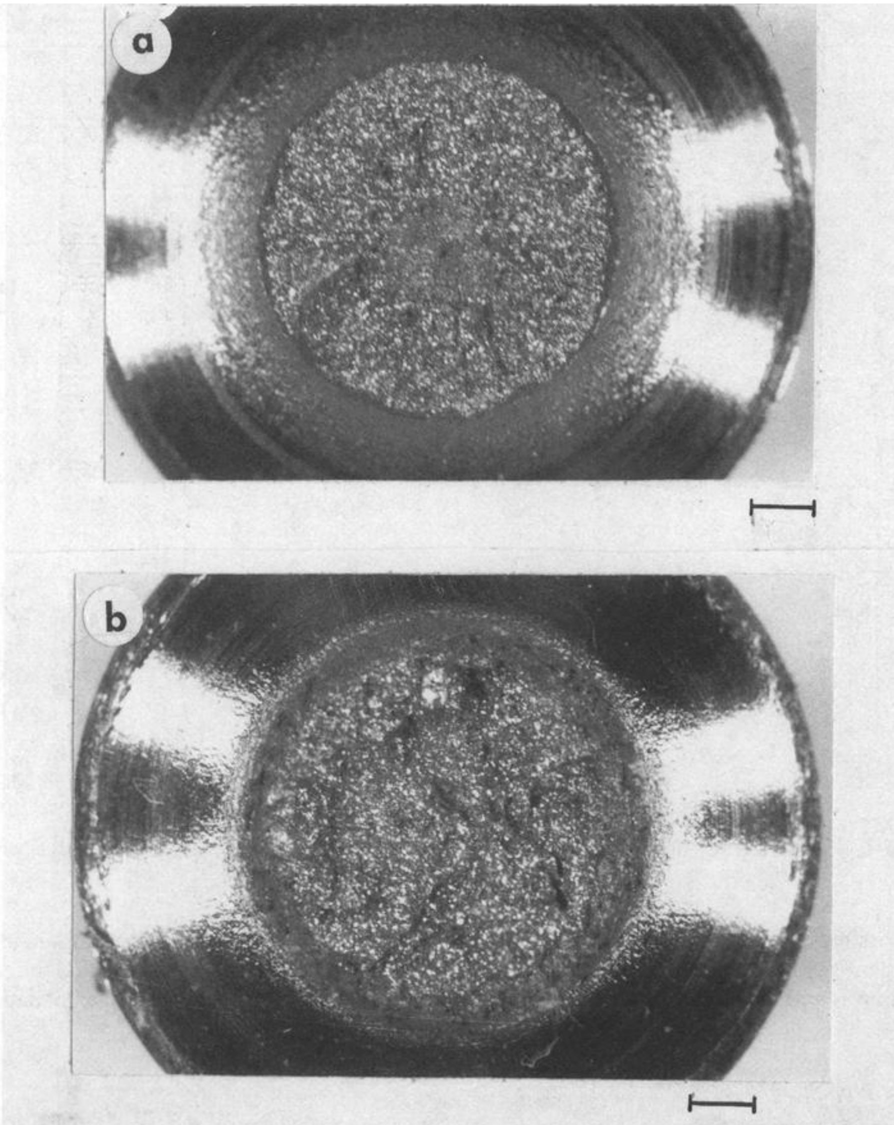

FIG. 6—*Fracture surfaces of specimens where ductile fracture initiated* (a) *at the central region (Type B specimen) and* (b) *at the perimeter (Type C specimen;)* ⊢⊣ = *1 mm.*

and 13 show the extent of cracking in Specimens A-4 and C-2, respectively. Because the as-polished surfaces of the aluminum contain many particles, making it difficult to separate cracks from artifacts, the local cracks are circled in these figures.

A comparison between Figs. 7 and 11 shows a similar trend, as expected, but the A710 results are to the right of the 6061-T6 results—the equivalent plastic strain required to initiate a crack is somewhat smaller for 6061-T6 than for A710 at the same constraint. Obviously, it

TABLE 2—*Summary of tension test results for A710.*

Specimen Number	Maximum Stress, MPa	Final Stress, MPa	Final Elongation, mm	D_0/D	Posttest Exam
A-1	291	291	0.44	1.061	MT[a]
A-2	291	173	1.81	1.35	MC[b]
A-6	297	222	1.66	1.43	...
A-7	295	295	0.46	1.06	MT
A-8	294	192	1.80	1.37	...
A-9	294	227	2.20	1.48	MT
B-1	352	309	1.01	1.198	MC
B-3	351	290	1.09	...	...
B-4	339	290	1.02	...	MT
B-5	340	293	1.02	1.214	MC
B-6	342	289	1.09	...	MT
B-7	346	346	0.44	1.068	MT
B-8	355	311	1.00	1.195	...
B-9	343	343	0.47	1.071	MC
B-10	350	288	1.12	...	...
C-1	387	387	0.50	1.068	MT
C-2	389	377	0.84	1.115	MT
C-3	383	383	0.50	1.072	MT
C-4	384	374	1.58	1.123	MC
C-5	389	336	1.05	1.172	...
C-6	380	312	1.07	...	...
C-7	372	282	1.19	...	...
C-8	382	382	0.50	1.067	MT
C-9	381	327	1.07	...	...
C-10	379	341	1.03	1.168	MC
C-3X	...	...	...	...	MT

[a] MT = microtopography.
[b] MC = sectioned and microscopy.

is possible to say that the 6061-T6 is more brittle than the A710. But additional work relative to identifying particles that initiated dimples, and their distribution and location, and the conditions required to initiate a void and coalescence will be required to provide an explanation.

Microtopography

A710—For specimens tested to failure, it was observed that Type B and C specimens all failed by cleavage after some dimple rupture. Therefore, microtopography could quantify only the extent of dimple rupture prior to cleavage failure. Figure 6 shows that dimple rupture initiated in the central region for Specimen B-4 and at the surface for Specimen C-3. The microtopography results for Specimen A-9, shown in Figs. 14*a* through *e*, are profiles similar to those found in topographic maps. Figure 14*a* shows the portion of the specimen that had the largest separation; this is the region where dimples were first initiated. Figures 14*b* and *c* show additional dimple formations and subsequent coalescence. Finally, Figs. 14*d* and *e* show the fracture process just prior to failure. The small squares observed in the figures are most likely due to bad data, as discussed in the Appendix.

The microtopography results are summarized in Table 3. These data were used to estimate

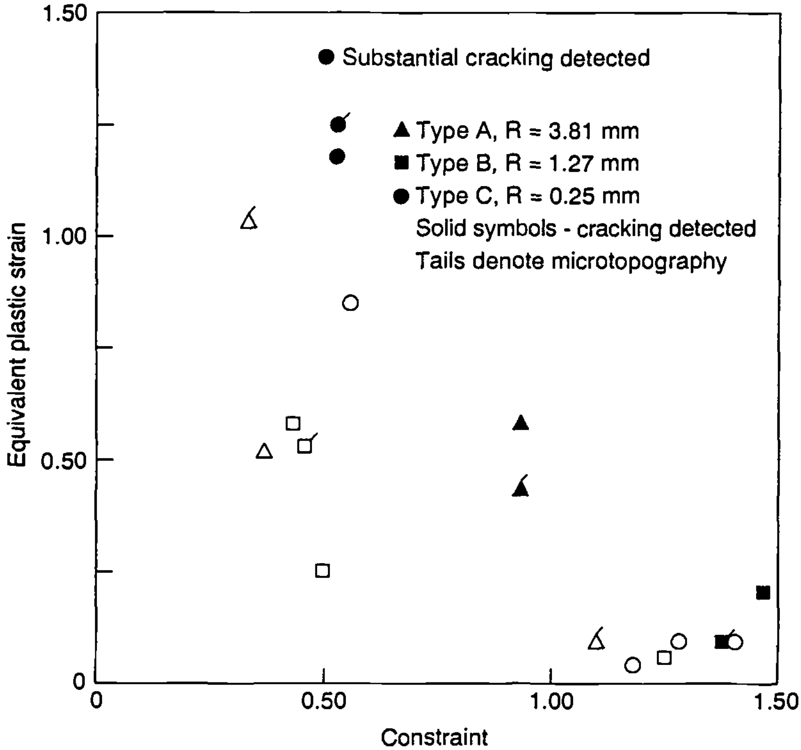

FIG. 7—*Equivalent plastic strain versus constraint for A710 steel.*

the stress, strain, and constraint associated with each initiation event. These results are included in Fig. 7. It is obvious that the microtopography results agreed well with the microscopy data in that the closed symbols with a tail (denoting microtopography) are adjacent to the other closed symbols. In Fig. 14, it is evident that cracking initiated in the central region and that initiation occurred at nominally 0.80 to 0.90 mm surface separation prior to failure.

6061-T6—The microtopography measurements revealed that fracture of the tension specimens was influenced significantly by texturing that occurred during rolling of the plate. The present technique did not provide useful information for these specimens.

TABLE 3—*Summary of A710 microtopography results.*

Notch Configuration	Location of Initiation	Plastic Displacement
A	center	0.43 (0.96)[a]
B	center	0.085 (1.37)
C	surface	1.25 (0.53)

[a] Constraint is provided in parentheses.

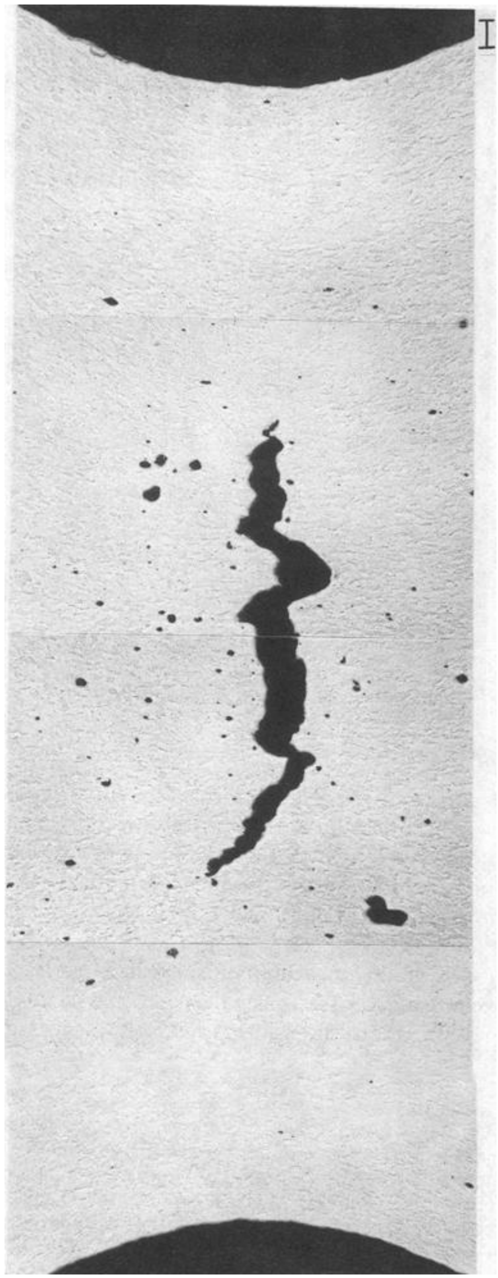

FIG. 8—*Photograph of substantial cracking in an A-notch A710 specimen;* I *= 100* μm.

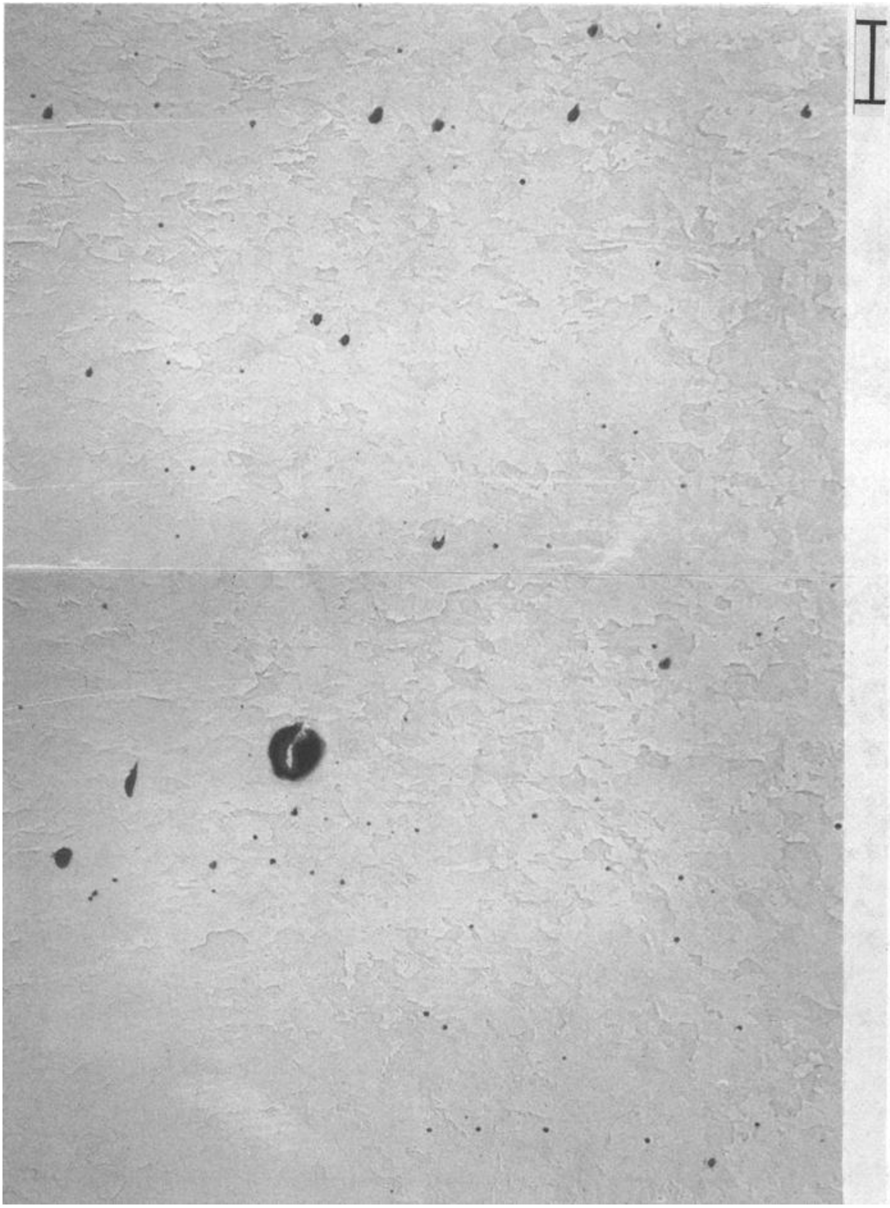

FIG. 9—*Photograph of cracking in a B-notch A710 specimen;* ⊢⊣ = *100 μm.*

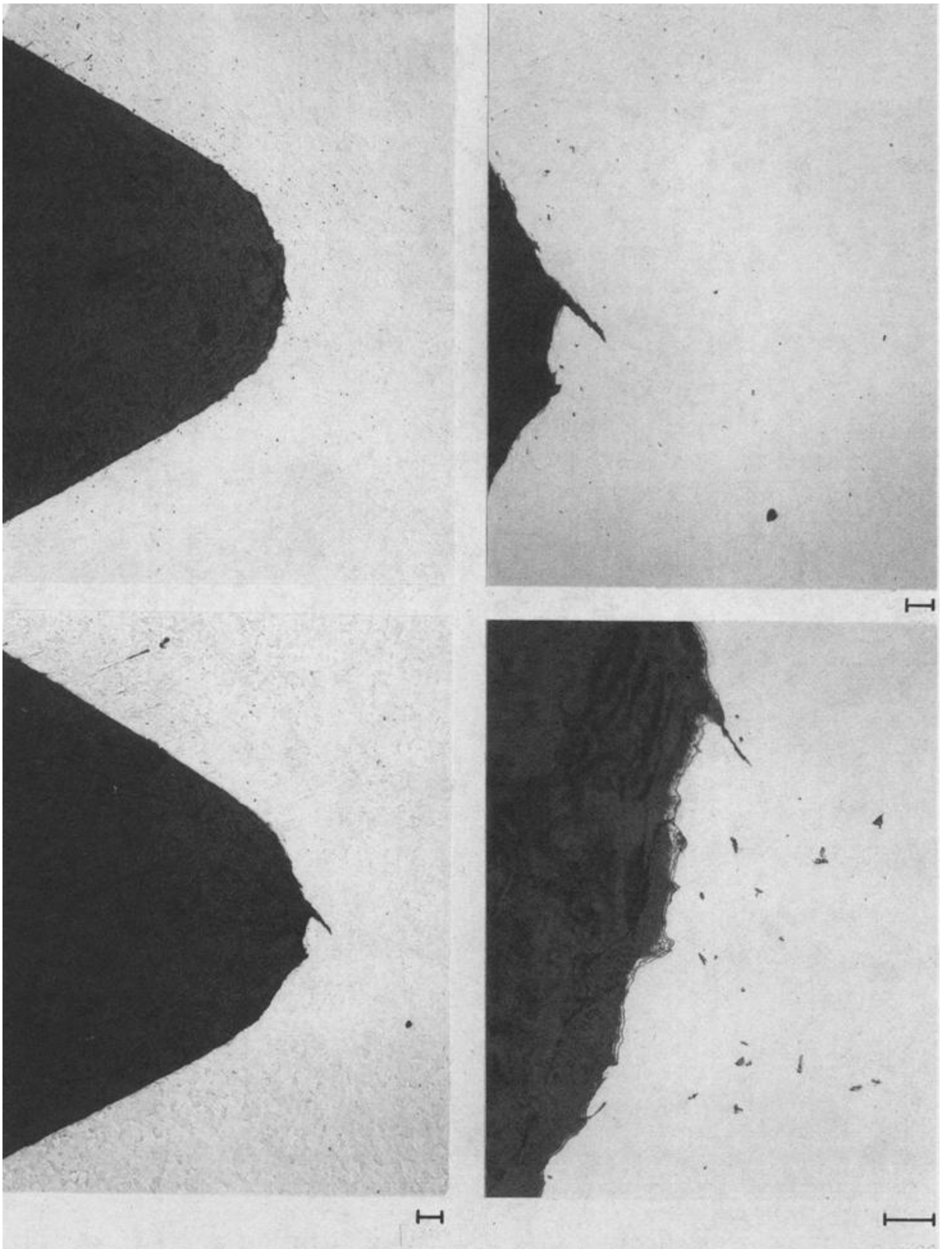

FIG. 10—*Photograph of cracking at notch tip in a C-notch A710 specimen;* ⊢⊣ *= 100 μm; and* ⊢ *= 25 μm.*

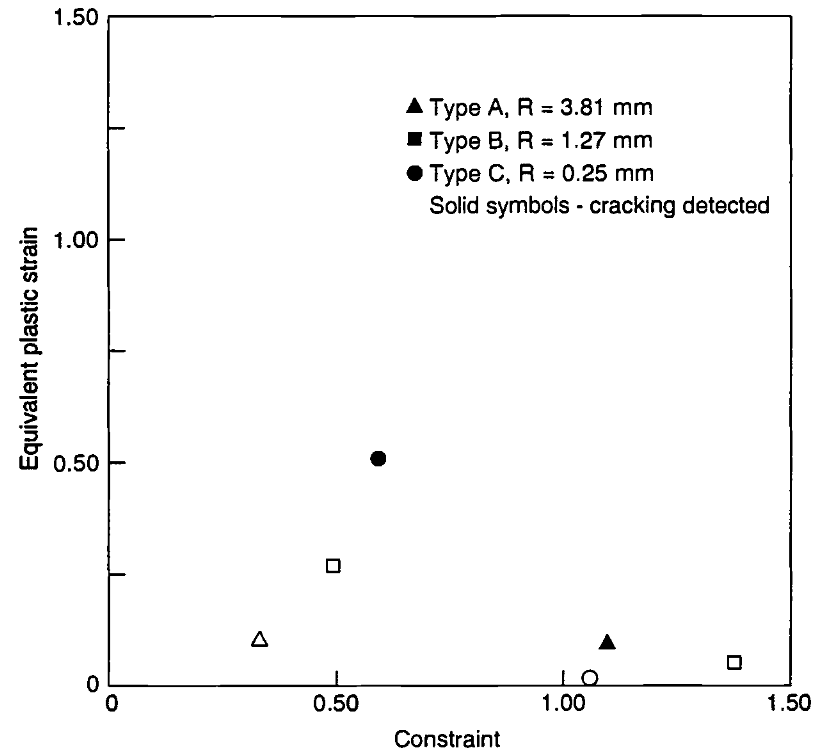

FIG. 11—*Equivalent plastic strain versus constraint for 6061-T6 aluminum.*

Summary

A710—The test data summarized in Fig. 7 shows a significant trend between equivalent plastic strain and constraint associated with initiation of cracking. This observation is in agreement with work by Hancock et al. [*2*], Hirth and Froes [*4*], and Harvey and Jolles [*5*]. The constraint in Hancock et al. [*2*] is based on the ratio of T/σ_0 where T is the T-stress, see Eq 3,

$$\sigma_{ij} = \frac{K}{\sqrt{2\pi r}} f_{ij}(\theta) + T_{ij}\delta_{ii}\delta_{ij} \tag{3}$$

and σ_0 is the yield strength. Rice [*8*] suggested the T-stress term for the second term of the Williams' expansion [*9*]. Obviously, this constraint term is not quantified in the same manner as constraint is in this paper. Hancock et al. [*2*] included a plot relating T/σ_0 to constraint, as defined here, showing that constraint ranged from 2 to 3. The constraint term in Reuter et al. [*1*], defined in the same manner as in this paper, shows values ranging from nominally 1.8 to 2.8. These values are considerably larger than the maximum of 1.5 used in Fig. 7. Figure 7 shows that the equivalent plastic strain, associated with initiation of cracks, ranges from 1.4 to 0.20 for constraint ranging from 0.5 to 1.5. But, when constraint exceeds 1.5, the critical value of equivalent plastic strain is limited to 0.20 or less. Therefore, for fracture toughness specimens, where constraint typically ranges from 1.8 to 2.8, there is only a limited amount of equivalent plastic strain available for initiation of a crack. The observation that crack initia-

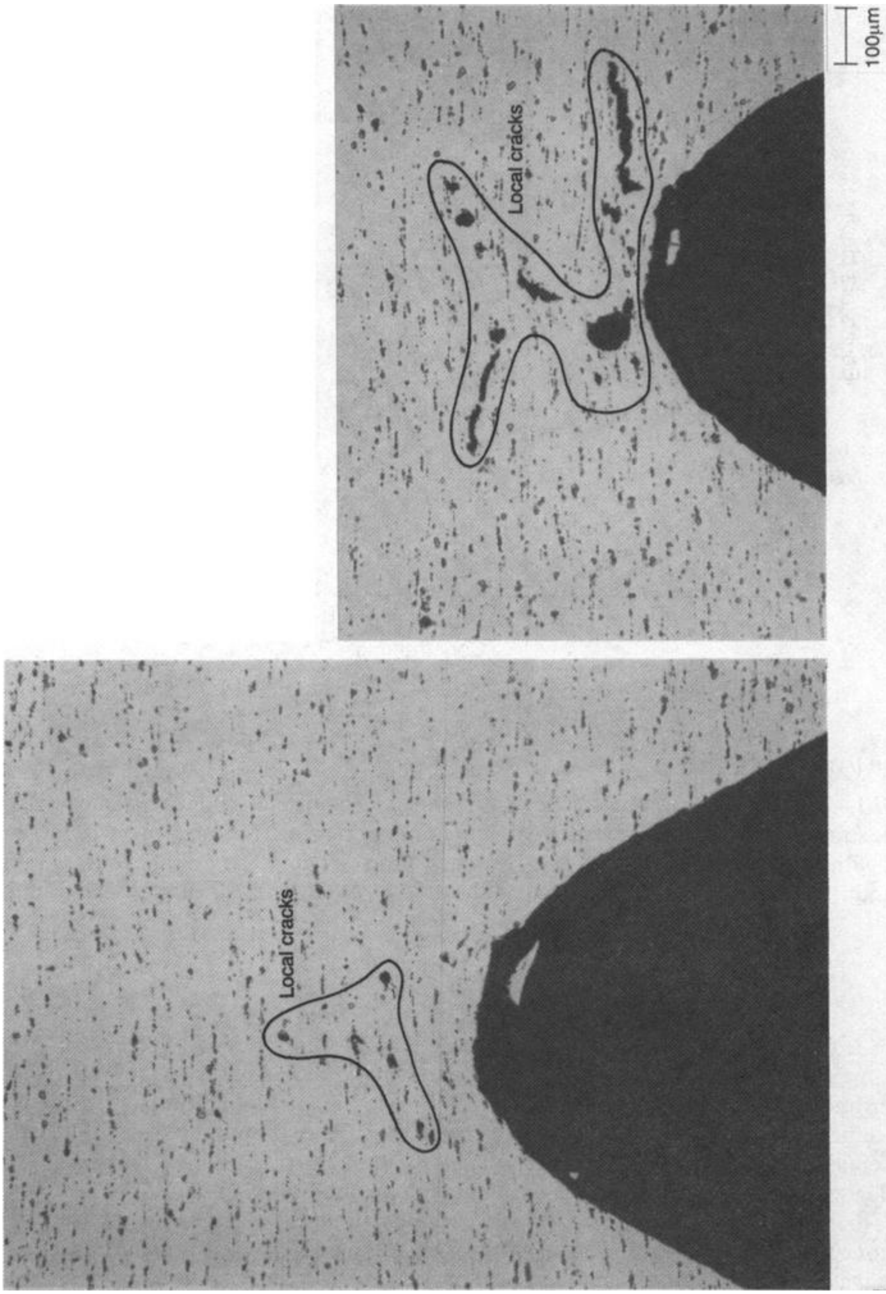

FIG. 12—*Photograph of cracking in an A-notch 6061-T6 specimen.*

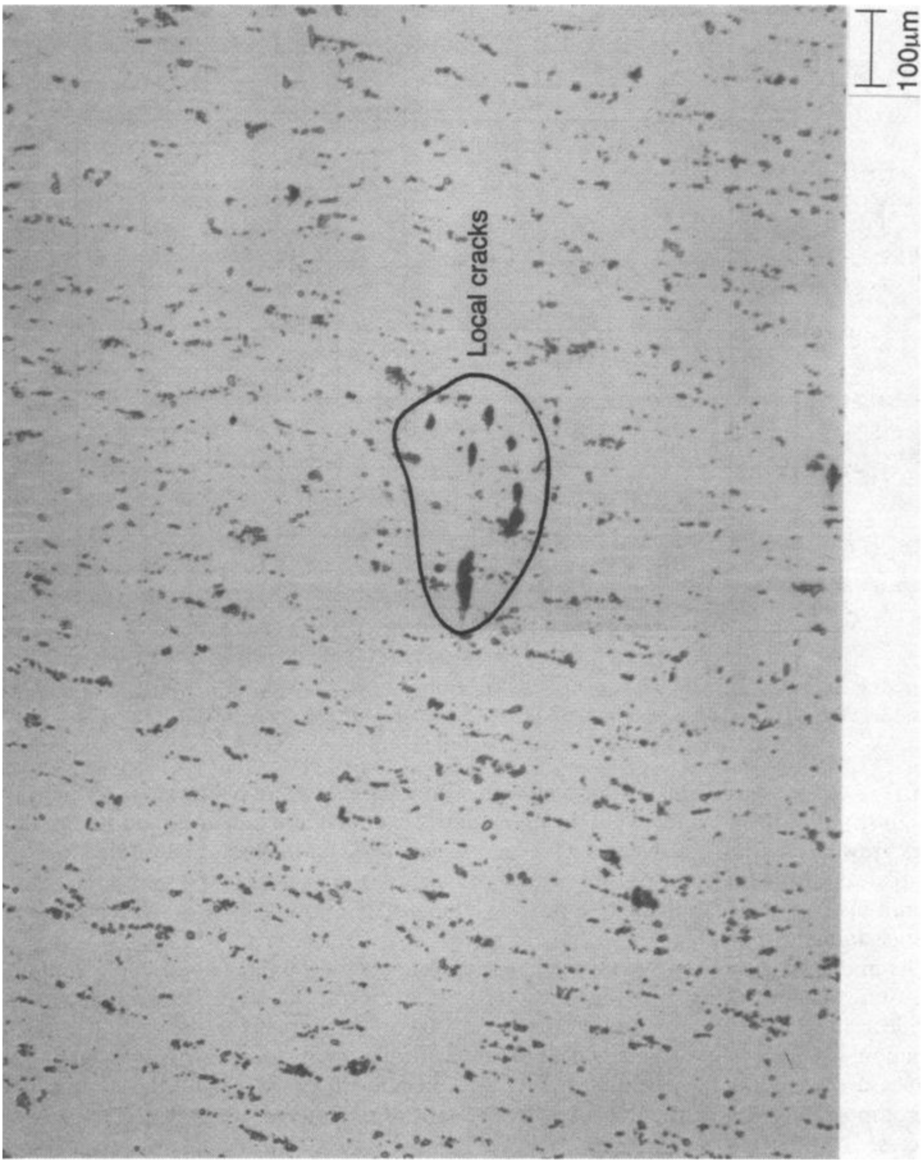

FIG. 13—*Photograph of cracking in a C-notch 6061-T6 specimen.*

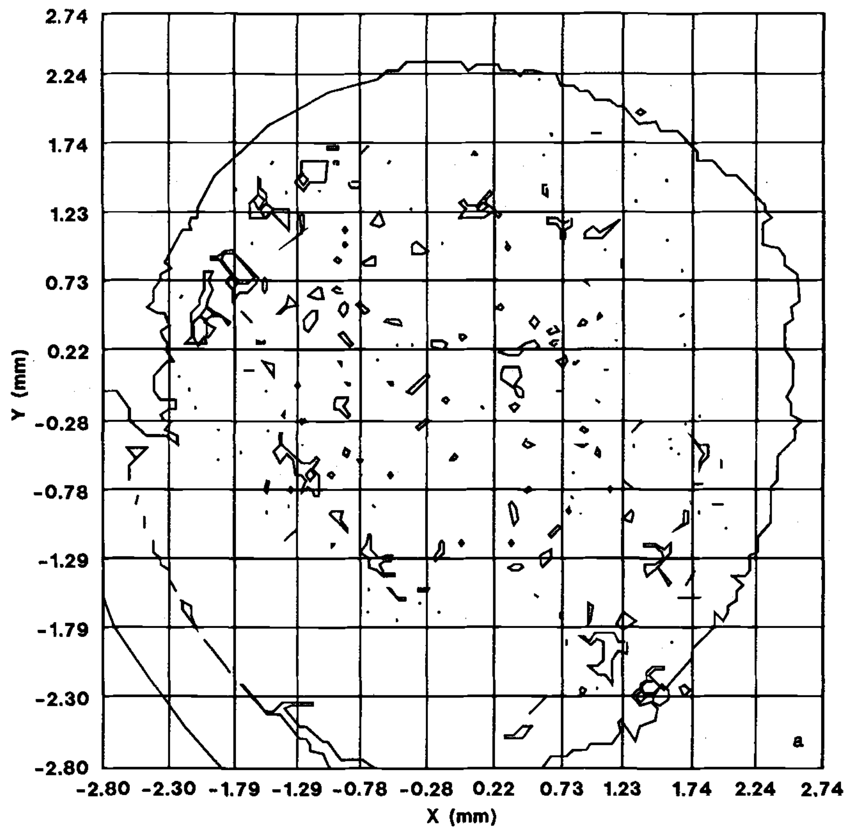

FIG. 14—*Microtopography results for an A-notch A710 specimen:* (a) *at 100 μm separation,* (b) *at 200 μm separation,* (c) *at 300 μm separation,* (d) *at 400 μm separation, and* (e) *at 500 μm separation.*

tion, for a tension specimen, is associated with decreasing equivalent plastic strain for increasing constraint is in agreement with the observation, from fracture toughness specimens, that crack growth initiation is associated with decreasing CTOD for increasing constraint. A more complete comparison is not possible because the constraint values for the two types of tests did not overlap, nor is it possible to provide a quantitative comparison between equivalent plastic strain and CTOD.

The microtopography system provided useful test data for the three notch configurations, suggesting that it was possible to accurately reconstruct the fracture process in these specimens. Verification of the reconstruction process was based on comparison of the location of crack initiation and the constraint/equivalent plastic deformation associated with crack initiation as measured using both microtopography and metallography. Successful development of microtopography will considerably reduce the cost of obtaining data on the crack growth process.

6061-T6—This material was used to obtain a measure of the sensitivity of crack initiation to specific materials. As was noted earlier, Fig. 11 showed a significant trend between constraint and equivalent plastic strain associated with initiation of cracking for this material. The comparison of the relationships between constraint and equivalent plastic strain for the two

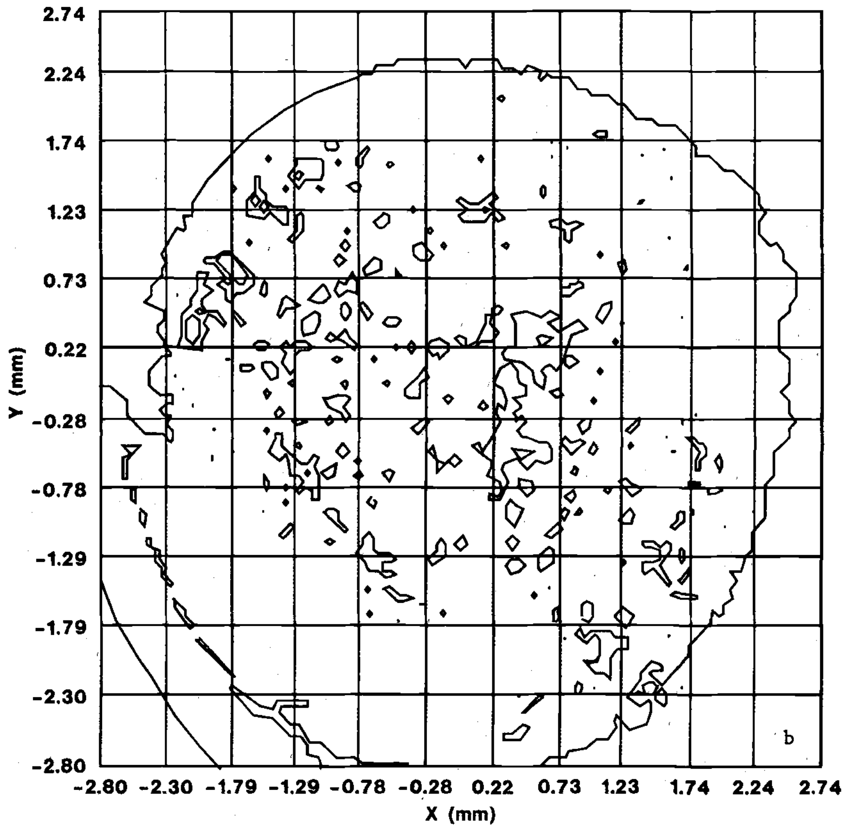

FIG. 14—*Continued.*

materials (Figs. 7 and 11) shows a significant difference between them. The additional work required to identify the particles that initiated dimple rupture, as well as their distribution and location, and the conditions required to initiate void formation and coalescence has not yet been performed.

Conclusions

The relationships between constraint and equivalent plastic strain at crack initiation for tension specimens fabricated from A710 and from 6061-T6 were identified. The observed sensitivity of equivalent plastic strain for crack initiation to constraint for the tension specimens fabricated from A710 is consistent with the conclusions of Reuter et al. [*1*] and Hancock et al. [*2*], who observed that crack growth initiation occurred at decreasing CTOD with increasing constraint. The constraint ranged from 0.5 to 1.5 for the tension specimens and from 1.8 to 2.8 for the fracture toughness specimens. From the tension test data, it is apparent that the equivalent plastic strain can range to a maximum of 0.2 for constraint in excess of 1.5. A quantitative relationship between equivalent plastic strain and CTOD is not available at this time.

The 6061-T6 showed a similar trend to the A710 in the relationship between equivalent

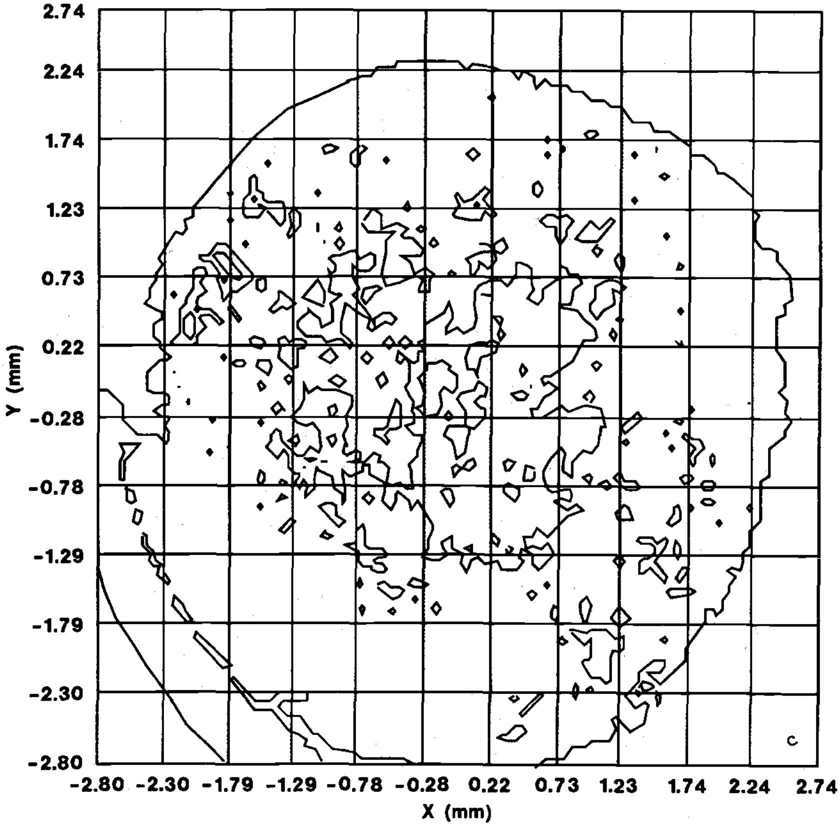

FIG. 14—*Continued.*

plastic strain and constraint, but the A710 data were shifted to a higher constraint. A definitive study relating microstructural features, for each material, to the crack initiation process as a function of constraint has not been performed.

Acknowledgments

This work was supported by the U.S. Department of Energy, Office of Energy Research, Office of Basic Energy Sciences, under DOE Contract No. DE-AC07-76ID01570. The authors express their appreciation to Dorothy A. Cullen for typing the manuscript and Gary L. Fletcher for metallography.

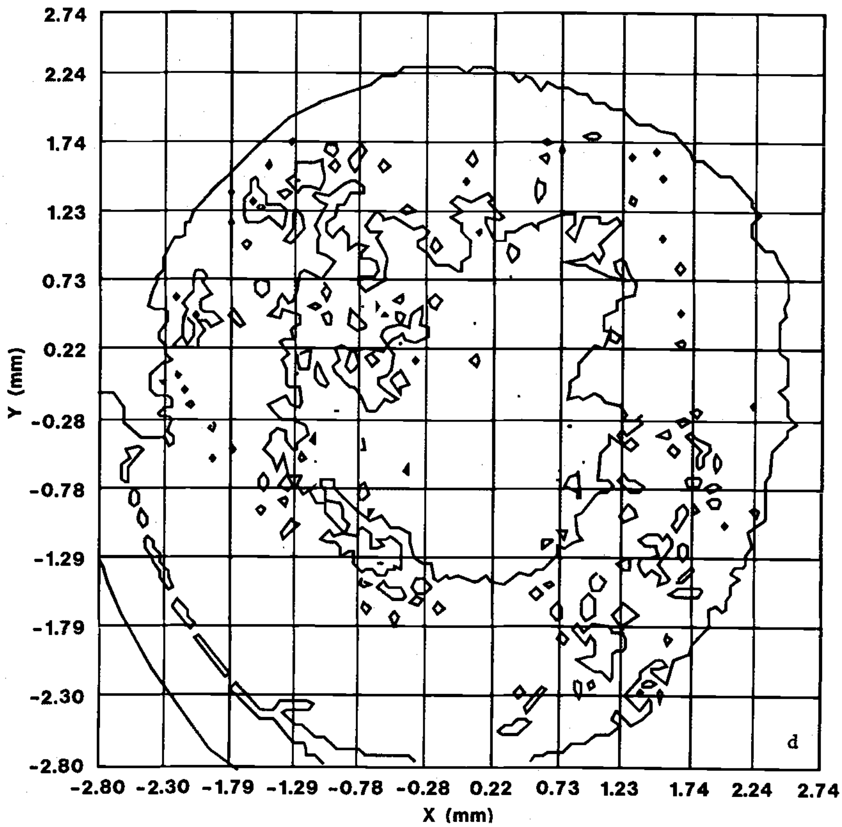

FIG. 14—*Continued.*

APPENDIX

Potential Error Sources and Error Management for Microtopography

The laser-point range sensor (PRS), which makes the actual height measurements, is somewhat sensitive to the reflective nature of the surface being measured. For irregular, specular surfaces, the PRS may have difficulty making a valid height reading; this is the case with a typical cleavage fracture in the A710 steels being measured. While Type A specimens failed solely by dimple rupture and Type C specimens showed mainly ductile fracture prior to ultimately failing by cleavage, the Type B specimens failed primarily by cleavage. Although it has not yet been used, a thin, diffusely reflecting coating may improve the PRS's ability to measure cleavage fracture surfaces.

Given that a certain percentage of locations in the scanned area will have a bad data flag on the height reading, some way of managing bad data points must be devised. The software and analysis techniques require data at regularly spaced intervals over the fracture surface. For this reason, scan points yielding bad data cannot be discarded nor ignored during data collection. Because of high measurement sensitivity, small spatial resolution, and (typically) highly irregular surface heights, extrapolation of surrounding "good" data to the point having a bad reading is not deemed (at present) an acceptable solution.

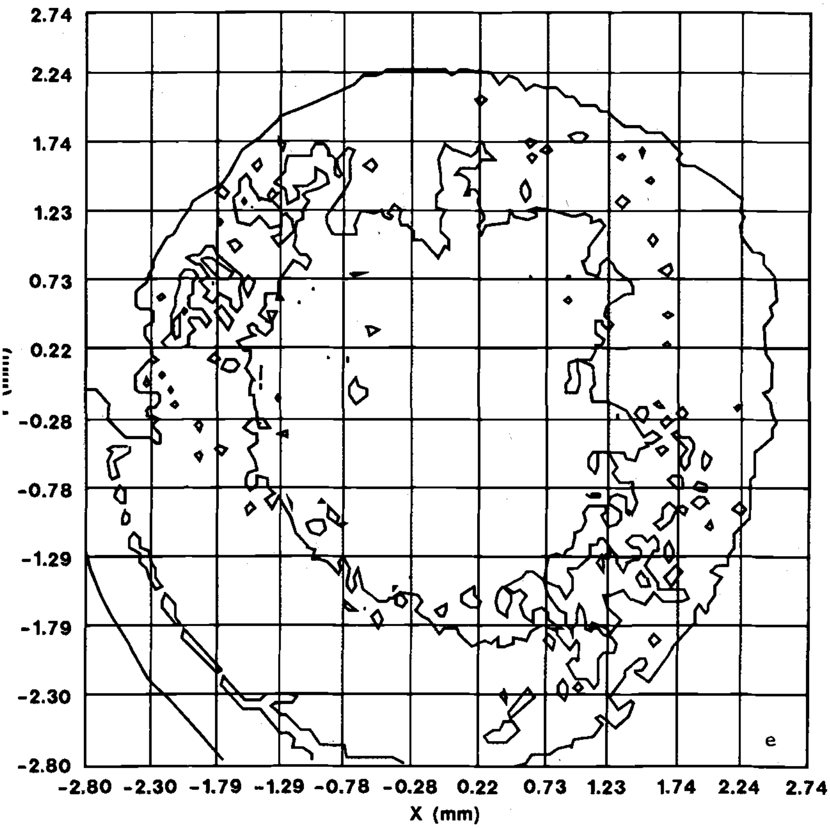

FIG. 14—*Continued.*

The current technique for managing bad data is to identify it as bad by adding a constant value to a selected decimal position that is higher than the resolution of the PRS. For example, if the PRS can measure to 0.1 μm, a constant can be added to the second decimal place to identify the reading as potentially bad, for example, xxx.x5. This height value can always be identified as bad in subsequent analyses, by checking for the nonzero value in the appropriate decimal position. For the purpose of graphing the data in topographic form, the bad data positions are set to a constant value lower than the minimum of the good values so that bad data areas appear as isolated points of low height on the contour maps. They are easy to identify visually and can be ignored in the qualitative interpretation of the "void height" contour maps. Other methods of managing bad data should be examined.

References

[*1*] Reuter, W. G., Graham, S. M., Lloyd, W. R., and Williamson, R. L., "Ability of Using Experimental Measurements of δ to Predict Crack Initiation for Structural Components," *Defect Assessment in Components—Fundamentals and Applications*, ESIS/EG F9, Mechanical Engineering Publications Ltd., London, U.K.

[*2*] Hancock, J. W., Reuter, W. G., and Parks, D. M., "Constraint and Toughness Parameterized by *T*," *Constraint Effects in Fracture, ASTM STP 1171*, E. M. Hackett, K.-H. Schwalbe, and R. H. Dodds, Jr., Eds., American Society for Testing and Materials, Philadelphia, 1993, pp. 21–40.

[3] Cox, T. B. and Low, J. R., Jr., *Metallurgical Transactions,* Vol. 5, 1974, pp. 1457–1470.
[4] Hirth, J. P. and Froes, F. H., "Interrelations Between Fracture Toughness and Other Mechanical Properties in Titanium Alloys," *Metallurgical Transactions, A,* Vol. 8A, July 1977, pp. 1165–1176.
[5] Harvey, D. P., II and Jolles, M. I., "Relationship Between Fractographic Features and Material Toughness," *Quantitative Methods in Fractography, ASTM STP 1085,* B. M. Strauss and S. K. Putatunda, Eds., American Society for Testing and Materials, Philadelphia, 1990, pp. 26–38.
[6] Hancock, J. W. and MacKenzie, A. C., *Journal of the Mechanics and Physics of Solids,* Vol. 24, 1976, pp. 147–169.
[7] Hibbitt, Karlsson, and Sorensen, Inc., Providence, RI, 1991.
[8] Rice, J. R., "Limitations to the Small Scale Yielding Approximation for Crack Tip Plasticity," *Journal of the Mechanics and Physics of Solids,* Vol. 2, 1974, pp. 17–26.
[9] Williams, M. L., "On the Stress Distribution at the Base of a Stationary Crack," *Journal of Applied Mechanics,* Vol. 24, 1957, pp. 111–114.

Donald E. McCabe[1]

A Comparison of Weibull and β_{Ic} Analyses of Transition Range Data

REFERENCE: McCabe, D. E., "**A Comparison of Weibull and β_{Ic} Analyses of Transition Range Data,**" *Fracture Mechanics: Twenty-Third Symposium, ASTM STP 1189,* Ravinder Chona, Ed., American Society for Testing and Materials, Philadelphia, 1993, pp. 80–94.

ABSTRACT: Specimen size effects on K_{Jc} data scatter in the transition range of fracture toughness have been explained by extremal (weakest link) statistics. In this investigation, compact specimens of A533 Grade B steel were tested in sizes ranging from ½TC(T) to 4TC(T) with sufficient replication to obtain good three-parameter Weibull characterization of data distributions. The optimum fitting parameters for an assumed Weibull slope of four were calculated. Extremal statistics analysis was applied to the ½TC(T) data to predict median K_{Jc} values for 1TC(T), 2TC(T), and 4TC(T) specimens. The distributions from experimentally developed 1TC(T), 2TC(T), and 4TC(T) data tended to confirm the predictions. However, the extremal prediction model does not work well at lower-shelf toughness. At $-150°C$, the extremal model predicts a specimen size effect where in reality there is no size effect.

Another model that has potential for dealing with data scatter effects in the transition range is the Irwin β_c–β_{Ic} relationship. This model uses breakdown in constraint as the argument for specimen size effects and suggests that data sets can be transposed from one size to another by operating on each individual datum with the following equation

$$K_{Ic} = K_{Jc}\sqrt{\beta_{Ic}/\beta_c}$$

Both models predict about the same distributions for specimens larger than 1TC(T), and only the extremal statistical model can predict correctly the smaller specimen distribution. With the β_c–β_{Ic} relationship, the limitation appears to be that $\beta_c \leq \pi$ must not be exceeded. Therefore, both the statistical and β_{Ic} models have limitations for their use. This study explores these limitations and makes specimen size requirement recommendations on K_{Jc} data.

KEY WORDS: transition temperature, Weibull analysis, size effects, constraint, cleavage fracture, size requirements, fracture mechanics, fatigue (materials)

The fact that section size has an effect on the transition temperature of ferritic steels has been known for several decades, but aside from empirical observations of constraint effects [*1,2*], no rationale in the form of analytically based models had been forthcoming until recently. Early application of statistical practices lacked a physical concept that could serve as the basis needed to contribute to an improved understanding of what had already been known empirically. Recently, Weibull fitting of data has been used to characterize data distributions, and the principle of extremal statistics (weakest link theory) has been shown to provide the needed size effect model. The accuracy of determinations requires considerable replication of tests, however. In the current project, over 120 compact specimens of A533-B base metal in sizes ranging from ½TC(T) to 4TC(T) and A533-B weld metal ranging from 1TC(T) to 8TC(T) have been tested in the transition range with sufficient replication at some of the test temperatures

[1] Senior engineer, Metals and Ceramics Division, Oak Ridge National Laboratory, Oak Ridge, TN 37831-6151.

for viable statistical analysis. Hence, the new methods that are used to predict trends in median toughness values due to specimen size can be effectively tested. The toughness parameter to be used herein is K_{Jc} that is defined as K_J at onset of cleavage instability, and it is derived by conversion from J-integral at instability, J_c. This paper will evaluate Weibull fitting methods and extremal statistics that are used to predict specimen size effects. An alternative predictive model, the β_{Ic} fracture toughness factor, that is derived from measured values of K_{Jc} and that uses a constraint based argument will also be reported.

Test Data

The test temperatures and numbers of specimens for the various specimen sizes of A553-B steel are given in Table 1. All specimens were proportionally dimensioned compacts with relative initial crack size, a/W, nominally at 0.5. Data scatter observed here is shown in Fig. 1. The dependence of data scatter on specimen size is most evident at −75°C. Specimens of small thickness tend to lose constraint earlier when entering the transition range because the volume of cross-slip type of plastic deformation relative to the material thickness controls the transition toughness development rate. Larger specimens require more ductility for proportional cross-slip, and essentially similar data scatter characteristics are delayed to higher temperatures. It can be noted also that specimen size effects do not exist on the lower shelf and tend to vanish again at high toughness levels on the transition curve. To add evidence for the data scatter characteristics of large specimens at high toughness, test data from the Fifth Irradiation Series at Oak Ridge National Laboratory (ORNL) [3] were added herein. There were two weld metals of identical chemistries, except for copper content, see Table 2. Extremal statistics had been applied in that project because there was a need for making specimen size predictions.

Extremal Statistics

An application of extremal statistics to transition temperature behavior was developed in 1979 by Landes and Shaffer [4]. Using a two-parameter Weibull model, they demonstrated how data from 1T compact specimens, 1TC(T), could be used to characterize the fracture toughness distribution of larger 4T compact specimens, 4TC(T). The scatter in fracture toughness between replicate specimens was proposed to be governed by occasional weak points or sources for brittle cleavage crack initiation that are distributed randomly throughout the microstructure. Specimens with through-thickness cracks have zones of concentrated stress at the crack tip, the volumes of which are proportional to the specimen thickness. Therefore, the probability for imperfections of critical size to cause cleavage fracture is relatable to specimen thickness. The mean fracture toughness was projected to be lower and the standard deviation

TABLE 1—*Test conditions and number of replicate specimens used in statistical analysis.*

Material	Test Temperature, °C	Number of Specimens					
		½TC(T)	1TC(T)	2TC(T)	4TC(T)	6TC(T)	8TC(T)
A533-B Plate 13A	−150	18	17	12	...	...	...
	−75	20	26	12	6	...	...
	−18	...	6	2	...	...	...
	24	...	5	...	...	...	...
A533-B welds							
72W	10	...	...	4	2	2	2
73W	−5	...	...	4	2	2	2

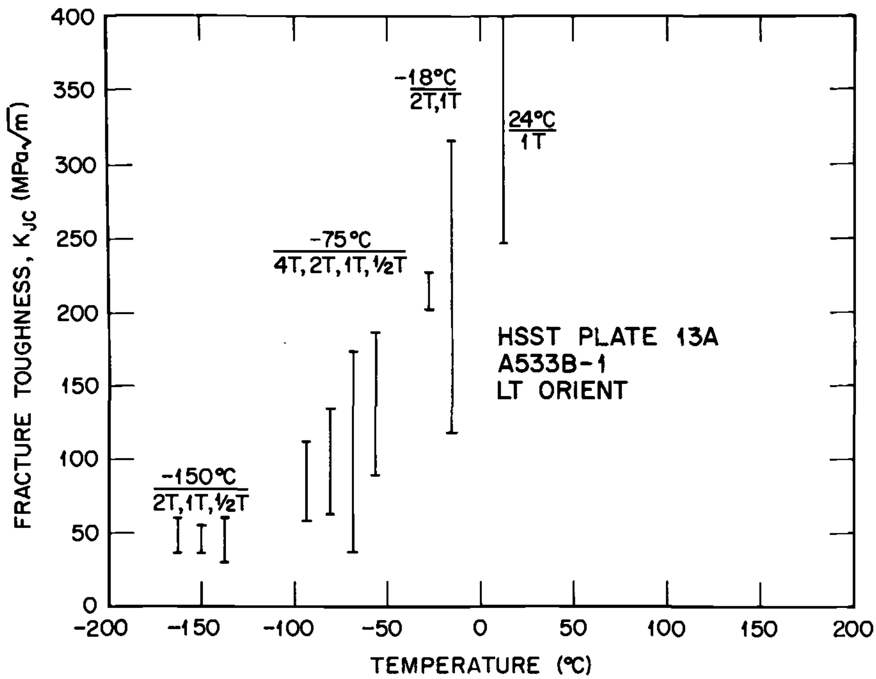

FIG. 1—*Data scatter of* K_{Jc} *values of A533-B Class 1 steel.*

smaller for larger specimens. The fracture toughness was expressed in terms of J_c, and the distribution for the baseline data was fitted to the following two-parameter Weibull model

$$P_{f1} = 1 - \exp\left[-(J/\theta_1)^b\right] \tag{1}$$

where P_{f1} is the probability that an arbitrarily chosen 1TC(T) specimen will have $J_c < J$, θ_1 is a scale parameter ($J_c = \theta_1$ when $P_{f1} = 0.632$), and b is the Weibull slope.

The fitting constants determined from the data are θ_1 and b. In using this model, it is assumed that the constraint is equal over all specimen sizes. Prior experience indicated that constraint does not vary sufficiently in compact specimens when the remaining ligament length is equal to or less than the specimen thickness [*5*]. Then if one were to test 4TC(T) specimens, the probability for J_c instability prior to reaching the toughness level, J, is given by

$$P_{f4} = 1 - \exp\left[-(J/\theta_4)^b\right] \tag{2}$$

where $\theta_4 = \theta_1(N)^{1/b}$ and $N = (4/1)$.

The preceding two-parameter model had predicted mean J_c for 4TC(T) specimens of ASTM A471 steel quite accurately at two of three test temperatures [*4*]. The Weibull slope (on J_c) was determined to be $b = 5$. Later experience suggests that they had an insufficient amount of data replication to obtain accurate Weibull slopes. Also a weakness not recognized was that the two-parameter extremal model will tend toward zero fracture toughness as the specimen size tends to infinity. Therefore, in a later publication [*6*], the weakness was corrected by introducing a three-parameter Weibull model. This has a lower-bound toughness value, J_{min}, that defines a lower limiting toughness for specimens of infinite thickness. The toughness parameter is

TABLE 2—*Materials.*

(a) *Yield and tensile strengths of test materials.*

Material	Strength, MPa (ksi) Yield	Ultimate
A533-B	444 (64.4)	600 (87.0)
A533-B SA weld		
72W	499 (72.4)	608 (88.2)
73W	490 (71.1)	600 (87.0)

(b) *Nominal chemical compositions.*

Material	C	Mn	P	S	Si	Cr	Ni	Mo	Cu	V
				A533-B[a] PLATE 13A						
	0.25	1.34	0.35[b]	0.040[b]	0.29		0.55	0.52		
				A533-B[a] WELDS						
72W	0.093	1.66	0.006	0.006	0.044	0.27	0.60	0.58	0.23	0.003
73W	0.098	1.56	0.005	0.005	0.045	0.25	0.60	0.58	0.31	0.003

[a] ASTM specifications for A533 Class 1.
[b] Maximum.

expressed as $(J_c - J_{min})$ and the denominator in Eq 1 becomes $(\theta_1 - J_{min})$. Figure 2 was used to illustrate the trial-and-error procedure used to identify an optimum J_{min} value on ½TC(T) specimens of A508 steel. The general form is

$$P_{f1/2} = 1 - \exp\left\{-\frac{(J - J_{min})}{(\theta - J_{min}}\right\}^b \tag{3}$$

Seven examples of three-parameter determinations gave four apparently reasonable J_{min} results for lower-bound toughness predictions. The three poor predictions were from data sets that had only four to seven data, and these were far too few to expect a good measure of the nonlinearity of a data population.

In current publications, it is more common to see three-parameter Weibull fitting to K_{Jc} data, where J_c is first calculated and then converted to K_{Jc} using

$$K_{Jc} = \sqrt{J_c E} \tag{4}$$

Weibull Constant Fitting Methods

Wallin [7] has performed Weibull analyses, using K_{Jc} data on numerous similar material data sets, large and small, and has concluded that toughness distributions generally show a fixed Weibull slope of 4 and that K_{min} also tends to be constant at about 20 MPa $\sqrt{m}$, independent of test temperature. Implicit in this argument is that all J_c distributions should have a slope of $b = 2$; noting that K is proportional to the square root of the J-integral. Brought into question is the initial finding of Landes and Shaffer where slope, b, was 5 for their J_c data on A471. The Wallin observation has been generally supported by the work of others [8,9] who have shown that a slope of 4 on K data has a basis in micromechanics theory. The assertion

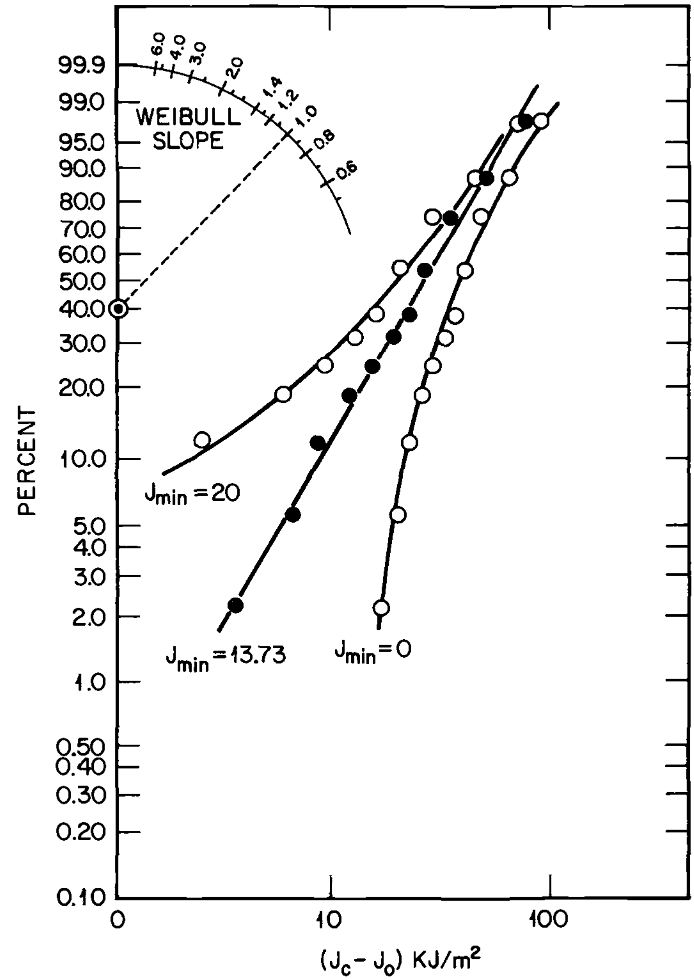

FIG. 2—*Example of the effect of minimum toughness parameter on data linearity and slope.*

that K_{min} is constant is less secure from a fundamental standpoint. Assuming K_{min} has physical meaning as a lower-bound toughness, some have suggested that lower bound K_{Ic} or K_{Ia} values obtained from ASME Code regulations could be used [*10*]. On the other hand, the best fits to the Weibull model are usually obtained with K_{min} values considerably lower than those indicated by the code curves. Figures 3 and 4 are representative of what results from seeking the best K_{min} values using the base metal data from the test matrix of Table 1. There are four specimen sizes and four test temperatures represented. The two fitting techniques used were (1) adjusting all three Weibull constants to get an optimum linear fit to the data and (2) setting the Weibull slope to 4 and then finding K_{min} for optimum fit. Table 3 lists the fitting constants and correlation coefficients of the two methods, and it appears that the fundamentally justified Weibull slope of 4 can provide a suitable representation of the distributions in most cases. One rule that was used, however, is that K_{min} was never allowed to be a negative value. Because of

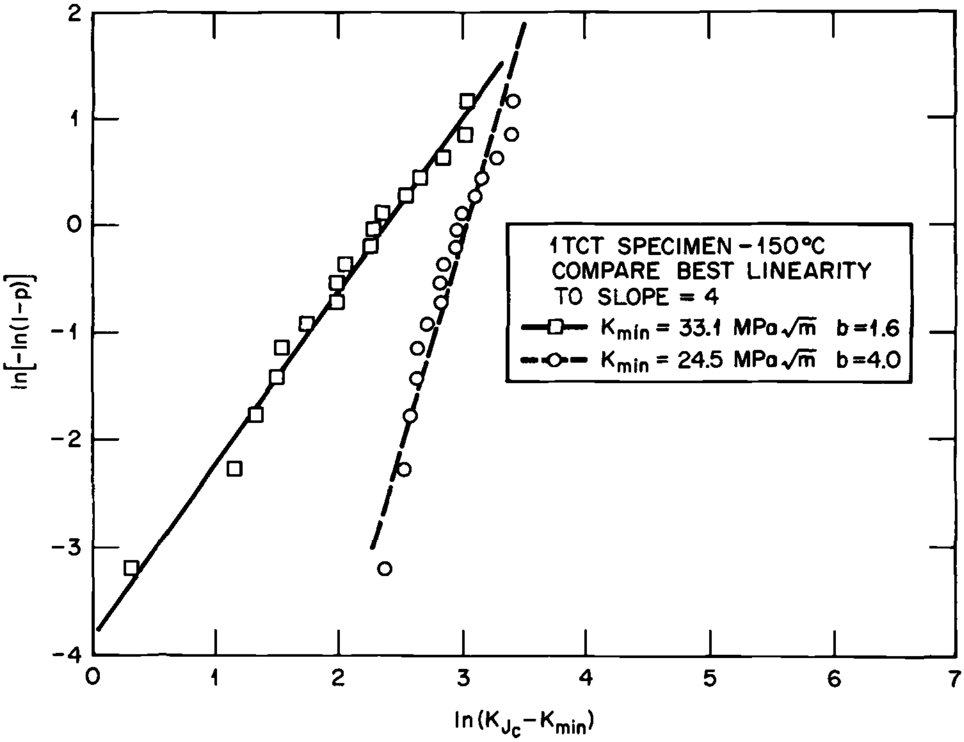

FIG. 3—*Example of best linearity with three variable parameters versus fixed slope and two variable parameters; 1TC(T) specimens tested at −150°C.*

TABLE 3—*Comparison of Weibull fitting parameters for best correlation coefficient.*

Test Temperature, °C	Size, C(T)	Three Fitting Parameters			Fixed Slope, Two Fitting Parameters		
		Slope	K_{min}[a]	Correlation Coefficient	Slope	K_{min}[b]	Correlation Coefficient
−150	½T	1.7	25	0.991	4	10.5	0.975
−150	1T	1.6	34	0.993	4	24.5	0.961
−150	2T	3.0	24	0.990	4	19.0	0.998
−75	½T	1.1	89	0.991	4	42.5	0.933
−75	1T	3.3	0	0.993	4	0	0.993
−75	2T	4.7	0	0.983	4	13.5	0.983
−75	4T	1.8	44	0.986	4	6.0	0.982
−18	1T	0.9	109	0.988	4	0	0.914
24	1T	3.2	0	0.913	4	0	0.913

[a] K_{min} for best fit with b, K_0, and K_{min} variable.
[b] K_{min} for best fit with K_0 and K_{min} variable.

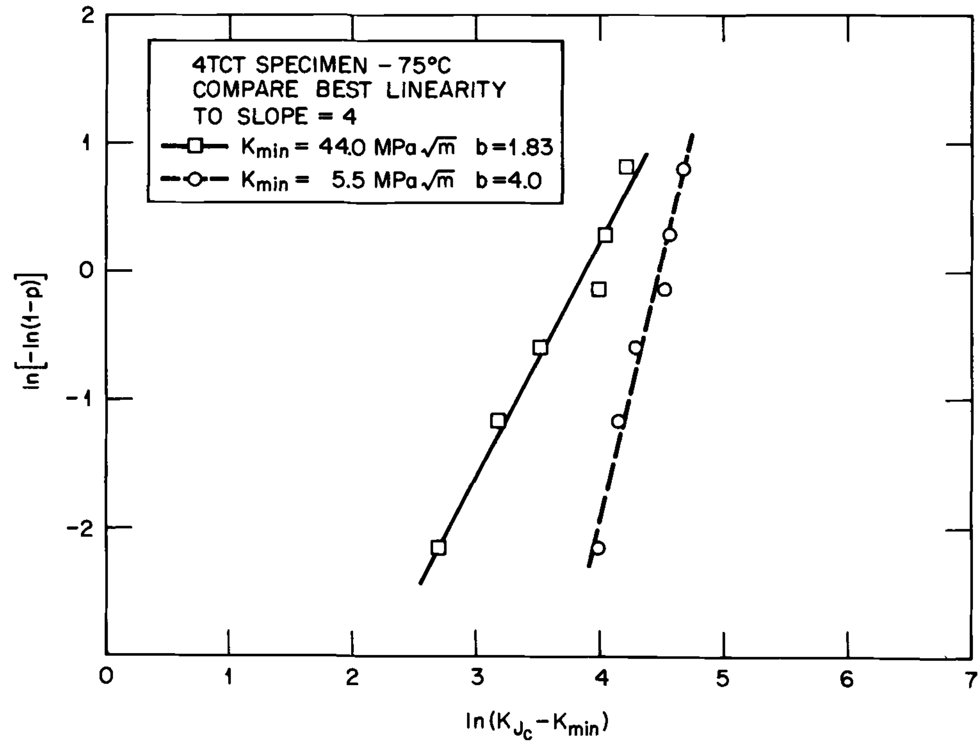

FIG. 4—*Example of best linearity with three variable parameters versus fixed slope and two variable parameters; 4TC(T) specimens tested at* −75°C.

this, a few slopes were only near to 4. There were two cases where good linearity and a Weibull slope of 4 were not entirely compatible, and these are shown in Figs. 5 and 6. Both cases had some data at relatively high toughness conditions for the size of specimen used, and their Weibull plots suggest bilinearity with an apparent break point at 125 MPa $\sqrt{m}$ for ½TC(T) and 192 MPa $\sqrt{m}$ for 1TC(T).

Prediction of Size Effects

The density function for the ½T compact specimens was used to predict median K_{Jc} values for the Weibull fits to 1T, 2T, and 4T compact specimen data generated at the same test temperature (−75°C), see Fig. 7 and Table 4. There are two sets of determinations in Table 4. In both cases, a fixed Weibull slope of 4 was used, with K_{min} variable in one case and fixed at 20 MPa$\sqrt{m}$ in the other case. The magnitude of median shift predicted for increased specimen size was reasonable in both cases.

The same exercise applied to tests made at −150°C (Table 4) was not as satisfactory. A specimen size effect was expected, but the distributions fitted to real data indicated no effect. The scatter bands of data for all tests made on A533-B plate on all specimen sizes and for all test temperatures was shown in Fig. 1. Note that at −150°C, the smallest specimens tested, ½TC(T), had both the highest and lowest K_{Jc} toughness values. Extremal statistics erroneously

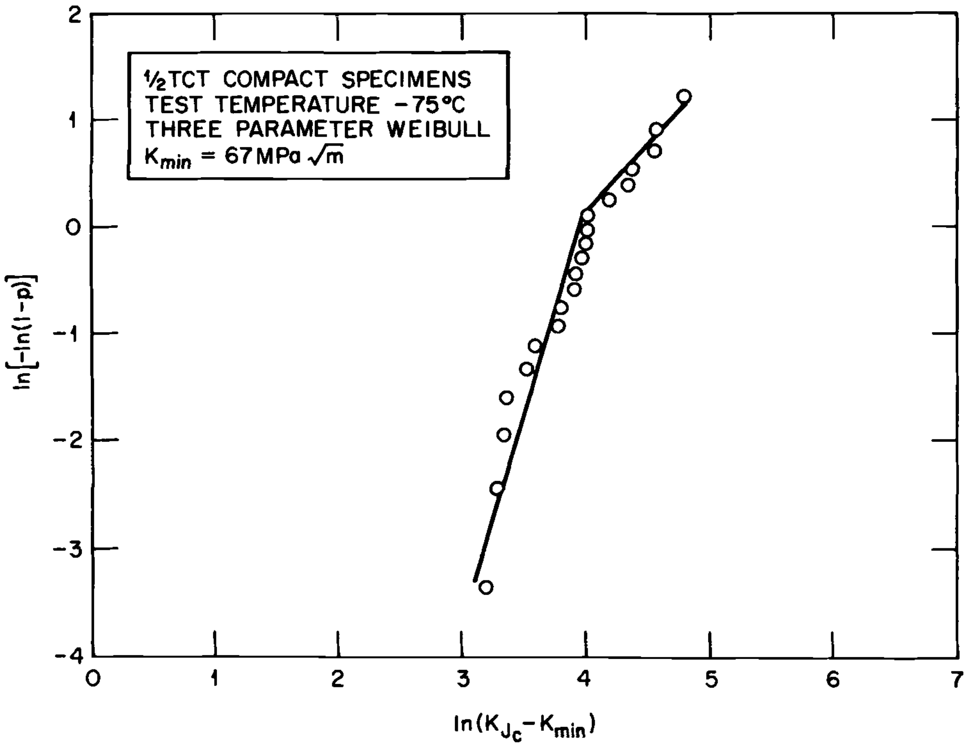

FIG. 5—*Bilinear Weibull slope development for ½TC(T) specimens tested at −75°C.*

TABLE 4—*Size effect predictions using extremal statistics (Weibull slope of four, comparing best* K_{min} *versus fixed* K_{min}.

Test Temperature, °C	Size C(T)	Median K_{Jc}, MPa $\sqrt{m}$: Fit Actual Data, Best K_{min}	Fit Actual Data, K_{min} = 20	Extremal Predictions from ½TC(T), Best K_{min}	Extremal Predictions from ½TC(T), K_{min} = 20
−75	½T	122.4	124.8	...	...
−75	1T	102.4	98.6	109.9	108.2
−75	2T	102.6	102.1	99.3	94.1
−75	4T	86.4	85.3	90.4	82.3
−150	½T	40.6	39.8	...	...
−150	1T	43.4	43.7	33.9	36.7
−150	2T	44.8	44.8	31.9	34.0
−150	4T	...	...	28.5	31.8

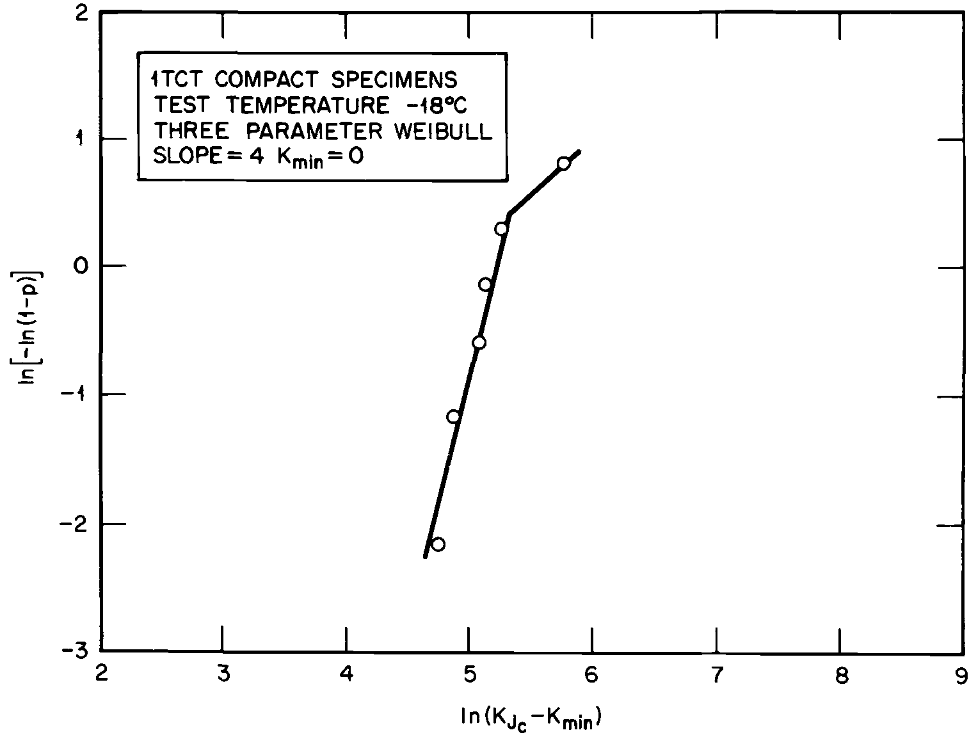

FIG. 6—*Apparent bilinear slope development for 1TC(T) specimens tested at* $-18°C$.

predicted a size effect because of a breakdown in the weakest link model. This will happen when the size of the imperfection needed to cause cleavage initiation becomes very small such that many cleavage sources exist at all points along the crack tip. Hence, there is a need to identify a lower toughness limit below which extremal statistics will not apply. A suggested approach will be addressed in the Discussion.

There can be some difficulty with the application of extremal statistics at the high toughness end of the material transition curve. This was experienced in the Heavy-Section Steel Irradiation Program in the Fifth Irradiation Series [*3*]. The objective of the experiment was to establish lower-bound K_{Ic} curves on two A533-B weld metals of different copper contents. Of special interest was the shift and potential change in shape of the lower bound due to irradiation damage. Four 8T compact specimens (two of each copper content) were to be tested at the highest possible toughness level that would be consistent with the ASTM validity requirements on K_{Ic}. It was determined that the maximum K_{Jc} would be a valid K_{Ic} at 150 MPa $\sqrt{m}$, and a temperature where this was likely to happen was chosen using smaller specimens. The sequence used was to first test four 2TC(T) specimens at the selected temperature to provide a baseline Weibull distribution for predicting the 8TC(T) distribution. One of the two plots made is shown in Fig. 8. Because median K_{Jc} was predicted to be 150 MPa $\sqrt{m}$, it was presumed that the chance of obtaining valid K_{Ic} should be one in two for each large specimen tested. Nevertheless, none of the four large specimens gave valid K_{Ic}. The trend indicated with 4TC(T) and 6TC(T) specimens gave no evidence that there might have been a breakdown in the extremal assumption, but the high toughness position on the transition curve evidently had broadened

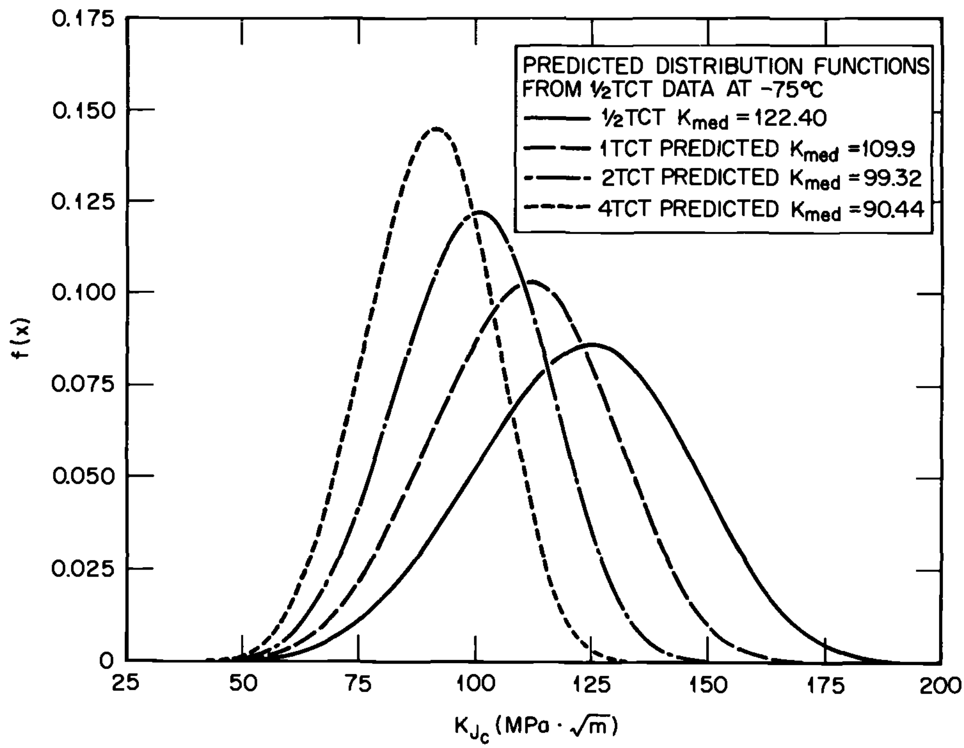

FIG. 7—*Density functions predicted from ½TC(T) specimens tested at −75°C.*

the scatter-band width for large specimens enough to make it difficult to assure an aim value. Hence, the utility of these predictions of size effects may be limited to a transition temperature window in the lower transition range.

β_c–β_{Ic} Fracture Toughness Correlation

Another perspective on the K_{Jc} data scatter phenomenon is to consider that the early (lower temperature) increase in K_{Jc} data scatter of small specimens is due to the lower constraint. Smaller specimens tend to respond nonlinearly with less crack-tip plastic deformation, readily losing constraint in the crack-tip region. Larger specimens require proportionately more cross slip, and similar data scatter is delayed to higher temperatures. To relate high and low constraint toughness, Irwin [*11*] had developed a semiempirical relationship based on the behavior of high-strength metallic materials. Merkle has investigated the potential of this relationship for use with the structural steels that are used in pressure vessels. It is as follows

$$\beta_c = \beta_{Ic} + 1.4\beta_{Ic}^3 \tag{5}$$

where $\beta_c = (1/B)(K_{Jc}/\sigma_{ys})^2$ and $\beta_{Ic} = (1/B)(K_{Ic}/\sigma_{ys})^2$.

The β_c value determined for each individual datum is picked out of a family of replicate tests. An estimate of K_{Ic} is made on each one, thereby establishing a family of K_{Ic} distributions. The procedure is to use β_c in Eq 5 and to determine the corresponding β_{Ic} either by iteration or by using a preformulated solution of the cubic equation. Then K_{Ic} is determined using

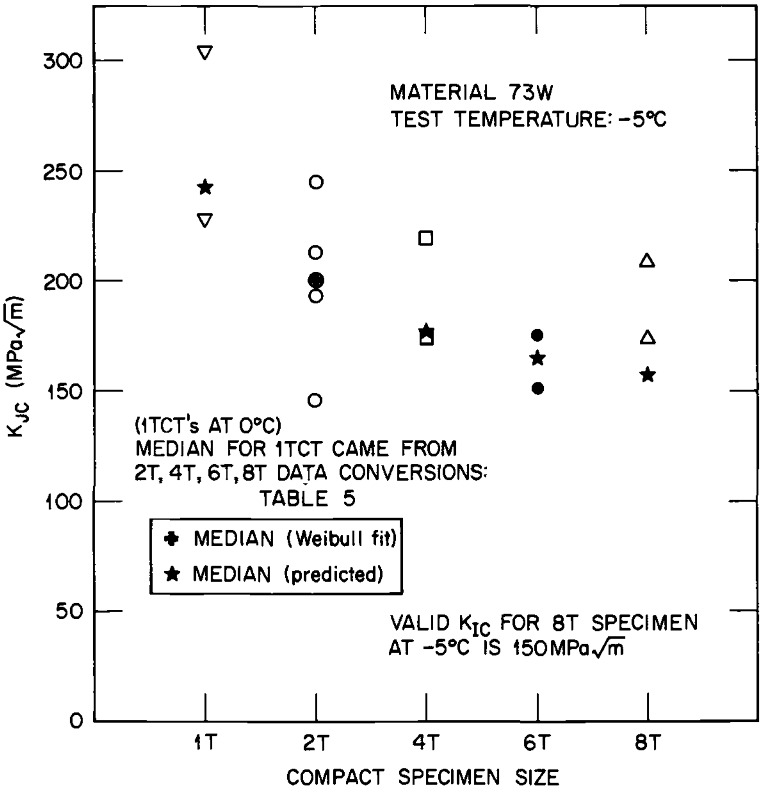

FIG. 8—*Example of extremal statistics used on 2TC(T)* K_{Jc} *data to predict median toughness for 8TC(T) specimens tested at the same temperature.*

$$K_{Ic} = K_{Jc}\sqrt{\frac{\beta_{Ic}}{\beta_c}} \tag{6}$$

The three-parameter Weibull can then be fitted to the K_{Ic} distribution or to interpolated values for intermediate specimen sizes. Equation 5 is used to interpolate in all cases. Figure 9 shows K_{Jc} data selected at three toughness levels from within the actual data sets for 1TC(T), 2TC(T), and 4TC(T) specimens (A533-B base metal tested at −75°C). These are the solid data points in Fig. 9. The interpolation and extrapolation by Eq 5 of the three specifically selected toughness levels are shown as open data points. The solid line represents the toughness trend over varied thicknesses that is implied by Eq 5. Irwin had cautioned that the semiempirical relationship should not be used when β_c is greater than π, and this limit is denoted in Fig. 9 as a dashed line. This limitation required that for the toughness of A533-B at −75°C, data from 1T or larger compact specimens must be used to develop the baseline Weibull plot. Figure 10 shows predictions of density functions from use of the 1TC(T) baseline data. Table 5 compares the predicted size effect on median K_{Jc} obtained from the density functions to those from the extremal statistical model. Again, this is using the 1TC(T) specimen data as baseline. Note that the beta method projects essentially the same result except for ½TC(T) where most of the projected values have β_c much greater than π.

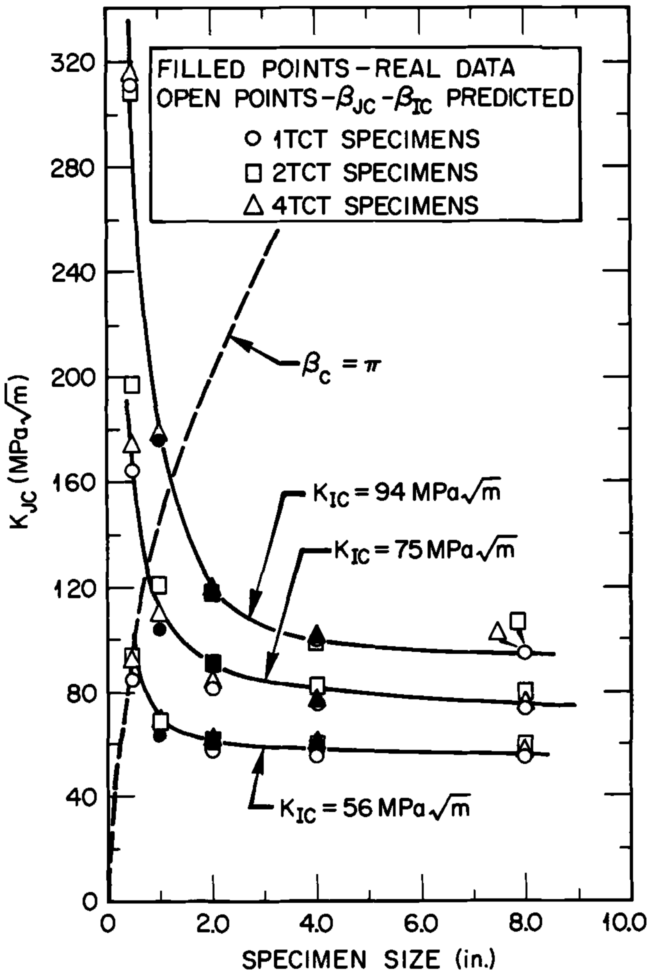

FIG. 9—*Fracture toughness trends for selected positions in* K_{Jc} *data scatter bands. Trend lines are from the Irwin* β_c–β_{Ic} *relationship.*

TABLE 5—*Predicted specimen size effect, comparing extremal statistics and beta methods.*

Test Temperature, °C	Size, C(T)	Median K_{Jc}, MPa √m		
		Fit Actual Data	Predictions from 1TC(T)	
			Extremal	Beta
−75	½T	122.4	121.3	159.8
−75	1T	102.4	...	...
−75	2T	102.6	85.8	81.1
−75	4T	86.4	72.1	74.2
−150	½T	40.6	48.2	47.2
−150	1T	43.7	...	...
−150	2T	44.8	39.9	42.6
−150	4T	...	36.8	42.4

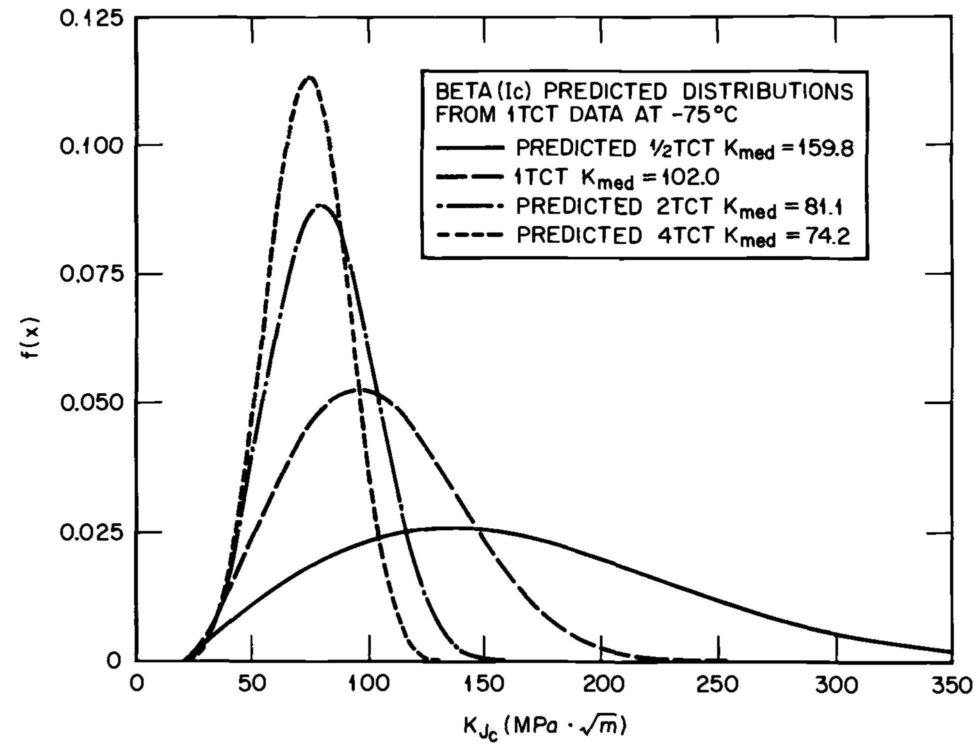

FIG. 10—*Distribution functions for ½TC(T), 2TC(T), and 4TC(T) specimens predicted from 1TC(T), K_{Jc} data and size effect prediction by constraint effects assumption.*

Discussion

The practical application for this work is to learn how data taken from small fracture-mechanics-type specimens can be used to infer the fracture toughness performance in full-scale structures. The general format of data development limitations is illustrated schematically in Fig. 11. This is for ½T compacts made of A533-B. From evidence in Figs. 5 and 6, it appears that constraint is controlled sufficiently for Weibull fitting and extremal statistics predictions for β_c up to 2π. The low toughness limitation for extremal statistics has not been determined, but a practical lower limit might be where $\beta_c = 0.4$. These limits would apply to distributions where a high percentage of the K_{Jc} values within the baseline distribution would satisfy the suggested criteria. Figure 11 indicates that the semiempirical β_c–β_{Ic} relationship might be suitable for toughness where β_c is equal to π or less. This model tends to plateau along with test data at the lower plateau of transition toughness, and median K_{Ic} can be more reasonably determined with this model.

If it can be established with reasonable confidence that the Weibull slope is almost always four for most structural steels, and that $K_{min} = 20$ MPa $\sqrt{m}$ is a reasonable compromise value, then the number of small specimens needed to establish a reasonable baseline Weibull distribution is highly reduced because only the scale parameter need be determined. Perhaps only a half-dozen specimens would suffice. Such a practice would only be suitable for establishing trends in mean toughness, however, because the tails of the fitted distribution curves would be quite unreliable and not usable to estimate lower-bound values. The utility would be for the determination of median transition curve shifts due to irradiation damage effects.

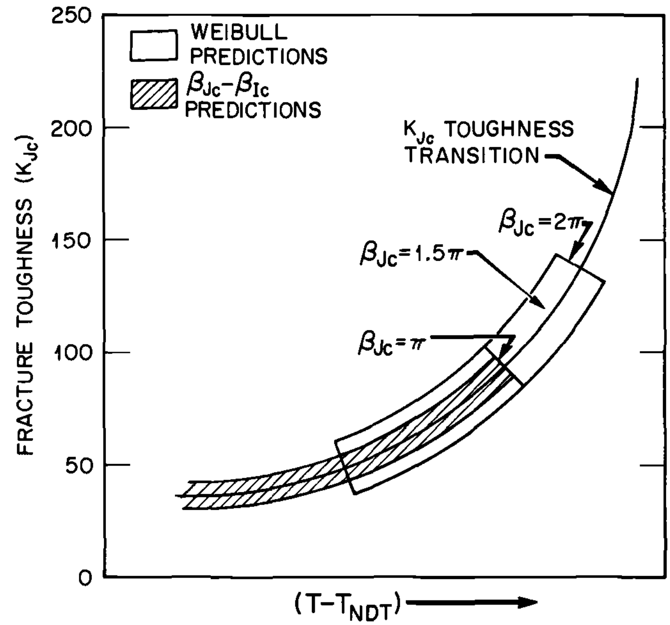

FIG. 11—*Zone of application for predictive models for* K_{Jc} *data from* ½ *TC(T) specimens.*

Conclusion

This paper has used selected data from two projects that were designed to study the fracture mechanics aspects of transition temperature behavior of structural steels. It is concluded that statistical methods and a constraint-based model can be incorporated into an overall plan to deal with size effects. Transition temperature shifts can be predicted for materials that are used in large structures using small-surveillance-size specimens. The establishment of lower-bound K_{Ic} curves by testing just a few small specimens is not suggested at the present time.

Acknowledgments

The author would like to give credit to Dr. John McGowan, who set up the experiment and developed the data. Also, the interest and support of Dr. Randy K. Nanstad, Mr. John G. Merkle, and the U.S. Nuclear Regulatory Commission is greatly appreciated.

This research was sponsored by the Office of Nuclear Regulatory Research, U.S. Nuclear Regulatory Commission, under Interagency Agreement DOE 1886-8011-9B with the U.S. Department of Energy under Contract DE-AC05-84OR21400 with Martin Marietta Energy Systems, Inc.

References

[*1*] Pellini, W. S. and Puzak, P. P., "Fracture Analysis Diagram Procedures for the Fracture Safe Engineering Design of Steel Structures," *Welding Research Council Bulletin 88*, Welding Research Council, New York, May 1963.

[*2*] Rolfe, S. T. and Barsom, J. M., *Fracture and Fatigue Control in Structures*, Prentice-Hall, New York, 1977.

[3] Nanstad, R. K. et al., "Effects of Radiation on K_{Ic} Curves for High-Copper Welds," *Effects of Radiation on Materials: Fourteenth International Symposium (Volume II), ASTM STP 1046,* N. H. Packan, R. E. Stoller, and A. S. Kumar, Eds., American Society for Testing and Materials, Philadelphia, 1990, pp. 214–233.
[4] Landes, J. D. and Shaffer, D. H., "Statistical Characterization of Fracture in the Transition Region," *Fracture Mechanics (Twelfth Conference), ASTM STP 700,* American Society for Testing and Materials, Philadelphia, 1980, pp. 368–382.
[5] McCabe, D. E. and Landes, J. D., "*J-R* Curve Testing of Large Compact Specimens," *Elastic-Plastic Fracture: Second Symposium, Volume II: Fracture Curves and Engineering Applications, ASTM STP 803,* C. F. Shih and J. P. Gudas, Eds., American Society for Testing and Materials, Philadelphia, 1983, pp. II-353–II-371.
[6] Landes, J. D. and McCabe, D. E., "Effect of Section Size on Transition Temperature Behavior of Structural Steels," *Fracture Mechanics: Fifteenth Symposium, ASTM STP 833,* R. J. Sanford, Ed., American Society for Testing and Materials, Philadelphia, 1984, pp. 378–392.
[7] Wallin, K., "Statistical Modeling of Fracture in the Ductile to Brittle Transition Region," *Defect Assessment in Components—Fundamentals and Applications,* J. G. Blauel and K. H. Schwalbe, Eds., ESIS/EGF9, Mechanical Engineering Publications, London, 1991, pp. 1–31.
[8] Mudry, F., "A Local Approach to Cleavage Fracture," *Nuclear Engineering and Design,* Vol. 105, 1987, pp. 65–76.
[9] Beremin, F. M., "A Local Criterion for Cleavage Fracture of a Nuclear Pressure Vessel Steel," *Metallurgical Transactions A,* Vol. 14A, Nov. 1983, pp. 2277–2287.
[10] "PVRC Recommendations on Toughness Requirements for Ferritic Materials," *Welding Research Council Bulletin 175,* Aug. 1972.
[11] Irwin, G. R., *Fracture Testing of High-Strength Sheet Materials Under Conditions Appropriate for Stress Analysis,* NRL Report 5486, Naval Research Laboratory, Washington, DC, 1960.

John G. Merkle[1]

Near-Crack-Tip Transverse Strain Effects Estimated with a Large Strain Hollow Cylinder Analogy

REFERENCE: Merkle, J. G., **"Near-Crack-Tip Transverse Strain Effects Estimated with a Large Strain Hollow Cylinder Analogy,"** *Fracture Mechanics: Twenty-Third Symposium, ASTM STP 1189*, Ravinder Chona, Ed., American Society for Testing and Materials, Philadelphia, 1993, pp. 95–114.

ABSTRACT: In order to study effects of constraint on fracture toughness, it is reasonable to study the region of large strains close to the crack tip within which the microscopic separations that lead to fracture often take place. The first step in this direction was taken in 1950 by Hill, who postulated that close to a circular notch tip the principal stress directions would be radial and circumferential, so that the plastic slip lines (maximum shear stress trajectories) would be logarithmic spirals. The resulting equation for stress normal to the notch symmetry plane, neglecting strain hardening, was identical to that for the circumferential stress near the bore of an ideally plastic thick-walled hollow cylinder under external radial tension, because the relevant geometries are identical. Hill's hypothesis was extended algebraically by Merkle to include strain hardening with a generalized-plane-strain small-strain hollow cylinder analogy, and numerically in a more general way geometrically for plane strain and large strains by Rice and Johnson. Large strain finite element analyses have shown that a wedge-shaped zone ahead of a blunting crack tip deforms like a hollow cylinder. This paper extends the generalized plane strain hollow cylinder analogy to large strains. The strain equations are derived by analyzing the constant volume deformation of a differential cylindrical element. The circumferential strain is singular at the tip of an initially sharp crack. With the strain distribution determined, the stresses are obtained by integrating the equation of radial equilibrium. An approximation is developed for the first increment of radial stress near the strain singularity. Calculations show that the in-plane stresses are only slightly sensitive to transverse plastic strain.

KEY WORDS: fracture mechanics, crack-tip blunting, transverse strain, constraint effects, large strains, fatigue (materials)

Nomenclature

b, b_0	Crack-tip opening, current and initial, respectively, mm
c	Radial displacement of point located at initial infinitely sharp crack tip, mm
E	Elastic modulus, MPa
e_z	Engineering strain in axial direction, dimensionless
$F(\varepsilon)$	Function of strain that is linear in distance from crack tip, dimensionless
h	Constraint factor, dimensionless
l	Height of ring element, mm
N	Strain hardening exponent, dimensionless
R	Original distance from crack tip, mm
r, r_i	Radial distance from coordinate origin, current and initial, respectively, mm

[1] Research specialist, Oak Ridge National Laboratory, Oak Ridge, TN 37831.

S	Stress parameter defined by Eq 46, MPa
u, u_r	Radial displacement, mm
u_θ	Circumferential displacement, mm
v	Displacement defined by Eq 57, mm
w	Axial displacement, mm
X	Undeformed horizontal coordinate, mm
X_0	Horizontal offset of hollow cylinder analogy coordinate origin from original crack tip, mm
x, y	Deformed coordinates, mm
δ_t	Crack-tip-opening displacement, mm
ε_1, ε_2, ε_3	Principal strains, dimensionless
ε_θ, ε_r, ε_z	Circumferential, radial, and axial strains, respectively, true strain unless otherwise noted, dimensionless
ε_a	Shear strain between characteristic directions at apex of large strain region, dimensionless
ε_0	Power law reference strain, dimensionless
$\bar{\varepsilon}$	Effective plastic strain, dimensionless
ε_y^{tr}	True crack opening strain, dimensionless
η	Maximum shear strain, dimensionless
θ	Angle measured from the crack plane, radians
λ	Strain function defined by Eq 6, dimensionless
ν	Poisson's ratio, dimensionless
ρ	Blunted crack or notch root radius, mm
σ	Stress, MPa
σ_1, σ_2, σ_3	Principal stresses, MPa
σ_θ, σ_r, σ_z	Circumferential, radial, and axial stresses, MPa
σ_Y	Yield stress, MPa
σ_0	Power law reference stress, MPa
σ_e	Effective stress, MPa
σ_m	Mean (hydrostatic) stress, MPa
χ	Distance from blunted crack tip, mm

Fracture mechanics is a collection of material testing and analysis procedures applied for the purpose of preventing fracture due to cracks in structures. It is recognized that yielding can and does occur near the tips of cracks, the result being lower stresses and higher strains perpendicular to the crack plane than would otherwise exist. However, yielding does not necessarily prevent the buildup of hydrostatic stresses relative to shear stresses in the crack-tip plastic zone but, in fact, can amplify this buildup. This is because of the restraint of attempted transverse contractions resulting from enforced compatibility with the adjacent regions subjected to lower stresses.

Existing fracture mechanics procedures are based on the premise that, by following prescribed methods, precracked laboratory specimens can be tested under conditions of effective maximum constraint and the results transferred conservatively to structures in terms of a material property called "fracture toughness." It has been demonstrated repeatedly that below the upper shelf, fracture toughness values measured with small laboratory specimens tend to develop increased upward scatter as specimen size decreases. In the smallest specimens, dimples are visible on the specimen surfaces at the crack ends, thus demonstrating the powerful tendency for transverse contraction to occur along a crack front. This is the inevitable consequence of the constant plastic volume condition, which is one of the physical conditions governing yielding. Realizing that cracks oriented circumferentially in a pressure vessel are subjected to a nominal transverse strain condition more severe than plane strain, it is prudent to consider the possibility that a positive out-of-plane strain condition can have an effect on toughness opposite to that of transverse contraction, namely, lowering the toughness.

To study the effects of constraint on fracture toughness, it is important to select the right location within the crack-tip stress and strain field for investigation. Despite the success achieved by treating K and J as single parameters that can be conveniently determined away from the crack-tip region but still assumed to control near-crack-tip behavior, understanding constraint effects has thus far not become amenable to this approach. Thus, it seems beneficial to select as a location for study the region of large strains close to the crack tip within which the microscopic separations that lead to fracture actually take place. This approach is not a new one. In fact, it predates linear-elastic fracture mechanics. However, without a mathematical or a computational connection with global structural behavior, there is no obvious way to transfer information from laboratory specimens to structures. Nevertheless, important information about the basic physical parameters governing fracture, including the nominal stress state at the flaw location, can be developed by this approach.

The first step applicable to studying the stress and strain distributions in the plastic zone immediately bordering a blunting crack tip was taken by Hill [*1*] in 1950. Considering a notch with a circular tip, Hill postulated that close to the notch tip the principal stress directions would be radial and circumferential and that the plastic slip-lines (maximum shear stress trajectories) would therefore be logarithmic spirals. The resulting equation for stress normal to the notch symmetry plane, neglecting strain hardening, is

$$\sigma = \sigma_Y \left[1 + \ln \left(1 + \frac{\chi}{\rho} \right) \right] \tag{1}$$

where χ is distance from the notch tip, ρ is root radius, and σ_Y is yield stress. Equation 1 is identical to the expression for the circumferential stress near the bore of an ideally plastic thick-walled hollow cylinder under external radial tension because the relevant geometries are identical.

Hill's analysis did not consider strain hardening nor attempt to relate the notch root radius to the remotely applied load. In 1969, Rice and Johnson [*2*] developed a near-crack-tip, plane strain, large-strain, rigid-plastic analysis considering strain hardening and assuming an infinitely sharp initial crack. Although the geometry analyzed was approximately a field of logarithmic spirals, the boundary displacement loading based on a singular shear strain distribution did not produce a perfectly circular-blunted crack tip, so the slip-lines were not exactly log spirals [*3*]. One strain distribution on the plane of symmetry was determined for ideally plastic conditions, and the stresses were then determined for various strain-hardening exponents by integrating the equation of equilibrium and applying the flow rule. The strain at the apex of the slip-line field was assumed to be zero [*3*] and, for strain hardening, a stress singularity occurred very close to the tip of the blunting crack. Because the calculated stresses at the apex of the slip-line field were finite, but the plastic strains were assumed zero and the elastic strains neglected, a state of pure hydrostatic tension was implied at that location. This result is not physically realistic enough to use in evaluating constraint effects, but the results are easily improved by assuming a finite strain at the apex, as explained in Ref *3*.

Assuming that the conditions of stress and strain near the apex of the near-tip slip-line field are only mildly sensitive to the exact shape of the blunted crack tip, Merkle [*4*], following Hill's suggestion [*1*], proposed an analysis of the stresses and strains ahead of a blunted crack tip on the plane of symmetry based on a circular-blunted crack tip. It was reasoned that, on the plane of symmetry, the equilibrium and strain-displacement equations should be identical to those for an axisymmetrically loaded thick-walled hollow cylinder. Actually, this is only true if

$\partial u_\theta/\partial_\theta = 0$, because u_θ changes sign at $\theta = 0$. However, as will be discussed later, numerical calculations show that this condition is approximately satisfied close to the plane of symmetry. Consequently, the hollow-cylinder analogy has the potential for illustrating details of near-crack-tip behavior without requiring complex or expensive analytical procedures. This is especially true with regard to the effects of transverse strain, because stress analysis solutions for thick-walled hollow cylinders under conditions of generalized plane strain include explicitly the effect of ε_z. The original hollow-cylinder analogy calculations [4] were based on small strain theory and therefore gave strain distributions that did not agree well with the Rice and Johnson results near the blunted crack tip. However, the original hollow-cylinder analogy did include the elastic strains, which the Rice and Johnson analysis neglected, and these strains may turn out to be important, especially the transverse (out-of-plane) elastic strain near the point of peak stress.

Basis for the Hollow-Cylinder Analogy

The basis for the hollow-cylinder analogy is Hill's approximation [1] that immediately ahead of a round-tipped notch, the slip-lines are orthogonal logarithmic spirals. Because these lines cross every radial and circumferential line at 45°, the principal directions of stress (and implicitly also of strain) are radial and circumferential, just as they are in an axisymmetrically loaded thick-walled hollow cylinder. The basic concept is thus illustrated in Fig. 1, showing that within the overall plastic zone there is a much smaller flame-shaped zone immediately

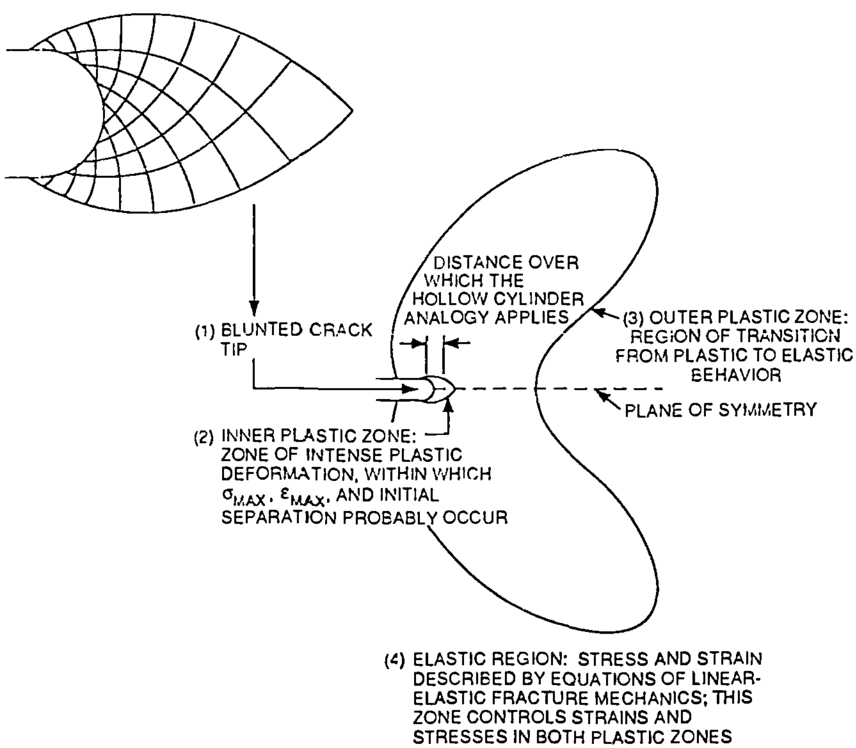

FIG. 1—*Schematic diagram of near-tip plastic zones of blunting crack (source: Ref 4).*

ahead of the blunting crack tip within which the slip-lines are approximately logarithmic spirals. Hill's model of the region immediately ahead of a circular notch tip did not consider strain hardening, and thus nothing was said explicitly about strains. Merkle [4] extended Hill's hypothesis to include strain hardening, reasoning that stress analysis solutions for axisymmetrically loaded thick-walled hollow cylinders should be applicable on the plane of symmetry ahead of a blunting crack tip as long as the through-thickness stress remains the intermediate principal stress. Using cylindrical coordinates and recognizing that the principal directions of stress and strain in the logarithmic spiral slip-line region are radial and circumferential, it follows that all the equilibrium and conventional strain-displacement equations reduce to those for an axisymmetrically loaded thick-walled hollow cylinder except the circumferential strain-displacement equation, which for small strains is

$$\varepsilon_\theta = \frac{1}{r}\frac{\partial u_\theta}{\partial_\theta} + \frac{u_r}{r} \tag{2}$$

For the hollow cylinder analogy to hold, $\partial u_\theta/\partial_\theta$ must be shown to be negligible or zero on the plane of symmetry. In Ref 4, symmetry was used as an argument for setting $\partial u_\theta/\partial_\theta = 0$ on $\theta = 0°$. However, because u_θ changes sign while passing through zero at $\theta = 0°$, $\partial u_\theta/\partial_\theta$ theoretically does not have to be zero on the plane of symmetry. Thus, additional information must be used to determine if $\partial u_\theta/\partial_\theta$ is actually small enough to neglect on the plane of symmetry.

Two separate studies of the stresses and strains very close to a blunting crack tip by the finite-element method have produced results that support the hollow-cylinder analogy. As indicated in Fig. 2, McMeeking [5] performed near-crack-tip, elastic-plastic large-strain calculations showing that the variation of effective plastic strain with polar angle, θ, near the plane of symmetry is very small. Needleman and Tvergaard [6] performed similar calculations, observing the details of deformation immediately surrounding the blunting crack tip. Figure 3 shows the existence of a wedge of finite elements bisected by the plane of symmetry that continues to subtend the same 22° angle as deformation proceeds. Together, Figs. 2 and 3 imply that, within a finite angular sector ahead of a blunting crack tip, material points displace only in the radial direction and circular arcs remain approximately circular. Consequently, within a finite angular sector ahead of a blunting crack tip, $u_\theta = 0$. For these conditions, Eq 2 reduces to

$$\varepsilon_\theta = \frac{u_r}{r} \tag{3}$$

thus providing an empirical basis for the hollow-cylinder analogy.

Derivation of Strain-Displacement Equations for Large Strains

The original hollow-cylinder analogy [4] was developed using the conventional small-strain, elastic-plastic stress and strain equations for a thick-walled hollow cylinder. However, comparing the calculated near-crack-tip strain distribution with the results obtained by Rice and Johnson [2] showed a discrepancy, the most likely cause of which appeared to be the existence of large strains very close to the blunted crack tip. The Rice and Johnson analysis [2] was based on large strain theory, so a large strain version of the hollow-cylinder analogy is necessary for a valid comparison between the two analytical models.

Consider a ring element within a thick-walled hollow cylinder with original inside radius, r_i, thickness, dr_i, and height, ℓ. Let the radial displacements corresponding to r_i and $r_i + dr_i$ be u

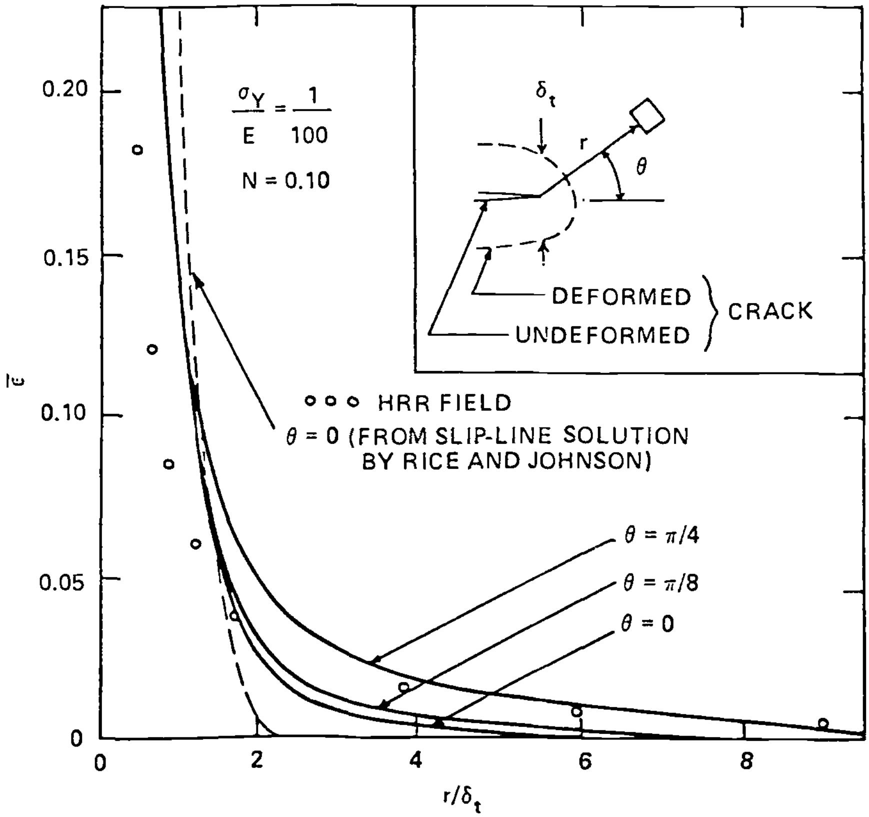

FIG. 2—*Effective plastic strain near a blunting crack tip (source: Ref 5).*

and $u + du$, and the uniform increase in height of the ring element be w. Neglecting elastic strains, the volume of the ring must remain constant. Thus

$$2\pi r_i dr_i \ell = (2\pi)(r_i + u)(dr_i + du)(\ell + w) \tag{4}$$

Define

$$e_z = \frac{w}{\ell} \tag{5}$$

and

$$\lambda = \frac{e_z}{1 + e_z} \tag{6}$$

Then

$$d(r_i u) + udu + \lambda r_i dr_i = 0 \tag{7}$$

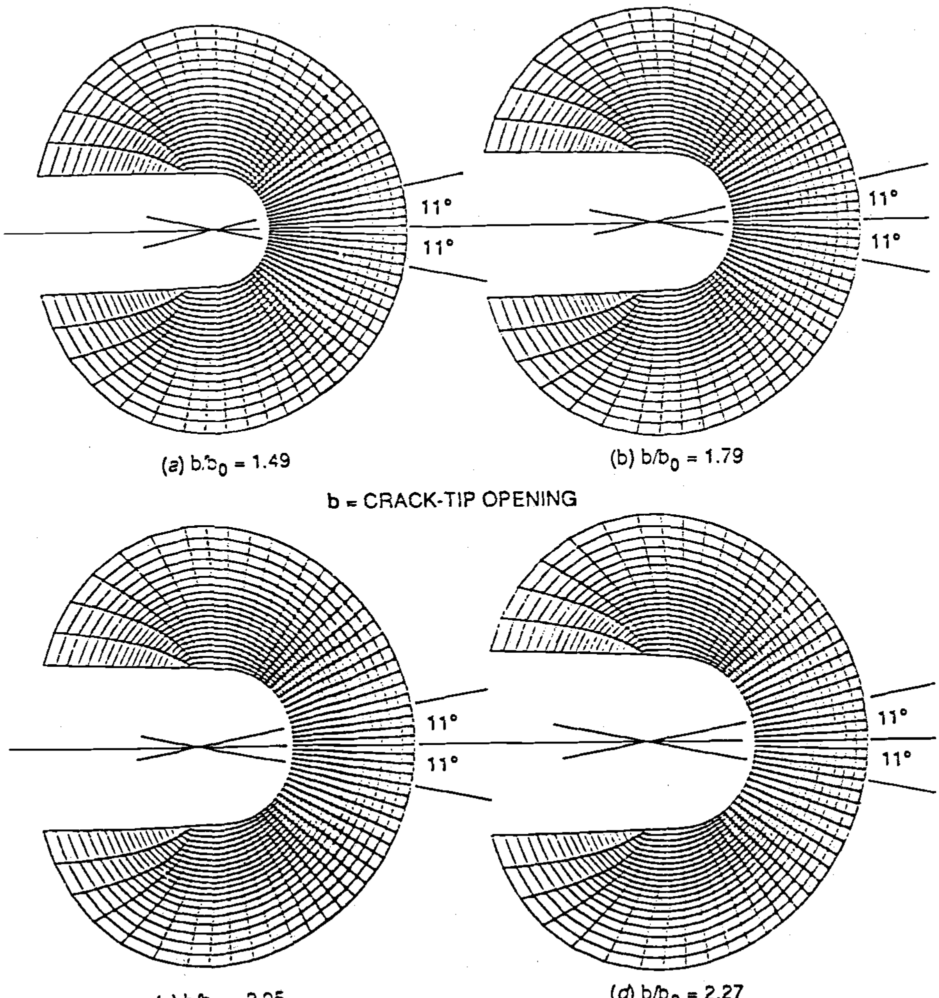

FIG. 3—*Deformed finite-element mesh diagrams for blunting crack tip (based on Ref 6).*

so that

$$u^2 + 2r_iu - (c^2 - \lambda r_i^2) = 0 \tag{8}$$

where c^2 is a constant of integration. From Eq 8, it follows that

$$u = \sqrt{(1 - \lambda)r_i^2 + c^2} - r_i \tag{9}$$

Setting $r_i = 0$ gives $u = c$, so c is the radial displacement of a point originally located at $r_i = 0$. In terms of the CTOD

$$c = \frac{\delta_t}{2} \tag{10}$$

For large strains, the circumferential strain is defined by

$$\varepsilon_\theta = \ln\left(1 + \frac{u}{r_i}\right) \tag{11}$$

so that, using Eq 9

$$\varepsilon_\theta = \frac{1}{2}\ln\left[(1 - \lambda) + \frac{c^2}{r_i^2}\right] \tag{12}$$

Note that a singularity in strain occurs for $r_i = 0$. For large strains, the axial strain is defined by

$$\varepsilon_z = \ln(1 + e_z) \tag{13}$$

so that, from Eq 6

$$\varepsilon_z = -\ln(1 - \lambda) \tag{14}$$

For large strains, the radial strain is defined by

$$\varepsilon_r = \ln\left(1 + \frac{du}{dr_i}\right) \tag{15}$$

so that, by using Eqs 9 and 14

$$\varepsilon_r = -\frac{1}{2}\ln\left[(1 - \lambda) + \frac{c^2}{r_i^2}\right] - \varepsilon_z \tag{16}$$

The foregoing equations agree with those published by McGregor et al. [7] in 1948.

For applications, it is useful to have the strain-displacement equations also expressed in terms of the deformed radius, r, defined by

$$r = r_i + u \tag{17}$$

Combining Eqs 17 and 9 gives

$$r_i^2 = \frac{r^2 - c^2}{1 - \lambda} \tag{18}$$

and by using Eq 14

$$r_i^2 = (r^2 - c^2)e^{\varepsilon_z} \tag{19}$$

From Eqs 11 and 17, it follows that

$$\varepsilon_\theta = \ln\left(\frac{r}{r_i}\right) \tag{20}$$

so that, by using Eqs 19 and 20

$$\varepsilon_\theta = -\frac{1}{2}\ln\left(1 - \frac{c^2}{r^2}\right) - \frac{\varepsilon_z}{2} \tag{21}$$

In Eq 21, ε_θ becomes singular at $r = c$. By substituting Eq 18 into Eq 16 and using Eq 14

$$\varepsilon_r = \frac{1}{2}\ln\left(1 - \frac{c^2}{r^2}\right) - \frac{\varepsilon_z}{2} \tag{22}$$

Note that the preceding strain-displacement equations do not include the elastic strains, which are assumed small, and also that their algebraic forms are independent of the shape of the stress-strain curve. This observation agrees with the finite-difference results obtained by Rice and Johnson [*2*] wherein, for plane strain, the same near-tip strain distribution was found to exist independent of the yield strain and the strain-hardening exponent.

The form of Eqs 21 and 22 can be examined by using Mohr's circle of strain. For generalized plane strain and constant plastic volume, if the maximum shear strain is denoted by η and

$$\varepsilon_2 = \varepsilon_z \tag{23}$$

then ε_1 and ε_3 must be given by

$$\varepsilon_1 = \eta - \frac{\varepsilon_z}{2} \tag{24}$$

and

$$\varepsilon_3 = -\eta - \frac{\varepsilon_z}{2} \tag{25}$$

Comparisons with Numerical Calculations

Because the basis for the hollow-cylinder analogy is partly empirical and direct experimental verification is not possible, it is important to establish its accuracy by means of comparisons with other independently performed analyses. The quantity of most interest is the maximum principal tensile strain, ε_θ, acting normal to the plane of symmetry. Because the near-crack-tip strain distribution is highly nonlinear, it is convenient to construct a function of ε_θ that is linear with distance from the crack tip. This is possible because there is only one term containing r_t in Eq 12. Thus, by rearranging Eq 12, for plane strain

$$\frac{1}{\sqrt{e^{2\varepsilon_\theta} - 1}} = \frac{r_t}{c} = F(\varepsilon_\theta) \tag{26}$$

Figure 4 shows the near-crack-tip strain distribution for $\theta = 0°$ based on undeformed positions, X, for small-scale yielding and fully plastic conditions, as calculated by Rice and Johnson [*2*] using the finite-difference method. Figure 4 also shows the plots of $F(\varepsilon_y^{tr})$, constructed for each case by scaling values from the strain curves and calculating $F(\varepsilon_y^{tr})$. Substantial linearity is observed. An added advantage of the linear plot is that no distance origin has to be assumed. While Fig. 4 shows that the calculated values of $F(\varepsilon_y^{tr})$ plot close to a straight line, the

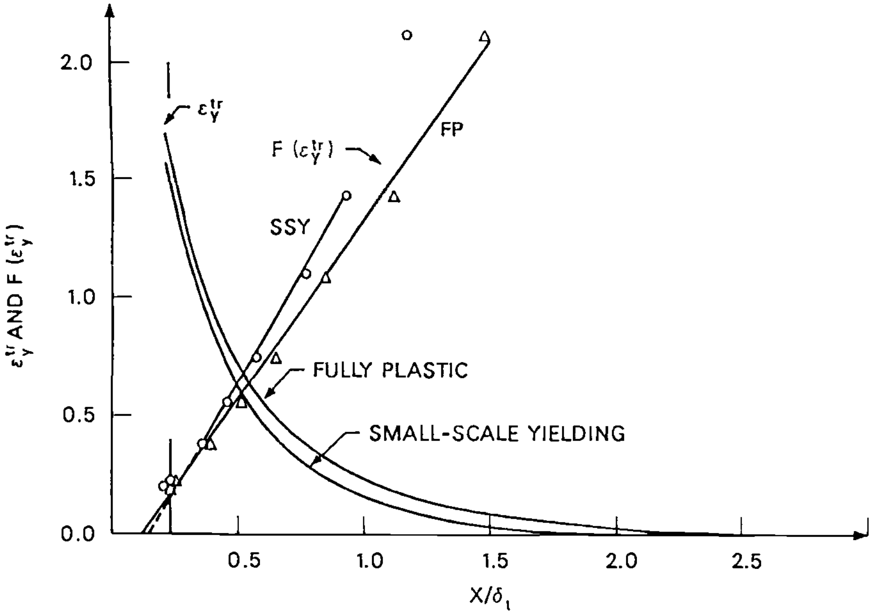

FIG. 4—*Near-crack-tip strain and linearized strain function plots for finite-difference analysis results of Rice and Johnson (based on Ref 2).*

distance origin is not at the original crack tip, but slightly ahead of it. This is qualitatively confirmed by Fig. 5 from Rice and Johnson [2] which shows that the curved portion of the blunted crack profile meets a horizontal segment of the crack profile slightly ahead of the original crack tip. Thus, in this case, the coordinate origin of the approximately logarithmic spiral slip-line region lies ahead of the original crack tip. A second comparison is shown in Fig. 6 using the

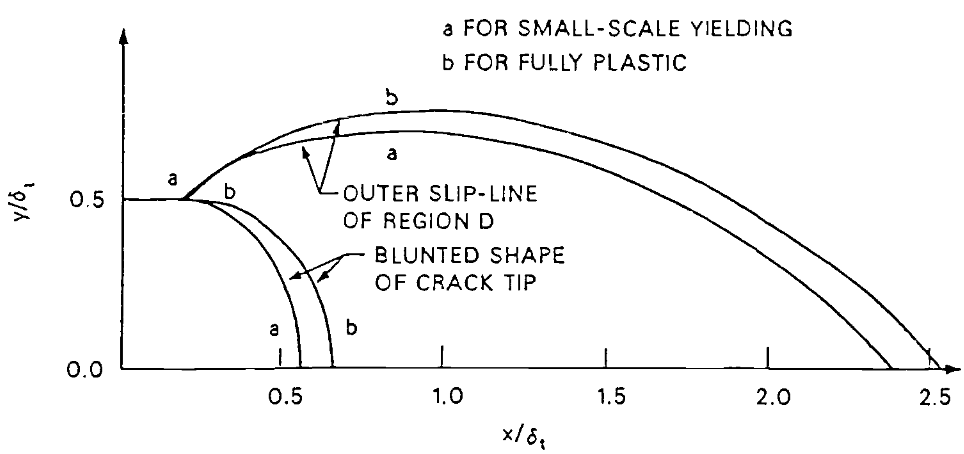

FIG. 5—*Deformed crack-tip and slip-line zone boundary results obtained by Rice and Johnson (source: Ref 2).*

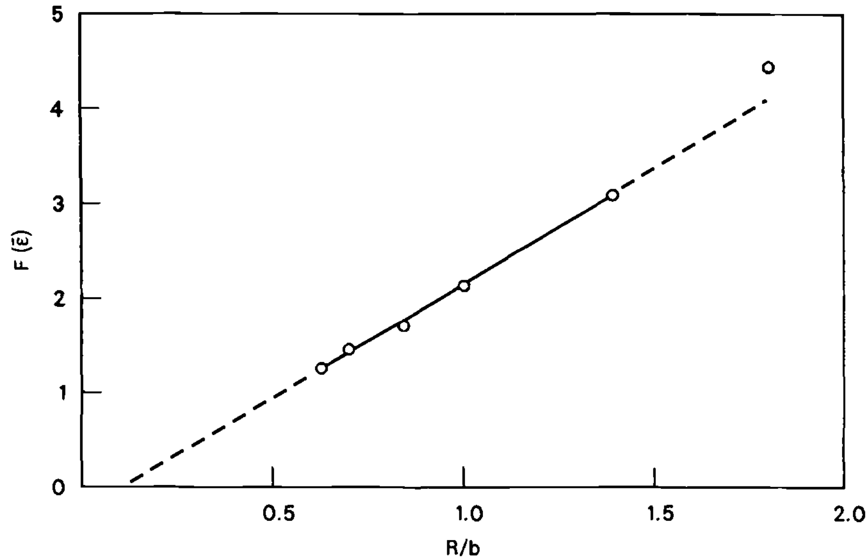

FIG. 6—*Linearized strain function plot for finite-element analysis results of McMeeking (based on Ref 5).*

effective plastic strain values for $\theta = 0°$ from Fig. 2 as calculated by McMeeking [*5*] using the finite-element method. Again $F(\varepsilon_\theta)$ is nearly linear over a substantial range of R/b, where R is the original distance from the crack tip and b is CTOD. Again, the curve intercept is slightly ahead of the original crack tip. Thus, two near-crack-tip analyses, the first being Rice's and Johnson's finite-difference analysis [*2*] and the second being McMeeking's finite-element analysis, [*4*] have both produced near-crack-tip strain distributions having forms close to that predicted by the hollow-cylinder analogy based on large strains.

Two other available strain distributions, calculated by the finite-element method by Needleman and Tvergaard [*6*] and by Goldthorpe, [*8*] produce plots of $F(\varepsilon_\theta)$ (not shown) that are linear until very close to $X = 0$ but then seem to approach a finite value of strain at $X = 0$. Both the latter analyses were begun with finite initial notch radii, as were McMeeking's, so the reason for the difference in result is not obvious. Because both Rice and Johnson [*2*] and McMeeking [*5*] clearly recognized and demonstrated the existence of a strain singularity for sharp cracks, preference is given here to their results because they are believed to be more accurate very close to the blunting crack tip.

Because a real material cannot stand infinite strain and the blunting crack surface is free of normal stress, and therefore under low triaxial constraint, shear fracture should tend to occur very close to the blunting crack tip. This is a possible explanation for the occurrence of stretch zones.

An additional comparison can be made between the strain distributions calculated by the Rice and Johnson slip-line analysis method and the hollow-cylinder analogy discussed in this chapter. In Ref *3*, two modifications were made to the Rice and Johnson slip-line analysis method to make it more useful and more realistic. The analysis was rederived for generalized plane strain, and the maximum principal tensile strain at the apex of the slip-line field was made nonzero. It is easily shown that for a nearly plane strain degree of constraint and $\nu = 0.3$, the elastically calculated maximum principal tensile strain at a distance of two times the

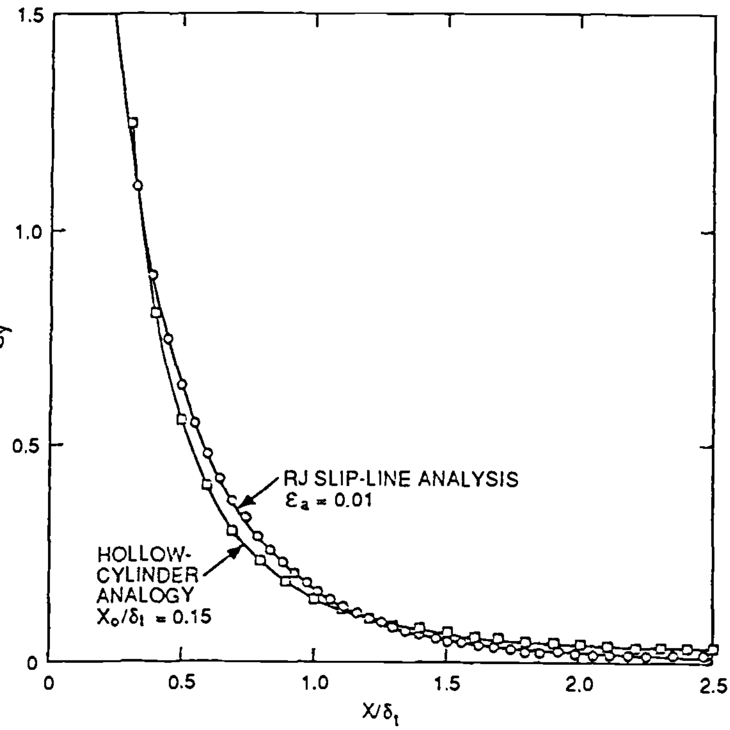

FIG. 7—*Comparison of near-crack-tip strain distribution curves obtained by Rice and Johnson method, as described in Ref 3, assuming* ε_a = *0.01, and by hollow-cylinder analogy based on large-strain theory, assuming* X_0/δ_t = *0.15.*

CTOD from the crack tip is ~1%. Thus, the total tensile strain at this location must equal or exceed this value. Assuming a total shear strain at the apex of 1%, the comparison between the modified slip-line analysis method results of Ref *3* and the hollow-cylinder analogy results are as shown in Fig. 7. Overall, the hollow-cylinder analogy is a good approximation. The assumed horizontal offset, X_0, for the hollow-cylinder analogy governs the accuracy of the strain approximation near the blunting crack tip but has no effect near the apex of the log spiral slip-line zone. The closeness of the hollow-cylinder approximation near the apex of the slip-line zone depends on the assumed value of the shear strain at that location in the modified slip-line analysis model. Because the hollow-cylinder analogy provides a satisfactory strain estimate, the next step is to calculate the stresses on the plane of symmetry.

Stress Calculations

For radial and circumferential principal stress directions, the equation of radial equilibrium, written in terms of current radii, has the familiar form

$$\frac{d\sigma_r}{dr} = \frac{\sigma_\theta - \sigma_r}{r} \tag{27}$$

In this analysis, the elastic strains are neglected. Thus, the usual superscript, p, on strain symbols indicating plastic strain is not used. The general equation for the von Mises effective plastic strain is

$$\bar{\varepsilon} = \frac{\sqrt{2}}{3}\sqrt{(\varepsilon_1 - \varepsilon_2)^2 + (\varepsilon_2 - \varepsilon_3)^2 + (\varepsilon_3 - \varepsilon_1)^2} \tag{28}$$

Using Eqs 21 through 25

$$\eta = \varepsilon_\theta + \frac{\varepsilon_z}{2} \tag{29}$$

and

$$\bar{\varepsilon} = \frac{2}{\sqrt{3}}\eta\sqrt{1 + \frac{3}{4}\left(\frac{\varepsilon_z}{\eta}\right)^2} \tag{30}$$

Eliminating η from Eq 30 gives

$$\bar{\varepsilon} = \frac{2}{\sqrt{3}}\varepsilon_\theta\sqrt{1 + \frac{\varepsilon_z}{\varepsilon_\theta} + \left(\frac{\varepsilon_z}{\varepsilon_\theta}\right)^2} \tag{31}$$

The general equation for the von Mises effective stress is

$$\sigma_e = \frac{1}{\sqrt{2}}\sqrt{(\sigma_1 - \sigma_2)^2 + (\sigma_2 - \sigma_3)^2 + (\sigma_3 - \sigma_1)^2} \tag{32}$$

For deformation theory, the principal plastic strains are given by the flow rule, which can be written in the form

$$\varepsilon_i = \frac{1}{2}\frac{\bar{\varepsilon}}{\sigma_e}\frac{\partial\sigma_e^2}{\partial\sigma_i} \tag{33}$$

Using Eqs 32 and 33

$$(\sigma_\theta - \sigma_r) = \frac{2}{\sqrt{3}}\sigma_e\sqrt{1 - \left(\frac{\varepsilon_z}{\bar{\varepsilon}}\right)^2} \tag{34}$$

as found by McGregor et al. [7]. From Eq 31

$$\left(\frac{\varepsilon_z}{\bar{\varepsilon}}\right)^2 = \frac{\frac{3}{4}\left(\frac{\varepsilon_z}{\varepsilon_\theta}\right)^2}{1 + \frac{\varepsilon_z}{\varepsilon_\theta} + \left(\frac{\varepsilon_z}{\varepsilon_\theta}\right)^2} \tag{35}$$

so that substituting Eq 35 into Eq 34 gives

$$(\sigma_\theta - \sigma_r) = \frac{2}{\sqrt{3}}\sigma_e \sqrt{\frac{1 + \frac{\varepsilon_z}{\varepsilon_\theta} + \frac{1}{4}\left(\frac{\varepsilon_z}{\varepsilon_\theta}\right)^2}{1 + \frac{\varepsilon_z}{\varepsilon_\theta} + \left(\frac{\varepsilon_z}{\varepsilon_\theta}\right)^2}} \tag{36}$$

From Eq 27

$$d\sigma_r = (\sigma_\theta - \sigma_r)\frac{dr}{r} \tag{37}$$

Therefore, the radial stress can be calculated incrementally, starting at the free surface of the blunted crack tip and using Eq 36 and the effective stress-strain relationship, which is general. In this analysis, the effective stress-strain relationship is assumed to be a pure power law, according to which

$$\sigma_e = \sigma_0\left(\frac{\bar{\varepsilon}}{\varepsilon_0}\right)^N \tag{38}$$

Thus, substituting Eq 31 into Eq 38, the result into Eq 36, and then using Eq 37 gives

$$\frac{d\sigma_r}{\sigma_0} = \frac{2}{\sqrt{3}}\left(\frac{2}{\sqrt{3}\varepsilon_0}\right)^N \left\{ \varepsilon_\theta^N \frac{\left[1 + \frac{\varepsilon_z}{\varepsilon_\theta} + \frac{1}{4}\left(\frac{\varepsilon_z}{\varepsilon_\theta}\right)^2\right]^{1/2}}{\left[1 + \frac{\varepsilon_z}{\varepsilon_\theta} + \left(\frac{\varepsilon_z}{\varepsilon_\theta}\right)^2\right]^{(1-N)/2}} \right\} \frac{dr}{r} \tag{39}$$

Also, by again using Eq 37

$$\frac{\sigma_\theta}{\sigma_0} = \frac{\sigma_r}{\sigma_0} + \frac{2}{\sqrt{3}}\left(\frac{2}{\sqrt{3}\varepsilon_0}\right)^N \left\{ \varepsilon_\theta^N \frac{\left[1 + \frac{\varepsilon_z}{\varepsilon_\theta} + \frac{1}{4}\left(\frac{\varepsilon_z}{\varepsilon_\theta}\right)^2\right]^{1/2}}{\left[1 + \frac{\varepsilon_z}{\varepsilon_\theta} + \left(\frac{\varepsilon_z}{\varepsilon_\theta}\right)^2\right]^{(1-N)/2}} \right\} \tag{40}$$

The stresses are calculated for the deformed radii. For calculating $d\sigma_r$ from Eq 39, the strain at the average radius over an increment of distance is used. For calculating σ_θ from Eq 40, the strain at the point of interest is used.

An equation for the transverse stress, σ_z, can be obtained by using the flow rule, Eq 33, and the effective stress-strain relationship. The result is

$$\frac{\sigma_z}{\sigma_0} = \left(\frac{\bar{\varepsilon}}{\varepsilon_0}\right)^N \left(\frac{\varepsilon_z}{\bar{\varepsilon}}\right) + \frac{1}{2}\left(\frac{\sigma_r}{\sigma_0} + \frac{\sigma_\theta}{\sigma_0}\right) \tag{41}$$

A constraint factor [9], h, defined by

$$h = \frac{\sigma_m}{\sigma_e} \tag{42}$$

where σ_m is the hydrostatic stress, is sometimes used for comparing the severity of different stress states with regard to the possibility of fracture. The quantity, h, can be calculated from

$$h = \frac{1}{3}\left(\frac{\varepsilon_z}{\bar{\varepsilon}}\right) + \frac{1}{2}\frac{\left(\dfrac{\sigma_r}{\sigma_0} + \dfrac{\sigma_\theta}{\sigma_0}\right)}{\left(\dfrac{\bar{\varepsilon}}{\varepsilon_0}\right)^N} \tag{43}$$

Effects of the Strain Singularity

The strain singularity that exists at the surface of the blunting crack tip, in the case of an infinitely sharp initial crack, has an effect on the stresses for strain-hardening material. The effect is to cause a singularity in the crack-opening stress, which in turn can cause a minimum to occur in that stress as a function of r, as the effects of the singularity decrease and the effects of triaxial constraint begin to dominate. Because the in-plane strains are large compared with the out-of-plane strain very close to the blunting crack tip, an analysis of the effects of the singularity for the case of plane strain should be adequately descriptive.

Solving the equation of radial equilibrium, Eq 27, for σ_θ and differentiating gives

$$\frac{d\sigma_\theta}{dr} = 2\frac{d\sigma_r}{dr} + r\frac{d\left(\dfrac{d\sigma_r}{dr}\right)}{dr} \tag{44}$$

For plane strain, Eq 39 gives

$$\frac{d\sigma_r}{dr} = \frac{2}{\sqrt{3}}\frac{\sigma_0}{r}\left(\frac{2}{\sqrt{3}\varepsilon_0}\right)^N \varepsilon_\theta^N \tag{45}$$

Let

$$S = \frac{2}{\sqrt{3}}\sigma_0\left(\frac{2}{\sqrt{3}\varepsilon_0}\right)^N \tag{46}$$

Then substituting Eq 46 into Eq 45 gives

$$\frac{d\sigma_r}{dr} = \frac{S}{r}\varepsilon_\theta^N \tag{47}$$

and substituting Eq 47 into Eq 44 leads to

$$\frac{d\sigma_\theta}{dr} = \frac{S\varepsilon_\theta^N}{r} + SN\varepsilon_\theta^{N-1}\frac{d\varepsilon_\theta}{dr} \tag{48}$$

For $d\sigma_\theta/dr = 0$, either $\varepsilon_\theta = 0$ or

$$\frac{d \ln \varepsilon_\theta}{d \ln r} = -\frac{1}{N} \tag{49}$$

Thus, stationary values of σ_θ occur at infinity and when Eq 49 is satisfied. If there are two stationary points and the curve of σ_θ is positive singular at $r = c$, then the first stationary point must be a local minimum because a local maximum would require three stationary values between $r = c$ and $r = \infty$. It is also possible to show that the first stationary value is a local minimum by using Eqs 48 and 49 to develop the expression for $d^2\sigma_\theta/d(\ln r)^2$ at the first stationary point. The result is

$$\frac{d^2\sigma_\theta}{d(\ln r)^2} = NS\varepsilon_\theta^N \frac{d^2 \ln \varepsilon_\theta}{d(\ln r)^2} \tag{50}$$

which gives a positive quantity.

For plane strain, the location of the local minimum can be calculated by applying Eq 49 to Eq 21, which gives

$$\varepsilon_\theta = \frac{N}{\left(\frac{r}{c}\right)^2 - 1} \tag{51}$$

Using Eq 19 for plane strain

$$\left(\frac{r}{c}\right)^2 - 1 = \left(\frac{r_i}{c}\right)^2 \tag{52}$$

so that substituting Eqs 21 and 52 into Eq 51 gives

$$\frac{\ln\left[1 + \left(\frac{c}{r_i}\right)^2\right]}{\left(\frac{c}{r_i}\right)^2} = 2N \tag{53}$$

The limit of the left side of Eq 53 as (c/r_i) approaches zero is unity. Thus, there is no local minimum for values of N exceeding 0.5. Equation 53 is plotted in Fig. 8, from which locations of the local minimum can be determined graphically.

Calculating the first increment of the radial stress very close to the blunting crack tip requires an approximation because of the singularity in the circumferential strain. For plane strain, Eq 39 reduces to

$$\frac{d\sigma_r}{\sigma_0} = \frac{2}{\sqrt{3}}\left(\frac{2}{\sqrt{3}\varepsilon_0}\right)^N \varepsilon_\theta^N \frac{dr}{r} \tag{54}$$

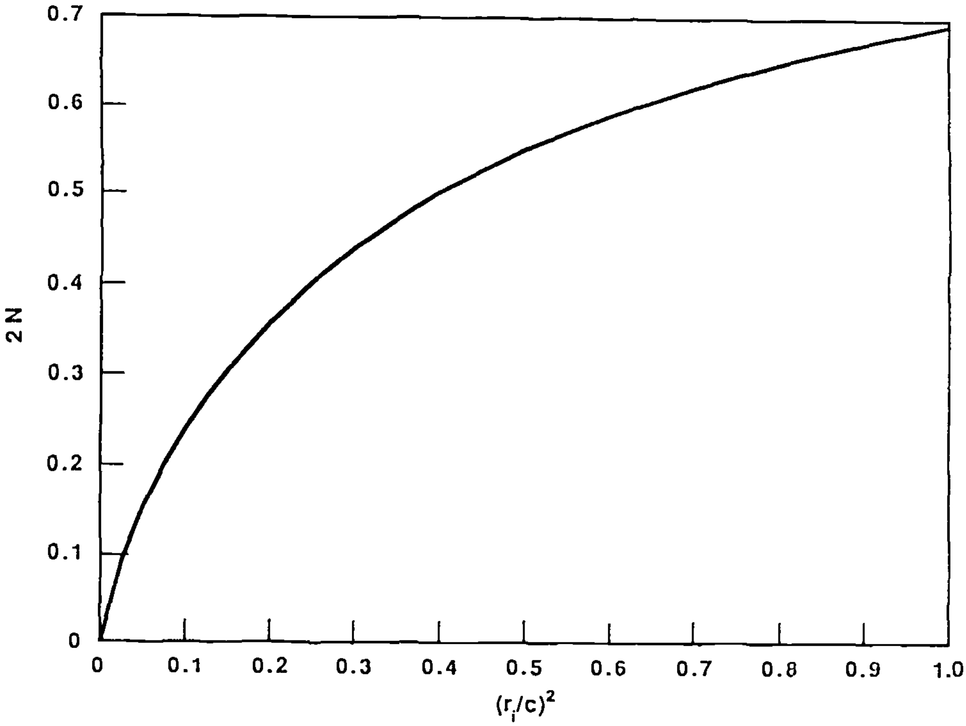

FIG. 8—*Curve for determining location of local minimum in crack-opening stress as a function of the strain-hardening exponent,* N.

Also, for plane strain, Eq 21 can be written in the form

$$\varepsilon_\theta = -\frac{1}{2}\ln\left[\left(1+\frac{c}{r}\right)\left(1-\frac{c}{r}\right)\right] \tag{55}$$

Near the singularity, $r \sim c$ so that

$$\varepsilon_\theta \sim -\frac{1}{2}\ln\left[\frac{2}{c}(r-c)\right] \tag{56}$$

Let

$$r - c = v \tag{57}$$

Then noting that

$$\frac{dr}{r} = \frac{1}{2}d\left(2\frac{v}{c}\right) \tag{58}$$

substituting Eq 57 into Eq 56 and the result, plus Eq 58 into Eq 54, gives

$$d\left(\frac{\sigma_r}{\sigma_0}\right) = \frac{\left(\ln \dfrac{1}{2\dfrac{v}{c}}\right)^N}{3^{(1+N)/2}\varepsilon_0}\, d\left(2\frac{v}{c}\right) \tag{59}$$

Integrating by parts, neglecting the second term as small, and using Eq 57 gives, for the first increment of radial stress

$$\frac{\sigma_r}{\sigma_0} = \frac{2\left(\dfrac{r}{c}-1\right)\left[\ln \dfrac{1}{2\left(\dfrac{r}{c}-1\right)}\right]^N}{3^{(1+N)/2}\varepsilon_0^N} \tag{60}$$

Effects of Transverse Strain

The foregoing equations were used to calculate the in-plane and transverse stresses for three example problems. The example problems were identical except for the values of transverse plastic strain, which were -1, 0, and $+1$%, respectively. The other parameters used were $\varepsilon_0 = 0.0025$, $N = 0.2$, and $c = 0.5\ \delta_t$. The results are plotted in Fig. 9, which shows that the effect of a given amount of transverse plastic strain of either algebraic sign is to reduce the circumferential stress from its plane strain value by the same relatively small amount. The same is true for the radial stress. This result was not anticipated because the elastic-plastic, small-strain, hollow-cylinder analogy equations [*4*] implied that positive transverse strain would increase the in-plane stresses and that negative transverse strain would do the opposite. Nevertheless, in retrospect, it is clear that the results obtained here are a direct consequence of Eqs 21, 29, 30, 34, and 37, because, from Eqs 21 and 29, η is independent of ε_z, only the square of ε_z appears in Eqs 30 and 34, and ε_z does not appear in Eq 37. Furthermore, the present results agree qualitatively with the more exact results obtained in Ref *3*. In the case of the transverse stress, also plotted in Fig. 9, positive transverse strain increases the transverse stress, and negative transverse strain does the opposite. Furthermore, the transverse stress is more affected by the transverse strain than are the in-plane stresses. The effect of increasing transverse strain is to increase the constraint factor, h, because of the increase in transverse stress, thereby potentially decreasing the fracture toughness.

Discussion

In comparing analyses, those presented here and in Ref *3* neglect elastic strains, therefore assuming that all the transverse strains are plastic strains. In contrast, the small-strain, hollow-cylinder analogy equations from Ref *4* were based on the Tresca yield criterion, which predicts no plastic strain in the direction of the intermediate principal stress, thus forcing the total strain in that direction to be completely elastic. It appears that transverse elastic and plastic strains may have different effects on the in-plane stresses, and therefore including the elastic strains in a near-tip analysis would be beneficial. It has also been estimated recently [*10*] that

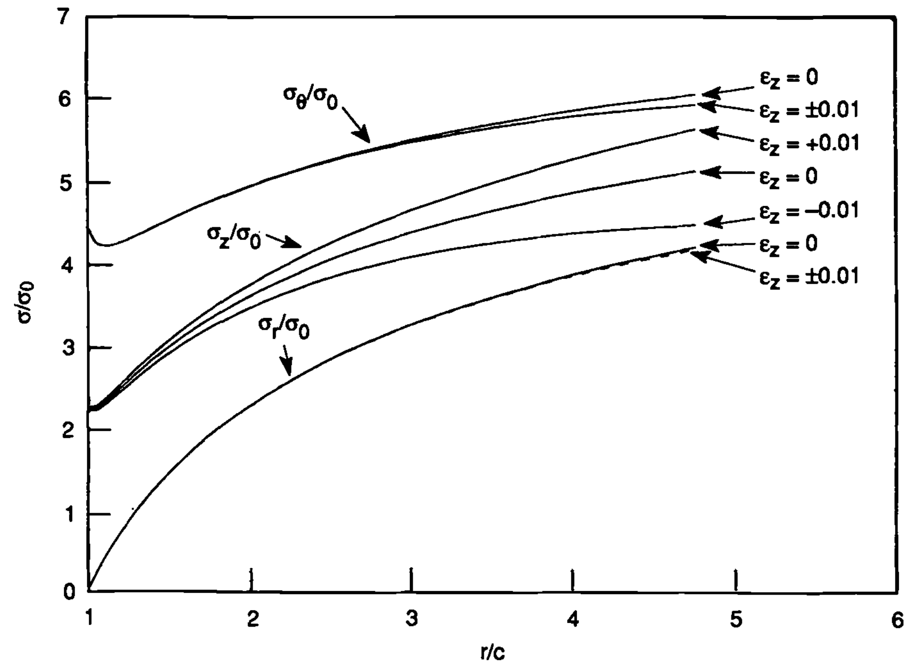

FIG. 9—*Stresses near a blunting crack tip, with transverse plastic strain as a parameter, as calculated by the hollow-cylinder analogy for large strains for* N = *0.2 and neglecting elastic strains.*

somewhat beyond the near-crack-tip large-strain region, positive and negative total transverse strains do not necessarily have either opposite or identical effects because the total strains are partitioned differently into elastic and plastic parts in the two cases. The present analysis does not explain the observed significant effects of geometrical constraint on cleavage fracture toughness, evidently because of what it omits; namely, elastic strains in the large-strain region and constraint-induced in-plane stress variations beyond the large-strain region. The effects of transverse strain on the latter, for three-dimensional problems, is presently not known. Despite their approximations, the analyses developed here and in Ref *3* have provided valuable new information about near-crack-tip stresses and strains, especially about their magnitudes at both ends of the large-strain region and the effects of transverse strain, and further developments appear feasible.

Conclusions

Large-strain finite element analyses have shown that a wedge-shaped zone ahead of a blunting crack tip deforms like a cylinder. Therefore, a hollow cylinder stress analysis analogy is valid in this region. Applications of this analogy based on large-strain theory have produced results in good agreement with those of Rice and Johnson, and McMeeking. Furthermore, they reveal that the stresses in the large-strain region ahead of a blunting crack tip are only mildly sensitive to transverse constraint, if elastic strains are neglected. Therefore, constraint effects on fracture toughness are likely to be caused by some combination of elastic strain effects in the large-strain region and constraint-induced stress variations just beyond the large-strain region.

Acknowledgment

This research was sponsored by the Office of Nuclear Regulatory Research, U.S. Nuclear Regulatory Commission under Interagency Agreement 1886-8011-9B with the U.S. Department of Energy under Contract DE-AC05-84OR21400 with Martin Marietta Energy Systems, Inc. The submitted manuscript has been authored by a contractor of the U.S. Government under Contract No. DE-AC05-84OR21400. Accordingly, the U.S. Government retains a nonexclusive, royalty-free license to publish or reproduce the published form of this contribution, or allow others to do so, for U.S. Government purposes.

References

[1] Hill, R., *The Mathematical Theory of Plasticity,* Oxford Press, Amen House, London, 1950.

[2] Rice, J. R. and Johnson, M. A., "The Role of Large Crack Tip Geometry Changes in Plane Strain Fracture," Report NYO-2394-38, Brown University, Providence, RI, Sept. 1969; see also, *Inelastic Behavior of Solids,* M. F. Kanninen et al., Eds., McGraw-Hill, New York, 1970.

[3] Shum, D. K. M., "Crack Initiation Under Generalized Plane-Strain Conditions," this publication.

[4] Merkle, J. G., "An Elastic-Plastic Thick-Walled Hollow Cylinder Analogy for Analyzing the Strains in the Plastic Zone Just Ahead of a Notch Tip," ORNL-TM-4071, Oak Ridge National Laboratory, Oak Ridge, TN, Jan. 1973.

[5] McMeeking, R. M., "Finite Deformation Analysis of Crack-Tip Opening in Elastic-Plastic Materials and Implications for Fracture," *Journal of the Mechanics and Physics of Solids,* Vol. 25, 1977, pp. 357–381.

[6] Needleman, A. and Tvergaard, V., "Crack-Tip Stress and Deformation Fields in a Solid with a Vertex on Its Yield Surface," *Elastic-Plastic Fracture: Second Symposium, Volume I: Inelastic Crack Analysis, ASTM STP 803,* C. F. Shih and J. P. Gudas, Eds., American Society for Testing and Materials, Philadelphia, 1983, pp. 80–115.

[7] MacGregor, C. W., Coffin, L. F., and Fisher, J. C., "The Plastic Flow of Thick-Walled Tubes with Large Strains," *Journal of Applied Physics,* Vol. 19, March 1946, pp. 291–297.

[8] Goldthorpe, M. R., "An Investigation of Size Effects in Compact Tension and Centre-Cracked Tension Specimens of an Austenitic Steel Using Elastic-Plastic Finite Element Analysis," Report under SERC Grant No. GR/E/79088, Structural Integrity Research Institute, University of Sheffield, Sheffield, UK, April 1989.

[9] Kordische, H., Sommer, E., and Schmidt, W., "The Influence of Triaxiality on Stable Crack Growth," *Nuclear Engineering and Design,* Vol. 112, 1989, pp. 27–35.

[10] Shum, D. K. M., Merkle, J. G., Keeney-Walker, J., and Bass, B. R., "Analytical Studies of Transverse Strain Effects on Fracture Toughness for Circumferentially Oriented Cracks," NUREG/CR-5592 (ORNL/TM-11581), Oak Ridge National Laboratory, Oak Ridge, TN, April 1991.

Robert J. Dexter[1] *and Samit Roy*[2]

The Conditions at Ductile Fracture in Tension Tests

REFERENCE: Dexter, R. J. and Roy, S., **"The Conditions at Ductile Fracture in Tension Tests,"** *Fracture Mechanics: Twenty-Third Symposium, ASTM STP 1189,* Ravinder Chona, Ed., American Society for Testing and Materials, Philadelphia, 1993, pp. 115–132.

ABSTRACT: The geometry dependence of several potential criteria for the onset of ductile fracture in tension tests was investigated for a modern tremethylcyclopentanone (TMCP) line pipe steel using an experimental/numerical approach. Large-strain finite-element simulations were used to estimate the state of stress and strain in highly instrumented notched and smooth tension tests of various geometries. The softening effect of void growth became significant only after the specimens had undergone extensive necking and had lost most of their load-carrying capacity. Therefore, for this steel, a practical fracture criterion can be based on the conditions at the onset of significant void growth, eliminating the need for void-growth modeling. At the onset of significant void growth, the maximum principal strain, the effective strain, and the strain energy density were independent of the tension-test geometry.

KEY WORDS: ductile fracture, steels, tension tests, large-deformation analysis, finite-element method, necking, fracture mechanics, fatigue (materials)

When materials fail in a brittle manner without exhibiting much plastic strain, the interpretation of tension test results is straightforward. However, when the specimen is loaded in displacement control and there is significant ductility, the plastic strain typically localizes in a way that is dependent on the specimen boundary conditions, geometry, and the associated stress state. Only the average stress and strain distributions can be inferred from the experimental data. Therefore, it is not clear how the tension test results should be used to predict the plastic behavior and failure (defined as actual separation) of components with other geometries.

A more complicated but possibly related problem is predicting ductile failure of cracked components. If the structure or component is subjected to load control, it is sufficient to make a prediction of the fracture load. It is not difficult to get a lower-bound estimate of the limit load [*1–3*], which corresponds to the yield strength. If brittle fracture and low-energy ductile fracture are avoided, the collapse load can be reached. The collapse load is usually estimated from the limit-load equations using the flow stress (usually defined as the average of the yield and engineering ultimate strength) in place of the yield strength. Because of the relatively flat slope of the load-deformation curve characteristic of steel components after yielding, the error in terms of the actual and predicted collapse loads is usually small. However, for structures that are loaded in displacement control (most structures with redundancy) or for localized failure regions restrained from collapse by surrounding elastic material, it would be useful to have a means of predicting stable extension of a crack.

[1] ATLSS Center, Lehigh University, Bethlehem, PA 18015-4729.
[2] Engineering and Materials Sciences Division, Southwest Research Institute, San Antonio, TX 78228-0510.

The ductile fracture mechanisms and models have been reviewed recently in a book by Thomason [4] and an article by Wilsdorf [5]. The ductile fracture process involves void growth that is generally thought to be controlled by a function of the stress and strain, for example, see Ref 6. (This is contrasted with cleavage fracture that is thought to be controlled primarily by the stress [7,8].) Because these local fracture criteria are very difficult to observe in the laboratory and calculate in the structural application (a large-strain numerical simulation is required), an indirect means of analyzing fracture has been developed, that is, fracture mechanics. Fracture mechanics has given us a methodology to relate the failure conditions in objects with various geometries containing discrete cracks [9].

Elastic-plastic fracture mechanics, based on the J-integral [10,11], allows a prediction of tearing. Under special conditions, the crack-tip stress and strain fields in a region within a radius of about six times the crack-tip opening displacement (CTOD) can be predicted as a function of J, the stress-strain law, and the spatial coordinates [12]. These conditions include a stationary crack loaded monotonically in bending with an uncracked ligament greater than about 30 times the CTOD. There are also very limited conditions under which the stress and strain fields of a growing crack may be similarly characterized [13–17]. Crack initiation and growth are controlled by the stress and strain, but since under these special circumstances the stress and strain fields are characterized by J, crack initiation and possibly a small increment of crack growth may be indirectly J-controlled.

Modern low-alloy steels in the upper-shelf of the toughness/temperature transition (such as the steels considered in this paper) typically exhibit too much plasticity during tearing to meet the requirements for J-controlled fracture in the available thicknesses. Consequently, the critical J-values measured from different specimens will exhibit specimen geometry dependence [18–21]. While this ductility is good for structural integrity, it unfortunately precludes the ability to analyze tearing with the J-integral.

If the J-integral approach will not work, it is logical to try to use the stress and strain directly as fracture criteria, as has been done for the case of crack initiation [22–24]. Because of the steep strain gradients and heterogeneous features of the material in the fracture process zone at the crack tip, the local criteria must be used in conjunction with a characteristic distance or area. If sufficiently general criteria could be found that governed the final separation of a material in tension tests of various geometries and stress states, these criteria should also apply to the same material ahead of a tearing crack. The unfortunate consequence of using these local fracture criteria is that simple relationships based on the load, displacement, and crack length (fracture mechanics) no longer can be used for tearing analysis. Rather, complex large-strain numerical analyses of the cracked body are required to determine the stress and strain fields ahead of the crack.

Micromechanical models have been developed to rationalize such fracture criteria, such as void nucleation, growth, and coalescence models [4,5]. However, these models are not practical for use in structural-scale models for failure prediction. A more practical model should be based on the history of variables that can be calculated from continuum mechanics, such as the stress and strain [6].

The major objection is using continuum mechanics to analyze ductile fracture is that the void growth process is not explicitly treated and therefore many important behaviors that lead to the final separation of material cannot be simulated [4]. Notwithstanding this objection, continuum mechanics can be used to simulate the conditions prior to these noncontinuum effects becoming significant.

For discussion purposes, a distinction will be made between two events leading to ductile fracture. These "events" are actually continuous processes that may be taking place simultaneously [4,5]. The first is void nucleation and the onset of significant void growth. Rather than try to detect these microscopic events, the first event will be defined as the onset of significant non-continuum effects, and referred to as damage initiation. The actual void nucleation may significantly precede what will be called "damage initiation." (As will be shown later, the onset of significant noncontinuum effects can be detected by a break in slope in the force-versus-displacement curve from a tension test.) After damage initiation, the effective (pseudocontinuum) yield surface contracts, which is called softening.

As shown later for a very clean (that is, lack of inclusions) X70 pipeline steel, at the time of damage initiation, the specimens have undergone extensive necking and have therefore lost most of their load-carrying capacity. (This may not be the case for "dirtier" steels with more inclusions that could cause earlier void nucleation and larger voids.) If it is possible to make geometry-independent predictions of damage initiation, this could constitute a conservative engineering approach to ductile fracture. Perhaps this approach is not satisfying on the micromechanical scale, but it is useful over a far greater range of conditions than the J-integral that is limited by the onset of gross plasticity.

The second and final event in the ductile fracture process is void coalescence, during which the material between voids necks and fractures. This event immediately precedes the actual separation of fracture surfaces. Predicting the behavior of the material between damage initiation and fracture is significantly more complex, for it requires equations for the rate of softening as a function of the stress and strain, that is, damage evolution equations. Also, it is in this phase that continuum mechanics is not strictly valid.

Accepting a continuum approach, failure criteria could be developed from experiments with various geometries and stress states. The histories of macroscopic stress and strain at material points on the failure plane are needed for this development. Because direct observation of the stress and strain distribution on the failure plane is not possible, an approximation of the history of the stress and strain must be obtained from a finite-element simulation of the experiments. This simulation must necessarily use accurate constitutive models and include the effect of large strains. The finite-element program, VISCRK, developed at Southwest Research Institute [*25,26*] is well suited for this purpose.

With this experimental/numerical approach in mind, an experimental program was conducted to investigate the conditions at failure in tension tests and tearing tests of various geometries. In addition to load and displacement, measurements were made in the experiments to determine the distribution of the large plastic strains on the specimen surfaces. The extra measurements were made to facilitate comparisons of the experiments to simulations performed with VISCRK.

This paper describes the tensile experiments and the results of numerical simulations of failure in tension tests. The focus is on the development and usefulness of the tools that can be used to investigate the failure criteria. The theory of the large-strain implementation, plasticity, and fracture simulation are presented in other papers [*25,26*]. The experimental tearing test data and simulations for the tearing tests are presented elsewhere [*21*]. Work is underway to develop consistent fracture criteria based on the experimental/numerical data. There are preliminary indications that something as simple as the maximum principal strain can be used as a damage initiation criteria for these modern clean steels.

Materials

Two line pipe-steels were selected for the ductile fracture experiments. The chemistry of these steels is given in Table 1. Both materials are clearly on the upper shelf of the Charpy toughness-temperature transition at room temperature and should therefore exhibit fully ductile behavior at all but the highest strain rates. The 27-J transition temperatures for the X46 and the X70 steel are 0°C and −128°C, respectively.

The material of primary interest is a "clean" (that is, low impurities and inclusions that serve

TABLE 1—*Chemical analysis for the pipeline steels (all values in percent by weight).*

Material	C	Mn	Si	P	S	Ni	Cr	Mo	Cu	Ti	Al	V	Cb	B
X46	0.24	1.20	0.26	0.020	0.022	0.02	0.04	0.01[a]	0.02	0.01[a]	0.01[a]	0.05	0.01[a]	0.0005
X70	0.06	1.50	0.30	0.013	0.008	0.24	0.02	0.01[a]	0.29	0.04	0.01	0.06	0.02	0.0005

[a] Less than 0.01%.

as void initiators) ultra-low carbon microalloyed thermo-mechanically controlled process-grade X70 steel. This steel has an acicular ferrite microstructure with islands of a second phase (probably bainite) and is among the toughest and most ductile steels available today.

This X70 steel has the fracture appearance referred to as a "shear fracture." Although shear fractures are still the result of void nucleation, growth, and coalescence under the influence of tension [*4*], the voids in these extremely ductile materials do not initiate until relatively late in the deformation process. At failure, the voids are still very fine, and hence the lack of the visibly "dimpled" failure appearance typical in ductile fracture and characteristic of the X46 steel.

The more conventional but still extremely tough X46 steel has a ferrite-pearlite microstructure. The X46 steel has a greater number of impurities and inclusions and therefore a lower fracture strain. Thus, the two steels represent different types of behavior in ductile fracture.

Test Specimen Geometries

For each material, two flat tension specimens with a 38-mm width and 9.4-mm thickness were tested. Also, round tension specimens with a nominal 6.4-mm diameter were prepared. Several of these were tested smooth, and two were tested with each of the three notch geometries shown in Fig. 1. These different notch geometries are known to produce different amounts of triaxial stress or pressure, thus these tests give a range of stress states during the evolution of plastic strain. For example, the flat specimens produce the lowest constraint. Round specimens initially provide uniaxial conditions but, after necking, significant triaxial constraint is developed. Notched specimens provide more consistent constraint throughout the deformation process.

The tension specimens were taken from the pipe such that the loading axis is parallel to the circumferential direction of the pipe, that is, transverse to the rolling direction. Flat tension specimens were taken from sections of pipe that had been flattened. Previous work showed an insignificant effect of flattening on the yield strength of these steels [*27*]. This observation was confirmed by comparing the yield stress from these tests to the yield stress from the round tension specimens that were not flattened.

Test Procedures

The round tension tests were performed in a 45-kN closed-loop servohydraulic testing machine under crosshead displacement control at a rate that gives a nominal strain rate of 10^{-4} s^{-1}. Simulations show that the strain rates increase during necking, reaching a maximum of about 0.006 s^{-1}. (During the final separation of material, the rates probably rapidly increase, however, for the reasons given in the introduction, it not necessary to understand this final behavior.) In order to investigate the effect of global strain rate, several of the tests were performed at a nominal strain rate of approximately 1 s^{-1}. Only the maximum load could be measured from these higher rate tests, and it did not seem to differ significantly from the quasi-static tests.

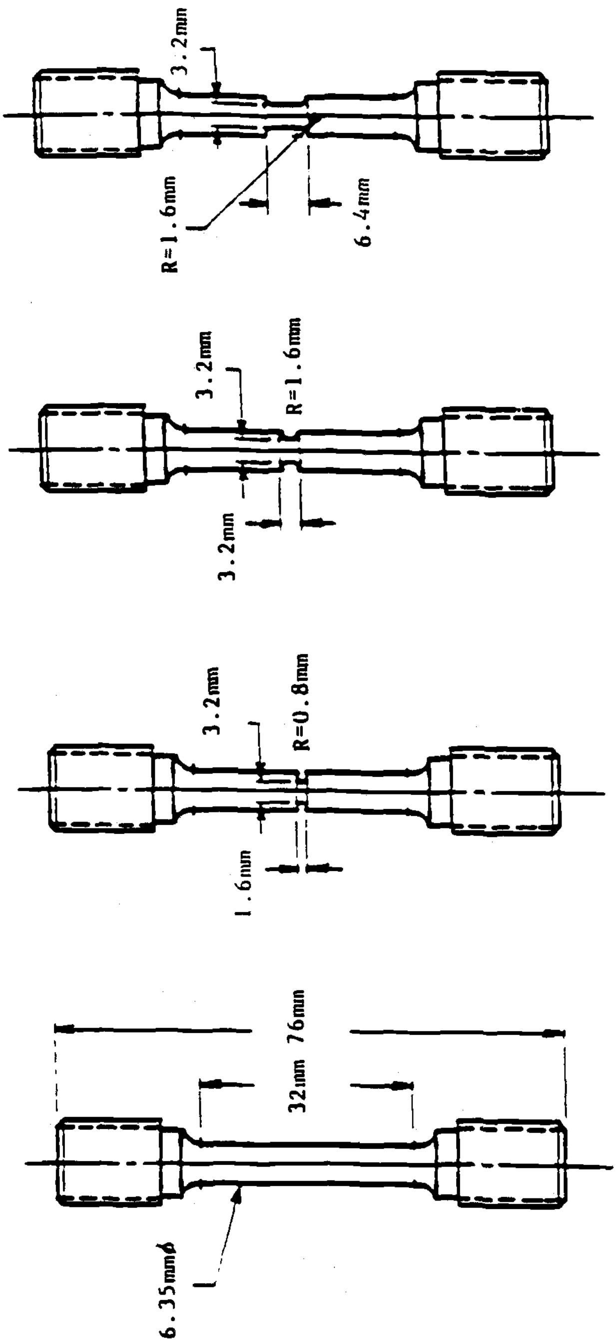

FIG. 1—*Round tension specimen geometries.*

The procedures were in accordance with the ASTM Test Methods and Definitions for Mechanical Testing of Steel Products (A 370-89). The time, load, and displacement in a centered 25-mm-gage extensometer and crosshead displacement were digitally recorded. The round tests were photographed periodically from one side and a video recording was made at a right angle from the line of the photographs. The diameters during necking were measured from the photographs and from the video. In addition, calipers were used to measure the necked diameter during the tests. Although some anisotropy is evident in the shape of the fracture at the neck, it was not significant enough that different diameters could be observed during the necking. Due to the lights used for the photography, the test temperature was 40°C.

The flat tension tests were also conducted in accordance with ASTM A 370-89 in a 450-kN closed-loop servohydraulic testing machine under crosshead displacement control at a rate that gives a nominal strain rate of 10^{-4} s^{-1}. Grids with 0.64-mm circles were photoetched on the front and back surfaces of the flat specimens. The flat specimens were photographed periodically and a continuous video recording was made; again the lights brought the test specimen temperature to 40°C. The time, load, and displacement in a centered 25-mm-gage extensometer and crosshead displacement were recorded digitally. The change in diameter of the grids was used to estimate the strain on the surface of the specimens. In addition, an automated stereoimaging machine [*28*] was used to compare before and after photographs, calculate the displacements, and make contour plots of the shear and in-plane displacement gradients (engineering strain).

Results of the Tension Tests

Complete test data are available in the original report [*21*]. The conventional engineering stress-strain data from duplicate unnotched specimens shows up to 10% variation in the 0.2% yield strength and up to 5% variation in the ultimate strength. The difference between flat and round specimens is within the range of the scatter. The ultimate strength of the flat specimens seems to be consistently lower than the round specimens.

The notched round tension-test data cannot be reduced in the conventional manner because the gage length is not known. However, taking the reduced areas into account, the average or apparent true axial stress can be determined. The stress is termed "average" because it is known that the stress distribution varies across the midplane, for example, Bridgman [*29*]. The stress determined from the load and current area (the apparent true stress) is affected by constraint. For example, the smaller the notch in the round tension tests the higher the apparent true axial stress.

It is commonly assumed that plastic flow is incompressible. Therefore, for a small disc-shaped element of the material at the neck and neglecting elastic compressibility, the engineering strain, e, can be determined from the relationship

$$\frac{A_0}{A} = \frac{L}{L_0} = 1 + e \tag{1}$$

where A_0 is the original, A is the current cross-sectional area, L_0 is the original, and L is the current length of the small element.

The average axial true strain at the neck (called the natural reduction) can be determined from the ratio of the original area, A_0, to the reduced area, A

$$\bar{\varepsilon} = \ln\left(\frac{A_0}{A}\right) \tag{2}$$

The notched round specimen data were first reduced in terms of the apparent true stress and the natural reduction. Specimen-dependent stress-strain curves are obtained from this procedure. The smaller the notch in general, the higher the average axial stress and the smaller the fracture strain. The apparent true axial stress contains the hydrostatic component (which does not cause plastic flow) and the deviatoric component. If the stress state were already known, these could be separated and an underlying effective Mises true stress-strain curve that is independent of the tension specimen geometry could be determined.

As shown later, the Bridgman analysis (and other similar analyses [*30*]) of the stress state are not accurate for very large strains. Therefore, it is necessary to perform simulations of the tension tests in an iterative manner using trial curves of effective true stress versus effective natural strain until the load-displacement curves match. The resulting effective stress-strain curve exhibits a saturation stress (much higher than the engineering ultimate strength) that is constant (660 MPa for the X70 steel) for the large strain region.

The fracture strains based on Eq 2 are dependent on the specimen geometry and the stress state. However, as will be shown later, Eq 2 is not valid for strains much larger than 50%; and it turns out that when properly modeled, the critical strain at the initiation of damage (about 225% for X70 steel) is specimen geometry independent.

For the flat tension specimens, the average axial engineering strain was determined from strain contours generated by stereoimaging photographs before and after the deformation. Examination of these strain maps shows consistent results between duplicate specimens. Also, the strain mapping system gave results consistent with the stretching of the grids on the surface. The results from the last photograph before fracture typically show the center contour is about 10 mm wide and 3 mm high and encloses an area where axial strains are greater than 84%. The strains are not uniform across the midplane but rather peak in the center.

Results of the Tension Test Simulations

The objective of this work was to develop the computational simulation tools and to demonstrate their use in simulation of ductile fracture. The large-strain formulation and details of the implementation are given in Refs *25* and *26*. The objective stress rate suggested by Dienes [*31*] known as the Green-Naghdi rate was used in the computations. The large-strain analyses require significant computational experience to perform. There are several parameters to select that have an impact on the accuracy and feasibility of the simulation.

The simulations require an effective stress-strain curve as input, but the curve cannot be determined directly from an experiment. A first guess of the effective stress-strain curve included the average axial true stress and natural reduction up to the engineering ultimate strength, that is, up to the onset of localization. The first trial curve was assumed to be flat, that is, a saturated effective flow stress was assumed. Adjustments of the effective stress-strain curve were then made until agreement with the measured force-versus-displacement curve was obtained. Usually, the adjustments were relatively minor, for example, if the maximum load was underpredicted, the saturated flow stress was increased or, if the load peaked to quickly, the point of saturation was adjusted to greater strain.

This iterative process involved some compromise because error between the measured and predicted force-versus-displacement curve from several specimens was minimized simultaneously. This process involved only judgment, although a more formal optimization could be employed. There is a strong cause-and-effect relationship between the adjustments and changes in the resultant predictions that builds confidence in the result, although it is not proven that the effective stress-strain curve arrived at by this process is unique. In view of the natural variation of the material properties of steel, this error is not thought to be significant.

Figure 2 shows an example of a result arrived at by this process. One curve was generated using the effective stress-strain curve shown in Fig. 3 that remains at a saturated flow stress, that is, without damage. The result is good except that it predicts continuous straining past the point where the experiment failed. The force decrease in this case comes entirely from the geometric effects of the necking.

The larger decrease in force toward the end of the experiment is due to a combination of this geometric effect and material softening or damage that sets in toward the end of the test. The point where the material softening effects become apparent, that is, where the slope of the force-versus-displacement curve changes, is defined as damage initiation. The apparent effect of damage evolution was included in the analysis in a very simple way. The effective stress-strain curve was altered such that at 133% strain the flow stress drops off as shown in Fig. 3. The effect of this damage evolution gives better agreement with the measured data as shown in Fig. 2. In this case, the initiation and evolution of damage were fixed to produce a given effect in a given specimen. For more general application, constitutive equations that include criteria for the initiation and evolution of this damage would be required.

Numerous micromechanical models have been developed to characterize the void growth or damage process. Atkins and Mai [*32,33*] and Clift et al. [*34*] have recently reviewed most of the published models. Basically, the useful models are variations on an integral that is postulated to be a controlling factor in void growth. The integrand is usually given as the increment of effective plastic strain multiplied by some nonlinear function of the ratio of the mean stress to the effective stress or other derivable stress quantities. This ratio is the ratio of the stress quantity that affects the dilatational growth of voids with respect to the stress quantity that affects their distortion [*33*].

An often-used void-growth model is an approximation for relatively high constraint factors

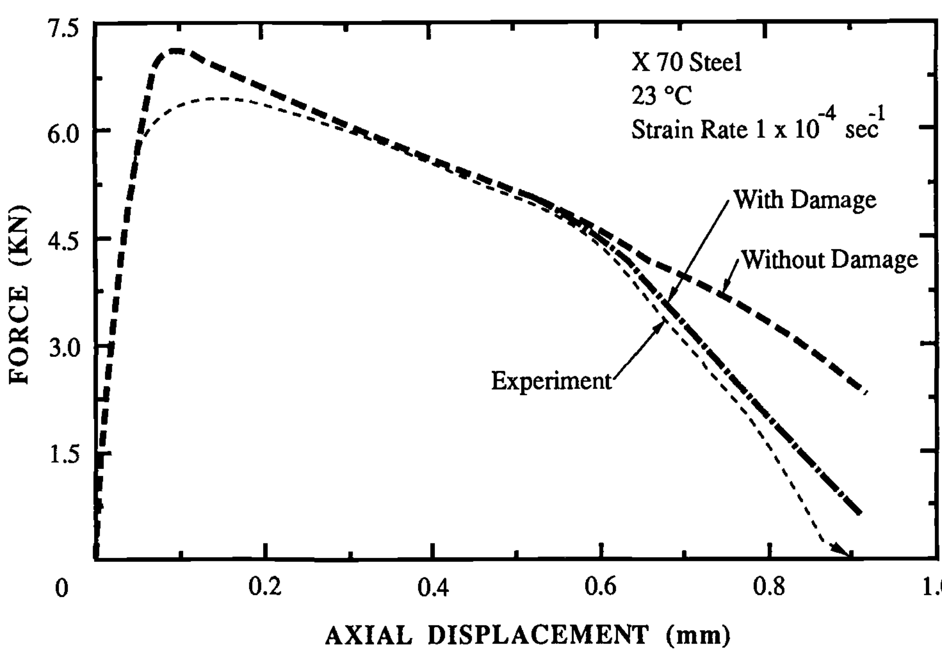

FIG. 2—*Comparison of measured force versus displacement to results computed with and without damage.*

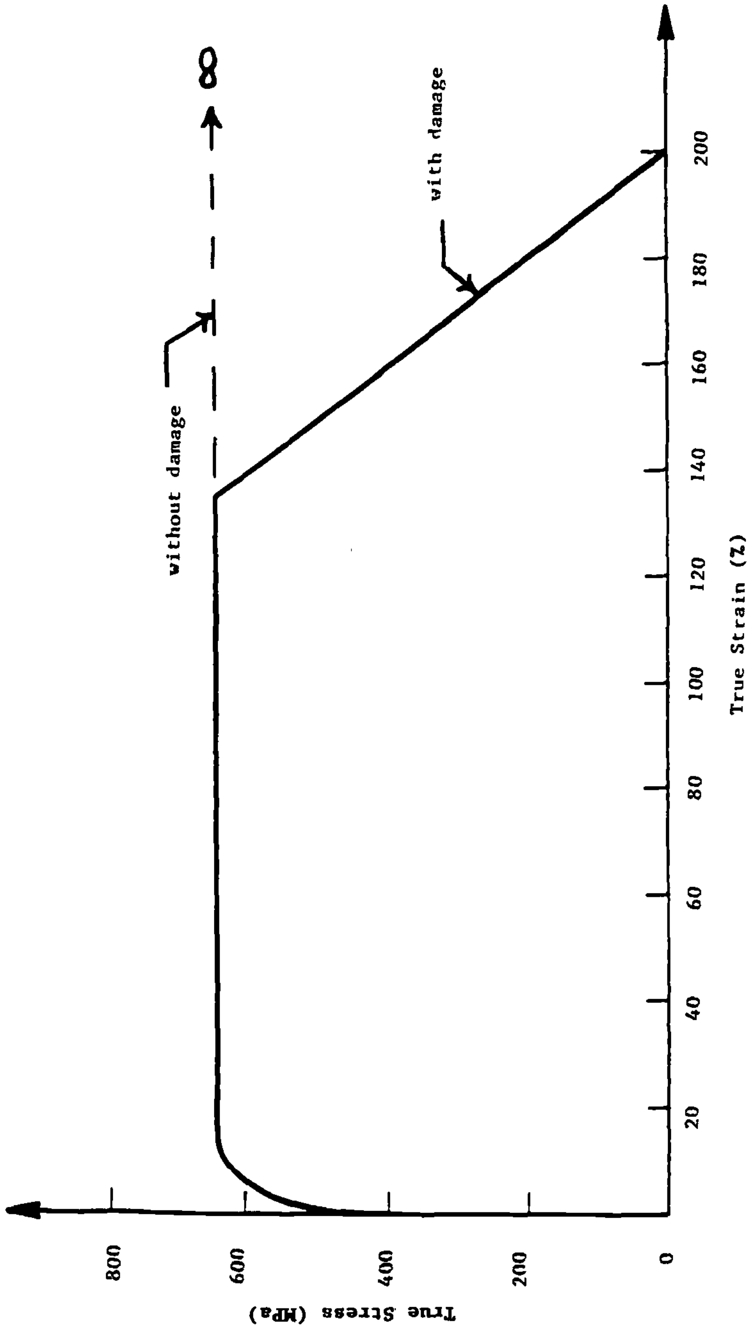

FIG. 3—*Effective stress-strain for X70 steel with and without damage.*

to the results of an analysis by Rice and Tracey [35]. The Rice and Tracey analysis represents the growth of the average diameter of an isolated two-dimensional void in an infinite medium.

$$\ln (R/R_o) = 0.283 * D \tag{3}$$

where

R = average radius of the void,
R_o = original average radius of the void, and
$D = \int_0^{\varepsilon^p} \exp\left(\frac{1.5\sigma_m}{\sigma_e}\right) d\varepsilon^p$

The integral, D, often appears in the form of a hyperbolic sine or hyperbolic cosine (with an appropriate change in the constants) rather than the exponential and is postulated to be a measure of damage [6,36]. Local failure is predicted when this level of damage reaches a critical value associated with void coalescence. The fracture criterion is stated as an integral that depends on the history of the deformation. As a fracture criterion, the critical value should therefore be independent of the history. For example, the critical value of the integral should be the same for an experiment with high constraint resulting in low fracture strains, and an experiment with low constraint resulting in high fracture strains.

There are many reasons why this may not be true in certain cases. For example, during the growth of voids from inclusions under high constraint, voids at smaller particles like carbides may be initiated that lead quickly to failure [37]. In this case, the void growth is terminated earlier than it would be under low constraint conditions. Despite the possible problems, many investigators have been able to correlate fracture using such simple void growth models to predict ductile fracture, even without explicit consideration of nucleation and coalescence [38–40].

Gurson [41] incorporated void growth equations like Eq 3 into constitutive equations such that the yield stress (corresponding to the unvoided cross-sectional area) is decreased according to the current volume fraction of the voids. The softening effect in the Gurson model causes localization of plastic flow that in effect is a prediction of void coalescence. Various modifications of the Gurson model (basically adding new fitting parameters) have been proposed, for example, Tveergard and Needleman [42,43].

The strain-energy density (SED) has been used by Sih [44,45] and Nemat-Nasser [46] as a fracture criterion. Often, this criterion has been employed as simply a critical plastic-work density [47–51]. This criterion is readily calculated and can be related to macroscopic fracture criteria as discussed later. Gillemot [52] has suggested that a critical SED of plain carbon steels is from 500 to 700 MJ/m^3 and for vacuum-remelted steels is from 1000 to 1050 MJ/m^3. As shown later, the critical SED for the X70 steel was 800 MJ/m^3, which is in approximate agreement with Gillemot considering that the steel is cleaner than most plain carbon steels.

$$\begin{aligned} \text{SED}\,(t) &= \int_0^t \sigma_{ij} d\varepsilon_{ij} \approx W^P \text{ the plastic work density} \\ W^P &= \int_0^t \sigma_{ij} d\varepsilon_{ij}^p = \int_0^t \sigma_e d\varepsilon^P \approx \sigma_f \int_0^t d\varepsilon^p = \sigma_f \varepsilon^p \end{aligned} \tag{4}$$

where

$\varepsilon^p = \sqrt{\tfrac{2}{3}\varepsilon_{ij}^p\varepsilon_{ij}^p}$ for proportional straining, and
σ_f = flow stress $\approx$ engineering ultimate stress.

Atkins and Mai [33] show that for the special case of the constant constraint factor or proportional loading, all of the integrated functions of stress and strain reduce to a constant (reflecting the hydrostatic stress term) times the critical plastic work per unit volume (W^p). This relationship may be approximately correct for loading that is nearly proportional. Therefore, for loading that is nearly proportional, there is approximately a one-to-one correspondence between the damage integral, the plastic-work density, and the effective plastic strain. For nearly proportional loading, it is therefore approximately equivalent to specify a critical value of a damage integral, the critical plastic-work density, or the critical effective plastic strain. The simulations of necking, discussed here, are highly nonproportional, however.

As shown in Fig. 2, the softening effect of void growth became significant only after the specimens had undergone extensive necking and had lost most of their load-carrying capacity. Therefore, for this steel, a practical fracture criterion can be based on the conditions at the onset of significant void growth (damage initiation), eliminating the need for void-growth or damage modeling. In the following discussion, various parameters are compared at the onset of damage initiation, that is, at the break in the slope of the force-versus-displacement curves. Since these results are at the initiation of damage, they are unaffected by the treatment of the end of the stress-strain curve.

Figure 4 shows profiles of the axial stress, the axial strain, the effective plastic strain, the SED, and the Gurson damage parameter for the 1.6-mm notch round specimen in X70 steel. The Gurson damage parameter, that is, D in Eq. 3, is essentially the same as the Rice and Tracey or McClintock parameters. The profiles in Fig. 4 are at damage initiation, that is, where the decreasing slope of the force-displacement curve changes. Similar profiles at damage initiation are shown for the 3.2-mm notch round specimen for the same material in Fig. 5. One observation that can be made is that the Bridgman [29] or Davidenkov [30] analyses that predict a maximum axial stress of 1.4 times the flow stress for the 1.6-mm notch and less for the 3.2-mm notch are clearly not applicable. Also, note that the plastic strain increases slightly toward the outside surface of the specimen. The Bridgman analysis predicts a uniform strain.

The profiles of the SED also increase slightly toward the outer radius, as does the strain normal to the fracture plane. The radial and circumferential strain components are not shown but are fairly constant across the fracture plane, about -40%. The large axial strain exceeds the sum of these other components. Therefore, the isochoric condition (that is, that the trace of the plastic rate of deformation tensor is zero) does not imply that the trace of the plastic strain tensor is zero, except at moderate strains. Note that this results from differences between the definition of strain and the deformation gradient in updated coordinates and has no implications with respect to volume change. This result is one reason that Eq 1 is not a valid way to estimate failure strain.

The effective plastic strain is computed by integrating the increments of the effective plastic strain rate in each time interval. This integral also tends to lose its meaning as the strain becomes large. The effective plastic strain is the internal variable upon which the constitutive model (an effective stress-strain curve) is based, therefore, the use of such a constitutive model is questionable at very large strains. However, the effective stress-strain curve used for these calculations is flat at large strains and is therefore not sensitive to the precise value of the effective strain.

The round smooth tension specimen for X70 steel was also simulated. Necking under fixed-grip conditions is naturally resisted by hardening that forces the straining to be uniform. The strain at which necking occurs is therefore controlled by saturation of the hardening in the effective stress-strain curve. The location at which necking occurs is another matter. At first, necking was predicted to occur at a location about one third of the height of the gage length, which was consistent with the experimental result for three out of four of these tests. (One test specimen necked at the midplane.) Although this prediction was quite pleasing, the simulation

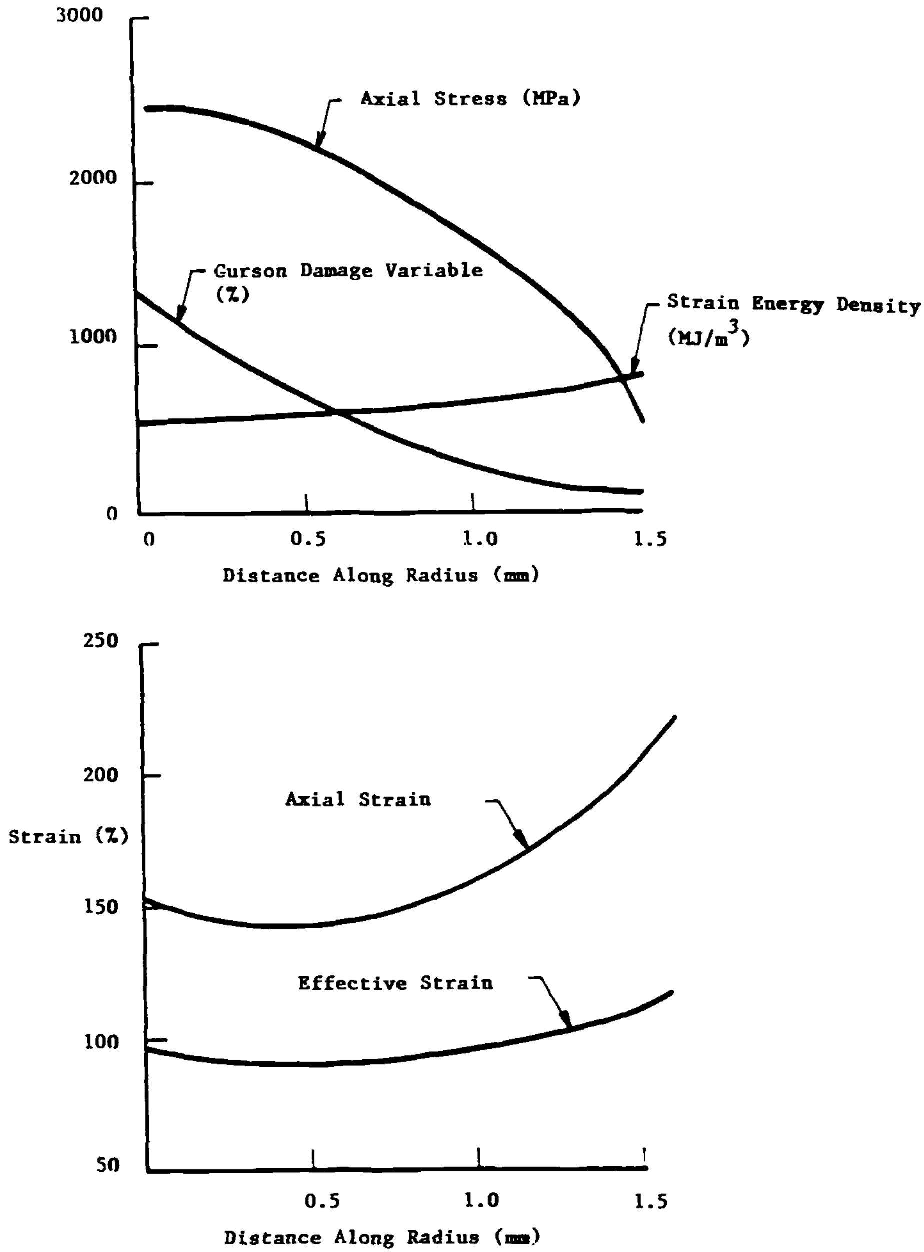

FIG. 4—*Profiles of results on the fracture plane for X70 steel round tension specimen with 1.6-mm notch.*

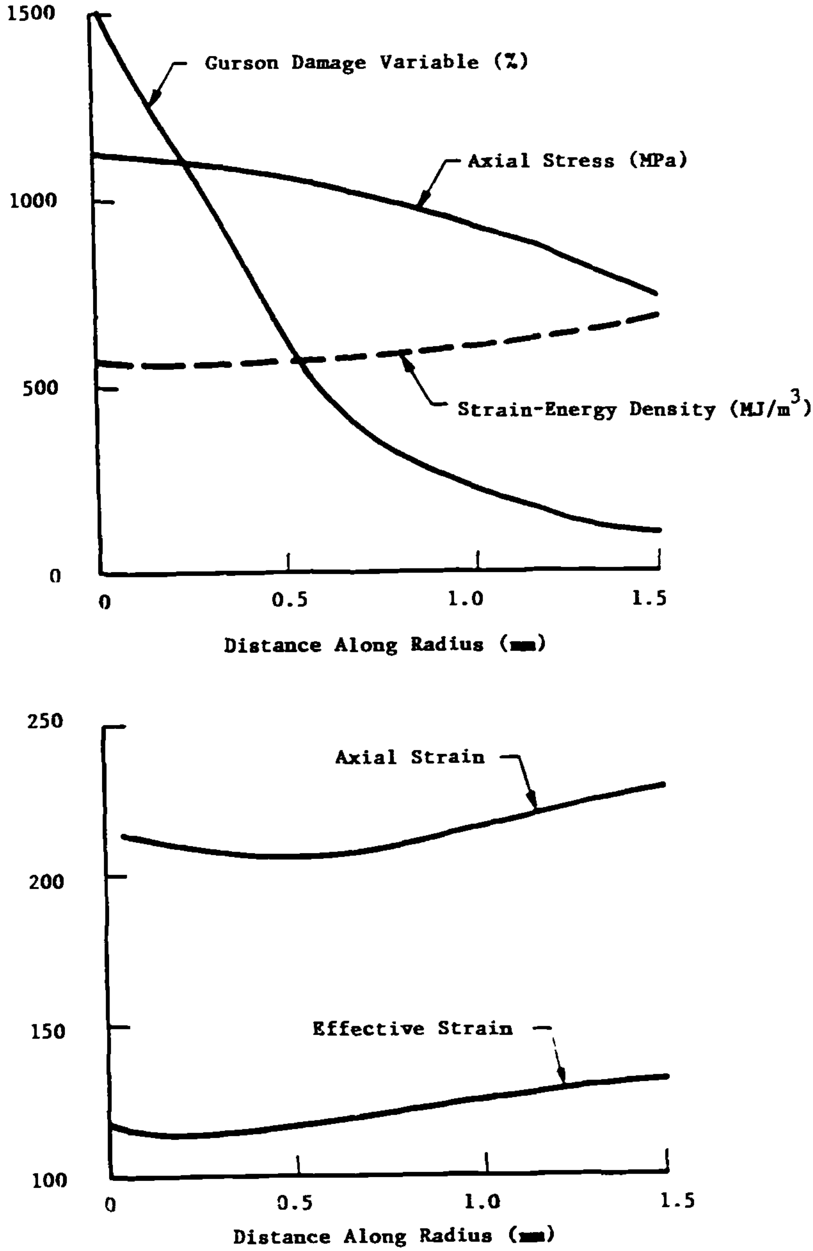

FIG. 5—*Profiles of results on the fracture plane for X70 steel round tension specimen with 3.2-mm notch.*

was repeated with some slightly different tolerances and necking was predicted at the midplane. It is concluded that the location of necking in round specimens with long gage length-to-diameter ratios is sensitive to small perturbations in the analysis. In other published simulations of necking in such specimens, a great deal of significance was placed on the predicted location of necking [*51*]. In view of the sensitivity of such a result, it is not clear whether these other results may have been fortuitous. Because of the long displacement history and associated expense, these simulations were not carried out until final separation was imminent.

The flat specimen exhibited necking at the midplane consistent with the experiment. The profiles of the results at damage initiation for the flat specimen of X70 steel are shown in Fig. 6. The strain normal to the fracture plane in Fig. 6 compares favorably to the measured strains. It is important to note that completely erroneous results would be obtained in any of these analyses if small-strain analysis were used, for example, necking would not occur.

A similar simulation of a flat specimen, done with a three-dimensional Eulerian finite-difference hydrodynamics code by Wilkens et al. [*53*], did not exhibit the axial strain gradient from a peak at the centerline of the specimen (obvious in Fig. 6*b*) when the Mises yield surface was used. Wilkens' calculations required an unusual yield surface with corners in order to exhibit this gradient of axial strain from the centerline to the sides of the specimen. In the plane-stress Lagrangian finite-element analysis with VISCRK, the strain gradient was properly accounted for with the Mises yield surface. The difference could be that the three-dimensional analysis will more accurately pick-up the through-thickness stress that will develop after necking.

The maximum value of the effective plastic strain and the SED only vary as much as 12% between specimens. Even better agreement is obtained between the maximum values of the strain normal to the fracture plane, which just exceeds 225% prior to failure. At this time, based on these preliminary results with only one material, it appears that either the effective plastic strain, the SED, or the axial strain could be used as geometry-independent damage initiation criteria or, conservatively, as fracture criteria.

This conclusion is contrary to the widely accepted notion that the effective strain at fracture in notched tension specimens is strongly geometry dependent, for example, see Ref *54* or the preliminary reduction of the tension test data in this project. However, these reports were based on the use of Eq 2 and analyses such as Bridgman's and Davidenkov's [*29,30*] that assume that the trace of the plastic strain tensor vanishes and that the effective strain is constant across the radius. Our computer simulations have shown that these assumptions are not valid for strains greater than about 50%.

From comparing the profiles of the stress and the Gurson damage variables in the various tension specimens, it is clear that they are strongly dependent on the geometry and are therefore not suitable as damage initiation criteria. This is contrary to the results in Refs *38* through *40*. A possible explanation for this difference is the failure mode. As discussed earlier, the X70 steel is very clean and therefore void nucleation is delayed until very late in the deformation process. The results in Refs *38* through *40* were obtained with dirtier steels, and void nucleation probably occurred earlier, playing a more significant role in the fracture process. Equation 3 is more suitable as a damage-evolution equation than as a damage-initiation criterion.

Conclusions

1. This work has demonstrated the experimental and simulation techniques that may be useful in the process of investigating potential criteria for ductile fracture.
2. The large-strain analysis capability is essential for these simulations.

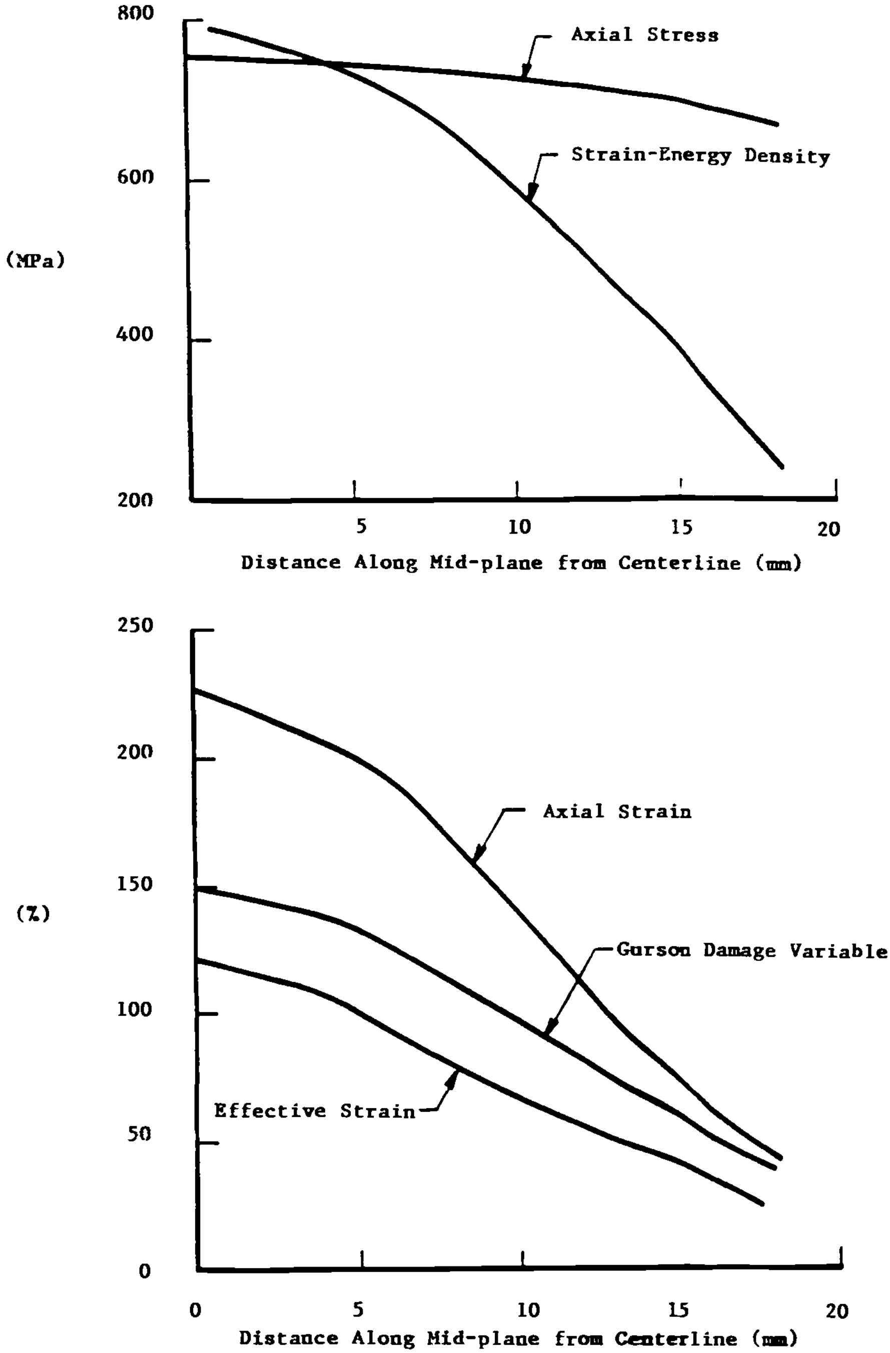

FIG. 6—*Profiles of results on the fracture plane for X70 steel flat tension specimen.*

3. The damage criteria commonly attributed to Rice and Tracey or to Gurson are dependent on the test specimen geometry.
4. The Bridgman analysis of notch tension specimens is only valid for moderate strains, that is, less than 50%.
5. There are preliminary indications that for the very clean X70 pipeline steel, the maximum principal strain (normal to the fracture surface), the maximum effective strain, and the maximum strain-energy density at fracture all appear to be geometry independent within 12% at damage initiation.
6. Based on the latter conclusion, a predictive analysis is possible where material softening is rapidly induced after the strain exceeds the critical damage initiation strain. This diminishing load-carrying capacity would then cause failure in tension specimens and could be used (in combination with a critical distance or area parameter) to advance the crack in fracture simulations.

Acknowledgments

The authors wish to express their appreciation of the support of the Southwest Research Institute advisory committee for research. The authors also acknowledge the useful discussions with Arlo Fossum of RE-SPEC Corporation, Ulric Lindholm of Southwest Research Institute, Andre Pellissier-Tanon of Framatome, Karl Frank at the University of Texas, and Ted Anderson from Texas A&M University. The careful and innovative experimental work of Tom Masden is also appreciated.

References

[1] Miller, A. G., "Review of Limit Loads of Structures Containing Defects," *International Journal of Pressure Vessels and Piping*, Vol. 32, 1988, pp. 107–327.
[2] Chen, X., Albrecht, P., and Joyce, J., "Limit Pressure Analysis of Cylindrical Vessel with Longitudinal Crack," in this volume.
[3] Hu, J. M., Cheng, J. G., Albrecht, P., and Joyce, J. A., "Ductile Crack Extension in Compact Specimens at Limit Load," *Proceedings*, Seventh International Conference on Fracture (ICF7), *Advances in Fracture Research*, Houston, March 1989, K. Salama et al., Eds., Pergamon Press, Oxford, UK, 1989.
[4] Thomason, P. F., *Ductile Fracture of Metals*, Pergamon Press, Oxford, UK, 1990.
[5] Wilsdorf, H. G. F., "Review Paper—The Ductile Fracture of Metals: A Microstructural Viewpoint," *Materials Science and Engineering*, Vol. 59, 1983, pp. 1–39.
[6] McClintock, F. A., "A Criterion for Ductile Fracture by the Growth of Holes," *Journal of Applied Mechanics, Transactions ASME Series E*, Vol. 35, June 1968, pp. 363–371.
[7] Knott, J. F., "Some Effects of Hydrostatic Tension on the Fracture Behavior of Mild Steel," *Journal of the Iron and Steel Institute*, Vol. 204, No. 2, Feb. 1966, pp. 104–111.
[8] Orowan, E., "Fracture and Strength of Solids," *Reports on Progress in Physics*, Vol. 12, pp. 185–232.
[9] Kanninen, M. F. and Popelar, C. H., *Advanced Fracture Mechanics*, Oxford University Press, New York, 1985.
[10] Rice, J. R., "A Path Independent Integral and the Approximate Analysis of Strain Concentration by Notches and Cracks," *Journal of Applied Mechanics*, June 1968, pp. 379–386.
[11] Hutchinson, J. W., "Fundamentals of the Phenomenological Theory of Nonlinear Fracture Mechanics," *Journal of Applied Mechanics*, Vol. 50, Dec. 1983, pp. 1042–1051.
[12] McMeeking, R. M. and Parks, D. M., "On Criteria for *J*-Dominance of Crack-Tip Fields in Large-Scale Yielding," *Elastic-Plastic Fracture, ASTM STP 668*, J. D. Landes, J. A. Begley, and G. A. Clarke, Eds. American Society for Testing and Materials, Philadelphia, 1979, pp. 175–194.
[13] Rice, J. R. and Sorensen, E. P., "Continuing Crack-Tip Deformation and Fracture for Plane-Strain Crack Growth in Elastic-Plastic Solids," *Journal of Mechanics and Physics of Solids*, Vol. 26, March 1978, pp. 163–186.

[14] Rice, J. R., *Proceedings*, Conference on Mechanics and Mechanisms of Crack Growth, Cambridge, UK, April 1973, M. J. May, Ed., British Steel Corp. Physical Metallurgy Centre Publication, 1975, pp. 14–39.
[15] Parks, D. M., Lam, P. S., and McMeeking, R. M., "Some Effects of Inelastic Constitutive Models on Crack Tip Fields in Steady Quasistatic Growth," *Proceedings*, Fifth International Conference on Fracture (ICF5), *Advances in Fracture Research*, Cannes, France, 1981, D. Francois, Ed., Pergamon Press, Oxford, UK, 1981, pp. 2607–2614.
[16] Shih, C. F., deLorenzi, H. G., and Andrews, W. R., "Studies on Crack Initiation and Stable Crack Growth," *Elastic-Plastic Fracture, ASTM STP 668*, J. D. Landes, J. A. Begley, and G. A. Clarke, Eds., American Society for Testing and Materials, Philadelphia, 1979, pp. 65–120.
[17] Hutchinson, J. W. and Paris, P. C., "Stability Analysis of *J*-Controlled Crack Growth," *Elastic-Plastic Fracture, ASTM STP 668*, J. D. Landes, J. A. Begley, and G. A. Clarke, Eds., American Society for Testing and Materials, Philadelphia, 1979, pp. 37–64.
[18] Zahoor, A. and Kanninen, M. F., "A Plastic Fracture Mechanics Prediction of Fracture Instability in a Circumferentially Cracked Pipe in Bending—Part I: J-Integral Analysis," *Journal of Pressure Vessel Technology*, Vol. 103, Nov. 1981, pp. 352–358.
[19] Garwood, S. J., "Geometry and Orientation Effects on Ductile Crack Growth Resistance," *International Journal of Pressure Vessel and Piping*, Vol. 10, 1982, pp. 297–319.
[20] Clausmeyer, H., Kussmaul, K., and Roos, E., "Influence of Stress State on the Failure Behavior of Cracked Components Made of Steel," *Applied Mechanics Review*, Vol. 44, No. 2, Feb. 1991, pp. 77–92.
[21] Roy, S. and Dexter, R., "Ductile Fracture of Viscoplastic Materials Involving Large Deformation," Final Report, SwRI Project 06-9563, Southwest Research Institute, San Antonio, TX, Oct. 1990.
[22] Rice, J. R. and Johnson, M. A., "The Role of Large Crack Tip Geometry Changes in Plane Strain Fracture," *Inelastic Behavior of Solids*, M. F. Kanninen et al., Eds., McGraw-Hill, New York, 1969, pp. 641–672.
[23] McMeeking, R. M., "Finite Deformation Analysis of Crack-Tip Opening in Elastic-Plastic Materials and Implications for Fracture," *Journal of the Mechanics and Physics of Solids*, Vol. 25, 1977, pp. 357–381.
[24] Ritchie, R. O., Server, W. L., and Wullaert, R. A., "Critical Fracture Stress and Fracture Strain Models for the Prediction of Lower and Upper Shelf Toughness in Nuclear Pressure Vessel Steels," *Metallurgical Transactions A*, Vol. 10A, Oct. 1979, pp. 1557–1570.
[25] Roy, S. and Dexter, R. J., "A Computational Procedure for the Simulation of Ductile Fracture with Large Plastic Deformation," *Engineering Fracture Mechanics*, 1993.
[26] Roy, S., Fossum, A. F., and Dexter, R. J., "On the Use of Polar Decomposition in the Integration of Hypoelastic Constitutive Laws," *Engineering Fracture Mechanics*, Vol. 30, No. 2, 1992, pp. 119–133.
[27] Dexter, R. J. and Kanninen, M. F., "Effect of Increased Yield-to-Ultimate Tensile Strength on Dynamic Fracture Toughness of Pipeline Steels," Final Report, SwRI Project 06-6147-009, Southwest Research Institute, San Antonio, TX, Oct. 1987.
[28] Williams, D. R., Davidson, D. L., and Lankford, J., "Fatigue-crack-tip Plastic Strains by the Stereoimaging Technique," *Experimental Mechanics*, Vol. 20, 1980, pp. 132–139.
[29] Bridgman, P. W., *Studies in Large Plastic Flow and Fracture*, McGraw-Hill, New York, 1952.
[30] Davidenkov, N. N. and Spiridonova, N. I., "Mechanical Methods of Testing, Analysis of the State of Stress in the Neck of a Tension Test Specimen," *Proceedings*, American Society for Testing and Materials, Philadelphia, Vol. 46, 1946, pp. 1147–1158.
[31] Dienes, J. K. "On the Analysis of Rotation and Stress Rates in Deforming Bodies," *Acta Mechanica*, Vol. 32, 1979, pp. 217–232.
[32] Atkins, A. G. and Mai, Y. W., "Fracture Strains in Sheet Metalforming and Specific Essential Work of Fracture," *Engineering Fracture Mechanics*, Vol. 27, No. 3, 1987, pp. 291–297.
[33] Atkins, A. G. and Mai, Y. W., *Elastic and Plastic Fracture*, Ellis Horwood/John Wiley, Chichester, UK, 1985.
[34] Clift, S. E., Hartley, P., Sturgess, C. E. N., and Rowe, G. W., "Fracture Prediction in Plastic Deformation Processes," *International Journal of Mechanics and Science*, Vol. 32, 1990, pp. 1–17.
[35] Rice, J. R. and Tracey, D. M., "On the Ductile Enlargement of Voids in Triaxial Stress Fields," *Journal of the Mechanics and Physics of Solids*, Vol. 17, 1969, pp. 201–217.
[36] McClintock, F. A., Kaplan, S. M., and Berg, C. A., "Ductile Fracture by Hole Growth in Shear Bands," *International Journal of Fracture Mechanics*, Vol. 2, No. 4, 1966, pp. 614–627.
[37] Bates, R. C., "Mechanics and Mechanisms of Fracture," *Proceedings*, USA-China Bilateral Conference, The Metallurgical Society of the American Institute of Mining, Metallurgical, and Petroleum Engineers, Warrendale, PA, 1981.

[38] Bethmont, M., Rousselier, G., and Devesa, G., "Effect of Specimen Geometry on *J*-Resistance Curves in Near Small-Scale Yielding Conditions," *Advances in Fracture Research, Proceedings*, Seventh International Conference on Fracture (ICF7), Houston, 20–24 March 1989, K. Salama et al., Eds., Pergamon Press, Oxford, UK, 1989.
[39] Schmitt, W., Sun, D.-Z., and Kienzler, R., "Application of Micro-Mechanical Models to the Prediction of Ductile Fracture," *Localized Damage Computer-Aided Assessment and Control, Vol. 1: Fatigue and Fracture Mechanics, Proceedings*, First International Conference on Computer-Aided Assessment and Control of Localized Damage, Portsmouth, UK, 26–28 June 1990.
[40] Sun, D.-Z., Siegele, D., Voss, B., and Schmitt, W., "Application of Local Damage Models to the Numerical Analysis of Ductile Rupture," *Fatigue Fracture Engineering Materials and Structures*, Vol. 12, No. 3, 1989, pp. 201-212.
[41] Gurson, A. L., "Continuum Theory of Ductile Rupture by Void Nucleation and Growth: Part 1—Yield Criteria and Flow Rules for Porous Ductile Media," *Journal of Engineering Materials and Technology*, Vol. 99, 1977, pp. 2–15.
[42] Tvergaard, V., "On Localization in Ductile Materials Containing Spherical Voids," *International Journal of Fracture*, "Vol. 18, 1984, pp. 237–252.
[43] Tvergaard, V. and Needleman, A. "Analysis of the Cup-Cone Fracture in a Round Tensile Bar," *Acta Metallurgica*, Vol. 32, 1984, pp. 157-169.
[44] Sih, G. C. and Madenci, E., "Prediction of Failure in Weldments—Part 1: Smooth Joint," *Theoretical and Applied Fracture Mechanics*, Vol. 3, 1985, pp. 23-29.
[45] Sih, G. C. and Madenci, E., "Fracture Initiation Under Gross Yielding: Strain Energy Density Criterion," *Engineering Fracture Mechanics*, Vol 18, No. 3, 1983, pp. 667-677.
[46] Nemat-Nasser, S., "Overview of the Basic Progress in Ductile Fracture," *Transactions*, Fourth International Conference on Structural Mechanics in Reactor Technology (SMIRT-4), San Francisco, Aug. 1977, pp. L2/1-11.
[47] Sih, G. C. and Madenci, E., "Crack Growth Resistance Characterized by the Strain Energy Density Function," *Engineering Fracture Mechanics*, Vol. 18, No. 6, 1983, pp. 1159-1171.
[48] Matic, P., "Numerically Predicting Ductile Material Behavior from Tensile Specimen Response," *Theoretical and Applied Fracture Mechanics*, Vol. 4, 1985, pp. 13-28.
[49] Matic, P. and Jolles, M. I., "The influence of Weld Metal Properties, Weld Geometry and Applied Load on Weld System Performance," *Naval Engineers Journal*, March 1988.
[50] Matic, P. and Jolles, M. I., "Defects, Constitutive Behavior and Continuum Toughness Consideration for Weld Integrity Analysis," NRL Memo No. 5935, Naval Research Laboratory, Washington, DC, 1987.
[51] Matic, P., Kirby, G. C., III, and Jolles, M. I., "The Relation of Tensile Specimen Size and Geometry Effects to Unique Constitutive Parameters for Ductile Materials," *Proceedings*, Royal Society London, Vol. A 417, 1988, pp. 309-333.
[52] Gillemot, F., "Criterion of Crack Initiation and Spreading," *Engineering Fracture Mechanics*, Vol. 8, 1976, pp. 239-253.
[53] Wilkins, M. L., Streit, R. D., and Reaugh, J. E., "Cumulative-Strain-Damage Model of Ductile Fracture: Simulation and Prediction of Engineering Fracture Tests," Report UCRL-53058, Lawrence Livermore National Laboratory, Oct. 1980.
[54] Hancock, J. W. and Mackenzie, A. C., "On the Mechanisms of Ductile Failure in High-Strength Steels Subjected to Multi-Axial Stress-States," *Journal of the Mechanics and Physics of Solids*, Vol. 24, June 1976, pp. 147-269.

Kang Lee[1] *and John D. Landes*[1]

Developing *J-R* Curves Without Displacement Measurement Using Normalization

REFERENCE: Lee, K. and Landes, J. D., "**Developing *J-R* Curves Without Displacement Measurement Using Normalization,**" *Fracture Mechanics: Twenty-Third Symposium, ASTM STP 1189,* Ravinder Chona, Eds., American Society for Testing and Materials, Philadelphia, 1993, pp. 133–167.

ABSTRACT: The method of normalization is used in a new inverse way to develop *J-R* curves from test records that contain only load-versus-crack length values with no measure of displacement. These data may represent a special case where measurement of crack length is easier experimentally than the measurement of displacement. The method of normalization uses the principle of load separation to relate the three variables of load, displacement, and crack length. This relationship is expressed by a functional form so that, given any of the two variables, the third can be determined. Previously, the method of normalization has been used to determine crack length when given only load and displacement; however, it can also be applied to determine displacement when given only load and crack length.

In this new way of applying normalization, some problems arise; namely, the calibration points needed to evaluate the functional form of normalized load are not available. A major thrust of this paper is to solve the problem of how to determine these calibration points. To do this, the method is first applied to data for which all of the three variables have been already determined. The displacement is assumed to be missing and the *J-R* curves are determined from only the load and crack length values; these *J-R* curves are then compared with the ones generated for the data with all of the variables available. Three methods of determining calibration points were used in the comparison. Of the three, an approach called the power law fit is the best for determining the calibration points. The method is then applied to data for which there are only load-versus-crack length data. The results of this study show that the method of normalization works well for developing *J-R* curves from load-versus-crack length data.

KEY WORDS: fracture mechanics, fatigue (materials), *J-R* curve, normalization, fracture toughness, displacement, loads, crack length, empirical formula, power law

J-R curves are used to measure fracture toughness in ductile materials. The ASTM Method for Determining the *J-R* Curves (E 1152-87) requires a simultaneous measurement of load, load-line displacement, and crack length. The crack length measurement is made by an on-line crack length monitor like the elastic unloading compliance system [*1,2*]. The method of normalization was developed as an alternate way to determine crack length without the need for an on-line crack monitoring system [*3–5*]. This method uses the relationship between the three variables of load, displacement, and crack length that comes from the principle of load separation [*6–8*]. These three variables are functionally related so that, given any two of the three, the third can be determined from the function. To date, the method of normalization has been used only to determine crack length, given the values of load and displacement. However, in principle, it could be used to predict any one of the three when given the other two.

For some fracture toughness test situations, it may be easier to measure crack length than

[1] Graduate assistant and professor, respectively, University of Tennessee, Knoxville, TN.

to measure displacement. Examples of this could be high-temperature testing where a conventional displacement gage may not operate or tests in a hot cell where the placement of a gage may be difficult. For the latter case, this may be especially true for some of the nuclear surveillance specimens that are small and do not have the correct design to accommodate the load-line displacement gage suggested by the standard test method. For these cases, the test could be conducted with a load-versus-crack length measurement rather than load versus displacement. The method of normalization would be used to determine the displacement when given load and crack length.

In this paper, the method of normalization is used to develop *J-R* curves from data that are given only as load-versus-crack length pairs. The procedure is developed in two steps. First, data from standard elastic unloading compliance tests are used. These data have the standard set of measurements: load, load line displacement, and crack length. The displacement is considered to be missing, and the method of normalization is used to determine the *J-R* curves from only the load-versus-crack length values. After this analysis is completed, the results developed with displacement measurement are used for comparison. This step is done to determine the best method for developing the calibration points needed in the separation functions. The second set of results have only load-versus-crack length data with no displacement measurement available. These data are analyzed to illustrate the application of the method. These data were supplied from Dr. Randy Nanstad of Oak Ridge National Laboratory. He actually has the full set of results from elastic compliance; however, the displacement data were never made available to the authors.

This paper begins with a review of the method of normalization and discusses some of the special problems involved in using it to develop *J-R* curves for the case of no displacement measurement, namely, the problem of developing calibration points to get the constants in the load separation functions. The data that have all the compliance measurements available are used to evaluate three different ways to get calibration points; these are labeled the Handbook method, an empirical formula, and a power law fit. Finally, the data for which there are actually no displacement measurements available are analyzed to illustrate the application of the method.

Method of Normalization

The method of normalization is based on the principle of load separation as developed originally by Ernst et al. [*6,7*] and confirmed experimentally by Sharobeam and Landes [*8*]. This principle has been demonstrated to work for all test geometries and for the growing crack as well as the stationary crack [*9,10*]. The principle represents load as a function of two separate variables, crack length and displacement, that are multiplied together.

$$P = G(a/W)H(v_{pl}/W) \tag{1}$$

where the displacement is given by its plastic component and both variables are normalized by a dimension parameter; here specimen width, W, is used. This format assumes that the total displacement can be represented as the sum of an elastic component and a plastic component

$$v = v_{el} + v_{pl} \tag{2}$$

When the load is divided by the crack length function, $G(a/W)$, a normalized load, P_N, results.

$$P_N = P/G(a/W) = H(v_{pl}/W) \tag{3}$$

The function in Eq 3 gives the plastic flow character of the material and specimen geometry. It represents the load-versus-plastic displacement for a stationary crack at any crack length. The elastic component of displacement is given by load and a compliance function $C(a/W)$

$$v_{el} = PC(a/W) \tag{4}$$

The function, $H(v_{pl}/W)$, in Eq 3 combined with the elastic compliance relates the three test variables of load, displacement, and crack length. When this function is known, it can be used to determine one of these variables when given the other two. In the past, this has been used to determine crack length when given the corresponding values of load and displacement [*4,5*]. In this way, the method can be used to develop *J-R* curves without an on-line crack length monitor. Since compliance calibrations are available for most geometries and $G(a/W)$ is related to the J calibration that is known for test geometries, the important part of using normalization is to determine the $H(v_{pl}/W)$ function. The original key curve method, which was used as a model for the normalization procedure, assumed that a universal "key curve" could be developed for a given material and specimen type [*7,11*]. That assumption is the same as choosing a universal $H(v_{pl}/W)$ function for all common specimens of the same material. Although this is nearly true, it was found that small specimen-to-specimen differences in this function could greatly influence the resulting *J-R* curve. The only way to use normalization to develop accurate *J-R* curves was to develop an individual $H(v_{pl}/W)$ function for each test specimen. This function could be obtained from the details of the test itself [*3*].

To determine $H(v_{pl}/W)$ for a given specimen, a functional form was assumed that had unknown fitting constants. These constants could be determined from calibration points in the test where load, displacement, and crack length are known simultaneously at the calibration point. Tests that do not use on-line crack length monitors have essentially two calibration points, one associated with an initial crack length and one associated with a final crack length. The crack lengths can be measured on the specimen fracture surface after the test is complete. Originally, a power law function with two constants was used for the $H(v_{pl}/W)$ function [*3*]. This function was taken from the idea that stress and strain would approximately follow a power law and also from the power law format used by the Electric Power Research Institute-General Electric (EPRI-G.E.) *Handbook* [*12*]. This form was convenient because it had two unknown constants and the two calibration points were sufficient to evaluate these constants.

However, in studying most test records, it was found that the deformation behavior did not follow a power law, especially for the more ductile materials that had extensive plastic deformation. The deformation seemed to have a combined power law and straight line character [*4,5*] that could be best fit by an equation suggested by Orange [*13*]. It has the form

$$P_N = H\left(\frac{v_{pl}}{W}\right) = \frac{L + M\left(\frac{v_{pl}}{W}\right)}{N + \frac{v_{pl}}{W}}\left(\frac{v_{pl}}{W}\right) \tag{5}$$

where L, M, and N are the unknown constants. This function has a power law character when v_{pl} is of the order of N. For $v_{pl} \gg N$, it follows a straight line. This function very closely approximates the deformation behavior observed for many steels [*5*]. The fact that there are three constants in this equation causes some problem in applying the method of normalization because there are two rather than three calibration points from which these constants can be evaluated. To use this function, a third calibration point must be invented. The development of calibration points for the previous use of normalization to analyze *J-R* curves is discussed in Ref 5. The three calibration points are illustrated in Fig. 1. These are labeled first point, corresponding to the point of final load, displacement, and crack length; second point, which are points employing a forced blunting assumption; and third points, which are an intermediate set of points that are used to optimize the fit of Eq 5. Figure 1 shows a P_N that is normalized by a_0 and is used to get the calibration points and the subsequent fit of the these points to get the P_N function of Eq 5.

Given these three sets of calibration points, the normalization procedure for determining the *J-R* curve is as follows. A load-versus-displacement record for a given test specimen is the starting point. Figure 2 shows an example for an HSLA-80 steel. For this test, the initial and final crack lengths must be known as well as the other specimen dimensions. The final crack length along with the final load and displacement are used to provide the first calibration point.

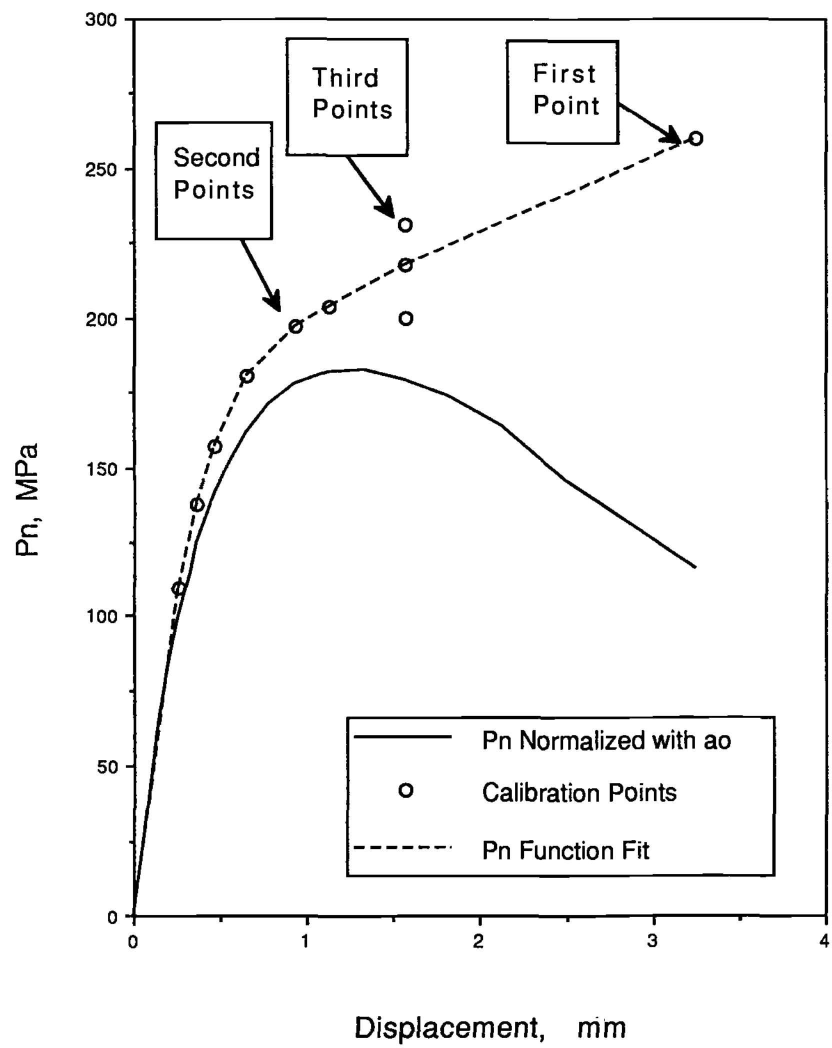

FIG. 1—*Normalized load versus displacement showing all calibration points.*

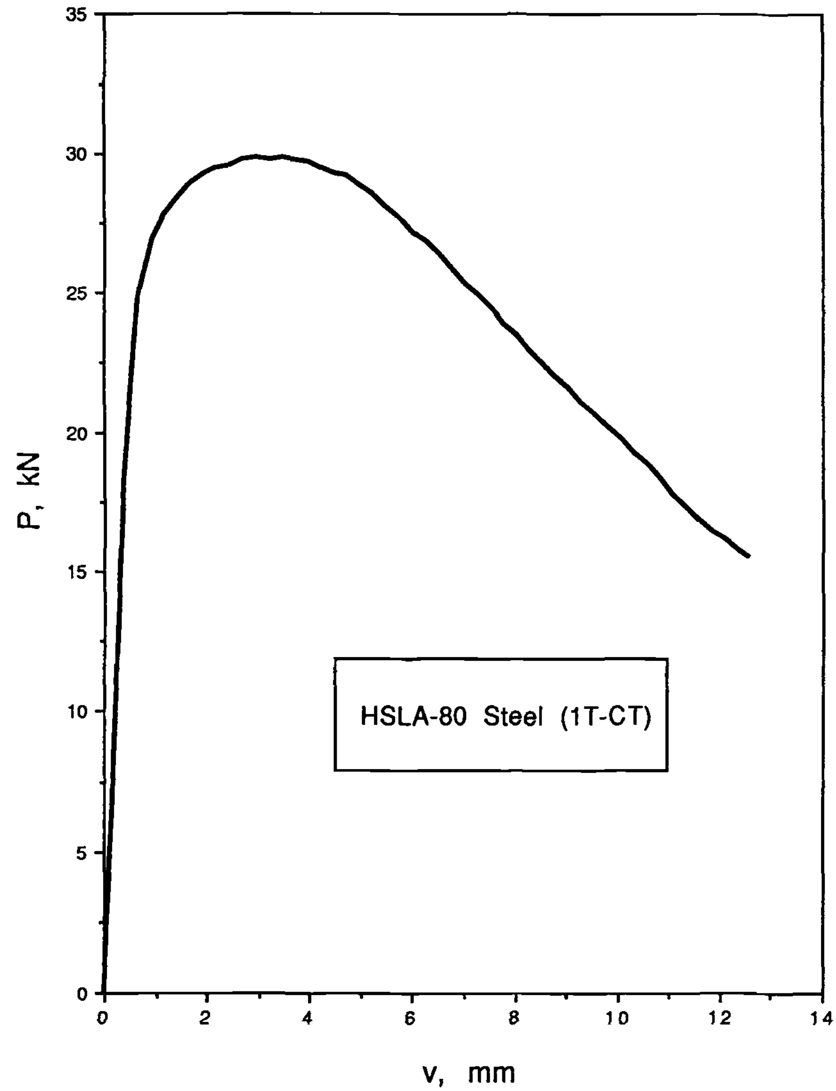

FIG. 2—*Load versus displacement for HSLA-80 steel, compact specimen.*

For this point, the displacement must be divided into elastic and plastic components and the load normalized with the final crack length. The second set of calibration points will consist of several points chosen between the first deviation from linearity and maximum load to which the forced blunting has been added. These points are separated into elastic and plastic displacement components and then the load is normalized using the initial crack length with a blunting addition. The third calibration is taken as a series of points at one-third of the final plastic displacement; no elastic displacement component is needed. The first of these points is taken at the normalized maximum test load, the others are higher.

The constants in Eq 5 are determined for the three sets of calibration points by selecting the first calibration point and one each in the second and third sets of calibration points. The fitting is done until an optimum fit is reached as described in Ref 5. This procedure defines the L, M, and N constants. The normalized load-versus-displacement curve for the data in Fig. 2 is shown in Fig. 3. From this curve, values of crack length can be determined using Eqs 2, 3, 4, and 5. The functional form of $G(a/W)$ used is

$$G(a/W) = BW\left(\frac{b}{W}\right)^{\eta_{pl}} \tag{6}$$

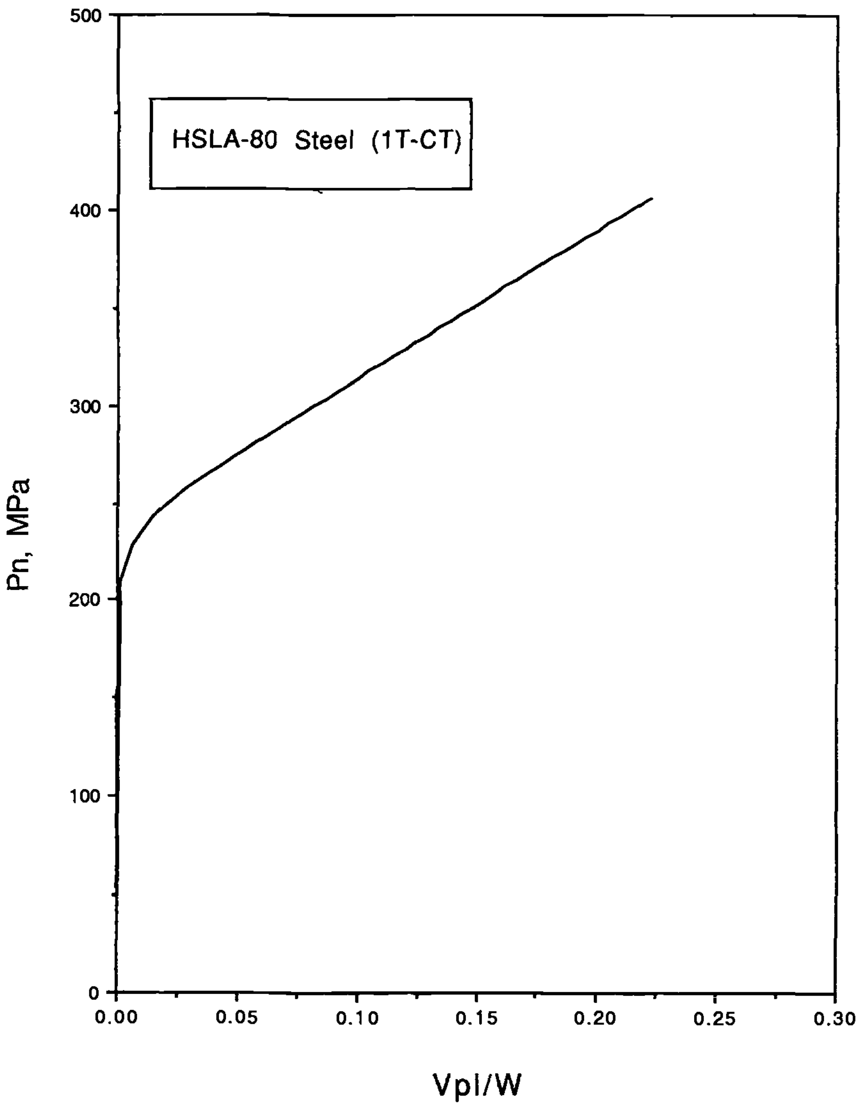

FIG. 3—*Normalized load versus plastic displacement for HSLA-80 steel, compact specimen.*

These equations cannot be solved explicitly so an iteration process is usually used. Once the crack length is known, the values of *J* can be determined by using the formula in ASTM E 1152-87 and the entire *J-R* curve can be determined. The *J-R* curve for the test record in Fig. 2 is given in Fig. 4.

Normalization With No Displacement Measurement

The idea of applying the method of normalization to the case of no displacement measurement was proposed because sometimes it may be easier to measure crack length than to mea-

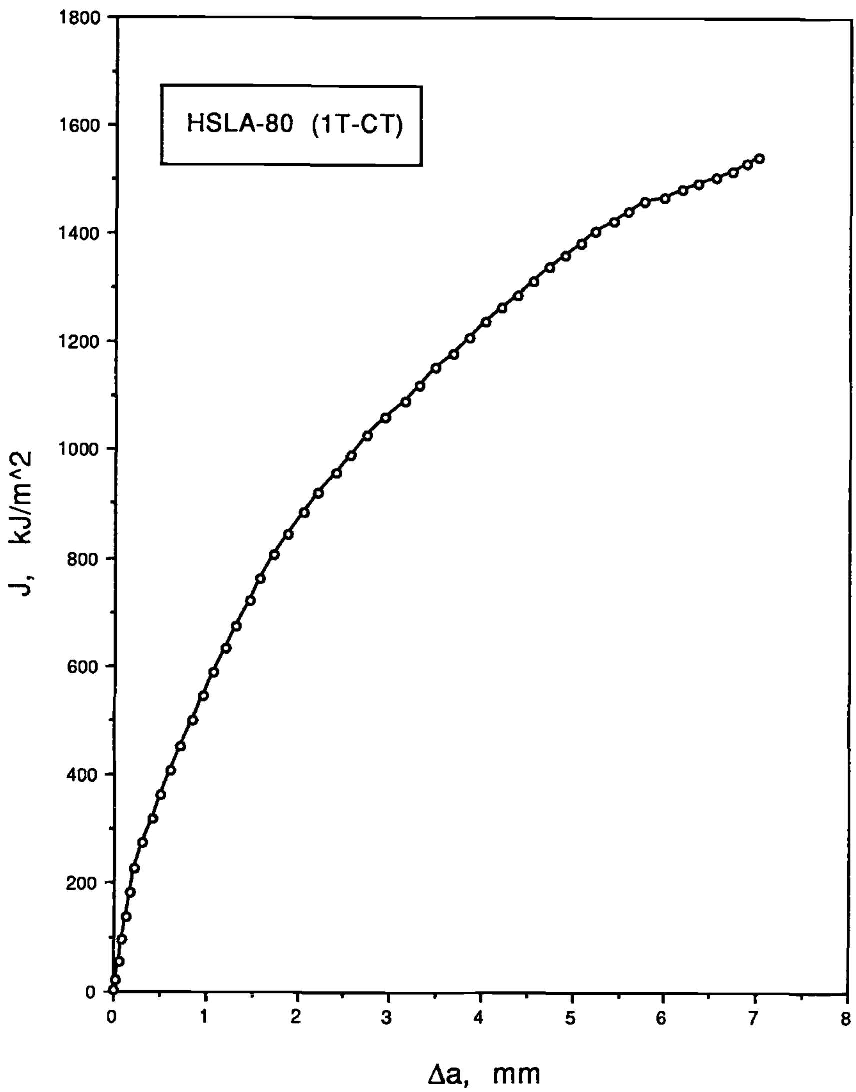

FIG. 4—J-R *curve for HSLA-80 steel, compact specimen.*

sure displacement. The crack length would likely be measured by a potential drop system; the elastic compliance method would not work when the displacement is not measured. The method works in principle the same way as before; two of the three variables are known so the third can be predicted from the normalization equations. However, in this case there are a few differences. The first calibration point cannot be determined when there is no final displacement measurement; in fact, there are no calibration points available when the displacement is not measured. As an alternative, the key curve method could be used; a universal "key curve" would be determined from a calibration specimen and used for all of the tests. Again, this seems to give too much scatter in the results. It appears to be important to develop a normalized P_N versus v_{pl}/W curve for each test. To get a calibration point corresponding with the final load and crack length, a plastic displacement can be measured from the permanent plastic set of the specimen at the end of the test. To do this, a length measurement is needed before and after the test at two points in the load line. This gives a final plastic displacement. The final elastic displacement can be determined from the final load, final crack length, and elastic compliance equation.

To determine the second set of calibration points, some additional consideration was needed. There is no initial portion of the load-versus-displacement curve to which a blunting correction could be added. A study was made to evaluate three alternative methods for getting the second calibration points. These are labeled (1) the Handbook method, (2) the empirical formula, and (3) the power law fit. The study of these points was made for the case where complete test information (load, displacement, and crack length) was known and *J-R* curves could also be developed from both the compliance and regular normalization method for comparison. The *J-R* curves were first generated for these data assuming that the displacement measurements were missing. Then the *J-R* curves were generated with the complete information so that the three alternatives for choosing a second set of calibration points could be evaluated. Note that the third calibration point is chosen arbitrarily and is evaluated from the fitting procedure for *L*, *M*, and *N*. Therefore, it does not depend on calibration values from the test and is not a problem to evaluate for this case.

The second calibration points correlate an initial crack length with an initial load and displacement. For the method to work well, these points must be chosen after some measurable plastic displacement but before any significant crack growth. Even for the regular normalization method it is sometimes difficult to define these points. When displacement is not being measured, it becomes even more difficult to define them. Three methods were used to try to establish these points; the Handbook method, an empirical formula, and a power law fit.

Handbook Method

The first method used to obtain the second calibration points used the equation in the *EPRI-G. E. Handbook* [*12*] that calculates plastic displacement from load. It has a general form that can be normalized and used as an $H(v_{pl}/W)$ function. Usually, it would not be very accurate because it has the wrong functional form, a power law. However, the beginning part of the load-versus-displacement curve, the portion before the maximum load is reached, may fit a power law well enough so that this function could be used to develop the set of second calibration points. The entire calibration curve can then be redefined using all three sets of calibration points. To look at the definition of second calibration points, four steels were studied: A106, A508, A533-B, and HSLA-80 steels. Work on these steels has been reported previously [*14–16*]. For each of these steels, there exists full test information to develop the *J-R* curves by compliance or by the regular normalization procedure so that the methods for developing calibration points can be evaluated by how well they work for the *J-R* curve as well as the P_N curve. To illustrate the development of the second calibration points, only the A106 and A508 steel results will be reported.

The set of second calibration points using the *Handbook* equation for v_{pl} is evaluated for each material. The examples for the two steels are given in Figs. 5 and 6. On each plot, the normalized load-versus-plastic displacement determined from the Handbook formula is compared with one determined from the on-line elastic compliance crack length measurement. Also included is the final point as determined from both methods. The Handbook fit looks

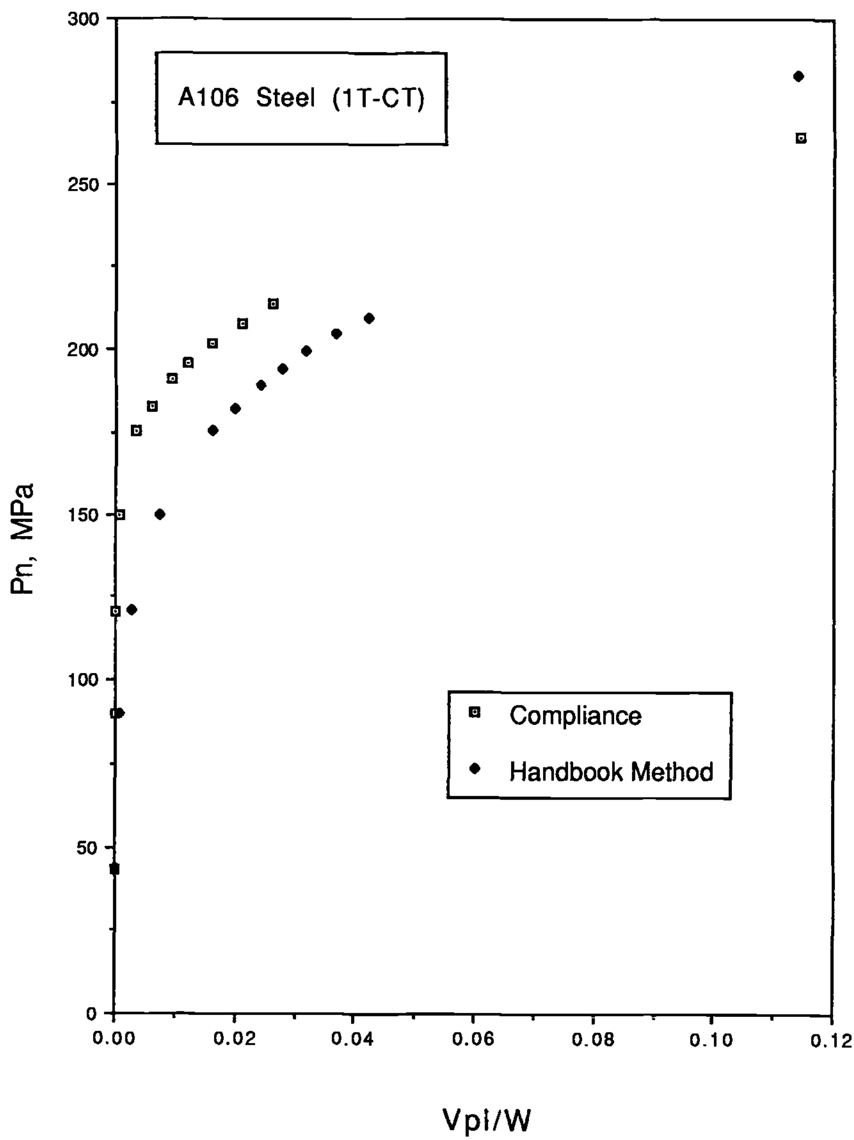

FIG. 5—*Normalized load versus plastic displacement: Handbook method, A106 steel.*

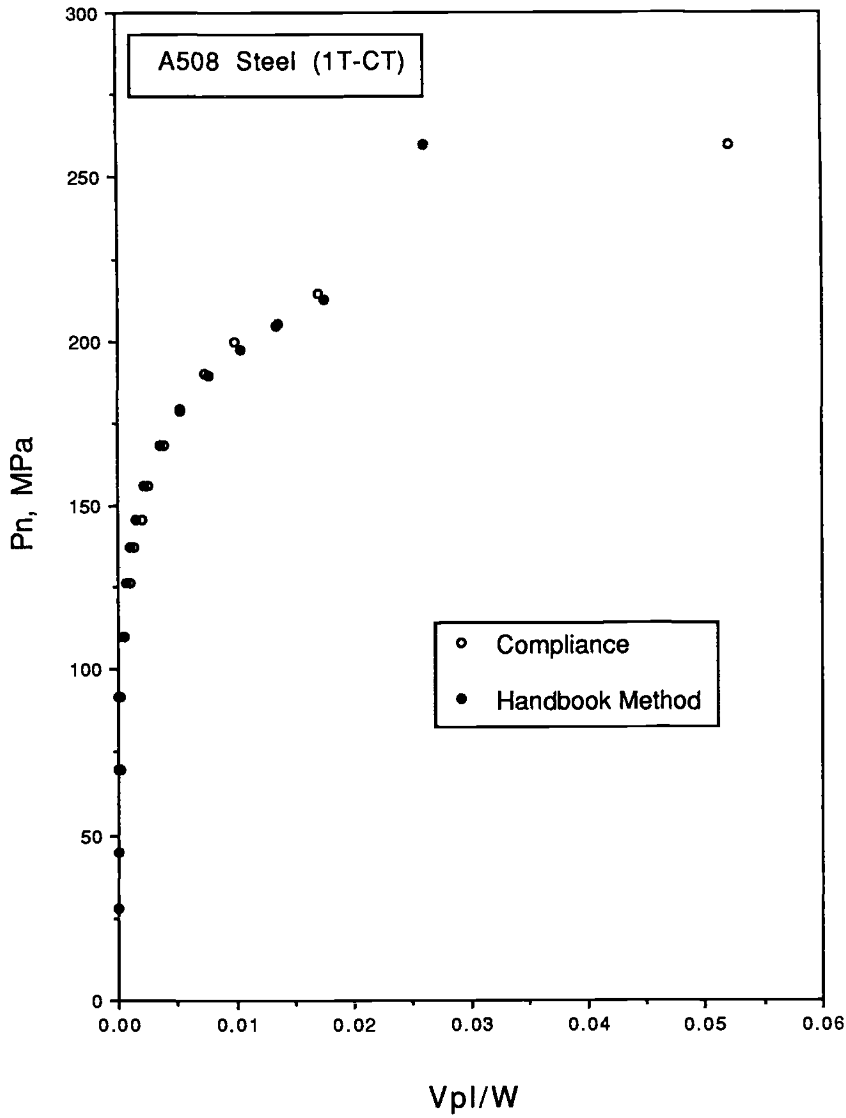

FIG. 6—*Normalized load versus plastic displacement: Handbook method, A508 steel.*

okay in some cases; it is best for the materials that do not have so much plastic displacement such as the A508 steel in Fig. 6. For the A106 steel (Fig. 5), the fit is not very good.

Empirical Formula

The second method used to obtain the second calibration points was labeled the empirical formula. This method used the tensile properties of the material to develop the constant, L, in Eq 5. This approach, in effect, eliminated the need for a set of second calibration points; however, the same format of evaluation was used. The expression used for L is

$$L = -204 + 8.58\sigma_Y - 0.108\sigma_Y^2 + 0.000472\sigma_Y^3 \qquad (7)$$

where σ_Y is the effective yield or flow stress usually taken as the average of the yield and ultimate tensile strengths. An average value of N was chosen, 0.0006, for all materials so it did not depend on the material properties. This procedure defined two of the three constants in the calibration equation. All that is needed to find M is one more calibration point. Therefore, the point taken at a_f, the final crack length, where plastic displacement as defined by the permanent set provides the needed calibration point. The example plots of the initial part of the P_N calibration curves are shown for the two steels in Figs. 7 and 8. The same information and

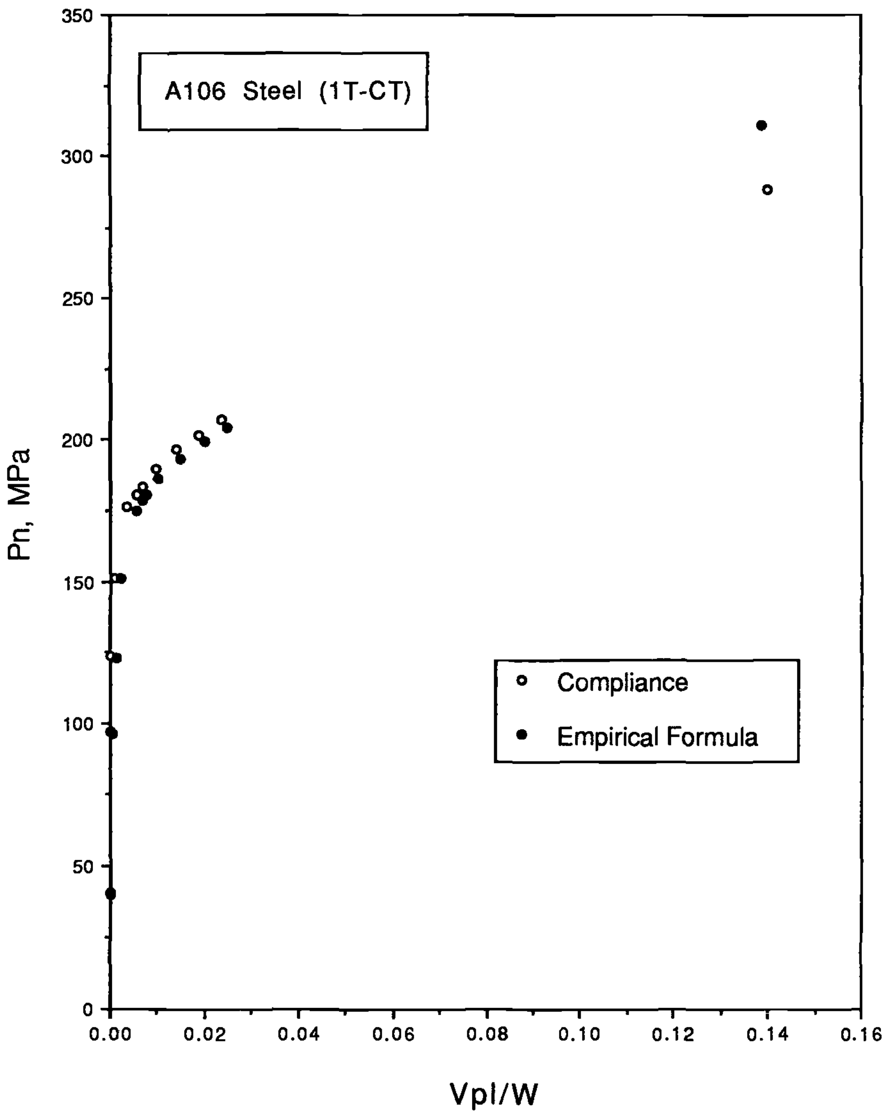

FIG. 7—*Normalized load versus plastic displacement: empirical formula, A106 steel.*

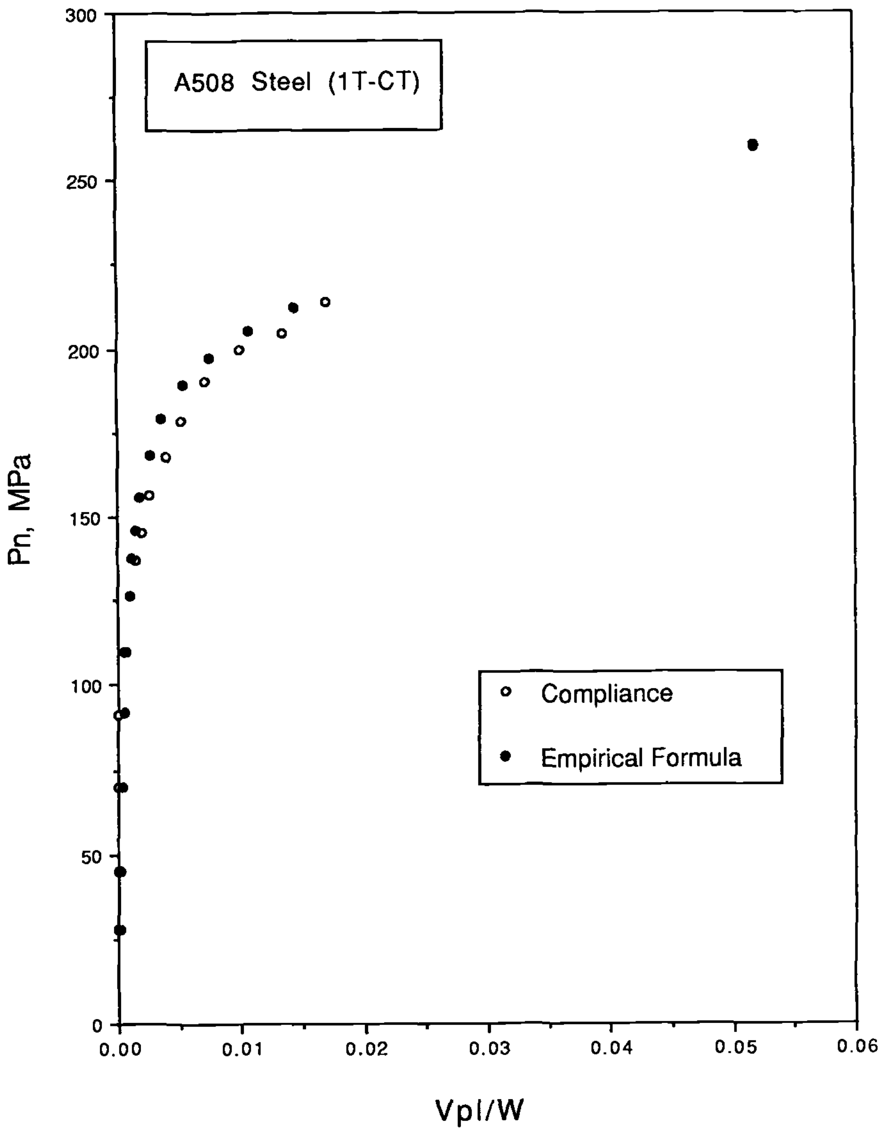

FIG. 8—*Normalized load versus plastic displacement: empirical formula, A508 steel.*

format that was used for the Handbook method was used here. In general, the empirical formula method seems to work better than the Handbook method.

Power Law Fit

The third method used to obtain second calibration points was labeled the power law fit. Although a power law is generally not a good fit over the entire range of plastic displacement, it could work well for the initial part of plastic displacement where the deformation is controlled more by the spread of the plastic zone than by the material deformation behavior. The form of the power law used was

$$P_N = \mu(v_{pl}/W)^{\kappa} \tag{8}$$

where μ and κ are fitting constants. The value of κ, the exponent, was taken to be a constant equal to 0.13, a value determined by trial and error. The value of μ was related to the material property, σ_Y, by the expression

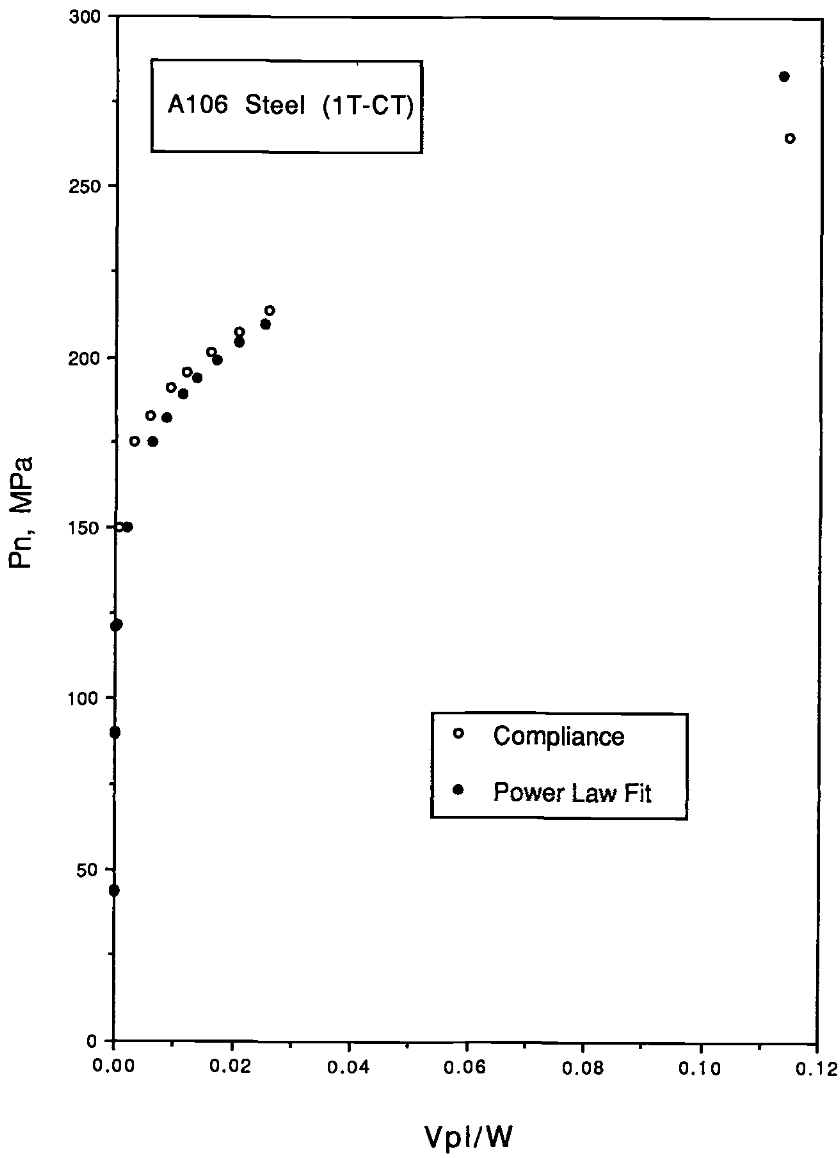

FIG. 9—*Normalized load versus plastic displacement: power law fit, A106 steel.*

$$\mu = 107.37 - 2.176\sigma_Y + 0.0197\sigma_Y^2 \tag{9}$$

The evaluation of the two steels for the initial part of the P_N curve is given in Figs. 9 and 10. Again, the same information and format used for the other two cases was used here. This fit also appears to work well. It is interesting to note that the Handbook approach that used a power law approach did not appear to work as well as the power law used here. In this case, the exponent was fixed and the Handbook fit used the power law from the stress-strain property. It does not appear that the stress-strain power law exponent is appropriate for the pre-

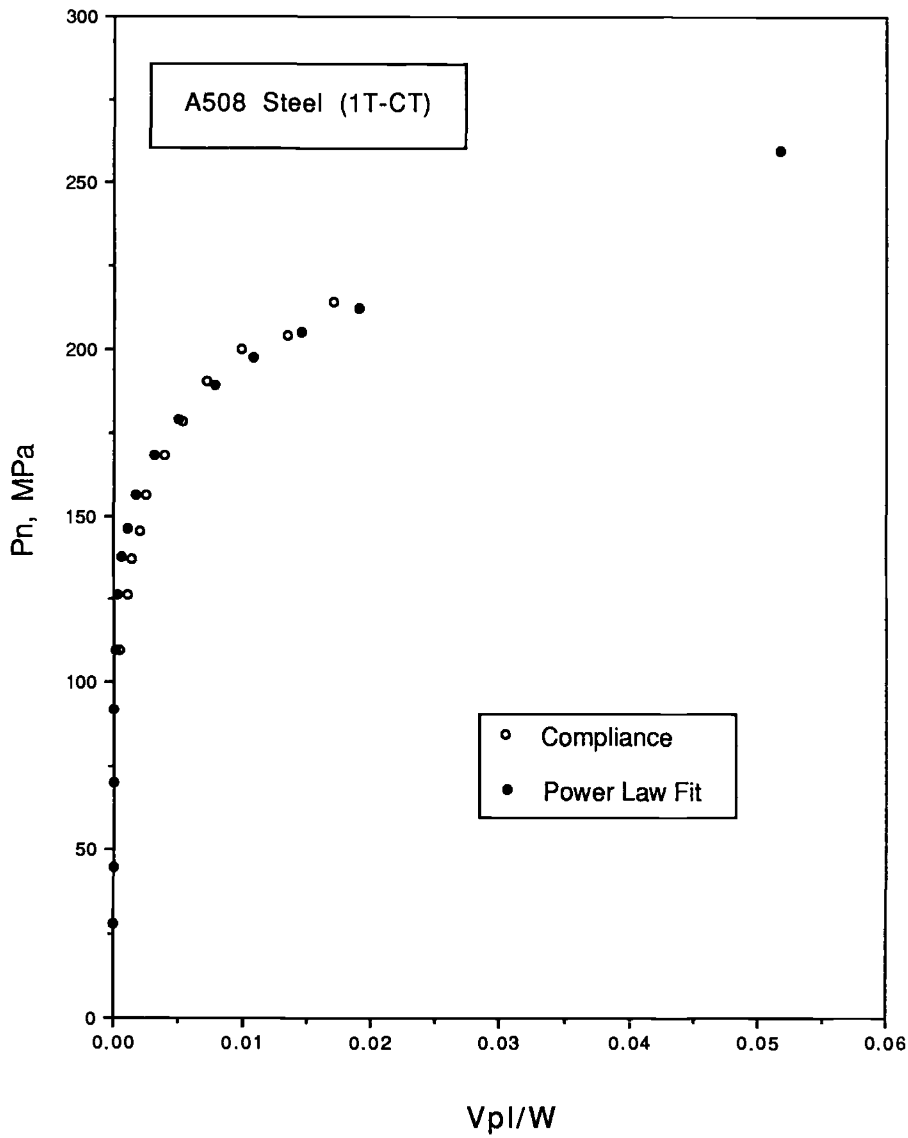

FIG. 10—*Normalized load versus plastic displacement: power law fit, A508 steel.*

cracked specimen, especially when they are loaded in bending [17]. For bend-type loading, there is spreading plasticity that gives a nonlinear behavior that is not particularly a function of the material property. Therefore, a constant exponent may be more appropriate.

Using Normalization for *J-R* Curves

The three methods of generating sets of second calibration points were used to obtain the L, M, and N values for Eq 10. This procedure gives the $H(v_{pl}/W)$ function needed to evaluate

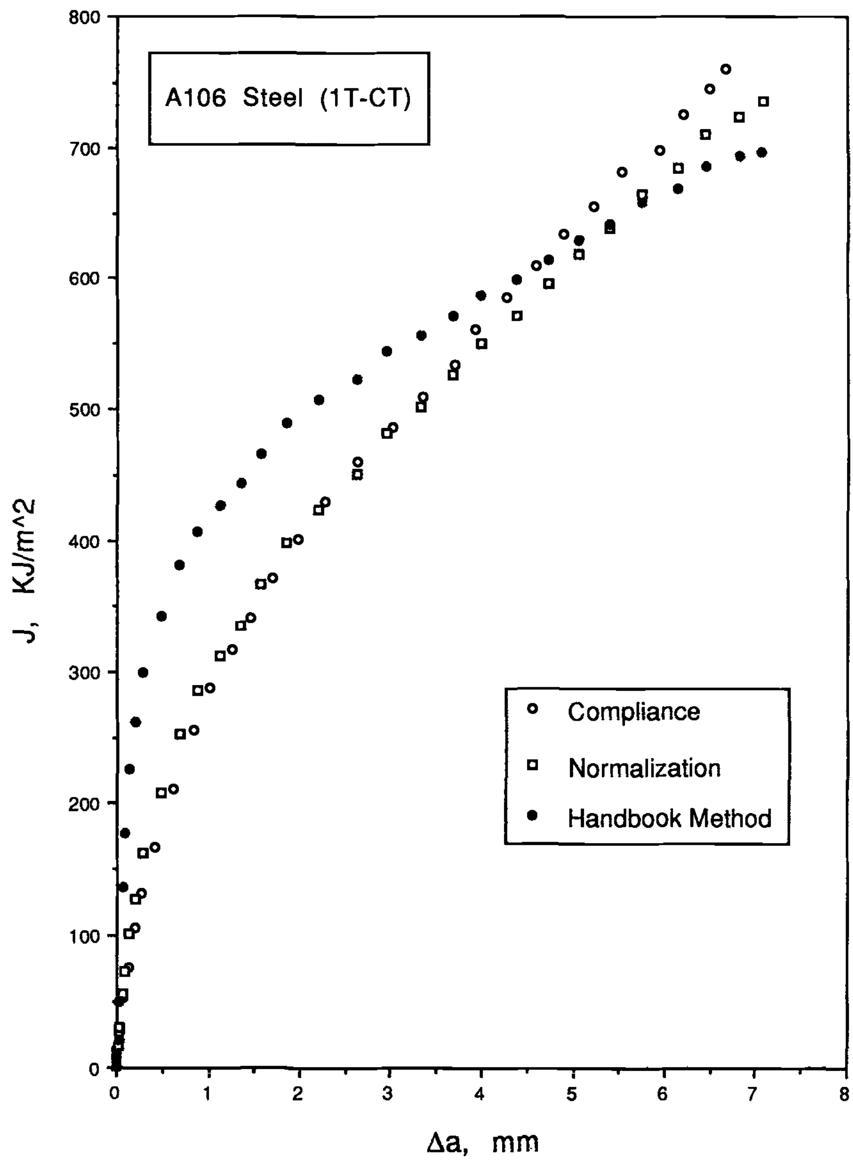

FIG. 11—J-R *curve for A106 steel comparing standard methods with the Handbook method.*

the unknown, in this case, displacement, from the two known quantities, load and crack length. The load-versus-crack length pairs were then used to obtain values of displacement so that J could be calculated and the J-R curve developed. This calculation was done for the twelve cases presented in the last section. They included four steels, A106, A508, A533B, and HSLA, and three methods of analysis to fit the early part of the normalized load-versus-plastic displacement curve, Handbook method, empirical formula, and power law fit. Examples of the J-R curves are plotted in Figs. 11 through 18. Again, only results from the A106 and A508 steels are presented.

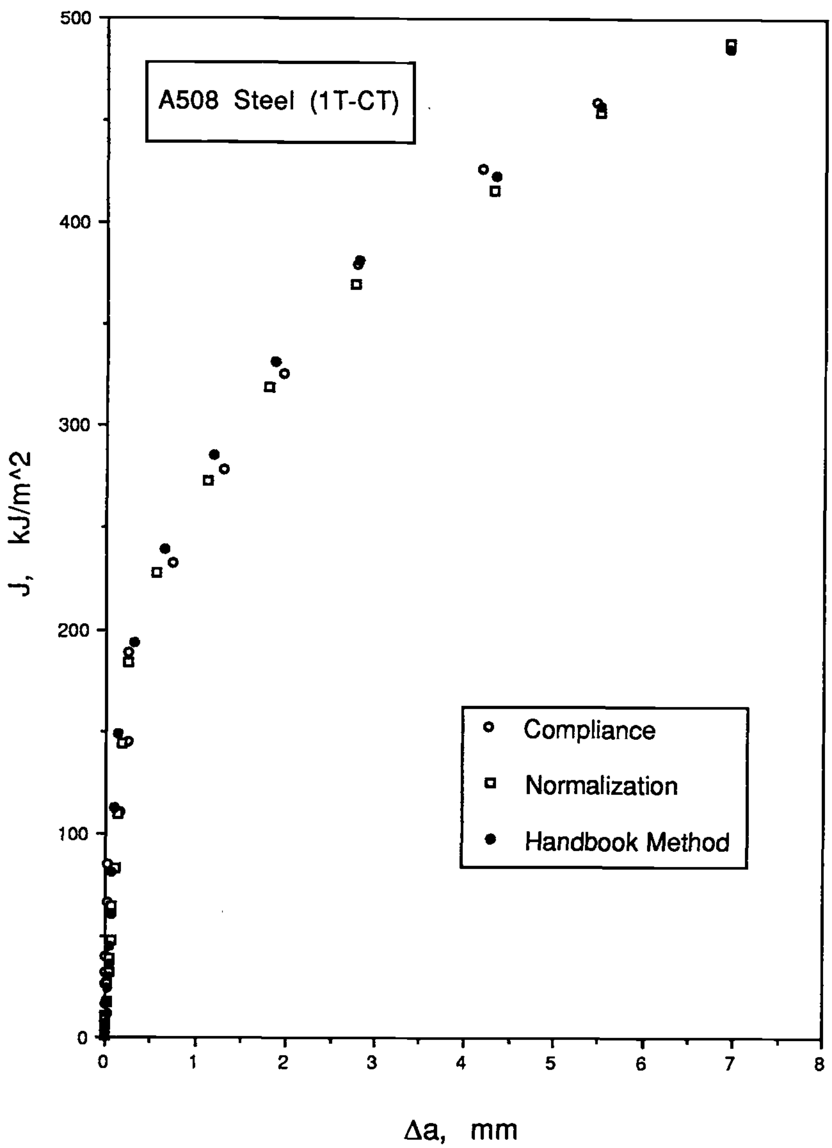

FIG. 12—J-R *curve for A508 steel comparing standard methods with Handbook method.*

The Handbook method was the first approach applied to the data. The results are presented in Figs. 11 and 12. This method did not work so well, especially for the A106 steel, Fig. 11. Here the two conventional methods, elastic unloading compliance and standard normalization, are also used to evaluate *J-R* curves, and the results are plotted with open symbols. The results of the method with no displacement measurement are all plotted using closed symbols. This format for plotting is used in all of the *J-R* curve comparisons. The Handbook method was used here only to get the initial points used for establishing the normalized calibration curve from Eq 10 and is not used in the *J-R* curve evaluation. The *J-R* curve was evaluated

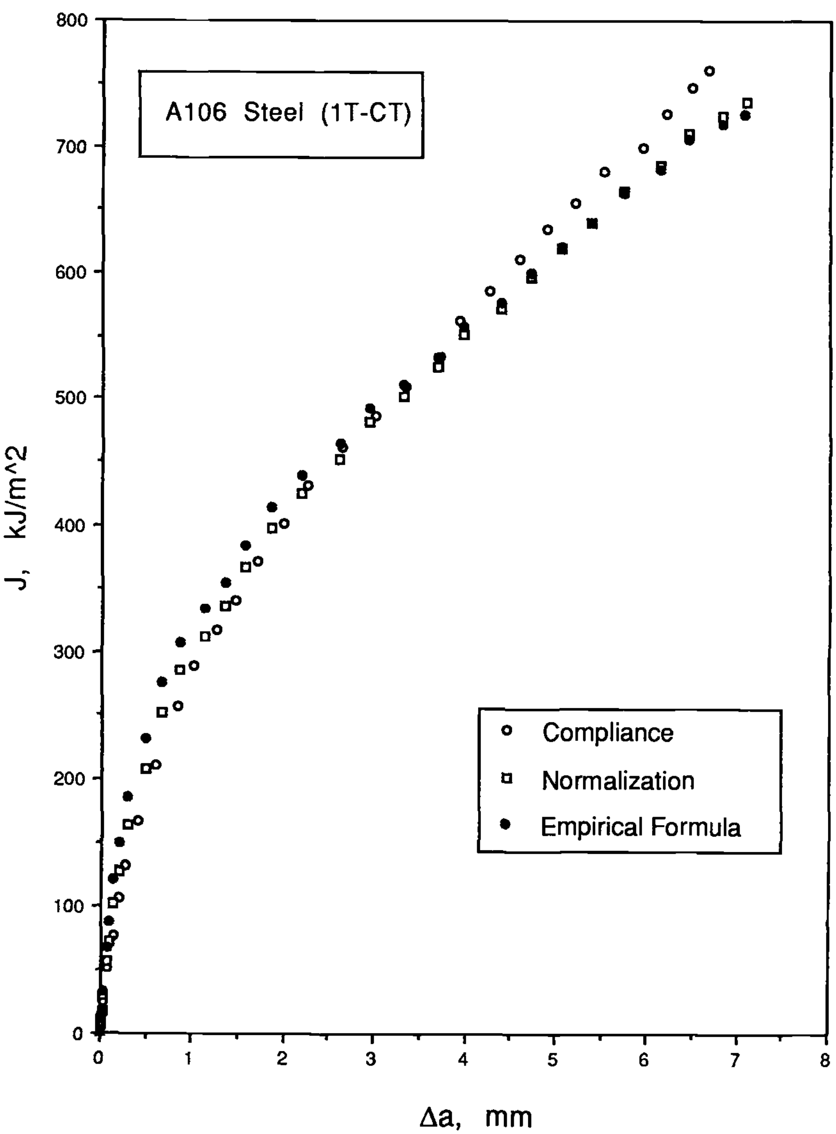

FIG. 13—J-R *curve for A106 steel comparing standards method with the empirical formula.*

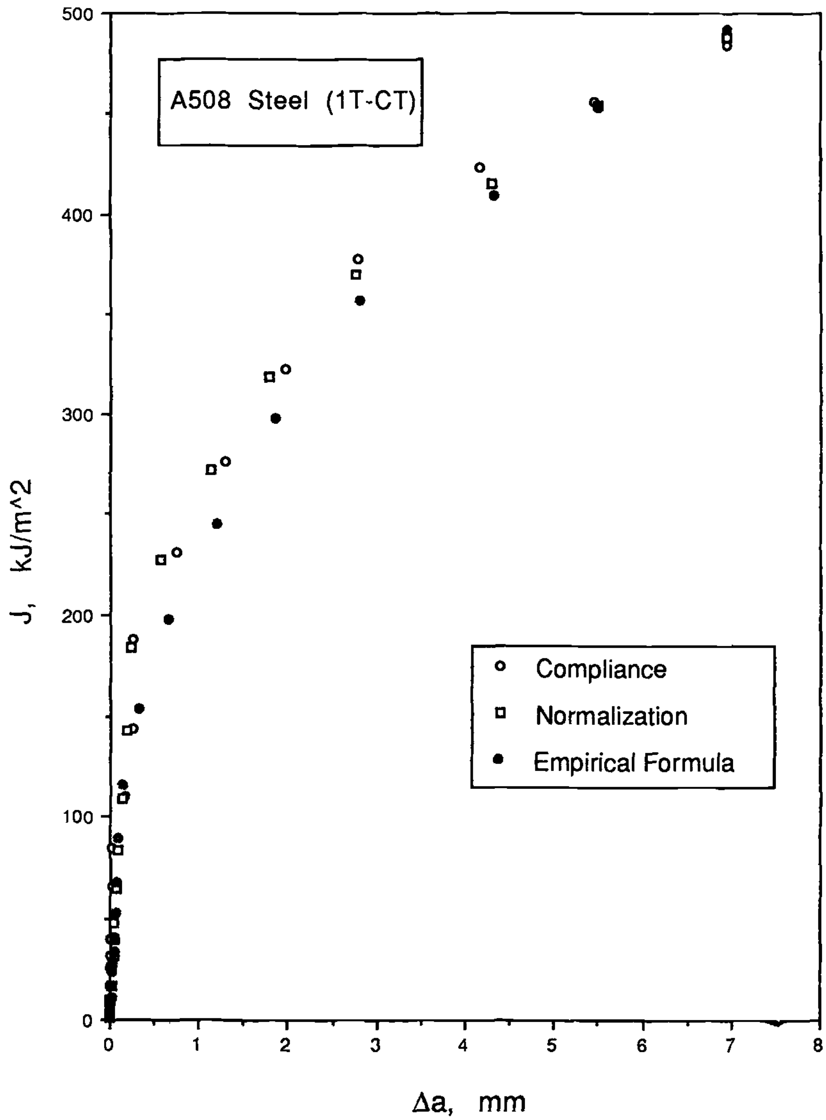

FIG. 14—J-R *curve for A508 steel comparing standard methods with the empirical formula.*

completely from normalization principles. For some of the other examples, the Handbook method works fairly well but overall it was judged to be inferior because it did not work for all of the materials.

The method using the empirical formula that takes its calibration from Eq 8, is plotted in Figs. 13 through 15. This method was better than the Handbook method but had a slight sensitivity to the material tensile properties. Compared with the Handbook method, the example for the A106 steel is much improved by the empirical formula, Fig. 13. The example showing

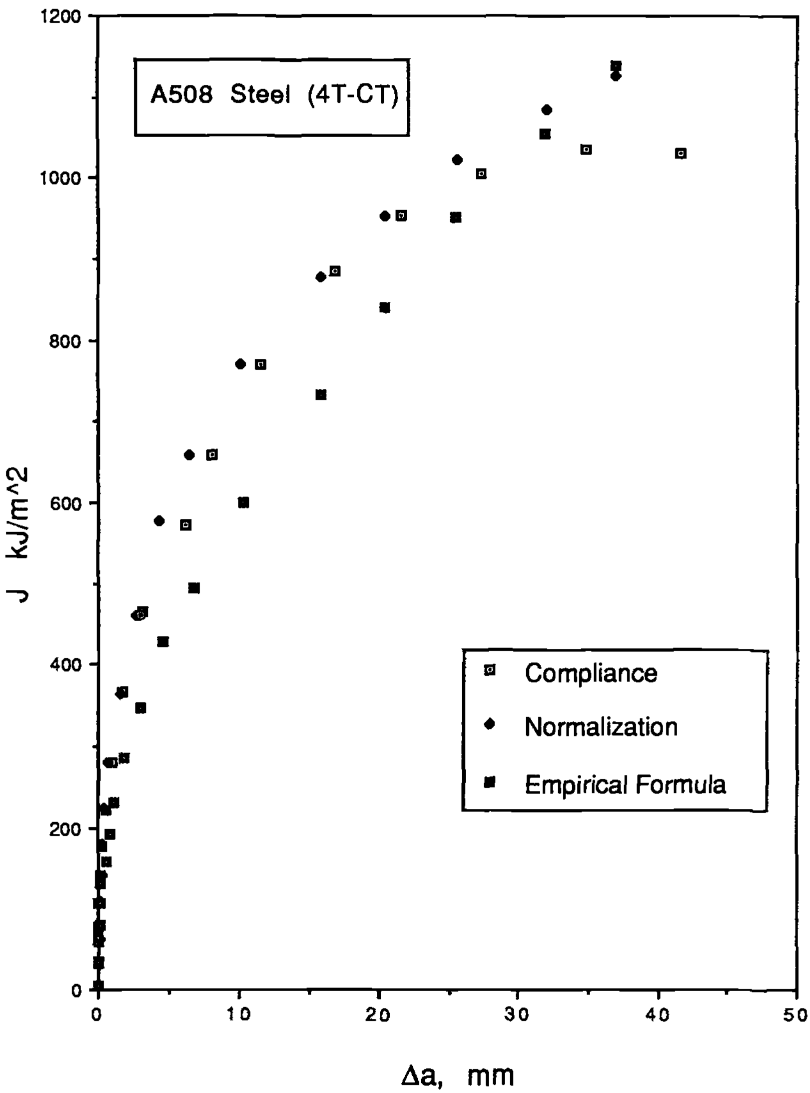

FIG. 15—J-R *curve for A508 steel comparing standard methods with the empirical formula.*

poor agreement came from the A508 steel where two cases, a 1T-CT (W = 50.4 mm) and a 4T-CT (W = 203 mm), are analyzed, Figs. 14 and 15, respectively. There is a difference in flow properties for these two cases, even though they are the same steel. This difference was enough to influence the method that bases the early calibration points on an empirical equation that is based on flow stress.

The power law fit was the last method used to analyze the *J-R* curves. It worked well for all four materials. Results are presented in Figs. 16 through 18. Comparing the two different examples for the A508 material, Figs. 17 and 18, the power law fit works well for both. Based on these results the power law fit was chosen as the best method for developing the early cali-

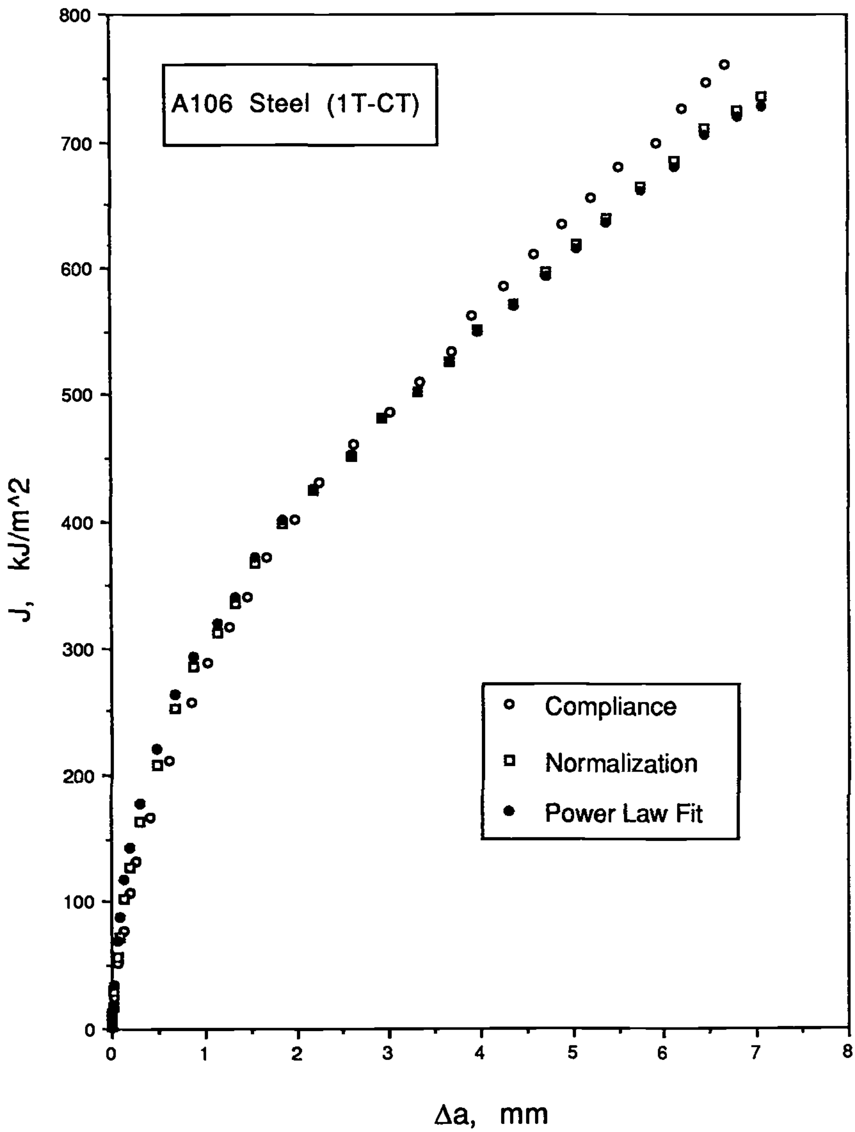

FIG. 16—J-R *curve for A106 steel comparing standard methods with the power law fit.*

bration points and was chosen for all subsequent analyses. In particular, it was used to evaluate the cases for which data were not available to evaluate the *J-R* curves from standard methods. These results are presented in the next section.

J-R Curves for Blind Specimens

In the previous section, the *J-R* curves were determined with no displacement measurement for specimens that originally had the full load, displacement, and crack length measurement

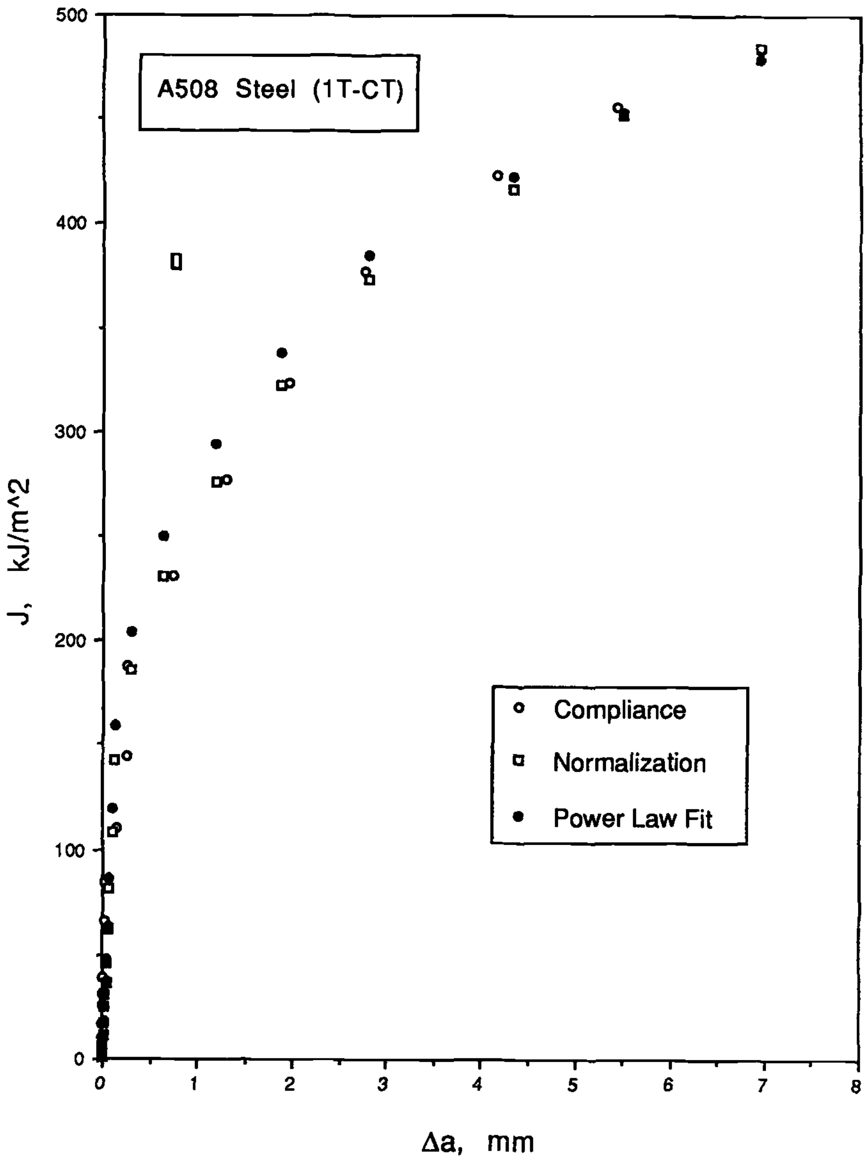

FIG. 17—J-R *curve for A508 steel comparing standard methods with the power law fit.*

available. The assumption was first made that the displacement was missing, and then the *J-R* curve was calculated by one of the three methods. After the *J-R* curve was calculated, the original displacement information was used to calculate *J-R* curves by the compliance and regular normalization methods for comparison. It was from this procedure that the power law fit was judged to be the best method to get the early calibration points.

The next step in demonstrating the method is to analyze data for which the displacement measurement is not available to us. These data were supplied by Randy Nanstad of Martin

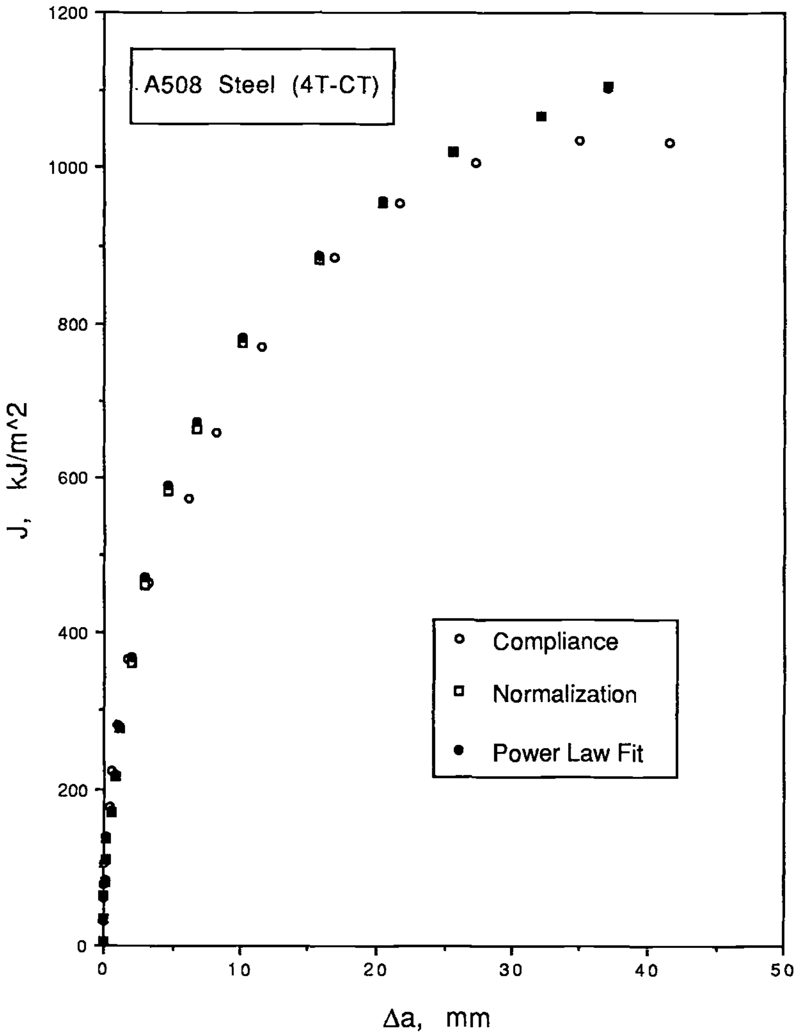

FIG. 18—J-R *curve for A508 steel comparing standard methods with the power law fit.*

Marietta for an A533-B steel in the form of only load-versus-crack length pairs. Also, the original and final crack lengths as measured on the fracture surface and final plastic displacement were provided. The set of data included eight specimens of an A533-B nuclear-grade pressure vessel steel. The analysis was done as described in the previous section using the power law fit to obtain the set of second calibration points. The final load, final plastic displacement, and final measured crack length were used to obtain the first calibration point, and the intermediate set of calibration points were used as the third points. From these points, the *L*, *M*, and *N* constants in Eq 5 could be determined. The load-versus-crack length pairs were then subjected to the method of normalization so that the plastic displacements could be determined for each load and crack length pair. Once displacement was determined, the values of J could be calculated at each point and the J-R curves could then be plotted.

The raw data were supplied as load-versus-crack length data; examples are given in Figs. 19 and 20. Also the initial and final crack lengths and the final plastic displacement were given.

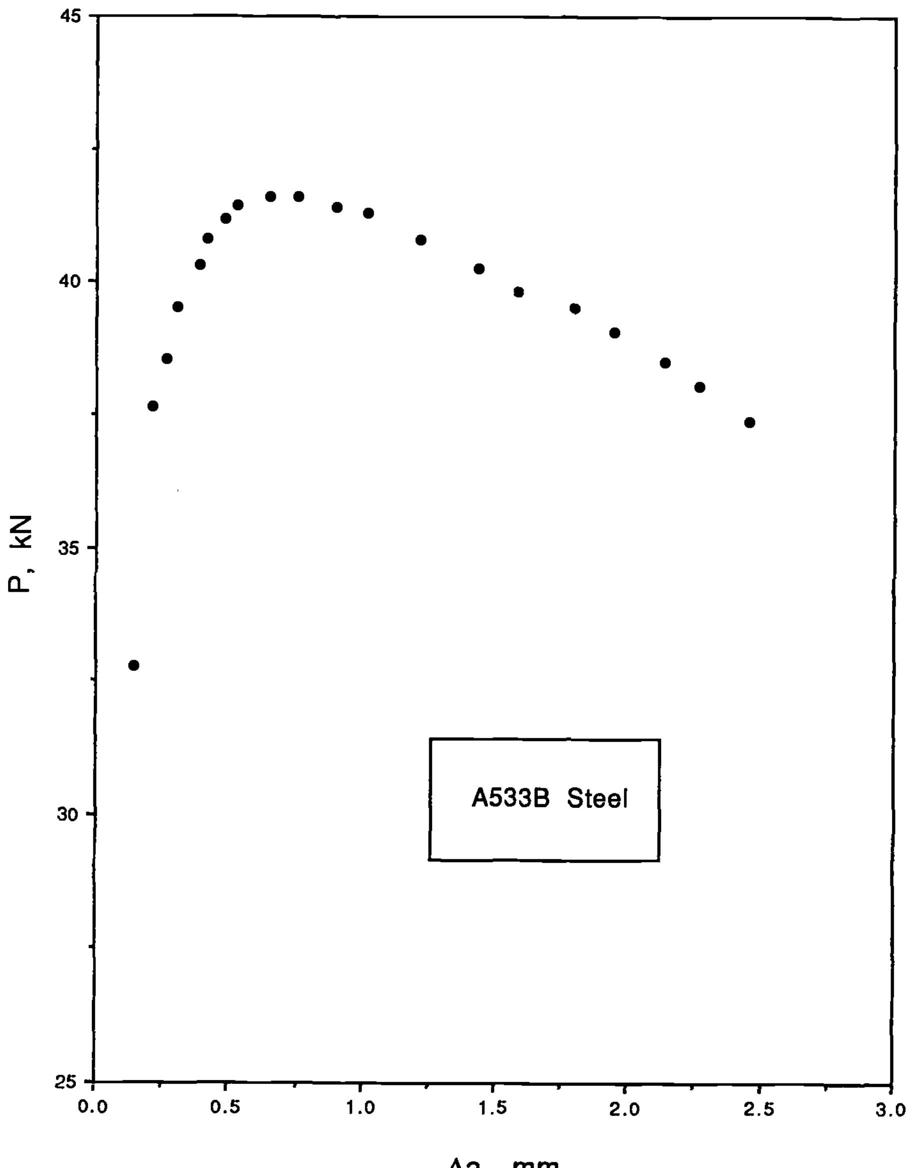

FIG. 19—*Load versus crack length for A533-B steel specimen, K54B.*

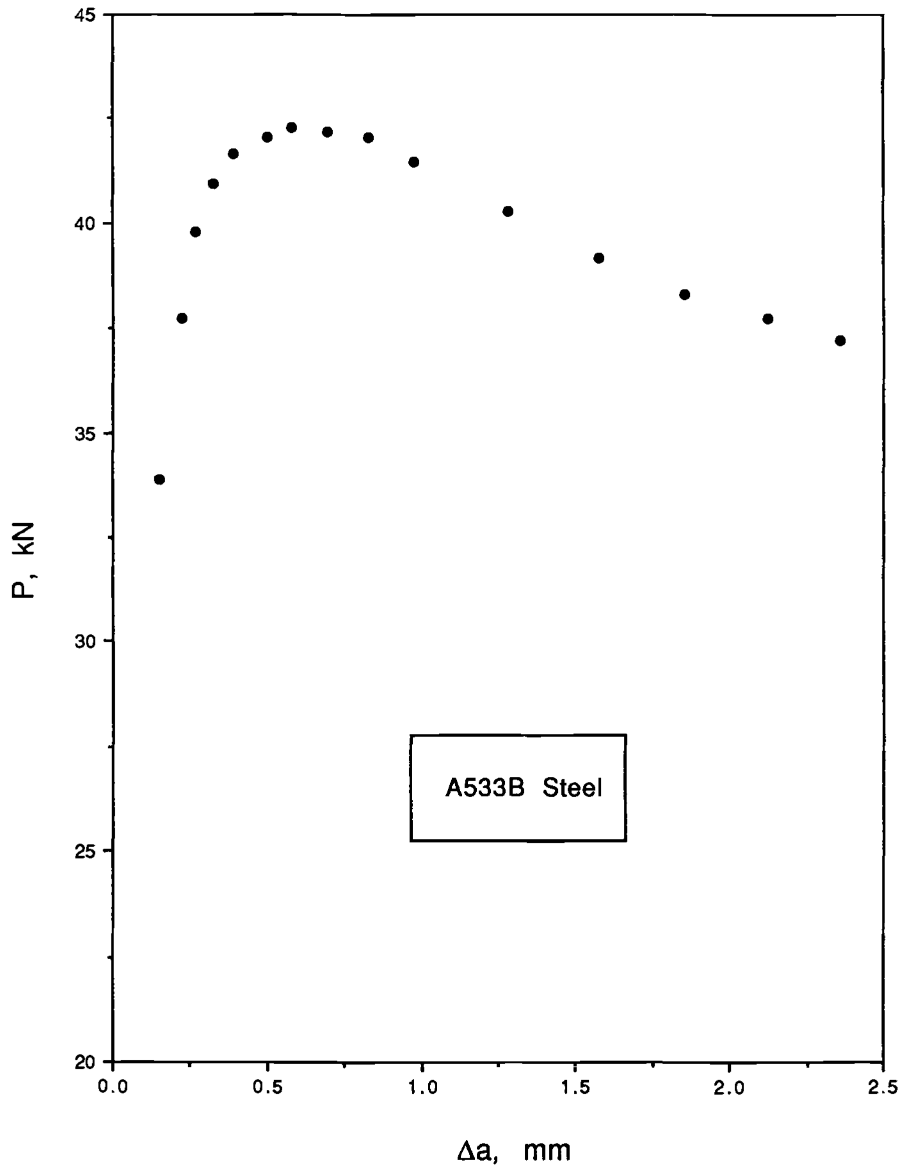

FIG. 20—*Load versus crack length for A533-B steel specimen, K53C.*

The *J-R* curves resulting from this analysis had two types of general characteristics. One type looked nearly correct, but the second type did not look correct near the end. Examples are given for four of the eight curves in Figs. 21 through 24. In Figs. 21 and 22, the *J-R* curves looked nearly correct. In Figs. 23 and 24, the end of the *J-R* curve did not look correct. The problem appeared to be related to this closeness of match between the final crack length given as a part of the load and crack length pairs and the final crack length measured on the fracture

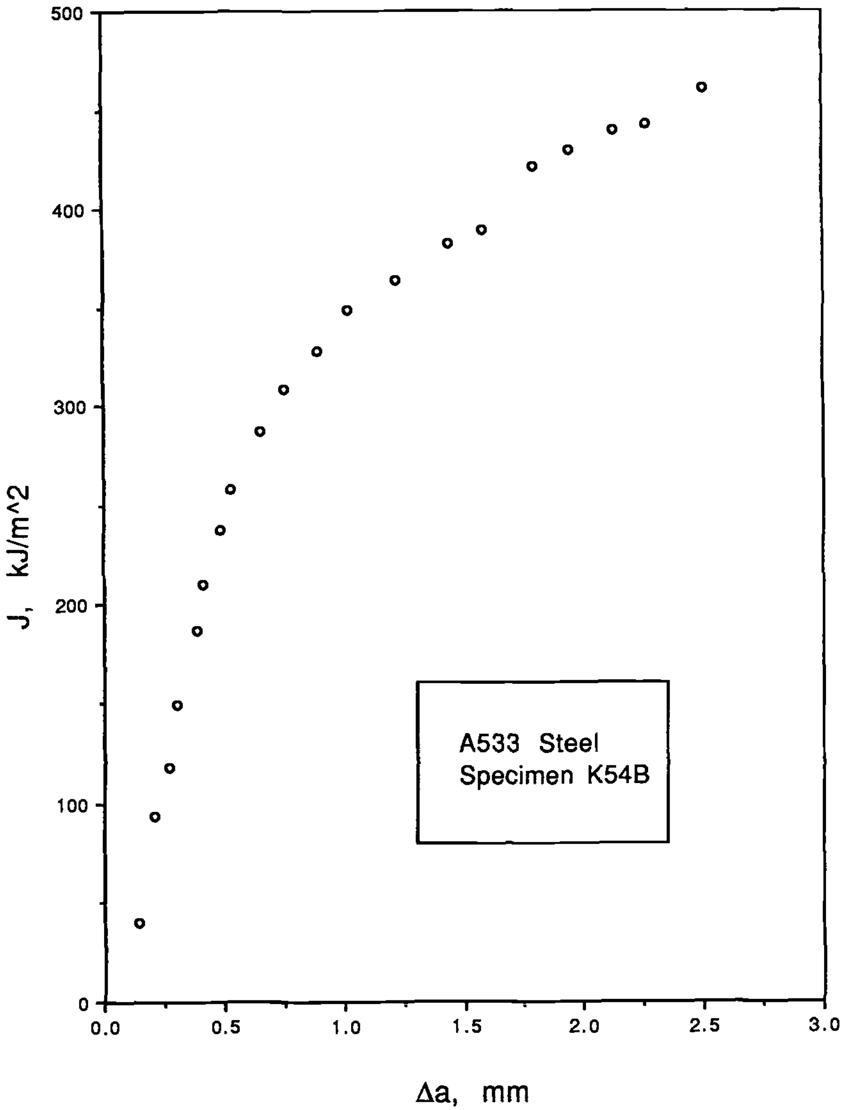

FIG. 21—J-R *curve for A533-B steel, K54B, analyzed with no displacement measurement.*

surface. For the first two cases, the match is fairly good. When the crack lengths supplied as data underestimate the measured crack lengths, the end of the *J-R* curve rises; when the opposite happens, it falls. In Fig. 21, a 2% difference causes an almost indistinguishable rise. In Fig. 22, a 6% overestimate causes a small final drop. For the latter two cases in Figs. 23 and 24, the final measured crack length and the final crack length from the crack length monitor had greater mismatch and the corresponding jumps in the end of the curves were greater. It is obvious that these trends near the end of the *J-R* curve are not correct. The method of normalization gives a result that terminates at the final physically measured crack length; however, when

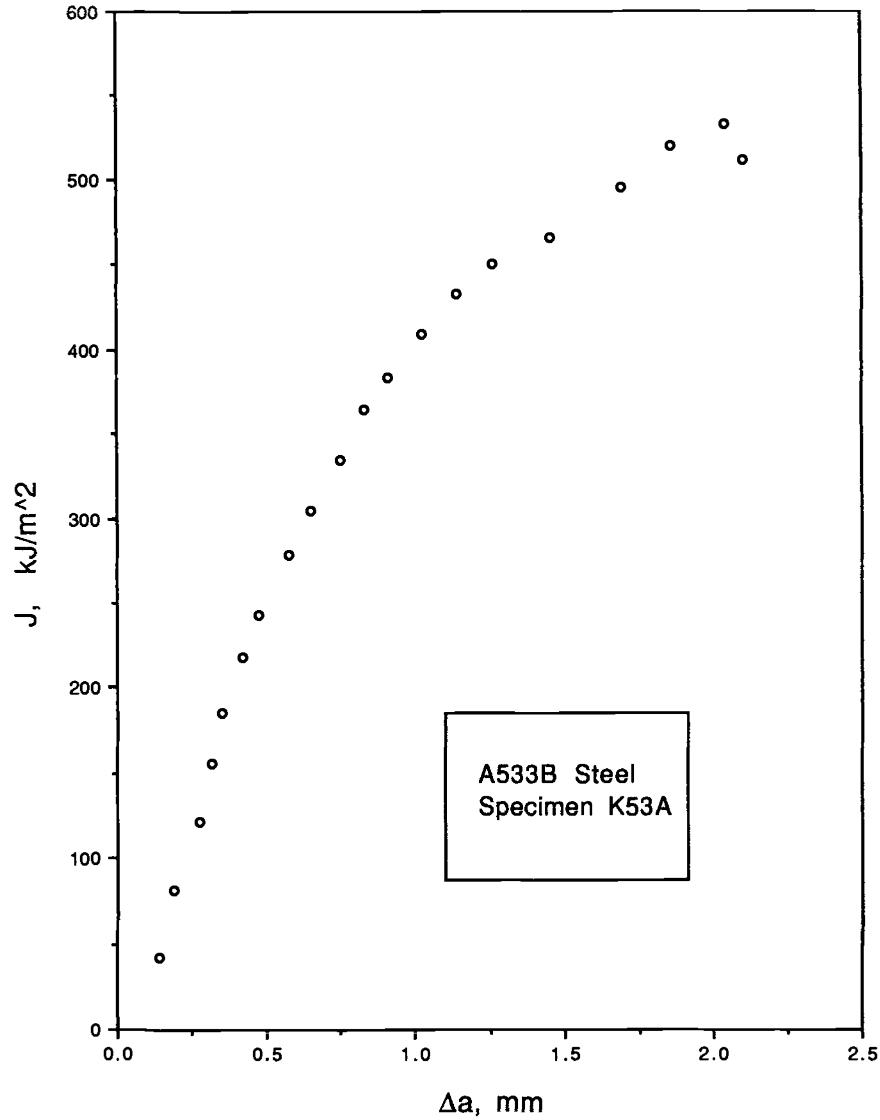

FIG. 22—J-R *curve for A533-B steel, K53A, analyzed with no displacement measurement.*

the crack length from the data monitor is not compatible with the physically measured crack length, the *J-R* curve will follow the monitored crack length until near the end and then jump to the physically measured crack length at the very end.

A correction scheme was devised to change the final trend of the *J-R* curve. This correction was accomplished by adjusting the plastic displacement to fall in line with the crack length data values given rather than the final measured crack length. The correction scheme was based on an empirical relationship between crack extension and normalized plastic displacement that was observed to be nearly linear after the maximum load point was passed. This

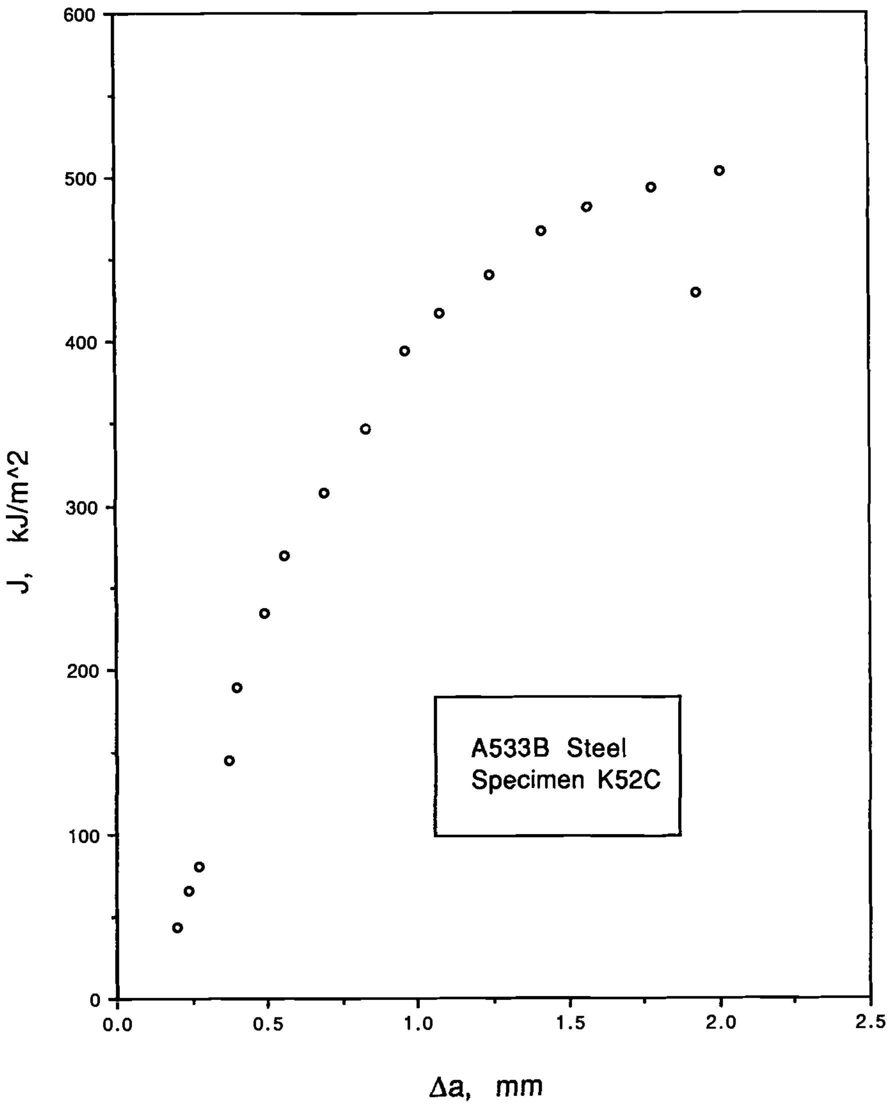

FIG. 23—J-R *curve for A533-B steel, K52C, analyzed with no displacement measurement.*

relationship is illustrated for the steels used previously, A106 and A508 in Figs. 25 and 26. A linear adjustment was taken for plastic displacement from the point of maximum load to the final point. It had the general form

$$(v_{pl}/W)_i = (v_{pl}/W)_{max} + [(\Delta a_i - \Delta a_{max})/(\Delta a_f - \Delta a_{max})][(v_{pl}/W)_f - (v_{pl}/W)_{max}] \quad (11)$$

where the subscript, i, refers to the current value of the term, f, to the final value and the subscript, max, refers to the value at maximum load. The correction in Eq 11 adjusts the normalized value of the plastic displacement to fall in line with the monitored values of crack

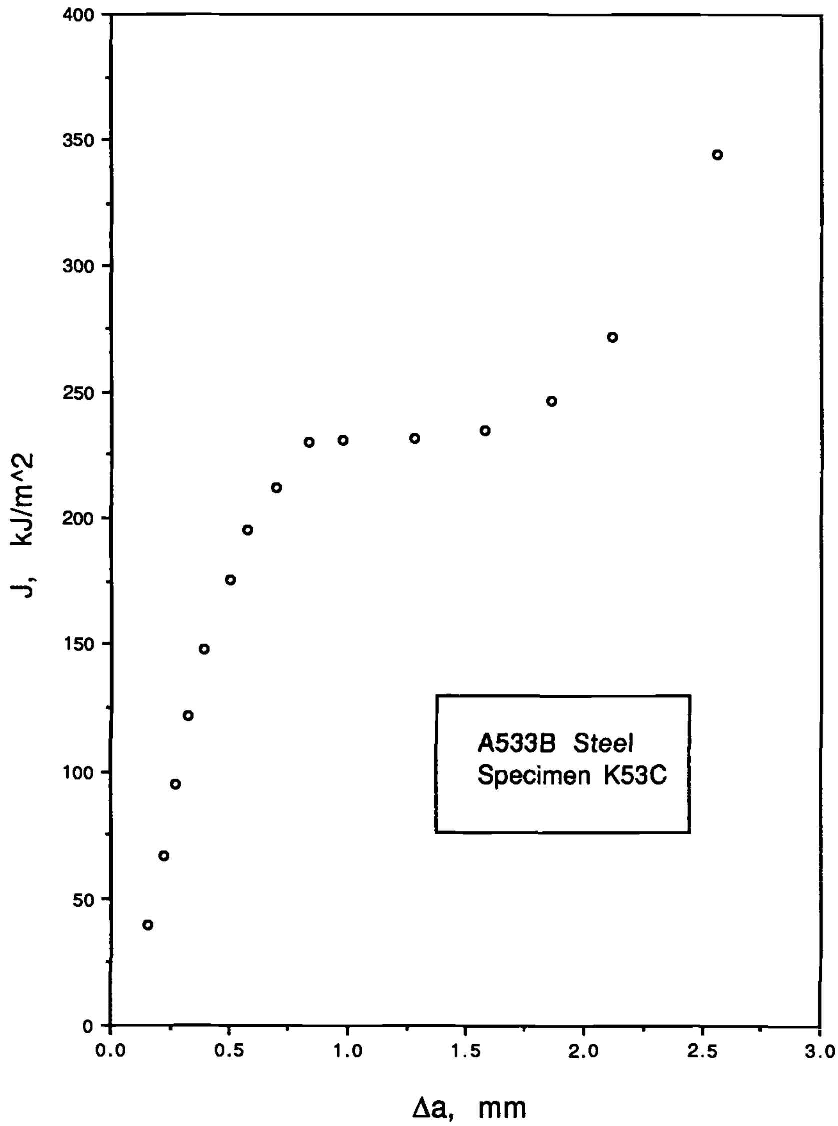

FIG. 24—J-R *curve for A533-B steel, K53C, analyzed with no displacement measurement.*

length rather than the physically measured values. These adjusted values of plastic displacement are then used with the load and the calibration function to get new values of crack extension. From all of these, the *J* values are calculated and the *J-R* curve is plotted.

This adjustment was given to the A533-B steel data in each of the eight cases and new *J-R* curves were evaluated. The results for the four cases previously shown are plotted in Figs. 27 through 30 where, for each example, the *J-R* curves determined before and after the adjustment are plotted. The effect of the adjustment is to shift the *J-R* curve so that it has a contin-

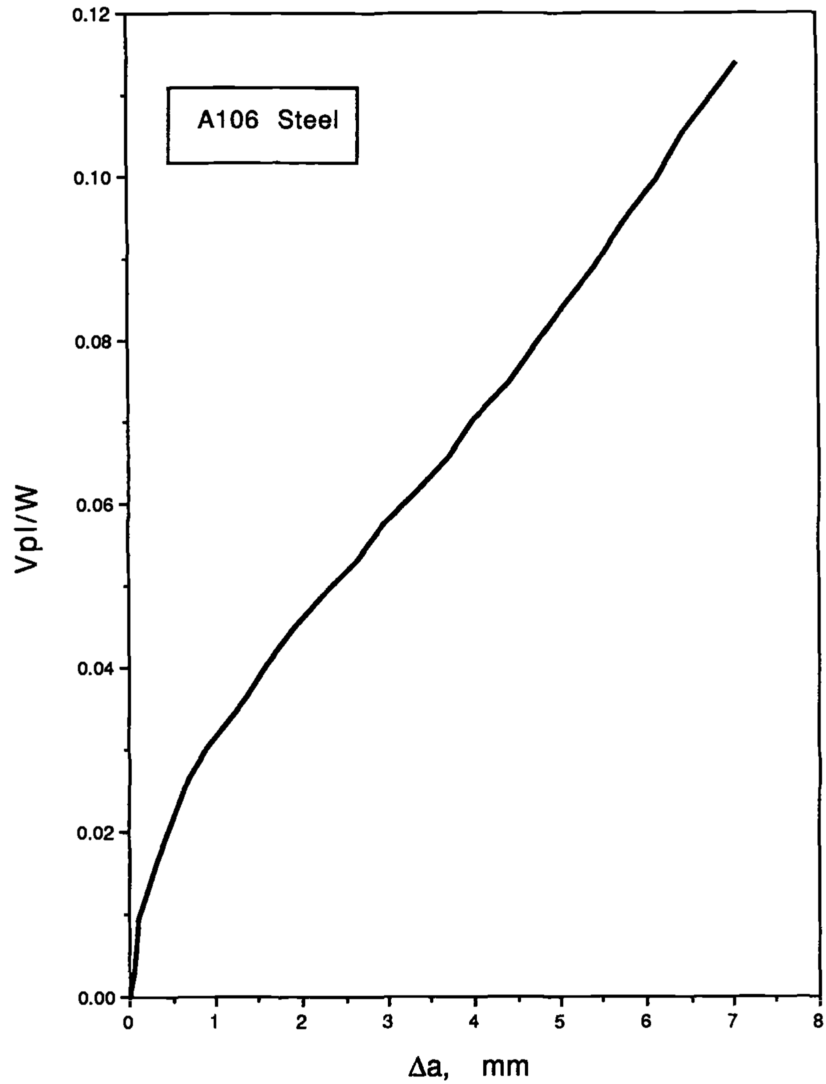

FIG. 25—*Normalized plastic displacement versus crack length showing linear relationship after maximum load, A106 steel.*

uous trend that ends at the final physically measured crack length rather than the trend that goes toward the final crack length supplied in the data pairs. When the final crack lengths supplied as data agree well with the final measured crack length, there is not much difference in the two *J-R* curves, but when this agreement is not good, the *R*-curve difference is significant. This difference is similar to the one observed between *J-R* curves measured by the regular normalization and the compliance method, when the final compliance estimated crack does not agree well with the physically measured crack length.

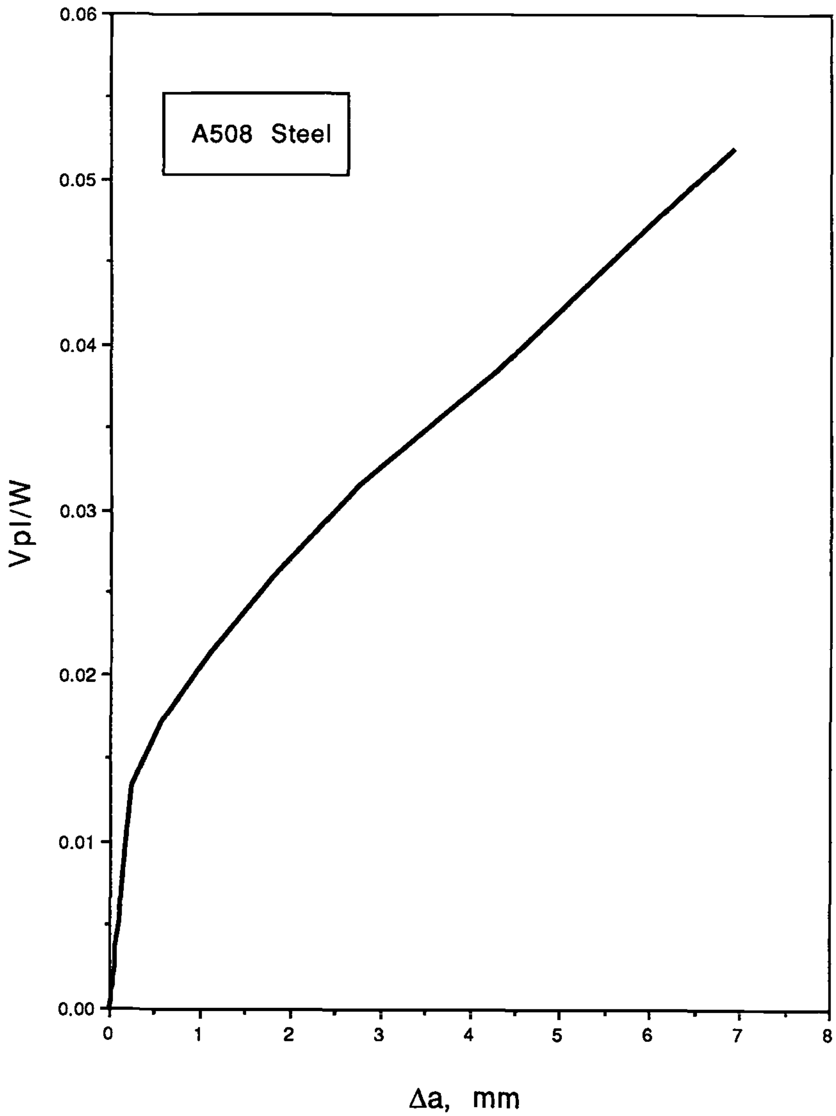

FIG. 26—*Normalized plastic displacement versus crack length showing linear relationship after maximum load, A508 steel.*

Summary

The method of normalization is used here to develop *J-R* curve fracture toughness data from tests where only load-versus-crack length is measured, and where no measurement of displacement is available. Two major problems were solved to obtain good *R*-curve results from these data. First, when no displacement measurement is available, there are no standard calibration points available from which to determine the normalized load-versus-displacement function that is necessary in the method of normalization. Calibration points were developed using a

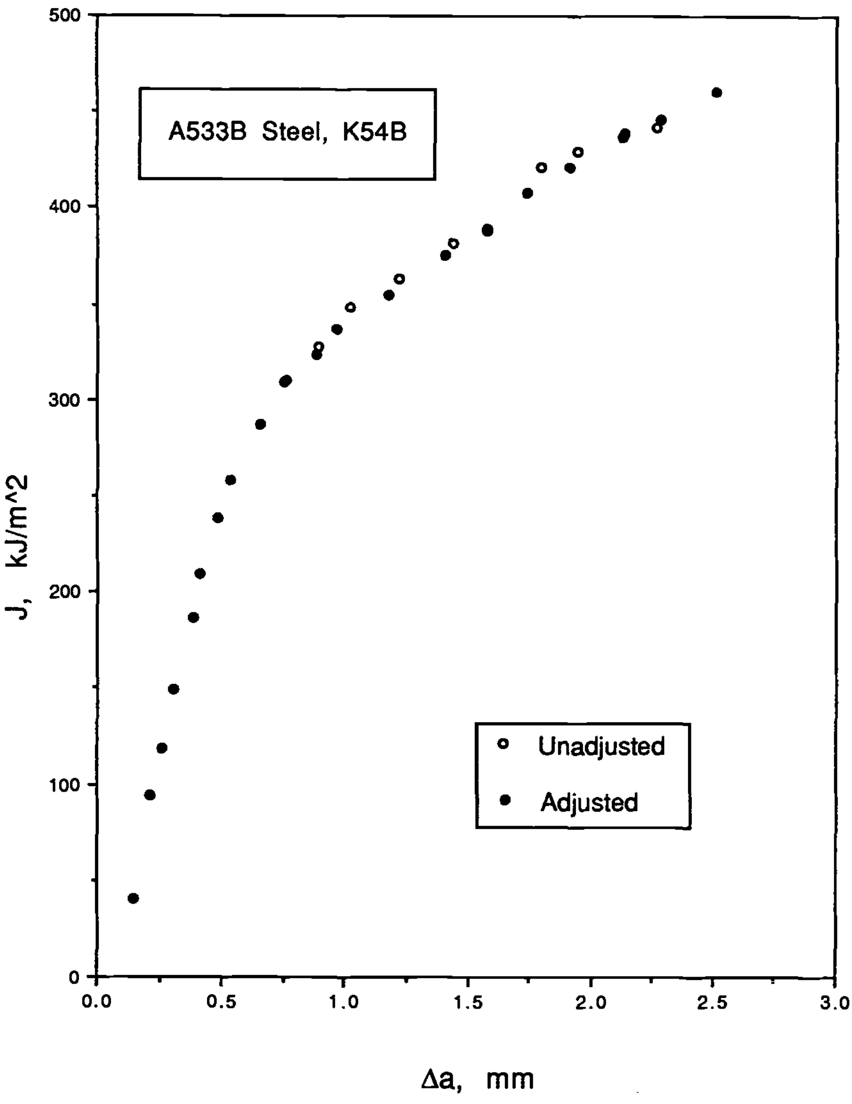

FIG. 27—J-R *curve for A533-B steel, K54B, with no displacement measurement comparing adjusted versus unadjusted.*

physical measurement of the final plastic displacement to obtain one point. Three fitting assumptions were tried in order to get a second set of calibration points; the Handbook method, an empirical formula, and a power law fit. From these calibration points the normalized load function could be determined.

A second problem was that the crack length measured during the test did not always match the physically measured crack length at the end of the test. When this happened, an adjustment was made to the plastic displacement so that the predicted plastic displacement would be consistent with the one that is correct for the physically measured crack length. After solving these

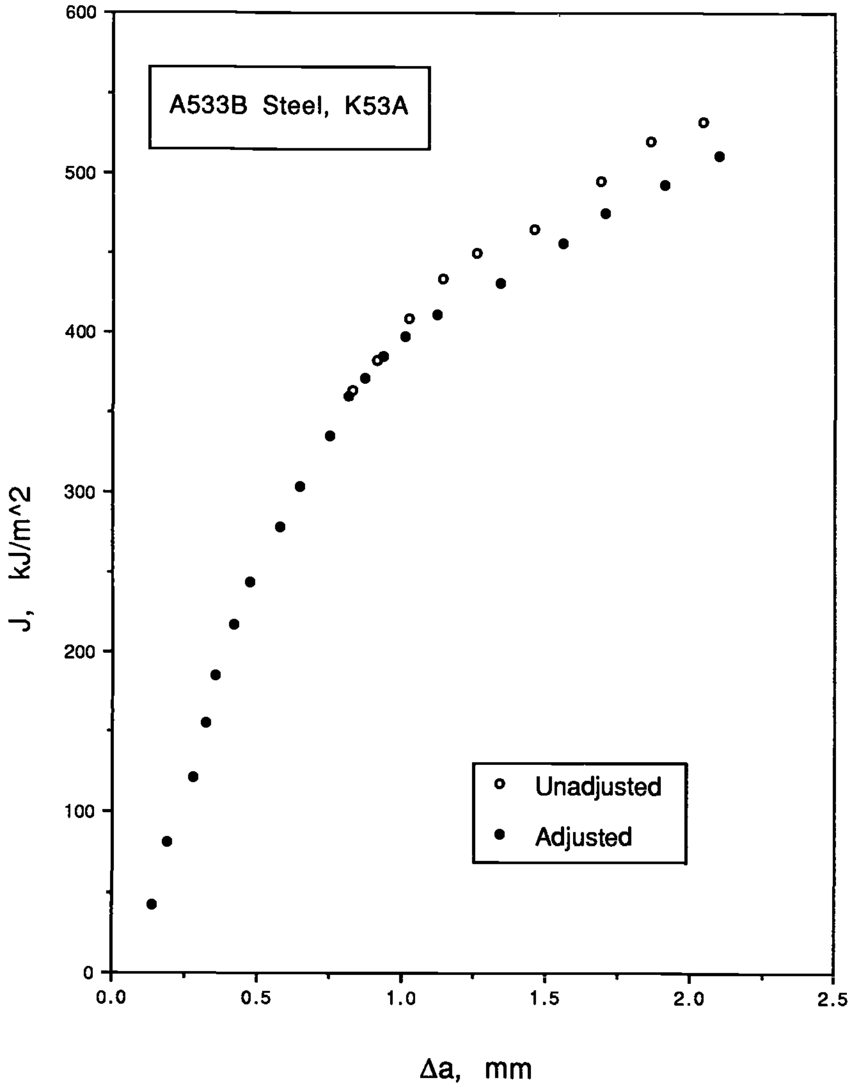

FIG. 28—J-R *curve for A533-B steel, K53A, with no displacement measurement comparing adjusted with unadjusted.*

problems, the method of normalization works well for determining *J-R* curves from the load-versus-crack length data.

Acknowledgment

This work was sponsored by the Oak Ridge National Laboratories. Dr. Randy Nanstad of ORNL was the contract monitor and technical contact.

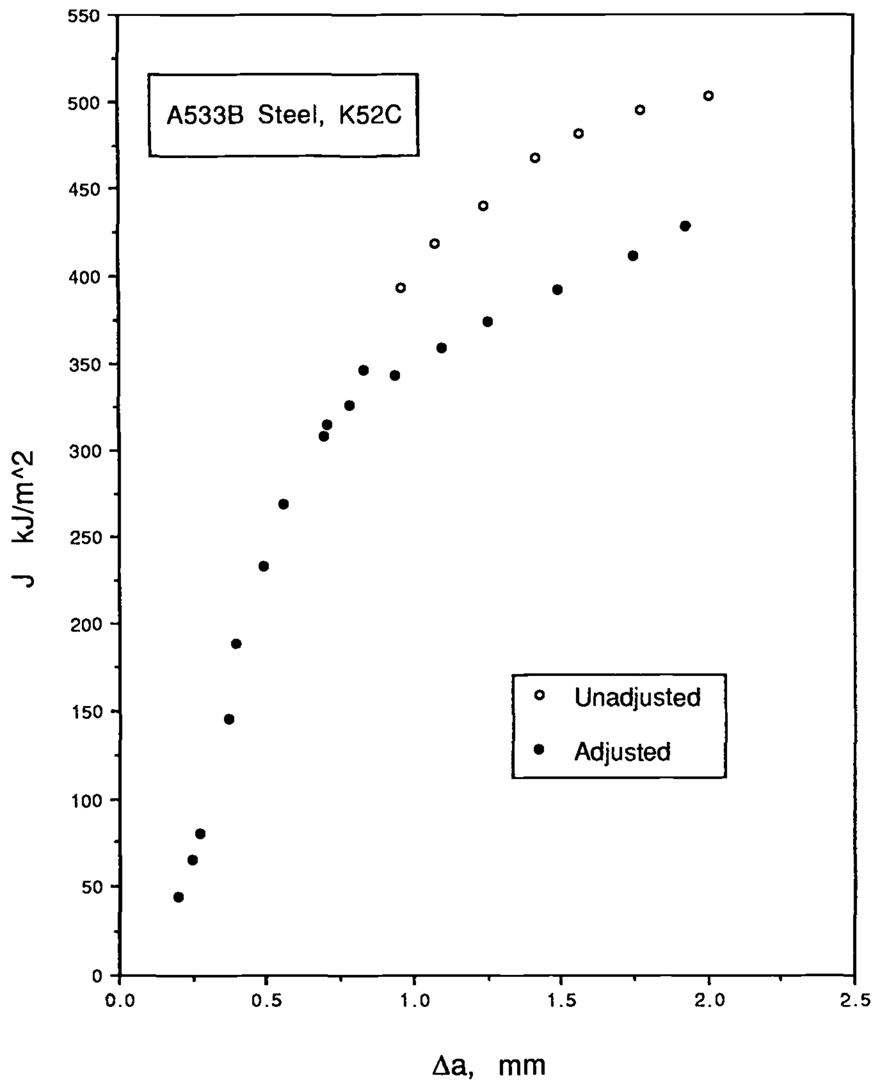

FIG. 29—J-R *curve for A533-B steel, K52C, with no displacement measurement comparing adjusted versus unadjusted.*

References

[1] Clarke, G. A., Andrews, W. R., Paris, P. C., and Schmidt, D. W., "Single Specimen Tests for J_{Ic} Determination," *Mechanics of Crack Growth, ASTM STP 590,* American Society for Testing and Materials, Philadelphia, 1976, pp. 24–42.

[2] Joyce, J. A. and Gudas, J. P., "Computer Interactive J_{Ic} Testing of Navy Alloys," *Elastic-Plastic Fracture, ASTM STP 668,* J. D. Landes, J. A. Begley, and G. A. Clarke, Eds., American Society for Testing and Materials, Philadelphia, 1979, pp. 451–468.

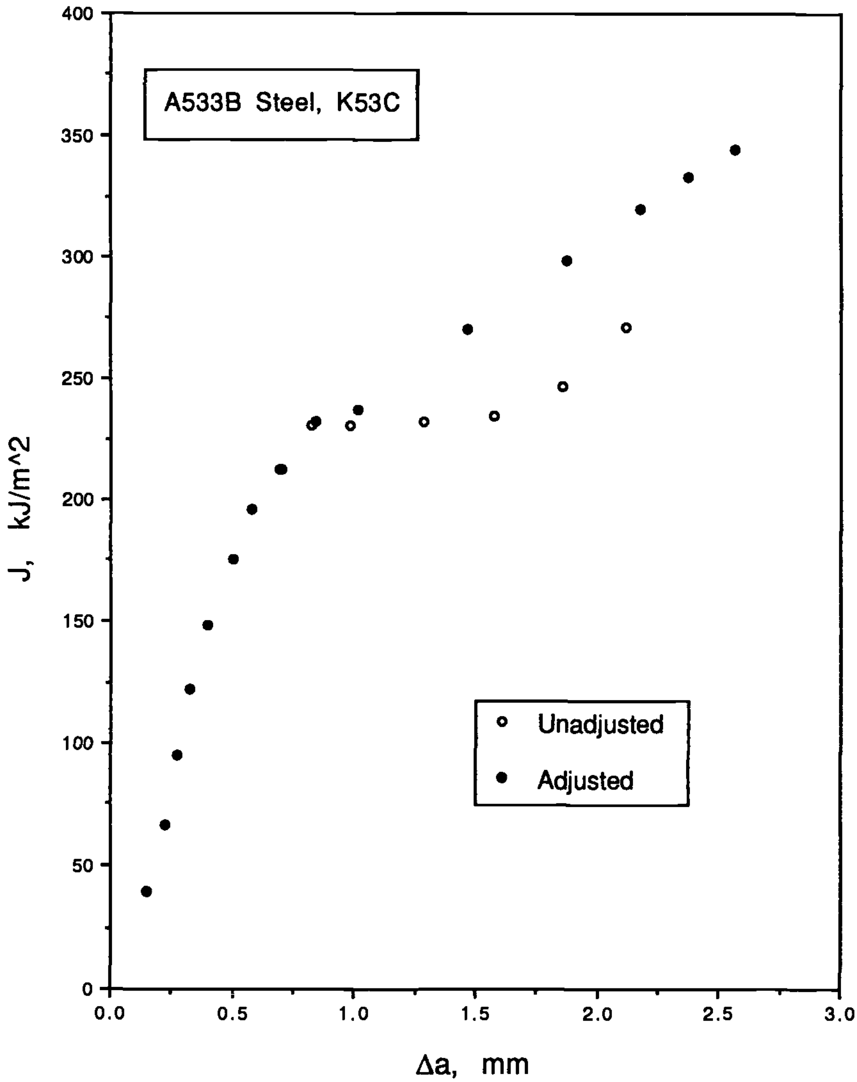

FIG. 30—J-R *curve for A533-B steel, K53C, with no displacement measurement comparing adjusted versus unadjusted.*

[3] Herrera, R. and Landes, J. D., "A Direct *J-R* Curve Analysis of Fracture Toughness Tests," *Journal of Testing and Evaluation*, Vol. 16, No. 5, Sept. 1988, pp. 427–449.

[4] Herrera, R. and Landes, J. D., "Direct *J-R* Curve Analysis: A Guide to the Methodology," *Fracture Mechanics: Twenty-First Symposium, ASTM STP 1074*, J. P. Gudas, J. A. Joyce, and E. M. Hackett, Eds., American Society for Testing and Materials, Philadelphia, 1990, pp. 24–43.

[5] Landes, J. D., Zhou, Z., Lee, K., and Herrera, R., "The Normalization Method to Develop *J-R* Curves with the LMN Function," *Journal of Testing and Evaluation*, Vol. 19, No. 4, July 1991, pp. 305–311.

[6] Ernst, H. A., Paris, P. C., and Landes, J. D., "Estimations on *J*-Integral and Tearing Modulus *T* From a Single Specimen Test Record," *Fracture Mechanics (13th Conference), ASTM STP 743,*

Richard Roberts, Eds., American Society for Testing and Materials, Philadelphia, 1981, pp. 476–502.

[7] Ernst, H. A., Paris, P. C., Rossow, M., and Hutchinson, J. W., "Analysis of Load Displacement Relationship to Determine *J-R* Curve and Tearing Instability Material Properties," *Fracture Mechanics (Eleventh Conference), ASTM STP 677*, C. W. Smith, Ed., American Society for Testing and Materials, Philadelphia, 1979, pp. 581–599.

[8] Sharobeam, M. H. and Landes, J. D., "The Separation Criterion and Methodology in Ductile Fracture Mechanics," *International Journal of Fracture*, Vol. 47, 1991, pp. 81–104.

[9] Sharobeam, M. H. and Landes, J. D., "Eta Factors in Elastic-Plastic Fracture Testing," *Elastic-Plastic Fracture Test Methods: The User's Experience (Second Volume), ASTM STP 1114*, J. A. Joyce, Ed., American Society for Testing and Materials, Philadelphia, 1991, pp. 114–132.

[10] Sharobeam, M. H. and Landes, J. D., "The Load Separation and η_{pl} Development in Precracked Specimen Test Records," *International Journal of Fracture*, Vol. 59, 1993, pp. 213–226.

[11] Joyce, J. A., Ernst, H. A., and Paris, P. C., "Direct Evaluation of *J*-Resistance Curves from Load Displacement Records," *Fracture Mechanics (Twelfth Conference), ASTM STP 700*, American Society for Testing and Materials, Philadelphia, 1980, pp. 222–236.

[12] Kumar, V., German, M. D., and Shih, C. F., "An Engineering Approach for Elastic-Plastic Fracture Analysis," NP 1931, EPRI Project 1237-1, Electric Power Research Institute, Palo Alto, CA, July 1981.

[13] Orange, T. W., "Methods and Models for *R*-Curve Instability Calculations," *Fracture Mechanics: Twenty-First Symposium, ASTM STP 1074*, J. P. Gudas, J. A. Joyce, and E. M. Hackett, Eds., American Society for Testing and Materials, Philadelphia, 1990, pp. 545–559.

[14] Zhou, Z., Lee, K., Herrera, R., and Landes, J. D., "Normalization: An Experimental Method for Developing *J-R* Curves," *Elastic Plastic Fracture Test Methods: The User's Experience (Second Volume), ASTM STP 1114*, J. A. Joyce, Ed., American Society for Testing and Materials, Philadelphia, 1991, pp. 42–56.

[15] Joyce, J. A., Davis, D. A., Hackett, E. M., and Hayes, R. A., "Application of the J-Integral and the Modified J-Integral to Cases of Large Crack Extension," NUREG CR-5143, Nuclear Regulatory Commission, Feb. 1989.

[16] Landes, J. D., McCabe, D. E., and Ernst, H. A., "Fracture Testing of Ductile Steels," NP 5014, Final Report of Research Project 1238-2, Electric Power Research Institute, Palo Alto, CA, Jan. 1987.

[17] Link, R. E., Landes, J. D., and Herrera, R., "Elastic-Plastic Handbook Solutions: Experimental Evaluations and User Guide," *Defect Assessment in Components—Fundamentals and Applications*, J. G. Blauel and K.-H. Schwalbe, Eds., Mechanical Engineering Publications Limited, London, 1991, pp. 985–1003.

Ruben Herrera,[1] Gabriel Carcagno,[1] and Luis A. de Vedia[2]

Evaluation of Dynamic Fracture Toughness Using the Normalization Method

REFERENCE: Herrera, R., Carcagno, G., and de Vedia, L. A., "**Evaluation of Dynamic Fracture Toughness Using the Normalization Method,**" *Fracture Mechanics: Twenty-Third Symposium, ASTM STP 1189,* Ravinder Chona, Ed., American Society for Testing and Materials, Philadelphia, 1993, pp. 168–184.

ABSTRACT: This paper presents a simple technique to determine dynamic *J-R* curves from a single, precracked Charpy-type specimen by means of an instrumented Charpy testing machine. This technique is based on the normalization method proposed originally by Landes and Herrera. This method eliminates the need for crack length monitoring that makes it particularly suitable under dynamic loading conditions.

The method used to generate *J-R* curves consisted of conducting precracked Charpy tests using a stop block. This simple device allows interruption of the test before the specimen is completely broken, furnishing the two calibration points necessary for applying the normalization method. *J-R* curves obtained with the normalization method were compared with values calculated following the multiple specimen technique.

KEY WORDS: dynamic fracture testing, *J-R* curves, normalization method, eta factor, instrumented Charpy test, fracture mechanics, fatigue (materials)

In the late 1960s, Rice [*1,2*] proposed the *J*-integral as a new parameter that characterized crack-tip singularity in elastic-plastic fracture behavior of metals. Since then, great effort has been directed towards the development of successful experimental procedures to evaluate *J*. The first approach was done by Landes and Begley [*3,4*], based on the energy rate interpretation of *J*. Despite the reliability and theoretical basis of this technique, it was not very successful because of the rising cost and time required for specimen preparation and testing. A new technique that required the testing of only one specimen was then proposed and widely accepted. It was based on the assumption that the load could be represented as the product of two separate functions; a crack geometry dependent function and a material deformation function (principle of normalization). This separable form, which was first proposed by Rice et al. [*5*], brought a new definition of *J* as a factor, defined later as η, times the area under the load-displacement record per unit of uncracked ligament area. Hence, *J* can be evaluated by testing one specimen, if this factor is known for the specimen configuration.

Recently, Sharobeam and Landes [*6,7*] studied the load displacement records of previously tested specimens of different geometries, materials, and constraints. They demonstrated the load separation in the plastic region under quasi-static loading conditions. In the present paper, the validity of the principle of normalization under impact loading conditions is analyzed and a value for η is reported for Charpy-type specimens. Consideration was first given

[1] Senior research officer and research officer, respectively, Center for Industrial Research, FUDETEC—Dr. Simini S/N, 2804 Campana, Argentina.

[2] Executive director, Fundacion Latinoamericana de Soldadura, 1672 V.Lynch, Buenos Aires, Argentina.

to the applicability of the J-integral parameter under dynamic loading conditions, since it makes no provision for the kinetic energy contribution. According to Refs *8* and *9*, if time to fracture exceeds a certain value, T (transition time), the kinetic energy component is much smaller than the deformation energy component, thus making the J-integral concept applicable. Transition time depends on the speed of sound in the material and on the specimen configuration. For Charpy-type specimens, the calculated value of T was about 30 μs, which is much smaller than typical maximum load times that were about 500 μs. The value obtained for the transition time in Charpy-type specimens was similar to the effective specimen oscillation period introduced by Ireland [*10*] that concerns the transition from a response dominated by individual stress waves to a response dominated by the fundamental structural mode. For low toughness materials, the time to fracture during Charpy testing can be significantly lower than 500 μs, thus precluding the application of J as a fracture characterizing parameters under dynamic loading conditions. Finally, dynamic J-R curves are obtained from precracked Charpy impact tests using the normalization method suggested by Landes and Herrera [*11–13*].

Principle of Normalization and η Calculation

Sharobeam and Landes [*6*] have introduced a new method to evaluate η_{pl} from experimental data using the normalization principle. This principle states that the load can be expressed as the product of two separate functions; functions of the crack length and plastic displacement, respectively

$$P = G(a/W)H(v_{pl}/W) \tag{1}$$

where

P = applied load,
a = crack length,
v_{pl} = plastic component of displacement, and
W = specimen width.

If the load is separable, the ratio, $S_{ij} = P(a_i)/P(a_j)$, corresponding to two identical specimens with different stationary crack lengths, a_i and a_j, respectively, must remain constant when the loads are determined for the same amount of plastic displacement. Figure 1 illustrates this principle for two test records of different stationary crack length. Mathematically, this principle can be explained as

$$\begin{aligned} S_{ij} &= \left.\frac{P(a_i)}{P(a_j)}\right|_{v_{pl}} = \left.\frac{G(a_i/W)H(v_{pl}/W)}{G(a_j/W)H(v_{pl}/W)}\right|_{v_{pl}} \\ &= \frac{G(a_i/W)}{G(a_j/W)} \\ &= \text{constant} \end{aligned} \tag{2}$$

for stationary cracks.

As mentioned before, this principle has been found to hold for a wide range of materials, configurations, and constraints under quasi-static loading conditions. As an example, Figs. 2 and 3, respectively, show the test record and the separation parameters for blunt notched HY 130 steel CT specimens [*14*].

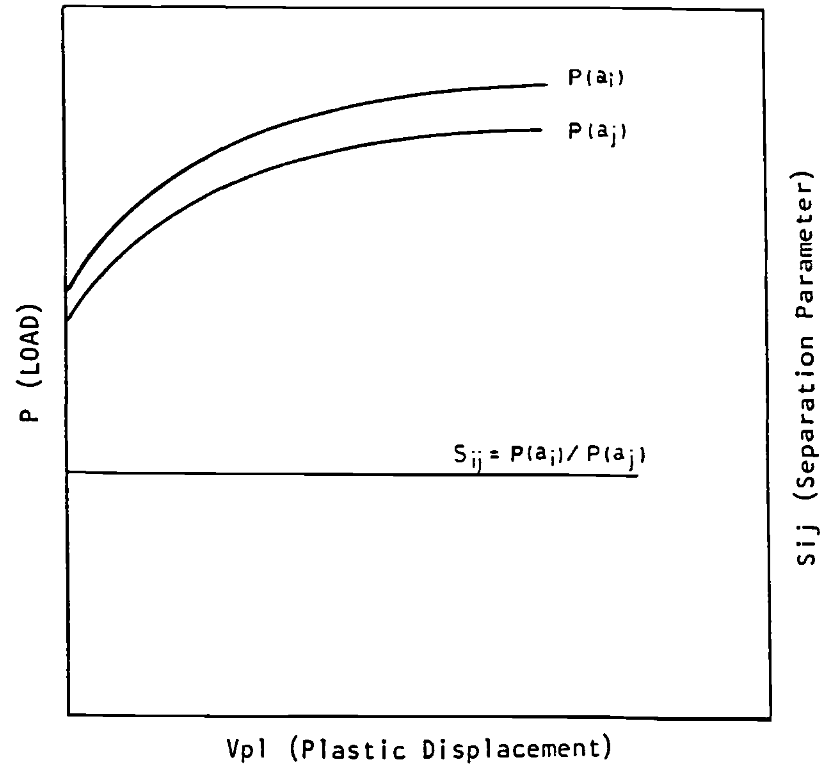

FIG. 1—*Load separability in the plastic region.*

In order to analyze the existence of load separability under impact loading conditions, blunt-notched Charpy-type specimens were tested in an instrumented Charpy impact testing system. Figure 4 shows typical specimen dimensions. Tables 1 and 2 present the chemical composition and mechanical properties of the low alloy steel tested. The specimens were tested at an impact speed of 1.7 m/s at room temperature. Load-versus-time records were obtained and translated into load-versus-displacement records using dynamic and kinematic considerations described in Ref *15*.

In order to obtain the plastic component of the displacement, a compliance expression was evaluated directly from experimental data. Figure 5 compares the calculated values with those reported by Kobayashi et al. [*16*]. The experimental values were closely fit by

TABLE 1—*Chemical composition of low alloy steel tested (% by weight).*

C = 0.21	Si = 0.30	Mn = 1.33
P = 0.008	S = 0.007	Cr = 0.13
Mo = 0.54	Ni = 0.76	Al = 0.025
Cu = 0.08	V = 0.01	Sn = 0.006
Co = 0.13		

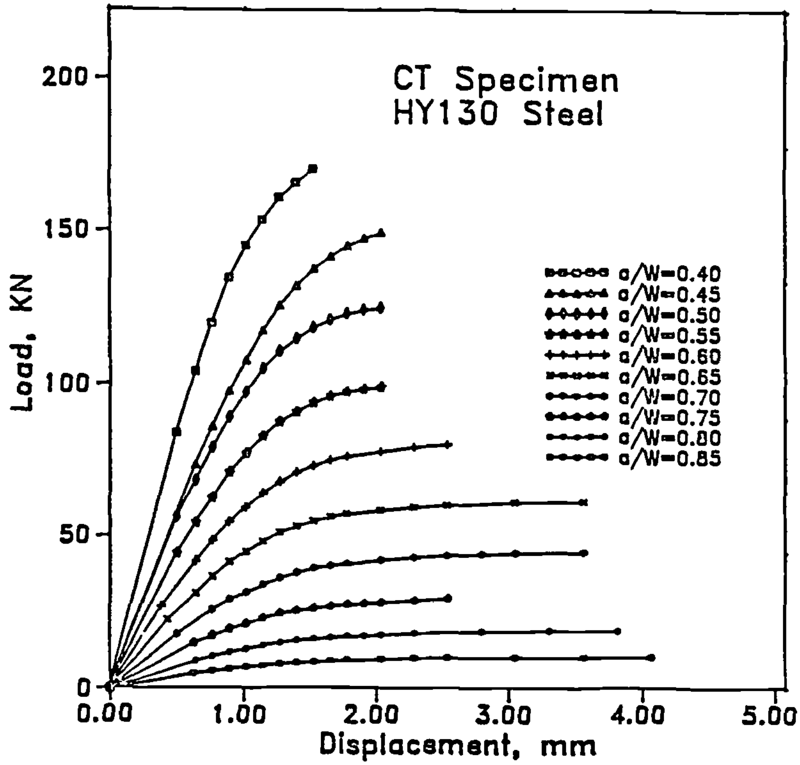

FIG. 2—*Test records of blunt-notched CT specimens* [14].

$$C_sEB = 32.35 - 159.2(a/W) + 479.05(a/W)^2 \tag{3}$$

where

C_s = specimen compliance,
B = specimen thickness, and
E = Young's modulus.

The use of this expression yields slightly higher compliance values than those obtained by Kobayashi.

Figure 6 shows the test records corresponding to blunt-notched specimens, and Fig. 7 presents the corresponding separation parameters. As can be seen, load separability exists except

TABLE 2—*Mechanical properties.*

Yield Stress, MPa	Ultimate Tensile Strength, MPa	Reduction of Area, %
450	640	45

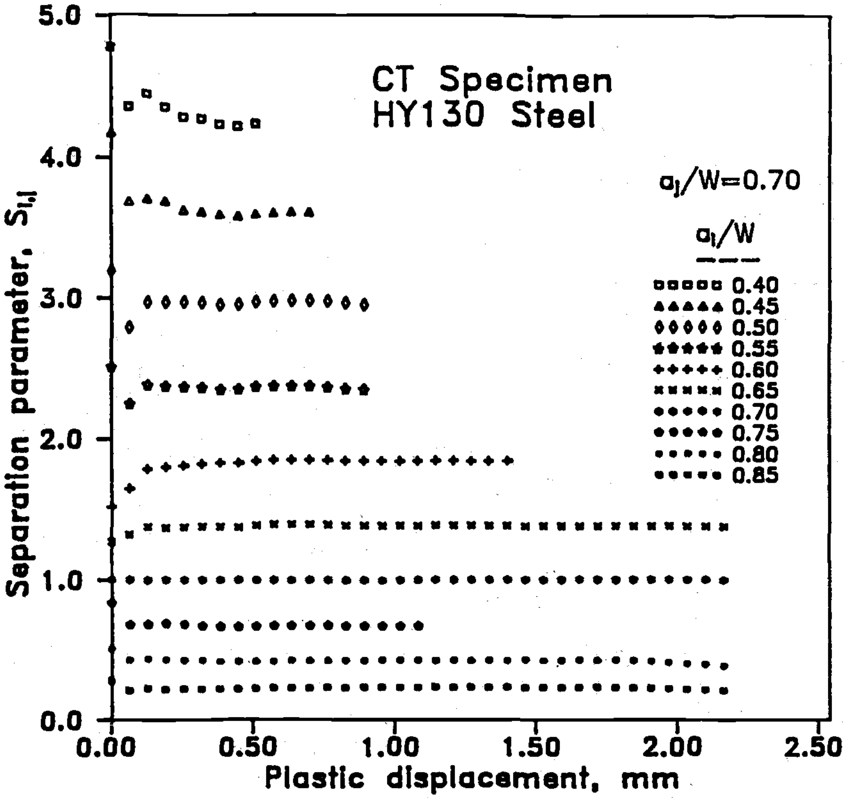

FIG. 3—*Separation parameter of blunt-notched CT specimens* [14].

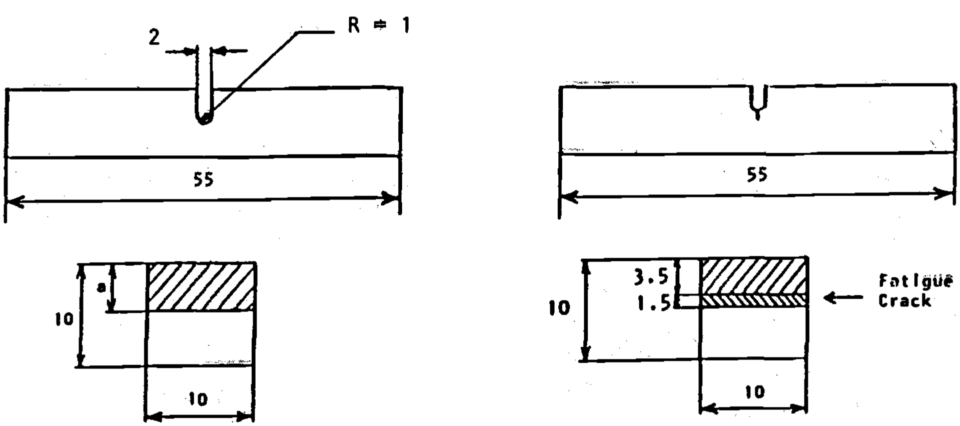

FIG. 4—*Specimen geometry and dimensions (in millimetres):* (left) *blunt-notched specimen and* (right) *fatigue-precracked specimen.*

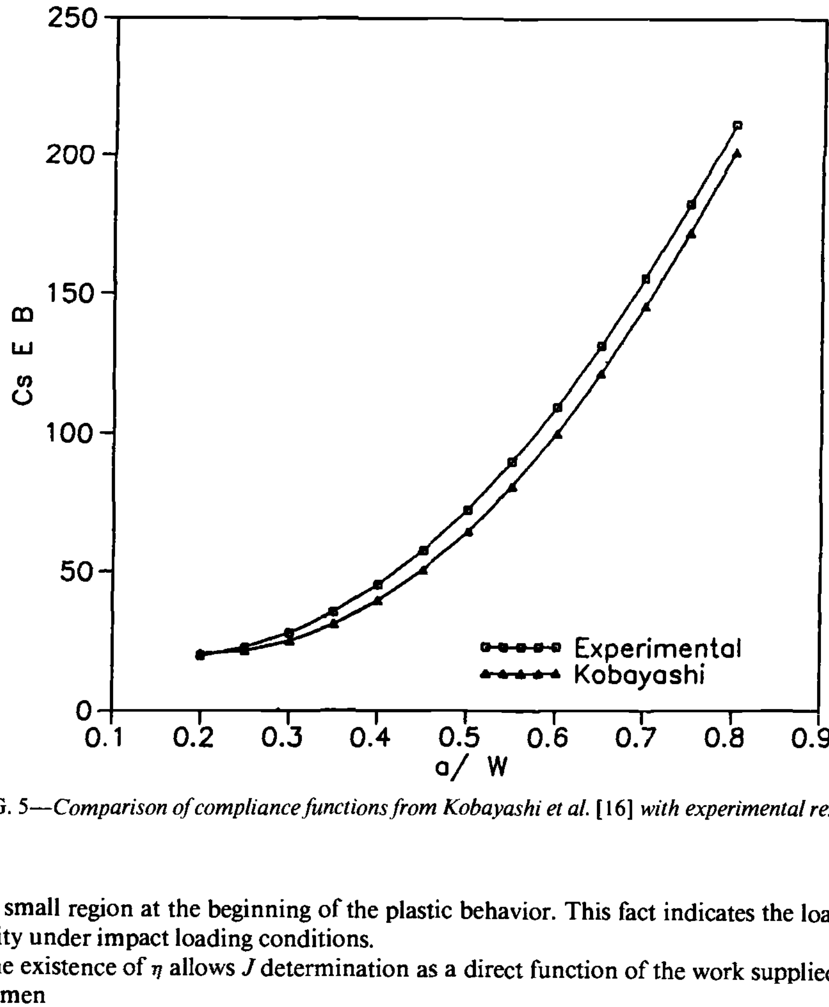

FIG. 5—*Comparison of compliance functions from Kobayashi et al.* [16] *with experimental results.*

for a small region at the beginning of the plastic behavior. This fact indicates the load separability under impact loading conditions.

The existence of η allows J determination as a direct function of the work supplied to the specimen

$$J = \frac{\eta}{bB} \int P\, dv \tag{4}$$

where $b = W - a$.

Combining this expression with the energy rate expression

$$J = -\frac{1}{B}\frac{dU}{da} \tag{5}$$

provides an expression for

$$\eta = b(-dU/da)/\left(\int P\, dv\right) \tag{6}$$

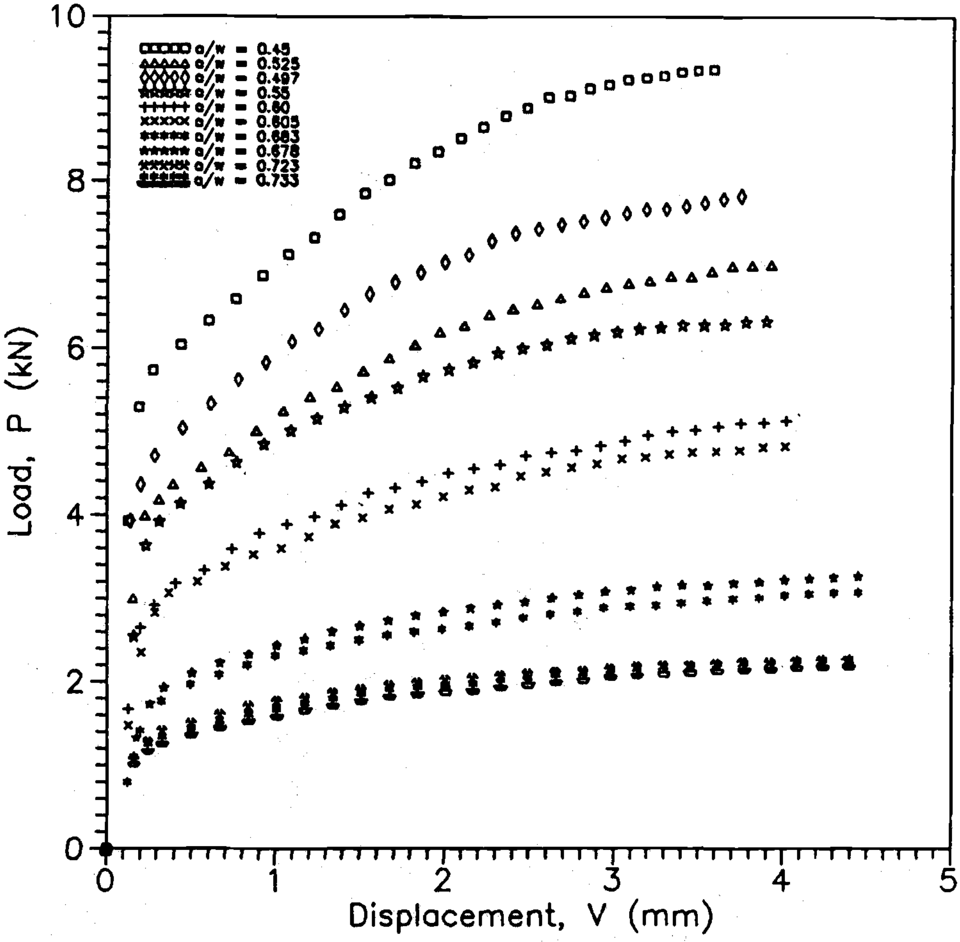

FIG. 6—*Blunt-notched specimens test records.*

In the case of η_{pl} evaluation instead of η, only the plastic area under the test records has to be included and v must be replaced by v_{pl}. Substituting Eq 1 into Eq 6 results in

$$\eta_{pl} = -\frac{G'(a/W)}{G(a/W)}(b/W) \tag{7}$$

where

$$G'(a/W) = \frac{dG(a/W)}{d(a/W)} = -\frac{dG(b/W)}{d(b/W)} \tag{8}$$

The method of calculating η proposed by Sharobeam and Landes [6] is based on the proportional relationship that exists between the separation parameter, S_{ij}, and the geometry dependent function, $G(a_i/W)$

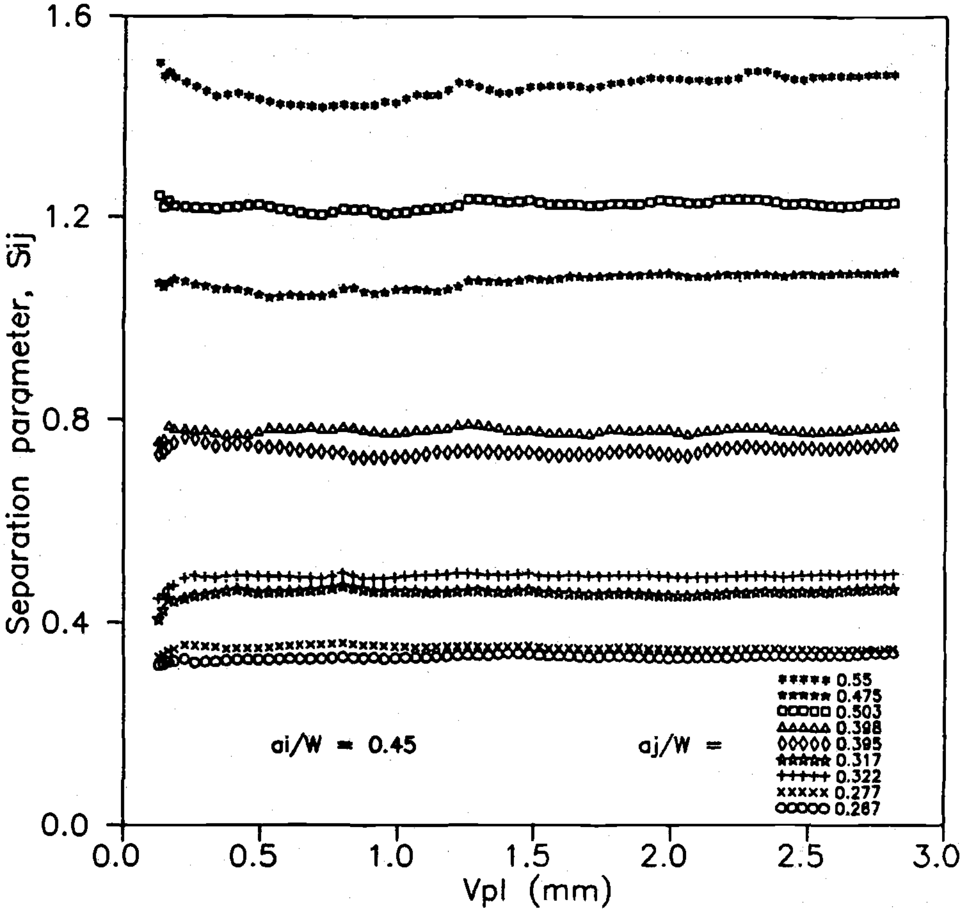

$$S_{ij} = A \cdot G(a_i/W) \tag{9}$$

where A is a constant.

This expression indicates that constructing the S_{ij} versus b_i/W fit will establish the relationship $G(b_i/W)$ versus b_i/W eventually. Then η_{pl} can be evaluated using Eq 7. Sharobeam and Landes demonstrated that under quasi-static loading conditions S_{ij}–b_i/W pairs were adequately fitted by a power law. Therefore, the geometry function becomes a power law function and can be represented as

$$G(b/W) = C(b/W)^m \tag{10}$$

where C is a constant.

Hence, Eq 7 yields

$$\eta_{pl} = m \tag{11}$$

Figure 8 shows a power law fit on S_{ij}–b_i/W pairs obtained from impact tests. As can be seen, the power law closely represents the experimental points. The value of η_{pl} was found to be 2.08, close to the theoretical value for a deep crack in bending.

J Calculation

The method of normalization was proposed as a technique to develop *J-R* curves from test specimen load-versus-displacement records without the need for automatic crack-length monitoring equipment [*11,12*]. It was based on the key curve approach [*17*], but rather than using a universal key curve for a given material, the method develops individual normalized calibration curves for each specimen based on some details of the test itself.

When the load, as written in Eq 1, is divided by the crack length function, a normalized load, P_N, is defined that is a function only of the plastic displacement

$$P_N = \frac{P}{G(a/W)} = H(v_{pl}/W) \tag{12}$$

In the method of normalization, the $H(v_{pl}/W)$ function is assumed to have a form with unknown constants that can be determined if enough calibration points are available where

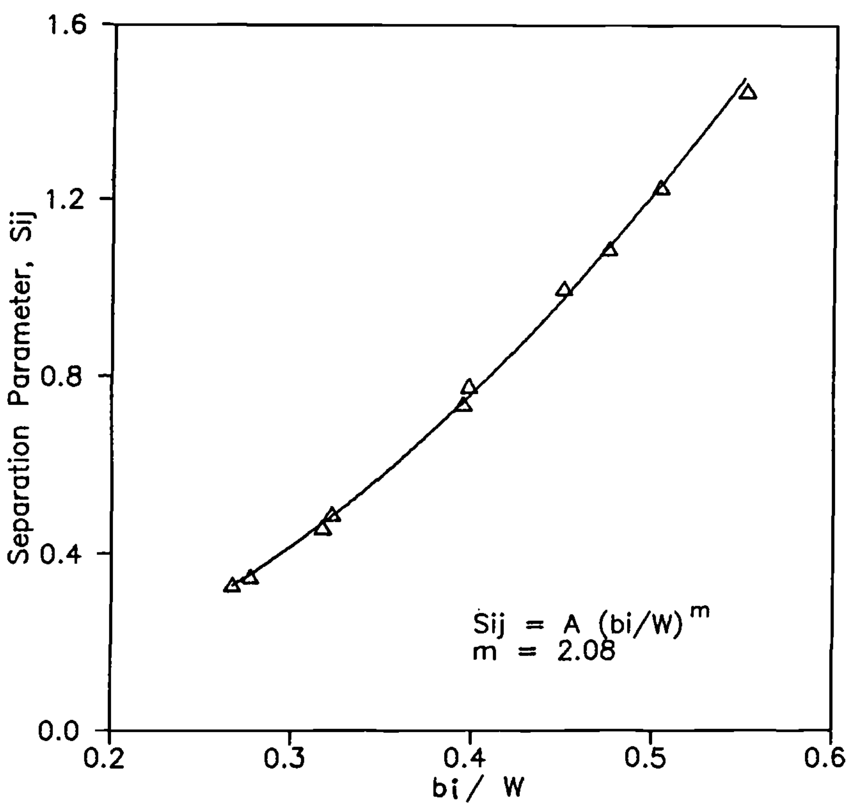

FIG. 8—*Separation parameters versus* b_i/W.

load, displacement, and crack length are known simultaneously. Therefore, a value of crack length, a, can be equated directly for each $P - v_{pl}$ pair from Eq 12. Under quasi-static loading conditions, two points, one corresponding to an initial crack length and the other to a final crack length, can be determined easily. Unfortunately, during conventional impact testing the specimen is broken completely, leaving only one calibration point. In order to study the evolution of plastic deformation and crack growth during the test, several specimens were tested up to different displacement levels. The striker was stopped using an adjustable block, Fig. 9. Figure 10 shows examples of typical load displacement records.

The next step in using the normalization method is to define a functional form for $H(v_{pl}/W)$. The power law is an example where two constants are used. However, Sharobeam et al. [14] showed that materials that experience extensive plastic deformation do not follow a power law throughout the entire load-versus-displacement history.

Knowing that normalized blunt-notch and precrack records will be represented by the same $H(v_{pl}/W)$, the different fits were tried on normalized blunt-notched test records. Figure 11 shows a power law fit on a typical blunt-notch test record. As can be seen, the fit follows closely

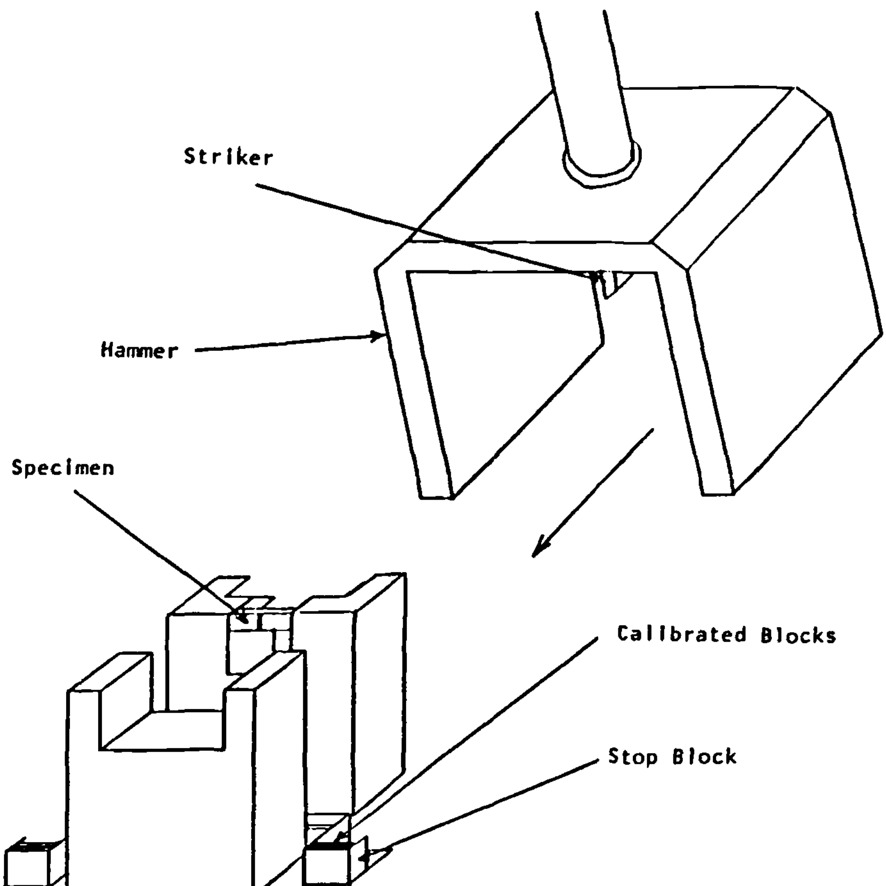

FIG. 9—*Stop block device.*

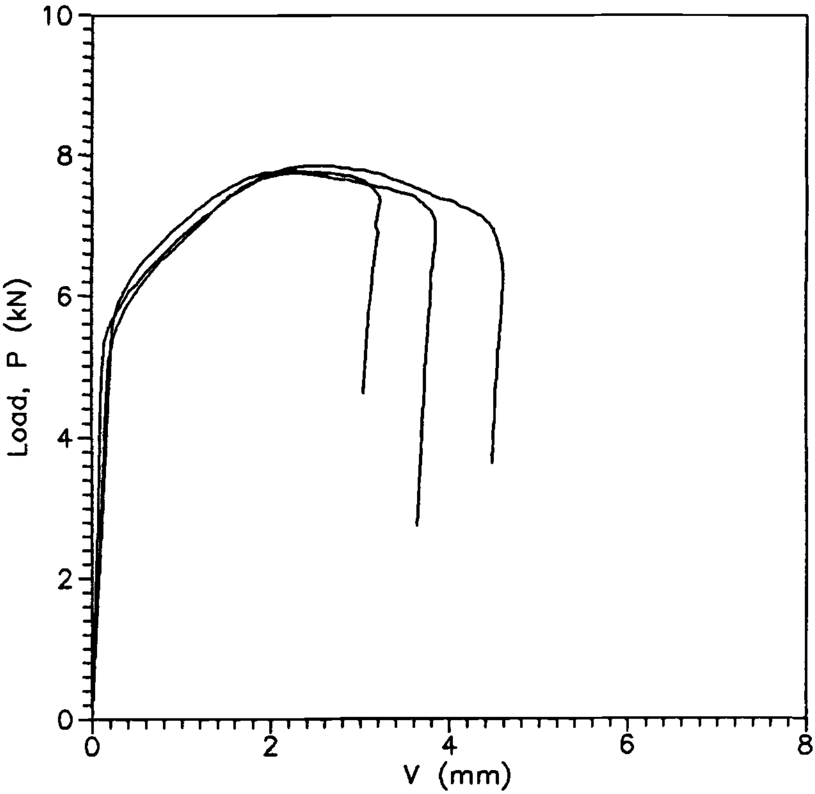

FIG. 10—*Typical load-displacement curves from stop-block tests.*

the experimental values. For this reason, in a first approach, the following P_N–v_{pl}/W relationship was adopted

$$v_{pl}/W = \beta P_N^m \tag{13}$$

Figure 12 shows P_N versus v_{pl}/W curves obtained from the normalization method for the stop-block tests. They collapse into a unique scatterband indicating a good crack length estimation.

Knowing the values of a, P, and v during the test, direct determination of the J-R curve becomes possible. J-values were calculated, according to ASTM Test Method for Determining J-R Curves (E 1152-87), as

$$J_{(i)} = J_{el(i)} + J_{pl(i)} \tag{14}$$

where (assuming plain-strain conditions)

$J_{el(i)} = K_{(i)}^2/E'$,
E' = effective Young's modulus = $E/(1 - \nu^2)$, and
ν = Poisson's ratio and

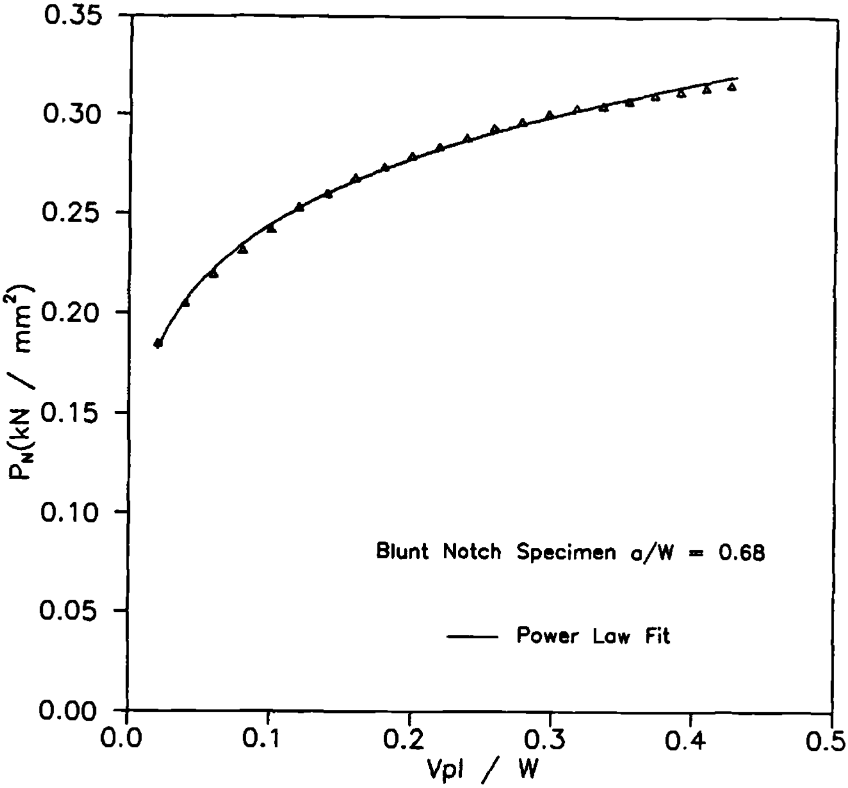

FIG. 11—*Power law fit on normalized blunt-notch test records.*

$$J_{pl(i)} = \left\{ J_{pl(i-1)} + \left(\frac{\eta_i}{b_i}\right) \frac{A_{pl(i)} - A_{pl(i-1)}}{B_N} \right\} \times \left\{ 1 - \gamma_i \frac{(a_i - a_{i-1})}{b_i} \right\}$$

where

$\eta_i = \eta = 2.0$,
$\gamma_i = \gamma = 1.0$, and
$A_{pl(i)} = A_{pl(i-1)} + (P_i + P_{i-1})(v_{pl(i)} - v_{pl(i-1)})/2$.

Figure 13 shows the *J-R* curves corresponding to stop-blocked specimens obtained with the normalization method. Solid symbols correspond to the last point of the test, where the crack length was measured directly from the fracture surface (multiple-specimen technique). There is a good agreement between solid points and predicted curves.

Figure 14 compares *J-R* curves from Fig. 13 with two other curves obtained with the normalization method when the striker was not stopped. Constants η and β were obtained directly by fitting on the initial portion of the normalized load-displacement record, Fig. 15. Values of P_N and v_{pl}/W were calculated using the value of crack length that results by equating

$$J = 2\sigma_0 \Delta a$$

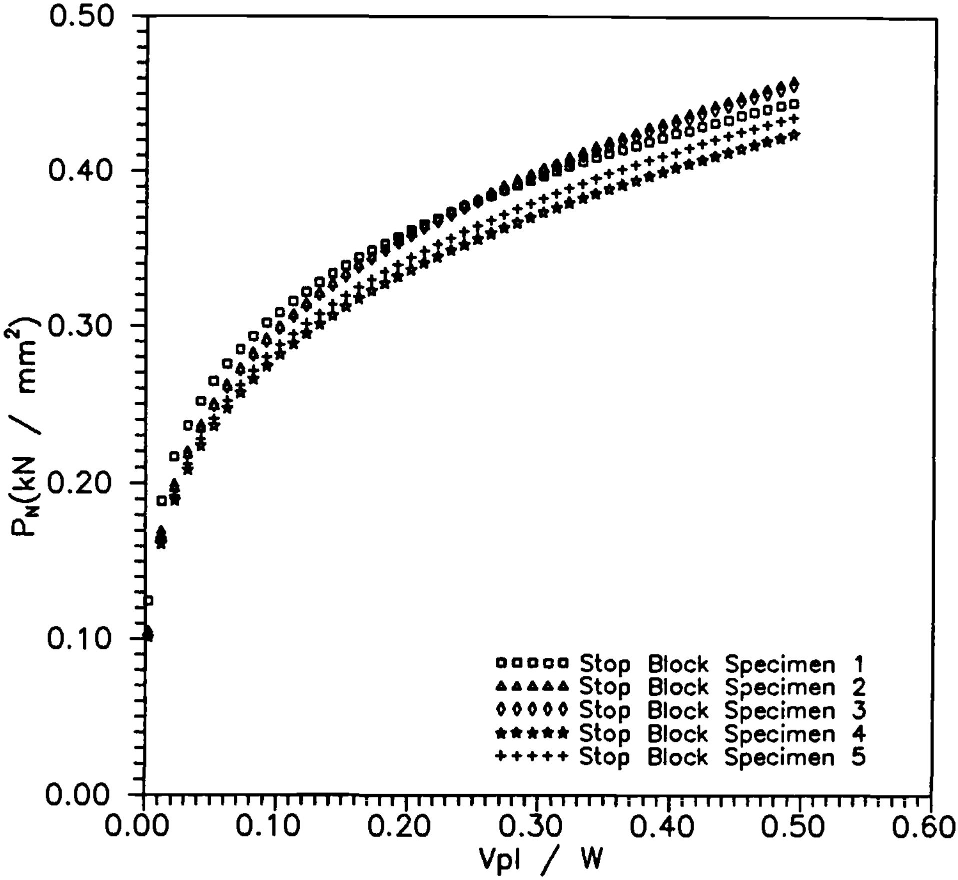

FIG. 12—*Normalized test records of precracked specimens.*

and

$$J = \frac{\eta}{Bb} \int P\, dv$$

where

σ_0 = dynamic flow stress = $(\sigma_y + \sigma_{mx})/2$,
σ_y = dynamic yield stress, and
σ_{mx} = dynamic maximum stress.

Following the procedure described in Ref *18*, σ_y and σ_{mx} were obtained for a calculated strain rate at the elastic-plastic boundary [*19*] of $10^2$1/s.

Conclusions

A simple technique was developed to determine dynamic *J-R* curves from a single precracked Charpy-type specimen for the steel used in the present work.

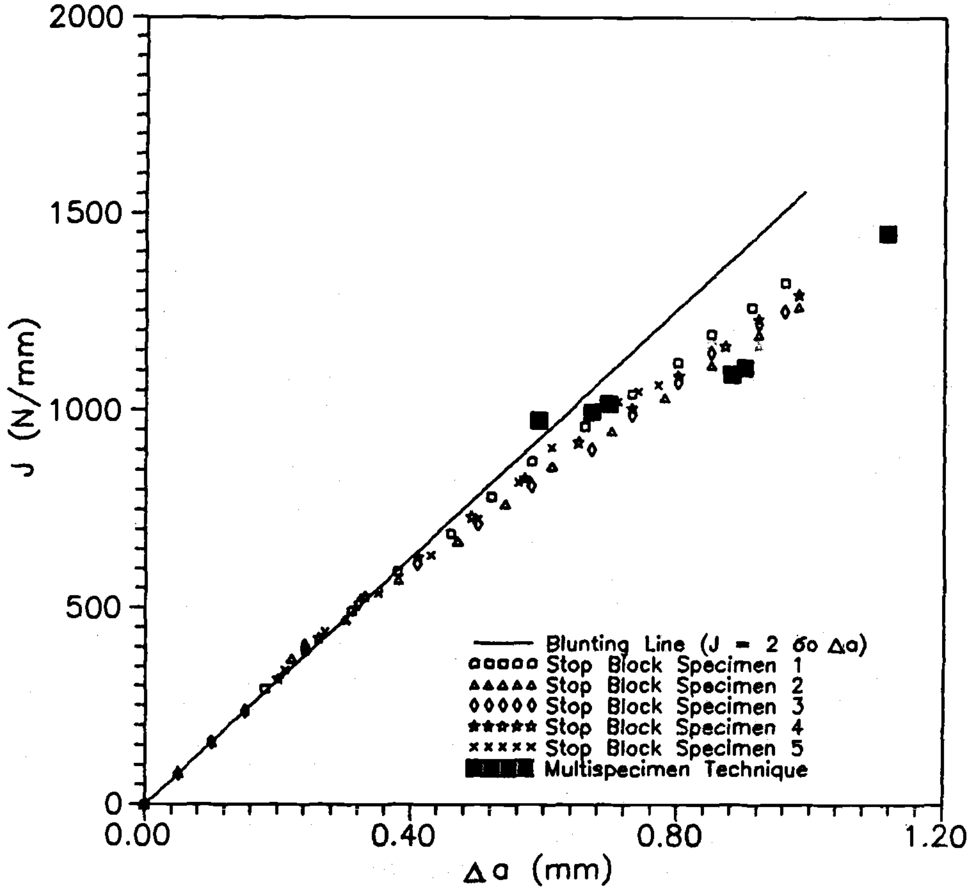

FIG. 13—J-R *curves corresponding to stop-blocked specimens.*

Load separability was demonstrated to exist under impact loading conditions. For Charpy-type specimens, a value of $\eta = 2.08$ was found. This estimation is close to the theoretical value of 2.0 for a deep crack under pure bending.

An expression approximating the elastic compliance of the Charpy-type specimens was obtained by means of blunt-notched testing. The expression found closely matches the experimental results.

J-R curves were obtained with the normalization method using precracked Charpy-type specimens and a simple mechanical device: a stop block that allows the striker to stop before the specimen is broken completely. The power law offered a good representation of $H(v_{pl}/W)$. For the material used in this work, adequate power law fittings were obtained in the initial portion of the normalized load–displacement records, as was shown for the specimens tested without interrupting the striker movement.

References

[1] Rice, J. R., "A Path Independent Integral and the Approximate Analysis of Strain Concentration by Notches and Cracks," *Journal of Applied Mechanics*, Vol. 35, 1968, pp. 379–386.

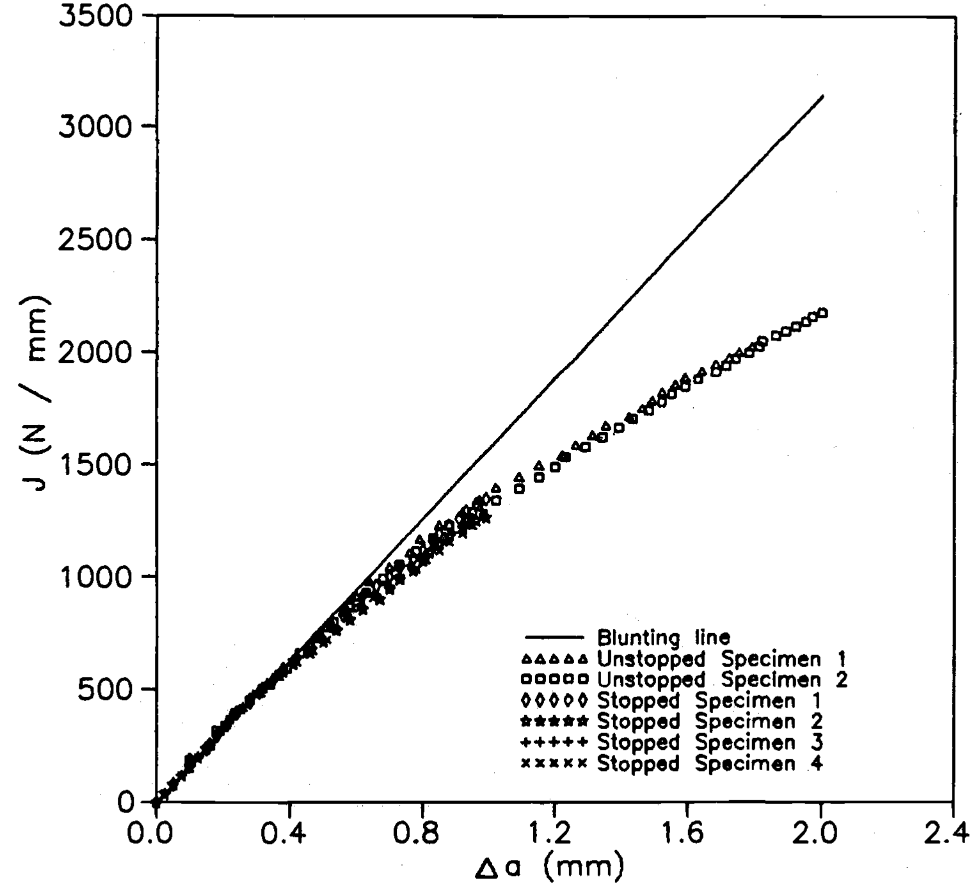

FIG. 14—*Comparison of stop-block* J-R *curves with those obtained when the striker was not stopped.*

[2] Rice, J. R., "Mathematical Analysis in the Mechanics of Fracture," *Fracture, and Advanced Treatise,* Vol. 2, H. Liebowitz, Ed., Academic Press, New York, 1968.

[3] Begley, J. A. and Landes, J. D., "The *J* Integral as a Fracture Criterion," *Fracture Toughness, ASTM STP 514,* American Society for Testing and Materials, Philadelphia, 1972, pp. 1–23.

[4] Landes, J. D. and Begley, J. A., "The Effect of Specimen Geometry on J_{Ic}," *Fracture Toughness, ASTM STP 514,* American Society for Testing and Materials, Philadelphia, 1972, pp. 24–39.

[5] Rice, J. R., Paris, P. C., and Merkle, J. G., "Some Further Results of *J*-Integral Analysis and Estimates," *Progress in Flaw Growth and Fracture Toughness Testing, ASTM STP 536.* American Society for Testing and Materials, Philadelphia, 1973, pp. 231–245.

[6] Sharobeam, M. H. and Landes, J. D., "The Separation Criterion and Methodology in Ductile Fracture Mechanics," *International Journal of Fracture,* Vol. 47, 1991, pp. 81–104.

[7] Sharobeam, M. H., "The Role of Geometry and Deformation in Ductile Fracture Methodology," Ph.D. thesis, University of Tennessee, Knoxville, 1990.

[8] Nakamura, T., Shih, C. F., and Freund, L. B., "Three-Dimensional Transient Analysis of a Dynamically Loaded Three Point Bend Ductile Fracture Specimen," *Nonlinear Fracture Mechanics, Volume 1: Time-Dependent Fracture, ASTM STP 995,* A. Saxena, J. D. Landes, and J. L. Bassani, Eds., American Society for Testing and Materials, Philadelphia, 1989, pp. 217–241.

[9] Hackett, E. M., Joyce, J. A., and Shih, C. F., "Measurement of Dynamic Fracture Toughness of Ductile Materials," *Nonlinear Fracture Mechanics, Volume 1: Time-Dependent Fracture, ASTM*

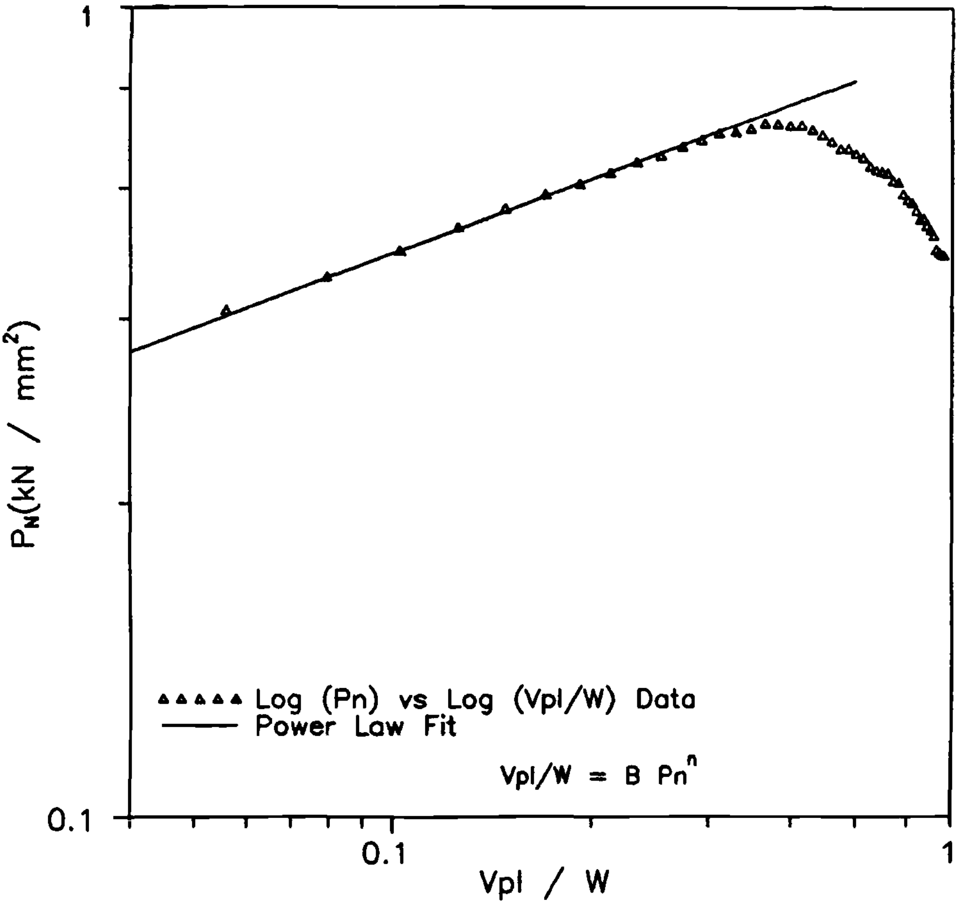

FIG. 15—*Power law fit on the initial region of the normalized load-displacement record of an unstopped specimen.*

STP 995, A. Saxena, J. D. Landes, and J. L. Bassani, Eds., American Society for Testing and Materials, Philadelphia, 1989, pp. 274–297.

[*10*] Ireland, D. R., "Procedures and Problems Associated with Reliable Control of the Instrumented Impact Test," *Instrumented Impact Testing, ASTM STP 563*, 1974, American Society for Testing and Materials, Philadelphia, pp. 3–29.

[*11*] Landes, J. D. and Herrera, R., "A New Look at J-R Curve Analysis," *International Journal of Fracture*, Vol. 36, 1988, pp. R9–R14.

[*12*] Herrera, R. and Landes, J. D., "A Direct *J-R* Curve Analysis of Fracture Toughness Tests," *Journal of Testing and Evaluation*, Vol. 16, No. 5, 1988, pp. 427–449.

[*13*] Herrera, R. and Landes, J. D., "Direct *J-R* Curve Analysis: A Guide to the Methodology," *Fracture Mechanics: Twenty-First Symposium, ASTM STP 1074*, J. P. Gudas, J. A. Joyce, and E. Hackett, Eds., American Society for Testing and Materials, Philadelphia, 1990, pp. 24–43.

[*14*] Sharobeam, M. H., Landes, J. D., and Herrera, R., "Development of Eta Factors in Elastic Plastic Fracture Testing Using a Load Separation Technique," *Elastic-Plastic Fracture Test Methods: The User's Experience (Second Volume), ASTM STP 1114*, J. A. Joyce, Ed., American Society for Testing and Materials, Philadelphia, 1989, pp. 114–132.

[*15*] Markowich, M., Rosenthal, Y., and Adam, G., "Experience with a Digitized Instrumented Impact Testing System," *Journal of Testing and Evaluation*, Vol. 15, No. 5, Sept. 1987, pp. 265–273.

[16] Kobayashi, T., "Analysis of Impact Properties of A533 Steel for Nuclear Reactor Pressure Vessel by Instrumented Charpy Test," *Engineering Fracture Mechanics*, Vol. 19, No. 1, 1984, pp. 49–65.
[17] Joyce, J. A., Ernst, H. A., and Paris, P. C., "Direct Evaluation of *J*-Resistance Curves from Load Displacement Records," *Fracture Mechanics (Twelfth Conference), ASTM STP 700*, American Society for Testing and Materials, Philadelphia, 1980, pp. 222–236.
[18] Server, W. L., "General Yielding of Charpy V-notch and Precracked Charpy Specimens," *Journal of Engineering Materials and Technology, Transactions*, ASME, Vol. 100, 1978, pp. 183–188.
[19] Barsom, J. M. and Rolfe, S. T., *Fracture and Fatigue Control in Structures*, 2nd ed., Prentice-Hall, Englewood Cliffs, NJ, 1987.

Huang Yuan[1] *and Alfred Cornec*[1]

Asymptotic Analysis of Steady-State Crack Extension of Combined Modes I and III in Elastic-Plastic Materials with Linear Hardening

REFERENCE: Yuan, H. and Cornec, A., "**Asymptotic Analysis of Steady-State Crack Extension of Combined Modes I and III in Elastic-Plastic Materials with Linear Hardening,**" *Fracture Mechanics: Twenty-Third Symposium, ASTM STP 1189,* Ravinder Chona, Ed., American Society for Testing and Materials, Philadelphia, 1993, pp. 185–207.

ABSTRACT: In this paper, asymptotic crack-tip fields of steady-state crack extension in materials with linear plastic hardening under combined in-plane (Mode I) and anti-plane shear (Mode III) loading conditions are investigated. Only the power singularity form of the in-plane and the anti-plane shear stresses is assumed, and the coupled differential equations are solved by means of the perturbation method. The governing equations of the asymptotic crack-tip field are formulated from two groups of angular functions: one for the in-plane mode and the other for the anti-plane shear mode. All stresses and deformations are of variable-separable forms of r and ϑ that represent the polar coordinates centered at the actual crack tip. Perturbation solutions of the governing equations have been carried out. The perturbation solutions predict that, regardless of the mixity of the crack-tip fields and strain-hardening, the in-plane stresses under the combined Mode I and Mode III loading conditions are generally more singular than the anti-plane shear stresses. The anti-plane shear stresses perturbed from the plane-strain Mode I field lose their singularity for small strain hardening, whereas the angular variation of stresses perturbed from the plane-stress Mode I behaves quite similarly to the pure Mode III solution. An obvious deviation between the perturbed and the unperturbed solutions can be observed under combined plane-strain and anti-plane Mode III loading conditions, but not under the plane-stress and Mode III conditions. The results imply that there exist no uniformly singular crack-tip fields under combined in-plane Mode I and anti-plane Mode III loading conditions.

KEY WORDS: asymptotic analysis, mixed-mode loading conditions, crack-tip field, plane-strain Mode I, plane-stress Mode I, anti-plane Mode III, steady-state crack extension, perturbation analysis, fracture mechanics, fatigue (materials)

Asymptotic solutions of stationary cracks of pure Mode I and pure Mode III in power-law materials in Refs *1* and *2* have provided a theoretical basis for nonlinear fracture mechanics. Compared with the asymptotic analysis of the stationary cracks under the deformation theory of plasticity [*1,2*], solutions of growing cracks is more complicated due to difficulties in the equation formulations and the inconsistency between the elastic and the plastic strain increments. Under the assumption of quasi-static crack growth and the small-strain elastic-perfect plasticity, asymptotic solutions have been found for the anti-plane mode in Ref *3*. For the plane-strain Mode I case, a complete near-tip solution for incompressible elastic-perfectly plastic solids has been generated in Ref *4*. Recently, a more general solution for a growing crack throughout the range from small-scale yielding up to general yielding has been reported in Ref *5*. However, little progress has been achieved in elastic-plastic solids with strain-hard-

[1] Research engineer and section head of Materials Mechanics, respectively. Institute of Materials Research, GKSS Research Center, W-2054 Geesthacht, Germany.

ening since the solution with the power singularity in linear hardening materials has been presented in Ref *6*. Based on this analysis, plastic reloading has been introduced in Ref *7*, similar to solutions for elastic-perfectly plastic materials, and it has been predicted that some stress components (σ_{rz} for the Mode III case and σ_{rr} for the Mode I case) become unbounded as the crack flank is approached ($\vartheta \rightarrow \pi$). These solutions of crack-tip fields for linear strain-hardening materials are expressed in the variable-separable form of r and ϑ, which are the polar coordinates centered at the crack tip. All works of asymptotic analyses of steady-state crack growth just mentioned are restricted to pure Mode I, pure Mode II, or Mode III.

Experimental results show that ductile crack extension occurs often under steady-state mixed-mode conditions. Observations in Ref *8* confirm that material points undergo failure under Mode I and Mode III conditions, especially, for thin specimens where the crack-tip field is turned from pure Mode I (normal stress failure) to combined Modes I and III (shear stress failure) immediately after crack initiation. From this observation, it is desirable to generate a study of the crack-tip field under the mixed-Mode I and III loading conditions. Recently, both asymptotic analysis [*9*] and finite element computations [*10*] for stationary crack-tip fields under combined anti-plane shear and in-plane modes for power-law hardening materials have been performed. It has been pointed out in Refs *9* and *10* that the singular behavior of the in-plane stresses differs from that of the anti-plane shear stresses, and these stresses generally cannot be expressed in a uniform variable-separable functional form of r and ϑ. The corresponding angular stress distribution can be changed from pure in-plane to anti-plane modes drastically.

To improve understanding of the crack-tip field under the combined Mode I and III loading conditions, we use for the first time the perturbation technique to analyze the steady-state crack growth in elastic-plastic materials. We are going to use the scheme proposed by Ref *7* and formulate the problem in terms of a system of first-order ordinary differential equations (ODEs) in the angular variations of all the components of the stress tensor and the velocity vector, instead of two higher-order equations in the stress functions as was done in Ref *9* for a stationary crack problem. We assume that the singularity of the in-plane stresses may differ from that of the anti-plane shear stresses. The subsequent differential equation systems are generally coupled with the coordinate, r, that cannot be solved as in Ref *7*. Following Ref *9*, the governing equations are perturbed for pure Mode I or Mode III, and numerical solutions of the perturbed equations are obtained. In this work, we will include the possibility of plastic reloading on the crack flanks of the linear-hardening J_2-flow theory problem. We will consider plane-strain Mode I and plane-stress Mode I combined with anti-plane shear mode (Mode III).

Assumptions and Governing Equations

Let x_i (i = 1,2,3) be a Cartesian coordinate system of fixed orientation traveling with the crack tip such that the x_3-axis coincides with the straight crack front and the x_1-axis is in the direction of crack advance, see Fig. 1. Also let $\mathbf{e}_i$ be the unit vector corresponding to the x_i direction. Similarly, let r and ϑ be polar coordinates corresponding to x_i (i = 1,2) and $\mathbf{e}_r$, $\mathbf{e}_\vartheta$ be the corresponding unit vectors. The crack tip moves with a velocity, $\mathbf{W} = W\mathbf{e}_1$, with respect to the stationary coordinate system, X_i. In our steady-state analysis, the crack-tip velocity is constant so that the material derivative is given by

$$(\dot{\ }) \equiv \frac{d}{d\tau} = W\left(-\cos\vartheta\,\frac{\partial}{\partial r} + \frac{\sin\vartheta}{r}\,\frac{\partial}{\partial\vartheta}\right) \tag{1}$$

where τ represents the time. Furthermore, the material derivatives of a vector, V_α, and a tensor, $A_{\alpha\beta}$ ($\alpha, \beta = r, \vartheta$), in the polar coordinates are given through

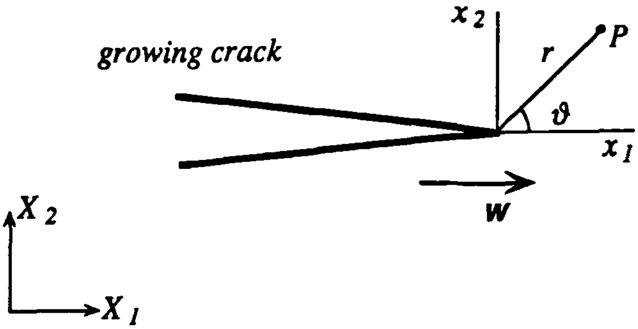

FIG. 1—*Local coordinate systems at crack tip.*

$$\dot{V}_\alpha = W\{-\cos\vartheta V_{\alpha,r} + r^{-1}\sin\vartheta(V_{\alpha,\vartheta} + V_\beta e_{\beta\alpha})\} \tag{2}$$

$$\dot{A}_{\alpha\beta} = W\{-\cos\vartheta A_{\alpha\beta,r} + r^{-1}\sin\vartheta(A_{\alpha\beta,\vartheta} + A_{\gamma\beta}e_{\gamma\alpha} + A_{\alpha\gamma}e_{\gamma\beta})\} \tag{3}$$

where $\alpha\beta$ and γ denote coordinates r, ϑ, respectively; and the two-dimensional permutation symbol is defined through $e_{\alpha\beta} = \beta - \alpha$ by assuming $r = 1$ and $\vartheta = 2$. Also, in the following context, we take the summation convention that all duplicated indices in one term mean summations of all in-plane components.

The stresses concerned in the in-plane field are σ_{rr}, $\sigma_{\vartheta\vartheta}$, $\sigma_{r\vartheta}$, and σ_{zz} (for the plane stress case, $\sigma_{zz} = 0$), and the nonzero and anti-plane shear stresses are σ_{rz} and $\sigma_{\vartheta z}$. Assume all components do not depend on the coordinate, z. The relevant deformation velocity components are $v_r(r,\vartheta)$, $v_\vartheta(r,\vartheta)$, and $v_z(r,\vartheta)$. The equilibrium equations require

$$\begin{aligned}
&(r\sigma_{rr})_{,r} + \sigma_{r\vartheta,\vartheta} - \sigma_{\vartheta\vartheta} = 0\\
&(r\sigma_{r\vartheta})_{,r} + \sigma_{\vartheta\vartheta,\vartheta} + \sigma_{r\vartheta} = 0\\
&(r\sigma_{rz})_{,r} + \sigma_{\vartheta z,\vartheta} = 0
\end{aligned} \tag{4}$$

The constitutive equation in the plastic loading zone, taking into account strain-hardening characterized by the J_2 flow theory and a bilinear effective stress-strain curve, is

$$E\dot{\varepsilon}_{ij} = (1 + \nu)\dot{\sigma}_{ij} - \nu\dot{\sigma}_{kk}\,\delta_{ij} + \tfrac{3}{2}(\underline{\alpha}^{-1} - 1)\sigma_e^{-1}\dot{\sigma}_e s_{ij} \tag{5}$$

where $\dot{\varepsilon}_{ij}$ is the strain-rate tensor, $\dot{\sigma}_{ij}$ is the stress-rate tensor, δ_{ij} is the Kronecker δ-symbol, s_{ij} is the stress deviator, ν is the Poisson's ratio, and $\underline{\alpha}$ is either α or unity, depending on whether the given material point is in an active plastic zone or in an elastic unloading zone. Here, $\alpha = E_t/E$, the ratio of the tangent modulus (E_t) to the elastic modulus (E), is the hardening parameter. The effective stress is defined as

$$\sigma_e^2 = \tfrac{1}{2}[(\sigma_{rr} - \sigma_{\vartheta\vartheta})^2 + (\sigma_{\vartheta\vartheta} - \sigma_{zz})^2 + (\sigma_{zz} - \sigma_{rr})^2] + 3(\sigma_{r\vartheta}^2 + \sigma_{rz}^2 + \sigma_{\vartheta z}^2) \tag{6}$$

where for the plane-stress case, $\sigma_{zz} = 0$. It can be seen that Eqs 4 and 5 form two systems with nine first-order partial differential equations (PDEs) under the plane-strain conditions, or eight PDEs under the plane stress conditions, in which the first system has three equations (two stresses and one velocity) deduced from anti-plane shear mode and the second has six equations for the plane strain cases (four for stresses and two for velocities) or five for plane-stress cases from the in-plane mode. The two systems of PDEs are coupled through the plastic dissipation terms, that is, only for the elastic case, the anti-plane shear and the in-plane fields can be solved separately. On the other hand, although some of the equations are nonlinear (namely, the constitutive equation), all equations are homogeneous in the radial measure, r, which suggests that we may look for solutions of the form

$$\left.\begin{aligned} v_z &= HW\sigma_0 \underline{r}^t z_1(\vartheta)/E \\ \sigma_{rz} &= H\sigma_0 \underline{r}^t z_2(\vartheta) \\ \sigma_{\vartheta z} &= H\sigma_0 \underline{r}^t z_3(\vartheta) \end{aligned}\right\} \text{for anti-plane shear mode} \tag{7}$$

$$\left.\begin{aligned} v_r &= KW\sigma_0 \underline{r}^s y_1(\vartheta)/E \\ v_\vartheta &= KW\sigma_0 \underline{r}^s y_2(\vartheta)/E \\ \sigma_{rr} &= K\sigma_0 \underline{r}^s y_3(\vartheta) \\ \sigma_{\vartheta\vartheta} &= K\sigma_0 \underline{r}^s y_4(\vartheta) \\ \sigma_{r\vartheta} &= K\sigma_0 \underline{r}^s y_5(\vartheta) \\ \sigma_{zz} &= K\sigma_0 \underline{r}^s y_6(\vartheta) \end{aligned}\right\} \text{for in-plane modes} \tag{8}$$

where $\underline{r}$ is nondimensionalized with respect to some measure of the plastic zone size. H and K are two stress amplitude factors for the anti-plane shear and the in-plane stresses, respectively. The eigenvalues of the homogeneous equations, s and t, characterize the singularities of the in-plane and the anti-plane shear crack-tip field.

Based on the observations of the stationary crack-tip fields in Refs *9* and *10*, we assume that the anti-plane shear and the in-plane stresses have different singularities. As indicated in Refs *9* and *10*, under the combined anti-plane shear and in-plane loading conditions, the singular behavior of the in-plane stresses is different from that of the anti-plane shear stresses. Actually, if we supposed $t = s$, we did not find a solution for $\alpha < 1$ in our numerical investigations with multiple shooting techniques [*11*]. Only for the perfectly elastic case ($\alpha = 1$) did the governing equations become uncoupled and the pure mode elastic solutions were found. Consequently, when we seek solutions of the singular crack-tip fields in the form of Eqs 7 and 8 under the combined anti-plane shear and in-plane loading conditions, the values of s and t are assumed to be different. Since we are seeking singular solutions in the immediate vicinity of the actual crack tip, we are interested in the solutions with both s and t being in the interval $(-0.5, 0)$. As r approaches 0, in-plane mode will dominate for $s < t$, whereas anti-plane shear mode will dominate for $t < s$. On the other side, the dominance of the crack-tip can be influenced strongly by either of the stress amplitude factors K and H.

As mentioned earlier, the coupling of the anti-plane shear and in-plane plastic deformation velocity is caused by the effective stress, σ_e, in the constitutive Eq 5. Substituting Eqs 7 and 8 into Eq 6, the effective stress is then expressed as

$$\sigma_e^2 = (K\sigma_0 \underline{r}^s)^2 T_i + (H\sigma_0 \underline{r}^t)^2 T_o \tag{9}$$

where

$$T_i = \tfrac{1}{2}((y_3 - y_4)^2 + (y_4 - y_6)^2 + (y_6 - y_3)^2) + 3y_5^2 \tag{10}$$

$$T_o = 3z_2^2 + 3z_3^2 \tag{11}$$

Note T_i and T_o are functions of ϑ only. More importantly, since we assume that s is not equal to t, σ_e cannot be expressed as a separable function of r and ϑ, such as those stresses in Eqs 7 and 8. We can define the magnitude of the ϑ variation, T_i and T_o, to be in the order of unit. Then, K and H represent the singularity amplitude of the in-plane stresses and the anti-plane shear stresses, respectively. In the next two sections, we will perturb the two ODE sytems with the assumption of either $H/K \ll 1$ or $K/H \ll 1$, although the final ODE systems obtained are independent of the intensity factors. The higher-order system has the same form of either pure Mode I or pure Mode III, whereas the lower-order system is strongly influenced by the higher-order solution.

Boundary Conditions and the Solution of Elastic Zone

We consider a material point in the crack-tip field, P, that moves along a line, L-L, with h = "constant" during crack growth, see Fig. 2. Due to the steady-state condition, the point goes through the plastic loading zone, then the elastic unloading zone, and last to the plastic reloading zone, if it exists. This corresponds to the loading history of any material particle in the crack-tip field discussed here, since the crack grows in the homogeneous medium with the velocity, W, and the crack-tip field does not change. It is important to note that the loading history of each material point can be described through this motion and therefore is determined only by the polar angle, ϑ, since, for any given material point, h is constant. It is common in asymptotic analysis of steady-state crack growth to assume that the elastic unloading and the plastic reloading angles are constant and are determined by the given material parameters and the loading configuration. The crack-tip field consists of angular sectors. Actually, this is a direct consequence of the general solution form assumed in Eqs 7 and 8. The elastic unloading occurs at ϑ_p when the effective stress-rate of the material point vanishes, or when

$$\left(-sT_i(\vartheta_p)\cos\vartheta_p + \frac{1}{2}T_i'(\vartheta_p)\sin\vartheta_p\right) + \left(\frac{H}{K}\right)^2 r^{2(t-s)}\left(-tT_o(\vartheta_p)\cos\vartheta_p + \frac{1}{2}T_o'(\vartheta_p)\sin\vartheta_p\right) = 0 \tag{12}$$

where $(\ )' = d/d\vartheta$.

In the elastic unloading zone, a material point retains the plastic strain state that it had in the plastic loading zone. Thus, it is expected that when the point is deep into the unloading, its associated effective stress can reach another yielding stress state, especially for some materials with small strain-hardening [7]. The plastic reloading occurs at some critical value of ϑ if the effective stress of the particle regains its unloading value, that is

$$(T_i(\vartheta_e)\sin^{-2s}\vartheta_e - T_i(\vartheta_p)\sin^{-2s}\vartheta_p) + \left(\frac{H}{K}\right)^2 r^{2(t-s)}(T_o(\vartheta_e)\sin^{-2t}\vartheta_e - T_o(\vartheta_p)\sin^{-2t}\vartheta_p) = 0 \tag{13}$$

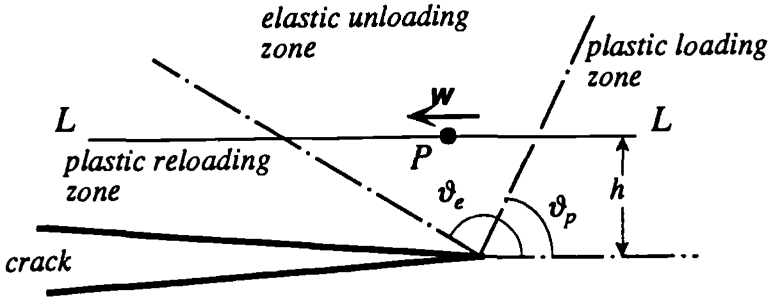

FIG. 2—*Angular sectors at the crack-tip field.*

Note that the effective stress must become singular at the crack flanks if the plastic reloading occurs, regardless of what kind of singularities will be assumed here and how the ODEs will be formulated [*12*].

Anti-plane symmetry ahead of the crack-tip for anti-plane shear mode reduces to two independent conditions

$$z_1(0) = z_2(0) = 0 \tag{14}$$

and Mode I symmetry of the in-plane mode requires

$$y_2(0) = y_5(0) = y_3'(0) = 0 \tag{15}$$

$$y_6'(0) = 0 \qquad \text{for plane-strain case} \tag{16}$$

Furthermore, we have vanishing tractions on the free crack surface and it requires

$$z_3(\pi) = 0 \tag{17}$$

$$y_4(\pi) = y_5(\pi) = 0 \tag{18}$$

Thus, we have nine homogeneous boundary conditions for the plane-strain case and eight for the plane-stress case to be satisfied by two ODE systems. As in pure Mode I or pure Mode III analysis, the strength of the singularities, s and t, will be determined as eigenvalues of the problem for each given α, and the stress amplitude factors, K and H, will be left undetermined in this asymptotic solution. Without loss of generality, we can set

$$\begin{aligned} y_4(0) &= 1 \\ z_3(0) &= 1 \end{aligned} \tag{19}$$

Next, we need to connect the solutions in the different zones through appropriate continuity conditions. Let [ ] denote the jump in a quantity as ϑ increases infinitesimally across such a boundary. Then it follows from equilibrium that the traction components of the stress tensor must be continuous

$$
\begin{aligned}
&[\sigma_{\vartheta z}] = 0 \\
&[\sigma_{r\vartheta}] = [\sigma_{\vartheta\vartheta}] = 0
\end{aligned}
\tag{20}
$$

and displacement fields must also be continuous

$$
\begin{aligned}
&[u_z] = 0 \\
&[u_r] = [u_\vartheta] = 0
\end{aligned}
\tag{21}
$$

The latter is consistent with the plastic rule to assume that the plastic strain tensor is continuous, and it follows from Eq 21

$$
\begin{aligned}
&[\varepsilon_{rz}] = 0 \\
&[\varepsilon_{rr}] = 0
\end{aligned}
\tag{22}
$$

From Eqs 21 and 22, we have

$$
\begin{aligned}
&[\sigma_{rz}] = 0 \\
&[\sigma_{rr}] = 0 \\
&[\sigma_{zz}] = 0 \qquad \text{for plane-strain case}
\end{aligned}
\tag{23}
$$

and also

$$[\sigma_e^2] = (K\sigma_0 r^{-s})^2[T_i(\vartheta)] + (H\sigma_0 r^{-t})^2[T_o(\vartheta)] = 0 \tag{24}$$

Thus, all strain-rate components are continuous and therefore

$$
\begin{aligned}
&[v_z] = 0 \\
&[v_r] = [v_\vartheta] = 0
\end{aligned}
\tag{25}
$$

Summarizing all continuity conditions, for the plane-strain case only, nine (for the plane-stress case, eight) of them are independent and they lead to the convenient form

$$
\begin{aligned}
&[z_1] = [z_2] = [z_3] = 0 \\
&[y_1] = \dots = [y_5] = 0 \\
&[y_6] = 0 \qquad \text{for plane-strain case}
\end{aligned}
\tag{26}
$$

We have to solve two ODE systems subject to boundary conditions and continuity conditions discussed earlier. We selected a semi-implicit extrapolation integrator to perform the numerical integration. The boundary value problems are solved by using the multiple shooting techniques of Ref *11*. In order to get started, we need to provide the values of $z_i(0)$, $y_i(0)$, s, and t for every given α and ν.

We have already shown in Eqs 14 and 15 that $z_1(0) = z_2(0) = 0$, $y_2(0) = y_5(0) = 0$, and $z_3(0) = y_4(0) = 1$. From Eqs 15 and 16 and making use of the implicit ODE systems in the Appendix, one obtains finally

$$\begin{aligned} y_6(0) &= (\nu + \lambda/2s)(y_3(0) + y_4(0))/(1 + \lambda/s) \\ y_1(0) &= -(1 + \lambda/s)y_3(0) + (\nu + \lambda/2s)(y_4(0) + y_6(0)) \end{aligned} \tag{27}$$

where

$$\lambda = -\left(\frac{1}{\alpha} - 1\right)\frac{\left[s + \left(\dfrac{H}{K}\right)^2 r^{2(t-s)}t\right]}{\left[1 + \left(\dfrac{H}{K}\right)^2 r^{2(t-s)}\right]} \tag{28}$$

It follows that $\lambda = -s(1/\alpha - 1)$ for the in-plane dominance, or $H/K = 0$, and $\lambda = -t(1/\alpha - 1)$ for the anti-plane shear stress dominance, or $K/H = 0$. According to Eq 19 only one stress component, $y_3(0)$, and both eigenvalues, s and t, must be guessed before integrating.

Note that $z_2(\vartheta)$, $y_3(\vartheta)$, and $y_5(\vartheta)$ obtain singular solutions in the form $(\sin\vartheta)^{-\lambda}$. To overcome the consequent numerical difficulty in integration, the corresponding sine-function is set to approach a very small finite value for $\vartheta \rightarrow \pi$. Since all other variables are well behaved near the crack flanks, this approximation yields fine results.

In the elastic zone, both ODE systems are uncoupled for integration. One can solve the ODEs as pure Mode I and pure Mode III, and the result is for the anti-plane shear field

$$\begin{aligned} z_1 &= -2(1 + \nu)(M\cos t\vartheta + N\sin t\vartheta) \\ z_2 &= M\cos(t + 1)\vartheta + N\sin(t + 1)\vartheta - L\sin^t\vartheta\cos\vartheta \\ z_3 &= -M\sin(t + 1)\vartheta + N\cos(t + 1)\vartheta + L\sin^{t+1}\vartheta \end{aligned} \tag{29}$$

and for the in-plane field

$$\begin{aligned} y_3 &= -A\cos(s + 2)\vartheta - B\sin(s + 2)\vartheta - C(s - 2)\sin s\vartheta - D(s - 2)\cos s\vartheta \\ &\quad + F\sin^s\vartheta\cos\vartheta \\ y_4 &= A\cos(s + 2)\vartheta + B\sin(s + 2)\vartheta + C(s + 2)\sin s\vartheta + D(s + 2)\cos s\vartheta \\ &\quad + F\sin^{s+2}\vartheta \\ y_5 &= A\sin(s + 2)\vartheta - B\cos(s + 2)\vartheta - Cs\cos s\vartheta + Ds\sin s\vartheta + F\sin^{s+1}\vartheta\cos\vartheta \\ y_6 &= 4\nu C\sin s\vartheta + 4\nu D\cos s\vartheta + G\sin^s\vartheta \end{aligned} \tag{30}$$

$$\begin{aligned} y_1 &= \frac{1}{s}(\dot{y}_3 - \nu[\dot{y}_4 + \dot{y}_6]) \\ y_2 &= \frac{1}{s - 1}(2\dot{y}_5 - y_1') \end{aligned} \tag{31}$$

where A, B, C, D, G, F, L, M, and N are arbitrary constants that will be determined through the continuity conditions and the boundary conditions; and $\dot{y}_3$, $\dot{y}_4$, $\dot{y}_5$, and $\dot{y}_6$ in Eq 31 represent the angular functions of the stress-rate tensor that can be calculated according to Eq 3. Note that the stress components, σ_{rz}, σ_{rr}, and $\sigma_{\vartheta\vartheta}$, or correspondingly, z_2, y_3, and y_6, generally become soon unbounded as $\vartheta \to \pi$, since generally $s < 0$. It can be proven that these stresses are unbounded as $\vartheta \to \pi$, regardless of plastic reloading.

Perturbation from Dominant In-Plane Modes

Formulation of Perturbation ODEs

First, we consider the cases where the contribution of the anti-plane shear stresses to the effective stress is small compared to that of the in-plane stresses (or $H/K \ll 1$). Equation 9 can be rewritten as

$$\sigma_e^2 = (K\sigma_0 r^s)^2 \tilde{\sigma}_e^2 \tag{32}$$

where

$$\tilde{\sigma}_e^2 = T_i \left[1 + \left(\frac{H}{K}\right)^2 r^{2(t-s)} \frac{T_o}{T_i} \right] \tag{33}$$

The asymptotic analysis and finite-element computations for a stationary crack-tip field in Refs *9* and *10* show that the singularities of the in-plane stresses and the anti-plane shear stresses are different slightly. For small r, $r^{2(t-s)}$ in Eq 33 is finite with an order of unit. Therefore, $\tilde{\sigma}_e$ does have a weak dependence on r. Since T_i and T_o are defined to have the order of unit, (H/K) determines the order of magnitude for the second term on the right-hand side of Eq 33. In fact, $(H/K)^2 r^{2(t-s)}$ can be regarded as a mixed factor of in-plane mode and anti-plane shear mode [*9*]. This mixed factor depends upon r. The plastic dissipation term in the constitutive Eq 5 can be written in the form

$$\sigma_e^{-1}\dot{\sigma}_e = \frac{1}{r} \frac{-sT_i \cos\vartheta + \frac{1}{2} T_i' \sin\vartheta + \left(\frac{H}{K}\right)^2 r^{2(t-s)} \left(-tT_o \cos\vartheta + \frac{1}{2} T_o' \sin\vartheta\right)}{T_i + \left(\frac{H}{K}\right)^2 r^{2(t-s)} T_o} \tag{34}$$

Substitute Eq 34 together with Eqs 7 and 8 into the constitutive equation, one obtains nine ODEs of angular functions for the plane-strain case or eight for the plane-stress case. Note again, since $\tilde{\sigma}_e$ is a nonseparable function of r and ϑ when t is not equal to s, all ODEs become dependent on r. The ODEs commonly cannot be solved as pure Modes I and III in Refs *6* and *7*. Assuming $(H/K) \ll 1$, and all terms from the anti-plane shear stresses in Eq 34 are smaller than unity, we can perturb these ODEs from in-plane modes using

$$\sigma_e^{-1}\dot{\sigma}_e = \frac{1}{r}\left(-s\cos\vartheta + \frac{T_i'}{2T_i}\sin\vartheta\right)$$
$$+ \frac{1}{r}\left(\frac{H}{K}\right)^2 r^{2(t-s)} T_o \left\{1 - \left(-s\cos\vartheta + \frac{T_i'}{2T_i}\sin\vartheta\right)\left(1 + t\cos\vartheta - \frac{T_o'}{2T_o}\sin\vartheta\right)\right\} \tag{35}$$

The unperturbed equation from in-plane modes is the same as the ODEs derived in Ref 7, see Appendix. The lower-order perturbed equations for anti-plane mode are, however, coupled through T_i with the in-plane solution, see Appendix. Correspondingly, the elastic unloading condition (Eq 12) becomes

$$-sT_i(\vartheta_p)\cos\vartheta_p + \tfrac{1}{2}T_i'(\vartheta_p)\sin\vartheta_p = 0 \tag{36}$$

and the plastic reloading condition (Eq 13) becomes

$$T_i(\vartheta_e)\sin^{-2s}\vartheta_e - T_i(\vartheta_p)\sin^{-2s}\vartheta_p = 0 \tag{37}$$

Note that the perturbed equations are homogeneous in unknown functions. In fact, we are now seeking the solutions for anti-plane shear mode perturbed from an in-plane mode. We first solve the unperturbed equations for an in-plane mode with the start values discussed in the last section. The eigenvalue, t, is set equal to s at the beginning to integrate the perturbed governing equations for anti-plane shear mode.

Numerical Results Perturbed from the Plane-Strain Mode I Solutions

As noted in Refs 6 and 7, the dependence of the singularity and angular variations of the in-plane stresses on the Poisson's ratio, ν, is weak. It follows that the perturbed solutions of anti-plane shear mode are slightly affected by different ν values; whereas in pure Mode III anti-plane cases, influences of ν can be included in the strain-hardening factor. Thus, we will only show results for $\nu = 0.3$ in the following text.

To give a better understanding of the curves, we use the conventional symbols for stresses and velocities in all figures. All stresses and velocities are normalized through Eq 19, as mentioned before. Figures 3*a* and *b* show the angular variation of the Mode III solutions perturbed from the plane-strain Mode I for large strain-hardening ($\alpha = 0.50$) and for moderate strain-hardening ($\alpha = 0.15$), respectively. For smaller strain-hardening, the singularity of the crack-tip field vanishes when the stress distribution becomes uninteresting, as predicted in Table 1. For comparison, the corresponding pure Mode III solutions are also plotted in the figures. In

TABLE 1—*Mode III perturbed from plane-strain Mode I ($\nu = 0.3$).*

α	$-t$	$-t^*$	ϑ_p	ϑ_p^*	ϑ_e	ϑ_e^*
1.0	0.5000	0.5000	88.0347	90.0000	...	...
0.75	0.38809	0.44909	91.2272	87.4825	...	...
0.67	0.34012	0.43018	92.8671	86.4588	...	...
0.50	0.22039	0.38389	97.8070	83.7364	...	...
0.40	0.14461	0.35125	101.9540	81.6195	...	...
0.35	0.10787	0.33281	104.4891	80.3445	...	...
0.30	0.07353	0.31250	107.3818	78.8707	...	...
0.20	0.01935	0.26394	114.2134	75.0194	...	...
0.15	0.00310	0.23352	118.4430	72.3412	179.1456	...
0.10	−0.00758	0.19587	123.9320	68.6905	173.7774	...
0.05	−0.01754	0.14403	131.0838	62.9029	161.1481	179.7561
0.01	−0.03245	0.06857	135.3640	52.0822	145.6069	179.7582

* Results from the pure Mode III solutions.

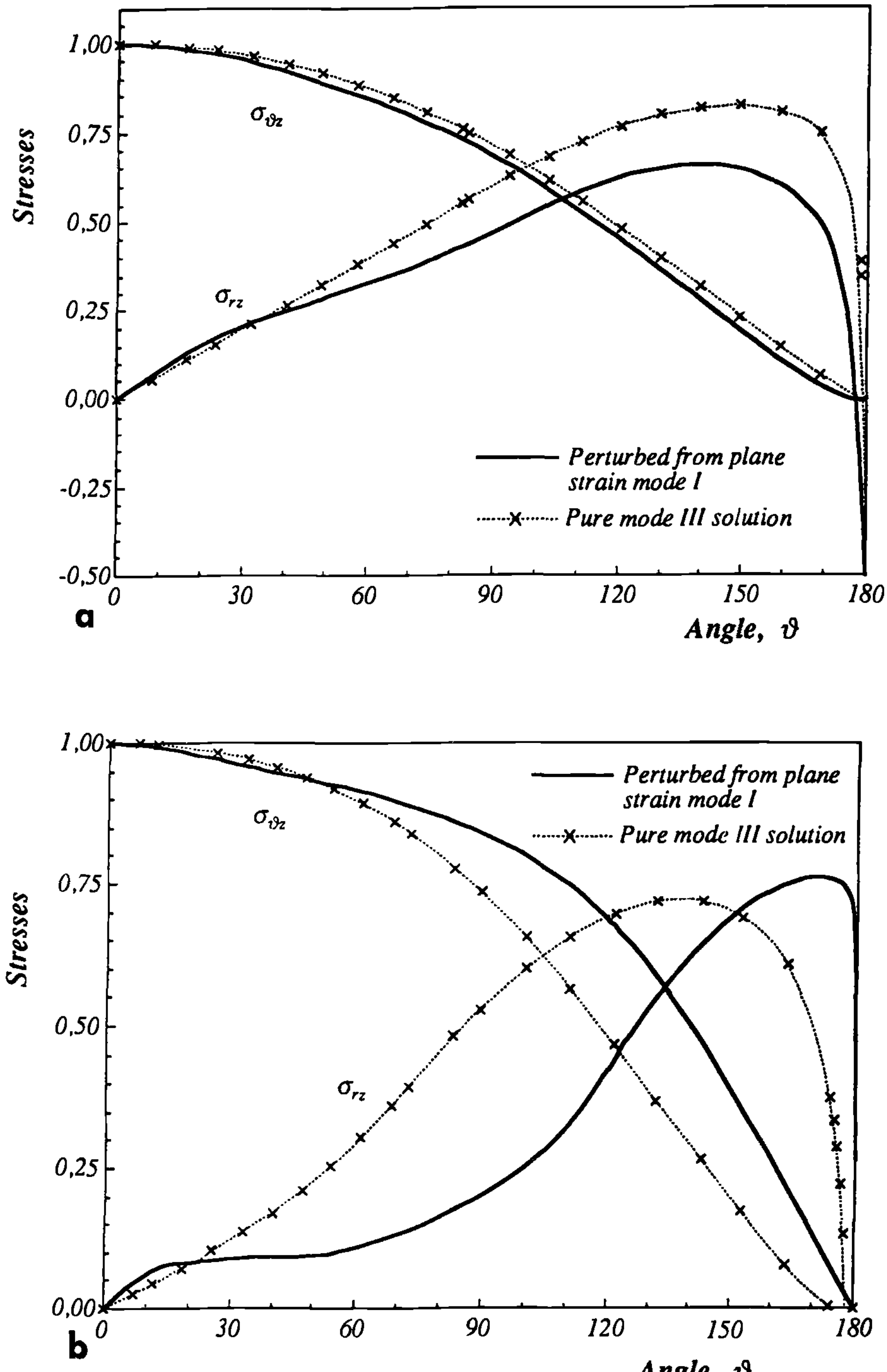

FIG. 3—*Angular stress distribution in the out-of-plane crack-tip field:* (a) *for large strain-hardening (α = 0.50) and* (b) *for moderate strain-hardening (α = 0.15).*

Figs. *3a* and *b*, variations of the angular function from pure Mode III curves depend significantly on the strain-hardening factor, whereas the shear stress component, σ_{rz}, has always an unbounded value for $\vartheta \rightarrow \pi$, similar to the pure Mode III case. As α becomes smaller, the stress level of σ_{rz} perturbed from plane-strain Mode I approaches a flat distribution, clearly below the pure Mode III curves. The material points near the crack flanks obviously undergo plastic reloading earlier than those in pure Mode III cases. The amplitude of the angular deformation velocity, v_z, around the crack tip shows a much more significant variation from the pure Mode III solutions, see Fig. *5a* for the large strain-hardening case, whereas the curve features are hardly changed. The perturbed angular velocity generally does allow normalization through its corresponding field singularity, as it does in Ref *7*.

The values of the shear stress singularity, t, are listed in Table 1 for various α. For comparison, we also list the values of pure Mode III. Note that the elastic unloading angles and the plastic reloading angles are determined by the dominant crack-tip field, that is, the plane-strain Mode I solutions in this case. For perfectly elastic materials, both shear stress fields singularities are the same, though the unloading angles are different due to different unloading conditions, comparing Eqs 36 and 41. The agreement of our solutions for $\alpha = 1$ serves as a check for our numerical procedure. As indicated in the table, the strength of the anti-plane shear stress singularity is generally weaker than those of the pure Mode III solutions and the dominant crack-tip fields. This characteristic was also observed in asymptotic analysis in Ref *13* for dynamic crack growth and Refs *9* and *10* for a stationary crack-tip field.

The most interesting features of the solution are that the singularity perturbed from plane-strain Mode I is reduced drastically, compared to the pure Mode III solutions, and t becomes positive for a further reduction of the strain-hardening factor. The singularity of the Mode III anti-plane shear stresses disappears for $\alpha \leq 0.1$. This result predicts that under the near plane-strain Mode I and III conditions in small strain-hardening materials the anti-plane shear stresses will not affect the fracture process dominated by plane-strain Mode I.

Numerical Results Perturbed from the Plane-Stress Mode I Solutions

In comparing the solutions perturbed from plane-strain Mode I, the perturbation from plane-stress Mode I brings no substantial changes into the anti-plane shear stress distribution, see Figs. *4a* for the large strain-hardening ($\alpha = 0.50$) and *4b* for the very small strain-hardening case ($\alpha = 0.0001$), respectively. Whereas for a stationary crack the perturbed tip field feature differs drastically from the pure Mode III stress solution, as discussed in Refs *9* and *10*, the figures show a nearly uniform agreement of the angular stress distribution with the pure Mode III solution for all linear-hardening and even nearly perfectly plastic materials. It implies that the crack-tip field combined by plane-stress Mode I and Mode III has the same stress distribution features as the pure plane-stress Mode I and Mode III (see the discussion of the plane-stress Mode I solutions perturbed from anti-plane mode in the next section).

The distribution of the deformation velocity shows, however, a large sensitivity again to the perturbation, see Fig. *5b*. The figures show that, as α decreases to 0.0001, the angular variations of the stresses and velocity undergo significant changes and they start taking the general shape of the perfectly plastic solution, see Ref *3*. This is a remarkable result because even the radial dependence of the velocity of the small α-problem, see Eq 7, does not approach that of the perfectly plastic problem ($\ln \underline{r}$), the angular variation of the velocity of the small α-problem does seem to approach the correspondent perfectly plastic distribution [*7*]. For this reason, one can assume that the anti-plane velocity of combined plane-stress Mode I and Mode III in perfectly plastic materials has a similar distribution feature as that in the pure Mode III solution.

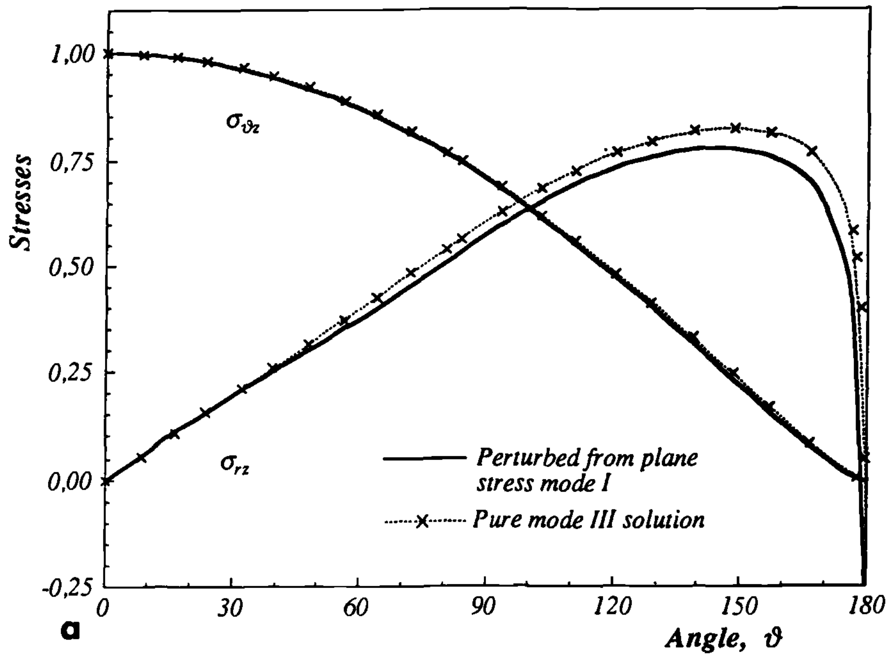

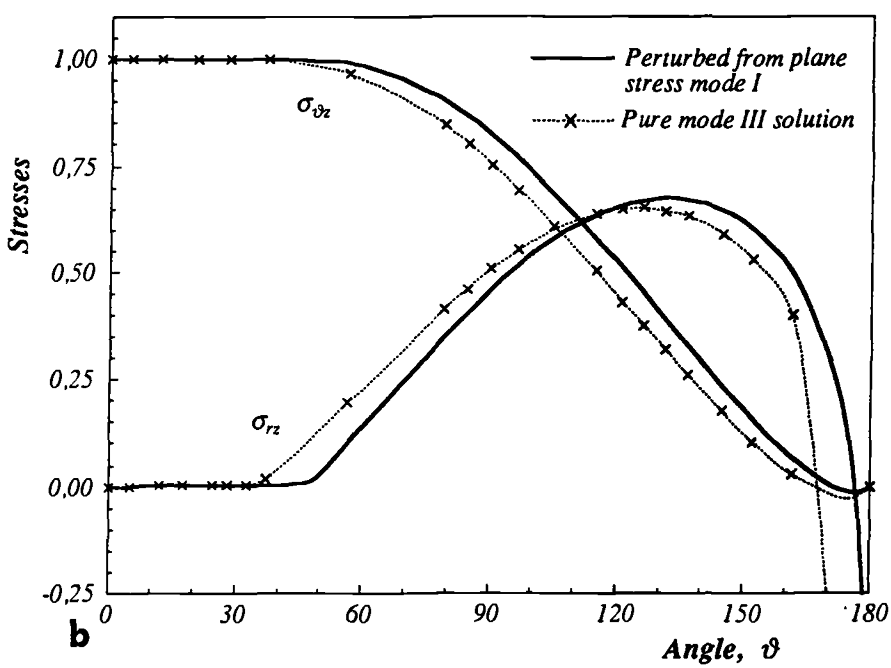

FIG. 4—*Angular stress distribution in the out-of-plane crack-tip field:* (a) *for large strain-hardening* (α = 0.50) *and* (b) *for small strain-hardening* (α = 0.0001).

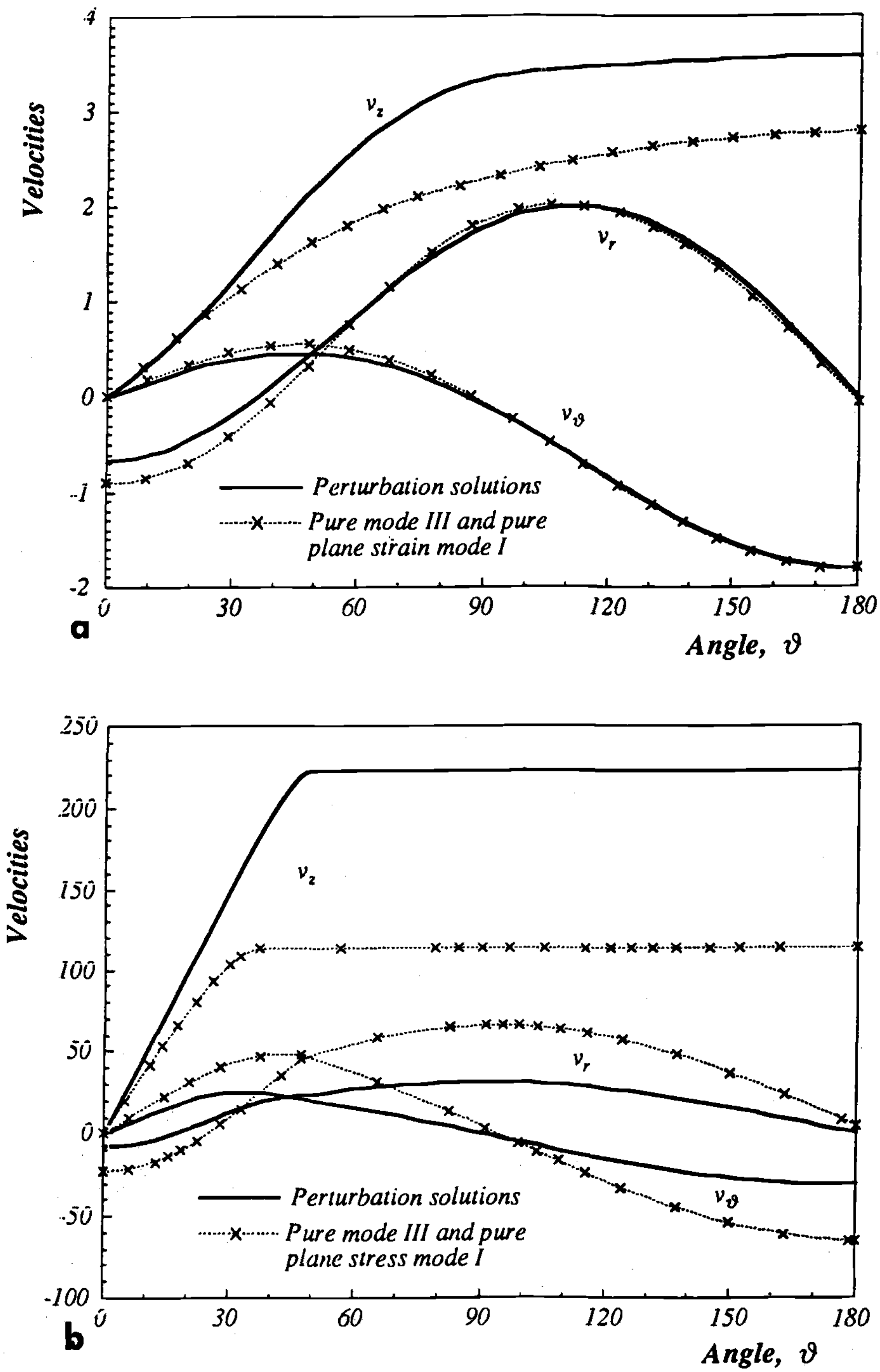

FIG. 5—*Angular velocity distribution in the combined Mode I and Mode III crack-tip field:* (a) *plane-strain case for large strain-hardening (α = 0.50) and* (b) *plane-stress case for small strain-hardening (α = 0.0001).*

TABLE 2—*Mode III perturbed from plane-stress Mode I (ν = 0.3).*

α	$-t$	$-t^*$	ϑ_p	ϑ_p^*	ϑ_e	ϑ_e^*
1.0	0.5	0.5	79.9177	90.0	...	...
0.75	0.43652	0.44909	80.7812	87.4825	...	...
0.67	0.41053	0.43018	80.9016	86.4588	...	...
0.50	0.34418	0.38389	80.7629	83.7364	...	...
0.30	0.24447	0.31250	79.3434	78.8707	...	...
0.20	0.18553	0.26394	77.5098	75.0194	...	...
0.10	0.11919	0.19587	73.6462	68.6905	...	...
0.05	0.07576	0.14403	69.5308	62.9029	...	179.7561
0.01	0.03418	0.06857	61.0908	52.0822	180.000	179.7582
0.005	0.02410	0.04940	58.2177	48.539	179.9999	179.7594
0.001	0.01080	0.02279	53.2020	42.4546	179.9999	179.7565
0.0001	0.00342	0.00739	49.0017	37.4571	179.999	179.7450

* Results from the pure Mode III solutions.

In Table 2, the values of singularity perturbed from plane-stress Mode I and the values of pure Mode III are summarized under t and t^*, respectively, for various α. As mentioned before, the unloading and the reloading angles are found in the analysis of the in-plane crack-tip fields, since we seek the solutions perturbed from plane-stress Mode I. Similar to those in Table 1, for each α less than 1, the value of t listed in Table 2 is smaller than the value of t^*. This indicates that the singularity of the anti-plane shear stresses under the combined plane stress and Mode III conditions is just slightly weaker than that of pure Modes III. Compared with the results perturbed from plane-strain Mode I, however, the values of t and t^* are much closer to each other. Table 2 shows no lower-limit of strain-hardening for vanishing anti-plane shear stress singularity, which is given in the plane-strain case of Table 1.

Perturbation from Dominant Anti-Plane Mode

The same procedure discussed in last section can also be used to analyze the cases where the contribution of the in-plane stresses to the effective stress is much smaller than that of the anti-plane shear stresses, or $K/H \ll 1$. Now we consider a crack-tip field dominated by the anti-plane shear stresses.

Formulation of Perturbation ODEs for the In-Plane Crack-Tip Field

We can rewrite Eq 9 as follows

$$\sigma_e^2 = (H\sigma_0 \underline{r}^{\,t})^2 \tilde{\sigma}_e^2 \tag{38}$$

where

$$\tilde{\sigma}_e^2 = T_o \left[1 + \left(\frac{K}{H}\right)^2 r^{2(s-t)} \frac{T_t}{T_o} \right] \tag{39}$$

As stated in the last section, under the condition, $K/H \ll 1$, one can assume the magnitude of the second term, which is indeed determined by the K/H, is small enough to deduce the perturbation equations. Thus, the plastic dissipation can be expressed as

$$\sigma_e^{-1}\dot{\sigma}_e = \frac{1}{r}\left(-t\cos\vartheta + \frac{T_o'}{2T_o}\sin\vartheta\right)$$

$$+\frac{1}{r}\left(\frac{K}{H}\right)^2 r^{2(s-t)}T_t\left\{1 - \left(-t\cos\vartheta + \frac{T_o'}{2T_o}\sin\vartheta\right)\left(1 + s\cos\vartheta - \frac{T_t'}{2T_t}\sin\vartheta\right)\right\} \quad (40)$$

The unperturbed equations for anti-plane shear mode are identical to the ODEs for pure Mode III, see Appendix. Therefore, the eigenvalue, t, should be the same as that in Ref 7. The lower-order perturbed equations for in-plane modes are however coupled through T_o with the anti-plane solution, see Appendix. Correspondingly, the elastic unloading angle will be determined by the anti-plane shear stresses as follows

$$-tT_o(\vartheta_p)\cos\vartheta_p + ½T_o'(\vartheta_p)\sin\vartheta_p = 0 \quad (41)$$

and the plastic reloading will be found under the condition

$$T_o(\vartheta_e)\sin^{-2s}\vartheta_e - T_o(\vartheta_p)\sin^{-2s}\vartheta_p = 0 \quad (42)$$

As the cases perturbed from in-plane modes, the equations for in-plane modes are homogeneous in unknown functions. We first solve the unperturbed equations for an anti-plane shear mode with the start values discussed before. The eigenvalue, s, is set equal to t at the beginning to integrate the perturbed governing equations for in-plane modes.

Numerical Results of Perturbed Plane-Strain Mode I Solutions

It has been shown that the value of ν very slightly changes the perturbed solutions of in-plane modes, as in pure in-plane modes [6,7]. Thus, we restrict our discussions only in cases with $\nu = 0.3$.

To give a better understanding of the curves, we also use the conventional symbol for stresses and the velocity in the following figures. All stresses and velocities are normalized through Eq 19, as mentioned before. Figures 6*a* and *b* show the plane-strain Mode I solutions perturbed from Mode III for larger strain-hardening ($\alpha = 0.50$) and small strain-hardening materials ($\alpha = 0.01$), respectively. For comparison, the pure Mode I solutions are also plotted in the figures. For the large strain-hardening case, the curve feature of the angular stresses is not changed drastically from the pure Mode I. Figure 6*a* shows a good agreement of both solutions for large strain-hardening materials. However, a great difference between pure Mode I and the perturbed solution can be found in small strain-hardening materials, see Fig. 6*b*. The effective stress ahead of the crack tip under the plane-strain conditions (Eq 19) is several times larger than that in pure Mode I, and all normal stress components develop a very distinct curve feature. In Fig. 6*b*, the stresses from the pure Mode I start to take the general shape of the Prandtl field and all normal components fall together behind the crack tip for a large angular sector, whereas stresses of the perturbed solution obtain a totally different distribution.

In Table 3, the values of the perturbed and the pure mode solutions are summarized for various strain-hardening values, α, under s and s^*, respectively. We seek solutions perturbed from Mode III, and the corresponding singularities of Mode III can be found in Table 1. For $\alpha = 1$, since the coupling term of plastic dissipation vanishes, the governing ODE systems become separable. It follows that numerical solutions of s are equal to the pure plane-strain Mode I value and the angular functions are identical to the linear elastic solution (Eq 30). As indicated in the table, the eigenvalue, s, is only slightly less than the corresponding pure Mode I value for each α less than 1. That is, also in Mode III dominance, the perturbed stresses of

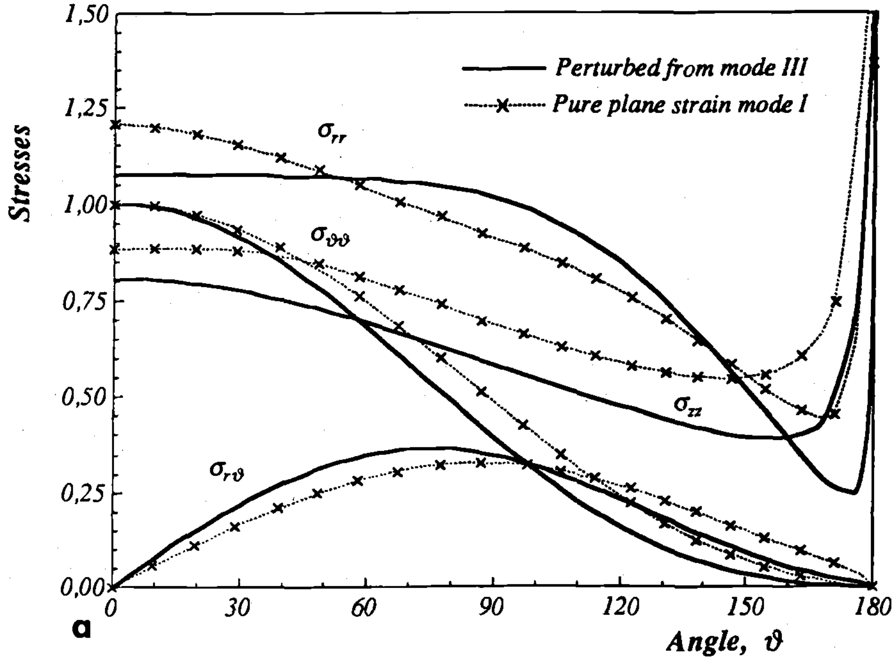

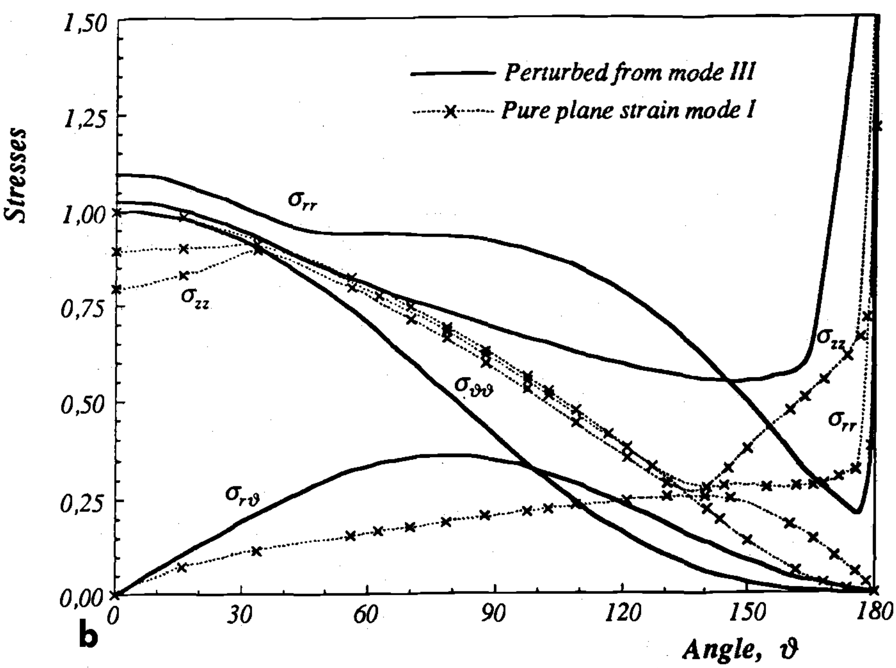

FIG. 6—*Angular stress distribution in the plane-strain Mode I crack-tip field:* (a) *for large strain-hardening (α = 0.50) and* (b) *for small strain-hardening (α = 0.01).*

TABLE 3—*Plane-strain Mode I perturbed from Mode III (ν = 0.3).*

α	$-s$	$-s^*$	ϑ_p	ϑ_p^*	ϑ_e	ϑ_e^*
1.0	0.5	0.5	90.0	88.0347	...	...
0.75	0.49164	0.47824	87.4825	91.2272	...	...
0.67	0.48901	0.46894	86.4588	92.8671	...	...
0.50	0.48331	0.4414	83.7364	97.8070	...	...
0.30	0.47581	0.37429	78.8707	107.3818	...	...
0.20	0.47101	0.30294	75.0194	114.2134	...	...
0.10	0.46362	0.20010	68.6905	123.9320	...	173.7774
0.05	0.45587	0.14360	62.9029	131.0838	179.7561	161.1481
0.01	0.43068	0.08045	52.0822	135.3640	179.7582	145.6069
0.005	0.41449	...	48.5390	...	179.7594	...
0.001	0.35897	...	42.4546	...	179.7565	...
0.0001	0.24037	...	37.4571	...	179.7450	...

* Results from the pure plane strain Mode I solutions.

plane-strain Mode I are generally more singular than those of the predominant pure Mode I crack-tip field. From this characteristic combining with the results in Table 1 it is predicted that the crack-tip field is dominated generally by the plane-strain field regardless of the mixity of the field. This is an important conclusion for characterization of cracks under the general Mode I and III loading conditions. The stress singularity decreases with reduction of α much more slowly than in pure Mode I cases. This result is also consistent with the variation of the singularities of the anti-plane shear stresses in Table 1. Comparing with Table 1, one can find that the perturbed singularity is stronger than that of the dominant part of the crack-tip field. This characteristic has been demonstrated in the analysis of a stationary crack [*9,10*].

Numerical Results of Perturbed Plane-Stress Mode I Solutions

Similar to results of the plane-stress Mode I dominance, the perturbation from Mode III has almost no influence to the angular stress fields, see Figs. 7*a* for the large strain-hardening and 7*b* for the small strain-hardening materials, respectively. The stress curve behavior ahead of the crack tip is independent of the mixity of combined anti-plane shear and in-plane stress loading. Following Figs. 4 and 7, one can assume the stress distribution under combined plane-stress Mode I and Mode III conditions is not significantly affected by the mode mixity ahead of the crack-tip field. One may use the pure Mode I and the pure Mode III solutions to estimate the stress distribution of the mixed mode.

As discussed for the plane-strain Mode I cases, though the stress angular distribution is not changed, the stress field under combined plane-stress Mode I and Mode III is generally more singular than those under the pure Mode I and the dominant Mode III conditions, see Table 4. As shown in the table, the singularities of the in-plane crack-tip stress field of pure Mode I and the perturbation solution are identical only in the elastic material, in which the governing ODE systems become separable due to the absence of the plastic dissipation term. Comparing the plane-strain analysis in Table 3, the singularity of plane-stress fields decreases less quickly. Because mixed-mode reduces the singularity of the anti-plane shear stresses, the combined Mode I and III loading conditions cause a stronger singularity of the in-plane stresses.

Discussions and Conclusions

In this paper, we present for the first time a systematic analysis of the asymptotic crack-tip stresses in steady-state crack growth based on the perturbed governing equations. In the whole analysis, only the power singularity form solutions in the crack-tip fields are assumed. These

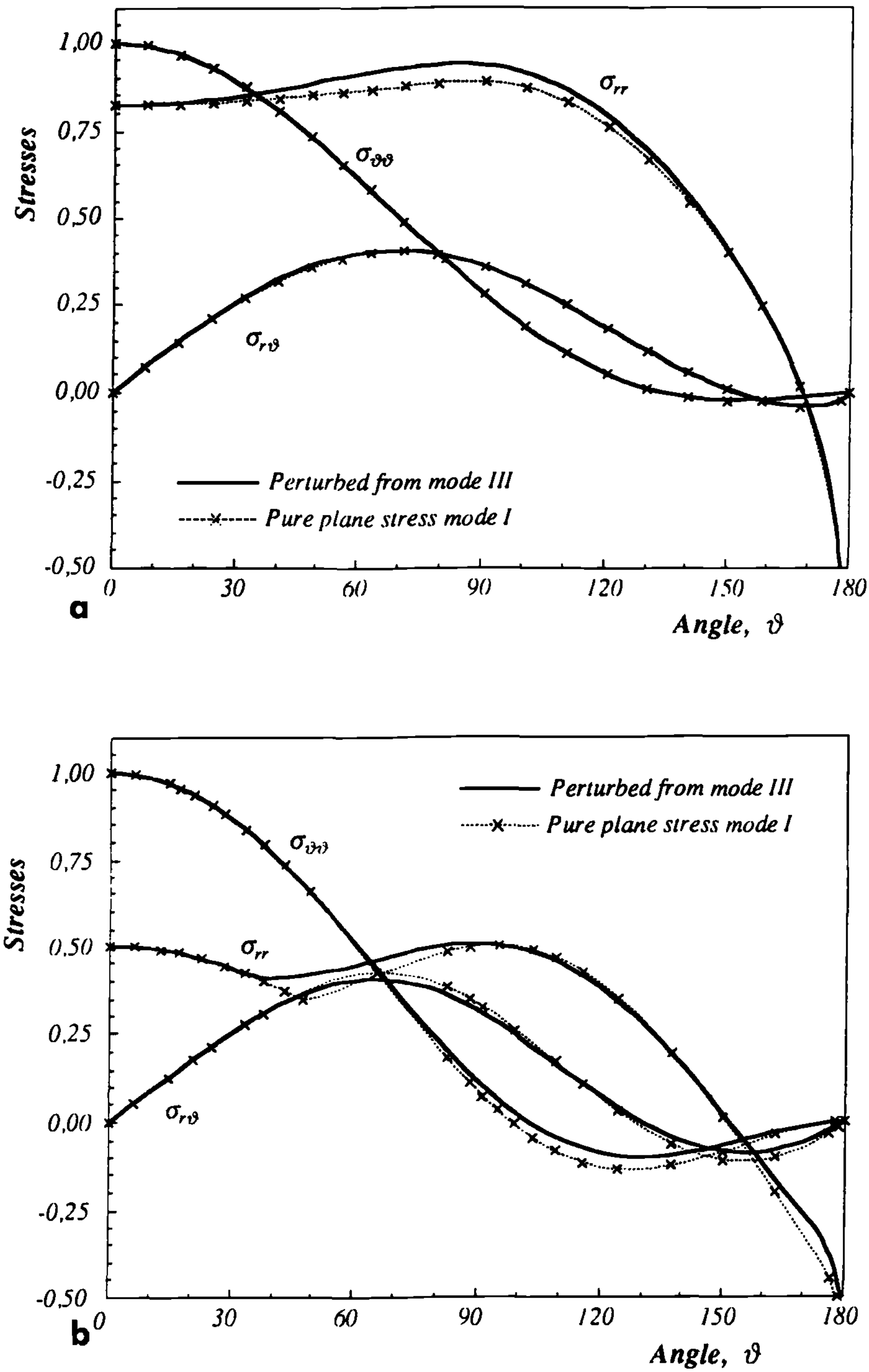

FIG. 7—*Angular stress distribution in the plane-stress Mode I crack-tip field:* (a) *for large strain-hardening (α = 0.50) and* (b) *for small strain-hardening (α = 0.0001).*

TABLE 4—*Plane-stress Mode I perturbed from Mode III (ν = 0.3).*

α	$-s$	$-s^*$	ϑ_p	$\vartheta_p{}^*$	ϑ_e	$\vartheta_e{}^*$
1.0	0.5	0.5	90.0	79.9177	...	...
0.75	0.47508	0.4684	87.4825	80.7812	...	...
0.67	0.46588	0.45519	86.4588	80.9016	...	...
0.50	0.44307	0.41971	83.7364	80.7629	...	...
0.30	0.40562	0.35708	78.8707	79.3434	...	...
0.20	0.37683	0.30959	75.0194	77.5098	...	...
0.10	0.32752	0.23722	68.6905	73.6462	...	...
0.05	0.27686	0.17787	62.9029	69.5308	179.7561	...
0.01	0.12530	0.08629	52.0822	61.0908	179.7582	180.000
0.005	0.16491	0.06226	48.539	58.2177	179.7594	179.9999
0.001	0.06131	0.02866	42.4546	53.2020	179.7565	179.9999
0.0001	0.02051	0.00925	37.4571	49.0017	179.745	179.999

* Results from the pure plane stress Mode I solutions.

perturbation solutions are approximately valid in the ranges of small r where either in-plane mode or anti-plane shear mode is much smaller than the other. They provide a partial picture of the near-tip fields under combined anti-plane shear and in-plane conditions. But these perturbation solutions do provide a correct understanding of the combined-mode near-tip field in steady-state crack extension problems.

According to the perturbation solutions, under combined Mode I and Mode III conditions, the singularity of the Mode I stresses is always stronger than that of the Mode III shear stresses when the contribution of either of the crack-tip stresses to the effective stress is smaller than that of the other. A combined mode will increase the in-plane stress singularity and decrease the anti-plane stress singularity. Similar results are also observed in the dynamic crack growth crack analysis in Ref *13*. A very interesting feature is the singularity of the anti-plane shear stresses in small strain-hardening materials that disappears under combined near-plane-strain Mode I and Mode III, but not under plane-stress Mode I and Mode III conditions. From the variation of the singularity, it may be assumed that the dominance zone of the solutions perturbed from the in-plane Mode I cases will be larger than those perturbed from the anti-plane shear field.

Variation of the stress angular functions under combined plane strain Mode I and Mode III is much more sensitive to the strain-hardening factor than that under combined plane-stress Mode I and Mode III. Whereas the stress angular distribution under plane-stress Mode I and Mode III is only very slightly changed from the pure Mode I or pure Mode III solutions, plane-strain Mode I exerts a large influence on the anti-plane shear and the in-plane stress singular distributions, especially for small strain-hardening materials.

APPENDIX

The Governing Ordinary Differential Equations

The homogeneous ODEs can be written generally as follows

$$A_{ij}y_j' + B_{ik}z_k' + C_i = 0 \qquad i = 1, \ldots 9 \tag{43}$$

where A_{ij} ($j = 1, \ldots, 6$) and B_{ik} ($k = 1, \ldots, 3$) are two coefficient matrices that will be defined in the following text. We suppose that all matrix components undefined in the following text are equal to zero. To simplify the formulation, we introduce following symbols

$$S_{rr} = -sy_3 \cos\vartheta - 2y_5 \sin\vartheta \qquad S_{\vartheta\vartheta} = -sy_4 \cos\vartheta - sy_5 \sin\vartheta$$
$$S_{r\vartheta} = -sy_5 \cos\vartheta - sy_3 \sin\vartheta \qquad S_{zz} = -sy_6 \cos\vartheta$$
$$S_{rz} = -tz_2 \cos\vartheta - z_3 \sin\vartheta \qquad S_{\vartheta z} = -tz_3 \cos\vartheta - tz_2 \sin\vartheta$$
$$x_3 = y_3 - \frac{1}{2}(y_4 + y_6) \qquad x_4 = y_4 - \frac{1}{2}(y_3 + y_6)$$
$$x_6 = y_6 - \frac{1}{2}(y_3 + y_4) \qquad \omega = \frac{1}{\alpha} - 1$$
$$R_i = -s\cos\vartheta + \frac{y_5}{T_i}\left[(1-s)y_4 - \left(\frac{5}{2}s + 2\right)y_3 + \left(\frac{1}{2}s + 1\right)y_6\right]\sin\vartheta$$
$$R_o = -t\cos\vartheta - \frac{3}{T_o}(t+1)z_2 z_3 \sin\vartheta$$

For plane-stress cases, y_6 vanishes and Eq 43 has only eight ODEs. In the following formulations the last three equations describe the anti-plane, shear crack-tip field and the other equations define the in-plane mode. Note that all perturbed equations are linear to the unknown eigenfunctions.

Perturbation from the Plane-Strain Mode I

$$A_{22} = -1 \qquad A_{31} = -\frac{1}{2}$$
$$A_{13} = \left(1 + \omega\frac{x_3^2}{T_i}\right)\sin\vartheta \qquad A_{16} = \left(-\nu + \omega\frac{x_3x_6}{T_i}\right)\sin\vartheta$$
$$A_{23} = \left(-\nu + \omega\frac{x_3x_4}{T_i}\right)\sin\vartheta \qquad A_{26} = \left(-\nu + \omega\frac{x_4x_6}{T_i}\right)\sin\vartheta$$
$$A_{33} = \frac{3}{2}\omega\frac{x_3}{T_i}y_5\sin\vartheta \qquad A_{36} = \frac{3}{2}\omega\frac{x_6}{T_i}y_5\sin\vartheta$$
$$A_{43} = \left(-\nu + \omega\frac{x_3x_6}{T_i}\right)\sin\vartheta \qquad A_{46} = \left(-\nu + \omega\frac{x_3^2}{T_i}\right)\sin\vartheta$$
$$A_{55} = 1 \qquad A_{64} = 1$$
$$A_{73} = \frac{3}{2}\omega\frac{x_3}{T_i}z_2\sin\vartheta \qquad A_{76} = \frac{3}{2}\omega\frac{x_6}{T_i}z_2\sin\vartheta$$
$$A_{83} = \frac{3}{2}\omega\frac{x_3}{T_i}z_3\sin\vartheta \qquad A_{86} = \frac{3}{2}\omega\frac{x_6}{T_i}z_3\sin\vartheta$$
$$B_{72} = (1+\nu)\sin\vartheta \qquad B_{81} = -\frac{1}{2}$$
$$B_{93} = 1$$
$$C_1 = S_{rr} - \nu(S_{\vartheta\vartheta} + S_{zz}) + \omega x_3 R_i - sy_1 \qquad C_2 = S_{\vartheta\vartheta} - \nu(S_{rr} + S_{zz}) + \omega x_4 R_i - y_1$$
$$C_3 = (1+\nu)S_{r\vartheta} + \frac{3}{2}\omega y_5 R_i + \frac{1-s}{2}y_2 \qquad C_4 = S_{zz} - \nu(S_{rr} + S_{\vartheta\vartheta}) + \omega x_6 R_i$$
$$C_5 = y_4 - (s+1)y_3 \qquad C_6 = -(s+2)y_5$$
$$C_7 = (1+\nu)S_{rz} + \frac{3}{2}\omega z_2 R_i - \frac{1}{2}tz_1 \qquad C_8 = (1+\nu)S_{\vartheta z} + \frac{3}{2}\omega z_3 R_i$$
$$C_9 = -(t+1)z_2$$

Perturbation from the Plane-Stress Mode I

$$A_{22} = -1 \qquad A_{31} = -\frac{1}{2}$$
$$A_{13} = \left(1 + \omega\frac{x_3^2}{T_i}\right)\sin\vartheta \qquad A_{23} = \left(-\nu + \omega\frac{x_3x_4}{T_i}\right)\sin\vartheta$$

$$A_{33} = \frac{3}{2}\,\omega\,\frac{x_3}{T_i}\,y_5 \sin\vartheta \qquad A_{45} = 1$$

$$A_{54} = 1 \qquad A_{63} = \frac{3}{2}\,\omega\,\frac{x_3}{T_i}\,z_2 \sin\vartheta$$

$$A_{74} = \frac{3}{2}\,\omega\,\frac{x_3}{T_i}\,z_3 \sin\vartheta$$

$$B_{62} = (1 + \nu)\sin\vartheta \qquad B_{71} = -\frac{1}{2}$$

$$B_{83} = 1$$

$$C_1 = S_{rr} - \nu S_{\vartheta\vartheta} + \omega x_3 R_i - s y_1 \qquad C_2 = S_{\vartheta\vartheta} - \nu S_{rr} + \omega x_4 R_i - y_1$$

$$C_3 = (1 + \nu)S_{r\vartheta} + \frac{3}{2}\,\omega y_5 R_i + \frac{1 - s}{2}\,y_2 \qquad C_4 = y_4 - (s + 1)y_3$$

$$C_5 = -(s + 2)y_5 \qquad C_6 = (1 + \nu)S_{rz} + \frac{3}{2}\,\omega z_2 R_i - \frac{1}{2}\,t z_1$$

$$C_7 = (1 + \nu)S_{\vartheta z} + \frac{3}{2}\,\omega z_3 R_i \qquad C_8 = -(t + 1)z_2$$

Perturbation from the Anti-Plane Mode (Plane-Strain Case)

$$A_{22} = -1 \qquad A_{31} = -\frac{1}{2}$$

$$A_{13} = \sin\vartheta \qquad A_{16} = -\nu\sin\vartheta$$

$$A_{23} = -\nu\sin\vartheta \qquad A_{26} = -\nu\sin\vartheta$$

$$A_{43} = -\nu\sin\vartheta \qquad A_{46} = \sin\vartheta$$

$$A_{55} = 1 \qquad A_{64} = 1$$

$$B_{12} = \omega\,\frac{3x_3}{T_o}\,z_2\sin\vartheta \qquad B_{22} = \omega\,\frac{3x_4}{T_o}\,z_2\sin\vartheta$$

$$B_{32} = \omega\,\frac{9y_5}{2T_o}\,z_2\sin\vartheta \qquad B_{42} = \omega\,\frac{3x_6}{T_o}\,z_2\sin\vartheta$$

$$B_{72} = \left(1 + \nu + \omega\,\frac{9y_5}{2T_o}\,z_2\right)\sin\vartheta \qquad B_{82} = \omega\,\frac{9z_3}{2T_o}\,z_2\sin\vartheta$$

$$B_{81} = -\frac{1}{2} \qquad B_{93} = 1$$

$$C_1 = S_{rr} - \nu(S_{\vartheta\vartheta} + S_{zz}) + \omega x_3 R_o - s y_1 \qquad C_2 = S_{\vartheta\vartheta} - \nu(S_{rr} + S_{zz}) + \omega x_4 R_o - y_1$$

$$C_3 = (1 + \nu)S_{r\vartheta} + \frac{3}{2}\,\omega y_5 R_o + \frac{1 - s}{2}\,y_2 \qquad C_4 = S_{zz} - \nu(S_{rr} + S_{\vartheta\vartheta}) + \omega x_6 R_o$$

$$C_5 = y_4 - (s + 1)y_3 \qquad C_6 = -(s + 2)y_5$$

$$C_7 = (1 + \nu)S_{rz} + \frac{3}{2}\,\omega z_2 R_o - \frac{1}{2}\,t z_1 \qquad C_8 = (1 + \nu)S_{\vartheta z} + \frac{3}{2}\,\omega z_3 R_o$$

$$C_9 = -(t + 1)z_2$$

Perturbation from the Anti-Plane Mode (Plane Stress Case)

$$A_{22} = -1 \qquad A_{31} = -\frac{1}{2}$$

$$A_{13} = \sin\vartheta \qquad A_{23} = -\nu\sin\vartheta$$

$$A_{45} = 1 \qquad A_{54} = 1$$

$$B_{12} = \omega\,\frac{3x_3}{T_o}\,z_2\sin\vartheta \qquad B_{22} = \omega\,\frac{3x_4}{T_o}\,z_2\sin\vartheta$$

$$B_{32} = \omega \frac{9y_5}{2T_o} z_2 \sin \vartheta \qquad B_{62} = \left(1 + \nu + \omega \frac{9y_5}{2T_o} z_2\right) \sin \vartheta$$

$$B_{72} = \omega \frac{9z_3}{2T_o} z_2 \sin \vartheta \qquad B_{71} = -\frac{1}{2}$$

$$B_{83} = 1$$

$$C_1 = S_{rr} - \nu S_{\vartheta\vartheta} + \omega x_3 R_o - s y_1 \qquad C_2 = S_{\vartheta\vartheta} - \nu S_{rr} + \omega x_4 R_o - y_1$$

$$C_3 = (1 + \nu) S_{r\vartheta} + \frac{3}{2} \omega y_5 R_o + \frac{1 - s}{2} y_2 \qquad C_4 = y_4 - (s + 1) y_3$$

$$C_5 = -(s + 2) y_5 \qquad C_6 = (1 + \nu) S_{rz} + \frac{3}{2} \omega z_2 R_o - \frac{1}{2} t z_1$$

$$C_7 = (1 + \nu) S_{\vartheta z} + \frac{3}{2} \omega z_3 R_o \qquad C_8 = -(t + 1) z_2$$

References

[1] Hutchinson, J. W., "Singular Behavior at the End of a Tensile Crack in a Hardening Material," *Journal of Mechanics and Physics of Solids*, Vol. 16, 1968, pp. 13–31.

[2] Rice, J. R. and Rosengren, G. F., "Plane Strain Deformation Near a Crack Tip in a Power-Law Hardening Material," *Journal of Mechanics and Physics of Solids*, Vol. 16, 1968, pp. 1–12.

[3] Chitaley, A. D. and McClintock, F. A., "Elastic-Plastic Mechanics of Steady-State Crack Growth Under Anti-Plane Shear," *Journal of Mechanics and Physics of Solids*, Vol. 19, 1971, pp. 147–163.

[4] Drugan, W. J., Rice, J. R., and Sham, T.-L., "Asymptotic Analysis of Growing Plane Strain Tensile Cracks in Elastic-Ideally Plastic Solids," *Journal of Mechanics and Physics of Solids*, Vol. 30, 1982, pp. 447–473.

[5] Drugan, W. J. and Chen, X.-Y., "Plane Strain Elastic-Ideally Plastic Crack Fields for Mode I Quasi-Static Growth at Large Scale Yielding—I. A New Family of Analytical Solutions," *Journal of Mechanics and Physics of Solids*, Vol. 37, 1989, pp. 1–26.

[6] Amazigo, J. C. and Hutchinson, J. W., "Crack Tip Fields in Steady Crack-Growth with Linear Strain-Hardening," *Journal of Mechanics and Physics of Solids*, Vol. 25, 1977, pp. 81–97.

[7] Ponte Castañeda, P., "Asymptotic Fields in Steady Crack Growth with Linear Strain Hardening," *Journal of Mechanics and Physics of Solids*, Vol. 35, 1987, pp. 227–268.

[8] Cornec, A., unpublished experimental observations, 1989.

[9] Pan, J., "Asymptotic Analysis of a Crack in a Power-Law Material Under Combined In-Plane and Out-of-Plane Shear Loading Conditions," *Journal of Mechanics and Physics of Solids*, Vol. 38, 1990, pp. 133–159.

[10] Pan, J. and Shih, C. F., "Elastic-Plastic Analysis of Combined Mode I and III Crack-Tip Fields Under Small-Scale Yielding Conditions," *Journal of Mechanics and Physics of Solids*, Vol. 38, 1990, pp. 161–181.

[11] Deuflhard, P. and Bader, G., "Multiple Shooting Techniques Revised," Technical Report 163, University of Heidelberg, Sonderforschangsbereich, 123, Heidelberg, Germany, 1982.

[12] Yuan, H. and Brocks, W., "Notes on Plastic Reloading Zone in the Asymptotic Analysis of Elastic-Plastic Crack Extension," *Archive of Applied Mechanics*, Vol. 61, 1991, pp. 471–478.

[13] Yuan, H., "A Perturbation Analysis of Dynamic Crack Growth Under Combined Mode I and III Loading Conditions," *Acta Mechanics*, in press.

Huang Yuan[1] *and Karl-Heinz Schwalbe*[1]

An Asymptotic Analysis of Static and Dynamic Crack Extension Along a Ductile Bimaterial Interface/Anti-Plane Case

REFERENCE: Yuan, H. and Schwalbe, K.-H., **"An Asymptotic Analysis of Static and Dynamic Crack Extension Along a Ductile Bimaterial Interface/Anti-Plane Case,"** *Fracture Mechanics: Twenty-Third Symposium, ASTM STP 1189,* Ravinder Chona, Ed., American Society for Testing and Materials, Philadelphia, 1993, pp. 208–226.

ABSTRACT: In the present paper, the asymptotic near-tip stress and velocity fields of a quasi-statically and dynamically growing crack under steady-state conditions along an interface between two ductile materials are presented. The ductile materials are characterized by J_2-flow theory with linear plastic hardening. Only the antiplane strain case is considered in the present paper. The linear hardening solutions are assumed to be of variable-separable form with a power-law singularity in the radial distance to the crack tip. Results are given for the singularity and for the distribution of the stress and velocity fields as functions of the hardening parameter and the crack propagation velocity. It is found that an interface between two ductile materials with large plastic hardening only slightly affects the angular distributions of stress and deformation velocity, whereas the singularity in this case is determined by both strain-hardening factors. If a crack is lies along on an interface with a small strain hardening, the singularity is dominantly determined by the lower strain-hardening material and the angular variation of stress and deformation velocity fields in the higher hardening material will be changed drastically. Differences of the elastic shear moduli will mainly influence the deformation velocity distribution, the stress variation will hardly be affected. Increasing the elastic modulus in the small strain-hardening material can slow down the appearance of the plastic reloading. The crack propagation velocity can enlarge the plastic loading zone and diminish the singularity.

KEY WORDS: asymptotic analysis, bimaterial interface, plastic linear-hardening materials, anti-plane Mode III, quasi-static crack growth, dynamic crack growth, fracture mechanics, fatigue (materials)

Interfacial crack problems are present in many important inhomogeneous materials (for example, in composite materials, cements, and in weldments) and it is often the case that such materials fail by growth and coalescence of preexisting or nucleated cracks along these interfaces. Many previous works on interfacial cracks [*1–4*] have shown that the stress and deformation fields around a stationary crack tip between two elastic-plastic materials are strongly influenced by the existing interface. Thus, one may assume that the growth of microscopic and macroscopic cracks along the interfaces can be an important factor in determining the overall strength, toughness, and reliability of such inhomogeneous materials.

Due to the analytical difficulties involved, the bulk of the research on the near-tip asymptotic field has been associated with homogeneous materials, characterized by the infinitesimal flow theory with either linear hardening or perfect plasticity for both quasi-static and dynamic

[1] Research engineer and head, respectively, Institute of Materials Research, GKSS Research Center, W-2054 Geesthacht, Germany.

crack growth problems. The successful assembly of the near-tip fields for the anti-plane shear case in a Mises elastic-perfectly plastic material was given in Ref *5* for quasi-static and in Refs *6* and *7* for dynamic crack growth. The corresponding linear-hardening problems were considered in Ref *8* for quasi-static and in Ref *10* for dynamic crack growth, and these solutions are extended to include plastic reloading in Refs *9* and *11*. All works on quasi-static and dynamic crack growth mentioned here are restricted to homogeneous materials.

Recently, quasi-static stable crack growth along an interface between an elastic material and an elastic-plastic one has been considered in Ref *12*, whereas most of the published papers on interfacial cracks deal with the stationary case, see Refs *1* through *4*. In Ref *12*, the interfacial crack-tip fields are treated as elastic-plastic crack growth under mixed-mode conditions by means of known elastic solutions, so that only one half of the crack-tip field has to be solved numerically.

The main objective of the present paper is to understand the asymptotic singular crack-tip fields of a steadily, quasi-statically, and dynamically growing anti-plane Mode III crack along an interface between two different elastic-plastic materials with linear strain hardening under steady-state conditions. Note, it is of course possible that a given crack at the interface would branch off the interface and penetrate into either material. But if the interface is assumed to be inherently weaker than both materials, then the crack would most likely propagate along the interface. This assumption is implicitly made in this work. In investigations of stationary interfacial in-plane cracks, it was shown that the near-tip asymptotic stress and deformation fields are oscillatory in nature leading to interpenetration of the crack faces, unless contact is enforced near the crack tip [*13*], whereas in the anti-plane shear mode, no stress and deformation oscillations are expected, regardless of the material behavior.

We are going to use the scheme proposed by Ref *9* and formulate the problem in terms of a system of first-order ordinary differential equations (ODEs) in the angular variations of all stress components and the anti-plane shear deformation velocity. In this work, both materials joining at the interface are assumed to be bilinear elastic-plastic. Both quasi-static and dynamic crack propagation are considered. Effects of different material parameters are investigated. The possibility of the plastic reloading on the crack flanks under the J_2-flow theory is included. We will consider only anti-plane shear mode (Mode III).

Formulation of Crack-Tip Fields

Governing Equations

Let x_i (i = 1,2,3) be a Cartesian coordinate system of fixed orientation traveling with the crack tip such that the x_3-axis coincides with the straight crack front and the x_1-axis is in the direction of crack advance. Figure 1 refers to a two-dimensional crack propagating steadily and dynamically along the interface between two ductile materials (abbreviated as Materials I and II in the following text). Let $\mathbf{e}_i$ be the unit vector corresponding to the x_i direction. Similarly, let r and ϑ be polar coordinates corresponding to x_i (i = 1,2) and $\mathbf{e}_r$, $\mathbf{e}_\vartheta$ be the corresponding unit vectors. The crack tip moves with a velocity, $\mathbf{W} = w\mathbf{e}_1$, with respect to the stationary coordinate system, X_i. In our steady-state analysis, the crack-tip velocity is constant so that the material derivative is given by

$$(\dot{\ }) \equiv \frac{d}{dt} = w\left(-\cos\vartheta\,\frac{\partial}{\partial r} + \frac{\sin\vartheta}{r}\,\frac{\partial}{\partial\vartheta}\right) \tag{1}$$

The undetermined variables under consideration are two anti-plane shear stresses, τ_r and τ_ϑ, and an antiplane shear deformation velocity component, υ_3 that are functions of the in-

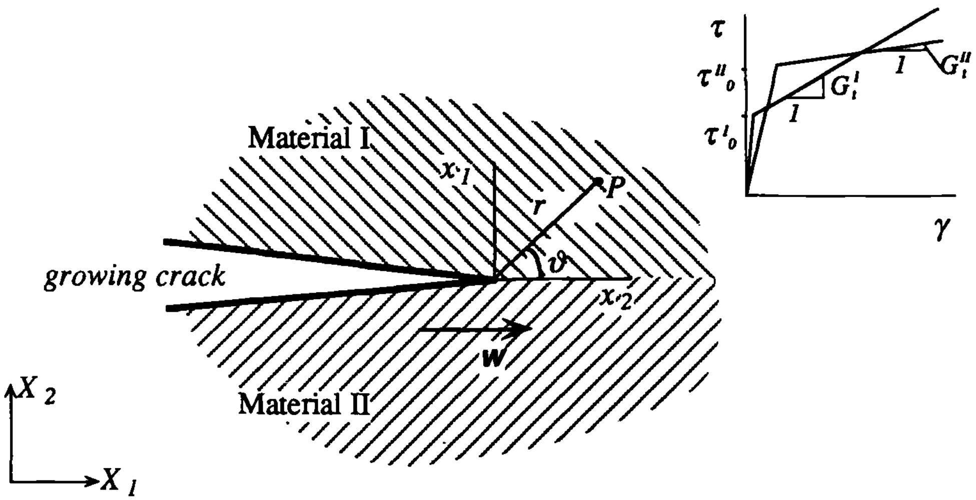

FIG. 1—*Local coordinate systems at a crack tip moving along a bimaterial interface.*

plane coordinates, x_i, only. In terms of the polar components of the stress vector, τ, and the velocity, v_3, the equation of motion requires

$$(r\tau_r)_{,r} + \tau_{\vartheta,\vartheta} = \rho\dot{v}_3 \tag{2}$$

where ρ denotes the mass density of the material considered, which takes the value of ρ^{I} for the material point in Material I or ρ^{II} in Material II.

Taking into account the strain-hardening characterized by J_2 flow theory and a bilinear effective stress-strain curve, the constitutive equations in the plastic loading zone are

$$G\dot{\gamma}_\alpha = \dot{\tau}_\alpha + (\underline{\alpha}^{-1} - 1)\tau_e^{-1}\dot{\tau}_e\tau_\alpha \qquad \alpha = r, \vartheta \tag{3}$$

where $\dot{\gamma}_\alpha$ is the engineering anti-plane shear strain-rate vector, $\dot{\tau}_\alpha$ is the shear stress-rate vector, and $\underline{\alpha}$ is either α or unity, depending on whether the given material point is in an active plastic zone or in an elastic unloading zone. Here, α is equal to $\alpha^{\mathrm{I}} = G_t^{\mathrm{I}}/G^{\mathrm{I}}$ for the material point in Material I or $\alpha^{\mathrm{II}} = G_t^{\mathrm{II}}/G^{\mathrm{II}}$ for the point in Material II, the ratio of the tangent shear modulus to the elastic shear modulus, see Fig. 1. The elastic shear modulus, G, in Eq 3 takes the value of G^{I} in Material I or G^{II} in Material II. $\tau_e = \sqrt{(\tau_r^2 + \tau_\vartheta^2)}$ is the effective stress.

It can be seen that Eqs 2 and 3 form a system with three first-order partial differential equations (PDEs) in the two stress components and the single velocity component for each material. Summarizing the equations for both materials, we have six PDEs for the whole crack-tip field. Regardless of the material behavior, all equations are homogeneous in the radial measure, r, which suggests that we may seek solutions of the form

$$\left.\begin{aligned} v_3 &= Kw\tau_0 r^s y_1^{\mathrm{I}}(\vartheta)/G^{\mathrm{I}} \\ \tau_r &= K\tau_0 r^s y_2^{\mathrm{I}}(\vartheta) \\ \tau_\vartheta &= K\tau_0 r^s y_3^{\mathrm{I}}(\vartheta) \end{aligned}\right\} \text{ for Material I} \tag{4}$$

$$\left.\begin{aligned} v_3 &= Kw\tau_0 r^s y_1^{\mathrm{II}}(\vartheta)/G^{\mathrm{II}} \\ \tau_r &= K\tau_0 r^s y_2^{\mathrm{II}}(\vartheta) \\ \tau_\vartheta &= K\tau_0 r^s y_3^{\mathrm{II}}(\vartheta) \end{aligned}\right\} \text{ for Material II} \tag{5}$$

where r is nondimensionalized with respect to some measure of the plastic zone size. K is a stress amplitude factor for the antiplane shear stresses, which cannot be determined in the present asymptotic analysis. $\tau_0 = (\tau_0^{\mathrm{I}} + \tau_0^{\mathrm{II}})/2$ denotes the mean yield stress of the two materials that will not influence the asymptotic solutions here. The single eigenvalue of the homogeneous equations, s, characterizes the singularity of the anti-plane shear stresses and the deformation velocity. Comparing with analyses of a crack tip in a homogeneous material [*8–10*], the difference is that we have a sole eigenvalue for two analogous ODE systems.

Substituting Eqs 4 and 5 into 2 and 3, along with Eq 1, results in two analogous systems of six first-order ODEs such that

$$\sum_{j=1,2,3} A_{ij}(\vartheta,y^{\mathrm{I}};M^{\mathrm{I}},s,\alpha^{\mathrm{I}}) \frac{d}{d\vartheta} y_j^{\mathrm{I}}(\vartheta) = B_i(\vartheta,y^{\mathrm{I}};M^{\mathrm{I}},s,\alpha^{\mathrm{I}}) \text{ for Material I} \tag{6}$$

$$\sum_{j=1,2,3} A_{ij}(\vartheta,y^{\mathrm{II}};M^{\mathrm{II}},s,\alpha^{\mathrm{II}}) \frac{d}{d\vartheta} y_j^{\mathrm{II}}(\vartheta) = B_i(\vartheta,y^{\mathrm{II}};M^{\mathrm{II}},s,\alpha^{\mathrm{II}}) \text{ for Material II} \tag{7}$$

$$j = 1,2,3$$

where $M^{\mathrm{I}} = w/\sqrt{(G^{\mathrm{I}}/\rho^{\mathrm{I}})}$ and $M^{\mathrm{II}} = w/\sqrt{(G^{\mathrm{II}}/\rho^{\mathrm{II}})}$ denote the Mach numbers for the dynamic crack growth in Materials I and II, respectively, which vanish for the quasi-static cases. The coefficient matrices, A_{ij}, and the coefficient vector, B_i, are analogous for different materials, which are summarized in Appendix A.

Boundary Conditions and Continuity Conditions

We imagine a material point in the crack-tip field, P, which moves along a line, L-L, with h = "constant" during crack growth, Fig. 2. Due to the steady-state condition, the point goes through the plastic loading zone and then the elastic unloading zone, and finally to the plastic reloading zone, if it exists. This corresponds to the loading history of a material particle in the crack-tip field discussed here, since the crack grows along a bimaterial interface with a constant velocity, w, and the crack-tip field does not change. It is important to note that the loading history of each material point can be described through this motion and therefore is determined only by the polar angle, ϑ, since for any given material point, h is constant. The elastic unloading occurs at ϑ_p when the effective stress-rate of the material point vanishes, or when

$$-sT(\vartheta_p) \cos \vartheta_p + T'(\vartheta_p) \sin \vartheta_p = 0 \tag{8}$$

where $(\ )' = d/d\vartheta$ and $T = (y_2^2 + y_3^2)^{1/2}$ defines the angular function of the effective stress.

In the elastic unloading zone, a material point retains the plastic strain values it had in the plastic loading zone. Thus it is expected that when the point is deep into the unloading, its associated effective stress can reach another yielding stress state, especially for some materials

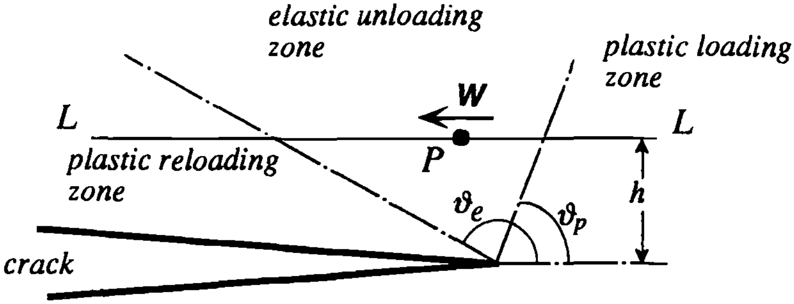

FIG. 2—*Angular sectors at the crack tip.*

with small strain hardening [*9,11*]. The plastic reloading occurs at some critical value of ϑ, ϑ_e, if the effective stress of the particle regains its previous value at unloading, that is

$$T(\vartheta_e)\sin^{-s}\vartheta_e - T(\vartheta_p)\sin^{-s}\vartheta_p = 0 \tag{9}$$

Note that the distribution of the effective stress in Materials I and II can be different; consequently, the elastic unloading angle and the plastic reloading angle can also be different in the materials. They must be independently determined for both halves of the crack-tip field according the conditions in Eqs 8 and 9.

Unlike the anti-plane strain crack-tip field in a homogeneous material in Refs *8* through *11*, the interfacial fields have no anti-plane shear symmetry ahead of the crack-tip. We can only assume that all stress components and the deformation velocity are regular as $\vartheta \rightarrow 0$. It follows that the ODE systems will be bounded if and only if the conditions

$$\begin{aligned} y_1^{\mathrm{I}}(0) + y_2^{\mathrm{I}}(0)/\alpha^{\mathrm{I}} &= 0 \\ y_1^{\mathrm{II}}(0) + y_2^{\mathrm{II}}(0)/\alpha^{\mathrm{II}} &= 0 \end{aligned} \tag{10}$$

are satisfied (see ODEs in Appendix I for more details).

As mentioned earlier, there exist no stress oscillations in the interfacial anti-plane shear mode, although it is well known for the in-plane modes [*1–4*]. Thus, as no contact zone is expected in such a case, we can simply suppose vanishing tractions on the free crack surface, which requires

$$\begin{aligned} y_3^{\mathrm{I}}(\pi) &= 0 \\ y_3^{\mathrm{II}}(\pi) &= 0 \end{aligned} \tag{11}$$

As in the analyses in homogeneous materials [*8–11*], the strength of the singularity, s, will be determined as an eigenvalue of the problem for each given material and each given crack propagation velocity. Hence, the stress amplitude factor, K, however, will be left undetermined in this asymptotic analysis. Without loss of generality in solving the eigenvalue problem, we can set

$$y_3^{\mathrm{I}}(0) = 1 \tag{12}$$

Next we need to connect the solutions in the different zones and in different materials through appropriate continuity conditions. Let [ ] denote the jump in a quantity as ϑ increases infinitesimally across such a boundary. Then it follows from equilibrium that the traction components of the shear stress must be continuous

$$[\tau_\vartheta] = 0 \tag{13}$$

and displacement fields must also be continuous

$$[u_3] = 0 \tag{14}$$

According to the analyses in Refs *14* and *15*, all stress components in elastic-plastic materials must be continuous across a moving surface. From this follows the second continuity condition for the unloading and the reloading boundary

$$[\tau_r] = 0 \tag{15}$$

Substituting Eqs 13 and 15 into the constitutive equations and combining with Eq 14, one finds that the velocity must also be continuous across the elastic unloading and the plastic reloading boundary, that is

$$[v_3] = 0 \tag{16}$$

Summarizing all conditions just mentioned, for the elastic unloading and the plastic reloading boundary, three continuity conditions are independent and they lead to continuous angular functions in each material, that is

$$[y_1] = [y_2] = [y_3] = 0 \tag{17}$$

These conditions must be satisfied along each unloading and reloading boundary.

The second set that requires the continuity of the traction stress and the displacement across the interface ahead of the crack tip, see Eqs 13 and 14, reduces to

$$\begin{aligned} y_1^{\mathrm{I}}(0^+) &= \eta y_1^{\mathrm{II}}(0^-) \\ y_3^{\mathrm{I}}(0^+) &= y_3^{\mathrm{II}}(0^-) \end{aligned} \tag{18}$$

where $\eta = G^{\mathrm{I}}/G^{\mathrm{II}}$ defines the ratio of the elastic shear moduli in the crack-tip field.

Numerical Solution Strategy

The Mode III solution for the elastic unloading zone in both quasi-static and dynamic crack growth can be deduced analytically, see Ref *16*. As a reference, both solutions are listed in Appendix II. It is to see that the elastic solutions contain generally three undetermined integration constants. To improve convergence of the numerical iteration procedure used in the present work, the elastic solutions are implemented in the numerical procedure directly. The loading plastic zones will be connected with the plastic reloading zones through the elastic solution.

Note that $y_2^{\mathrm{I}}(\vartheta)$ and $y_2^{\mathrm{II}}(\vartheta)$ get singular solutions near $\vartheta = \pi$ in the form $(\sin \vartheta)^s$ with $s < 0$. To overcome the consequent numerical difficulties in integration, the corresponding "sine-" function is set to approach a very small finite value for $\vartheta \rightarrow \pi$. Since all other variables are well behaved near the crack flanks, this approximation yields very fine results.

We have to solve two ODE systems subject to boundary conditions and continuity conditions as discussed earlier. The boundary value problems are solved by the shooting techniques making use of a semi-implicit extrapolation integrator. As discussed in Ref *12* for a combination of an elastic material with a plastic one, we have only one variable to be assumed in the beginning; the eigenvalue will be assumed such that the boundary condition at the free crack flank is satisfied. Using the elastic solution provided in Appendix II, one can find that the boundary values for the combination of an elastic material ($\alpha^{I} = 1$) and a plastic one are

$$\begin{aligned} y_1(0^-) &= -\frac{\eta}{(1 - M^2)}\cot(s\pi) \\ y_2(0^-) &= \frac{\eta\alpha^{II}}{(1 - M^2)}\cot(s\pi) \\ y_3(0^-) &= 1 \end{aligned} \tag{19}$$

Thus one guesses the value of s for given α^{II}, M^{II}, and η, and hence determine the initial values of $y(\vartheta)$ for $0 < \vartheta \leq \pi$, checking to determine when unloading and reloading occur in order to make use of the appropriate value of α^{II}. Once one has angular values at $\vartheta = \pi$, one checks whether $y_3^{II}(\pi)$ is zero, and iterates in his guess for s until convergence is achieved by means of an appropriate numerical scheme.

For cases in which the crack-tip field consists of two elastic-plastic materials, by means of continuity conditions discussed earlier, one has two variables to be assumed at the beginning, the eigenvalue, s, and the angular velocity, $y^{I}(0)$. Making use of Eqs 10, 12, and 18, one has

$$\begin{aligned} y_2^{I}(0) &= -y_1^{I}(0)/\alpha^{I} \\ y_3^{I}(0) &= 1 \\ y_1^{II}(0) &= y_1^{I}(0)/\eta \\ y_2^{II}(0) &= y_1^{II}(0)/\alpha^{II} \\ y_3^{II}(0) &= 1 \end{aligned} \tag{20}$$

One can take an analogous technique discussed earlier for the elastic/elastic-plastic interface to solve the cases with two elastic-plastic materials. Here, one must guess two initial values.

It is worth mentioning that the case of an interface on a rigid border, that is, $\eta = 0$, corresponds exactly to the case of crack propagation in a homogeneous linear hardening material. This is due to the anti-symmetries ahead of the crack tip in the Mode III problem. Based on this reason, our further discussions are restricted to two elastic-plastic materials or an elastic-plastic material combined with an elastic one. The latter has been discussed in Ref *12* for quasi-static crack propagation.

Results for Quasi-Static Crack Propagation

Our numerical solutions for an interfacial crack between an elastic material and a plastic one for quasi-static crack growth along an interface have confirmed results in Ref *12*. The numerical solution procedure shows rapid convergence in iterations. In the present paper, two groups of numerical results will be discussed. We set the strain-hardening factor of Material II in the interfacial crack-tip field, see Fig. 1, equal to $\alpha^{II} = 0.5$ for a large strain-hardening case and $\alpha^{II} = 0.01$ for a small strain-hardening case. Furthermore, we consider the influences of the difference of the elastic shear modulus: $\eta = 0.2$, $\eta = 1$, and $\eta = 5$. The shear stress singularity, s, and the elastic unloading and reloading angles, ϑ_p and ϑ_e, are summarized in Tables 1 and 2, correspondingly.

In cases with $\alpha^{II} = 0.5$, the stress singularity distribution is affected only if α^{I} is larger than

TABLE 1—*Strength of the singularity, unloading, and reloading angles versus hardening in quasi-static crack growth with α^{II} = 0.5.*

	$\eta = 0.2$				$\eta = 1$				$\eta = 5$		
α^I	$-s$	ϑ_p^I	ϑ_e^I	ϑ_p^{II}	$-s$	ϑ_p^I	ϑ_e^I	ϑ_p^{II}	$-s$	ϑ_p^I	ϑ_p^{II}
1.0	0.4777	90	...	−88.339	0.4393	90	...	−86.486	0.40794	90	−85.007
0.75	0.4431	87.535	...	−86.670	0.4218	87.099	...	−85.656	0.4008	86.741	−84.779
0.67	0.4296	86.637	...	−86.023	0.4145	86.217	...	−85.314	0.4008	85.850	−84.678
0.50	0.3944	84.385	...	−84.385	0.3944	84.385	...	−84.385	0.3944	84.385	−84.385
0.30	0.3344	80.461	...	−81.792	0.3550	81.952	...	−82.644	0.3799	83.751	−83.729
0.20	0.2893	77.236	...	−80.153	0.3204	80.081	...	−81.249	0.3644	84.005	−83.048
0.10	0.2207	71.574	...	−78.614	0.2588	76.310	...	−79.287	0.3282	84.291	−81.546
0.05	0.1649	66.020	...	−78.819	0.2005	71.828	...	−78.497	0.2803	83.212	−79.873
0.01	0.0798	54.955	179.96	−82.971	0.1007	61.126	179.99	−81.504	0.1599	75.389	−78.925
0.005	0.0577	51.200	179.93	−84.777	0.0731	57.144	179.97	−83.494	0.1188	71.222	−80.456
0.001	0.0267	44.660	179.86	−87.560	...	...	...	...	...	...	...

or nearly equal to α^{II} and, in the small hardening region ($\alpha^I \ll \alpha^{II}$), the singularity is determined mainly by the smaller hardening factor, α^I. It is observed, as pointed out in asymptotic analyses in homogeneous materials in Refs *8* and *9*, that $-s$ is approximately proportional to $\alpha^{1/2}$, Fig. 3, where the strength of the singularity versus the square root of the hardening parameter is plotted. The variation of the ratio of elastic shear moduli (η = 0.2) leads to deviation of the distribution of singularity. Whereas $\eta > 1$ for $\alpha^I < \alpha^{II}$ yields a stronger stress singularity, $\eta < 1$ leads to reduction of the singularity compared to the uniform elastic shear modulus cases. Similar behaviors can also be observed in the distribution of the elastic unloading angle for these two series of results. Both series show more obvious deviation from the homogeneous material analysis in the combination with weaker strain-hardening materials ($\alpha^I < \alpha^{II}$) than with stiffer materials ($\alpha^I \geq \alpha^{II}$). The interface enlarges the plastic loading zone in both series and slows down the appearance of the plastic reloading near to the crack flanks.

The shear stress singularity is dramatically changed by Material II with a small strain-hardening Table 2. The strength of the singularity is determined primarily by the smaller strain-hardening material alone. The variation of the ratio of the elastic shear moduli changes the singularity further. The distribution of the singularity has a feature similar to that in Table 1. It is interesting to see that the singularity attains a maximum value near the elastic limit case,

TABLE 2—*Strength of the singularity, unloading, and reloading angles versus hardening in quasi-static crack growth with α^{II} = 0.01.*

	$\eta = 1$					$\eta = 5$				
α^I	$-s$	ϑ_p^I	ϑ_e^I	ϑ_p^{II}	ϑ_e^{II}	$-s$	ϑ_p^I	ϑ_e^I	ϑ_p^{II}	ϑ_e^{II}
1.0	0.09937	90	...	−60.761	−179.990	0.07933	90	...	−54.801	−179.961
0.75	0.10018	87.138	...	−60.988	−179.990	0.07960	87.671	...	−54.883	−179.961
0.67	0.10040	85.768	...	−61.050	−179.989	0.07968	86.548	...	−54.909	−179.961
0.50	0.10067	81.504	...	−61.126	−179.990	0.07983	82.971	...	−54.955	−179.962
0.30	0.10011	72.071	...	−60.971	−179.990	0.07981	74.241	...	−54.951	−179.962
0.20	0.09900	64.556	...	−60.656	−179.989	0.07959	65.980	179.997	−54.880	−179.961
0.10	0.09638	56.261	179.972	−59.909	−179.987	0.07901	55.963	179.963	−54.700	−179.960
0.05	0.09251	53.271	179.954	−58.789	−179.982	0.07822	50.867	179.933	−54.452	−179.958
0.01	0.07325	52.874	179.947	−52.874	−179.947	0.07325	52.874	179.947	−52.874	−179.947
0.005	0.06043	48.643	179.908	−52.308	−179.940	0.06805	55.264	179.961	−51.182	−179.932
0.001	0.03205	48.646	179.903	−38.922	−179.795	...	...	...	...	...

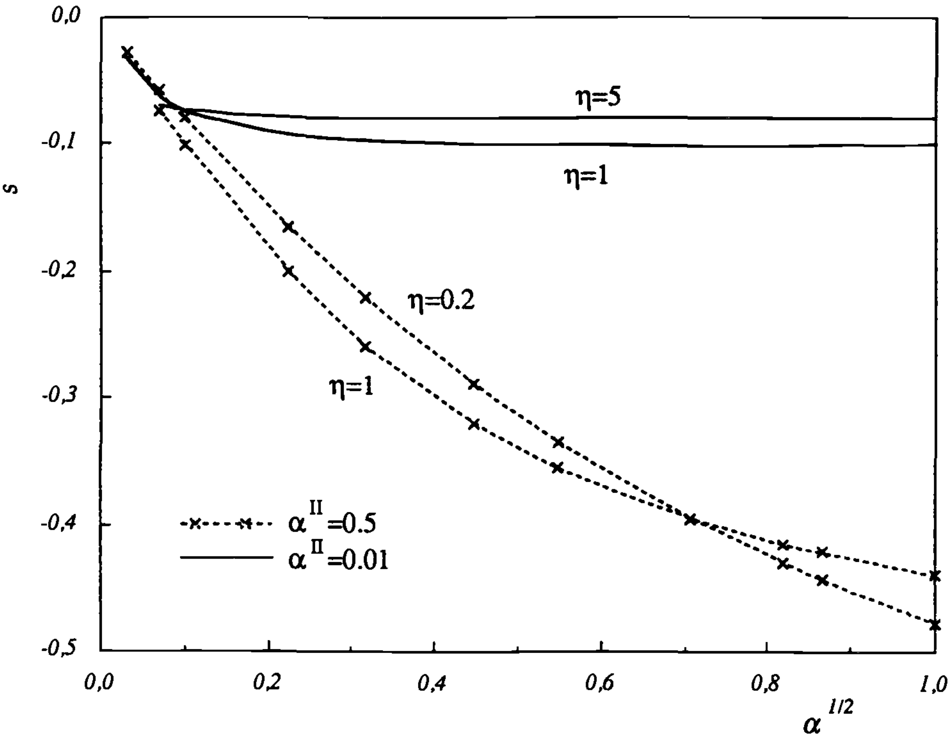

FIG. 3—*Strength of the singularity as a function of the strain-hardening factor in quasi-static crack propagation.*

but not in the elastic material, which have not been observed anywhere else. The elastic unloading angle in Material I is reduced due to a smaller elastic shear modulus of Material II and an increment of the elastic modulus results in an enlarged unloading angle. The combination with a small hardening material enforces a larger plastic reloading zone. Whereas the reloading occurs only for $\alpha \leq 0.05$ in homogeneous crack-tip fields, in the interfacial analysis with $\alpha^{II} = 0.01$, the material point will undergo plastic reloading if $\alpha^{I} \leq 0.1$ for $\eta = 1$ and even if $\alpha^{I} \leq 0.2$ for $\eta = 5$.

As a consequence of the continuity conditions in Eq 18, the shear stress component, τ_r, loses it continuity across the interface, Fig. 4. Actually, if one summarizes the continuity condition, Eq 18, and the boundary conditions ahead of the crack tip, it follows

$$y_2^{I}(0^+) - y_2^{II}(0^-) = (\alpha^{I} - \alpha^{II}/\eta)y_1^{I}(0^+) \tag{21}$$

It is to show that $y_1^{I}(0^+)$ vanishes only in homogeneous materials, that is, in crack extension along an interface the discontinuity of the stress component τ_r, is not avoidable.

Figure 4 shows the angular distribution of shear stresses and deformation velocity around the crack tip; herein, the velocity angular function, $y_1(\vartheta)$, is multiplied by the corresponding singularity, s, so that the velocity angular variation remains bounded as $\alpha \rightarrow 0$, as suggested in Ref 9. To study the effects of the interface, the solution of a homogeneous material with $\alpha = 0.005$ is also plotted in the figure. It can be seen that in the material with $\alpha = 0.005$ stress and velocity distributions are almost unchanged by the existence of the interface. The stress

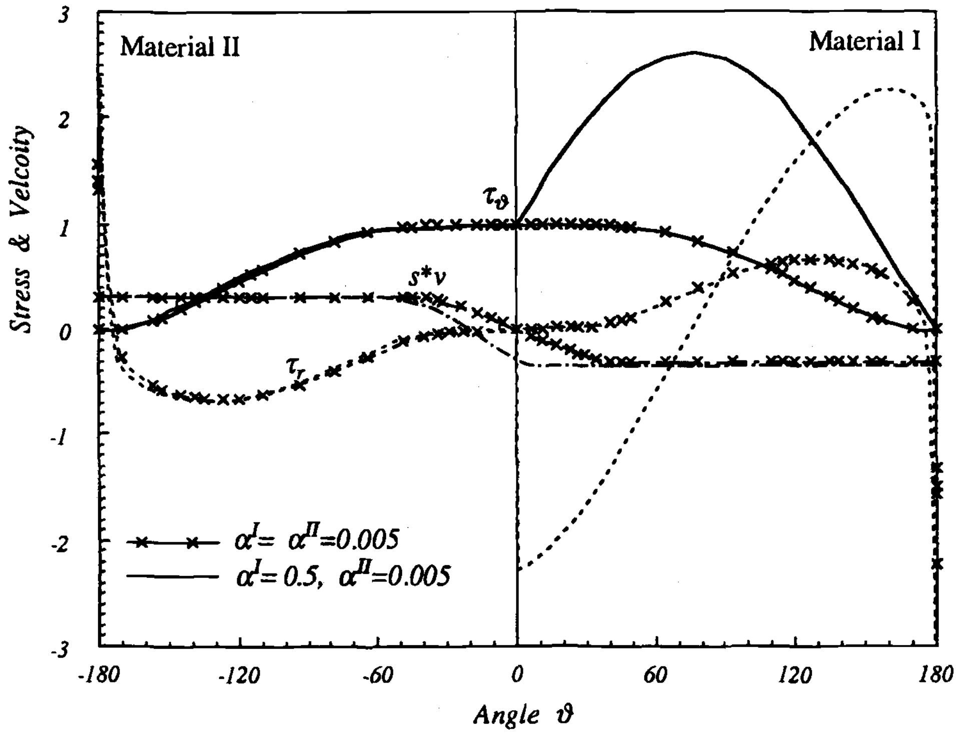

FIG. 4—*Angular variation of the stress and deformation velocity fields in quasi-static crack extension with* $\alpha^I = 0.5$, $\alpha^{II} = 0.005$, *and* $\eta = 1$.

level ahead of the crack tip approaches a flat distribution and a tiny reloading zone appears on the crack flank. In the other material, however, the angular stress functions show a totally different behavior as compared to a homogeneous material, whereas the velocity distribution is only slightly affected by the interface. The angular variation of stress and velocity fields around an interfacial crack in two large hardening materials is shown in Fig. 5. Only a very slight difference from the homogeneous solution can be seen. The interface between two large strain-hardening materials yields little contribution to the angular distribution. Influences of the ratio of elastic shear moduli on the angular variation, η, are shown in Fig. 6, where results for an interfacial crack between an intermediate ($\alpha^I = 0.1$) and a small strain-hardening material ($\alpha^{II} = 0.01$) are plotted. It is confirmed that the η yields a large variation in velocity distribution, but not in stresses. Changes of stress distribution are much more strongly dependent on the difference of two plastic hardening factors than that of elastic shear moduli. This feature can also be seen in Fig. 5 where the variation of the velocity distribution is not so obvious due to large strain hardening.

Variations of the effective stress of a material point in the crack-tip field are shown in Fig. 7, which shows the effective stress distribution along a horizontal line with fixed $x_2 = h$, see Fig. 2. The positive and the negative polar angle denotes Materials I and II of the tip field, respectively. One can simultaneously find influences of material parameters assumed on the singularity and the angular functions. Similar to Fig. 4, the stress variation in Material I (α^I = 0.5) shows a large deviation from that in Material II. Interesting to note is that the stress variation in Material II ($\alpha^{II} = 0.005$) also shows a clear difference from the homogeneous solution

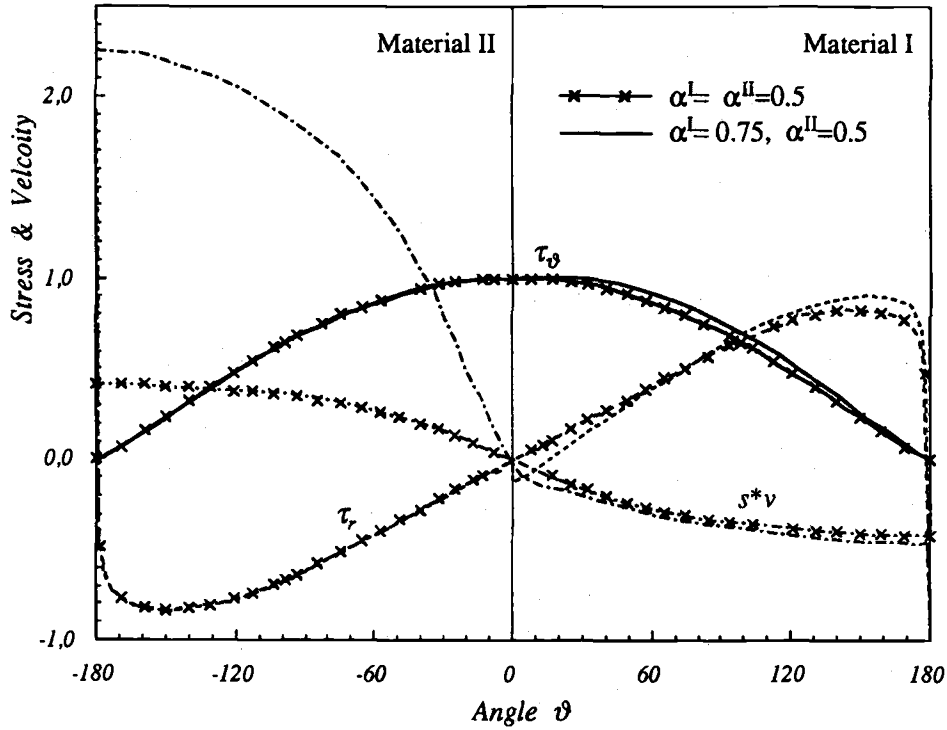

FIG. 5—*Angular variation of the stress and deformation velocity fields in quasi-static crack extension with* $\eta = 0.2$.

due to different strengths of the singularity, whereas in Fig. 4, nearly no difference between them can be recognized. Again, for large strain-hardening materials, the interface brings only a slight influence on the stress distribution.

Results for Dynamic Crack Propagation

In our numerical investigations, we can simply set the Mach number in the ODE system for dynamic crack propagation to zero, in order to obtain the quasi-static solution. Thus, in the anti-plane shear mode of the present work, there is no problem with evaluating the dynamic solution due to the decrease of the crack propagation velocity. It is also observed that the dynamic solutions are numerically more difficult to obtain than the static ones, especially for cases with very small strain-hardening factors. The solution procedure is very sensitive to the initial input values. We use simply the static solutions as initial values for the dynamic cases and let the crack propagation velocity increase. With $\alpha^{I} = \alpha^{II}$ and $\eta = 1$, we have a crack-tip field problem in a homogeneous material. The solution for homogeneous materials in Ref *11* is confirmed in the present work. Similar to analysis of quasi-static crack cases discussed earlier, we set the strain-hardening factor, $\alpha^{II} = 0.5$, for the large strain-hardening case and $\alpha^{II} = 0.05$ for the small strain-hardening case. Furthermore, we consider the influences of the difference of the elastic shear moduli and the Mach number. The shear stress singularity, s, and the elastic unloading and reloading angles, ϑ_p and ϑ_e, are summarized in Tables 3 and 4, correspondingly.

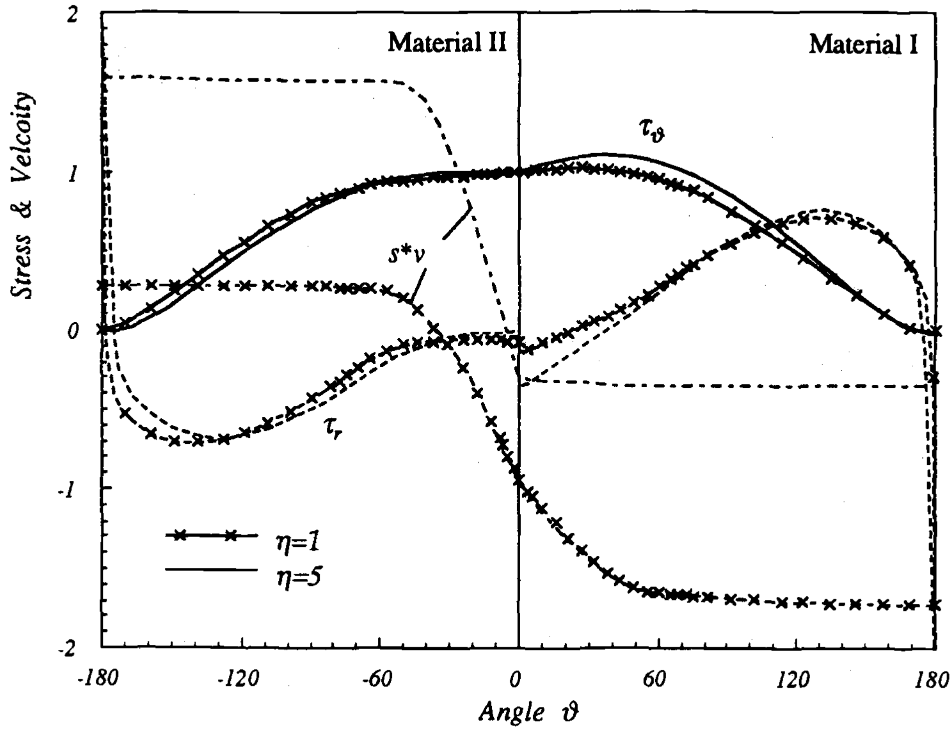

FIG. 6—*Angular variation of the stress and deformation velocity fields in quasi-static crack extension with $\alpha^I = 0.1$ and $\alpha^{II} = 0.01$.*

Similar to the quasi-static cases, for $\alpha^{II} = 0.5$, the stress singularity ahead of the crack tip is determined by both hardening factors if α^I is larger than or nearly equal to α^{II}. For $\alpha^I \ll \alpha^{II}$, the singularity is mainly determined by α^I alone. Figure 8 shows that the variation of singularity with $\alpha^{1/2}$ is affected by both the elastic shear moduli and the Mach number, wherein the different Mach number for a crack growth process is caused by distinct mass densities and distinct elastic moduli. Increasing the Mach number will weaken the stress singularity, whereas

TABLE 3—*Strength of the singularity, unloading, and reloading angles versus hardening in dynamic crack growth with $\alpha^{II} = 0.5$.*

	$\eta = 1, M^I = M^{II} = 0.1$				$\eta = 1, M^I = M^{II} = 0.3$				$\eta = 5, M^I = 0.02, M^{II} = 0.1$		
α^I	$-s$	ϑ_p^I	ϑ_e^I	ϑ_p^{II}	$-s$	ϑ_p^I	ϑ_e^I	ϑ_p^{II}	$-s$	ϑ_p^I	ϑ_p^{II}
1.0	0.4393	90.00	...	−86.49	0.4307	92.47	...	−89.13	0.4077	91.086	−85.31
0.75	0.4214	87.39	...	−85.95	0.4178	89.67	...	−88.30	0.4025	87.920	−85.08
0.67	0.4141	86.510	...	−85.61	0.4102	88.81	...	−87.97	0.4003	87.053	−84.97
0.50	0.3939	84.683	...	−84.68	0.3891	87.04	...	−87.04	0.3936	85.636	−84.67
0.30	0.3543	82.263	....	−82.94	0.3472	84.73	...	−85.28	0.3785	85.072	−83.99
0.20	0.3194	80.408	...	−81.55	0.3098	83.02	...	−83.85	0.3621	85.403	−83.28
0.10	0.2571	76.084	...	−79.58	0.2394	79.87	...	−81.81	0.3229	85.988	−81.68
0.05	0.1977	72.300	180.00	−78.81	0.1661	77.461	180.00	−81.11	0.2681	85.791	−79.86
0.01	0.0919	63.05	179.99	−82.29	...	...	...	...	...	...	...

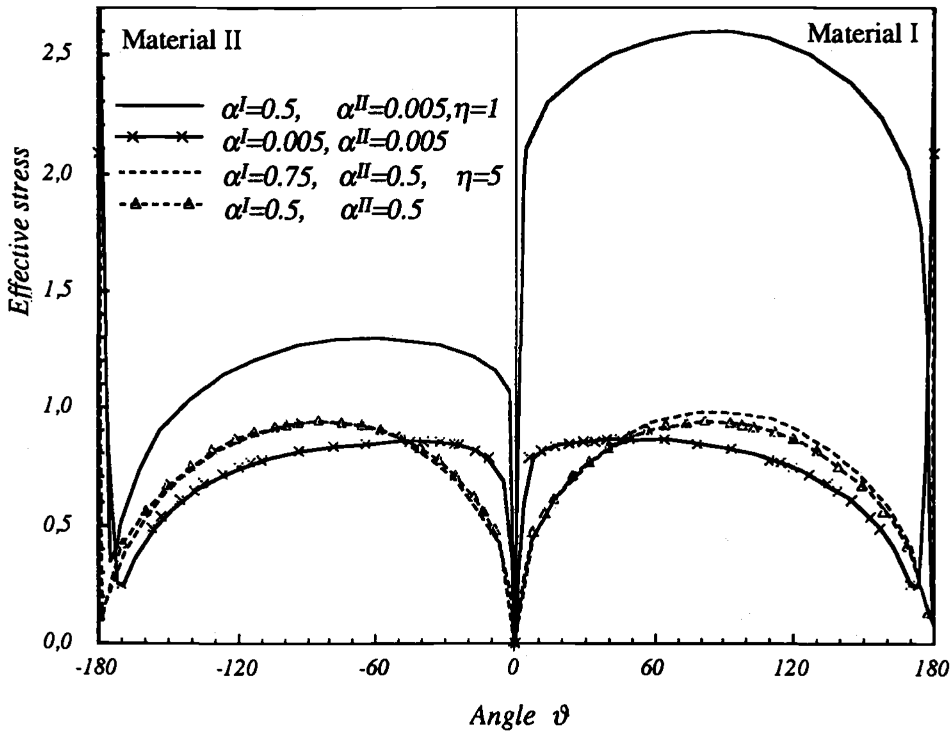

FIG. 7—*Variation of the effective stress of a material particle (x_2 fixed) in quasi-static crack extension.*

variations of η cannot change the singularity distribution uniformly, as pointed out in the quasi-static analysis. The series with $\eta = 5$, $M^I = 0.2$, and $M^{II} = 0.1$ in Table 3 confirms this prediction further. Generally, one can also find that the crack propagation velocity can enlarge the plastic loading zone and increase the elastic unloading angle, as observed in solutions for homogeneous materials [*11*]. It is interesting to note that the crack propagation velocity does not change the plastic reloading behavior, and increasing the elastic shear modulus will slow down the plastic reloading, which can also be seen in Table 4.

Table 4 shows results of the numerical analysis for an interface combined with a small

TABLE 4—*Strength of the singularity, unloading, and reloading angles versus hardening in dynamic crack growth with α^{II} = 0.05.*

	$\eta = 1, M^I = M^{II} = 0.1$					$\eta = 5, M^I = 0.2, M^{II} = 0.1$				
α^I	$-s$	ϑ_p^I	ϑ_e^I	ϑ_p^{II}	ϑ_e^{II}	$-s$	ϑ_p^I	ϑ_e^I	ϑ_p^{II}	ϑ_e^{II}
1.0	0.2012	90.168	...	−72.85	...	0.3039	90.917	...	−87.075	...
0.75	0.2005	85.642	...	−72.738	−180.000	0.29455	86.451	....	−85.925	...
0.67	0.19993	83.735	...	−72.646	−180.000	0.29029	84.831	...	−85.393	...
0.50	0.19774	78.812	...	−72.300	−180.000	0.27804	81.144	...	−83.831	...
0.30	0.19203	71.871	180.000	−71.390	−179.999	0.25319	76.420	...	−80.511	...
0.20	0.18592	68.500	179.999	−70.402	−179.999	0.23065	73.687	...	−77.310	...
0.10	0.17136	65.744	179.999	−67.991	−179.999	0.18778	69.754	180.000	−70.703	−180.00
0.05	0.15049	64.405	179.906	−64.405	−179.906	0.15297	63.979	179.999	−63.979	−179.999

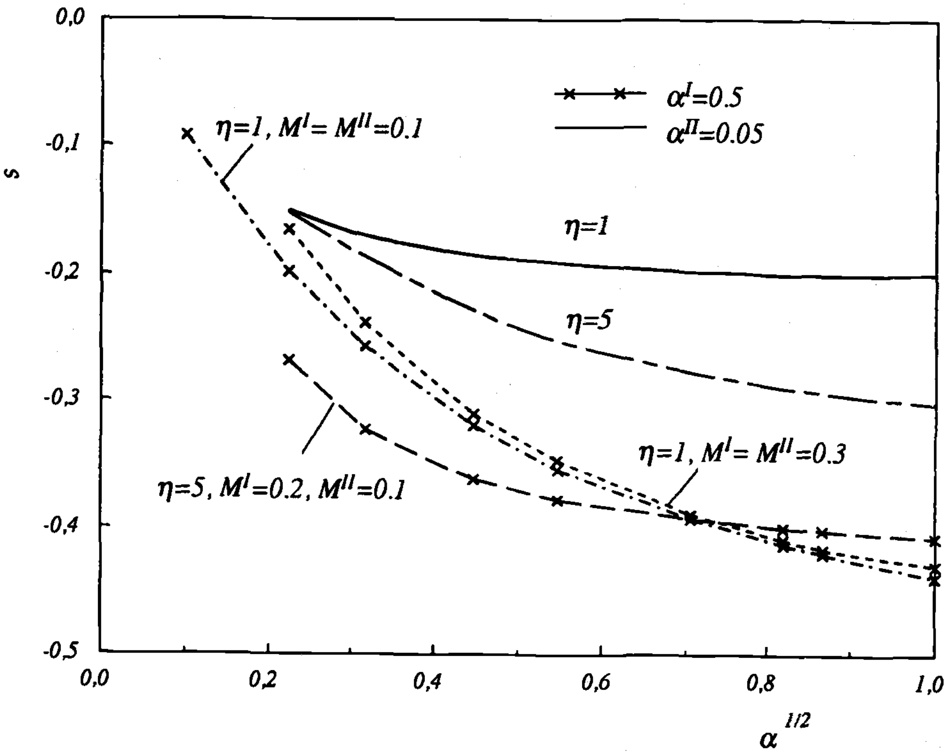

FIG. 8—*Strength of the singularity as a function of the strain-hardening factor in dynamic crack propagation.*

strain-hardening Material II. As in the quasi-static analysis, small α^{II} results in great differences of the singularity distribution versus $\alpha^{1/2}$, see Fig. 8. The strength of the singularity is almost exclusively determined by the smaller strain-hardening material alone. Increasing the crack velocity and changes of the elastic shear moduli affect the variation of the singularity more clearly than in Table 3. Comparing the two series of numerical results, one can see that increasing the elastic shear modulus in the material with less strain-hardening will diminish the plastic reloading zone, and an increase of the stress singularity can also occur.

A similar behavior as plotted in Figs. 4 and 5 is also observed in the dynamic analysis, that is, the large strain-hardening materials produce only slight deviations in the angular variation of stress and deformation velocity fields, but can cause large variations in an interface with a small hardening material. Figure 9 shows the effects of the crack propagation velocity on the angular variation of the stress and deformation velocity field. Due to the large difference between the two strain-hardening factors, the discontinuity of the stress component, τ_{rr}, is very large, as pointed out in Eq 21, the discontinuity of the stress is linearly proportional to the difference of the two hardening factors. Figure 9 displays only a slight deviation due to different crack extension velocities. Effects of different elastic shear moduli on the dynamic solution of two intermediate hardening materials are plotted in Fig. 10. It is confirmed that only the deformation velocity shows a large sensitivity to the crack velocity, as pointed out in the corresponding quasi-static analysis in Fig. 6. The angular stress functions are nearly independent of the increment, though the stress singularity is obviously changed. That means the stress distribu-

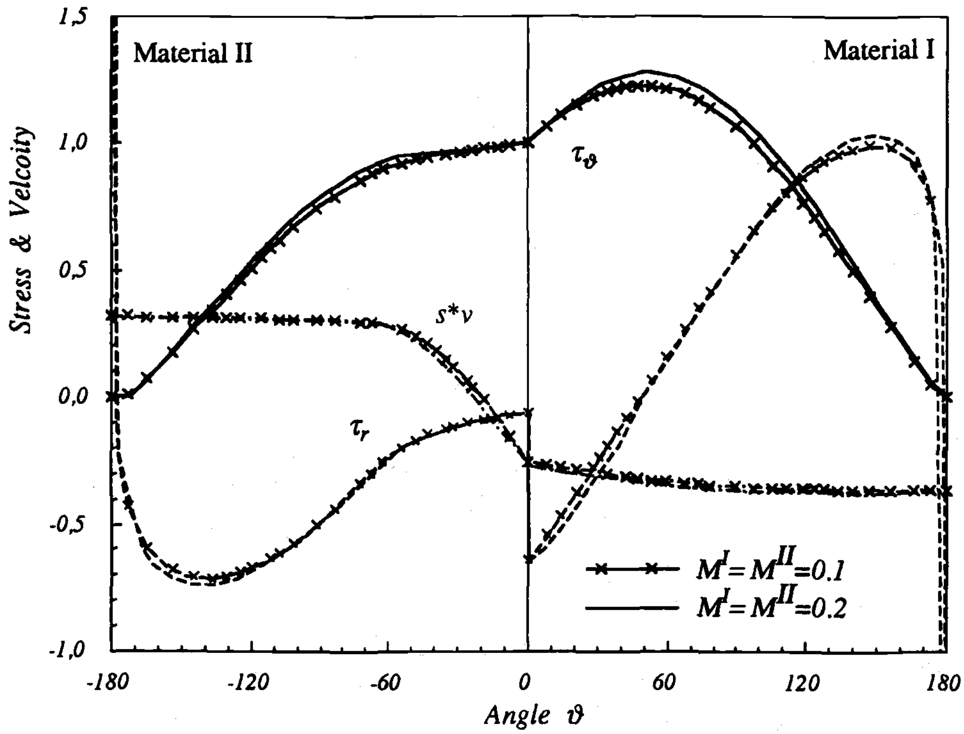

FIG. 9—*Angular variation of the stress deformation velocity fields in dynamic crack extension with* $\alpha^I = 0.5$, $\alpha^{II} = 0.05$, *and* $\eta = 1$.

tions of a material point in these two crack-tip fields can be quite different, although their angular functions are rather similar; the corresponding static behavior is shown in Fig. 7.

Discussion and Conclusions

In the present paper, the asymptotic near-tip stress and velocity fields of a quasi-statically or dynamically growing crack under steady-state conditions along an interface between two ductile materials are presented. The ductile materials are characterized by J_2-flow theory with linear hardening. Only the anti-plane strain case is considered in the present paper. The linear-hardening solutions are assumed to be of variable-separable form with a power-law singularity in the radial distance from the crack tip.

Analyses of both quasi-static and dynamic crack extensions show, for an interface with two very different hardening materials, that the stress singularity is mainly determined by the smaller hardening material, and the angular variation of stress and deformation velocity fields in the material with a smaller strain-hardening factor will be slightly changed; but in the material with a large hardening factor, the stress distributions can be changed drastically. For the interface with two similar strain-hardening factors, the stress singularity is affected by the properties of both materials, and the angular variation is close to that of the homogeneous material solution.

The difference in the elastic shear moduli can cause large variations in the deformation velocity distribution, whereas the angular stress function is hardly affected by this difference.

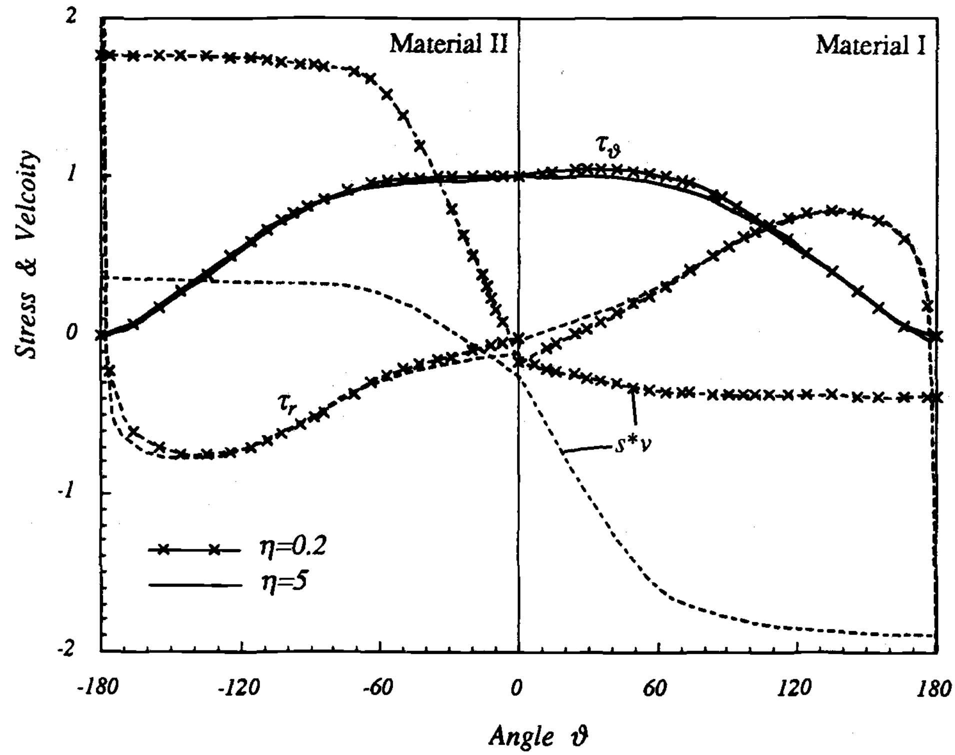

FIG. 10—*Angular variation of the stress and deformation velocity fields in dynamic crack extension with* $\alpha^I = 0.2$, $\alpha^{II} = 0.1$, *and* $M^I = M^{II} = 0.3$.

Changes of the elastic shear moduli, however, can result in different stress singularities and, consequently, the stress state of a material point in the crack-tip field will be changed. Increasing the elastic modulus in the material with less strain hardening can decrease plastic reloading.

In dynamic propagation problems, the crack velocity can change the variation of the stress singularity much more clearly than the angular distribution of the stress and deformation velocity. Increasing the crack velocity will diminish the stress singularity and enlarge the plastic loading zone ahead of the crack tip.

APPENDIX I

The Governing Ordinary Differential Equations

To simplify the terminology in formulations of the governing equations, we omit the indices for Materials I and II. Actually, the equation forms for the upper and the lower material are the same. One needs only to substitute the correspondent material parameters into the equations.

The homogeneous ODEs can be written generally as follows

$$\sum_{i=1,2,3} A_{ij}(\vartheta,y;M,s,\alpha)y_j(\vartheta) = B_i(\vartheta,y;M,s,\alpha) \qquad i = 1,2,3 \tag{22}$$

where A_{ij} and $B_i = 1,2,3$ are coefficient matrices that will be defined in the following text. We suppose that all matrix components undefined in the following text are equal to zero.

Dynamic Crack Propagation

$$A_{11} = \kappa\left(\frac{M}{T}\right)^2 y_2 y_3 \sin^2\vartheta \qquad A_{12} = \left(1 + \frac{\kappa y_2^2}{T^2}\right)\sin\vartheta$$

$$A_{21} = M^2\left(1 + \frac{\kappa y_3^2}{T^2}\right)\sin^2\vartheta - 1 \qquad A_{22} = \kappa\frac{y_2 y_3}{T^2}\sin\vartheta$$

$$A_{31} = M^2\sin\vartheta \qquad A_{33} = 1$$

$$B_1 = sy_1 + s(1+\kappa)y_2\cos\vartheta + \left(1 + (1+s)\frac{\kappa y_2^2}{T^2}\right)y_3\sin\vartheta + M^2\frac{\kappa s y_1 y_2 y_3}{T^2}\cos\vartheta\sin\vartheta$$

$$B_2 = s(1+\kappa)y_3\cos\vartheta - y_2\sin\vartheta + \left(1 + \frac{\kappa y_3^2}{T^2}\right)(M^2 s y_1\cos\vartheta + (s+1)y_2)\sin\vartheta$$

$$B_3 = -(1+s)y_2 - M^2 s y_1\cos\vartheta$$

where $\kappa = (1/\alpha - 1)$.

Quasi-Static Crack Propagation

$$A_{12} = \left(1 + \frac{\kappa y_2^2}{T^2}\right)\sin\vartheta \qquad A_{21} = -1$$

$$A_{22} = \kappa\frac{y_2 y_3}{T^2}\sin\vartheta \qquad A_{33} = 1$$

$$B_1 = sy_1 + s(1+\kappa)y_2\cos\vartheta + \left(1 + (1+s)\frac{\kappa y_2^2}{T^2}\right)y_3\sin\vartheta$$

$$B_2 = s(1+\kappa)y_3\cos\vartheta - y_2\sin\vartheta + (s+1)\left(1 + \frac{\kappa y_3^2}{T^2}\right)y_2\sin\vartheta$$

$$B_3 = -(1+s)y_2$$

APPENDIX II

Solution of Elastic Unloading Zone

To simplify the terminology in deductions of the solutions for the elastic unloading zone, we omit the indices for Materials I and II. Actually, the solutions are valid for both elastic unloading zones in the upper and the lower material. One needs only to substitute the corresponding material parameters into the equations.

Dynamic Crack Propagation

The Mode III solution for the elastic unloading zone in the dynamic crack propagation case follows from a slight generalization of Achenbach and Bazant [*15*]. It is possible to derive a solution of the form

$$u_3(r, \vartheta) = K\tau_0 r^{s+1}\tilde{u}(M, \vartheta)/G \tag{23}$$

where $M = w/(G/\rho)^{1/2}$ denotes the Mach number due to dynamic crack extension and the angular deformation, $\tilde{u}(M, \vartheta)$, may be written as [15]

$$\tilde{u}(M, \vartheta) = (1 - M^2 \sin^2 \vartheta)^{(s+1)/2}[A \sin\{(s + 1)(\omega - \pi)\} + B \cos\{(s + 1)(\omega - \pi)\}] \tag{24}$$

with

$$\tan \omega = (1 - M^2)^{1/2} \tan \vartheta \tag{25}$$

where $0 \leq \omega \leq \pi$ if $0 \leq \vartheta \leq \pi$ and $0 \geq \omega \geq -\pi$ if $0 \geq \vartheta \geq -\pi$. In Eq 24, A and B are two integration constants that will be determined by the boundary conditions or the continuity conditions. Comparing with Eqs 4 and 5, if the displacement velocity in the elastic unloading zone is defined as

$$\dot{u}_3 \equiv v_3 = Kw\tau_0 r^s y_1(M, \vartheta)/G \tag{26}$$

then follows from Eqs 23 and 24

$$y_1 = -(s + 1)\tilde{u} \cos \vartheta + \tilde{u}' \sin \vartheta \tag{27}$$

Substituting Eq 23 into the constitutive equations (Eq 3), in which the plastic dissipation vanishes, we have

$$\begin{aligned} y_2 &= (s + 1)\tilde{u} - C \sin^s \vartheta \cos \vartheta \\ y_3 &= \tilde{u}' + C \sin^{s+1} \vartheta \end{aligned} \tag{28}$$

where C is the third integration constant to be determined.

Quasi-Static Crack Propagation

In a similar way, one can formulate the quasi-static solution for the elastic unloading zone. The solution can be written explicitly

$$\begin{aligned} y_1 &= -A \cos s\vartheta - B \sin s\vartheta \\ y_2 &= A \cos(s + 1)\vartheta + B \sin(s + 1)\vartheta - C \sin^s \vartheta \cos \vartheta \\ y_3 &= -A \sin(s + 1)\vartheta + B \cos(s + 1)\vartheta + C \sin^{s+1} \vartheta \end{aligned} \tag{29}$$

Similar to the dynamic solutions, the integration constants, A, B, and C, must be determined by the boundary conditions or the continuity conditions.

References

[1] Willis, J. R., "Fracture Mechanics of Interfacial Cracks," *Journal of Mechanics and Physics of Solids*, Vol. 19, 1971, pp. 353–368.

[2] Shih, C. F. and Asaro, R. J., "Elastic-Plastic Analysis of Cracks on Bimaterial Interfaces: Part I—Small Scale Yielding," *Journal of Applied Mechanics*, Vol. 55, 1988, pp. 299–316.

[3] Shih, C. F. and Asaro, R. J., "Elastic-Plastic Analysis of Cracks on Bimaterial Interfaces: Part II—Structure of Small-Scale Yielding Fields," *Journal of Applied Mechanics*, Vol. 56, 1989, pp. 763–779.

[4] Shih, C. F. and Asaro, R. J., "Elastic-Plastic and Asymptotic Fields of Interface Cracks," *International Journal of Fracture*, Vol. 42, 1990, pp. 101–116.

[5] Chitaley, A. D. and McClintock, F. A., "Elastic-Plastic Mechanics of Steady Crack Growth under Anti-Plane Shear," *Journal of Mechanics and Physics of Solids*, Vol. 19, 1971, pp. 147–163.

[6] Achenbach, J. D. and Dunayevsky, V., "Fields Near a Rapidly Propagating Crack Tip in an Elastic-Perfectly Plastic Material," *Journal of Mechanics and Physics of Solids*, Vol. 29, 1981, pp. 283–303.
[7] Gao, Y. C. and Nemat-Nasser, S. "Dynamic Fields Near a Crack Tip Growing in an Elastic-Perfectly Plastic Solid," *Mechanics of Materials*, Vol. 2, 1983, pp. 47–60.
[8] Amazigo, J. C. and Hutchinson, J. W., "Crack Tip Fields in Steady Crack-Growth with Linear Strain-Hardening," *Journal of Mechanics and Physics of Solids*, Vol. 25, 1977, pp. 81–97.
[9] Ponte Castañeda, P., "Asymptotic Fields in Steady Crack Growth with Linear Strain Hardening," *Journal of Mechanics and Physics of Solids*, Vol. 35, 1987, pp. 227–268.
[10] Achenbach, J. D., Kanninen, M. F., and Popelar, C. H., "Crack Tip Fields for Fast Fracture of an Elastic-Plastic Material," *Journal of Mechanics and Physics of Solids*, Vol. 29, 1981, pp. 211–225.
[11] Östlund, S. and Gundmundson, P., "Asymptotic Crack Tip Fields for Dynamic Fracture of Linear Strain-Hardening Solids," *International Journal of Solids and Structures*, Vol. 24, 1988, pp. 1141–1158.
[12] Ponte Castañeda, P. and Mataga, P. A., "Stable Crack Growth Along a Brittle/Ductile Interface—I. Near-Tip Fields," *International Journal of Solids and Structures*, Vol. 27, 1991, pp. 105–133.
[13] Comninou, M. "The Interface Crack," *Journal of Applied Mechanics*, Vol. 44, 1977, pp. 631–636.
[14] Drugan, W. J. and Rice, J. R., "Restrictions on Dynamically Propagating Surfaces of Strong Discontinuity in Elastic-Plastic Solids," *Mechanics of Material Behavior: The D. C. Drucker Anniversary Volume*, G. J. Dvorak and R. T. Shield, Eds., Elsevier, Amsterdam, 1984, pp. 59–73.
[15] Drugan, W. J. and Shen, Y., "Restrictions on Quasi-Statically Moving Surfaces of Strong Discontinuity in Elastic-Plastic Solids," *Journal of Mechanics and Physics of Solids*, Vol. 35, 1987, pp. 771–787.
[16] Achenbach, J. D. and Bazant, Z. P., "Elastodynamic Near Tip Stress and Displacement Fields for Rapidly Propagating Cracks in Orthotropic Materials," *Journal of Applied Mechanics*, Vol. 42, 1975, pp. 183–189.

Elastic-Plastic Fracture Mechanics—Applications

John D. Landes,[1] Zhen Zhou,[1] and Kevin H. Brown[1]

An Application Methodology for Ductile Fracture Mechanics

REFERENCE: Landes, J. D., Zhou, Z., and Brown, K. H., "**An Application Methodology for Ductile Fracture Mechanics,**" *Fracture Mechanics: Twenty-Third Symposium, ASTM STP 1189*, Ravinder Chona, Ed., American Society for Testing and Materials, Philadelphia, 1993, pp. 229–264.

ABSTRACT: A ductile fracture methodology is presented here that takes the load-versus-displacement data from a precracked laboratory test specimen, such as a compact specimen, and through a series of analysis steps that will allow direct prediction of the load-versus-displacement behavior of a structural component containing a crack-like defect. This is based on a ductile fracture methodology originally presented by Ernst and Landes that was used to evaluate maximum load in a structure under complex loading. The load versus displacement from the test is analyzed by using the methodology in reverse so that it can be divided into two outputs, calibration functions, and fracture toughness. The calibration functions used here are based upon the load separation principle; the fracture toughness is given in terms of the *J-R* curve. The calibration functions and fracture toughness are then transferred from those relevant for the test specimen to those for the structure to be analyzed. Having done this, the methodology is used to predict the load-versus-displacement behavior of the structural component.

A critical step in the methodology is the transfer of the calibration functions and fracture toughness from those for the specimen to those for the structure. The fracture toughness transfer must be made knowing the effects of three categories on toughness; size, geometry, and thickness constraint. Presently, the data in the literature show conflicting trends for the effect of size and constraint. Therefore, a transfer based on known principles is not possible. The approach used here is to try to get a conservative value of the fracture toughness. Fortunately, for many structural components, the fracture toughness is not the controlling input, and the calibration functions have more influence on such things as maximum load prediction.

A procedure for transferring the test specimen calibration function to the structural calibration functions has been developed. Two important things must be addressed for this transfer. A functional form for the calibration function is needed for the structure. This form can be based on the *J*-calibration equation and is known for common geometrical shapes. For more complex geometries, this form must be determined.

In this paper, several example structural components are taken to illustrate the methodology. A compact specimen is used for the laboratory specimen geometry and six structural component models are analyzed to illustrate how well the method works and to evaluate the importance of the various steps in the method. From these examples, suggestions are made for further work that could improve the overall method.

KEY WORDS: ductile fracture mechanics, applications, methodologies, calibrations, toughness, predictions, structural components, fracture mechanics, fatigue (materials)

A major goal of the fracture mechanics approach has been the prediction of fracture behavior in structural components containing defects from the results of laboratory tests. In the past, the approaches that have often been suggested are very limited in scope. For example, K_{Ic} was used to predict a failure load for linear elasticity plane-strain conditions; the *K-R* curve was

[1] Professor and graduate assistants, respectively, University of Tennessee, Knoxville, TN 37996-2030.

used for linear elastic, plane stress conditions; J_{Ic} and tearing modulus, T, were applied to elastic-plastic conditions; and limit load was used for fully plastic conditions. These approaches were used to predict instability loads under fixed conditions of structural stiffness.

A methodology suggested by Ernst and Landes [*1*,*2*] and further developed by Link et al. [*3*] used two inputs, a set of calibration curves, and a fracture toughness result to predict the load-versus-displacement behavior of a structural component during the fracture process. This approach gave a more complete description of the structural behavior in terms of parameters like load and displacement that are easier to work with in a structural design. The result could be combined with the overall structural stiffness to determine instability. The calibration functions describe relationships between load, displacement, and crack length for the nongrowing crack and represent the deformation behavior of the structural component. The fracture behavior gives a method for keeping track of crack length during the loading process. This method represented both the deformation and fracture behavior as a linear sum of elastic and plastic components. As such, it can be used across the range of deformation behavior and is not limited to either linear-elastic or elastic-plastic behavior. The fracture behavior was generally taken as ductile and characterized by a *J-R* curve. However, unstable brittle fracture can be viewed as an interruption of a ductile fracture process [*4*]. When the instability toughness can be identified for the structure, it can be predicted on the ductile load-versus-displacement record. In this way, the method can be used to predict the overall behavior of the structural component for both linear elastic or elastic deformation and for ductile or brittle fracture behavior.

To use the method, inputs are needed for both calibration functions and for fracture toughness. In the past, the demonstrations of the method have been restricted mostly to minor differences between structural component and test specimen because the inputs for the structural component were not easy to develop. Very often, the behavior of a compact specimen was predicted from another and perhaps smaller compact specimen. For components of a different geometry, the calibration curves were often developed numerically.

Using the method described in this paper, the calibration functions for most two-dimensional geometries can be developed from the compact specimen calibration function, at least in principle. The fracture toughness behavior for a structural component is more difficult to determine from the compact specimen test because many of the factors that influence toughness have not been resolved [*5*]. However, a conservative estimate of toughness is often sufficient.

This paper describes a complete fracture methodology that can be used to predict the load-versus-displacement behavior of a structural component directly from the load-versus-displacement record of a laboratory test specimen. The major emphasis is on the procedure to transfer the calibration function. To illustrate the method, six examples of structural component models are analyzed.

Background

The method uses the load-versus-displacement behavior for a laboratory test specimen, here the compact geometry is used to predict the load-versus-displacement behavior of a structural component. The basic steps in the process are illustrated in Fig. 1. The load-versus-displacement record for the compact specimen is reduced to provide two pieces of information, the calibration function and the fracture toughness for the compact specimen. These two are transferred to develop calibration functions and fracture toughness for the structure. The methodology then combines these two to get load versus displacement for the structure.

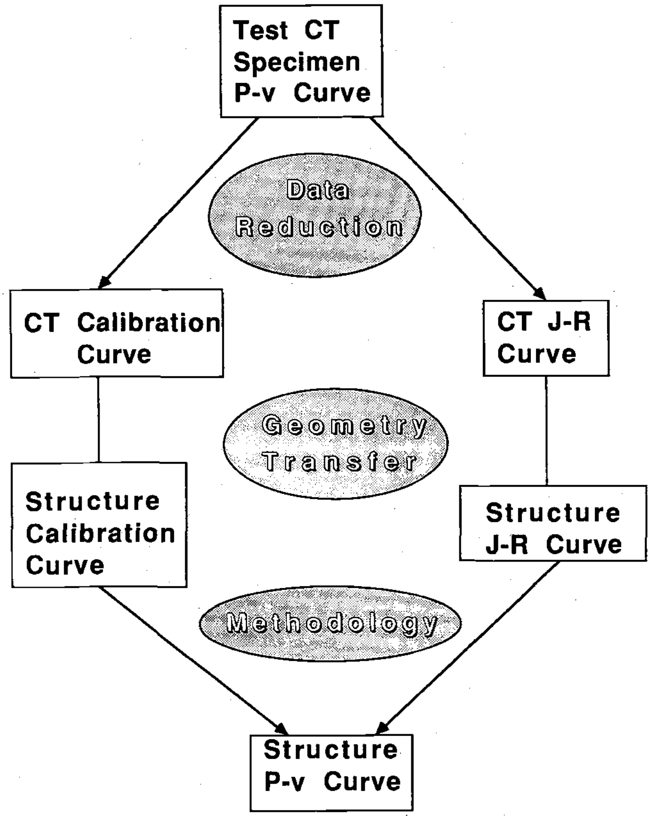

FIG. 1—*Flow chart of component model load-versus-displacement prediction from test specimen.*

The overall method assumes that the load separates into multiplicative functions of crack length, a, and plastic deformation, v_{pl}

$$P = G(a/W)H(v_{pl}/W) \tag{1}$$

for all of the geometries and that this function depends on current values of a and v_{pl}, not on the path taken to arrive at these values. The separation assumption [*6,7*] has been demonstrated for many two-dimensional geometries, and the path independence has been verified for a few cases involving compact geometries [*8,9*].

The first step for developing calibration functions and fracture toughness for compact specimens has been described previously as a method primarily to develop *J-R* curves directly from load-versus-displacement records without the need for online crack monitoring equipment [*10–12*]. It is labeled the method of normalization. The latest approach assumes a deformation function $H(v_{pl}/W)$ in the format

$$H(v_{pl}/W) = \frac{L + M\dfrac{v_{pl}}{W}}{N + \dfrac{v_{pl}}{W}}\left(\frac{v_{pl}}{W}\right) \tag{2}$$

where L, M, and N are constants [12]. This has been shown to describe the deformation results for most metals better than other functional forms such as the power law. The fracture toughness is given in the format of the J-R curve.

The resulting calibration function and J-R curve from this step are the ones appropriate for compact specimens. If they are used in the methodology to predict load versus displacement for a structural component, they would work only when the structure is another compact specimen. To apply the method to a structure of another geometry, the calibration functions and J-R curve must be transferred to ones relevant for that geometry.

The calibration functions are often the most important in determining structural behavior, particularly in determining a maximum or failure load. Previously, these functions were developed from tensile properties of the material. Approaches using numerical analysis, for example, the *GE-EPRI Handbook* [13], would use properties of the material to be developed from a tension test to obtain calibration functions. These were generally inaccurate because the numerical solution would be developed from a two-dimensional analysis that was either plane stress or plane strain, neither of which was correct for the actual structural component. Other approaches could estimate calibration functions from a limit load solution that did not incorporate the strain-hardening aspects of loading the structure [14,15]. These solutions could provide an estimate of the calibration function; however, it was found that the test specimen itself gave a better estimate of the deformation character of a cracked body than the tension test [16]. Therefore, an approach that could develop the calibration functions for the structure directly from those of the fracture toughness test specimen would give a more accurate result.

The fracture toughness of the structure could be obtained from the J-R curve of the test specimen, if the influence of geometry and constraint were well understood. Many of the results reported in the literature do not follow consistent trends, so these influences cannot be incorporated quantitatively [5]. Therefore, in this work, the J-R curve from the compact specimen was used directly as a lower bound estimate. It will be shown later that the behavior of the structure is often more sensitive to the calibration curve than to the J-R curve, and the lower bound given from the test works very well.

When the calibration curve and J-R curve toughness for the geometry have been determined, they can be recombined using the ductile fracture methodology [1-3] to give the load-versus-displacement behavior of the structure. This has been illustrated in the past and will be demonstrated only briefly in this paper.

Calibration Functions

The structure of the calibration function comes from the principle of load separation. What is needed is a relationship between the primary variables load, displacement and crack length, and a separate relationship between these variables and a fracture parameter. Since the fracture toughness is given in the format of the J-R curve, J is the fracture parameter used here. If the load separates, as expressed by Eq 1, what is needed for the calibration function is the $G(a/W)$ function that expresses the functional relationship between load and crack length and the $H(v_{pl}/W)$ function that expresses the relationship between load and plastic deformation.

The $G(a/W)$ function is fixed for a given geometry. Therefore, for the geometry of the structural component, this function must be determined. This can be done experimentally by testing blunt-notched specimens or numerically; here blunt-notch finite element models can be used for this as will be shown later. The J-value can be determined as a sum of an elastic and a plastic component

$$\begin{aligned} J &= J_{el} + J_{pl} \qquad (3) \\ &= \frac{K^2}{E'} + \frac{\eta_{pl}}{Bb}\int_0^{v_{pl}} P\,dv_{pl} \end{aligned}$$

where E' is an effective modulus, K is the linear elastic crack-tip stress intensity factor, η_{pl} is a coefficient for the plastic area, B is thickness, and b is an uncracked ligament length ($W - a$). From the separation equation

$$\eta_{pl} = -\frac{b}{W}\frac{G'(a/W)}{G(a/W)} \tag{4}$$

where G' is the derivative of G with respect to a/W. Therefore $G(a/W)$ can be determined if the η_{pl} coefficient is known or vice versa. Since η_{pl} is known for many common geometries, $G(v_{pl}/W)$ is also known for these geometries. In some cases, the $G(a/W)$ from a simple geometry can be used to estimate the one for a more complex geometry.

The total displacement is also written as a sum of elastic and plastic components

$$v = v_{el} + v_{pl} \tag{5}$$

and v_{el}

$$v_{el} = C(a/W)P \tag{6}$$

where $C(a/W)$ is a compliance function. Therefore, the calibration functions needed for a new geometrical shape, not regarding material, are the compliance $C(a/W)$, the K solution, and the $G(a/W)$ function or η_{pl}. All of these calibration functions can be obtained with a knowledge only of the cracked geometry. The elastic modulus comes into the compliance solution in the relationship between K and J_{el}, but in a linear manner, so that it really does not need to be known in determining the functions.

When a specific material is considered, the $H(v_{pl}/W)$ must be determined for that material and the specific geometry. This is the function that incorporates the material plastic deformation characteristics. By the approach used here, this function can be determined from the laboratory test of the compact specimen. The transfer of calibration function from test specimen to structural component in Fig. 1 then involves the determination of the new $H(v_{pl}/W)$ function.

The determination of this new $H(v_{pl}/W)$ function for the structural component is an important step and is a major focus of this paper. The procedure presented in this paper is only one of many possible. It is essentially empirically based and could be a topic for further work and is explained in the next section.

Transfer of Calibration Function

The material calibration function from the test of a compact specimen has the functional character given in Eq 2. This has been shown to fit many steels and some other metals [12,15]. The same functional form can be used for the geometry of the structural component. Let us assume that is has the form

$$h\left(\frac{v_{pl}}{W}\right) = \frac{l + m\dfrac{v_{pl}}{W}}{n + \dfrac{v_{pl}}{W}}\left(\frac{v_{pl}}{W}\right) \tag{7}$$

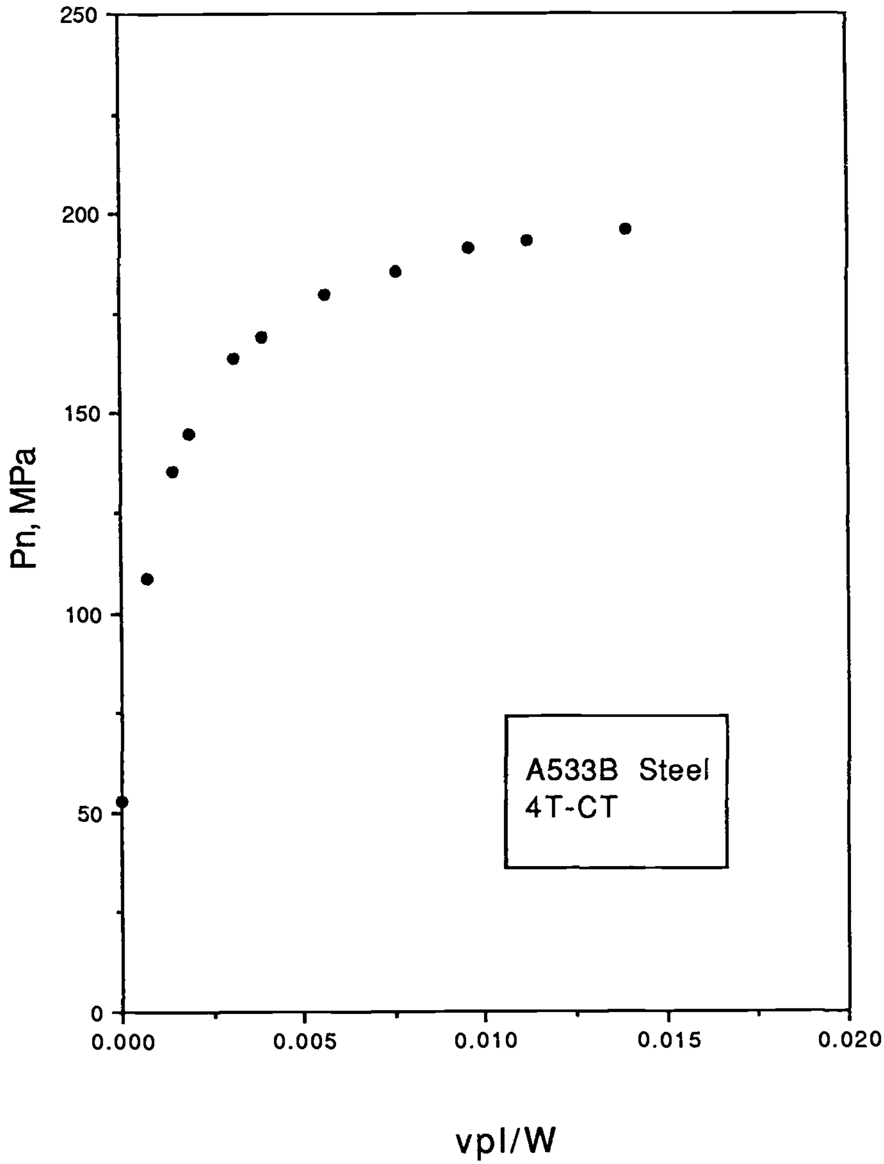

FIG. 2—*Normalized load-versus-plastic displacement for A533-B compact specimen.*

Then, given L, M, N from the laboratory test, the l, m, n of the structure must be determined. The following procedure is a suggestion for doing this. This is illustrated for an A533-B steel [*17*]. Figure 2 shows the calibration curve for the A533-B compact specimen. It is expressed here as P_N versus v_{pl}/W where

$$P_N = \frac{P}{G(a/W)} = H\left(\frac{v_{pl}}{W}\right) \tag{8}$$

is a normalized load. To make the transformation from the L, M, N of the compact test result to the new structure, both axes of Fig. 2 are normalized. The P_N axis becomes p_n where

$$p_n = P_N f \tag{9}$$

and f is a factor that is the ratio of limit load for the structure to limit load for the compact specimen. The abscissa, v_{pl}/W, is divided by v_{el}/W so that it becomes v_{pl}/v_{el}. The limit-load ratio factor, f, could be taken from a number of sources, but they must have a consistent format. Here, the limit load expressions in the *Handbook* [13] are used. They are based on a combination of rigid plastic models with some numerical modifications.

The normalized elastic displacement, v_{el}/W, would be a function of load.

$$\begin{aligned} v_{el} &= C(a/W)P \\ &= C(a/W)G(a/W)H(v_{pl}/W) \end{aligned} \tag{10}$$

The product of compliance and $G(a/W)$ function, CG, is used at a given v_{pl}/W (where $H(v_{pl}/W)$ has a known value.) This is dependent upon a/W but is not a strong function of a/W. Therefore, for a changing crack length, an average value can be used. The normalized calibration function, p_n, versus v_{pl}/v_{el} is shown in Fig. 3 for the A533-B compact. The structural components used in this example are three specimen types: the double-edge-notched tension, DENT (ASTM DE(T)); center-cracked tension, CCT (ASTM M(T)); and single-edge-notched tension, SENT (ASTM SE(T)). Their calibration functions in the form of fP_N versus v_{pl}/v_{el} are also given in Fig. 3. The factor, fP_n, is the desired normalized load, p_n, for the structural component so the abscissa must be converted back to v_{pl}/W by multiplying v_{pl}/v_{el} of Fig. 3 by v_{el}/W for the structural component. The same approach of using an average CG product is used. The resulting p_n versus v_{pl}/W is given in Fig. 4. This represents the calibration function for the structures, that is, the three specimen types DENT, CCT, and SENT. This plot can be fit to obtain Constants l, m, n by fitting the points. This set of calibration functions along with the appropriate *J-R* curve can then be recombined to develop the load-versus-displacement behavior of the structure [1–3]. In this paper, no procedure has been developed for the transfer of the *J-R* curve for the test specimen to the structural component. It is hoped that the *J-R* curve from a bend-type test specimen like the compact will provide a lower bound. Examples are given in the next section to show how the complete method is applied and to show the relative success of the prediction, despite the fact that the *J-R* curve is not always the appropriate one.

Examples

Examples of the application of the method are given here, starting with the simple case for predicting the load versus displacement of one compact specimen from another. The second example is given for the DENT, CCT, and SENT specimen types in Figs. 2, 3, and 4. These have different loading modes from the compact specimen and are a good test to see how well the method can handle changes in both geometry and loading mode. All of these are predicted from a compact specimen of the same material. An example is then given for a circumferentially through-cracked pipe in four-point bending. For all of these examples, a complete load-versus-displacement behavior of the component is available from a test for comparison with the prediction. A more complex geometry is then analyzed, that is, the three-holed specimen from a predictive round robin [18]. For this, only maximum failure loads are available. This example is used to illustrate an alternative method for obtaining calibration functions based on simple numerical calculations.

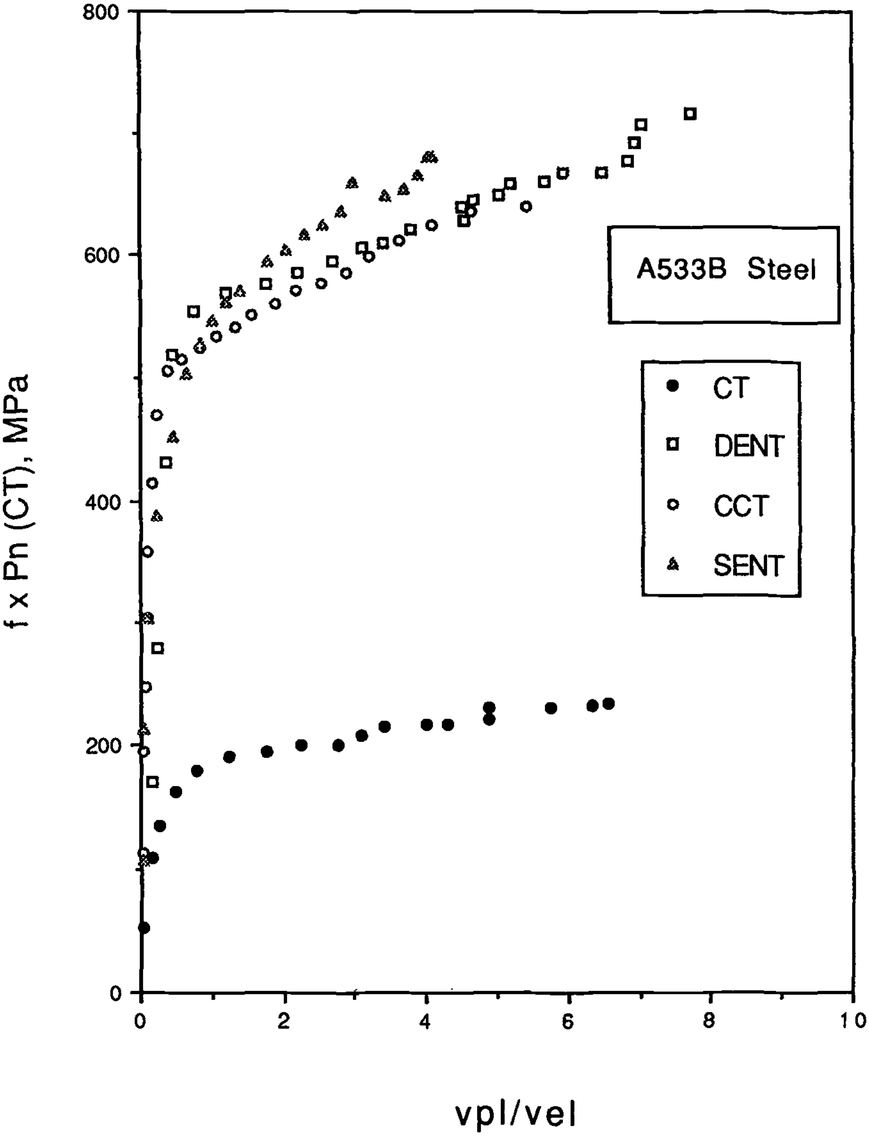

FIG. 3—*Construction to transfer from calibration of the compact specimen to CCT, DENT, and SENT.*

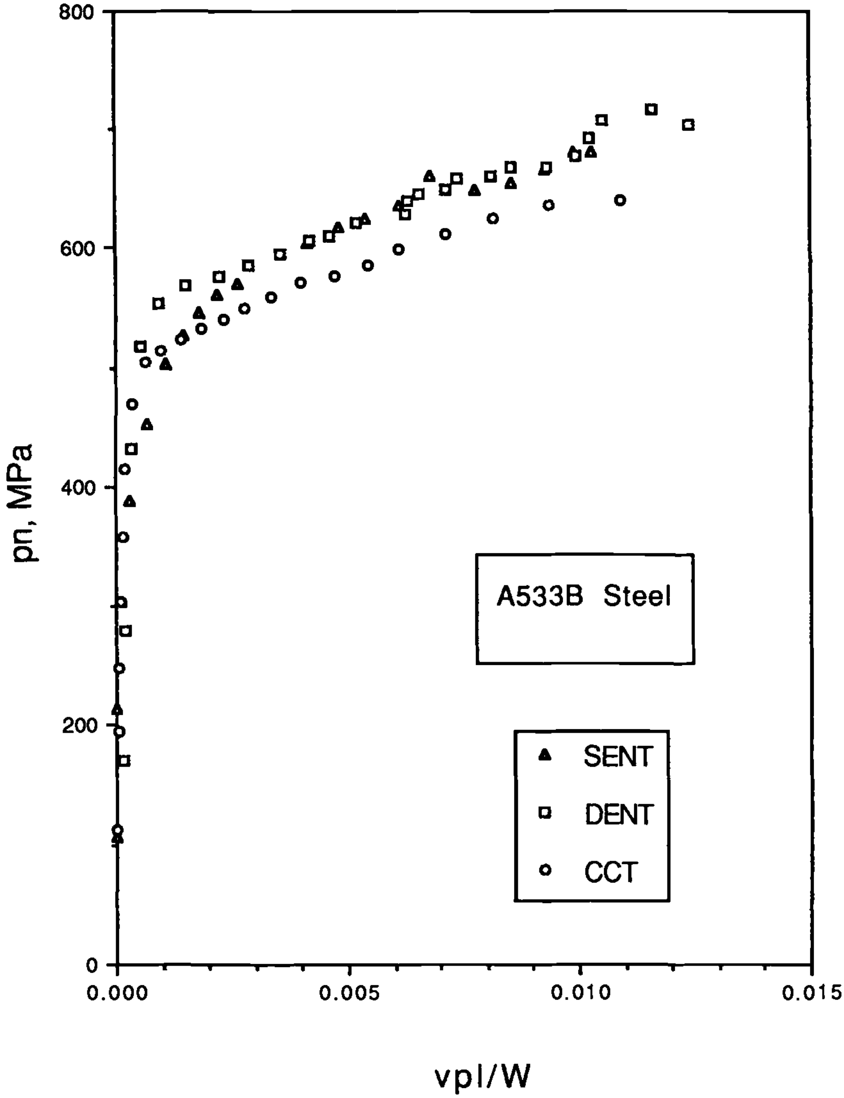

FIG. 4—*Normalized load-versus-plastic displacement transferred from the compact specimen to CCT, DENT, and SENT.*

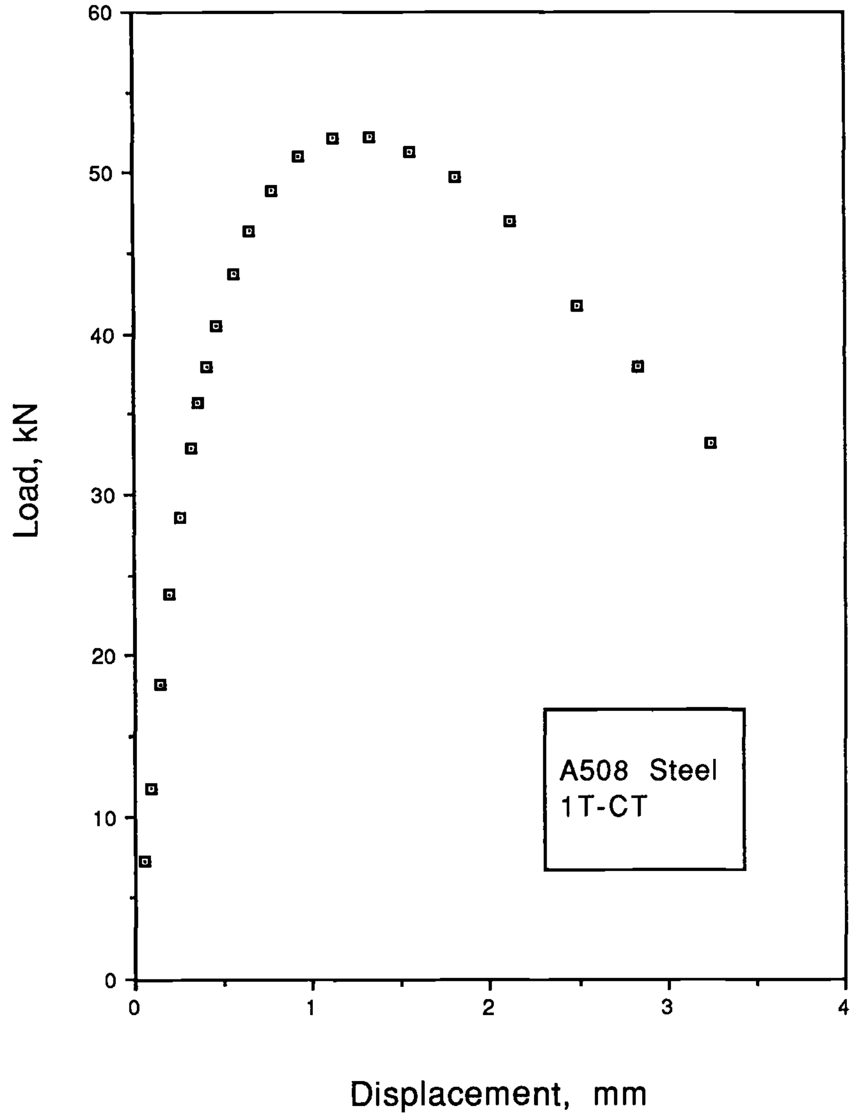

FIG. 5—*Load versus displacement from A508 steel 1T-CT.*

Compact from Compact Prediction

The compact from compact prediction illustrates the method without the transfer step in the middle of Fig. 1. The P_N function for one compact specimen is the same as the p_n for the second. All of the other calibration functions, K, $C(a/w)$, and $G(a/W)$, also remain the same. Given a test record for an A508 steel, 25-mm-thick compact specimen (1T-CT), Fig. 5; the method of normalization is used to obtain the calibration curve, P_N versus v_{pl}/W, in Fig. 6 and the J-R curve in Fig. 7. These are now direct inputs for predicting the behavior of another compact specimen of a different size. An example is given for a 10T-CT (W = 508 mm) of

254 mm thickness. The load versus displacement for this is solved by choosing an independent variable to increment, for example, v_{pl}/W. For a given value of this v_{pl}/W, Eqs 1, 3, and 5 must be satisfied as well as the *J-R* curve that could also be represented functionally

$$J = C_1(\Delta a)^{C_2} \tag{11}$$

These equations usually cannot be solved directly, and an iterative approach must be used. A suggested approach is given in Ref *3*. The resulting load-versus-displacement prediction is given in Fig. 8 where the test result is included for comparison.

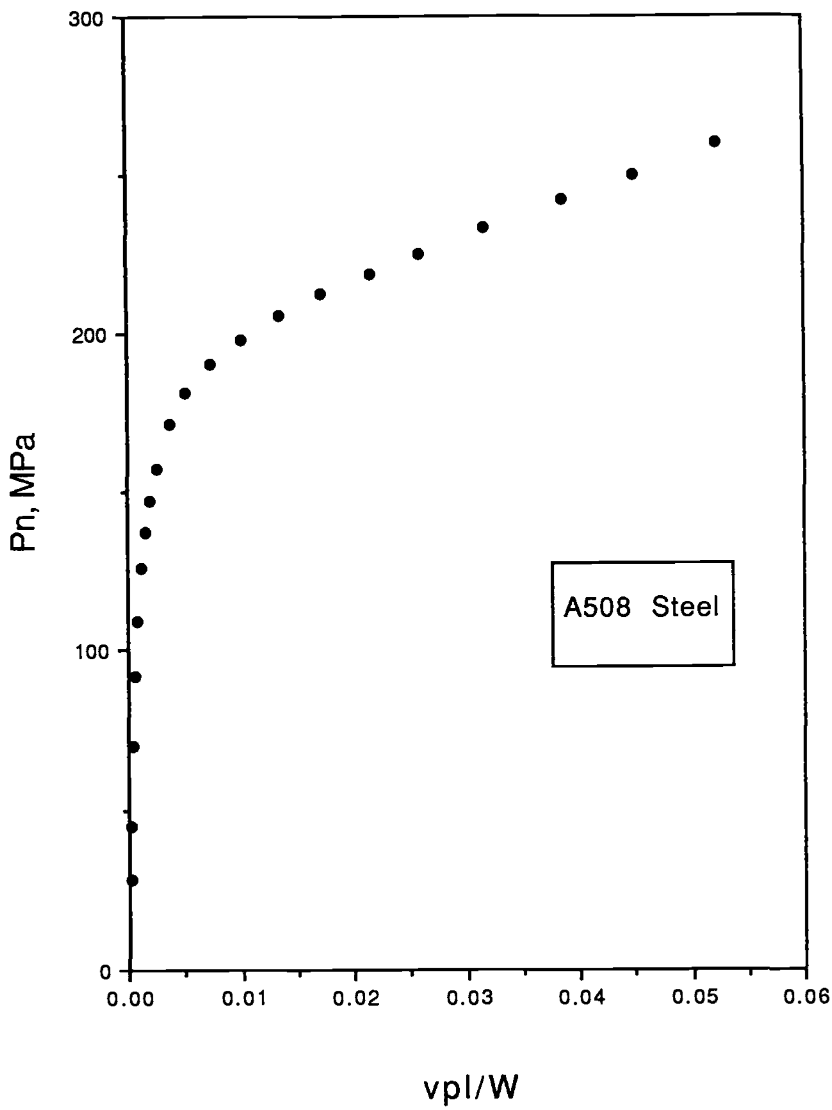

FIG. 6—*Normalized load-versus-plastic displacement for A508, 1T-CT.*

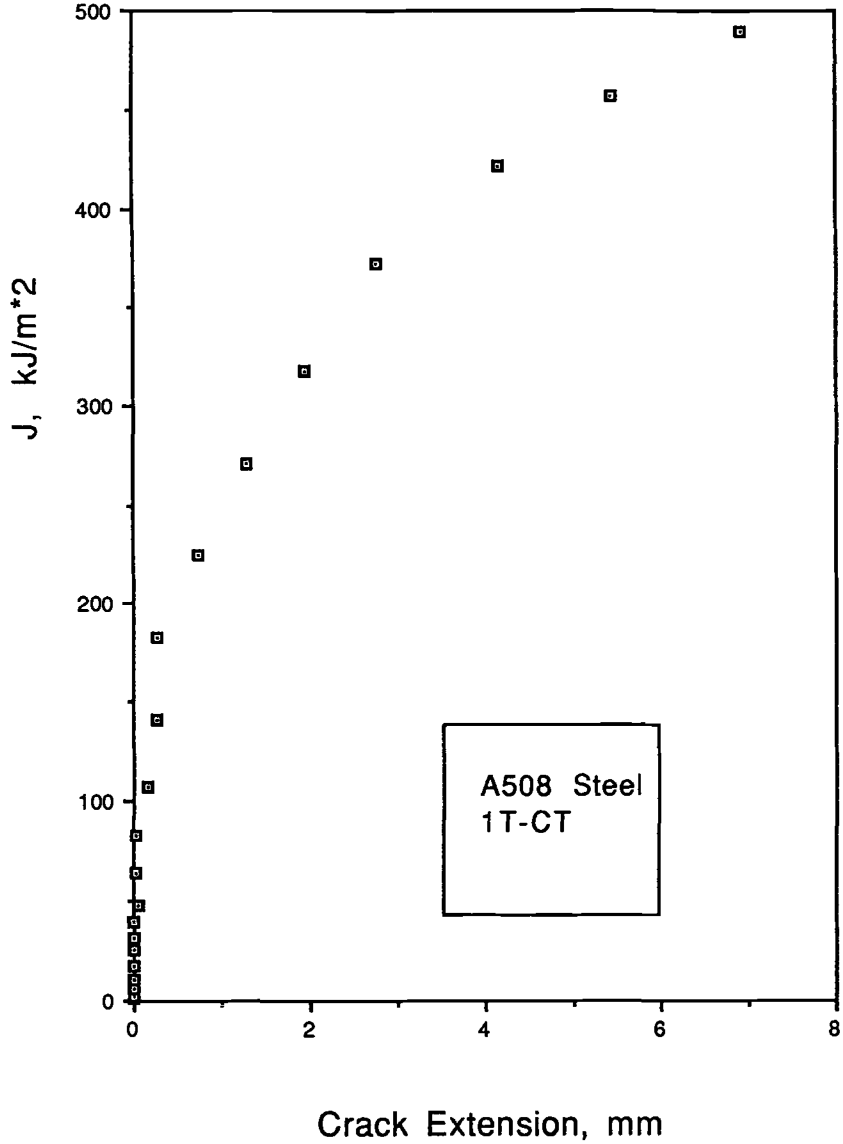

FIG. 7—J-R *curve for A508 steel, 1T-CT.*

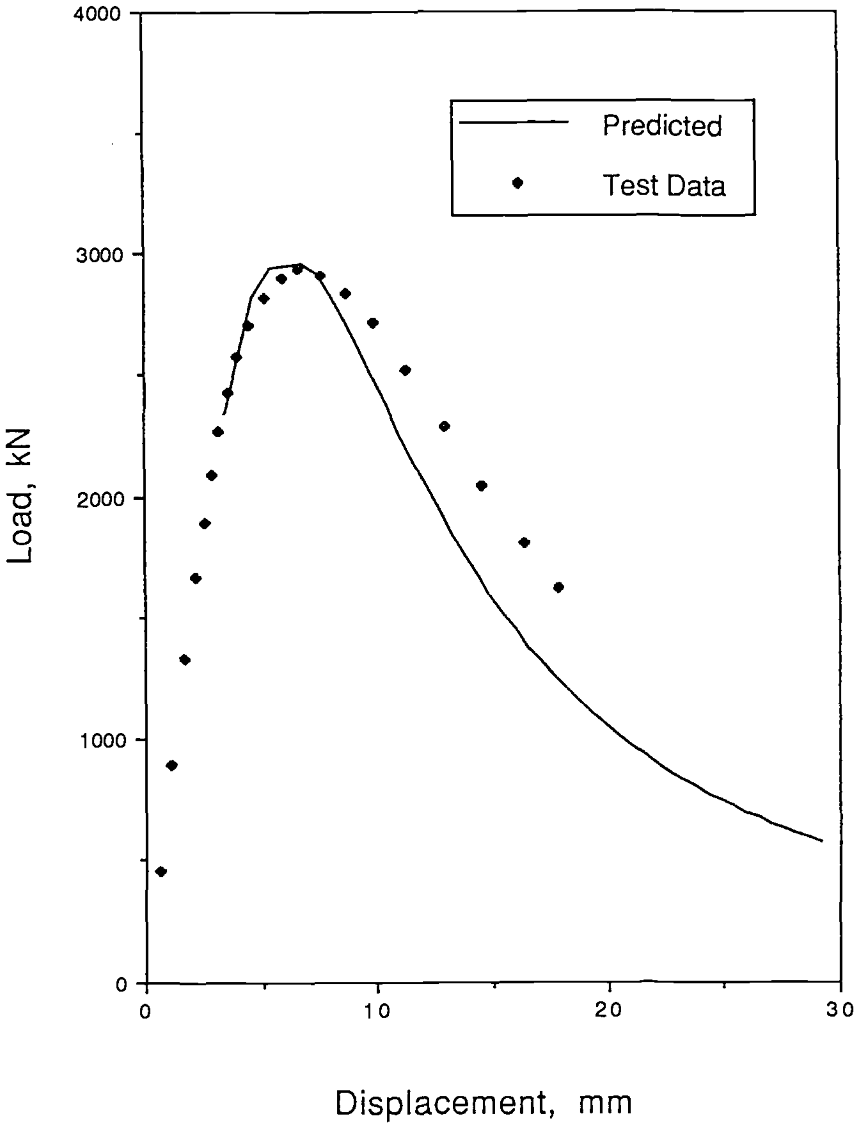

FIG. 8—*Load versus displacement for A508 steel, 10T-CT; predicted and test data.*

SENT, CCT, and DENT from Compact Prediction

The second example uses the geometry transfer step of Figs. 2, 3, and 4. The SENT, CCT, and DENT geometries with different loading modes, Fig. 9, are predicted from a compact specimen. In this case, all have the same constraint, that of plane stress. The load versus displacement for a compact specimen of A533-B steel, Fig. 10, is subjected to the normalization

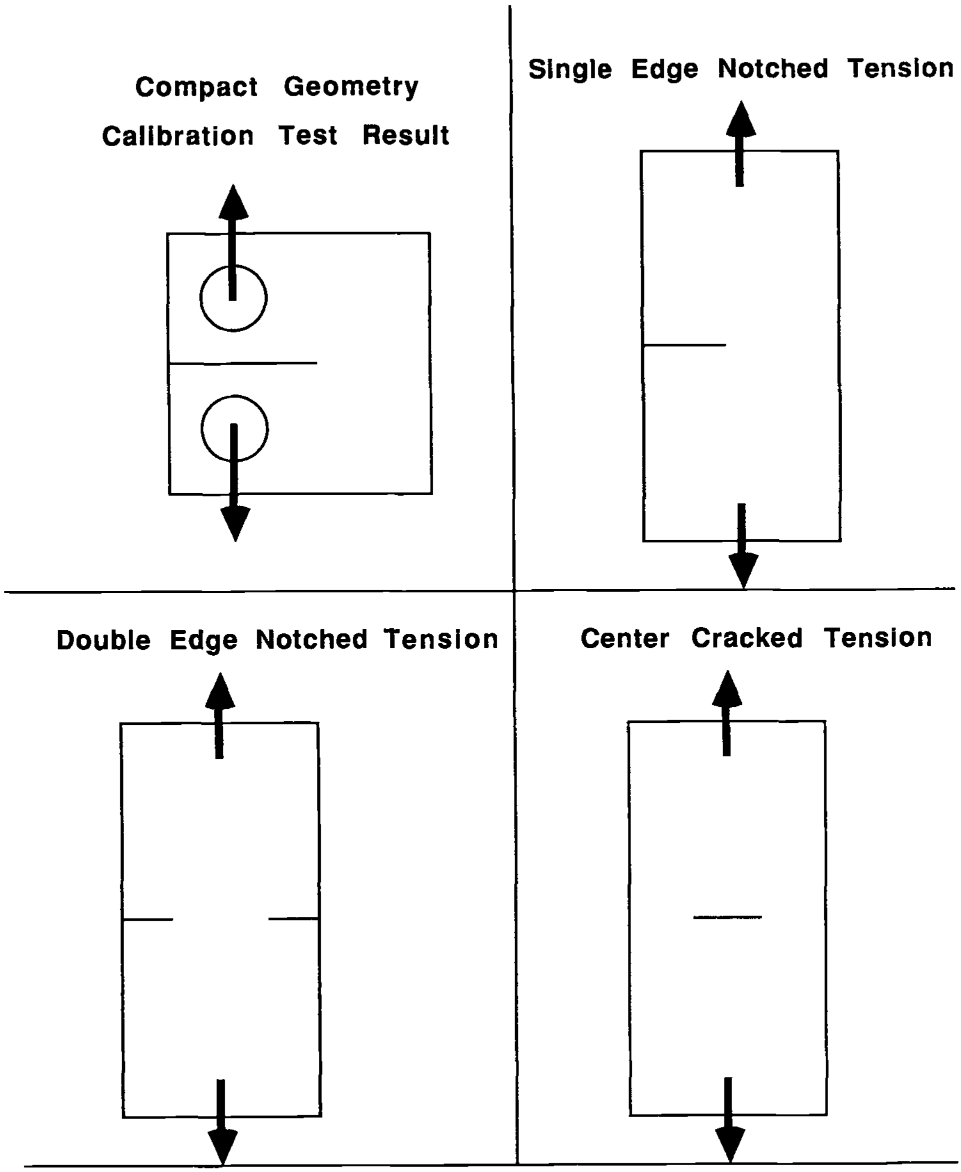

FIG. 9—*Schematic of four component geometries used in calibration curve transfer.*

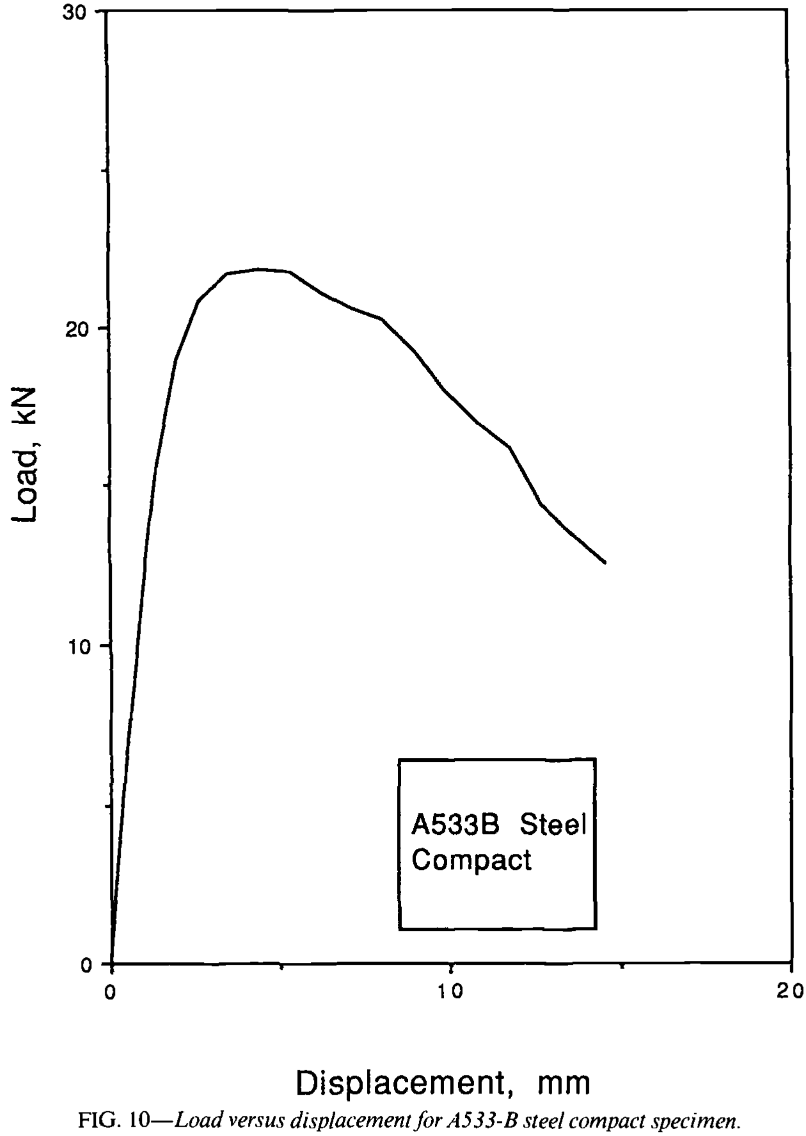

FIG. 10—*Load versus displacement for A533-B steel compact specimen.*

procedure to obtain the calibration curve, Fig. 2, and the *J-R* curve, Fig. 11. The calibration curve in Fig. 2 is not correct for any of the other geometries and must be transferred, in each case, to the one for the new geometry. The *J-R* curve for this material has been shown to also have geometry dependence, with the compact result in Fig. 11 being a lower bound [*5*]. Since the *J-R* curve transfer has not been developed, this lower bound curve will be used.

Using the procedure from the previous section, the calibration curve in Fig. 2 is transferred to one for the CCT and DENT, Fig. 12. The calibration curves of Fig. 12 and the *J-R* curve of Fig. 11 are combined to predict load versus displacement for the two cases, that is, CCT in Fig.

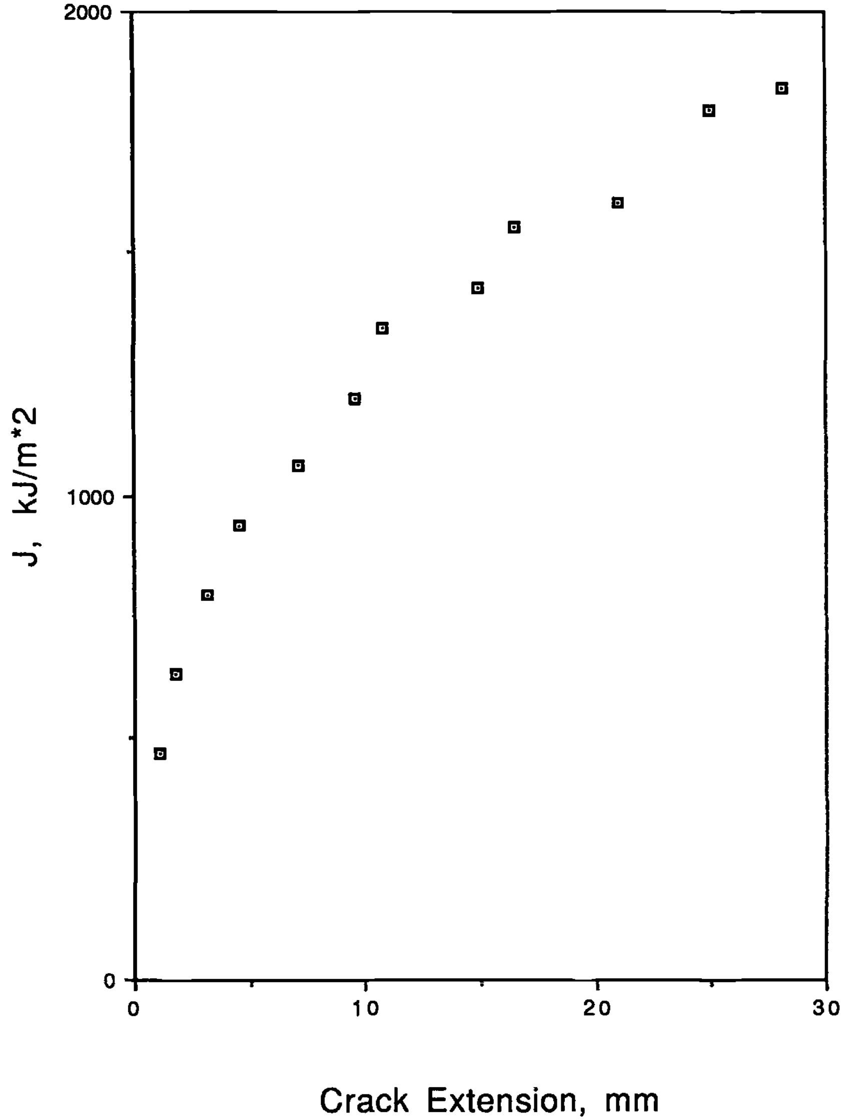

FIG. 11—J-R *curve for A533-B steel compact.*

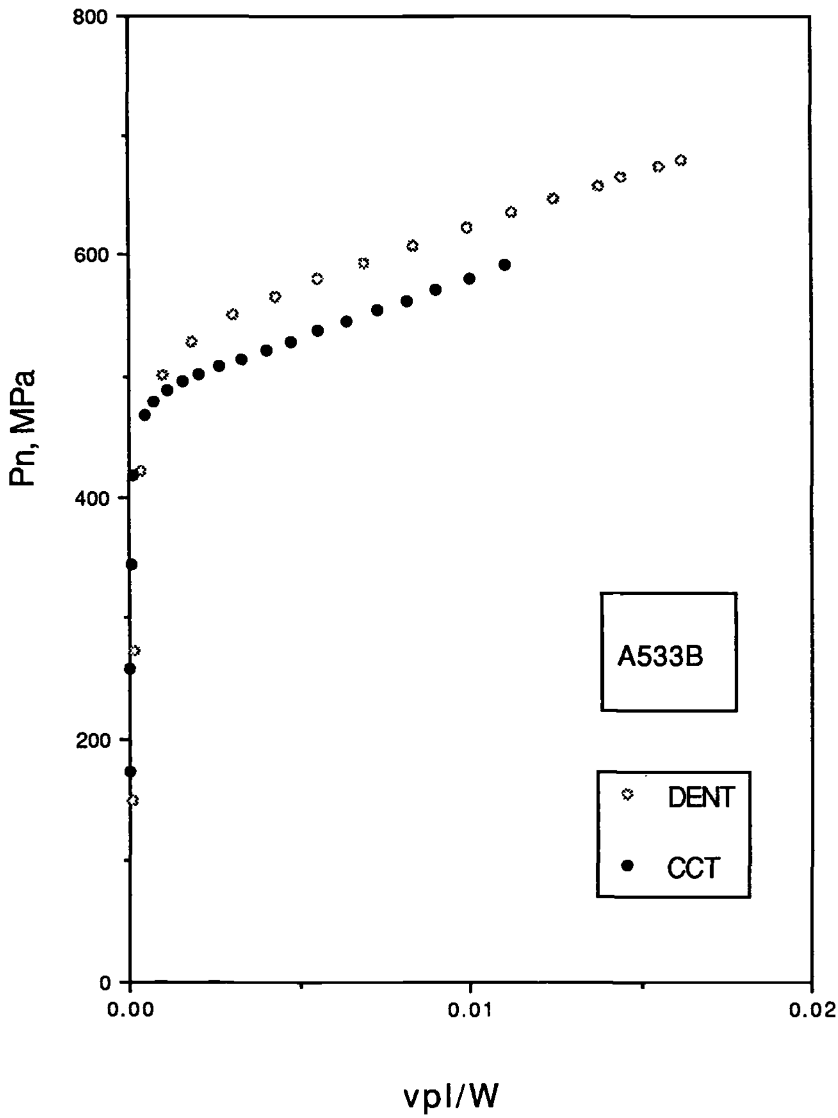

FIG. 12—*Normalized load-versus-plastic displacement for A533-B CCT and DENT.*

13 and DENT in Fig. 14. The predicted results are compared with the test results [*17*]. The fact that the *J-R* curve is not correct for that geometry does not greatly influence the prediction. This is often the case when the ductile fracture occurs on the relatively flat part of the P_N calibration curve. This would not be correct in all cases, especially where the ductile crack advance occurs on the steeply rising part of this curve.

The SENT tests have a range of a/W values so that they also have a range of loading mode.

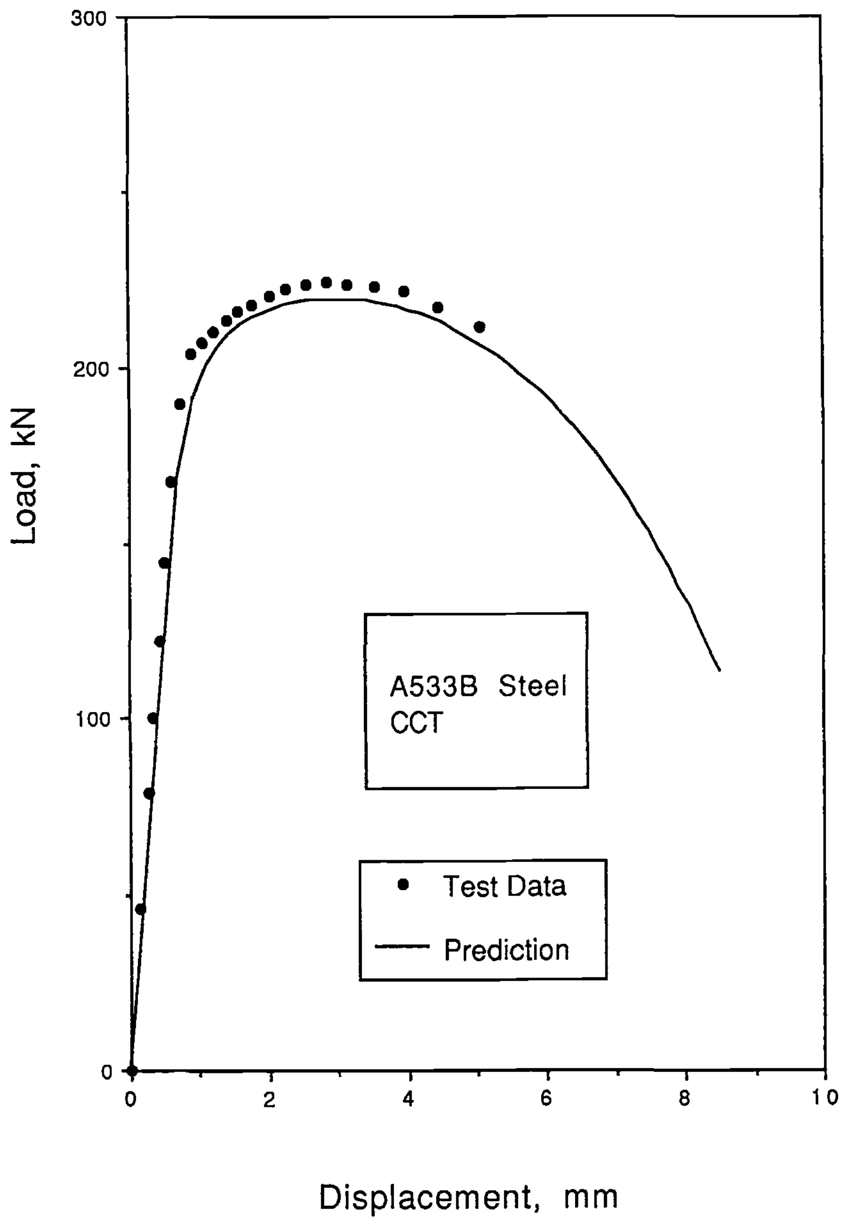

FIG. 13—*Load versus displacement for A533-B steel CCT: prediction versus test data.*

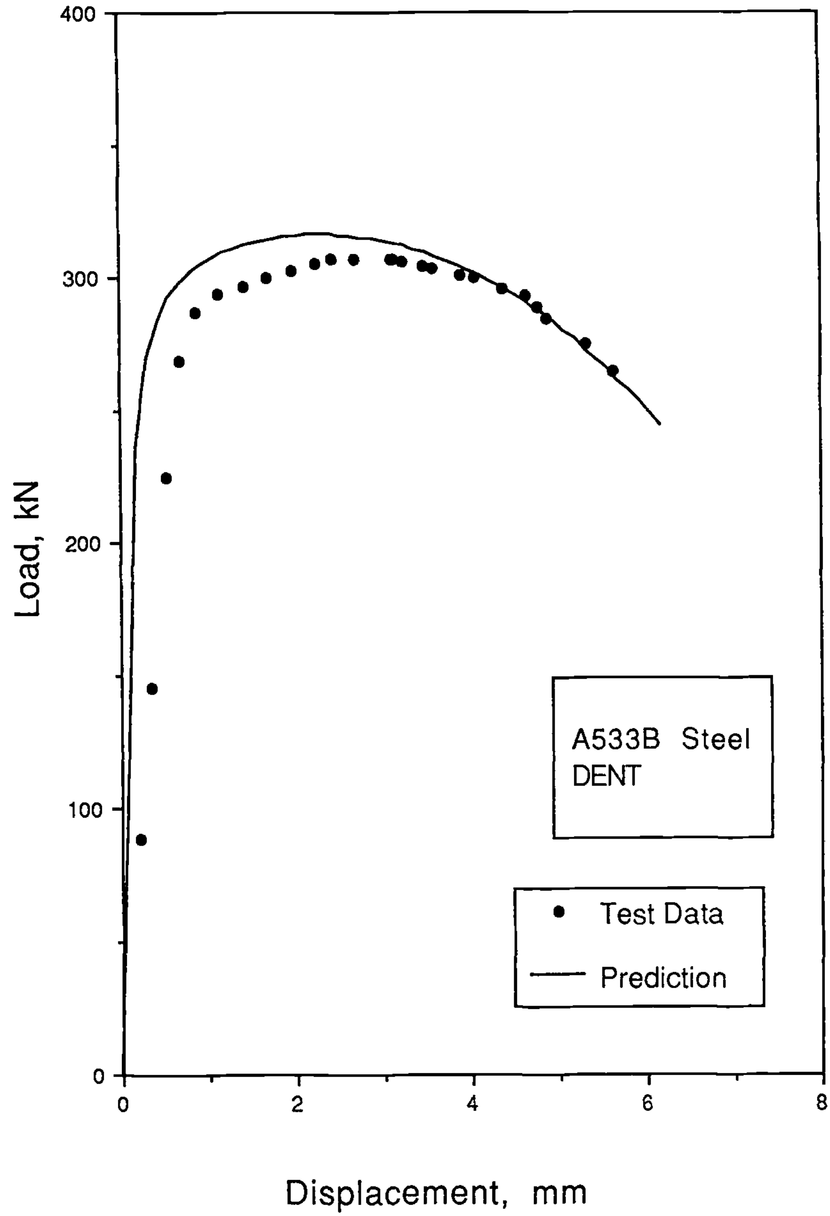

FIG. 14—*Load versus displacement for A533-B DENT specimen: prediction versus test.*

The prediction is given in Fig. 15 for a/W ranging from 0.4 to 0.7. The test result is also included [*17*]. The prediction is very good in this example for the longer a/W, but not as good for the shorter a/W. This may reflect an effect of the variation in J-R curve or could indicate that the calibration function transfer procedure cannot handle such a range of loading mode.

In all of the preceding cases, the geometry calibration function, K, J, $C(a/W)$, and $G(a/W)$, are well known. The next example illustrates a case where it is not as well known.

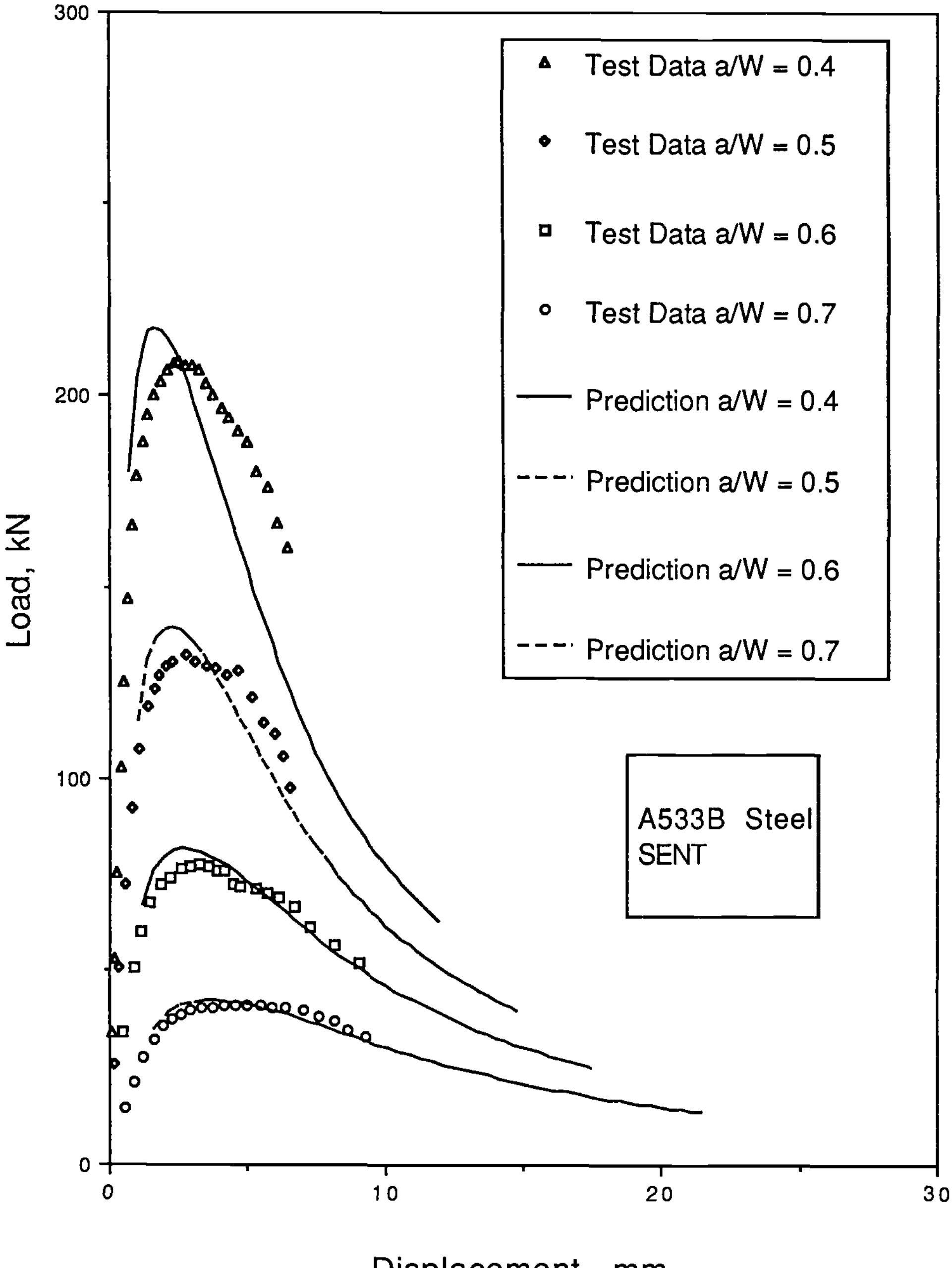

FIG. 15—*Load versus displacement for A533-B steel SENT: prediction versus test.*

Pipe from Compact Prediction

A circumferentially cracked pipe of Type 304 stainless steel was tested in four-point bend loading, Fig. 16 [*19,20*]. For this case, the test result used for prediction is again a compact specimen. The load versus displacement is given in Fig. 17. This result was taken from a test in the literature of a similar Type 304 stainless steel material and not that of the pipe [*21*]. This result was normalized to give the P_N calibration, Fig. 18, and the *J-R* curve, Fig. 19. The P_N curve in Fig. 18 must then be taken through the transfer steps to go from the compact P_N function to the pipe p_n function. To do this, the geometry calibration functions are also needed.

The K calibration and elastic compliance for the pipe were given in the literature [*19,20*]; however, the $G(a/W)$ function and η_{pl} were not available. In order to solve this, a limit-load estimation procedure was used. Since the format of most limit-load solutions is

$$P_L = F(a/W)\sigma_Y \tag{12}$$

where the $F(a/W)$ can be used as a $G(a/W)$ calibration function and η_{pl} is given by Eq 4. In using this approach, it was found that the four-point bending load for the pipe gave a $G(a/W)$ function similar to that of a four-point loaded, single-edge-cracked bend specimen when the circumferential crack is treated as a two-dimensional edge crack. So, in this case, $\eta_{pl} = 2$ was used. This example illustrates a case where the substitution of a similar geometry can be used to estimate $G(a/W)$.

The predicted p_n function for the pipe is given in Fig. 20. From the results presented in the literature, a p_n could also be estimated from the test data; this is also presented in Fig. 20. It can be seen that prediction and test result differ by approximately 10%. The prediction of load versus displacement is given in Fig. 21. Despite the error in the p_n prediction, the prediction of maximum load has much less error. Considering that the calibration and *J-R* curves came from another material, this result is either not very sensitive to material differences or is fortuitous. In this case, errors in calibration and fracture toughness could be offsetting.

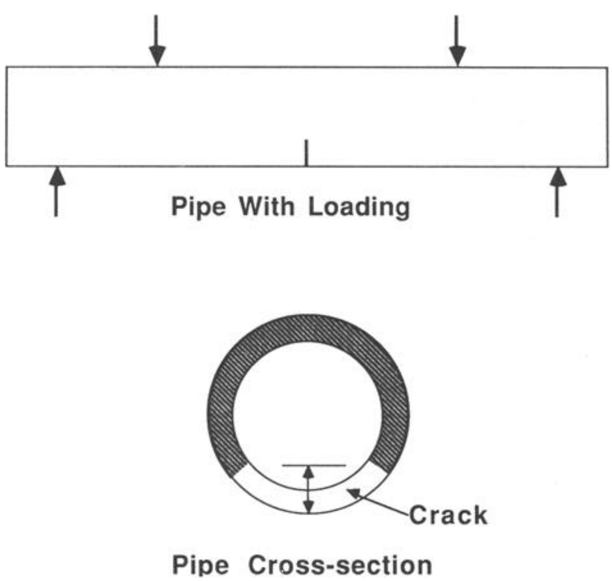

FIG. 16—*Circumferentially through-notched pipe in four-point bend loading.*

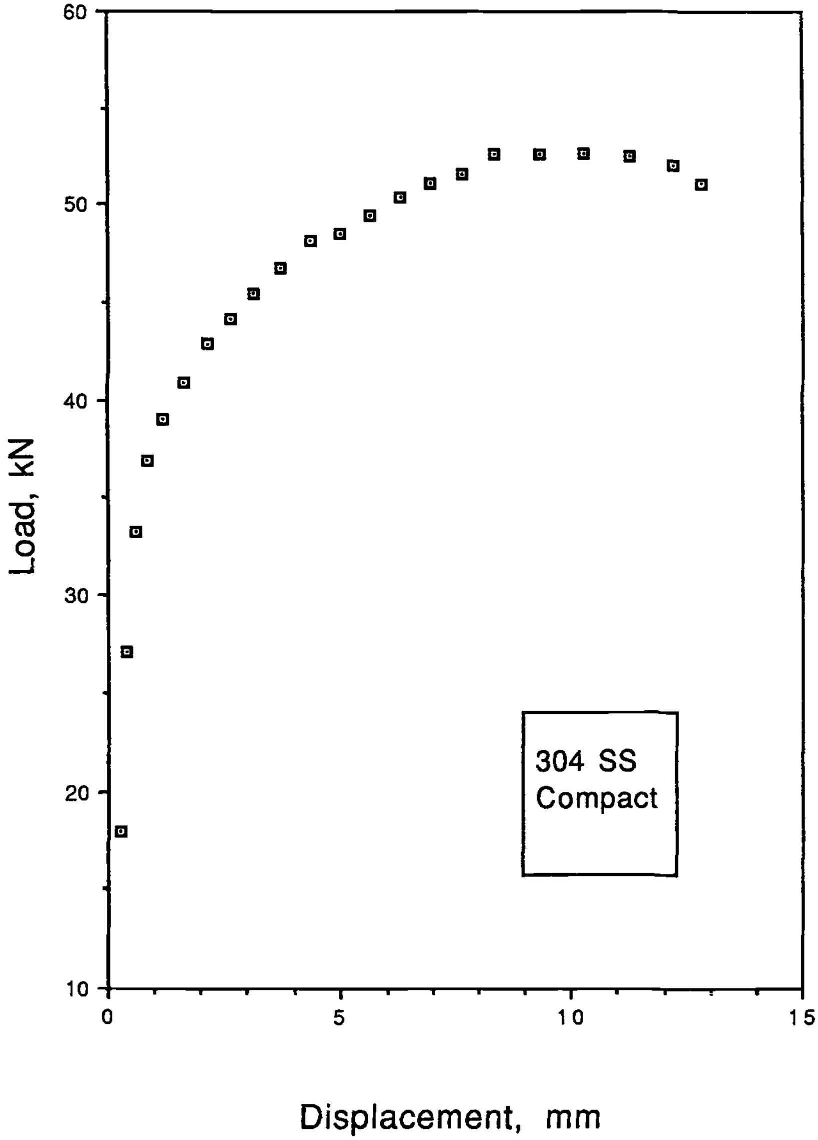

FIG. 17—*Load versus displacement for Type 304 stainless steel compact.*

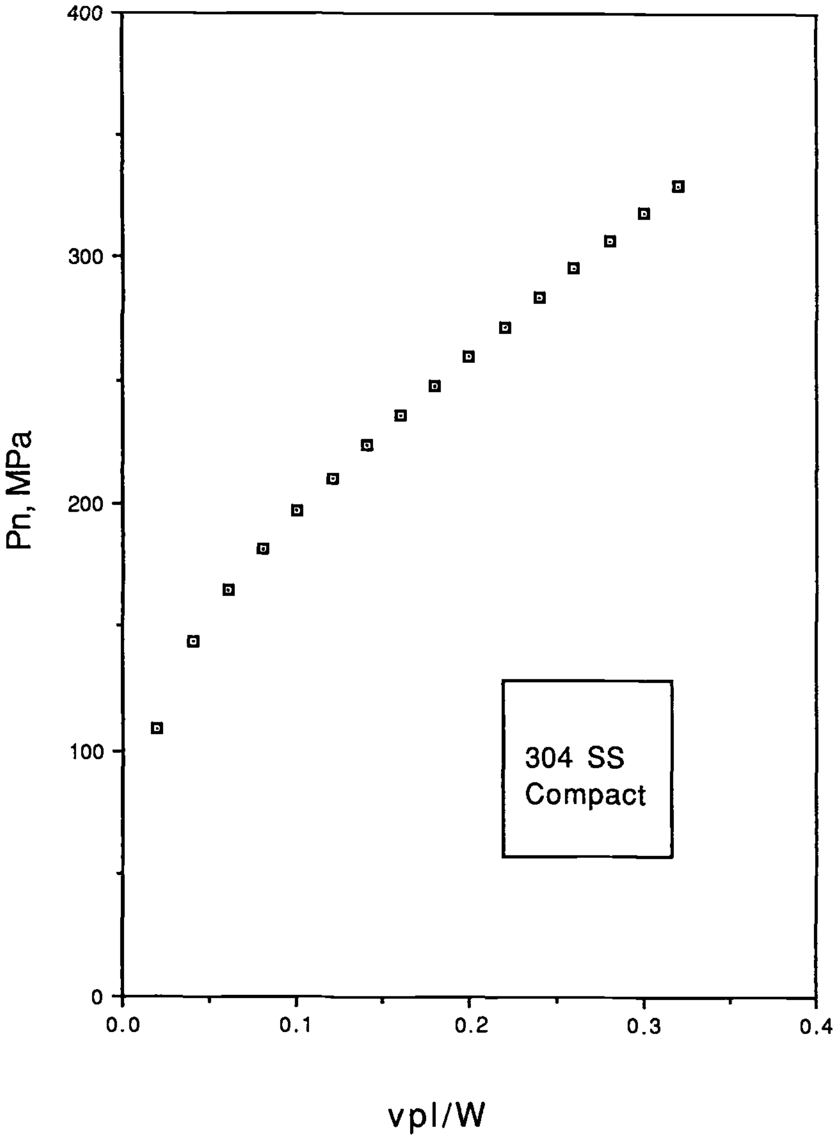

FIG. 18—*Normalized load-versus-plastic displacement for Type 304 stainless steel compact.*

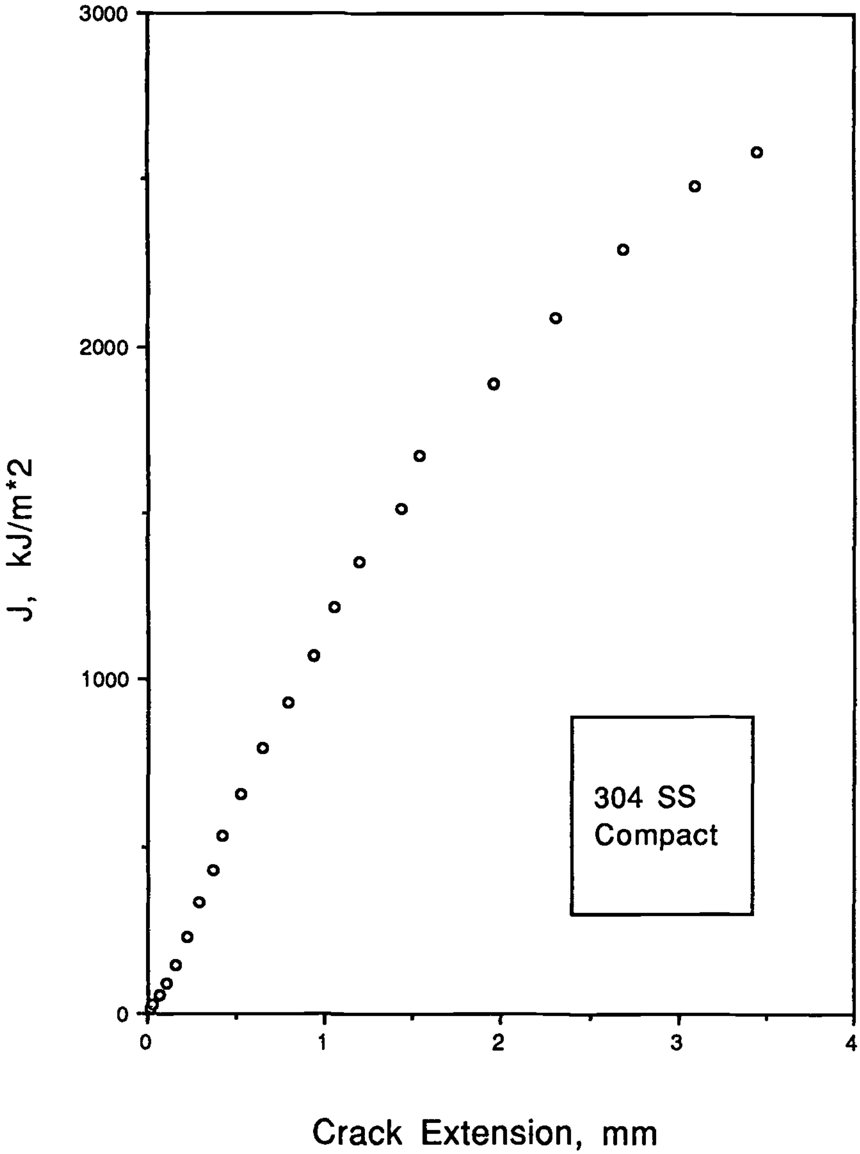

FIG. 19—J-R *curve for Type 304 stainless steel compact.*

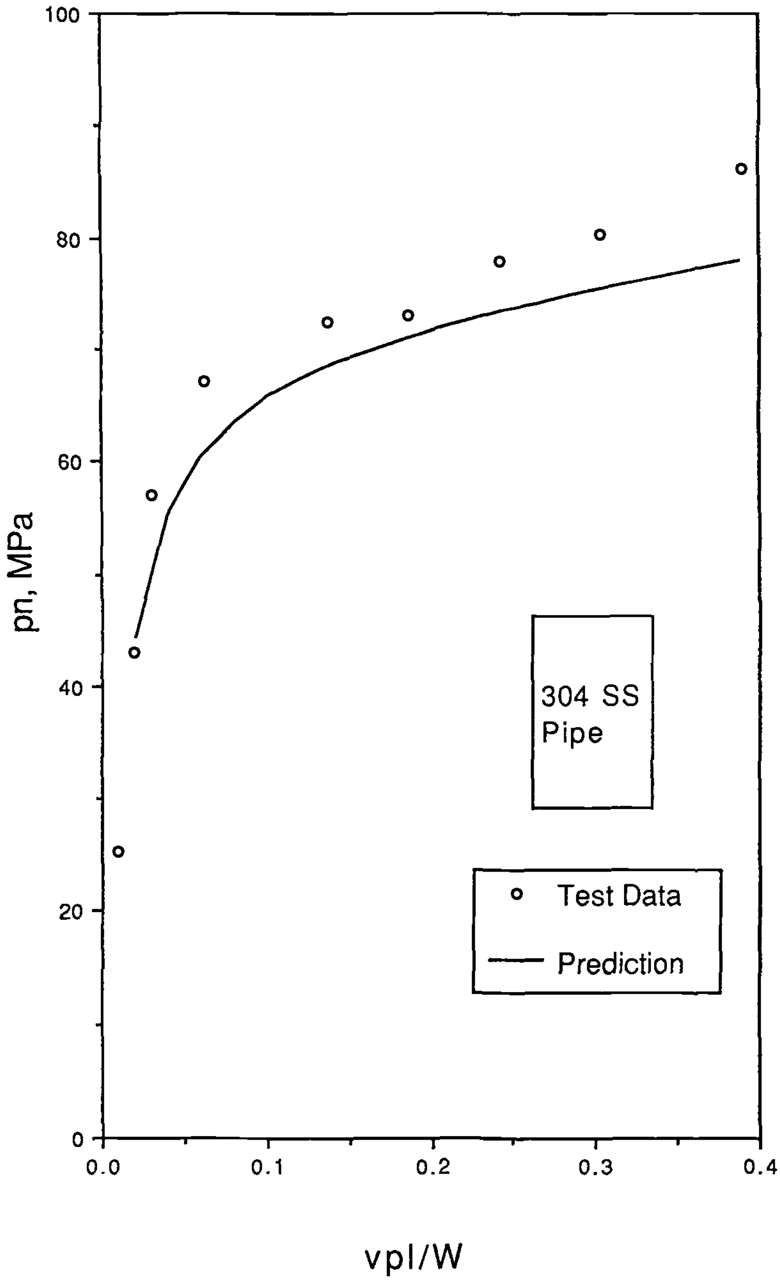

FIG. 20—*Normalized load-versus-plastic displacement predicted for Type 304 stainless steel pipe.*

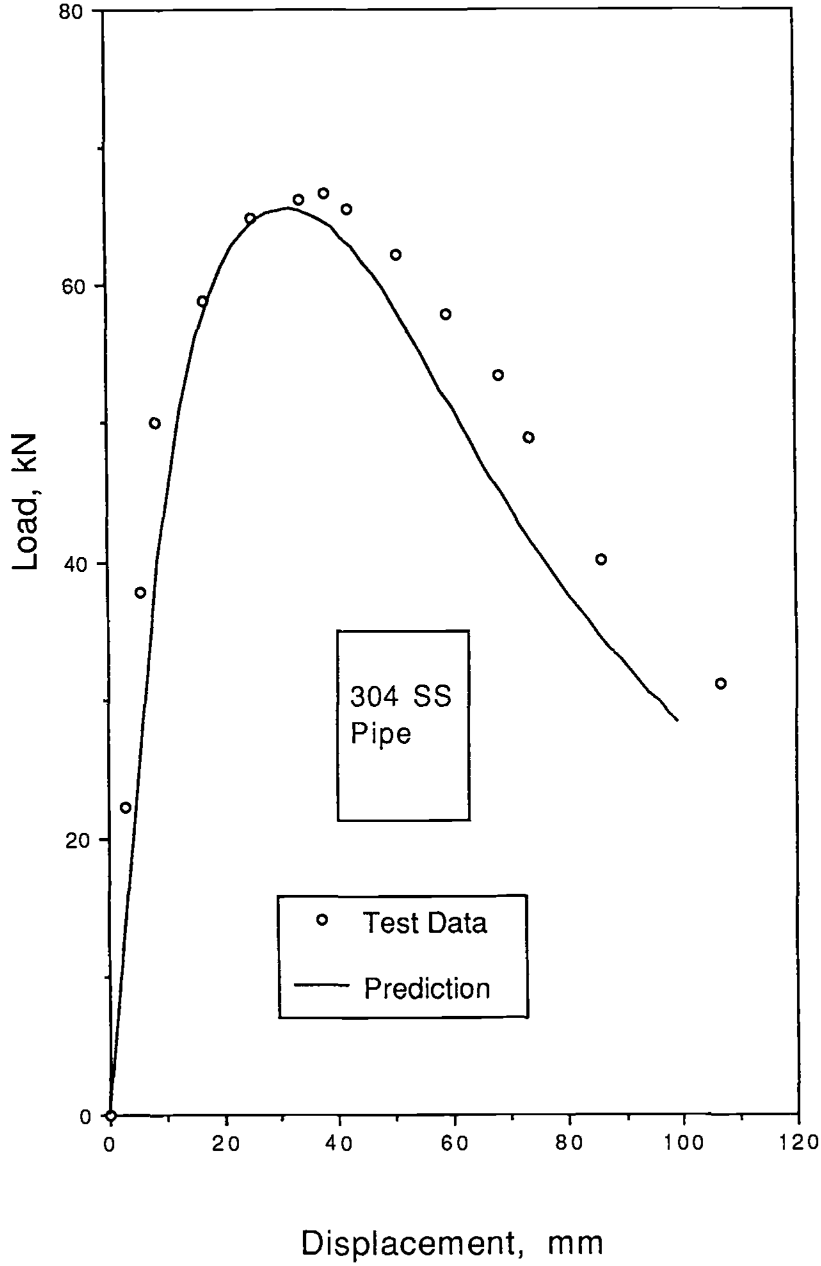

FIG. 21—*Load versus displacement for Type 304 stainless steel pipe: prediction versus test.*

Three-Hole Specimen

A final example is given for a three-hole tension loaded specimen, shown schematically in Fig. 22. This specimen was used in an analytical round robin to see how well failure loads of test specimens could be predicted starting from given compact specimen tests, the same objective as this paper. In the round robin, only maximum loads were predicted so those are the only test results available, however, the analysis here will predict full load-versus-displacement results.

For this specimen geometry, the K solution was given [*18*]; however, none of the other calibration solutions were available. The compliance function could be estimated from the K-solution [*22*], however, the $G(a/W)$ or η_{pl} are more difficult to obtain. To illustrate an alternative method for obtaining these values, a finite-element analysis of blunt-notched specimens was conducted and a load separation analysis was applied [*7*].

The finite-element analysis was conducted for blunt-notched three-hole specimens using a nonlinear version of the COSMOS program with the Macintosh II computer. All that is needed are the plots of load versus displacement for a range of notch lengths. The notch lengths analyzed ranged from $a/W = 0.05$ to $a/W = 0.4$. Eight cases in a/W increments of 0.5 were run corresponding to the range of precracked specimens tested. Three examples of these results are given in Fig. 23. The material properties that were used as input came from the tensile results in Ref *18* for the Type 304 stainless steel material.

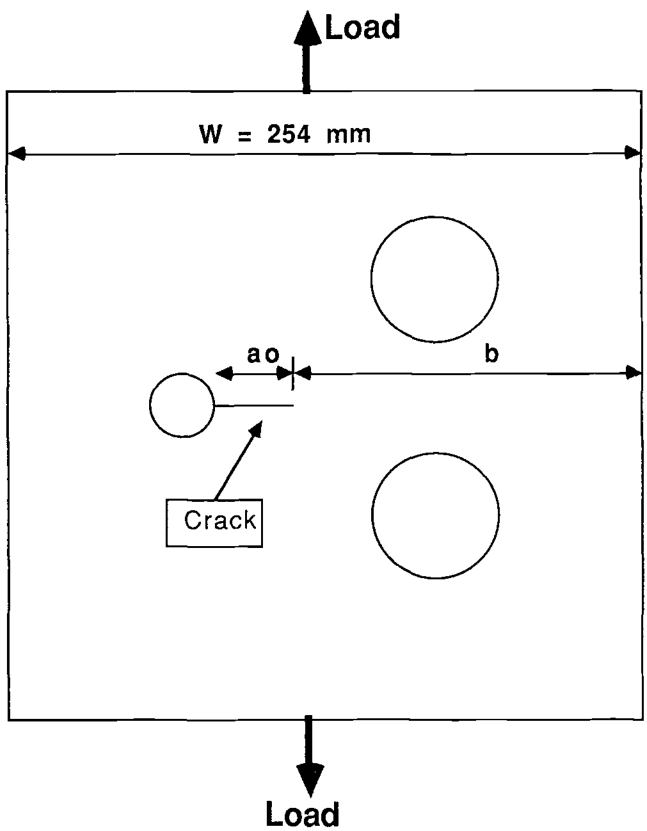

FIG. 22—*Schematic of three-hole specimen.*

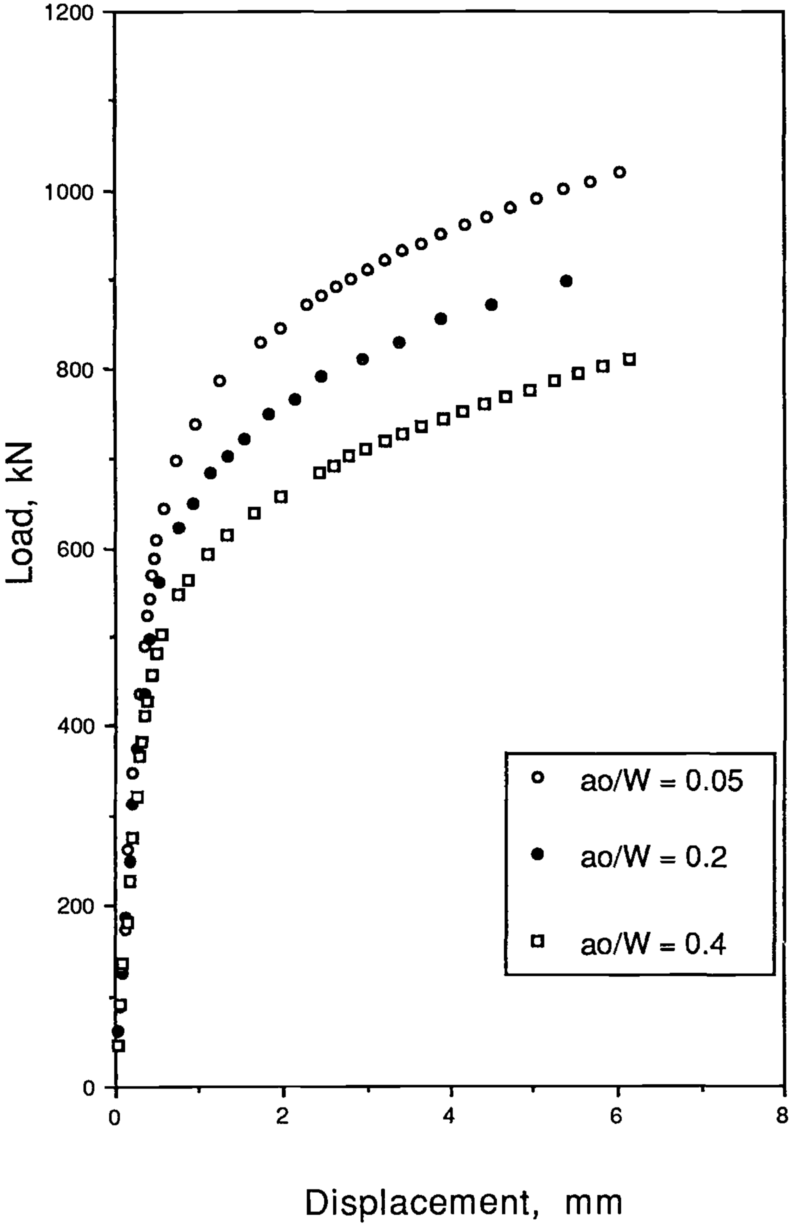

FIG. 23—*Load versus displacement for three-hole specimen blunt-notch finite element, Type 304 stainless steel.*

The load separation procedure divides the load for a crack length, a_i, by the load for crack length, a_j, at fixed values of v_{pl}/W. This ratio is called the load separation parameter, S_{ij}. It is plotted for some of the examples in Fig. 24. If the separation parameter is constant as a function of v_{pl}/W, the J_{pl} expression of Eq 5 can be used. If not, a J-calibration is more difficult. The result of Fig. 24 shows reasonable separation for higher values of v_{pl}/W. Based on this, the procedure used in Ref 7 was followed to obtain the $G(a/W)$ function. A log-log plot was first made of S_{ij} as a function of b/W, Fig. 25. This gives a power law format for $G(a/W)$ when the results can be fit by a straight line. Figure 25 shows that the straight line fit is not very good, suggesting that another functional form could be used. However, as a first attempt, the power law was used. It had an exponent of 0.43, which is also the value of η_{pl}. The $G(a/W)$ function is successful if it collapses the calibration curves when plotted as P_n versus v_{pl}/W. This was tried and had reasonable success, Fig. 26. This result represents the calibration function that can be

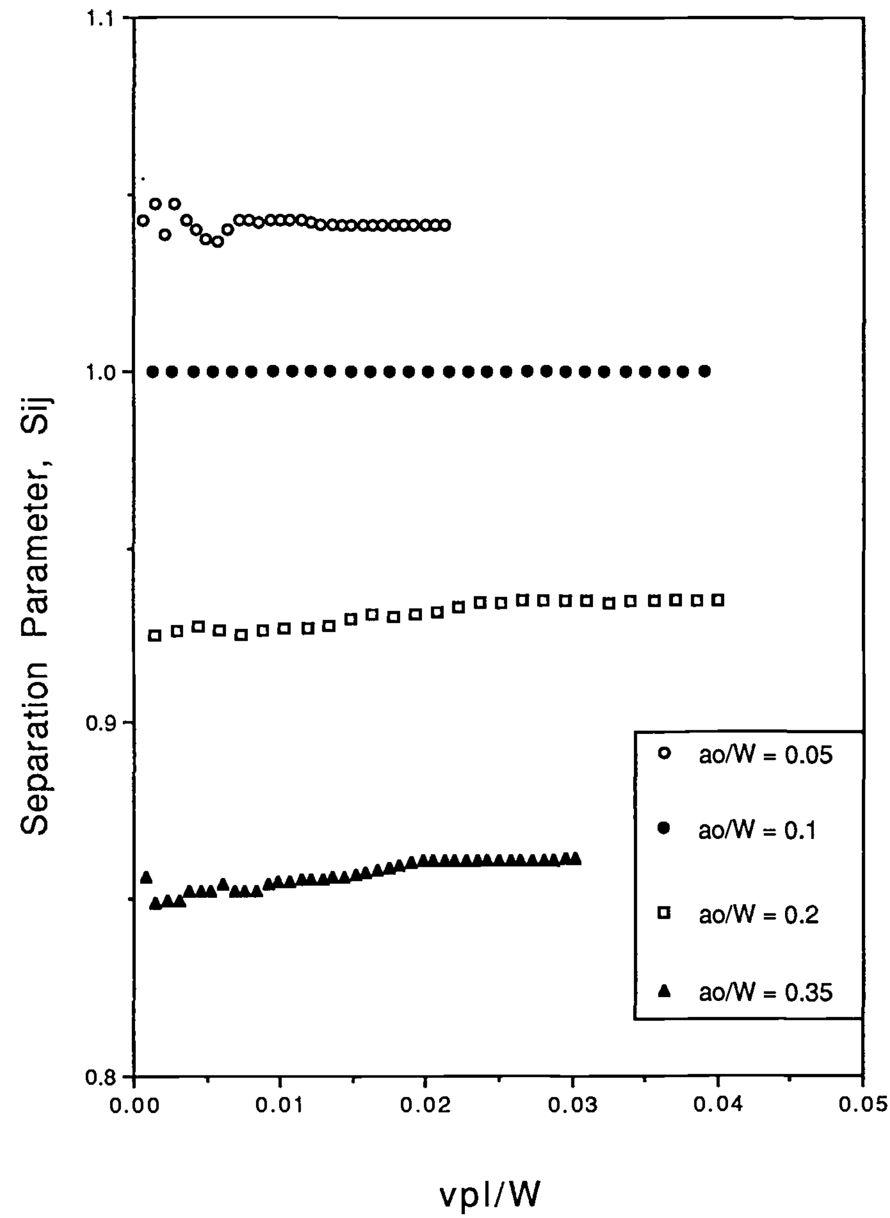

FIG. 24—*Separation parameter-versus-normalized plastic displacement for Type 304 stainless steel three-hole blunt-notch finite element results.*

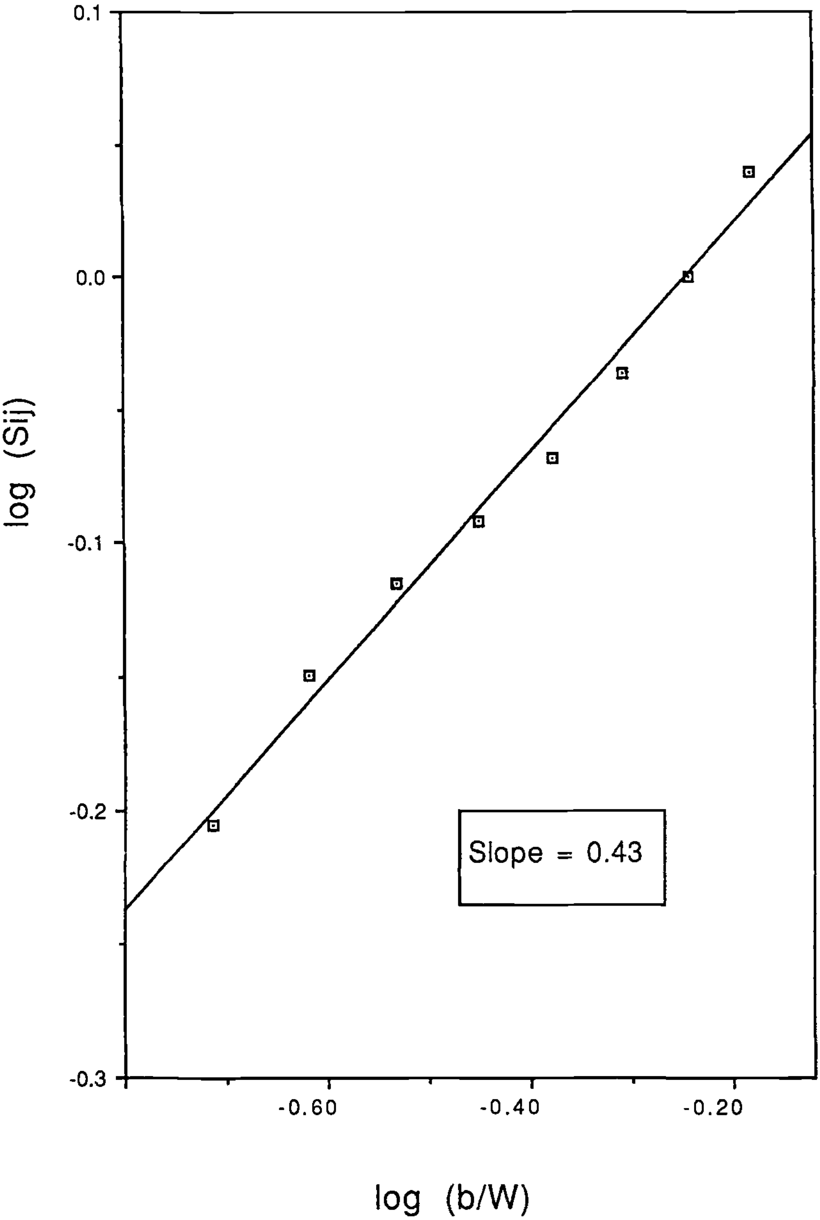

FIG. 25—*Log-log plot of separation constant,* S_{ij}*, versus normalized remaining ligament for three-hole blunt-notch finite element result.*

used for the analysis of the precracked specimen. The *J-R* curve was taken from Ref *18*. The resulting load-versus-displacement predictions are given in Fig. 27. Again, eight examples were analyzed corresponding to the eight initial values of crack length tested. Only four of the eight results are shown for clarity. The test results in Ref *18* measured only the maximum failure load. To compare the predicted maximum load with the failure load, the ratio of predicted-to-test failure load is plotted for each of the eight specimens in Fig. 28. The results show some variations but fall within a ± 10% scatterband. This is a better result than most reported by the round-robin participants [*18*].

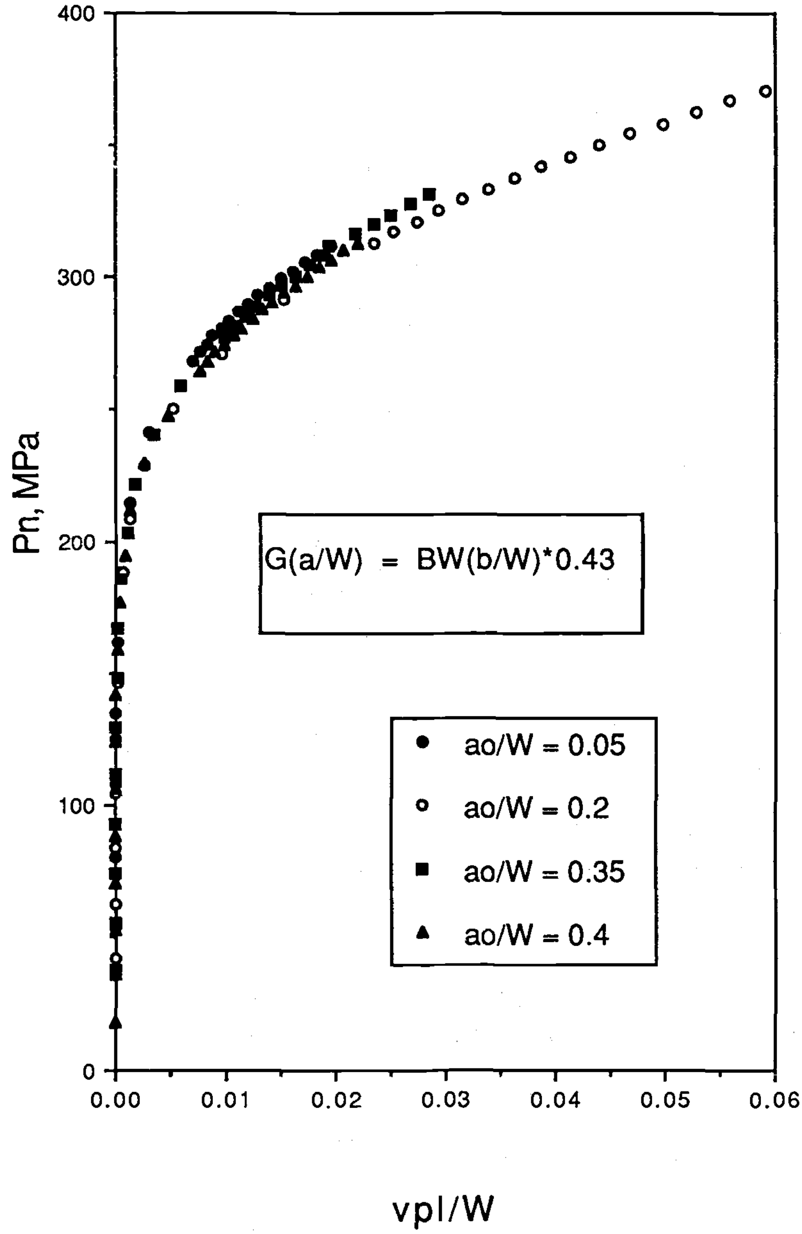

FIG. 26—*Normalized load-versus-plastic displacement for Type 304 stainless steel three-hole specimen.*

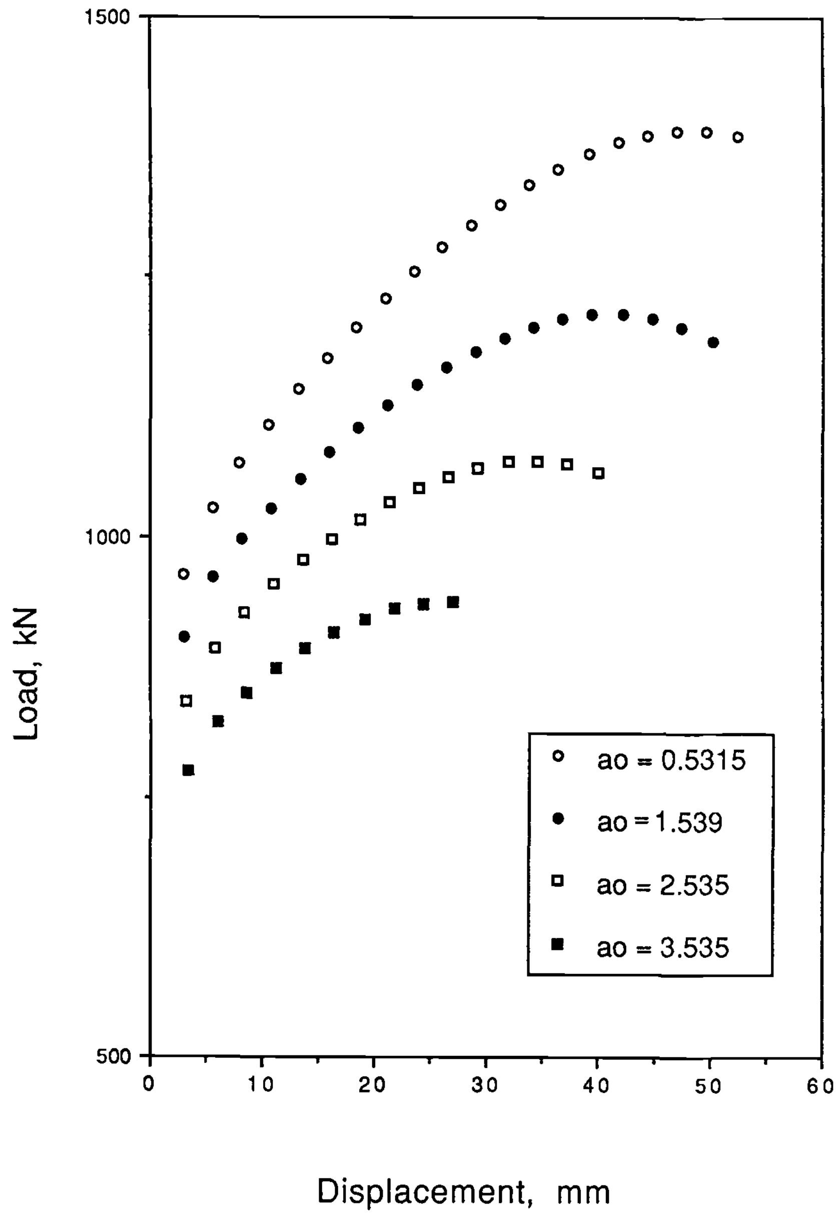

FIG. 27—*Load-versus-displacement predictions for Type 304 stainless steel three-hole specimens.*

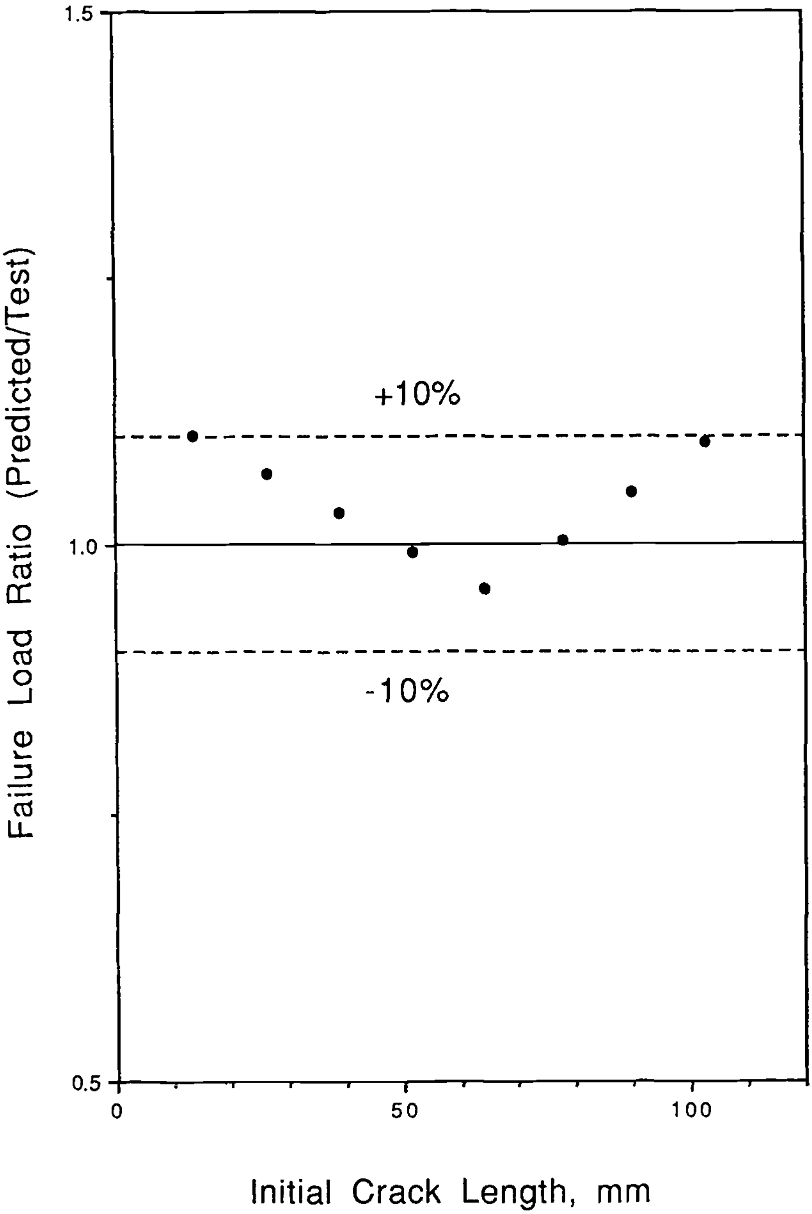

FIG. 28—*Comparison of predicted maximum load with test results for Type 304 stainless steel three-hole specimen.*

Discussion

The methodology presented in this paper is a fairly simple procedure but gives a more detailed prediction of structural behavior than most procedures. In this approach, the entire load-versus-displacement behavior of the structure is predicted rather than simply an instability load or some other more obscure parameter. The method is essentially a complete prediction of the failure behavior for structural components in that it covers the range from linear elastic to fully plastic behavior because it uses a sum of elastic and plastic components. This has been illustrated here for ductile fracture; however, if brittle fracture is viewed as an event that interrupts the ductile fracture process, the point of brittle fracture could be determined as the end point of the load-versus-displacement curve. To do this, the uncertainty in determining a brittle fracture point for a structure would need to be resolved.

In some structures load and displacement are not parameters that can be related to structural behavior. In these cases, other parameters involved in the set of calibration functions could be used. For example, a pressure vessel has neither load or a clearly identifiable displacement. However, in this case, the pressure analyzed as a function of J can identify a maximum failure pressure.

The transfer approach here did not specifically consider the effect of constraint. Although these effects are well known for their effect on the J-R curve, they also affect the calibration functions. One approach might be to use the geometry transfer approach incorporating limit-load solutions that reflect the difference between plane strain and plane stress. These may work for extremes of constraint but would probably not be very accurate for the general case.

To make the method work better, more effort could be given to the development of the $G(a/W)$ function for complex geometries. For the three-hole specimen, the power law function for $G(a/W)$ was not correct, but it still gave reasonable predictions. For other complex geometry shapes, a transfer from the compact to the structural component could be done using a procedure that may be better than the one given in Figs. 2, 3, and 4. However, for a first attempt, this procedure of calibration curve transfer works reasonably well.

The other procedure that needs to be developed is the transfer of the J-R curve from that for the compact specimen to one for the structural component geometry. This procedure will require more study of the effects of size geometry and constraint on the J-R curve before it can be completed. For now, using a conservative J-R curve works well when the fracture process is occurring on the flat part of the calibration curve. This illustrates the point that getting correct calibration curves is often more important than getting correct J-R curves.

The procedure used here was applied to two-dimensional geometries. Obviously, the three-dimensional part-through crack is often the one more encountered in an application, and a procedure to develop calibration curves for three-dimensional cases is needed.

Summary

A ductile fracture methodology is presented here that takes the load-versus-displacement behavior measured on a compact specimen in a laboratory test and uses this result to directly predict the load-versus-displacement behavior of a structural component containing a crack-like defect. Six examples of structural component models were used to demonstrate the methodology. The important new result presented here is a procedure to transfer calibration functions from that for the compact test specimen to one for the structural component. In one case, a simple finite-element analysis of a blunt-notched geometry is used to develop the calibration functions. In all of the cases presented here, there were test results for the structural models that were compared with the predicted load versus displacement. In most cases, the entire load-versus-displacement record may not be predicted exactly but the maximum load, corresponding to failure under a soft loading, was predicted within a few percent.

Acknowledgment

Some of the results presented in this paper were developed under a contract supported by the David Taylor Research Center (DTRC). Richard Link of DTRC was the contract monitor for this project.

References

[*1*] Ernst, H. A. and Landes, J. D., "Elastic-Plastic Fracture Mechanics Methodology Using the Modified J, J_M Resistance Curve Approach," *Journal of Pressure Vessel Technology, Transactions*, American Society of Mechanical Engineers, Vol. 108, No. 1, Feb. 1986, pp. 50–56.

[*2*] Ernst, H. A. and Landes, J. D., "Predictions of Instability Using the Modified J, J_M, Resistance Curve Approach," *Elastic-Plastic Fracture Mechanics Technology, ASTM STP 896*, J. C. Newman and F. J. Loss, Eds., American Society for Testing and Materials, Philadelphia, 1985, pp. 128–138.

[*3*] Link, R. E., Herrera, R., and Landes, J. D., "General Methodology for Predicting Structural Behavior Under Ductile Fracture Conditions," *Advances in Fracture Research, Proceedings*, ICF-7, Pergamon Press, New York, Vol. I, March 1989, pp. 205–212.

[*4*] Landes, J. D. and Herrera, R., "Micromechanics of Elastic/Plastic Fracture Toughness, J_{Ic}," *Fracture Mechanics: Microstructure and Micromechanics, Proceedings*, 1987 ASM Materials Science Seminar, American Society for Metals, Metals Park, OH, Oct. 1987, pp. 111–130.

[*5*] Link, R. E., Landes, J. D., Herrera, R., and Zhou, Z., "Something New on Size and Constraint Effects for J-R Curves," *Defect Assessment in Components—Fundamentals and Applications*, ESIS/EGF9 (S. G. Blauel and K. H. Schwalbe, Eds.) Mechanical Engineering Publications, London, 1991, pp. 707–721.

[*6*] Ernst, H. A., Paris, P. C., and Landes, J. D., "Estimations of *J*-Integral and Tearing Modulus *T* from a Single Specimen Test Record," *Fracture Mechanics (13th Conference), ASTM STP 743*, Richard Roberts, Ed., American Society for Testing and Materials, Philadelphia, 1981, pp. 476–502.

[*7*] Sharobeam, M. H. and Landes, J. D., "The Load Separation Criterion and Methodology in Ductile Fracture Mechanics," *International Journal of Fracture*, Vol. 47, Jan. 1991, pp. 81–104.

[*8*] Joyce, J. A., Davis, D. A., Hackett, E. M., and Hayes, R. A., "Application of the *J*-Integral and the Modified *J*-Integral to Cases of Large Crack Extension," NUREG CR-5143, U.S. Nuclear Regulatory Commission, Washington, DC, Feb. 1989.

[*9*] Sharobeam, M. H. and Landes, J. D., "The Load Separation and η_{pl} Development in Precracked Specimen Test Records," *International Journal of Fracture*, Vol. 59, 1993, pp. 213–226.

[*10*] Herrera, R. and Landes, J. D., "A Direct *J-R* Curve Analysis of Fracture Toughness Tests," *Journal of Testing and Evaluation*, Vol. 16, No. 5, Sept. 1988, pp. 427–449.

[*11*] Herrera, R. and Landes, J. D., "Direct *J-R* Curve Analysis: A Guide to the Methodology," *Fracture Mechanics: Twenty-First Symposium, ASTM STP 1074*, J. P. Gudas, J. A. Joyce, and E. M. Hackett, Eds., American Society for Testing and Materials, Philadelphia, 1990, pp. 24–43.

[*12*] Landes, J. D., Zhou, Z., Lee, K., and Herrera, R., "The Normalization Method to Develop *J-R* Curves with the *LMN* Function," *Journal of Testing and Evaluation*, Vol. 19, No. 4, July 1991, pp. 305–311.

[*13*] Kumar, V., German, M. D., and Shih, C. F., "An Engineering Approach for Elastic-Plastic Fracture Analysis," NP 1931, EPRI Project 1237-1, Electric Power Research Institute, Palo Alto, CA, July 1981.

[*14*] Hu, J. M. and Albrecht, P., "Analyses of Deformation Behavior During Plastic Fracture," *Elastic-Plastic Fracture Test Methods: The User's Experience (Second Volume), ASTM STP 1114*, J. A. Joyce, Ed., American Society for Testing and Materials, Philadelphia, 1991, pp. 178–196.

[*15*] Landes, J. D., Brown, K. H., and Herrera, R., "Determining Failure Load: Ductile Fracture Methodology versus Limit Load," *Fracture Mechanics: Twenty-Second Symposium* (Volume I), *ASTM STP 1131*, H. A. Ernst, A. Saxena, and D. L. McDowell, Eds., American Society for Testing and Materials, Philadelphia, 1992, pp. 158–177.

[*16*] Link. R. E., Landes, J. D., and Herrera, R., "Elastic-Plastic Handbook Solutions: Experimental Evaluations and User Guide," *Defect Assessment in Components—Fundamentals and Applications*, ESIS/EGF9, S. G. Blauel and K. H. Schwalbe, Eds., Mechanical Engineering Publications, London, 1991, pp. 985–1003.

[*17*] Landes, J. D., McCabe, D. E., and Ernst, H. A., "Elastic-Plastic Methodology to Establish R-Curves and Instability Criteria," Final Report, EPRI Contract RP-1238-2, Electric Power Research Institute, Palo Alto, CA, March 1983.

[*18*] Newman, J. C., Jr., "An Evaluation of Fracture Analysis Methods," *Elastic-Plastic Fracture*

Mechanics Technology, ASTM STP 896, J. C. Newman, Jr., and F. J. Loss, Eds., American Society for Testing and Materials, Philadelphia, 1985, pp. 5–96.
[*19*] Kanninen, M. F. et al., "Instability Predictions for Circumferentially Cracked Type 304 Stainless Steel Pipe Under Dynamic Loading-Vols. I & II," EPRI NP-2347, Project T118-2, Final Report, Electric Power Research Institute, Palo Alto, CA, April 1982.
[*20*] Kanninen, M. F. et al., "The Development of a Plan for the Assessment of Degraded Nuclear Pipe by Experimentation and Tearing Instability Fracture Mechanics Analysis," NRC-04-81-178, Final Report, Battelle Columbus Laboratories, Columbus, OH, Sept. 1982.
[*21*] Landes, J. D. and McCabe, D. E., "Toughness of Austenitic Stainless Steel Pipe Welds," NP-4768, Topical Report on Research Project 1238-2, Electric Power Research Institute, EPRI, Palo Alto, CA, Oct. 1986.
[*22*] Tada, H., Paris, P. C., and Irwin, G. R., *The Stress Analysis of Cracks Handbook,* Paris Productions, Inc., St. Louis, MO, 1985.

R. Craig McClung,[1] Stephen J. Hudak, Jr.,[1] Martin L. Bartlett,[1] and John H. FitzGerald[1]

Growth of Surface Cracks During Large Elastic-Plastic Loading Cycles

REFERENCE: McClung, R. C., Hudak, S. J., Jr., Bartlett, M. L., and FitzGerald, J. H., **"Growth of Surface Cracks During Large Elastic-Plastic Loading Cycles,"** *Fracture Mechanics: Twenty-Third Symposium, ASTM STP 1189,* Ravinder Chona, Ed., American Society for Testing and Materials, Philadelphia, 1993, pp. 265–283.

ABSTRACT: Thin Inconel 718 plates with deep elliptical surface flaws are subjected to large loading cycles under both load and displacement control. Closed-form estimates of the *J*-integral for surface flaws in finite thickness plates are derived with a modified reference stress method and compared with recent elastic-plastic finite element results. A *J*-resistance curve for the surface-cracked configuration is developed and compared with data from thick compact tension specimens. Special attention is given to the apparent relationship between ductile tearing and low-cycle fatigue crack growth mechanisms and rates.

KEY WORDS: elastic-plastic fracture mechanics, *J*-integral, resistance curves, surface cracks, fatigue crack growth, ductile tearing, range marking, crack shape, crack closure, fracture mechanics, fatigue (materials)

Fracture mechanics is often a very powerful tool for ensuring the structural reliability of critical engineering components and structures. There is frequently a tension, however, between the idealized world of fracture mechanics laboratories and textbooks and the real world of engineering applications. One good example of an engineering application that challenges the current limits of accepted fracture mechanics practice is the Space Shuttle Main Engine (SSME). The SSME is subjected to exceptionally severe temperature and stress cycles during repeated missions, and component failure can have catastrophic implications. Flaws of potential concern include complex weldment defects such as porosity, lack of penetration, and microfissures. Flaw geometries are often three-dimensional and typically intersect only one surface (that is, part-through configurations rather than two-dimensional laboratory through-cracks). Due to the high toughness of many SSME materials, small defect sizes, thin component sections, and severe stresses, flaw growth is associated typically with significant plasticity (that is, elastic-plastic fracture mechanics).

Conventional nondestructive evaluation (NDE) methods are the preferred approach to crack detection in the SSME, but NDE techniques alone are occasionally inadequate due to geometric complexities of the component or structure. Under these conditions, proof testing has been utilized as a supplement to NDE for various SSME components and structures. The design and interpretation of these proof tests is complicated, however, by the complex fracture mechanics issued involved, most notably the elastic-plastic nature of the problem. Traditional proof testing logic is based on "brittle" linear elastic fracture mechanics: loading of a cracked

[1] Senior research engineer, manager, research engineer, and senior engineering technologist, respectively, Materials and Mechanics Department, Southwest Research Institute, San Antonio, TX 78228-0510.

structure results in either unstable crack growth to failure (for cracks larger than the critical size) or zero crack growth (for cracks smaller than the critical size.) Elastic-plastic fracture mechanics admits a third possibility, stable crack extension without failure.

The current SSME subcontractor, Rocketdyne, utilizes a modified version of conventional single-cycle proof testing (SCPT) involving multiple proof cycles. This approach has been motivated by failures of components that had survived an initial single-cycle test and were subsequently re-tested, often failing at pressures significantly less than the initial proof. Although this phenomenon is consistent with the earlier observation about stable elastic-plastic crack extension during a proof cycle, there is not yet a well-established theoretical basis to establish the superiority of multiple-cycle proof testing (MCPT), in comparison to conventional SCPT, or to optimize MCPT parameters. The primary justification for current MCPT protocol is experience: the successful record of performance of Rocketdyne engines whenever the procedure has been implemented.

The ultimate goal of the current research program is to develop a rigorous understanding of crack growth behavior during SCPT and MCPT in order to optimize proof testing procedures for SSME and related applications. This paper reports on some of the first steps towards that goal. A series of experiments and analyses are conducted to characterize the crack driving force and material resistance associated with surface-cracked plates under single-cycle loading conditions, based on a *J-R* curve approach, and the relationship between this ductile crack extension and low-cycle fatigue crack growth is explored.

Experimental Procedures

Material Characterization

Due to its wide application in SSME components, Inconel 718, a precipitation hardenable, nickel-base superalloy, was chosen for the experimental investigations. Age hardening in this

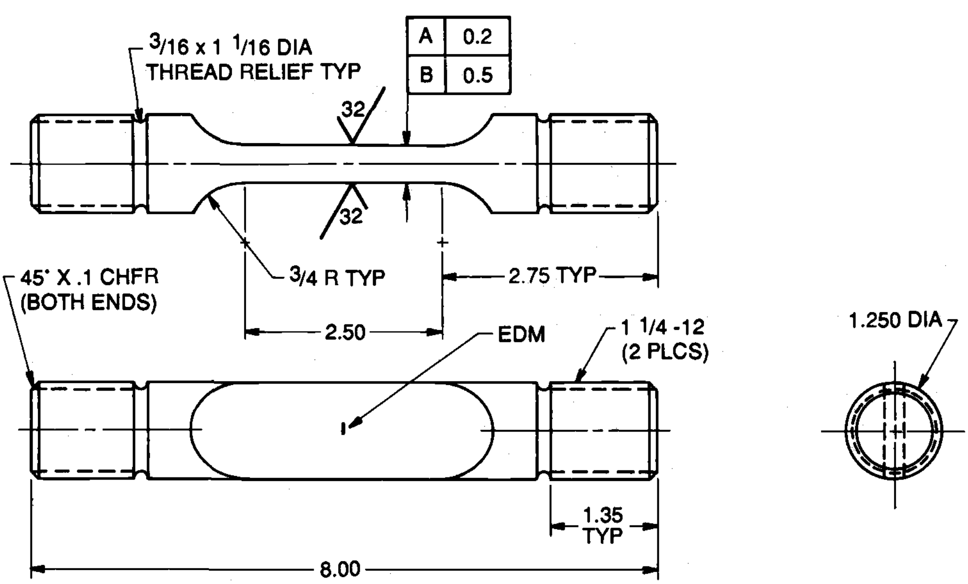

FIG. 1—*Specimen geometry showing location of surface flaw for fatigue and resistance curve testing.*

TABLE 1—*Chemical composition of the Inconel 718 test material, Heat 6L9364.*

C	Mn	Si	S	P	Cr	Ni	Mo	Co
0.044	0.09	0.12	0.001	0.006	18.5	52.3	3.03	0.31
Cu	Al	Ti	Cb+Ta	Mg	Pb	Sn	Fe	
0.05	0.53	0.99	5.17	23 ppm	0.8 ppm	25 ppm	balance	

alloy is achieved through precipitation of a columbium-rich intermetallic phase that results in good corrosion and oxidation resistance, as well as good mechanical properties which permit its use to temperatures of 649°C (1200°F).

To ensure that the results generated were applicable to SSME components, the test material was purchased according to Rockwell Specification RB0170-153 in the form of 31.8-mm (1.25-in.) diameter round bars. The Inconel 718 was machined into center-cracked tension specimens, shown in Fig. 1, and then heat treated according to the following procedures:

1. Vacuum solution treat at 1038°C (1900°F) for 10 to 30 min.
2. Argon back fill, cool to room temperature.
3. Age in vacuum at 760°C (1400°F) for 10 h.
4. Furnace cool to 649°C (1200°F) and hold for a total time at 760°C (1400°F) plus furnace cool plus hold time at 649°C (1200°F), of 20 h.
5. Argon back fill, cool to room temperature.

This particular heat treatment is used in SSME components to achieve optimum resistance to hydrogen embrittlement.

The chemical composition of the Inconel 718 material used is given in Table 1, and the basic mechanical properties are given in Table 2. These tension test results are in conformance with the RB0170-153 specifications. Analysis of the load-displacement records from these tension tests produced a relationship between stress (in ksi) and plastic strain of the form

$$\sigma = 248.4\varepsilon_p^{0.0633} \tag{1}$$

The elastic modulus is 204.7 GPa (29.69 $\times$ 10^3 ksi). The stress–total strain relationship may also be written in the general Ramberg-Osgood form

$$\frac{\varepsilon}{\varepsilon_0} = \frac{\sigma}{\sigma_0} + \alpha\left(\frac{\sigma}{\sigma_0}\right)^n \tag{2}$$

where $\varepsilon_0 = 0.006$, $\sigma_0 = 1240$ MPa (179.8 ksi), $\alpha = 1$, and $n = 15.8$.

TABLE 2—*Mechanical properties of the Inconel 718 test material.*

0.2% Yield Strength, ksi	Ultimate Tensile Strength, ksi	Elongation, %	Reduction in Area, %
161.2	205.5	22.2	33.3

Fatigue Crack Growth Testing and Range Marking Procedure

Fatigue crack growth (FCG) rate tests were conducted on through-thickness cracked panels to determine both baseline fatigue data and information regarding fatigue range marking [1]. The range marking technique is based on the fact that the topography of the fatigue fracture surface is altered with changes in loading variables. The cyclic stress ratio, $R' = K_{min}/K_{max}$, and the cyclic stress intensity factor range, ΔK, can be changed to place a coarse mark on a fine surface, or vice versa, leaving a dark band on the fracture surface. The production of a well-defined range mark depends on prior knowledge of the fracture surface appearance. The crack growth rates correlated with the fracture surface morphology were used to select loading levels for the range marking necessary for the crack shape studies. Metallic materials exhibit a general fracture morphology trend of coarse-to-fine-to-coarse that occurs with transitions at crack growth rates of about 1.27×10^{-5} and 1.27×10^{-3} mm/cycle (5×10^{-7} and 5×10^{-5} in./cycle), respectively [1].

Figure 2 provides a summary of the resulting crack growth rate data (*da/dN*) plotted as a function of ΔK for three specimens. Two tests were run on 5-mm (0.2-in.) thick specimens to provide data over a wide range of growth rates. Crack lengths for these through-crack specimens were measured by optical inspection at the surface. As indicated by the figure, the data obeyed a power law above 20 MPa $\sqrt{m}$ (ΔK = 18 ksi $\sqrt{in.}$), with good agreement in the mid-range where results from the two specimens overlapped. The third test was conducted on a 12.7-mm (0.5-in.) thick specimen. Results from the two thicknesses were in excellent agree-

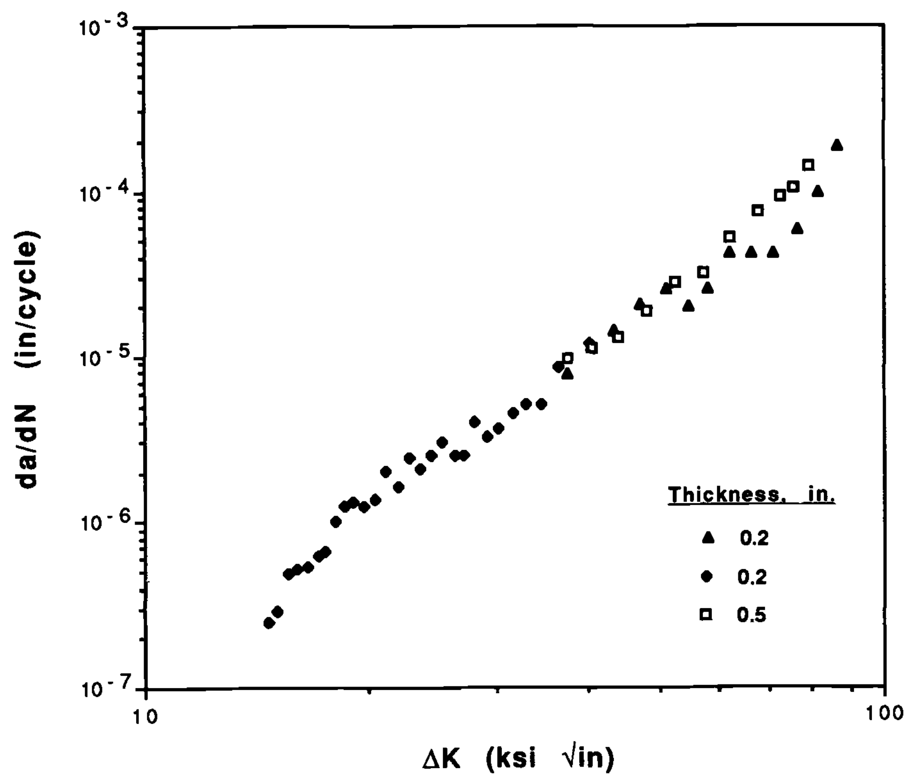

FIG. 2—*Fatigue crack growth rate data for Inconel 718.*

ment, except in the region near 71 MPa $\sqrt{m}$ (ΔK = 65 ksi $\sqrt{in.}$). The deviation in this region was believed to be due to the occurrence of noticeable crack branching in the 5-mm (0.2-in.) thick specimen, which apparently resulted in retardation of the growth rates in this specimen.

Visual examination of the fracture surfaces of the preceding experiments revealed significant differences in the fracture surface morphology at high and low growth rates. This observation provided verification that range marking could be employed successfully to mark crack extension in the following experiments on surface-cracked specimens. Fatigue range marking bands were used to verify changes in the crack shape and to monitor the crack growth during the resistance curve testing.

The crack shape study experiments were conducted on surface-flawed 5-mm (0.2-in.) thick specimens. All specimens were first polished down to a 1-μm diamond polish to provide easy viewing of the crack during the test. Electro-discharge machining (EDM) slots were introduced into the surface of the specimens to provide a starter for the crack. The slot sizes for the 5-mm (0.2-in.) thick specimens were 1.27-mm (0.05-in.) deep by 0.100-in. (2.54-mm) long, and, in the 12.7-mm (0.5-in.) thick specimens, they were 3.18-mm (0.125-in.) deep by 6.35-mm (0.25 in.) long. Prior to the precracking, the specimens were prepared with photographic grids, having 0.254-mm (0.010-in.) spacing, to provide reference lines for the visual crack length measurements. Three specimens were then precracked and tested under fatigue loading at a stress ratio of 0.1 using a closed-loop, servohydraulic testing machine.

The shape of the growing crack was recorded periodically using fatigue range marking. On the first attempt at range marking, fine marks were applied to the fracture surface. When the specimen was broken open, these marks were indistinct, indicating that a coarser marking was necessary. For the second attempt, a coarse-on-fine scheme was employed to produce the marker band. The stress ratio needed to produce a marker band (R^{σ}_{mark}) was estimated from the following empirical relationship [2]

$$\frac{(da/dN)_{\text{Ref}}}{(da/dN)_{\text{mark}}} = \left\{\frac{1 - R^{\sigma}_{\text{Ref}}}{1 - R^{\sigma}_{\text{mark}}}\right\}^2 \tag{3}$$

where $(da/dN)_{\text{Ref}}$ is the reference crack growth rate at R^{σ}_{Ref} = 0.1 and $(da/dN)_{\text{mark}}$ is the crack growth rate at the stress ratio chosen to produce the marker band (R^{σ}_{mark}). Based on the fracture surface morphology, $(da/dN)_{\text{mark}}$ was chosen to be 2.54×10^{-6} mm/cycle (1×10^{-7} in./cycle) and R^{σ}_{mark} was determined from Eq 3. In FCG testing, R^{σ}_{mark} varied as $(da/dN)_{\text{Ref}}$ increased, whereas in R-curve testing, R^{σ}_{mark} was fixed at 0.8. Prior to marking the specimen, the load was dropped 30%. This drop in maximum load is desirable during the resistance curve testing, so that only small crack extension will occur during the marking.

A range-marked part-through fatigue crack fracture surface is shown in Fig. 3. Note that the crack shape was nearly constant throughout the growth of the crack, varying from 0.493 to 0.549 at the seven marker bands (Fig. 4). The aspect ratio, $a/2c$, appears to drop off only slightly as the deepest point of the crack approaches the back face of the specimen.

Surface Crack J*-Resistance Curve*

In order to develop resistance curves for part-through crack configurations, crack growth tests were conducted with surface-cracked panels of Inconel 718 under both load and displacement control. Initial crack depths ranged from a/t = 0.36 to 0.73, and initial crack aspect ratios were typically around $a/2c$ = 0.5.

In the load control experiments, the applied load was used as the feedback signal for the servohydraulic test machine. During these tests, a crack opening displacement (COD) gage

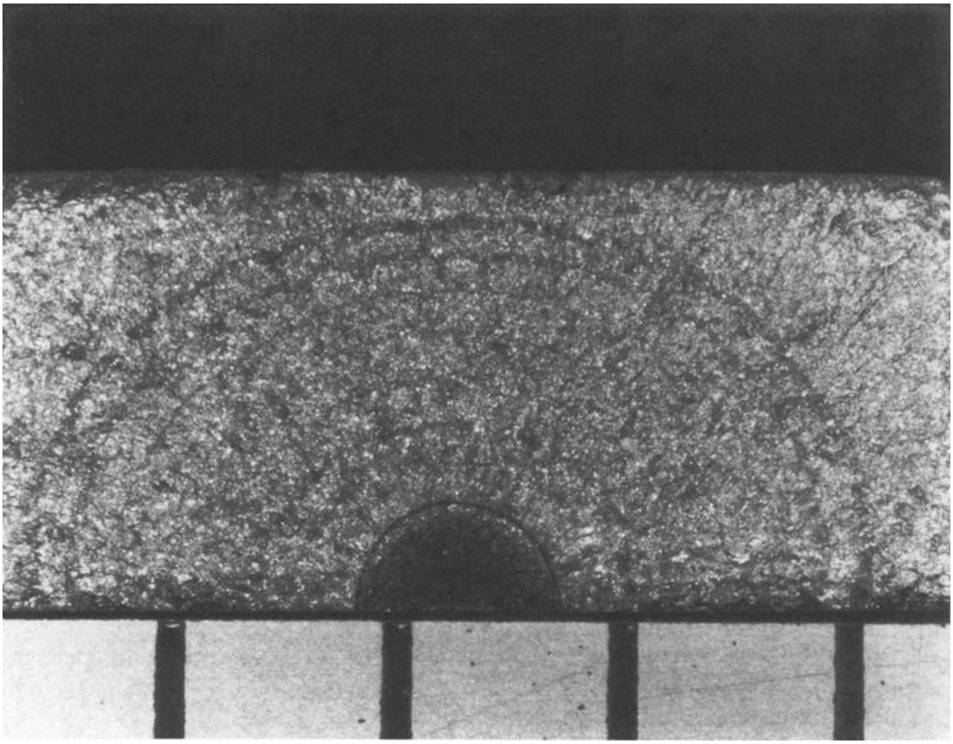

FIG. 3—*Fracture surface of range-marked FCG specimen.*

with a gage length of 5 mm (0.20 in.) was placed across the crack mouth, the gage pins located in diamond indentations on the front surface of the plate. Two methods were attempted to monitor crack extension during loading: changes in elastic compliance during periodic unloading of the specimen, and fatigue marker bands introduced by periodic cyclic loading at a high R ratio. However, due to the small amount of crack extension that occurred in the experiments, crack extension could not be reliably detected with either of these techniques. Nevertheless, it was possible to generate a resistance curve by testing multiple specimens. In each case, the specimen was loaded to produce different amounts of crack extension as determined by postmortem analysis of the fracture surface. The initial crack length was marked following fatigue precracking by heat tinting. The final crack length at the end of the R-curve loading was distinguished by growing the crack to final fracture under high stress ratio cyclic loading, which created a distinctively different fracture surface morphology.

Only small amounts of crack extension (less than 0.2 mm (0.008 in.)) were obtained in the load control tests. In addition, the low strain hardening behavior of the material, when coupled with the large loads required to initiate crack growth, made control of the experiment difficult. The crack mouth displacement tended to run rapidly as yielding spread throughout the net section, and fast fracture occasionally intervened before the loading could be interrupted.

In response to these experimental difficulties, a series of displacement control tests were conducted. During these tests, the specimen was driven to a set crack mouth displacement (and at a fixed rate of crack mouth displacement), allowing the load to increase as necessary to reach that displacement. In this case, the COD gage was modified to obtain a gage length of 1.27 mm (0.05 in.). By conducting the test in this manner, it was possible to achieve virtually any displacement (and thus any amount of crack growth), since the applied J decreased as the crack extended. Larger Δa values were thus obtained in the displacement-controlled tests than in the load-controlled tests. No significant changes in crack aspect ratios were observed with crack growth. Crack growth increments reported for both load and displacement control tests were measured at the deepest point of the surface crack.

Analytical Procedures

Due to the high toughness of this material and the small absolute sizes of the flaws, all specimens exhibited significant yielding before the onset of instability. This phenomenon required the use of elastic-plastic analysis techniques to establish the resistance curve. The J-integral was selected as the correlating parameter for crack growth.

J-integral estimation schemes for compact tension specimens, edge-cracked plates, and many other "standard" specimen and component geometries are readily available. Closed-form estimates for surface or embedded cracks in finite thickness plates or shells, however, have not been developed. A limited number of finite element results for specific crack and specimen geometries and materials have been published, but these have not yet led to generalized analytical expressions.

An alternative approach to J estimation is the reference stress approach developed by Ainsworth and colleagues at the Central Electricity Generating Board (CEGB) of the United Kingdom [3]. This technique requires only three basic pieces of information: (1) a complete solu-

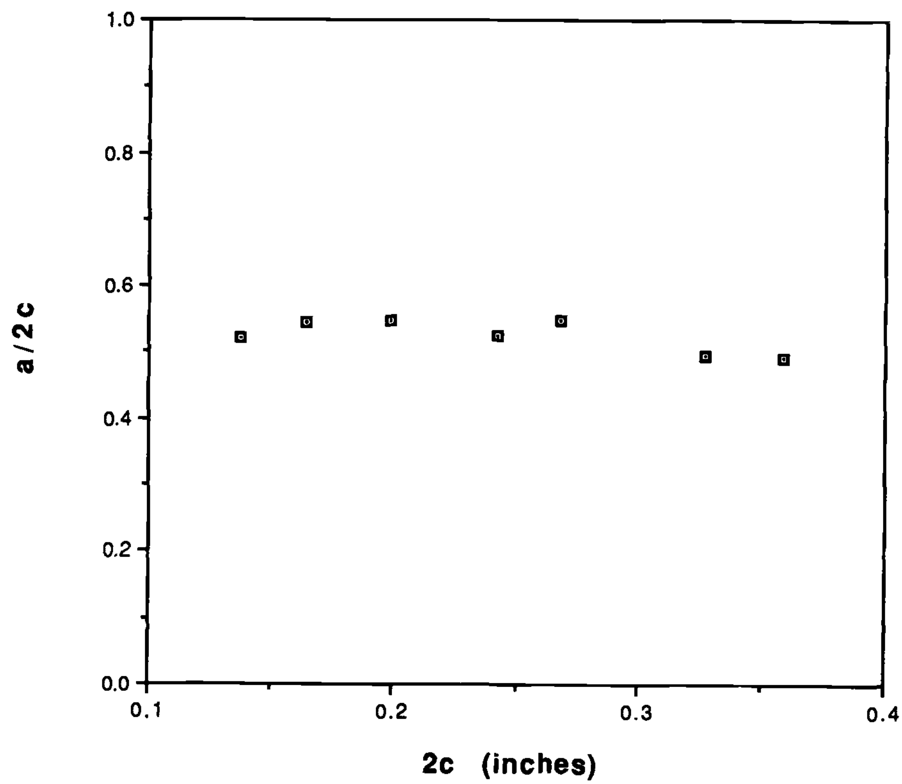

FIG. 4—*Variation of surface crack shape with crack size.*

tion for the linear elastic stress intensity K factor; (2) a description of the elastic-plastic constitutive material response (which does not have to be of the Ramberg-Osgood form); and (3) an estimate of the plastic collapse limit load for the cracked member, assuming an elastic-perfectly plastic material. All three of these are available for the surface-cracked plate and the Inconel 718 material. A remaining ambiguity for the surface-cracked plate is whether the limit load should represent the local limit load for break-through to the back surface or the global limit load for failure of the entire plate. Investigations by Miller of the CEGB [4] suggested that the global limit load provides better J estimates, and his comparisons of reference stress estimates with the limited number of "exact" solutions available at that time found the estimate to be acceptable.

The general form of the reference stress estimate for J used here was given by the expression

$$J = K^2 \frac{\varepsilon_{\text{ref}}}{\sigma_{\text{ref}}} \left\{ 1 + \frac{1}{2} \left(\frac{\sigma_{\text{ref}}}{\sigma_{\text{ys}}} \right)^2 \left(\frac{\sigma_{\text{ref}}}{E \varepsilon_{\text{ref}}} \right)^2 \right\} \tag{4}$$

This equation includes an effective crack length term to approximately account for plasticity in the intermediate yielding regime [5]. The reference stress for a surface-cracked plate was calculated as

$$\sigma_{\text{ref}} = \frac{\sigma_\infty}{1 - (\pi a c)/(2tW)} \tag{5}$$

where t and W are the thickness and width of the specimen and σ_∞ is the nominal applied stress. The reference strain, ε_{ref}, was calculated from the constitutive relationship as the uniaxial strain corresponding to σ_{ref}. The linear elastic stress intensity factor, K, for the surface cracks was calculated from the expressions of Newman and Raju [6].

These reference stress estimates for surface cracks in finite thickness elastic-plastic plates are compared with recent finite element results published by Parks and Wang [7] in Fig. 5, where J is normalized by $\sigma_0 \varepsilon_0 t$ and the applied stress is normalized as σ_∞/σ_0. The material constants, σ_0 and ε_0, are based on the Ramberg-Osgood description of the elastic-plastic constitutive relationship, Eq 2. The reference stress J estimate was found to be significantly low for both crack shapes, and this prompted additional analysis.

Dowling [8] has previously studied J estimates for semicircular flaws in infinite bodies. He derived an equation of the general form

$$J = \frac{K^2}{E'} \left\{ 1 + \frac{J_z}{J_e} + h_0 \frac{E'}{E} \frac{\alpha(\sigma/\sigma_0)^n}{\sigma/\sigma_0} \right\} \tag{6}$$

where $E' = E$ for plane stress, $E' = E/(1 - \nu^2)$ for plane strain, J_z/J_e is an effective crack length (plastic zone) correction term, and h_0 is a function of the strain hardening exponent. Dowling found an equation of this form to give very similar results to the elastic-plastic finite element analysis of Trantina et al. [9].

For infinite bodies, the reference stress is equal to the applied stress, and so we may rewrite the previous equation (for plane stress) as

$$J = \frac{K^2}{E} \left\{ 1 + \frac{J_z}{J_e} + h_0 \left(\frac{\varepsilon_{\text{ref}} E}{\sigma_{\text{ref}}} - 1 \right) \right\} \tag{7}$$

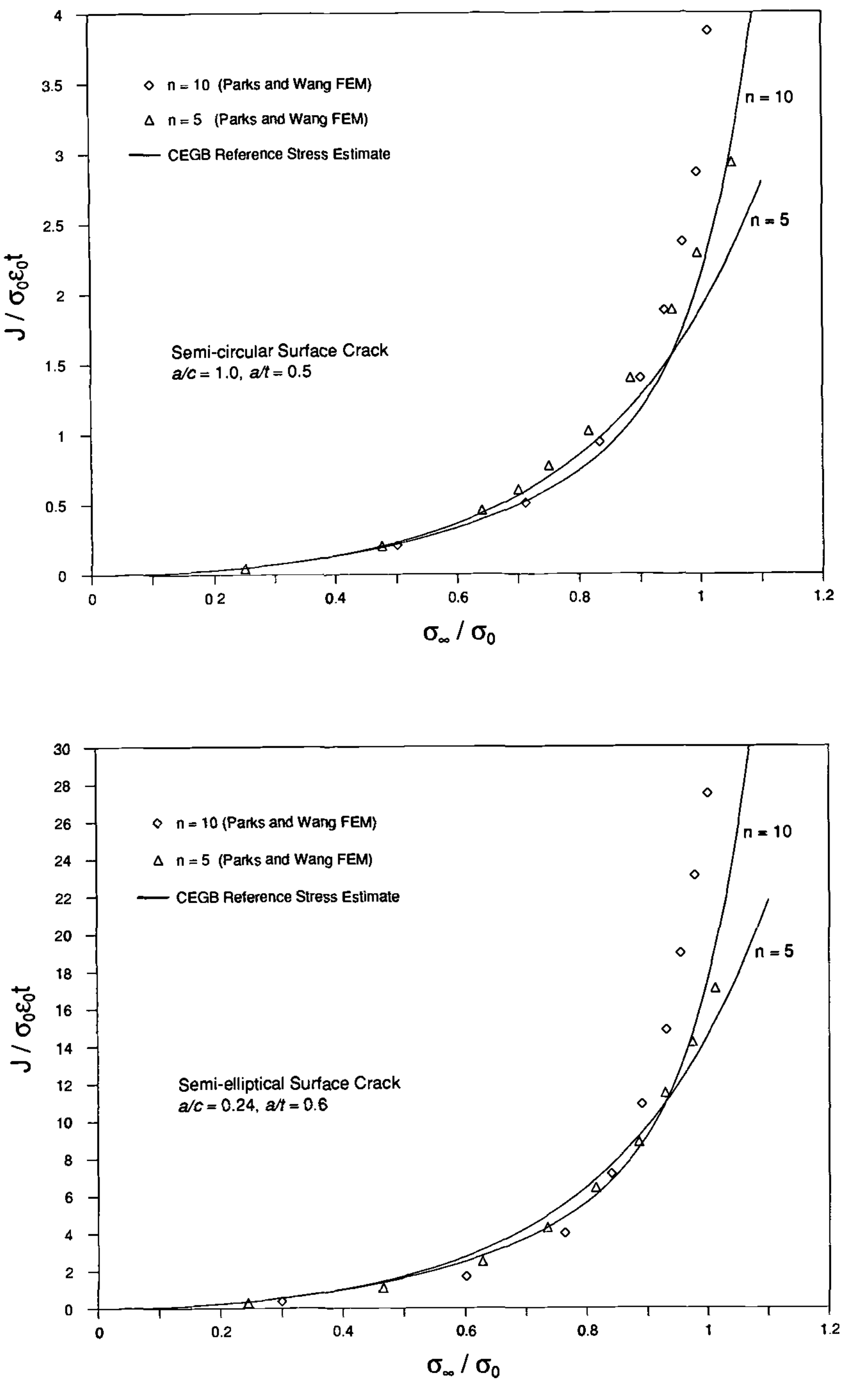

FIG. 5—*Comparison of reference stress method for* J *estimation with finite element results of Parks and Wang* [7] *for surface cracks in finite plates.*

Ignoring for the moment the effective crack length term, J_z/J_e, this equation differs from the basic CEGB reference stress equation only by the h_0 factor, which the CEGB estimate for an infinite body would set equal to 1. An arbitrary modification to the reference stress J estimate can then be made by applying this last equation to the general case of a finite body, where the reference stress and strain will be higher than the nominal applied values. These new estimates are compared with the Parks and Wang results in Fig. 6, and the agreement is clearly much improved. These results are promising, although further study is needed to confirm this modified estimation procedure.

A second method of estimating J for the surface crack tests is an "equivalent energy" approach suggested by McCabe et al. [*10*]. They proposed that J could be calculated as

$$J = \frac{(K_R)^2}{E} \tag{8}$$

where K_R is a plasticity-modified stress intensity factor given by

$$K_R = K_{Ie} \sqrt{\frac{A_T}{A_e}} \tag{9}$$

Here, A_T and A_e are the total and elastic areas under the load-displacement curves and K_{Ie} is the linear-elastically determined stress intensity factor; see Fig. 7. Since this method requires experimental information about local displacements, it is not entirely suitable for engineering applications to actual structures. Nevertheless, it serves as a useful independent check on the modified reference stress technique for the experiments reported in this paper.

Actually, of course, the value of the J-integral varies around the perimeter of the crack [*7*], and the specific variation of J along the crack front changes with the crack aspect ratio, a/c, the applied stress, σ_∞/σ_0, and the strain hardening properties of the material. At lower applied stresses, this angular variation largely mirrors the well-documented variation in K around the perimeter, although this is less true at applied stresses on the order of the flow stress. In view of the relatively uniform crack growth around the perimeter observed in the experiments discussed earlier, and in view of the relatively uniform analytical values of J around the perimeter for semicircular cracks at applied stresses of interest, variations of J around the perimeter were ignored in the development of simple J estimates for the current research. In the modified reference stress estimate, the K-solution used corresponded to the deepest point of the crack, and the resulting J-estimate was assumed to correspond to this location as well (the finite element results shown in Figs. 5 and 6 also correspond to the deepest point of the crack). Further studies are required to determine if the reference stress approach can adequately address more significant variations in J around the perimeter. A more complete treatment of the surface crack ductile fracture problem must address not only variations in driving force around the perimeter but also variations in crack growth resistance (with stress state, for example) around the perimeter. These issues are beyond the scope of the present work.

Results and Discussion

Resistance Curves for Surface-Cracked Plates

The resulting resistance curves for the surface-cracked Inconel 718 are shown in Fig. 8. Note that the modified reference stress and equivalent energy estimates gave similar values for J, typically differing by about 10%. The primary exception to this agreement is the data point corresponding to the displacement-controlled test with the greatest amount of crack extension.

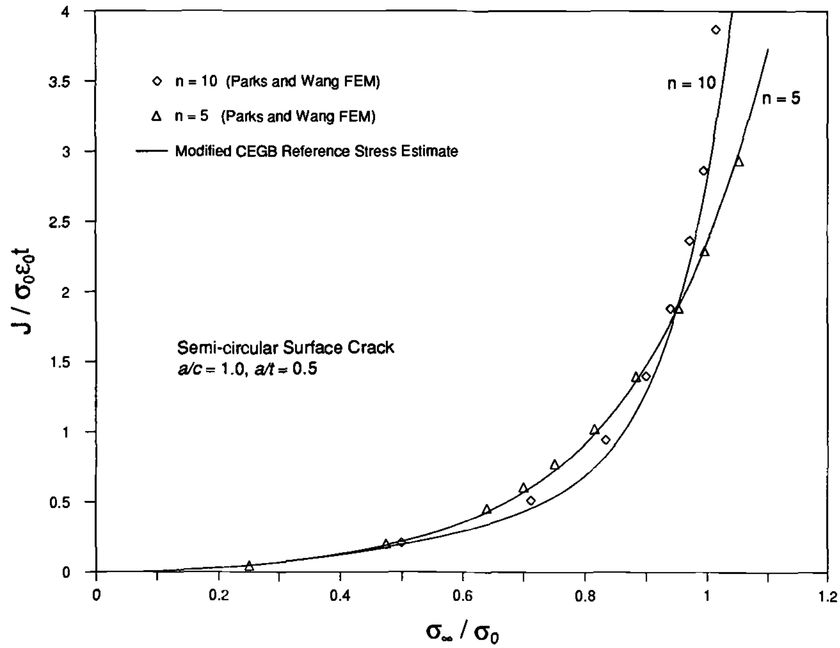

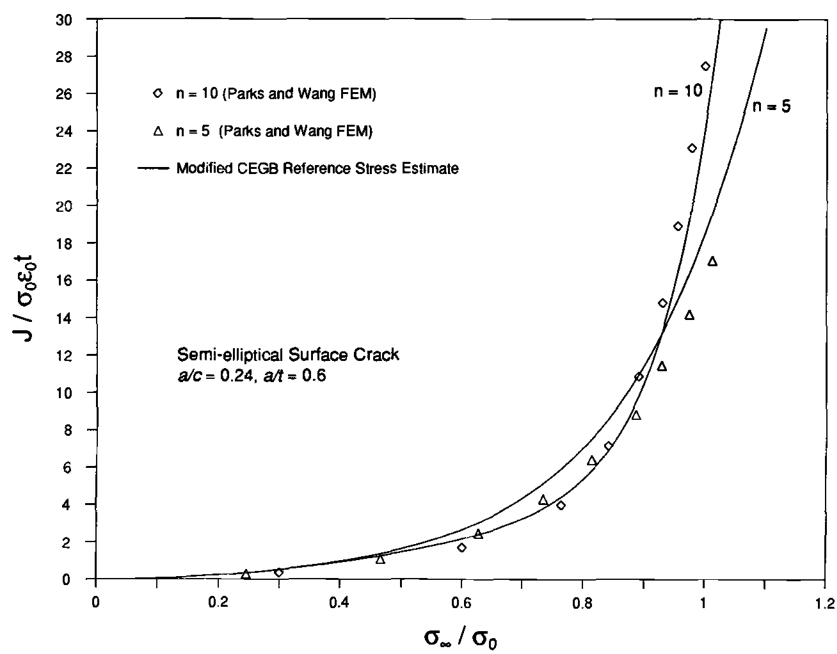

FIG. 6—*Comparison of modified reference stress method for* J *estimation with finite element results of Parks and Wang* [7] *for surface cracks in finite plates.*

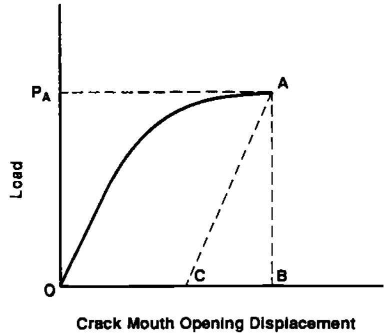

$$K_R = (K_{Ie})_A \sqrt{\frac{A_T}{A_e}}$$

Where $(K_{Ie})_A$ is the linear-elastic K at load P_A
A_T = Total Area (O-A-B)
A_e = Elastic Area (C-A-B)

FIG. 7—*Schematic of equivalent energy method for estimating* J *for surface cracks (adapted from Ref 10).*

This discrepancy may reflect the uncertainty associated with J following large amounts of crack advance with associated elastic unloading in the wake of the crack. It may also indicate differences in J for stationary cracks under load control (the basis of the analysis) and growing cracks under displacement control (the conditions of the experiment), differences that would be magnified with extensive crack advance.

Also shown in this figure for comparison are resistance curve data obtained by Rocketdyne[2] from relatively thick (B = 15.24 mm (0.6 in.)) compact tension (CT) specimens of a similar Inconel 718. These CT data meet the specimen size validity requirements of ASTM Test Method for J_{Ic}, a Measure of Fracture Toughness (E 813-89). The resistance curve for surface cracks is clearly different from the CT resistance curve. The initial slope (associated with the blunting line and early crack growth) appears to be about the same, but the critical J value at which large amounts of crack extension begin to occur is much higher. This indication of higher toughness is consistent with a possible change from high constraint in the thick-section CT tests to lower constraint in the thin-section, deeply-cracked surface flaw tests. Other factors may also be involved, including the loss of J-dominance (discussed further later). Similar surface crack behavior has been previously observed by others [*11–13*]. Furthermore, there appears to be a more gradual change in the slope of the surface crack resistance curve in the vicinity of the "knee." It is difficult to evaluate the possible changes in the tearing slope with specimen geometry in this case, since only a few points are available to calculate this slope for the surface crack tests. It is possible that the tearing modulus remains unchanged with the specimen geometry, but it is also possible that the tearing modulus increases (perhaps due also to loss of constraint) for the surface crack. Both phenomena have been reported in the literature for other materials. Additional tests would be needed to better characterize the tearing slope, particularly for small amounts of crack extension.

[2] K. A. Garr, unpublished data.

This difference in the resistance curves for CT and surface-cracked geometries is consistent with recent research on constraint effects in fracture. Shih et al. [*14*] and Hancock et al. [*15*] have both recently presented rigorous numerical frameworks to explain the geometry dependence of J_c values in terms of the elastic T-stress [*15*], the nonsingular stress term parallel to the crack [*16*], or its elastic-plastic analog, the so-called Q-stress [*14*]. The nondimensional biaxiality parameter, $\beta = T\sqrt{\pi a}/K_I$ [*17*], is relatively low, around $\beta = -1$, for low constraint geometries such as the center-cracked plate and the deep surface crack, while β is positive for CT and deeply cracked single-edge-notch configurations. J_c typically reaches a constant minimum value for normalized T-stresses greater than zero, while J_c increases at progressively more negative T-values.

These changes in apparent fracture resistance with geometry/constraint have also been shown to be related to the loss of rigorous J-dominance (the failure of J to adequately describe the crack-tip fields). J-dominance is lost more quickly under low constraint configurations. Conventional fracture mechanics wisdom would question even the use of J under such low constraint (and large applied stress) conditions. The ongoing work on constraint effects seems to suggest, however, that a two-parameter approach (J and either T or Q) may provide a means of explaining some geometry effects on ductile fracture and perhaps even correcting R-curve data to some geometry-independent representation of material resistance. Further work is clearly needed.

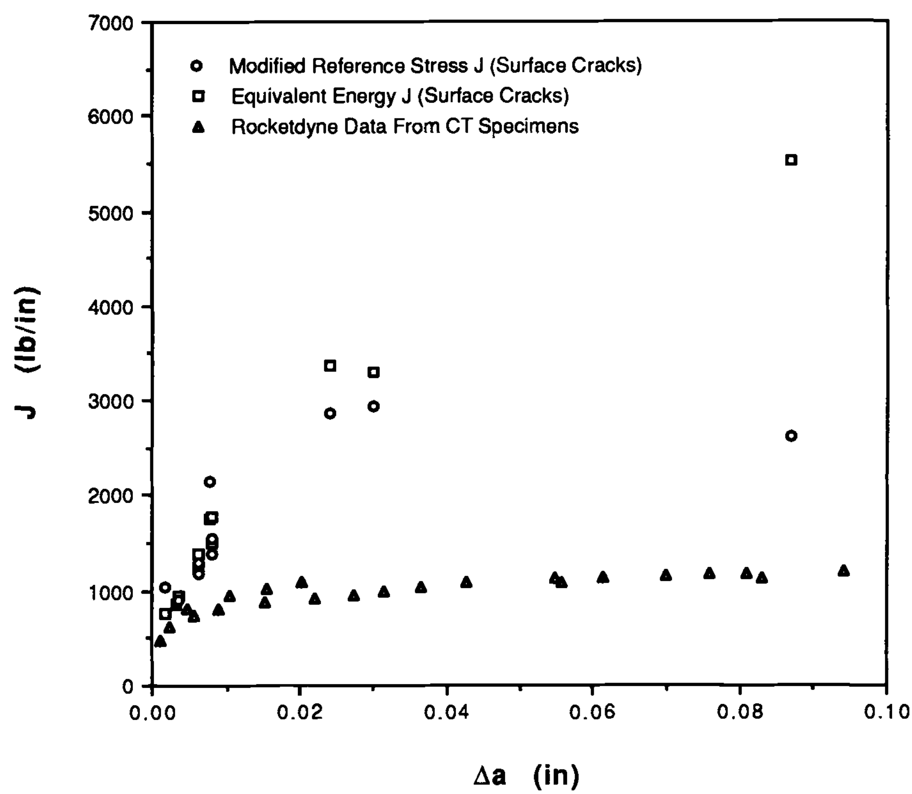

FIG. 8—*Resistance curve data for surface-cracked Inconel 718 based on two different J-estimation methods and compared with data from CT specimens.*

Relationship Between Ductile Fracture and Fatigue Crack Growth

The engineering application that is motivating this research (multiple-cycle proof testing of SSME hardware), however, requires a more difficult problem to be addressed. Crack growth behavior must be characterized not only for single monotonic loadings (traditional ductile fracture) but for multiple large load-unload cycles. Crack growth during these cycles can conceivably occur by several different mechanisms, including (1) rupture mechanisms such as ductile tearing; (2) true fatigue mechanisms, such as those associated with striation formation; and (3) interactions between rupture and fatigue. Potential contributions due to creep mechanisms do not appear to be significant, since these proof tests and experiments are conducted at room temperature.

Perhaps the most common approach to estimating crack growth during large load-unload cycles is an independent linear summation of contributions from fatigue and ductile tearing [*18,19*]. No interaction between the two crack growth mechanisms is considered. Other [*20*] have suggested that some acceleration in the fatigue crack growth rate may occur as ductile fracture instability is approached, similar to the increase in da/dN in linear elastic systems subject to cleavage fracture as K_{max} approaches K_{Ic}. Kobayashi et al. [*21*] have recently proposed more direct relationships between monotonic and cyclic elastic-plastic crack growth behavior.

An important first step in characterizing crack growth during large load-unload cycles, then, is to investigate the relationship between crack growth during fatigue (da/dN) and ductile tearing (R-curve) experiments. In order to study this relationship, data from the earlier fatigue crack growth tests on Inconel 718 (which belong to the small-scale yielding regime and hence were originally correlated with ΔK) were re-expressed in terms of the more general elastic-plastic parameter, ΔJ, according to the usual relationship, $J = K^2/E$. An estimate of the crack closure level was made by noting that the original FCG tests satisfied plane strain conditions, for which $\sigma_{open}/\sigma_{max} = 0.2$ has been shown to be a reasonable approximation at $R = 0$ [*22*]. The FCG data were then expressed as da/dN versus ΔJ_{eff} values, and the central tendency line (in log-log space) was identified via least-squares regression.

Data from the J-resistance curves were superimposed on the FCG plot by recognizing that for one "cycle" of monotonic loading with no previous history, $J_{max} = \Delta J_{eff}$ and $\Delta a = da/dN$. Both types of R-curve data were included in this exercise: CT specimens with through-cracks and plate specimens with surface cracks. J values for the surface cracks were estimated by both equivalent energy and reference stress methods.

The FCG and R-curve data are shown together in Fig. 9 on the traditional log-log FCG graph. Note that the R-curve data are entirely consistent with the latter stages of FCG. The form of these data is similar to the usual upturn in da/dN-ΔK data near instability (for example, near K_{Ic} or plastic collapse). This upturn occurs at a lower value for the CT specimen, where constraint is higher. The upturn occurs at a considerably higher value for the surface-cracked plates, where deep flaws and high stresses cause a reduction in constraint, and many of the R-curve data points are shown to lie directly on the FCG central tendency line. The FCG line must be extrapolated beyond the region of the FCG data to pass through the region of the R-curve data, of course, but previous experience with ΔJ indicates that this should be a reliable extrapolation. Dowling, for example, found that the linear Paris law form of the ΔJ-da/dN relationship was consistent over five orders of magnitude in crack growth rates [*23*].

The relationship between FCG and R-curve data is shown from a different perspective in Fig. 10, which superimposes the central tendency FCG line on the traditional J-resistance curves. The central tendencies of the R-curve data are also identified with empirical fits of the data to an exponential form proposed by Orange [*24*]. For the surface crack data, the modified reference stress and equivalent energy estimates were averaged to obtain a "best estimate" of

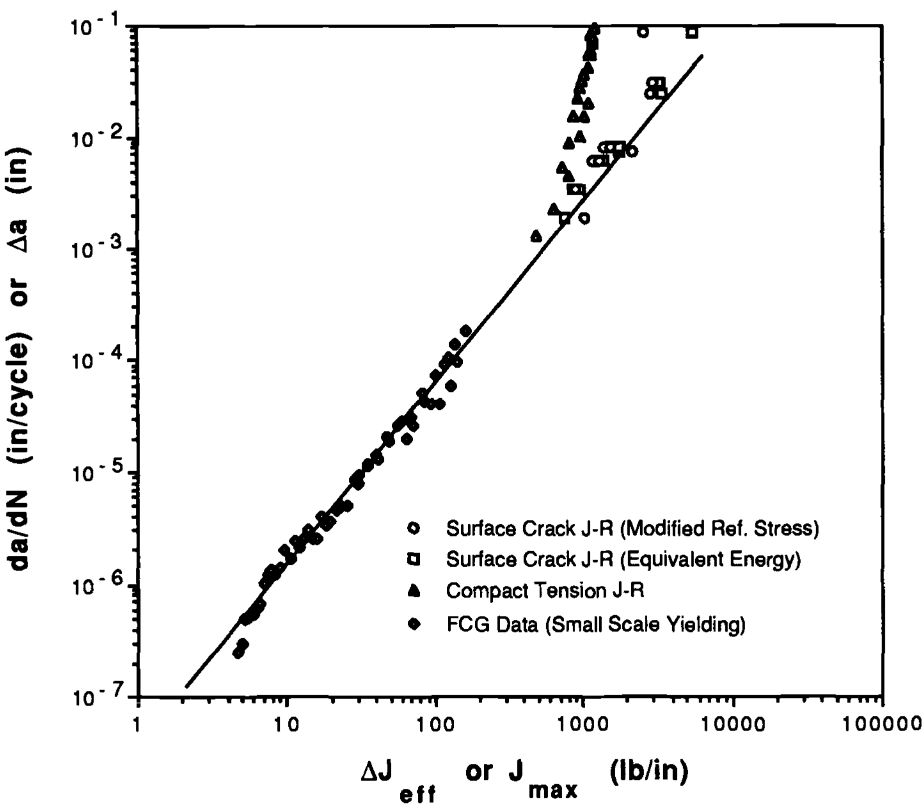

FIG. 9—*Fatigue crack growth data for Inconel 718 with superimposed resistance curve data.*

J at each Δa value for the least squares regression. Note that the FCG curve corresponds almost exactly to the "blunting line" portion of the R-curve, but that as additional ductile tearing begins to occur at higher J values, the R-curve line begins to deviate from the baseline FCG curve.

This apparent coincidence of the R-curve blunting line and low-cycle FCG curve should not be surprising in view of the crack growth mechanisms involved. The so-called blunting line of the R-curve, as its name implies, is thought to describe the crack extension during initial loading that occurs due to crack-tip blunting alone, before the initiation of ductile tearing (or brittle cleavage) [*25*]. On the other hand, the mechanism of Stage II crack growth during low-cycle fatigue is widely believed to be a progressive plastic blunting process [26]. The broadening of slip zones at the crack tip and the associated blunting of the crack tip during the tensile loading excursion in low-cycle fatigue define the extent of crack advance during that particular cycle, before the application of reversed loading (locally compressive) causes a reversal of slip directions and a crushing/folding of the new crack surfaces. The point to be made is that the basic mechanism of crack extension is apparently initially the same in both "ductile fracture" and "low-cycle fatigue crack growth" processes. In fact, the material at the crack tip is largely unaware of whether initial blunting will be followed by further loading to tearing or by unloading. The primary difference in the two processes is the more complex residual stress/deformation field that develops in the vicinity of the fatigue crack tip due to previous load/unload

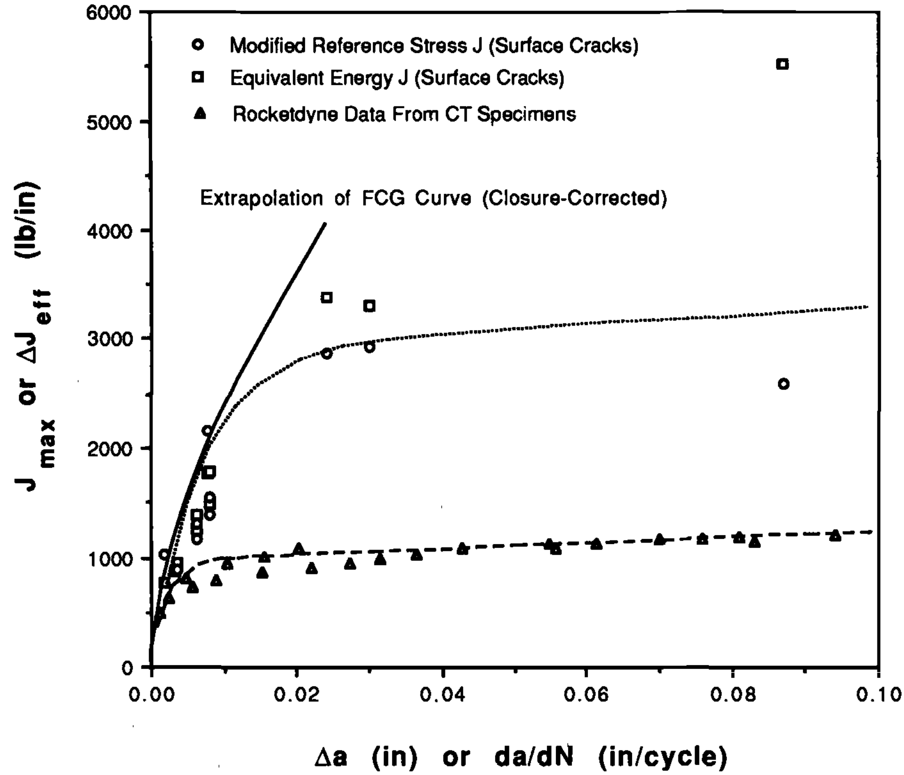

FIG. 10—*Resistance curves for Inconel 718 with superimposed FCG curve.*

and crack growth histories. Consideration of crack closure effects, as we have done earlier, represents a first-order compensation for this difference.

Wilhem and Ratwani [*27*] previously suggested a similar relationship between fatigue and fracture data as described by the linear elastic stress intensity factor (ΔK and K_R), based on their empirical observations of crack growth in 2024-T3 aluminum. They proposed a "full range resistance curve" that was a continuous, monotonically increasing function of crack extension and that was composed of both fatigue (da versus K_{max}) and fracture (Δa versus K_R) data. Their primary goal was apparently to reconcile thickness effects in FCG rate data by relating them to thickness effects on the R-curve. Wilhem and Ratwani went on to suggest that there may not be a smooth transition between fatigue resistance and fracture resistance portions of the curve, based on their supposition that the crack-tip plastic zone in fatigue was different in size from that developed during static (monotonic) loading. Actually, however, the size of the "forward" plastic zone has been shown to be essentially the same under monotonic and cyclic loading [*28*]. Any apparent discontinuities between fatigue and fracture data may instead be due to uncompensated differences in crack closure behavior.

This line of thinking is consistent with the ideas of Kobayashi et al. [*21*], who suggested that the Paris law (striation mechanism) portion of the FCG curve was parallel to the blunting line. The difference between the two lines was attributed to plasticity-induced crack closure. The specific data generated by Kobayashi et al. to evaluate these ideas are somewhat difficult to interpret, however, due in part to the wide range of stress ratios ($R = -1.5$ to $+0.5$) and applied loads (elastic to elastic-plastic) considered. Crack closure levels (which were not measured) are certain to change considerably with both stress ratio and applied load, and the CT geometry employed was not an ideal choice for load histories with large compressive excursions. The present investigations were simplified by considering only a single stress ratio for all tests ($R = 0$).

A final consideration addresses the conditions for final instability from the FCG perspective (Fig. 9). It was noted earlier in discussions of R-curve behavior that the onset of tearing was influenced by constraint, which in turn was influenced by specimen or component geometry. The value of J_{max}, which might be used to characterize the latter stages of crack growth in a FCG equation [20], then, will change with specimen geometry and also, in some cases, with applied load and crack length. It should be possible, in theory, to predict this value of J_{max} (which is related to J_c) based on the apparent functional relationship between J_c and a measure of constraint such as the T-stress [15]. The gradual transition of crack growth rates near J_c is likely to be further complicated by gradual changes in crack closure behavior as net section yield is approached [29].

Experimental investigations are currently underway to evaluate further the issues associated with crack growth during large load-unload cycles. Surface-cracked specimens identical to those used earlier to generate the resistance curve are being subjected to repeated loading cycles under displacement control with various minimum and maximum loads and displacements. Crack growth behavior during these cycles is being measured and compared to expectations from both fatigue and ductile fracture perspectives, with the ultimate goal of developing an analytical model for MCPT. A preliminary model of crack growth during MCPT based only on a resistance curve approach was developed previously [30] as an aid to designing and interpreting the MCPT experiments. But the observations made earlier in this paper about the relationship between fatigue and ductile fracture crack growth processes suggest that it should be possible to develop a model of crack growth during multiple cycle proof testing that incorporates both fatigue and fracture information on a unified basis. This model must also address several complicating issues, such as the effects of constraint and control mode (load versus displacement) on crack behavior during not only loading (as discussed earlier) but also unloading.

Conclusions

1. A modified reference stress estimate of the J-integral has been developed for semielliptical surface cracks in finite thickness plates. This simple closed-form estimate compares favorably with available three-dimensional finite element solutions for several different applied stresses, strain hardening exponents, crack shapes, and crack depths.
2. A J-resistance curve has been developed for semicircular surface flaws in finite-thickness Inconel 718 plates. The blunting line of the surface crack R-curve is coincident with the blunting line for resistance curve data from thick compact tension specimens, but the onset of stable tearing occurs at much higher apparent J values in the surface-cracked configurations. The difference is apparently due to loss of constraint in the severely loaded surface crack configuration.
3. A comparison of resistance curve data with fatigue crack growth data for Inconel 718 suggests that the blunting line of the R-curve is coincident with the fatigue crack growth curve in the low-cycle regime when plasticity-induced crack closure is taken into account. This phenomenon is consistent with the similarity in proposed crack growth mechanisms for low-cycle fatigue crack growth and the initial blunting process in ductile fracture.

Acknowledgments

V. D. Aaron of the Southwest Research Institute provided invaluable assistance in conducting the crack growth experiments. D. A. Russell and K. A. Garr of the Rocketdyne Division, Rockwell International Corporation, are thanked for their cooperation and, especially, for providing the resistance curve data from Inconel 718 compact tension specimens. Financial support for this program was provided by the NASA–George C. Marshall Space Flight Center, Contract NAS8-37451. The continuing interest and encouragement of G. C. Faile, H. M. Lee, and R. Stallworth of NASA-MSFC is gratefully acknowledged.

References

[*1*] Wilhem, D. P., FitzGerald, J. H., Carter, J., and Dittmer, D., "An Empirical Approach to Determining *K* for Surface Cracks," *Advances in Fracture Research, Proceedings,* Fifth International Conference on Fracture, 1981, pp. 11–22.

[*2*] FitzGerald, J. H., "Empirical Formulations for the Analysis and Prediction of Trends for Steady-State Fatigue and Crack Growth Rates," *Journal of Testing and Evaluation,* Vol. 5, 1977, pp. 343–353.

[*3*] Ainsworth, R. A., "The Assessment of Defects in Structures of Strain Hardening Material," *Engineering Fracture Mechanics,* Vol. 19, 1984, pp. 633–642.

[*4*] Miller, A. G., "J Estimation for Surface Defects," TPRD/B/0811/R86, Central Electricity Generating Board, U.K., July 1986.

[*5*] Ainsworth, R. A., "Approximate Non-Linear Fracture Mechanics Calculations Using Reference Stress Techniques," *Innovative Approaches to Irradiation Damage and Fracture Analysis,* PVP-Vol. 170, American Society of Mechanical Engineers, New York, 1989, pp. 13–20.

[*6*] Newman, J. C., Jr., and Raju, I. S. "An Empirical Stress Intensity Factor Equation for the Surface Crack," *Engineering Fracture Mechanics,* Vol. 15, 1981, pp. 185–192.

[*7*] Parks, D. M. and Wang, Y.-Y., "Elastic-Plastic Analysis of Part-Through Surface Cracks," *Analytical, Numerical, and Experimental Aspects of Three Dimensional Fracture Processes,* AMD-Vol. 91, American Society of Mechanical Engineers, New York, 1988, pp. 19–32.

[*8*] Dowling, N. E., "*J*-Integral Estimates for Cracks in Infinite Bodies," *Engineering Fracture Mechanics,* Vol. 26, 1987, pp. 333–348.

[*9*] Trantina, G. G., deLorenzi, H. G., and Wilkening, W. W., "Three-Dimensional Elastic-Plastic Finite Element Analysis of Small Surface Cracks," *Engineering Fracture Mechanics,* Vol. 18, 1983, pp. 925–938.

[*10*] McCabe, D. E., Ernst, H. A., and Newman, J. C., Jr., "Application of Elastic and Elastic-Plastic Fracture Mechanics Methods to Surface Flaws," *Fracture Mechanics: Twenty-Second Symposium (Volume I), ASTM STP 1131,* H. A. Ernst, A. Saxena, and D. L. McDowell, Eds., American Society for Testing and Materials, Philadelphia, 1992, pp. 495–518.

[*11*] White, C. S., Ritchie, R. O., and Parks, D. M., "Ductile Growth of Part-Through Surface Cracks: Experiment and Analysis," *Elastic-Plastic Fracture: Second Symposium, Volume I: Inelastic Crack Analysis, ASTM STP 803,* C. F. Shih and J. P. Gudas, Eds., American Society for Testing and Materials, Philadelphia, 1983, pp. I-384, I-409.

[*12*] Hodulak, L., "Growth of Surface Cracks Under Fatigue and Monotonic Increasing Load," *Surface-Crack Growth: Models, Experiments, and Structures, ASTM STP 1060,* W. G. Reuter, J. H. Underwood, and J. C. Newman, Jr., Eds., American Society for Testing and Materials, Philadelphia, 1990. pp. 315–332.

[*13*] Bauschke, H.-M., Read, D. T., and Schwalbe, K.-H., "Crack Growth Resistance at Surface Cracks in Three Aluminum Alloys," *Defect Assessment in Components—Fundamentals and Applications, ESIS/EGF 9,* Mechanical Engineering Publications, London, 1991, pp. 749–769.

[*14*] Shih, C. F., O'Dowd, N. P., and Kirk, M. T., "A Framework for Quantifying Crack Tip Constraint," *Constraint Effects in Fracture, ASTM STP 1171,* E. M. Hackett, K.-H. Schwalbe, and R. H. Dodds, Eds., American Society for Testing and Materials, Philadelphia, 1992, pp. 2–20.

[*15*] Hancock, J. W., Reuter, W. G., and Parks, D. M., "Constraint and Toughness, Parameterized by T," *Constraint Effects in Fracture, ASTM STP 1171,* E. M. Hackett, Schwalbe, and R. H. Dodds, Eds., American Society for Testing and Materials, Philadelphia, pp. 21–40.

[*16*] Larsson, S. G. and Carsson, A. J., "Influence of Non-Singular Stress Terms and Specimen Geometry on Small-Scale Yielding at Crack Tips in Elastic-Plastic Materials," *Journal of the Mechanics and Physics of Solids,* Vol. 21, 1973, pp. 263–277.

[17] Leevers, P. S. and Radon, J. C., "Inherent Stress Biaxiality in Various Fracture Specimen Geometries," *International Journal of Fracture*, Vol. 19, 1982, pp. 311–325.
[18] Kaiser, S., "On the Relation Between Stable Crack Growth and Fatigue," *Fatigue of Engineering Materials and Structures*, Vol. 6, 1983, pp. 33–49.
[19] Marshall, C. W. and Wilkowski, G. W., "Effect of Cyclic Loads on Ductile Fracture Resistance," *Advances in Fracture and Fatigue for the 1990's, Vol. I: Load History Effects of Fracture Resistance*, PVP–Vol. 166, American Society of Mechanical Engineers, New York, 1989, pp. 1–13.
[20] Mogami, K., Hayashi, T., Ando, K., and Ogura, N., "Elastic-Plastic J-R Curve and Tearing Instability Characteristics Under Cyclic Load," *Advances in Fracture and Fatigue for the 1990's, Vol. I: Load History Effects of Fracture Resistance*, PVP–Vol. 166, American Society of Mechanical Engineers, New York, 1989, pp. 71–76.
[21] Kobayashi, H., Kusumoto, T., and Nakazawa, H., "Cyclic J-R Curve and Upper Limit Characteristic of Fatigue Crack Growth in 2-¼ Cr-Mo Steel," *Advances in Fracture and Fatigue for the 1990's, Vol. I: Load History Effects of Fracture Resistance*, PVP–Vol. 166, American Society of Mechanical Engineers, 1989, pp. 55–63.
[22] McClung, R. C., Thacker, B. H., and Roy, S., "Finite Element Visualization of Fatigue Crack Closure in Plane Stress and Plane Strain," *International Journal of Fracture*, Vol. 50, 1991, pp. 27–49.
[23] Dowling, N. E., "Geometry Effects and the *J*-Integral Approach to Elastic-Plastic Fatigue Crack Growth," *Cracks and Fracture (Ninth Conference), ASTM STP 601*, American Society for Testing and Materials, Philadelphia, 1976, pp. 19–32.
[24] Orange, T. W., "Methods and Models for R-Curve Instability Calculations," NASA TM 100935, National Aeronautics and Space Administration, Washington, DC, 1988.
[25] Rice, J. R., "Elastic-Plastic Fracture Mechanics," *The Mechanics of Fracture*, AMD–Vol. 19, American Society of Mechanical Engineers, 1976, pp. 23–53.
[26] Laird, C., "The Influence of Metallurgical Structure on the Mechanisms of Fatigue Crack Propagation," *Fatigue Crack Propagation, ASTM STP 415*, American Society for Testing and Materials, Philadelphia, 1967, pp. 131–168.
[27] Wilhem, D. P. and Ratwani, M. M., "Application of the R-Curve Concept to Fatigue Crack Growth," *Journal of Engineering Materials and Technology, Transactions*, ASME, Vol. 100, 1978, pp. 416–420.
[28] McClung, R. C., "Crack Closure and Plastic Zone Sizes in Fatigue," *Fatigue and Fracture of Engineering Materials and Structures*, Vol. 14, No. 4, 1991, pp. 455–468.
[29] McClung, R. C., "The Influence of Applied Stress, Crack Length, and Stress Intensity Factor on Crack Closure," *Metallurgical Transactions A*, Vol. 22A, 1991, pp. 1559–1571.
[30] McClung, R. C., Hudak, S. J., Jr., and Russell, D. A., "Towards an Analysis of Multiple-Cycle Proof Testing Based on *J*-Resistance Curves," *Fatigue, Degradation, and Fracture*, PVP–Vol. 195, American Society of Mechanical Engineers, 1990, pp. 57–65.

Stig Berge,[1] Oddvar I. Eide,[2] and Masahiko Fujikubo[3]

Level-3 Crack-Tip Opening Displacement (CTOD) Assessment of Welded Wide Plates in Bending—Effect of Overmatching Weld Metal

REFERENCE: Berge, S., Eide, O. I., and Fujikubo, M., "**Level-3 Crack-Tip Opening Displacement (CTOD) Assessment of Welded Wide Plates in Bending—Effect of Overmatching Weld Metal,**" *Fracture Mechanics: Twenty-Third Symposium, ASTM STP 1189,* Ravinder Chona, Ed., American Society for Testing and Materials, Philadelphia, 1993, pp. 284–309.

ABSTRACT: Butt-welded wide plates with semi-elliptical surface cracks along the fusion line were tested in four-point bending. The material was normalized low-carbon microalloyed steel that conformed to offshore specifications. The testing temperature was in the range of $-40°$ to $0°C$. The test results were analyzed by the crack-tip opening displacement (CTOD) Level-3 method that compared different assumptions for the reference strain in order to assess the effect of overmatching weld metal. The original Level-3 plane stress model and a proposed plane strain model with a modified definition of effective primary stress were compared. Consistent results were obtained by the latter method. A detailed finite-element method (FEM) model was validated, and results from comprehensive analyses of welded and nonwelded models are presented.

KEY WORDS: crack-tip opening displacement, elastic-plastic fracture mechanics, weldments, wide plate tests, fracture mechanics, defect assessment, structural analysis, fatigue (materials)

Nomenclature

- a Depth of surface crack
- a_e Effective a with plastic zone correction
- $\bar{a}$ Half length of equivalent through-thickness crack
- c Half length of surface crack
- E Young's modulus
- J J-integral
- K Stress intensity factor
- K_I^P Stress intensity factor due to primary stresses
- K_I^S Stress intensity factor due to secondary stresses
- m J-CTOD proportionality constant
- P Applied load
- P_0 Characteristic load
- P_L Plastic limit load
- δ Crack-tip opening displacement (CTOD)
- δ_c CTOD at unstable fracture with no prior crack extension
- δ_m CTOD at maximum load (no fracture)
- δ_u CTOD at unstable fracture after stable crack extension

[1] Professor, The Norwegian Institute of Technology, Trondheim, Norway.
[2] Senior scientist, SINTEF, Trondheim, Norway.
[3] Associate professor, Hiroshima University, Hiroshima, Japan.

ε_L Local strain in cross section of crack
ε_N Nominal strain not influenced by crack
ε^P Strain in parent plate material
ε^W Strain in weld
ε_{ys} Yield strain, σ_{ys}/E
ν Poisson's ratio
σ_b Nominal bending stress
σ_P Effective primary stress
σ_{ref} Reference stress
σ_s Effective secondary stress
σ_{ys} Yield stress
Φ Nondimensional CTOD

In offshore structures, fracture mechanics is used regularly in two areas:

1. Materials characterization and selection when evaluating welding procedures.
2. Fitness for purpose evaluation of structures in the as-built condition.

Fracture mechanics is less frequently applied in the design stage because, in the field of offshore structural steels and technology, fracture can be avoided by the proper selection of materials and fabrication procedures. Thus, design criteria are based on ductile material behavior.

In more optimized structures, particularly with the increased use of high-strength steels, fracture mechanics evaluations become more important, and may gradually become an integral element of structural design [1].

In present-day design practices, there is a need for fracture mechanics-based criteria. Offshore structures are designed for accidental and abnormal loads in a progressive collapse limit state (PLS) design. According to the Norwegian Petroleum Directorate regulations [2], a two-step procedure is followed. First, the design analysis should demonstrate that the structure experiences purely local damage when exposed to abnormal load effects. Second, after assessment of calculated or specified local damages, the structure must have a proved capacity to resist defined environmental conditions without collapse. The procedure implies structural analysis with nonlinear effects associated with yielding and buckling, that is, large deflections and strains. Due to the built-in redundancy of offshore structures, plastic capacity is important, and the contribution from strain hardening effects may be significant. Whereas the ultimate limit state design (ULS) is essentially a check of "load" (stress) capacity, the PLS design is, in many cases, a check of "ductility" (strain) capacity.

In Fig. 1 (schematic), the design of a tubular structure subjected to falling objects or collision

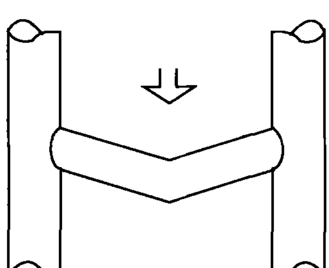

FIG. 1—*Design case (schematic) for falling object or collision against an offshore structure.*

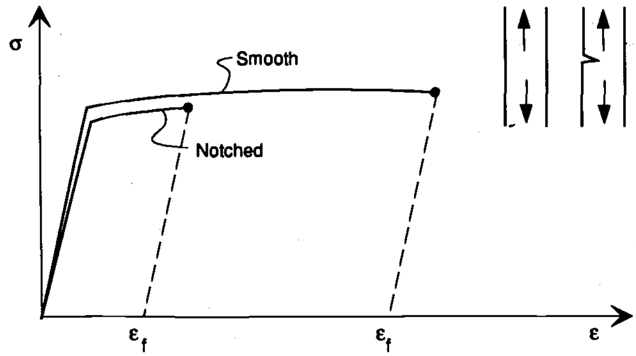

FIG. 2—*Stress versus strain curves for smooth and notched tension specimen (schematic).*

is shown. This is a relatively common structural damage, and the structural integrity following local damage due to impact loading must be checked. Here, the load effect is defined in terms of impact energy, and the corresponding capacity criterion is energy absorption by plastic deformation of structural elements (represented by the area under the curves shown in Fig. 2). The implication for material properties is that ductility is a design parameter as equally important as strength.

In current PLS design procedures, the ductility of a structural component is deduced from tension test data for the base material, where strains to fracture are typically in the 0.1 to 0.2 range. For a dynamically loaded and welded structure with possible weld defects and fatigue cracks, this could be over-optimistic. Figure 2 shows schematically the load/deflection curves for smooth and notched tension specimens, respectively. For ductile materials, the load capacity is generally unaffected by defects, provided these are not excessive. The ductility and the capacity for energy absorption may, however, be strongly affected, even for small defects. It has been shown that a rational approach to the analysis of ductile behavior for welded structures should include the interaction between cracks and ductile behavior, that is, fracture criteria for large strains in strain-controlled load cases [*3*].

In this study, butt-welded wide plates with surface cracks along the fusion line were tested to failure. The objectives of the tests were twofold:

1. To investigate the application of the CTOD Level-3 (reference strain) method for fracture assessment of welded structures at large strains.
2. To assess the effect of overmatching weld metal on fracture.

The experimental work was supported by numerical analysis through which a proposed plane strain CTOD Level-3 method was validated.

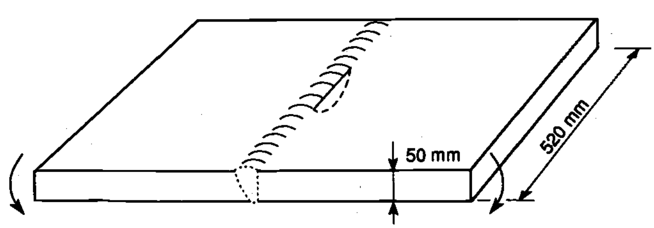

FIG. 3—*Wide-plate specimen with crack.*

TABLE 1—*Tensile properties for steel.*

	Yield Strength, MPa	Ultimate Tensile Strength, MPA
Parent plate	377	507
Weld metal	480	580

Experimental

The work reported here is based mainly on tests with butt-welded plates conforming to offshore specifications, described later. In the analysis section, reference is also made to tests on an unwelded bridge steel, reported in Ref *4*. The reader is referred to Ref *4* for details of those tests.

Materials and Welding

Butt-welded wide-plate specimens were produced by manual metal arc welding. The specimens are shown in Fig. 3. The material was normalized low-carbon microalloyed steel that conformed to offshore specifications [*5*].

Welding was done manually with covered electrodes according to a prequalified procedure for offshore structural welding. The electrodes were in compliance with ASME BPV-Code-IIc SFA-5.5:E7018-G (1983), and the mechanical properties are shown in Table 1. No post-weld heat treatment was applied.

CTOD Testing

CTOD testing was performed according to British Standards Institution BS 5762:1979 using B × B specimens as shown in Fig. 4. The notch was located in the weld metal (WM series) and at the fusion line (FL series). No attempt was made to sample specific features of the microstructure [*6*].

The CTOD values are shown in Table 2 and in Fig. 5. From the values listed in Table 2, it is apparent that the material was very tough, even at a temperature of −40°C. Ductile crack extension prior to fracture was typically 1 mm or less. For higher temperatures, only δ_m values

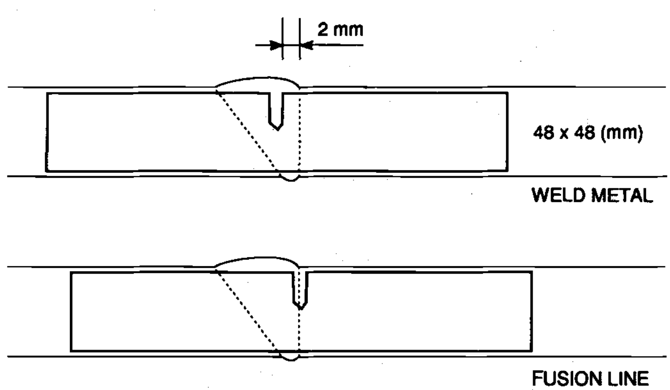

FIG. 4—*CTOD specimens, B × B geometry.*

TABLE 2—*CTOD values, B × B specimens.*

Specimen	Temperature, °C	CTOD, mm	Comment
WM-1	0.5	0.87	δ_m
WM-2	−20.0	1.26	δ_m
WM-3	−39.5	1.26	δ_u
WM-4	−40.0	1.36	δ_u
FL-1	−41.0	0.69	σ_c, slag
FL-2	−20.0	>1.4	δ_m
FL-3	−39.5	1.38	δ_u
FL-4	−20.0	>1.4	δ_m
FL-5	−40.0	1.12	δ_u

were obtained. In two cases, the deflection limitation of the fixtures was reached before maximum load was attained (run-outs).

As shown in Ref *4*, CTOD at fracture in nonwelded wide-plate specimens tends to fall on the lower bound temperature transition curve from small-scale tests, which in Ref *4* was based on 15 tests. For the welded plates, a much smaller number of CTOD tests were carried out, and the assessment of a lower bound curve for materials characterization was somewhat uncertain. With more tests, lower values of CTOD would undoubtedly have come in. With this

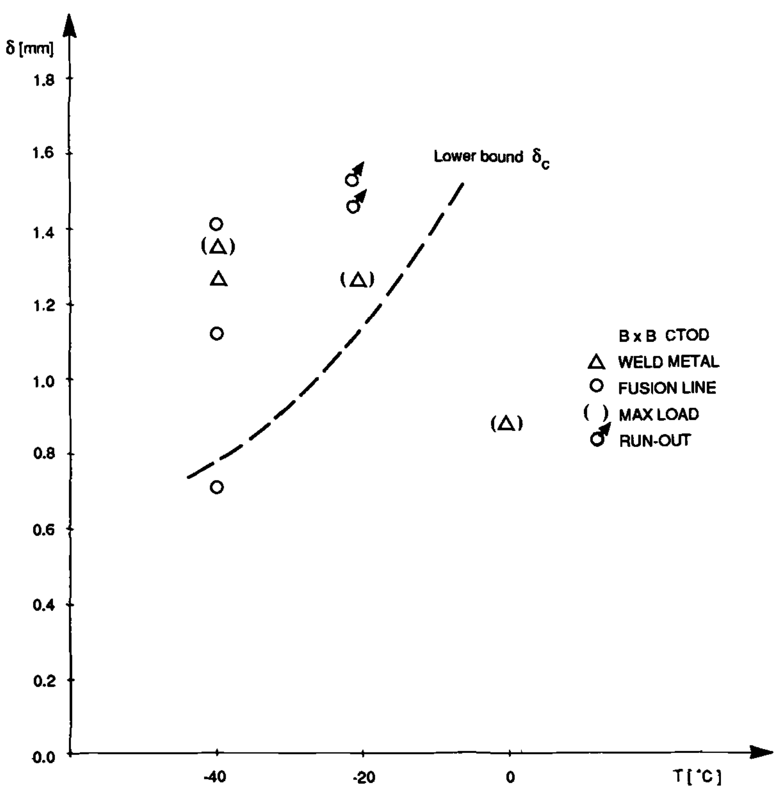

FIG. 5—*CTOD data from B × B tests, temperature transition curve.*

consideration in mind, a temperature transition curve was drawn on the following basis, Fig. 5:

1. The fracture surfaces of FL-1 revealed the presence of slag at the crack initiation site. Due to the slag, the crack profile was in violation of the requirements of BS5762, and the result was discarded.
2. The δ_m value for the weld metal tested at 0°C was taken as a ductile collapse criterion for the specimen, and not relevant for fracture design, that is, considered as a run-out.

The curve shown in Fig. 5 is used as a reference for the fracture toughness of the weldments in the ensuing fracture assessments. Admittedly, the basis for this curve is somewhat meager. A main point for discussion is the relevance of the CTOD test procedure for materials with toughness properties in this range, and the use of δ_m value for fracture characterization.

Wide-Plate Specimens

Cracks were produced with spark erosion. The spark-erosion electrodes were made from 1-mm copper sheet formed to the desired semi-elliptical crack shape. The cracks were located along the fusion line as shown in Fig. 6 where fatigue cracks are most likely to develop, simulating typical fatigue crack geometries. The cracks were oriented at a 5° angle relative to the fusion line, sampling material along the crack tip through the heat-affected zone, fusion line, and weld metal. Thus, fractures would be initiated from the weakest link of the weldment [7].

The spark-eroded cracks were extended by fatigue precycling. The length of the fatigue crack and the applied stress intensity during precycling were according to the specifications for CTOD testing (BS 5762:1979). Fracture testing was performed in a four-point bend fixture as shown in Fig. 7.

Strain Measurements

The leading load parameter entered into CTOD Level-3 design is a reference strain, ε^S_{ref}, calculated from the applied loading and the uniaxial stress/strain curve for the material [8]. As shown by the authors [9], this stress-based reference strain, ε^S_{ref} is highly sensitive to the flow properties of the material and carries along significant uncertainties. Therefore analysis was based on a strain-based reference strain, ε^m_{ref}, either measured on the specimens or calculated by the finite-element method (FEM), hereafter denoted ε_{ref}.

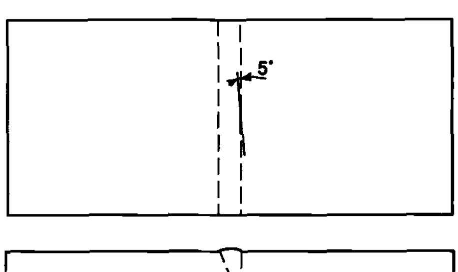

FIG. 6—*Crack location for the wide-plate tests.*

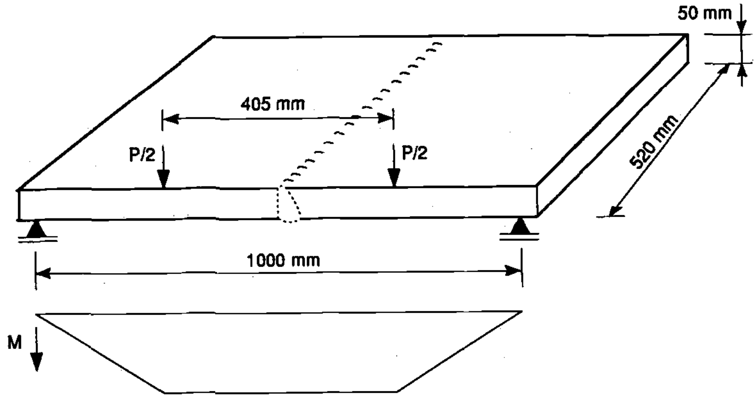

FIG. 7—*Four-point bend fixture (schematic).*

It has been shown that the definition of a characteristic strain in wide-plate tests may have a major influence on the interpretation of test data, even with nonwelded plate material [*4*]. In the presence of a weld with nonmatching properties, the definition of strain becomes even more difficult. Strain was measured with strain gages at three locations, denoted as follows, see Fig. 8:

ε_L^P = local strain in parent plate material, 10 mm from fusion line;
ε_L^W = local strain in weld material; and
ε_N = nominal strain in parent plate material.

The strain measurements were made on both sides of the plate. The differences were generally within 10% and average values are plotted. The welds were locally machined for attachment of the strain gages.

Local strain was measured in the cross section of the crack, and would be influenced by the overmatched weld metal and by any hinge mechanism developing from the crack. Nominal strain was measured outside the strain shadow of the crack [*4*], but within the span of the

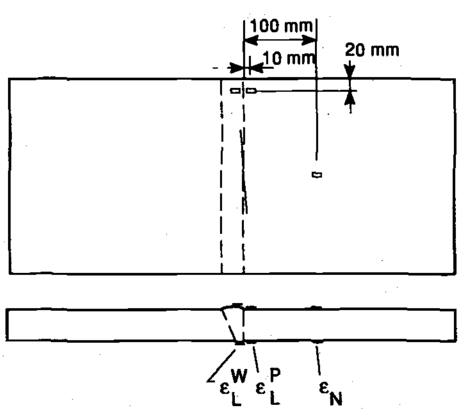

FIG. 8—*Location of strain measurements.*

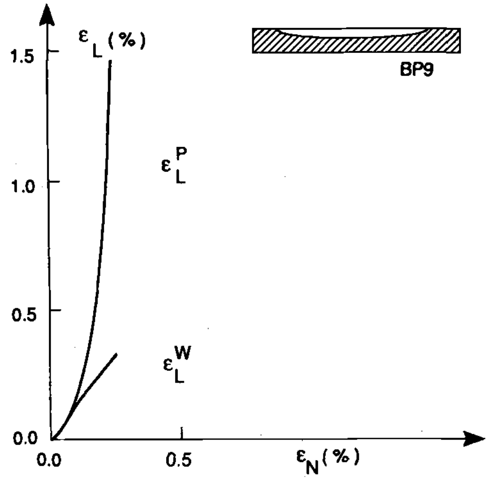

FIG. 9—*Strain measurements, Specimen BP9.*

constant bending moment, and was a measure of the strain of the plate material in an uncracked section. For the current CTOD Level-1 design, this would be the design strain [*10*].

In Figs. 9 through 11, the three measures of strain are compared by graphs showing ε_L^P and ε_L^W as functions of ε_N. At small strains, all strains were essentially equal. At a strain exceeding approximately 0.2%, that is, above the elastic limit, significant differences developed, due to the yield strength overmatching of the weld metal, and the development of a hinge for large cracks.

In Fig. 9, the strains in Specimen BP9 that had a very large initial crack are shown. The crack is also shown drawn to scale. The local strain in the weld and the nominal strain were approximately equal, whereas the local plate strain increased to more than five times the nominal

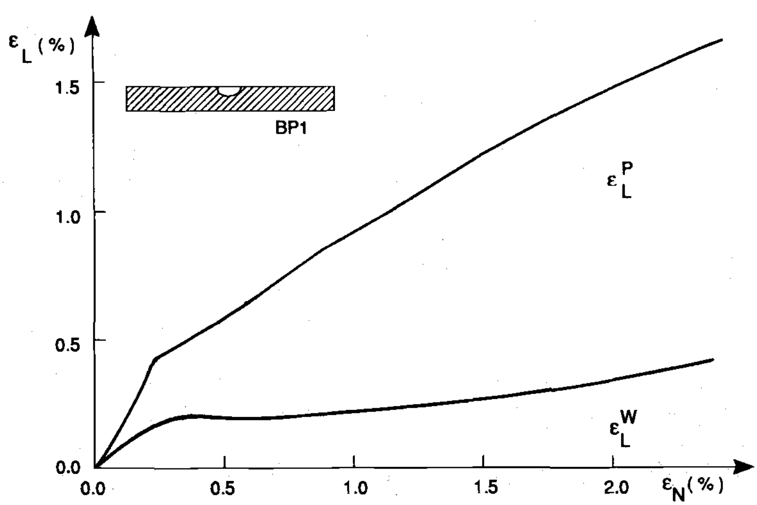

FIG. 10—*Strain measurements, Specimen BP1.*

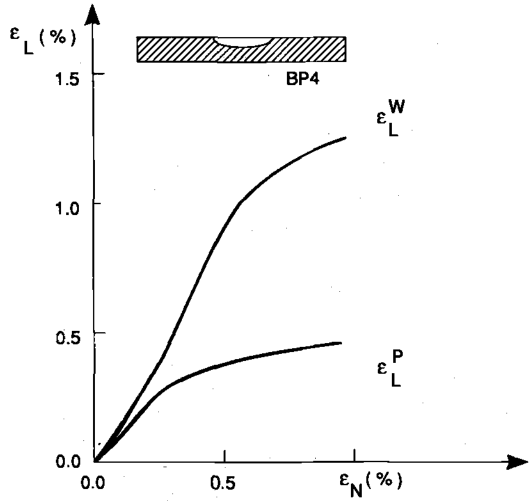

FIG. 11—*Strain measurements, Specimen BP4.*

strain, reflecting the hinge development. Due to the hinge, fracture took place at a very small nominal strain.

The initial crack in Specimen BP1 was comparatively small, Fig. 10. In this case, the strain in the weld did not develop much beyond yield. An interesting feature is that ε_N was larger than ε_L^P. This was apparently because the plastic flow in the parent material was constrained by the weld that remained in an essentially elastic stress state. This means that for cracks that are small compared to the cross section, an overmatching weld could provide strain shielding for cracks at the fusion line. This plate did not fracture, and the test was stopped at maximum deflection of the rig.

Figure 11 shows strains for Specimen BP4 that had an intermediate size crack compared to Specimens BP1 and BP9. There was some hinge development, and the strain in the weld went beyond yield.

The data shown in Figs. 9 through 11 clearly underline the problem of assessing a relevant strain for fracture analysis of welds.

Wide-Plate Fracture Appearance

Plates that had cracks with an aspect ratio, $a/2c = 0.2$ (Fig. 10), did not fracture, even at a temperature of $-40°C$. The tests had to be stopped due to the deflection limitations of the fixtures. At this point, the nominal strain of the specimens was more than ten times yield, and the local plate strain was around six times yield, see Table 3.

Plates with larger cracks failed by fracture at a temperature of $-40°C$ and, in one case, at $-20°C$. Contrary to the small-scale specimens, the fracture surfaces indicated that fracture was initiated with no prior ductile crack growth. The same discrepancy between small- and large-scale tests was observed with nonwelded plates [*4*]. This may indicate that for ductile materials, the small-scale B × B specimen is not fully representative of the conditions of constraint in wide plates.

The fracture surfaces indicated that fracture initiation took place in the deepest part of the cracks that coincided generally with the region of the fusion line. There appeared to be no preferential path for crack propagation with respect to microstructure. From the initiation

TABLE 3—*Wide-plate test data at fracture/end-of-test.*

Test	Temperature, °C	a, mm	$2c$, mm	P, MN	$E\varepsilon_L^W/\sigma_{ys}^W$	$E\varepsilon_L^P/\sigma_{ys}^P$	$E\varepsilon_N/\sigma_{ys}^P$
BP1[NFa]	0	14	70	0.832	2.0	7.0	12.0
BP2[NF]	−40	15	70	0.902	2.6	6.2	12.3
BP3[NF]	−40	16	70	0.877	2.1	5.9	11.2
BP4[Fb]	−40	20	174	0.818	1.7	5.9	5.3
BP5[NF]	−20	18	175	0.861	3.0	7.8	8.4
BP6[F]	−40	20	173	0.937	3.8	13.3	3.2
BP7[F]	−20	27	360	0.726	3.0	13.3	3.2
BP8[NF]	−20	20	340	0.858	2.8	11.5	8.8
BP9[F]	−40	21	320	0.816	1.5	8.1	4.6

[a] NF = no fracture, data at end of test.
[b] F = fracture.

point, the crack had propagated around the perimeter of the precrack and from there into the plate material in a direction normal to the stress axis; that is, the crack ran partly through the weld metal, partly through the plate material, with crack surfaces at an angle reflecting the location along the front of the initial crack from where the crack propagation ran off, Fig. 12.

Based on these observations, the fracture behavior was analyzed in terms of mechanistic models. Microstructure was assumed to have a less important role relative to the stress and strain field in the characterization of the fracture limit state [*6*]. Test data are summarized in Table 3.

CTOD Fracture Assessment

The crack-tip opening displacement (CTOD) approach to assessment of elastic-plastic fracture has been expanded recently to a three-tier approach, referred to as Levels 1, 2, and 3. These methods have been extensively reviewed in the literature [*11–13*], and only the basic equations will be given here.

Level-1 is the conventional CTOD design by the so-called CTOD design curve [*10*]. For large strains, this curve is essentially empirical, derived from wide-plate tests with through-thickness cracks. It has been shown that for strains approaching yield, the curve may become

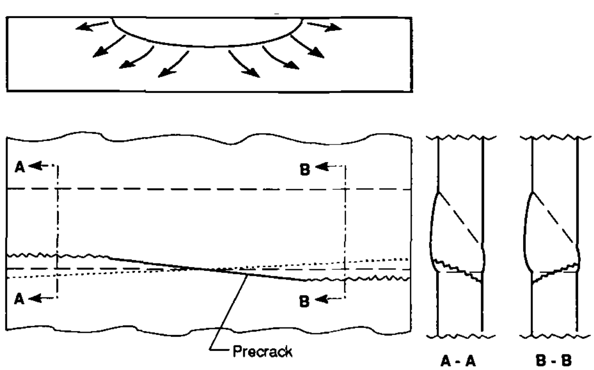

FIG. 12—*Typical crack path.*

unconservative. For this reason, the validity range for Level-1 method has been restricted to $\varepsilon/\varepsilon_{ys} \leq 0.8$ [*13*].

Level-2 is based on the Dugdale strip-yield model for plane stress conditions. Ductile collapse is implied, due to the fact that for $\sigma_{net}/\sigma_{ys} = 1.0$ the model predicts an infinite CTOD, that is, failure regardless of toughness properties of the material. For a strain hardening material, this is clearly conservative. Furthermore, for a strain-controlled situation, that is, a collapse analysis of a redundant structure in which member loads may exceed gross yielding, the model cannot readily be used.

Level-3, also called the reference strain method, includes strain hardening and is conceptually valid for very large strains. Hence, this model was chosen for analysis of the results. It should be noted that the purpose of the analysis is to investigate the mechanistics of the fracture assessment model, and not to evaluate specific fracture design procedures.

CTOD Level-3 Method

The governing equation of the Level-3 CTOD method proposed by Anderson et al. [*11,12*] is given by

$$\frac{\delta E}{\pi \sigma_{ys} a} = \left[\frac{\sigma_p}{\sigma_{ys}}\right] \left[\left(\frac{a_e}{a} + \frac{E\varepsilon_{ref}}{\sigma_{ref}} - 1\right)^{1/2} + \frac{\sigma_s}{\sigma_{ys}}\right]^2 \tag{1}$$

Here, the effective crack length, a_e, is

$$a_e = a + \frac{1}{2\pi}\left(\frac{K_I^p}{\sigma_{ys}}\right)^2 \frac{1}{1 + (\sigma_{ref}/\sigma_{ys})^2} \tag{2}$$

Equation 1 is derived for a through-thickness crack. Effects of crack geometry are accounted for by an effective primary stress

$$\sigma_p = \frac{K_I^p}{\sqrt{(\pi a)}} \tag{3}$$

Equation 1 was derived from the following expression of the J-integral proposed by Ainsworth [*8*]

$$J = \frac{K^2(a_e)}{E'} + \frac{\mu K^2(a)}{E}\left(\frac{E\varepsilon_{ref}}{\sigma_{ref}} - 1\right) \tag{4}$$

where $E' = E$, $\mu = 1$ in plane stress, $E' = E(1 - \nu^2)$, $\mu = 0.75$ in plane strain, and the reference stress

$$\sigma_{ref} = \frac{P}{P_0}\sigma_0 \tag{5}$$

where σ_0 is a reference point on the materials stress/strain curve (usually σ_{ys}), P is the remotely applied load, and P_0 is a characteristic load, for example, the plastic limit load, P_L. ε_{ref} is the point on the uniaxial stress-strain curve for the material corresponding to σ_{ref}.

Assuming plane stress and expressing K in terms of an effective primary stress, Eq 4 may be written as

$$J = \frac{\sigma_p^2 \pi a}{E}\left(\frac{a_e}{a} + \frac{E\varepsilon_{\text{ref}}}{\sigma_{\text{ref}}} - 1\right) \tag{6}$$

The relationship between CTOD and J-integral is

$$J = m\sigma_{ys}\delta \tag{7}$$

where m in the elastic-plastic range depends on the plastic constraint factor, accumulated plastic strain, and work hardening rate of the material [14]. In plane stress with an ideal plastic material $m = 1$, in plane strain $m \simeq 2$.

Equating Eqs 6 and 7, setting $m = 1$, and introducing the contribution of the secondary stress $(\sigma_s^2 \pi a/E)$ to J, Eq 1 can be derived. Level-3 method is thus derived for plane-stress conditions.

Plane Strain CTOD Level-3 Method

As shown by the authors [9], Eq 1 can be modified into a CTOD equation for plane strain by combining Eqs 4 and 7

$$\frac{\delta E}{\pi \sigma_{ys} a} = \frac{1}{m}\left\{\frac{\sigma_p}{\sigma_{ys}}\left[\frac{a_e}{a}\frac{E}{E'} + \mu\left(\frac{E\varepsilon_{\text{ref}}}{\sigma_{\text{ref}}} - 1\right)\right]^{1/2} + \sqrt{\frac{E}{E'}}\left(\frac{\sigma_s}{\sigma_{ys}}\right)\right\}^2 \tag{8}$$

where $m = 2$, $\mu = 0.75$, $E' = E/(1 - \nu^2)$, and

$$a_e = a + \frac{1}{6\pi}\left(\frac{K_I^p}{\sigma_{ys}}\right)^2 \frac{1}{1 + (\sigma_{\text{ref}}/\sigma_{ys})^2} \tag{9}$$

In Eq 8, the contribution of secondary stress to the J-integral was assumed as $\sigma_s^2 \pi a/E'$.

Numerical Analysis

Finite-Element Model and Verification

Three-dimensional elastic-plastic finite-element analyses were performed using the ABAQUS finite-element code [15]. The plate model was partitioned into a solid part near the crack plane and a shell part, Fig. 13. By preliminary analysis, it was shown that the stress in the shell part was little affected by the presence of a crack.

In Fig. 13, a model is shown with a crack in the center of the weld, where only one quarter of the plate was modeled. With a crack at the fusion line, symmetry along the weld was lost, and one half of the plate was modeled.

The load was applied as uniformly distributed forced displacements, shown in Fig. 13, simulating the actual experimental conditions. The flow characteristics of the material were input from uniaxial stress-strain curves with piecewise linearization. Nonlinear material behavior was evaluated by the incremental theory of plasticity with the von Mises yield criterion, associated flow rule, and isotropic strain hardening.

The solid part consisted of 20-node isoparametric brick elements. For crack-tip modeling,

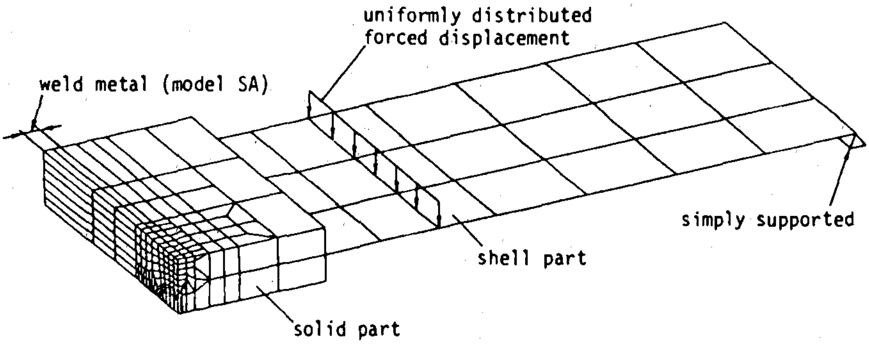

FIG. 13—*FEM model of surface-cracked plate with the crack located in the center of the weld.*

this element was degenerated into a wedge shape as shown in Fig. 14*a*. The nodes at the crack tip, which were given the same initial coordinates, were allowed to displace independently. CTOD was extracted from the nodal displacements at Point A as shown in Fig. 14*b*. This was shown to correspond within 1% of the 90° intercept method [*16*]. The model was verified by calculations simulating the wide-plate tests reported in Ref *4*, showing good agreement with CTOD at fracture measured by scanning electron microscopy by the 90° intercept method [*9*].

The *J*-integral was calculated using the virtual crack extension method [*17,18*]. For this purpose, a focused mesh shown in Fig. 14*c*, was employed along the crack front. Three *J*-integral paths were selected, and a satisfactory path independence was established. The *J*-integrals calculated along each path were averaged. Stress intensity factors were calculated from the aver-

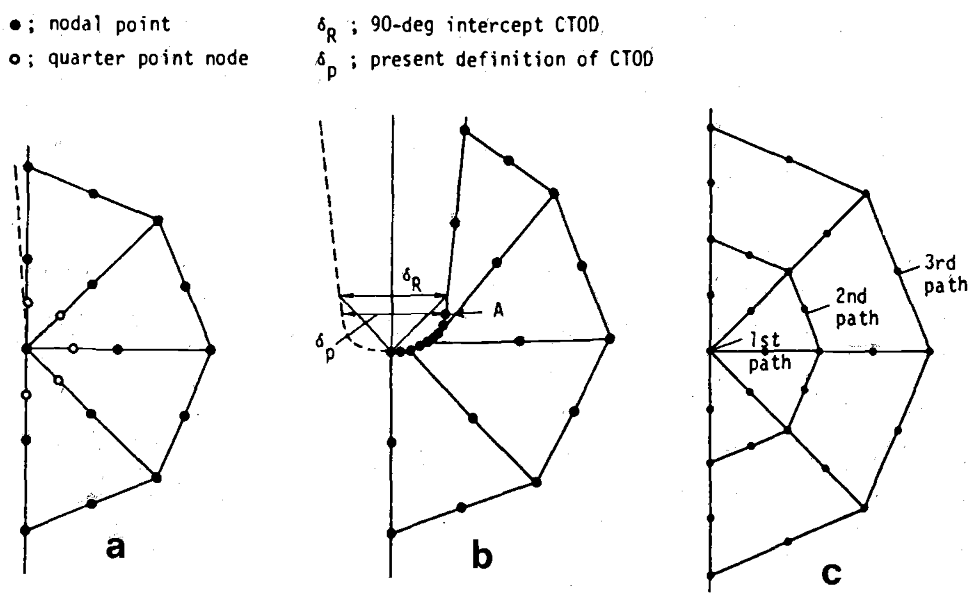

FIG. 14—*Finite-element representation of the crack-tip region:* (a) *collapse node and quarter-point node,* (b) *definition of CTOD, and* (c) *focused mesh.*

age value of J-integrals assuming plane strain conditions. Good agreement with the Newman-Raju solutions [*19*] was found except at the free surface, which was clearly not in plane strain. Further details about the modeling and the actual computations are given in Ref *20*.

Three plate models were analyzed, see Fig. 15; unwelded with two crack geometries (WA, WB), welded with a crack in the center of the weld (SA), and welded with a crack at the fusion line (SB). The latter corresponds to the tests reported herein.

CTOD Level-3 Predictions for Unwelded Plate

The purpose of discussing results for unwelded plate is to establish some basic relationships, and to utilize the data for verification of the fracture mechanics model, without the additional complication of an overmatched weld.

For unwelded plate, the relationship between CTOD and J-integral at the crack bottom obtained by finite-element analysis is shown in Fig. 16. Calculations were performed for two crack geometries, $a/2c = 0.1$ (WA) and 0.2 (WB), respectively. The CTOD/J relationship of Eq 7 is shown for two values of m; 2.0 and 2.5. The analysis shows that the value of m is around 2.0 for both models, implying plane strain. For large strains, the value of m appears to approach 2.5, indicating inaccuracies in the model in this region.

In Fig. 17, CTOD calculated by Level-3 for plane stress (Eq 1) and plane strain (Eq 8) for a surface crack with $a/2c = 0.1$ are shown. The data are plotted on the Level-1 CTOD format with an effective crack length, see Eq 3 [*10*]

$$\bar{a} = a\left(\frac{K_I^P}{\sqrt{(\pi a)}}\right)^2 \tag{10}$$

Local strain calculated by FEM was assumed as reference strain. Also shown is CTOD calculated directly by FEM, and experimental values from two tests [*4*]. The data are plotted on the CTOD design curve (Level-1) format. Also shown is the plane strain calculation using experimentally measured local strain as input. The plane strain equation is seen to give very

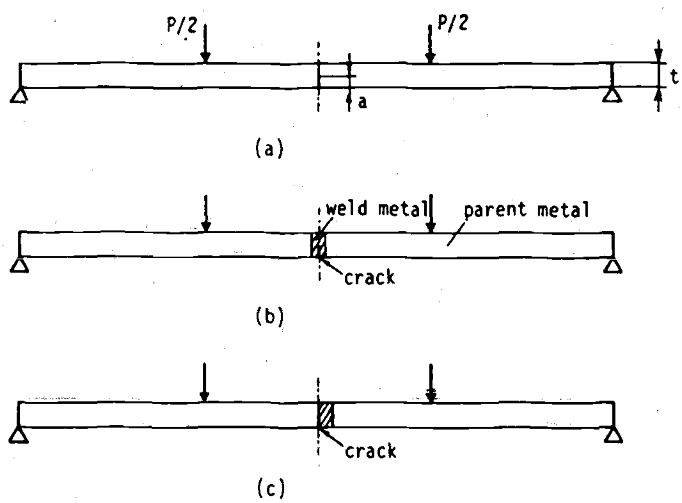

FIG. 15—*FEM models of* (a) *nonwelded (model WB),* (b) *crack in center of weld (model SA), and* (c) *crack at fusion line (model SB).*

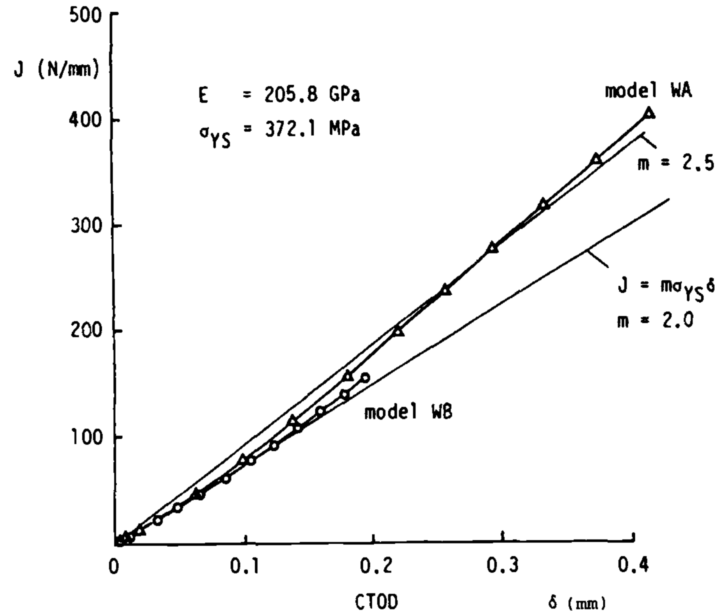

FIG. 16—*Relationship between* J *and CTOD at crack bottom for nonwelded model, calculated by FEM model.*

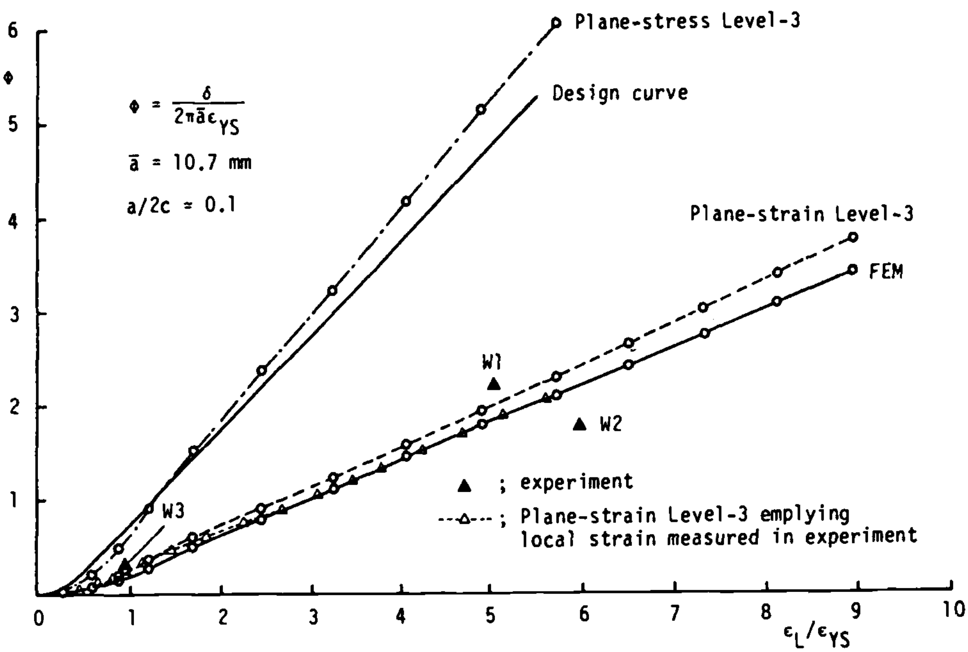

FIG. 17—*CTOD estimates by Level 3-methods for nonwelded plate, calculated by FEM model, experimental data from Ref* 4.

accurate predictions, whereas the plane stress solution is overpredicting applied CTOD by a factor close to three. Similar results were obtained with a model with $a/2c = 0.2$.

Conclusions of the analyses for parent plate models were that the FEM model was well behaving and gave results in good agreement with tests. With this model, the plane strain CTOD model was verified for surface-cracked plates in bending.

CTOD Predictions for Overmatched Weld

For the welded plate analysis, a crack geometry with $a/2c = 0.2$ was modeled, corresponding to Specimens BP1 through BP3. Analysis was performed for a crack at the fusion line (SB) corresponding to the test conditions, and for a crack at the center of the weld (SA) for comparison.

In Fig. 18, CTOD calculated by FEM for unwelded plate (WB), welded with crack in center (SA), and welded with crack at fusion line (SB), are shown. For the latter, the CTOD is split into two contributions: from the weld and from the plate side of the crack tip. All CTOD curves are plotted on the basis of nominal strain in the plate and parent plate yield strength. For the model SA, CTOD is separated into δ^P and δ^W, and the contribution, δ^P, from the plate materials is seen to be dominating. CTOD for a crack in HAZ (SB) is about half the size of CTOD for the same crack in nonwelded plate (WB). With the crack in the middle of a weld (SA), the CTOD is even less.

For model SA, CTOD was replotted on the basis of the local strain in the weld (dotted line

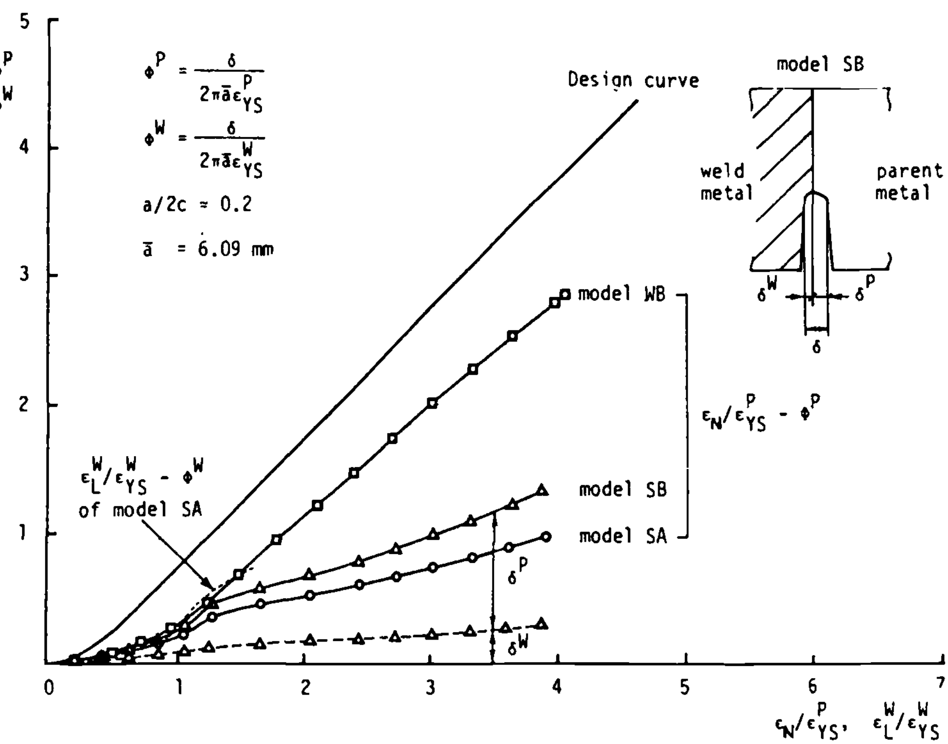

FIG. 18—*CTOD from FEM analysis, plotted on the design curve format: WB = nonwelded parent plate, SA = crack in weld, and SB = crack at fusion line, see Fig. 15.*

in Fig. 18). CTOD and strain were nondimensionalized by the weld metal properties. For this crack geometry, the nominal strain was much larger than the local strain, see Fig. 10. The CTOD curve then appears to follow closely the curve for nonwelded plate, giving support to the proposal that the reference strain in a CTOD assessment should be the local strain, taking into account the effect of an overmatching weld and of a crack.

In Fig. 19, this idea is pursued in more detail. CTOD calculated by FEM is plotted without nondimensionalizing the parameters. Models SA and SB (crack in the middle of the weld) and Model WB (nonwelded plate) show a similar behavior on an absolute strain scale. If this behavior is assumed as a reference then CTOD of the model SB (crack at fusion line), which samples from plate and weld material, is overpredicted when plotted versus weld properties, underpredicted when plotted versus plate material.

In Fig. 19, applied CTOD increases markedly for ε_L around 0.25%, particularly for the welded models. This was found to coincide with the onset of gross section yielding of the plate, causing a change of the applied bending moment distribution along the welded line in the following mechanism.

In the analysis, bending loading is applied as incremental force displacements uniformly distributed in the width direction of the plate, see Fig. 13. In the elastic state, the corresponding bending moment increment applied to the weld metal is larger in the intact part of the plate than in the cracked part, as illustrated in Fig. 19*b*, owing to a smaller bending stiffness in the cracked part. In the design equation, this effect is accounted for by the effective primary stress term, Eq 3, that is based on the linear-elastic fracture mechanics (LEFM) theory. After onset of gross section yielding, which tends to take place in the cracked section, the applied bending moment is redistributed as depicted by the dashed line in Fig. 19*b*, because of the reduction of stiffness in the plastic hinge relative to the adjacent sections. As a result, the rate of plastification of the crack ligament increases and the CTOD increases markedly. With an overmatched weld at the cracked section, this effect would be enhanced as shown in Fig. 19. This effect of load redistribution is not taken into account in the CTOD design equations.

Fracture Assessment of Welded Plate

The procedure for fracture assessment using the CTOD Level-3 method may be summarized as follows:

(*a*) Calculate stress intensity factor, K_I^P due to primary stress.
(*b*) Calculate effective primary stress, σ_P, from K_I^P, Eq 3.
(*c*) Calculate reference stress, σ_{ref}, by Eq 5.
(*d*) Obtain reference strain, ε_{ref}, corresponding to σ_{ref}.
(*e*) Calculate effective crack length, a_e.
(*f*) Calculate applied δ from Eqs 1 or 8.

K_I^P was calculated from the Newman-Raju solutions [*19*], assuming linear elastic distribution of the nominal bending stress.

σ_{ref} was calculated from Eq 5. P_L was calculated assuming elastic-perfectly plastic material, recategorizing the surface cracks as rectangular surface flaws with equal depth and area and computing the value of P that would balance the resisting bending moment [*12*]. (In the analysis of the FEM data, a different recategorization scheme was applied, with essentially the same results [*9*]). As explained earlier, ε_{ref} was measured experimentally, or calculated by three-dimensional FEM, see Fig. 8.

The analyses were aimed at load cases that would give gross section yielding, and residual stresses were neglected [*13*].

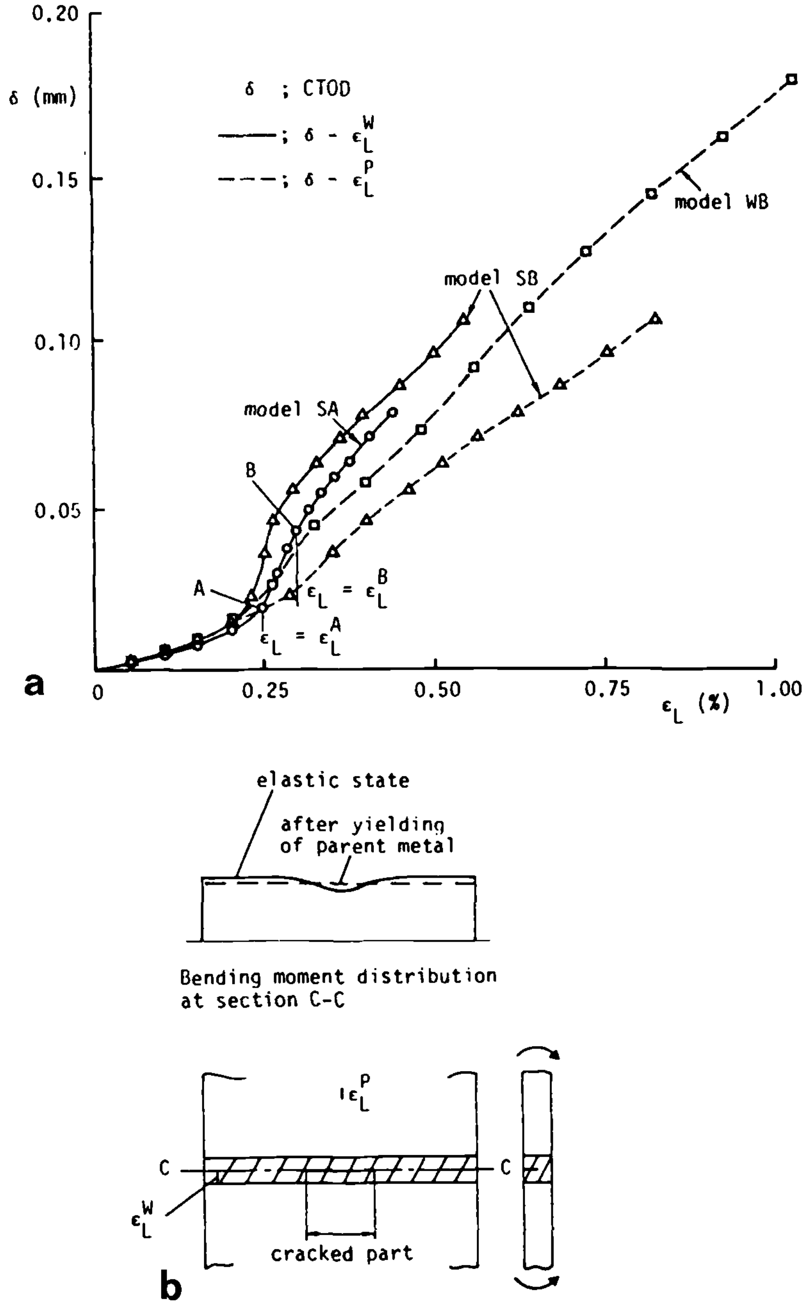

FIG. 19—*Relationship between CTOD and local strain from FEM analysis; WB = nonwelded parent plate, SA = crack in weld, and SB = crack at fusion line, see Fig. 15:* (a) *CTOD/local strain relationship and* (b) *distribution of applied bending moment increment along welded line.*

CTOD Level-3 Predictions from FEM Analysis

In Fig. 20, applied CTOD calculated by Level-3 plain stress (Eq 1) and plain strain (Eq 8) methods for the model SA (crack in the middle of the weld) are shown. Also shown is CTOD calculated with FEM. The calculated CTODs were compared with direct FEM calculations. Computed strain in the weld metal was assumed for ε_{ref}. Also shown is the Level-1 design curve. Assuming the FEM model to give accurate predictions, the plane stress model is overpredicting applied CTOD by a factor in the 2 to 3 range. The plane strain model gives reasonable predictions. However, at strains above gross section yielding, the model is underpredicting CTOD, due to the neglected effect of load redistribution over the crack ligament.

For the model SB (crack along fusion line), there is no clear definition of ε_{ref}, which may be taken in the weld metal or in the parent plate. In Fig. 21, the same curves are shown for the model SB (crack along fusion line), ε_{ref} in the weld. The curves are quite identical to the curves in Fig. 20, with a somewhat more pronounced underprediction of the plane strain method for large strains. The reason appears to be the dominating contribution to the CTOD from the parent plate side of the crack, δ_P, in combination with the load redistribution, see Fig. 18.

The same data, again for the model SB, are plotted in Fig. 22, with ε_{ref} taken in the parent plate close to the fusion line. This strain samples more of the gross yielding of the plate that was constrained by the weld, and the steep increase in CTOD due to load redistribution does not appear. In this case, due to the contribution of, δ^W, from the weld side of the crack being smaller than predicted by the Level-3 method, the plane strain method overpredicts CTOD compared to FEM. The plane stress method appears to be overconservative.

It should be noted that the FEM model of a crack along the fusion line is much idealized. In a real weld, there is no abrupt transition in material properties at the fusion line, due to intermixing of parent and weld material and effects of local thermal cycling during welding.

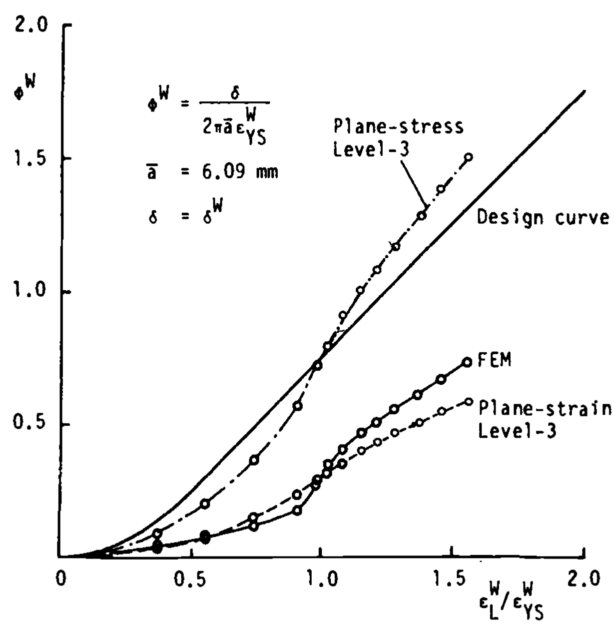

FIG. 20—*CTOD estimates with Level-3 method for the model SA (see Fig. 15), reference strain in weld metal.*

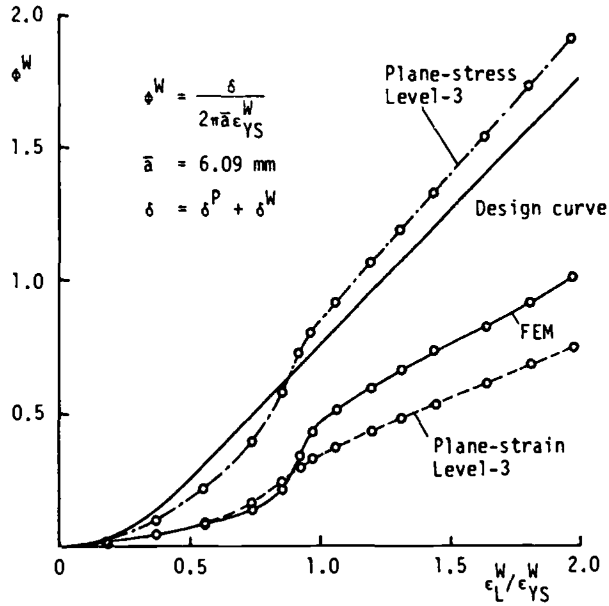

FIG. 21—*CTOD estimates with Level-3 method for the model SB (see Fig. 15), reference strain in weld metal.*

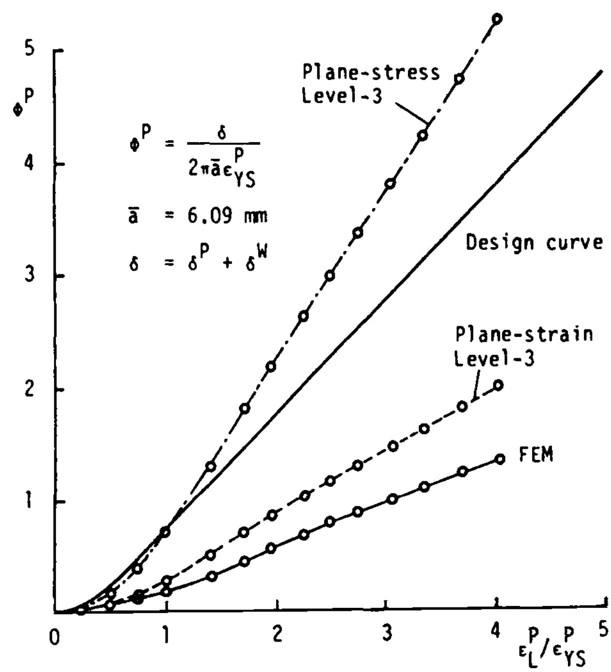

FIG. 22—*CTOD estimates with Level-3 method for the model SB (see Fig. 15), reference strain in parent plate material.*

TABLE 4—*CTOD (δ) of wide plates at fracture/end-of-test calculated by plane strain Level-3 method (Eq 8) for three measures of reference strain.*

Test	Temperature, °C	$a/2c$	$E\varepsilon_L^W/\sigma_{ref}$, δ (mm)	$E\varepsilon_L^P/\sigma_{ref}$, δ (mm)	$E\varepsilon_N/\sigma_{ref}$, δ (mm)	Comment
BP1	0	0.20	0.1	0.2	0.3	no fracture
BP2	−40	0.21	0.1	0.2	0.4	no fracture
BP3	−40	0.23	0.1	0.2	0.3	no fracture
BP4	−40	0.11	0.1	0.3	0.2	fracture
BP5	−20	0.11	0.2	0.4	0.4	no fracture
BP6	−40	0.11	0.3	0.4	0.4	fracture
BP7	−20	0.08	0.3	0.6	0.2	fracture
BP8	−20	0.06	0.3	0.7	0.5	no fracture
BP9	−40	0.06	0.1	0.4	0.3	fracture

Wide-Plate Tests—Comparison with Small-Scale CTOD Data

Evaluation of the CTOD Level-3 procedures from the experimental values was based on the assumption that fracture in a wide plate takes place at the same critical CTOD as in small-scale specimens [*4*]. Level-3 CTOD at fracture (or end of test) of the wide plates was calculated, using measured values of ε_{ref} and other parameters that enter Eqs 1 and 8. The resulting CTODs were compared to the temperature transition curve from small-scale tests, Fig. 5.

Whereas in the FEM study only one crack geometry was analyzed, the wide plate tests had three different crack geometries, causing very different behavior with regard to hinge development, see Figs. 9 through 11. For this reason, the analysis was carried out using all three measured strains as ε_{ref}, namely, ε_L^P, ε_L^W, and ε_N, see Fig. 8, using the plane stress as well as the plane strain models (Eqs 1 and 8). The results of the calculations are shown in Tables 4 and 5.

The purpose of this exercise was to investigate which model and set of input parameters would give the best predictions of Level-3 CTODs in the wide plates. The evaluation of the goodness of the predictions was based on two criteria:

1. Best fit to the temperature transition curve established from a small-scale test (Fig. 5) and
2. Consistency in that CTOD values at fracture should generally be larger than CTOD at the end of a test for plates that did not fracture.

TABLE 5—*CTOD (δ) of wide plates at fracture/end-of-test calculated by plane stress Level-3 method (Eq 1) for three measures of reference strain.*

Test	Temperature, °C	$a/2c$	$E\varepsilon_L^W/\sigma_{ref}$, δ (mm)	$E\varepsilon_L^P/\sigma_{ref}$, δ (mm)	$E\varepsilon_N/\sigma_{ref}$, δ (mm)	Comment
BP1	0	0.20	0.3	0.5	0.9	no fracture
BP2	−40	0.21	0.3	0.5	1.0	no fracture
BP3	−40	0.23	0.3	0.4	0.8	no fracture
BP4	−40	0.11	0.3	0.7	0.6	fracture
BP5	−20	0.11	0.6	0.9	1.0	no fracture
BP6	−40	0.11	0.7	1.1	1.0	fracture
BP7	−20	0.08	0.7	1.7	0.4	fracture
BP8	−20	0.06	0.8	1.9	1.5	no fracture
BP9	−40	0.06	0.4	1.1	0.7	fracture

In Fig. 23, CTOD values a fracture/end-of-test calculated on the basis of nominal strain, ε_N, are shown. The difference between plane stress (Eq 1) and plane strain (Eq 8) predictions is evident. It is also apparent that with this definition of ε_{ref} the results become inconsistent, because the "no fracture" values of CTOD are generally above the values at fracture. The reason is that hinge effects are not accounted for by ε_N.

In Fig. 24, the results calculated with $\varepsilon_{ref} = \varepsilon_L^W$ are shown. The plain strain model gives in this case unrealistically low values of CTOD. Even the values calculated by the plane stress model, which according to the FEM analysis is overpredicting CTOD, appear to be on the low side compared to the temperature transition curve. For cracks along the fusion line, design based on strain in the weld would therefore be unconservative.

In Fig. 25, the results are shown using $\varepsilon_{ref} = \varepsilon_L^P$, which in the FEM analysis was shown to give the best agreement. The resulting CTOD values appear to be more consistent than in the two preceeding figures. The plane stress model is overpredicting CTOD values, whereas the plane strain model appears to be underpredicting. The latter is somewhat in disagreement with the FEM results. One reason could be the neglect of the Level-3 design equation to account for the increase in applied CTOD due to load redistribution following gross section yielding, see Figs. 20 and 21.

As a simple approximation, the load redistribution may be modeled by assuming $a/2c \rightarrow 0$ at the onset of gross section yielding, that is, substituting the Newman-Raju solution for K_I^P in

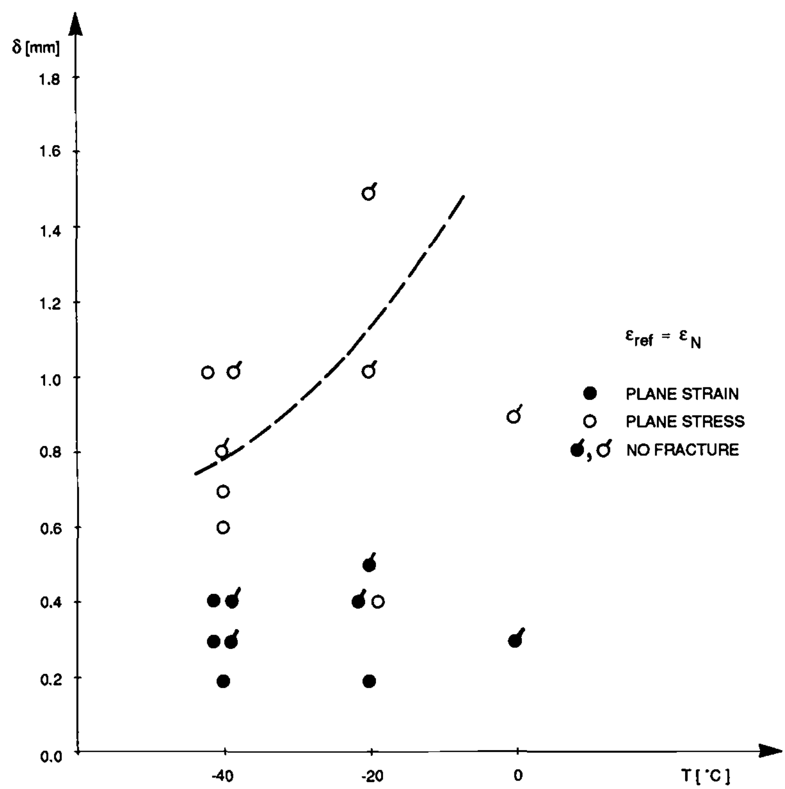

FIG. 23—*CTOD estimates by Level-3 method from test data, nominal strain. Temperature transition curve from Fig. 5.*

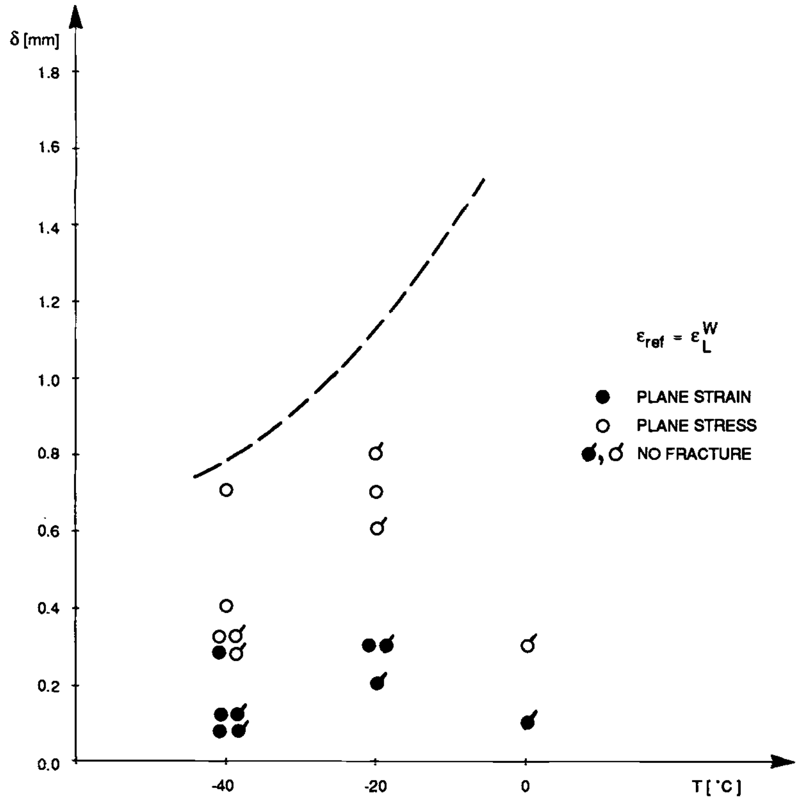

FIG. 24—*CTOD estimates by Level-3 method from test data, local strain in weld metal. Temperature transition curve from Fig. 5.*

Eq 2 by the edge crack solution $1.12\sigma_b\sqrt{(\pi a)}$. The resulting CTOD values, Table 6, are shown in Fig. 26, with the same definition of ε_{ref} as in Fig. 25. The results of Fig. 26 show an improved consistency, and the agreement with the temperature transition curve is very good. It is interesting to note that the same exercise was carried out in the analysis of fracture tests on girth-welded tubulars with a similar improvement [*21*]. The results may indicate that the derivation of an effective primary stress where crack geometry is accounted for by LEFM (Eq 3) is not valid in the regime of gross yielding.

Conclusions

Butt-welded plates of low-carbon microalloyed and normalized steel that conform to offshore specifications with surface fatigue cracks along the fusion line were tested in bending. Plate thickness was 50 mm, and the crack fronts sampled material in HAZ, fusion line, and weld metal.

The material was found to have excellent toughness properties for temperatures down to $-40°C$. In B × B tests of the material, there was some ductile crack extension prior to fracture. In the wide plates, there was no evidence of ductile tearing, indicating that the B × B tests did not reproduce the conditions of constraint in wide plates. Data were insufficient for a further exploration of this issue.

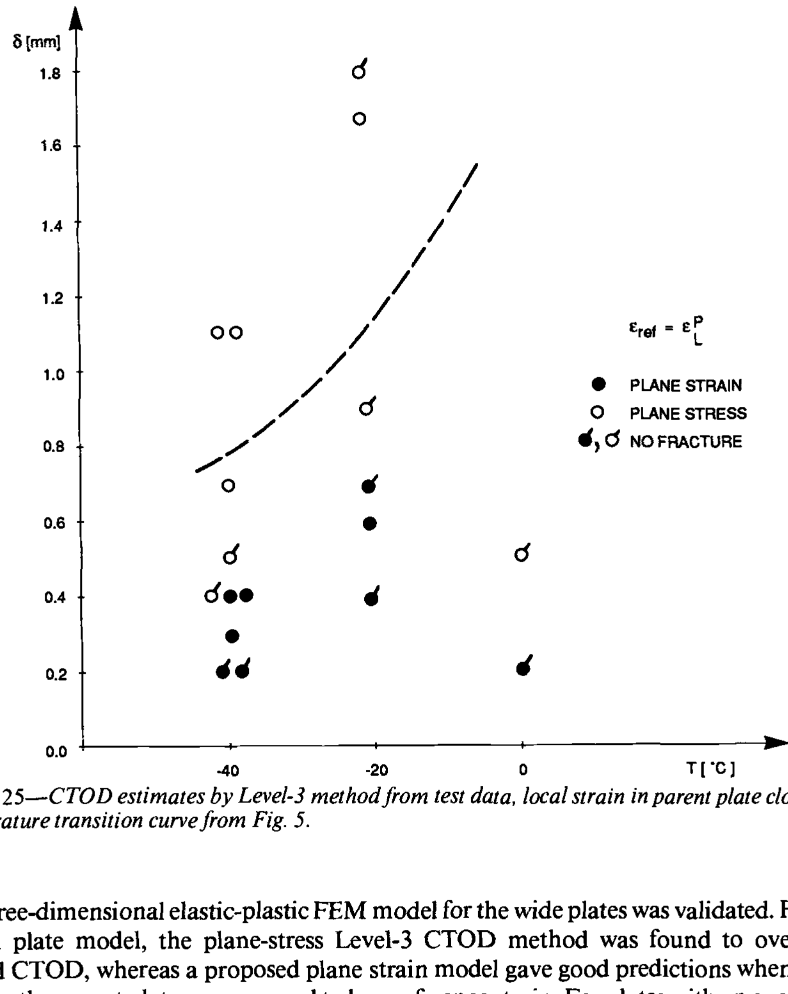

FIG. 25—*CTOD estimates by Level-3 method from test data, local strain in parent plate close to weld. Temperature transition curve from Fig. 5.*

A three-dimensional elastic-plastic FEM model for the wide plates was validated. For a non-welded plate model, the plane-stress Level-3 CTOD method was found to overestimate applied CTOD, whereas a proposed plane strain model gave good predictions when the local strain in the parent plate was assumed to be a reference strain. For plates with an overmatched

TABLE 6—*CTOD (δ) of wide plates at fracture/end-of-test calculated by plane strain Level-3 method (Eq 8) assuming* $K_I^P = 1.12\ \sigma_b \sqrt{(\pi a)}$ *in Eq 3, for three measures of reference strain.*

Test	Temperature, °C	$a/2c$	$E\varepsilon_L^W/\sigma_{ref}$, δ (mm)	$E\varepsilon_L^P/\sigma_{ref}$, δ (mm)	$E\varepsilon_N/\sigma_{ref}$, δ (mm)	Comment
BP1	0	0.20	0.3	0.6	1.0	no fracture
BP2	−40	0.21	0.4	0.6	1.2	no fracture
BP3	−40	0.23	0.4	0.6	1.1	no fracture
BP4	−40	0.11	0.3	0.6	0.6	fracture
BP5	−20	0.11	0.5	0.8	0.8	no fracture
BP6	−40	0.11	0.7	1.1	1.0	fracture
BP7	−20	0.08	0.5	1.2	0.3	fracture
BP8	−20	0.06	0.5	1.0	0.8	no fracture
BP9	−40	0.06	0.3	0.7	0.4	fracture

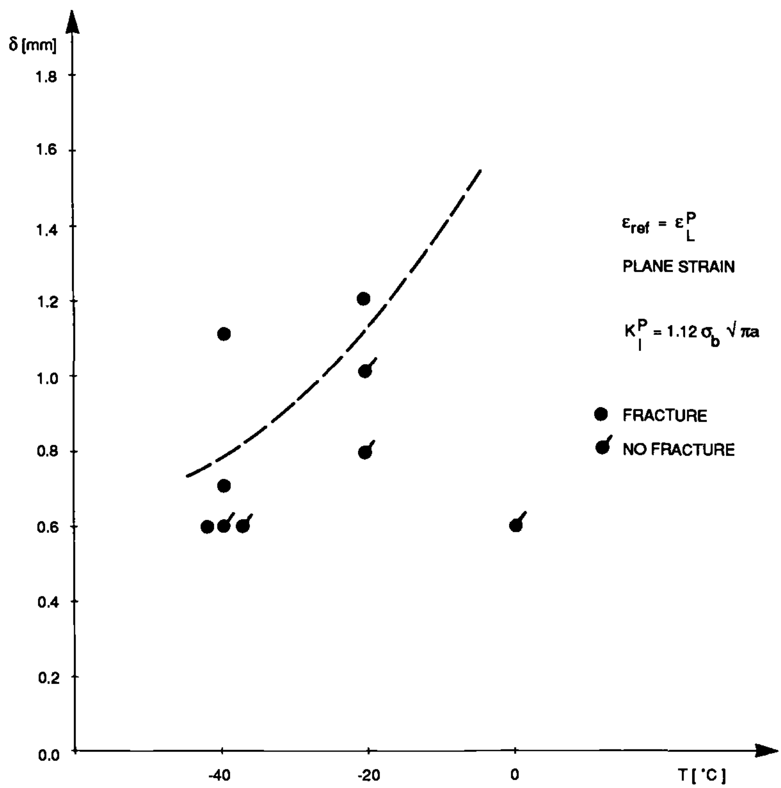

FIG. 26—*CTOD estimates by Level-3 method from test data, local strain in parent plate close to weld, effect of plastic load redistribution included. Temperature transition curve from Fig. 5.*

weld, a load redistribution effect not accounted for in the CTOD design equation was found to significantly enhance CTOD after gross section yielding.

Based on experimental data, applied CTOD at fracture/end-of-test in the wide plates was calculated by the Level-3 CTOD method and compared with the temperature transition curve from B × B tests. The results of the FEM analysis were generally confirmed. For assessment of surface defects in the heat-affected zone of overmatching welds subjected to bending, the following conclusions were drawn:

1. For a material with good toughness, assessment of characteristic values of δ_c by standard test procedures is difficult and leads to large uncertainties in the corresponding temperature transition curve.
2. The reference strain should be measured in the parent plate material, taking into account hinge effects and effects of constraint from the overmatching weld.
3. The plane stress Level-3 CTOD method appears to overpredict applied δ.
4. A proposed plane-strain Level-3 CTOD method with the conventional definition of a primary stress that takes into account the linear-elastic effects of crack geometry appears to underpredict applied δ.
5. A proposed plane-strain Level-3 CTOD method with a primary stress corrected for plastic load redistribution gave results for the wide-plate tests with good consistency and good agreement with small-scale CTOD tests.

Acknowledgment

The experimental work was carried out under Research Programme for Marine Structures supported by NTNF, Statoil, and Norsk Hydro. Dr. Fujikubo received a scholarship from NTNF and NAVF while doing this work. Financial support is gratefully acknowledged.

References

[*1*] Lereim, J., "Fracture Toughness in the Ductile Regime and the Significance on Structural Collapse Mechanisms," *Proceedings*, Fourth Scandinavian Symposium on Materials Science, Trondheim, Norway, 1986.

[*2*] *Regulations for the Structural Design of Load Bearing Structures Intended for Exploitation of Petroleum Resources*, Norwegian Petroleum Directorate, Stavanger, Norway, 1984.

[*3*] *Proceedings*, Tenth International Ship and Offshore Structures Congress (ISSC), Report of Committee III.1, Ductile Collapse, Copenhagen, Denmark, 1988, pp. 315–404.

[*4*] Berge, S., Ebrahimi, F., and Read, D. T., "Wide Plates in Bending: Application of CTOD Design Approach," *Fracture Mechanics: Eighteenth Symposium, ASTM STP 945*, D. T. Read and R. P. Reed, Eds., American Society for Testing and Materials, Philadelphia, 1988, pp. 516–534.

[*5*] Thaulow, C. and Paauw, A. J., "Effects of Notch Depth and Orientation with Respect to Fracture Toughness of the HAZ of Structural Steel," *Proceedings*, 7th Conference of Offshore Mechanics and Arctic Engineering (OMAE), Houston, TX, Vol. III, 1988, pp. 275–286.

[*6*] de Konig, A. C., Harston, J. D., Nayler, K. D., and Ohm, R. K., "Feeling Free–Despite HAZ," *Proceedings*, 7th Conference of Offshore Mechanics and Arctic Engineering, Houston, TX, Vol. III, 1988, pp. 161–179.

[*7*] Denys, R. M., "Advances in Fracture Toughness Testing," *Proceedings*, 6th Conference of Offshore Mechanics and Arctic Engineering (OMAE), Houston, TX, 1987, pp. 269–278.

[*8*] Ainsworth, R. A., "The Assessment of Defects in Structures of Strain Hardening Material," *Engineering Fracture Mechanics*, Vol. 19, No. 4, 1984, pp. 633–642.

[*9*] Fujikubo, M., Berge, S., and Moan, T., "CTOD Estimates of Surface Cracked Wide Plates in Bending—II. Level-3 CTOD Method," *Engineering Fracture Mechanics*, Vol. 40, No. 3, 1991, pp. 641–651.

[*10*] *Guidance on Some Methods for the Derivation of Acceptance Levels for Defects in Fusion Welded Joints*, PD 6493, British Standards Institution, London, UK, 1980.

[*11*] Anderson, T. L., "Elastic-Plastic Fracture Assessments Based on CTOD," Report 276/1985, The Welding Institute, Cambridge, UK, 1985.

[*12*] Anderson, T. L., Leggatt, R. H., and Garwood, S. J., "The Use of CTOD Methods in Fitness for Purpose Analysis," *Proceedings*, Workshop on CTOD Methodology, GKSS-Forschungszentrum, Geesthacht, Germany, 1985, pp. 281–313.

[*13*] Garwood, S. J., Willoughby, A. A., Leggatt, R. H., and Jutla, T., "Crack Tip Opening Displacement (CTOD) Method for Fracture Mechanics Assessments: Proposals for Revisions to PD 6493," *The Assessment of Cracked Components by Fracture Mechanics, Proceedings*, 6th Advanced Seminar on Fracture Mechanics (ASFM6), L. H. Larsson, Ed., Mechanical Engineering Publications Ltd., London, UK, 1989, pp. 267–302.

[*14*] Hancock, J. W., "The Role of the State of Stress on Crack Tip Failure Processes," *Proceedings*, Conference on Micromechanics of Crack Extension, Cambridge, UK, 1980.

[*15*] *ABAQUS Users Manual: Version 4.7*, Hibbitt, Karlsson & Sorensen Inc., Palo Alto, CA, 1988.

[*16*] Rice, J. R., "A Path Independent Integral and the Approximate Analysis of Strain Concentration by Notches and Cracks," *Journal of Applied Mechanics, Transactions*, American Society of Mechanical Engineers, Vol. 35, June 1968, pp. 231–245.

[*17*] Parks, D. M., "A Stiffness Derivative Finite Element Technique for Determination of Crack Tip Stress Intensity Factors," *International Journal of Fracture*, Vol. 10, No. 4, 1974, pp. 487–502.

[*18*] Hellen, T. K., "On the Method of Virtual Crack Extensions," *International Journal for Numerical Methods in Engineering*, Vol. 9, 1975, pp. 187–207.

[*19*] Newman, J. C. and Raju, I. S., "An Empirical Stress-Intensity Factor Equation for the Surface Crack," *Engineering Fracture Mechanics*, Vol. 15, Nos. 1–2, 1981, pp. 185–192.

[*20*] Fujikubo, M., Berge, S., and Moan, T., "CTOD Estimates of Surface Cracked Wide Plates in Bending—I. Finite Element Analysis," *Engineering Fracture Mechanics*, Vol. 40, No. 3, 1991, pp. 639–672.

[*21*] Eide, O. I., Berge, S., and Lereim, J., "Fracture Tests of Girth Welded Tubular Models with Surface Cracks," *Proceedings*, Conference on Welded Structures, The Welding Institute, Cambridge, UK, 1988.

Xiaoguang Chen,[1] *Pedro Albrecht,*[1] *and James Joyce*[2]

Limit Pressure Analysis of a Cylindrical Vessel with Longitudinal Crack

REFERENCE: Chen, X. G., Albrecht, P., and Joyce, J., **"Limit Pressure Analysis of a Cylindrical Vessel with Longitudinal Crack,"** *Fracture Mechanics: Twenty-Third Symposium, ASTM STP 1189,* Ravinder Chona, Ed., American Society for Testing and Materials, Philadelphia, 1993, pp. 310–329.

ABSTRACT: This paper presents equations for the limit pressure of a cylindrical vessel with a longitudinal crack. The calculations are based on a log-spiral slip-line and plane-strain conditions. The calculated limit pressure is compared with the pressure measured in the Pressurized-Thermal-Shock Experiment No. 2, PTSE-2, performed at the Oak Ridge National Laboratory. It was found that in the PTSE-2A test the short crack extended in a region of thermal tensile stress at a measured pressure lower than the calculated limit pressure. However, in the PTSE-2B test, the long crack extended in a region of decreasing temperature gradient at à pressure about equal to the calculated limit pressure. The vessel collapsed when the pressure exceeded the limit pressure. In comparison, the crack in compact specimens [C(T)] fabricated from the same steel as the vessel extended at the limit load calculated on the basis of the flow stress. The differences in fracture behavior likely resulted from differences in degree of constraint in the C(T) specimens and the vessel.

KEY WORDS: limit pressure, cracks, fracture (materials), slip line, pressure vessels, thermal shock, fracture mechanics, fatigue (materials)

The present study evolved from observations that (1) cracks in many compact tension, C(T), specimens extended at loads greater than the limit load calculated on the basis of yield stress, and (2) J versus crack extension ($J_R - \Delta a$) data from C(T) specimen tests poorly predicted crack extension in a thick-wall cylindrical vessel.

Regarding the first observation, Hu et al. [*1,2*] have shown that the limit load predicted well the load versus crack extension behavior of 0.5T and 1T C(T) specimens fabricated from A710 steel, A533-B steel, A508 steel, HY 80 steel, A302-B steel, and CS19 aluminum. All specimens were tested at room temperature or higher. The limit load also predicted well the data for 2T, 4T, and 10T C(T) specimens of A508 steel. The predictions were generally better for small specimen sizes and long cracks.

In their work, Hu et al. have emphasized the need to clearly distinguish between elastic-plastic and plastic fractures. Crack extension is controlled in the former case by a crack-tip singularity parameter such as the J-integral and in the latter case by plastic hinge rotation at limit load.

Regarding the suitability of $J_R - \Delta a$ data, Oak Ridge National Laboratory (ORNL) researchers concluded that [*3*]

> Posttest analysis of the four distinct phases of stable ductile tearing in PTSE-2 (pressurized-thermal-shock experiment No. 2) failed to demonstrate quantitative agreement between $J_R - \Delta a$ data and

[1] Ph.D. candidate and professor, respectively, Department of Civil Engineering, University of Maryland, College Park, MD 20742.
[2] Professor, Mechanical Engineering Department, U.S. Naval Academy, Annapolis, MD 21402.

tearing in the experiment. J_R curves that fit the early phases of the experiment were poor fits for the later phases and vice versa.

Also,

The tearing analysis of both experiments indicate that the quantitative effect cannot be predicted well from $J_R - \Delta a$ data. This experience and the imprecision of similar tearing predictions for the isothermal hydrostatic test of intermediate test vessel V-8A suggest that it would be useful to investigate the applicability of other theoretical procedures based on tensile properties.

Based on the findings just cited, the authors were asked to calculate the limit pressure of the PTSE-2 vessel during Transients A and B. The result was to serve as a test of the utility of slip-line analysis in predicting the strength of a pressurized vessel.

PTSE-2 Vessel

Dimensions

The cylindrical vessel that was tested in the PTSE-2 had an inner radius of R_i = 343.0 mm, outer radius of R_o = 490.6 mm, and wall thickness of W = 147.6 mm (Fig. 1). The 2160-mm-long cylindrical portion was capped with spherical ends.

A longitudinal, full-thickness insert was welded into the cylindrical portion of the vessel. It contained a longitudinal crack of initial depth, a = 14.5 mm, and surface length, L = 1000 mm, on the front wall.

Tensile Properties

The insert piece was made of 2¼ Cr — 1 Mo steel of low tearing resistance, designated Material A in Refs *3* and *4*.

The tensile properties of Material A were measured with two sets of specimens. The Set 5 specimens were machined from a piece of material that was cut from the insert before the

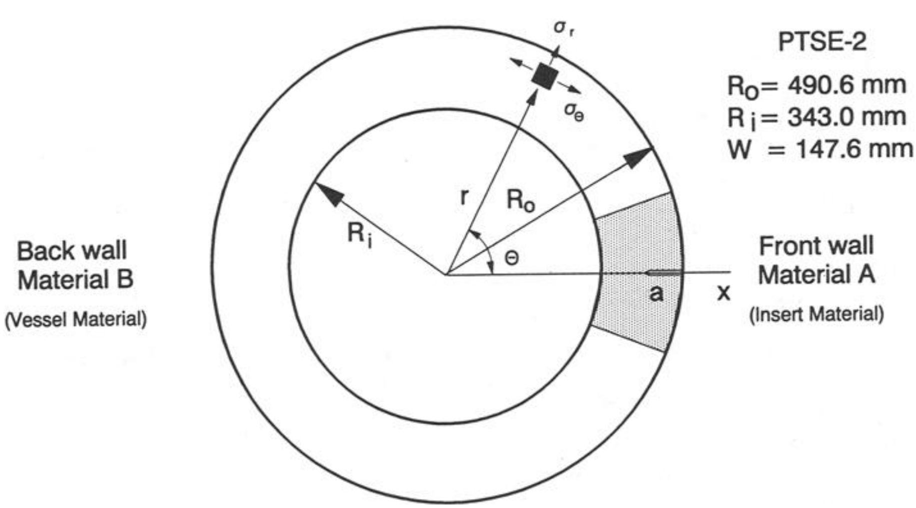

FIG. 1—*Cylinder with a longitudinal outer crack.*

insert was welded into the vessel. This characterization piece had a yield strength of 255 MPa and a tensile strength of 518 MPa. The Set 7 specimens were cut from the insert after the completion of the PTSE-2 vessel test. This posttest piece had a yield strength of 375 MPa. Its tensile strength was not reported.

The yield strength of the posttest piece, $\sigma_y = 375$ MPa, was about the same as the flow stress of the characterization piece, $\sigma_0 = 386$ MPa. The flow stress was calculated as the mean of the measured yield and tensile strengths. Evidently, the insert steel strain hardened during the pressurized-thermal-shock event.

The vessel itself was made of A533-B steel, designated Material B in Refs *3* and *4*. It had a yield strength of 430 MPa. Its tensile strength was not reported.

Elastic Compliance Data

The ORNL staff also performed elastic compliance tests of two sets of 1*T* C(T) specimens fabricated from the insert Material A. Similar to the tensile specimens, the Set 5 C(T) specimens came from the characterization piece and the Set 7 C(T) specimens from the posttest piece.

The authors reanalyzed the elastic compliance data in terms of load versus crack length. The measured loads were compared with the limit load of the 1*T* C(T) specimen, calculated as [*1,2*]

$$P_L = \frac{2}{\sqrt{3}} B\sigma_0 \left(2.572 \frac{R}{b} - 1\right) b \tag{1}$$

where the radius of the circular segment of the slip-line in the C(T) specimen is (see Fig. 2 in Ref *1*)

$$R = \sqrt{0.699a^2 + 0.409W^2} - 1.052a \tag{2}$$

and

B = specimen thickness,
W = specimen width, and
$b = W - a$ = ligament width.

Figures 2 and 3 show typical results for the Set 5 and 7 specimens. Both were 20% side grooved. For ease of comparing the data, the load and the crack length were normalized. Two predicted limit load curves were plotted, one based on the yield strength and the other on the flow stress of Material A. The latter accounts for strain hardening.

The load in the Set 5 specimens reached the limit load calculated on the basis of the flow stress after a crack extension of about $\Delta a/W = 0.03$. Thereafter, the crack extended at loads higher than the flow stress limit load.

The load in the Set 7 specimens reached the limit load calculated on the basis of the yield stress. The yield strength of the Set 7 specimens was much higher than that of the Set 5 specimens, on average $\sigma_y = 375$ MPa versus $\sigma_y = 255$ MPa. It was comparable to the flow stress of the Set 5 specimens ($\sigma_0 = 386$ MPa). It is believed that the prestrain to which the posttest piece was subjected during the PTSE-2 test kept the Set 7 specimens from strain hardening further in the elastic compliance tests.

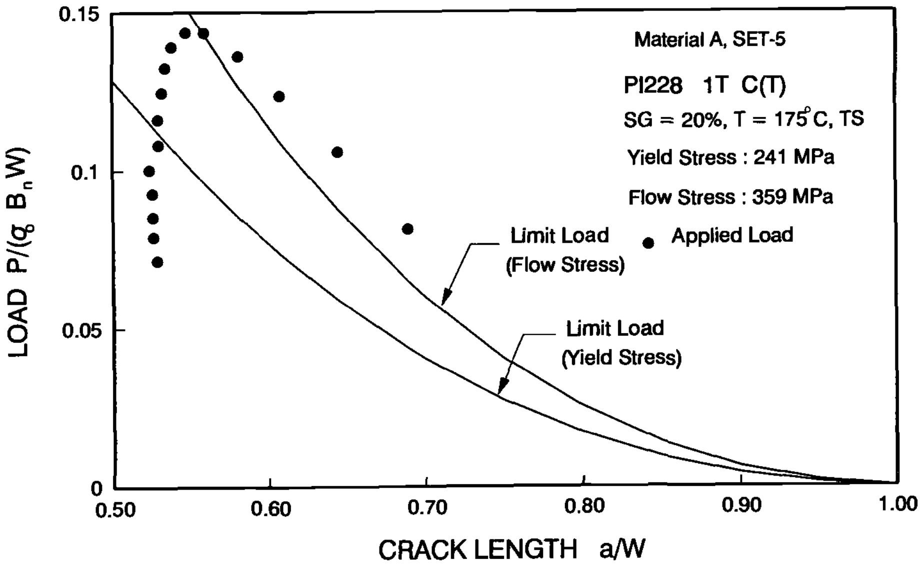

FIG. 2—*Comparison of the applied load,* p, *with limit load,* p_L, *for pretest C(T) Specimen PI228 made of insert Material A.*

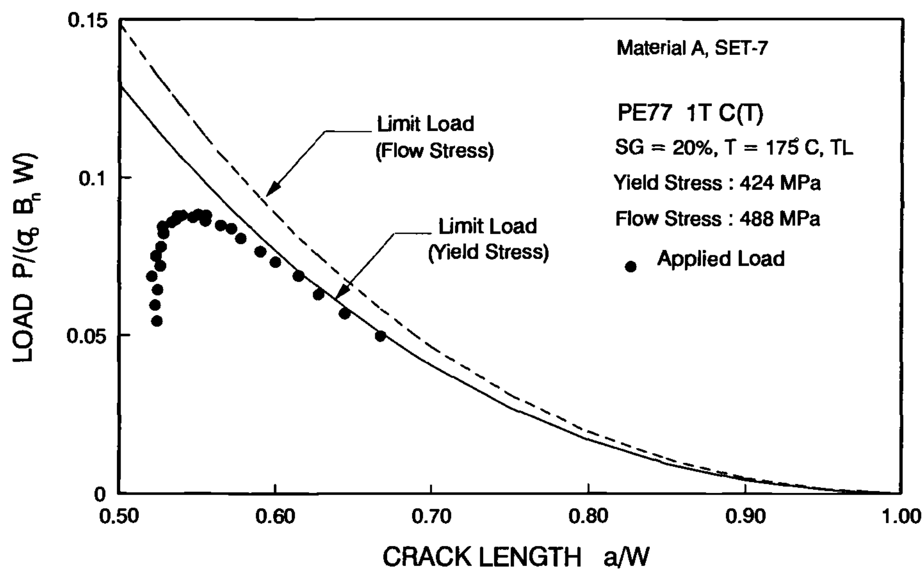

FIG. 3—*Comparison of the applied load,* p, *with limit load,* p_L, *for posttest C(T) Specimen PE77 made of insert Material A.*

Cylinder Without Crack

To determine the limit pressure of a cracked vessel, it is necessary to first obtain the stress distribution through the wall thickness of a cylindrical vessel without a crack. As a first step towards calculating the limit pressure of a cracked vessel, equations were obtained for the internal pressure as well as the elastic, elastic-plastic, and plastic stresses in the cylindrical portion of a noncracked vessel. Knowledge of these stresses provides guidance on the location and formation of the plastic hinges that are needed for an upper-bound mechanism analysis, and the stress diagrams for a lower-bound static analysis.

Elastic Solution

The elastic solution for stresses in the wall of an axisymmetric cylinder subjected to internal pressure can be found in the literature [5]. The solution of interest in this study assumes that the cylinder wall is thick; the material is homogeneous, isotropic, and linear elastic; and the moment at the cylinder to cap junction does not significantly affect the stresses in the cylinder wall away from the ends. Under those conditions the circumferential and radial stresses through the wall thickness, Fig. 1, are given by [5]

$$\sigma_\theta = p \frac{\left(\frac{R_o}{r}\right)^2 + 1}{\left(\frac{R_o}{R_i}\right)^2 - 1} \tag{3}$$

$$\sigma_r = -p \frac{\left(\frac{R_o}{r}\right)^2 - 1}{\left(\frac{R_o}{R_i}\right)^2 - 1} \tag{4}$$

where

R_i = inner radius,
R_o = outer radius,
r = radial location between R_i and R_o, and
p = internal pressure.

The stress component, σ_z, in the longitudinal direction of the cylinder is

$$\sigma_z = 2\nu p \frac{1}{\left(\frac{R_o}{R_i}\right)^2 - 1} + E\varepsilon_0 \tag{5}$$

where

E = modules of elasticity,
ν = Poisson's ratio, and
ε_0 = longitudinal strain.

The preceding equations are valid until the yield condition is reached at the inner surface of the cylinder, where the circumferential stress is highest.

Yield Criteria

The yield condition in this study is based on the von Mises yield criterion written in the form

$$\frac{1}{\sqrt{2}}\sqrt{(\sigma_1-\sigma_2)^2+(\sigma_2-\sigma_3)^2+(\sigma_3-\sigma_1)^2}=\sigma_y \tag{6}$$

where

$\sigma_1, \sigma_2, \sigma_3$ = principal stresses, and
σ_y = tensile yield stress.

Since the directions of the principal stresses do not change during loading, one can assume that σ_2 is the longitudinal stress, σ_z. Thus, $\sigma_1 = \sigma_\theta$, $\sigma_2 = \sigma_z$, $\sigma_3 = \sigma_r$. Also, one can show that $\sigma_z = (\sigma_r + \sigma_\theta)/2$. For plane strain ($\epsilon_0 = 0$) and rigid-perfectly plastic material behavior, the von Mises yield criterion has the form

$$\sigma_1 - \sigma_3 = 2k \tag{7}$$

where $k = \sigma_y/\sqrt{3}$ is the shear yield stress. Equation 7 is valid at first yielding as well as during rigid-perfectly plastic deformation, because for both cases $\sigma_z = (\sigma_r + \sigma_\theta)/2$.

Elastic-Plastic Solution

The cylinder begins to yield when the difference between the circumferential and radial stresses, Eqs 3 and 4, is equal to two times the shear yield stress. The corresponding pressure at first yielding, p_y, is given by

$$p_y = \frac{1}{2}\left[1-\left(\frac{R_i}{R_o}\right)^2\right]2k \tag{8}$$

A cylinder subjected to a pressure greater than the yield pressure (Eq 8) develops elastic-plastic stresses through the wall thickness. The cylinder can be thought of as a two-ring composite. The radius to the boundary between the elastic and plastic rings is labeled r_y.

The stresses in the "inner plastic ring," $R_i \leq r \leq r_y$, are

$$\sigma_\theta = -p + 2k\left(1 + \ln\frac{r}{R_i}\right) \tag{9}$$

$$\sigma_r = -p + 2k\ln\frac{r}{R_i} \tag{10}$$

The stresses in the "outer elastic ring," $r_y \leq r \leq R_o$, are

$$\sigma_\theta = \frac{r_y^2}{2R_o^2}2k\left(1+\frac{R_o^2}{r^2}\right) \tag{11}$$

$$\sigma_r = \frac{r_y^2}{2R_o^2}2k\left(1-\frac{R_o^2}{r^2}\right) \tag{12}$$

Plastic Solution [7]

The noncracked cylinder fully yields through the wall thickness when $r_y = R_o$. The limit pressure of the noncracked cylinder then becomes

$$p_L = 2k \ln \frac{R_o}{R_i} \tag{13}$$

Substituting the limit pressure, p_L, from Eq 13 into Eqs 9 and 10 gives the following expressions for the circumferential and radial stresses of the fully yielded cylinder, with $R_i \leq r \leq R_o$

$$\sigma_\theta = 2k\left(1 + \ln \frac{r}{R_o}\right) \tag{14}$$

$$\sigma_r = 2k \ln \frac{r}{R_o} \tag{15}$$

Application to Vessel Without Crack

The stresses in the wall of a pressurized cylinder of dimensions equal to those of the PTSE-2 vessel were calculated for two conditions: a cylinder made entirely of the insert Material A (characterization piece, Set 5); and a cylinder made entirely of the vessel Material B.

The right part of Fig. 4 shows the circumferential and radial stress distributions for a noncracked cylinder made entirely of the insert Material A, with yield strength of σ_y = 255 MPa. The circumferential stress is shown for three pressures, the radial stress only for the limit pressure. The three curves represent: (*a*) elastic stresses at the yield pressure, p_y = 75.3 MPa, causing first yielding of the steel on the inner surface of the wall; (*b*) elastic-plastic stresses at an intermediate pressure, p = 98.9 MPa; and (*c*) plastic stresses at the limit pressure, p_L = 105.4 MPa.

The stresses are shown for the front wall section of the cylinder (where the insert is located in the PTSE-2 vessel) at an angle, $\theta = 0$, from the x-axis. As Fig. 4 shows, the wall of the noncracked cylinder yields from the inside out as the pressure is increased. Indeed, the value of the elastic circumferential stress induced by the yield pressure decreases from σ_θ = 219.1 MPa at the inner surface to σ_θ = 144.0 MPa at the outer surface. At the limit pressure, the value of the plastic circumferential stress increases from $\sigma_\theta = 2\sigma_y/\sqrt{3} - p_L$ = 189.0 MPa at the inner surface to $\sigma_\theta = 2\sigma_y/\sqrt{3}$ = 294 MPa at the outer surface. The radial stress is much smaller than the circumferential stress. It varies from $\sigma_r = -p$ at the inner surface to zero at the outer surface.

Similarly, the left part of Fig. 4 shows the circumferential and radial stresses for a noncracked cylinder made entirely of the vessel Material B, with yield strength of σ_y = 430 MPa. They are shown for the back wall section of the cylinder at a counter-clockwise angle, $\theta = \pi$, from the x-axis (Fig. 1). The curves represent: (*a*) elastic stresses at the yield pressure, p_y = 126.9 MPa, causing first yielding of the steel on the inner surface of the back wall; (*b*) elastic-plastic stresses at an intermediate pressure; and (*c*) plastic stresses at the limit pressure, p_L = 177.7 MPa. The back wall stresses for the higher yield strength Material B are much higher than the corresponding front wall stresses for the lower yield strength Material A.

The implication of the results for a crack-free PTSE-2 vessel is that the back wall remains elastic even as the front wall fully yields. This suggests a failure mechanism, in which a plastic tensile link forms in the front wall (Fig. 5*a*) followed by a plastic hinge in the back wall (Fig. 5*b*). The vessel would then collapse.

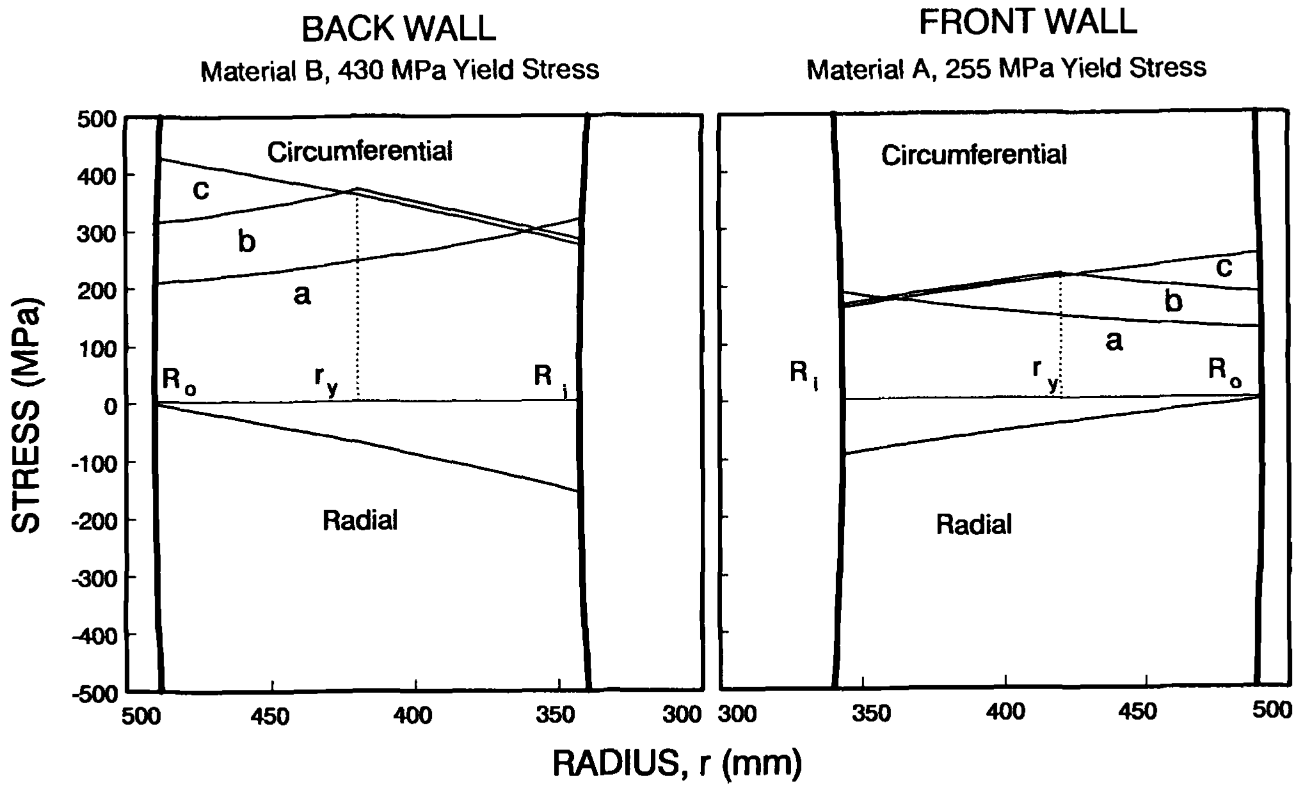

(a) elastic stresses at yield pressure
(b) elastic-plastic stresses at intermediate pressure
(c) plastic stresses at limit pressure

FIG. 4—*Typical circumferential and radial stress in front and back walls of the cylinder without crack.*

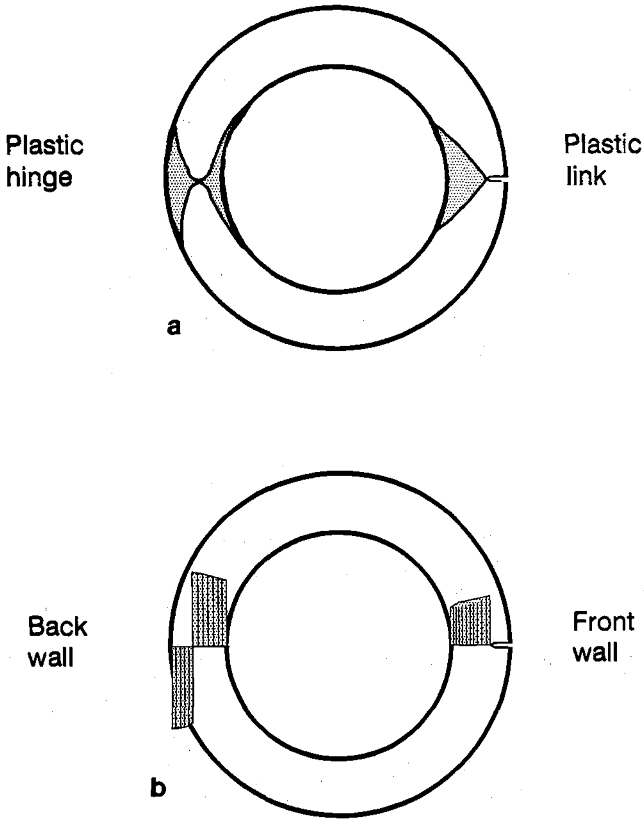

FIG. 5—*Vessel with plastic link in front wall and plastic hinge at back wall:* (a) *plastic region and* (b) *circumferential stress.*

Cylinder with Outer Crack

The limit pressure is calculated with the slip-line method at the different crack lengths that were measured during the PTSE-2A and PTSE-2B tests. The governing equations are summarized briefly in the following section. The reader should refer to Ref *6* for a detailed analysis.

Plastic Link in Front Wall

Equations for Slip-Line Field—The plane strain condition is the main assumption made in developing the slip-line solution. With this assumption, the basic equations for the stress components are

$$\sigma_\theta = \sigma_m + k \sin[2(\alpha - \theta)] \tag{16}$$

$$\sigma_r = \sigma_m - k \sin[2(\alpha - \theta)] \tag{17}$$

$$\tau_{r\theta} = k \cos[2(\alpha - \theta)] \tag{18}$$

where $\alpha - \theta$ is the angle between the α-line and the x-axis in Fig. 6. Equations 16 through 18 are solved for the tangential stress

$$\sigma_\theta = \sigma_r \pm 2\sqrt{k^2 - \tau_{r\theta}^2} \tag{19}$$

hydrostatic stress

$$\sigma_m = \sigma_r \pm \sqrt{k^2 - \tau_{r\theta}^2} \tag{20}$$

and angle of the slip-line angle

$$\alpha = \theta \pm \frac{1}{2}\arccos\frac{\tau_{r\theta}}{k} \tag{21}$$

The shear stress, $\tau_{r\theta}$, in the wall of a pressurized cylinder is assumed to be zero. Thus, the tangent on the α-line is sloped at an angle, $\alpha = \theta + \pi/4$, from the x-axis. The equations for the α- and β-lines then take the form

$$\begin{aligned} \theta &= -\theta_0 + \ln\frac{r}{R_i} \\ \theta &= +\theta_0 - \ln\frac{r}{R_i} \end{aligned} \tag{22}$$

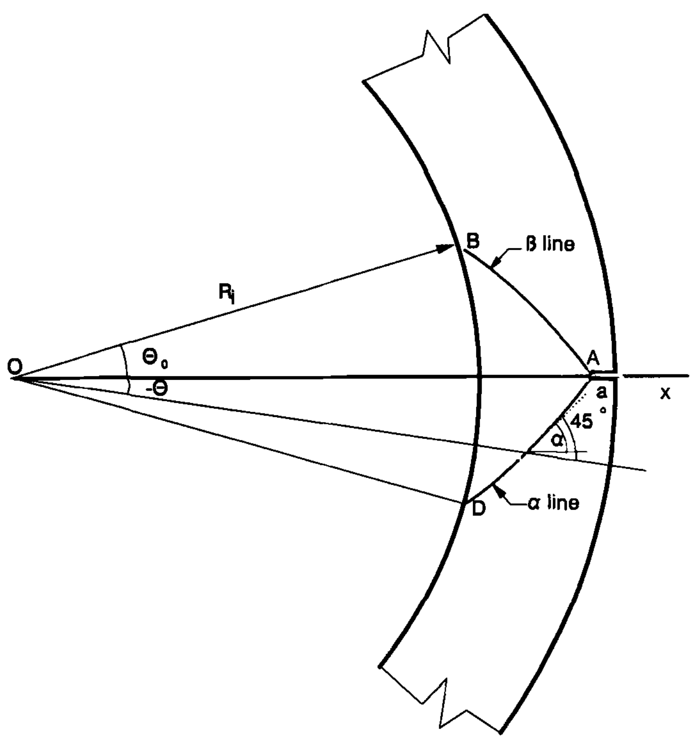

FIG. 6—*Log-spiral slip line in pressurized cylinder with longitudinal outer crack.*

Limit Pressure—The pressure when a plastic link forms in the front wall is loosely called the limit pressure in this study, even though the vessel does not collapse until a plastic hinge forms in the back wall. This pressure is assigned the symbol, p_{L1}, in which the numeric subscript stands for the first cross section to fully yield. To calculate the limit pressure, the circumferential stress, σ_θ, must be known in the front and back walls of the vessel. The stress in the back wall is still elastic when the front wall fully yields, because the yield strength of the vessel Material B is much higher than that of the insert Material A.

The circumferential stress in the front wall is calculated first at Point A, $\sigma_{\theta A}$, and then at other points along the x-axis, $\sigma_{\theta=0}$ (Fig. 6). Using the basic slip-line equation for the α-line, $\delta\sigma_m = 2k\,\delta\alpha$, and knowing the hydrostatic stress at Point D, $\sigma_m = -p + k$, the hydrostatic stress at Point A can be obtained. Inserting the resulting expression, $\sigma_{mA} = -p + k + 2k\ln(r/R_i)$, into Eq 16, leads to the equation for the circumferential stress at Point A.

$$\sigma_{\theta_A} = -p + 2k\left(1 + \ln\frac{r}{R_i}\right) \tag{23}$$

Since the boundary conditions for all points on the inner surface between the x-axis and D (Fig. 6) are the same as those for Point D, one can show that the circumferential stress at all points on the x-axis between the inner surface and the crack tip must be equal to the circumferential stress at the crack tip. In other words, Eq 23 is valid for all other points along the x-axis, that is

$$\sigma_\theta|_{\theta=0} = \sigma_{\theta_A} \tag{24}$$

The limit pressure is obtained by writing an equation of force equilibrium for one half of the cylinder.

$$p_{L1} = 2k\ln\frac{R_o - a}{R_i} \tag{25}$$

Figure 7 shows, as an example, the circumferential and radial stresses in the front and back walls, at a pressure of $p_{L1} = 96.5$ MPa and initial crack length of $a = 14.5$ mm (Eq 25), as calculated with the von Mises shear yield stress, $k = \sigma_y/\sqrt{3}$.

Plastic Hinge in Back Wall

As the pressure is further increased, the plastic link elongates at constant resistance, and the lower and upper halves of the cylinder are assumed to rotate about a point in the back wall. The vessel eventually collapses when a plastic hinge forms in the back wall under combined tension and bending. The increment in pressure between the formation of the plastic link in the front wall and the plastic hinge in the back wall is equivalent to a pressure resisted by a ring split at the front wall.

The pressure at the time of collapse is assigned the symbol p_{L2} in which the numeric subscript stands for the second cross section to fully yield. Similar to the deviation of p_{L1}, the limit pressure, p_{L2}, is obtained from the equations of force and moment equilibrium for a unit length of one half of the cylinder. The circumferential stress in the front wall is given by Eq 23.

Equations for Stress Field—The circumferential stress distribution for combined tension and bending of the back wall is assumed in such a way that the stress satisfies the yield criterion at all points. According to Eq 14, this stress is in the region under tension

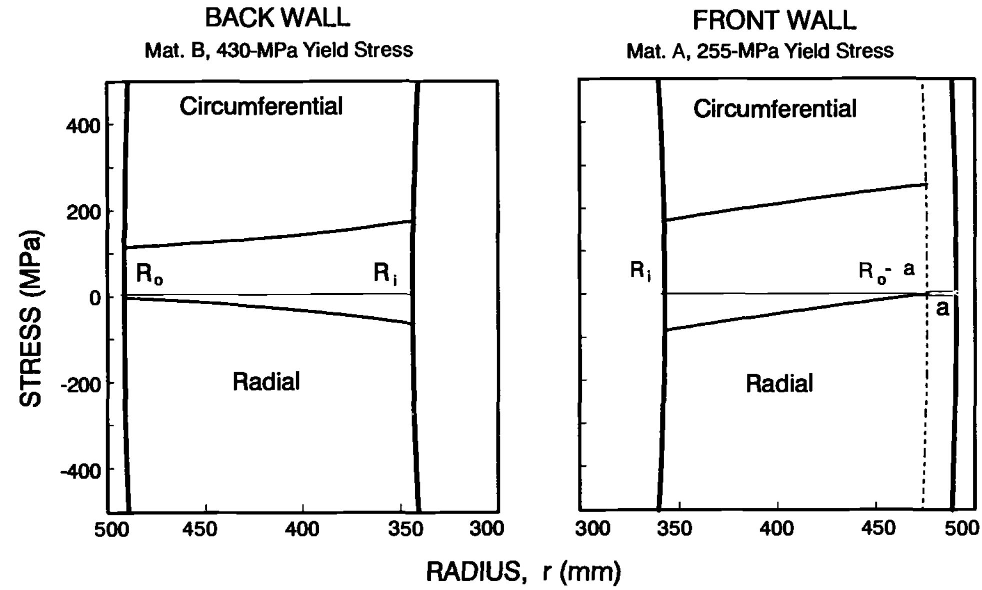

FIG. 7—*Stresses in cracked cylinder at formation of plastic link in front wall.*

$$\sigma_\theta = 2k_B\left(1 + \ln\frac{r}{R_o}\right) \tag{26}$$

and in the region under compression

$$\sigma_\theta = -2k_B\left(1 + \ln\frac{r}{R_o}\right) \tag{27}$$

The shear yield strength, $k_B = \sigma_{yB}/\sqrt{3}$, is that of the vessel Material B.

Limit Pressure—The force equilibrium equation is then

$$\Sigma F_y = 2p_{L2}R_i - \int_{\text{front wall}} \sigma_\theta\, dr - \int_{\text{back wall}} \sigma_\theta\, dr = 0 \tag{28}$$

where p_{L2} is the limit pressure when the plastic hinge forms. The stress state in the front wall does not change as the pressure is increased from p_{L1} to p_{L2}, meaning that the plastic link elongates at constant resistance. Therefore, the integral of the circumferential stress in the front wall remains equal to $p_{L1}R_i$ according to the plastic link calculations. Substituting this value for the first integral in Eq 28, along with the expression for the circumferential stress in the back wall (Eqs 26 and 27), gives

$$2p_{L2}R_i - P_{L1}R_i - \int_{R_i}^{r_{NA}} 2k_B\left(1 + \ln\frac{r}{R_o}\right) dr + \int_{r_{NA}}^{R_o} 2k_B\left(1 + \ln\frac{r}{R_o}\right) dr = 0 \tag{29}$$

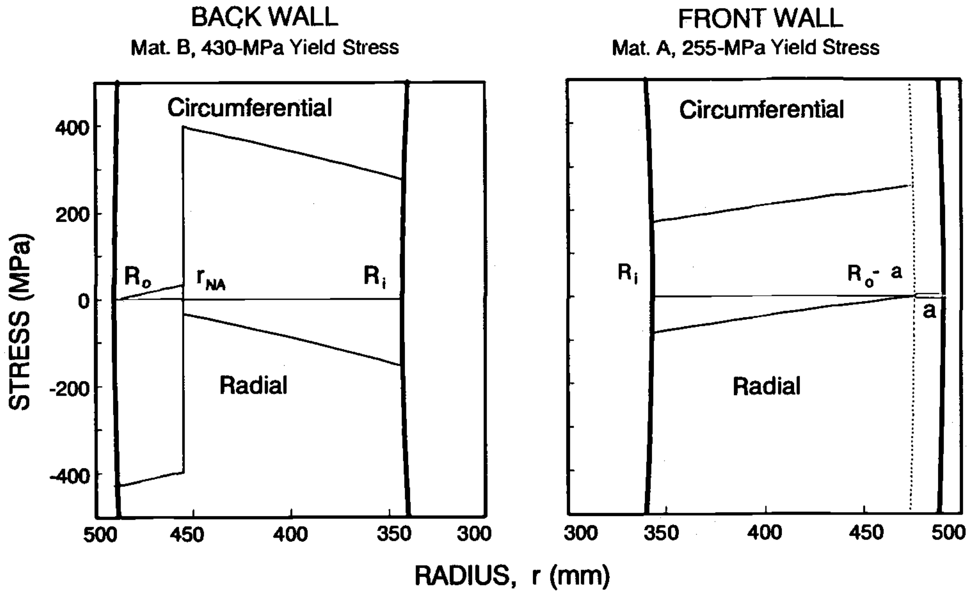

FIG. 8—*Stresses in cracked cylinder at formation of plastic hinge in back wall.*

Moment equilibrium about the axis of the cylinder requires that

$$\Sigma M_o = \int_{\text{front wall}} \sigma_\theta r \, dr - \int_{\text{back wall}} \sigma_\theta r \, dr = 0 \tag{30}$$

Substituting the front wall stress from Eq 24 and the back wall stress from Eqs 26 and 27 leads to

$$\int_{R_i}^{R_o-a} \left[-P_{L1} + 2k_A\left(1 + \ln\frac{r}{R_i}\right)\right] r\,dr - \int_{R_i}^{r_{NA}} 2k_B\left(1 + \ln\frac{r}{R_o}\right) r\,dr + \int_{r_{NA}}^{R_o} 2k_B\left(1 + \ln\frac{r}{R_o}\right) r\,dr = 0 \tag{31}$$

The term, r_{NA}, is the radius to the plastic neutral axis in the back wall. The position of the neutral axis was calculated by solving the moment equilibrium Eq 31. The result was then substituted into the force equilibrium Eq 29 giving the limit pressure, p_{L2}. Both equations were solved numerically with MathCAD.

Figure 8 shows, as an example, the circumferential and radial stresses in the front and back walls at the limit pressure, p_{L2} = 100.4 MPa, and initial crack length of a = 14.5 mm. The stresses in the front wall are the same as those plotted in Fig. 7, because in both cases a plastic link has formed in the front wall.

Results

Table 1 summarizes the fracture events during the PTSE-2A and PTSE-2B tests, their time of occurrence, and the measured pressure and crack length at each event. This information was taken from Ref *3*.

Table 2 lists the values of the limit pressure, p_{L1}, when the plastic link forms in the front wall and the values of the limit pressure, p_{L2}, when the plastic hinge forms in the back wall. The von Mises shear yield stress is $k = \sigma_y/\sqrt{3}$, where $\sigma_{yA} = 255$ MPa for the insert Material A in the front wall and $\sigma_{yB} = 430$ MPa for the vessel Material B in the back wall.

The limit pressure, p_{L2}, is higher than p_{L1} by an amount varying from 4% at 14.5-mm crack length to 7% at 78.8-mm crack length. This difference is not significant, and, for practical purposes, the limit pressure, p_{L1}, at the formation of the plastic link in the front wall could be taken as the collapse pressure.

Completing the calculations, Table 2 also lists the limit pressures, p_{L1} and p_{L2}, calculated with the von Mises shear flow stress for the insert Material A in the front wall, $k = \sigma_{0A}/\sqrt{3} = 386/\sqrt{3} = 223$ MPa, and the shear yield stress for the vessel Material B in the back wall, $k = \sigma_{yB}/\sqrt{3} = 430/\sqrt{3} = 248$ MPa. The flow stress was chosen for the insert Material A, because the tension tests of specimens from the posttest piece showed evidence of strain hardening during the PTSE-2 tests. The yield stress is the appropriate value for the vessel Material B. Since the hinge in the back wall is the last to form and does not have to rotate for the vessel to collapse, the yield stress of the vessel material should not be raised to the level of the flow stress.

Figures 9 and 10 compare the calculated limit pressure with the pressure measured during the PTSE-2A and PTSE-2B tests, respectively. The limit pressure was calculated at all measured crack lengths and was plotted at the corresponding times from scan start (Tables 1 and 2). The limit pressure was calculated for the following cases: formation of the plastic link in the front wall, based on the yield stress of the insert material; formation of the plastic hinge in the back wall, based on the yield stresses of the insert and vessel materials; and formation of the plastic hinge in the back wall, based on the flow stress of the insert material and the yield stress of the vessel material. The measured pressure was plotted at all elapsed times listed in Tables 10.10 and 10.11 of Ref *3*. Table 2 of the present study gives only the data at the times

TABLE 1—*Measured pressure and crack lengths during PTSE-2A and PTSE-2B tests (adapted from Tables 9.1, 10.10, 10.11, and 10.12 of Ref 3).*

Event	Time, s	Measured Position	Crack Length, a (mm)	Measured Pressure, p (MPa)	SIF, K_I (MPa $\sqrt{m}$)	Crack-Tip Temperature, T (°C)
		PTSE-2A				
Initiation of thermal shock	~112	a	14.5	~60.0		302.8
Onset of initial tearing	<184.6	b	19.6	62.8	195.7	128.0
First maximum K_I	184.6	c	19.6	62.8	171.0	77.0
Minimum K_I, onset of precleavage tearing	241.8	c	19.6	~13.1	171.0	77.0
Initial cleavage propagation	361.4	d	22.5	47.7	198.9	80.7
Cleavage arrest	361.4	e	39.3	47.7	261.4	130.6
End of postcleavage tearing (second maximum K_I)	365.6	f	42.4	52.1	278.7	138.0
		PTSE-2B				
Initiation of thermal shock	~155	g	42.4	2.7		274.9
Onset of precleavage tearing	>575.8	h	42.4	66.6		
Initial cleavage propagation	575.82	i	46.1	66.6	248.1	102.4
Interruption of cleavage by ductile tearing and cleavage reinitiation	575.82	j	69.2	66.6	361.6	146.8
Final cleavage arrest	575.82	k	78.8	66.6	419.3	162.9
Onset of postcleavage tearing	576.2	l	78.8	64.3	406.5	162.9
Rupture of vessel wall	576.7		147.6	62.3		216.4

TABLE 2—*Comparison of measured pressure and calculated limit pressure.*

Crack Position	Measured Crack Length a (mm)	a/W (MPa)	Measured Pressure, p (MPa)	Limit Pressure Based on Yield Stress: Plastic Link[a] in Front Wall, p_{L1} (MPa)	Limit Pressure Based on Yield Stress: Plastic Hinge[b] in Back Wall, p_{L2} (MPa)	Limit Pressure Based on Combined Flow and Yield Stresses: Plastic Link[c] in Front Wall, p_{L1} (MPa)	Limit Pressure Based on Combined Flow and Yield Stresses: Plastic Hinge[d] in Back Wall, p_{L2} (MPa)
				PTSE-2A			
a	14.5	0.098	60.0	96.5	100.4	146.1	147.0
b	19.6	0.133	62.8	93.4	97.2	141.3	142.1
c	19.6	0.133	13.1	93.4	97.2	141.3	142.1
d	22.5	0.152	47.7	91.6	95.3	138.6	139.3
e	39.3	0.266	47.7	80.8	84.3	122.3	122.9
f	42.4	0.287	52.1	78.8	82.2	119.2	119.8
				PTSE-2B			
g	42.4	0.287	2.7	78.8	82.2	119.2	119.8
h	42.4	0.287	66.6	78.8	82.2	119.2	119.8
i	46.1	0.312	66.6	76.3	79.8	115.5	116.2
j	69.2	0.469	66.6	60.6	64.2	91.8	92.9
k	78.8	0.534	66.6	53.8	57.6	81.5	83.0
l	78.8	0.534	64.3	53.8	57.6	81.5	83.0
	147.6	1.000	62.3				

[a] Yield stress of Material A (insert material).
[b] Yield stresses for both insert and base materials.
[c] Flow stress of Material A.
[d] Flow stress of Material A and yield stress of Material B.

when the crack length was measured. The comparisons in Figs. 9 and 10 suggest that the measured pressure exceeded the limit pressure during the second half of crack extension in the PTSE-2B test.

Interpretation

An alternate way of comparing pressures is to plot them against crack length instead of time. This was done in Fig. 11 for the same three cases cited in the previous paragraph. As the legend in the figure indicates, the crack extended alternately under cleavage and tearing in both the PTSE-2A and PTSE-2B tests. Yet, the measured pressure was always lower than any of the three calculated limit pressures in the PTSE-2A test (Points a through f) and changed from being lower to falling within the range of calculated limit pressures in the PTSE-2B test (Points g through l). Beyond Point l, the crack extended through the remaining ligament of the vessel wall in ductile tearing at a pressure equal to and greater than the calculated limit pressure. In the end, slip-line analysis correctly predicted plastic collapse.

PTSE-2A Test

A more detailed interpretation must consider two important factors, namely, the plastic zone size and the temperature gradient that was induced in the test by applying a thermal shock (cooling) to the outside wall of the vessel. The temperature gradient induced a self-equil-

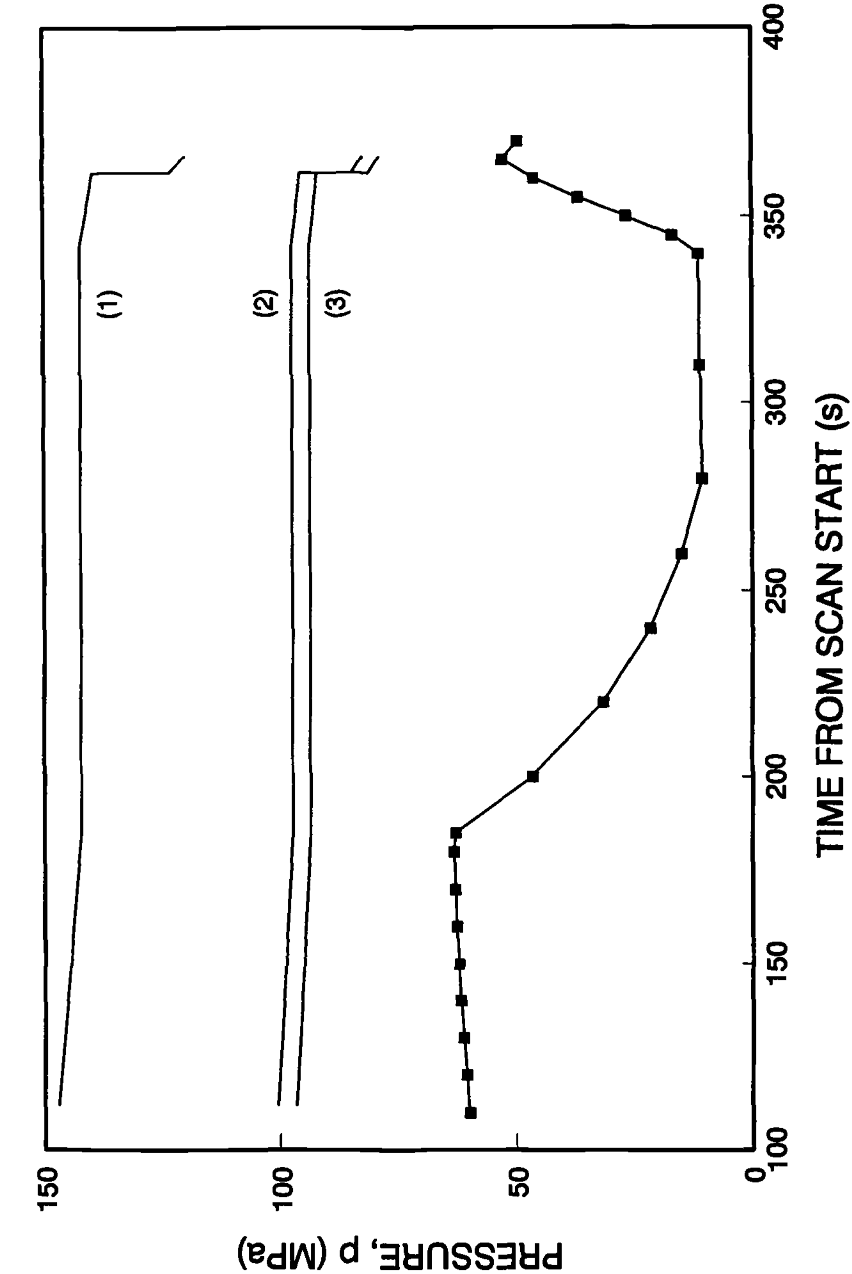

(1) plastic hinge : flow stress for insert material and yield stress for vessel material
(2) plastic hinge : yield stresses for both insert material and vessel material
(3) plastic link : yield stress for insert material and vessel material

FIG. 9—*History of pressure versus time in PTSE-2A test.*

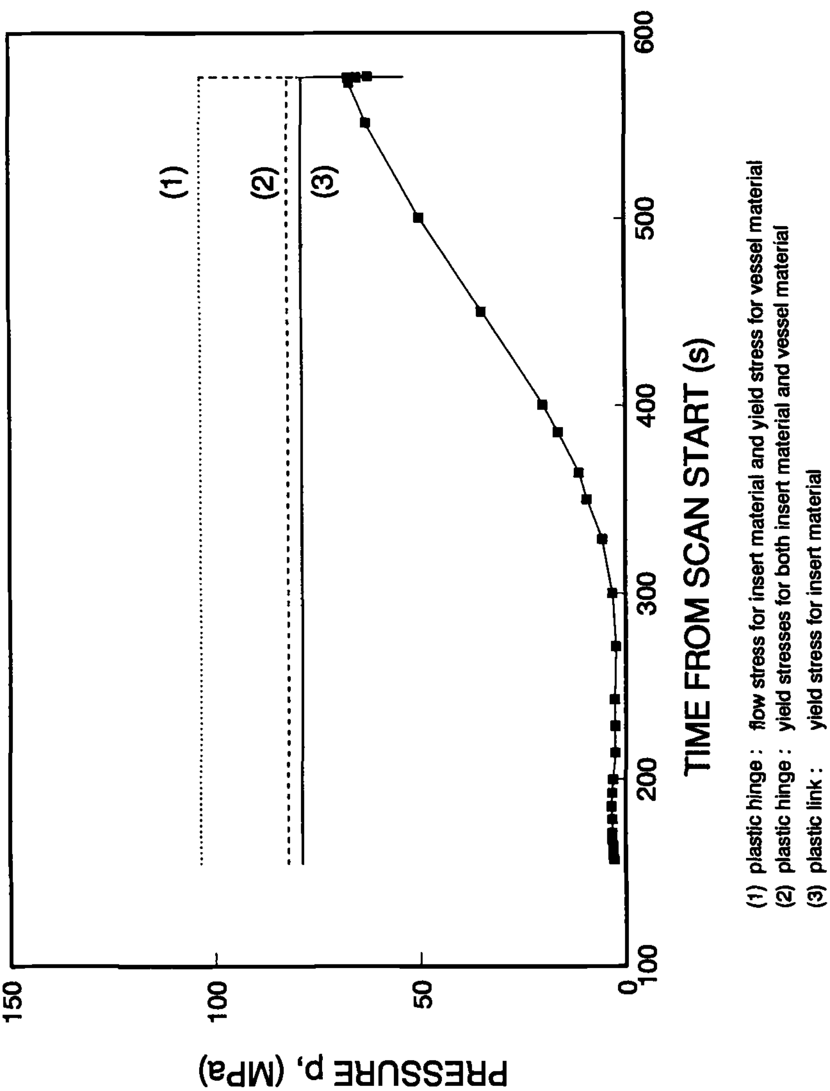

FIG. 10—*History of pressure versus time in PTSE-2B test.*

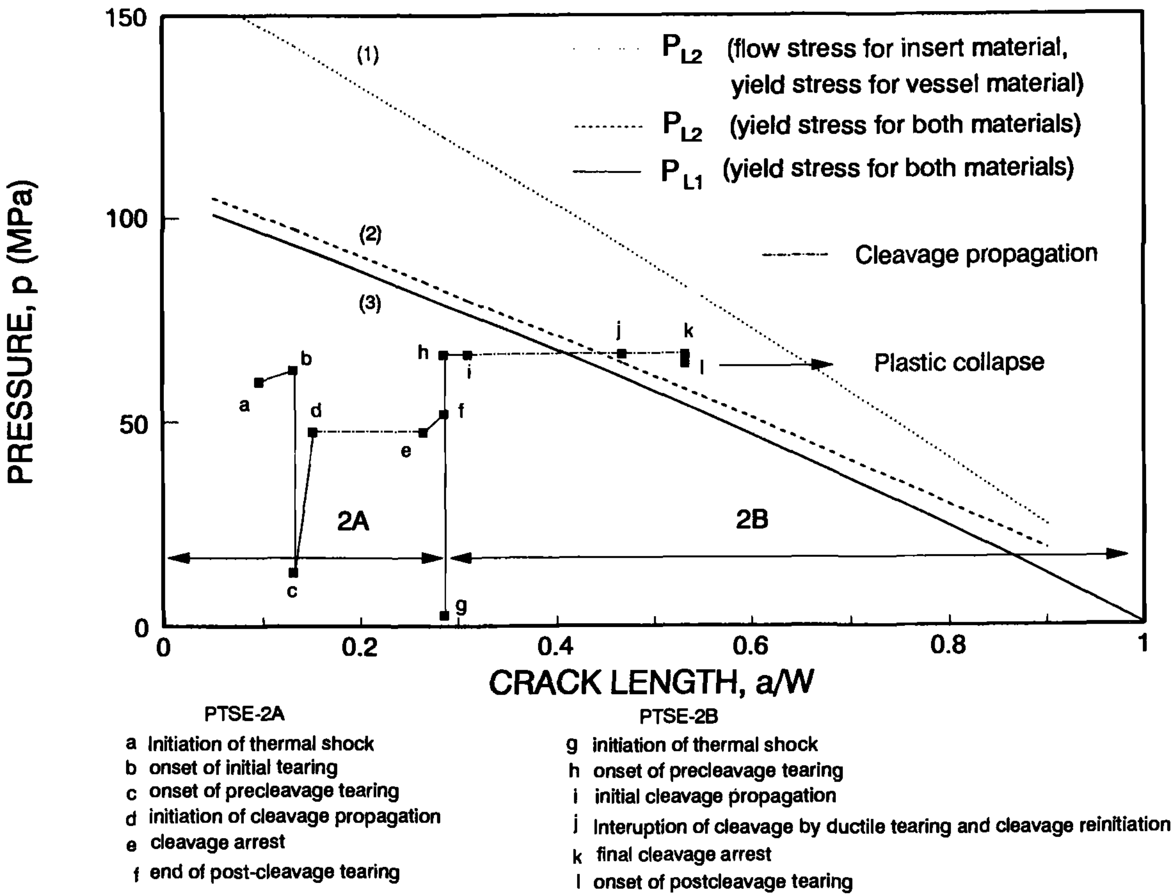

FIG. 11—*History of pressure versus crack length in PTSE-2A and PTSE-2B tests.*

ibrated stress field in the vessel wall that—in the absence of internal pressure—would change from tension at the crack tip to compression at the inner surface of the wall.

The plastic zone size along the line of crack extension can be estimated from the results of the elastic-plastic finite-element analysis performed in Ref *3*. In that analysis, the vessel was subjected to the internal pressure and the measured temperature gradient. The results reported in Table 10.12 of Ref *3* show K_I values of 196 MPa $\sqrt{m}$ for a crack length of a = 19.6 mm (a/W = 19.6/147.6 = 0.13, Point b in Fig. 11). The corresponding plastic zone size, calculated approximately with Irwin's equation for small-scale yielding

$$2r_y = \frac{1}{\pi}\left(\frac{K_I}{\sqrt{3}\,\sigma_y}\right)^2 \qquad (32)$$

is $2r_y$ = 63 mm, which corresponds to 49% of the remaining ligament [$2r_y/(W - a)$ = 63/(147.6 − 19.6) = 0.49]. This plastic zone size implies large-scale plasticity and suggests the vessel is near or even at collapse. Yet, according to Table 2, the measured pressure is only 67% of the calculated limit pressure, p_{L1}, when the plastic link forms in the front wall (p/p_{L1} = 62.8/93.4 = 0.67 in Table 2).

The discrepancy may be attributed to the steep temperature gradient in the vessel wall. According to calculations based on the data reported in Fig. A.1 of Ref *3*, the temperature gradient in the vicinity of the crack tip was 4.8°C/mm at onset of initial tearing (Point b in Fig. 11) and 3.5°C/mm at initiation of cleavage propagation (Point d). The stress field induced by the temperature gradient increased the crack-tip opening displacement, adding to the driving force and causing the crack in the PTSE-2A test to extend at a pressure lower than the limit pressure predicted by slip-line analysis.

It is emphasized that slip-line analysis cannot account for temperature gradients. Also, it was not an objective of the present study to determine the contribution of temperature gradients to crack extension.

PTSE-2B Test

The temperature gradient in the vicinity of the crack tip was much smaller in the PTSE-2B test than in the PTSE-2A test. For example, the gradient was 1.9°C/mm at initiation of cleavage propagation (Point h in Fig. 11) and 1.6°C/mm at onset of postcleavage tearing (Point l).

The predicted value of K_I at the onset of postcleavage tearing (Point l) was 406 MPa $\sqrt{m}$ [*3*]. The corresponding plastic zone size is $2r_y$ = 125 mm, a value nearly twice as large as the remaining ligament, $b = W - a$ = 147.6 − 78.8 = 68.8 mm, suggesting that the vessel was at collapse as shown in Fig. 11. So both the small-scale yielding estimate of plastic zone size and the slip-line analysis predict full yielding of the remaining ligament. Indeed, the crack suddenly tore through the vessel wall after reaching Point l.

Conclusions

In conclusion, limit pressure analysis was performed for an externally cracked, thick walled, cylindrical pressure vessel made of two materials. The calculated limit pressure corresponded well with the measured pressure for the long cracks in the PTSE-2B test, but not for the short cracks in the PTSE-2A test. Limit pressure analysis predicted the observed collapse of the vessel in the PTSE-2B test.

Calculations based on K_I imply that the remaining ligament was predominantly plastic in both the PTSE-2A and PTSE-2B tests, and the vessel should have failed at a pressure near the limit pressure. The discrepancy in the PTSE-2A test, in which the crack extended at a pressure lower than the limit pressure, seems to result from the steep temperature gradient at the crack tip. The effect of this gradient cannot be modeled with slip-line analysis.

In the authors' opinion, the resistance to crack extension in a vessel made of ductile material should be characterized in terms of a global limit load analysis as well as a local crack-tip singularity parameter. Designers need to know how close the pressure is to the limit pressure in assessing the safety of a cracked vessel. The R6-diagram approach, for example, calls for such a dual analysis [8, 9].

References

[1] Hu, J. M. and Albrecht, P., "Limit Load Solution and Loading Behavior of C(T) Fracture Specimen," *International Journal of Fracture*, Vol. 52, 1991, pp. 19–45.

[2] Hu, J. M., Cheng, J. G., Albrecht, P., and Joyce, J. A., "Ductile Crack Extension in Compact Specimens at Limit Load," *Advances in Fracture Research, Proceedings*, Seventh International Conference on Fracture, Vol. 1 Brittle Fracture, Ductile Fracture and Dynamic Fracture, Houston, TX, March 1989, Pergamon Press, New York, pp. 339–358.

[3] Bryan, R. H., Bass, B. R., Bolt, S. E., Bryson, J. W., Corwin, W. R., Merkle, J. G., Nanstad, R. K., and Robinson, G. C., "Pressurized-Thermal-Shock Test of 6-in-Thick Pressure Vessels. PTSE-2: Investigation of Low Tearing Resistance and Warm Prestressing," Report No. NUREG/CR-4888, ORNL-6377, Oak Ridge National Laboratory, Oak Ridge, TN, Dec. 1987.

[4] Pugh, C. and Bass, B. R., "Second HSST Pressurized-Thermal-Shock Experiment (PTSE-2): Detailed Description of Test, Test Data, Material Properties, Analysis Methods, and Results of Analyses," CSNI Reference Experiment No. 2, CSNI/FAG Project for Fracture Analyses of Large-Scale International Reference Experiments (Project FALSIRE), Report No. CSNI-RE-2, Committee on the Safety of Nuclear Installations, Sept. 1989.

[5] Timoshenko, S. P. and Goodier, J. N., *Theory of Elasticity*, 3rd Ed., McGraw-Hill, New York, 1970.

[6] Albrecht, P., Chen, X. G., and Joyce, J. A., "Limit Pressure Analysis of PTSE-2 Vessel," Final Report to Oak Ridge National Laboratory, Oak Ridge, TN, Dec. 1990.

[7] Hill, R., *Mathematical Theory of Plasticity*, Oxford University Press, Oxford, UK, 1950.

[8] Harrison, R. P., Loosemore, K., and Milne, I., "Assessment of the Integrity of Structure Containing Defects," CEGB Report No. R/H/6, Central Electricity Generating Board, UK, 1976.

[9] Bloom, J. M., "Validation of the Deformation Plasticity Failure Assessment Diagram (DPFAD) Approach—The Case of An Axial Flaw in a Pressurized Cylinder," *Journal of Pressure Vessel Technology*, Vol. 112, Aug. 1990, pp. 213–217.

Lieh Chen,[1] *Paul C. Paris,*[1] *and Hiroshi Tada*[1]

A Deep Part-Through All-Around Circumferential Crack in a Cylindrical Vessel Subject to Combined Thermal and Pressure Load

REFERENCE: Chen, L., Paris, P. C., and Tada, H., "**A Deep Part-Through All-Around Circumferential Crack in a Cylindrical Vessel Subject to Combined Thermal and Pressure Load,**" *Fracture Mechanics: Twenty-Third Symposium, ASTM STP 1189,* Ravinder Chona, Ed., American Society for Testing and Materials, Philadelphia, 1993, pp. 330–343.

ABSTRACT: The primary purpose of this work is to develop analytical solutions that could be used to assess the safety of irradiated nuclear reactor pressure vessels against unstable fracture during thermal shock events with repressurization present. This methodology makes use of a constraint straight beam model under combined tension and bending for simplicity. It will be shown that this model can represent the deep part-through circumferential crack in a cylindrical vessel under pressure and thermal load. The thermal load can be treated as an induced equivalent bending moment. Elastic and fully plastic solutions are presented for such deep cracks at the inner surface of the wall. The results show that such a crack would be stable under pressurized thermal shock load.

KEY WORDS: fracture mechanics, pressurized thermal shock, elastic-plastic fracture mechanics, pressure vessel, part-through flaw, fatigue (materials)

Pressurized thermal shock (PTS) in pressurized water reactor nuclear vessels has been a problem of concern for the safety of nuclear power plants. This type of event could occur if emergency core cooling water is required after a loss of coolant accident (LOCA). When this water is injected into a reactor core, it causes a sharp drop in temperature and, in some cases, repressurization may occur inside the reactor vessel. A result of the rapid temperature change and the possibility of also sustaining high pressure is that a very large tensile stress may occur at the inside surface of the vessel wall. Rapid crack growth from small flaws in welds or base materials at the reactor beltline region, where irradiation damage is greatest, might occur. If the growth of the flaws is not arrested, it may result in unstable crack propagation at the ends of the crack around the vessel. Therefore, such a flaw may become an all-around part-through circumferential crack, as a worst case. Then it becomes appropriate to consider whether such a crack may propagate through the wall.

The application of fracture mechanics analysis for evaluating the structural integrity of nuclear vessels under PTS events has been attempted for many years. In most of the studies, linear elastic fracture mechanics (LEFM) is used alone as a crack propagation and arrest criterion. However, the materials used for nuclear reactors display a very high fracture toughness in the operating temperature range, and the application of elastic fracture analysis can result

[1] Graduate student, professor of Mechanics, and affiliate professor, respectively, Department of Mechanical Engineering, Washington University, St. Louis, MO 63130.

in an erroneous failure prediction where substantial plasticity can occur. In particular, the validity of LEFM is restricted to situations where the size of the plastic zone occurring at the crack tip must be small compared to the other significant dimensions. The plane-strain plastic zone size is estimated by

$$r_p = \frac{1}{3\pi}\left(\frac{K}{\sigma_y}\right)^2 \tag{1}$$

where K is the stress intensity factor of the crack tip and σ_y is the yield stress of the material. Substituting K-solutions for a shallow circumferential crack in a cylindrical vessel subjected to thermal load [*1*] into Eq 1, the extent of the plasticity normally approaches one half of the remaining ligament, b, when the crack depth reaches only 30% of the wall thickness. Thus, the situation rarely remains linear elastic even with no appreciable pressure present during a LOCA. Moreover, if the repressurization is taken into account, the plastic zone will become even larger. Hence, for such conditions, a linear elastic analysis is not appropriate. As a consequence, there is a clear need for plastic fracture mechanics solutions that can establish the real response of a thermally shocked and repressurized reactor vessel with a deep postulated flaw.

With the preceding objective in mind, this analysis shall proceed to development of a fully plastic solution that recognizes the plasticity associated with the ductile nature of nuclear vessel materials; but, first, a deep crack elastic solution is developed for comparative purposes.

Development of the Elastic Solution

Although the elastic approach is not by itself appropriate for PTS analysis, it is felt that the availability of an accurate elastic solution can be of considerable importance for assessing elastic-plastic failure behavior over the full range of elastic to fully plastic fracture behavior. Indeed, a plastic zone corrected elastic solution can be viewed as a bound on the complete elastic-plastic analysis. Thus, the elastic solution will be developed before starting an elastic-plastic approach.

Consider a cracked straight beam subjected to a bending moment and an axial force both at its fixed ends as shown in Fig. 1. This model can represent the deep part-through all-around circumferential crack in a cylindrical vessel subjected to combinations of thermal and pressure loads. The thermal load can be treated as an induced equivalent bending moment. The pressure load is treated as an axial force. The superposition principle is then used to determine the stress intensity factor solution under these combined loads.

Figure 2 schematically shows the principle. In the figure, the axial force per unit thickness (circumference) and the moment per unit thickness on the uncracked section of the shell are denoted by P_{sh} and M_{sh}, respectively. The axial force per unit thickness and the moment per unit thickness on the remaining ligament are denoted by P_{Lig} and M_{Lig}, respectively. The thermally induced moment is remotely applied and denoted as M_t. Considering the eccentricity between the axial force, P_{sh}, on the shell and the axial force, P_{Lig}, on the ligament, the total moment on the ligament is

$$M_{Lig} = M_t + P_{sh}e \tag{2}$$

where

M_t = thermally induced bending moment per unit thickness,
P_{sh} = axial force on uncracked shell,

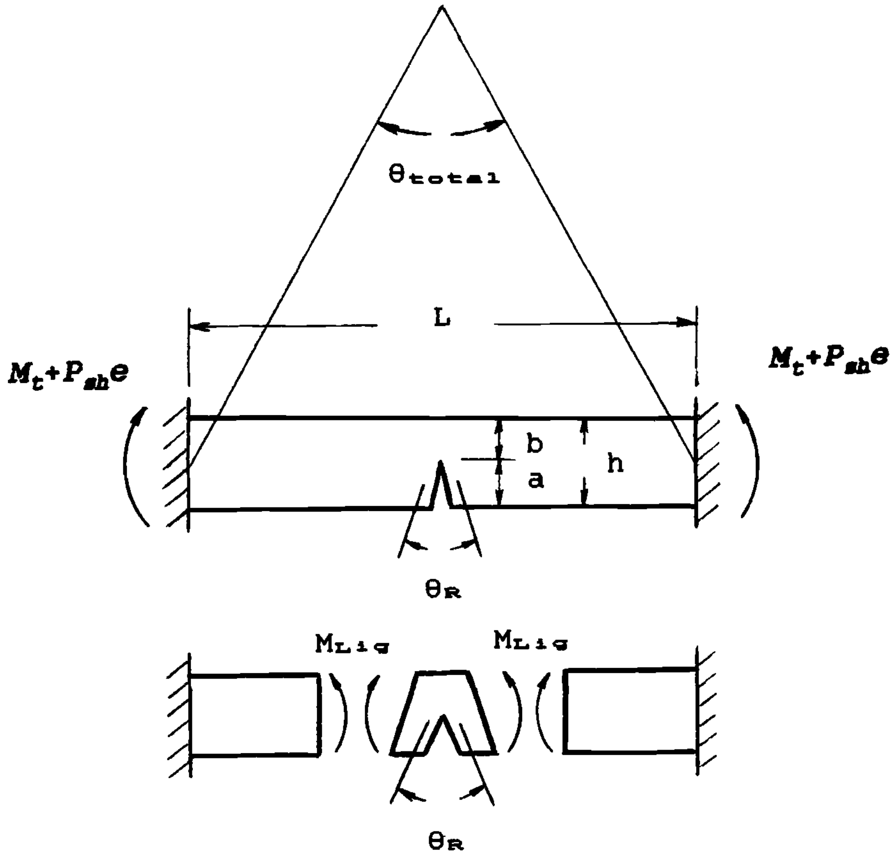

FIG. 1—*The equivalent constrained beam that represents the shell effect on the cracked section.*

e = $h/2 - 0.736b$ [2],
h = wall thickness of the shell, and
b = remaining ligament.

The axial force on the uncracked shell, P_{sh}, and the axial force, including the effects of pressure on the crack surface on the remaining ligament, P_{Lig}, are given respectively by

$$P_{sh} = \frac{p \cdot R_i}{2} \tag{3}$$

$$P_{Lig} = \frac{p[\pi(R_i + a)^2]}{2\pi(R_o - h/2 + e)} \approx \frac{p}{2}(R_o - 1.264b) \tag{4}$$

where

p = internal pressure,
R_i = inner radius of shell, and
R_o = outer radius of shell.

Furthermore, the restraint effect of actual geometry of pressure vessel should be considered since stress intensity factors are very sensitive to the degree of restraint of the structure. From the configuration shown in Fig. 1, the total angle of rotation between fixed ends under combined tension and bending (without a crack) is

$$\theta_{\text{total}} = \frac{(M_t + P_{sh}e)L}{EI} \tag{5}$$

where

L = length of the beam,
E = Young's modulus of elasticity, and
I = $h3/12$.

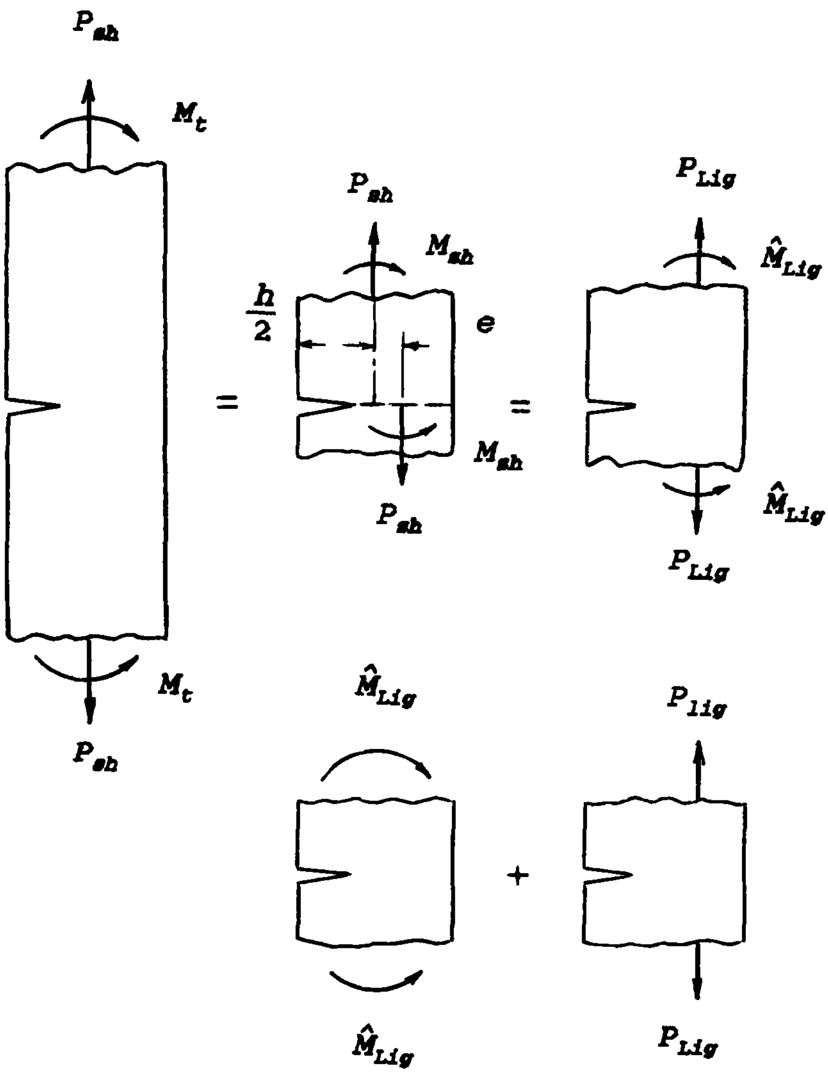

FIG. 2—*Determination of stress intensity factor by means of super-position principle.*

The total angle of rotation, θ_{total}, and the angle of recovery, θ_R, are related by

$$\theta_{\text{total}} - \theta_R = \frac{M_{Lig}L}{EI} \tag{6}$$

where the recovery angle, θ_R, is given [2] by

$$\theta_R = \frac{16(1 - \nu^2)M_{Lig}}{Eb^2} \tag{7}$$

The ν is the Poisson's ratio of the elastic shell material. Combining Eqs 5, 6, and 7, the total moment on the ligament can then be expressed by

$$M_{Lig} = (M_t + P_{sh}e)\frac{1}{1 + \dfrac{16(1 - \nu^2)}{b^2}\dfrac{I}{L}} \tag{8}$$

Now, from the configuration shown in Fig. 2, the stress intensity factor can be deduced by the superposition principle

$$K_I = (K_I)^{M_{Lig}} + (K_I)^{P_{Lig}} \tag{9}$$

The $(K_I)M_{Lig}$ is the stress intensity factor for a deeply notched plate subjected to bending that is given [2] by

$$(K_I)^{M_{Lig}} = \frac{4M_{Lig}}{b^{3/2}} \tag{10}$$

Substituting Eq 8 into Eq 10, the result is

$$(K_I)^{M_{Lig}} = \frac{4(M_t + P_{sh}e)}{b^{3/2}}\frac{1}{1 + \dfrac{16(1 - \nu^2)}{b^2}\dfrac{I}{L}} \tag{11}$$

Moreover, the stress intensity factor of a cylindrical shell having a part-through circumferential crack can be regarded as being represented by an equivalent length, L_{eff}, of a fixed-ended straight beam as shown by Fig. 1 for which Eq 11 applies or

$$(K_I)^{M_{Lig}} = \frac{4(M_t + P_{sh}e)}{b^{3/2}}\frac{1}{1 + \dfrac{16(1 - \nu^2)}{b^2}\dfrac{I}{L_{\text{eff}}}} \tag{12}$$

In Eq 12, the effective length of the fixed beam equivalent for the cylindrical shell under bending load can be determined by the fundamentals of elasticity. Now, consider a shell subject to a bending moment $(M_{th} + P_{sh}e)$ as shown in Fig. 3. The end rotation angle, θ, on the shell [3] is

$$\theta = \frac{dw}{dx} = \frac{2}{\beta D} \cdot (M_{th} + P_{sh}) \tag{13}$$

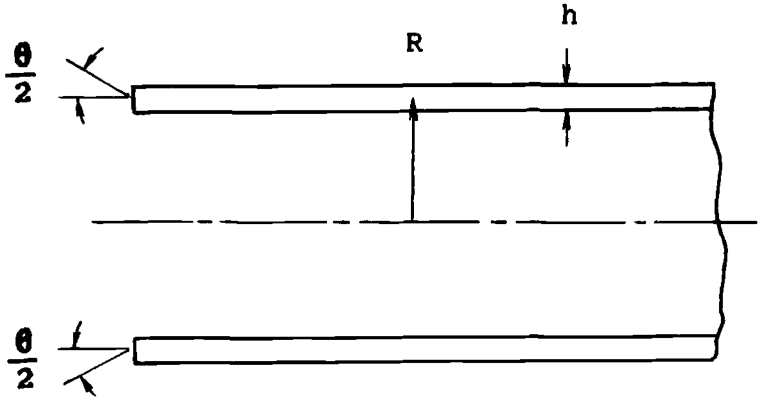

FIG. 3—*Schematic representation of the shell with the angle of rotation.*

where

w = radial displacement,
$\beta = (Eh/4R2D)^{1/4}$,
$D = Eh^3/12(1 - \nu^2)$,
R = mean radius of the shell, and
h = thickness of the shell.

Equating Eq 13 to 5, the effective length of the shell, L_{eff}, is obtained

$$L_{eff} = 1.52 \cdot (1 - \nu^2)^{3/4}\sqrt{Rh} \tag{14}$$

Substituting Eq 14 into 12, the stress intensity factor for the deeply cracked shell subject to the moment due to a thermal load and an eccentrical axial load is

$$K_{bend} = \frac{4(M_{th} + P_{sh} \cdot e)}{b^{3/2}} \frac{1}{1 + 0.88(1 - \nu^2)^{1/4}\left(\frac{h}{b}\right)^2 \sqrt{\frac{h}{R}}} \tag{15}$$

Another contribution to the elastic solution is the stress intensity factor due to the pressure load as described in Eq 9. Also from Ref *2*, the $(K_I)P_{Lig}$ for a deeply notched plate subject to tension load is given by

$$(K_I)^{P_{Lig}} = 1.297 \cdot \frac{2P_{Lig}}{\sqrt{\pi b}} \tag{16}$$

Substituting Eq 4 into 16, it becomes

$$(K_I)^{P_{Lig}} = 0.732 \cdot p\left(\frac{R_o}{L} - 1.264\right)\sqrt{b} \tag{17}$$

Combining Eqs 3, 15, and 17, the stress intensity factor for a shell under both thermal and pressure load is

$$K_{\mathrm{I}} = \left[\frac{4\left[\frac{M_{th}}{b^2} + \frac{p}{4}\left(\frac{R}{b}\right)\left(\frac{h}{b} - 1.472\right)\right]}{1 + 0.88(1 - \nu^2)^{1/4}\left(\frac{h}{b}\right)^2 \sqrt{\frac{h}{R}}} + 0.732 \cdot p\left(\frac{R_o}{b} - 1.264\right) \right] \sqrt{b} \quad (18)$$

The stress intensity factor presented in Eq 18 is for a deep part-through all-around circumferential crack in a cylindrical vessel subject to thermal and pressure loads. The stress intensity factor profile through the wall is then determined by varying the ligament length, b, in Eq 18. The same procedure can be repeated at various time intervals during the pressurized thermal shock transient. For elastic conditions, it is noted that J may be obtained from K by

$$J = \frac{(1 - \nu^2)K_{\mathrm{I}}^2}{E} \quad (19)$$

The Stress Block Model

In this section, plastic fracture mechanics techniques will be used to develop a more accurate fully plastic solution for a shell with a deep part-through circumferential crack under combined bending and tension. A plasticity model for determining the limit load of an edge-notched plate under combined tension and bending is proposed. It assumed that plasticity has fully developed over the remaining ligament ahead of the crack. Further assume no strain hardening for the material. Figure 4 shows the model. The shell wall is subjected to a combined limit load, P_L and M_L, at the midpoint of remaining ligament. The combined limit loads carried by the ligament, P_L and M_L, can be expressed by

$$P_L = \sigma_o \cdot c \quad (20)$$

$$M_L = \alpha\sigma_o b^2\left[1 - \left(\frac{c}{b}\right)^2\right] \quad (21)$$

where α is about 0.36 for plane strain and 0.25 for plane stress. The limit load, P_L is caused by internal pressure that is

$$P_L = \frac{p}{2}(R_o - 0.5 \cdot b) \quad (22)$$

By equating Eq 20 to Eq 22, the ratio of c to b is

$$\frac{c}{b} = \frac{p}{\sigma_o}\left(\frac{R_o}{2b} - \frac{1}{4}\right) \quad (23)$$

If this is introduced in Eq 21, the plastic limit moment can be written as

$$M_L = \alpha \cdot \sigma_o b^2\left[1 - \left(\frac{p}{\sigma_o}\right)^2\left(\frac{R_o}{2b} - \frac{1}{4}\right)^2\right] \quad (24)$$

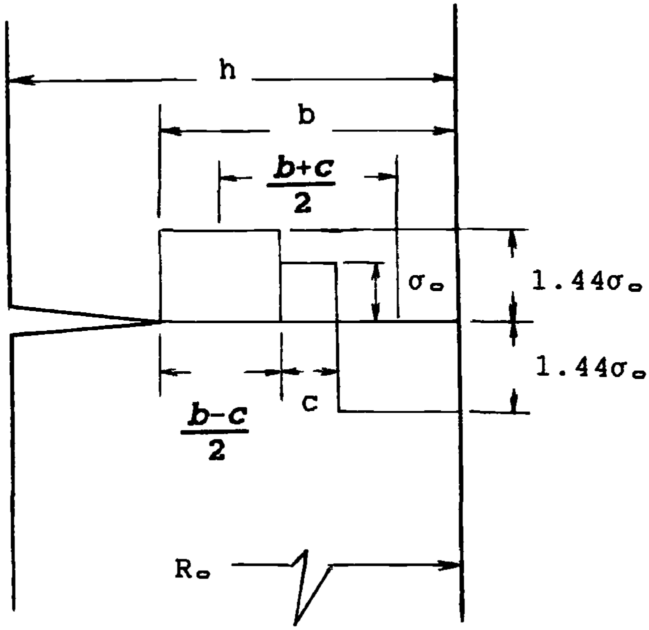

FIG. 4—*The stress block model.*

From Eq 24, it is important to note that the condition to avoid plastic tensile instability at the remaining ligament is

$$1 > \frac{p}{\sigma_o}\left(\frac{R_o}{2b} - \frac{1}{4}\right) \tag{25}$$

The two reference quantities, P_o and M_o, are further defined as

$$P_o = \sigma_o b \tag{26}$$

$$M_o = \alpha\sigma_o b^2 \tag{27}$$

Nondimensionalization of Eqs 20 and 21 by using Eqs 26 and 27 leads to

$$\frac{P_L}{P_o} = \frac{c}{b} \tag{28}$$

$$\frac{M_L}{M_o} = 1 - \left(\frac{c}{b}\right)^2 \tag{29}$$

From Eqs 28 and 29, the (M_L/M_o) can be expressed in terms of (P_L/P_o)

$$\frac{M_L}{M_o} = 1 - \left(\frac{P_L}{P_o}\right)^2 \tag{30}$$

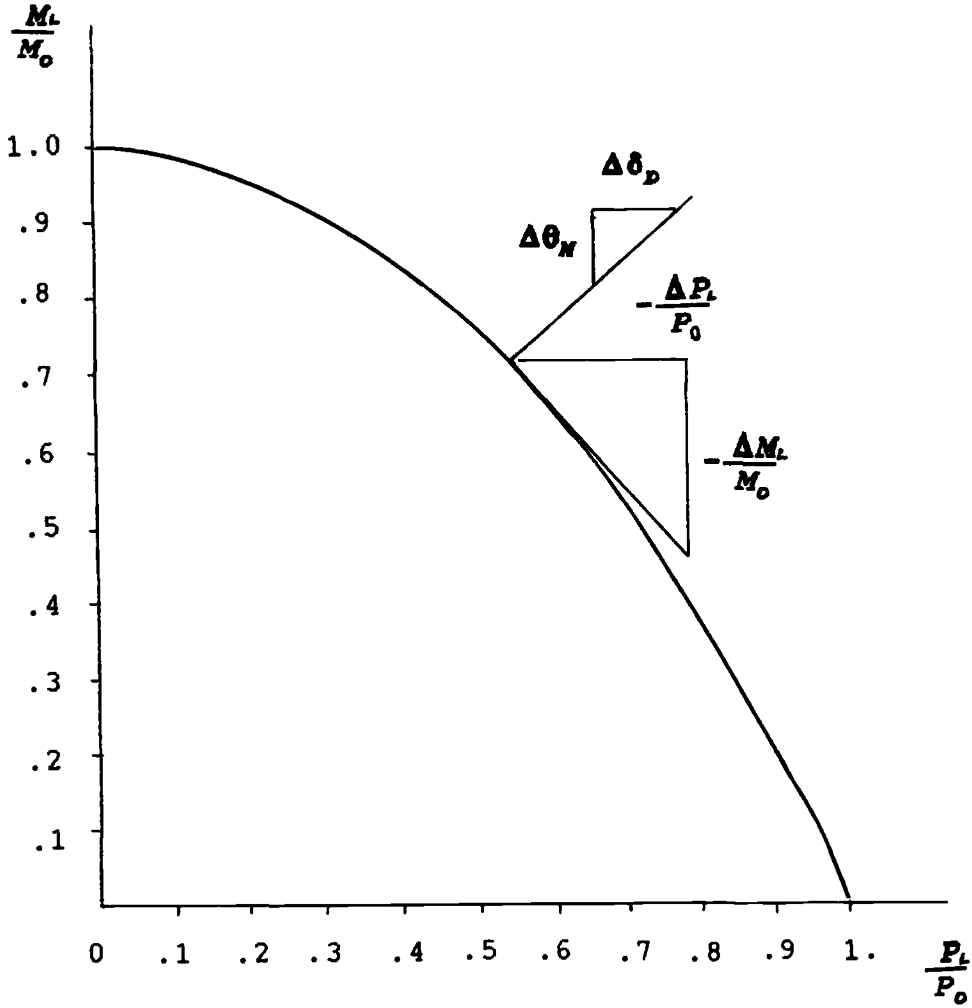

FIG. 5—*Interaction diagram for stress block model.*

Equation 30 maps as a parabola on the interaction diagram as shown on Fig. 5. This will be used for computing J, which is discussed in the next section.

The Fully Plastic Solution for *J*

The fully plastic solution for a circumferentially cracked shell subject to combined bending and tension is carried out by using the following relationship [*4*]

$$J = \frac{\sigma_o \delta_t}{\gamma} \tag{31}$$

where

δ_t = crack opening stretch and
$\gamma \approx 0.7$ for plane strain and 1.0 for plane stress.

In evaluating δ_t, the geometrical relationship in Fig. 6 is considered

$$d = \frac{\delta_p}{\theta_M} \tag{32}$$

where d is the distance from the load point to the actual plastic hinge location, δ_p is the load point displacement, and θ_M is the final angle of rotation of the shell. Since the interaction diagram in Fig. 4 can be regarded as a yield surface, and the "strain" (displacement, δ_p, and angle, θ_M) is normal to the yield surface, the relationship between hinge distance and loading becomes

$$d = \frac{\Delta\delta_p}{\Delta\theta_M} = -\frac{\Delta M_L}{\Delta P_L} = -\frac{\dfrac{\Delta M_L}{M_o}}{\dfrac{\Delta P_L}{P_o}} \cdot \frac{M_o}{P_o} \tag{33}$$

Differentiating Eq 30 leads to

$$\frac{\dfrac{\Delta M_L}{M_o}}{\dfrac{\Delta P_L}{P_o}} = -2 \cdot \frac{c}{b} \tag{34}$$

Substituting Eqs 23 and 34 into Eq 33, the hinge distance, d, becomes

$$d = 2\alpha c = 2\alpha b\left(\frac{c}{b}\right) = 2\alpha b\frac{p}{\sigma_o}\left(\frac{R_o}{2b} - \frac{1}{4}\right) \tag{35}$$

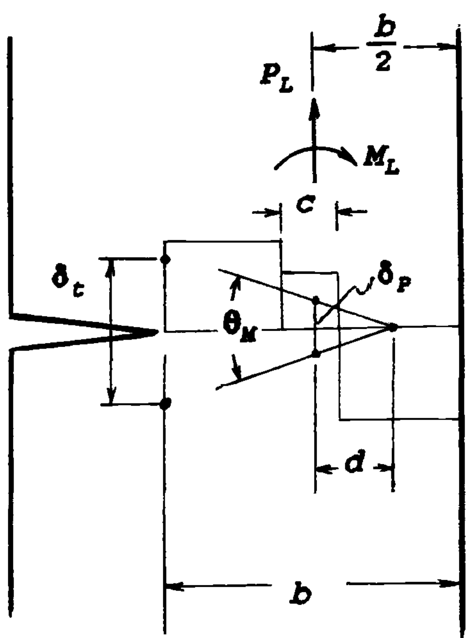

FIG. 6—*The configuration of stress block model.*

The corresponding crack opening stretch is given through

$$\delta_t = \left(\frac{b}{2} + d\right)\theta_f \tag{36}$$

where θ_f can be determined by

$$\theta_f = (M_{th} - M_{sh}) \cdot \frac{L_{\text{eff}}}{EI} \tag{37}$$

where M_{sh} is the recovery moment of elastic shell. From Fig. 2, the moment on ligament, M_{Lig}, and on shell, M_{sh}, can be related by

$$M_{Lig} = M_{sh} + P_{sh} \cdot e \tag{38}$$

When fully plastic behavior is assumed, the M_{sh} can be obtained by equating Eq 39 to Eq 24

$$M_{sh} = \alpha\sigma_o b^2 \left[1 - \left(\frac{p}{\sigma_o}\right)^2 \left(\frac{R_o}{2b} - \frac{1}{4}\right)^2\right] - \frac{pR}{4}(h - b) \tag{39}$$

Noting the P_{sh} and e in the fully plastic case are

$$P_{sh} = \frac{pR}{2} \tag{40}$$

$$e = \frac{h}{2} - \frac{b}{2} \tag{41}$$

Finally, combine Eqs 14, 36, 37, and 39, and then substitute into Eq 31, the result leads to

$$J = 26 \cdot (1 - \nu^2)^{3/4} \frac{\sigma_o}{Eh^2} \sqrt{\frac{R}{h}} \cdot \left(\frac{b}{2} + d\right) \left[M_{th} - \alpha\sigma_o b^2 \left[1 - \left(\frac{p}{\sigma_o}\right)^2 \left(\frac{R_o}{2b} - \frac{1}{4}\right)^2\right] + \frac{pR}{4}(h - b)\right] \tag{42}$$

where d is hinge distance from the midpoint of the remaining ligament in the shell wall that is defined in Eq 35. This model presented is for a deep part-through all-around circumferential crack in a cylindrical vessel subject to local fully plastic bending and tension load at the uncracked ligament.

It is noted that Eq 42 used to estimate J is applicable only for large-scale yielding. In order to ensure fully plastic behavior, the ratio of elastic moment to plastic moment must be greater than 1, that is

$$\frac{M_{\text{el}}}{M_{\text{pl}}} > 1 \tag{43}$$

M_{el} can be obtained by substituting Eqs 14 and 3 into Eq 8, and using L_{eff} instead of L, thus leading to

$$M_{el} = \frac{M_{th} + \frac{pR_i}{4}(h - 1.472b)}{1 + 0.88(1 - \nu^2)^{1/4}\left(\frac{h}{b}\right)^2 \sqrt{\frac{h}{R}}} \tag{44}$$

Then substituting Eqs 44 and 24 into Eq 43, the condition for fully plastic action is obtained

$$\frac{M_{el}}{M_{pl}} = \frac{M_{th} + \frac{pR_i}{4}(h - 1.472b)}{\alpha\sigma_o b^2\left[1 - \left(\frac{p}{\sigma_o}\right)^2\left(\frac{R_o}{2b} - \frac{1}{4}\right)^2\right]} \cdot \frac{1}{1 + 0.88(1 - \nu^2)^{1/4}\left(\frac{h}{b}\right)^2 \sqrt{\frac{h}{R}}} > 1 \tag{45}$$

The general applicability of Eq 42 requires satisfying the condition given by Eq 45 to ensure fully plastic behavior.

Analysis and Discussion

For a postulated LOCA, it is assumed that the wall at the inside surface is subjected to sudden chilling and its temperature equals the minimum coolant temperature from the emergency storage tank (ambient). Thus, the thermal stress transient follows the simple heat conduction equations. The solution to the heat conduction and corresponding thermal stresses can be determined analytically from Ref *5* and will not be discussed here. However, it is noted that assuming the temperature of the wall at the inside surface equals the minimum coolant temperature of the emergency tank is very conservative. The actual wall temperature will be greatly increased by mixing the reactor coolant from the cold leg with the cooling water from the emergency storage tank.

The geometric dimensions of a reactor vessel used in this analysis are ~2413 mm (95.24 in.) for outer radius and ~220 mm (8.844 in.) for the wall thickness. The flow stress, σ_∞, of the material varies with neutron fluence and temperature. It can be adjusted to each point along the wall thickness and is averaged to obtain conservative results. Then using the thermal stress transient as described earlier and assuming a constant repressurization pressure [15 858 kPa (2300 psi)], the ranges of J for elastic to fully plastic solutions were calculated using Eqs 18 and 42. Figure 7 shows the J profile obtained at various time intervals during a transient. It is apparent in Fig. 7 that the applied J-curve reaches a maximum and then decreases ($dJ/da < 0$) with increasing crack length. A negative slope of the applied J-curve would indicate stability, considering the fact that the material in the deep crack region has both high temperature and toughness. For such behavior, the material properties can best be shown for the stability analysis by making use of a J versus T diagram, as considered in Ref *6*. Therefore, the stability of a deep circumferential crack under a PTS transient can be expected.

Conclusions

1. For the case of combined bending and axial tension acting on a deeply circumferentially cracked cylindrical vessel, explicit formulas have been derived for J for elastic and fully plastic behavior.

2. A deep part-through all-around circumferential crack would be stable during a postulated loss of coolant accident even with reactor repressurization.

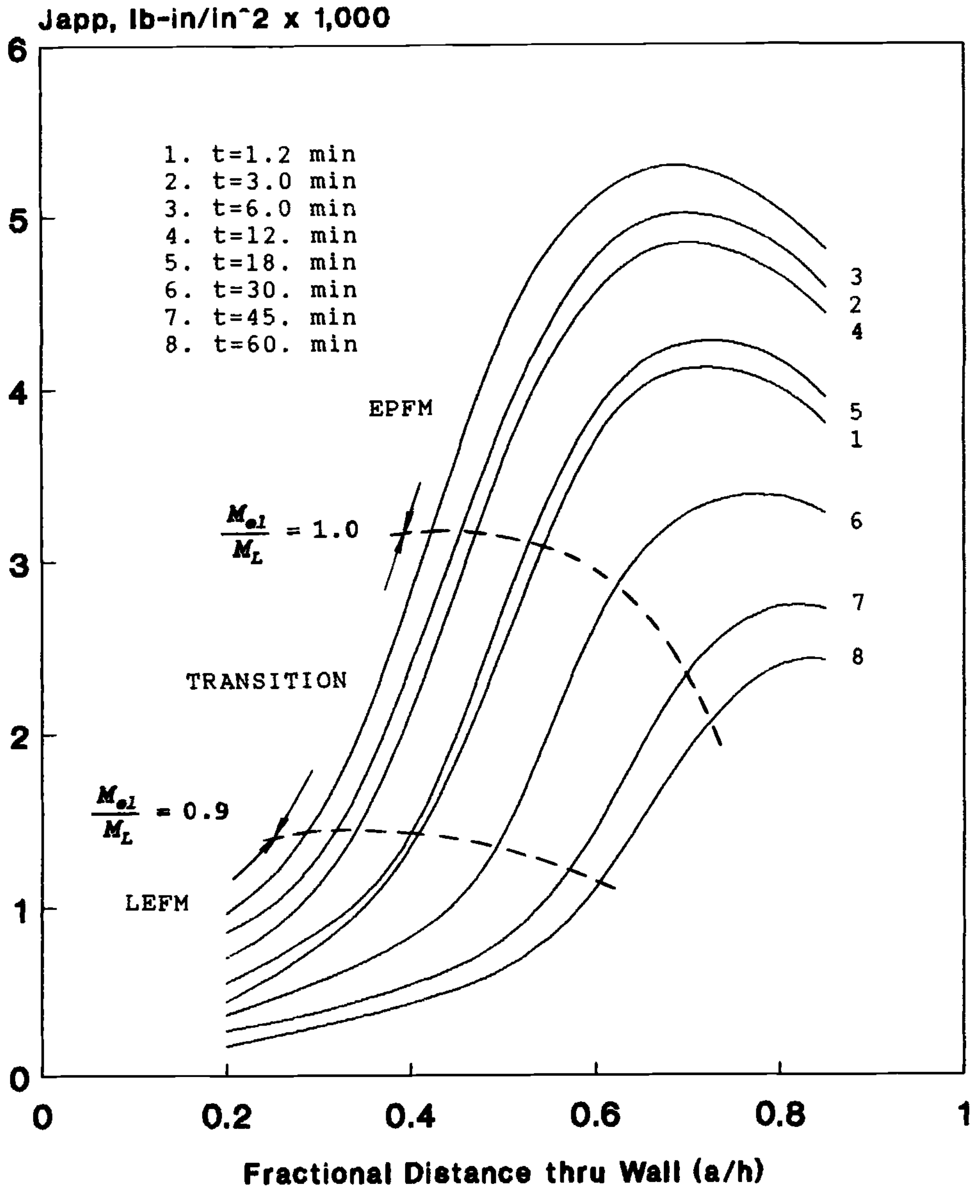

FIG. 7—*J-integral profiles (1 in. lb/in. = 0.17512 kJ/m²).*

3. An advantage of the present approach is that it leads to a simple new closed-form crack stability criterion for pressurized thermal shock of nuclear pressure vessels.

Acknowledgments

This work was a part of Mr. Chen's doctoral thesis research under the direction of Professor Paris. Professor Tada provided considerable analytic assistance. Mr. Chen also wishes to acknowledge the financial support of the National Science Council and the Taiwan Power Company during his study at Washington University.

References

[*1*] Chen, L., Paris, P. C., and Tada, H., "A Deep Part-Through All Around Circumferential Crack in a Cylindrical Vessel Subject to Thermal Stresses," 1991 ASME Pressure Vessel & Piping Conference, San Diego, 23–27 June 1991, to be published.

[*2*] Tada, H., Paris, P. C., and Irwin, G. R., *The Stress Analysis of Cracks Handbook*, Del Research Corp., St. Louis, 1985.

[*3*] Timoshenko, S. P. and Woinowsky-Krieger, "Theory of Plates and Shells," 2nd ed., McGraw-Hill, New York, 1959, p. 466.

[*4*] Rice, J. R., "A Path Independent Integral and the Approximate Analysis of Strain Concentration by Notches and Cracks," *Journal of Applied Mechanics*, Vol. 35, 1968, pp. 379–386.

[*5*] Paris, P. C. and Johnson, R. E., "A Method of Application of Elastic-Plastic Fracture Mechanics to Nuclear Vessel Analysis," *Elastic-Plastic Fracture: Second Symposium, Volume II: Fracture Curves and Engineering Applications, ASTM STP 803*, C. F. Shih and J. P. Gudas, Eds., American Society for Testing and Materials, Philadelphia, 1983.

[*6*] Boley, B. A. and Weiner, J. H. *Theory of Thermal Stresses*, Wiley, New York, 1960.

Cesar A. Sciammarella,[1] Armando Albertazzi, Jr.,[2] and John Mourikes[3]

Study of a Crack-Tip Region Under Small-Scale Yielding Conditions

REFERENCE: Sciammarella, C. A., Albertazzi, A., Jr., and Mourikes, J., "**Study of a Crack-Tip Region Under Small-Scale Yielding Conditions,**" *Fracture Mechanics: Twenty-Third Symposium, ASTM STP 1189,* Ravinder Chona, Ed., American Society for Testing and Materials, Philadelphia, 1993, pp. 344–364.

ABSTRACT: The computer-assisted moire technique was used to measure displacements and strains in the neighborhood of a crack tip. An aluminum 6061-T6 compact tension specimen was utilized to perform the measurements. The u (parallel to the crack direction) and v displacement fields (perpendicular to the crack direction) were determined, as well as the corresponding strains. Tension and fracture tests were performed to obtain the properties of the material. The stress-strain curve was fitted with a Ramberg-Osgood type of constitutive law. The stresses were computed from the strains using a two-dimensional generalization of the Ramberg-Osgood constitutive equation. The J-integral was computed along several paths. Good agreement was found between the K_I computed from the J-integral with the K_I obtained from the application of the ASTM Test Method for Plane-Strain Fracture Toughness of Metallic Materials (E 399-83) standard polynomial. The HRR solution was compared to the experimental results. Some important conclusions can be obtained:

1. In small-scale yielding, the HRR field can only be observed very close to the crack tip.
2. The region dominated by the HRR field is only a few crystalline grains in size.
3. The HRR field models the radial stresses very poorly but gives a good estimate of the tangential stresses.
4. The experimental results support the view point that in small-scale yielding, the J-dominance is independent of the validity of the HRR solution.

KEY WORDS: linear fracture mechanics, small-scale yielding, J-integral, HRR stress field, plastic zone, plastic radius, crack opening, fracture mechanics, fatigue (materials)

The discrepancy between observed and theoretical strengths of materials led to the consideration of cracks to provide an explanation for this difference. The work of Griffith on glass laid down the foundations for the generalization of this model to the process of fracture of other materials. Aside from brittle materials, all other materials must develop a region of plastic deformations in the neighborhood of the tip of a crack. Consequently, the process of fracture must take place in this region of intense plastic deformations. This is true whether these deformations correspond to the conditions referred to in the literature as small-scale yielding or generalized yielding, as in the case of elasto-plastic fracture mechanics. The concept of

[1] Professor and director of Experimental Mechanics of Materials Laboratory, Illinois Institute of Technology, Chicago, IL 60616.
[2] Assistant professor, University Federal de Santa Catarina, Brazil.
[3] Research assistant, Illinois Institute of Technology, Chicago, IL 60616.

small-scale yielding is an essential feature of linear elastic fracture mechanics. However, in spite of the vast amount of literature (analytical, numerical and experimental) accumulated over the years, there are some fundamental issues concerning the strain and stress fields near a crack tip that have not been settled completely. These problems have been studied through numerical methods, particularly under Mode I loading in the plane-strain model of fracture. These studies [1-3] provided support to the asymptotic analysis of Hutchinson [4,5], Rice and Rosengren [6] (HRR). The HRR theory gives a rational basis for the use of the J-integral as a fracture parameter both in the linear and nonlinear regimes and to the work of Begley and Landes [7,8]. The fact that equivalent K_{Ic} can be computed from J_{Ic} specimen measurements led Paris [9] to the following speculation. For identical J-values, identical stresses and strain values should be present at the onset of crack growth.

The fully plastic solution is applicable if the J-field dominates over a certain length scale that is large compared to the process zone or zone where the actual fracture process takes place. Since the introduced theories do not model the process zone and do not merge with the existing elastic fields away from the crack tip, scale factors are missing and have been estimated from numerical results and from speculative assumptions. However, the actual scale factors are vital for a complete understanding of the phenomena involved. Numerical fracture mechanics studies have dealt mainly with plane-strain conditions, although the actual problem is three dimensional. Parsons, Hall, and Rosakis [10] conducted an elastic finite-element investigation of the strain and stress fields near an edge crack and concluded that the conditions of generalized plane stress are reached at a distance from the crack-tip equal to half of the thickness of the plate, and no region was found where pure plane-strain exists. Lately, in a number of experimental papers, the J-integral has been computed from displacement data [11-15]. In Refs 13 and 15, it has been pointed out that only one of the displacement field components agrees with the HRR prediction.

The purpose of this investigation is to observe experimentally the surface displacement field in the neighborhood of a crack tip under conditions of small-scale yielding.

Experimental Method

The computer-assisted moiré method [16-18] was used to determine the surface displacement fields. The details of the experimental aspects of the study are given in Ref 19. A compact specimen with the dimensions indicated in Fig. 1 was used. The specimen material is 6061-T6 aluminum alloy. Three round specimens were manufactured from the same plate and were used to perform tension tests. A compact specimen was also manufactured to measure the critical stress intensity factor. The mechanical properties of the aluminum alloy are shown in Table 1. Figure 2 shows the stress-strain curve together with the fitted curve using a Ramberg-Osgood stress-strain relationship.

The displacements were measured at a load 60.6% of the critical load obtained from the measurement of K_{Ic}. A 12.5 μm pitch metallic grating was applied to the specimen surface after the specimen was precracked by fatigue loading.

Measurements were performed with a microscope focused on the crack tip of the specimen while the load was applied by a servohydraulic testing machine. Different magnifications were used to observe different regions of lengths 30 to 1800 μm in the direction of the crack length. Figure 3 shows the u and v displacement patterns (u parallel to the x-axes, v parallel to the y-axis). Each fringe corresponds to a displacement of 0.416 μm. Figure 4 shows the u and v displacements obtained from the fringe pattern analysis. From the displacements, the ϵ_x, ϵ_y, and ϵ_{xy} strains were obtained. Using the corresponding tensor equations, the principal strains were obtained and the results are shown in Fig. 5.

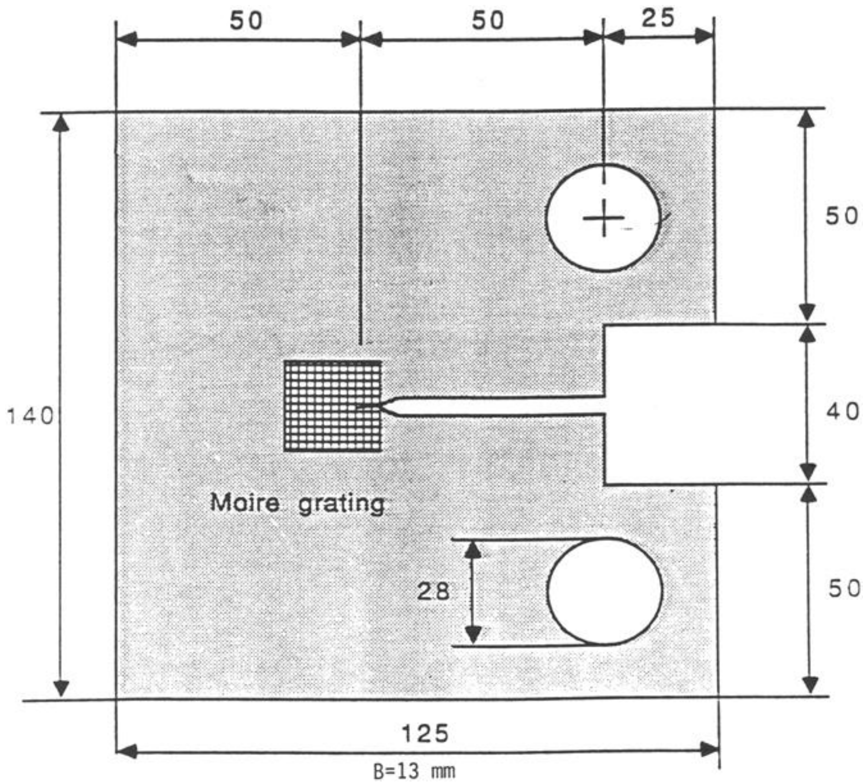

FIG. 1—*Dimensions (in millimeters) of the compact specimen.*

Data Analysis

From the strains, stresses can be obtained by adopting constitutive laws. In the region near the crack tip, it is assumed that proportional loading exists, so that the deformation theory of plasticity can be applied. The material is modeled as an elasto-plastic material obeying the generalized Ramberg-Osgood law

$$\epsilon_{ij} = \frac{1+\nu}{E} S_{ij} + \frac{1-2\nu}{3E} \sigma_{kk} \delta_{ij} + \frac{3}{2} \alpha \epsilon_{ys} \left(\frac{\sigma}{\sigma_{ys}}\right)^{n-1} \frac{S_{ij}}{\sigma_{ys}} \quad (1)$$

TABLE 1—*Mechanical properties of the 6061-T6 aluminum sample.*

σ_{os},[a] MPa	σ_u, MPa	K_{Ic}, MPa $\sqrt{m}$	E, GPa	n[b]	α[c]	σ_{ys},[d] MPa	ϵ_{ys},[e] 10^{-3}
280	410	32.9	69.3	5	1	272.2	2.915

[a] 0.2% yield limit.
[b] Hardening coefficient.
[c,d,e] Constants in the Ramberg-Osgood Law.

where ν is the Poisson's ratio; $s_{ij} = \sigma_{ij} - \frac{1}{3}\sigma_{kk}\,\delta_{ij}$ is the deviatoric stress; $\sigma = (3J_2)^{1/2} = (\frac{3}{2}s_{ij}s_{ij})^{1/2}$ is the effective stress; and σ_{ys}, ϵ_{ys}, α, and n are constants obtained by fitting the Ramberg-Osgood relationship to the tension test data. For a biaxial field, the corresponding equations are

$$\epsilon_x = \frac{1}{E}(\sigma_x - \nu\sigma_y) + \left(\sigma_x - \frac{1}{2}\sigma_y\right)\alpha\frac{\epsilon_{ys}}{\sigma_{ys}}\left(\frac{\sigma}{\sigma_{ys}}\right)^{n-1} \tag{2}$$

$$\epsilon_{xy} = \frac{1+\nu}{E}\tau_{xy} + \frac{3}{2}\tau_{xy}\alpha\frac{\epsilon_{ys}}{\sigma_{ys}}\left(\frac{\sigma}{\sigma_{ys}}\right)^{n-1} \tag{3}$$

$$\epsilon_y = \frac{1}{E}(\sigma_y - \nu\sigma_x) + \left(\sigma_y - \frac{1}{2}\sigma_x\right)\alpha\frac{\epsilon_{ys}}{\sigma_{ys}}\left(\frac{\sigma}{\sigma_{ys}}\right)^{n-1} \tag{4}$$

where

$$\sigma = (\sigma_x^2 + \sigma_x^2 - \sigma_x\sigma_y + 3\tau_{xy}^2)^{1/2} \tag{5}$$

In Eqs 2 to 4, ϵ_x, ϵ_y, and ϵ_{xy} are known values, and σ_x, σ_y, and τ_{xy} are unknowns. We have a system of three nonlinear equations with three unknowns. This system can be solved by using the Newton-Rapson method to minimize the functional

$$F(\sigma_x,\sigma_y,\tau_{xy}) = (\epsilon_x - \epsilon_{xc})^2 + (\epsilon_y - \epsilon_{yc})^2 + (\epsilon_{xy} - \epsilon_{xyc})^2 \tag{6}$$

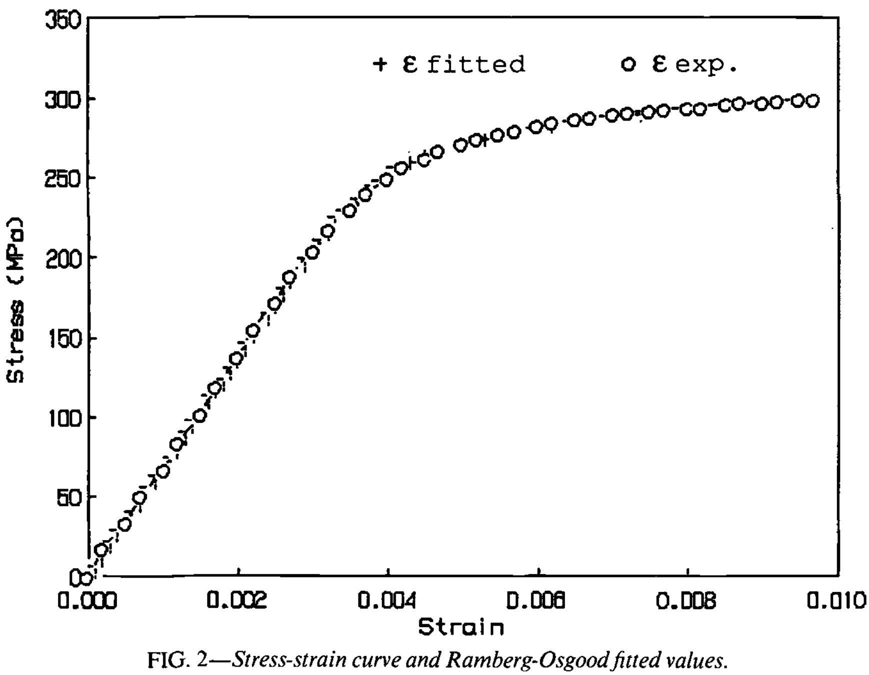

FIG. 2—*Stress-strain curve and Ramberg-Osgood fitted values.*

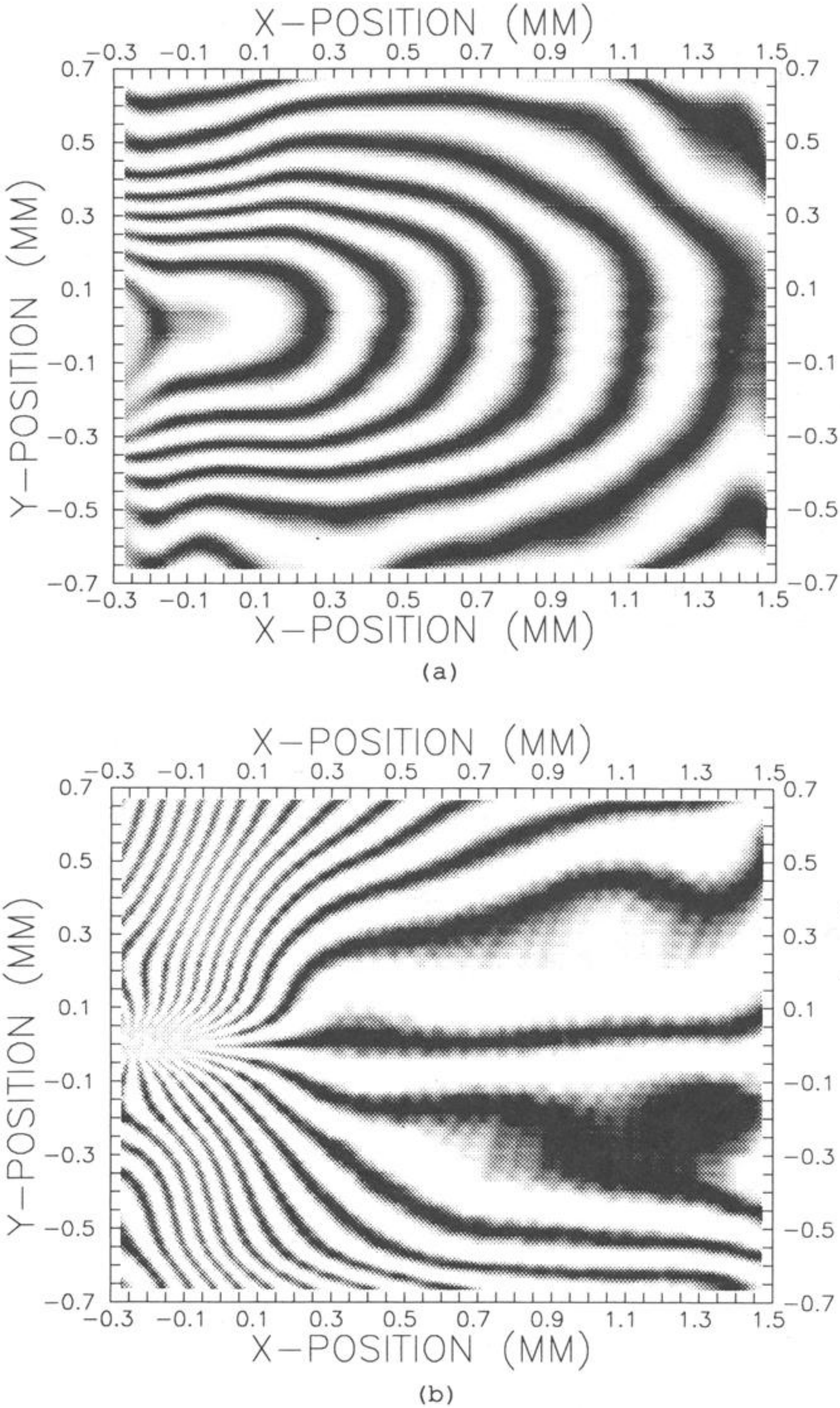

FIG. 3—*Moiré pattern of the* u *and* v *displacements in the neighborhood of the crack tip. Fringes correspond to 0.42 μm displacements.*

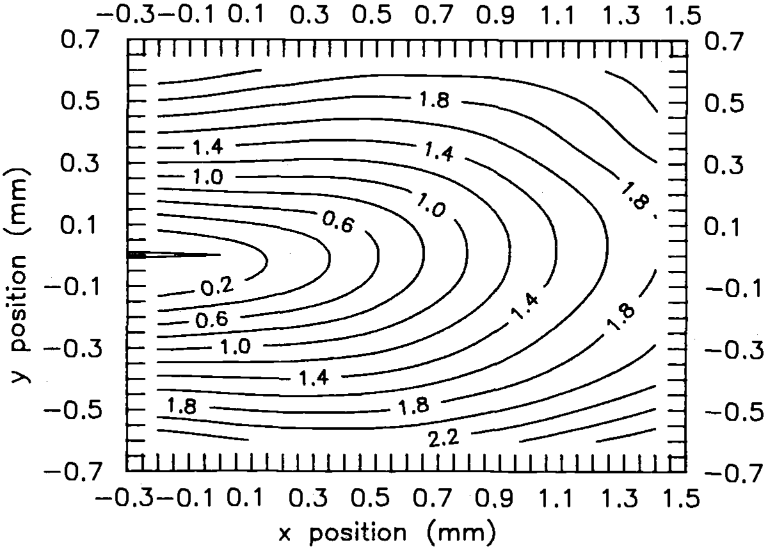

(a)

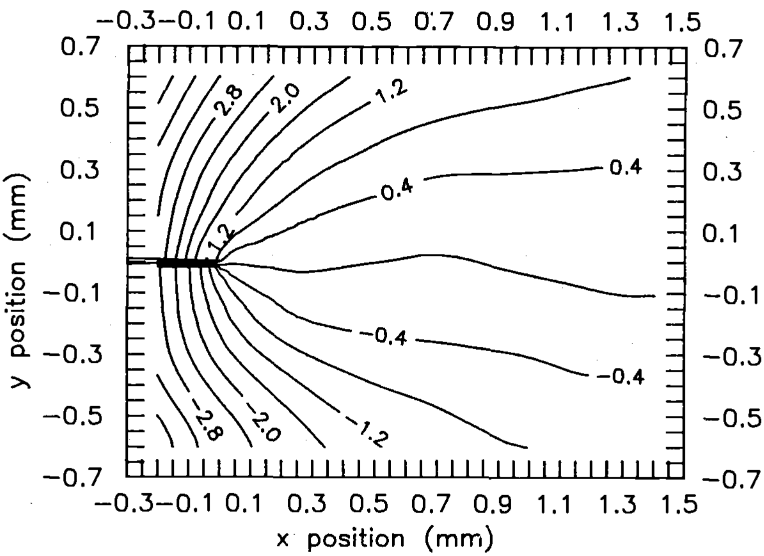

(b)

FIG. 4—(a) u-*displacements (microns) and* (b) v-*displacements (microns).*

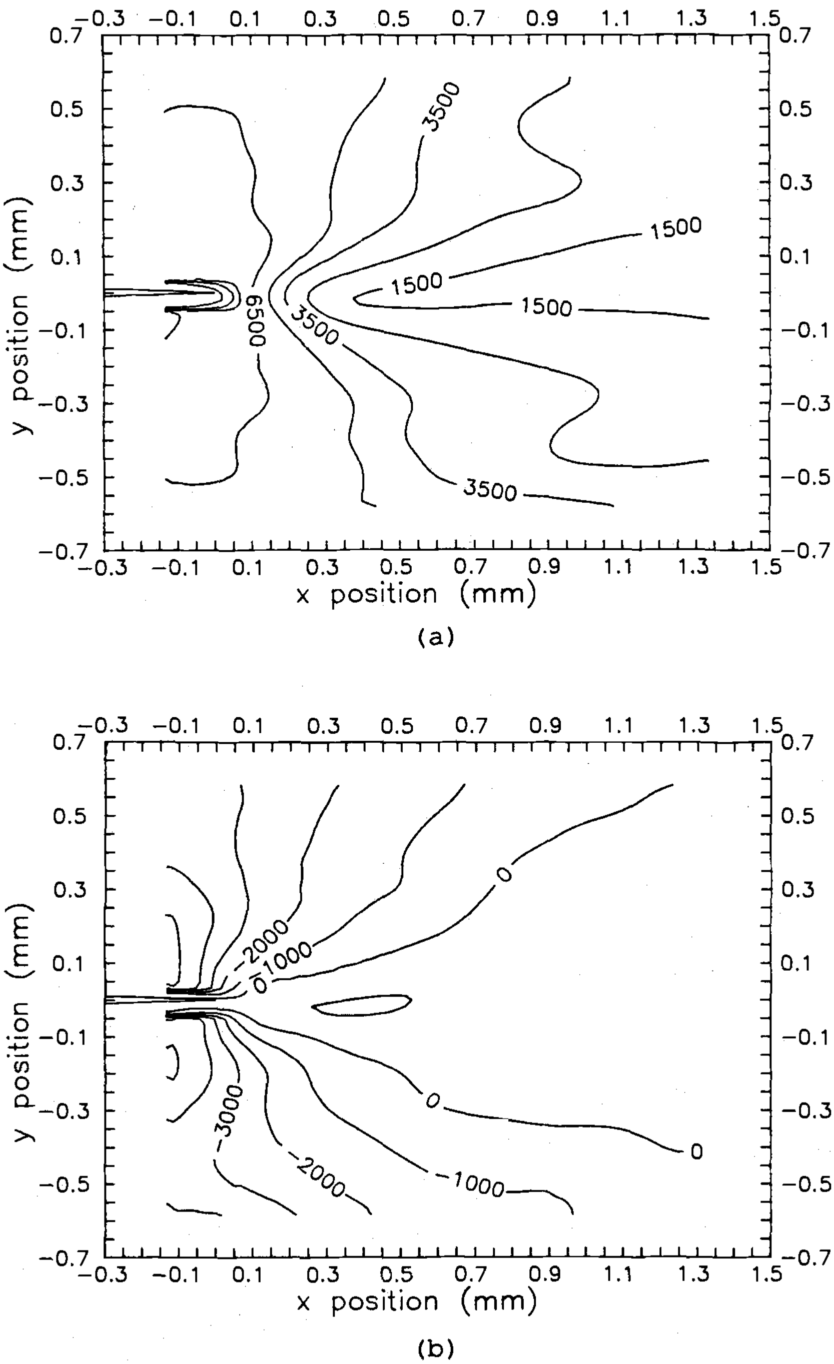

FIG. 5—*Principal strains (microstrains);* (a) *maximum principal,* ϵ_1 *and* (b) *minimum principal,* ϵ_2.

in σ_x, σ_y, and τ_{xy}. In Eq 6, ϵ_x, ϵ_y, and ϵ_{xy} are the measured strain values and ϵ_{xc}, ϵ_{yc}, and ϵ_{xyc} are the calculated values resulting from Eqs 2 to 4. For minimization, an iterative procedure was followed using Eq 7

$$\begin{Bmatrix} \sigma_x \\ \sigma_y \\ \tau_{xy} \end{Bmatrix}_{i+1} = \begin{Bmatrix} \sigma_x \\ \sigma_y \\ \tau_{xy} \end{Bmatrix}_i - P_{i+1} \begin{bmatrix} \frac{\partial^2 F}{\partial\sigma_x \partial\sigma_x} & \frac{\partial^2 F}{\partial\sigma_x \partial\sigma_y} & \frac{\partial^2 F}{\partial\sigma_x \partial\tau_{xy}} \\ \frac{\partial^2 F}{\partial\sigma_x \partial\sigma_y} & \frac{\partial^2 F}{\partial\sigma_y \partial\sigma_y} & \frac{\partial^2 F}{\partial\sigma_y \partial\tau_{xy}} \\ \frac{\partial^2 F}{\partial\sigma_x \partial\tau_{xy}} & \frac{\partial^2 F}{\partial\sigma_y \partial\tau_{xy}} & \frac{\partial^2 F}{\partial\tau_{xy} \partial\tau_{xy}} \end{bmatrix}^{-1} \begin{Bmatrix} \frac{\partial F}{\partial\sigma_x} \\ \frac{\partial F}{\partial\sigma_y} \\ \frac{\partial F}{\partial\tau_{xy}} \end{Bmatrix} \tag{7}$$

where P is a parameter that is optimized for the ith step of the iterative process by the one-dimensional Newton-Rapson procedure, expressed as

$$P_{i+1} = P_i - \frac{\dfrac{\partial F}{\partial P}}{\dfrac{\partial^2 F}{\partial P^2}} \tag{8}$$

This method of computation was applied to a grid of points containing the strain tensor information and, from this grid, three new grids were generated corresponding to the three components of the stress tensor. From these data, the principal stresses and the principal directions were computed, Figs. 6 to 8. The isostatic lines were drawn on the basis of isoclinic lines obtained from the stress tensor data.

The plastic zone was obtained by applying the von Mises yield condition. Several lines are shown in Fig. 9, corresponding to increasing permanent plastic strains up to the conventional limit of 0.2%. As anticipated, the dimensions and shape of the plastic zone depend on the amount of permanent plastic deformation used to define the yield limit.

Values of the J-integral were computed using a technique similar to that introduced in Ref *12*. The path of integration is separated into vertical and horizontal components as indicated in Fig. 10, and J is computed from

$$J = J_V + J_H \tag{9}$$

The vertical component is equal to

$$J_V = \int_{V1} \left[W - \left(\sigma_x \frac{\partial u}{\partial x} + \tau_{xy} \frac{\partial v}{\partial x} \right) \right] dy - \int_{V2} \left[W - \left(\sigma_x \frac{\partial u}{\partial x} + \tau_{xy} \frac{\partial v}{\partial x} \right) \right] dy \tag{10}$$

where

$$W = \frac{1}{2E}(\sigma_x^2 + \sigma_y^2 - 2\nu\sigma_x\sigma_y) + \frac{\tau_{xy}^2}{2G} \tag{11}$$

and the horizontal component is equal to

$$J_H = - \int_{H1} \left(\sigma_y \frac{\partial v}{\partial x} + \tau_{xy} \frac{\partial u}{\partial x} \right) dx + \int_{H2} \left(\sigma_y \frac{\partial v}{\partial x} + \tau_{xy} \frac{\partial u}{\partial x} \right) dx \tag{12}$$

The contours and the positive sense are indicated in Fig. 10.

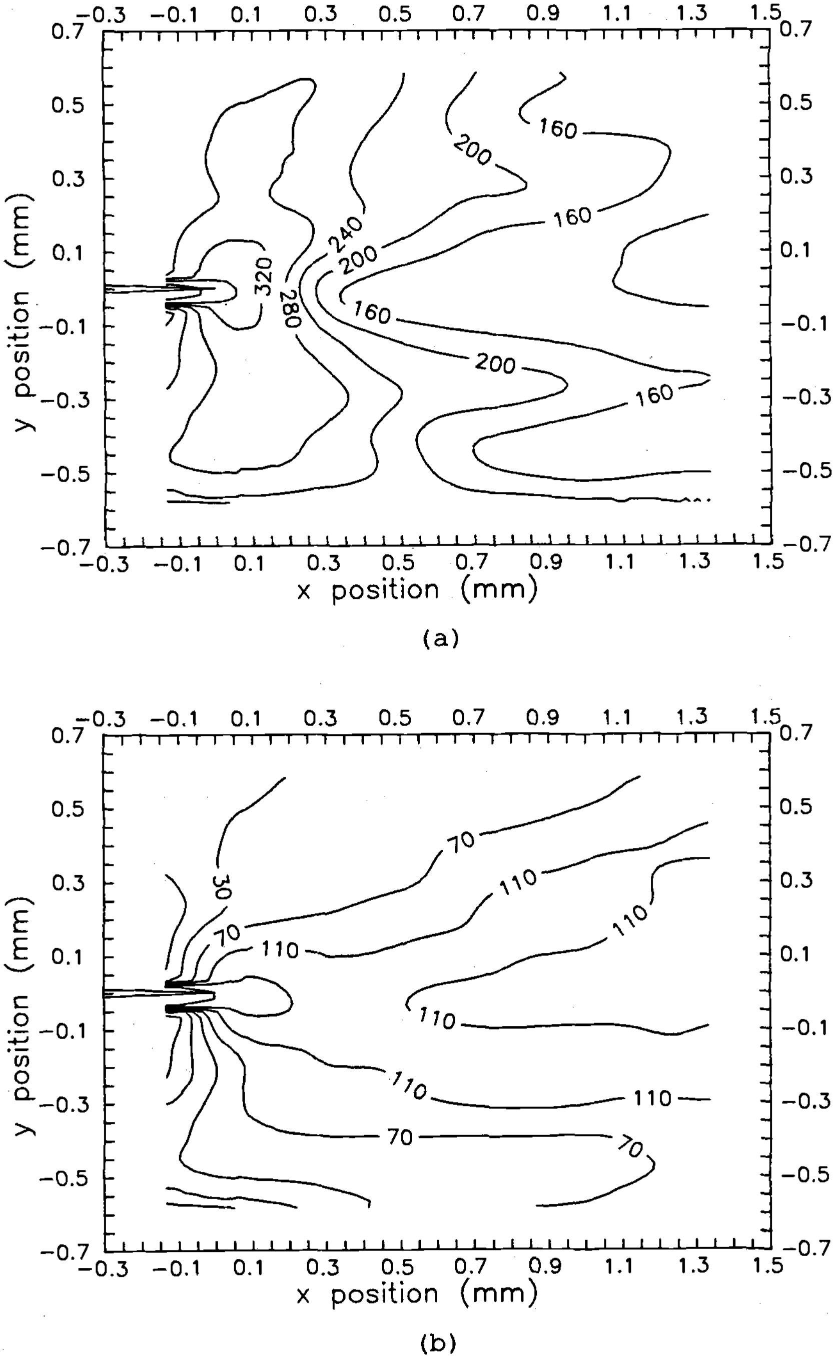

FIG. 6—*Principal stresses (MPa);* (a) *maximum principal, σ_1 and* (b) *minimum principal, σ_2.*

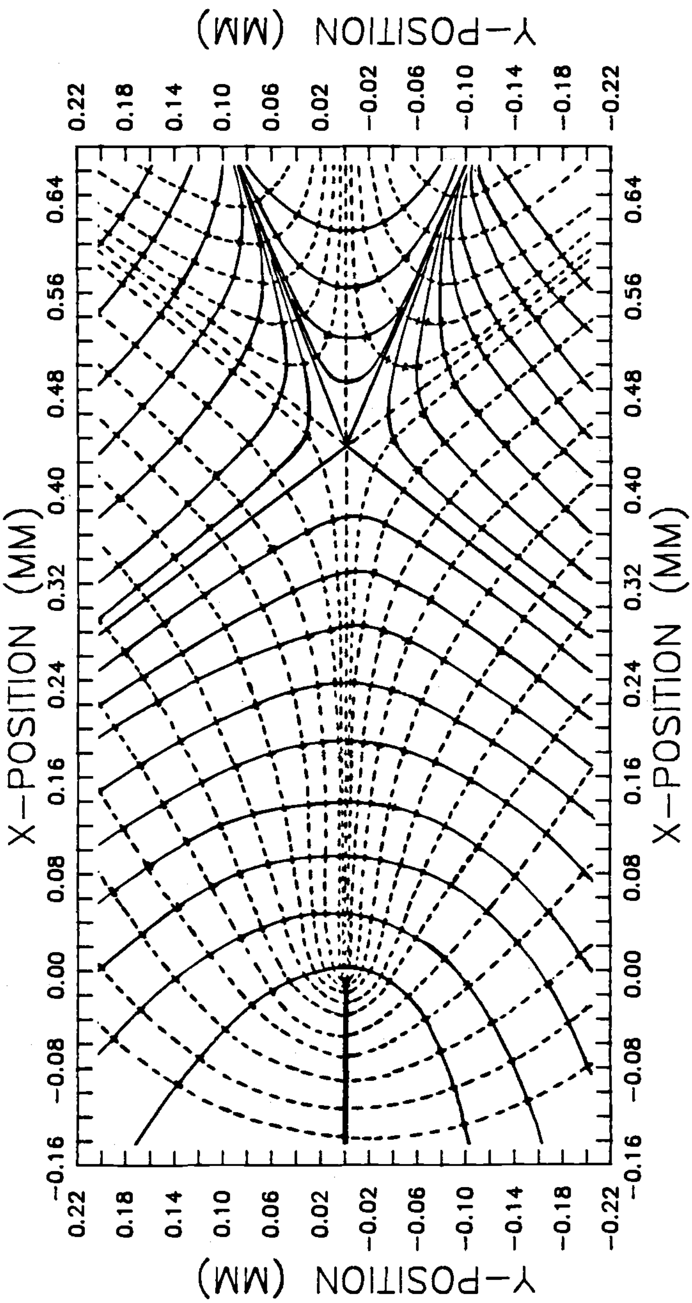

FIG. 7—Isostatic lines.

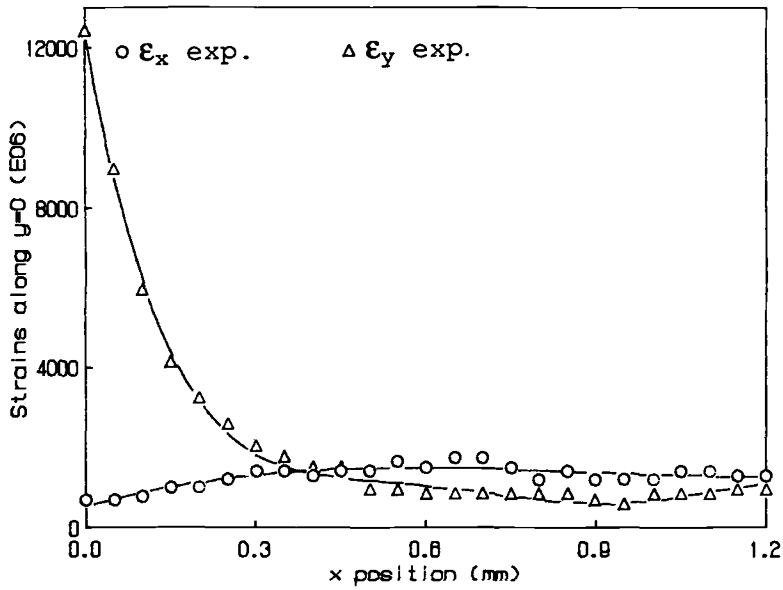

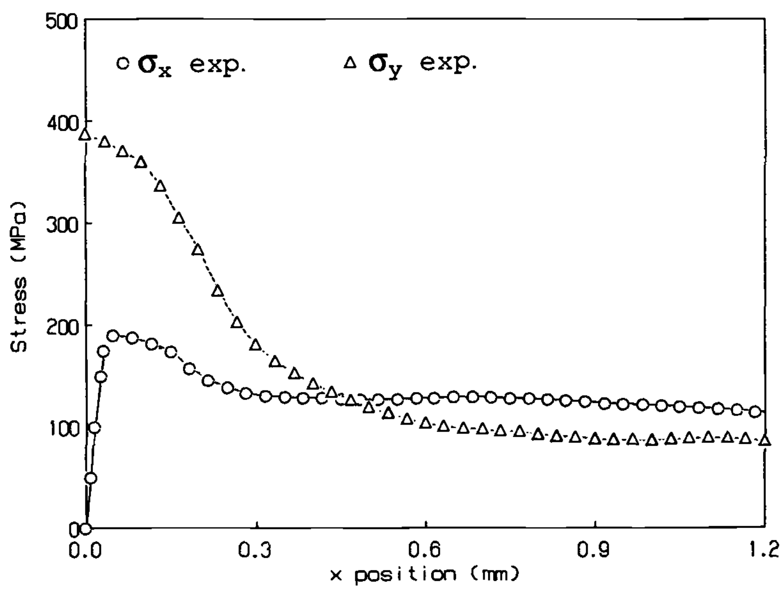

FIG. 8—*Experimental strains and stresses along the crack direction.*

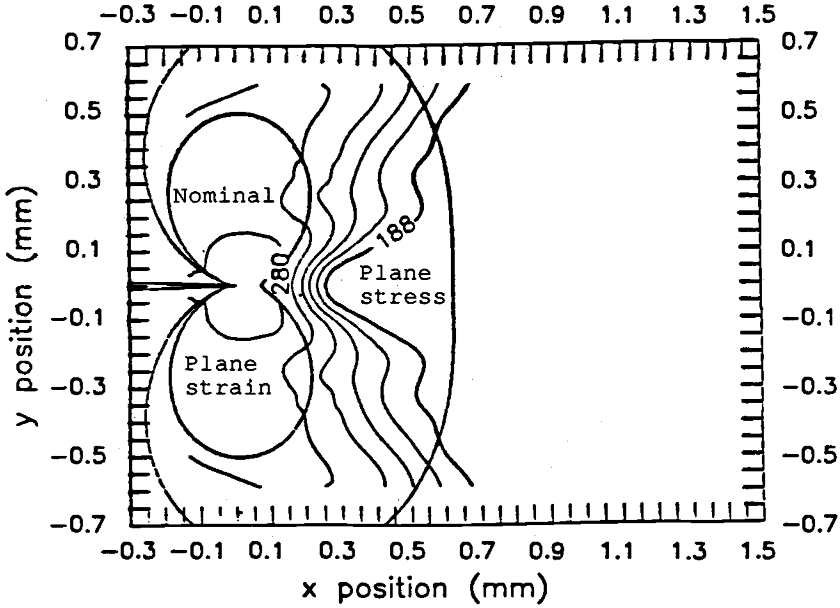

FIG. 9—*Plastic regions corresponding to the von Mises criterion: 280 MPa, nominal 0.2% yields stress; and 188 MPa, 0.1% yields stress. Empirical approximations are included for comparison.*

The values of J-integral are given in Table 2 as well as the equivalent Ks. The value of K_I computed by applying the polynomial provided by ASTM Test Method for Plane-Strain Fracture Toughness of Metallic Materials (E 399-83) is $K_I = 20$ MPa $\sqrt{m}$. The equivalent stress intensity value for the surface was computed using the method introduced in Ref *20*. The method was applied to elastic displacement values taken from a region located at $x = 0.4$ mm

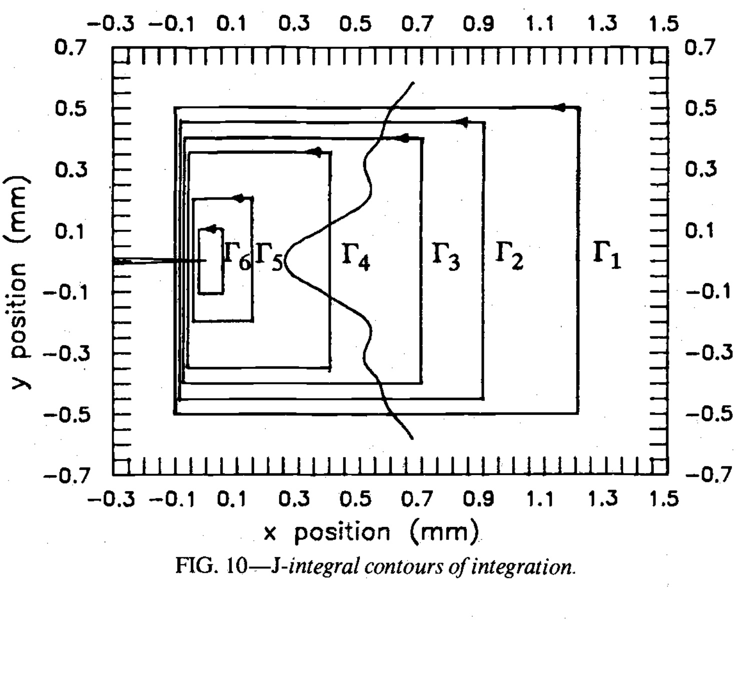

FIG. 10—J-*integral contours of integration.*

TABLE 2—*Contour coordinates and J-integral values.*

Contour	x-position, mm	y-position, mm	J-integral, Pa m	K_I, MPa $\sqrt{m}$	K_I/K_{IE399}
Γ_1	1.20	0.50	5663	19.8	0.99
Γ_2	0.90	0.45	5189	19.0	0.95
Γ_3	0.70	0.40	4661	18.0	0.90
Γ_4	0.40	0.35	4148	17.0	0.85
Γ_5	0.15	0.20	2917	14.2	0.71
Γ_6	0.05	0.10	2783	14.0	0.70

from the crack tip to x = 0.9 mm; the resulting value was K_I = 18.05 MPa $\sqrt{m}$. The average of the K values resulting from the J-contours ending at the previously indicated coordinates is K_I = 18.0 MPa $\sqrt{m}$.

One of the foundations of the current theories on fracture mechanics is the predominance of the HRR field in the neighborhood of the crack tip. The stress and strain fields corresponding to the HRR field are

$$\sigma_{ij} = \sigma_{ys}\left[\frac{J}{\alpha\sigma_{ys}\epsilon_{ys}I_n r}\right]^{1/n+1}\overline{\sigma_{ij}}(\theta,n) \tag{13}$$

and

$$\epsilon_{ij} = \alpha_{ys}\left[\frac{J}{\alpha\sigma_{ys}\epsilon_{ys}I_n r}\right]^{n/n+1}\overline{\epsilon_{ij}}(\theta,n) \tag{14}$$

Equations 13 and 14 were applied using the values of α, σ_{ys}, ϵ_{ys}, and n obtained by fitting the Ramberg-Osgood stress-strain relationship to the experimental stress-strain curve and taking the dimensionless constants, $\overline{\sigma_{ij}}(\theta,n)$ and $\overline{\epsilon_{ij}}(\theta,n)$, from the tabulated values for plane stress given in Ref *21*. The J-value was taken as the average of Γ4, Γ5, and Γ6 contours that are within the plastic region.

The HRR field has been computed for the plane stress case, because the experimental values correspond to the surface stresses of the three-dimensional problem. Therefore, differences exist between the numerical values of both cases. To compare the shapes of the in-plane fields corresponding to the two solutions, a normalization procedure was used. The HRR values have been matched to the experimental values by using the following procedure. A 50 by 50 μm region with its centroid along the crack length at a distance of 150 μm from the crack tip was selected. The tangential stresses of the points located in the matching area were averaged. The average of the theoretical values was equated to the average of the experimental values, and the resulting number was used to match the two fields. This procedure was motivated by an observation from finite-element results. These results show that for the strain-hardening exponent, n = 5, the HHR and numerical radial stresses start to agree at a dimensionless distance from the crack tip of the order of $2 \times 10^{-4}J/\alpha\sigma_{ys}\epsilon_{ys}$. This distance corresponds to the selected zone. Figure 11 shows the radial components and Fig. 12 shows the tangential components. Figure 13 shows a plot of the radial and tangential components along the x-axes. Figure 14 shows the field of isostatics near the crack tip and Fig. 15 shows the lines of maximum shear. The region at the crack tip where the field features are not indicated, are regions where the deformations are predominantly out of plane (dimple region).

Two other quantities are of interest, the plastic radius (generally interpreted as the extension of the plastic zone in the direction of the crack length) and the crack-tip opening displacement. The plastic radius can be expressed

$$r_p = b\left[\frac{K}{\sigma_{os}}\right]^2 \tag{15}$$

where b is a constant. The crack-tip opening displacement can be computed from

$$\delta_t = c\left[\frac{J}{\sigma_{os}}\right]$$

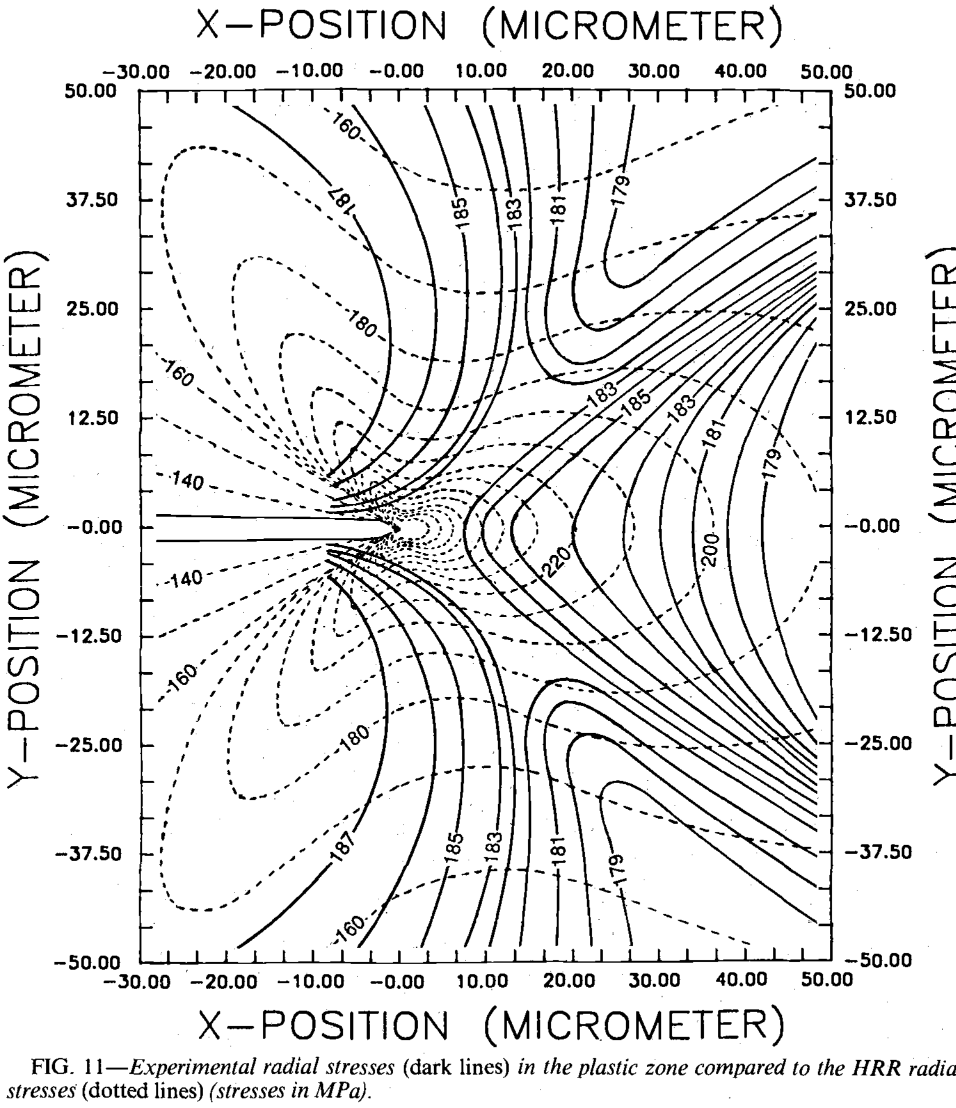

FIG. 11—*Experimental radial stresses* (dark lines) *in the plastic zone compared to the HRR radial stresses* (dotted lines) *(stresses in MPa).*

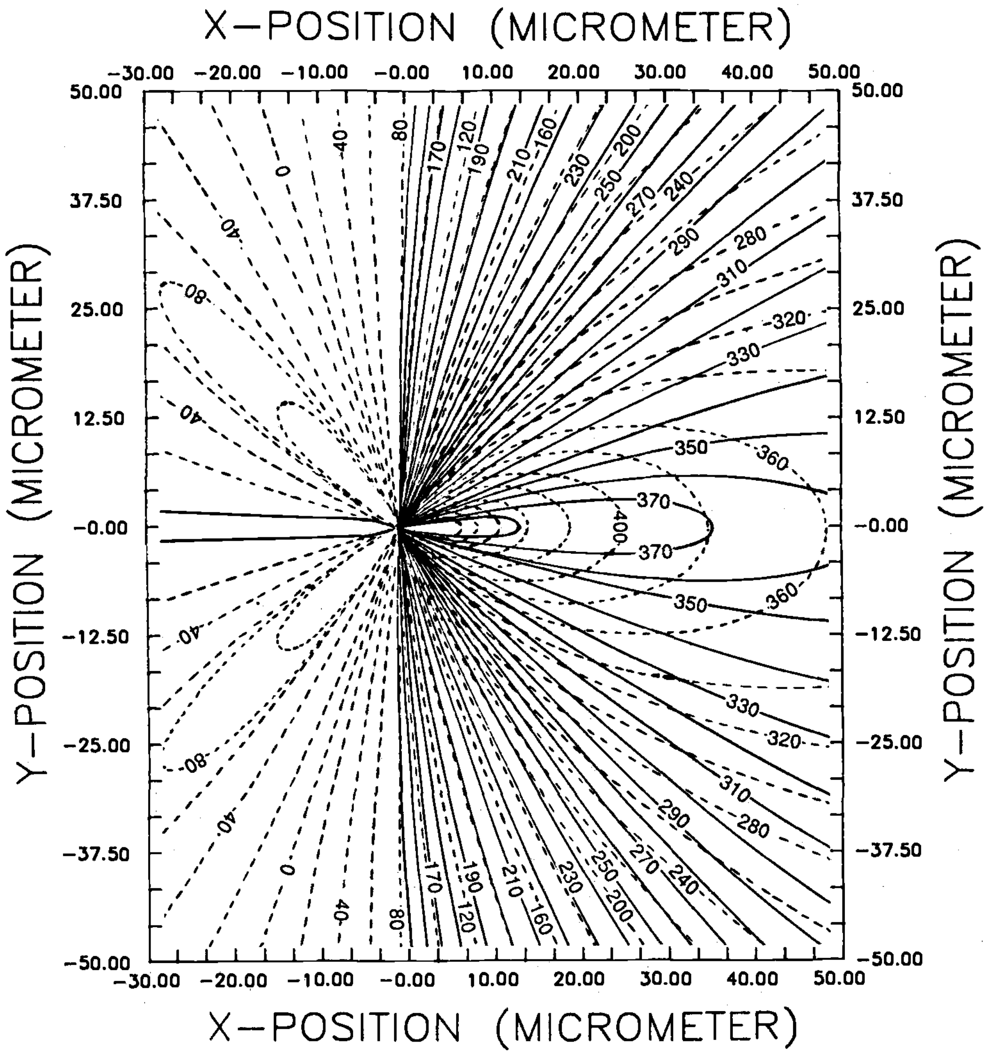

FIG. 12—*Experimental tangential stresses* (dark lines) *in the plastic zone compared to the HRR tangential stresses* (dotted lines) *(stresses in MPa).*

where c is a constant. Table 3 contains the experimental values and values coming from either theoretical analysis or numerical results [*22–25*]. The experimental values have been computed using the following values; $K = 19.8$ MPa $\sqrt{\text{m}}$, and $J = 5663$ Pa m. The values given in Table 3 correspond to the plane-strain condition.

Another quantity that was measured, was the crack opening load. The measurement was performed at three points (A, B, and C) within 30 μm of the crack tip (A the farthest away, C the closest). The load was increased and the crack opening at these three points was measured. The result of the measurements is given in Fig. 16. According to this graph a load of 1348 N is necessary to cause a crack opening at Points B and C.

Discussion and Conclusions

The experimental results that have been presented in this paper provide some answers to the questions that arise in small-scale yielding fracture problems.

One of the first observations that we must make is the fact that we are measuring values corresponding to the surface of a three-dimensional problem. If we look at the finite element solution presented in Ref *10*, we can see that the deformations and stresses in the neighborhood of the crack tip on the surface are smaller than in the center of the specimen where they have their maximum. A similar picture comes from the results of a three-dimensional, finite element elasto-plastic analysis presented in Ref *26*. This picture is consistent with the fact that the *J*-integral values computed in the present investigation are decreasing as the circuits of integration become closer to the crack tip. This reduction in value is a consequence of the decreasing stress and strain fields in the neighborhood of the crack tip as the surface of the specimen is approached. A similar drop of the *J*-integral towards the surface is shown in Ref *26* for a definition of *J*-integral consistent with a three-dimensional field.

We will discuss the following points: (*a*) scale factors, (*b*) *J*-dominance and the HHR field, and (*c*) Paris' conjecture.

We can see (Table 3) that the plastic radius in the direction of the crack is very close to the value coming from a numerical analysis and from an approximated method, resulting from applying the von Mises yield criterion to the Mode I elastic stress field. However, there is a considerable difference from the more commonly used value of the plastic radius in plane strain, r_p = ⅙π. The experimental value has been obtained on the surface of the specimen. Although the surface is in a plane-stress condition, it reflects the three-dimensional state of the specimen stresses. The experimental evidence obtained in Ref *27* by etching sections parallel

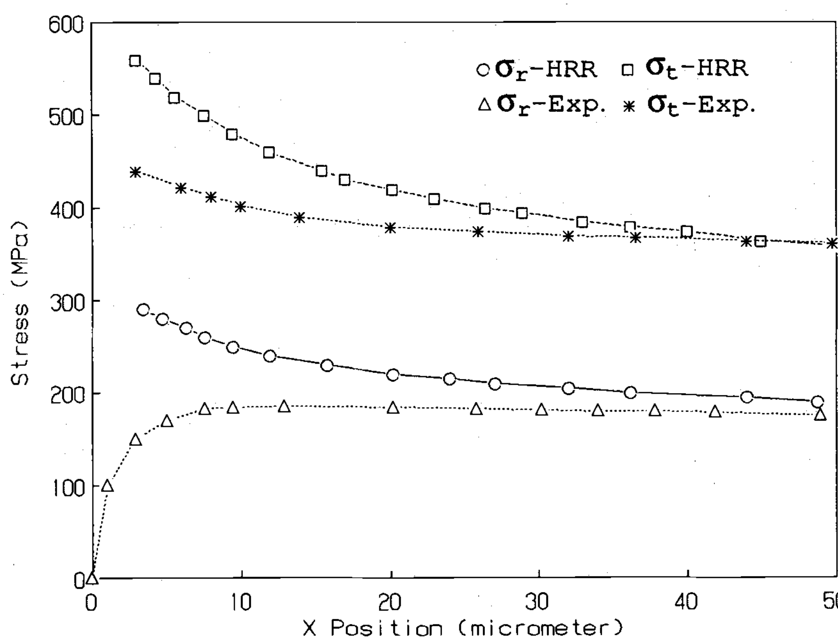

FIG. 13—*Experimental radial and tangential stresses compared to the HRR values along the crack direction.*

to the plate surfaces shows that for constrained plastic deformations, plastic zone sizes remain practically invariant through the thickness.

The crack-tip opening displacement provided by the HRR field [25] agrees in order of magnitude with the experimental value (3 μm versus 6 μm). The factor, c, in Eq 16 is a function of the mechanical properties of the material. In the HRR solution, c is a function of the hardening coefficient and of the ratio, σ_{os}/E. We can see from Table 3, that the crack-tip opening is of the order of magnitude predicted by theoretical and numerical results, but the experimental values are about one half of the predicted values.

The difference between predicted and measured values of the crack-tip opening can be partly due to the presence of residual stresses caused by the precracking fatigue loading.

Let us look at the practical consequences of the scale factors. The region that shows predominant out-of-plane deformation has an approximate size twice the crack-tip opening, about 6 μm, and can be equated to the process zone, where the fracture process will take place. The blunting of the crack tip creates a notch and at the same time local necking occurs. It is in this region of high localized plastic deformations that the crack will propagate. It is also in this region where the necessary conditions for the nucleation of a crack will be met, and the local tensile stress will reach the theoretical cohesive stress, triggering (in the case of brittle materials)

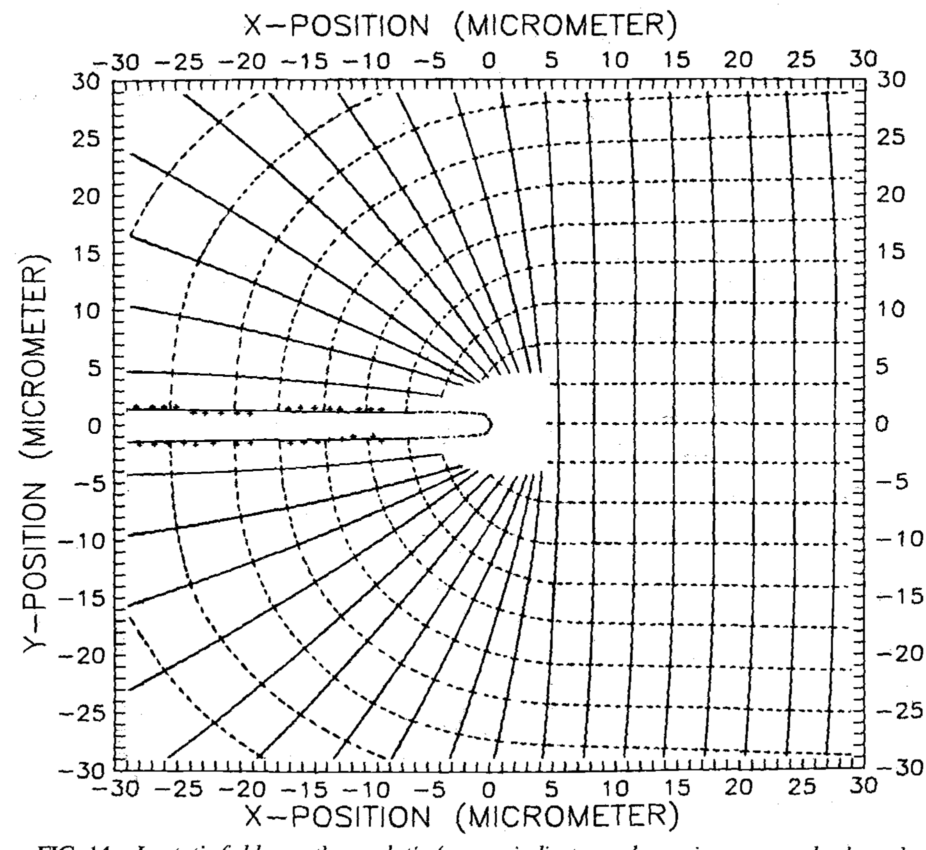

FIG. 14—*Isostatic field near the crack tip (crosses indicate crack opening measured values; the dash and dot region is undefined in the microscopic image).*

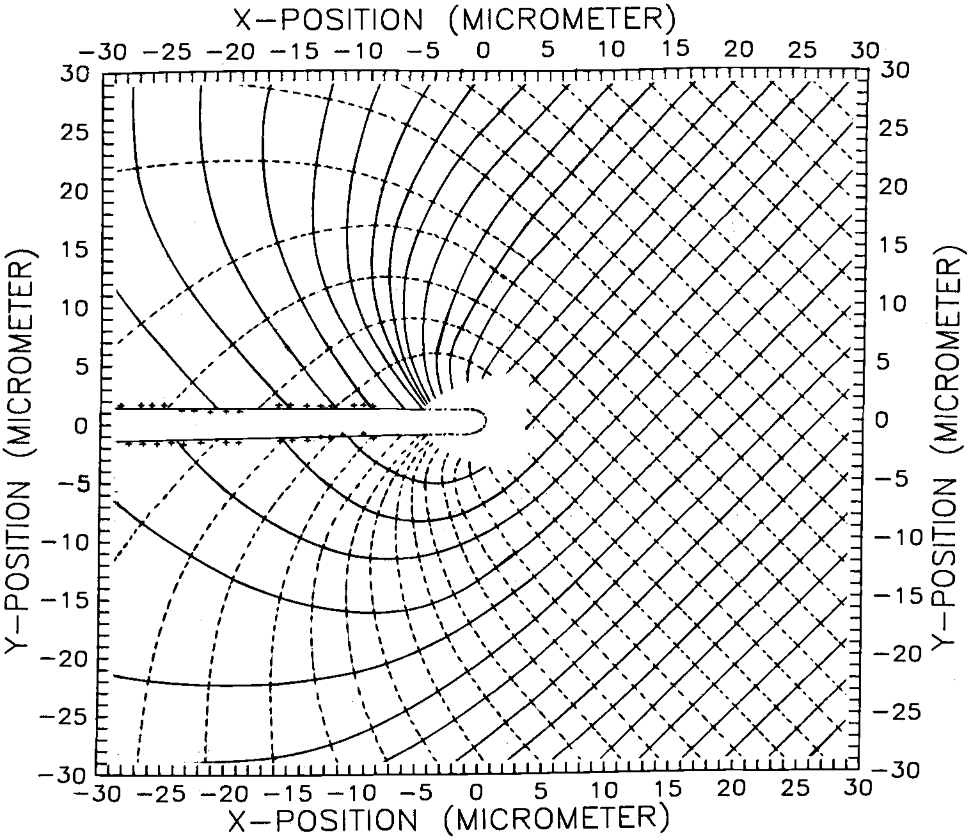

FIG. 15—*Lines of maximum shear stresses.*

the sudden fracture of the specimen. The region where the damage is concentrated has the size of, roughly, 10 μm at about 60% of the critical K_{Ic}. Within this region, there may be a secondary crack where the conditions for crack instability will be met at failure. From the preceding discussion, it is clear that the corresponding dimensions are of the order of magnitude of a crystalline grain, and, at most, few crystalline grains will be involved in the failure process.

Concerning J-dominance and the validity of the HRR solution, the following observations can be made. As pointed out in the introduction, a number of experimental papers have shown discrepancies between observed and HRR-predicted displacement fields. Dadkhah and Kobayashi [*13*] indicate that in their investigation only the v-displacement field seems to be

TABLE 3—*Plastic radius and crack opening displacement.*

	r_p				δ_t		
σ_{os}, MPa	Exp, b = 0.022, μm	b = 0.032 [*22*], μm	b = 0.0255 [*23*], μm	b = 0.106 [*24*], μm	Exp, c = 0.149, μm	c = 0.49 [*22*], μm	c = 0.341 [*25*], μm
280	112	159.9	127	530	3	9.9	6.9

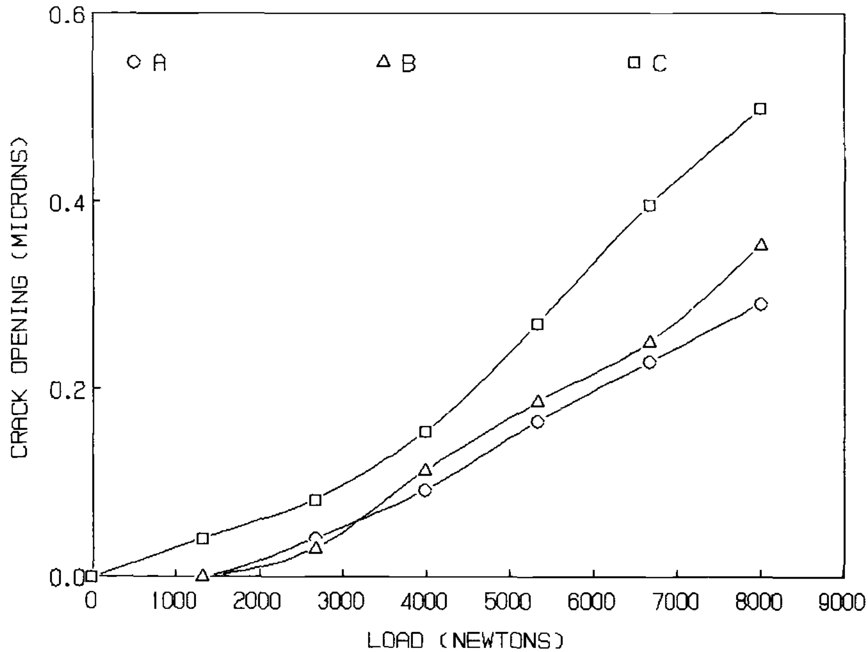

FIG. 16—*Crack opening in a region 30 μm from the crack tip.*

following the trend corresponding to the HRR field while the *u*-field does not. This discrepancy can be explained as follows. At the elastic-plastic boundary, the plastic and the elastic fields must be matched and, therefore, the plastic field must evolve inside the plastic zone before the effect of the boundary is no longer noticeable. Consequently, to observe the HRR field, one must look at a region very close to the crack tip. This conclusion is supported by the experimental results obtained in this paper. Near the crack tip, a second effect takes place. Figure 11 shows the field of the radial stresses near the crack tip. The experimental field is completely different from the HRR field. This difference is to be expected since the singular solution predicts an infinite radial stress at the crack tip while the experimental values show a decreasing field that goes to zero at the crack tip. We can conclude that the singular solution is a poor model to approximate the radial stresses near the crack tip. Since the *u*-displacement is highly influenced by the radial stresses, the observations of Dadkhah and Kobayashi [*13*] and Kang [*14*] concerning this field are explained. If we look at the tangential stresses, a different picture emerges. Although not identical, the two fields approximately agree in shape and in magnitude. Figure 13 shows the plot of the radial and tangential fields along the crack direction. The HRR solution provides a good estimate of the tangential stresses in a region that is about five times the size of the process zone. This region is well within the plastic field. Since the *v*-field depends on the tangential stresses, this explains the observations of Kobayashi and Kang. In the neighborhood of the crack tip, the radial stresses are low, hence, the stress field is very closely uniaxial and the HRR solution gives a good estimate of the tensile stresses. Therefore, the *J*-integral is a good predictor of the onset of the crack instability under the conditions of small-scale yielding. We can look at the Mode I prediction of crack instability as a modern version of the maximum tensile stress theory of fracture for brittle materials. Indeed, the specimen breaks in the direction of the maximum principal tensile stress and follows the trajectory of the isostatic orthogonal to it (crack axis).

Returning to the scale factors, there are only few crystalline grains in the direction of the crack that are affected by the HRR field. Of course, along the crack front there are many grains that are involved in the fracture process.

From a different approach, Anderson [*28*] reaches a similar conclusion; the HRR singularity is a special case of a more general relationship that can be derived on the basis of dimensional analysis. This relationship shows that J is the controlling factor of the principal stress perpendicular to the crack direction. He concludes also that the crack-tip stress field need not to agree with the HRR solution for J-controlled fracture.

We can also see that the conjecture of Paris [*9*] (that linear elastic fracture mechanics is just a special case of J-controlled fracture) is supported by the findings of this research work. Under small-scale yielding conditions, the critical stress causing the onset of crack instability is J-controlled, independent of the mechanism of failure.

The two previous observations can be summarized by the following quote from Anderson [*28*]: "Thus there is a very limited region were the HRR applies; crack tip stress fields in finite specimens should be compared to complete small scale yielding solutions rather than the HRR singularity."

Acknowledgment

The work presented in this paper has been supported by the National Science Foundation through Grant No. MSM-9020082.

References

[*1*] Rice, J. R. and Tracey, M. D., "Computational Fracture Mechanics," *Numerical and Computer Methods in Structural Mechanics*, S. J. Fenves et al., Eds. Academic Press, New York, 1973, pp. 585–673.

[*2*] Tracey, D. M., "Finite Element Solution for Crack Tip Behavior in Small Scale Yielding," *Transactions*, American Society of Mechanical Engineers, *Journal of Engineering Materials and Technology*, Vol. 98, 1976, pp. 146–151.

[*3*] Shih, C. F., "Elastic-Plastic Analysis of Combined Mode Fracture Problems," Ph.D. thesis, Harvard University, Cambridge, MA, 1976.

[*4*] Hutchinson, J. W., "Singular Behavior at the End of a Tensile Crack in a Hardening Material," *Journal of the Mechanics and Physics of Solids*, Vol. 16, 1968, pp. 13–31.

[*5*] Hutchinson, J. W., "Plastic Stresses and Strain Fields at a Crack Tip," *Journal of the Mechanics and Physics of Solids*, Vol. 16, 1968, pp. 337–347.

[*6*] Rice, J. R. and Rosengren, G. F., "Plane Strain Deformation Near a Crack Tip in a Power-Law Hardening Material," *Journal of the Mechanics and Physics of Solids*, Vol. 16, 1968, pp. 1–12.

[*7*] Begley, J. A. and Landes, J. D., "The *J*-integral as a Fracture Criterion," *Fracture Toughness, Part II, ASTM STP 515*, American Society for Testing and Materials, Philadelphia, 1972, pp. 1–20.

[*8*] Landes, J. D. and Begley, J. A., "Test Results from J-integral Studies: An Attempt to Establish a J_{Ic} Testing Procedure," *Fracture Analysis, ASTM STP 560*, American Society for Testing and Materials, Philadelphia, 1974, pp. 170–186.

[*9*] Paris, P. C., "Fracture Mechanics in the Elastic-Plastic Regime," Flow Growth and Fracture, *ASTM STP 731*, American Society for Testing and Material, Philadelphia, 1977, pp. 3–27.

[*10*] Parsons, I. D., Hall, J. R., and Rosakis, A. J., "A Finite Element Investigation of the Elastostatic State Near a Three-Dimensional Edge Crack," SM Report 86-24, California Institute of Technology, Pasadena, 1986.

[*11*] Kang, B. S., Kobayashi, A. S., and Post, D., "Stable Crack Growth in Aluminum Tensile Specimens," *Experimental Mechanics*, Vol. 27, No. 3, 1987, pp. 234–245.

[*12*] Dadkhah, M. S., Kobayashi, A. S., Wang, F. X., and Graesnen, D. L., "J-integral Measurement Using Moire Interferometry," *Proceedings*, VI International Congress on Experimental Mechanics, Portland, OR, 1988, pp. 227–234.

[*13*] Dadkhah, M. S. and Kobayashi, A. S., "HRR Field in Aluminum SEN Specimen, *Proceedings*, Society of Experimental Mechanics, Boston, MA, 1989, pp. 311–316.

[14] Kang, B. S-J., Dadkhah, M. S., and Kobayashi, A. S., "J-Resistance Curves of Aluminum Specimens Using Moire Interferometry," *Proceedings*, 1989 SEM Spring Conference on Experimental Mechanics, Cambridge, MA, Society of Experimental Mechanics, Boston, MA, 1989, pp. 317–322.
[15] Kang, B. S-J. and Liu, O.-K., "Crack Tip Blunting, Initiation and Growth Analysis of Aluminum SEN Specimens by Moiré Interferometry," *Experimental Mechanics*.
[16] Sciammarella, C. A. and Bhat, G., "Computer Assisted 3-D Moire Method, Euromechanics Colloquium No. 256 on Nondestructive 3-D Stress Analysis," Institute of Cybernetics, Estonian Academy of Sciences, Tallinn, USSR, Oct. 1989, to be published.
[17] Sciammarella, C. A., Bhat, G., and Albertazzi, A., Jr., "An Optical Technique to Measure Microdisplacements," *Applied Stress Analysis*, T. H. Hyde and E. Ollerton, Eds., Elsevier Applied Science, London, 1990, pp. 689–700.
[18] Assundi, A. and Bubbins, B. M., "Digital Moire of Moire," Hologram Interferometry and Speckle Metrology," *Proceedings*, Society of Experimental Mechanics, Boston, MA, 1990, pp. 14–20.
[19] Sciammarella, C. A., Albertazzi, A., Jr., and Mourikes, J., "Application of Computer Assisted Moire to the Study of a Crack Tip," *Proceedings*, 1991 SEM Spring Conference on Experimental Mechanics, Milwaukee, WI, Society of Experimental Mechanics, Boston, MA, 1991.
[20] Dally, J. W., Sciammarella, C. A., and Shareef, I., "Extraction of the Stress Intensity Factor from In-plane Displacements Measured by Holographic Interferometry," *Surface Crack Growth: Models, Experiments, and Structures, ASTM STP 1060*, W. G. Reuter, J. H. Underwood, and J. C. Newman, Jr., Eds., American Society for Testing and Materials, Philadelphia, 1990, pp. 130–141.
[21] Shih, C. F., "Tables of Hutchinson-Rice-Rosengren Singular Field Quantities," MLR E-147, Materials Research Laboratory, Brown University, Providence, RI, June 1983.
[22] Knott, J. M., *Fundamentals of Fracture Mechanics*, Wiley, New York, 1976, p. 89.
[23] Kanninen, M. and Popelar, C. H., *Advanced Fracture Mechanics*, Oxford University Press, Claredon Press Oxford, 1985, p. 175.
[24] Irwin, G. R., "Linear Fracture Mechanics, Fracture Transition and Fracture Control," *Engineering Fracture Mechanics*, Vol. 1, 1968, pp. 257–271.
[25] Shih, C. F., "Relationship Between the J-integral and the Crack Opening Displacement for Stationary and Extending Cracks," *Journal of Mechanics and Physics of Solids*, Vol. 29, 1981, pp. 305–326.
[26] Narasimhan, R., Rosakis, A. J., and Maran, B., "A Three Dimensional Numerical Investigation of Fracture Initiation by Ductile Failure Mechanisms in A4340 Steel," SM Report 89-5, California Institute of Technology, Pasadena, CA, 1989.
[27] Hahn, G. T. and Rosenfield, A. R., "Local Yielding and Extension of a Crack Under Plane Stress," *Acta Metallurgica*, Vol. 13, 1965, pp. 293–306.
[28] Anderson, T. L., "Elastic-Plastic Fracture Mechanics," SSC Report No. 345, Ship Structure Committee, Washington, DC, 1990.

David J. Alexander[1] *and Richard D. Cheverton*[2]

Fracture Properties of Specially Heat-Treated ASTM A508 Class 2 Pressure Vessel Steel

REFERENCE: Alexander, D. J. and Cheverton, R. D., **"Fracture Properties of Specially Heat-Treated ASTM A508 Class 2 Pressure Vessel Steel,"** *Fracture Mechanics: Twenty-Third Symposium, ASTM STP 1189,* Ravinder Chona, Ed., American Society for Testing and Materials, Philadelphia, 1993, pp. 365–380.

ABSTRACT: The mechanical properties of ASTM A508 Class 2 pressure vessel steel quenched and tempered to simulate the effects of irradiation have been measured. The tensile, Charpy impact, fracture toughness, and crack arrest properties were measured as a function of temperature. The fracture toughness was measured using 1T, 2T, and 4T compact specimens. The maximum dimensions of the 4T specimens exceeded the test cylinder thickness, so compound specimens were successfully fabricated by electron-beam welding arms to the material. Compact crack arrest specimens were used to determine the arrest toughness. Two sizes of specimens were tested: 150 by 150 by 32 mm and 75 by 75 by 25 mm. The larger specimens used a brittle weld bead and notch as the crack starter. Two different notches (blunt and fatigue precracked) were used with the smaller specimens. The blunt notch was not successful, but the fatigue-precracked specimens provided valid data without the need for warm prestressing. The results from the small fatigue-precracked specimens were consistent with the data from the larger weld-embrittled specimens.

KEY WORDS: fracture toughness, crack arrest toughness, ductile-to-brittle transition temperature, Charpy specimen, compact crack arrest specimen, electron beam welding, fracture mechanics

One of the postulated accident conditions for nuclear pressure vessels involves the sudden quenching of a heated vessel. The resultant thermal shock will produce large tensile stresses in the inner portion of the vessel wall and this, in conjunction with radiation embrittlement, may result in the propagation of existing flaws in the vessel. It is of critical interest to determine whether the flaws will extend and, if so, whether the running cracks will be arrested, as well as to determine the possible beneficial effects of cladding applied to the inner surface of the vessel. Recent work at Oak Ridge National Laboratory has studied this problem with large cylinders subjected to severe thermal shocks. The results of these experiments are presented elsewhere [*1,2*]. This paper reports on some of the materials characterization work done in support of this thermal shock program.

[1] Development staff member, Fracture Mechanics Group, Metals and Ceramics Division, Oak Ridge National Laboratory, Oak Ridge, TN 37831-6151.
[2] Section head, Pressure Vessel Technology Group, Engineering Technology Division, Oak Ridge National Laboratory, Oak Ridge, TN 37831-8047.

Experimental Procedure

Material and Heat Treatment

The material used for this program was typical light-water reactor pressure vessel material, conforming to ASTM A508 Class 2 chemical composition specifications. The actual composition is given in Table 1.

The test cylinder used for the thermal shock experiments was given a heat treatment intended to simulate the properties of an irradiated vessel; therefore, it was quenched and only slightly tempered. The test cylinder was normalized at 888°C (1630°F) for 9 h, then austenitized at 861°C (1580°F) for 7 h, and water quenched to room temperature. Several different tempering heat treatments were given to different pieces of material used in this study. The test cylinder was given a tempering treatment that was described as 7 h at 621°C (1150°F). However, examination at a later date of the temperature record from thermocouples attached to the test cylinder indicated that this treatment was more accurately described as 10 h at 621°C. The time-temperature history of the test cylinder is shown in Fig. 1, and is called CYLINDER.

An initial heat treatment was performed on specimens that already had been machined in the as-quenched condition. This included Charpy, tension, and drop weight specimens, as well as two blocks of material. These specimens were sealed inside evacuated cans and tempered for 7 h at 621°C, to match the apparent heat treatment of the vessel. This heat treatment has been designated CAN in Fig. 1. Another heat treatment of four blocks cut from a piece of the test cylinder prolongation is identified as BLOCKS in Fig. 1, and matches the test cylinder heat treatment quite well. The possible effect of these various heat treatments must be kept in mind when evaluating the results of the mechanical testing.

Charpy Testing

All Charpy testing was conducted on a 407-J (300-ft·lb) pendulum-type impact tester equipped with a semiautomated transfer device [*3*] that held the specimen in a chamber until the desired temperature was reached, and then quickly transferred it from the chamber to the anvils where it was positioned and then broken. Heating of the specimens was provided by a hot air gun system, and cooling was provided with vapor from liquid nitrogen. A thermocouple mounted in the specimen holder was used to monitor the temperature. Specimens were either overcooled or overheated, as required, and then tested as they drifted back through the target temperature.

Following the testing, the data were analyzed with the help of a computer program that fitted the data to a hyperbolic tangent function, and allowed the temperature at specified levels of

TABLE 1—*Chemical composition for ASTM A508 Class 2 material.*

	Composition, % by weight								
	C	Mn	P	S	Si	Cr	Ni	Mo	V
Heat analysis[a]	0.22	0.59	0.008	0.010	0.28	0.35	0.76	0.64	<0.01
Check analysis	0.21	0.57	0.007	0.012	0.24	0.35	0.74	0.66	<0.01
ASME specification A508 Class 2[b]	0.27	0.50	0.012	0.015	0.15	0.25	0.50	0.55	0.05
		1.00			0.40	0.45	1.00	0.70	

[a] Bethlehem Steel Heat 122S238.
[b] Single values are maxima.

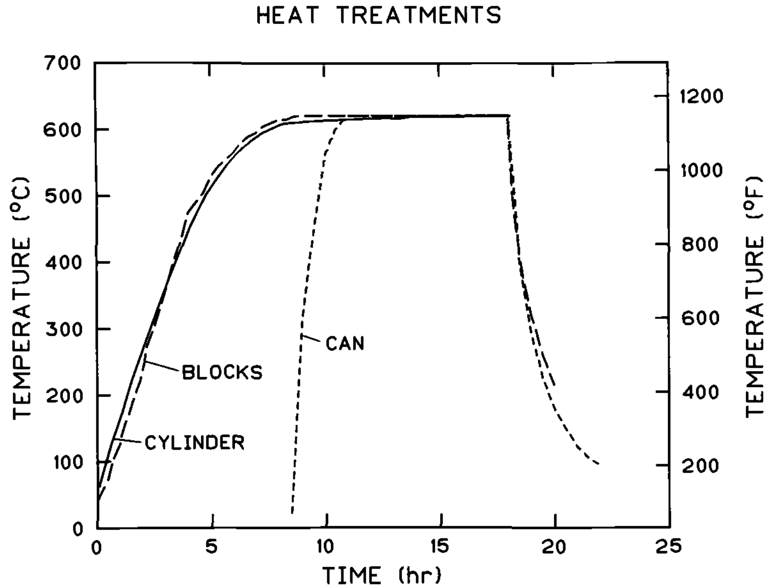

FIG. 1—*A comparison of the different tempering treatments. CYLINDER shows the treatment of the actual test cylinder; BLOCKS shows the treatment for large blocks of material; CAN shows the treatment for specimens sealed in evacuated cans. The curves have been plotted with a common end of time-at-temperature.*

energy, lateral expansion, or amount of ductile fracture, to be evaluated. The lateral expansion was measured from the broken specimens using a dial gage, and the percent of ductile fracture was estimated from the dimensions of the cleavage region, in accordance with procedures in ASTM Methods for Notched Bar Impact Testing of Metallic Materials (E 23–86).

Several sets of specimens were tested; the results are given in Table 2. A set of specimens (designated as series CAN in Table 2) was machined from material in the as-quenched condition, and then tempered in evacuated cans for 7 h at 621°C (heat treatment CAN). Another set (designated series BLOCK in Table 2) was machined after the material had undergone the same heat treatment. This set was designed to evaluate any possible effect of machining before rather than after heat treatment. Seven sets of 22 to 24 Charpy specimens were machined and tested to determine the azimuthal variation in the impact properties of the material in the test cylinder. The material was sampled every 60° around the cylinder. Testing was conducted according to a test matrix that was designed to emphasize behavior in the transition region. Therefore, five specimens were tested at each of −101 and −46°C (−150 and −50°F); three each at −18, 10, 38, and 66°C (0, 50, 100, and 150°F); and the remainder at 93°C (200°F). This resulted in only a few data points on the upper shelf. Therefore, the values of the upper-shelf energies given in Table 2 for these seven sets of specimens must be considered as rough estimates only.

All of these specimens were notched to simulate the crack propagating through the thickness of the vessel, with the crack plane parallel to the vessel axis of symmetry (C-R orientation[3]).

[3] The nomenclature used for specimen orientation is according to ASTM Terminology Relating to Fracture Testing (E 616-89).

TABLE 2—*Charpy impact properties.*

Specimen Series	Transition Temperature[a], °C					Upper-Shelf Energy, J
	T_0	40.7 J (30 ft·lb)	67.8 J (50 ft·lb)	0.89 mm (35 mil)	50% Shear	
5[b]	36	11	28	27	44	164
11[b]	30	4	23	14	40	157
15[b]	28	4	21	21	40	157
16[b]	28	2	22	15	40	150
17[b]	42	19	37	37	45	152
24[b]	24	2	24	16	41	134
26[b]	36	13	31	26	41	153
BLOCK[c]	28	14	27	26	45	133
CAN[d]	50	5	49	59	70	135

[a] T_0 = transition temperature at average of upper- and lower-shelf energies; 30 ft·lb = transition temperature at 30-ft·lb energy level; 50 ft·lb ≐ transition temperature at 50-ft·lb energy level; 35 mils = transition temperature at 35-mils lateral expansion; and 50% shear = transition temperature at 50% ductile fracture.

[b] Heat treated for 10 h at 621°C (1150°F) before machining.

[c] Heat treated for 7 h at 621°C (1150°F) before machining.

[d] Heat treated for 7 h at 621°C (1150°F) after machining.

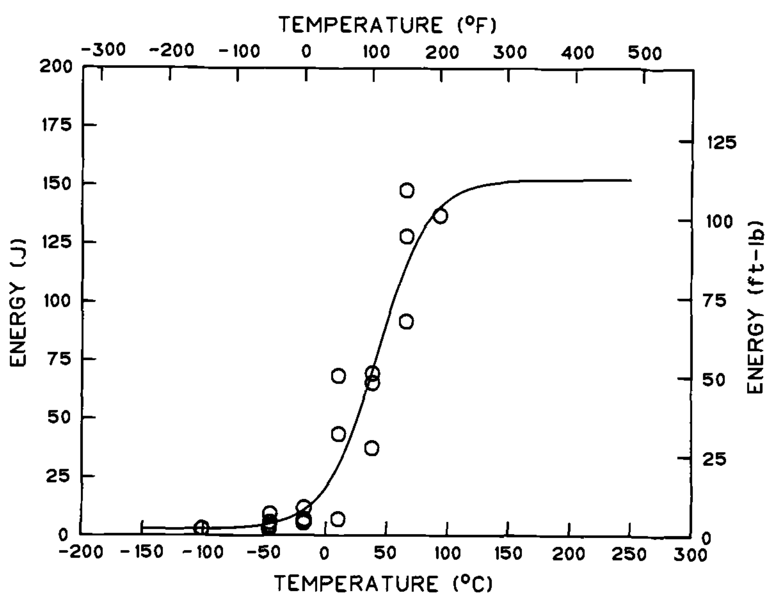

FIG. 2—*Typical energy versus temperature transition curve from one of the azimuthal variation data sets (Series 17), showing scatter commonly found in impact testing. Note that very few specimens were tested at higher temperatures, so the upper shelf indicated is only a rough estimate.*

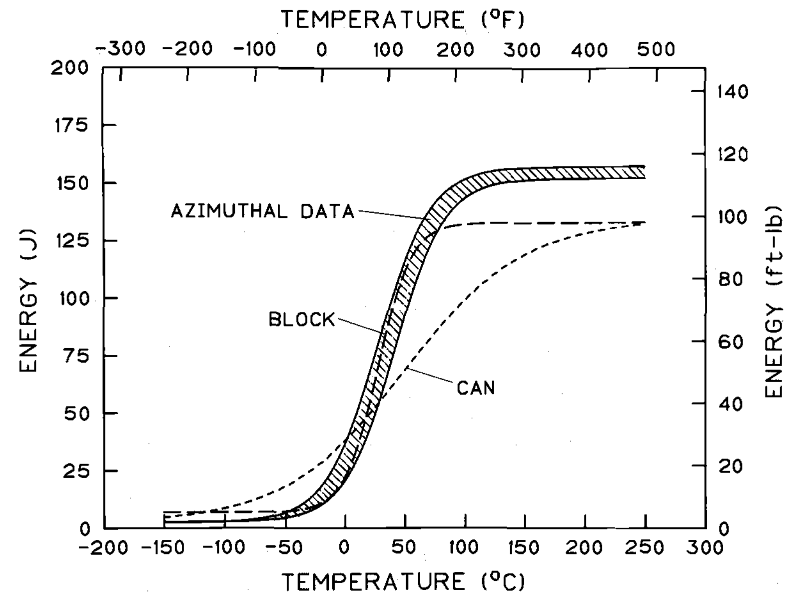

FIG. 3—*A comparison of the impact energy versus temperature curves of the various Charpy test sets. The azimuthal specimen sets are represented by the band of data; BLOCK indicates specimens machined from material after tempering for 7 h at 621°C; CAN refers to specimens machined from as-quenched material and then tempered in evacuated cans. The CAN treatment results in a wider transition region and a higher 67.8-J transition temperature than for the other series.*

The results for all the specimens are similar, despite the slightly different histories of each set of specimens. The data are presented in Table 2, and a typical data set is shown in Fig. 2; there is considerable scatter in the data, as is frequently observed for impact testing. A comparison of the curve fits for all the data sets is shown in Fig. 3. The azimuthal sets are shown by the band of data. The specimens machined from the tempered block fall within this band, but the specimens machined and then tempered show a wider transition region and a higher 67.8-J (50-ft·lb) transition temperature.

Tensile Properties

The tensile specimens were machined and then tempered for 7 h at 621°C (heat treatment CAN). All of these specimens had a reduced section length of 31.8 mm (1.25 in.), a diameter of 4.5 mm (0.18 in.), and were oriented in the C (circumferential) direction. The specimens were tested at a crosshead speed of 8.5×10^{-3} mm/s (0.02 in./min), corresponding to an initial strain rate of $3 \times 10^{-4}\ s^{-1}$.

Almost all of the specimens were tested on a mechanically screw-driven machine. The specimens were held in a frame that was fastened beneath the machine crosshead. This assembly was immersed in a bath contained in a vacuum dewar that was raised to cover the specimen and maintain the desired test temperature. For low temperature testing near room temperature, a bath of propylene glycol cooled with granulated dry ice was used, while for lower temperatures, isopentane cooled with liquid nitrogen was necessary. Tests above room temperature were conducted with a bath of light mineral oil, heated with an electric immersion heater. In all cases, a stirrer was used to agitate the bath to obtain an even temperature distribution. The vacuum dewar maintained the temperature very well. A thermocouple wire was wound around the gage length of the specimen and monitored continuously throughout the test. Load was recorded during the test as a function of time, corresponding to crosshead motion. This record was analyzed to determine the specimen's stress-strain curve. In addition to the load versus time record, the specimens were tested with an extensometer fastened to the gage length that was used to measure the specimen elongation directly.

Two specimens were tested on a servohydraulic machine at high temperature. A box furnace with resistance heater elements was used to maintain the test temperature. The results of the tensile tests on the base metal are given in Table 3 and are shown in Fig. 4.

Drop-Weight Testing

Drop-weight testing was performed in accordance with ASTM Method for Conducting Drop-Weight Test to Determine Nil-Ductility Transition Temperature of Ferritic Steels (E 208-87) on a vertical drop tower. Specimen blanks for P3-type specimens were machined in the as-quenched condition and then sealed in evacuated cans and tempered for 7 h at 621°C (heat treatment CAN). A single-pass weld bead was deposited on the specimens after they had been machined to size.

Considerable scatter in the behavior of the material required that 12 specimens be tested to determine the nil-ductility temperature (NDT). The lowest temperature at which two no-break specimens were tested was 70°C (158°F). Therefore, NDT = 65°C (149°F). The tests conducted are listed in Table 4.

Fracture Toughness

Static crack initiation and crack arrest fracture toughness measurements were made as an aid in the design of the thermal shock experiments, for which cleavage fracture was of dominant interest. It had been demonstrated previously that valid small specimen data accurately represented the effective fracture toughness of the test cylinder for flaw depths $\geq$12mm [*4*]. Thus, this was not an intent of the more recent thermal shock experiment. Furthermore, for these latter experiments, the initial flaws were three dimensional in shape and behavior, making a determination of critical values of the stress intensity value (K_I) corresponding to the initiation (K_{Ic}) and arrest (K_{Ia}) events very uncertain.

TABLE 3—*Tensile properties; specimens machined and tempered 7 h at 621°C (1150°F).*

Specimen	Temperature, °C (°F)	Yield Strength, MPa (ksi)	Ultimate Strength, MPa (ksi)	Elongation, %		Reduction of Area, %
				Uniform	Total	
KD102	−129 (−200)	720 (104)	843 (122)	11.7	21.9	55.6
KD111		778 (113)	913 (132)	10.6	18.2	38.6
KD104	−73 (−100)	563 (82)	726 (105)	11.7	21.4	64.1
KD116		585 (85)	740 (107)	12.0	23.7	63.7
KD110	−18 (0)	524 (76)	681 (99)	9.4	17.6	61.0
KD113		518 (75)	671 (97)	9.9	18.4	63.2
KD100	20 (68)	558 (81)	701 (102)	9.4	17.6	61.7
KD103		495 (72)	647 (94)	7.7	14.8	59.3
KD107		577 (84)	734 (107)	8.3	16.4	62.5
KD105	38 (100)	579 (84)	712 (103)	8.1	17.7	62.1
KD114		523 (76)	653 (95)	8.4	17.0	64.8
KD108	93 (200)	507 (74)	644 (92)	6.1	13.2	61.8
KD101		491 (71)	631 (92)	6.6	12.8	53.6

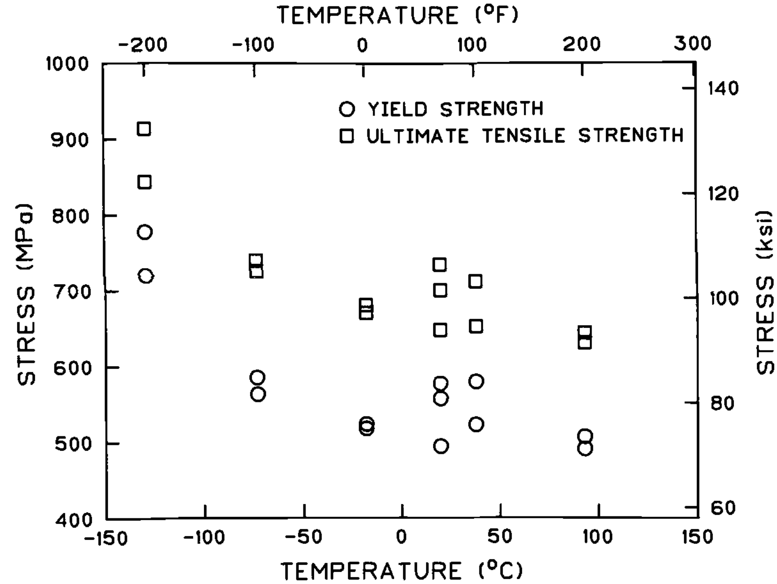

FIG. 4—*Tensile data for specimens machined in the as-quenched condition and then tempered 7 h at 621°C in evacuated cans.*

Because of restrictions on material availability and costs, specimen size was such that much of the data (particularly the initiation data) were invalid in accordance with ASTM Test Method for Plane-Strain Fracture Toughness of Metallic Materials (E 399-83). In the previous thermal shock experiment program, however, it was determined that the lower bound of a "large" set of data was sufficient for experiment design purposes, and that is the approach taken in the most recent program. A comparison of the new data included here is limited to a comparison with the ASME Section XI Appendix A lower-bound K_{Ia} curve.

Initiation Toughness—Compact specimens were used to measure the initiation fracture toughness of the test cylinder material. Several different batches of specimens were fabricated. Twenty 1T specimens were machined in the as-quenched condition and then sealed in evac-

TABLE 4—*Drop-weight testing.*

Specimen	Temperature, °C (°F)	Test Result: Break	Test Result: No Break
KD206	0 (32)	X	...
KD200	20 (68)	X	...
KD202	50 (122)	X	...
KD203	75 (167)	...	X
KD201	65 (149)	...	X
KD204	60 (140)	...	X
KD205	55 (131)	...	X
KD207	60 (140)	X	...
KD208	65 (149)	X	...
KD209	75 (167)	...	X
KD210	70 (158)	...	X
KD211	70 (158)	...	X

uated cans and tempered for 7 h at 621°C (heat treatment CAN). Ten 2T compact specimens were also machined from material tempered for 10 h at 621°C (heat treatment BLOCKS).

Five sections for 4T compact specimens were cut from the test cylinder. Because the vessel thickness was only nominally 150 mm (6 in.), it was necessary to attach stubs to these sections to achieve the desired width of 250 mm (10 in.). Pieces of A533 Grade B steel from an earlier test program were used for this purpose. Electron beam (EB) welding was used for the fabrication to achieve a narrow heat-affected zone (HAZ) that would not alter the mechanical properties of the base metal. Figure 5 shows a section through a successful trial piece used for development of the welding technique. Complete penetration was achieved. The sections were ground and etched to reveal the HAZ. It is apparent that the HAZ is quite narrow, and the material at the final crack-tip location, approximately 50 mm from the fusion line, would not be altered by the welding procedure. Figure 6 shows the welded blanks.

All compact specimens were precracked and tested in accordance with ASTM Test Method for J_{Ic}, a Measure of Fracture Toughness (E 813-87). The 1T specimen tests were performed on a 20-kip MTS servohydraulic system, while the 2T and 4T specimens were tested on a 220-kip Instron servohydraulic machine. In all cases, the test machine was computer-controlled using a clip gage mounted on knife edges screwed to the specimen. The specimens were loaded until the slope of the load-displacement trace had decreased by 5%, as determined by the computer. Small unloadings were then applied at regular intervals to those specimens that had not yet fractured. This allowed the J-integral to be calculated for those specimens that did not fracture with sufficiently low plasticity for a K_{Ic} determination.

The toughness values calculated at the onset of cleavage are given in Table 5 and shown in Fig. 7. Note that the data for the 4T specimens have been plotted displaced to slightly lower temperatures for clarity. These results were checked to determine whether they were valid according to ASTM E 399-83. For the 1T specimens, five of the results at −73°C (−100°F) and two results at −18°C (0°F) are valid. These are the lowest values in each data set.

Nine 2T compact specimens were tested, four at −18°C (0°F) and five at 10°C (50°F). No valid tests were achieved at −18°C, but there was one valid test at 10°C.

All five of the 4T specimens were tested at −18°C (0°F). Four of the specimens fractured during their initial loading cycle. One specimen had a significant popin during the first cycle. Since this changed the specimen compliance, the computer test program caused the specimen load to be cycled, as for a J-R type test. The specimen received three cycles, and then fractured. However, the load-displacement record indicated that the specimen was still behaving elasti-

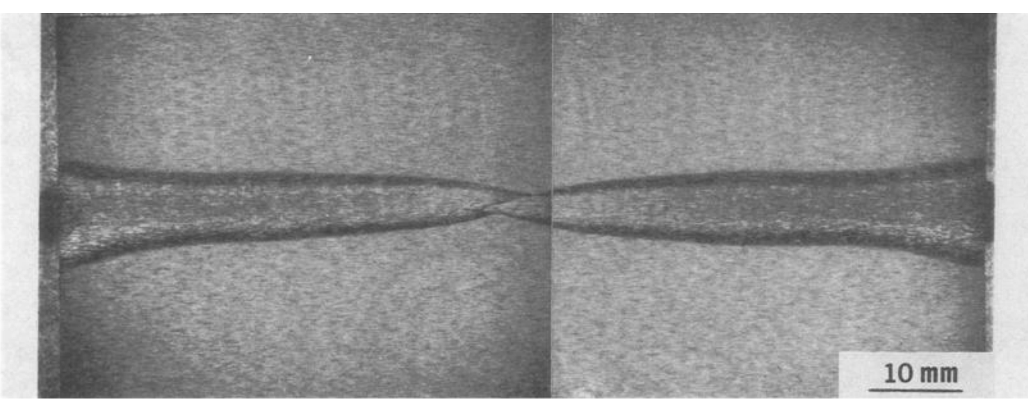

FIG. 5—*Ground and etched section through a successful trial for the EB welding process. Full penetration has been achieved. The heat-affected zone is quite narrow.*

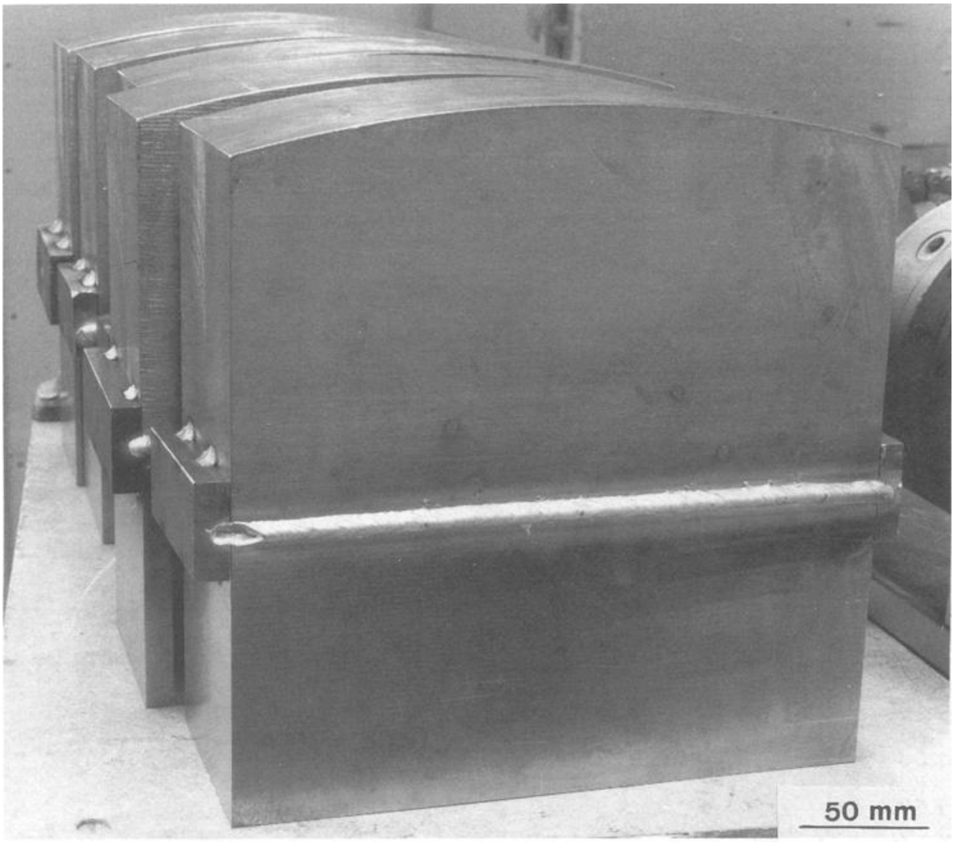

FIG. 6—*View of the EB-welded blanks for the 4T compact specimens, showing the base metal on the upper part of the specimen, the welded stubs below, and the EB weld and run-off tabs. The curved surface is the outer surface of the cylinder.*

cally. The stress intensity at which the popin occurred was 50 MPa $\sqrt{m}$ (45 ksi $\sqrt{in.}$), the lowest value for the 4T specimens. Notice, however, that the next lowest value, 54 MPa $\sqrt{m}$ (49 ksi $\sqrt{in.}$), represents a specimen that fractured with no popin, and the next higher value, 59 MPa $\sqrt{m}$ (54 ksi $\sqrt{in.}$), is the stress intensity at final fracture for the pop-in specimen, determined from the final load and the estimated crack length after the popin, based on the specimen compliance. The other 4T tests were valid according to ASTM E 399-83. The yield strength of this material is 524 MPa (76 ksi) at -18°C so the maximum allowable toughness that could be measured with a 4T specimen is 106 MPa $\sqrt{m}$ (96 ksi $\sqrt{in}$).

Crack-Arrest Toughness—Crack-arrest testing was conducted to determine the arrest toughness of the test cylinder. Testing was conducted in accordance with ASTM Test Method for Determining the Plane-Strain Crack Arrest Fracture Toughness K_{Ia} of Ferritic Steels (E 1221-88). In order to mark the crack front after arrest, the specimens were heat tinted by placing them on a hot plate until they became discolored. The specimens were cooled in liquid nitrogen and then broken open by driving a wedge into one end of the specimen.

Several different batches of specimens were made. Eight 6$\times$6 compact crack-arrest (CCA) specimens (150 by 150 by 32 mm) were machined from material that had been tempered for

TABLE 5—*Fracture toughness results.*

Specimen	Temperature, °C (°F)	K^{a}_{Jc}, MPa $\sqrt{m}$ (ksi $\sqrt{in.}$)	Validity[b]
		1T SPECIMENS	
KB04	−73 (−100)	104 (95)	N
KB17		54 (49)	Y
KB02		39 (36)	Y
KB09		102 (93)	N
KB20		100 (91)	N
KB19		117 (106)	N
KB12		46 (42)	Y
KB03		77 (70)	N
KB07		40 (36)	Y
KB14		48 (44)	Y
KB05	−18 (0)	70 (63)	N
KB10		91 (83)	N
KB13		53 (49)	Y
KB01		91 (83)	N
KB15		79 (72)	N
KB08		82 (75)	N
KB18		51 (47)	Y
KB06		130 (118)	N
KB11		95 (87)	N
KB16		107 (97)	N
		2T SPECIMENS	
KR03	−18 (0)	101 (92)	N
KR01		102 (93)	N
KQ04		155 (141)	N
KR05		102 (93)	N
KQ05	10 (50)	63 (57)	Y
KR04		122 (111)	N
KQ03		202 (184)	N
KQ01		105 (96)	N
KR02		102 (93)	N
		4T SPECIMENS	
10-1	−18 (0)	65 (59)	Y
20-1[c]		50 (45)	N
		59 (54)	N
20-2	−18 (0)	77 (70)	Y
30-1		54 (49)	Y
30-2		68 (62)	Y

[a] Modified J-integral value calculated at cleavage onset.
[b] Valid K_{Ic} values per ASTM E 399-83; Y = yes, N = no.
[c] This specimen exhibited pop-in. The first toughness value is for the pop-in and the second is for the final fracture.

10 h at 621°C (heat treatment BLOCKS). The crack orientation in these specimens matched the axial flaw of the test cylinder, running from the inner surface toward the outer surface. A brittle weld deposit was used to initiate the running crack.

Ten 3×3 CCA specimens (75 by 75 by 25 mm) were machined from material that had been tempered for 10 h at 621°C (heat treatment BLOCKS). These smaller specimens were used to determine whether this small size of specimen could generate valid arrest data. Five of these specimens had a blunt notch and side grooves while five had a chevron notch and were pre-cracked in fatigue and then side-grooved 25% (Fig. 8). The fatiguing was started at 40 kN

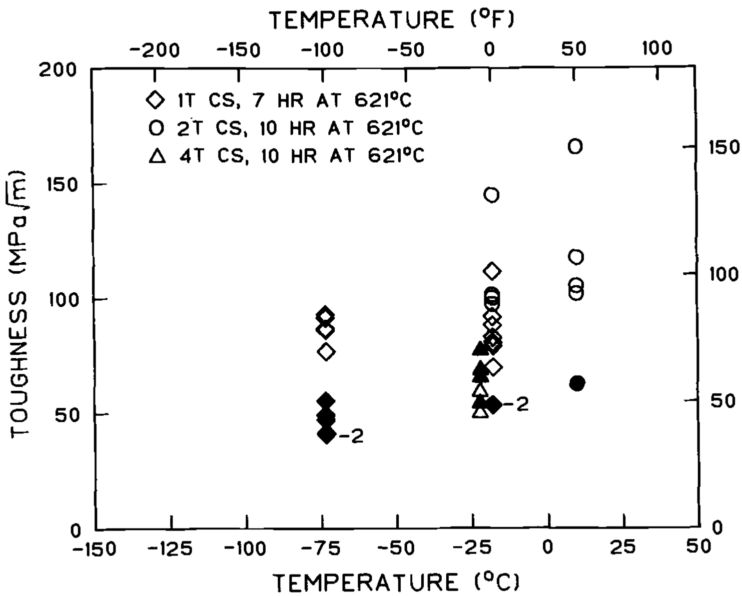

FIG. 7—*Fracture toughness data calculated from the final loads at fracture. The "2" indicates virtually identical results from two specimens. The filled symbols indicate valid* K_{Ic} *data.*

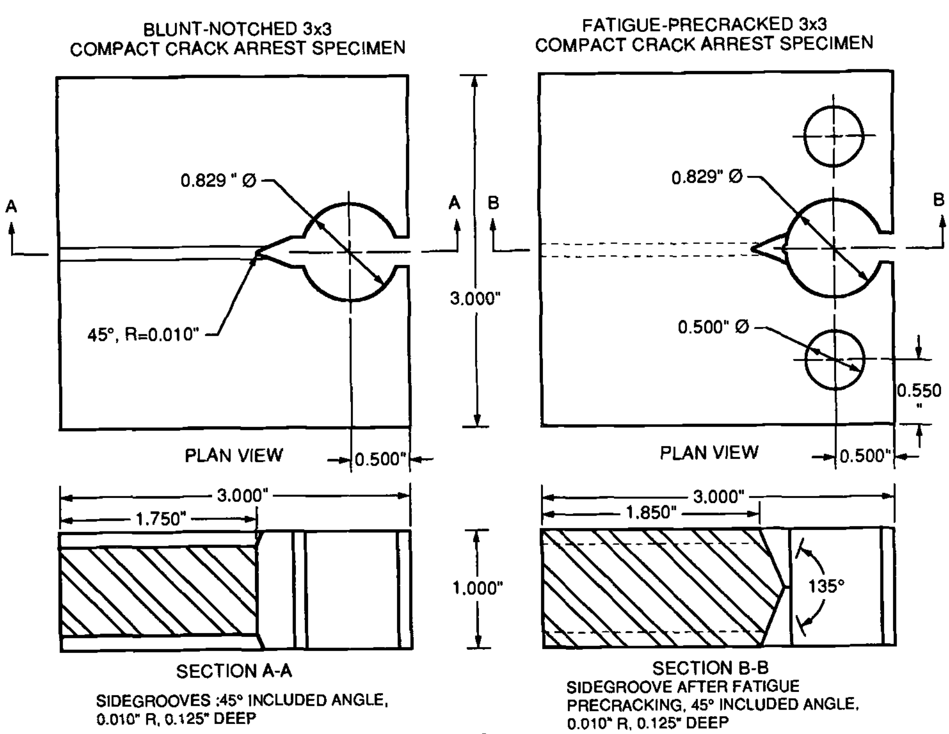

FIG. 8—*Plan views of the two 3×3 CCA specimens.*

(9000 lb) maximum load, and finished at 26.7 kN (6000 lb), with the final $a/W = 0.3$. The final maximum stress intensity was estimated to be about 27.5 MPa $\sqrt{m}$ (25 ksi $\sqrt{in.}$), assuming that the equation for a compact specimen could be used. Although the geometry of the two specimens is not identical, they are similar enough to justify this approach as a first approximation. In any case, the exact value of the stress intensity does not matter as long as it is fairly low at the end of precracking. Following the precracking, the specimens were side-grooved and then tested.

Tests with the 3×3 blunt notched specimens were unsuccessful, as the initiation loads were so great that no crack arrest occurred. The first fatigue precracked specimen was warm prestressed, as it was expected that the crack initiation would need to be suppressed to achieve valid crack jump lengths. This specimen was prestressed to a stress intensity of approximately 90 MPa $\sqrt{m}$ at 80°C and then tested at −18°C. The stress intensity factor at initiation was so large that the crack jump exceeded the allowable limits, giving an invalid test. The second specimen was tested at −18°C without any prestressing, and gave a valid result. The third specimen was tested at −73°C (−100°F) without any prestressing and also gave a valid result. Based on these results, it was apparent that 3×3 CCA specimens could be successfully tested after fatigue precracking without any prestressing. Therefore, an additional ten specimens were machined.

Successful tests were conducted at −18 and −73°C (0 and −100°F). One specimen was tested at 38°C (100°F), but stable crack growth rather than cleavage occurred. Apparently, this type of specimen will only work at relatively low temperatures where ductile crack extension is unlikely.

The 6×6 CCA specimens were tested at 38 and 66°C (100 and 150°F). The results of all the crack arrest tests are given in Table 6 and are shown in Fig. 9. The data were analyzed for validity according to the criteria in ASTM E 1221-88. The validity of each test is indicated in Table 6, and any reason for invalidity is indicated.

Discussion

The majority of the material characterization specimens were machined from test cylinder prolongation material in the as-quenched condition and were subsequently sealed in evacuated cans and tempered for 7 h at 621°C. The 1T compact, tensile, and drop weight specimens were prepared in this manner. The Charpy specimens in the azimuthal study were machined from the test cylinder material (tempered 10 h at 621°C). Examination of Table 2 indicates that there is appreciable scatter in the transition temperatures for the azimuthal material alone. The 67.8-J (50-ft·lb) transition temperature ranges from 21 to 37°C (70 to 98°F), a difference of 16°C (28°F). An even greater difference is observed for the 35 mils lateral expansion transition temperature.

The data in Table 2 show that there is also a significant effect of the fabrication or heat treatment history or both on the mechanical properties of the material. In general, the test cylinder material is noticeably tougher than the prolongation material. For instance, the 67.8-J transition temperature for the CAN material, typical of the 1T compact and drop weight specimens, is 49°C (120°F), much higher than even the highest of the test cylinder material (Series 17), which has a transition temperature of 37°C (98°F). The average 67.8-J transition temperature for the seven series of specimens from the test cylinder material is 26°C. Thus, there is roughly 23°C difference between the vessel material and the CAN series material. The difference in the 0.89-mm (35 mil) transition temperature is even greater. Furthermore, the upper shelf for the cylinder material is higher than that of the CAN material, by about 20 J. This may be due, in part, to the small number of specimens from the azimuthal sets that were tested on the upper shelf. Thus, the estimates of the upper-shelf energy are not very accurate.

TABLE 6—*Crack arrest toughness results.*

Specimen	Size	Temperature, °C (°F)	Arrest Toughness, MPa $\sqrt{m}$ (ksi $\sqrt{in.}$)	Validity[a]
KT07	3×3	−73 (−100)	26.4 (24.0)	Y
KT09			31.6 (28.8)	Y
KT11			38.1 (34.7)	Y
KT12			30.7 (27.9)	Y
KT16			39.4 (35.8)	Y
KT19			39.8 (36.2)	Y
KT03	3×3	−18 (0)	56.8 (51.7)	L
KT06			60.6 (55.1)	L
KT08			46.1 (41.9)	Y
KT10			40.8 (37.1)	Y
KT13			117.9 (107.3)	L,T
KT14			78.6 (71.5)	L
KT15			43.7 (39.8)	Y
KT17			49.2 (44.8)	Y
KT20			54.8 (49.9)	L
KS01	6×6	38 (100)	80.6 (73.3)	Y
KS03			108.5 (98.7)	Y
KS04			59.8 (54.4)	Y
KS05			89.8 (81.7)	Y
KS02	6×6	66 (150)	87.1 (79.2)	Y
KS06			194.7 (177.2)	J,L,T
KS07			160.7 (146.2)	L,T
KS08			77.3 (70.3)	Y

[a] Y = yes, test was valid; L = not valid due to insufficient remaining ligament; T = not valid due to insufficient thickness; and J = not valid due to insufficient crack jump.

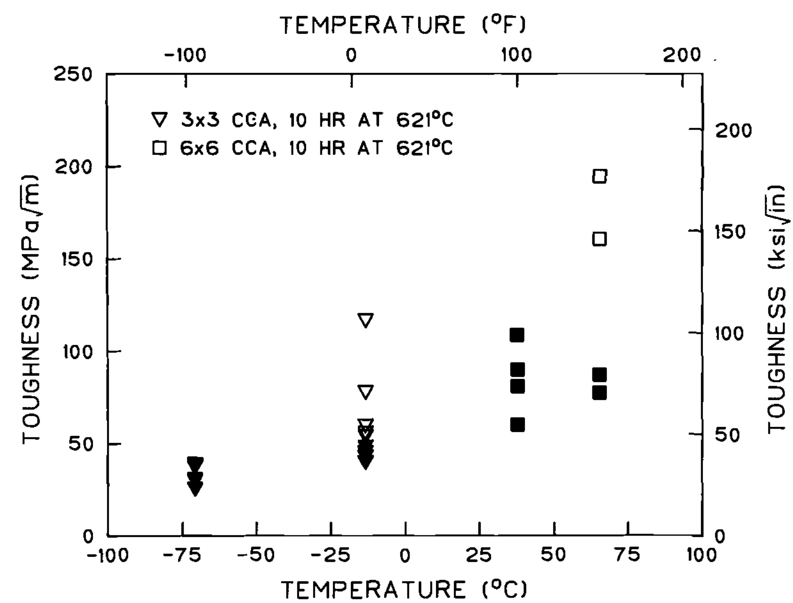

FIG. 9—*Crack arrest toughness data for the 6×6 weld-embrittled CCA specimens and the 3×3 fatigue-precracked CCA specimens. The filled symbols indicate valid* K_{Ia} *data.*

Figure 10 shows both the crack arrest data and the initiation data from the compact specimens for comparison. Note that the data for the 3 × 3 CCA specimens have been plotted displaced to slightly higher temperatures for clarity. The K_{Ia} curve from the ASME *Boiler and Pressure Vessel Code,* Section XI, given by

$$K_{Ia} = 29.4 + 1.344 \exp[0.0261(T - \text{NDT} + 89)]$$

where K_{Ia} is in MPa $\sqrt{m}$, T is in °C, and NDT = 65°C, is also shown for comparison. It is evident that the ASME K_{Ia} curve is a reasonable lower bound, with only a single K_{Ia} value below the curve.

It is interesting to compare the fracture toughness values from the 4T specimens to those from smaller specimens. As Fig. 10 shows, the range of values from the 4T specimens is considerably less than for the 1T specimens at the same temperature, although there is still a spread of over 50% in the results (from 50 to 77 MPa $\sqrt{m}$). Notice also that the lowest values obtained from the 4T specimens are very similar to the lowest values from the 1T specimens, suggesting that if enough 1T specimens are tested, the same lower bound can be found.

No problems were encountered with the precracking or testing of the compound 4T compact specimens. The electron beam welding of stubs to the vessel material proved to be a satisfactory method of obtaining larger specimen dimensions. The fracture surface from one of the 4T specimens is shown in Fig. 11. All of the fracture surfaces were similar. The shape of the fatigue precrack is very interesting. The crack front is fairly uniform, but does contain a noticeable undulation, similar for all of the specimens. The variation in crack length is within the limits prescribed by ASTM E 399-83 and does not affect the test validity. It is not clear whether this crack length variation is a result of residual stresses from the electron beam welding or is due to the material itself. The crack front is nearly 50 mm from the weld, so residual stresses seem an unlikely explanation. However, none of the other unwelded fracture tough-

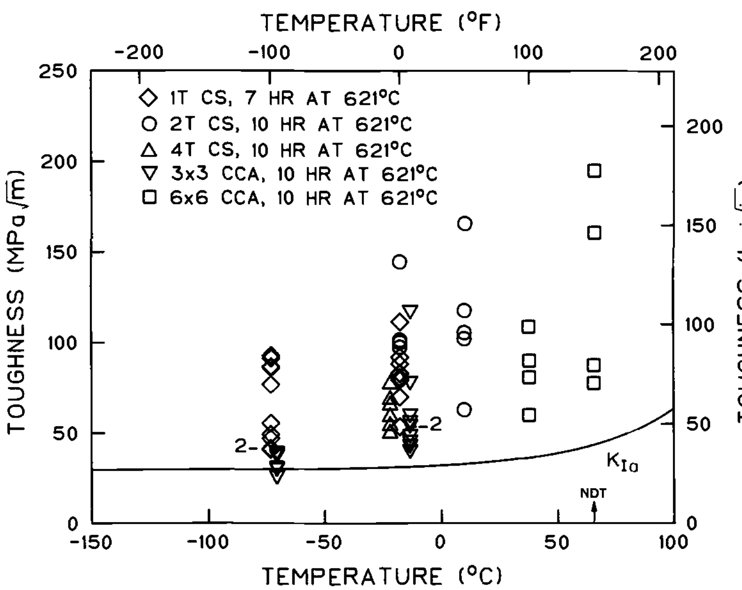

FIG. 10—*A comparison of all the toughness data. The* K_{Ia} *curve is shown for reference.*

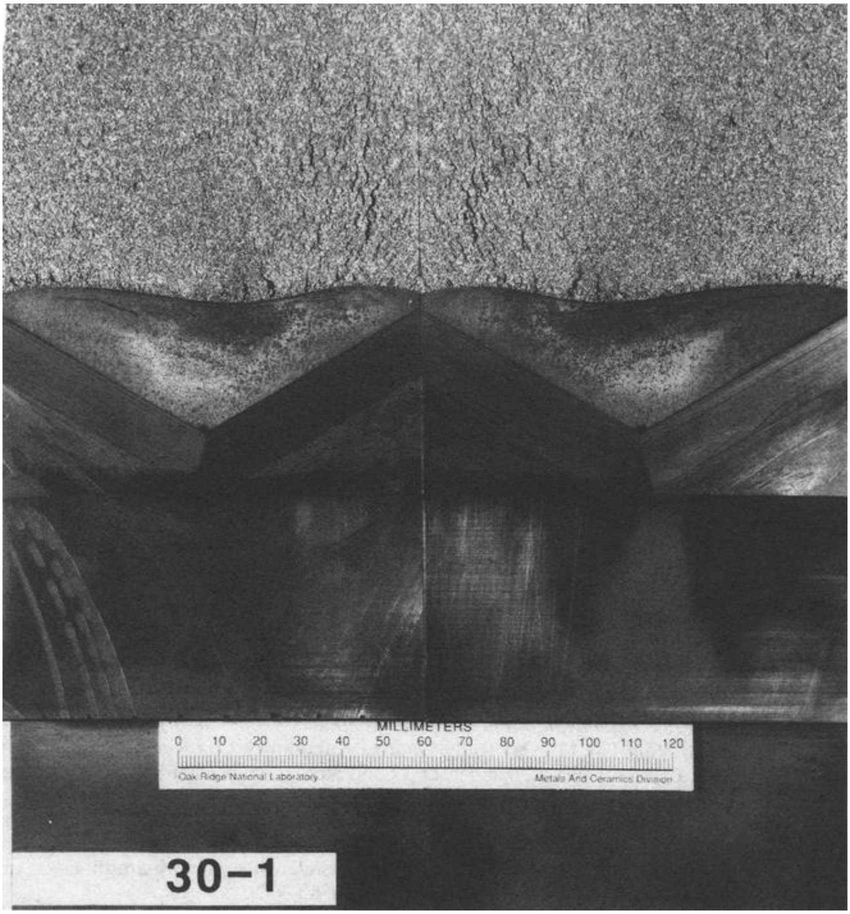

FIG. 11—*Typical fracture surfaces from a 4T compact specimen. The EB weld is located at the tip of the chevron. Note the undulation in the fatigue precrack.*

ness specimens showed any tendency toward crack front curvature. The curvature may be due to the chevron notch. Perhaps if the precracking had been extended further from the notch, the undulations would have disappeared. Again, the notch geometry was similar for all of the specimen sizes, and none of the smaller specimens showed such undulations. In any case, the curvature is not believed to be significant.

The test results from the 3×3 fatigue precracked CCA specimens compare very favorably with the results from the larger 6×6 CCA weld-embrittled specimens. For this material, at least, the smaller specimens provided a viable alternative for the generation of crack arrest toughness data, although only at lower temperatures. The fatigue precracking is a simple procedure, and the total specimen cost is less than for a similar weld-embrittled specimen, as there are fewer fabrication steps. Further effort is needed to determine whether other materials would allow successful crack arrest testing with these smaller fatigue precracked specimens. Other materials may require warm prestressing, although it was not necessary in this case.

Conclusions

The mechanical properties of a specially heat-treated quenched and tempered ASTM A508 Class 2 pressure vessel steel have been measured. These tests showed there was significant variability in the vessel material, with considerable scatter in the Charpy, drop-weight, and fracture toughness tests. The 1T compact specimens showed a great deal of scatter, but the lower bound was similar to that measured with larger specimens. Large 4T compact specimens were successfully fabricated by electron-beam welding stubs to the vessel material to allow the necessary specimen dimensions to be attained. Small fatigue-precracked CCA specimens gave values in good agreement with larger standard CCA specimens without requiring warm prestressing. Further work is needed to determine whether these smaller specimens can be successfully used for other materials.

Acknowledgments

Oak Ridge National Laboratory is managed by Martin Marietta Energy Systems, Inc., under Contract DE-AC05-84OR21400 for the U.S. Department of Energy. The mechanical testing was performed by R. L. Swain and E. T. Manneschmidt. The electron-beam welding was performed by the Materials Joining Group at Oak Ridge National Laboratory. We appreciate helpful reviews of the manuscript by S. K. Iskander and R. K. Nanstad. The manuscript was prepared by J. L. Bishop.

References

[*1*] Cheverton, R. D., Alexander, D. J., Bolt, S. E., Bryson, J. W., Nanstad, R. K., and Robinson, G. C., *Studies Pertaining to the Behavior of Flaws in Clad Cylinders Subjected to Thermal-Shock Loading,* ORNL/TM-11156, Vols. I and II, Oak Ridge National Laboratory, Oak Ridge, TN, Aug. 1989.

[*2*] Cheverton, R. D., Bryson, J. W., Alexander, D. J., and Slot, T., "Thermal-Shock Experiments with Flawed Clad Cylinders," *Nuclear Engineering and Design,* Vol. 124, 1990, pp. 109–119.

[*3*] Alexander, D. J., Nanstad, R. K., Corwin, W. R., and Hutton, J. T., "A Semiautomated Computer-Interactive Dynamic Impact Testing System," *Applications of Automation Technology to Fatigue and Fracture Testing, ASTM STP 1092,* A. A. Braun, N. E. Ashbaugh, and F. M. Smith, Eds., American Society for Testing and Materials, Philadelphia, 1990, pp. 83–94.

[*4*] Cheverton, R. D., Iskander, S. K., and Ball, D. G., "Review of Pressurized-Water-Reactor-Related Thermal Shock Studies," *Fracture Mechanics: Nineteenth Symposium, ASTM STP 969,* T. A. Cruse, Ed., American Society for Testing and Materials, Philadelphia, 1988, pp. 752–766.

Linear-Elastic Fracture Mechanics—Analyses

O. Selçuk Yahşi[1] *and Yücel Demir*[1]

Cracked Strip Problem Subjected to a Nonsymmetric Transverse Loading by a Stamp

REFERENCE: Yahşi, O. S. and Demir, Y., "**Cracked Strip Problem Subjected to a Nonsymmetric Transverse Loading by a Stamp,**" *Fracture Mechanics: Twenty-Third Symposium, ASTM STP 1189,* Ravinder Chona, Ed., American Society for Testing and Materials, Philadelphia, 1993, pp. 383–395.

ABSTRACT: In this study, the problem of an infinite elastic strip that contains a crack perpendicular to its boundaries and subjected to a nonsymmetric transverse loading is considered. The problem is a coupled crack-contact problem in which the distribution of the transverse loads is not known and is dependent on the geometry of the crack as well as the stamp. The effect of friction that may exist at the punches is taken into consideration in formulating the problem by prescribing the tangential as well as the normal tractions on the boundaries.

The solution of the problem is given for two stamp geometries, namely, a rigid flat-ended stamp with sharp corners and a curved elastic stamp.

To solve the problem, the stress and displacement fields of the strip were obtained by using Fourier transforms and then crack solution was added. As a result, three singular integral equations were obtained.

These singular integral equations are solved for the discrete values of contact stresses at certain collocation points, and stress intensity factors are obtained and tabulated for various geometries and material combinations.

KEY WORDS: contact stresses, cracked strip, integral transform techniques, fracture mechanics, fatigue (materials)

Today, as in the past, there has been considerable interest in cracked strip problems and rolling contact problems involving strips. Some of these studies are listed in Refs *1* through *7*. In all of these studies, either the contact stresses under the stamp or the dislocation densities are not known.

In this study, plane elastic contact between a thin strip, which contains a crack perpendicular to its boundaries, and symmetric stamps are considered (Fig. 1). Similar to Ref *8*, the problem differs from the standard cracked strip problems considered, because it is a coupled crack-contact problem where the distribution of the transverse load is not known and is dependent on the geometry of the crack as well as that of the stamp.

When solving the contact problems, a point of practical interest is the estimation of the effect of friction that may exist at the punches. This effect is taken into consideration in this problem by assuming that the tangential as well as the normal tractions are prescribed on the boundaries.

The results are given for a rigid flat stamp with sharp edges and for an elastic curved stamp for various crack and strip geometries.

[1] Professor and graduate student, respectively, Mechanical Engineering Department, Middle East Technical University, 06531 Ankara, Turkey.

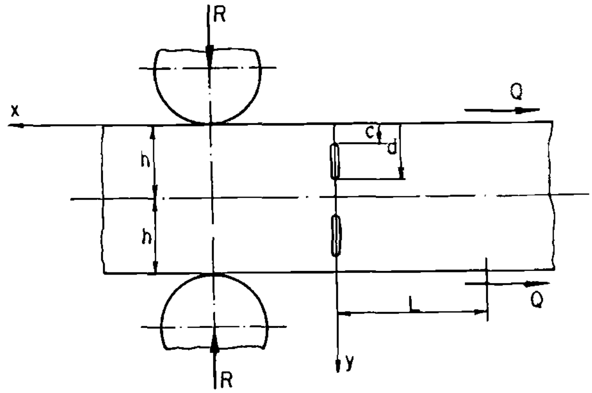

FIG. 1—*An elastic strip containing a crack that is loaded through stamps.*

Formulation of the Problem

Consider the plane elasticity problem for an infinite strip as in Fig. 2. Let $y = h$ be a plane of symmetry. For the purpose of deriving the integral equations, one may express the stress state at a point (x,y) in the cracked strip as follows

$$\sigma_{ij}(x,y) = \sigma_{1ij}(x,y) + \sigma_{2ij}(x,y), \ (i,j = x,y) \tag{1}$$

where the stress components, σ_{1ij} are associated with an infinite plane containing two cracks along $(x = 0, c < y < d, 2h - d < y < 2h - c)$, and σ_{2ij} are associated with an infinite strip.

First, by integrating the solutions given in Ref 7 for a pair of point dislocations with f and g densities located at some point $(0,y_0)$ and defined by

$$\frac{\partial}{\partial y}[v(0,y_0 + 0) - v(0,y_0 - 0)] = f(y_0)\delta(y - y_0) \tag{2a}$$

$$\frac{\partial}{\partial y}[u(0,y_0 + 0) - u(0,y_0 - 0)] = g(y_0)\delta(y - y_0) \tag{2b}$$

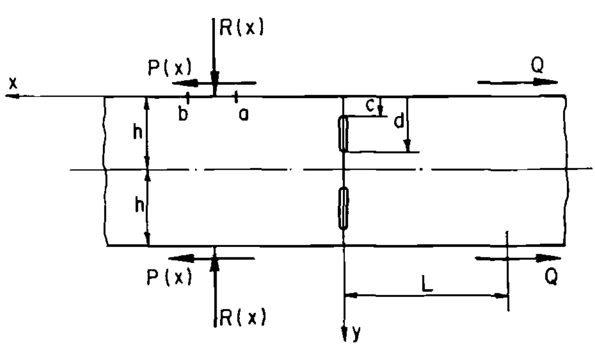

FIG. 2—*External loads acting on the elastic strip.*

where δ is the Dirac delta function, and the stress components, σ_{1ij}, can be found as

$$\sigma_{1xx}(x,y) = \frac{2\mu}{\pi(\kappa+1)}\left\{ -\int_c^d g(t)(2h-t-y)\left[\frac{3x^2+(2h-t-y)^2}{[x^2+(2h-t-y)^2]^2}\right]dt + \int_c^d f(t)x\left[\frac{x^2-(2h-t-y)^2}{[x^2+(2h-t-y)^2]^2}\right]dt + \int_c^d g(t)(t-y)\left[\frac{3x^2+(t-y)^2}{[x^2+(t-y)^2]^2}\right]dt + \int_c^d f(t)x\left[\frac{x^2-(t-y)^2}{[x^2+(t-y)^2]^2}\right]dt\right\}, \quad -\infty < x < \infty \quad 0 \le y \le 2h \tag{3a}$$

$$\sigma_{1yy}(x,y) = \frac{2\mu}{\pi(\kappa+1)}\left\{ -\int_c^d g(t)(2h-t-y)\left[\frac{(2h-t-y)^2-x^2}{[x^2+(2h-t-y)^2]^2}\right]dt + \int_c^d f(t)x\left[\frac{x^2+3(2h-t-y)^2}{[x^2+(2h-t-y)^2]^2}\right]dt + \int_c^d g(t)(t-y)\left[\frac{(t-y)^2-x^2}{[x^2+(t-y)^2]^2}\right]dt + \int_c^d f(t)x\left[\frac{x^2+3(t-y)^2}{[x^2+(t-y)^2]^2}\right]dt\right\}, \quad -\infty < x < \infty \quad 0 \le y \le 2h \tag{3b}$$

$$\sigma_{1xy}(x,y) = \frac{2\mu}{\pi(\kappa+1)}\left\{ -\int_c^d g(t)x\left[\frac{x^2-(2h-t-y)^2}{[x^2+(2h-t-y)^2]^2}\right]dt + \int_c^d f(t)(2h-t-y)\left[\frac{(2h-t-y)^2-x^2}{[x^2+(2h-t-y)^2]^2}\right]dt + \int_c^d g(t)x\left[\frac{x^2-(t-y)^2}{[x^2+(t-y)^2]^2}\right]dt + \int_c^d f(t)(t-y)\left[\frac{(t-y)^2-x^2}{[x^2+(t-y)^2]^2}\right]dt\right\}, \quad -\infty < x < \infty \quad 0 \le y \le 2h \tag{3c}$$

where μ is the shear modulus and $\kappa = 3 - 4\nu$ for plane strain and $\kappa = (3-\nu)/(1+\nu)$ for plane stress, ν being the Poisson's ratio.

Finally, by using Fourier transforms, the stresses in an infinite strip $0 < y < 2h$, $-\infty < x < \infty$ may be expressed as

$$\sigma_{2xx}(x,y) = \frac{1}{2\pi}\int_{-\infty}^{\infty}\left\{\alpha^2(A_1+B_1y)e^{-|\alpha|y} + \alpha^2(A_2+B_2y)e^{|\alpha|y} - 2|\alpha|B_1e^{-|\alpha|y} + 2|\alpha|B_2e^{|\alpha|y}\right\}e^{-i\alpha x}\,d\alpha \tag{4a}$$

$$\sigma_{2yy}(x,y) = -\frac{1}{2\pi}\int_{-\infty}^{\infty}\alpha^2\left\{(A_1+B_1y)e^{-|\alpha|y} + (A_2+B_2y)e^{|\alpha|y}\right\}e^{-i\alpha x}\,d\alpha \tag{4b}$$

$$\sigma_{2xy}(x,y) = \frac{1}{2\pi}\int_{-\infty}^{\infty} i\alpha\left\{-|\alpha|(A_1+B_1y)e^{-|\alpha|y} + |\alpha|(A_2+B_2y)e^{|\alpha|y} + B_1e^{-|\alpha|y} + B_2e^{|\alpha|y}\right\}e^{-i\alpha x}\,d\alpha \tag{4c}$$

In these equations, A_1, A_2, B_1, and B_2 are all unknown functions of α and they should be determined from the following symmetry and boundary conditions

$$v(x,h) = 0, \qquad \sigma_{xy}(x,h) = 0, \qquad -\infty < x < \infty \tag{5a,b}$$

$$\sigma_{yy}(x,0) = -R(t)\delta(x - t) \tag{6a}$$

$$\sigma_{xy}(x,0) = -P(t)\delta(x - t) + Q\delta(x + L) \tag{6b}$$

By substituting Eqs 4a through c and 3a through c into Eq 1 and then by substituting the resulting equations into Eqs 5 and 6, by taking Fourier inverse transforms, four simultaneous linear algebraic equations in terms of the unknown functions, A_1, A_2, B_1, and B_2, can be obtained [9]. By solving these simultaneous equations, all unknowns of the problem can be expressed in terms of contact stresses, $P(t)$ and $R(t)$, and dislocation density functions, $g(t)$ and $f(t)$.

Now let us assume that the strip is loaded by stamps on the $y = 0$ and $y = 2h$ boundaries, and the coefficient of friction, μ_f, on the contact, area is constant, that is, $P(x) = \mu_f R(x)$.

To complete the formulation of the problem, the contribution of the elastic stamp has to be incorporated into the integral equations. Considering only cúrved elastic stamps that are in "smooth" contact with the strip and assuming that they have relatively large local radii of curvature and they are under the $P(x)$ and $R(x)$ tractions, the derivative of the normal displacement in the stamp may be expressed as [8]

$$\frac{\partial}{\partial x} V_s(x,-0) = + \frac{\kappa_s - 1}{4\mu_s} P(x) - \frac{1}{\pi}\frac{\kappa_s + 1}{4\mu_s} \int_M \frac{R(t)}{t - x} dt \tag{7}$$

Where the subscript, s, refers to the quantities in the stamp. The integral equation giving the contact pressure, R, may then be obtained from [8]

$$\frac{\partial}{\partial x} [v(x,+0) - V_s(x,-0)] = \frac{d}{dx} V_o(x), \; a \leq x \leq b \tag{8}$$

where $V_0(x)$ describes the profile of the stamp.

The other integral equations are obtained by assuming that the crack surfaces are traction free, that is

$$\sigma_{xx}(0,y) = 0, \; c \leq y \leq d \tag{9a}$$

$$\sigma_{xy}(0,y) = 0, \; c \leq y \leq d \tag{9b}$$

Now expressing $\sigma_{xx}(0,y)$, $\sigma_{xy}(0,y)$, and $(\partial/\partial x)v(x,+0)$ in terms of the unknown functions, R, f, and g, and using Eqs 8, 9a and b after a lengthy but straightforward analysis (details of which can be found in Ref 9) the following singular integral equations can be obtained

$$\beta_1 R(x) + \frac{\beta_2}{\pi} \int_b^a \frac{R(t)\, dt}{t - x} + C_1 \int_a^b k_{11}(x,t)R(t)\, dt + C_2 \int_c^d [k_{12}(t,x) - k_{12}(2h - t,x)]g(t)\, dt$$
$$+ C_2 \int_c^d [k_{13}(t,x) + k_{13}(2h - t,x)]f(t)\, dt = C_1 M_1(L,x)Q + \frac{d}{dx} V_0(x), \; a < x < b \tag{10a}$$

$$\int_c^d \left[\frac{g(t)}{t-y} - \frac{g(t)}{2h-t-y}\right] dt + \frac{1}{C_3}\int_a^b k_{21}(t,y)R(t)\,dt + \int_c^d [k_{22}(t,y) - k_{22}(2h-t,y)]g(t)\,dt = \frac{M_2(L,y)}{C_3}Q,\ c<y<d \quad (10b)$$

$$\int_c^d \left[\frac{f(t)}{t-y} + \frac{f(t)}{2h-t-y}\right] dt + \frac{1}{C_3}\int_a^b k_{31}(t,y)R(t)\,dt + \int_c^d [k_{32}(t,y) + k_{32}(2h-t,y)]f(t)\,dt = \frac{M_3(L,y)}{C_3}Q,\ c<y<d \quad (10c)$$

If the strip contains a single symmetrically located crack, that is, for $d = h$, $c > 0$, by using the symmetry of the problem and by observing that $f(t) = f(2h - t)$, $g(t) = -g(2h - t)$, (Eqs $10a$ through c) may be expressed as

$$\beta_1 R(x) + \frac{\beta_2}{\pi}\int_a^b R(t)\frac{1}{t-x}\,dt + C_1\int_a^b k_{11}(t,x)R(t)\,dt + C_2\int_c^{2h-c} k_{12}(t,x)g(t)\,dt + C_2\int_c^{2h-c} k_{13}(t,x)f(t)\,dt = \frac{d}{dx}V_0(x) + C_1 M_1(L,x)Q,\ a \le x \le b \quad (11a)$$

$$\int_c^{2h-c}\frac{g(t)}{t-y}\,dt + \frac{1}{C_3}\int_a^b k_{21}(t,y)R(t)\,dt + \int_c^{2h-c} g(t)k_{22}(t,y)\,dt = \frac{M_2(L,y)}{C_3}Q,\ c<y<2h-c \quad (11b)$$

$$\int_c^{2h-c}\frac{f(t)}{t-y}\,dt + \frac{1}{C_3}\int_a^b k_{31}(t,y)R(t)\,dt + \int_c^{2h-c} f(t)k_{32}(t,y)\,dt = +\frac{M_3(L,x)}{C_3}Q,\ c<y<2h-c \quad (11c)$$

where

$$\beta_1 = \frac{1}{4}\left(\frac{\kappa-1}{\mu} - \frac{\kappa_s-1}{\mu_s}\right)\mu_f,\ \beta_2 = \frac{1}{4}\left(\frac{\kappa+1}{\mu} + \frac{\kappa_s+1}{\mu_s}\right)$$
$$C_1 = \frac{-1}{8\mu\pi},\ C_2 = \frac{-1}{2\pi(\kappa+1)},\ C_3 = \frac{2\mu}{\kappa+1} \quad (12a\text{–}c)$$

and the kernels, k_{11}, k_{12}, k_{13}, k_{21}, k_{22}, k_{31}, k_{32}, and functions, M_1, M_2, and M_3, are given in Appendix C of Ref 9.

Equations $11a$, b, and c are three singular integral equations that can be solved simultaneously to determine the unknown contact force, R, and the dislocation densities, $g(t)$ and $f(t)$.

The contact force, R, is subjected to the following equilibrium equation

$$Q = \mu_f\int_a^b R(t)\,dt \quad (13)$$

Also referring to the definition of the density functions, $f(t)$ and $g(t)$ must satisfy the following single-valued conditions

$$\int_c^{2h-c} f(t)\,dt = 0 \tag{14a}$$

$$\int_c^{2h-c} g(t)\,dt = 0 \tag{14b}$$

After determining the unknown functions, $R(x)$, $g(t)$, and $f(t)$, all physical quantities of the problem can be found by substituting these functions into the stress and displacement expressions.

In the integral Eqs 11*a* through *c*, k_{ij} values are Fredholm kernels whereas the others are Cauchy kernels.

The k_{ij} values are technically bounded in the respective closed domains of definition of their arguments and hence may be evaluated numerically without any difficulty. In this problem, the Gauss-Quadrature formula is used to evaluate the related infinite integrals. However, since the integrands have a singularity at $a = 0$, considered individually, most of these integrals are divergent. Expanding the integrands around $a = 0$, the divergent part of the integrals can be separated. By using the equilibrium condition (Eq 13), it can then be shown that the sum of the divergent parts of the kernels is zero. Even though somewhat lengthy, this procedure is necessary for the accurate evaluation of the kernels.

Numerical Solution and Stress Intensity Factors

After normalizing the intervals, (a,b) and $(c,2h - c)$, through the transformations

$$x = \frac{b+a}{2} + \frac{b-a}{2}\eta,\ t = \frac{b+a}{2} + \frac{b-a}{2}\tau,\ a < t < b \tag{15a,b}$$

$$y = h + (h - c)\gamma,\ t = h + (h - c)\varepsilon,\ c < t < h - c \tag{15c,d}$$

the singular integral Eqs 11*a* through *c* may be solved numerically by using the Gauss-Chebyshev integration formulas [*10*].

Refering to Ref 10, for example, it is known that the solution of the system of singular integral equations may be expressed as

$$R(\tau) = \Omega(\tau)(1 - \tau)^{\alpha}(1 - \tau)^{\beta},\ -1 \le \tau \le 1 \tag{16a}$$

$$G(\varepsilon) = g(h + (h - c)\varepsilon) = \theta(\varepsilon)(1 - \varepsilon^2)^{-1/2},\ -1 \le \varepsilon \le 1 \tag{16b}$$

$$F(\varepsilon) = f(h + (h - c)\varepsilon) = \psi(\varepsilon)(1 - \varepsilon^2)^{-1/2},\ -1 \le \varepsilon \le 1 \tag{16c}$$
$$S = -(\alpha + \beta)$$

where the functions, $\Omega(\tau)$, $\theta(\varepsilon)$, and $\psi(\varepsilon)$, are all bounded and unknown in the closed domain $[-1, 1]$ and S is the index of an integral equation.

The singular integral equation in Eq 11*a* is the second kind and the values of α and β can be found as follows [*10*]

$$\alpha = \frac{1}{2\pi i}\log\left(\frac{a - bi}{a + bi}\right) + N \tag{17a}$$

$$\beta = -\frac{1}{2\pi i}\log\left(\frac{a-bi}{a+bi}\right) + M, S = -(N+M) \tag{17b}$$

In order to get integrable singularities, S must be restricted to $-1, 0, 1$, and $S = 1$ represents sharp, $S = 0$ represents smooth-sharp, and $S = -1$ represents smooth contact at the end points of the contact region under the indenter [*10*].

Therefore, N and M are selected according to the singular behavior at the end points of the contact region [*10*].

After α, β are determined, using Gauss-Chebyshev and Gauss-Jacobi integration formulas and using the quadrature formula for singular integral equations of the second kind as given in Ref *10*, the problem can easily be solved in terms of discrete values of the unknown functions.

For a flat rigid stamp (that is, $S = 1$) and an elastic curved stamp (that is, $S = -1$), the integral equations (Eqs 11*a* through *c*) are valid with $V(x) = 0$, $\beta_1 = \mu_f(\kappa - 1)/4\mu$, $\beta_2 = (\kappa + 1)/4\mu$, and $V(x) = -x/R$, respectively.

Here it should be noted that for the flat rigid stamp the contact zone is known and the integral equations (Eqs 11*a* through *c*) subject to the conditions (Eqs 13, 14*a*, and *b*) can be solved easily. The position and the magnitude of the load, Q, contact width of the stamp, (that is, a and b) can be prescribed freely.

On the other hand for the elastic curved stamp, neither a nor b is known and they should be evaluated. For this case, collocation points in Eq 11*a* outnumber integration points by one, so there is an extra equation. On the other hand, contact width that is dependent on the total load exerted by the stamp is an additional unknown. Then, limits of contact region, a and b, can be prescribed and a solution can be obtained by solving n of $n + 1$ equations. The equation that is disregarded in the solution may be used to find the exact contact width by a trial-error procedure.

After obtaining the limits of the contact region, the total load on the stamp can be found by using Eq 13.

For the problem under consideration and for similar fracture mechanics problems, the main concern is the evaluation of the stress intensity factors that are defined as follows

$$k_I(c) = \lim_{y \to c} [2(c - y)]^{1/2} \sigma_{xx}(0,y) \tag{18a}$$

$$k_{II}(c) = \lim_{y \to c} [2(c - y)]^{1/2} \sigma_{xy}(0,y) \tag{18b}$$

After solving the integral equations, $k_I(c)$ and $k_{II}(c)$ may be evaluated as

$$k_I(c) = -\frac{2\mu}{\kappa + 1}\sqrt{h - c}\,\theta(+1) \tag{19a}$$

and

$$k_{II}(c) = -\frac{2\mu}{\kappa + 1}\sqrt{h - c}\,\psi(+1) \tag{19b}$$

TABLE 1—*Material constants used in numerical examples.*

	Steel	Aluminum
μ	80.77 GPa	26.32 GPa
ν	0.30	0.36

Then normalized Mode I and Mode II stress intensity factors can be defined as

$$k_{\mathrm{I}}^{*}(c) = -\frac{\theta(+1)}{Q/h}\frac{2\mu}{\kappa + 1} \tag{20a}$$

and

$$k_{\mathrm{II}}^{*}(c) = -\frac{\psi(+1)}{Q/h}\frac{2\mu}{\kappa + 1} \tag{20b}$$

Results and Conclusions

The stress intensity factors, $k_{\mathrm{I}}^{*}(c)$, $k_{\mathrm{II}}^{*}(c)$, obtained by using the materials shown in Table 1 are given in Figs. 3 through 6 and Tables 2 through 4.

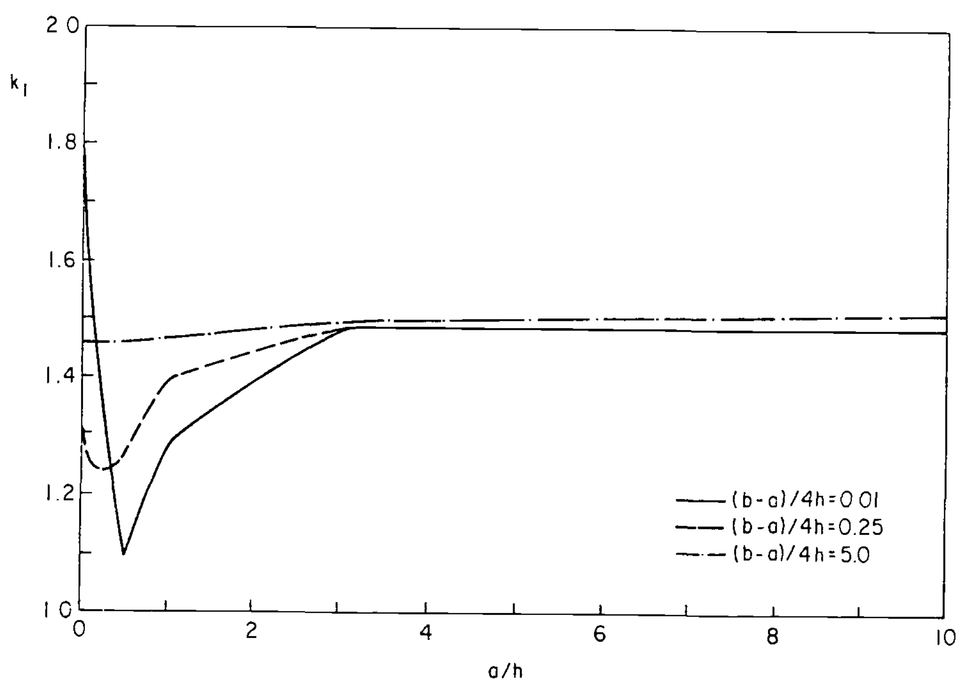

FIG. 3—*First mode stress intensity factors in a steel strip with an internal crack loaded by a rigid flat stamp;* (h − c)/h = *0.7.*

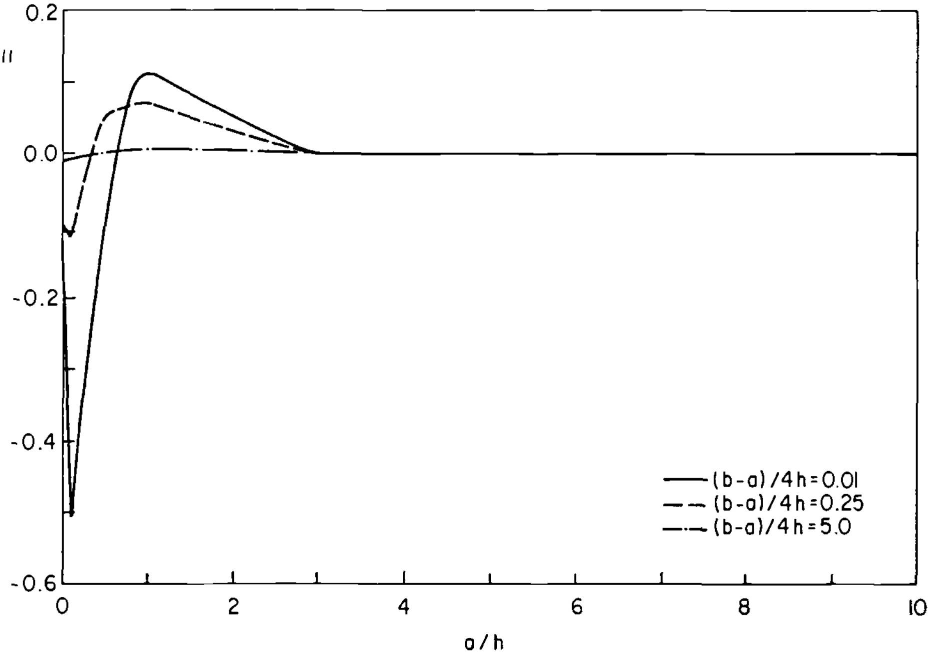

FIG. 4—*Second mode stress intensity factors in a steel strip with an internal crack loaded by a rigid flat stamp;* (h − c)/h = *0.7.*

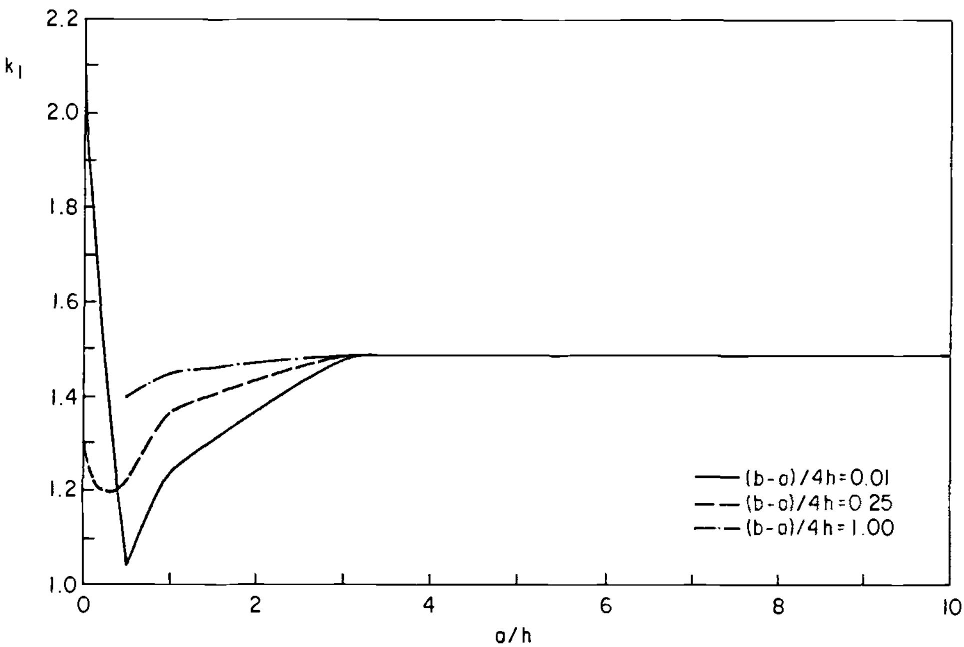

FIG. 5—*First mode stress intensity factors in an aluminum strip with an internal crack loaded by a rigid flat stamp;* (h − c)/h = *0.7.*

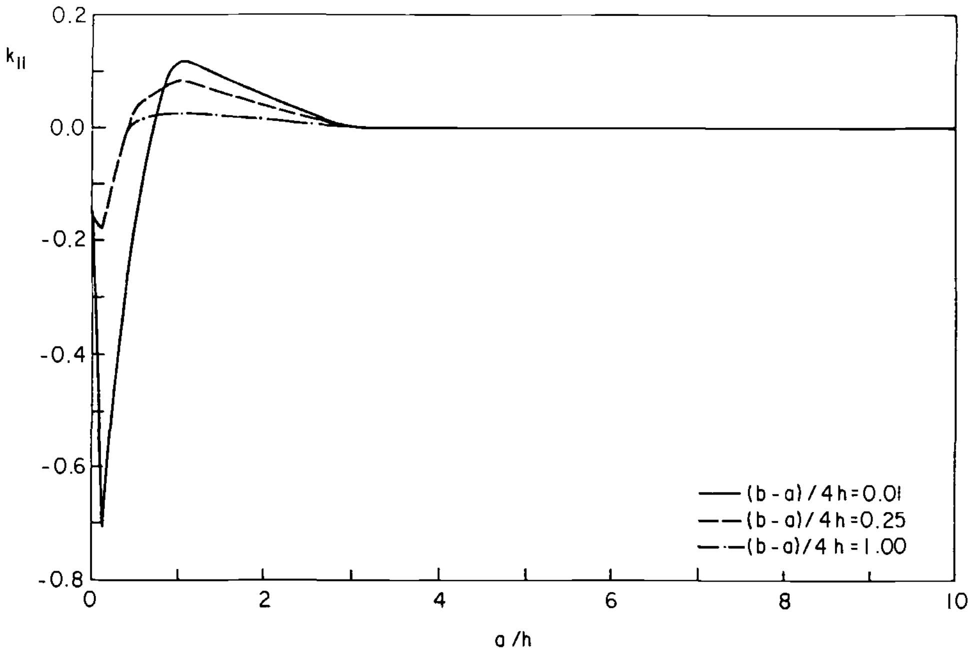

FIG. 6—*Second mode stress intensity factors in an aluminum strip with an internal crack loaded by a rigid flat stamp;* (h − c)/h = *0.7.*

Figures 7 and 8 give the pressure distribution under the rigid flat stamp for a fixed crack length and for selected values of the stamp width ($b - a$). In these figures, the abscissa η is the normalized distance from the center of the stamp. The pressure distribution is approximately symmetric except in the case where the stamp width is equal to ten times of width of the strip. From the analysis of Fig. 7, if the width of the stamp is equal to ten times the width of strip, then separation begins when the edge of the stamp is just above the crack.

If the strip is made of aluminum (Fig. 8), then separation begins when the contact width is equal to two times the strip width and pressure distribution under the stamp is more sensitive to the change of the contact width than that of steel strip. Here it should be noted that when separation begins (for a given crack length and stamp width greater than a certain critical value), the solution would not be applicable as outlined in this paper.

TABLE 2—*Stress intensity factors in an infinite steel strip with an internal crack loaded by a rigid flat stamp;* a/h = *0,* (b − a)/4h = *0.25, and* μ_f = *0.4.*

$(h - c)/h$	$k_I^*(c)$	$k_{II}^*(c)$
0.9	2.287	−0.164
0.7	1.093	−0.084
0.5	0.709	−0.049
0.3	0.481	−0.024
0.1	0.262	−0.005

TABLE 3—*Stress intensity factors in an infinite steel strip with an internal crack loaded through a steel curved stamp;* a/h = *0.05*, (b − a)/4h = *0.125* × 10^{-3}, *and* μ_f = *0.4*.

$(h - c)/h$	$k_I^*(c)$	$k_{II}^*(c)$
0.9	2.700	−1.254
0.7	1.758	−0.274
0.5	1.375	−0.105
0.3	1.120	−0.044
0.1	1.125	−0.013

TABLE 4—*Stress intensity factors in an infinite aluminum strip with an internal crack loaded through a steel curved stamp;* a/h = *0.05*, (b − a)/4h = *0.125* × 10^{-3}, *and* μ_f = *0.3*.

$(h - c)/h$	$k_I^*(c)$	$k_{II}^*(c)$
0.9	3.135	−1.751
0.7	2.094	−0.377
0.5	1.634	−0.146
0.3	1.421	−0.063
0.1	1.332	−0.018

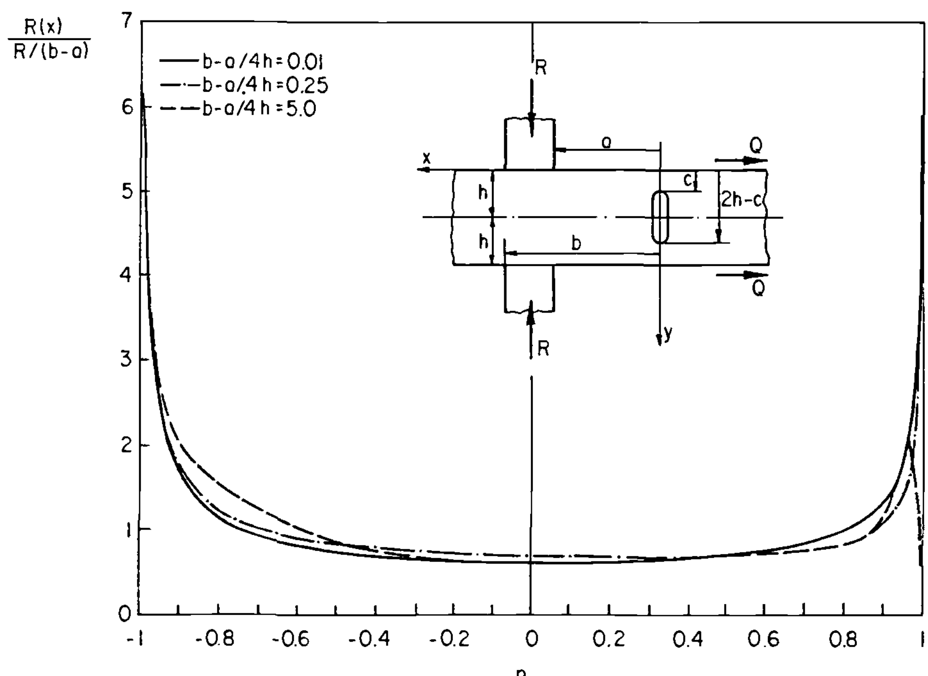

FIG. 7—*Normalized pressure distribution under a flat rigid stamp with sharp edges in a steel strip, with an internal crack;* a/h = *0.0*, (h − c)/h = *0.7*, *and* μ_f = *0.4*.

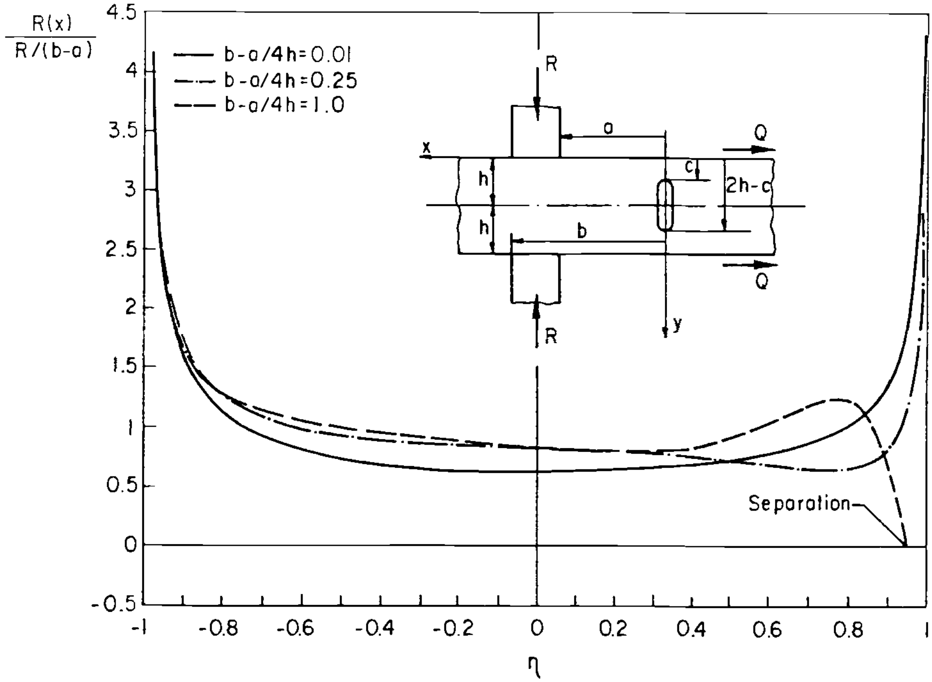

FIG. 8—*Normalized pressure distribution under a flat rigid stamp with sharp edges in an aluminum strip, with an internal crack;* a/h = *0.0,* (h − c)/h = *0.7, and* μ_f = *0.3.*

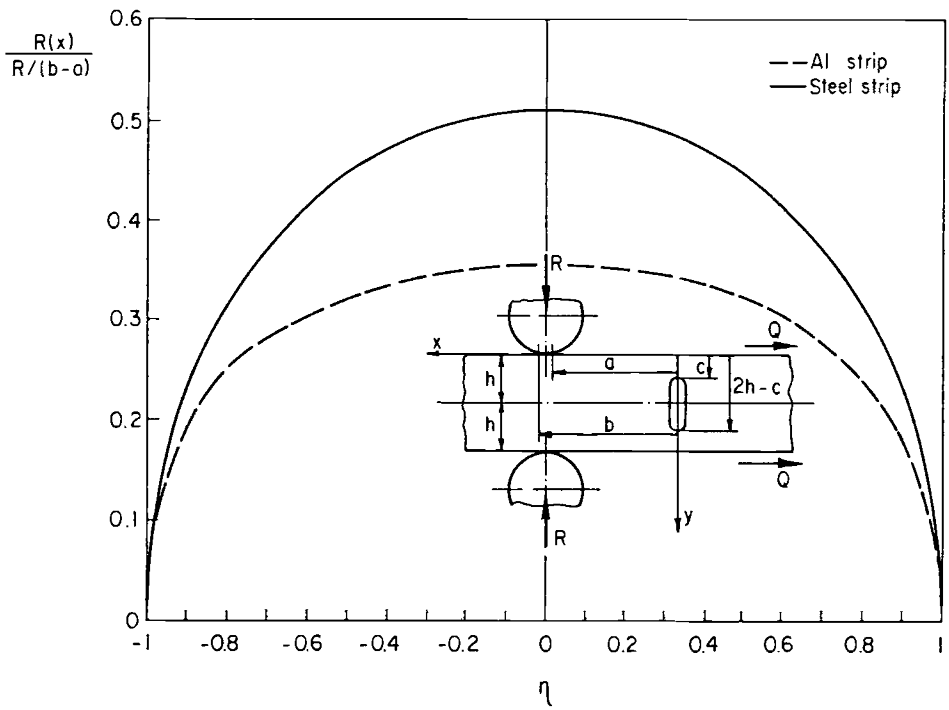

FIG. 9—*Normalized pressure distribution under a curved steel stamp in an aluminum and steel strip with an internal crack;* (h − c)/h = *0.7,* a/h = *0.0, and* μ_f = *0.4.*

Figure 9 gives the stress distribution for steel curved stamp and steel strip and steel stamp and aluminum strip combinations. From the analysis of Fig. 9, it is clear that as the strip material gets weaker the pressure in the mid portion of the contact area decreases.

Stress intensity factors for a cracked strip loaded by a flat rigid stamp are shown in Figs. 3 through 6.

Figures 3 through 6 show that as expected the first mode of stress intensity factor is the dominant stress intensity factor. As the crack moves away from the stamp, the second mode of stress intensity factor goes to zero. The largest first mode stress intensity factor is obtained when the stamp width is equal to 4% of the half strip width and the edge of the stamp is just above the crack. Since the contact zone is very small, this case can also represent the point load on the strip. As the stamp moves away from the crack, the first mode of stress intensity factor first decreases and then increases and finally converges to a value. This convergence is due to the decreasing effect of the stamp as it moves away from the crack and, finally, the effect of stamp disappears.

Contrary to the point load cases, as the width of the stamp increases, the largest stress intensity factors are found when the edge of the stamp is away from the crack.

For the aluminum strip when the stamp width is two times larger than the strip width for certain values of crack length, separation begins. For this typical "receding contact" problem in which the contact area is not known, the solution would not be applicable as outlined in this paper. The effect of crack length on stress intensity factors is shown in Table 2, and, as expected, stress intensity factors increase as the crack length increases.

The calculated results obtained for the loading by a curved stamp are summarized in Tables 3 and 4. From the analysis of these tables, similar conclusions are valid for these cases.

References

[1] Koiter, W. T., "Rectangular Tensile Sheet with Symmetric Edge Cracks," *Journal of Applied Mechanics, Transactions,* American Society of Mechanical Engineers, Vol. 32, 1965, p. 237.

[2] Sneddon, I. N. and Srivastav, R. P., "The Stress Field in the Vicinity of a Griffith Crack in a Strip of Finite Width," *International Journal of Engineering Science,* Vol. 9, 1971, pp. 479–488.

[3] Gupta, G. D. and Erdogan, F., "The Problem of Edge Cracks in an Infinite Strip," *Journal of Applied Mechanics, Transactions,* American Society of Mechanical Engineers, Vol. 41, 1974, pp. 1001–1006.

[4] Keer, L. M. and Schonberg, W. P., "Smooth Indentation of an Isotropic Cantilever Beam," *International Journal of Solids and Structures,* Vol. 22, No. 1, 1986, pp. 87–106.

[5] Nowell, D. and Hills, D. A., "Contact Problems Incorporating Elastic Layers," *International Journal of Solids and Structures,* Vol. 24, No. 1, 1988, pp. 105–115.

[6] Bentall, R. H. and Johnson, K. L., "An Elastic Strip in Plane Rolling Contact," *International Journal of Mechanical Science,* Vol. 30, 1968, pp. 637–663.

[7] Civelek, M. B. and Erdogan, F., "Crack Problems for a Rectangular Plate and an Infinite Strip," *International Journal of Fracture,* Vol. 19, 1982, pp. 139–159.

[8] Nied, H. F. and Erdogan, F., "A Cracked Beam or Plate Transversely Loaded by a Stamp," *International Journal of Solids and Structures,* Vol. 15, 1979, pp. 951–965.

[9] Yücel, D., "Cracked Strip Problem Subjected to a Nonsymmetric Transverse Loading by a Stamp," Master of Science thesis, Department of Mechanical Engineering, Middle East Technical University, Ankara, Turkey, 1989.

[10] Erdogan, F., "Mixed Boundary-Value Problems in Mechanics," *Mechanics Today,* Vol. 4, S. Nemat-Nasser, Ed., Pergamon Press, Oxford, 1978, pp. 1–85.

Kuan-Luen Chen,[1] *An-Yu Kuo,*[1] *and Simon Shvarts*[1]

Stress Intensity Factor Solutions for Partial Elliptical Surface Cracks in Cylindrical Shafts

REFERENCE: Chen, K.-L., Kuo, A.-Y., and Shvarts, S., "**Stress Intensity Factor Solutions for Partial Elliptical Surface Cracks in Cylindrical Shafts,**" *Fracture Mechanics: Twenty-Third Symposium, ASTM STP 1189,* Ravinder Chona, Ed., American Society for Testing and Materials, Philadelphia, 1993, pp. 396–416.

ABSTRACT: Pump shaft cracking has become an emergent issue recently in power industry. Prediction of residual life for a cracked shaft relies on accurate stress intensity factor calculations. Because of the three-dimensional nature of the cracked shaft problem, it is prohibitively expensive to obtain a complete stress intensity factor solutions library with three-dimensional finite-element method.

The expensive task of performing the three-dimensional fracture analyses can be alleviated by using an alternating analytical procedure. The alternating analytical procedure utilizes two analytical solutions: (*a*) the solution for an elliptical crack embedded in an infinite domain and (*b*) the solution for an infinitely long, uncracked cylinder subjected to arbitrary surface loadings. Because no finite-element mesh is required in the alternating analytical technique, the efforts to accomplish this study has been reduced significantly.

Cracked shafts under tensile, bending, and torsional loads are studied in this paper. *K* solutions for a wide range of crack geometries are presented. The *K* solutions can be applied in shaft residual life studies.

KEY WORDS: alternating technique, stress intensity factor, shaft residual life, three-dimensional crack analysis, mixed-mode fracture, partial elliptical cracks, fracture mechanics, fatigue (materials)

Many fracture mechanics problems associated with structural components, such as cracks in pump shafts or pipes, can be idealized as an elliptical or partial elliptical crack in a cylindrical shaft (Fig. 1). Numerical methods, such as the finite-element method (FEM) and the boundary integral evaluation (BIE), have been used by many researchers, for example, Raju and Newman [*1*], to obtain the three-dimensional fracture mechanics solutions. However, such conventional numerical methods as FEM and BIE often require not only a lengthy computation time, but also a large amount of manpower in preparing the numerical model. Worst of all, for problems involving different geometries, the previously mentioned labor-intensive numerical procedure has to be repeated for each case.

Until 1981, analytical solutions for an elliptical crack embedded in an infinite space were available only for polynomial crack surface loads up to the sixth order. A general solution for an embedded elliptical crack in an infinite space subjected to polynomial crack surface loads of any order was first obtained by Vijayakumar and Atluri [*2*] and then by Nishioka and Atluri [*3*]. This solution has often been referred as the VNA solution, which is the abbreviation of the first letters of Vijayakumar, Nishioka, and Atluri. By applying the VNA solution, Nishioka

[1] Senior engineer, associate, and engineer, respectively, Structural Integrity Associates, Inc., San Jose, CA 95118.

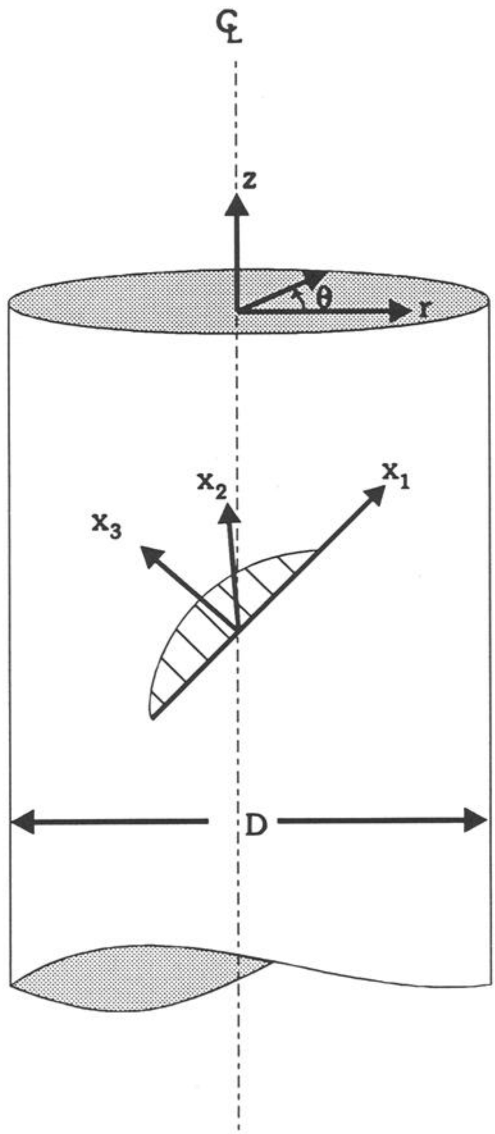

FIG. 1—*Global* r − θ − z *coordinate system and crack* $x_1 - x_2 - x_3$ *coordinate system of a cracked shaft.*

and Atluri [3] have successfully demonstrated the concept of an alternating finite-element method for the problem of an elliptical crack in a structural component of any shape. With this alternating finite-element method, the computation time and the modeling effort can be reduced dramatically relative to the usual numerical methods, since only an uncracked structure needs to be analyzed in the alternating finite-element analysis. However, the alternating finite-element method still requires the three-dimensional FEM mesh preparation for the uncracked structure.

Presented in this paper is an analytical alternating procedure (AAP) for an elliptical or partial elliptical crack in a pump shaft. Because of the simple geometry associated with the pump shaft, the finite-element analysis of an uncracked shaft in the alternating finite-element method can be replaced by a Fourier series analysis. Kuo and Shvarts [4] had presented a similar analytical alternating procedure for cracked flat plates. The cracked shaft is assumed to be subjected to arbitrarily distributed crack surface tractions. Availability of this analytical alternating method enables the user to simply enter shaft radius, crack location, and orientation relative to the shaft, crack dimensions, and crack surface loads and obtain K_{I}, K_{II}, and K_{III} solutions at the crack front, without going through the previously mentioned tedious numerical procedures.

Assumptions

The following assumptions were made to simplify the analysis:

1. As shown in Fig. 1, the shaft of the diameter, D, extends infinitely in the z-direction, that is, the shaft is infinitely long.
2. The shaft material is assumed to be isotropic, homogeneous, and linear elastic.
3. It is assumed that the stress singularity at the free edge vicinity is still $-\frac{1}{2}$ [5–10].

Boundary Conditions

As shown in Fig. 1, boundary conditions for the three-dimensional crack problem are:

1. on $r = D/2$

$$\sigma_{rr}(D/2,\theta,z) = \sigma_{r\theta}(D/2,\theta,z) = \sigma_{rz}(D/2,\theta,z) = 0$$

2. on the crack surfaces

$$x_3 = 0, (x_1/a_1)^2 + (x_2/a_2)^2 \leq 1, (a_1 > a_2)$$

the tractions are prescribed in the following form [11]

$$\sigma_{3\alpha}(x_1,x_2,0) = \sum_{i=0}^{1} \sum_{j=0}^{1} \sum_{m=0}^{M} \sum_{n=0}^{m} A^{(i,j)}_{\alpha,m-n,n}\, x_1^{2m-2n+i}\, x_2^{2n+j} \quad (1)$$

where $\alpha = 1, 2, 3$, $A^{(i,j)}_{\alpha,m-n,n}$ are known constants of the prescribed crack surface loading; and $x_1 - x_2 - x_3$ is a Cartesian coordinate system. As illustrated in Figs. 1 and 2, the Cartesian coordinate system is attached to elliptical crack surface and is related to the global cylindrical coordinate system, $r - \theta - z$, by three translations and three rotations. In the preceding equations, a_1 and a_2 are lengths of the major and the minor axes of the bounding ellipse of the crack, respectively.

Alternating Analytical Procedure (AAP)

The AAP is composed of two fundamental analytical solutions: (1) an elliptical crack in an infinite space and (2) an uncracked shaft with arbitrary surface loads. By applying three stress

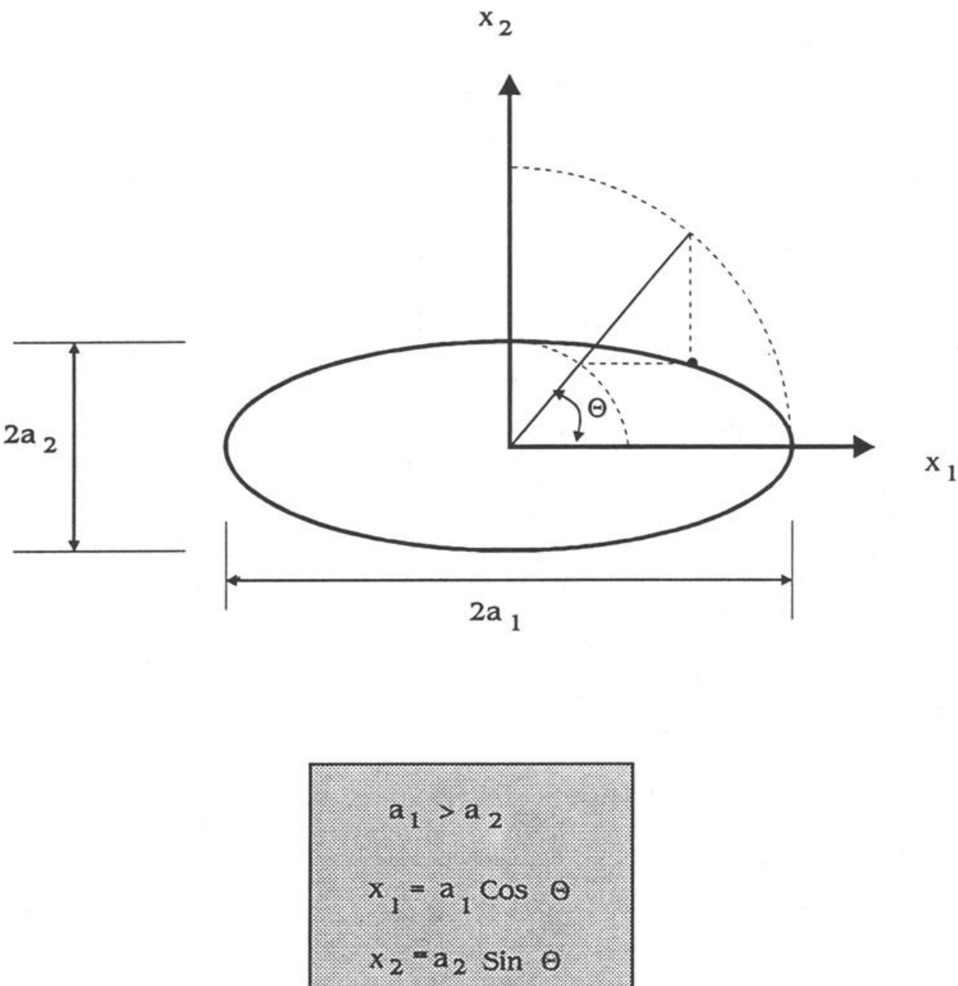

FIG. 2—*Definition of crack coordinate system and crack front angle, θ.*

functions in the Trefftz's formulation [*12,13*], the VNA solution can provide stresses at any location of an infinite domain with an elliptical crack subjected to arbitrary crack surface loads. Stress intensity factors along the crack front can also be evaluated. Detail formulations have been provided in Vijayakumar and Atluri's paper [*2*], and thus are not repeated in this paper.

In general, stress solutions resulting from the VNA solution do not satisfy the stress-free boundary conditions at the outside surface of the shaft, even though they do satisfy the governing equations and the crack surface loading conditions. That is, σ_{rr}, $\sigma_{r\theta}$, and σ_{rz} derived from the VNA solution do not, in general, satisfy Eq 1 on the shaft surface, $r = D/2$. To cancel out the nonzero stresses, σ_{ri} ($r = r, \theta, z$), on the boundary surfaces of the shaft, another analytical solution is required.

The second fundamental problem is an uncracked, infinitely long shaft of outside diameter, D, subjected to arbitrary tractions on the boundary surfaces [3,4]. Stress solutions to the second fundamental problem can be expressed in terms of three Papkovich-Neuber stress functions, Φ_o, Φ_r, and Φ_θ. Once the residual boundary traction is known (from the VNA solution), the stress functions, Φ_i ($i = o, r, \theta$), can be expressed in terms of modified Bessel functions. Since the complete formulation of the uncracked shaft solution has been presented in a relevant paper [14], detail derivation will not be repeated here.

The stress solutions to the elliptical (or partial elliptical) crack problem in a circular shaft can be obtained by summing a series of the two analytical solutions according to the following procedure until a convergence condition is met:

(*a*) Fit the crack surface loads into polynomials in the crack surface coordinate ($x_1 - x_2 - x_3$). Calculate stress intensity factors at crack fronts and stresses at $r = D/2$ by the VNA solution.
(*b*) Fit negatives of the stresses resulting from the VNA solution at $r = D/2$ into a Fourier series and calculate stresses at the fictitious crack location for an uncracked shaft by the second analytical solution.
(*c*) Check if convergence is achieved. If "no," go back to (*a*). If "yes," continue to the next step.
(*d*) Output K_i (i = I, II, III) at different crack front locations.

Several different convergence conditions, such as percentage change of residual crack surface stresses and percentage change of K-values, can be applied. A relative K-value change less than 1% was chosen as the convergence criterion in the present study.

Stress Intensity Factor for Various Cracked Shafts

To account for shafts of different size, normalized stress intensity factors will be presented. A normalized stress intensity factor, F, can be defined as follows

$$F_i = K_i/(S\sqrt{\pi a_2/Q}) \tag{2}$$

where i = I, II, or III for the three fracture modes, $S = S_t$ (maximum tensile stress), S_b (maximum bending stress), or S_q (maximum torsional stress) as defined in Fig. 3, and

$$Q = 1 + 1.464(2a_2/L)^{1.65} \tag{3}$$

where L is also defined in Fig. 3.

To examine the validity of the analytical alternating procedure, two different surface crack cases were studied and the F-factors at the deepest crack fronts were compared against Raju and Newman's (R-N) solutions [1]. The comparisons are as follows

Case 1: $2a_2/L = 0.6$, $a_2/D = 0.2$
tension:
$F_{\mathrm{I}} = 1.316$ (R-N)
$F_{\mathrm{I}} = 1.336$ (AAP)
bending:
$F_{\mathrm{I}} = 0.985$ (R-N)
$F_{\mathrm{I}} = 0.998$ (AAP)

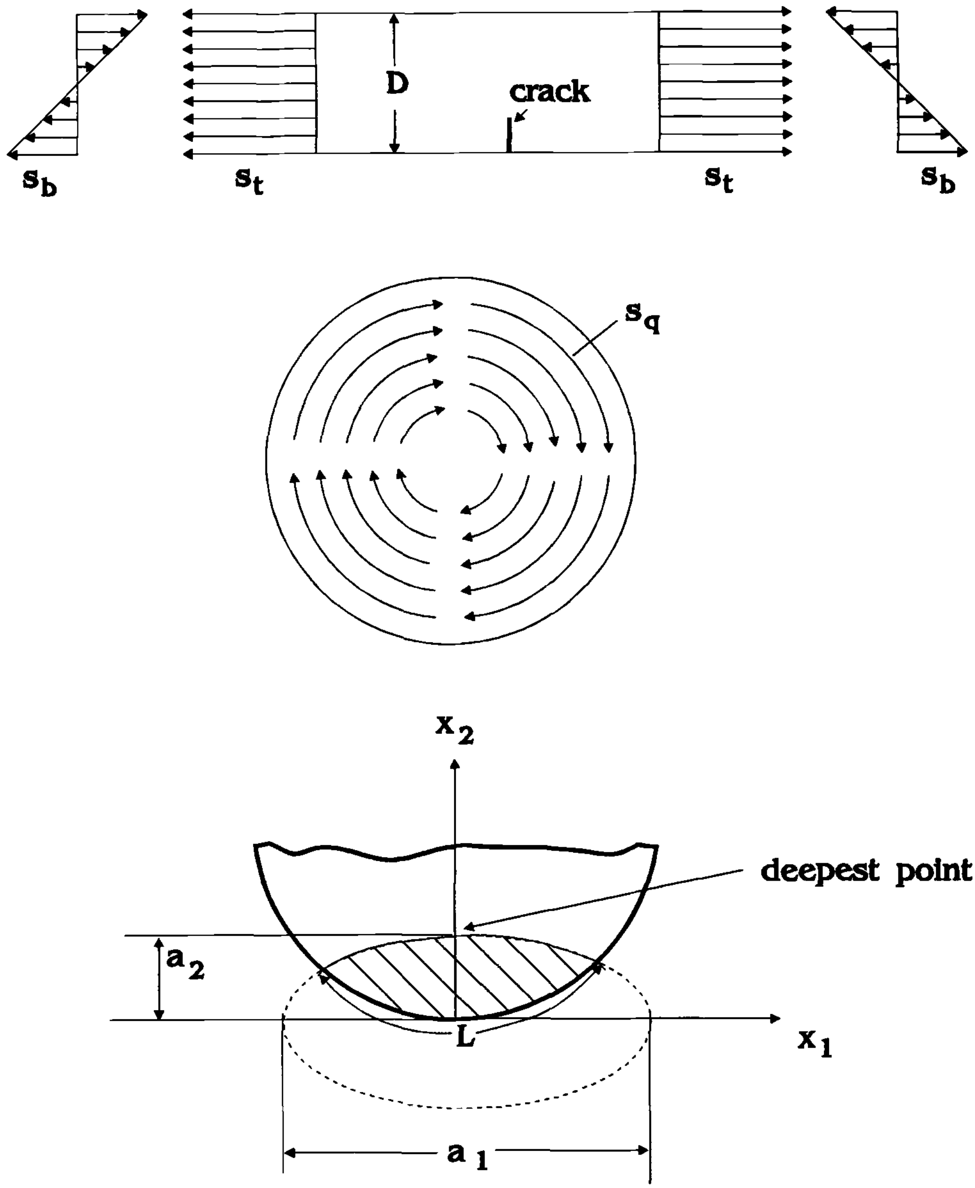

FIG. 3—*Loadings applied to the shaft and dimensions for surface crack.*

Case 2: $2a_2/L = 0.6$, $a_2/D = 0.35$

tension:

$F_{\rm I} = 1.835$ (R-N)

$F_{\rm I} = 1.762$ (AAP)

bending:

$F_{\rm I} = 1.056$ (R-N)

$F_{\rm I} = 0.999$ (AAP)

The AAP results were found to fall within a 5% error band of the reference solutions. Traditionally, for the three-dimensional linear elastic fracture mechanics problem, the 5% discrepancy is considered acceptable.

Figure 4 shows the geometries and loading conditions of various cracked shafts that were chosen to be the second example. Normalized stress intensity factors at the deepest point of a

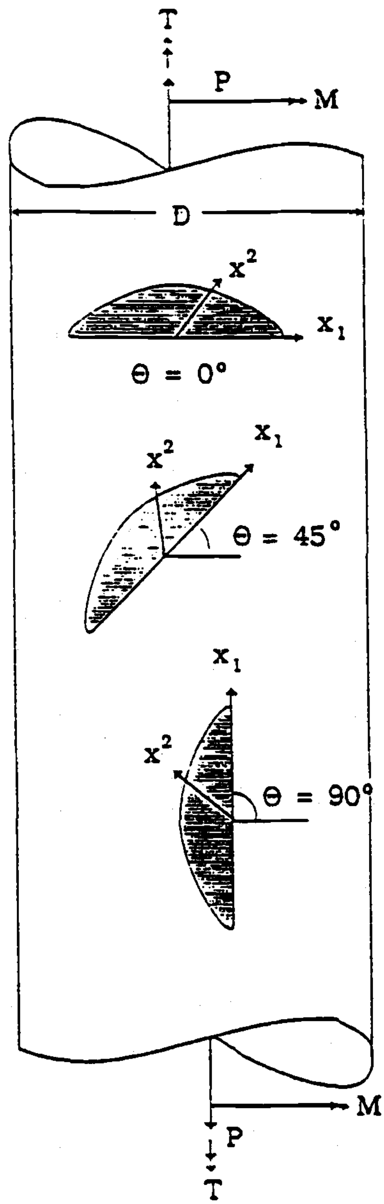

FIG. 4—*Definition of orientation of surface cracks.*

particular crack geometry ($a_2/D = 0.15$, $a_2/L = 0.25$) at three crack orientations ($\Theta = 0°, 45°, 90°$) subjected to three different loading conditions (tension, bending, and torsion) have been calculated as shown in Table 1.

Figures 5 through 16 show the variation of the normalized stress intensity factors, F, of the surface cracks as a function of the crack front angle (θ) at a particular crack orientation angle, $\Theta = 0°$. Curves in different figures represent different combinations of crack shapes (a_2/a_1), crack sizes (a_2/D), and loading conditions (tension, bending, or torsion). The following observations can be drawn:

(*a*) According to Figs. 6, 8, 10, 12, 14, and 16, Mode III fracture dominates the deepest crack point under the torsional loading while Mode II fracture dominates surface region.

(*b*) According to Figs. 5, 7, 9, 11, 13, and 15, F_Is near the free surface for curved cracks ($a_2/a_1 = 0.8$) are larger than F_Is for straight cracks ($a_2/a_1 = 0.3$). This probably explains why curve cracks tend to propagate into straight curves in pump shafts.

(*c*) For shallow curved cracks ($a_2/a_1 = 0.8$, $a_2/D \leq 0.1$), the maximum F_Is under tension loading occur at the deepest crack point (Figs. 5, 7, and 9). However, for deep curved cracks ($a_2/a_1 = 0.8$, $a_2/D > 0.1$), the larger F_Is occur near the free surface (Figs. 11, 13, and 15).

(*d*) Discrepancies of F_Is between tension and bending loading are more profound for deep cracks ($a_2/D = 0.25$, Fig. 15) than for shallow cracks ($a_2/D = 0.025$, Fig. 5).

Conclusions

A broad range of stress intensity factor solutions for cracked shafts under tensile, bending, and torsional loads have been presented in this paper. An analytical alternating procedure has been developed for this catalog of problems. With the AAP approach, the three-dimensional crack problem can be solved with great ease, in shorter computer time, and more importantly, with no FEM model preparation. Of course, AAP's shortcoming with respect to the conventional FEM [*1*] or the alternating FEM [*2,3*] is that it can only handle a specific (cylindrical shaft) geometry.

Acknowledgment

The authors wish to express their gratitude to Dr. Peter C. Riccardella of Structural Integrity Associates, Inc., for his encouragement during the course of the study.

TABLE 1—*Normalized stress intensity factors of various crack orientations and loading conditions.*

	$\Theta = 0°$	$\Theta = 45°$	$\Theta = 90°$
Tension	$F_I = 1.22$	$F_I = 0.87$ $F_{III} = 0.65$	NA[a]
Bending	$F_I = 0.99$	$F_I = 0.69$ $F_{III} = 0.51$	NA
Torsion	$F_{III} = 0.75$	$F_I = 0.75$ $F_{III} = 0.56$	$F_{III} = 0.79$

[a] NA = not available.

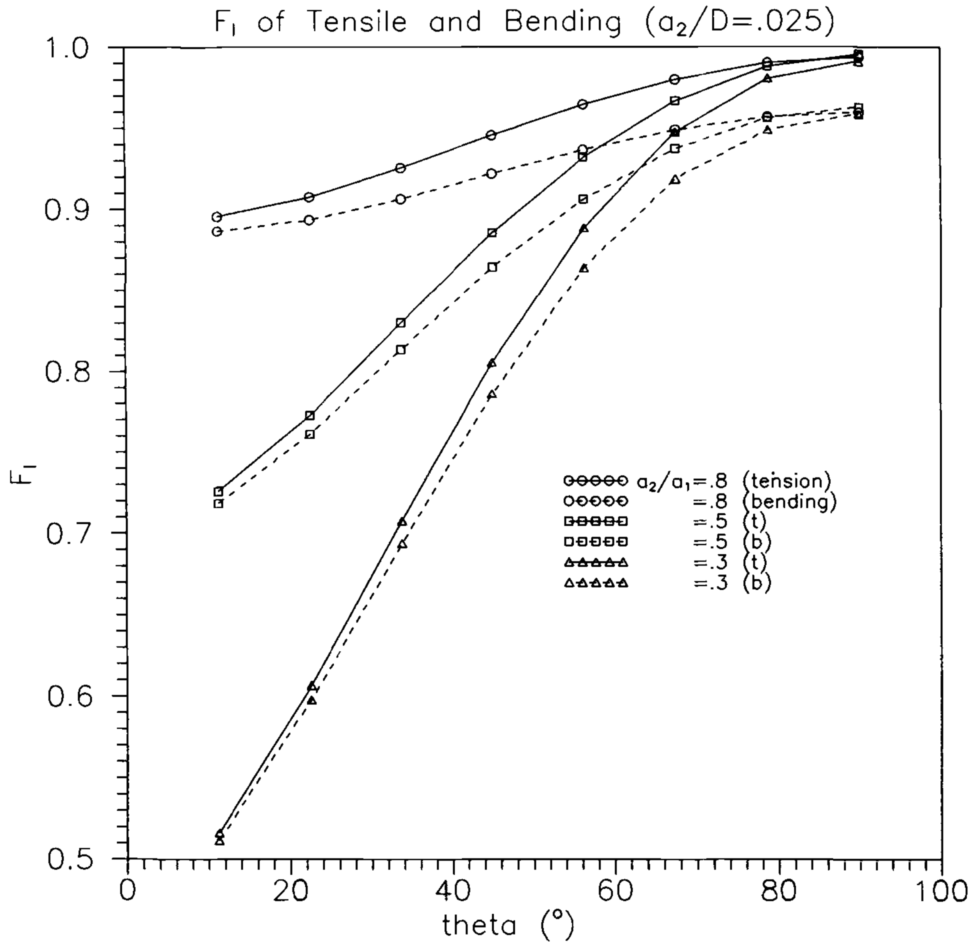

FIG. 5—F_I *of* a_2/D = *0.025.*

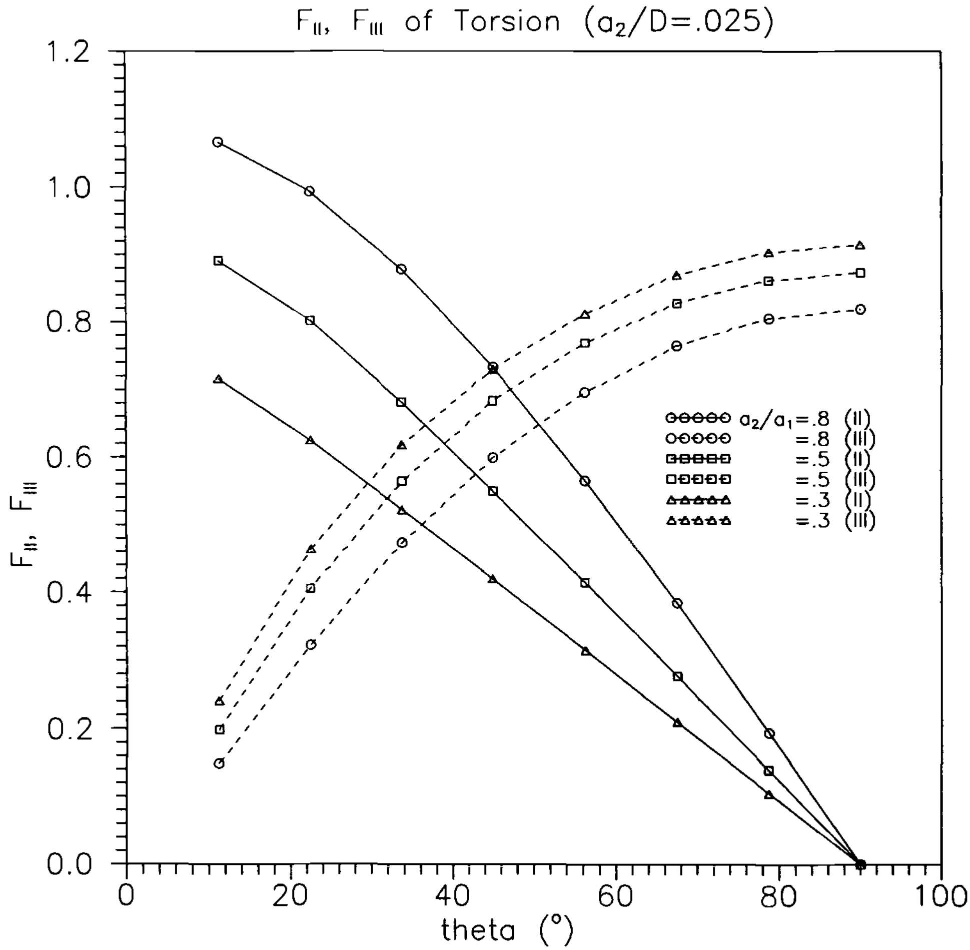

FIG. 6—F_{II} *and* F_{III} *of* a_2/D = *0.025.*

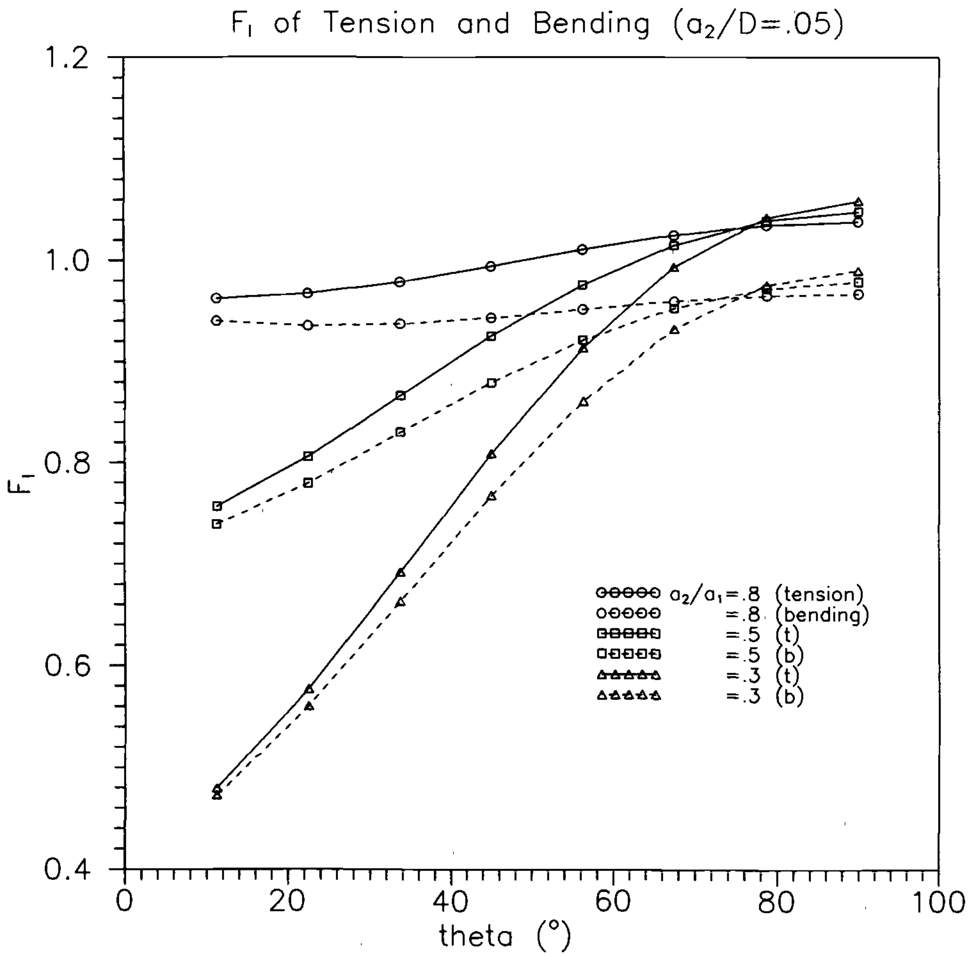

FIG. 7—F_I *of* a_2/D = *0.05.*

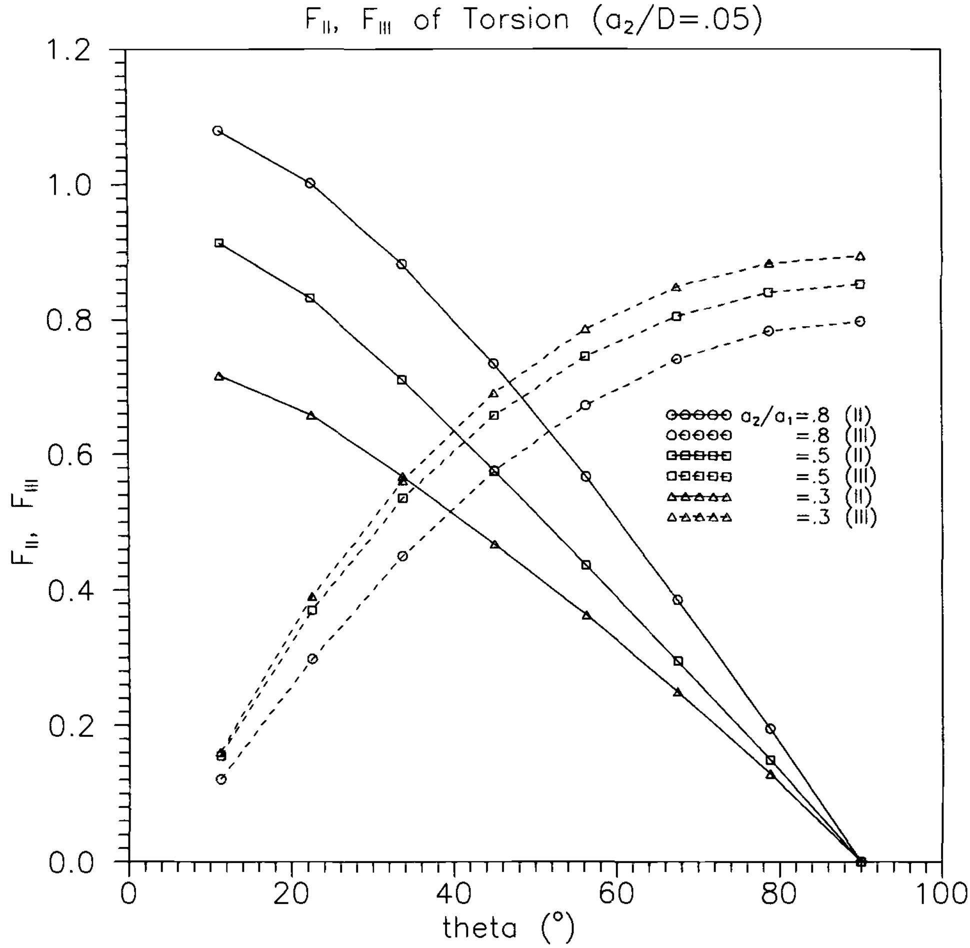

FIG. 8—F_{II} *and* F_{III} *of* a_2/D = *0.05.*

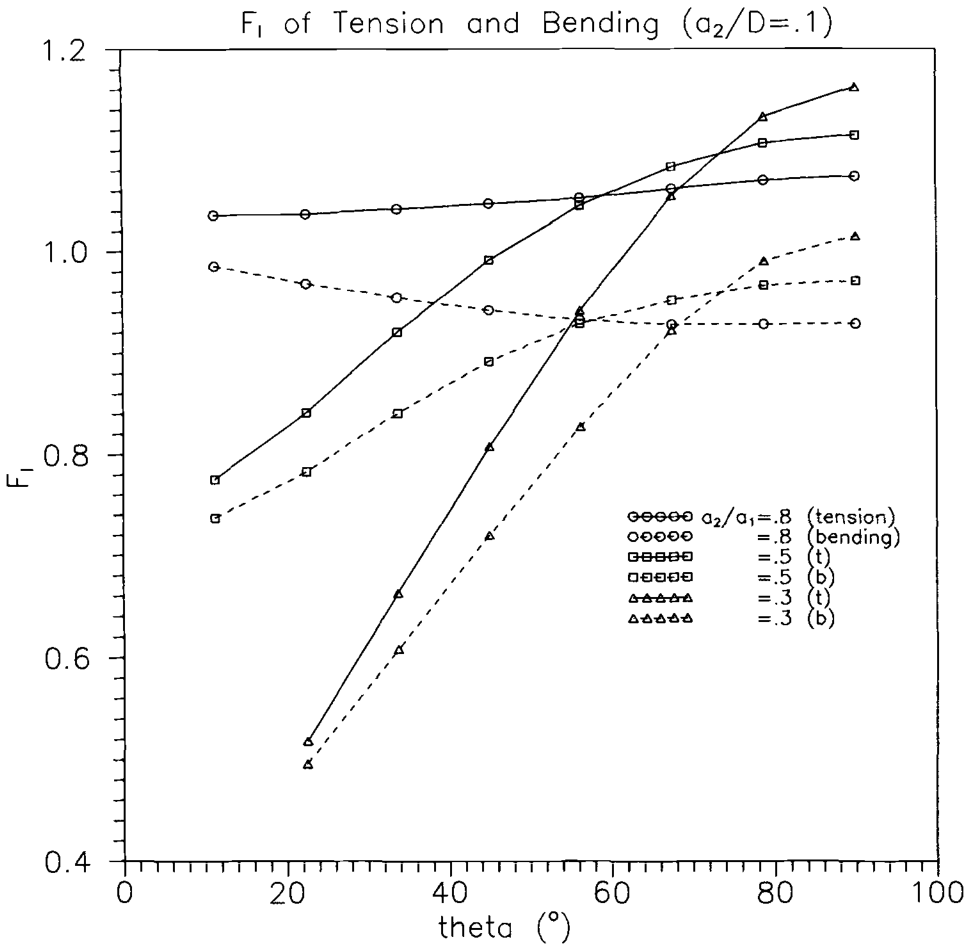

FIG. 9—F_I *of* a_2/D = *0.1.*

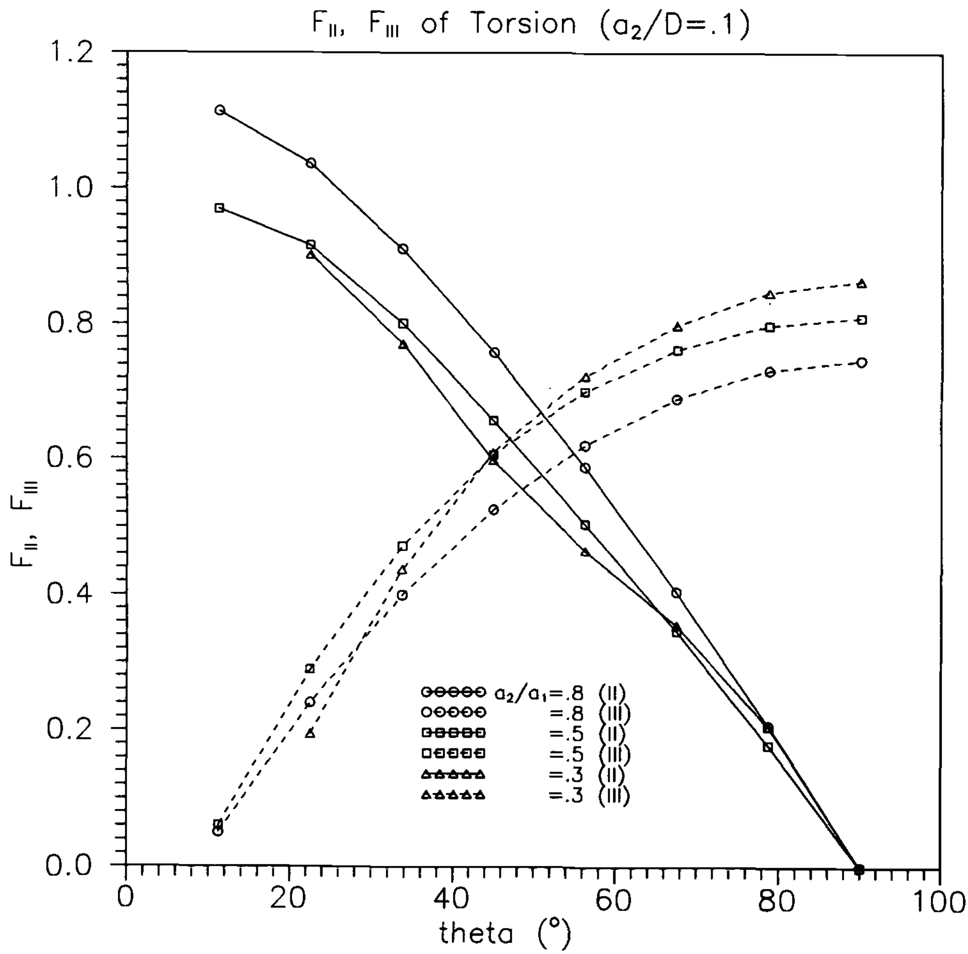

FIG. 10—F_{II} *and* F_{III} *of* a_2/D = *0.1.*

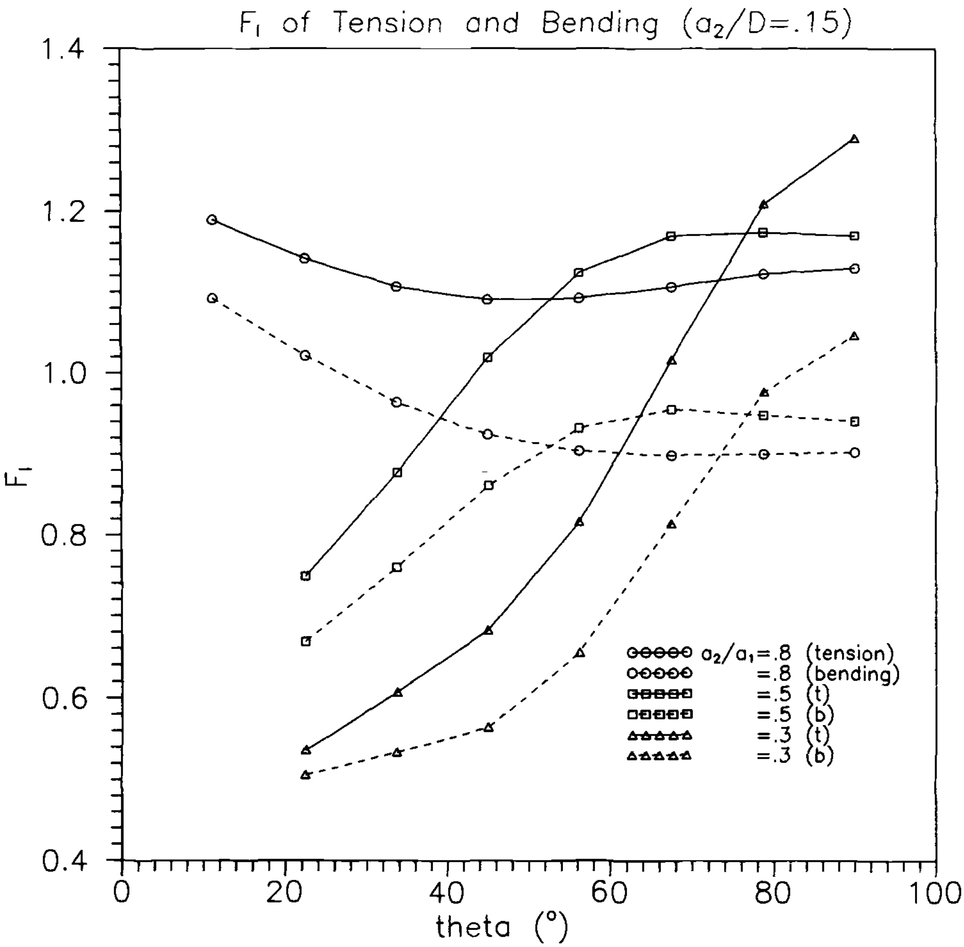

FIG. 11—F_I *of* a_2/D = *0.15*.

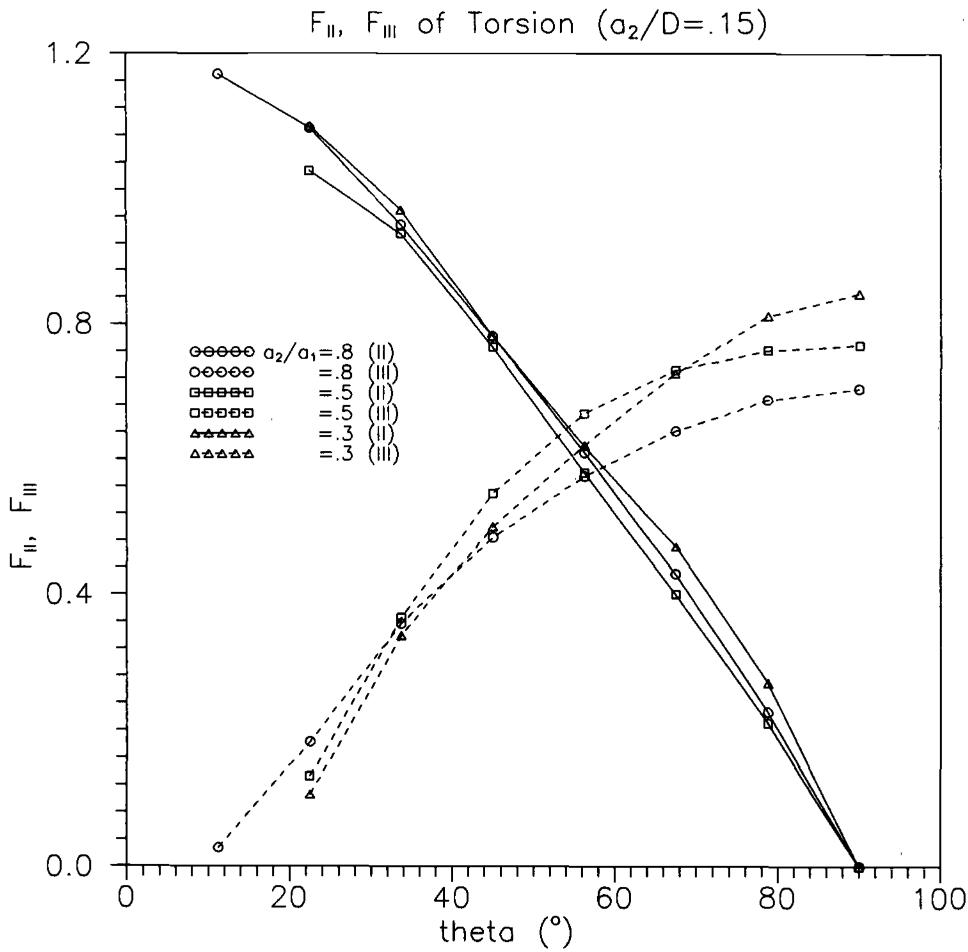

FIG. 12—F_{II} *and* F_{III} *of* a_2/D = *0.15*.

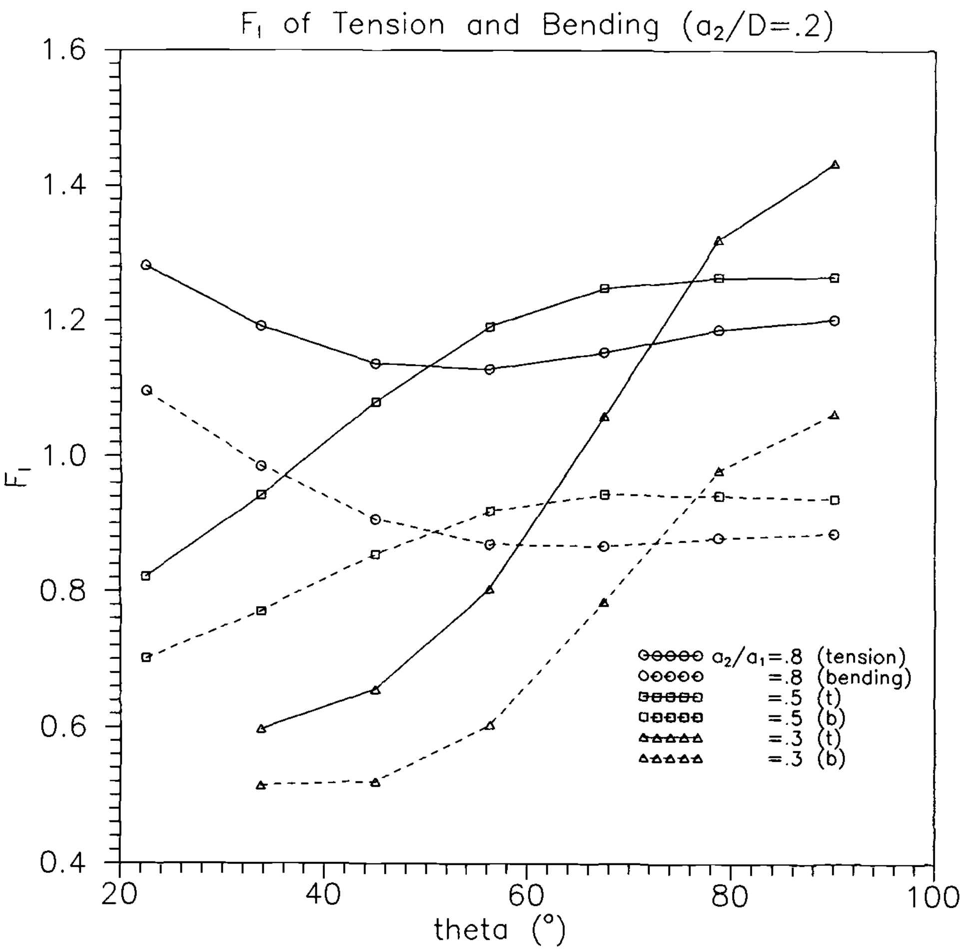

FIG. 13—F_I of $a_2/D = 0.2$.

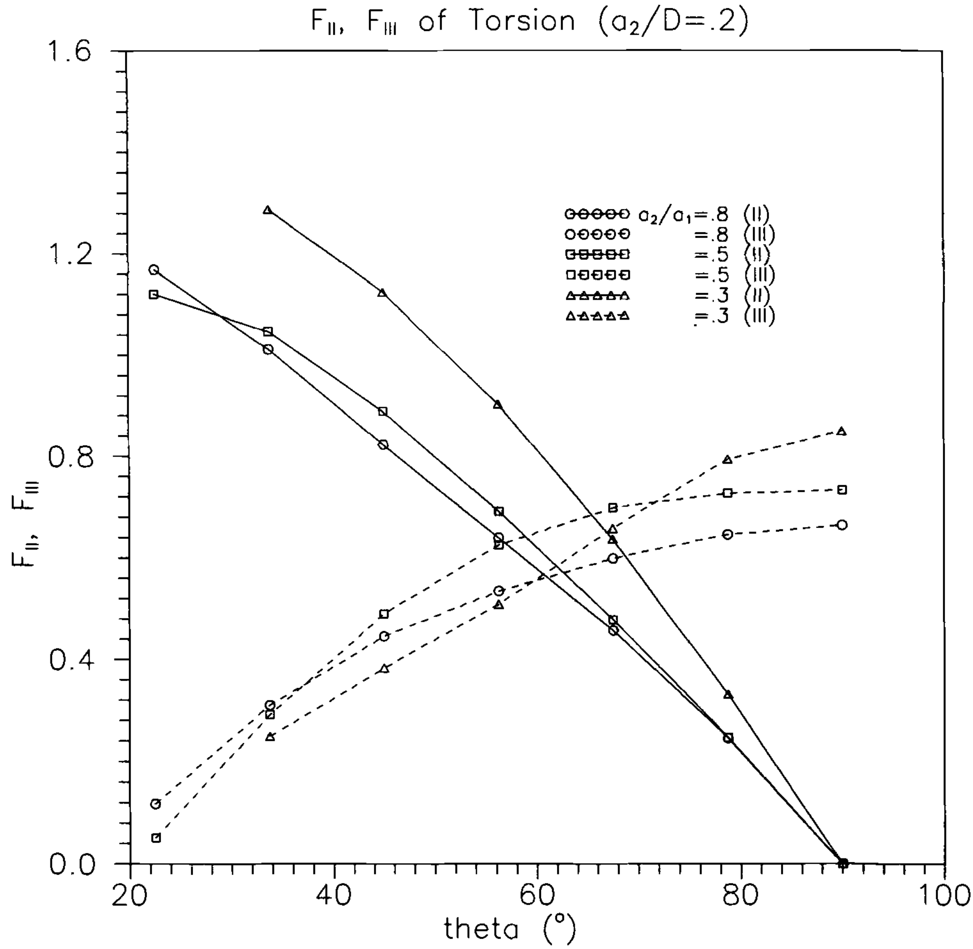

FIG. 14—F_{II} *and* F_{III} *of* a_2/D = *0.2.*

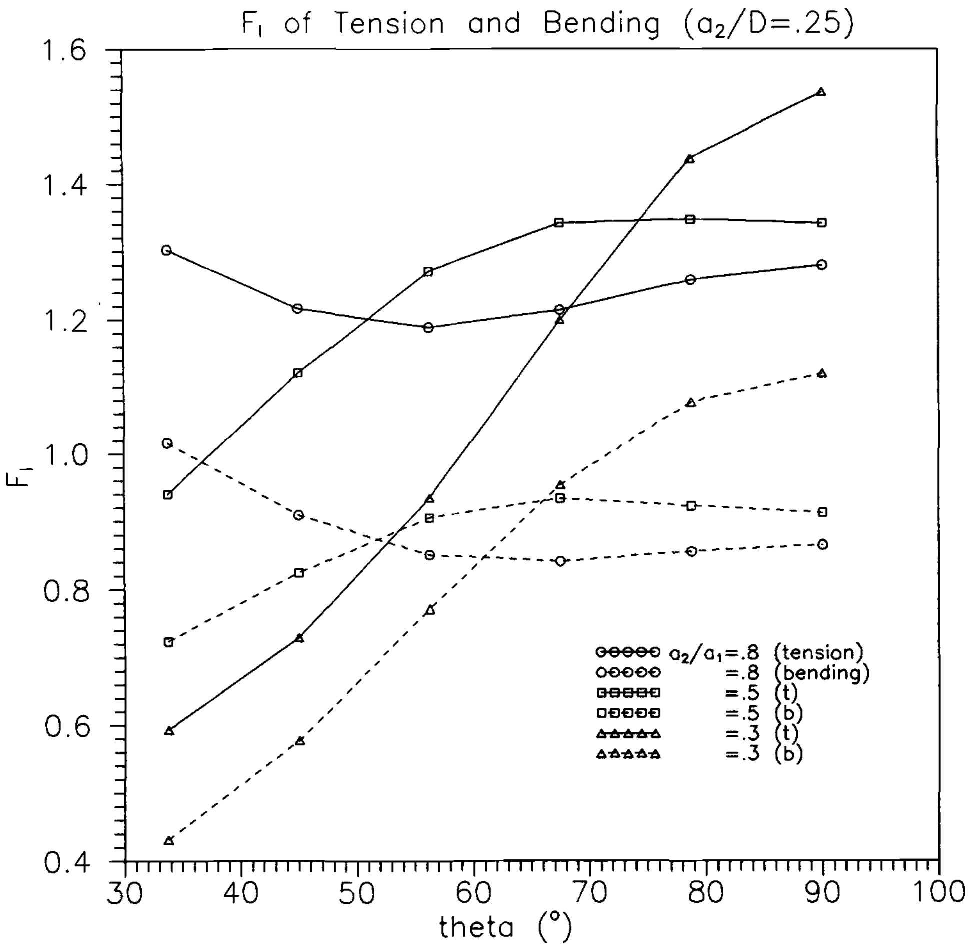

FIG. 15—F_I of a_2/D = 0.25.

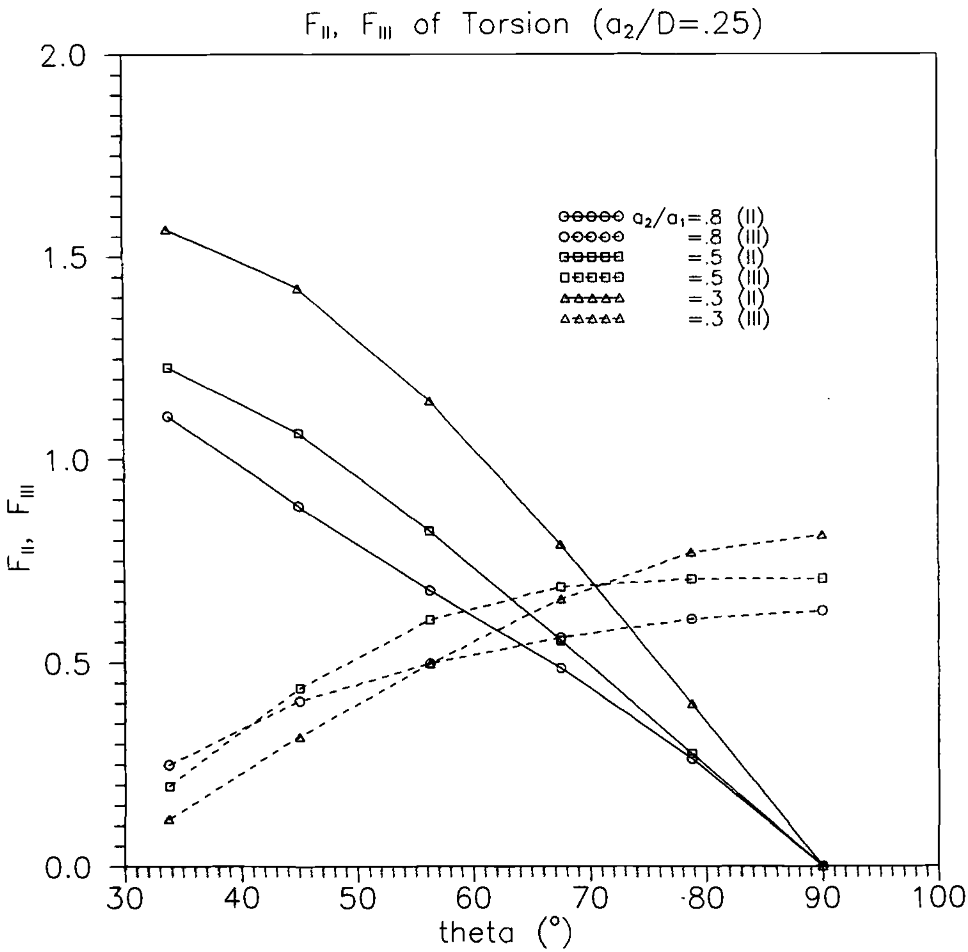

FIG. 16—F_{II} *and* F_{III} *of* a_2/D = *0.25.*

References

[1] Raju, I. S. and Newman, J. C., "Stress-Intensity Factors for Circumferential Surface Cracks in Pipes and Rods under Tension and Bending Loads," *Fracture Mechanics: Seventeenth Volume, ASTM STP 905*, J. H. Underwood, R. Chait, C. W. Smith, D. P. Wilhem, W. A. Andrews, and J. C. Newman, Eds., American Society for Testing and Materials, Philadelphia, 1986, pp. 789–805.

[2] Vijayakumar, K. and Atluri, S. N., "An Embedded Elliptical Crack in an Infinite Solid, Subject to Arbitrary Crack-Face Tractions," *Journal of Applied Mechanics*, Vol. 48, 1981, pp. 88–96.

[3] Nishioka, T. and Atluri, S. N., "Analytical Solution for Embedded Elliptical Cracks, and Finite Element Alternating Method for Elliptical Surface Cracks, Subjected to Arbitrary Loadings," *Engineering Fracture Mechanics*, Vol. 17, 1983, pp. 247–268.

[4] Kuo, A. Y. and Shvarts, S., "An Analytical Solution for an Elliptical Crack in a Flat Plate Subjected to Arbitrary Loading," *Fracture Mechanics: Twenty-Second Symposium, ASTM STP 1131*, Vol. 2, S. N. Atluri, J. C. Newman, Jr., and J. S. Epstein, Eds., American Society for Testing and Materials, Philadelphia, 1992, pp. 347–367.

[5] Sih, G. C., "A Review of the Three-Dimensional Stress Problem for a Cracked Plate," *International Journal of Fracture Mechanics*, Vol. 7, 1971, pp. 39–61.

[6] Benthem, J. P., "State of Stress at the Vortex of a Quarter-Infinite Crack in a Half-Space," *International Journal of Solids Structures*. Vol. 13, 1977, pp. 479–492.

[7] Benthem, J. P., "The Quarter-Infinite Crack in a Half-Space; Alternative and Additional Solutions," *International Journal of Solids Structures*, Vol. 16, 1980, pp. 119–130.

[8] Bazant, Z. P. and Estenssoro, L. F., "General Numerical Method for Three Dimensional Singularities in Cracked or Notched Elastic Solids," *Advances in Research on the Strength and Fracture of Materials*, Vol. 3A, D. M. R. Taplin, Ed., Pergamon Press, Oxford, 1977, pp. 371–385.

[9] Bazant, Z. P. and Estenssoro, L. F., "Surface Singularity and Crack Propagation," *International Journal of Solids Structures*, Vol. 15, 1979, pp. 405–426.

[10] Shivakumar, K. N. and Raju, I. S., "Treatment of Singularities in a Middle-Crack Tension Specimen," *Fracture Mechanics: Twenty-First Symposium, ASTM STP 1074*, J. P. Gudas, J. A. Joyce, and E. M. Hackett, Eds., American Society for Testing and Materials, Philadelphia, 1990, pp. 470–489.

[11] Atluri, S. N., *Computational Methods in Mechanics, Vol. 2—Computational Methods in the Mechanics of Fracture*. Elsevier, New York, 1986.

[12] Trefftz, E., *Handbuch der Physik*, Vol. 6, Springer-Verlag, Berlin, 1928.

[13] Kassir, M. K. and Sih, G. C., "Embedded Elliptical Crack," *Mechanics of Fracture, Vol. 2, Three-Dimensional Crack Problems*, Noordhoff International Publishing, Leyden, 1975, pp. 74–117.

[14] Chen, K. L., Kuo, A. Y., and Shvarts, S., "An Alternating Analytical Procedure for Cracked Cylindrical Structures Subjected to Arbitrary Loading," *Journal of Applied Mechanics*, submitted for publication.

Sambi R. Mettu[1] *and Royce G. Forman*[2]

Analysis of Circumferential Cracks in Circular Cylinders Using the Weight-Function Method

REFERENCE: Mettu, S. R. and Forman, R. G., "**Analysis of Circumferential Cracks in Circular Cylinders Using the Weight-Function Method,**" *Fracture Mechanics: Twenty-Third Symposium, ASTM STP 1189,* Ravinder Chona, Ed., American Society for Testing and Materials, Philadelphia, 1993, pp. 417–440.

ABSTRACT: Circumferential cracks in hollow circular cylinders are often used as idealizations of flaws in weldments caused by lack of penetration. The most common cases occur for butt welds in pipes, nozzles, and cylindrical pressure vessels. The objective of the present work is to develop a methodology to compute accurately values of stress intensity factor for the entire range of radius ratio, R_i/R_o (inner to outer), from 0 to 0.9999 and crack-depth-to-thickness ratio, a/t, from 0 to 1.0 for general loading using the weight-function approach. The *p*-version of the finite-element method was used to obtain stress intensity factors and crack face displacements for the reference loading of uniform tension. The reference solution was obtained for selected values of the geometrical parameters, R_i/R_o and a/t, covering their whole range. Both internal and external cracks were treated. Piecewise cubic Hermite interpolation techniques were then used to compute the quantities corresponding to intermediate values of the geometrical parameters. The derivatives of crack face displacements needed in the weight function method were obtained numerically from a three-term Williams series fit to the displacements obtained from the finite-element analysis. The results obtained were compared to existing solutions for uniform tension loading and excellent agreement was found. Results for uniform tension loading obtained from the weight function method were compared with those from finite-element analysis and error bounds were established.

KEY WORDS: fracture mechanics, circumferential cracks, hollow cylinder, pipes, weight function, stress intensity factor, *p*-version finite element, axisymmetric loading, fatigue (materials)

Circumferential cracks in hollow circular cylinders are often used as idealizations of flaws in weldments caused by lack of penetration. The most common cases occur for butt welds in pipes, nozzles, and cylindrical pressure vessels. The flaws could be present either internally or externally. The idealization referred to is performed usually during the assessment of structural integrity of the pressure vessels or pipelines using fatigue and fracture mechanics concepts. Current work is motivated by the need to perform safe-life and fracture control analyses of critical hardware used in the Space Shuttle, the Space Station, and associated payloads. In particular, accurate values of the stress intensity factors are essential for any such assessment.

The available stress intensity factors for these crack cases are limited to uniform tension and bending loading [*1*]. In these solutions, the ratio of crack depth to thickness (a/t) is also limited to 0 to 0.6, and extrapolated values are shown by Tada [*1*] for the deeper cracks. Moreover, for the case of very thin cylindrical parts, where the ratio of internal to external radius (R_i/R_o) is more than 0.9, no solution is available in the open literature. Residual stresses with arbitrary

[1] Advanced systems engineering specialist, Lockheed Engineering and Sciences Company, Houston, TX 77058.
[2] Senior materials engineer, NASA Lyndon B. Johnson Space Center, Houston, TX 77058.

variation across the thickness occur quite often in these cylindrical vessels and hence stress intensity factor solutions for this type of axisymmetric loading are desirable. Labbens et al. [2] derived influence functions for various planar crack cases including the internal crack in an axisymmetric body subjected to general loading, but the numerical results were presented for only one ratio of R_i/t. Another attempt at obtaining a somewhat general solution for the circumferential crack in a cylinder was made by Buchalet and Bamford [3] who used the conventional finite-element method to compute the stress intensity factors when the cylinder is subjected to constant, linear, quadratic, and cubic variations of load. These component solutions were then used in a superposition type of fit for a general applied stress. The results were again presented only for one ratio of t/R_i.

In the present work, the weight function approach [4] was used to provide the desired solution by specializing it to the axisymmetric case from the three-dimensional formulation. The key to the success of the approach is the ability to compute accurately stress intensity factors and crack surface displacements for a reference loading such as uniform tension. Once a reference solution is known, the weight function method provides solutions for arbitrary through-the-thickness stress distribution such as thermal or bending stresses by way of numerical quadrature. In order to provide a solution for any given value of the geometrical parameters, R_i/R_o and a/t, it is apparent that the reference solution should be obtained for selected values of these geometrical parameters covering their whole range. Interpolation techniques can then be used to obtain the solution for the desired values of the parameters.

In order to generate the reference solution, use of the general-purpose finite-element programs CSA/NASTRAN [5] and MSC/PROBE [6] was considered. NASTRAN uses the more common h-version of the finite-element formulation whereas PROBE uses the p-version formulation. It was evident from a few trials that for the present problems, MSC/PROBE was more accurate and efficient than NASTRAN. PROBE also has a solution-extraction facility including computation of the strain energy release rate. Axisymmetric loading was considered in all cases, and solutions were obtained for the entire range of radius ratio and crack-depth ratio for the reference case of uniform tension. The weight-function approach was used to generalize the solution for arbitrary axisymmetric loading. The following sections present the details of the finite-element analysis, the method of weight function for axisymmetric bodies, and a discussion of the results.

Finite-Element Analysis

In order to obtain the stress intensity factors and crack face displacements for arbitrary geometrical parameters of the hollow cylinder with an internal or external crack, numerical finite-element methods seemed to be the only choice. The general-purpose finite-element software CSA/NASTRAN was considered initially, and trial runs were made. Two meshes were constructed, one having 48 elements along the plane of symmetry and the second having 96 elements along the plane of symmetry. Figure 1 shows the geometry of the cracked hollow cylinder and Fig. 2 shows the meshes used. The same configuration was analyzed using MSC/PROBE by using a much coarser mesh as shown in Fig. 3. Comparison of the results for these pilot cases is summarized in Table 1. The ease of preparing the mesh and the efficiency as well as accuracy of PROBE compared to CSA/NASTRAN for this class of problems weighed heavily in favor of PROBE. All subsequent analyses were conducted using the axisymmetric module of PROBE.

It may be noted that the detailed view of the mesh in Fig. 3, where very small elements around the crack tip rapidly increased in size away from it, was the mesh pattern that yielded

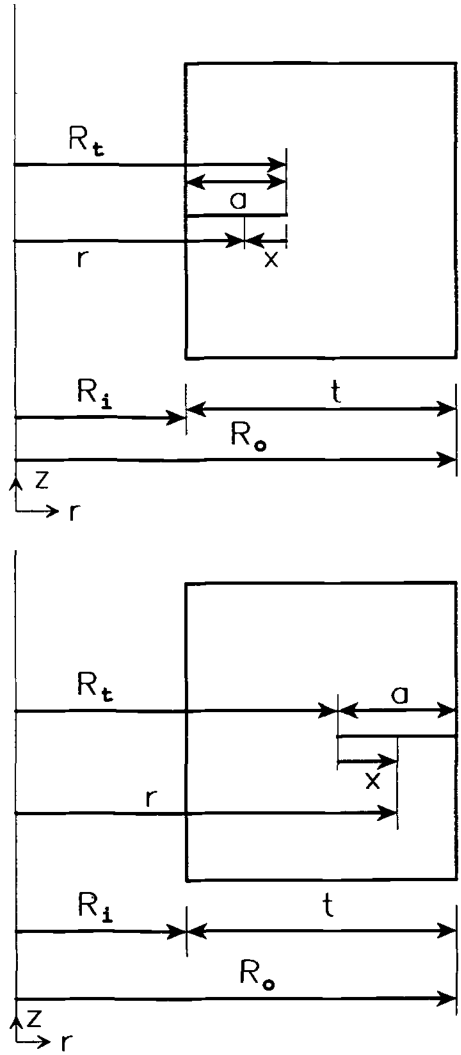

FIG. 1—*Geometry of cracked hollow cylinders: internal and external.*

TABLE 1—*Comparison of results, NASTRAN versus PROBE; internal crack,* R_i/R_o = *0.5,* a/t = *0.5, and* t = *1 m.*

Software Used	Mesh or p	Elements	Degrees of Freedom	Strain energy, N-m	CMOD,[a] m
CSA/NASTRAN	M-48	2408	2678	0.31984586E-5	0.4352E-6
CSA/NASTRAN	M-96	3320	3652	0.31985511E-5	0.4411E-6
MSC/PROBE	CYL5, p = 6	22	845	0.31995647E-5	0.4583E-6
MSC/PROBE	CYL5, p = 7	22	1129	0.31996307E-5	0.4588E-6
MSC/PROBE	CYL5, p = 8	22	1457	0.31996421E-5	0.4589E-6

[a] CMOD—crack mouth opening displacement from Ref *1* = 0.4625E-6 m.

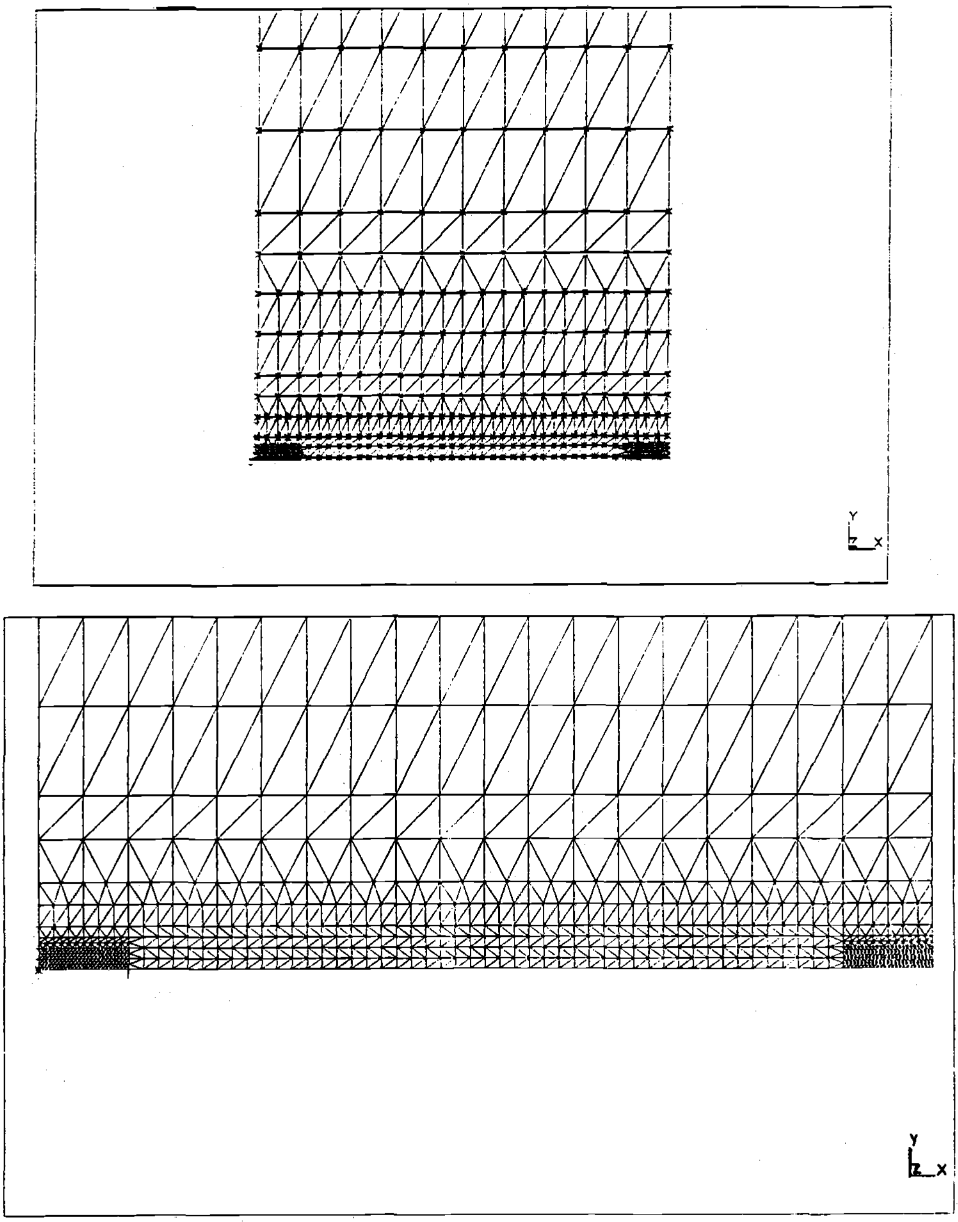

FIG. 2—*NASTRAN models of the cylinder.*

good results. For convenience in modeling, the thickness of the cylinder was set to unity, so that the same mesh could be used for various ratios of the inner to outer radii. In order to cover the entire range of crack lengths, three meshes were used, as shown in Figs. 3, 4, and 5. Two local coordinate systems were defined, one with the origin at the inner wall (S1) and the other at the crack tip (S2). The S1 system was redefined for each ratio of R_i/R_o. The S2 system was

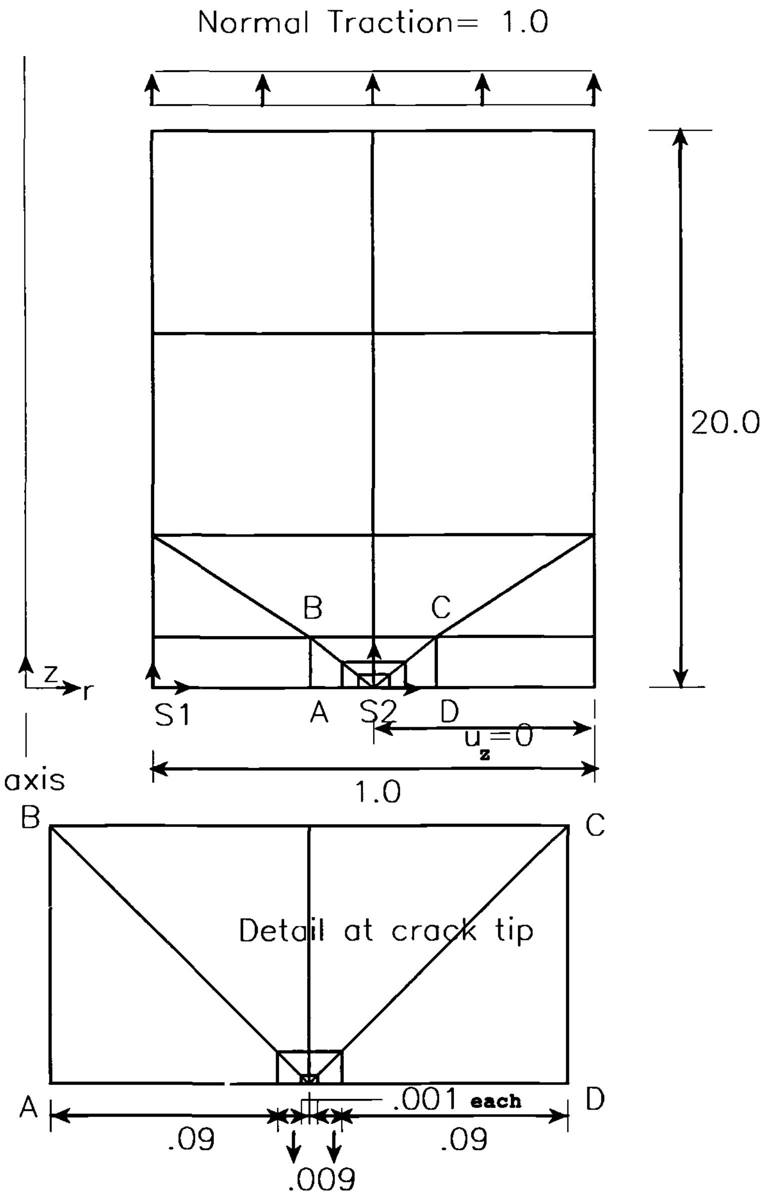

FIG. 3—*PROBE model of the cylinder for* a/t = *0.15 to 0.85.*

redefined for each crack length to thickness ratio (a/t). For the internal crack case, the mesh in Fig. 3 was used for shallow cracks, that is, with a/t ratios of 0.02, 0.05, and 0.1. The same mesh was used for deep external cracks, that is, a/t ratios of 0.9, 0.95, 0.985. The mesh in Fig. 4 was used for the midrange of a/t ratios from 0.15 to 0.85 for both internal and external cracks. Similarly, the mesh in Fig. 5 was used for deep internal cracks and shallow external cracks. Thus, just these three meshes were used repeatedly for generating the entire spectrum

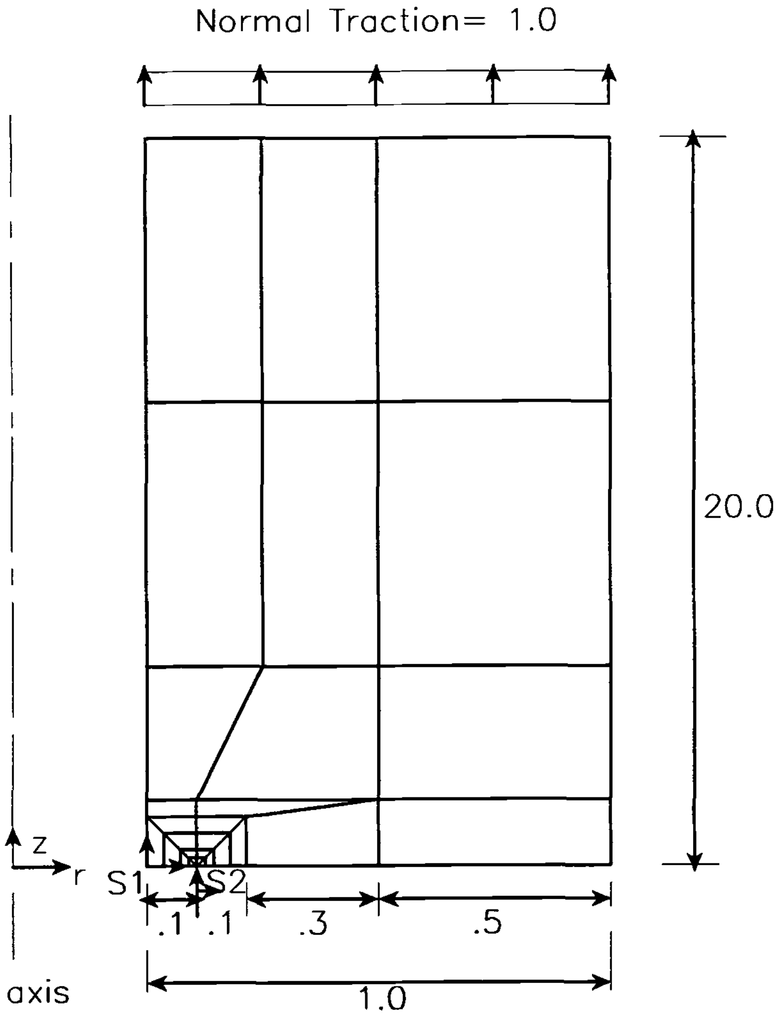

FIG. 4—*PROBE model of the cylinder for* a/t = *0.02 to 0.1.*

of solutions by simply redefining the local coordinate systems. Table 2 shows a sample set of results including the error in energy norm for a radius ratio of $R_i/R_o = 0.5$. The error in the energy norm is computed by PROBE as part of the solution whenever three successive values of the polynomial order (p, used for defining element shape functions) are specified. In the current work, all solutions were obtained for Orders 6, 7, and 8 that are the three highest possible with PROBE. Values from Order $p = 8$ were taken to be the most accurate and used in subsequent analysis. Table 2 also shows a comparison of strain energy release rates obtained by two methods with those from results found in Tada [*1*]. The column showing G calculated from U is obtained by a central difference method on successive values of the total strain energy given in the second column. PROBE also directly gives values of the strain energy release rate, using the stiffness derivative method internally. The results show excellent agreement with those of Ref *1*. Table 3 lists the stress intensity correction factor, F_{int}, as defined in

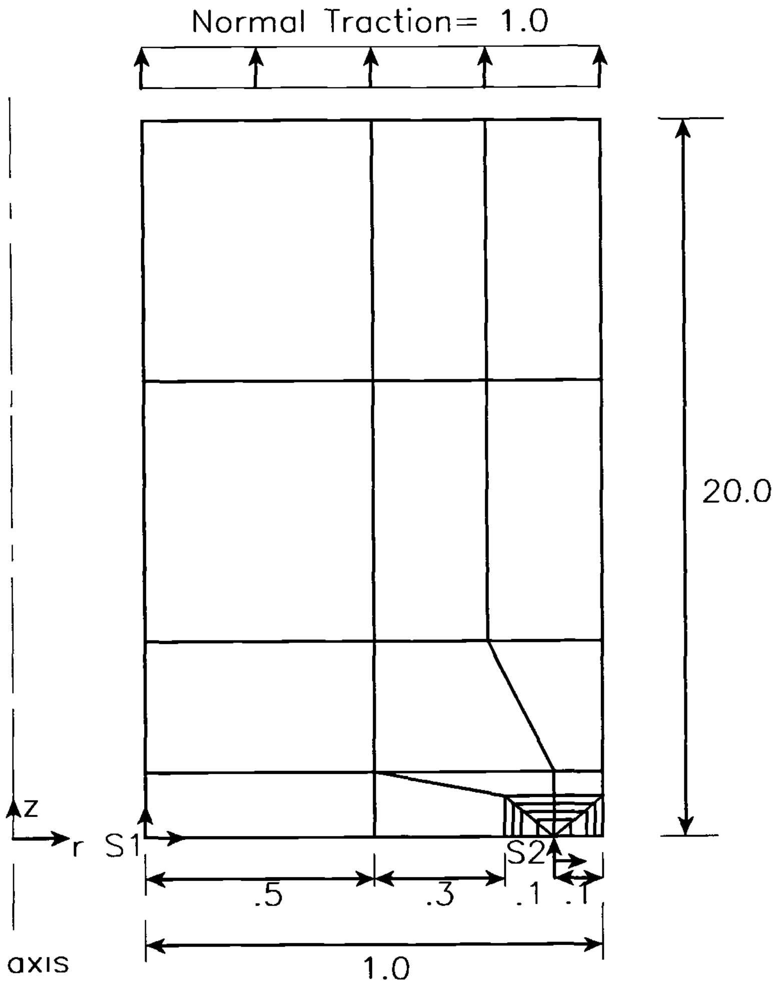

FIG. 5—*PROBE model of the cylinder for* a/t = *0.9 to 0.985.*

Ref *1* for each of the parameters, R_i/R_o and a/t, for the internal crack. The stress intensity factor is defined by

$$K_I = \sigma_0 F_0 \sqrt{\pi a} \tag{1}$$

where σ_0 is the applied uniform tensile stress. The correction factors listed in Table 3 are defined as

$$F_{int} = F_0 \sqrt{1 - a/t} \tag{2}$$

Table 4 lists similar results for the external crack. Here, the stress intensity factor is defined as in Eq 1 but the correction factors are defined as

$$F_{ext} = F_0 \sqrt{1 - a/t}/(1 + R_o/R_i \tag{3}$$

TABLE 2—*Strain energy release rates; internal crack,* R_i/R_o = *0.5.*

Crack Length	Total Strain Energy from PROBE, $U/2\pi$ (N-M)	Error in U, %	Energy Release Rates G from U, N/m	G-PROBE, N/m	G-Tada, N/m
0.02	0.500011898602E-6	0.04	...	0.231E-8	0.245E-8
0.05	0.500074337211E-6	0.08	0.569E-8	0.561E-8	...
0.10	0.500298633244E-6	0.09	0.110D-7	0.109E-7	0.109E-7
0.15	0.500678639535E-6	0.06	0.161D-7	0.160E-7	...
0.20	0.501224824881E-6	0.06	0.212E-7	0.211E-7	0.213E-7
0.25	0.501952678092E-6	0.07	0.265E-7	0.263E-7	...
0.30	0.502882231740E-6	0.09	0.321E-7	0.319E-7	0.322E-7
0.35	0.504038927616E-6	0.10	0.381E-7	0.378E-7	...
0.40	0.505454734349E-6	0.10	0.447E-7	0.444E-7	0.451E-7
0.45	0.507170530015E-6	0.10	0.522E-7	0.518E-7	...
0.50	0.509238881717E-6	0.10	0.608E-7	0.603E-7	0.617E-7
0.55	0.511728752117E-6	0.10	0.709E-7	0.703E-7	...
0.60	0.514733435320E-6	0.10	0.832E-7	0.823E-7	0.836E-7
0.65	0.518382319681E-6	0.11	0.985E-7	0.974E-7	...
0.70	0.522863665248E-6	0.13	0.119E-6	0.117E-6	0.119E-6
0.75	0.528465995935E-6	0.16	0.146E-6	0.144E-6	...
0.80	0.535667611660E-6	0.19	0.188E-6	0.183E-6	0.181E-6
0.85	0.545355901859E-6	0.24	0.258E-6	0.247E-6	...
0.90	0.559506750351E-6	0.22	0.411E-6	0.372E-6	0.361E-6
0.95	0.584370634122E-6	0.40	0.705E-6	0.741E-6	...
0.985	0.628214014703E-6	0.62	...	0.245E-5	0.241E-5

TABLE 3—*Stress intensity correction factors; internal crack,* F_{int}.

Crack Length, a/t	Values of R_i/R_o 0.1	0.2	0.3	0.4	0.5	0.6	0.7	0.8	0.9	0.95	0.99	0.995	0.999	0.9999
0.02	0.997	1.050	1.071	1.082	1.089	1.094	1.098	1.101	1.103	1.105	1.106	1.106	1.105	1.166
0.05	0.891	0.976	1.017	1.042	1.058	1.070	1.080	1.088	1.095	1.099	1.103	1.104	1.105	1.107
0.10	0.792	0.887	0.944	0.983	1.013	1.037	1.057	1.076	1.094	1.105	1.117	1.120	1.124	1.133
0.15	0.733	0.823	0.887	0.935	0.975	1.009	1.040	1.071	1.103	1.124	1.148	1.153	1.164	1.168
0.20	0.688	0.773	0.839	0.893	0.941	0.984	1.026	1.069	1.119	1.151	1.191	1.202	1.220	1.226
0.25	0.654	0.732	0.799	0.857	0.911	0.962	1.014	1.070	1.139	1.185	1.246	1.265	1.292	1.298
0.30	0.625	0.698	0.764	0.825	0.883	0.942	1.004	1.073	1.162	1.225	1.313	1.340	1.383	1.386
0.35	0.601	0.670	0.734	0.797	0.859	0.923	0.993	1.076	1.185	1.269	1.390	1.429	1.492	1.500
0.40	0.580	0.645	0.708	0.771	0.836	0.905	0.983	1.078	1.210	1.315	1.477	1.533	1.624	1.634
0.45	0.560	0.622	0.684	0.748	0.815	0.888	0.973	1.078	1.233	1.362	1.575	1.651	1.782	1.797
0.50	0.543	0.603	0.664	0.727	0.795	0.871	0.961	1.076	1.253	1.407	1.677	1.786	1.974	1.996
0.55	0.528	0.585	0.645	0.708	0.777	0.855	0.948	1.071	1.267	1.447	1.793	1.936	2.208	2.239
0.60	0.514	0.569	0.628	0.690	0.759	0.838	0.933	1.062	1.274	1.479	1.908	2.102	2.499	2.547
0.65	0.502	0.555	0.612	0.674	0.742	0.820	0.916	1.047	1.271	1.498	2.019	2.279	2.868	2.944
0.70	0.491	0.543	0.599	0.659	0.725	0.802	0.897	1.027	1.255	1.499	2.114	2.456	3.347	3.474
0.75	0.481	0.532	0.586	0.644	0.709	0.783	0.875	1.001	1.225	1.474	2.171	2.611	3.987	4.219
0.80	0.473	0.523	0.575	0.631	0.692	0.763	0.849	0.966	1.176	1.417	2.161	2.701	4.873	5.334
0.85	0.467	0.514	0.565	0.618	0.676	0.741	0.819	0.924	1.108	1.324	2.047	2.649	6.123	7.191
0.90	0.462	0.508	0.555	0.605	0.658	0.717	0.785	0.872	1.019	1.187	1.789	2.354	7.756	10.887
0.95	0.458	0.502	0.546	0.592	0.640	0.690	0.745	0.811	0.910	1.012	1.371	1.733	8.347	21.728
0.985	0.456	0.498	0.540	0.583	0.626	0.670	0.715	0.764	0.823	0.869	0.996	1.118	4.274	61.478

TABLE 4—*Stress intensity correction factors; external crack,* F_{ext}.

Crack Length, a/t	Values of R_i/R_o													
	0.1	0.2	0.3	0.4	0.5	0.6	0.7	0.8	0.9	0.95	0.99	0.995	0.999	0.9999
0.02	0.102	0.186	0.258	0.319	0.371	0.418	0.458	0.494	0.526	0.541	0.552	0.554	0.555	0.566
0.05	0.101	0.186	0.257	0.318	0.370	0.416	0.456	0.492	0.524	0.539	0.551	0.553	0.554	0.577
0.10	0.101	0.185	0.256	0.316	0.369	0.415	0.455	0.492	0.526	0.542	0.557	0.560	0.563	0.560
0.15	0.101	0.184	0.255	0.315	0.368	0.414	0.456	0.495	0.533	0.553	0.572	0.576	0.582	0.579
0.20	0.101	0.184	0.254	0.314	0.367	0.415	0.458	0.500	0.543	0.567	0.594	0.600	0.610	0.607
0.25	0.102	0.184	0.254	0.314	0.367	0.416	0.461	0.507	0.556	0.586	0.622	0.632	0.646	0.646
0.30	0.103	0.185	0.254	0.314	0.367	0.417	0.465	0.514	0.570	0.607	0.655	0.670	0.691	0.695
0.35	0.104	0.187	0.256	0.315	0.368	0.418	0.467	0.521	0.585	0.631	0.694	0.714	0.746	0.748
0.40	0.107	0.190	0.257	0.316	0.369	0.419	0.470	0.527	0.600	0.655	0.738	0.766	0.812	0.817
0.45	0.110	0.193	0.260	0.317	0.370	0.420	0.472	0.532	0.615	0.680	0.787	0.826	0.891	0.898
0.50	0.114	0.197	0.264	0.320	0.371	0.421	0.473	0.536	0.627	0.705	0.841	0.893	0.987	0.997
0.55	0.119	0.203	0.268	0.323	0.373	0.421	0.474	0.539	0.637	0.726	0.897	0.969	1.104	1.119
0.60	0.125	0.210	0.274	0.327	0.375	0.422	0.473	0.539	0.643	0.744	0.956	1.052	1.250	1.273
0.65	0.133	0.218	0.281	0.332	0.377	0.422	0.472	0.536	0.644	0.755	1.012	1.141	1.434	1.472
0.70	0.143	0.229	0.289	0.337	0.379	0.421	0.468	0.530	0.638	0.756	1.059	1.230	1.674	1.737
0.75	0.156	0.242	0.299	0.344	0.383	0.421	0.463	0.521	0.625	0.745	1.088	1.307	1.994	2.109
0.80	0.173	0.258	0.312	0.352	0.386	0.419	0.457	0.508	0.602	0.717	1.083	1.352	2.438	2.667
0.85	0.197	0.279	0.327	0.361	0.390	0.418	0.448	0.490	0.570	0.670	1.026	1.326	3.063	3.596
0.90	0.232	0.306	0.346	0.373	0.395	0.415	0.438	0.468	0.527	0.603	0.897	1.178	3.880	5.444
0.95	0.288	0.345	0.372	0.389	0.401	0.413	0.425	0.442	0.474	0.516	0.688	0.868	4.175	10.865
0.985	0.358	0.386	0.397	0.403	0.408	0.412	0.416	0.421	0.432	0.445	0.500	0.560	2.138	30.741

Weight-Function Method

The basic formulation of the weight-function method was given by Rice [*4*]. Specializing the three-dimensional formulation given in the appendix of Ref *4*, one can write the stress intensity factor for an axisymmetric body in the following form

$$K_{\rm I} = \frac{1}{2\pi R_t}\int_{r_1}^{r_2} h(r,a)\sigma(r)2\pi r dr \tag{4}$$

Here, r_1, r_2 are two radii between which the stress, $\sigma(r)$ (arbitrary stress distribution), is applied at the location of the crack across the thickness of the cylinder. Referring to the coordinate system shown in Fig. 1 and changing the variable of integration to x, (noting $r = R_t + cx$, $dr = cdx$, etc.) one gets

$$K_{\rm I} = \frac{1}{2\pi R_t}\int_{0}^{a} h(x,a)\sigma(x)2\pi(R_t + cx)dx \tag{5}$$

where the weight function, $h(x,a)$, is given by

$$h(x,a) = \frac{H}{K_{\rm ref}}\frac{\partial u(x,a)}{\partial a} \tag{6}$$

where R_t is crack tip radius, $H = E/(1 - \nu^2)$ is a material parameter, E being Young's modulus, and ν being Poisson's ratio. The constant, c, should be set to -1 for an internal crack and $+1$ for an external crack so that the radial coordinate is measured from the center to a typical point, whereas the coordinate, x, is always measured from the crack tip towards the open end of the crack. The $K_{\rm ref}$ quantity is the stress intensity factor and the $u(x,a)$ quantity is the crack face displacement for the reference loading case. The usual factor 2 in the denominator of the right-hand side of Eq 6 is omitted due to the symmetry about the crack plane and integration is performed on only the upper crack face.

In order to proceed with the numerical integration, one needs the crack-face displacements expressed in a convenient equation form. Approximate equations describing the crack surface displacement profile were proposed by Orange [*7*] and Petroski and Achenbach [*8*]. Orange used a two-parameter conic section form for the displacement whereas Petroski and Achenbach used a two-parameter form based on stress intensity factor alone. In the present work, crack surface displacements obtained from PROBE for the reference loading case were curve-fitted using a three-term Williams series. The equation for the displacement normal to the crack face is assumed to be of the form

$$u(x,a) = A_1(a)x^{1/2} + A_2(a)x + A_3(a)x^{3/2} \tag{7}$$

for any given crack length. The crack length-dependent A_1, A_2, A_3 coefficients were determined from the finite-element displacement solution as follows. The first term represents the dominant singular term (in stresses) directly related to the stress intensity factor. Hence the constant, A_1, is given by

$$A_1 = \frac{4K_{\text{ref}}}{H\sqrt{2\pi}} \tag{8}$$

The remaining two coefficients were determined by making Eq 7 satisfy the displacement values at distances $x = (9/19)\,a$ and $x = a$. Figure 6 shows that the present three-term approach fits the finite-element results well. A trial-and-error method of fitting is necessary to obtain the conic-section parameter, m, if one uses the method of Ref *5*. Hence, the three-term method was used to fit the displacements from the finite-element results, as shown in Fig. 7 for the internal crack and Fig. 8 for the external crack at one of the radius ratios (0.5). Similar good fits were obtained for all the radius ratios. Minor deviations were observed for very deep cracks in relatively thick cylinders. A table of the three fitting coefficients for the chosen discrete values of R_i/R_o and a/t were prepared and used in conjunction with an interpolation scheme to determine values for arbitrary geometric parameters. Since there are 1764 ($2 \times 3 \times 14 \times 21$) values of these fitting coefficients, and they cannot be tabulated in hardcopy with good accuracy, they are not presented in this paper. However, they can be supplied electronically to interested users. The stress intensity solution was also tabulated (as in Tables 3 and 4) for the reference loading in a two-dimensional array form for similar use with the weight-function method. The partial derivative of the displacement is given by

$$\frac{\partial u(x,a)}{\partial a} = B_1(a)x^{1/2} + B_2(a)x + B_3(a)x^{3/2} + \frac{1}{2}A_1(a)x^{-1/2} + A_2(a) + A_3(a)x^{1/2} \tag{9}$$

The coefficients in the first three terms, $B_1(a)$, $B_2(a)$, and $B_3(a)$, are a result of direct numerical differentiation of the $A_1(a)$, $A_2(a)$, and $A_3(a)$ coefficients with respect to a. The latter three terms arise from the fact that the radial coordinate, x, measured from the crack tip varies with the crack length. This may be seen by rewriting Eq 7 in terms of a distance coordinate, z, of a generic point on the crack face such that $x = (a - z)$, differentiating with respect to a and changing the $(a - z)$ back to x.

The equation for the stress intensity factor was then applied for determining the solution for an arbitrary stress distribution across the thickness of the cylinder. The arbitrary stress can be

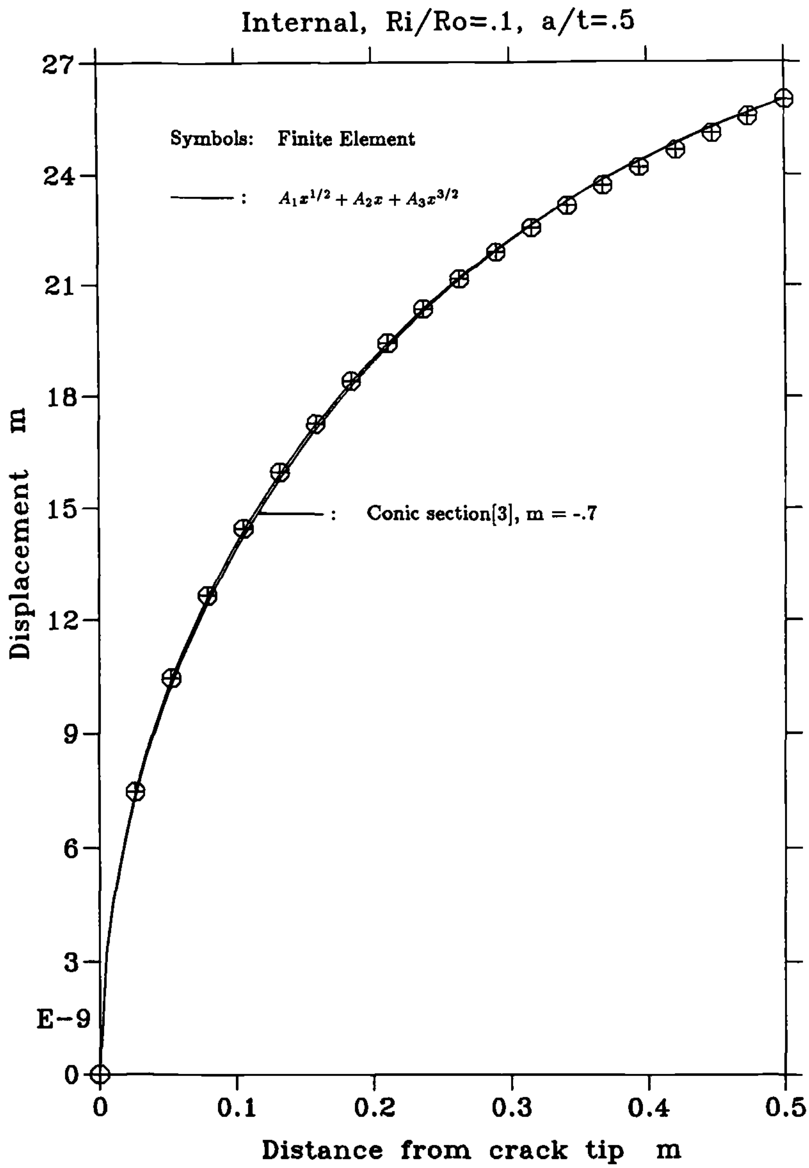

FIG. 6—*Comparison of displacement fit equations.*

expressed numerically as a function of nondimensional position along the crack face. The resulting stress intensity factor was computed by numerical quadrature. Since the integrand is singular at the crack tip, the singular term was dealt with separately. It was transformed into a nonsingular integrand by a change of variable (setting $y = \sqrt{x}$). Both the singular and the nonsingular parts were integrated using Simpson's rule. It was found that about 500 points were adequate for an accurate evaluation of the integral. FORTRAN routines were developed for these calculations and were incorporated into the NASA/FLAGRO software [9] used for fracture control analysis of Space Shuttle, payload, and Space Station structures.

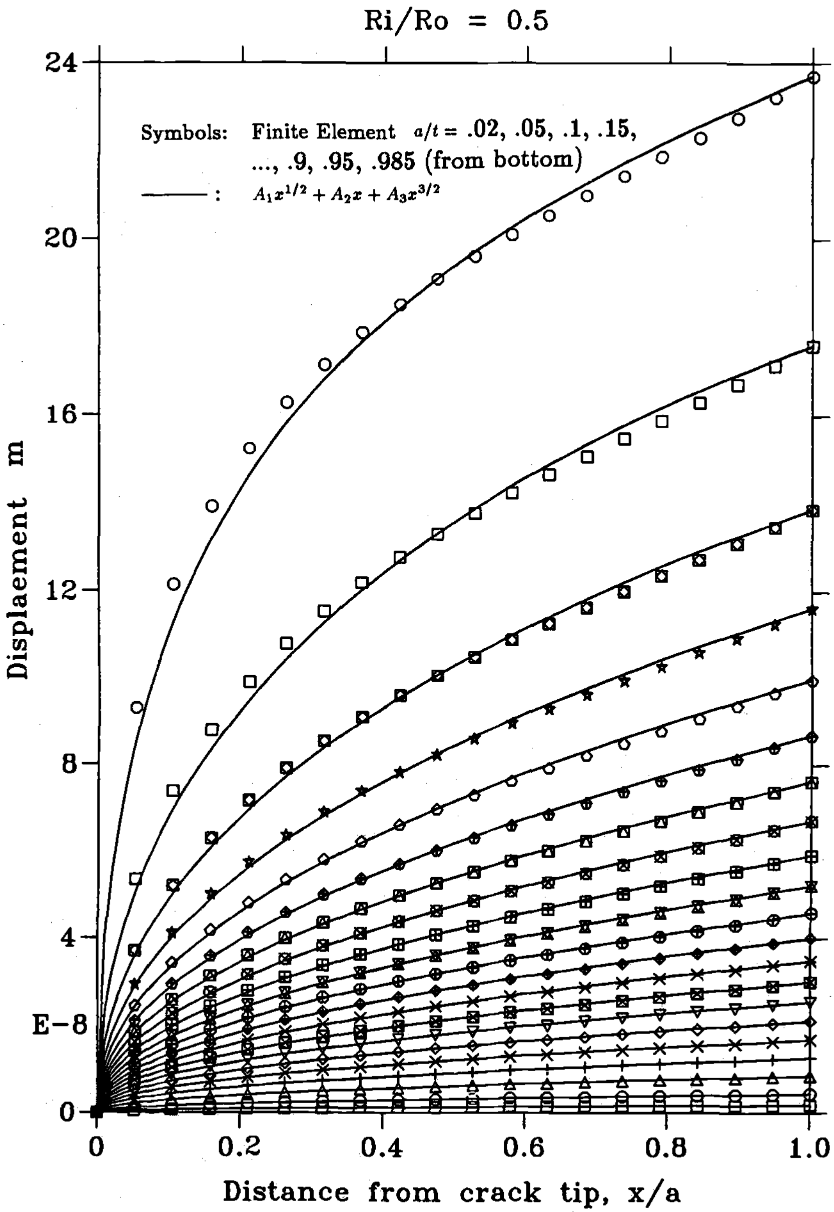

FIG. 7—*Crack surface displacements for an internal crack,* R_i/R_o = *0.5.*

Discussion

The stress intensity factors from finite-element analysis agreed to within 1% with known solutions [*1*]. The trends for very thin cylinders also appear to be reasonable. Solutions for the internal crack case are shown in Fig. 9, where the dashed line corresponding to the ratio, R_i/R_o = 0.9999, approaches the limiting solution of an edge crack in a plate. Similar results are

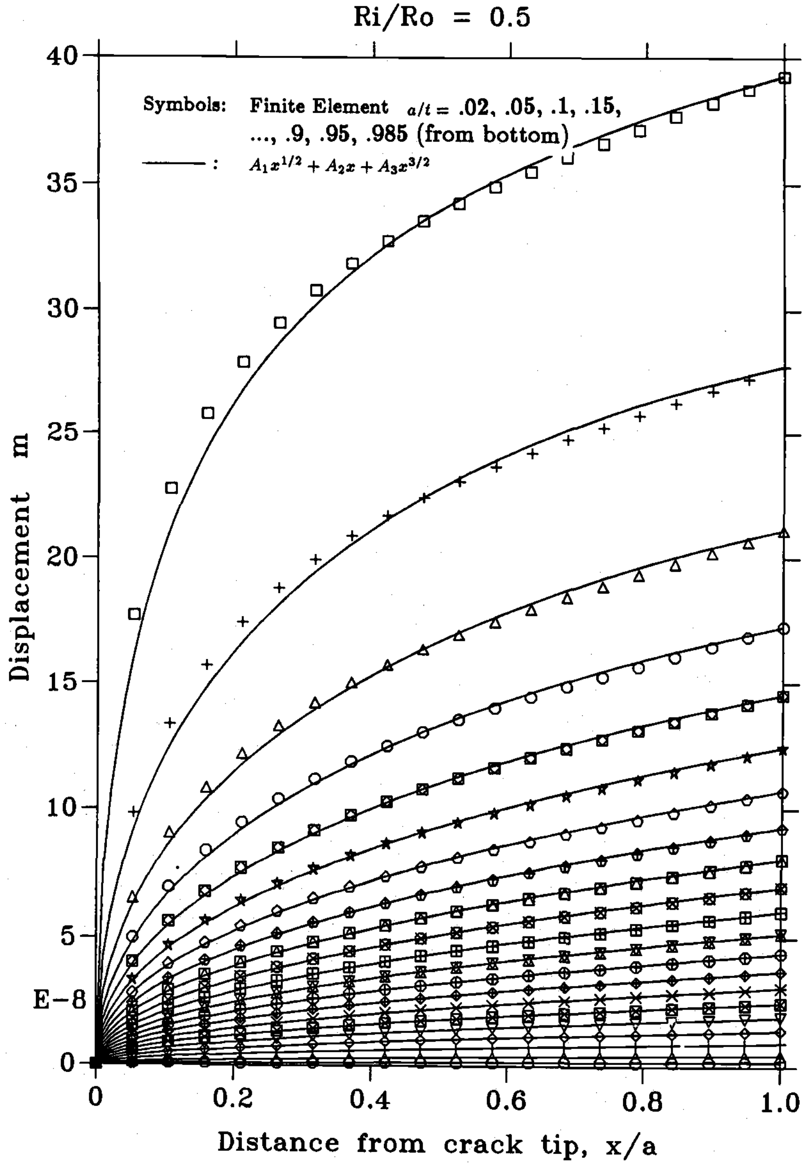

FIG. 8—*Crack surface displacements for an external crack,* R_i/R_o = *0.5.*

also shown for the case of an external crack in a cylinder in Fig. 10 where excellent agreement is found with the existing results. Assessment of errors in the weight-function approach was done as follows. For the uniform tension case, stress intensity factors were calculated using the weight function approach in order to compare them with the results obtained directly from PROBE. Figures 11 and 12 show these comparisons for internal and external cracks, respectively. In these two plots, the solid curves are the direct PROBE results, while the symbols denote results obtained from the weight-function method. The errors for each of the data

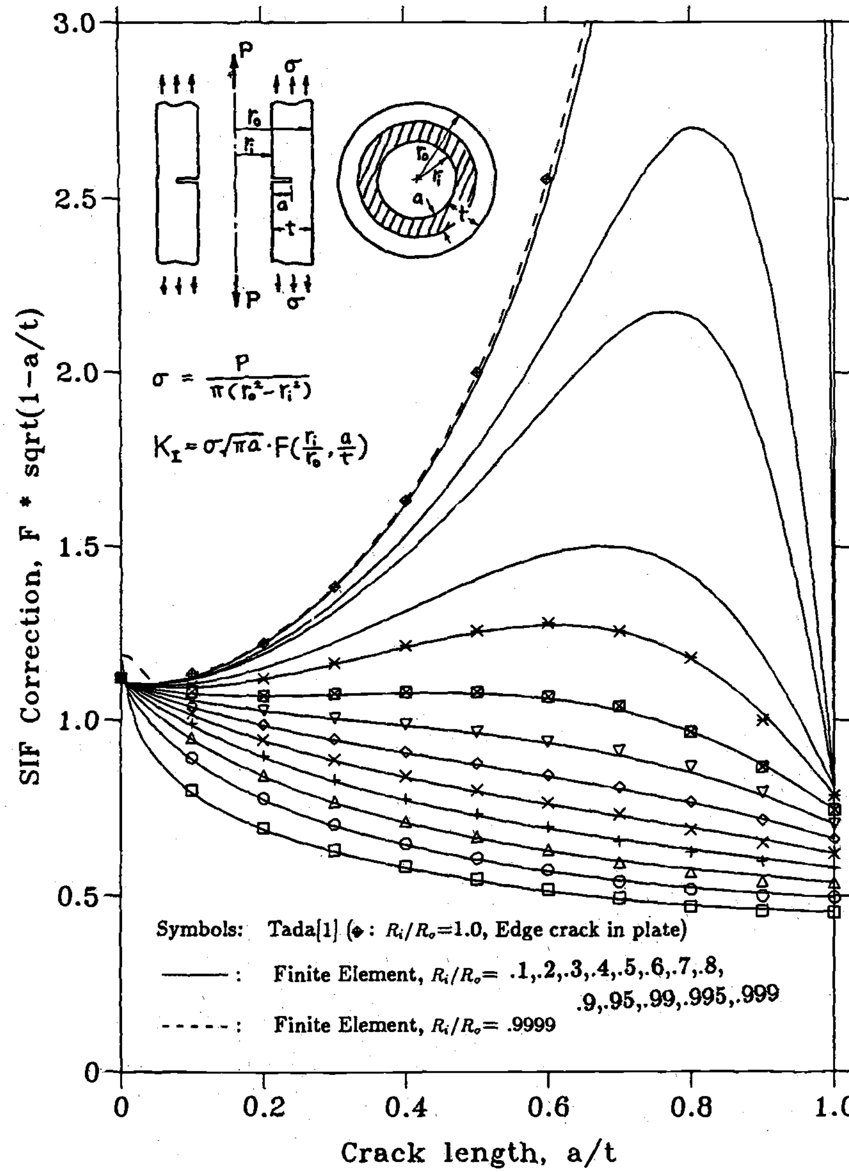

FIG. 9—*Correction factors, PROBE versus Ref* 1 *for an internal crack.*

points were calculated and plotted as in Figs. 13 and 14. It is found that the errors for the most part are less than about 2%. The exceptions are for very shallow (a/t = 0.02) internal cracks in thick cylinders where the error could be up to about 9% and deep ($a/t > 0.8$) cracks in both internal and external cases where the errors could be even higher. In order to establish the source of the error, the numerical integration was verified by a closed-form integration procedure for selected polynomial equations for the stress distribution (up to a cubic). Table 5 shows a sample of stress-intensity-factor values for a cylinder subjected to nonuniform loading

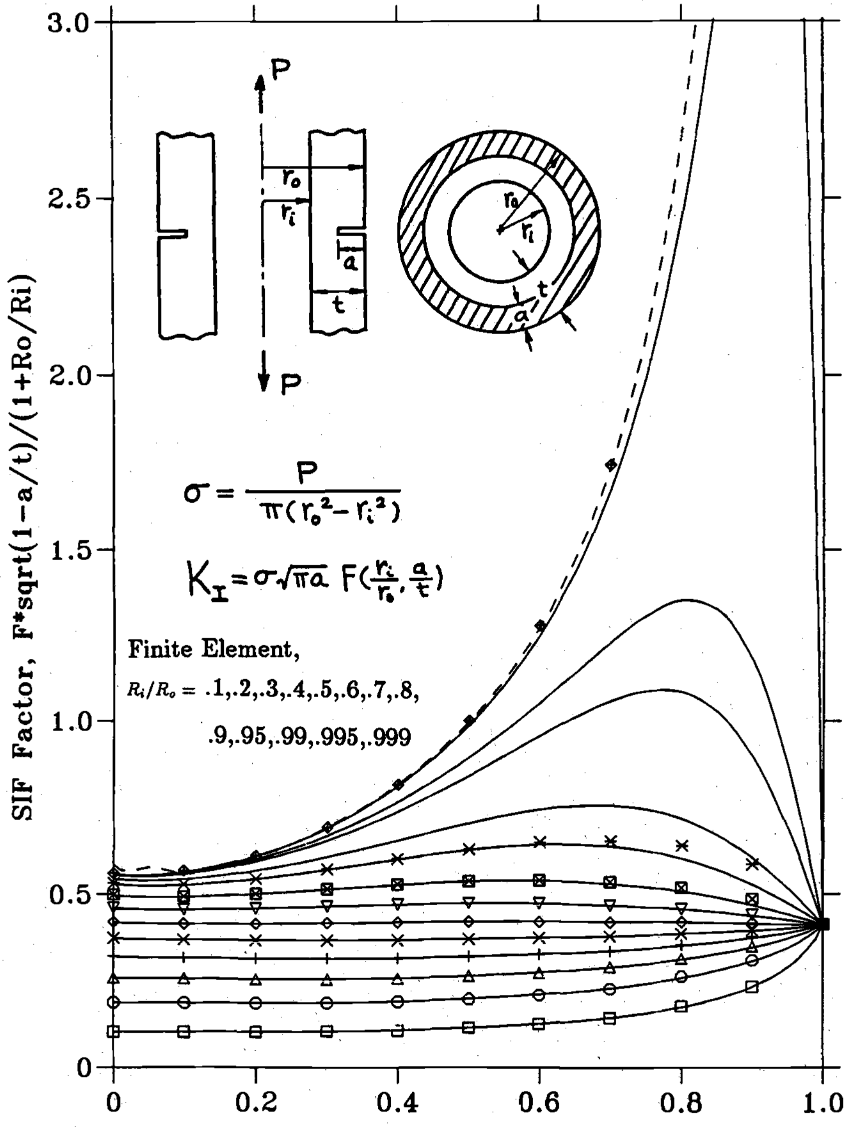

FIG. 10—*Correction factors, PROBE versus Ref* 1 *for an external crack.*

with a ratio of $R_i/R_o = 0.5$ having an internal crack of depth $a/t = 0.5$. It was found that the numerical integration agrees very well with closed-form values for about 500 integration points. This indicates that the source of error is the deviation in the displacement fits, as shown in Figs. 7 and 8 and the numerical differentiation of the A_1, A_2, A_3 coefficients to obtain B_1, B_2, B_3 values. Hermite polynomial fits were used both for interpolating a particular quantity as well as obtaining its derivative. In particular, piecewise cubic fits were used for obtaining a smooth curve fit through any given set of data. Plots of the A_1, A_2, A_3 coefficients and their B_1,

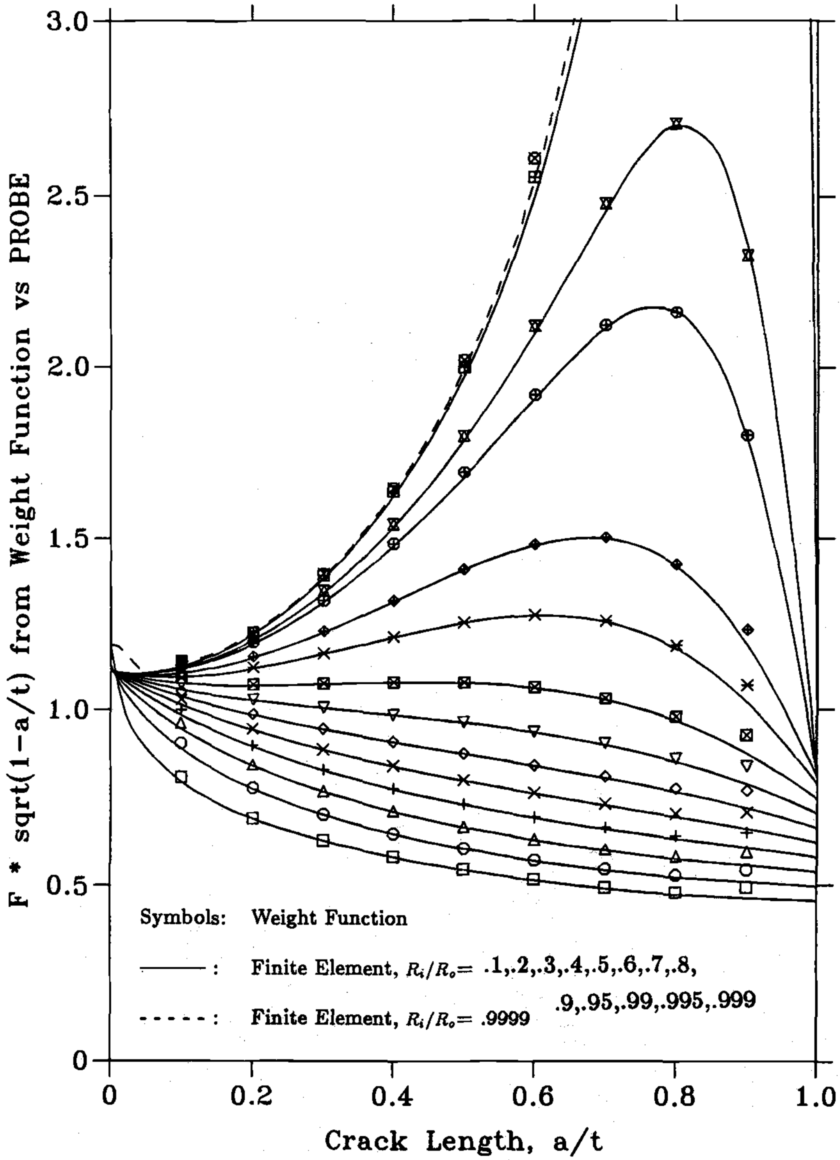

FIG. 11—*Correction factors, PROBE versus weight function for an internal crack.*

B_2, B_3 derivatives are shown for one radius ratio, R_i/R_o = 0.5 in Figs. 15, 16, and 17. These figures show rapid changes in the derivatives near a/t = 1.0, indicating an increase in error for very deep cracks. Since most practical situations would have crack lengths in the range of a/t = 0.0 to 0.8 where the errors are minimal, the level of accuracy achieved was considered satisfactory. For arbitrary distributions of stress, the accuracy may vary and the only way to ascertain the actual error in the weight-function solution is by obtaining an accurate finite-element solution for the stress distribution of interest.

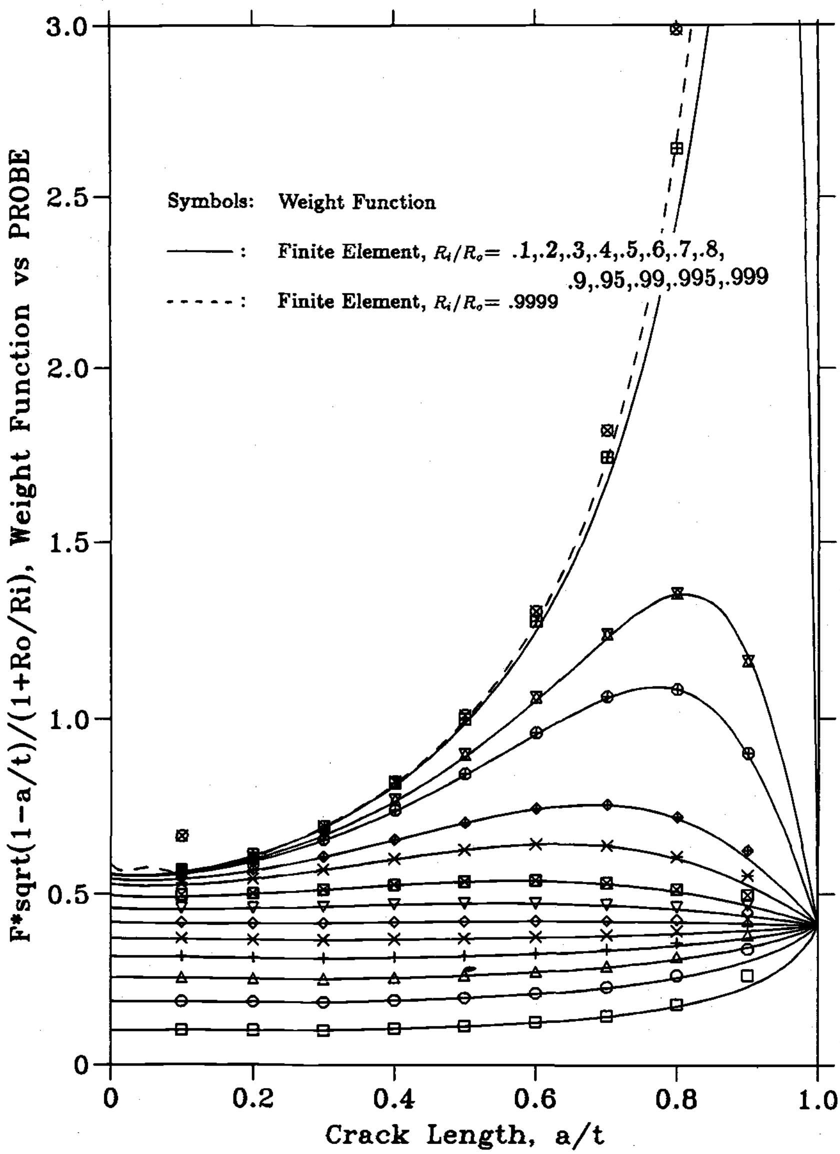

FIG. 12—*Correction factors, PROBE versus weight function for an external crack.*

Conclusion

A methodology was established for obtaining stress intensity factor solutions for general axisymmetric loading based on the weight-function method. Numerical finite-element solutions for the stress intensity factor were obtained for the whole array of geometrical parameters for the reference loading case of uniform tension. New solutions are provided for the practically important case of very thin cylindrical vessels. The stress intensity solution for uniform tension was established to be within 1% via direct interpolation and within about 2% via the weight-function method for most practical crack geometries ($0.02 < a/t < 0.8$).

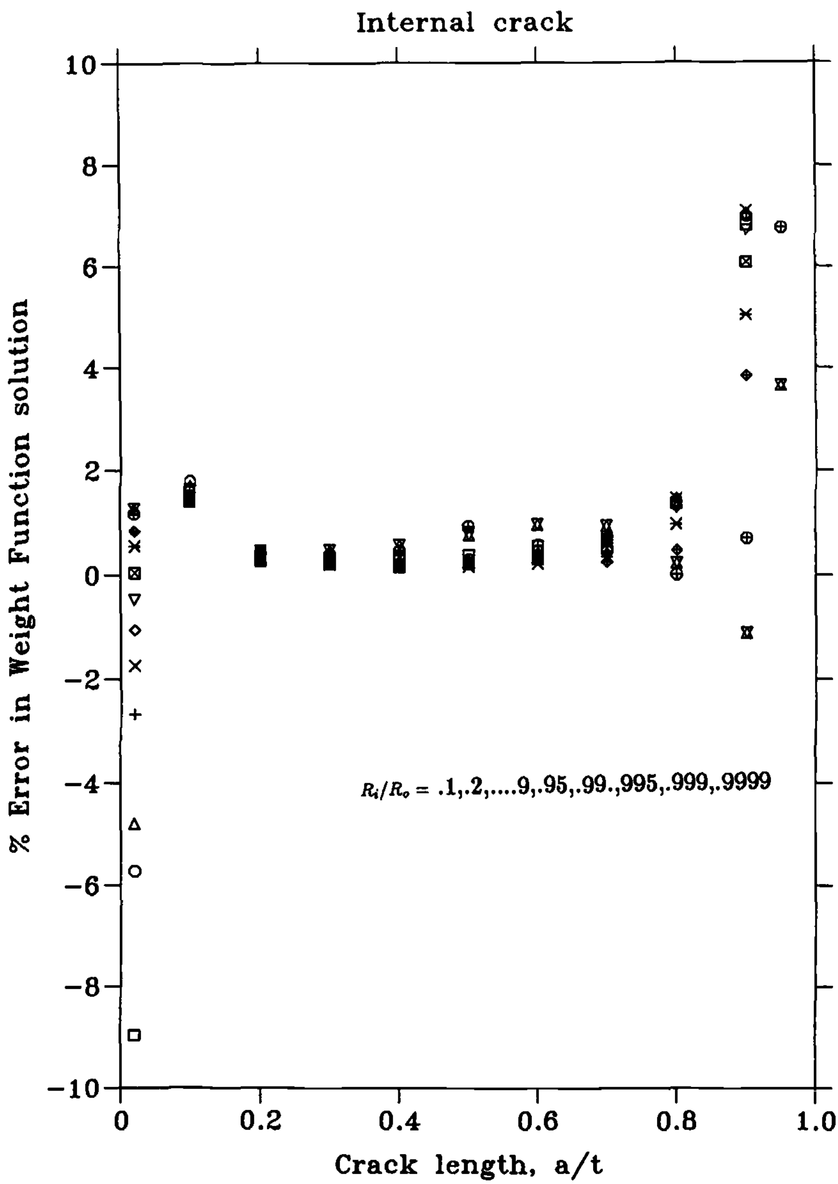

FIG. 13—*Errors in weight function results for an internal crack.*

TABLE 5—*Stress intensity factors for nonuniform loading; internal crack,* $R_i/R_o = 0.5$, $a/t = 0.5$, $t = 1$ *m.*

Loading Type	Distance $(r - r_i)/t$	Stress	Number of Integration Points	Weight Function Method Numerical	Weight Function Method Closed Form
Uniform	0.0	1.0	51	1.3903	1.4160
	1.0	1.0	101	1.4032	1.4160
			201	1.4096	1.4160
			501	1.4136	1.4160
Linear	0.0	0.5	51	0.9125	0.9255
	1.0	1.0	101	0.9190	0.9255
			201	0.9223	0.9255
			501	0.9242	0.9255
Quadratic	0.0	0.25	51	0.6108	0.6132
	0.5	0.5625	101	0.6141	0.6132
	1.0	1.0	201	0.6157	0.6132
			501	0.6126	0.6132
Cubic	0.0	0.125	51	0.4083	0.4114
	0.25	0.2441	101	0.4099	0.4114
	0.5	0.4219	201	0.4108	0.4114
	0.75	0.6667	501	0.4112	0.4114
	1.0	1.0			

Acknowledgments

The authors appreciate the helpful discussions they had with M. J. Heskitt of MSC-Noetic Inc. and J. McMahon of NASA-JSC regarding modeling for PROBE. The computational assistance provided by R. Giamona of Lockheed ESC in using PROBE is greatly appreciated. The NASTRAN modeling support provided by J. Myers and J. Woods of Lockheed ESC is also acknowledged with appreciation. The first author, Dr. S. R. Mettu, thanks Dr. V. Shivakumar for helpful discussions and the Lockheed management for their encouragement.

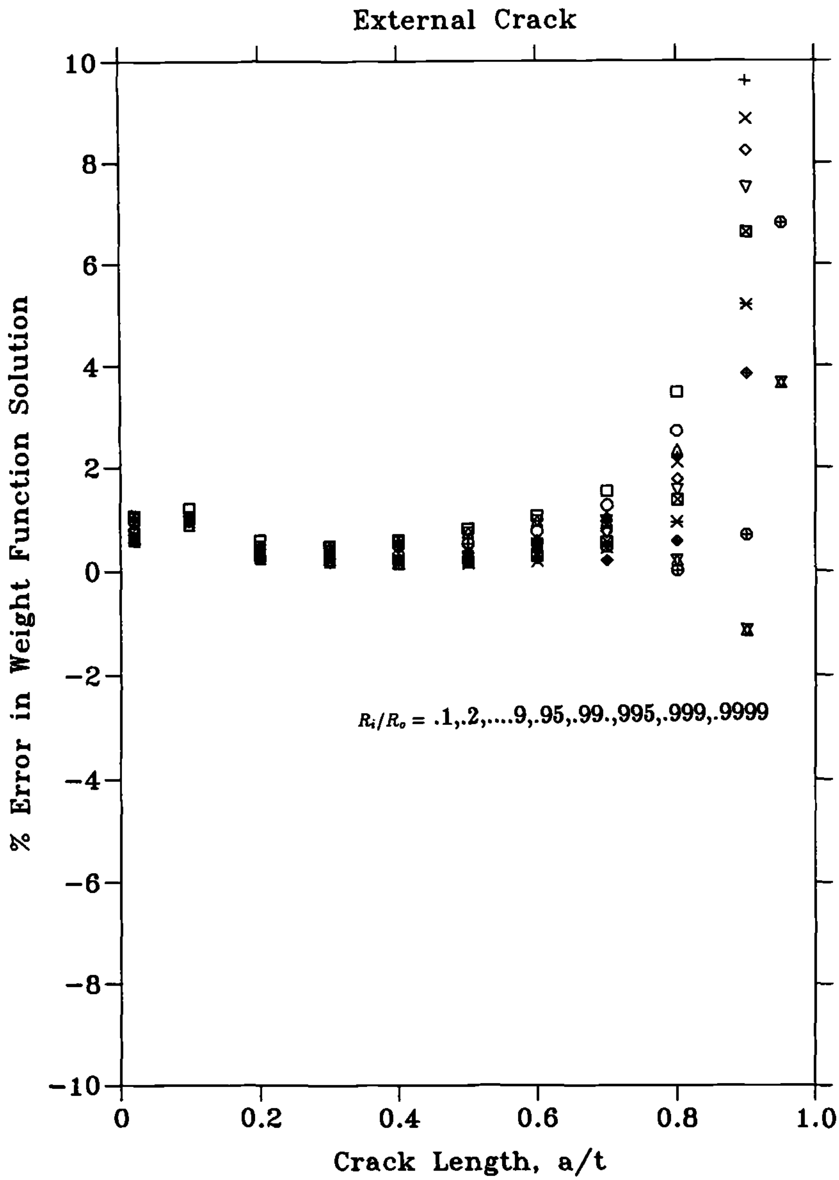

FIG. 14—*Errors in weight function results for an external crack.*

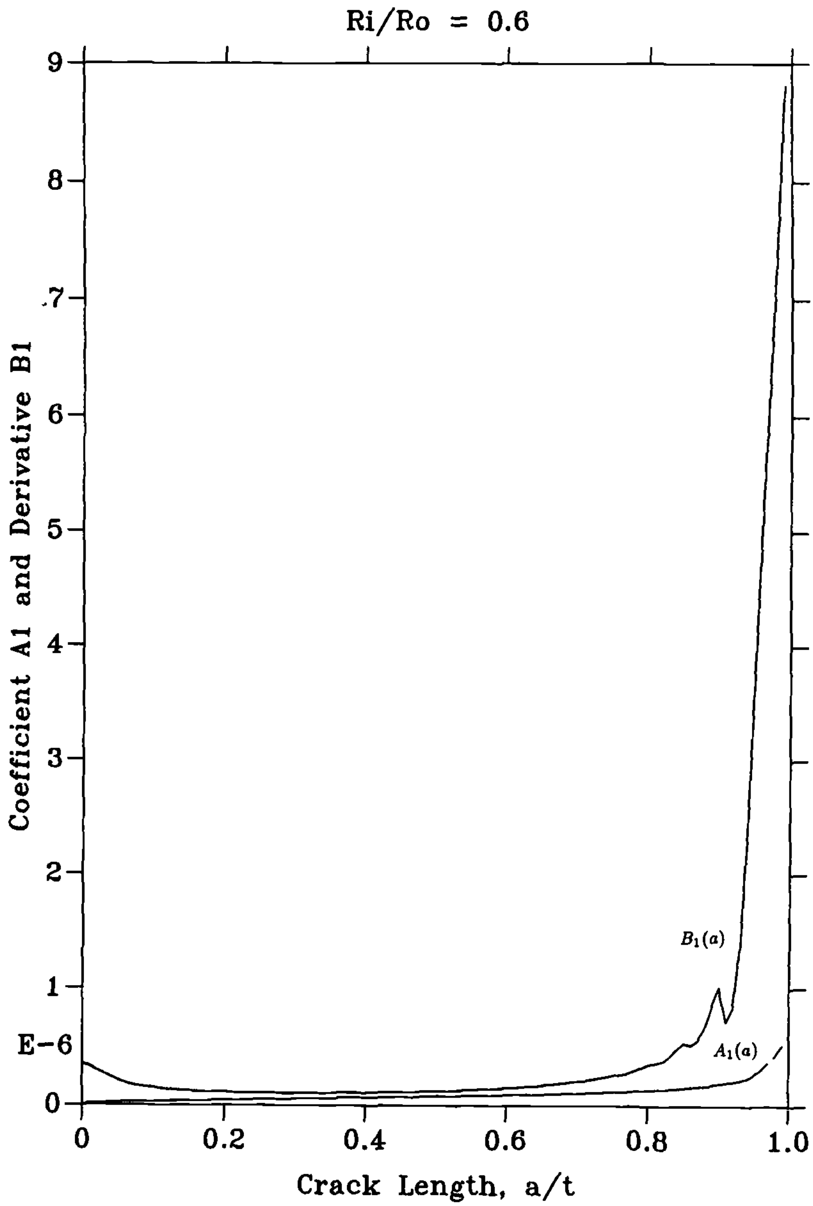

FIG. 15—*Coefficient* $A_1(a)$ *and its derivative,* $B_1(a)$.

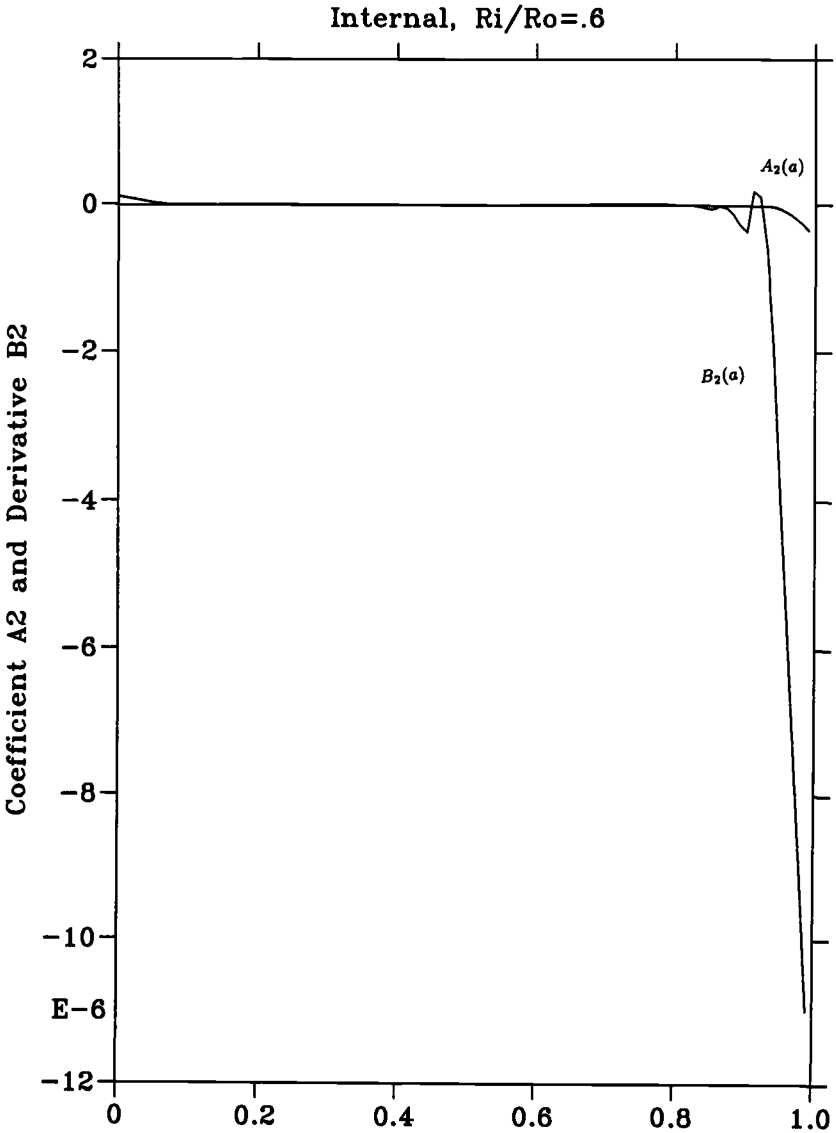

FIG. 16—*Coefficient* $A_2(a)$ *and its derivative,* $B_2(a)$.

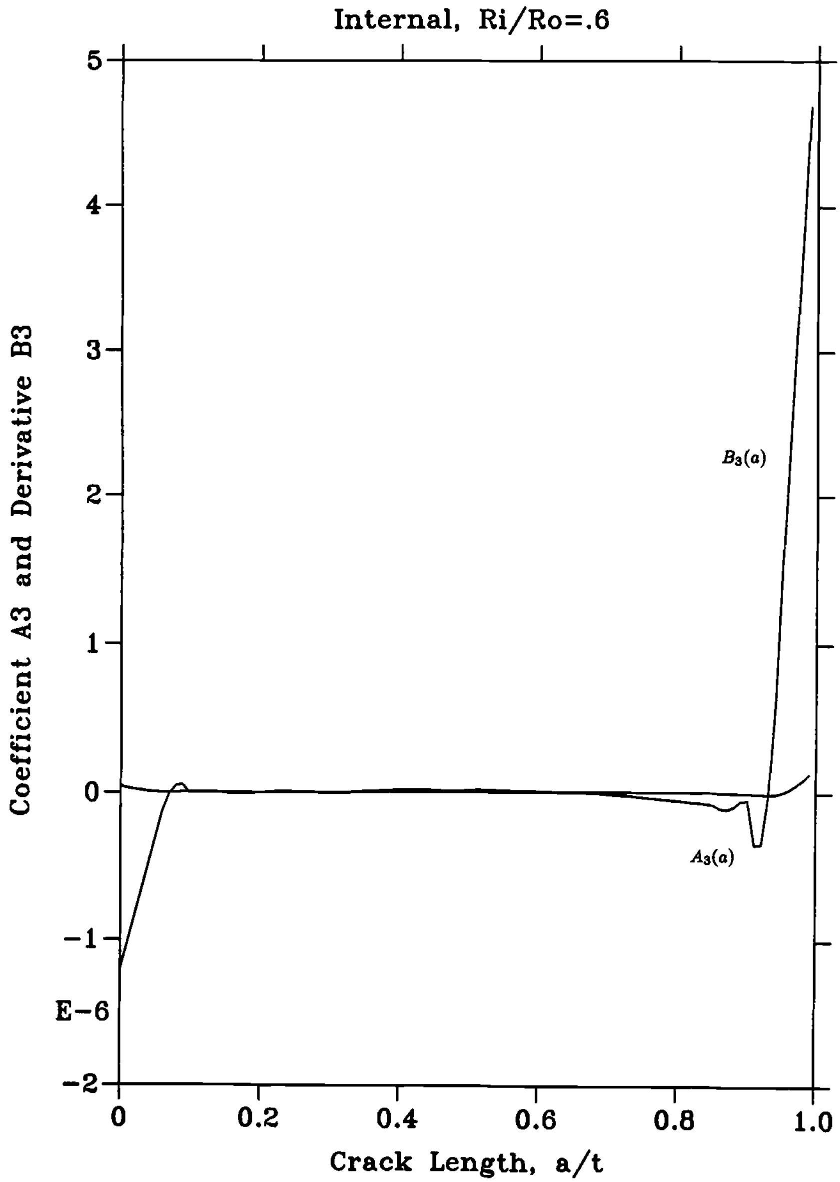

FIG. 17—*Coefficient* $A_3(a)$ *and its derivative,* $B_3(a)$.

References

[1] Tada, H., Paris, P. C., and Irwin, G. R., *The Stress Analysis of Cracks Handbook*, 2nd ed., Del Research Corporation, St. Louis, MO, 1985.
[2] Lubbens, R., Pellissier-Tanon, A., and Heliot, J., "Practical Method for Calculating Stress-Intensity Factors Through Weight Functions," *Mechanics of Crack Growth, ASTM STP 590*, American Society for Testing and Materials, Philadelphia, 1976, pp. 368–384.
[3] Buchalet, C. B. and Bamford, W. H., "Stress-Intensity Factor Solutions for Continuous Surface Flaws in Reactor Pressure Vessels," *Mechanics of Crack Growth, ASTM STP 590*, American Society for Testing and Materials, Philadelphia, 1976, pp. 385–402.
[4] Rice, J. R., "Some Remarks on Elastic Crack-tip Stress Fields," *International Journal of Solids and Structures*, Vol. 8, 1972, pp. 751–758.
[5] *CSA/NASTRAN Users Manual*, Computerized Structural Analysis and Research Corporation, Northridge, CA, Sept. 1988.
[6] *MSC/PROBE Users Manual*, Version 4.1, The MacNeal-Schwendler Corporation, Los Angeles, CA, 1990.
[7] Orange, T. W., "Crack Shapes and Stress Intensity Factors for Edge-Cracked Specimens," *Stress Analysis and Growth of Cracks, ASTM STP 513*, American Society for Testing and Materials, Philadelphia, 1972, pp. 71–78.
[8] Petroski, H. J. and Achenbach, J. D., "Computation of the Weight Function from a Stress Intensity Factor," *Engineering Fracture Mechanics*, Vol. 10, 1978, pp. 257–266.
[9] "Fatigue Crack Growth Computer Program NASA/FLAGRO," JSC-22267, NASA Lyndon B. Johnson Space Center, Houston, TX, March 1989.

Linear-Elastic Fracture Mechanics—Applications

John H. Underwood,[1] Vincent J. Olmstead,[1] John C. Askew,[1] Anthony A. Kapusta,[1] and George A. Young[1]

Environmentally Controlled Fracture of an Overstrained A723 Steel Thick-Wall Cylinder

REFERENCE: Underwood, J. H., Olmstead, V. J., Askew, J. C., Kapusta, A. A., and Young, G. A., "**Environmentally Controlled Fracture of an Overstrained A723 Steel Thick-Wall Cylinder,**" *Fracture Mechanics: Twenty-Third Symposium, ASTM STP 1189,* Ravinder Chona, Ed., American Society for Testing and Materials, Philadelphia, 1993, pp. 443–460.

ABSTRACT: A through-wall, 1.7-m-long crack grew suddenly from an outer diameter (OD) notch in a 285-mm-OD A723 steel overstrained tube that was undergoing plating operations with no externally applied loads. A description is given of the fracture mechanics tests and analyses and the fractography that were performed to characterize the cracking. Key material, residual stress, and environment information are: 1200 MPa yield strength; 150 MPa $\sqrt{m}$ fracture toughness; composition typical of air-melt A723 steel; tensile residual stress at the OD of about 600 MPa; and electro-polishing bath of sulfuric and phosphoric acids at 54°C.

The bolt-loaded test for threshold stress intensity factor for environmentally controlled cracking described by Wei and Novak was used here with two significant modifications. Some tests included only a notch with radius matching that of the tube, and a new expression for K in terms of crack-mouth displacement was developed and used. Scanning electron microscopy (SEM) fractography and energy dispersive X-ray spectra were used to identify cracking mechanisms.

Results of the investigation include: (*a*) a measured threshold of hydrogen stress cracking for the material/environment below 20 MPa $\sqrt{m}$, (*b*) da/dt versus K behavior typical of classic environmental control, (*c*) an improved K/v expression for the bolt-loaded specimen and associated criteria for determining plane strain test conditions in relation to the Irwin plastic zone.

KEY WORDS: environmental cracking, test methods, hydrogen stress cracking, thick-wall cylinder, K analysis, scanning electron microscopy, residual stress, fracture mechanics, fatigue (materials)

"Postmortem" studies of crack-growth-induced structural failure are often prompted by an unanticipated failure that also has economic significance. Such is the case here. In August 1990, a nearly finished cannon tube suffered an unexpected and complete failure. A crack grew from a notch in the 285-mm outer diameter (OD) of the tube, down the tube axis for a distance of 1.7 m, and through to the 157-mm inner diameter (ID) over most of the 1.7-m length, thereby ruining the tube. Figure 1 shows some aspects of the configuration. At the time of the failure, the tube was undergoing chrome plating operations with no externally applied mechanical loads. The plating baths were above the tube ambient temperature, which could result in applied transient thermal stress, but as will be shown in upcoming analysis, these thermal stresses would be of too low a level to have been a primary cause of the failure.

The unique residual stress state of the tube was considered from the start to be a significant factor in the failure. Prior work showed the important and deleterious effects of overstrain residual stresses on crack growth from a similar notch and tube configuration [*1*]. However,

[1] Materials engineer, mechanical engineer, chemical engineer, physical science technician, and metallurgist, respectively, Army Armament RD&E Center, Benet Laboratories, Watervliet, NY 12189.

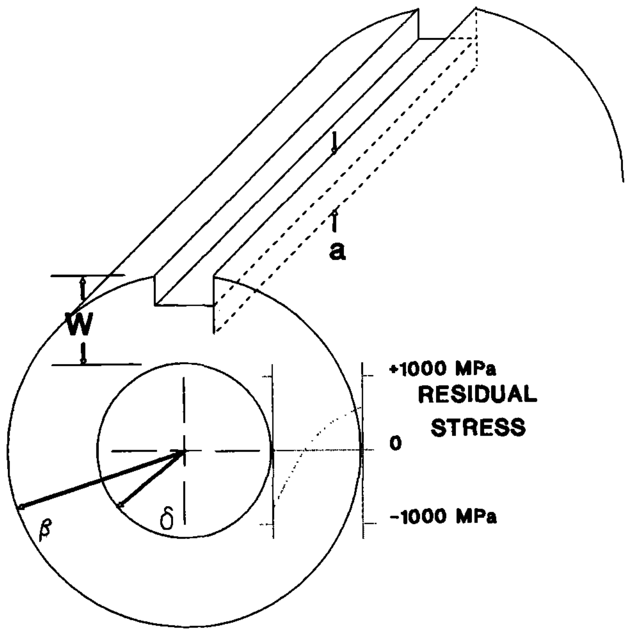

FIG. 1—*Sketch of overstrained tube configuration.*

unlike the previous work that involved fatigue loading, this failure involved only the sustained loads due to overstrain residual stresses and the low-level thermal stresses mentioned previously. Thus, environmentally controlled cracking was the suspected cause of the failure, particularly upon consideration of the acids commonly used in plating operations.

The objective here is to describe the tests and analyses used to identify the specific cause of the cracking and related failure and to describe both the overall macrofailure process of the tube as a structure as well as the micromechanisms of the cracking that led to the failure. As the investigation proceeded, some of the available fracture test and analysis methods from the technical literature were modified in order to broaden their usefulness or improve their accuracy. Thus, a secondary object of the work became the development of modified and new test and analysis procedures for use in the investigation and for general use in fracture testing.

Materials and Environments

The tube that failed was machined from an A723 steel forging with mechanical properties and chemical analysis as shown in Table 1. The tension and fracture test results were the mean of two circumferential orientation samples from a location near the failure. The circumferential orientation is critical in most pressurized tubes and was the orientation of the failure, see again Fig. 1. The chemical analysis was from direct reading emission spectrometer results from specimens near the failure location. In general, the Table 1 results meet the requirements of A723, Grade 1, Class 4. The only exceptions are the molybdenum content of 0.51%, which is somewhat above the 0.40% upper limit of Grade 1, and the Charpy energy of 25 J at −40°C, which is not the same as the 27 J at +5°C requirement of Class 4. However, these differences are not considered to be significant. There appears to be no deficiency with the tube based on material properties.

TABLE 1—*Properties of steel and chemical environment.*

	A723 Steel: Mechanical Properties Circumferential		C-R Orientation	
	Yield Strength	Tensile Strength	Charpy Energy	Fracture Toughness
Measured	1207 MPa	1282 MPa	25 J −40°C	157 MPa $\sqrt{m}$ +20°C
Specified	1105 MPa min	1205 MPa min	27 J +5°C	...

Chemical Analysis, % by Weight	C	Mn	Mo	Si	Cr	Ni	V	P	S
Measured	0.33	0.60	0.51	0.13	1.03	2.11	0.11	0.010	0.009
Specified	0.35 max	0.90 max	0.40 max	0.35 max	0.80 to 2.00	1.50 to 2.25	0.20 max	0.015 max	0.015 max

Acid Solution		Test Temperature	
Concentrated H_2SO_4 (98% by weight)	Concentrated H_3PO_4 (85% by weight)	Cylinder	Specimens
50% by volume	50% by volume	54°C	20 to 54°C

The chemical baths that were used with the tube are those typically used in chrome plating: NaOH in H_2O for electrocleaning; concentrated H_2SO_4 + H_3PO_4 for electropolishing; CrO_3 + H_2SO_4 in H_2O (water) for plating; and NaOH in H_2O for stripping of the plated chrome, if necessary. The prime suspect environment for this failure was the electropolish bath, because it was a mixture of concentrated acids including sulfuric acid, which is known to be highly aggressive toward steels. The concentrations and test temperatures used for the electropolish solution with the tube (and the subsequent modeling tests) are shown in Table 1.

Failure Details and Modeling Tests

The sequence of critical events of the failure are the following. The tube was subjected to the plating baths mentioned previously, including the stripping bath, which was required to remove uneven plating products. The sequence of baths was repeated and the failure was noted as the tube was removed from the stripping bath, which was again required to remove uneven plating. The fact that the failure was noted following exposure to the NaOH stripping bath placed the initial attention on this environment. However, attention quickly shifted to the H_2SO_4 + H_3PO_4 environment, because the latter is so much more aggressive. The electrolytic cleaning, polishing, plating, and stripping operations were performed with an electrode inserted in the ID of the tube and with the entire tube subjected to the baths. Therefore, the failure, which was initiated at the OD of the tube, was considered to be controlled by chemical environment and not by any electrochemical process.

The crack extended 1.7 m along the tube axis and into the ID surface, as mentioned previously. It initiated from and was guided by a 9.8-mm-deep, 24-mm-wide, 1.7-m-long notch in the OD surface, (shown skematically in Fig. 1) with notch root radii of 1.1 mm. The maximum opening of the crack at the notch root was 11.7 mm, at a location about midway along the 1.7-

m length of the crack. The fracture surface was removed and examined and showed two distinct regions. The first was a dark-colored region emanating from one of the notch roots at the approximate middle of the 1.7-m-long overall fracture surface, and is believed to be an area of environmentally controlled fracture. This region was generally covered with corrosion product and had a length of 430 mm, an average depth (from the notch root) of 5.6 mm, and a maximum depth of 11.9 mm. The corrosion-covered region included two distinct areas, one near the notch root having thinner, more uniform, and adherent corrosion, and an area further from the notch having darker, thicker, and more brittle and porous corrosion. The nature of these two areas is consistent with the two complete plating cycles that were applied, with the second cycle removing some of the corrosion product near the notch. The second region of the fracture surface had no corrosion and made up the remainder of the fracture surface. It is believed to be an area of fast fracture.

To be sure that the understanding of the failure was correct—that residual stress and the presence of the acids caused environmental cracking that led to fast cracking—the following modeling tests and analysis were performed. Environmental cracking threshold tests and plain strain fracture toughness tests were performed using samples of the failed tube and samples of the acid bath used in electropolishing the tube. Scanning electron fractographs and energy dispersive X-ray spectra of the tube fracture surface were compared with like results from the controlled laboratory tests. Stress intensity factor relationsips were developed for the tube configuration and residual stress conditions, and comparisons were made between the experimental and analytical results.

Subsequent sections of this report describe the tests and analyses and their results and implications.

Test Procedures

The most important test results required to model and understand the tube failure are a demonstration of environmental cracking in the suspect environment and a measurement of a threshold K value for cracking. Bolt loaded specimens have clear advantages of simplicity for environmental testing, and the work of Wei and Novak [*2*] provides a comprehensive basis for this type of test. Reference *2* describes a bolt-loaded compact specimen with generic "arm" height-to-depth ratio, H/W, of 0.486 and the detailed test procedures for environmental cracking tests with this specimen. Figure 2 shows the specimen used here, as suggested in Ref *2*.

Several aspects of the Wei and Novak procedure for environmental cracking tests should be emphasized. One recommendation found to be critical in interlaboratory tests of environmentally assisted cracking [*2*] is believed to be equally important in these tests, that is, the application of the test environment "before" application of the load. As will be shown by the test results, had not this recommendation been followed, the fast environmental cracking may not have been observed, and it was this fast cracking that led to the failure of the tube. The recommendation to apply environment before load allows breakage of protective layers at the notch tip and thereby the exposure to environment of fresh metal, a mechanism often proposed for environmental cracking.

Two aspects of the procedure [*2*] were modified in the tests here. First, in two of the tests, the usual fatigue precrack was omitted in order to duplicate the 1.1-mm notch root radius of the tube that failed. Other tests used a precrack, as shown in Table 2. A second modification of the Wei and Novak procedure was the development and use of a different expression for the ratio of applied stress intensity to applied crack mouth opening, K/v. The expression from Ref *2* is

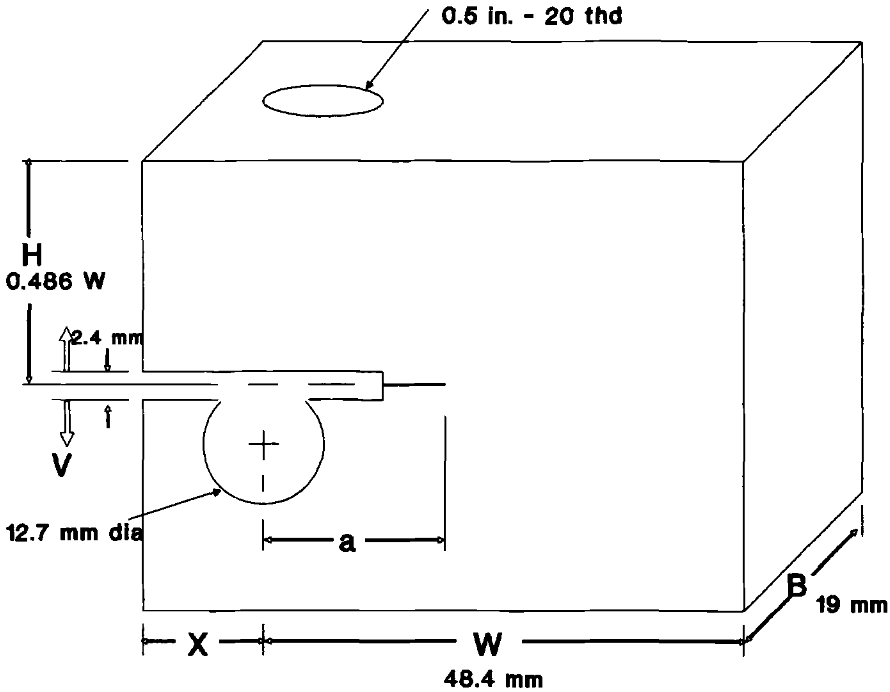

FIG. 2—*Bolt-loaded compact specimen for environmentally controlled fracture tests.*

$$KW^{1/2}(a/W)^{1/2}/Ev = f_1(a/W)/f_2(a/W) \quad (1)$$
$$f_1 = 30.96(a/W) - 195.8(a/W)^2 + 730.6(a/W)^3 - 1186.3(a/W)^4 + 754.6(a/W)^5$$
$$f_2 = \exp[4.495 - 16.130(a/W) + 63.838(a/W)^2 - 89.125(a/W)^3 + 46.815(a/W)^4]$$

for $X/W = 0.255$, $H/W = 0.486$, and $0.3 \geq a/W \geq 0.8$; where E is elastic modulus and the other symbols are defined in Fig. 2. Equation 1 was fitted to reliable numerical results [*3*], but it is relatively complex, and, as stated in Ref *2*, "there are uncertainties associated with the K

TABLE 2—*Specimens and test conditions.*

	Notch Conditions		Initial Load Application			
Test	a_0/W	Precrack	In	v_0, mm	K_0, MPa $\sqrt{m}$	Test Duration, h
3	0.39	none	air	0.62	100	120
10	0.45	2 mm	acid	0.70	114	4
7	0.44	2 mm	acid	0.66	110	2400
15	0.44	2 mm	acid	0.50	82	1540
16	0.44	2 mm	acid	0.33	54	1540
17	0.40	none	acid	0.93	168	0.1

calibration which have not been fully addressed." Therefore, a different K expression was developed, as shown in Fig. 3. A much lower order polynomial was used to fit a parameter that included the ratio, K/v, of prime importance for the bolt-loaded compact specimen, but also including the functional form of the deep crack limit of K/v for the specimen. This limit can be obtained from two limit solutions for remotely applied moment, M, available from Tada, Paris, and Irwin [*4*], in a manner similar to that from prior work [*5*]

$$\lim_{a \to W} K = 3.975\ M/B(W - a)^{3/2} \tag{2}$$

$$\lim_{a \to W} \theta = 15.8\ M/EB(W - a)^2 \tag{3}$$

combined with the limit relationship for crack opening angle, θ

$$\lim_{a \to W} \theta = v/(W + x) \tag{4}$$

The general result for compact specimens (independent of H/W) is

$$\lim_{a \to W} [KW^{1/2}/Ev(1 - a/W)^{1/2}] = 0.2516/(1 + X/W) \tag{5}$$

and for the $X/W = 0.255$ of interest here

$$\lim_{a \to W} [KW^{1/2}/Ev(1 - a/W)^{1/2}] = 0.2005 \tag{6}$$

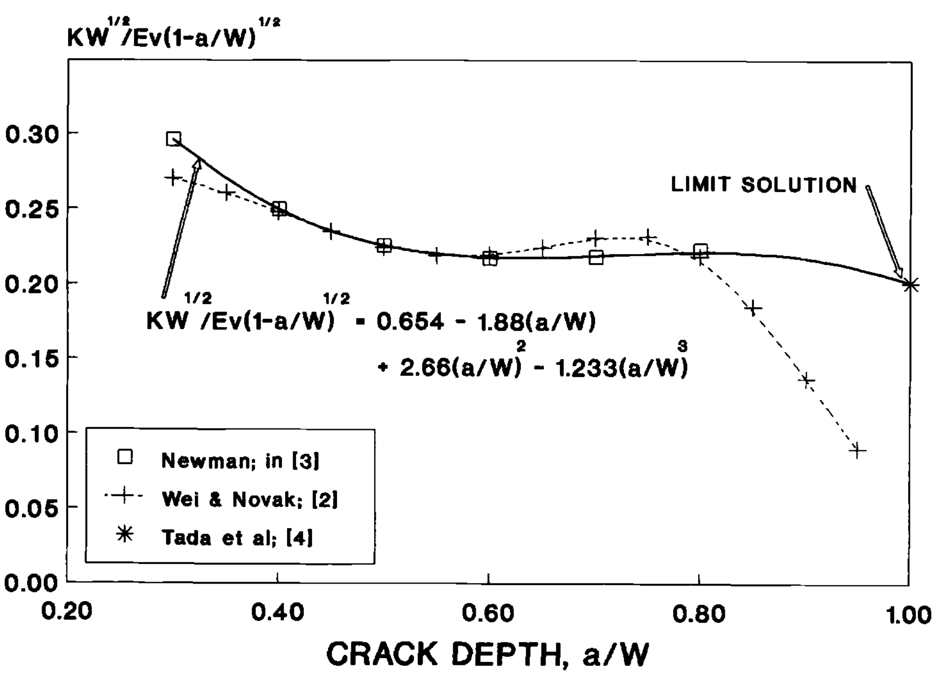

FIG. 3—*Comparison of* K/v *analyses for bolt-loaded compact specimen.*

TABLE 3—*1540-h threshold values for* K *for A723 steel in H_2SO_4 + H_3PO_4 acid environment at 54°C.*

Test	Crack Depth, a/W	Initial Load, K_0 (MPa $\sqrt{m}$)	Test Duration, h		Threshold, K_{th} (MPa $\sqrt{m}$)
7	0.98	110	1588		18.6
15	0.96	82	1540		19.0
16	0.94	54	1540		16.2
				Mean	17.9
				Standard Deviation	1.5

This is the limit shown in Fig. 3 and used in a cubic polynomial fit, resulting in the following K/v expression

$$KW^{1/2}/Ev(1 - a/W)^{1/2} = 0.654 - 1.88(a/W) + 2.66(a/W)^2 - 1.233(a/W)^3 \quad (7)$$

for $X/W = 0.255$, $H/W = 0.486$, and $0.3 \geq a/W \geq 1.0$.

This expression fits the numerical results of Newman [*3*] over the range $0.3 \geq a/W \geq 0.8$ within 0.6% and the deep crack limit within 0.2%. Note that the fit of the Wei and Novak expression to Newman's results is not as good. Also, for $a/W > 0.8$, crack lengths of importance in these tests and in general for displacement-loaded compact specimens, the Wei and Novak expression does not approach the deep crack limit. Equation 7 was used for all calculations of applied K in the bolt-loaded tests.

Two K_{Ic} tests were done using the arc tension specimen of ASTM Test Method for Plane-Strain Fracture Toughness of Metallic Materials (E 399-83) with a thickness of B = 38 mm. The results, 156 and 159 MPa $\sqrt{m}$, had a mean K_{max}/K_{Ic} value of 1.03, well within the 1.10 requirement, but had a mean 2.5 $(K_{Ic}/\sigma_{ys})^2$ value of 43 mm, somewhat larger than B. Since only one of these basic test requirements was not met, and by a relatively small margin, the test results are believed to give a good measure of fracture toughness.

Referring again to Table 2, the general test procedure was to precrack (except for Specimens 3 and 17) at a maximum K of about 50 MPa $\sqrt{m}$, apply a few drops of the acid solution at laboratory ambient temperature (20°C), and immediately (within 1 min) apply an initial displacement, v_0, and then immerse (within about 5 min) in the acid solution held at a temperature of 54°C. The total test durations are listed in Table 2. The mean crack depth was determined from microscope measurements on both surfaces, with various inspection frequencies, based on growth rates observed. The first sample listed in Table 3 was not subjected to the few drops of acid solution before load application, and the results were quite different, as discussed in the next section.

Results and Discussion

Least Severe Model Test

Of the six specimens tested, the first, Specimen 3, had a notch of the same radius as the tube, no precrack, and was loaded in air to K_0 = 100 MPa $\sqrt{m}$. These test conditions were intended to model the least severe conditions that could have been present in the tube, that is, no sharpening of the notch and no acid present as the stress was applied. The K_0 value of 100 MPa $\sqrt{m}$ was selected based on the following. The circumferential direction residual stress, σ_R, at the tube OD was calculated using [*6*]

$$\sigma_R/\sigma_{ys} = 1 - 2 \ln (\beta/\delta)/[(\beta/\delta)^2 - 1] \quad (8)$$

where β and δ are the outer and inner radii of the tube, as in Fig. 1. Equation 8 gives the stress for a 100% overstrained tube, that is, one in which the plastic straining has proceeded completely through the tube wall due to application of overpressure or mandrel expansion to the tube. The failed tube was 100% overstrained, as verified by a destructive slitting test of a ring from the tube. The result from Eq 8, $\sigma_R = 578$ MPa, used with the expression for K for a short edge crack under remote tension

$$K_R = 1.12\sigma_R(\pi a)^{1/2} \tag{9}$$

gives a calculated value of $K_R = 114$ MPa $\sqrt{\text{m}}$ for a 9.8-mm-deep notch. This value may be only an estimate of the effective K in the tube, because Eq 9 assumes a sharp crack and the tube contained a notch, and because the equation ignores the stress gradient through the tube wall. Nevertheless, Eq 9 does give a reasonable estimate of K for a cracked tube with residual stress, based on the following comparison of K_R with K_{Ic}. Using $\sigma_R = 578$ MPa, as before, and the average and maximum total crack depths, 15.4 and 21.7 mm, gives K_R values of 142 and 169 MPa $\sqrt{\text{m}}$, respectively, that bracket the measured K_{Ic}, 157 MPa $\sqrt{\text{m}}$. Note that a in these calculations is the total depth of the notch (9.8 mm) plus the crack depth.

The results of the Specimen 3 test of the least severe conditions that could have been present in the tube were essentially negative. Although small cracks were noted in the disturbed area near the machined surfaces of the notch, no crack growth was observed by optical or electron microscopic examination following 120 h of acid exposure at 54°C. This indicates that the conditions were more severe in the failed tube. Although no large inclusions were noted on the tube fracture surface, manganese sulfide inclusions are always present to some extent in this type of steel and could have effectively sharpened the notch.

Precracked Tests

The next four specimens were precracked (about 2 mm extension of notch), subjected to a few drops of acid, and then loaded, two specimens to a high load that corresponded to the tube loading and one each to an intermediate and low load. The high load tests were dramatically different in result than Test 3. Cracking was noted almost immediately upon loading of Specimens 10 and 7; about 5 min after applying drops of acid to the notch and crack area and about 3 min after applying the load, several millimetres of crack growth could be seen with the unaided eye on both sides of the specimen. The tests were continued in the 54°C acid bath as described previously; Test 10 was ended at 4 h, in an attempt to obtain a fracture surface relatively unaffected by corrosion products, and Test 7 continued for 2400 h to obtain a K threshold for cracking in this environment.

Figure 4 is a plot of crack depth and applied K versus exposure time for the two high-load precracked tests. The fast "three minute" cracking noted earlier has occurred very near the left ordinate; for Specimen 7, the first two points show crack growth from 21 mm (the total depth of notch plus precrack) to 28 mm, while K changes from $K_0 = 110$ MPa $\sqrt{\text{m}}$ to $K = 88$ MPa $\sqrt{\text{m}}$, after 0.05-h exposure. This "three minute" cracking is followed by a region of steadily increasing crack depth and decreasing K, and finally by a region of relatively constant crack depth and K.

The nature of the cracking in this tube is essentially the same as hydrogen stress cracking described by Uhlig and Revie [7]. They describe cracking of martensitic steels that occurs within a few minutes upon exposure to acid solutions and an applied or residual tensile stress. All of these conditions are met in the case of this cylinder, and, as already noted, both the acid environment and the tensile stress are particularly severe.

The three regions of behavior in Fig. 4 can be explained by a plot of crack growth rate versus

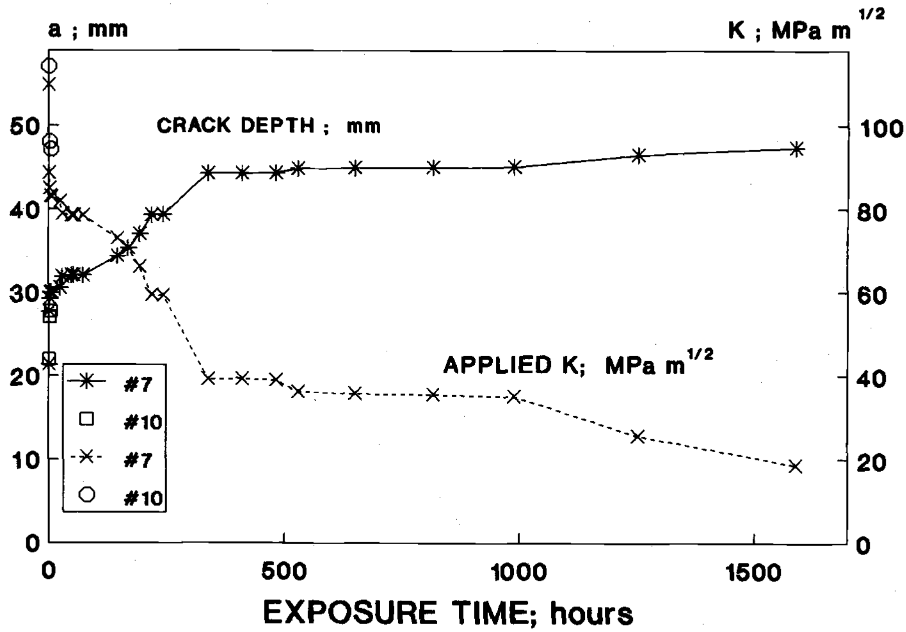

FIG. 4—*Crack growth and applied K for A723 steel exposed for 1600 h to 50% H_2SO_4/50% H_3PO_4 at 54°C.*

applied K (Fig. 5). A five-point floating average procedure was used to calculate *da/dt,* in a manner similar to the secant method of ASTM Test Method for Constant-Load-Amplitude Fatigue Crack Growth Rates Above 10^{-8}m/Cycle (E 647-83). The crack depth and time values for the $n + 2$ and the $n - 2$ data points were used to calculate $\Delta a/\Delta t$, which was plotted versus the K of the middle data point of the set of five. Had the $n + 1$ and $n - 1$ data points been used in Fig. 5, the result would have been similar but with more scatter. It is interesting to note the similarity of the trend of the data with the classic three regions of environmental crack growth rate behavior [7]: Region I at low K approaching a threshold; Region II at intermediate K and a constant *da/dt;* and Region III at high K approaching the critical K for fast fracture. This similarity to the classic behavior gives further verification that environmental effects controlled the tube failure.

Figures 6 and 7 compare results of crack depth and applied K versus exposure time for three levels of initial load, K_0. The intermediate and low initial K_0 tests, Tests 15 and 16, respectively, showed no initial fast cracking, but otherwise the three sets of results were generally similar. Note in Fig. 7 that the applied K after about 1500-h exposure approached a relatively constant K value for very deep cracks in the three tests. These results are a useful measurement of a threshold K for cracking for these tests and are summarized in Table 3. One of the three tests (Test 7) was continued further, to a total of 2404-h exposure. There was no significant change in a/W (still 0.98) or applied K (18.0 MPa $\sqrt{m}$).

Plane-Strain Limit

One aspect of concern in the apparent threshold values under discussion in Fig. 7 and Table 3 was the notably deep cracks in the tests. Even though the expression used to calculate K, Eq 7, was shown to be accurate for $a/W \rightarrow 1$, there is still the concern that the Irwin plastic zone

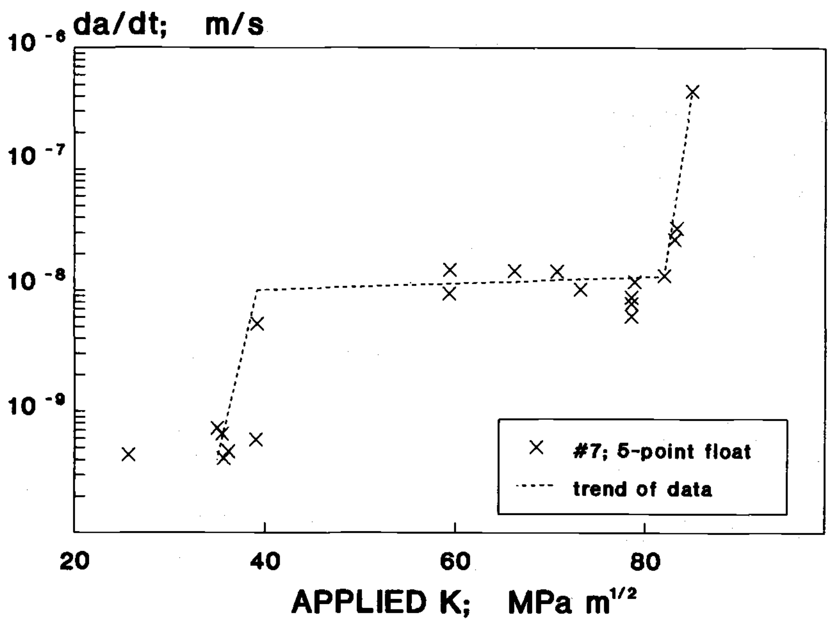

FIG. 5—*Crack growth rate versus applied* K *for A723 steel exposed to 50%* H_2SO_4*/50%* H_3PO_4 *at 54°C.*

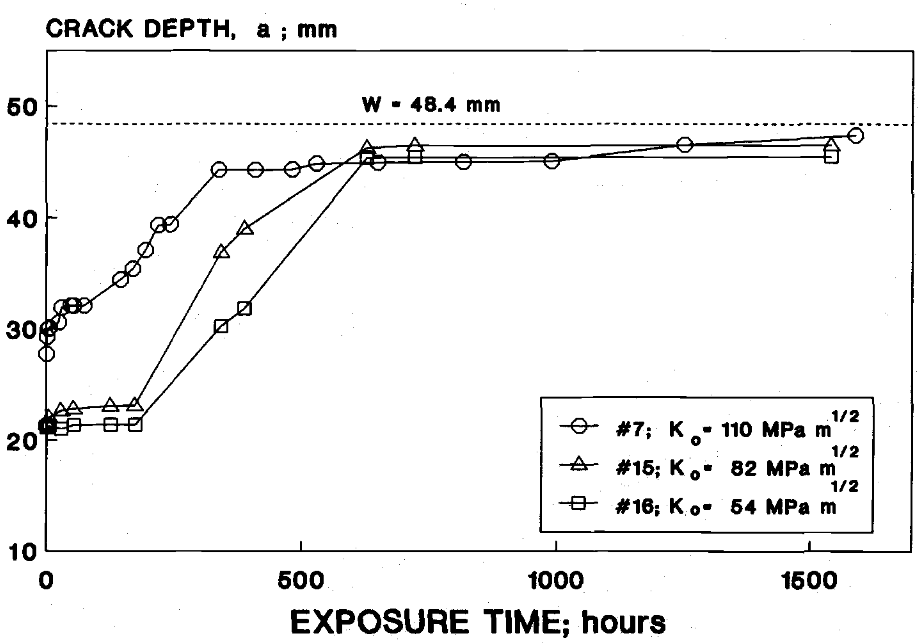

FIG. 6—*Crack growth for A723 steel exposed for 1600 h to 50%* H_2SO_4*/50%* H_3PO_4 *at 54°C with various initial applied* K *values.*

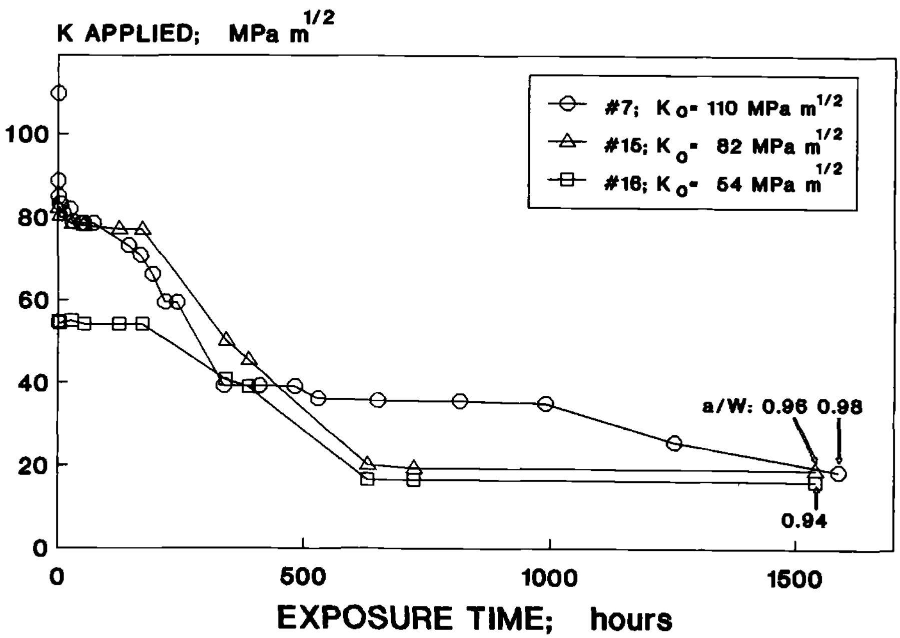

FIG. 7—*Applied* K *for A723 steel exposed for 1500 h to 50% H_2SO_4/50% H_3PO_4 at 54°C with various initial applied* K *values.*

may become significant in size relative to the remaining uncracked ligament as $a/W \rightarrow 1$. If this were to occur, the threshold values would be suspect due to loss of plane-strain constraint. The following analysis was performed to develop specimen size and crack depth criteria for the displacement-loaded compact specimen that would ensure small enough plastic zones to maintain plane-strain conditions. Starting with the relationship for adequate specimen size relative to plastic zone size used in ASTM E 399

$$(W - a) \geq 2.5(K_{Ic}/\sigma_{ys})^2 \tag{10}$$

and combining Eq 10 with Eq 5, gives an expression for a dimensionless factor that defines the ratio of v_0 to W required for plane-strain conditions

$$\gamma_{Ic} = Ev_0/\sigma_{ys}W \leq 2.51\ (1 + X/W) \tag{11}$$

For a material with given values of σ_{ys} and E, if the factor that could be called a plane-strain limit factor, γ_{Ic}, is less than the specified value, then the test results are valid with respect to plastic zone size. Note the simplicity of the expression, particularly that valid results can be predicted for the deepest of cracks. However, considering the similar form of Eqs 5 and 10, specifically the fact that $(W - a)$ varies as K^2 in both expressions, the simple result is not surprising. A physical interpretation is that the plastic zone size and the remaining ligament size have a constant ratio for the displacement-loaded specimen. Therefore, for cracks deep enough that the limit solution of Eq 5 controls K/v, Eq 11 can be used and cracks of any depth can give valid results. And it is clear from the nearly constant values in Fig. 3 for $0.6 \leq a/W \leq 1$ that the limit solution controls K/v over this range.

Expressions for the plane-strain limit factor for two commonly used displacement-loaded specimens follow directly from Eq 11. For the bolt-loaded compact specimen, the expression is

$$\gamma_{Ic} = Ev_0/\sigma_{ys}W \leq 3.15 \tag{12}$$

for $X/W = 0.255$.

Referring to Table 2, the first five listed tests met this criteria, which includes all the tests with deep cracks. For the wedge-loaded compact specimen of ASTM Test Method for Determining Plane-Strain Crack Arrest Fracture Toughness K_{Ia} of Ferritic Steels (E 1221-88) the expression is

$$\gamma_{Ic} = Ev_0/\sigma_{ys}W \leq 3.14 \tag{13}$$

for $X/W = 0.250$.

Notched Test and Thermal Stress

One further crack growth test was performed, Test 17 listed in Table 2. The sample had the 1.1-mm radius notch with no precrack and was subjected to acid in the notch (at 20°C) and then bolt-loaded to a v_0 about 50% higher than Test 3. Since Specimen 3 had shown no crack growth from a notch when loading preceded the application of the acid, this further test explored the application of acid before loading and loading to a higher level. The displacement was increased gradually so that K increased from 100 to 168 MPa $\sqrt{m}$ in about 2 min, whereupon cracking began. After about 3 min, the crack had grown 16 mm and the specimen was broken apart for fracture surface examination.

The results of Specimen 17 suggest that a precrack is not required for fast environmental cracking in this material and environment, but environmental contact before loading does seem to be required. A question can arise as to a source of loading in the tube that would have occurred after contact with the acid. The following answer is proposed. Transient thermal stresses caused by the sudden entry of the tube into the hot acid would reach their maximum level several seconds after entry of the tube. The magnitude of these stresses can be approximated by the steady-state stresses in a tube with the OD held at the higher temperature, 54°C, and the ID at ambient, 20°C. An expression for the stress at the tube OD under these conditions [*8*] and concentrated by the stress concentration factor, k, of the notch is

$$\sigma_T = k\Delta T\alpha E[1 - 2\ln(\beta/\delta)/(\beta^2/\delta^2 - 1)]/[2(1 - \mu)\ln(\beta/\delta)] \tag{14}$$

Using Eq 14 with $\Delta T = 34°C$, $k = 6$ from prior work [*1*], $\alpha = 12/°C$ [*9*], and Poisson's ratio, $\mu = 0.3$, a compressive thermal stress at the notch tip of 293 MPa is predicted. If the effect of the loading following environmental contact is to break brittle protective films and thereby expose fresh metal to the acid, it should not matter whether the stress is compressive or tensile, particularly when it is concentrated at the notch tip. Following this reasoning, thermal loading could have provided the critical loading that followed acid contact in the tube failure process.

Fractography and Spectra

This final section gives fractographic results corresponding to some of the crack growth results already presented. The objective was to corroborate (or refute) the belief that hydrogen stress cracking was the cause of the tube failure and to show other important features of the tests.

Figure 8 shows low-magnification views of two fracture surfaces with corrosion products present. In the optical photo, Fig. 8*a*, the corrosion did not obscure the area near the fatigue precrack *(bottom)* nor the area near the last ligament that was broken in air after removal from the acid *(top)*, both of which showed that the crack front was quite straight. The light-shaded corrosion product has the appearance of a nonstraight crack front, but careful examination showed the crack to be straight in this area as well. A straight crack is an important requirement for the deep crack tests here, in complement to the proposed K/v expression and plane-strain requirements already discussed. The scanning electron microscope (SEM) photo, Fig. 8*b*, is a portion of the fatigue precrack *(bottom)* and the subsequent environmental crack. Secondary cracking can be seen in the environmentally affected area of the fracture surface.

A few areas could be found on the environmental cracking fracture surfaces that were relatively free of corrosion products. Figure 9 shows high magnification SEM fractographs that compare a corrosion-product free area from the tube with an area ahead of the environmental cracking. Figure 9*a*, from an area just ahead of the notch, shows areas of secondary cracking and intergranular cracking, both of which have been associated with environmental cracking. Evidence of manganese sulfide stringers is also clear, aligned with the tube axis (horizontal in the photo). Immediately ahead of the area of environmental cracking, the appearance is typical dimpled rupture, as would be expected for fast, K_{Ic}-type fracture, see Fig. 9*b*. Figure 10 shows relatively corrosion-free areas of two specimens that were believed to be areas of environmental cracking, and the clear indications of secondary cracking and intergranular cracking confirm this belief. Note the similarity of the fracture appearance in the modeling specimens of Fig. 10 and that from the tube in Fig. 9*a*.

Energy dispersive X-ray spectra were taken at many of the areas of SEM study. Figure 11 is a presentation of key results from areas believed to be areas of environmental cracking, two from the failed tube and two from a test specimen. The results were obtained using a relatively low voltage for this process, 10 kv, in order to focus more on the surface layers of the sample than on the metal substrate. Spectra *a* and *b* are from the tube in areas comparatively free of

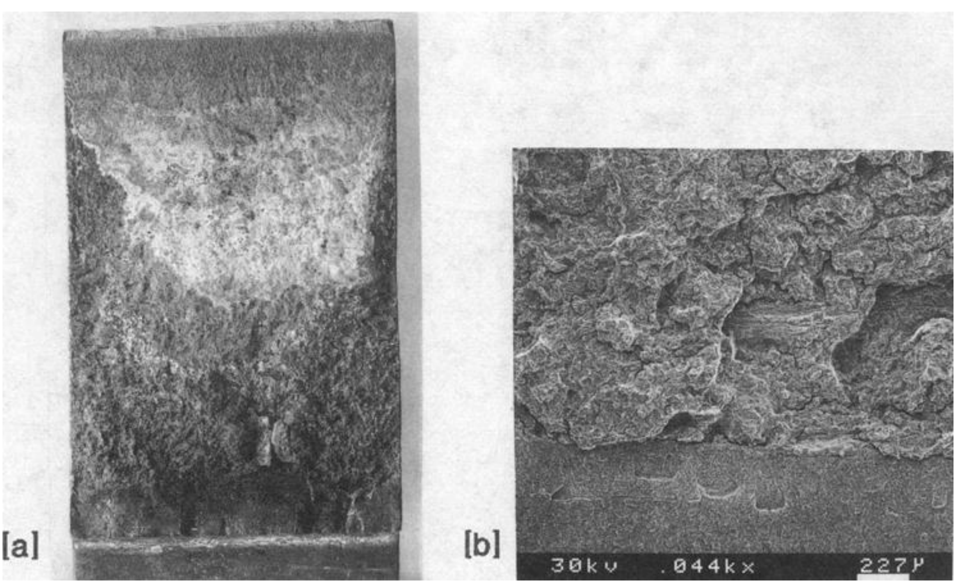

FIG. 8—*Optical and SEM fractographs of A723 steel exposed for 1600 h to 50%* H_2SO_4/50% H_3PO_4 *at 54°C:* (a) *macrophoto of Specimen 7 at ×3.2 original magnification and* (b) *SEM fractograph of Specimen 10 at ×44 original magnification.*

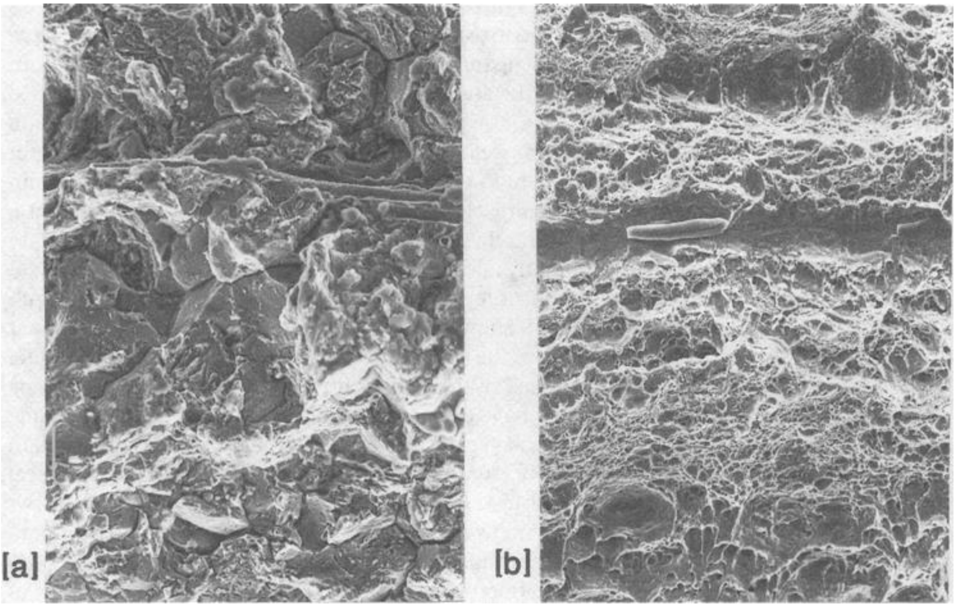

FIG. 9—*SEM fractographs of failed A723 steel tube exposed to 50%* H_2SO_4*/50%* H_3PO_4 *at 54°C and other environments;* ×*1000 original magnification:* (a) *area of apparent environmental cracking, 2 mm ahead of notch; and* (b) *area of apparent fast cracking, 7 mm ahead of notch.*

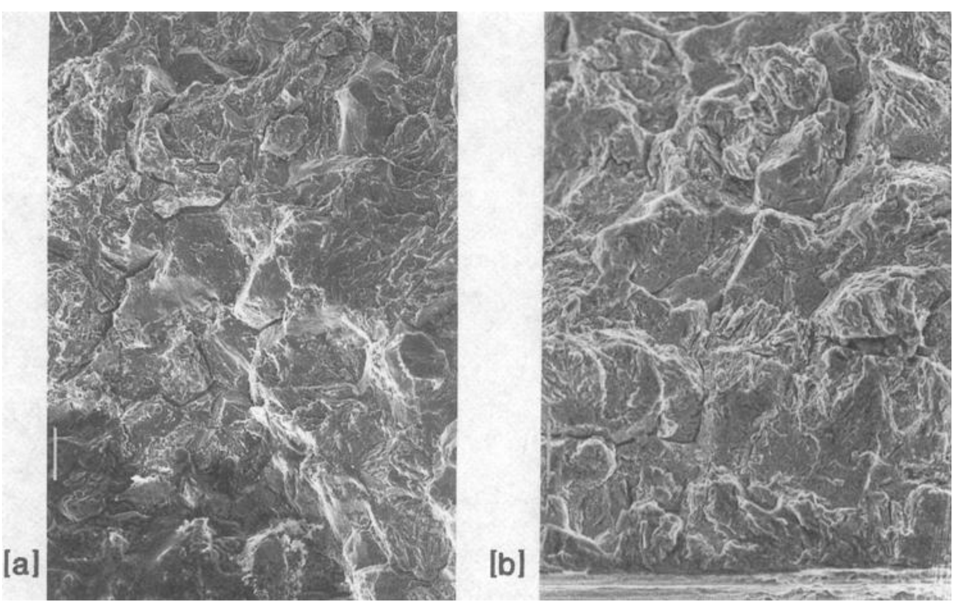

FIG. 10—*SEM fractographs of A723 steel exposed to 50%* H_2SO_4*/50%* H_3PO_4 *at 54°C;* ×*1000 original magnification:* (a) *Specimen 10, area near the end of apparent environmental cracking; and* (b) *Specimen 17, area adjacent to notch.*

corrosion and covered with corrosion, respectively, (Spectrum *a* is from near the area of the SEM photo of Fig. 9*a*). In Spectrum *a*, the sulfur and phosphorous indications are consistent with the sulfuric and phosphoric acid mixture being the cause of the cracking. Spectrum *b* is consistent with the presence of all the chemicals applied to the tube, which were H_2SO_4, H_3PO_4, NaOH, and CrO_3. This indicates that identification of the most obvious and heavy corrosion product does not necessarily identify the specific cause of cracking.

Spectra *c* and *d* are from Specimen 10 in areas comparatively free of corrosion and covered with corrosion, respectively (Spectra *c* is from near the area of the SEM photo of Fig. 10*a*). In Spectrum *c*, a phosphorous indication can be seen, and perhaps a sulfur indication, although it has not been designated. Spectra *d*, of a heavy corrosion area, includes clear indications of phosphorous, sulfur, and oxygen. The presence of oxygen is evidence that the corrosion product includes an oxide of sulfur or phosphorous or perhaps iron.

Implications

The results suggest, as in any study of environmental cracking, that cracking could be avoided by eliminating the aggressive environment or by eliminating or reducing the tensile stress. Neither the acid nor the residual stress could be eliminated without significant changes in the design and manufacturing process of the component. However, the concentration of the stress by the notch can be reduced with relatively little bother. Referring to a compendium of stress concentration factors [*10*], if the 9.8-mm depth of the notch remained the same and the notch radii were increased to a significant portion of the depth, say 8 mm, the result would be $k = 2.16$. Thus, by replacing the nearly square-cornered notch with one approaching a semicircle, the maximum stress would reduce to 36% of its former value. This would significantly reduce the likelihood of environmental cracking and failure of the tube by reducing both the concentrated residual stress that initiates and drives the cracking and the thermal stress that may accelerate the initiation process. An added bonus would be improved nondestructive inspection access to cracking, should it occur.

Summary and Conclusions

The key results and conclusions of the work regarding the environmental cracking in the tube and associated modeling tests are the following:

1. Hydrogen stress cracking was identified as the cause of the cracking of the tube and was modeled in bolt-loaded compact specimen tests of the same material and environment. Overstrain residual stress, concentrated at an OD notch, provided the sustained tensile stress, and a mixture of concentrated sulfuric and phosphoric acids at 54°C was the aggressive environment.
2. Modeling tests showed fast environmentally controlled cracking, with several millimetres of growth occurring typically in 3 min at applied K levels above 80 MPa $\sqrt{m}$. A threshold of environmental cracking was observed following 1540 h of acid exposure; three tests at different initial K levels resulted in threshold values of 16 to 19 MPa $\sqrt{m}$. A da/dt versus K plot of results showed the classic Phase I-III environmental cracking behavior.
3. Scanning electron fractography and energy dispersive X-ray spectra of tube and model specimen fracture surfaces corroborated the fracture mechanics test results. Secondary cracking and intergranular cracking were observed in the few areas of the fracture surface that were not obscured by corrosion product. Spectra of tube and modeling surfaces showed clear sulfur and phosphorous indications in the areas in which secondary and intergranular cracking were observed.

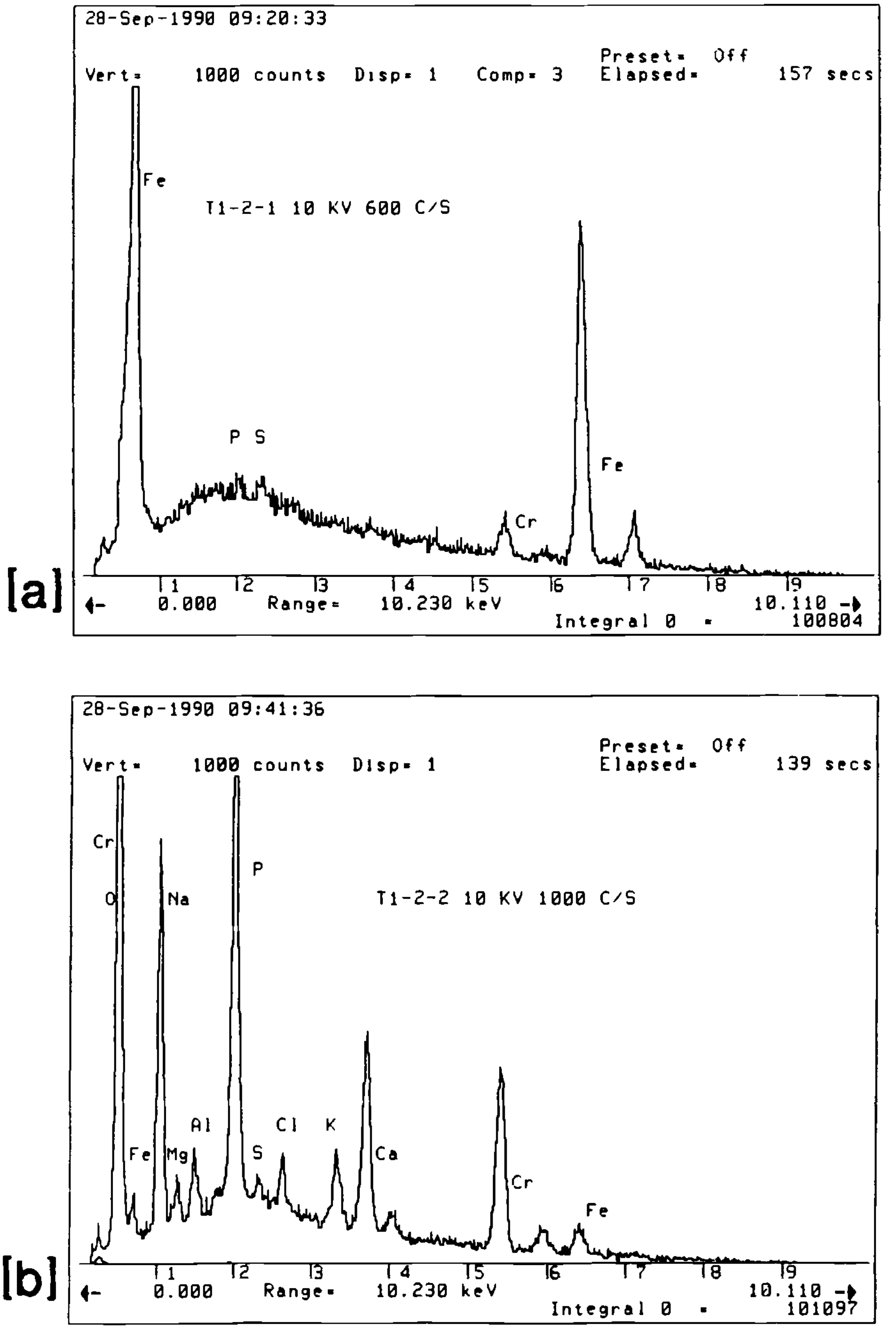

FIG. 11—*Energy dispersive X-ray spectra of A723 steel fracture surfaces subjected to various environments:* (a) *failed tube—area of apparent environmental cracking, but relatively free of corrosion products;* (b) *failed tube—area of apparent environmental cracking, with corrosion products;* (c) *Specimen 10—area of apparent environmental cracking, but relatively free of corrosion products; and* (d) *Specimen 10—area of apparent environmental cracking, with corrosion products.*

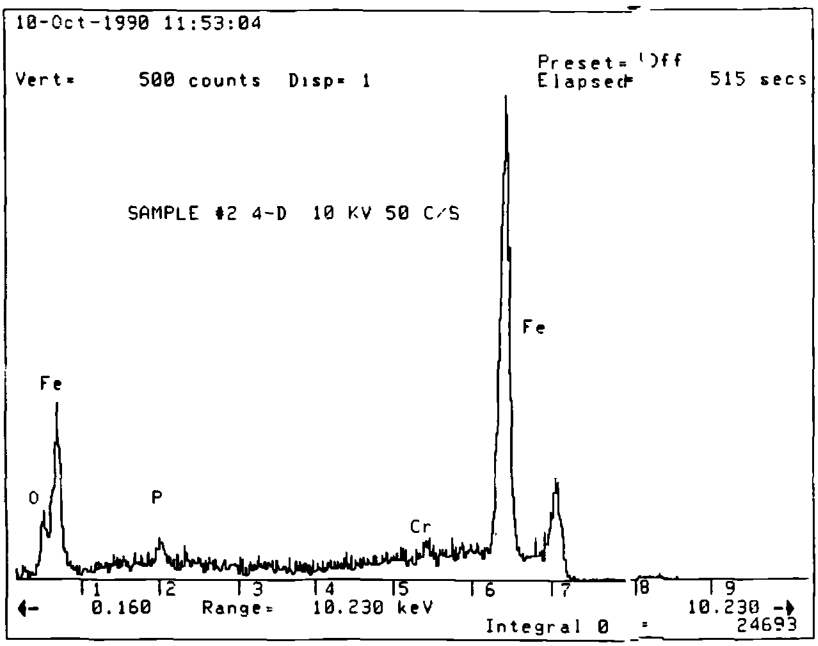

[c]

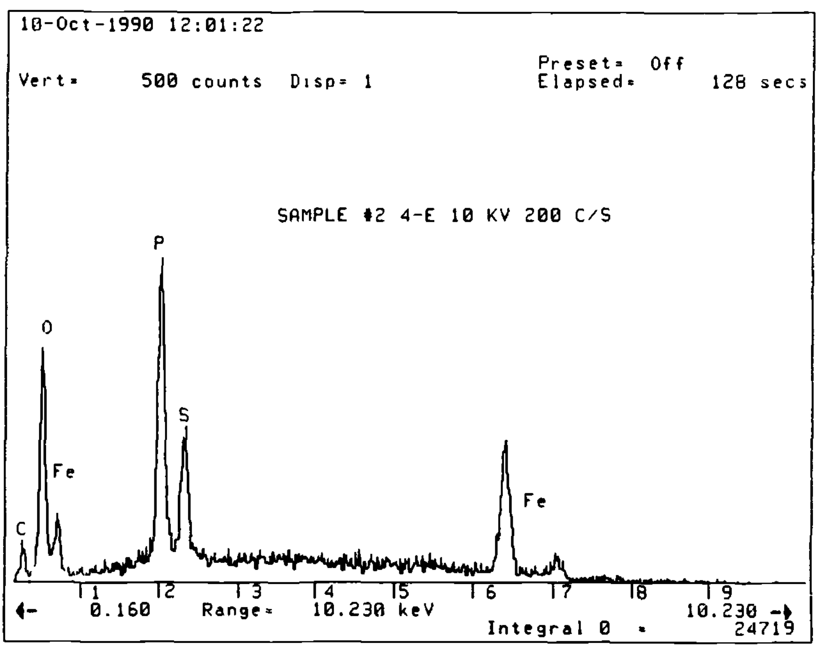

[d]

FIG. 11—*Continued.*

4. Thermal stresses concentrated by the notch were proposed as the source of the critical loading that followed environmental contact and broke the protective layers and thereby accelerated the environmental cracking of the tube.

The key results here with regard to the development of new test and analysis procedures for environmental cracking studies are the following:

1. A new K expression was developed for the $H/W = 0.486$ bolt-loaded specimen that is simpler, a better fit to Newman's numerical results, and fits a wider range of a/W, including the deep crack limit solution for this specimen.
2. A new criterion was developed for the specimen size required to maintain plane-strain constraint for displacement-loaded compact specimens. The similar form of the relationships for the Irwin plastic zone and the K limit for the specimen resulted in a simple size criterion.
3. A floating five-point average da/dt calculation procedure was shown to give a good description of environmental crack growth for a bolt-loaded specimen.

Acknowledgments

We are pleased to credit Mr. J. Zalinka and Mr. D. Corrigan for performing mechanical and fracture testing and Mr. C. Rickard for optical measurements and fractography.

References

[*1*] Kapp, J. A. and Underwood, J. H., "Service Simulation Tests to Determine the Fatigue Life of Outside-Diameter-Notched Thick-Wall Cylinders," *Experimental Mechanics*, Vol. 22, No. 3, March 1982, pp. 96–100.
[*2*] Wei, R. P. and Novak, S. R., "Interlaboratory Evaluation of K_{Iscc} and *da/dt* Determination Procedures for High-Strength Steels," *Journal of Testing and Evaluation*, Vol. 15, No. 1, Jan. 1987, pp. 38–75.
[*3*] James, L. A., "Compliance Relationships for the WOL Specimen Revisited," report to ASTM Subcommittee E-24.04 on Subcritical Crack Growth, July 1989.
[*4*] Tada, H., Paris, P. C., and Irwin, G. R., *The Stress Analysis of Cracks Handbook*, Paris Productions Inc., St. Louis, MO, 1985, p. 9.1.
[*5*] Underwood, J. H., Burch, I. A., and Ritter, J. C., "Crack-Arrest and Static Fracture Toughness Tests of a Ship Plate Steel," *Rapid Load Fracture Testing, ASTM STP 1130*, American Society for Testing and Materials, Philadelphia, 1991, pp. 147–160.
[*6*] Davidson, T. E., Barton, C. S., Reiner, A. N., and Kendall, D. P., "Overstrain of High Strength Open End Cylinders of Intermediate Diameter Ratio," *Proceedings*, First International Congress on Experimental Mechanics, Pergamon Press, Oxford, 1963.
[*7*] Uhlig, H. H. and Revie, R. W., *Corrosion and Corrosion Control*, Wiley, New York, 1985, pp. 123–147.
[*8*] Roark, R. J. and Young, W. C., *Formulas for Stress and Strain*, McGraw-Hill, New York, 1975, pp. 582–587.
[*9*] Smithells, C. J., *Metals Reference Book*, Butterworths, Washington, 1962, pp. 705–711.
[*10*] Peterson, R. E., *Stress Concentration Factors*, Wiley, New York, 1974, p. 40.

Anthony P. Parker,[1] *Robert C. A. Plant,*[2] *and Adib A. Becker*[3]

Fatigue Lifetimes for Pressurized, Eroded, Cracked, Autofrettaged Thick Cylinders

REFERENCE: Parker, A. P., Plant, R. C. A., and Becker, A. A., **"Fatigue Lifetimes for Pressurized, Eroded, Cracked, Autofrettaged Thick Cylinders,"** *Fracture Mechanics: Twenty-Third Symposium, ASTM STP 1189,* Ravinder Chona, Ed., American Society for Testing and Materials, Philadelphia, 1993, pp. 461–473.

ABSTRACT: This paper summarizes Boundary Element Method Stress Intensity Factor solutions, obtained by the authors and presented elsewhere, for internally pressurized thick cylinders having a single longitudinal, semicircular erosion on the internal bore with radial straight-fronted and elliptical cracks emanating from the deepest point of the bore erosion.

A ratio of external to internal cylinder radii (R_0/R_1) of 2.0 is employed and a range of semicircular erosion depths varying from 0 to 40% of the wall thickness. Care is taken to determine accurate stress concentration factors for the various erosion depths in order to accurately quantify limiting values of stress intensity factor at very short crack lengths.

Employing a standard fatigue crack growth law, lifetime calculations are presented for cyclic pressurization of the bore. The results indicate that the presence of a modest semicircular erosion at the bore serves to reduce the fatigue lifetime by an order of magnitude. A similar reduction in lifetime results from the elimination of the autofrettage residual stress field.

KEY WORDS: crack growth, fatigue cracks, cylinders, erosion, fracture (materials), fracture mechanics, residual stress, stress intensity factor, fatigue (materials)

Nomenclature

a	Crack depth, bore to crack tip
a^*	Crack depth, erosion to crack tip
$2b$	Surface crack length
C	Coefficient in Paris' crack growth law
K	Stress intensity factor
ΔK	Stress intensity factor range
m	Exponent in Paris' crack growth law
max	Maximum
min	Minimum
N	Number of loading cycles
p	Pressure
r	Radius
R_1	Tube inner radius

[1] Dean, Faculty of Engineering, Science and Technology, University of Northumbria at Newcastle, Newcastle upon Tyne, NE1 8ST, UK.

[2] Research assistant, Department of Mechanical and Computer Aided Engineering, University of Staffordshire, Stafford, ST1 OAD, UK.

[3] Lecturer, Mechanical Engineering Department, University of Nottingham, University Park, Nottingham, NG7 2RD, UK.

R_0 Tube outer radius
W Wall thickness ($R_0 - R_1$)

Fatigue crack growth arising from the cyclic pressurization of thick-walled cylinders tends to produce radial fatigue cracks emanating from the bore. A knowledge of the crack-tip intensity factor, K, is necessary in order to predict the fatigue crack growth rate, critical length, and lifetime of such cracks. It is common practice to produce an advantageous stress distribution by autofrettage (overstrain) of the cylinder in order to slow or prevent crack growth. This autofrettage process may involve plastic strain throughout the wall thickness (100% overstrain), or any lesser proportion of the wall thickness, depending upon the degree of overstrain applied to the cylinder by over pressure or by an over-sized mandrel swage process.

Reference *1* provides background on stress intensity solutions for a single, straight-fronted radial crack in a thick cylinder with an external to internal radius ratio (R_0/R_1) of 2.0, Fig. 1*a*. Solutions are provided for internal pressure (on bore and crack face) and for any proportion of overstrain from 0 to 100%. Reference *1* also proposes and employs a "crack shape correction factor" to account for the fact that cracks are frequently semi-elliptical in shape, Fig. 1*b*. The total crack depth (that is, semiminor axis) is a and the major axis is $2b$. Subsequent work, particularly that due to Tan and Shim [*2*] has provided more accurate solutions, based on the boundary element method (BEM) for the problem of a semi-elliptical crack in a pressurized, autofrettaged thick cylinder.

There are clear indications in Ref *1* that the presence of the autofrettage residual stress field may enhance fatigue lifetimes in typical materials and operating conditions by up to an order of magnitude.

Erosion at Bore

The purpose of this paper is to extend the types of analyses and predictions referred to earlier to a modified form of the geometry illustrated in Fig. 1. The modification is illustrated in Fig. 2 and consists of a single additional, longitudinal, semicircular erosion with a crack of depth

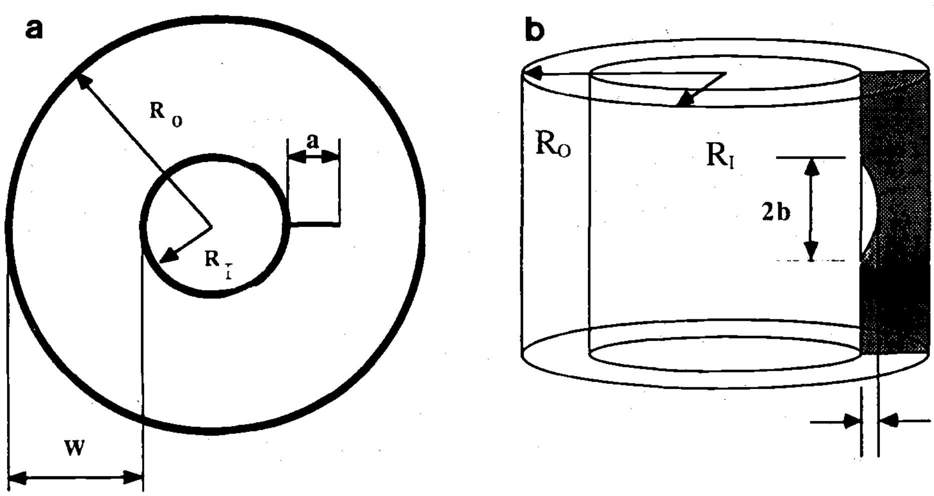

FIG. 1—(a) *Thick cylinder with single internal radial through crack.* (b) *Thick cylinder with intern radial semi-elliptical crack.*

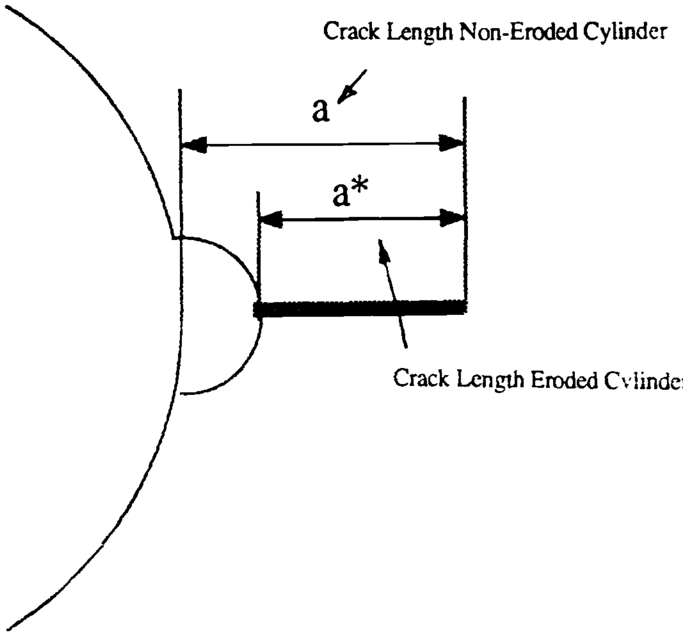

FIG. 2—*Schematic of cylinder bore showing semicircular erosion groove and associated radial crack.*

a^* (whether straight-fronted or semi-elliptical) emerging radially from the deepest point of the erosion. The reason for the concern over such geometries is that, under certain operating conditions, it is possible to produce a long, semicircular erosion groove in thick-walled tubes early in the fatigue lifetime of such tubes. It is further noted that such grooving effects appear to be associated with a reduction in fatigue lifetime of around one order of magnitude.

The authors have determined stress intensity factors for the eroded geometries referred to earlier with both straight-fronted and radial cracks by use of BEM employing quadratic elements. These results are reported in full in Refs *3* and *4* where the extensive use of superposition techniques is also explained. Where comparison is possible with the two-dimensional results reported in Ref *1* and the three-dimensional results reported in Ref *2*, agreement is generally within 0.5 and 2%, respectively. Examples of the solutions obtained for the two-dimensional and three-dimensional noneroded cases are presented in Figs. 3 and 4, respectively. For two-dimensional cases (Fig. 3), the minimum crack depth was 2.5% of wall thickness, while for three-dimensional cases (Fig. 4), it was 10% of wall thickness. These figures present normalized stress intensity solutions for a pressurized, autofrettaged thick cylinder having 100% overstrain and a ratio of yield strength/internal pressure of 3.55, a figure typical of certain high-pressure applications. Such pressure produces a hoop stress at the bore of 1.66 p (where p is internal pressure), while such autofrettage produces a compressive hoop stress at the bore amounting to 85% of the yield strength of the material.

Stress intensity factor solutions were obtained for various locations on the curved crack front from $\alpha = 0$ (deepest point) to $\alpha = 90°$ (bore surface). Results for $\alpha = 0$, 45, and 90° are presented in Fig. 4. In all subsequent lifetime calculations, the stress intensity factor employed is that for the deepest point on the crack front.

Referring to Figs. 3 and 4, a feature of high levels of autofrettage is noted, namely, the reduction of K below zero at short crack lengths. The implication of this result is that short cracks will be held closed, even at the peak of the pressure cycle, and no fatigue crack growth will

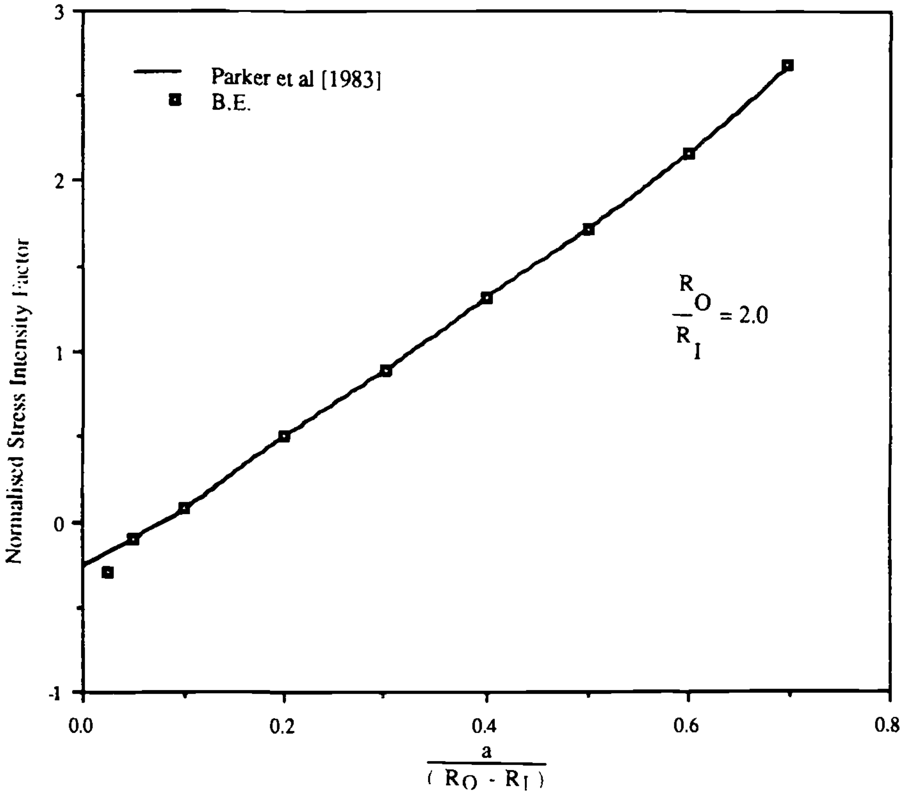

FIG. 3—*Stress intensity factors, normalized using* $p\sqrt{\pi a}$, *for a through-cracked pressurized, fully-autofrettaged thick cylinder radius ratio,* $R_O/R_I = 2.0$.

occur. In practice, even in cylinders subjected to 100% overstrain, it is unlikely that the idealized residual stress field will be achieved. The most straight forward indication of this effect is the opening of cut, autofrettaged tubes. Reference *1* reports work on this aspect and, for the purposes of fatigue calculations in this paper, it is assumed that only 0.7 of the magnitude of the idealized, 100% overstrain residual stress field is obtained, and hence only 0.7 of the associated negative contribution to stress intensity is available.

Stress Concentration Effects

It is important to appreciate the stress concentration effects arising from the introduction of the erosion. This is illustrated for the case of 5% erosion (that is, the depth of the erosion is 5% of the wall thickness) and internal pressure in Fig. 5. Here the familiar Lame's hoop stress distribution is increased dramatically near the erosion. This emphasizes two points, first, the stress concentration effect itself and, second, the impact on stress intensity factor at very short crack lengths. By this method, it is possible to determine, very accurately, limiting values of K as the crack length approaches zero. The range of erosion depths studied is between 5 and 40% of the wall thickness. The limiting value as erosion depth tends to zero is obtained from stan-

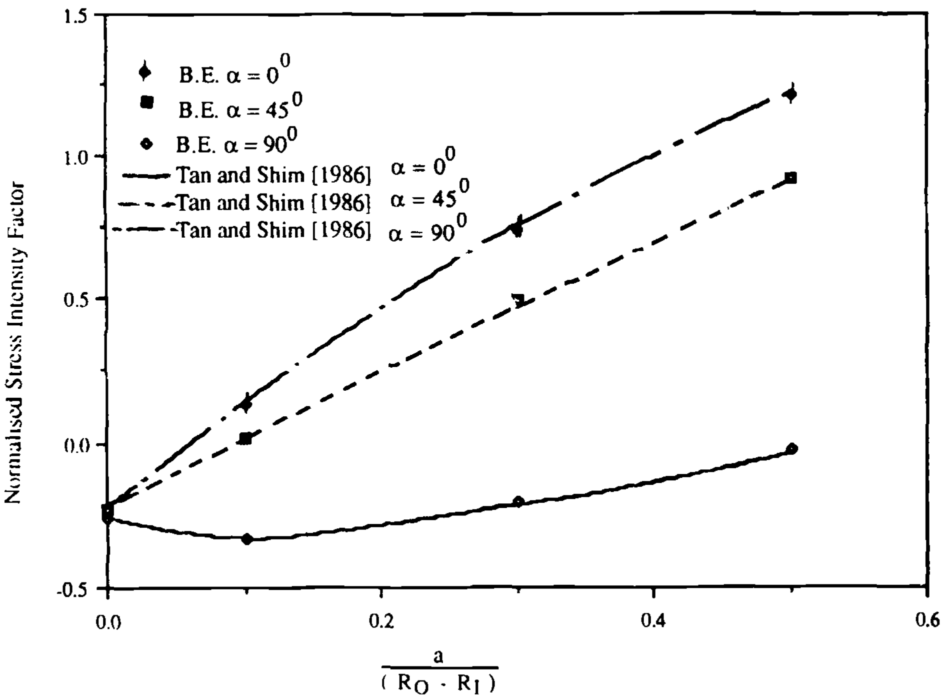

FIG. 4—*Stress intensity factors, normalized using* $p\sqrt{\pi a}$, *for a pressurized, fully-autofrettaged thick cylinder radius ratio*, R_0/R_I = *2.0, with semi-elliptical crack of eccentricity*, a/b = *0.8.*

dard limit solutions for edge-notched plates. The associated stress concentration factors are relatively constant varying over the range of 4.25 to 3.6 when calculated as the ratio hoop stress erosion tip/hoop stress at bore without erosion, Fig. 6. The limiting value as erosion depth approaches 0% is 4.30. Equivalent calculations were performed for the case of the semicircular erosion within the autofrettage field.

A problem does, however, arise when considering the stress concentration effects resulting from erosion within the residual stress field. The stress at the deepest point of the erosion is approximately three times that at the bore of the equivalent (100% overstrain) cylinder. Such an overstrained cylinder already contains hoop stresses near the bore that are very close to the compressive stress level for reversed yielding, and, therefore, this increased level of compressive stress will cause plastic flow at the tip of the erosion and a new, stable residual stress field to be created. All the analyses referred to earlier are linear-elastic, and it is therefore necessary to make some assumption as to the form of the new stress field. For the purposes of this work, it is assumed that the new stress field created ahead of the erosion is essentially the same as that adjacent to the bore in the noneroded cylinder, and that the stress intensity factors determined for the noneroded autofrettaged cylinder may be employed. While it is appreciated that such an assumption is, indeed, approximate, it is argued that it is pragmatically justified and that available evidence on the level of residual stress achieved in autofrettaged cylinders (and hence the associated negative contribution to stress intensity factor) is consistently lower than that predicted by the normal elastic/perfectly plastic analysis.

Typical stress intensity factor solutions for the case of the cracked, 5% eroded thick cylinder

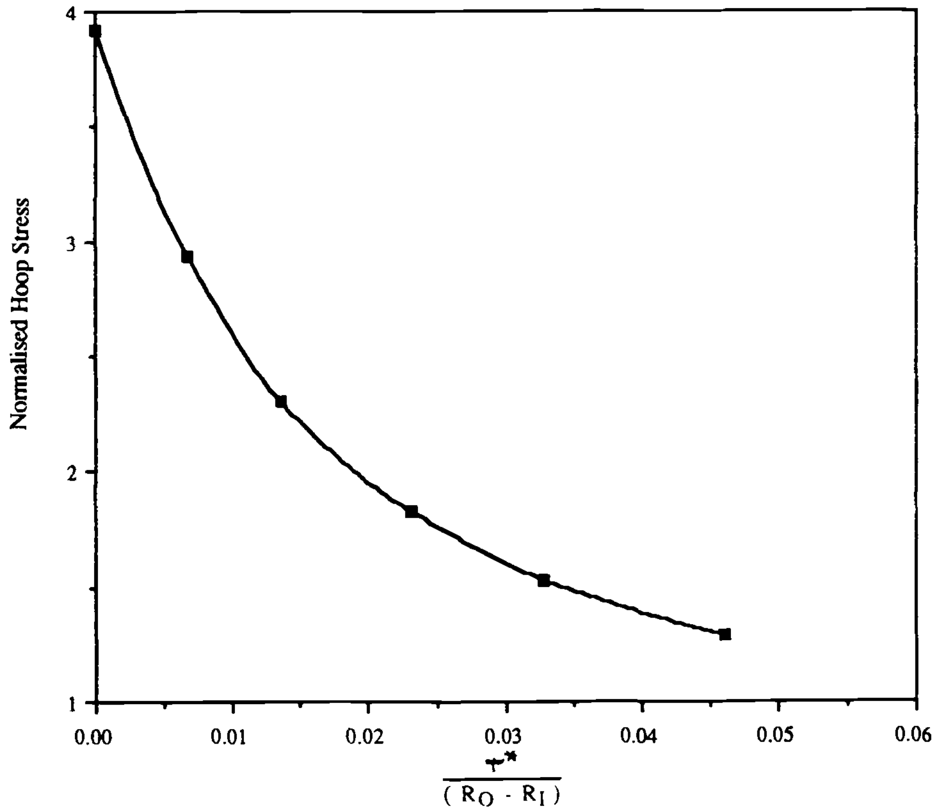

FIG. 5—*Pressurized thick cylinder: hoop stress at distance* r* *from tip of 5% erosion normalized with hoop stress at bore for noneroded case.*

with a semi-elliptical crack are presented in Fig. 7. The presentation adopted (namely, normalization of K with respect to $p\sqrt{\pi a}$) permits comparison with the equivalent set of results for the non-eroded cylinder and makes clear the asymptotic nature of the convergence of the eroded and noneroded solutions. The reader is cautioned that this presentation gives the "appearance" of lower stress intensity for the eroded cylinder. This is caused by the nature of the normalization at short crack lengths, the actual stress intensity for the eroded case is higher, in proportion to the stress concentration effect, than in the noneroded case.

Life Calculations

The fatigue growth rate of cracks subjected to cyclic loading may be expressed in terms of Paris' law [*1*]

$$\frac{da}{dN} = C(\Delta K)^m \tag{1}$$

where da/dN is the fatigue crack growth per loading cycle, C and m are empirical constants, and ΔK is the range of stress intensity defined by

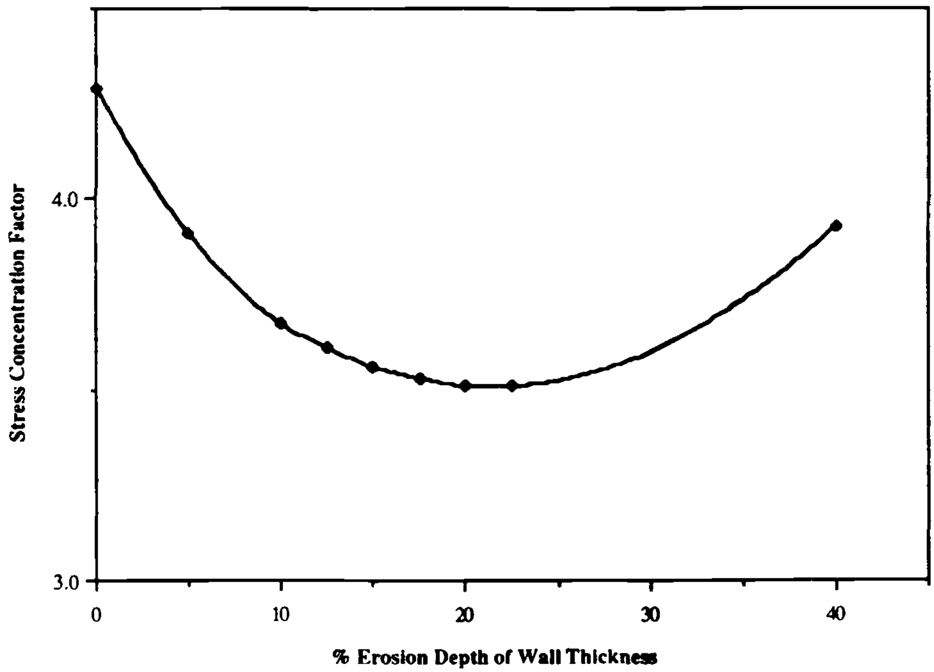

FIG. 6—*Pressurized thick cylinder: stress concentration factors for various erosion depths.*

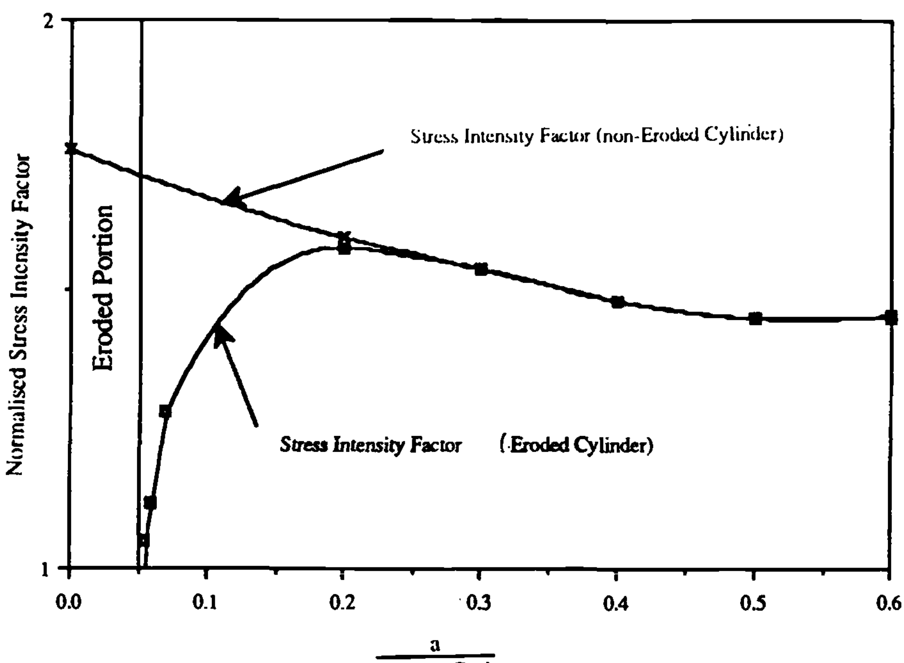

FIG. 7—*Stress intensity factors for pressurized thick cylinder with elliptical crack with and without erosion.*

$$\Delta K = K_{max} - K_{min'}, (K_{min} \geq 0) \tag{2}$$

$$\Delta K = K_{max'}, (K_{min} < 0) \tag{3}$$

where K_{max} and K_{min} are the maximum and minimum values of stress intensity during the loading cycle, respectively. Note that the possibility of "overlapping" or touching of the crack surfaces at some point on the crack line remote from the crack tip is not considered in this paper [5]. During the lifetime of a particular cracked cylinder, the crack will propagate from some initial depth, a_i, after N_i cycles to some final depth, a_f, after N_f cycles, where a_f is the total wall thickness of the cylinder, $R_0 - R_1$ or such shorter length that is required to attain a critical value of stress intensity. In order to predict the propagation life, Eq 1 is rearranged to give

$$\int_{a_i}^{a_f} \frac{da}{C(\Delta K)^m} = N_f - N_i \tag{4}$$

Crack growth (a versus N) predictions are made for both straight-fronted cracks and for semi-elliptical cracks. In the case of the semi-elliptical cracks, the eccentricity, a/b, is 0.8. The predictions are based on cylinders with an internal radius of R_1 of 50 mm and a ratio R_0/R_1 of 2.0. The cyclic pressurization is 0 to 344 MN m^{-2}. The cylinder material is assumed to have a yield strength of 1221 MN m^{-2}; this property can be slightly different after overstrain, due to the plastic strain, which can be up to 1% at the inner radius of 100% overstrained cylinders. Considering this small amount of plastic strain relative to reduction in area, no significant effect on fatigue life is expected as a result of the material property changes due to the overstrain process.

In general the integral of Eq 4 was evaluated numerically using Simpson's rule. A typical value of $C = 2.209 \times 10^{-11}$ and $m = 2.75$ for crack growth in metres per cycle and ΔK in MN m$^{-(3/2)}$ are employed. In all cases where the crack reaches a critical length, the critical crack length was calculated on the basis of a fracture toughness value of 150 MN m$^{-(3/2)}$.

Lifetimes have been calculated for the following load and geometry conditions for both two- and three-dimensional cases:

(*a*) internal pressure,
(*b*) internal pressure and autofrettage,
(*c*) internal pressure with erosion, and
(*d*) internal pressure and autofrettage with erosion.

In each case, the erosion occupies 5% of the wall thickness. Because the erosion is taken to occur early in the lifetime, it is assumed that cracks of a specific initial crack length (0.125, 0.25, 0.5, or 1 mm) exist in each of Configurations *a* to *d* listed earlier, that is, for the non-eroded case the initial crack size is the same as that for the eroded case. The smallest straight-fronted crack (0.125 mm) produces a minimum stress intensity of 4.5 MN m$^{-(3/2)}$ in the non-eroded, autofrettage tube and of 17.4 MN m$^{-(3/2)}$ in the equivalent eroded tube. In the case of semi-elliptical crack of depth 0.125 mm, the minimum stress intensities are 3.5 MN m$^{-(3/2)}$ and 13.5 MN m$^{-(3/2)}$, respectively.

Two-Dimensional Case, Straight-Fronted Cracks

Results for each of the cases just listed are presented in Figs. 8 to 11 for the range of initial crack lengths listed earlier.

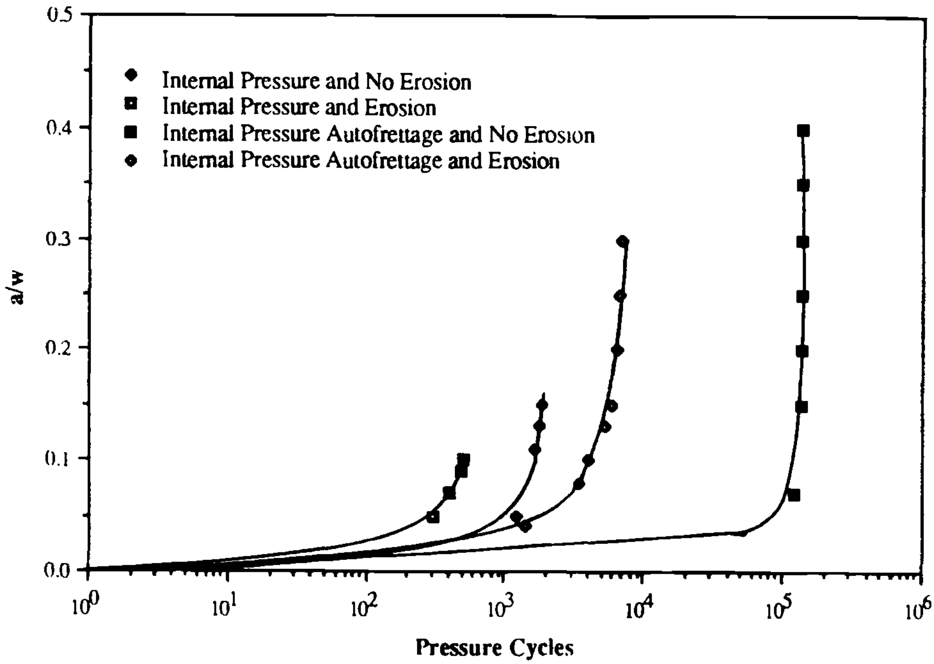

FIG. 8—*Fatigue crack growth, straight-fronted crack, initial depth 1.0 mm.*

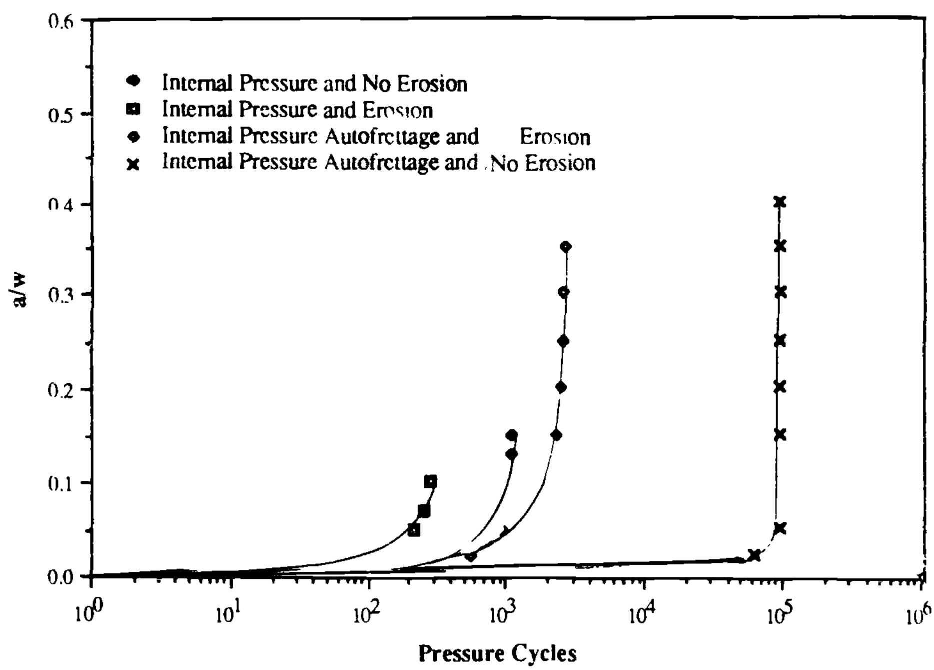

FIG. 9—*Fatigue crack growth, straight-fronted crack, initial depth 0.5 mm.*

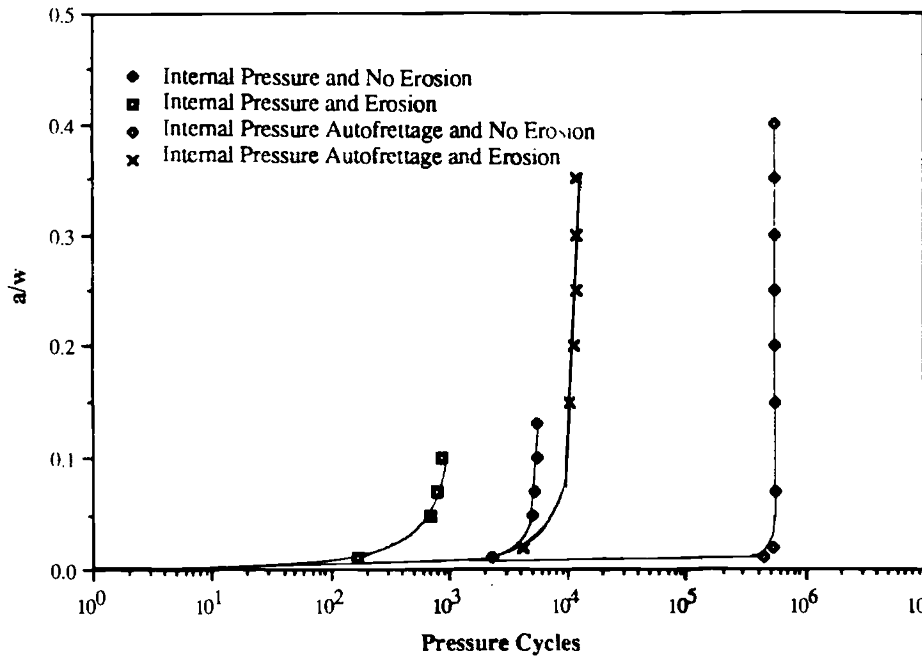

FIG. 10—*Fatigue crack growth, straight-fronted crack, initial depth 0.25 mm.*

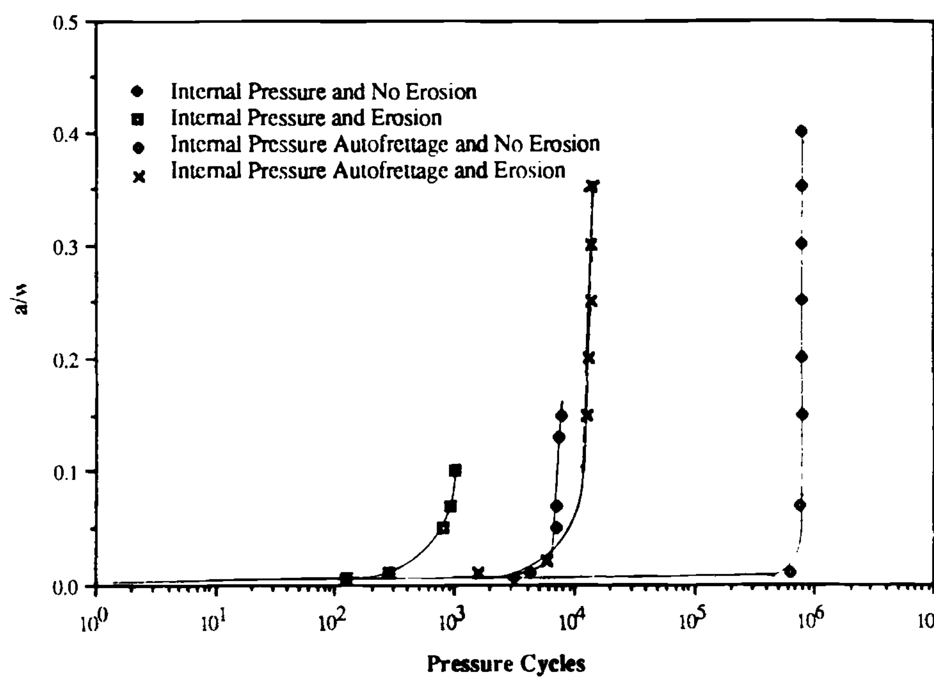

FIG. 11—*Fatigue crack growth, straight-fronted crack, initial depth 0.125 mm.*

In all cases where autofrettage is present, it is assumed that 0.7 of K due to idealized 100% overstrain has been achieved.

Three-Dimensional Case, Semi-Elliptical Cracks

Equivalent results are presented in Figs. 12 to 15 for the range of initial crack lengths just listed. Again the proportion of K due to overstrain achieved is 0.7 of that due to 100% overstrain.

Discussion and Conclusions

Life predictions for cracked tubes require an accurate knowledge of stress intensity factor at short and medium crack length. In this paper, two-dimensional straight-fronted cracks and three-dimensional semi-elliptical crack solutions obtained by use of the Boundary Element Method were presented. These represent the problem of pressurized thick cylinders with cracks emanating from the bore or from a single longitudinal, semicircular erosion groove in tubes with and without autofrettage.

Lifetime predictions for all two- and three-dimensional configurations generally conform to the following pattern:

(*a*) The combination of zero autofrettage, erosion, and internal pressure produces the shortest lifetimes.
(*b*) Lifetimes in (*a*) may be improved by an order of magnitude by autofrettage.
(*c*) Lifetimes in (*a*) may be improved by an order of magnitude by elimination of the erosion.

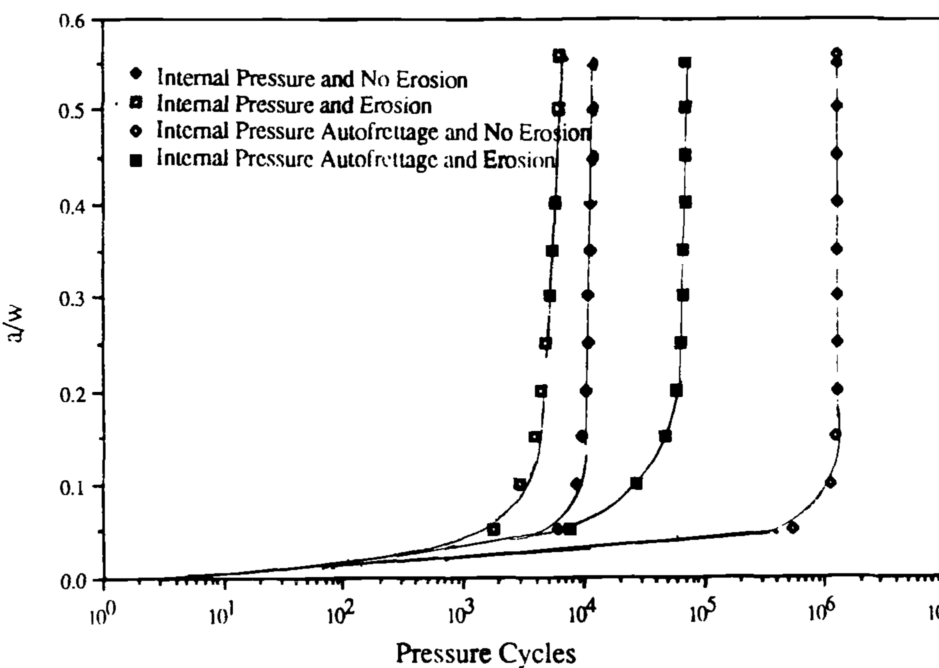

FIG. 12—*Fatigue crack growth, semi-elliptical crack, initial depth 1.0 mm.*

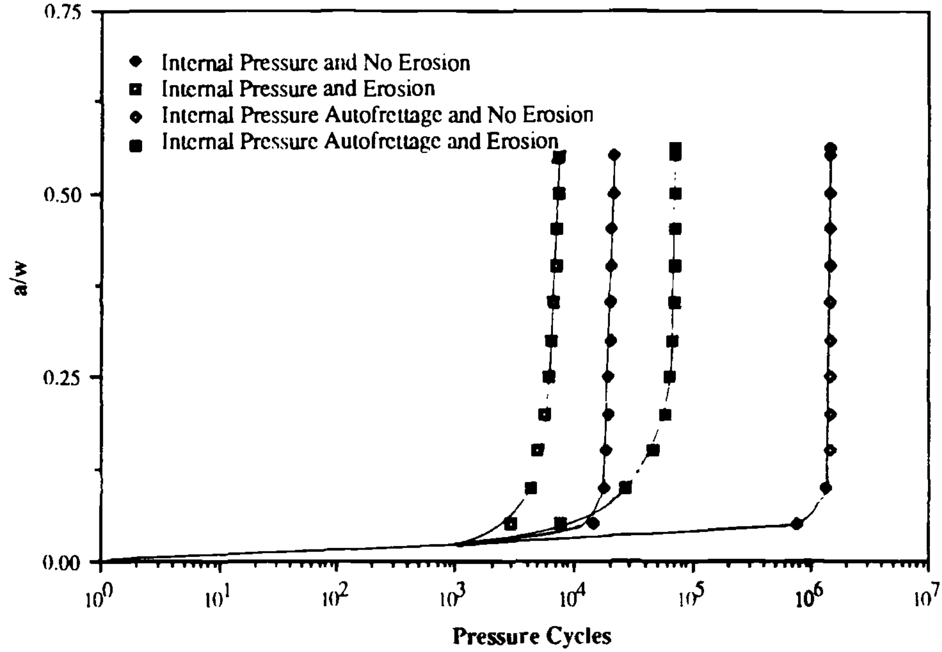

FIG. 13—*Fatigue crack growth, semi-elliptical crack, initial depth 0.5 mm.*

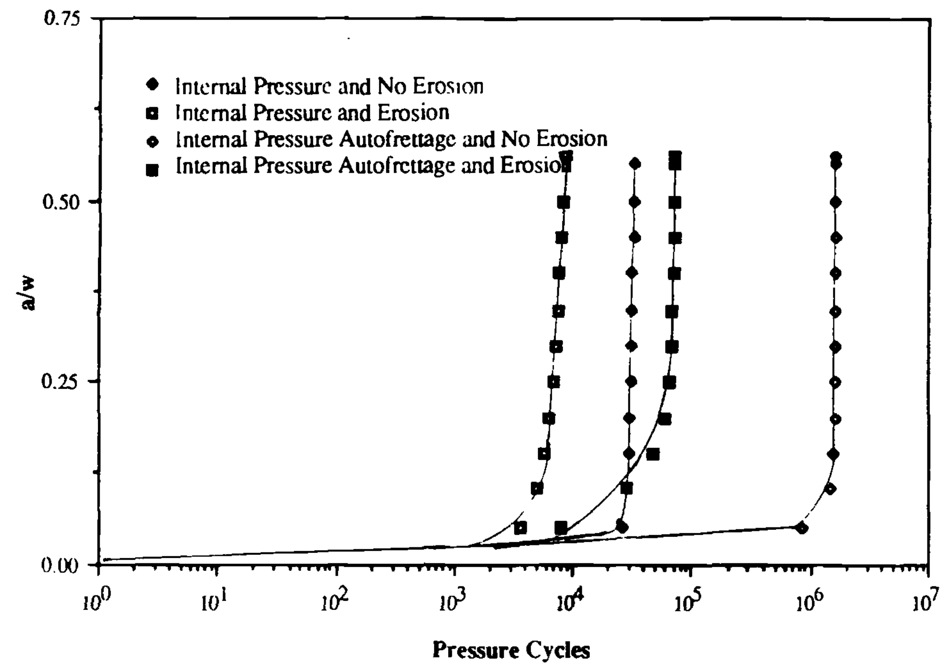

FIG. 14—*Fatigue crack growth, semi-elliptical crack, initial depth 0.25 mm.*

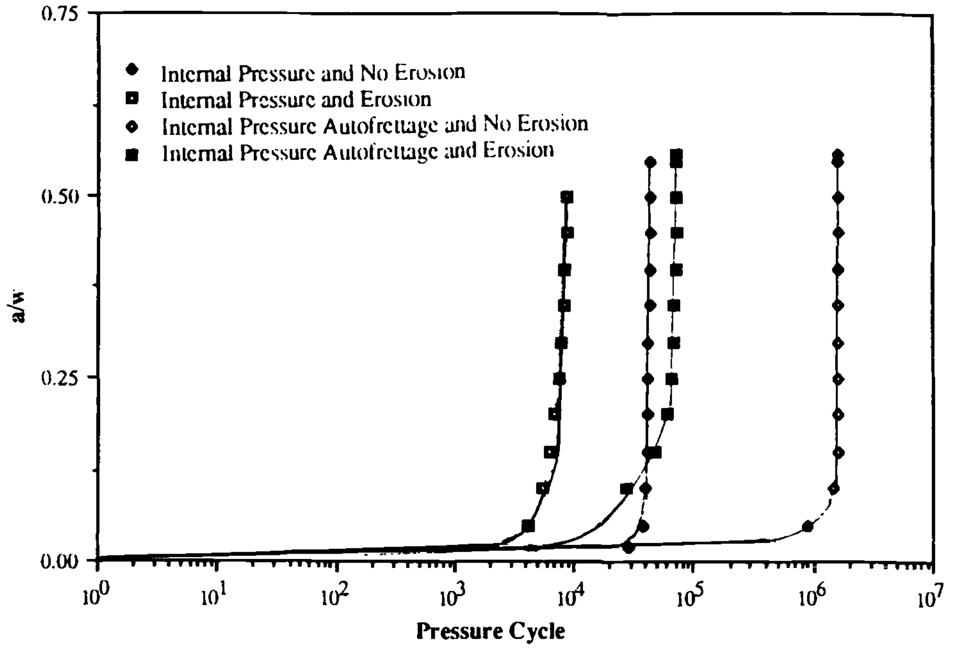

FIG. 15—*Fatigue crack growth, semi-elliptical crack, initial depth 0.125 mm.*

(*d*) Lifetimes in (*a*) may be improved by between two and three orders of magnitude by inclusion of autofrettage and elimination of the erosion.

The reader is cautioned not to treat the predictions as a precise representation of real-life effects. The two major caveats relate to the possibility that full pressure does not infiltrate the cracks [*1*] and that it is not possible to achieve the predicted (ideal elastic/plastic) residual stress field as evidenced by experimental work on cut, autofrettaged tubes [*1*].

Acknowledgments

The authors wish to acknowledge support from a UK Ministry of Defence research contract, and the advice and support of Mr. B. D. Goldthorpe.

References

[*1*] Parker, A. P., Underwood, J. H., Throop, J. F., and Andrasic, C. P., "Stress Intensity and Fatigue Crack Growth in a Pressurized Autofrettaged Thick Cylinder," *Fracture Mechanics: 14th Symposium, Volume 1: Theory and Analysis, ASTM STP 791,* J. C. Lewis and G. Sines, Eds., American Society for Testing and Materials, Philadelphia, 1983, pp. I-216–I-237.

[*2*] Tan, C. L. and Shim, M. L., "Stress Intensity Factor Influence Coefficients for Internal Surface Cracks in Thick Walled Cylinders," *International Journal of Pressure Vessels and Piping,* Vol. 24, 1986, pp. 49–72.

[*3*] Becker, A. A., Plant, R. C. A., and Parker, A. P., "Axial Cracks in Pressurised, Eroded, Autofrettaged Thick Cylinders," in preparation.

[*4*] Plant, R. C. A., Becker, A. A., and Parker, A. P., "Three Dimensional Semi-Elliptical Cracks in Pressurised, Eroded, Autofrettaged Thick Cylinders," in preparation.

[*5*] Parker, A. P. in *Residual Stress Effects in Fatigue, ASTM STP 776,* American Society for Testing and Materials, Philadelphia, 1982, pp. 13–31.

Julie A. Henkener,[1] Victor B. Lawrence,[1] and Royce G. Forman[2]

An Evaluation of Fracture Mechanics Properties of Various Aerospace Materials

REFERENCE: Henkener, J. A., Lawrence, V. B., and Forman, R. G., "**An Evaluation of Fracture Mechanics Properties of Various Aerospace Materials,**" *Fracture Mechanics: Twenty-Third Symposium, ASTM STP 1189*, Ravinder Chona, Ed., American Society for Testing and Materials, Philadelphia, 1993, pp. 474–497.

ABSTRACT: This paper presents results from a series of fracture mechanics tests that used a variety of aerospace materials, including 6063 aluminum in the T5 and T6 tempers, 2014-T651 aluminum welded with a 4043 filler material, Inconel 718, A286 steel, superalloy MP35N, beryllium SR-200E, magnesium AZ-31B-H24 and ZK-60A-T5, beryllium-copper CDA172, and aluminum-bronze CDA630. The fatigue crack growth data for these materials were curve fit using the crack propagation and other related equations that will be incorporated into an updated version of the NASA/FLAGRO computer program. This program will help achieve more reliable fracture mechanics assessments of space systems hardware.

KEY WORDS: crack propagation, fatigue (materials), fracture mechanics, toughness, aerospace materials, fatigue crack growth

Nomenclature

a	Depth, length, or half length of crack
c	Width or half width of crack
f	Crack opening function, Eq 2
n, p, q	Exponents in Eq 1
t	Thickness of plate, sheet, or forging
w	Specimen width
t_0	Thickness to meet plane-strain condition, Eq 9
A_0, A_1, A_2, A_3	Coefficients for crack opening function, Eqs 3 through 6
A_k, B_k	Fit parameters in Eq 8
C_k	Fit parameter in Eq 10
C	Growth rate coefficient
K_{Ic}	Plane strain fracture toughness
K_{Ie}	Effective fracture toughness for surface or elliptically shaped crack
$K_{Ie(a)}$	K_{Ie} evaluated in the thickness direction
$K_{Ie(c)}$	K_{Ie} evaluated in the width direction
ΔK_0	Threshold stress intensity factor range at $R = 0$
ΔK_{th}	Threshold stress intensity factor range
N	Number of applied fatigue cycles
R	Stress ratio
S_{max}	Maximum applied stress

[1] Senior associate engineers, Lockheed Engineering & Sciences Co., Houston TX 77258.
[2] Senior materials engineer, NASA Lyndon B. Johnson Space Center, Houston, TX 77058.

α	Plane stress/strain constraint factor
σ_0	Flow stress
σ_{ys}	Tensile yield strength

The need for a method of performing safe life analyses for Space Shuttle payloads and, in the future, for the Space Station Freedom, has prompted the development of the NASA/FLAGRO computer program [1,2]. In support of this program, an extensive database of fracture mechanics properties, surveying a variety of materials that are used for aerospace applications, is required. Fracture toughness data are especially important and should include plane strain fracture toughness (K_{Ic}) values, part-through fracture toughness (K_{Ie}) values, and any other available fracture toughness (K_c) values as a function of thickness. This paper investigates the role of fracture toughness in curve fitting fatigue crack growth data to the equations included in NASA/FLAGRO. In addition, the results from a series of fracture mechanics tests, using aluminum alloys, high-strength bolt alloys, and other alloys used for specialized aerospace applications, are presented with the resultant fatigue crack growth curve fits.

Theoretical Background

Crack growth rate calculations in the next release of the NASA/FLAGRO computer program will use the NASGRO 2.0 crack growth relationship [3], which is given by

$$da/dN = \frac{C(1-f)^n \Delta K^n \left(1 - \frac{\Delta K_{th}}{\Delta K}\right)^p}{(1-R)^n \left(1 - \frac{\Delta K}{(1-R)K_c}\right)^q} \tag{1}$$

where

N = number of applied fatigue cycles,
a = crack length,
R = stress ratio,
ΔK = stress intensity factor range,
ΔK_{th} = threshold stress intensity factor range, and
C, n, p, q = empirically derived constants.

The crack opening function, f, for plasticity-induced crack closure has been defined [4] as

$$f = \frac{K_{op}}{K_{max}} = \begin{cases} A_0 + A_1 R + A_2 R^2 + A_3 R^3 & R \geq 0 \\ A_0 + A_1 R & -1 \leq R < 0 \end{cases} \tag{2}$$

and the coefficients are given by

$$A_0 = (0.825 - 0.34\alpha + 0.05\alpha^2)\left[\cos\left(\frac{\pi}{2} S_{max}/\sigma_0\right)\right]^{1/\alpha} \tag{3}$$

$$A_1 = (0.415 - 0.071\alpha) S_{max}/\sigma_0 \tag{4}$$

$$A_2 = 1 - A_0 - A_1 - A_3 \tag{5}$$

$$A_3 = 2A_0 + A_1 - 1 \tag{6}$$

In these equations, α, which is a plane stress/strain constraint factor, is treated as a constant for the purposes of curve fitting the crack growth data for a particular material system. Values range from 1, which would indicate a plane stress condition, to 3, which would indicate a condition of plane strain. Materials, such as high-strength steels, for which the K_{Ic}/σ_{ys} ratio is relatively low, are usually assigned relatively high α values, while materials with higher K_{Ic}/σ_{ys} ratios usually have α values ranging from 1.5 to 2.0. While better correlation with experimental results may be obtained by allowing α to vary with K_{max} [4], reasonable agreement has been obtained by using it strictly as a fitting parameter. In addition, S_{max}/σ_0, the ratio of the maximum applied stress to the flow stress, is assumed to be constant. All materials that are being fit for NASA/FLAGRO use an average value of $S_{max}/\sigma_0 = 0.3$. Since the effect of S_{max}/σ_0 on the crack opening function is relatively small for positive stress ratios, using this parameter as a constant has been shown to produce acceptable results [3]. It should be noted that the crack opening function was derived from an analysis of center-cracked panels, subjected to a constant load amplitude condition, in which the crack front advances through a zone of plastically deformed material. Johnson Space Center is currently sponsoring research where elastic-plastic finite-element techniques are used to investigate the effects of thickness and combined tension/bending loads on the three-dimensional closure behavior of through-cracks. Also, the validity of applying the crack opening function (Eq 2) to part-through-cracks is not clear at this time. Future elastic-plastic finite-element work on part-through-crack configurations will be required to adequately address this question.

The threshold stress intensity factor range, ΔK_{th}, is approximated as a function of the stress ratio, R, and the threshold stress intensity factor range at $R = 0$, ΔK_0, by the following equation [3]

$$\Delta K_{th} = \Delta K_0 \left[\frac{4}{\pi} \arctan(1 - R) \right] \tag{7}$$

A comparison of ΔK_{th} versus R data for several aluminum alloys with a curve fit according to Eq 7, indicates good agreement in Fig. 1.

The following relationship has been adopted to describe the K_c versus thickness behavior of various materials [1]

$$K_c/K_{Ic} = 1 + B_k e^{-(A_k t/t_0)^2} \tag{8}$$

where

$$t_0 = 2.5(K_{Ic}/\sigma_{ys})^2 \tag{9}$$

For through-crack geometries, these equations are used by NASA/FLAGRO to calculate a K_c value for Eq 1. On the other hand, for calculations using part-through-crack geometries, K_c in Eq 1 is set equal to a constant value of K_{Ie} (evaluated in the thickness direction). Surface-cracked toughness data often show a high degree of scatter and are known to vary greatly with crack size. However, using a constant value of K_{Ie} simplifies crack growth predictions and is justified since K_{Ie} values do not show a significant thickness effect. It may be shown that K_{Ie} is related to K_{Ic} according to

$$K_{Ie} = K_{Ic}(1 + C_k K_{Ic}/\sigma_{ys}) \tag{10}$$

where C_k is an empirical constant with units of length$^{-1/2}$. This relationship holds for a variety of materials (Fig. 2), and may be used to approximate K_{Ie} for materials that have insufficient

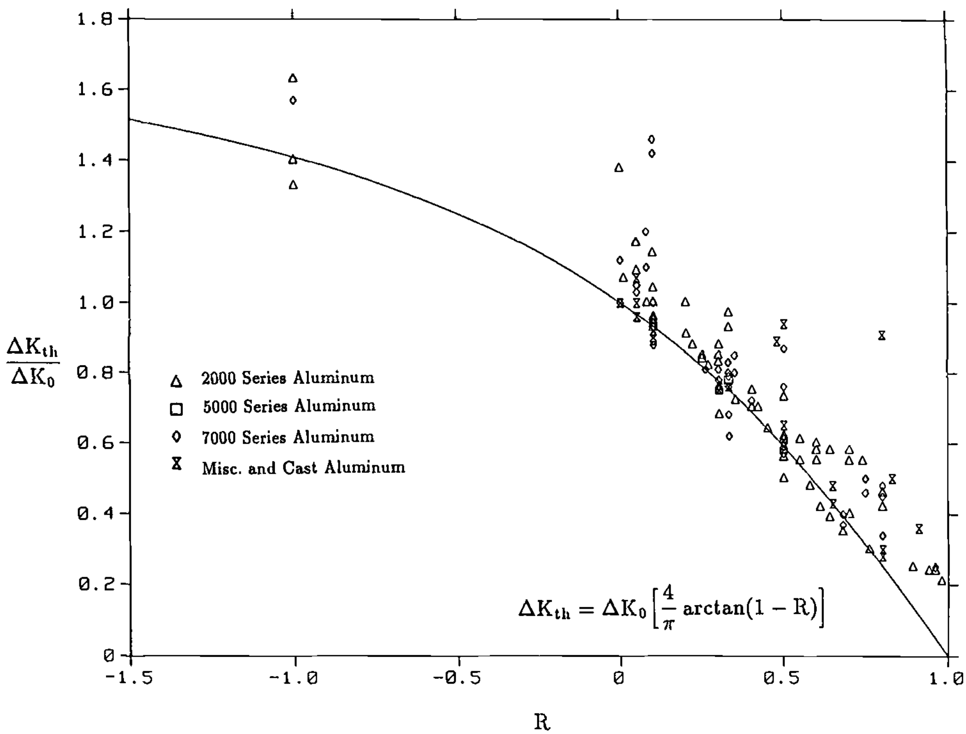

FIG. 1—*Comparison of* $\Delta K_{th}/\Delta K_0$ *versus* R *data for several aluminum alloys with curve fit relationship.*

surface-cracked toughness data. For materials that have a very high K_{Ic}/σ_{ys} ratio, K_{Ie} values calculated by this equation are limited to 1.4 times the K_{Ic} values in NASA fracture control analyses.

Experimental Details

Fracture toughness tests were performed according to ASTM Test Method for Plane-Strain Fracture Toughness of Metallic Materials (E 399-83) [*5*] using C(T) (compact tension) specimens machined in both the C-L and C-R orientations from beryllium-copper alloy CDA172. In addition, toughness tests were conducted in the L-C orientation using beryllium-copper M(T) (center-cracked) and PS(T) (surface-cracked) specimens of varying thickness. Details regarding these tests may be found in Ref *6*.

Constant-load-amplitude fatigue crack growth tests were conducted according to the procedures in ASTM Test Method for Measurements of Fatigue Crack Growth Rates (E 647-88) [*7*]. All crack growth tests were performed in laboratory air conditions in a frequency range of 1 to 50 Hz, using an automated data acquisition system. The crack length during each test was monitored using an indirect d-c potential method [*8*]. The materials tested were beryllium-copper (Be-Cu) alloy CDA172 [*6*]; aluminum 2014-T651 and aluminum 2014-T651 welded with a 4043 filler material [*9*]; aluminum 6063 in the T5 and T6 tempers, beryllium SR-200E, aluminum-bronze CDA630, and magnesium alloys AZ-31B-H24 and ZK-60A-T5 [*10*]; and A286 steel, Inconel 718, and MP35N. Table 1 presents information regarding the specimens used for the crack growth tests for each material type.

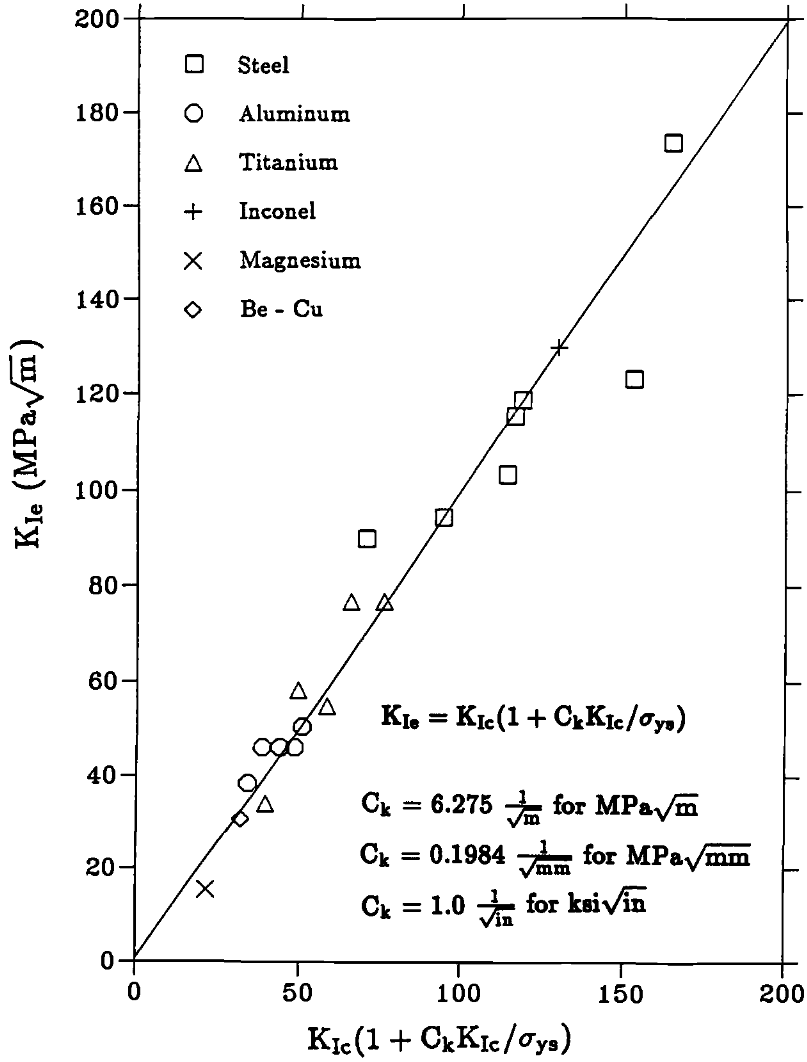

FIG. 2—*Comparison of* K_{Ie} *versus* K_{Ic} *for several classes of materials.*

Discussion of Results

Fracture Toughness Results

The K_{Ic} values obtained in the C-L and C-R orientations from the Be-Cu C(T) specimens were found to be comparable, producing an average toughness of 28.0 MPa $\sqrt{m}$. Average K_{Ie} values from the PS(T) specimens were determined to be $K_{Ie(a)}$ = 30.1 MPa $\sqrt{m}$ and $K_{Ie(c)}$ = 27.2 MPa $\sqrt{m}$. This average $K_{Ie(a)}$ was in good agreement with a K_{Ie} value of 32.5 MPa $\sqrt{m}$, which was calculated from Eq 10. For the materials in this study, average K_{Ic} values and the K_{Ie} values calculated from Eq 10 are listed in Table 2.

Fracture toughness values from both the through- and part-through-crack geometries are plotted as a function of thickness in (Fig. 3). Using the constants A_k = 0.35 and B_k = 0.5, the

TABLE 1—*Summary of fatigue crack growth tests.*

Material	Specimen Type	Orientation	w, mm	t, mm	Number of Tests
6063-T5	C(T)	T-L	76.20	12.70	10
6063-T6	C(T)	T-L	76.20	12.70	5
2014-T651	C(T)	T-L	76.20	12.70	6
2014-T651 GTA welded	C(T)	parallel to weld	76.20	12.70	13
Inconel 718 STA	SE(B)	L-R	30.48	15.24	12
Inconel 718 STCWA	SE(B)	L-R	30.48	15.24	10
A286 (950 MPa)	SE(B)	L-R	27.94	13.97	7
A286 (1100 MPa)	SE(B)	L-R	27.94	13.97	10
A286 (1375 MPa)	SE(B)	L-R	25.40	12.70	8
MP35N	SE(B)	L-R	19.05	8.89	2
Al-bronze	DC(T)	C-R	76.20	12.70	11
Be SR-200E	C(T)	unknown	50.80	1.98	8
Be SR-200E	M(T)	unknown	50.80	1.98	7
AZ-31B-H24	C(T)	T-L	76.20	12.70	8
ZK-60A-T5	C(T)	T-L	76.20	12.70	9
Be-Cu CDA172	C(T)	C-R	50.80	8.89	12
Be-Cu CDA172	C(T)	C-L	50.80	8.89	10

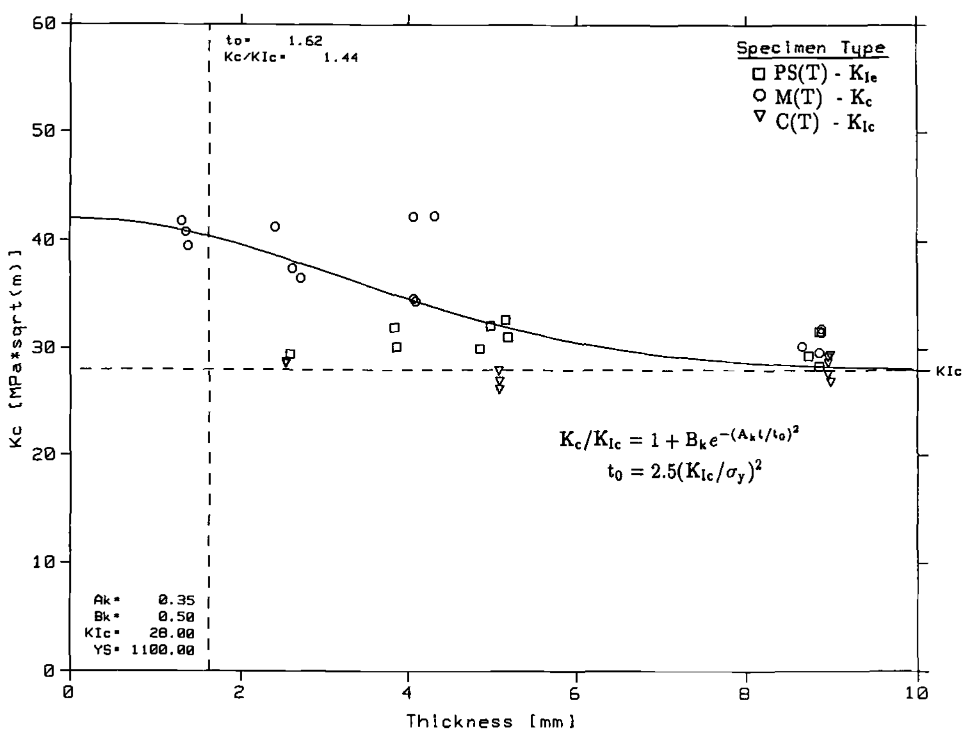

FIG. 3—K_c *versus thickness behavior of Be-Cu alloy CDA172.*

TABLE 2—*Curve fit constants for the next release of NASA/FLAGRO.*

Material	S_{max}/σ_0	α	K_{Ic}, MPa $\sqrt{m}$	σ_{ys}, MPa	A_k	B_k	t, mm	p	q	ΔK_0, MPa $\sqrt{m}$	C	n	K_{Ie}, MPa $\sqrt{m}$
Al 6063-T5	0.3	1.90	25.2	144.8	1.00	0.75	12.70	0.50	0.75	3.3	0.163E-6	3.635	52.7
Al 6063-T6	0.3	1.90	23.1	213.7	1.00	0.75	12.70	0.50	0.50	5.5	0.122E-6	3.090	38.7
Al 2014-T651	0.3	1.90	22.0	441.3	1.00	1.00	12.70	0.50	0.50	3.3	0.350E-7	3.957	28.8
Al 2014-T651 GTA welded	0.3	1.90	17.6	165.5	1.00	1.00	12.70	0.50	0.50	11.0	0.402E-8	5.815	29.3
Inconel 718 STA	0.3	2.50	76.9	1241.1	0.75	0.50	15.24	0.25	0.50	4.4	0.236E-8	3.627	106.8
Inconel 718 STCWA	0.3	2.50	58.2	1413.5	0.75	0.50	15.24	0.25	0.50	3.3	0.146E-7	2.838	73.3
A286 (950 MPa)	0.3	2.00	104.4	724.0	1.00	0.50	13.97	0.50	0.50	5.5	0.353E-8	3.153	198.8
A286 (1100 MPa)	0.3	2.50	104.4	1168.7	1.00	0.50	13.97	0.50	0.50	5.5	0.808E-7	2.213	168.4
A286 (1375 MPa)	0.3	2.50	104.4	1344.5	1.00	0.50	12.70	0.50	0.50	5.5	0.762E-7	2.146	155.2
MP35N	0.3	2.50	87.9	1765.1	1.00	0.50	8.89	0.25	0.25	3.3	0.541E-7	2.280	115.4
Al-bronze CDA 630	0.3	2.50	58.2	565.4	1.00	0.50	12.70	0.50	0.50	9.3	0.282E-7	3.190	95.9
Be SR-200E	0.3	1.75	10.4	310.3	1.00	1.00	1.98	0.50	0.50	8.8	0.151E-6	1.926	12.6
Mg AZ-31B-H24	0.3	1.50	22.0	179.3	1.00	0.50	12.70	0.25	0.25	1.5	0.578E-5	2.717	38.9
Mg ZK-60A-T5	0.3	1.50	22.0	268.9	1.00	0.50	12.70	0.25	0.25	1.5	0.582E-5	2.576	33.2
Be-Cu CDA172	0.3	2.00	28.0	1096.3	0.35	0.50	8.89	0.50	1.00	8.8	0.876E-9	4.595	32.5

data were fit according to Eq 8. While the C(T) specimen data show a consistent K_{Ic} value for all thicknesses tested, the M(T) data indicate a shallow transition from plane stress to plane strain, and PS(T) data indicate a fairly constant K_{Ie} value, slightly higher than K_{Ic}. The t_0 parameter (Eq 9) is often used to define the minimum thickness for obtaining plane strain behavior, and is required explicitly by ASTM E 399-83 for a valid K_{Ic} test. This relationship works well for describing the plane strain limit for Be-Cu C(T) data, but using t_0 to define the limit of this behavior for M(T) data is problematic. This discrepancy between C(T) and M(T) data at thicknesses equal to or greater than t_0 has been reported previously (for example, for high-strength maraging steel [*11*]), but no explanation for this behavior has yet been developed.

Fatigue Crack Growth Results

Fatigue crack growth data and curve fits for the aluminum materials are shown in Figs. 4 through 7, crack growth data and curve fits for the high-strength bolt materials are shown in (Figs. 8 through 13), and the data and curve fits for the other miscellaneous aerospace materials are shown in (Figs. 14 through 18). The curve fit constants for Eq 1 and 8 are listed for all the materials in Table 2.

The aluminum crack growth data agreed well with the curve fits. An α value of 1.9 rather than 1.75, which was used previously, was chosen for fitting the aluminum alloys. This was due to evidence that variable amplitude life predictions, using an α of 1.9, agreed better with experimental results than predictions that used 1.7 for α [*12*]. In addition, the fatigue crack growth data for the welded 2014-T651 indicated a very high ΔK_0 that made correlation with the curve fit difficult at $R = 0.1$. It is possible that this high threshold was caused by the presence of compressive residual stresses in the weld. Stress relieving the welds at 400°C for 2 h reduced ΔK_{th} at $R = 0.1$ by approximately 5 MPa $\sqrt{m}$ [*9*].

The high-strength bolt materials agreed fairly well with their respective curve fits. However, these materials generally exhibit high toughness in addition to high strength. For this reason, it was especially difficult to obtain valid toughness data that are crucial for accurate curve fits and life predictions. The high-strength A286 steels (Figs. 11 and 12) did not exhibit a large stress ratio effect, and the curve fits do not agree with the data points at a stress ratio of 0.7. Some of this difference may be attributed to the fact that the crack closure behavior in the analytic solution was derived for the M(T) specimen geometry, while the data points were generated using SE(B) specimens. These curve fits are acceptable for fracture mechanics calculations, however, since they are conservative to the data.

The crack growth data from the miscellaneous aerospace materials also compared favorably with the curve fits. However, for some materials, agreement was more difficult to achieve at higher crack growth rates. This may be caused by plastic hinging of the C(T) specimens and the fact that the net section stress approaches the yield stress at high crack growth rates.

Summary

Fracture toughness and fatigue crack growth data were obtained for a variety of aerospace materials. The data were curve fit to the empirical equations that will be used by the next release of NASA/FLAGRO. Fracture mechanics analyses of aerospace structural materials are made feasible by a procedure of selecting conservative curve fits for the fatigue crack propagation data with these equations that incorporate the effect of plasticity-induced fatigue crack closure.

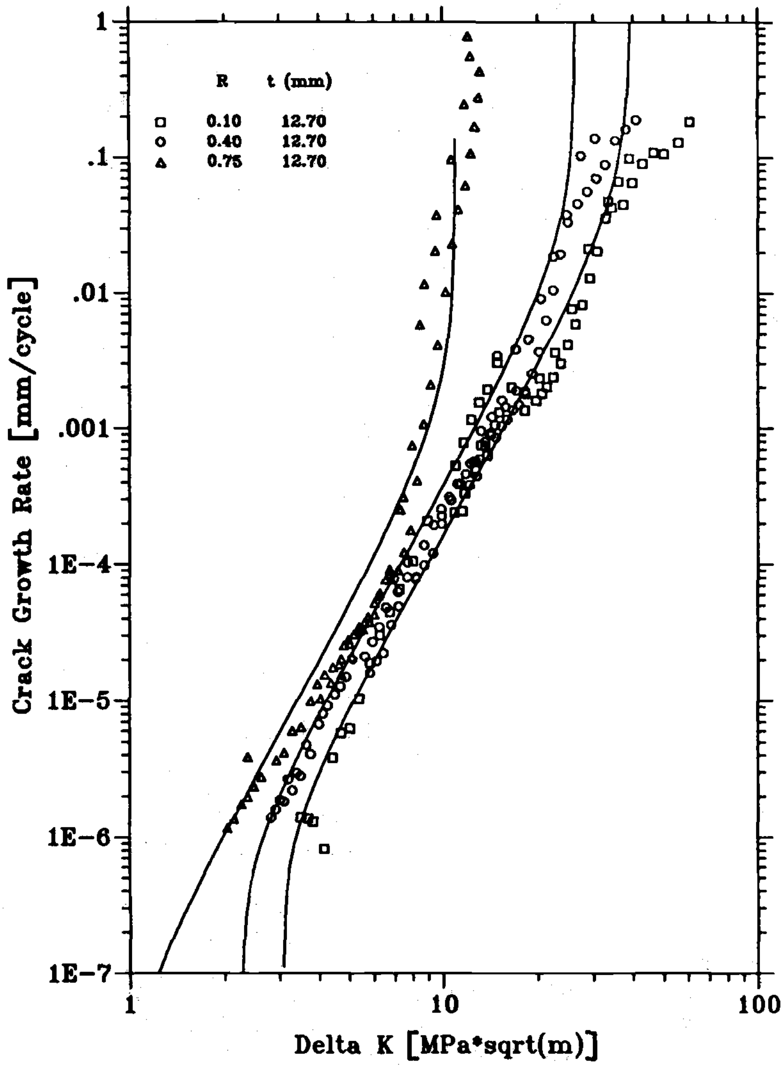

FIG. 4—*Curve fit of fatigue crack growth data for aluminum 6063-T5 (T-L) at* R = *0.1, 0.4, and 0.75.*

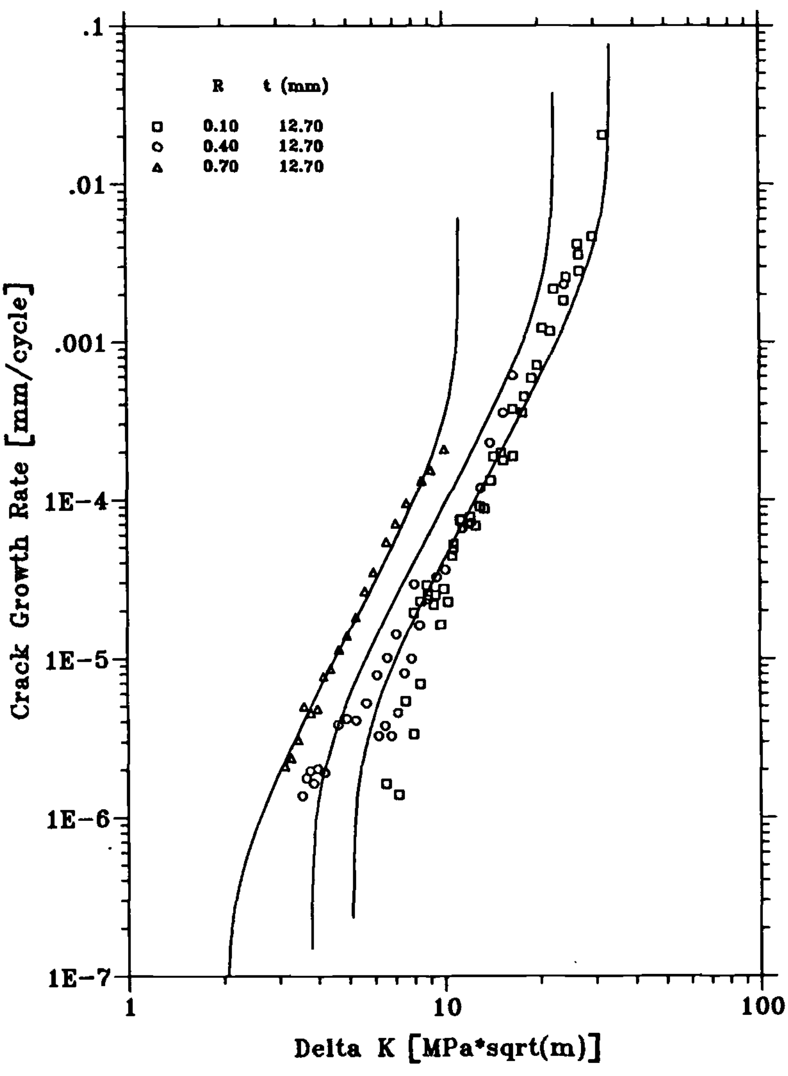

FIG. 5—*Curve fit of fatigue crack growth data for aluminum 6063-T6 (T-L) at* R = *0.1, 0.4, and 0.7.*

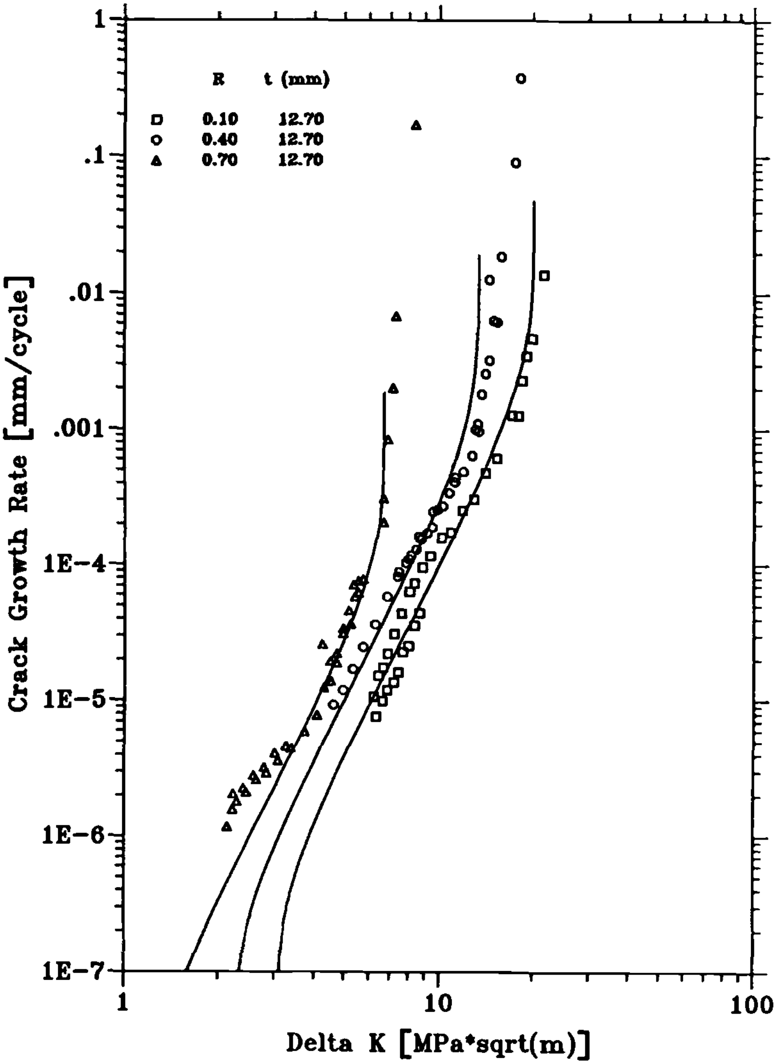

FIG. 6—*Curve fit of fatigue crack growth data for aluminum 2014-T651 (T-L) at* R = *0.1, 0.4, and 0.7.*

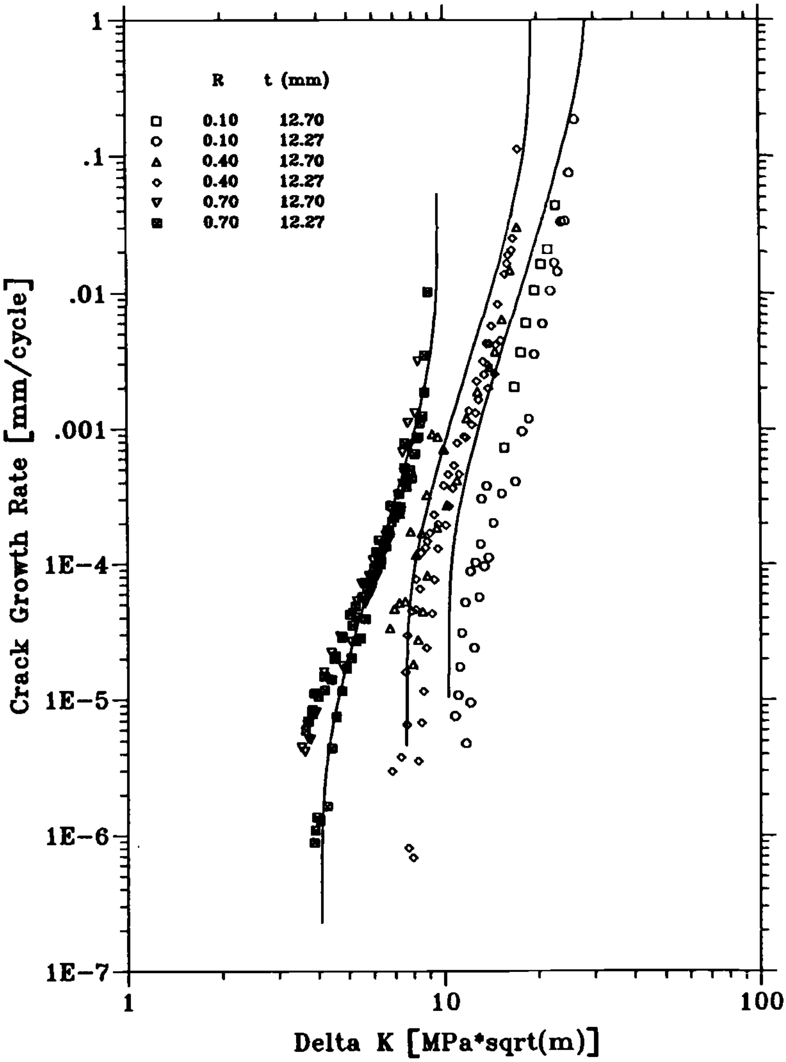

FIG. 7—*Curve fit of fatigue crack growth for aluminum 2014-T651 GTA welded with 4043 filler material at* R = *0.1, 0.4, and 0.7.*

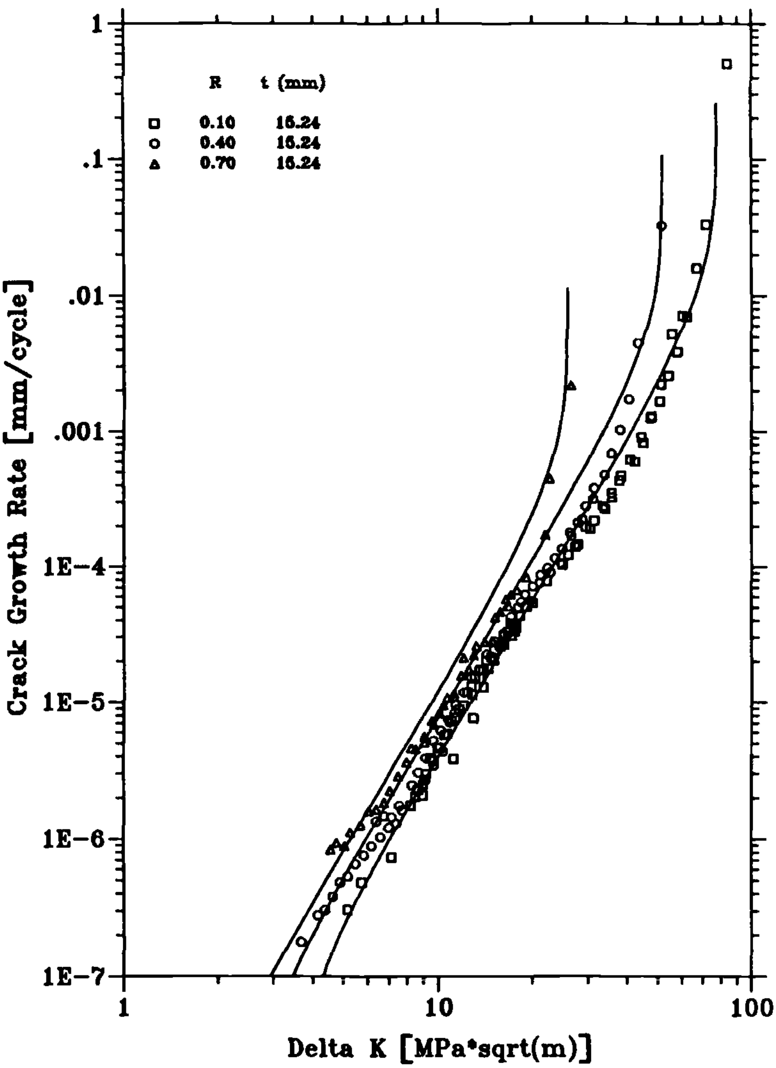

FIG. 8—*Curve fit of fatigue crack growth data for Inconel 718 STA (L-R) at* R = *0.1, 0.4, and 0.7.*

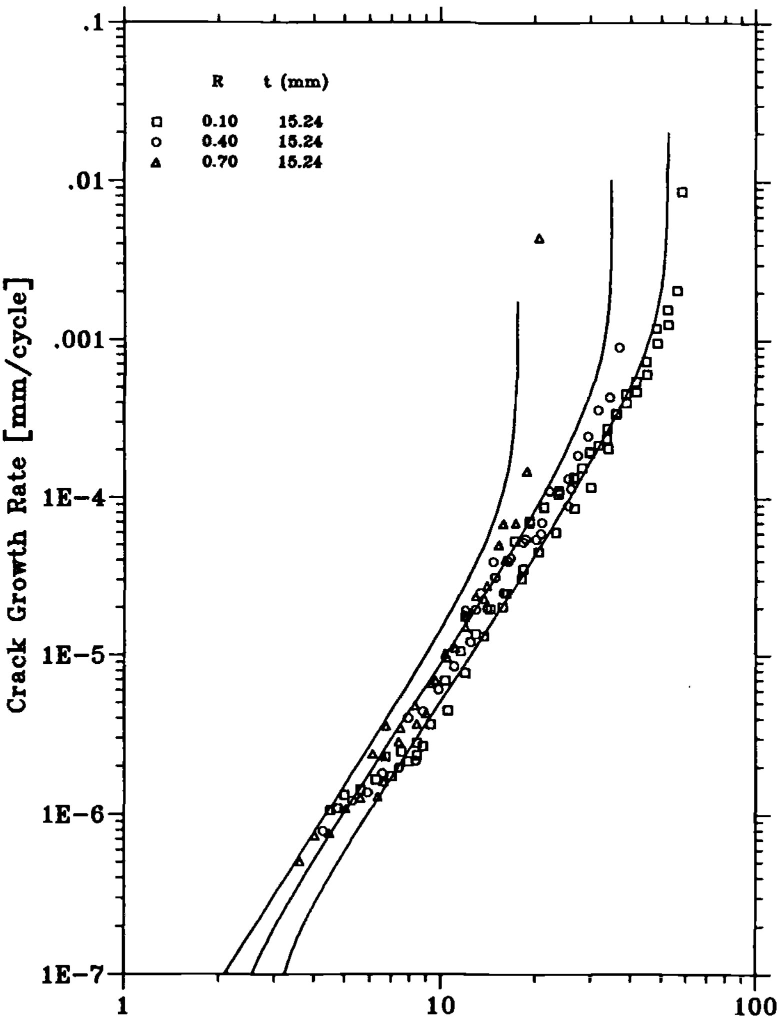

FIG. 9—*Curve fit of fatigue crack growth data for Inconel 718 ST-CW-A (L-R) at* R = *0.1, 0.4, and 0.7.*

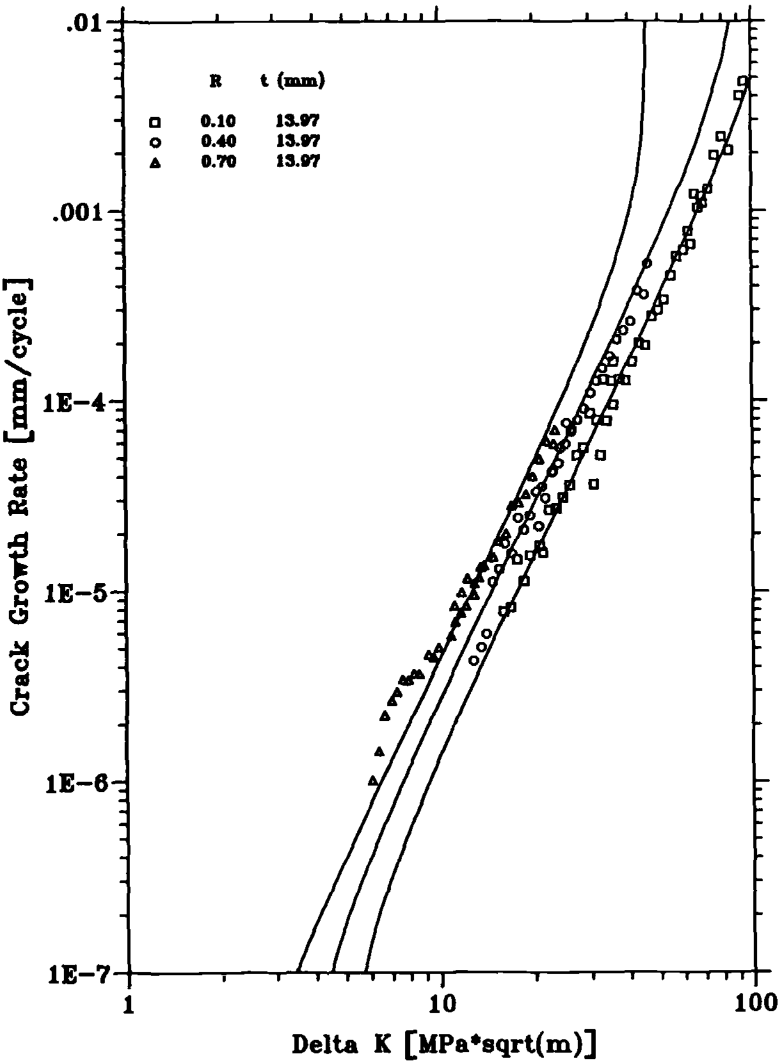

FIG. 10—*Curve fit of fatigue crack growth data for 950 MPa A286 steel (L-R) at* R = *0.1, 0.4, and 0.7.*

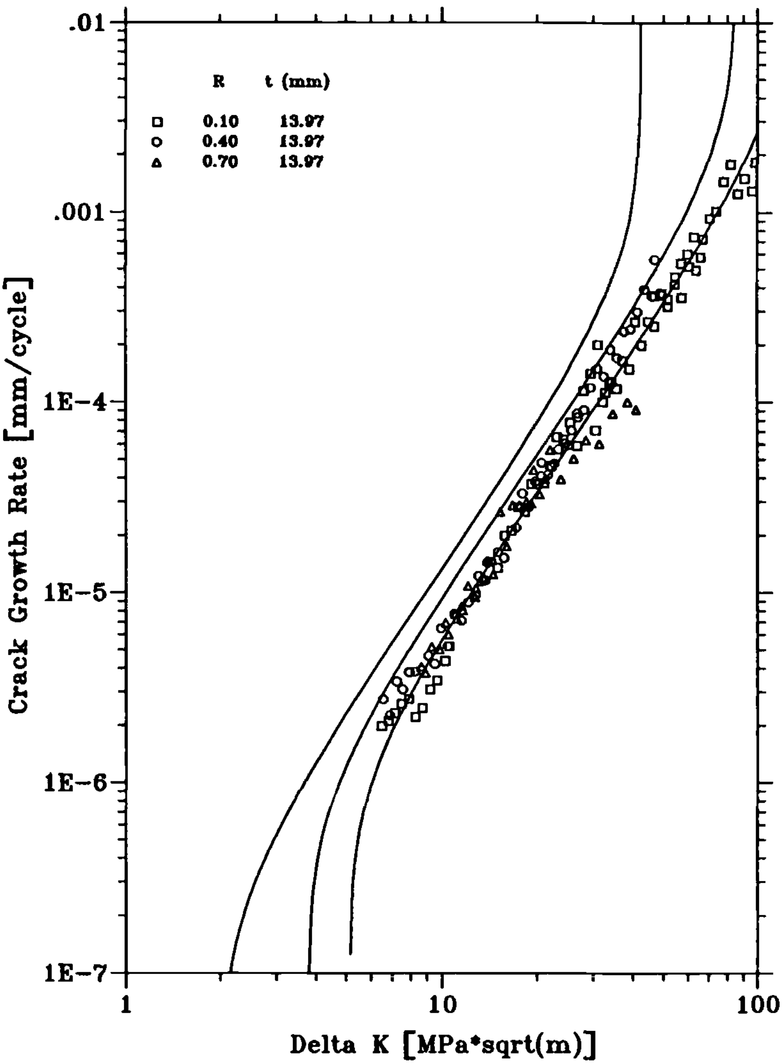

FIG. 11—*Curve fit of fatigue crack growth data for 1100 MPa A286 steel (L-R) at* R = *0.1, 0.4, and 0.7.*

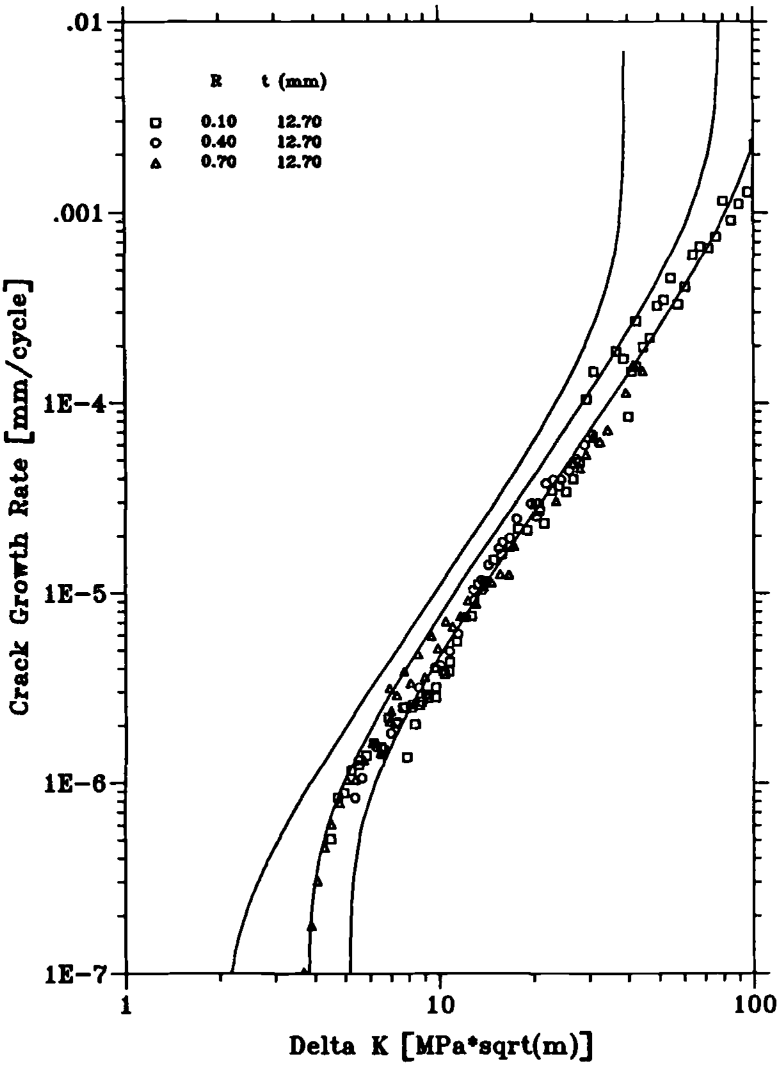

FIG. 12—*Curve fit of fatigue crack growth data for 1375 MPa A286 steel (L-R) at* R = *0.1, 0.4, and 0.7.*

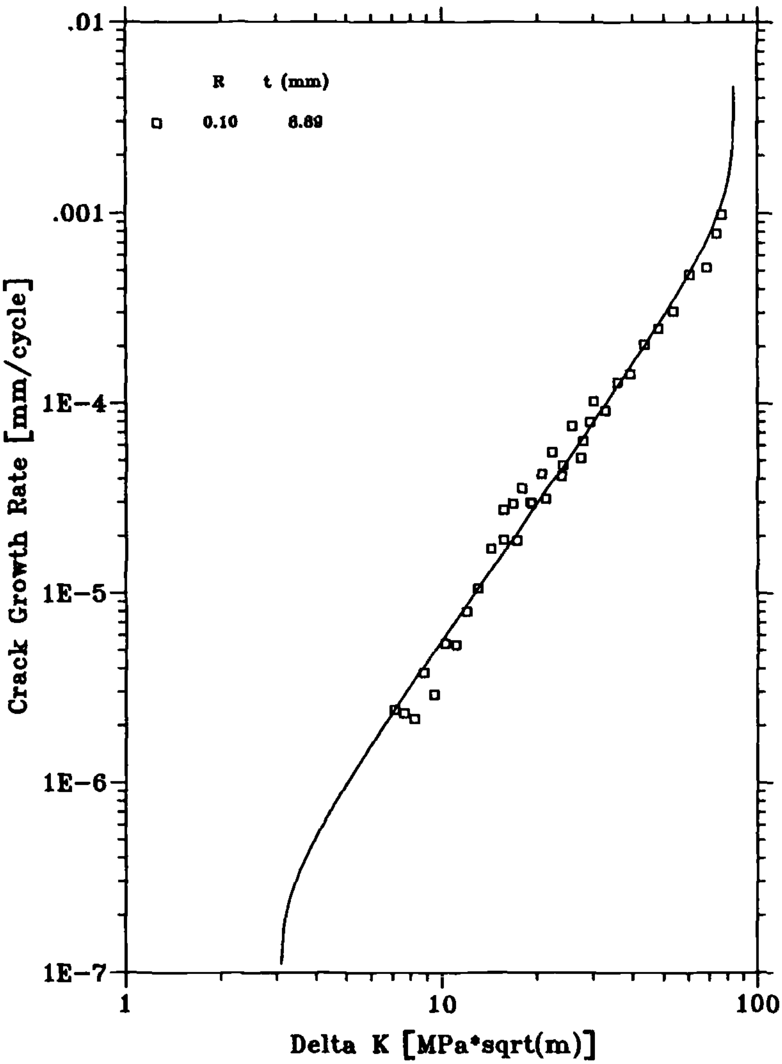

FIG. 13—*Curve fit of fatigue crack growth data for MP35N bolt material (L-R) at* R = *0.1.*

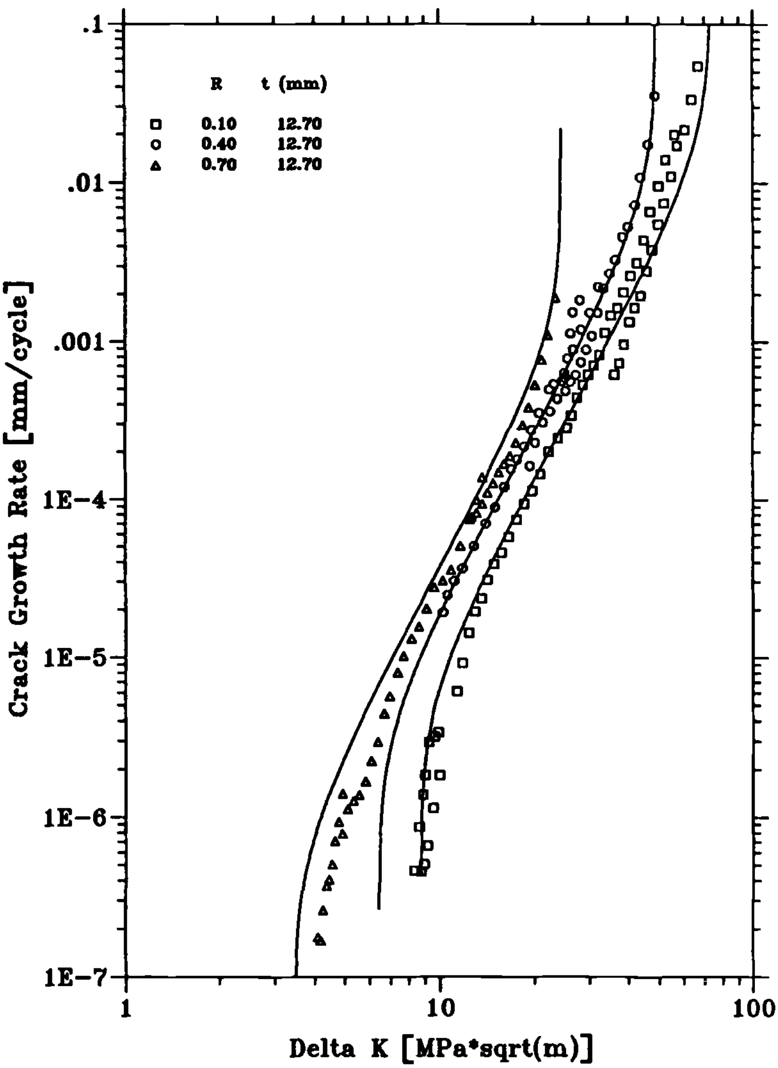

FIG. 14—*Curve fit of fatigue crack growth data for 102-mm-diameter aluminum-bronze CDA630 (C-R) at* R = *0.1, 0.4, and 0.7.*

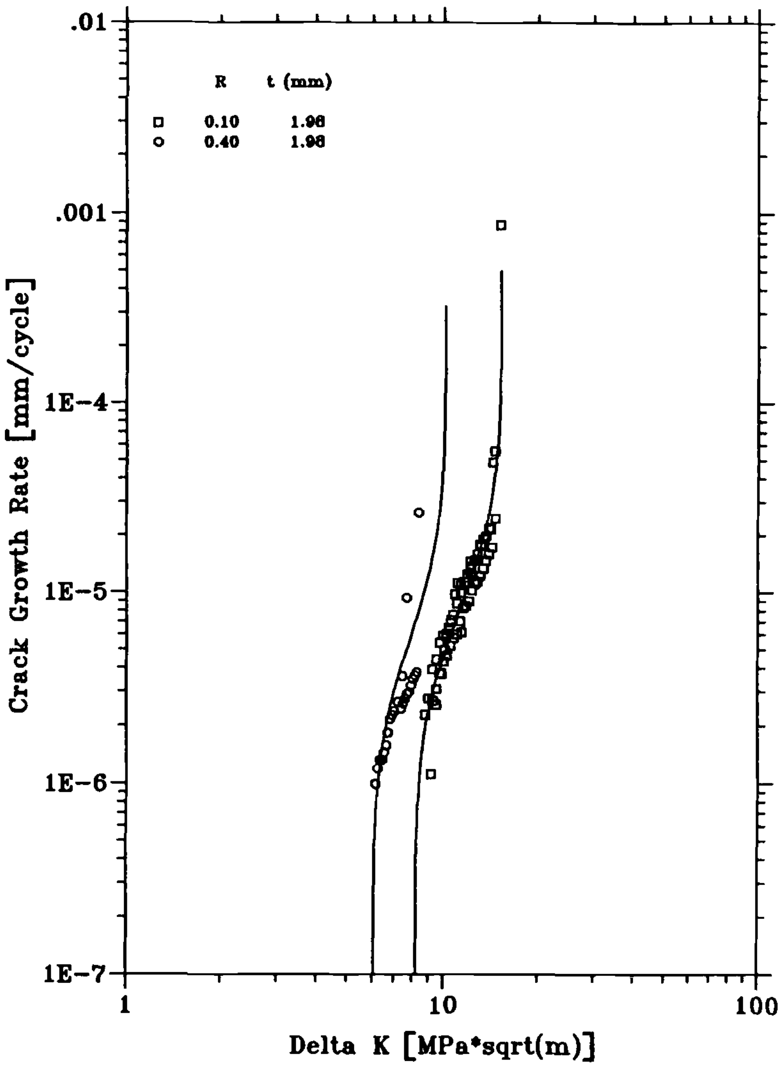

FIG. 15—*Curve fit of fatigue crack growth data for 1.98-mm-thick Be SR-200E cross-rolled sheet at* R *= 0.1 and 0.4.*

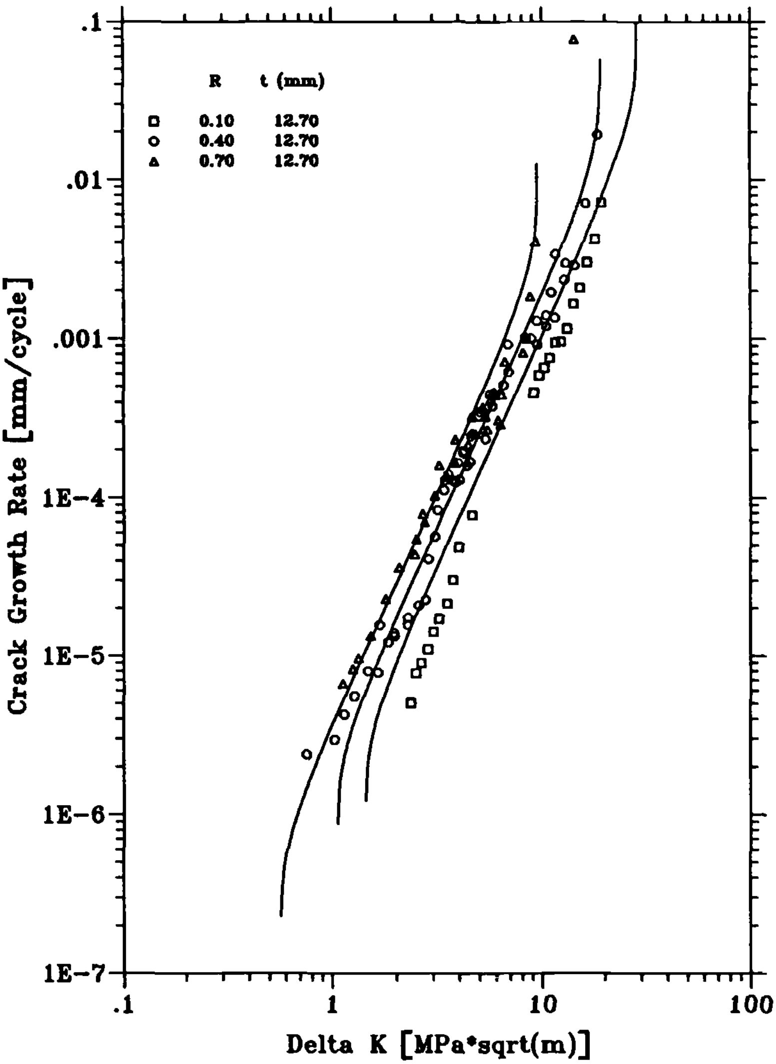

FIG. 16—*Curve fit of fatigue crack growth data for forged Mg AZ-31B-H24 (T-L) at* R = *0.1, 0.4, and 0.7.*

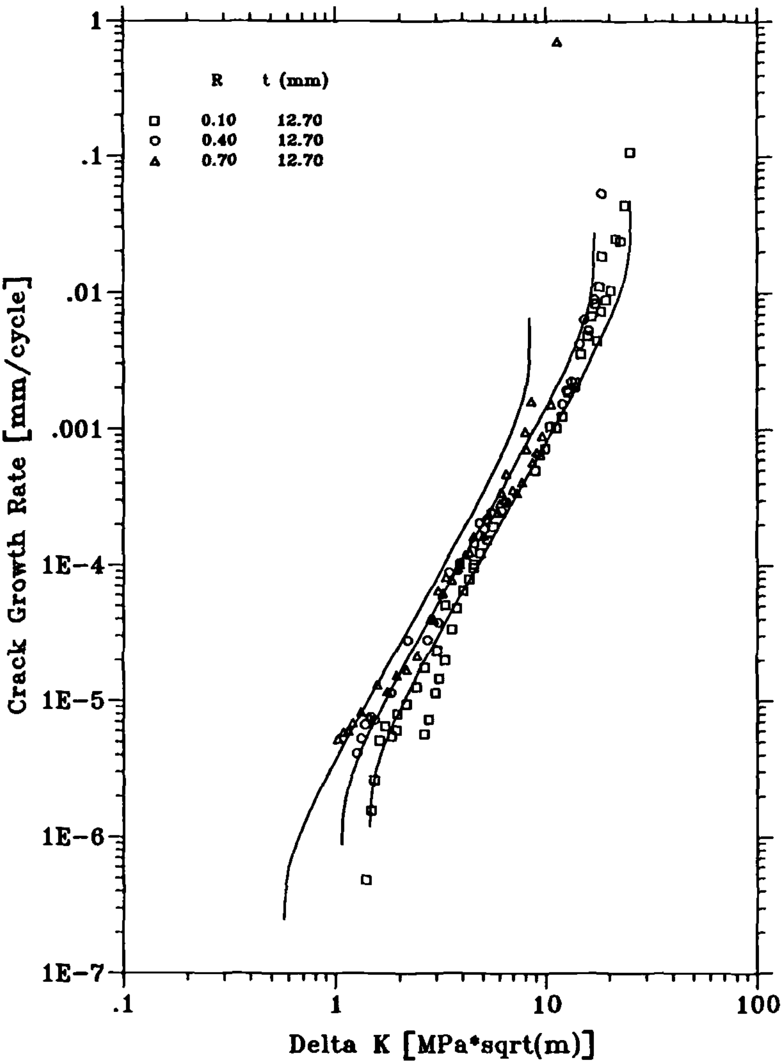

FIG. 17—*Curve fit of fatigue crack growth data for forged Mg ZK-60A-T5 (T-L) at* R = *0.1, 0.4, and 0.7.*

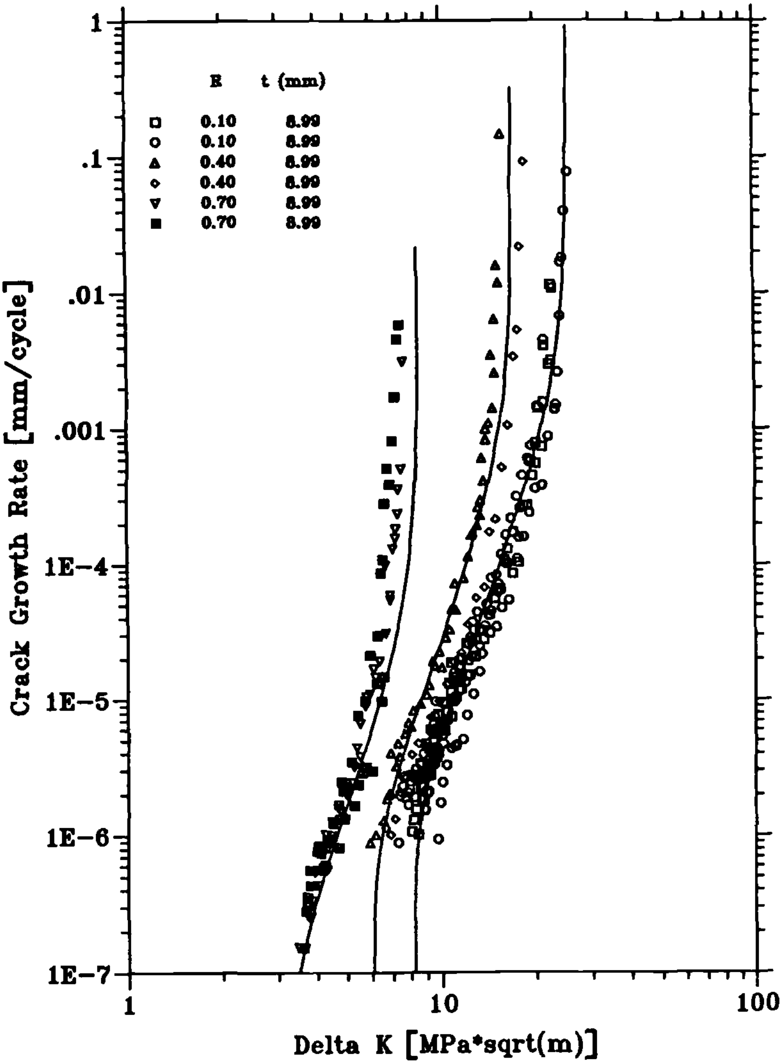

FIG. 18—*Curve fit of fatigue crack growth for 152-mm-diameter Be-Cu CDA172 (C-R and C-L) at* R = *0.1, 0.4, and 0.7.*

Acknowledgment

This research was partially sponsored by Marshall Space Flight Center's Fatigue, Fracture, and Life Working Group of the Earth-to-Orbit Propulsion Technology Program, Office of Aeronautics and Exploration Technology. This working group is chaired by Gwyn C. Faile.

References

[*1*] Forman, R. G., Shivakumar, V., Newman, J. C., Jr., Piotrowski, S. M., and Williams, L. C., "Development of the NASA/FLAGRO Computer Program," *Fracture Mechanics: Eighteenth Symposium, ASTM STP 945,* D. T. Read and R. P. Reed, Eds., American Society for Testing and Materials, Philadelphia, 1988, pp. 781–803.

[*2*] Forman, R. G., et al., "Fatigue Crack Growth Computer Program NASA/FLAGRO," JSC-22267, NASA Lyndon B. Johnson Space Center, Houston, TX, March 1989.

[*3*] Forman, R. G. and Mettu, S. R., "Behavior of Surface and Corner Cracks Subjected to Tensile and Bending Loads in Ti-6Al-4V Alloy," *Fracture Mechanics: Twenty-Second Symposium (Volume I), ASTM STP 1131,* H. A. Ernst, A. Saxena, and D. L. McDowell, Eds., American Society for Testing and Materials, 1992, pp. 519–546.

[*4*] Newman, J. C., Jr, "A Crack Opening Stress Equation for Fatigue Crack Growth," *International Journal of Fracture,* Vol. 24, No. 3, March 1984, pp. R131–R135.

[*5*] Test Method for Plane-Strain Fracture Toughness of Metallic Materials (E 399-83), *1988 Annual Book of ASTM Standards,* Vol. 3.01, American Society for Testing and Materials, Philadelphia, 1988, pp. 480–504.

[*6*] Forman, R. G. and Henkener, J. A., "An Evaluation of the Fatigue Crack Growth and Fracture Toughness Properties of Be-Cu Alloy CDA172," NASA TM-102166, National Aeronautics and Space Administration, Houston, TX, 1990.

[*7*] Test Method for Measurements of Fatigue Crack Growth Rates (E 647-88), *1988 Annual Book of ASTM Standards,* Vol. 3.01, American Society for Testing and Materials, Philadelphia, 1988, pp. 714–736.

[*8*] Liaw, P. K., Logsdon, W. A., Roth, L. D., and Hartmann, H. R., "Krak-Gages for Automated Fatigue Crack Growth Testing: A Review," *Automated Test Methods for Fracture and Fatigue Crack Growth, ASTM STP 877,* W. H. Cullen, R. W. Landgraf, L. R. Kaisand, and J. H. Underwood, Eds., American Society for Testing and Materials, Philadelphia, 1985, pp. 177–196.

[*9*] Henkener, J. A. and Forman, R. G., "Fatigue Crack Growth and Fracture Toughness Properties of Welded 2014-T651 Aluminum," JSC-24645, NASA Lyndon B. Johnson Space Center, Houston, TX, Sept. 1990.

[*10*] Henkener, J. A. and Forman, R. G., "Fatigue Crack Growth and Fracture Toughness Data for Selected Space Systems Structural Alloys," JSC-24976, NASA Lyndon B. Johnson Space Center, Houston, TX, March 1991.

[*11*] Rolfe, S. T. and Barsom, J. M., *Fracture and Fatigue Control in Structures: Applications of Fracture Mechanics,* Prentice-Hall, Inc., Englewood Cliffs, NJ, 1977, p. 100.

[*12*] Newman, J. C., Jr., and Dawicke, D. S., "Prediction of Fatigue-Crack Growth in a High Strength Aluminum Alloy Under Variable-Amplitude Loading," NASA-TM-101544, National Aeronautics and Space Administration, Hampton, VA, 1989.

Gouri S. Bhuyan[1]

Leak-Before-Break and Fatigue Crack Growth Analysis of All-Steel On-Board Natural Gas Cylinders

REFERENCE: Bhuyan, G. S., "**Leak-Before-Break and Fatigue Crack Growth Analysis of All-Steel On-Board Natural Gas Cylinders,**" *Fracture Mechanics: Twenty-Third Symposium, ASTM STP 1189,* Ravinder Chona, Ed., American Society for Testing and Materials, Philadelphia, 1993, pp. 498–511.

ABSTRACT: Fracture-mechanics methods have been used to provide a basis for assessing the structural integrity of the all-steel (AISI 4130 grade, 31 HRC) compressed natural gas cylinders used as storage fuel tanks on vehicles. A leak-before-break (LBB) failure mode of the cylinders in the event of fatigue crack growth has been established from the cylinder tests as well as from the analysis. Results indicated a safety factor of 1.3 on the materials' fracture toughness for the LBB performance in the worst operating condition. Length of the leaks varied from 2.6 to 3.5 times the cylinder wall thickness for the single-crack-initiated fatigue cracks. Average growth for internal cracks, pressurized with water, was found to be 1.5 times faster than that of external cracks. Flaws shallower than the 30% of wall thickness were not critical for the subsequent five-year service period.

KEY WORDS: compressed natural gas, steel on-board cylinders, leak-before-break failure, fatigue crack growth, crack shape development, fracture toughness, allowable flaw size, fracture mechanics, fatigue (materials)

Compressed natural gas (CNG) is becoming increasingly attractive as a vehicle fuel. Natural gas is economical and its combustion products are less harmful compared with conventional liquid petroleum fuels (as an example, 85% reduction in carbon monoxide (CO) and 23% reduction in carbon dioxide (CO_2). However, for the widespread acceptance of natural gas vehicles (NGV), a critical issue is the safe on-board storage of this fuel. The use of CNG as a vehicle fuel involves on-board storage in cylinders at a service pressure of 20.6 MPa. At present, various types of on-board NGV cylinders are available in the market, that is, all-steel, filament wound on steel or aluminum alloy liner, and all-composite cylinders. The design burst pressure of a typical steel or metal-lined fiber-reinforced plastic (FRP), hoop-wrapped cylinder is equal to 2.5 times the service pressure. These cylinders are subjected to cyclic pressure during refueling operations. The ratio of minimum to maximum pressure during this operation is about 0.1. The maximum refueling frequency could be as high as 25 times a week.

Although a stringent quality assurance procedure is followed at the fabrication step, defects can be introduced in NGV cylinders during their design life, arising from manufacturing processes, mechanical damage, and service operations. Currently, all steel as well as metal-lined FRP cylinders are required to be tested hydrostatically after a five- and three-year interval, respectively, for recertification purposes. These hydrostatic tests are conducted at a pressure of 34.5 MPa, which is about 1.67 times the design service pressure. Steel cylinders are consid-

[1] Fracture mechanics specialist, Powertech Labs, Surrey, British Columbia, Canada V3W 7R7.

ered acceptable for further service if the permanent volume expansion is less than 10% of the total expansion at the pressure of 34.5 MPa. This acceptance criterion is not rationally based, because one may or may not obtain a detectable permanent volume expansion during a hydrostatic retest for a cylinder containing a critical defect. Since sharp discontinuities in the NGV steel cylinders are bound to be introduced during service, the requalification procedure should be based on fracture-safe design principles. In order to achieve this, knowledge of wall stress distribution, fatigue crack growth and crack shape development in the cylinder wall, and the failure behavior of cylinders during service is essential. This paper addresses these aspects with reference to all steel NGV on-board cylinders.

Cylinder Specification

The most commonly used material for the all-steel NGV cylinders is a modified form of quenched and tempered low-alloy AISI 4130X steel. Fabrication of the cylinder tube is done by a deep drawing process with intermittent annealing. The open end is then hot spun to close it. An opening is bored through the closed neck. The cylinders are quenched and tempered to the desired hardness. The size and capacity of the cylinders analyzed here are given in Table 1. It was found from the stress analysis [*1*] that the midsection of the cylinder would start to yield at an internal pressure of 41.4 MPa. Magnitudes of the hoop stress at the midsection, upper transition, and neck area of the cylinder (Fig. 1) under the service pressure are about 56, 46, and 24% of the yield strength, respectively.

Material Properties

Tension specimens were machined from a steel cylinder. The yield strength, ultimate tensile strength, and elongation were found to be 822 MPa, 948 MPa, and 20%, respectively. The average value of hardness was found to be 31 HRC. The chemical composition of the steel is given in Table 2.

Fracture Toughness

The material's Charpy impact energies at different test temperatures were obtained (shown in Fig. 2) from the subsized specimen tests. All the specimens were prepared from a cylinder and fracture plane orientation was in *C-R* direction. An upper self charpy V-notch (CVN) energy value of 80 *J* was obtained. A transition temperature of −27°C, for ductile-to-brittle fracture, was observed.

The toughness of the material near the onset of crack extension (J_{Ic}) was obtained by testing specimens, in *C-R* direction, in accordance with ASTM Test Method for J_{Ic}, a Measure of Fracture Toughness (E 813-89), using a multiple-specimen technique. A power law regression curve, defined by Eq 1, was fitted to the valid data points obtained at 20°C.

$$J = 345.3(\Delta a)^{0.594} \tag{1}$$

TABLE 1—*Dimensions of the NGV on-board steel cylinders.*

Capacity, L	Outside Diameter, mm	Wall Thickness, T (mm)	Length, mm
60	316.6	7.5	972.8
50	316.6	7.5	835.0

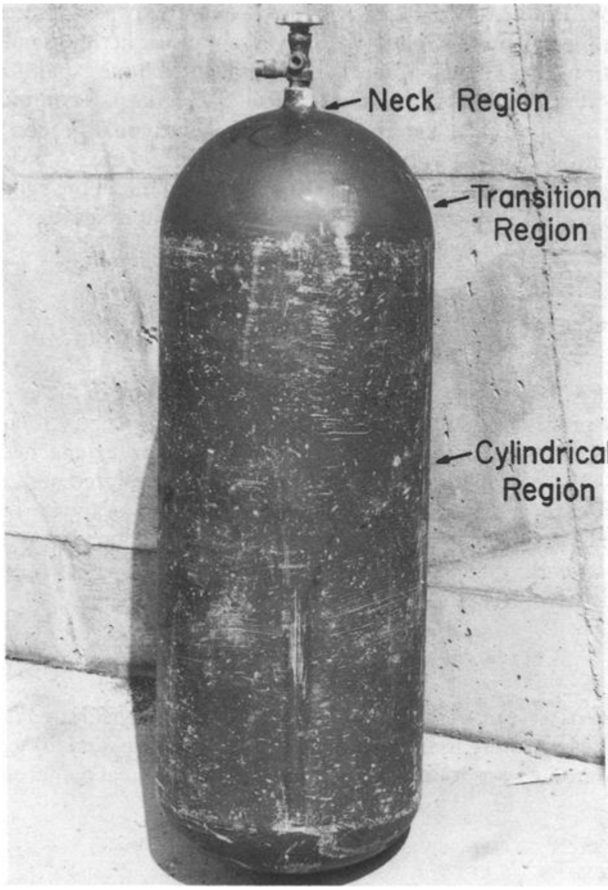

FIG. 1—*Photograph of a typical all-steel on-board NGV cylinder.*

A J_{Ic} value of 54 N/mm, corresponding to the intersection of the regression curve with the blunting line, was obtained. The corresponding plane-strain fracture toughness value at 20°C is 105 MPa $\sqrt{m}$. K_Q values of 82 MPa $\sqrt{m}$ and 78 MPa $\sqrt{m}$ were obtained from the plane-strain fracture toughness tests, conducted according to ASTM Test Method for Plane-Strain Fracture Toughness of Metallic Materials (E 399-83) at −40°C and −50°C, respectively (shown in Fig. 2).

TABLE 2—*Chemical composition and mechanical properties of the steel.*[a]

Chemical Analysis, Percent by Weight						
C	Mn	P	S	Si	Cr	Mo
0.33	0.61	0.026	0.018	0.4	1.1	0.28

[a] Mechanical properties: yield strength = 822 MPa, ultimate tensile strength = 948 MPa, and elongation = 20.1%.

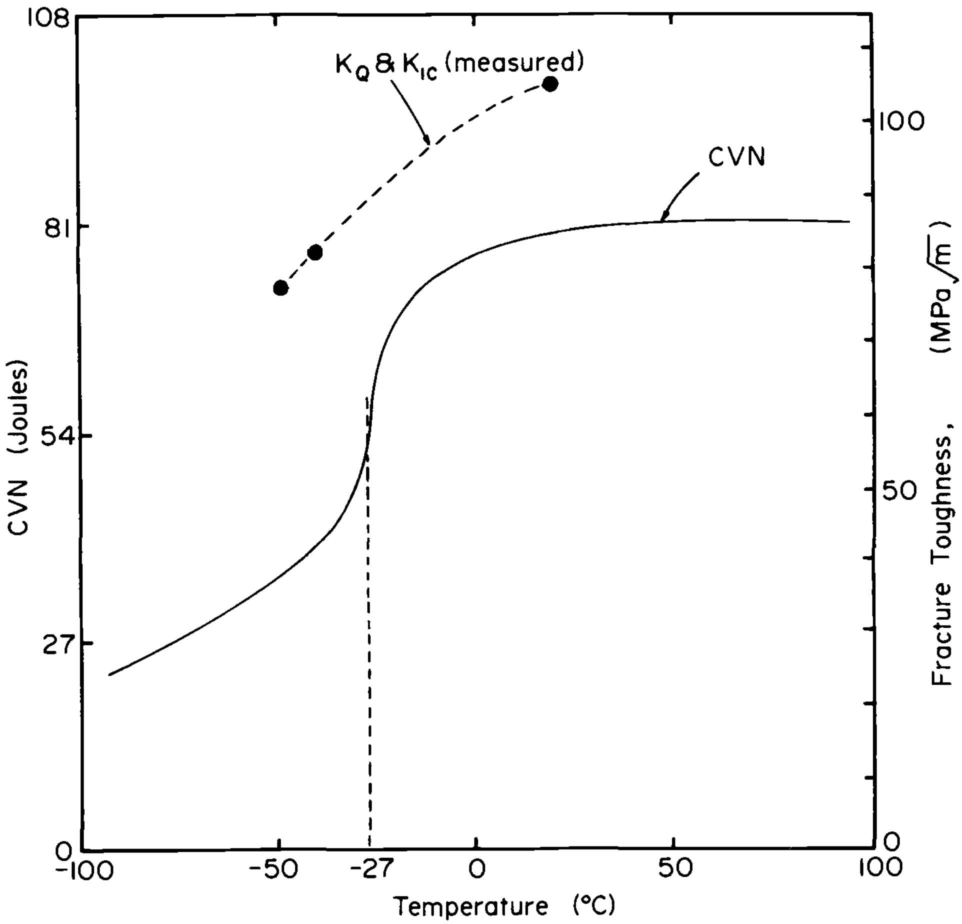

FIG. 2—*Charpy impact energy as well as fracture toughness of the cylinder material at different temperatures.*

Fatigue Crack Growth Rate in Air

Fatigue crack growth rates in air at room temperature are measured on three-point bend specimens with *C-R* and *C-L* crack orientations. Tests were conducted at a load ratio of 0.1 at two loading frequencies (5 and 10 Hz) according to ASTM Test Method for Measurements of Fatigue Crack Growth Rates (E 647-88a). Data were obtained over a stress intensity range (ΔK) of 12 to 55 MPa $\sqrt{\text{m}}$. A best regression line, defined by Eq 2 and also shown in Fig. 3, has been fitted to the air data using the Paris equation.

$$\frac{da}{dN} = 1.58 \times 10^{-11}(\Delta K)^{2.67} \tag{2}$$

where da/dN is expressed in metres/cycle and ΔK in MPa $\sqrt{\text{m}}$. A slight increase of crack growth rate in the length direction (*C-L*), compared to the growth rate in the thickness direction (*C-R*), was observed at the low stress intensity factor range. This anistropic behavior of

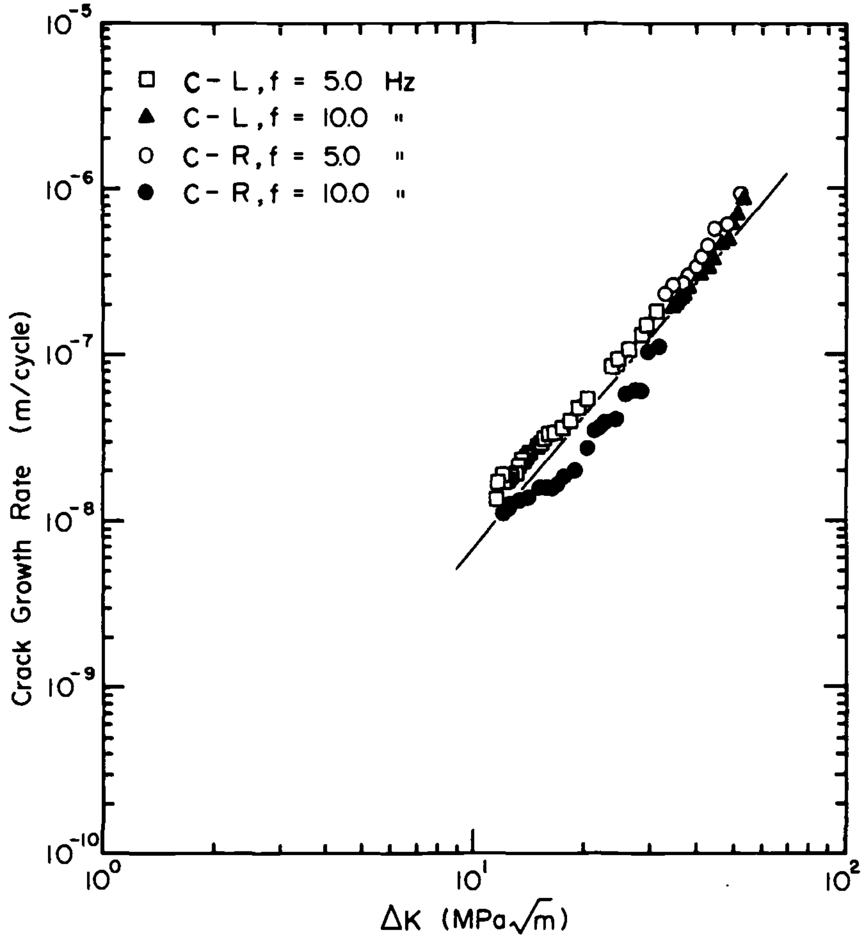

FIG. 3—*Small-scale-specimen fatigue crack growth rate data, in air, at a load ratio of 0.1.*

the material could be attributed to the deep drawing process used for the manufacture of the cylinder.

Corrosion Fatigue Crack Growth Rate

Knowledge of the corrosion fatigue crack growth rate in the natural gas environment is essential to assess the flaw tolerance of the on-board steel cylinders. Small-scale specimens (*C-R* orientation) were tested in a modified National Association of Corrosion Engineers environment test (NACE TM-01-77) at 1.0 and 0.1 Hz. This solution was prepared by bubbling a 90% CO_2 plus 10% hydrogen sulfide (H_2S) gas in the NACE environment. The H_2S gas in the NACE environment was refreshed continuously. Tests were conducted at a load ratio of 0.1. Corrosion fatigue crack growth rates at 0.1 Hz were increased by 6.8, 8.9, and 13.0 times the air growth rate, at ΔK values of 40, 30, and 20 MPa $\sqrt{\text{m}}$, respectively (Table 3). Corresponding growth rate increases were 1.4, 2.4, and 5.1 times for a loading frequency of 1.0 Hz. Details of the test results have been reported in Ref *2*.

TABLE 3—*Magnification factor for corrosion-fatigue crack growth rate in a modified NACE solution.*

ΔK, MPa $\sqrt{m}$	Magnification Factor with Respect to the Growth Rate in Air — Loading Frequency, Hz: 1.0	0.1
20	5.1	13.0
30	2.4	8.9
40	1.4	6.8

Cylinder Tests

Two sets of cylinder tests were carried out. In the first set of testing, axially orientated semi-elliptical flaws were introduced on the external surface of the cylinder, at the midsection, using an electric-discharge-machining (EDM) process. Then the cylinders were pressurized with water from 2.4 to 24.1 MPa, to initiate fatigue cracks from the EDM cuts. The maximum pressure of 24.1 MPa, instead of the design service pressure of 20.6 MPa, was used to account for the temperature compensation during refueling operations. Cylinders were pressure cycled at a rate of four times a minute (or at a loading frequency of 0.07 Hz). Surface fatigue crack growth in the axial direction was monitored using the Fractomat-Krak-Gage instrumentation, while the crack depth was monitored using an a-c potential drop system. In the second set of experiments, cylinders were pressure cycled without introducing any artificial defect. Natural fatigue cracks from the inside surface of the cylinder were developed. Crack growth in one of the cylinders was monitored by the heat tinting process. All the cylinders were cycled to failure. The size of the EDM cuts and the final crack sizes at the failure, for tested cylinders, are shown in Table 4.

TABLE 4—*Results of cylinder tests.*

Cylinder Identification	Initial Flaw (external or internal) Depth, mm	Length, mm	Final Flaw Depth, mm	Length, mm	Applied Maximum Hoop Stress, MPa	Type of Loading	Failure Mode
1	2.3[a]	9.6[a]	4.3	12.3	945.9	monotonic	rupture
3	internal[b]	...	7.5	24.2	509.4	cyclic	LBB
	1.32	5.2	1.57	5.2			
5	2.8	9.1	7.5	19.8	509.4	cyclic	LBB
8	internal[c]		7.5	44.4	506.8	cyclic	LBB
9	internal		7.5	26.0	506.8	cyclic	LBB
10	internal		7.5	31.0	506.8	cyclic	LBB
11	internal		7.5	22.0	506.8	cyclic	LBB
12	internal		7.5	26.0	506.8	cyclic	LBB

[a] Fatigue precrack initiated from an EDM cut of 1.5 mm by 8.7 mm.
[b] Crack initiated from two silicate inclusions (2.1 mm by 0.1 mm deep and 2.3 mm by 0.06 mm deep).
[c] Nine small crack coalesced to form a large crack.

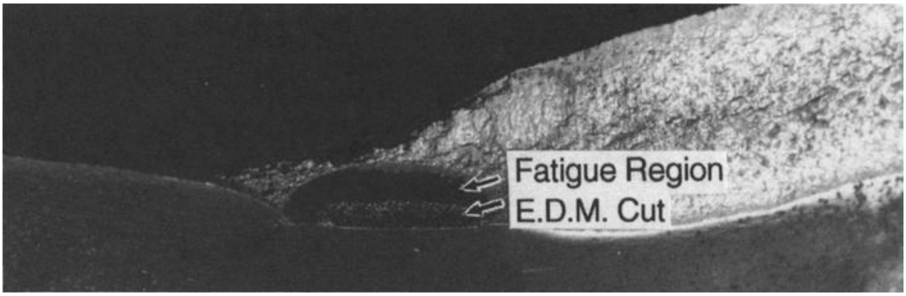

FIG. 4—*Photograph of the fracture surface of Cylinder 1 that failed in the rupture mode at a monotonic pressure of 45.5 MPa. Fracture surface shows the final crack (4.3 mm deep and 12.3 mm long) that was initiated from an EDM cut (1.5 mm deep and 8.7 mm long) by fatigue cycling. Wall thickness is 7.5 mm.*

Details of the test results have been reported in Ref *1*. Figure 4 shows the fracture surface of Cylinder 1. This cylinder failed in the rupture mode at a pressure of 45.5 MPa under monotonic loading. Cylinder 3 began to leak from a natural crack initiated from the inside surface before a through-thickness growth occurred at the EDM cut. It was found that a leak was due to a fatigue crack originating in the area of two silicate inclusions near the inside surface. A fatigue crack, initiated from the EDM cut (9.1 mm long and 2.8 mm deep) of Cylinder 5, became a through-thickness crack (Fig. 5). For Cylinder 8, nine small cracks originated at the midsection of the cylinder, and coalesced to form a single crack that eventually grew into a through-thickness crack.

Leak-Before-Break Analysis

From the defect tolerance standpoint, the leak-before-break (LBB) performance of the cylinders is considered a desirable fracture characteristic. The significance of the LBB concept is that a flaw in the cylinder can penetrate through the wall thickness (T) and allow stored gas to be discharged without rupturing the vessel.

The maximum applied stress intensity factor (K_I) for the final cracks at the failure condition, under the maximum service pressure of 24.1 MPa, was calculated using Eq 3.

$$K_I = \sigma_h \sqrt{\pi T}\, F \tag{3}$$

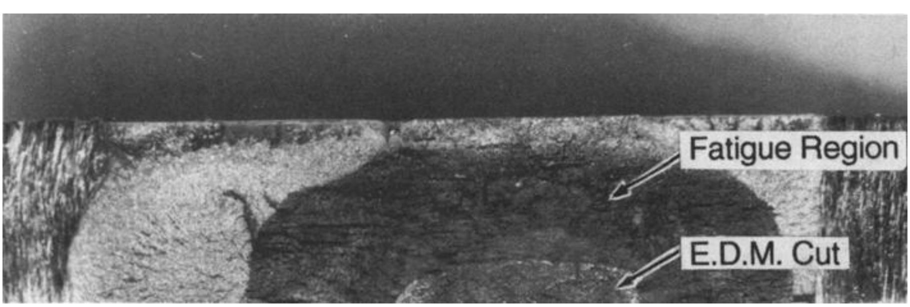

FIG. 5—*Photograph of the fracture surface of Cylinder 5 that leaked during the fatigue cycles. The leak, 19.8 mm long at the outside surface, was initiated from an EDM cut (2.8 mm deep and 9.1 mm long). Wall thickness is 7.5 mm.*

where σ_h is the hoop stress. Factor F was calculated using Raju and Newman's equation [3] for the internal surface cracks, and this factor includes the influence of the internal pressure acting on the crack surface. Since the actual cylinder wall thickness of 7.5 mm is less than the plane-strain limit thickness requirement of 38 mm according to ASTM E 399-83, the cylinder section experiences a plane stress fracture state at the leak condition. In order to compare the applied stress intensity factor, K_I, with the measured plane-strain fracture toughness, K_{Ic}, of the material at the testing temperature as well as at the minimum possible operating temperature (-50°C), K_I was converted to K^*_{Ic} using the following relationship (Eqs 4 through 6) between plane-strain and plane stress fracture toughness, proposed by Irwin et al. [4].

$$K_I = K^*_{Ic}(1 + 1.4\beta_{Ic}^2)^{1/2} \tag{4}$$

$$\beta_{Ic} = (1/T)(K^*_{Ic}/\sigma_y)^2 \tag{5}$$

$$\beta_c = (1/T)(K_I/\sigma_y)^2 \tag{6}$$

The accuracy of Eq 4 is sufficient if $\beta_{Ic} < 1$ and $\beta_c < \pi$.

If K^*_{Ic} exceeds the measured fracture toughness of the cylinder material at a particular temperature, then the cylinder could fail in the rupture mode. The ratio of K_{Ic} (measured)/K^*_{Ic} translates into a safety factor for the LBB performance of the cylinder. These safety factors, at the testing temperature (20°C) and at the minimum operating temperature (-50°C), were calculated and are given in Table 5. The most significant observation from this table and also from Fig. 6 is that in all tests the required fracture toughness to initiate fracture, when the crack penetrates the wall of the cylinder, are significantly less than the measured K_{Ic} value of 105 MPa $\sqrt{\text{m}}$. The average values of K^*_{Ic} under the maximum service pressure are about 58 and 79% of the measured material's toughness at 20 and -50°C, respectively. This results in the cylinder design having a safety factor of 1.3 in terms of fracture toughness for the worst operating condition. Figure 6, which shows the extrapolation line for the average K^*_{Ic}/K_{Ic} (measured) value at the testing temperature for a pressure of 34.4 MPa, also suggests that the cylinders with through-the-wall thickness axial cracks will not have unstable crack propagation under the hydrostatic test pressure.

Crack Shape Development

In order to assess the integrity of the on-board steel cylinders, it is necessary to understand the fatigue crack shape development through the cylinder wall. The amount of the crack

TABLE 5—*Leak-before-break (LBB) analysis results.*

Cylinder Identification	Factor of Safety for LBB Performance, K_{Ic} (measured)/K^*_{Ic}: At Testing Temperature, 20°C	At Worst Operating Temperature, -50°C
3	1.75	1.30
5	1.89	1.40
8	1.45	1.07
9	1.75	1.30
10	1.67	1.23
11	1.82	1.35
12	1.69	1.26

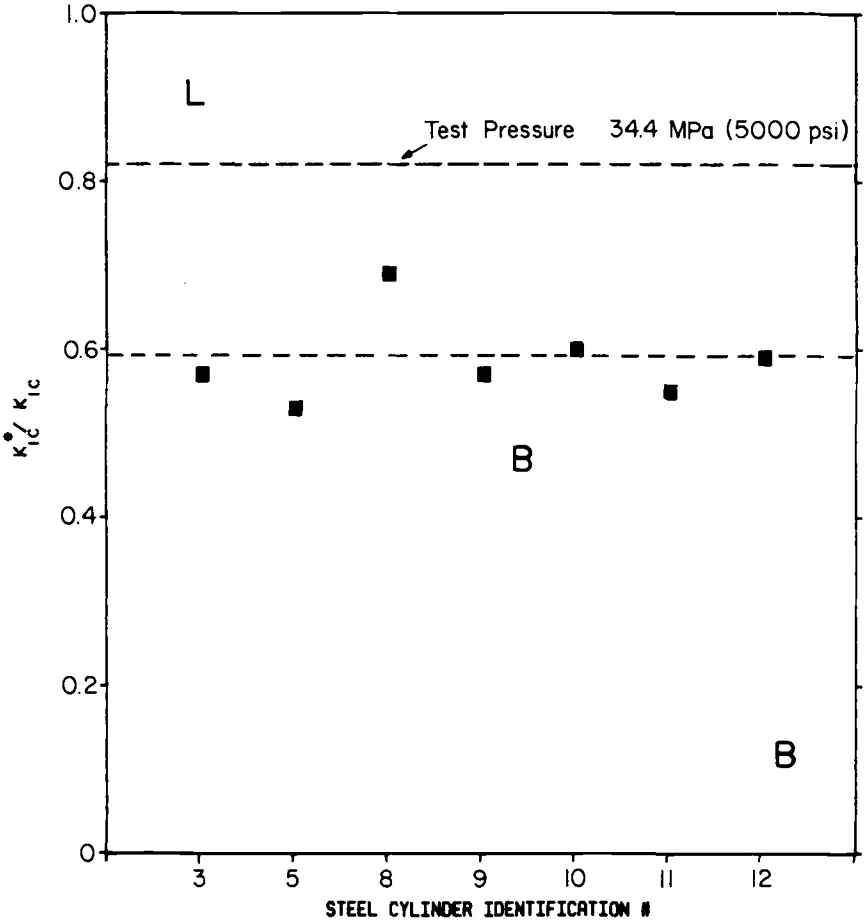

FIG. 6—*Failure behavior of the all-steel on-board cylinders under a maximum service pressure of 24.1 MPa at a testing temperature of 20°C.*

growth (for an external crack) in both cylinder surface and thickness directions (that is, Δc and Δa) between certain numbers of refueling cycles (N) were estimated using Eqs 7 and 8.

$$\Delta a = \sum_{i=1}^{N} 1.58 \times 10^{-11}(0.9K_{LAi})^{2.67} \tag{7a}$$

$$\Delta c = \sum_{i=1}^{N} 1.58 \times 10^{-11}(0.9K_{IBi})^{2.67} \tag{7b}$$

$$K_{LAi} = \sigma_h \sqrt{\pi a_i}\, F_i \tag{8a}$$

$$K_{IBi} = \sigma_h \sqrt{\pi a_i}\, F'_i \tag{8b}$$

where K_{LAi} and K_{IBi} are the applied stress intensity factors at the maximum depth and the surface of a crack front, respectively, for the ith refueling cycle; σ_h is the hoop stress corresponding to the maximum service pressure of 24.1 MPa; a_i is the instantaneous crack depth; and Factors F_i and F_i', which depend on the cylinder dimensions, crack aspect ratio, were calculated using the Raju and Newman equation [*3*].

Crack growths were calculated for initial crack aspect ratios (depth/half length), a/c, of 1.0, 0.67, 0.5, and 0.4. These predicted crack shape development for the external cracks compared, in Fig. 7, with the experimental results obtained from the cylinder tests. It can be seen from this figure that with increasing crack depth the crack shape changes asymptotically towards $a/c \approx 0.75$. The predicted crack shape development for an initial crack aspect ratio of 0.5 compares well with the experimental data obtained from the Cylinder 5 test; and these shape changes can be described by Eq 9

$$\log(a/c) = -0.141 - 0.137 \log(a/T) - 0.942 [\log(a/T)]^2 \tag{9}$$

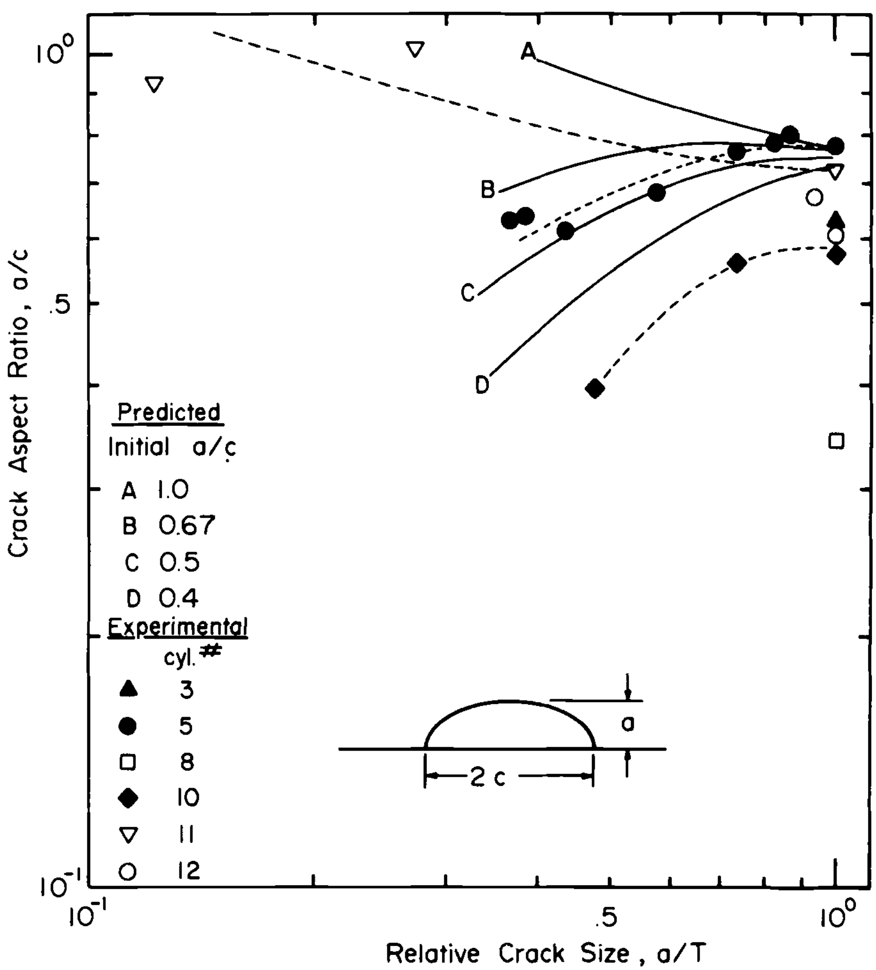

FIG. 7—*Comparison of the predicted and the experimental crack shape development through the cylinder wall. Predicted results are shown as solid lines, whereas data obtained from the cylinder tests are shown as symbols. The dashed lines are drawn to the data obtained from Cylinder 5, 10, and 11 tests.*

where T is the cylinder wall thickness. At the leak condition, the observed aspect ratio (a/c) of the cracks varied from 0.77 to 0.57. It should be noted that data shown for Cylinders 3, 8, 10, 11, and 12 were obtained from internal cracks for which the growth rates could be different. Moreover, coalescence of multiple cracks into a single crack at the initial stage (which was the case for Cylinder 8) is not considered in the present prediction scheme.

Cylinder Crack Growth

The fatigue crack growth rates in the wall thickness direction (da/dN) as well as in the surface direction (dc/dN) were calculated as a function of stress intensity factor ranges, ΔK, from the data obtained from three cylinder tests with external cracks. These calculated (growth rate versus ΔK) data for cylinders are compared, in Fig. 8, with the three-point-bend specimen test results from Fig. 3.

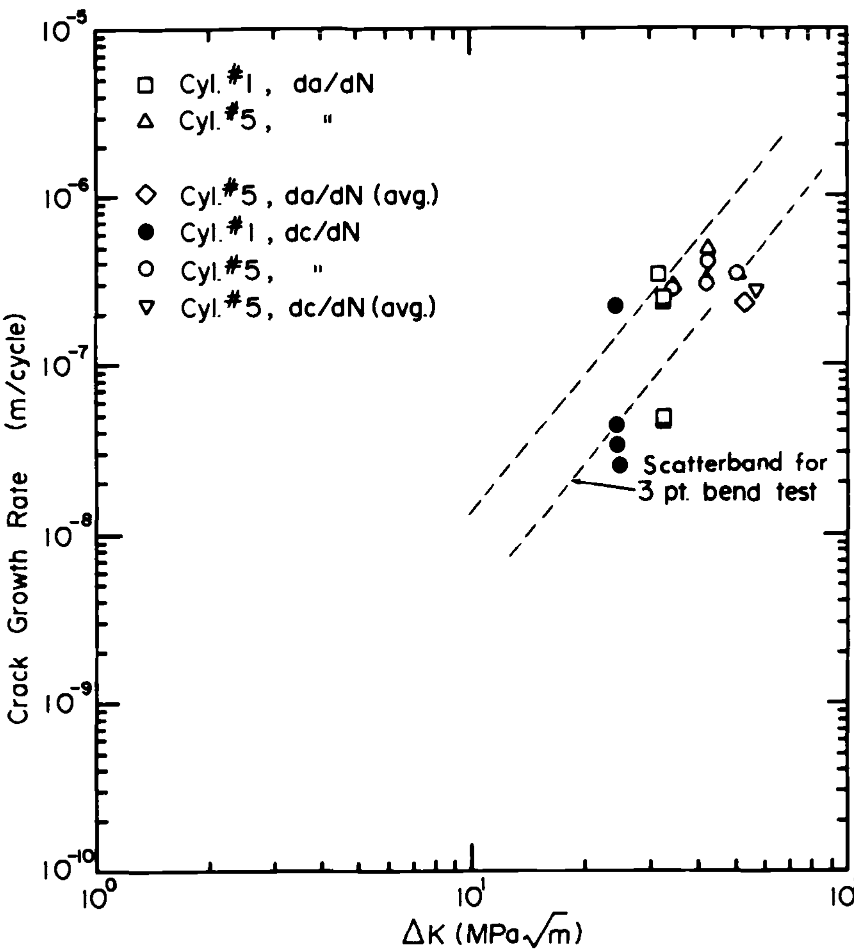

FIG. 8—*Comparison of the fatigue crack growth rate between the three-point-bend specimen test and the cylinder test results. Cylinder growth rates were obtained from the external cracks only.*

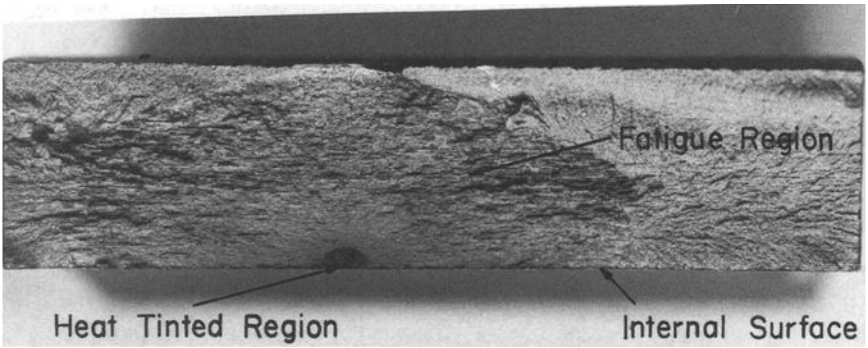

FIG. 9—*Photograph of the fracture surface of Cylinder 11 that leaked after 44 600 cycles. The leak (26 mm long) was initiated from the inside surface. The crack was 0.9 mm deep and 2 mm long (shown as dark region) at 31 456 cycles. Wall thickness is 7.5 mm.*

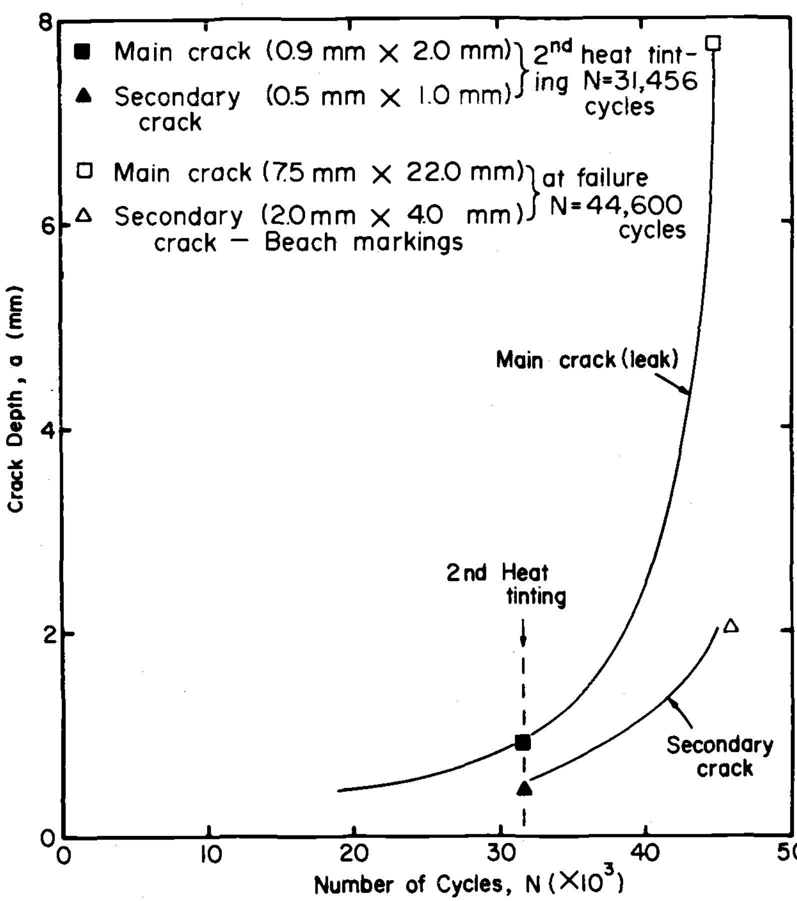

FIG. 10—*Fatigue crack growth behavior of the internal cracks for Cylinder 11. Predicted growths are shown as solid lines.*

The cylinder data are reasonably represented by the small specimen data. The higher susceptibility for crack initiation and growth of the internal surface crack compared with the external surface crack requires a better determination of the fatigue crack growth behavior of internal surface cracks. Figure 9 shows the fracture surface of Cylinder 11 at the main crack that became a leak after 44 600 cyles. The size of the crack at the end of the heat tinting process (31 456 cycles) was 0.9 mm deep and is shown as a dark region in the figure. Fatigue crack growth behavior (crack versus number of pressure cycles) of Cylinder 11 was initially predicted using the crack growth rate equation (Eq 2) that represents the actual growth behavior reasonably well for the external surface crack. But the predicted crack depths were higher than those actually observed for the main and secondary cracks through the heat tinting process. This overestimation of crack depths is due to the exclusion of the environmental effect on the internal surface crack growth. Using the same slope of the Paris equation (Eq 2), that is, 2.67, but increasing the intercept to successively higher values, crack growth curves were generated until the predicted data fit the observed through-wall defect at 44 600 cycles and a 0.9 mm crack (heat tint) at 31 456 cycles (Fig. 10). The crack growth rate for the internal surface crack in the presence of water turned out to be 1.5 times higher than those for the external surface crack.

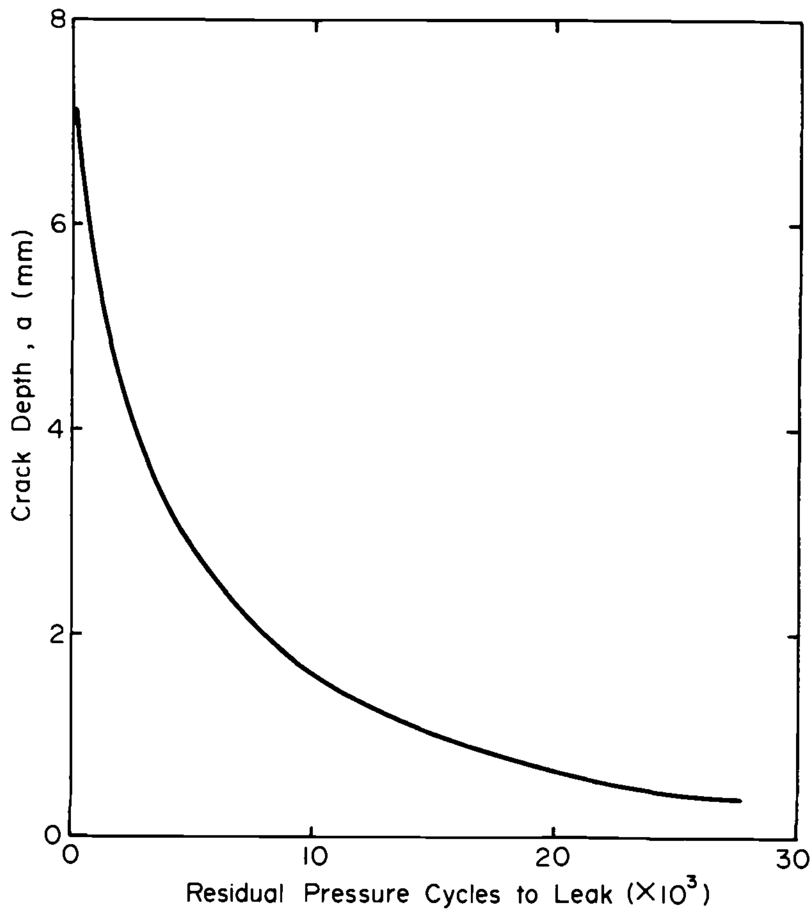

FIG. 11—*Effect of the size of axial internal defects on the residual fatigue life of the cylinder.*

This 1.5 times magnification in the growth rate is half of the observed average crack growth magnification factor of 3.0 in the modified NACE solution (Table 3) at the similar loading frequency and the stress intensity factor ranges.

The number of times the steel cylinder could be refueled was predicted as a function of initial starter internal defect depth, *a*, and shown in Fig. 11. An initial crack length/crack depth of 4 was used for the calculation. Crack shape change during the growth was accounted for in the analysis. Residual life of the cylinder, having a crack that is about 30% of wall thickness (2.25 mm deep), is 6800 cycles. This number of cycles is slightly more than the maximum number of times (6500) an on-board cylinder could be subjected to the refueling operation during a 5-year period.

Conclusions

Structural integrity of an all-steel compressed natural gas on-board cylinder is assessed based on fracture mechanics methods. Based on the results, the following conclusions can be drawn:

(*a*) The on-board steel cylinders will leak before break, should the fatigue crack growth occur in service.
(*b*) The cylinder has a safety factor of 1.3, in terms of the fracture toughness for the LBB failure mode, at the worst operating condition.
(*c*) The average crack growth for an internal surface crack in the cylinder, pressurized with water, is about 1.5 times faster than the growth of an external surface crack.
(*d*) Fatigue cracks, with depths less than 30% of the cylinder wall thickness, would not become leaks during a 5-year service period.

Acknowledgment

Major funding for this work has been provided by the Canadian Gas Association. Collaboration from Dr. A. Akhtar, Mr. C. T. L. Webster, and Mr. J. Wong is acknowledged.

References

[*1*] Bhuyan, G. S., Akhtar, A., Webster, C. T. L., Wong, J. Y., and Carter, D. M., "Integrity of On-board and Ground Storage NGV Cylinders," *Proceedings*, Second International Conference, NGV'90, Paper No. 31, Beunos Aires, IANGV, Argentina, 1990.
[*2*] Bhuyan, G. S. and Brezden, W. J., "Influence of Environmental Variables and Intermittent Overloading on Fatigue Crack Growth in On-Board NGV Steel," *International Journal of Pressure Vessels and Piping*, Vol. 40, 1989, pp. 139–149.
[*3*] Raju, I. S. and Newman, J. C., Jr., "Stress Intensity Factors for Internal and External Surface Cracks in Cylindrical Vessels," *Journal of Pressure Vessel Technology*, Vol. 104, 1982.
[*4*] Irwin, G. R., Kraft, J. M., Paris, P. C., and Wells, A. A., "Basic Aspects of Crack Growth and Fracture," Naval Research Lab Report 6598, U.S. Dept. of Commerce, 1967.

Fatigue and Nondestructive Evaluation

Peter C. McKeighan,[1] *Ben M. Hillberry,*[2] *and Thomas H. Sanders, Jr.*[3]

Intergranular Delamination and the Role of Artificial Aging Conditions on the Fracture of an Unrecrystallized Aluminum-Lithium-Zirconium (Al-Li-Zr) Alloy

REFERENCE: McKeighan, P. C. Hillberry, B. M., and Sanders, T. H., Jr., "**Intergranular Delamination and the Role of Artificial Aging Conditions on the Fracture of an Unrecrystallized Aluminum-Lithium-Zirconium (Al-Li-Zr) Alloy,**" *Fracture Mechanics: Twenty-Third Symposium, ASTM STP 1189,* Ravinder Chona, Ed., American Society for Testing and Materials, Philadelphia, 1993, pp. 515–535.

ABSTRACT: The influence of aging and grain morphology on the fracture behavior of an Al-2.6Li-0.09Zr alloy was investigated by varying the extrusion parameters that affect grain structure; namely, extrusion ratio and product geometry. Fracture specimens were partially fractured and serially sectioned to characterize crack progression into the plastic zone and to assess the interaction between the crack front and the grain structure. Fracture in the higher toughness, underaged condition is characterized by crack tunneling and grain boundary microcracking in a zone surrounding the continuous crack surface. The fracture process for the overaged material is distinguished by large, intergranular delamination cracks perpendicular to the main fracture surface and extending deep into the plastic zone. This delamination cracking phenomenon was investigated using linear, two-dimensional finite-element simulations of the delaminations at the crack tip. The results indicate that when a delamination crack is longer than one half of the section thickness, the stress intensity factor (K_I) for the delamination crack is independent of crack length. Furthermore, a section with multiple delamination cracks has a higher load carrying capacity than a section with only one crack, assuming that failure is K_I dependent. This delamination formation reduces through-thickness constraint and hastens development of plane-stress conditions. The effect of this delamination cracking on the toughness of aluminum-lithium (Al-Li-X) alloys is in accordance with the functional form of the Bilby, Cottrell, and Swinden model developed for plane-stress fracture and defined by $K_c \propto (B_l E \sigma_f)$ where B_l is delamination spacing, E is Young's modulus, and σ_f is the flow stress.

KEY WORDS: fracture behavior, fracture toughness, delamination, aluminum-lithium alloys, grain morphology, delamination toughening, plane-stress fracture, thickness effect, finite-element modeling, fracture mechanics, fatigue (materials)

Aluminum-lithium (Al-Li) alloys are appealing to the aerospace industry since they typically exhibit lower densities and higher elastic moduli when compared to conventional aluminum alloys. The property tradeoffs associated with these gains include increased anisotropy and low ductility levels. A common fatigue and fracture behavior characteristic of these alloys

[1] Research associate, Department of Mechanical Engineering, University of Bristol, Bristol, UK; former graduate research assistant, Purdue University.
[2] Professor, School of Mechanical Engineering, Purdue University, West Lafayette, IN 47907.
[3] Professor, School of Materials Engineering, Georgia Institute of Technology, Atlanta, GA 30332-0245.

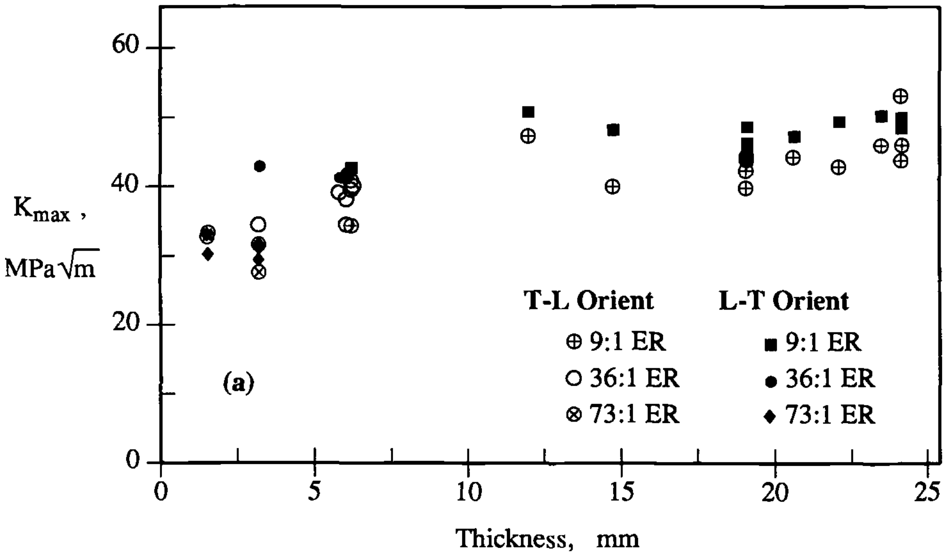

FIG. 1—*Fracture toughness,* K_{max}, *as a function of specimen orientation, extrusion ratio (ER), and thickness for near peak-aged Al-2.6Li-0.09Zr C(T) specimens evaluated at room temperature* [6].

is the formation of highly nonplanar, branched, and deflected crack profiles that result in beneficial fatigue crack growth properties [*1,2*] and generally higher fracture toughness values [*3,4*] as a consequence of mixed-mode loading. Metallographic study of the fracture surfaces of Al-Li alloys indicates a strong propensity for short-transverse delamination independent of the expected crack advance direction [*2,5*].

Studies investigating fracture toughness as a function of specimen thickness have shown that Al-Li-X alloys do not exhibit the classical behavior of higher toughness in thin plane-stress sections and lower toughness in thick plane-strain sections. In fact, the toughness is relatively high through a wide range of specimen thicknesses [*5,6*] as can be observed in Fig. 1 for an Al-Li-Zr alloy in various extruded forms. Rao and Ritchie [*5*] and McKeighan et al. [*6*] have suggested that this is a consequence of a thick, nominally plane-strain specimen behaving as if in plane-stress due to through-thickness constraint relaxation. This mechanism is termed thin sheet toughening [*7*] or crack-divider delamination toughening [*8*] and occurs in Al-Li-X alloys as a result of intergranular delamination through the thickness of the specimen.

The objectives of this investigation were to investigate the degree of intergranular delamination in an Al-Li-X alloy for different aging conditions and, in the extreme case of severe grain boundary delamination, to model the corresponding affect on toughness. Conventional J_{Ic}, K_c, and K_{max} fracture toughness measures were used to quantify the toughness of rod and

TABLE 1—*Chemical composition of the Al-Li-Zr alloy as determined by spectrophotometry and listed in percent by weight.*

Li	Zr	Cu	Mg	Si	Fe	Ti	B, Na, Ca	Al
2.6	0.09	0.11	0.07	0.04	0.03	0.01	<0.001	bal

TABLE 2—*Parameters for each of the extrusion geometries considered.*

Extrusion Dimensions and Product Shape		Extrusion Ratio	Aspect Ratio	Approximate Extruded Length
0.64 by 8.9 cm	(bar)	36:1	14:1	9.3 m
5.33 cm diameter	(rod)	9:1	1:1	2.3 m

bar extrusions of an Al-2.6Li-0.09Zr alloy aged to various conditions. The extrusion geometry (round rod and flat bar) and extrusion ratio (9:1 and 36:1) affected the size and shape of the unrecrystallized grains. The fracture behavior of sharp-notched and fatigue precracked specimens was characterized with elastic-plastic J_{Ic} evaluations. Metallographic characterization of the fracture mode was performed with particular attention directed toward the interaction between the crack path and the grain structure of the material. Finite-element modeling was employed to investigate the phenomena of Mode I delamination cracking in the direction of the applied load. These numerical simulations examined the stress intensity factor for a delamination crack, its effect on stress levels in the ligament, and the interaction between two delamination cracks.

Material and Methods

Material

A 2250-kg ingot, with the chemical composition listed in Table 1 and nominally described as Al-2.6Li-0.09Zr, was cast.[4] Once formed, it was preheated in a gas furnace for 8 h at 482 to 538°C followed by 12 h at 527 to 538°C. The ingot was then sectioned and machined into cylindrical billets suitable for extrusion.[5] The extrusion parameters for the material considered in this study are listed in Table 2. The extruded products include a bar with an extrusion ratio of 36:1 and a round rod with an extrusion ratio of 9:1. The extrusion ratio (ER) is defined as the ratio of the original billet cross-sectional area to the final product cross-sectional area and can be considered as a relative measure of the homogeneous strain required to form the extruded shape [*9*]. The aspect ratio is a measure of the axisymmetry of the extruded shape and is defined by the ratio of the length to the width of the cross section.

The alloy was solution heat treated (SHT) for 1 h at 550°C, stretched 2 to 3%, and isothermally aged at 185°C. The thermal operations, SHT and aging, were carried out in molten sodium nitrate salt. A near-peak aging time of 48 h has been determined with this material in various unstretched, extruded forms [*9*]. Furthermore, this near-peak aging time of 48 h is not affected by any post-SHT stretch processing of the alloy [*10*]. In this investigation, at least two underaged (UA), the peak-aged (PA) and one over-aged (OA), conditions were evaluated using the rod and bar geometries detailed in Table 2.

Mechanical Testing

All monotonic tension testing was performed in accordance with the ASTM Method of Tension Testing Wrought and Cast Aluminum- and Magnesium-Alloy Products (Metric) (B 557M-84) specifications [*11*]. Either round or rectangular specimens were used with the geom-

[4] ALCOA Technical Center, Alcoa Center, PA.

[5] ALCOA Lafayette Extrusion Works, Lafayette, IN.

etry of the specimen reflecting the original bar or rod extrusion form. The specimen dimensions correspond to the standard subsize specimen except that the grip length was reduced to limit the specimen length to 88.9 mm. The algorithm used to analyze the tension test data is described in detail in Ref *12*. The percent of elongation at failure, ε_f, was measured from an extensometer mounted on the gage length of the specimen. Although the tensile behavior of this alloy has been extensively studied in detail [*10,13*] for a variety of aging and processing parameters, in this study only the conditions evaluated in the fracture toughness testing part of the program are presented.

Fracture toughness testing was performed using the J_{Ic} procedure detailed in ASTM Test Method for J_{Ic}, a Measure of Fracture Toughness (E 813-89) [*10*] with all testing performed under computer control [*14*]. The single specimen procedure [*11*] was utilized with crack extension derived from unloading compliance. Single-edge-notched specimens with a nominal width of 19.1 mm and thickness of 6.4 mm were loaded in three-point bending. The nominal width-to-normalized crack length ratio at the onset of toughness testing was 0.6 a/W. Specimens from the 36:1 ER bar were tested in the *L-T* orientation whereas the 9:1 ER rod product was tested with rectangular cross-section specimens in the *L-R* orientation.

Specimen precracking was either formed by fatigue loading the specimen in the conventional manner or by machining a notch into the specimen with a well-lubricated, single-point cutter operating at a low speed. The measured root radius of the machined V-notch was less than 25 μm. The fracture tests performed on these V-notch specimens were interrupted when the load had dropped to 70 to 80% of its maximum value. These partial fracture tests yielded a complete set of fracture data while the specimen remained in one piece. This facilitated post-test metallographic investigation.

The fracture test data were analyzed using several different techniques. First, the standard J_q analysis described in the ASTM E 813-89 test procedure was used to characterize the toughness of the material. It should be noted that the inclusion of a K_{J_q} parameter is not intended to suggest that elastic conditions dominate the fracture behavior but rather is utilized for comparison purposes with other toughness measures. The load-displacement data recorded during testing were also used to generate the *K-R* curve by applying the secant method outlined in ASTM Recommended Practice for *R*-Curve Determination (E 561-86) [*11*]. Consequently, the K_c fracture toughness describing the instability condition and defined by the tangency point between the *K-R* curve and specimen *K*-curve was also determined. Finally, a K_{max} toughness measure was calculated based upon the maximum sustained load and the pre-fracture crack length.

Fracture Specimen Sectioning

Metallographic work was performed to characterize how the crack progressed into the plastic zone and the interaction between the crack front and the grain structure. Crack progression was evaluated by serially sectioning the plastic zone through the specimen thickness ahead of the crack and normal to the crack plane. The initial section was close to the precrack tip with subsequent sections deeper into the specimen. This technique was particularly useful with the partially fractured specimens since both halves adjacent to the fracture surface remained attached.

The sections were mechanically polished and then electropolished or etched with Keller's reagent to show the grain structure. The electropolish was applied with a 30-s exposure at 18 V in an electrolyte of 948-mL H_2O, 55-mL HBF_4, and 7-g H_3BO_3. The sample was viewed under bright-field or polarized light conditions. UA, PA, and OA specimens from the 36:1 ER bar and 9:1 ER rod were studied using this serial sectioning technique.

Finite-Element Simulations

A finite-element model of a $2T$ by $6T$ plate with a centrally located delamination crack, as illustrated in Fig. 2*a*, was studied using the ANSYS[6] finite-element code. The quadrant modeled is illustrated in Fig. 2*b*. Different constraint boundary conditions were applied to the $x/T = 1$ edge depending on the problem analyzed. Three specific problems were investigated to access the following:

1. the influence of a delamination crack on the local transverse stress, σ_x, in the plate;
2. the variation of the Mode I stress intensity factor (K_I) for a delamination crack subjected to various degrees of x constraint along the $x/T = 1$ edge; and
3. the variations in K_I for delamination cracks at $x/T = 0$ and $x/T = ½$ as a function of the length of each crack.

These linear elastic analyses were compared to the stress state results from a simple baseline model of a fully constrained infinite plate. In this model, the $x/T = 0$ and $x/T = 1$ edges were constrained in the x-direction, and the $y = 0$ edge was constrained in the y-direction. A constant displacement boundary condition in the y-direction was applied along the $y = 3T$ edge. This same boundary condition was used in all the finite-element analyses performed in these studies. The component stresses are designated $\tilde{\sigma}_y$ and $\tilde{\sigma}_x$.

The "modified crack closure integral" described by Rybicki and Kanninen [*15*] was used to calculate the strain energy release rate, G, from the finite-element load and displacement data in the vicinity of the crack tip. This method uses the theory that if a crack extends by a small amount, Δa, the energy absorbed in the process is equal to the work required to close the crack to its original length. One advantage of this method is that a relatively coarse mesh will yield accurate results. Sun and Jih [*16*] have reported less than 10% error between this method and theoretical stress intensity factors for a mesh with $\Delta a/a = 0.1$ or less. This guideline was strictly adhered to in these analyses. The elements utilized in the mesh were two-dimensional, 8 degree-of-freedom, isoparametric solids. Models with higher order elements yielded virtually the same results as that of a more refined mesh of lower order elements.

Results

Fracture Toughness

The different toughness measures and tensile properties as a function of aging time and extrusion geometry are shown in Table 3. In general, the K_{max} fracture toughness for both extrusions exhibits a 5 to 10% increase as aging progresses. The K_{max} values are approximately the same for both the rod and bar extrusions. These observations of a fairly constant K_{max} are not surprising since K_{max} does not account for the effect of plasticity and slow stable crack advance that are both theoretically accounted for in K_c and K_{J_q}. Furthermore, the general trend of K_c and K_{J_q} as a function of aging shows higher values in the UA condition, a decrease until near the PA condition, followed by a slight increase with further aging. Though there is no directly comparable strength condition, the difference in toughness magnitude between the two extrusions appears minimal.

This Al-Li-Zr alloy exhibits considerably less sensitivity to precrack sharpness when compared with a reference 7075-T6511 material. The fracture toughness of the 7075 specimen with a machined V-notch was observed to increase by approximately a factor of two when

[6] Copyright by Swanson Analysis Systems, Inc.

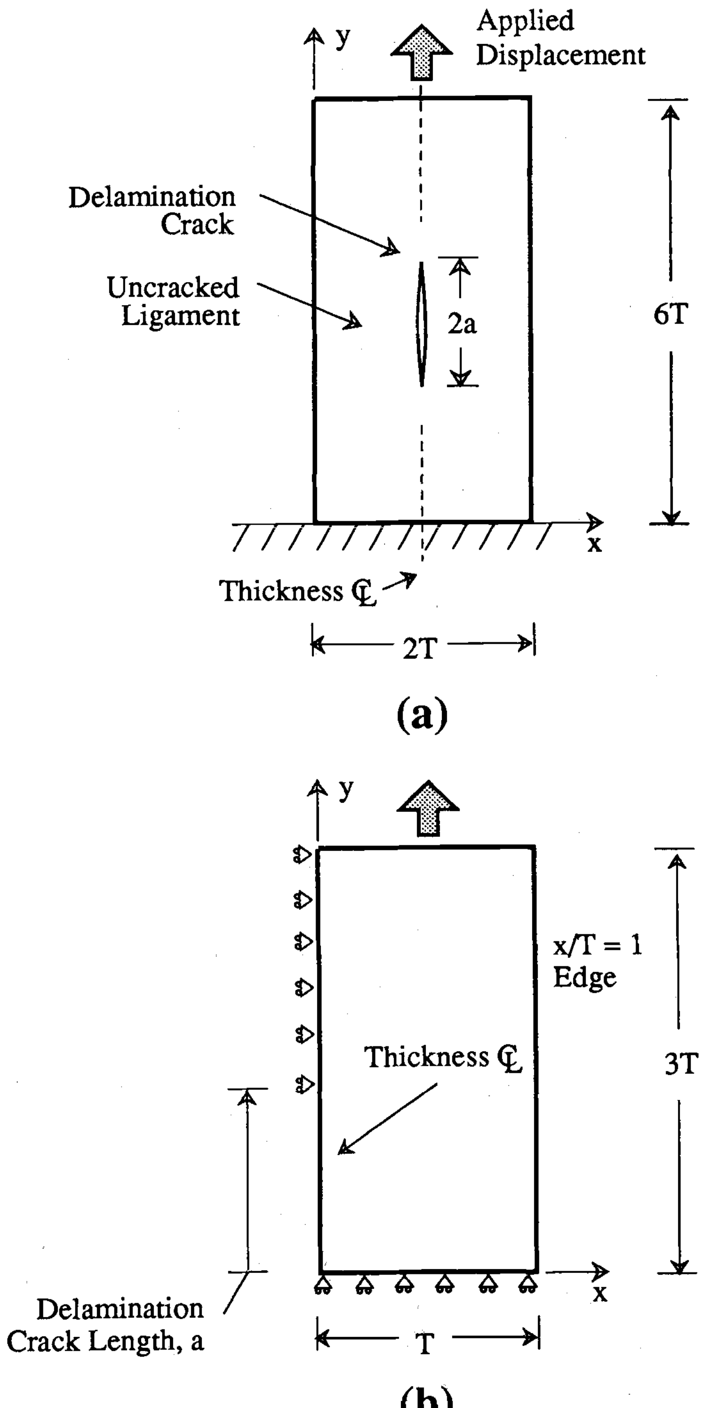

FIG. 2—*Schematic of* (a) *the section with a delamination crack and* (b) *the finite-element model for this section.*

TABLE 3—*Fracture properties as determined from SEN(B) specimens nominally 6.2 mm thick. The prefracture crack was a machined V-notch unless otherwise noted.*

Material Extrusion Ratio and Form	Aging Time, h	Tensile Properties σ_{TS}, MPa	σ_{YS}, MPa	ε_f, %	Fracture Properties K_{max}, MPa $\sqrt{m}$	K_c, MPa $\sqrt{m}$	J_q, kPa m	K_{J_q}, MPa $\sqrt{m}$
36:1 Bar	1	366	274	6.9	29.0	48.2	33.4	54.6
	12	406	309	2.6	31.0	43.5	24.2	46.4
	48	430	333	3.3	33.8	50.4	...	...
	225	425	334	4.2	32.4	50.2	36.1	56.7
9:1 Rod	1	395	365	1.3	32.2[a]	59.3	34.7	55.3
					30.4	51.2	41.5	60.4
	2	410	389	0.8	32.5[a]	57.8	27.5	50.8
					30.3	42.6	30.8	53.9
	12	447	433	0.5	32.2[a]	37.7	17.7	41.3
					32.2	42.3	20.7	44.6
					32.6	47.2	24.1	48.3
	48	475	434	3.0	37.5[a]	49.2	14.0	35.6
					31.6	39.7	18.6	41.0
	96	462	405	5.1	36.1[a]	50.0	...	...
					35.9	45.8	24.7	46.7

[a] Fatigue precracked specimens.

compared to a fatigue-cracked specimen. For the Al-Li-Zr alloy, the V-notched specimen K_{max} or K_c toughness in Table 3 decreases 10 to 20% when compared to similar fatigue-cracked specimens while K_{J_q} increases 5 to 10%. The specimen compliance recorded during testing indicates that this difference is a consequence of slightly more slow, stable crack growth for the fatigue-cracked specimens (1 to 4% of the initial crack length) compared to the V-notch specimens (0.3 to 2%). Notch sharpness may be less critical in this alloy since during fracture, specimens exhibited a high net section stress exceeding yield (undoubtedly accompanied by significant crack-tip blunting) and a crack path morphology that was globally rough and tortuous.

Fracture Specimen Sectioning

The three-dimensional grain structures for the rod and bar extrusions are illustrated in Fig. 3. The grain structures shown in Fig. 3 are unrecrystallized as a consequence of the zirconium addition to the alloy [*17*]. In general, an unrecrystallized grain structure is associated with the highest combination of strength and toughness although properties tend to be more anisotropic [*18*]. The highly elongated grains observed in Fig. 3 are typical for unrecrystallized aluminum alloys and have been described as resembling a deck of cards or stack of pancakes. The longitudinal grain length was approximately 1 to 5 mm. The through-thickness grain width was found to be a function of the extrusion considered. For the 9:1 ER rod, the mean measured grain width was approximately 65 μm, whereas for the 36:1 ER bar, it was 15 μm. These values should be considered approximate since the grain size varied significantly in a given section.

A through-thickness section of the crack in the underaged 36:1 ER bar is shown in Fig. 4. This section of a partially fractured specimen is 1.52 mm in front of the notch tip (measured on the specimen surface). The photomicrograph illustrates crack tunneling in this section since the crack is not completely through the specimen thickness. Tunneling was apparent in virtually all of the specimens examined. Evidence of remote microcracking in the direction of the applied load was observed to be confined to a 500-μm zone surrounding the continuous

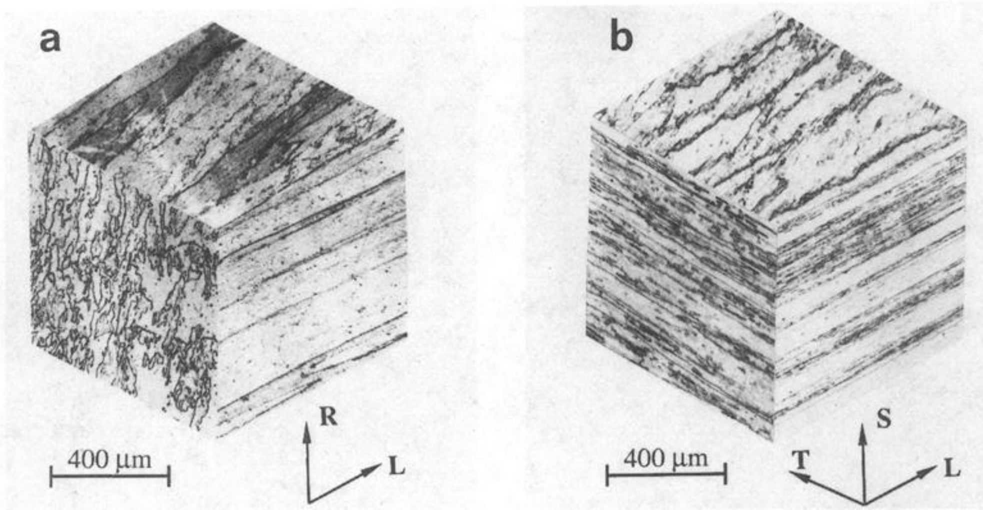

FIG. 3—*Grain structure of the* (a) *9:1 ER rod and* (b) *36:1 ER bar.*

crack. This microcracking in the *L*-direction was also observed in the as-polished condition of the sample and therefore was not a consequence of the electropolish. The majority of this microcrack damage consisted of short intergranular delaminations approximately 20 to 50 μm in length. Little damage was observed outside the 500-μm zone surrounding the main, continuous crack. It is theorized that crack formation in this UA condition is a result of a joining or coalescing of microcrack damage remote from the continuous crack.

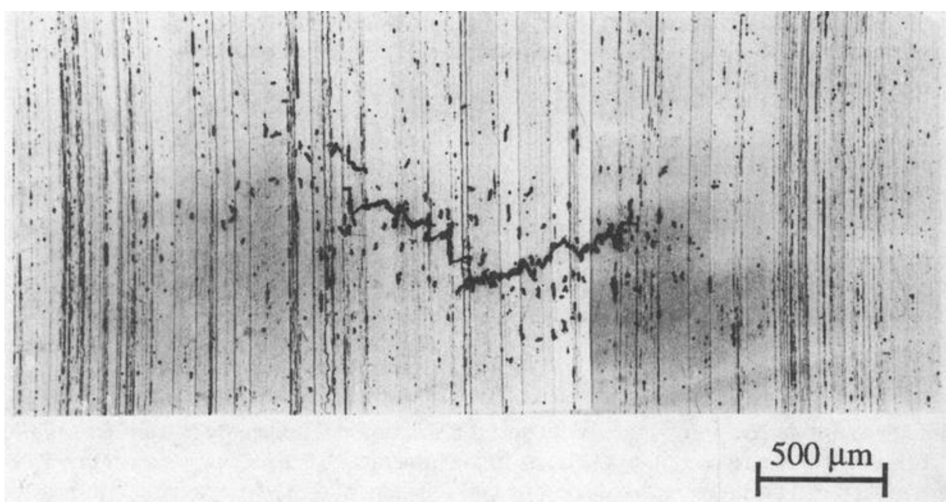

FIG. 4—*Thickness section at 1.52 mm from the notch tip into the plastic zone for the 36:1 ER bar extrusion aged for 1 h (UA). The tunneled crack is approximately in the midthickness of the specimen. The crack growth direction* (T) *is into the paper.*

A considerably different fracture profile is shown in Fig. 5 for an overaged specimen of the same 36:1 ER bar product. Three major longitudinal grain delamination cracks can be observed in each section shown in Fig. 5. These three cracks effectively split the specimen into four nearly equal ligaments. The delamination in the midthickness is the longest, whereas the flanking delaminations are each shorter. Additional delaminations are evident in each of the four major ligaments in all of the three sections. Furthermore, transgranular failure has resulted in a crack through the entire thickness in the shallowest 0.13-mm section as shown in Fig. 5*a*. There is little evidence of microcracking separate from the main fracture surface in this condition. Evidence of crack tunneling can be observed in this specimen as the amount of through-thickness transgranular cracking is reduced for the sections deeper into the process zone.

Specimen sections for aging conditions between the UA (Fig. 4) and OA (Fig. 5) exhibit behavior with characteristics of both UA and OA conditions. For instance, microcracking separate from the continuous crack is less evident and is confined to a much narrower region around the main crack for the PA condition. Furthermore, there is less evidence of major delaminations splitting the thickness, though some were observed. It should also be noted that the observed nature of the crack progression and the fracture mode appearance were independent of position in the plastic zone (that is, the distance from the notch tip). Thickness sections deeper in the plastic zone did exhibit crack tunneling as evidenced by material separation confined to the midthickness portion of the specimen.

Average delamination spacings measured from the photomicrographs are listed in Table 4 for the peakaged and overaged specimens. This delamination spacing, B_l, appears to decrease as the alloy is aged. Although the measured variation (quantified with ± 2 standard deviations) also increases. Furthermore, the delamination spacing is 20 to 30% greater for the coarser grained rod product compared with similarly aged bar extrusion. The delamination spacing is not a linear function of grain size since the grain size of the rod is over four times greater than that for the bar.

Specimens fabricated from the round rod extrusion exhibited behavior similar to that described for the bar extrusion. A thickness section 1.91 mm deep into the plastic zone for an OA 9:1 ER rod specimen is depicted in Fig. 6. Delamination behavior similar to that of the bar can be observed even though the macroscopic grain structure for the rod, Fig. 3*a*, is much coarser than that for the bar, Fig. 3*b*.

Finite-Element Simulations

The component stresses in the fully constrained baseline model, denoted $\tilde{\sigma}_y$ and $\tilde{\sigma}_x$, are used as the reference condition for all the finite-element results. Recall that the loading for all the models was fixed. The stress state in the fully constrained model was observed to be constant in each direction and in accordance with the fundamental theory that $\tilde{\sigma}_x = \nu\tilde{\sigma}_y$, where ν = Poisson's ratio.

TABLE 4—*Measured delamination spacing,* B_l, *for various-aged fracture specimens from both extrusions.*

ER and Shape	Aging Condition	B_l, mm
36:1 □	48 h (PA)	0.67 ± 0.12
	225 h (OA)	0.51 ± 0.06
9:1 ○	48 h (PA)	0.88 ± 0.31
	96 h (OA)	0.61 ± 0.24

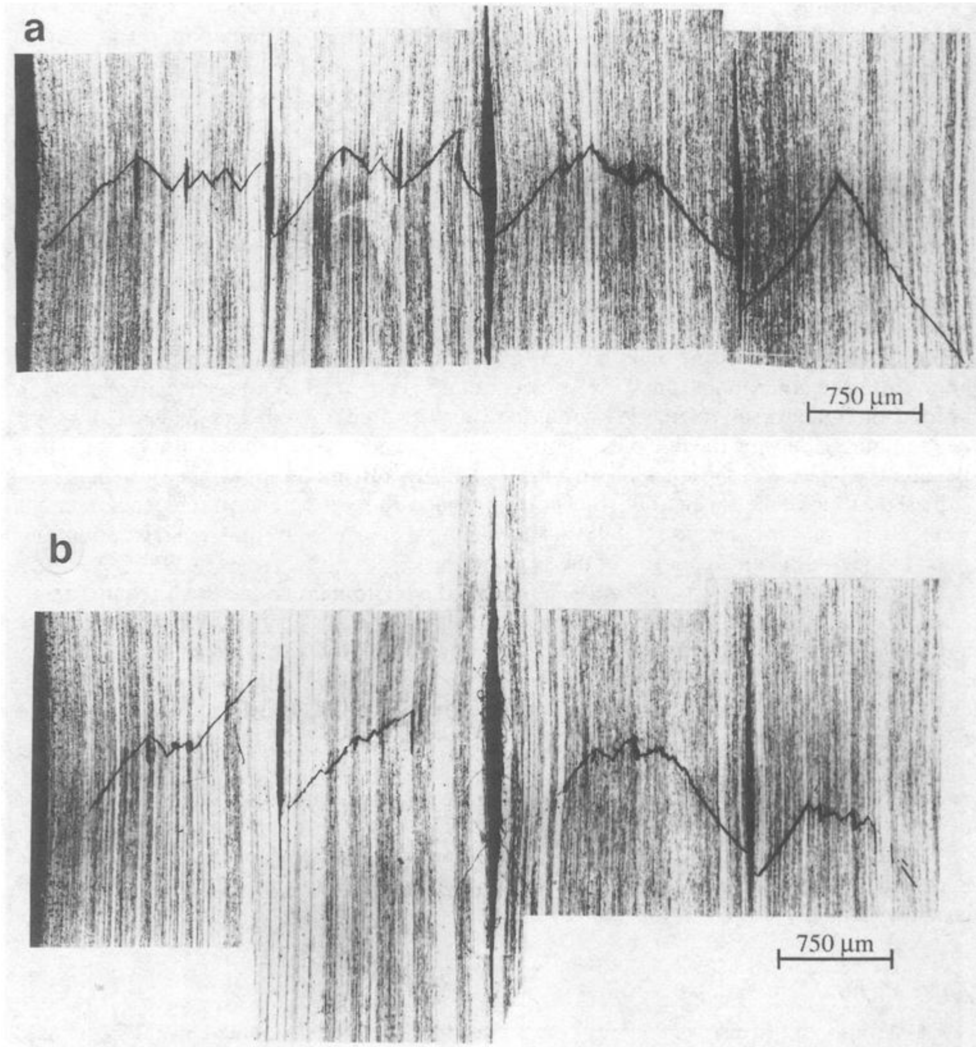

FIG. 5—*Thickness sections at* (a) *0.13 mm,* (b) *0.76 mm, and* (c) *1.65 mm from the notch tip into the plastic zone for the 36:1 ER bar extrusion aged for 225 h (OA). The crack growth directions are into the paper.*

The first series of finite-element analyses examined the influence of a delamination crack at $x/T = 0$ on the σ_x stress state along $y = 0$ in the ligament. The σ_x stress, normalized with the reference $\tilde{\sigma}_x$, is shown in Fig. 7 for four different delamination crack sizes, (a/T). The decrease in σ_x with decreasing x/T is indicative of the constraint relaxation due to free crack surface. The decrease in normalized σ_x as a/T increases is caused by the greater constraint relaxation of a longer delamination crack.

The symmetry of this model as a consequence of the lateral constraint applied along the $x/T = 1$ edge means the geometry also models the case of an array of delamination cracks positioned at $x/T = 0$, $x/T = 2$, $x/T = 4$, etc. Considering the results in this manner suggests

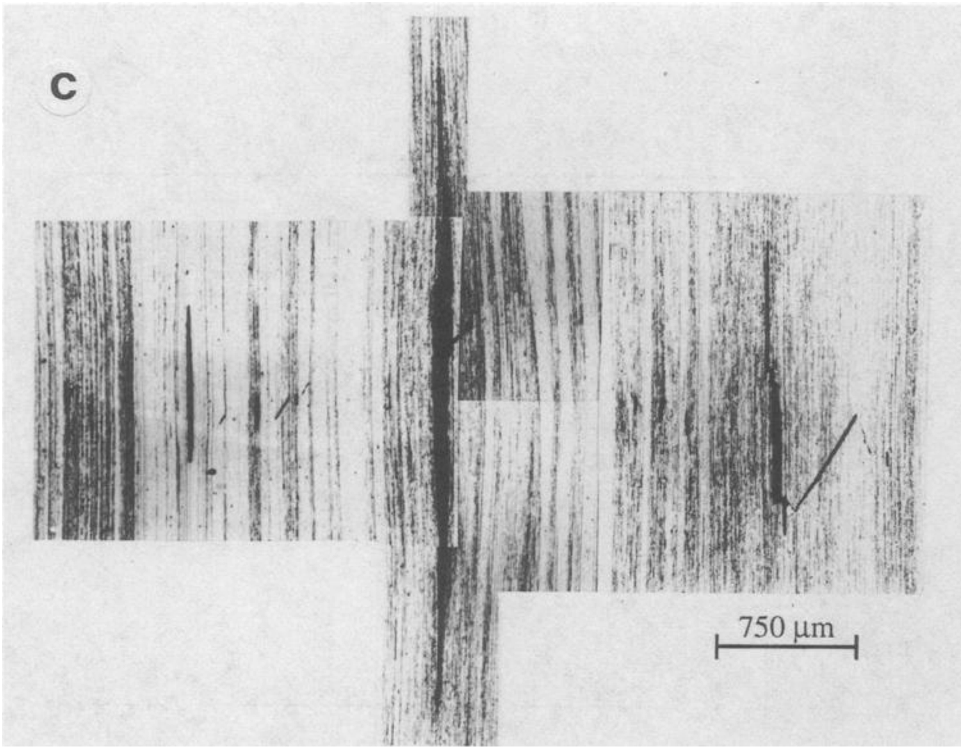

FIG. 5—*Continued.*

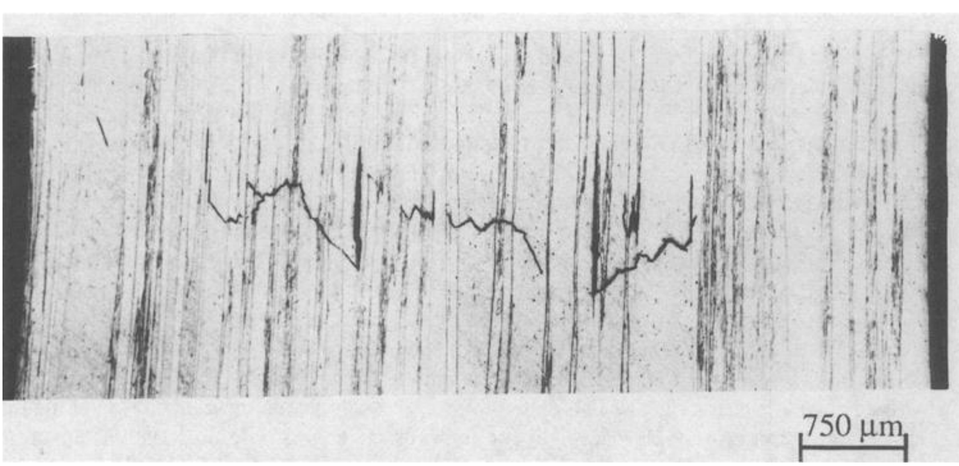

FIG. 6—*Thickness section at 1.91 mm from the notch tip into the plastic zone for the 9:1 ER rod extrusion aged for 96 h (OA). The crack growth direction is into the paper.*

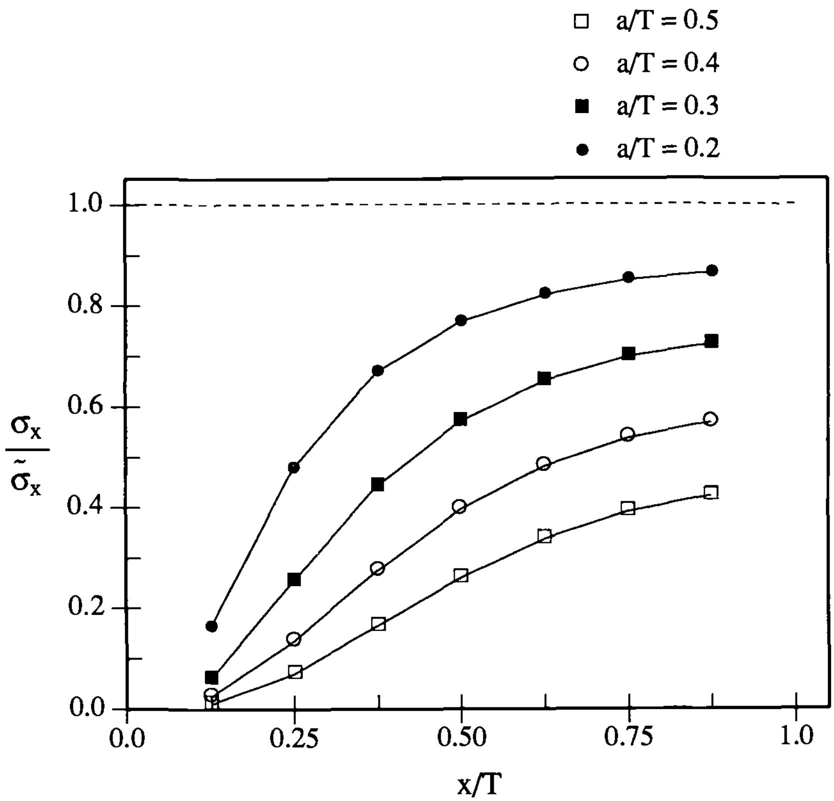

FIG. 7—*The effect of delamination crack size,* a/T, *on local* σ_x *stresses at* y $\approx$ *0. The delamination crack is located at* x/T = *0 and the edge at* x/T = *1 is constrained in the* x*-direction.*

that the center of the $2T$ ligament at $x/T = 1$ is the position of maximum σ_x stress along the lower $y = 0$ edge.

The second finite-element simulation evaluated the Mode I stress intensity factor, K_I, of a delamination crack located at $x/T = 0$ in the presence of a second delamination crack of various lengths located along the $x/T = 1$ edge (Fig. 8). For the fully constrained case, the K_I follows the expected $\sqrt{\pi a}$ behavior for short crack lengths ($a/T < 0.25$) but remains at a constant value for longer cracks ($a/T > 0.5$). This crack length, independent stress intensity factor behavior was initially unexpected. Further review of the literature showed that similar behavior has been reported for other delamination studies [*19,20*]. Furthermore, it can also be inferred from Tada et al. [*21*] who presented the solution $K_I = \sigma\sqrt{T}$ which applies for an array of parallel cracks spaced $2T$ apart and subjected to a remote Mode I stress, σ. For K_I to be independent of crack length means that as the crack grows, the remote stress driving it also decreases. For a delamination crack, this is a consequence of the constraint relaxation along the crack surface causing σ_x to decrease in the uncracked ligament (see Fig. 7).

As a delamination crack grows in a plate of finite size, some constraint relaxation along the $x/T = 1$ edge seems reasonable, especially for longer crack lengths. The effect of this relaxation on K_I is shown in Fig. 8 for three relaxation levels, each a function of crack length. Constraint relaxation is achieved in the finite-element model by allowing both x and y displacements

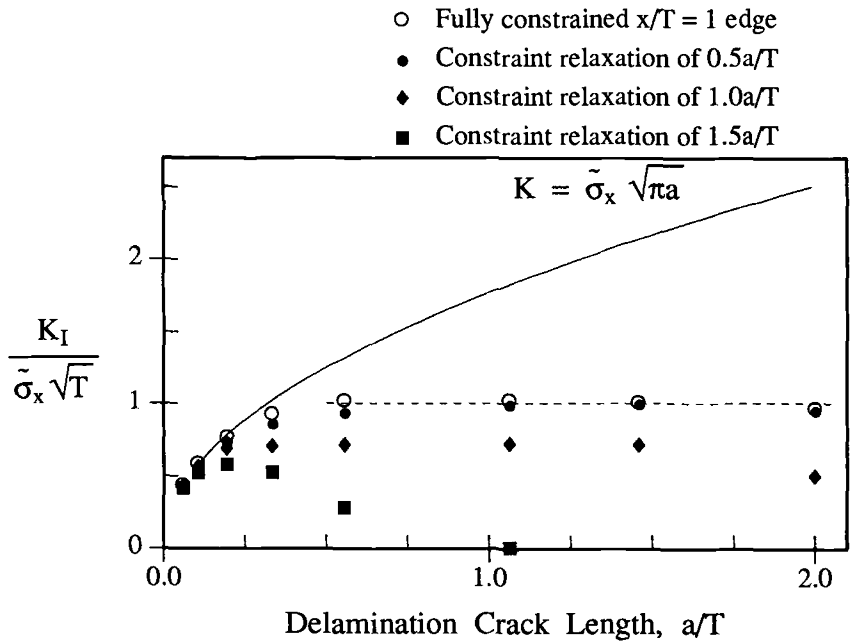

FIG. 8—*Finite element results indicating* K_I *for a delamination crack plotted as a function of crack length. The crack is located at* x/T = 0 *and the edge constraint at* x/T = 1 *is reduced in the* x- *and* y-*directions by releasing nodes (see Fig. 2).*

along the $x/T = 1$ edge to be nonzero (that is, simply releasing the nodes previously constrained in the x and y directions). As the relaxation along the edge increases, K_I for the delamination crack decreases. The smallest constraint relaxation ($0.5a/T$ or corresponding to a length of $0.5a/T$ beginning at $y = 0$) has little effect on K_I because the σ_x levels in the model for $y < 0.5a/T$ are relatively low. Conversely, K_I decreases to the point of crack arrest for the most severe constraint relaxation ($1.5a/T$). Furthermore, K_I decreases as crack length increases only when the constraint relaxation is equal to, or greater than, the length of the delamination crack.

The final series of finite-element analyses examined K_I for two delamination cracks, one located at the midthickness ($x/T = 0$) and the other at one quarter thickness ($x/T = ½$). Results are plotted in Fig. 9 for two fixed lengths of the midthickness crack. Whereas symmetry dictates no K_{II} for the midthickness crack, the ligament (quarter thickness) crack is subject to a Mode II effect. The results from Fig. 8 clearly indicate that the K_{II} effect is negligible for the crack lengths considered. Furthermore, as the ligament crack grows, K_I for the midthickness crack decreases. The plots for the two K_I values intersect when the a/T for the ligament crack is 5 to 10% shorter than the midthickness crack. The magnitude of K_I at this intersection is approximately 60% of the initial K_I for the fixed crack.

The applicability of these linear, two-dimensional finite-element approximations to the crack-tip region can be questioned since plasticity dominates locally. Furthermore, the nature of the actual physical problem dictates that a highly complex, three-dimensional solution would be required for accurate analysis. Nevertheless, these models provide insight into the influence of the delamination cracks.

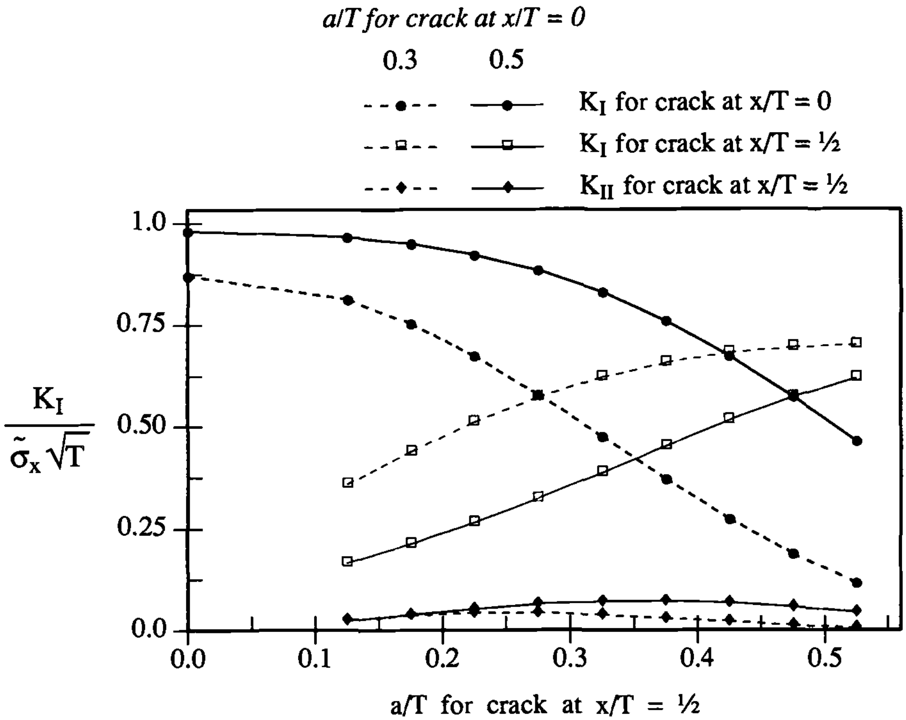

FIG. 9—*Variation of* K_I *for two sizes of a delamination crack at* x/T = 0 *when an* x/T = ½ *crack is introduced and allowed to grow. The applied load is fixed for all conditions and the edge at* x/T = 1 *is constrained in the* x*-direction.*

Discussion

Quantifying Fracture Toughness

The fracture surface crack profiles depicted in Figs. 4 through 6 clearly illustrate the three-dimensional nature of the fracture process. The delaminations occurring in the material as fracture progresses will inevitably result in some degree of constraint relaxation through the thickness of the specimen. Accompanying this constraint change, from an initial more plane-strain condition to a final more plane-stress dominant condition, is an increase in compliance. For the limiting case, the compliance increase can be described with the factor $1/(1 - \nu^2)$ that predicts approximately a 10% compliance increase. This compliance increase will be reflected subsequently in a flattening of the load-displacement behavior recorded from a specimen undergoing delaminations during a fracture test.

Analysis of the load-displacement behavior is a crucial characteristic of the conventional fracture toughness measures; namely, K_{Ic}, K_c from the *K-R* curve and J_{Ic} from the *J-R* curve. Clearly any compliance variation not resulting from plasticity or stable crack advance (in the conventional sense, not delamination formation) will have a deleterious effect on the measured toughness. This implies that an accurate fracture toughness measurement using the typical testing methods may not be possible for these alloys which exhibit large, intergranular delaminations. Of the toughness measures used in this study, the K_c and K_{J_q} parameters that rely more heavily on accurate compliance measurement could be largely affected by these delaminations.

The Delamination Fracture Process

Though the photomicrographs in Fig. 5 are from a single, partially fractured OA specimen, they can be considered a sequential illustration of the fracture process. For example the planar view closest to the notch, Fig. 5*a*, depicts a fully broken section in the latest stage of fracture. Conversely, the deepest section, Fig. 5*c*, illustrates the fracture process in its earlier stages. As such, it is clear from these planar sections that material separation is driven by the formation of through-thickness delaminations. This is the conceptual basis for the mechanistic-based approach to fracture described in this discussion.

Two possible mechanical criteria for delamination initiation include

1. exceeding a through-thickness, grain boundary strength (the fracture stress criteria), and
2. exceeding an *S-T* fracture toughness at a pre-existing flaw (the fracture mechanics criteria).

A necessary condition for grain delamination for either of these criteria is the buildup of through-thickness stress, σ_x. This will occur only if some degree of plane-strain constraint is initially present in the specimen.

The stress state in the thickness section must be estimated to apply these criteria. It is assumed that the crack or notch is sharp enough to cause crack-tip stress levels to at least locally exceed the yield strength of the material. The maximum stress in the plane-strain plastic zone perpendicular and parallel to the crack face will exceed the uniaxial yield stress and can be estimated by the product of σ_{YS} and the plastic constraint factor (PCF), defined as the ratio of the maximum sustained stress to the yield stress. The Irwin estimation of PCF = 1.68 [*22*] will be assumed due to the absence of reported experimentally measured values for Al-Li-X alloys. Consequently, the through-thickness stress with plane-strain conditions globally prevailing is $\sigma_x = 2\nu\sigma_{\max}$ or $\sigma_x = 2\nu(\text{PCF})\sigma_{YS} \approx \sigma_{YS}$.

The best estimate available for tensile grain boundary strength is the *S-T* yield strength. A survey of tensile properties for the commercial Al-Li-X alloys 2090, 8090, and 8091 in various tempers indicates that the ratio of *S-T* strength to *L* strength ranges from 0.76 to 0.89 with a mean value of 0.8 [*2,23,24*]. Since this value is less than σ_{YS}, the local through-thickness stress, σ_x, would be high enough to cause grain delamination. Hence the local σ_x stress is of the approximate magnitude to cause delamination based upon a relatively high tensile grain boundary strength. The extensive delamination observed in the photomicrographs of Figs. 4 through 6 may imply that the grain boundary strength is significantly lower than the 0.76 to 0.89 estimate.

A grain boundary fracture toughness must be known to apply the fracture mechanics criteria to delamination initiation in this material. Grain boundary fracture toughness can be estimated from the *S-L* or *S-T* toughness range of 8 to 20 MPa $\sqrt{m}$ reported in the literature [*2,5,23,24*] for Al-Li-X alloys. Furthermore, assume that K_I for a delamination crack can be represented by $K_I = \beta\sigma\sqrt{\pi a}$, where $\beta = 1$ for a crack of half-length a and $\beta = \pi/2 \approx 1.5$ for a circular internal crack of radius a. The predicted initiation flaw size based upon a mean toughness of 14 MPa $\sqrt{m}$ and $\sigma = \sigma_{YS} \approx 500$ MPa is between 100 and 250 μm with the range of β values noted. A finite flaw of this size consequently must exist in the material for this fracture mechanics criteria to apply. Based upon a review of the macroscopic thickness profiles in Figs. 4 through 6, there is no clear evidence of initiation sites of this size. In fact, some microstructural features expected to introduce discontinuities or flaws; namely, slip band width and spacing, are 2 to 3 orders of magnitude smaller, 0.1 to 2 μm [*25*]. This argument appears to favor the fracture stress criteria for delamination initiation.

The arrest of a delamination that has formed is probably a consequence of two factors:

growth out of the highly stressed fracture zone and global constraint relaxation. The first factor is more important for the initially appearing, longer delaminations. For example, the half length of the midthickness delamination in Figs. 5*b* and *c* is approximately 1.7 mm. For this specimen, the plane-strain plastic zone radius at fracture from Irwin's well-known expression is 0.5 mm. Hence, the delamination has extended beyond the plastic zone and into the less highly stressed material.

The finite-element results in Fig. 9 indicate that when a midthickness delamination crack extends beyond 0.25 to 0.5 a/T, K_I at the tip of a delamination crack is no longer a function of crack length. This corresponds to 0.8 to 1.6 mm for the specimen in Fig. 5 that compares well with the measured delamination length of 1.7 mm. The fact that K_I is no longer a function of crack length does not in itself result in crack arrest. Rather, crack arrest may occur because of subsequent constraint relaxation that causes K_I to decrease since it is no longer increasing with crack length. This was numerically verified in the finite-element results detailed in Fig. 9 for the higher levels of constraint relaxation.

The discussion so far has been limited to the formation and arrest of the first largest delamination, the delamination process is speculated to continue in each of the one-half thickness ligaments adjacent to the first midthickness delamination. Delaminations in these ligaments are evident in Fig. 5*c*. Recall that the finite-element study assessing the influence of a delamination crack on ligament σ_x stress state indicates that the region of highest stress is in the center of the ligament. This is reasonably close to where the ligamental delaminations in Fig. 5 appear.

The delamination lengths in the one-half thickness ligaments in Fig. 5*c* are 47 and 29% of the major midthickness delamination length. Since each adjacent ligament is approximately one half of the original specimen thickness, it is expected that these delaminations lengths would be 50% of the midthickness delamination. Furthermore, the lengths of these same delaminations can be measured in the shallower thickness section in Fig. 5*b*. These measured values of 46 and 57% agree more closely with the expected 50% because in this section the delaminations are mature and fully arrested. The evidence for this is the initial appearance of transgranular failure in Fig. 5*b*. Whereas intergranular failure is denoted as vertical lines in the photomicrographs, the transgranular fracture feature is slanted at an angle measured from the horizontal that is typically in excess of 30°.

The delamination size and spacing appears to support the idea that fracture progresses by sequential ligament splitting. This splitting continues until the remaining ligament widths are too thin to build up sufficient through-thickness stress, σ_x, to cause delamination. Furthermore, the finite-element results in Fig. 9 indicate that for the case of multiple delamination cracks, the stress intensity factor for each of these cracks is less than if a single crack existed in the section. If unstable delamination fracture is assumed to occur when the stress intensity factor exceeds a toughness level, the obvious implication is that a section with multiple delamination cracks has a higher load-carrying capacity than a section with only one crack.

Plane-Stress Fracture

The fracture process described in the previous section suggests that fracture in Al-Li-X alloys occurs in primarily a plane-stress constraint condition since the delaminations lead to stress relaxation through the thickness. This is also evident in Fig. 5*b* by the plane-stress type, transverse contraction of the ligament remaining between the delamination. The sequential delamination process simply transforms a thick, constrained section into a series of thin, unconstrained sheets each of which fails in plane-stress. If this is indeed the case, a fracture model for plane-stress failure should be able to predict the toughness of Al-Li-X alloys. This concept, originally suggested by Rao and Ritchie [5], was used in this work to assess the toughening effect associated with the slant fracture that occurs in the less constrained ligaments. Rao and Ritchie [5] also used the Bilby, Cottrell, and Swinden [BCS] theory [26] to describe this toughening behavior. The BCS theory treats plane-stress failure by modeling the plastic relaxation around the crack tip by the motion of screw dislocations. It assumes that the plane-stress material separation, even though in nominal Mode I loading, is driven by an antiplane Mode III shear mechanism. The BCS model simulates the plastic zone and crack-tip discontinuity with a distribution of dislocations from which a critical sliding displacement can be defined. This critical sliding displacement, δ_{crit}, is the length of the plane-stress failure and can be defined by

$$\delta_{crit} = \frac{4a\tau_{YS}}{\pi G} \ln \left[\sec \left(\frac{\pi \tau_c}{2\tau_{YS}} \right) \right] \tag{1}$$

where

τ_{YS} = shear yield stress,
G = shear modulus,
a = crack length, and
τ_c = critical shear stress for fracture.

Using only the first term of the Taylor series expansion for the exponential-trigonometric function in Eq 1 yields an expression of the form

$$\delta_{crit} = \frac{\pi a \tau_c^2}{2G\tau_{YS}} \tag{2}$$

Further simplification can be made by following a procedure outlined by Knott [27]. For a pure slant 45° plane-stress failure, $\delta_{crit} = \sqrt{2}B$, where B is the thickness of the ligament. Furthermore, the shear stresses can be transformed to axial stresses with $\tau_c = \sigma_c/2$ and $\tau_{YS} = \sigma_{YS}/2$. If these substitutions and $E = 2G(1 + \nu)$ are made in Eq 2, the resulting expression is

$$\sigma_c = \sqrt{\frac{2\sqrt{2}B\sigma_{YS}E}{\pi a(1 + \nu)}} \tag{3}$$

where σ_c is the remote applied stress for a ligament to fail in plane-stress at 45°. This stress can be transformed into a stress intensity by assuming $K_c = \sigma_c\sqrt{\pi a}$. The final result is

$$\begin{aligned} K_c &= \sqrt{\frac{2\sqrt{2}BE\sigma_{YS}}{1 + v}} \\ &= 1.48\sqrt{BE\sigma_{YS}} \end{aligned} \tag{4}$$

for $\nu = 0.3$.

This BCS model for fracture can be used to predict toughness based upon flow strength, σ_f, and ligament size, B_1, provided plane-stress conditions dominate. The functional form of this model, namely, $K_c \propto \sqrt{B_1 E\sigma_f}$, is evaluated in Fig. 10 for the Al-Li-Zr material and other commercial Al-Li-X alloys using reported toughness values and ligament thicknesses, B_1, in the delamination region [5,28]. K_{max} is plotted as the toughness measure for the Al-Li-Zr alloy because it is less dependent on accurate compliance measurements that are difficult to obtain

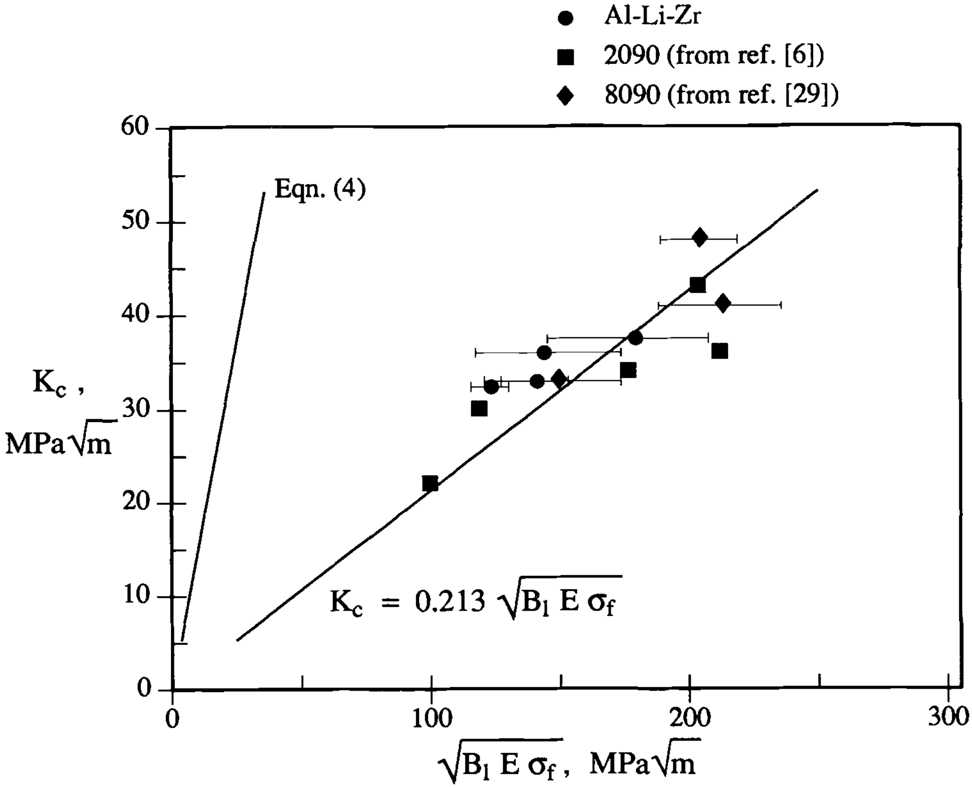

FIG. 10—*Experimentally measured fracture toughness plotted against the functional form of the BCS plane-stress fracture theory with data from this study (Al-Li-Zr) and data from the literature for two commercial Al-Li-X alloys* [5,28].

in the presence of intergranular delaminations. The alloys included in Fig. 10 exhibit a flow strength range of 380 to 575 MPa. The flow strength is utilized instead of the yield strength to partially account for the strength increase associated with work hardening. The horizontal error bars on the data points in Fig. 10 account for the variability in the reported delamination size, B_l [*5,28*]. The line through the data in Fig. 10 is a linear least squares fit passing through the origin. However, the slope of this line, 0.213, is lower than the expected value of 1.48.

There are several potential explanations for the difference between the BCS model and the experimental results. First, the BCS model does not account for the influence of slow, stable crack advance, section necking, nor section thinning. Also, it does not account for the influence of delamination cracks that will inevitably create a slip initiation site at the delamination crack tip. Furthermore, the applicability of the dislocation distribution assumed in the BCS model to Al-Li-X alloys conducive to planar slip is unknown. Whereas the BCS model assumes plane-stress conditions at the beginning of the fracture process, this alloy achieves a plane-stress condition only after delamination cracks have initiated. The formation of these delamination cracks will inevitably introduce damage and slip paths into the microstructure that would effectively lower the strength of the material.

The magnitude of the difference between the experimental and theoretical responses in Fig. 10 may indicate that the micromechanics of failure in Al-Li-X alloys may be different than that considered with the BCS model. Nevertheless, the functional form for the BCS model for plane-stress fracture predicts the experimental trend for these alloys since the observed behavior in Fig. 10 is nearly linear. Assuming that toughness decreases with increasing flow strength, this model predicts that delamination spacing must also decrease as strength increases. A decrease in ligament width suggests less ability to sustain through-thickness stress or a weakening in the *S-T* direction. This implies that *S-T* strength is sacrificed in order to achieve higher strength Al-Li-X alloys.

The specific mechanical conditions or material characteristics that cause a slant-type fracture to occur in the ligaments have not been analyzed in this investigation. It could be either {111} slip plane fracture, shear deformation fracture, or a combination thereof. Furthermore, the existence of slant fracture and the dominance of plane-stress conditions, both presupposed in the BCS model, may not be sufficient conditions to utilize the model to predict toughness. Nevertheless, the trend of the data suggests that the functional form of the model is in accordance with the experimental trends. This implies that the BCS model provides a first-order indication of the toughness changes observed with specimens exhibiting various ligament sizes and alloy strength levels.

Concluding Remarks

1. Fracture of this Al-2.6Li-0.09Zr alloy in the underaged condition is characterized by crack tunneling and significant grain boundary microcracking. This microcracking is separate from the continuous crack and confined to a zone surrounding it. It is believed that crack formation results from a linking of the microcrack damage.
2. The fracture profile of the alloy in the overaged condition is distinguished by large, intergranular delamination cracks perpendicular to the main fracture surface and extending deep into the specimen. The delamination spacing results in ligaments 0.5 to 0.9 mm thick that then fail by transgranular slant fracture.
3. A mechanistic-based fracture process is described for the alloy in the overaged condition whereby fracture appears to be driven by the formation of the through-thickness delaminations. This delamination process continues until the uncracked ligaments in the specimen behave in a plane-stress manner. Furthermore, this alloy and other Al-Li-X alloys appear to follow the functional form of the BCS model for plane-stress fracture with $K_c \propto \sqrt{B_1 E \sigma_f}$.
4. The notch sensitivity of the alloy, as measured by fracture testing with machined-notched and fatigue-cracked specimens, is less than that observed with 7075 aluminum alloy. For the Al-Li-Zr alloy, the fracture toughness for specimens with these two types of notches was essentially the same whereas for 7075 the machined notch nearly doubled the measured toughness.
5. The complexity and irregularity of the fracture surface and the changes in constraint caused by delamination cracking leads to serious questioning of the validity of conventional fracture toughness measures and test procedures for this class of alloys.

Acknowledgments

This work was supported in part by the National Science Foundation under Grant CDR 8803017 to the Engineering Research Center for Intelligent Manufacturing Systems and CIDMAC at Purdue University. The material utilized in this study was cast and extruded by the Aluminum Company of America.

References

[*1*] Henkener, J. A., Scheumann, T. D., and Grandt, A. F., Jr., "Fatigue Crack Growth Behavior of a Peakaged Al-2.6Li-0.09Zr Alloy," *Proceedings*, Fourth International Conference on Fatigue and Fatigue Thresholds, Materials and Component Engineering Publications Ltd, Birmingham, UK, Vol. 2, 1990, pp. 957–962.

[*2*] Bucci, R. J., Malcolm, R. C., Colvin, E. L., Murtha, S., and James, R. S., "Cooperative Test Program for the Evaluation of Engineering Properties of Al-Li Alloy 2090-T8X Sheet, Plate and Extrusion Products," Final Report, Department of the Navy, Naval Surface Warfare Center, Silver Springs, MD, 1989, pp. 1–162.

[*3*] Vasudevan, A. K. and Suresh, S., "Microstructural Effects on Quasi-static Fracture Mechanisms in Al-Li Alloys: The Role of Crack Geometry," *Materials Science and Engineering*, Vol. 72, 1985, pp. 37–49.

[*4*] Suresh, S., Vasudevan, A. K., Tosten, M., and Howell, P. R., "Microscopic and Macroscopic Aspects of Fracture in Lithium-Containing Aluminum Alloys," *Acta Metallurgica*, Vol. 35, No. 1, 1987, pp. 25–46.

[*5*] Venkateswara Rao, K. T. and Ritchie, R. O., "Mechanisms Influencing the Cryogenic Fracture-Toughness Behavior of Aluminum-Lithium Alloys," *Acta Metallurgica*, Vol. 38, No. 11, Nov. 1990, pp. 2309–2326.

[*6*] McKeighan, P. C., Henkener, J. A., Kistler, G. P., Sanders, T. H., Jr., Grandt, A. F., Jr., and Hillberry, B. M., "Mechanical Properties of a Peak-aged Al-2.6Li-0.09Zr Alloy," *Proceedings*, Fifth International Aluminum-Lithium Conference, Materials and Component Engineering Publications Ltd, Birmingham, UK, 1989, pp. 849–858.

[*7*] Chan, K. S., "Evidence of a Thin Sheet Toughening Mechanism in Al-Fe-X Alloys," *Metallurgical Transactions A*, Vol. 20A, 1989, pp. 155–164.

[*8*] Venkateswara Rao, K. T., Yu, W., and Ritchie, R. O., Cryogenic Toughness of Commercial Aluminum-Lithium Alloys: Role of Delamination Toughening," *Metallurgical Transactions A*, Vol. 20A, 1989, pp. 485–497.

[*9*] Sanders, T. H., Jr., Grandt, A. F., Jr., Hillberry, B. M., Fragomeni, J. M., Henkener, J. A., Kistler, G. P., McKeighan, P. C., Pegram, J. E., Sater, J. M., and Valentine, M. G., "An Extrusion Program Designed to Relate Processing Parameters to Microstructure and Properties of an Al-Li-Zr Alloy," *Proceedings*, Fifth International Aluminum-Lithium Conference, Materials and Component Engineering Publications Ltd, Birmingham, UK, 1989, pp. 273–285.

[*10*] McKeighan, P. C. and Hillberry, B. M., "The Effect of Extrusion and Processing Variables on the Tensile Properties of an Al-2.6Li-0.09Zr Alloy," *Proceedings*, Sixth International Aluminum-Lithium Conference, to be published.

[*11*] *1990 Annual Book of ASTM Standards*, Section 3, Metals Test Methods and Analytical Procedures, American Society for Testing and Materials, Philadelphia, 1990.

[*12*] McKeighan, P. C. and Hillberry, B. M., "An Algorithm for Determining Tensile Properties from Digitally Recorded Tensile Test Data," *Experimental Techniques*, Society for Experimental Mechanics, 1991, accepted for publication.

[*13*] Pegram, J. E., Sanders, T. H., Jr., Hartshorn, C. J., McKeighan, P. C., Valentine, M. G., and Hillberry, B. M., "Tensile Properties of an Al-2.6Li-0.09Zr Alloy," *Proceedings*, Fifth International Aluminum-Lithium Conference, Materials and Component Engineering Publications Ltd, Birmingham, UK, 1989, pp. 261–273.

[*14*] McKeighan, P. C., Evans, R. D., and Hillberry, B. M., "Fatigue and Fracture Testing Using a Multitasking Minicomputer Workstation," *Applications of Automation Technology to Fatigue and Fracture Testing, ASTM STP 1092*, American Society for Testing and Materials, Philadelphia, 1990, pp. 52–67.

[*15*] Rybicki, E. F. and Kanninen, M. F., "A Finite Element Calculation of Stress Intensity Factors by a Modified Crack Closure Integral," *Engineering Fracture Mechanics*, Vol. 9, 1977, pp. 931–938.

[*16*] Sun, C. T. and Jih, C. J., "On Strain Energy Release Rates for Interfacial Cracks in Bi-Material Media," *Engineering Fracture Mechanics*, Vol. 28, 1987, pp. 13–20.

[*17*] Starke, E. A., Sanders, T. H., Jr., and Palmer, I. G., "New Approaches to Alloy Development in the Al-Li System," *Journal of Metals*, Vol. 33, No. 8, 1981, pp. 24–33.

[*18*] Palmer, I. G., Miller, W. S., Lloyd, D. J., and Bull, M. J., "Effect of Grain Structure and Texture on Mechanical Properties of Al-Li Base Alloys," *Proceedings*, Third International Aluminum-Lithium Conference, 1985, pp. 565–575.

[*19*] Russell, A. J., "Micromechanics of Interlaminar Fracture and Fatigue," *Polymer Composites*, Vol. 8, No. 5, 1987, pp. 342–351.

[20] Lee, S. M., "Failure Mechanism of Delamination Fracture," *Composite Materials: Testing and Design (Eighth Conference), ASTM STP 972,* American Society for Testing and Materials, Philadelphia, 1988, pp. 356–365.
[21] Tada, H., Paris, P. C., and Irwin, G. R., *The Stress Analyses of Cracks Handbook,* Del Research Corporation, St. Louis, MO, 1985.
[22] Irwin, G. R., "Plastic Zone Near a Crack and Fracture Toughness," *Proceedings,* Seventh Sagamore Conference, Racquette Lake, NY, Vol. 4, 1961, pp. 63–78.
[23] "Aluminum-Lithium Alloys: Current Data," British Alcan Aluminum, Sept. 1986.
[24] Cieslak, S. J., Hart, R. M., Mehr, P. L., and Mueller, L. N., "Alcoa Alithalite Alloy 2090 Technical Information," Seventeenth International SAMPE Technical Conference, Rianesha Lake, NY, Oct. 1985.
[25] Jata, K. V. and Starke, E. A., Jr., "Fatigue Crack Growth and Fracture Toughness Behavior of an Al-Li-Cu Alloy," *Metallurgical Transactions A,* Vol. 17A, 1986, pp. 1011–1026.
[26] Bilby, B. A., Cottrell, A. H., and Swinden, K. H., "The Spread of Plastic Yield from a Notch," *Proceedings of the Royal Society A,* Vol. 272, 1963, pp. 304–310.
[27] Knott, J. F., *Fundamentals of Fracture Mechanics,* Butterworths, London, UK, 1973.
[28] Blankenship, C. P., Jr., Roven, H. J., and Starke, E. A., "The Fracture and Fatigue Behavior of Al-Li-X Alloys," *Proceedings,* Fourth International Conference on Fatigue and Fatigue Thresholds, Materials and Component Engineering Publications Ltd, Birmingham, UK, Vol. 2, 1990, pp. 937–955.

Young-Jin Kim,[1] *Yong-Shick Choy,*[2] *and Jin-Ho Lee*[2]

Development of Fatigue Life Prediction Program for Multiple Surface Cracks

REFERENCE: Kim, Y.-J., Choy, Y.-S., and Lee, J.-H., **"Development of Fatigue Life Prediction Program for Multiple Surface Cracks,"** *Fracture Mechanics: Twenty-Third Symposium, ASTM STP 1189,* Ravinder Chona, Ed., American Society for Testing and Materials, Philadelphia, 1993, pp. 536–550.

ABSTRACT: The objective of this paper is to develop a computational model and a software for predicting the fatigue propagation of collinear multiple surface cracks under constant-amplitude and variable-amplitude loading. After examining fatigue crack growth rate data for compact tension (CT) specimens and single surface crack specimens, an empirical equation is proposed for the prediction of fatigue life in a multiple surface crack geometry. The accuracy of the proposed model is verified using a life prediction computer program. The predictions are compared with the results from several case studies to check the accuracy of the proposed model and to verify the usefulness of the developed program. Good agreement is observed between the numerical results based on the proposed model and the published experimental data.

KEY WORDS: surface crack, fatigue (materials), life prediction, interaction effect, crack closure, random loading, fracture mechanics

In machine components subjected to severe temperature gradients, small surface cracks are formed that can coalesce before developing as a main crack. It is therefore important to assess the growth of multiple surface cracks to ensure the integrity of a structural component under fatigue loading. Life prediction of multiple surface cracks is difficult because of problems in using the Paris' power law type material constants (C and m) for compact tension (CT) and center-cracked tension (CCT) specimens, variation of crack aspect ratio, and an interaction effect of multiple cracks.

Some analyses [*1–7*] and experiments [*5–10*] have been carried out for interacting and coalescing coplanar surface cracks. Soboyejo and Knott [*11*] also performed an experimental investigation of the fatigue growth of noncoplanar surface cracks. However, such studies were limited to idealized geometries because of inherent complexities involved in modeling the problem.

In order to predict crack growth behavior more conveniently, various computer programs have been developed. Peterson and Vroman [*12*] developed a fatigue life prediction program for a single surface crack under constant-amplitude loading and Chang [*13*] reported ASTM round-robin prediction results for CCT specimen behavior under random amplitude loading. Forman et al. [*14*] developed a general-purpose fatigue life prediction program for single surface crack behavior. Yuuki and Yoshida [*15*] developed a computer program for predicting the fatigue growth behavior of multiple surface cracks under constant-amplitude loading.

[1] Associate professor, Department of Mechanical Design, Sung Kyun Kwan University, Suwon, Korea.
[2] Professor and graduate student, respectively, Department of Mechanical Engineering, Sung Kyun Kwan University, Suwon, Korea.

The objective of this paper is to propose an improved life prediction model for multiple surface cracks under constant-amplitude and variable-amplitude loading. Accordingly, a computer program based on the proposed model is developed, and various case studies are performed to check the usefulness of the proposed life prediction method.

Life Prediction Method

Fatigue growth behavior of a surface crack can be predicted by applying the Elber's crack closure model [*16*] for a through-thickness crack to the deepest point and the surface point of a surface crack, respectively. Information such as stress intensity factor, crack opening ratio, and material constants for a surface crack are required for fatigue life prediction.

Stress Intensity Factor

The stress intensity factor for a semi-elliptical surface crack (depth, a, and length, $2c$) in a plate subjected to membrane stress, σ_m, and bending stress, σ_b, can be expressed as

$$K_I = (M_m \cdot \sigma_m + M_b \cdot \sigma_b)\sqrt{\pi a/Q} \quad (1)$$

where Q is the shape factor, and M_m and M_b are the correction coefficients for stress intensity factor. In this paper, the Fett equation [*17*] that is the modified form of the Newman-Raju equation [*18*] is used.

The stress intensity factor for multiple surface cracks can be obtained by multiplying the interaction coefficient and the stress intensity factor for a single surface crack. In this paper, the following Yuuki-Yoshida equation [*15*] is adopted

$$M_m = \{1 + r_m(F - 1)\} \cdot (M_m)_{n-r} \quad (2a)$$

$$M_b = \{1 + r_b(F - 1)\} \cdot (M_b)_{n-r} \quad (2b)$$

where $(M_m)_{n-r}$ and $(M_b)_{n-r}$ are the correction coefficients for a single surface crack proposed by Fett [*17*], and F is the interaction coefficient for a through-thickness crack. In addition, the values of the correction coefficients, r_m and r_b, which are introduced to account for the effect of crack aspect ratio, are 0.8 and 0.4, respectively, as obtained by Yuuki and Yoshida [*15*].

Crack Opening Ratio

Crack closure, which has a significant effect on the shape change during surface crack growth, varies along the surface crack front and can be explained by the difference in crack opening ratio between the deepest point and the surface point of a surface crack. After examining fatigue crack growth rate data obtained from various fracture mechanics specimens [*9–10,19–20*], The following relationship can be established between the crack opening ratio at the deepest points (U_A) and those at the surface points (U_B):

Aluminum Alloys

$$U_A = \begin{cases} 1.1\ U_B & \text{for } R \leq 0.5 \\ U_B & \text{for } R > 0.5 \end{cases} \quad (3)$$

Stainless Steels

$$U_A = \begin{cases} 1.21\ U_B & \text{for } R \leq 0.5 \\ U_B & \text{for } R > 0.5 \end{cases} \tag{4}$$

Since the crack opening ratio, U, for a through-thickness crack is obtained by measuring at the specimen surface (approximately plane stress state), the following assumption can be justified

$$U \doteq U_B \tag{5}$$

Determination of Material Constants

By considering the crack-closure phenomenon, the fatigue crack growth behavior of fracture mechanics specimens can be expressed as

$$da/dN = C_{\text{eff}} \cdot (\Delta K_{\text{eff}})^m \tag{6}$$

where C_{eff} is a material constant. Also, the fatigue crack growth behavior at the deepest point and at the surface point of a surface crack can be respectively expressed as

$$da/dN = C'_{\text{eff}} \cdot (\Delta K_{\text{eff}})_A^m \tag{7a}$$

$$dc/dN = C'_{\text{eff}} \cdot (\Delta K_{\text{eff}})_B^m \tag{7b}$$

where C'_{eff} is the material constant obtained by analyzing the fatigue crack growth data in terms of ΔK_{eff}. Since the difference in the slope of the two lines in Eqs 6 and 7 is negligible, m is assumed to be constant.

Figure 1 shows the relationship between the fatigue crack growth rate and range of effective stress intensity factor for a through-thickness crack and a surface crack. Since the material constants, C_{eff}, C'_{eff}, and m, are independent of the stress ratio, R, the distance between the two lines can be regarded as a material property. In this paper, the material constant correction factor, MFACTOR, is proposed for crack growth in the Paris regime as

$$\text{MFACTOR} = C'_{\text{eff}}/C_{\text{eff}} \tag{8}$$

$$C_{\text{eff}} = C/U^m \tag{9}$$

where C is the material constant obtained by analyzing the fatigue crack growth rate data in terms of ΔK.

Life Prediction Model

Based on the preceding crack closure model, the fatigue crack growth model under constant-amplitude loadings is proposed as

$$\begin{aligned} da/dN &= C'_{\text{eff}} \cdot (\Delta K_{\text{eff}})_A^m \\ &= \text{MFACTOR} \cdot C_{\text{eff}} \cdot (U_A \cdot \Delta K_A)^m \\ &= \text{MFACTOR} \cdot C_{\text{eff}} \cdot (\gamma \cdot U_B \cdot \Delta K_A)^m \\ &= \text{MFACTOR} \cdot C_{\text{eff}} \cdot (\gamma \cdot U \cdot \Delta K_A)^m \\ &= \text{MFACTOR} \cdot C \cdot (\gamma \cdot \Delta K_A)^m \end{aligned} \tag{10a}$$

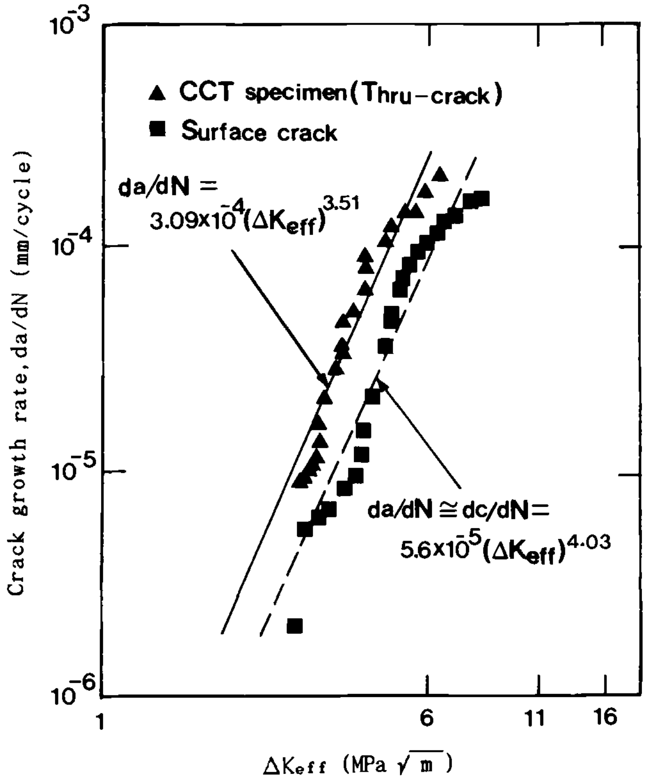

FIG. 1—*Relationship between crack growth rate and range of effective stress intensity factor for through-thickness crack and surface crack* [20].

$$\begin{aligned} dc/dN &= C'_{\text{eff}} \cdot (\Delta K_{\text{eff}})_B^m \\ &= \text{MFACTOR} \cdot C_{\text{eff}} \cdot (U_B \cdot \Delta K_B)^m \\ &= \text{MFACTOR} \cdot C_{\text{eff}} \cdot (U \cdot \Delta K_B)^m \\ &= \text{MFACTOR} \cdot C \cdot (\Delta K_B)^m \end{aligned} \tag{10b}$$

where γ is the opening ratio that is defined as U_B/U_A.

By combining the preceding life prediction model for a surface crack under constant-amplitude loading with Socie's model [*21*] for through-thickness cracks under variable amplitude loading, the following equation is proposed for a surface crack subjected variable amplitude loading

$$\begin{aligned} \frac{\Delta a}{\Delta B} &= \text{MFACTOR} \cdot C_{\text{eff}} \cdot \sum_1^N (\gamma \cdot U \cdot \Delta K_A)^m \\ &= \text{MFACTOR} \cdot C \cdot \sum_1^N (\gamma \cdot \Delta K_A)^m \end{aligned} \tag{11a}$$

$$\begin{aligned} \frac{\Delta c}{\Delta B} &= \text{MFACTOR} \cdot C_{\text{eff}} \cdot \sum_1^N (U \cdot \Delta K_B)^m \\ &= \text{MFACTOR} \cdot C \cdot \sum_1^N (\Delta K_B)^m \end{aligned} \tag{11b}$$

where the unit loading block is defined as the period of load history in which the characteristics of idealized, representative load appear repeatedly, ΔB is the increment of loading block, and N is the total number of cycles of variable amplitude loading within a unit loading block.

Determination of MFACTOR

From Eqs 9 and 5, the MFACTOR value can be defined respectively as the following expressions

$$\text{MFACTOR} = \left(\frac{C_A}{C}\right)\left(\frac{U}{U_A}\right)^m \tag{12}$$

$$\text{MFACTOR} = \left(\frac{C_A}{C}\right)\left(\frac{U_B}{U_A}\right)^m \tag{13}$$

Appropriate U_A and U_B values are given in Eqs 3 and 4. Therefore, in order to predict the fatigue crack growth using the MFACTOR value, the relationship between C_A and C is required. As shown in Fig. 2, several researchers [*9,18*] have predicted the fatigue lives of surface crack configuration by assuming that $C_A \doteq C$. However, as shown in Fig. 1, the values of C_A and C are clearly different in the range where the stress ratio, R, is greater than 0.5 (no crack closure) range. Therefore, the assumption that $C_A \doteq C$ is limited to cases where $R > 0.5$.

The newly proposed material constant MFACTOR can be determined in the Paris regime from the following expressions for stress ratios in the range where $C_A \doteq C$

$$\begin{aligned} \text{MFACTOR} &= \left(\frac{U_B}{U_A}\right)^m \\ &= \left(\frac{1}{\gamma}\right)^m \end{aligned} \tag{14}$$

Since the material constant MFACTOR value is independent of R, this value can be applied in the range of $R > 0.5$ as well.

Computer Program Development

In order to predict the fatigue life of multiple surface cracks more efficiently, a computer program based on the proposed method has been developed. As shown in Fig. 3, the program consists of three parts: an input section, an analysis section, and an output section. For the convenience of computer graphics, *C* language was used for programming purposes.

Input Subroutines

The input portion of the program consists of two sections: an input section and an *a-N* data processing section. In the input section, required input information such as analysis model geometry (width and thickness of the model, crack geometry, and location), loading conditions (constant and variable, membrane and bending), and material constants (ΔK_{th} and K_c, C and m) are provided. The *a-N* data processing section is used to obtain C (or C_{eff}) and m values when material constants are not given. After obtaining the graphical output of $da/dN - \Delta K$ (or ΔK_{eff}) relationship from the *a-N* data by the seven-point incremental method, material constant values are determined by curve fitting of the specified data points.

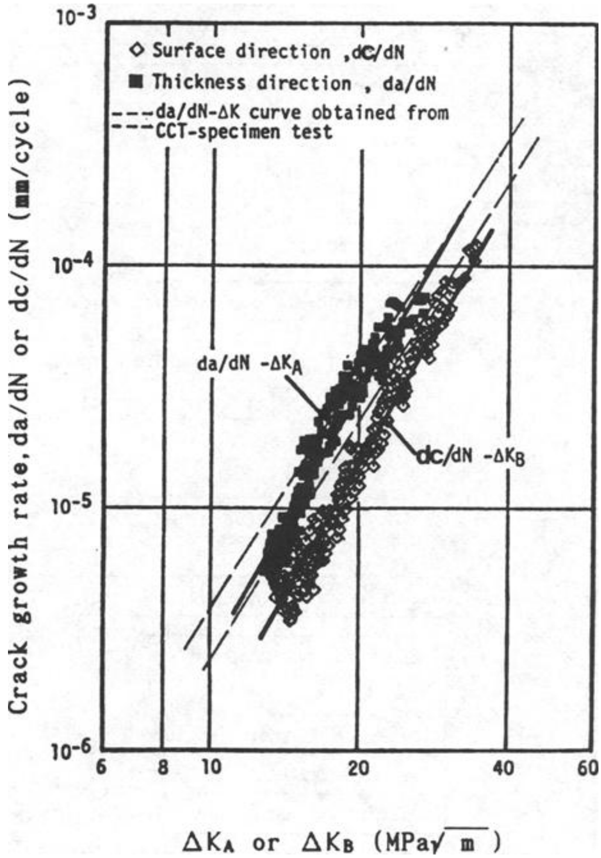

FIG. 2—*Relationship between crack growth rate and range of stress intensity factor in thickness and surface direction* [9].

Analysis Subroutines

In the analysis subroutines, the crack growth simulation is performed based on Eq 10, and the onset of crack coalescence is established using one of the following three methods [*15*]

1. ASME Sec. XI Code

$$\delta_0 = \min(a_1, a_2) \times 2$$

2. BSI PD 6493 Code

$$\delta_0 = C_1 + C_2$$

3. Coalescence of Surface Points

$$\delta_0 = 0$$

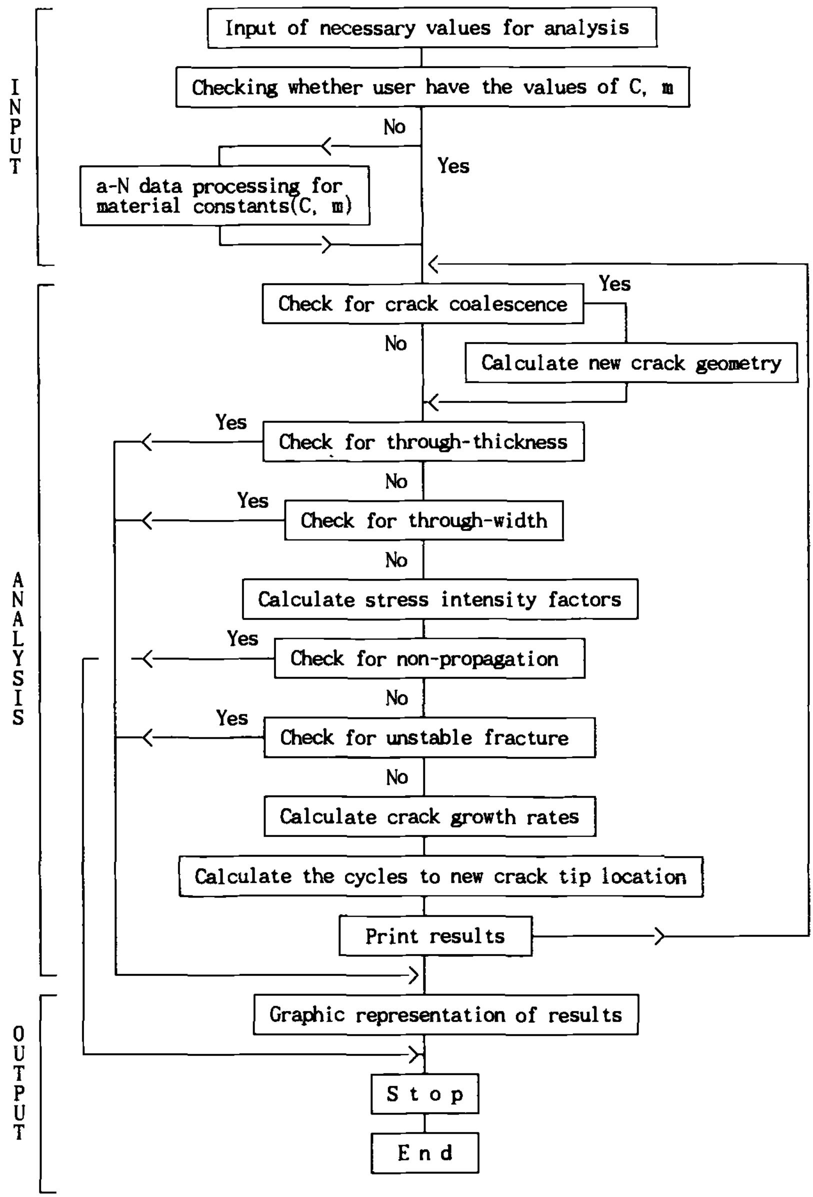

FIG. 3—*Flow chart of life prediction program for multiple surface cracks.*

where

δ_0 = separation between two adjacent surface cracks for coalescence condition,
a_1 and a_2 = crack depth values, and
c_1 and c_2 = half crack lengths.

Coalescence occurs when the separation between two adjacent surface cracks reaches δ_0, and the crack length is recomputed after coalescence. The semi-elliptical crack dimensions assumed at the point of coalescence are given by

$$a = \max(a_1, a_2)$$

$$2c = 2(C_1 + C_2 + \delta/2)$$

The crack length and crack depth are recomputed when the coalescence occurred. If the recomputed crack depth exceeds the plate thickness, a decision on through-thickness is made and the program is terminated. If the recomputed crack length exceeds the plate width, a decision on through-width is made and the program is terminated. In the next phase of the analysis, the stress intensity factor for multiple surface cracks is computed. Crack growth simulation is performed if the maximum stress intensity factor range (ΔK_{max}) is larger than the threshold stress intensity factor range (ΔK_{th}), and a decision on unstable fracture is made by comparing the maximum stress intensity factor (K_{max}) against the fracture toughness (K_{Ic}). Subsequently, both the amount of crack extension and the number of cycles required to reach to the new crack location are computed based on the stress intensity factor and the crack growth model.

Output Subroutines

In the output subroutines, analysis results that are stored in a file format can be displayed on the screen, printer, and plotter for the user's convenience. Currently, the following information is available:

1. crack aspect ratios,
2. $a/c - a/t$ diagrams, and
3. $K_{max} - N$ diagrams.

Case Studies

In order to verify the proposed life prediction method and the developed computer program, several case studies were conducted. The predicted results were compared with published experimental data (SUS Type 304L stainless steel plates and cylinder) by Shibata et al. [*9,10*]. As summarized in Table 1, Cases I, II, and III are surface crack plates under tensile loading and Case IV is straight pipe under internal pressure. Crack length measurements were made by beach mark and ultrasonic methods [*9,10*].

TABLE 1—*Test conditions of SUS Type 304L stainless steel plates and cylinder* [9,10].

Items/Case No.	Case I	Case II	Case III	Case IV
Number of cracks	1	2	2	3
Crack spacing	...	42 mm	60 mm	57.3 mm
Membrane stress range		$\Delta\sigma_m$ = 137 MPa		$\Delta\sigma_m$ = 115.6 MPa
Bending stress range		$\Delta\sigma_b$ = 0 MPa		$\Delta\sigma_b$ = 13.7 MPa
Stress ratio		R = 0.05		R = 0.1
Geometry of test section		t = 24 mm $2w$ = 200 mm		t = 35 mm $2w$ = 400 mm
Geometry of crack		a = 5 mm $2c$ = 12 mm		a = 8 mm $2c$ = 24 mm
Material constants (for m/cycle-MPa $\sqrt{m}$)		$C = 1.73 \times 10^{-12}$ [a] m = 3.26		$C = 4.63 \times 10^{-12}$ [b] m = 2.98

[a] Material constants obtained from CCT specimen.
[b] Material constants obtained from CC (center-cracked) cylinder specimen.

Constant-Amplitude Loading

Case I involves a single surface crack in a plate. By substituting $\gamma = 1.21$ and $m = 3.26$ (obtained from a CCT specimen) into Eq 14, the material constant MFACTOR value for stainless steel is computed as 0.537. As shown in Fig. 4, good agreement is observed between the predicted crack growth curves and the experimental data.

Cases II and III deal with the problem of twin surface cracks (in a plate) with different initial crack separations. The MFACTOR value of 0.537 obtained from Case I is used. Figures 5 and 6 show respective predicted results from the second and third case studies. Good agreement between the predicted crack dimensions and the experimental results is observed for precoalescence and postcoalescence ranges. The life prediction model proposed in this paper is therefore shown to simulate the interaction effect of a twin surface crack problem in a plate.

Case IV deals with triple, identical surface cracks located at the inner wall of a cylinder. By substituting $\gamma = 1.21$ and $m = 2.98$ (obtained from a center-cracked cylindrical specimen) into Eq 14, the material constant MFACTOR value is computed as 0.566.

Figure 7 shows that the maximum crack depth versus number of cycles diagram, and the predicted maximum depths are in good agreement with the experimental data within 2%. The life prediction model proposed in this paper can therefore appear to be applicable also to cylindrical geometries.

Figure 8 shows the progressive shape change with increasing the number of cycles. Coalescence occurs between 6.64×10^5 and 6.70×10^5 cycles.

Variable Amplitude Loading

It is difficult to obtain crack growth data for surface cracks subjected to random loading hysteresis. Therefore, the predicted results are shown here for demonstration purposes only.

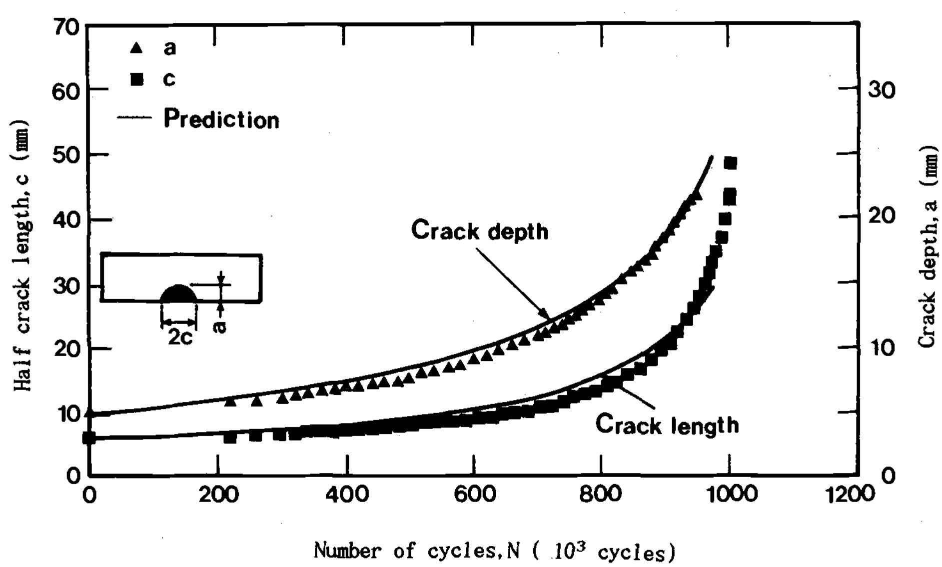

FIG. 4—*Comparison of crack growth curves between predicted results and experimental ones (Case I).*

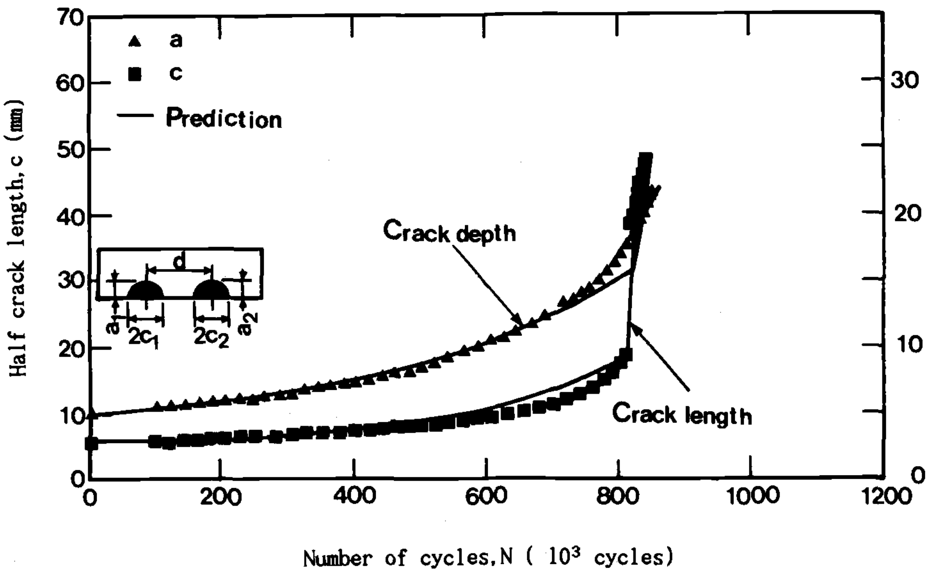

FIG. 5—*Comparison of crack growth curves between predicted results and experimental ones (Case II).*

The input conditions are identical to those employed in Case II. Instrumentation and Navigation Mission spectra from an ASTM round robin [*13*] are utilized for this demonstration.

Figure 9 shows the crack shape change and Fig. 10 shows the *a-N* and *c-N* diagrams, the variation in crack opening ratio is not significant when the unit loading block is approximately 500 cycles and the load variation is gradual. Therefore, it is still possible to make an approximate prediction of life using the proposed life prediction model.

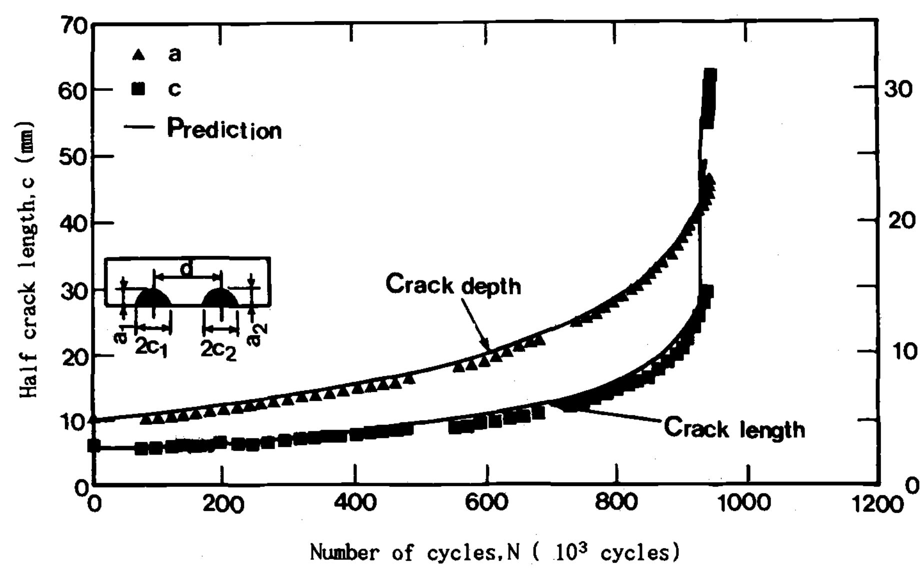

FIG. 6—*Comparison of crack growth curves between predicted results and experimental ones (Case III).*

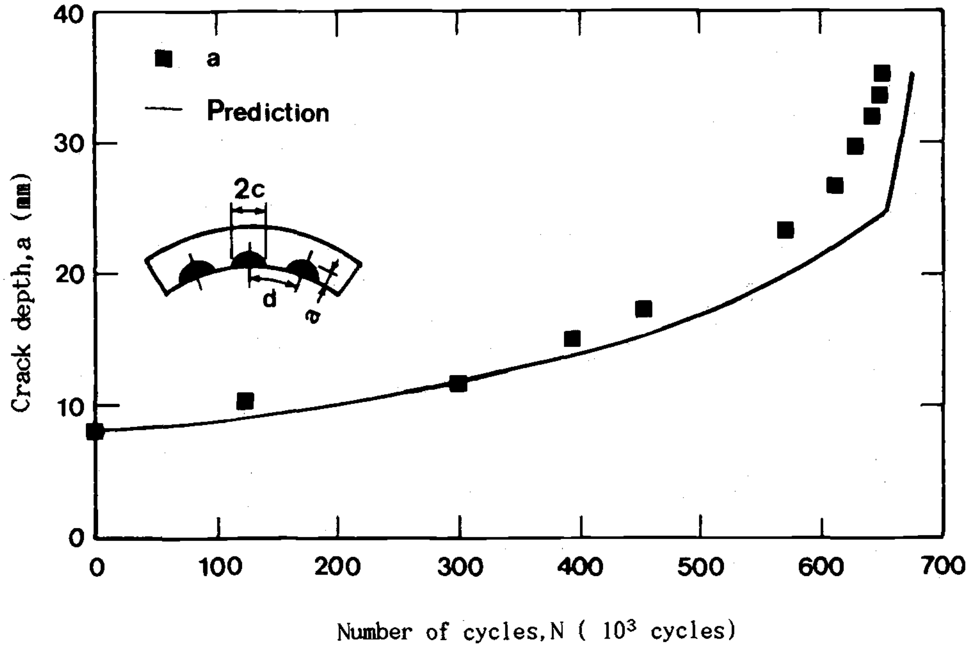

FIG. 7—*Comparison of crack growth curves between predicted results and experimental ones (Case IV).*

Conclusions

Based on the current life prediction study on multiple surface cracks, the following conclusions are made.

1. The newly proposed crack growth model that accounts for both multiple crack interaction and crack closure results in good predictions of the fatigue propagation of multiple surface cracks in plate and cylindrical geometries.
2. Reliable predictions of the propagation of multiple surface cracks in a plate or a cylinder can be achieved by using the computer program developed.

Acknowledgment

The authors wish to thank the Korea Science and Engineering Foundation for supporting this work through the Turbo and Power Machinery Research Center.

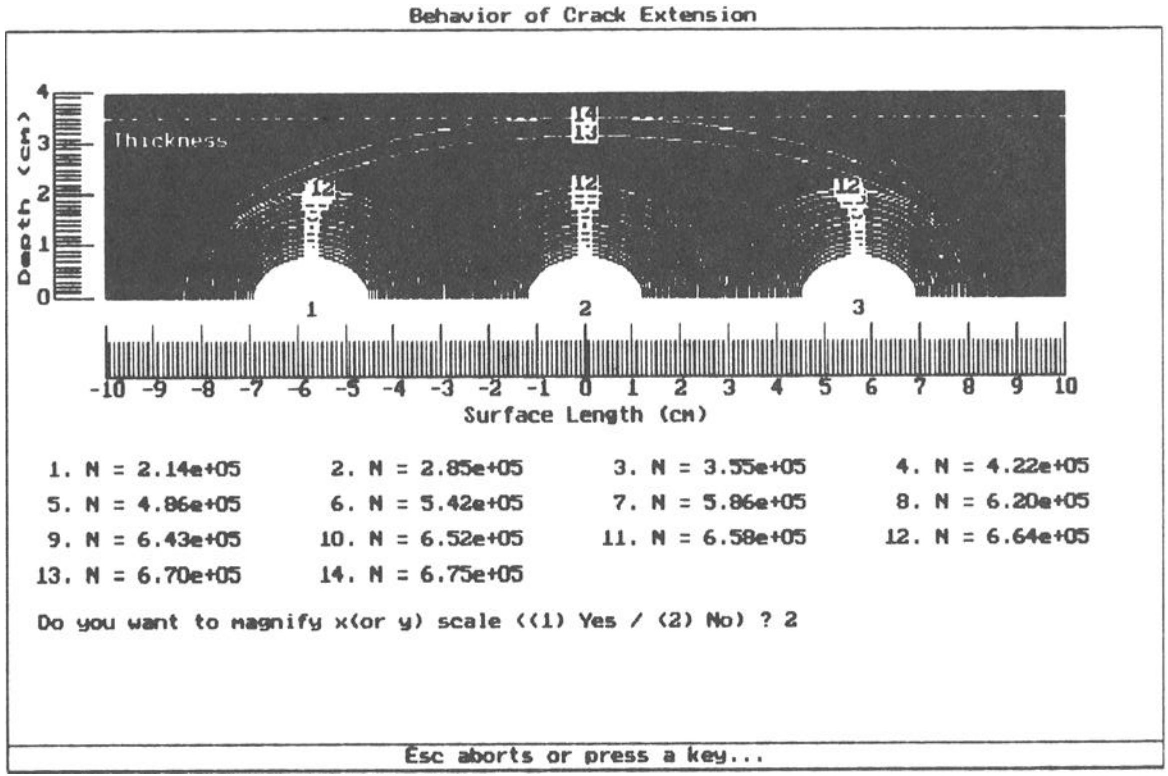

FIG. 8—*Prediction of crack shape change (Case IV).*

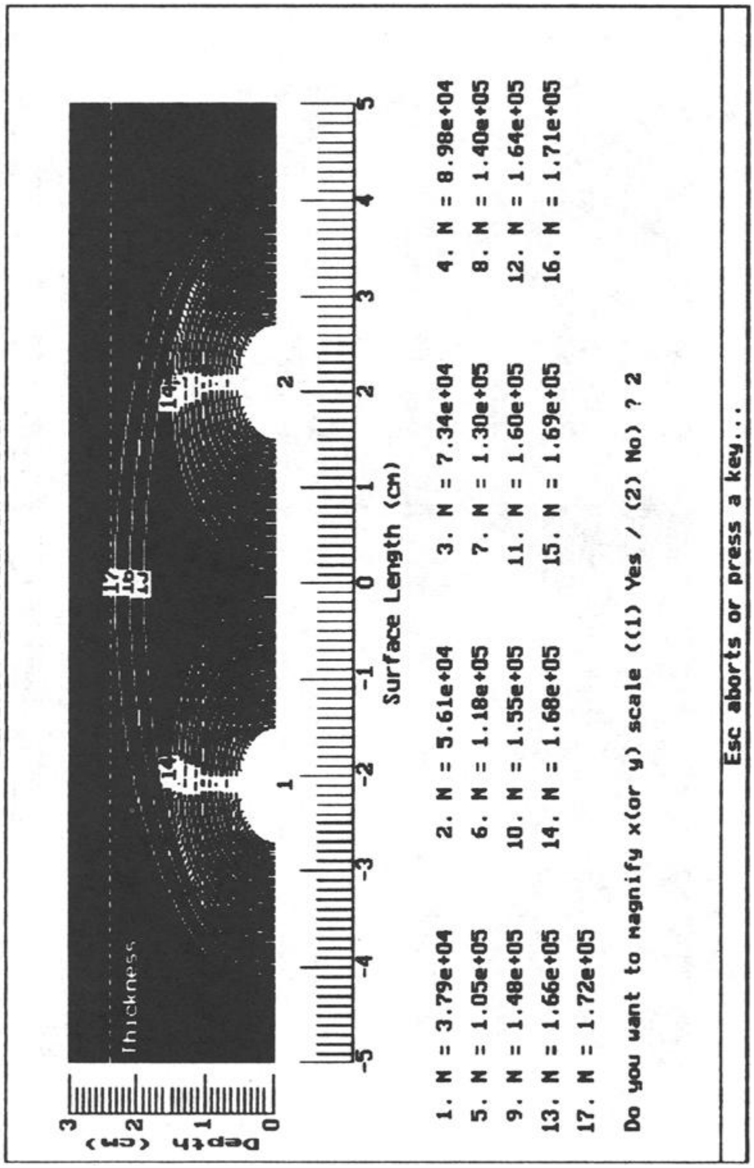

FIG. 9—*Prediction of crack shape change under random loading.*

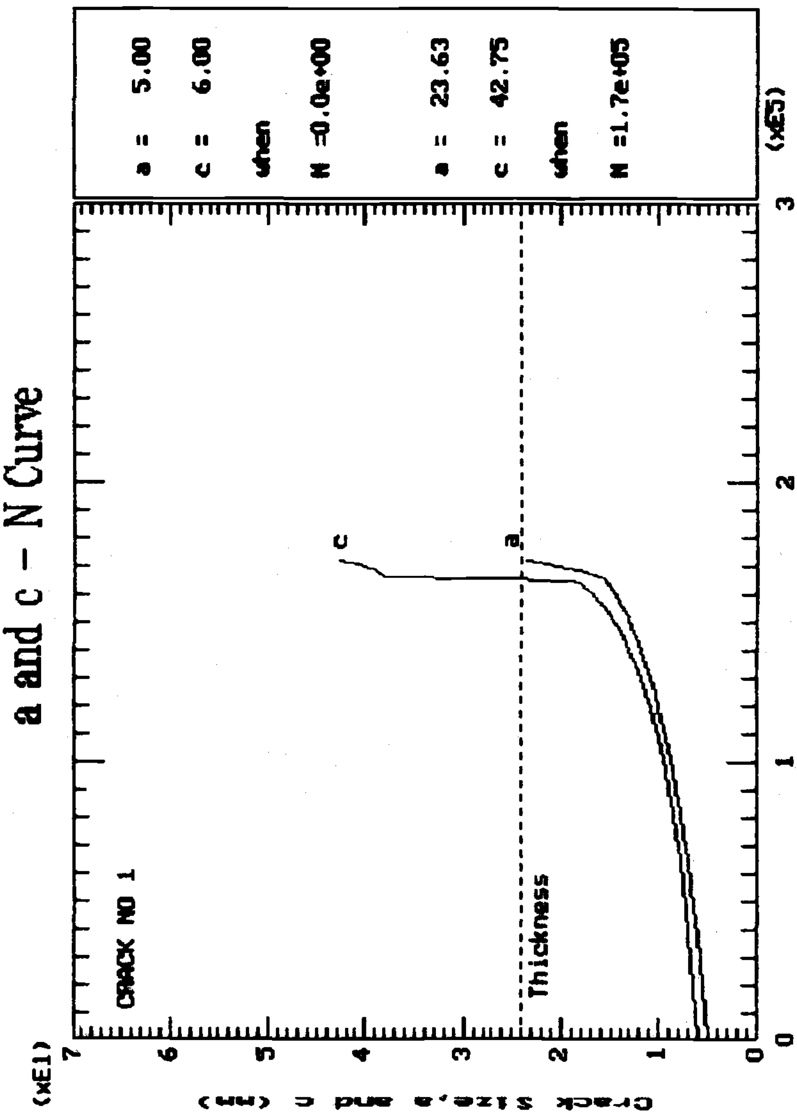

FIG. 10—*Predicted crack growth curves under random loading.*

References

[*1*] Murakami, Y. and Nemat-Nasser, S., "Interacting Dissimilar Semi-Elliptical Surface Flaws Under Tension and Bending," *Engineering Fracture Mechanics*, Vol. 16, No. 3, 1982, pp. 373–386.

[*2*] Murakami, Y. and Nemat-Nasser, S., "Growth and Stability of Interacting Surface Flaws of Arbitrary Shape," *Engineering Fracture Mechanics*, Vol. 17, No. 3, 1983, pp. 193–210.

[*3*] O'Donoghue, P. E., Nishioka, T., and Atluri, S. N., "Multiple Surface Cracks in Pressure Vessels," *Engineering Fracture Mechanics*, Vol. 20, No. 3, 1984, pp. 545–560.

[*4*] Heath, B. J. and Grandt, A. F., Jr., "Stress Intensity Factors for Coalescing and Single Corner Flaws Along a Hole Bore in a Plate," *Engineering Fracture Mechanics*, Vol. 19, No. 4, 1984, pp. 665–673.

[*5*] Grandt, A. F., Jr, "An Experimental and Numerical Investigation of the Growth and Coalescence of Multiple Fatigue Cracks at Notches," *Fracture Mechanics: Seventeenth Volume, ASTM STP 905*, J. H. Underwood, R. Chait, C. W. Smith, D. P. Wilhem, and J. C. Newman, Eds., American Society for Testing and Materials, Philadelphia, 1986, pp. 239–252.

[*6*] Soboyejo, W. O., Kishimoto, K., Smith, R. A., and Knott, J. F., "A Study of the Interaction and Coalescence of Two Coplaner Fatigue Cracks in Bending," *Fatigue Fracture of Engineering Materials and Structures*, Vol. 12, No. 3, 1989, pp. 167–174.

[*7*] Soboyejo, W. O., Knott, J. F., Walsh, M. J., and Cropper, K. R., "Fatigue Crack Propagation of Coplanar Semi-Elliptical Cracks in Pure Bending," *Engineering Fracture Mechanics*, Vol. 37, No. 2, 1990, pp. 323–340.

[*8*] McComb, T. H., Pope, J. E., and Grandt, A. F., Jr., "Growth and Coalescence of Multiple Fatigue Cracks in Polycarbonate Test Specimens," *Engineering Fracture Mechanics*, Vol. 24, 1986, pp. 601–608.

[*9*] Shibata, K., Yokoyama, N., Ohba, T., Kawamura, T., and Miyazono, S., "Growth Evaluation of Fatigue Cracks from Multiple Surface Flaws (I)," *Journal*, Japanese Nuclear Society, Vol. 28, No. 3, 1985, pp. 250–262.

[*10*] Shibata, K., Yokoyama, N., Ohba, T., Kawamura, T., and Miyazono, S., "Growth Evaluation of Fatigue Cracks from Multiple Surface Flaws (II)," *Journal*, Japanese Nuclear Society, Vol. 28, No. 3, 1986, pp. 258–265.

[*11*] Soboyejo, W. O. and Knott, J. F., "The Propagation of Non-Coplanar Semi-Elliptical Fatigue Cracks," *Fatigue Fracture of Engineering Materials and Structures*, Vol. 14, No. 1, 1991, pp. 37–49.

[*12*] Peterson, D. E. and Vroman, G. A., "Computer-Aided Fracture Mechanics Life Prediction Analysis," *Part-Through Crack Fatigue Life Prediction, ASTM STP 687*, J. B. Chang, Ed., American Society for Testing and Materials, Philadelphia, 1979, pp. 129–142.

[*13*] Chang, J. B., "Round-Robin Crack Growth Predictions on Center-Cracked Tension Specimens under Random Spectrum Loading," *Methods and Models for Predicting Fatigue Crack Growth Under Random Loading, ASTM STP 748*, J. B. Chang and C. M. Hudson, Eds., American Society for Testing and Materials, Philadelphia, 1981, pp. 3–40.

[*14*] Forman, R. G., Shivakumar, V., Newman, J. C., Jr., Piotrowski, S. M., and Williams, L. C., "Development of the NASA/FLAGO Computer Program," *Fracture Mechanics: Eighteenth Symposium, ASTM STP 945*, D. T. Read and R. P. Reed, Eds., American Society for Testing and Materials, Philadelphia, 1988, pp. 781–803.

[*15*] Yuuki, R. and Yoshida, T., "Fatigue Life Prediction System for Structures," *Journal of High Pressure Institute of Japan*, Vol. 24, No. 3, 1986, pp. 115–123.

[*16*] Elber, W., "The Significance of Fatigue Crack Closure," *Damage Tolerance in Aircraft Structures, ASTM STP 486*, American Society for Testing and Materials, Philadelphia, 1971, pp. 230–242.

[*17*] Fett, T., "An Extension of the Newman-Raju Formula," *International Journal of Fracture*, Vol. 33, 1987, pp. R47–R50.

[*18*] Newman, J. C. and Raju, I. S., "An Empirical Stress Intensity Factor Equation for the Surface Crack," *Engineering Fracture Mechanics*, Vols. 15, Nos. 1–2, 1981, pp. 185–192.

[*19*] Jolles, M. and Tortoriello, V., "Geometry Variations During Fatigue Growth of Surface Flaws," *Fracture Mechanics: Fourteenth Symposium, ASTM STP 791*, J. C. Lewis and G. Sines, Eds., American Society for Testing and Materials, Philadelphia, 1983, pp. 297–307.

[*20*] Chang, W., "Surface Crack Growth Behavior of 7075-T6 Aluminum Alloy," M.Sc. thesis, Korea Advanced Institute of Science and Technology, Seoul, Korea, 1989.

[*21*] Socie, D. F., "Prediction of Fatigue Crack Growth in Notched Members under Variable Amplitude Loading Histories," *Engineering Fracture Mechanics*, Vol. 9, 1977, pp. 849–865.

Stephen J. Balsone,[1] David C. Maxwell,[2] and Thomas F. Broderick[1]

Fatigue Crack Growth Behavior of Titanium Aluminide Ti-25Al-25Nb

REFERENCE: Balsone, S. J., Maxwell, D. C., and Broderick, T. F., "**Fatigue Crack Growth Behavior of Titanium Aluminide Ti-25Al-25Nb,**" *Fracture Mechanics: Twenty-Third Symposium, ASTM STP 1189,* Ravinder Chona, Ed., American Society for Testing and Materials, Philadelphia, 1993, pp. 551–567.

ABSTRACT: The fatigue crack growth rate of an orthorhombic + beta titanium aluminide, nominally Ti-25Al-25Nb, was studied as a function of temperature (25 to 750°C), environment (air and vacuum), frequency (0.001 to 1.0 Hz), and superimposed hold times (1 to 1000 s) under computer-controlled constant K_{max} testing conditions. In addition, fatigue crack growth rates from the near-threshold region to rates greater than approximately 10^{-7} m/cycle were determined at room and elevated temperatures. Results show that the fatigue crack growth rate exhibits a combination of cycle- and time-dependent behavior and is sensitive to environment over the entire temperature range. At elevated temperature, crack growth per cycle is found to increase with decreasing frequency in both laboratory air and vacuum, suggesting a contribution from environmentally assisted crack growth. Growth rates in vacuum are as much as an order of magnitude lower than those obtained in air. Further, hold times of increasing duration are found to slightly decrease and then increase the crack growth rate at elevated temperature. At elevated temperatures, crack growth behavior appears to be a complex interaction of environmental degradation at the crack tip, crack-tip blunting due to creep, and cyclic fatigue (resharpening of the crack tip). An attempt was made to correlate the observed fatigue crack growth rates with the mechanism, or mechanisms, of fracture. The crack growth characteristics were compared with those of the alpha-2 titanium aluminide, Ti-24Al-11Nb, and a conventional high-temperature titanium alloy, Ti-1100.

KEY WORDS: crack growth, environmental effects, fractography, frequency, hold times, intermetallic materials, temperature, titanium aluminide, fracture mechanics, fatigue (materials)

Advanced aerospace applications demand high-strength, light-weight, damage-tolerant materials that are capable of surviving in high-temperature environments. For a number of years, the titanium aluminide intermetallics based on the alpha-2 phase, Ti_3Al, have been the subject of intense investigation for such applications. Improvements in gas turbine engine performance and the development of hypersonic flight rely heavily on these lower density structural materials with high-temperature capability [*1,2*]. Development of the alpha-2 titanium aluminides would extend the service temperature of titanium-base materials beyond that of conventional alpha-beta alloys and would allow substitution for nickel-base superalloys in some applications. The alpha-2 titanium aluminides are being considered both as a monolithic material as well as the matrix material for continuous fiber-reinforced composites.

To date, much of the research conducted on alpha-2 titanium aluminides has used the Ti-24Al-11Nb (atomic percent) composition, a two-phase alloy containing alpha-2 and beta

[1] Materials research engineers, Air Force Wright Laboratory, Materials Directorate, Wright-Patterson AFB, OH 45433.
[2] Materials test specialist, University of Dayton Research Institute, Dayton, OH 45469.

phases. The composition was identified in 1977 by Blackburn and Smith as one that had a good combination of room-temperature ductility and elevated-temperature creep rupture properties [3]. Since that time, a significant database has been generated for this alloy both in monolithic and metal-matrix composite form [4,5]. However, from a design engineering point of view, this alloy suffers from limited room-temperature ductility and toughness. A number of investigations have been undertaken to improve the low ductility and toughness at room temperature through alloying and thermomechanical processing while trying to retain elevated-temperature strength and creep resistance in the same alloy [6–8]. Blackburn and Smith and other researchers have found that the tradeoff between low-temperature ductility and toughness with elevated-temperature creep resistance is a most difficult one. Recent progress in the understanding of microstructure-property relationships has resulted in alloys with microstructures having an improved balance of low- and high-temperature properties. During these investigations, titanium aluminide alloys with compositions near Ti-25Al-25Nb (atomic percent) were studied. The microstructure of these high-niobium alloys contains the ordered orthorhombic phase (O), ordered beta phase (B2), and the alpha-2 phase. The ordered orthorhombic phase was first identified by Banerjee as a distorted alpha-2 ordered structure with niobium occupying an additional sublattice [9]. The volume fraction and morphology of these three phases are strongly dependent on thermomechanical processing and heat treatment. Rowe has reported that these O + B2 titanium aluminide alloys have higher specific strength up to 760°C than the alpha-2 + beta titanium aluminides, such as Ti-24Al-11Nb, even though the O + B2 alloys have a higher density due to their higher niobium content [10]. They also possess higher fracture toughness (27.5 MPa $\sqrt{m}$ (25 ksi $\sqrt{in.}$)) while retaining creep resistance competitive with alloys such as Ti-24Al-11Nb. The tradeoffs among strength, ductility, toughness, and creep properties are strongly dependent on heat treatment. Much of the data on the Ti-25Al-25Nb class of alloys is preliminary, and much work needs to be done on the phase relationships, microstructural stability, minor alloying effects, and processing of these alloys.

The Ti-25Al-25Nb titanium aluminides have generated considerable interest as a monolithic material because of their higher specific strength and higher room-temperature ductility and fracture toughness without the major debit in creep resistance normally associated with increases in room temperature properties of the titanium aluminides. These characteristics appear to be a result of the large volume fraction of the more ductile orthorhombic phase and the ordered beta phase in the microstructure with only minor amounts of the more brittle alpha-2 phase [10]. Conversely, Ti-24Al-11Nb consists of predominantly the alpha-2 phase with little disordered beta phase. The Ti-25Al-25Nb alloys are also being considered as a matrix material for metal-matrix composites because of their higher ductility and toughness. Evidence has shown that a matrix microstructure that contains a high volume fraction of ductile, tough phases, for example, beta or orthorhombic or both, may be more effective in blunting cracks that initiate at the fiber/matrix interface in a metal-matrix composite [11]. In addition, the high niobium content appears to reduce the reaction zone and beta phase depleted zone that typically form around the silicon-carbide fibers that have been used as continuous reinforcement in titanium aluminide materials.

Preliminary mechanical properties generated on the orthorhombic + B2 titanium aluminide alloys have been predominantly under monotonic loading. Cyclic properties such as fatigue life and crack growth have not been investigated in any detail. This investigation was undertaken to determine the effects of environment, temperature, frequency, and superimposed hold times on the fatigue crack growth rate of a representative orthorhombic + B2 titanium aluminide, nominally Ti-25Al-25Nb. An attempt was made to correlate the observed fatigue crack growth rates with the mechanisms of fracture. Also, the crack growth characteristics were compared to those of the widely studied alpha-2 titanium aluminide Ti-24Al-11Nb and a conventional high-temperature titanium alloy, Ti-1100.

Experimental

The material used in this study was an orthorhombic + B2 titanium-aluminide intermetallic, nominally Ti-25Al-25Nb (atomic percent). Table 1 gives the analyzed alloy composition. The subject material was vacuum induction melted and cast into an ingot 6.99 cm in diameter and 81.28 cm in length (2.75 by 32 in.). The ingot was subsequently cut into 12.7-cm (5-in.) long sections. An ingot section was then forged after a 2 h soak at 1038°C (1900°F) to a pancake nominally 15.24 cm (6.0 in.) in diameter and 2.54 cm (1.0 in.) thick (80% reduction). The forged pancake was given a two-step heat treatment consisting of a direct salt quench to 816°C (1500°F) after forging, hold for 30 min, and an air cool to room temperature. The forged pancake was then aged at 649°C (1200°F) for 100 h and air cooled to room temperature. The resulting microstructure is shown in Fig. 1. The microstructure appears to consist of three phases. These phases include globular primary alpha-2 particles contained in a fine transformed matrix of orthorhombic (dark contrast) and beta (light contrast) phases. The forging and heat treatment produced an equiaxed prior beta grain structure with no preferred orientation. The prior beta grain size was approximately 1.5 mm in diameter. Specimens used in this study were electro-discharge machined (EDM) from the forged pancake with the crack growth direction perpendicular to radial lines of the pancake. Mini compact tension, C(T), specimens (B = 5 mm, W = 20 mm) were used for all fatigue crack growth tests.

Fatigue crack growth tests were conducted under either load shedding/constant load or constant K_{max} conditions using a computer-controlled servohydraulic test machine according to ASTM Test Method for Measurements of Fatigue Crack Growth Rates (E 647 88a). For the constant K_{max} tests, the fatigue crack growth rates reported in this paper were determined by fitting a linear equation to a-versus-N (crack length versus number of cycles) data after steady-state growth was established at each experimental test condition. Crack length was computed using a compliance measurement from an extensometer. This calculated crack length was periodically verified by optical measurements using a traveling microscope, and both results were within ± 0.0005 (a/w). Closure measurements were also made by compliance. Closure load levels were determined based on the first deviation from linearity in the load-versus-displacement curves. All specimens were precracked under identical conditions, and the final K_{max} from precracking was always kept lower than the initial K_{max} for starting the subsequent testing. In laboratory air, heating was done using a clamshell resistance furnace. Fatigue crack growth tests in vacuum were conducted at a vacuum level of 1.3×10^{-4} Pa (10^{-6} torr). The vacuum chamber was mounted on a computer-controlled servohydraulic test machine. A resistance furnace was used to heat the test specimen inside the vacuum chamber.

Fatigue crack growth rates from the near threshold region (less than 10^{-9} m/cycle) to rates greater than approximately 10^{-7} m/cycle were determined at room temperature, 550, and 650°C at a cyclic loading frequency of 1.0 Hz in laboratory air. A stress ratio, R, of 0.1 was used for all tests conducted in this study. These tests were conducted under decreasing ΔK

TABLE 1—*Composition of titanium aluminide.*

	Ti	Al	Nb	C	O	N
% by weight	balance	12.35	41.25	0.024	0.099	0.009
Atomic %	balance	24.40	23.66	0.107	0.330	0.034

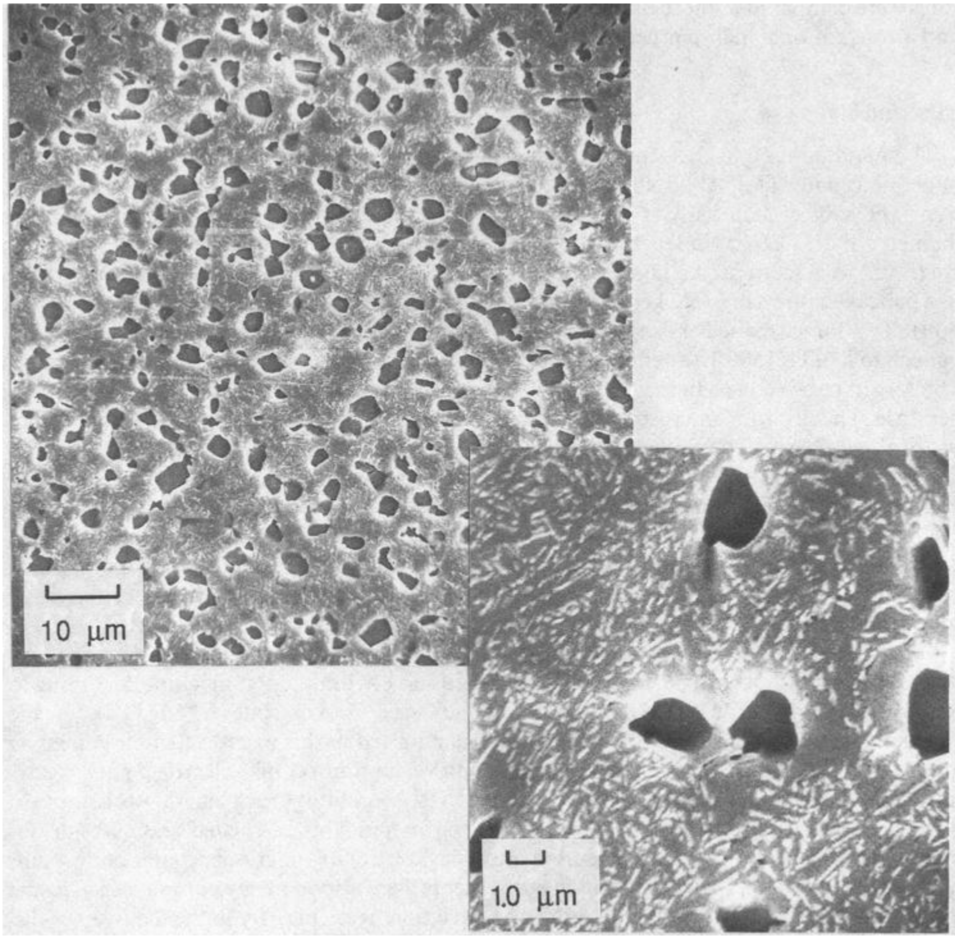

FIG. 1—*Microstructure of Ti-25Al-25Nb.*

conditions (at a load shedding rate of $c = -2$) until a threshold was established (threshold defined when crack length, plotted as a function of the number of cycles, asymptotically reached a constant value). The cracks were then grown under constant load conditions until specimen failure.

In addition, constant K_{max} fatigue crack growth rate tests were conducted at a $K_{max} = 11.1$ MPa $\sqrt{m}$ (10 ksi $\sqrt{in.}$) and a stress ratio of $R = 0.1$. These constant K_{max} tests were conducted at room temperature and at 100°C intervals from 150 to 750°C at cyclic loading frequencies of 0.01 and 1.0 Hz to determine the effects of temperature and frequency. Tests were conducted in both laboratory air and 1.3×10^{-4} Pa vacuum to investigate the effects of environment.

Testing at various frequencies and with superimposed hold times was conducted to investigate the contribution of environmentally-assisted crack growth to the overall fatigue crack growth rate. At 650 and 750°C, constant K_{max} fatigue crack growth rate tests were conducted at frequencies in the range from 0.001 to 1.0 Hz to define the regions of fully cycle-dependent and fully time-dependent crack growth. Superimposed hold times ranging from 1 to 1000 s were used to evaluate creep-fatigue-environment interactions at 650 and 750°C in laboratory air.

Results and Discussion

da/dN *versus* ΔK *Behavior*

Figure 2 shows the fatigue crack growth rate (FCGR) of Ti-25Al-25Nb at room temperature, 550, and 650°C. The *da/dN*-ΔK crack growth rate curve is very steep at room temperature, exhibiting a ΔK_{th} of approximately 5 MPa $\sqrt{m}$ and an apparent K_c (K_{max} at the point of specimen failure) of approximately 11 MPa $\sqrt{m}$. This apparent value of room-temperature K_c determined by extrapolating the crack growth rate curve is lower than the previously reported actual K_{Ic} value of 27.5 MPa $\sqrt{m}$ [*10*]. The data indicate that ΔK_{th} varies with increasing temperature from a ΔK_{th} value of approximately 5 MPa $\sqrt{m}$ at room temperature to 7 MPa $\sqrt{m}$ at 550°C and back to 5 MPa $\sqrt{m}$ at 650°C (if the data are indeed outside typical experimental scatter). Closure load levels were very low and did not vary significantly with temperature, and, therefore, it is difficult to discern to what degree closure affects the observed threshold values.

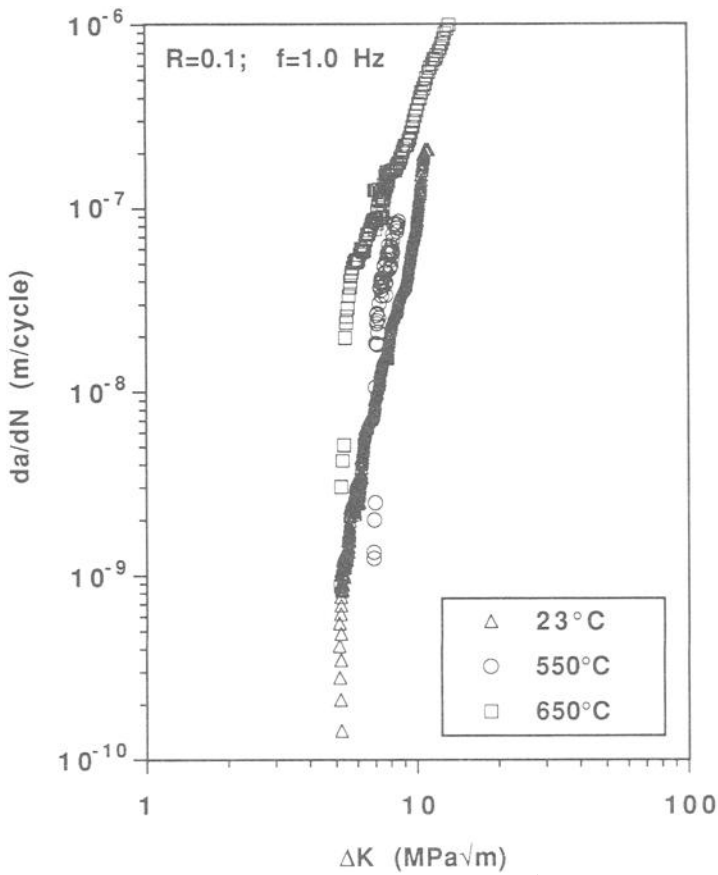

FIG. 2—*Fatigue crack growth behavior of Ti-25Al-25Nb.*

The FCGR increases with increasing temperature, and the slopes of the crack growth rate curves decrease with increasing temperature, resulting in a crossing of the curves at the higher growth rates. Changes in the slope of the curves are most likely a result of the higher ductility and toughness at elevated temperatures. At 650°C, the da/dN-ΔK crack growth rate curve exhibits a better defined inflection in the curve from the threshold region to steady-state crack growth. The data indicate a higher apparent K_c at 650°C as compared to room temperature, but extrapolation of the data to a K_c value is tenuous at best.

Figure 3 shows two distinct regions of fracture topography exhibited at room temperature. At low magnification, Fig. 3*a* shows a series of steps and ridges on the fracture surface typical of growth rates in the lower half of the FCGR curve. The large steps appear to be the result of cracking that occurs along multiple crack planes ahead of the main crack. As these multiple cracks link up with the main propagating crack, large steps form on the fracture surface. In many instances, ligaments of material linking the cracking on multiple crack planes remain intact well behind the propagating crack front. These ligaments similarly occur at elevated temperature and when viewed with the naked eye, are clearly heat tinted differently from the surrounding fracture surface. Fracture in regions of the surface between the steps, as shown at the higher magnification in Fig. 3*a*, occurs predominantly by transgranular cleavage. This transgranular fracture appears to occur in sheaths parallel to the crack growth and shows a series of much smaller ridges on the fracture surface. Fracture in these regions exhibits little ductility as evidenced by the large, flat cleavage surfaces. However, the large steps produced by the fracture of bridging ligaments joining multiple cracks are much finer in fracture detail, exhibiting a more ductile fracture on the step faces than surrounding regions. The cause of this fracture behavior is unclear at this time. No features in the bulk microstructure, such as inhomogeneity or segregation, have been identified that might account for such fracture behavior. Local chemical analyses and precision-sectioning metallography need to be conducted to further investigate this phenomenon.

Figure 3*b* shows the fracture surface typical of growth rates at room temperature in the upper half of the FCGR curve. The fracture surface is predominantly very flat, transgranular, and exhibits little ductility. In this region of crack growth, the large steps resulting from the fracture of bridging ligaments at low growth rates are not present. However, the regions of transgranular cleavage appear to fracture in sheaths parallel to the crack growth as in the low growth rate case, and the small ridges in the regions of cleavage fracture are also present. Although the relative roughness of the fracture surfaces suggest that high levels of crack closure would be present, measurements of crack closure as a function of crack length yielded very low crack closure loads under all the test conditions that were employed in this study. Similar results have been observed in Ti-24Al-11Nb by Aswath and Suresh using notched four-point flexure specimens [*12*].

Figure 4 shows the fracture surface of a specimen tested in laboratory air at 650°C. At elevated temperature, there is no distinction between the fracture in the low growth rate and high growth rate regimes. The fracture surface is flat, transgranular, and exhibits little ductility. The large steps that were present on the fracture surface at room temperature are not as prominent at elevated temperature. Features similar to the ridges observed at room temperature in the regions of transgranular cleavage are present on the fracture surfaces at elevated temperature, although they are somewhat obscured by the oxidation debris on the fracture surface. The cleavage fracture appears to be smaller in scale at elevated temperature than at room temperature and does not appear to occur in the large sheaths typical at room temperature. The faces of the shallow steps present on the fracture surface exhibit finer fracture features while typically appearing more ductile in nature.

Figure 5 compares the FCGR of Ti-25Al-25Nb to the widely studied alpha-2 titanium aluminide, Ti-24Al-11Nb, and a conventional high-temperature titanium alloy, Ti-1100 (Ti-6Al-

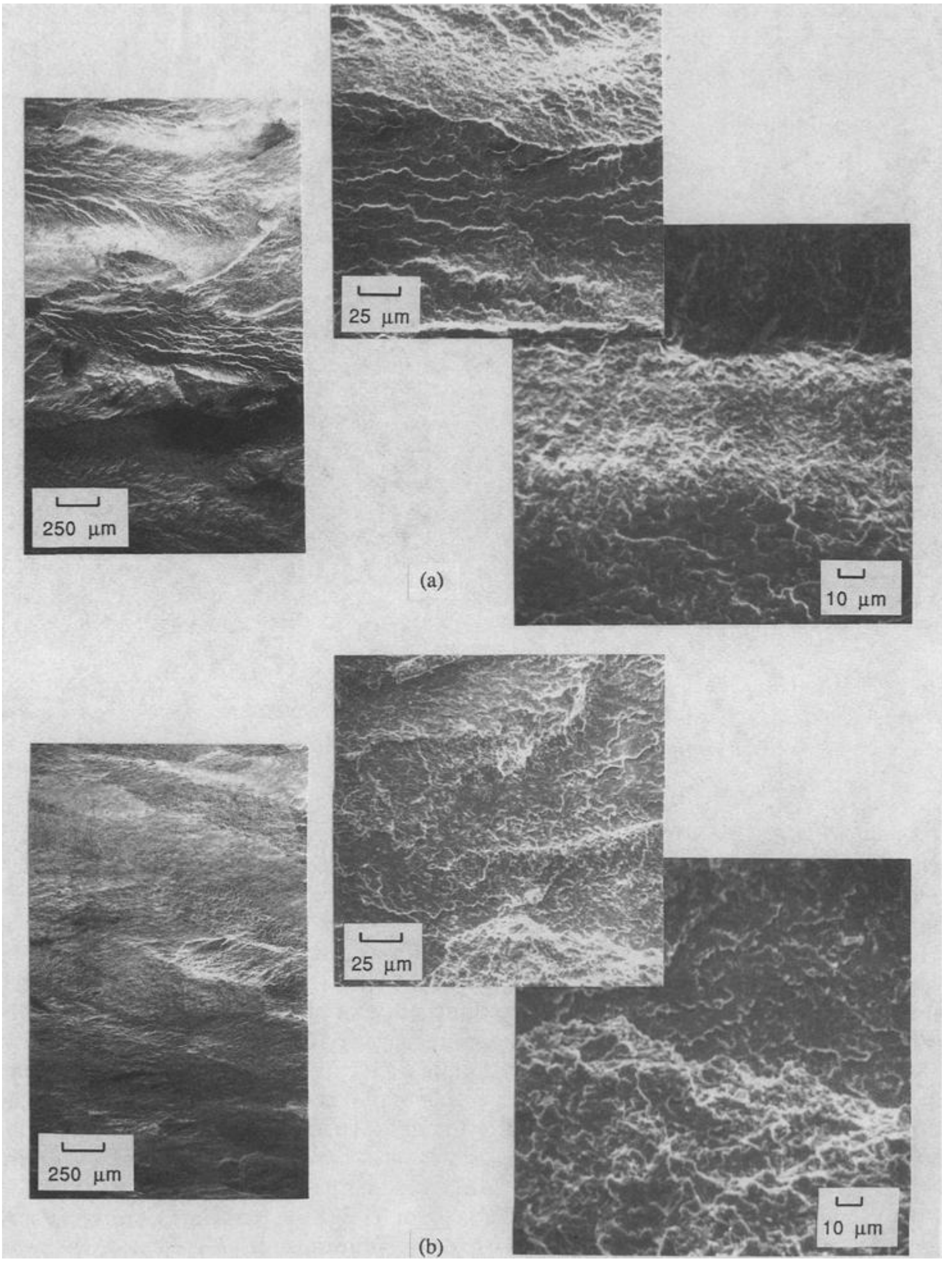

FIG. 3—*Fracture surface of specimen tested in laboratory air at room temperature:* (a) *low growth rates and* (b) *high growth rates.*

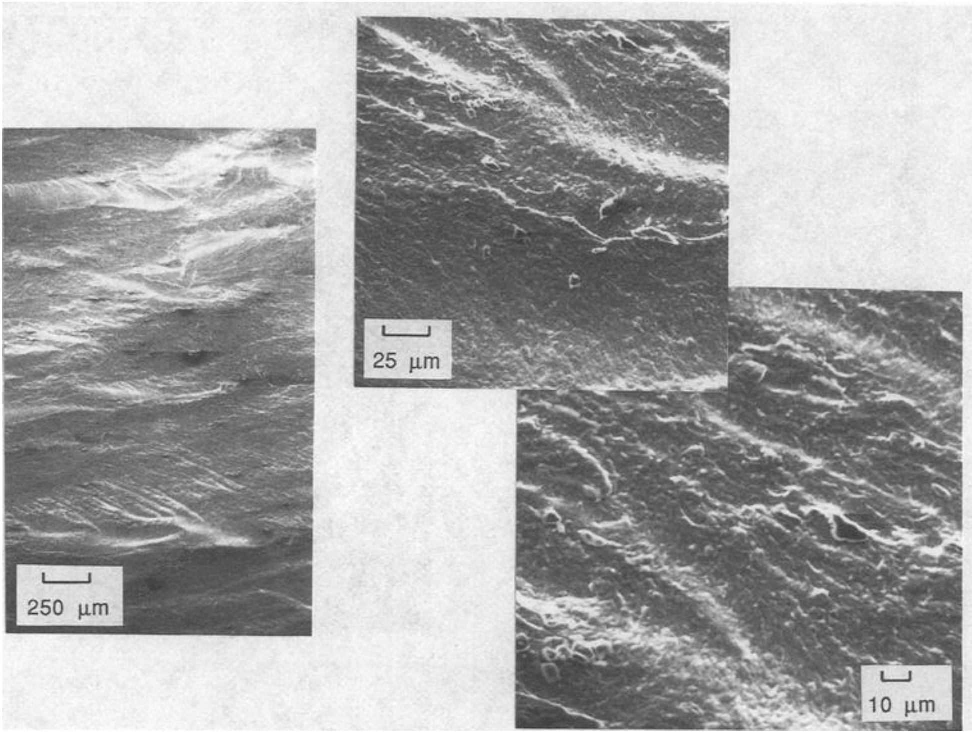

FIG. 4—*Fracture surface of specimen tested in laboratory air at 650°C.*

2.8Sn-4Zr-0.4Mo-0.45Si). The FCGR data for Ti-24Al-11Nb are from a beta heat-treated microstructure consisting of acicular alpha-2 platelets separated by thin films of beta phase in a basketweave, Widmanstätten morphology. The heat treatment included a solution at 1149°C (2100°F) for 1 h and an age at 760°C (1400°F) for 1 h [*13*]. The FCGR data for Ti-1100 are from a beta-processed microstructure that was beta forged at 1093°C (2000°F) and given a direct stabilization age at 593°C (1100°F) for 8 h [*14*]. At room temperature, the crack growth behavior of Ti-25Al-25Nb is very similar to that of Ti-24Al-11Nb. Ti-25Al-25Nb exhibits slightly higher growth rates over the entire range of ΔK presented, presumably a result of its finer microstructure. While the growth rate data tend to converge in the threshold regime, the FCGR of Ti-25Al-25Nb is significantly higher than that of Ti-1100, diverging to greater than an order of magnitude at the higher growth rates. At 650°C, the FCGR of Ti-25Al-25Nb is lower than that of Ti-24Al-11Nb. At high growth rates, the data are comparable but diverge as threshold is approached. The apparent ΔK_{th} value for Ti-25Al-25Nb is approximately 5 MPa $\sqrt{m}$ as compared to a value of 3 MPa $\sqrt{m}$ for Ti-24Al-11Nb. The FCGR of Ti-25Al-25Nb at 650°C is higher than that of Ti-1100 over the entire range of ΔK presented. The apparent ΔK_{th} value for Ti-1100 is approximately 7 MPa $\sqrt{m}$.

Effect of Temperature

Figure 6 shows the FCGR of Ti-25Al-25Nb as a function of temperature from 25 to 750°C in laboratory air at a K_{max} = 11.1 MPa $\sqrt{m}$ (10 ksi $\sqrt{in.}$). The FCGR at room temperature is relatively high and is almost equal to that observed at 650°C. Note also that the *da/dN*-ΔK

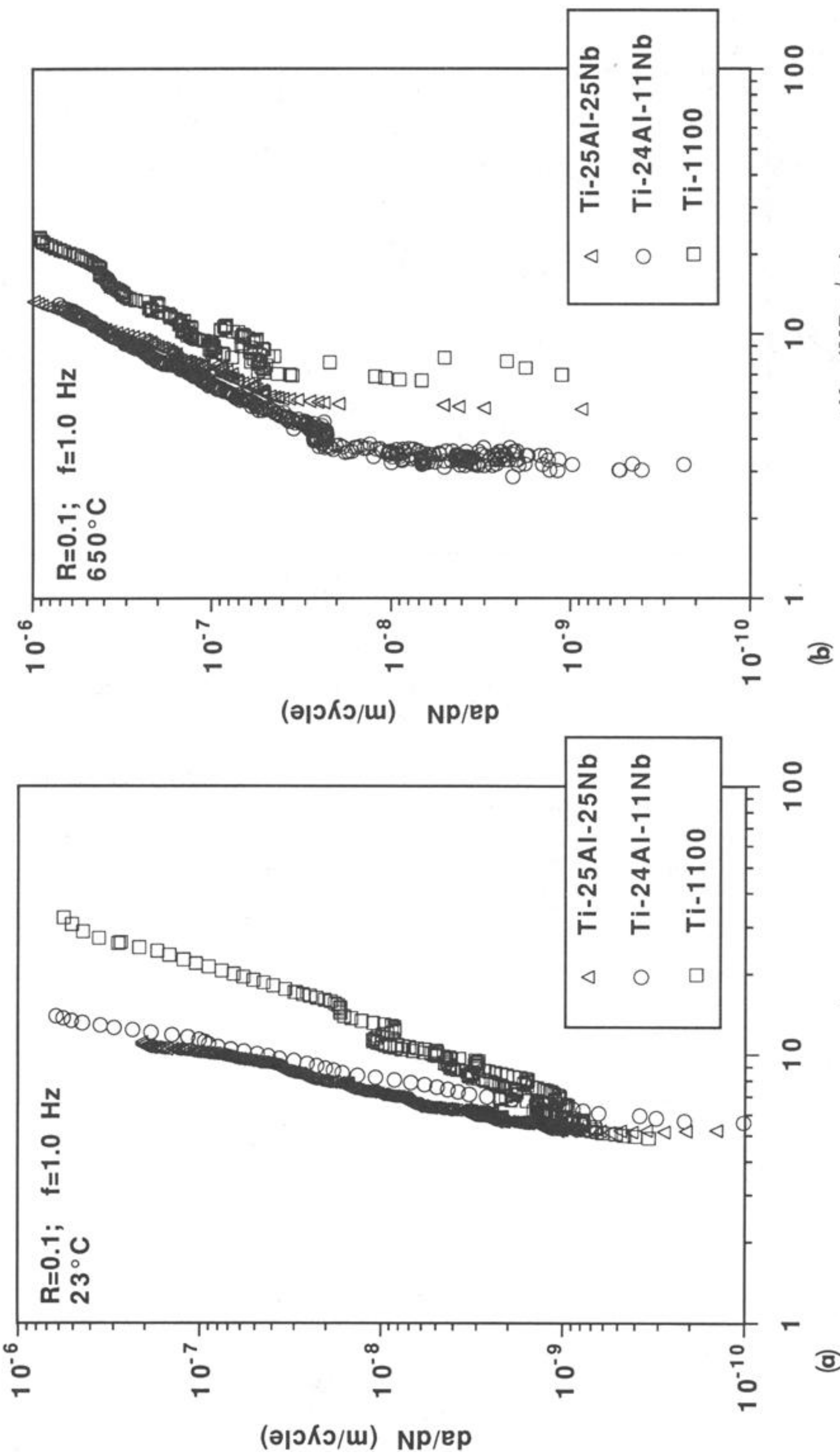

FIG. 5—*Comparison of fatigue crack growth behavior at* (a) *room temperature and* (b) *650°C.*

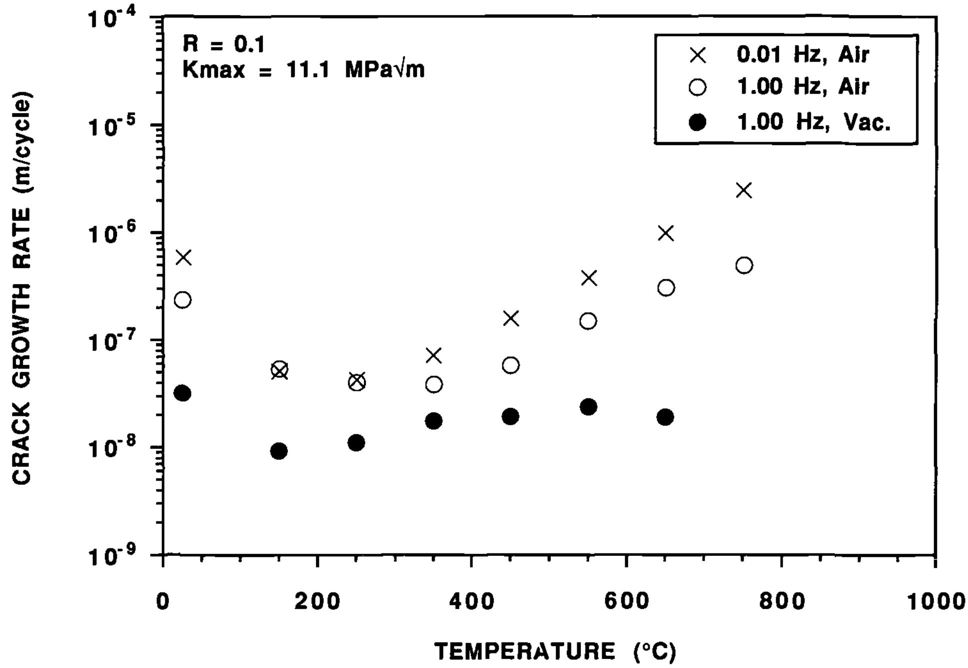

FIG. 6—*Effect of temperature on the fatigue crack growth rate of Ti-25Al-25Nb.*

crack growth rate curve is very steep at room temperature (Fig. 2). As temperature increases, the FCGR decreases until a minimum is reached at approximately 250 to 350°C depending on the test frequency. This minimum in FCGR at intermediate temperatures is consistent with the slightly higher ΔK_{th} at 550°C suggested by the *da/dN*-ΔK crack growth data shown in Fig. 2, although a direct correlation would not necessarily have to be true. Further increases in temperature result in increased growth rates as shown in Fig. 6. The initial decrease in FCGR from room temperature to 250 to 350°C is attributed to a gradual increase in the ductility and toughness of the Ti-25Al-25Nb with temperature or to the elimination of a moist environment at the crack tip or both (see discussion in the following paragraph). Further increase in temperature from 250 to 350°C results in an increase in growth rate that can be attributed to a gradual decrease in material strength with temperature, coupled with an increase in environmentally-assisted crack growth. Because closure load levels were very low and did not change significantly with increasing temperature, the effect of crack closure on the trends in crack growth rate as a function of temperature remains undetermined. Similar crack growth behavior with temperature has been reported for Ti-24Al-11Nb [*13*].

Effect of Frequency

Figure 6 shows that at 150 and 250°C, there is essentially no effect of frequency from 0.01 to 1.0 Hz on growth rates obtained in laboratory air. However, at room temperature there does appear to be a frequency effect, that is, higher FCGR at lower frequency. This finding is consistent with that of Aswath and Suresh who reported that for Ti-24Al-11Nb, a decrease in frequency from 20.0 to 1.0 Hz led to an order of magnitude increase in the FCGR at room temperature over the range of ΔK values from 5 to 20 MPa $\sqrt{m}$ [*12*]. They hypothesize that the acceleration in FCGR due to the reduction in test frequency could be attributed to a deleterious environmental attack from a moist environment in the highly stressed region of the crack tip. It would then follow that at 150 and 250°C, the heating of the test specimen may result in the evaporation of moisture from the crack tip, thus reducing the effect of frequency. At temperatures greater than 250°C, growth rates tend to diverge, and this results in as much as a factor of 5 increase in growth rate at 0.01 Hz than at 1.0 Hz. Therefore, at temperatures greater than 250°C, crack growth per cycle increases with decreasing test frequency, suggesting a contribution from environmentally-assisted crack growth to the overall FCGR. At lower test frequencies, the crack tip is exposed for longer times under load to the degrading effects of the environment.

Figure 7 shows FCGR as a function of frequency at 650 and 750°C. The data clearly show that the crack growth per cycle increases as the frequency decreases over the range from 1.0 to 0.001 Hz. As shown in Fig. 8, Weerasooriya defined three regions of fatigue crack growth in nickel-base superalloys, that is, (*a*) at low frequencies, fully time-dependent crack growth; (*b*) at high frequencies, fully cycle-dependent crack growth; and (*c*) a region of intermediate frequency exhibiting a mix of both time- and cycle-dependent behavior [*15*]. If FCGR is plotted versus frequency as shown schematically in Fig. 8, the corresponding slopes would range from -1 to 0 on a log-log plot. When the data for Ti-25Al-25Nb, as shown in Fig. 7, are approximated by a straight line, the slope of the least squares regression is -0.34 indicating that the fatigue crack growth is in the region of mixed time- and cycle-dependent behavior. For Ti-25Al-25Nb at a frequency of 1.0 Hz, Fig. 7 shows that the FCGR is not yet fully cycle dependent. One would expect as test frequency is increased, the FCGR would eventually reach a constant value indicating fully cycle-dependent crack growth. Under the conditions used in this study, fully cycle-dependent crack growth occurs at frequencies greater than 1.0 Hz. Con-

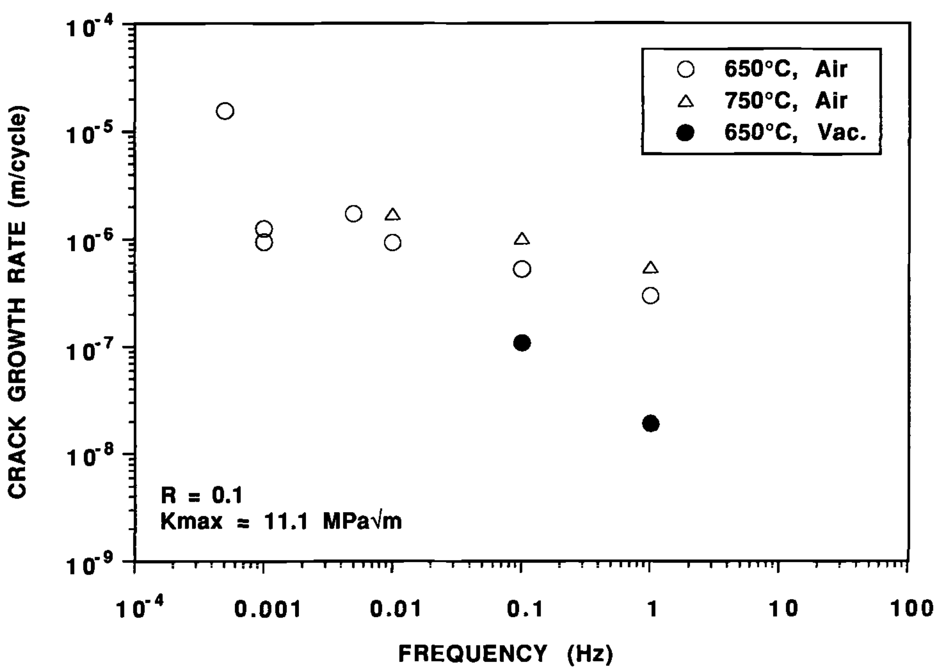

FIG. 7—*Effect of cyclic frequency on the fatigue crack growth rate of Ti-25Al-25Nb.*

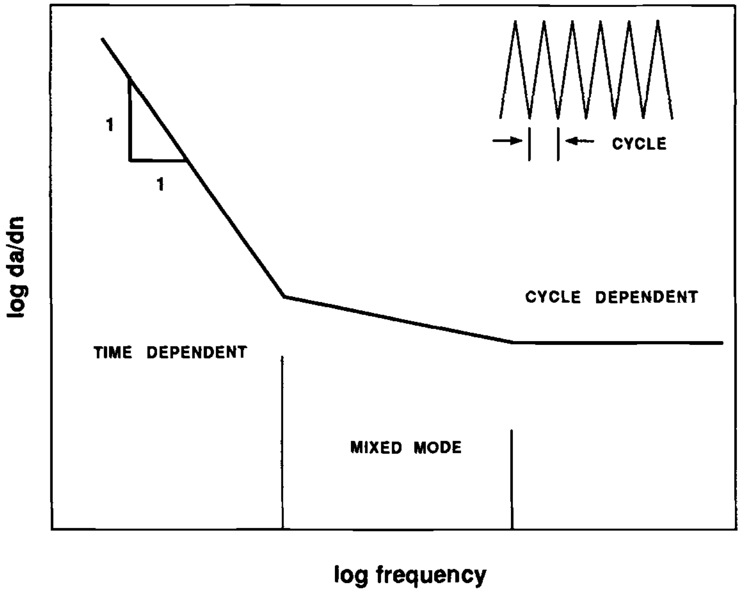

FIG. 8—*Schematic showing three regions of fatigue crack growth as a function of frequency.*

versely, at frequencies as low as 0.001 Hz, the data show that the fatigue crack growth had not yet reached a fully time-dependent condition. It is clear that over the frequency range of 0.001 to 1.0 Hz, Ti-25Al-25Nb exhibits a mixed mechanism of both time-dependent and cycle-dependent crack growth at 650 and 750°C. Note that a data point at 0.001 Hz and 750°C is not included in the plot of Fig. 7. Crack growth at these conditions was arrested due to creep deformation at the crack tip and subsequent crack-tip blunting. However, at frequencies higher than 0.001 Hz at 750°C, stable crack growth was achievable due to cyclic resharpening of the crack tip. Note also that additional tests are needed at the lower frequencies at 650°C to reduce the apparent scatter in the data at these test conditions.

Fractographic analyses of the fracture surfaces at 650 and 750°C showed remarkably similar features at all the frequencies examined and revealed no significant changes in fracture mechanisms as a function of frequency. As shown in Fig. 4, fracture at elevated temperatures occurs by transgranular cleavage. The fracture surface exhibits little evidence of ductility. As a result, there are no clear effects of frequency on the fracture mechanisms over the range of frequencies examined in this study.

Effect of Environment

As shown in Fig. 6, vacuum test results for Ti-25Al-25Nb show a trend in growth rate with temperature similar to that obtained in laboratory air, but at significantly lower growth rates over the entire temperature range 25 to 750°C. Testing in a vacuum environment apparently reduces the contribution of environmentally assisted crack growth to the overall FCGR. One might have expected that as temperature decreases, the data for FCGR in laboratory air and vacuum would converge at the lower temperatures approaching room temperature. While environmental contributions to crack growth can occur at room temperature, greater differences would be expected at elevated temperatures where interactions occur at greater rates. However, Fig. 6 clearly shows that the data do not converge at the lower temperatures. Similar results have been observed in Ti-24Al-11Nb tested in vacuum and under controlled humidity conditions [*13*]. FCGR at room temperature under these conditions increases with increasing humidity levels and is an order of magnitude higher in laboratory air with 55% relative humidity than in a vacuum environment. The lower FCGR at room temperature in a vacuum environment suggests that the Ti-25Al-25Nb alloy is also sensitive to the moisture content of the environment. This is consistent with the frequency effect on FCGR at room temperature in laboratory air as shown in Fig. 6 and discussed earlier. This is most probably a result of hydrogen interaction with the material in a moist environment at the highly stressed region of the crack tip under fatigue loading.

Figure 7 shows FCGR of Ti-25Al-25Nb as a function of frequency in laboratory air and a vacuum environment at 650°C. The growth rates obtained in vacuum at 0.1 and 1.0 Hz are significantly lower than corresponding rates obtained in laboratory air. However, the dependence of FCGR on test frequency is still present in the vacuum environment. If the frequency dependence is a result of a contribution from environmentally-assisted crack growth to the overall FCGR, then no frequency effect would be expected in vacuum testing where the deleterious effect of the environment is presumably removed. As shown in Fig. 7, this is clearly not the case. The FCGR of the Ti-25Al-25Nb alloy appears to be sensitive to environment even at the 1.3×10^{-4} Pa vacuum level. At a vacuum of this level, either the partial pressure of the aggressive species remains great enough to cause degradation at the crack tip, or there exists a strain rate effect on crack growth where at higher strain rates, that is, higher frequencies, the FCGR is lower (yield strength is higher). Further investigation of these effects is needed.

Figure 9 compares the fracture surfaces of specimens tested at 650°C in laboratory air and vacuum. The fracture surface of the specimen tested in vacuum does not show the large, flat regions of transgranular cleavage exhibited by fracture in laboratory air. The fracture surface in vacuum reveals a slightly higher degree of ductility, and the scale of the fracture features is on the order of the primary alpha-2 particle size and distribution in the microstructure. The fracture in vacuum does not occur in the large sheaths as demonstrated in laboratory air but appears to occur by a more ductile failure of the O + B2 matrix around the primary alpha-2 particles. Clearly, environment plays an important role in the fracture by transgranular cleavage in laboratory air.

Effect of Hold Time at Elevated Temperatures

Figure 10 shows the influence of superimposed hold times at maximum load on the cyclic crack growth rate (1.0 Hz) at 650 and 750°C. Growth rate is plotted as a function of total cycle time, that is, the 1.0 Hz cycle (1 s) plus the hold time at maximum load. Therefore, the data plotted at a total cycle time of 1 s are the results with no applied hold time. At 650°C, hold times ranging from 1 to 1000 s are shown to first decrease and then increase the growth rate per cycle with increasing hold times. At small hold times, crack-tip blunting occurs, and the growth rate per cycle decreases. At larger hold times, crack-tip blunting still occurs. However, the crack tip is now held open to the environment for a longer time that degrades the material ahead of the crack tip resulting in higher growth rates upon subsequent cycling (a resharpening of the crack tip). No sustained-load creep crack growth during the hold times was observed. The increase in FCGR as a result of the larger hold times is greater in the Ti-25Al-25Nb alloy than that reported for Ti-24Al-11Nb at the same test conditions [*13*]. The smaller increase in FCGR of Ti-24Al-11Nb is due to its poorer creep resistance resulting in greater crack-tip blunting during hold times at elevated temperature. In addition, Nicholas and Mall showed a decrease in growth rate in Ti-24Al-11Nb by a factor of 3 when a 48-s hold time is superimposed on a 0.01 Hz cycle and attribute the effect to creep blunting at the crack tip [*16*].

At 750°C, the same trend of a decrease and then an increase in FCGR of Ti-25Al-25Nb with

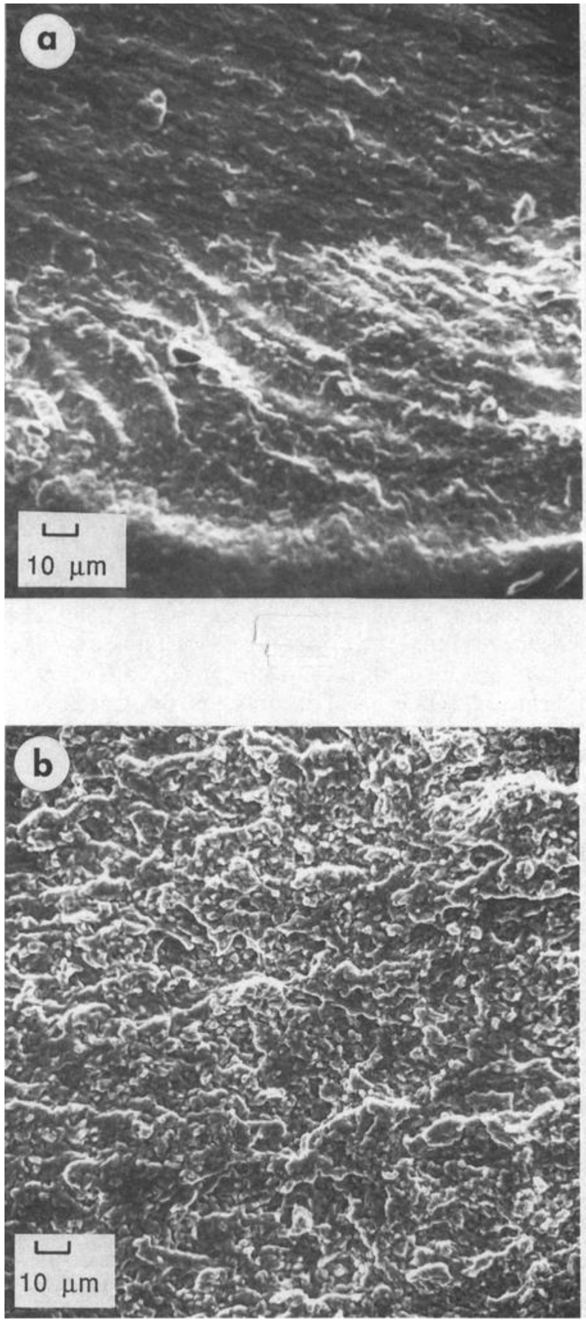

FIG. 9—*Fracture surface of specimens tested at 650°C in* (a) *laboratory air and* (b) *vacuum.*

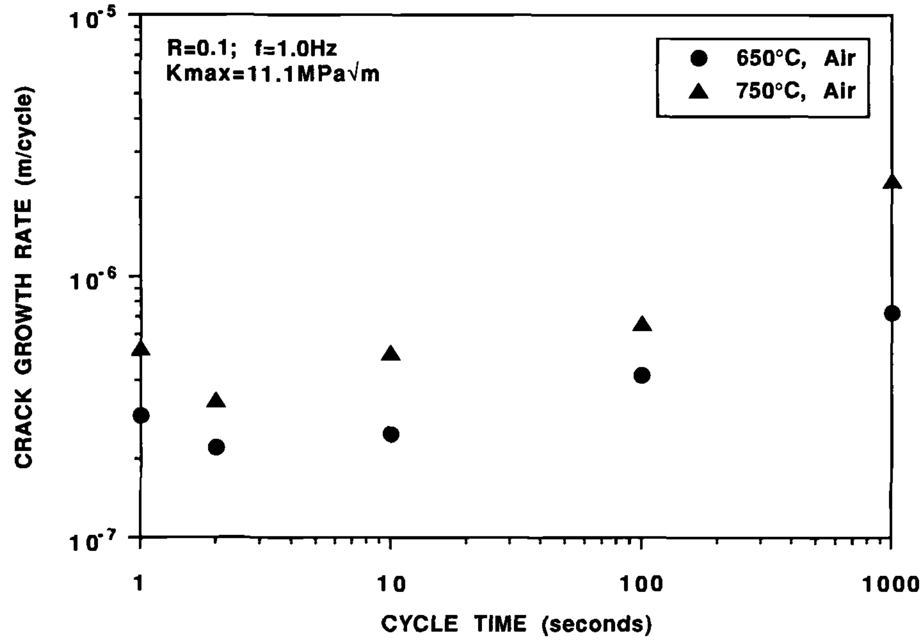

FIG. 10—*Effect of hold time on the fatigue crack growth rate of Ti-25Al-25Nb.*

increasing hold times was observed. Experiments by Mall et al. on Ti-24Al-11Nb involving the addition of hold times to a 0.1 Hz, R = 0.3, cycle showed similar trends at 750°C [*17*]. In these tests, the addition of 30- and 120-s hold times resulted in a doubling of the cyclic growth rate while hold times of 300 and 600 s tripled the rate. However, an analysis of those data showed that the increase in growth rate in Ti-24Al-11Nb due to the addition of a hold time was less than predicted from a linear summation model based on cyclic- and sustained-load data. Therefore, at both 650 and 750°C, it appears that the growth rate under fatigue cycles with superimposed hold times results from a combination of competing phenomena involving both environmental and creep effects. Blunting of the crack tip due to creep during the hold at maximum load results in a decrease in subsequent crack growth rates, while environmental degradation ahead of the crack tip during the hold time accelerates the crack growth during subsequent fatigue cycling. No sustained-load creep crack growth data for Ti-25Al-25Nb has been generated. Therefore, a prediction of the FCGR under fatigue cycles with superimposed hold times resulting from a linear summation model (based on cyclic- and sustained-load data) cannot be made at this time. However, Ti-25Al-25Nb appears to behave in an analogous manner to Ti-24Al-11Nb [*13*].

Summary and Concluding Remarks

The results of this study show that environment plays an important role in the fatigue crack growth of the orthorhombic + B2 titanium aluminide Ti-25Al-25Nb. The data support the notion that laboratory air (oxygen, nitrogen, and hydrogen in moist air) degrades the material in the highly stressed region ahead of propagating fatigue crack resulting in greater crack advance per cycle. The contribution from environmentally-assisted crack growth to the overall fatigue crack growth is significant in the titanium aluminide materials and can result in much higher fatigue crack growth rates. At elevated temperatures, crack growth behavior appears to be a complex interaction of environmental degradation at the crack tip, crack-tip blunting due to creep that simultaneously tends to retard the growth rate, and cyclic fatigue (resharpening of the crack tip). Specific findings in this study include:

(*a*) The fatigue crack growth rate of Ti-25Al-25Nb exhibits a combination of cyclic- and time-dependent behavior.
(*b*) The fatigue crack growth rates of Ti-25Al-25Nb determined at a constant K_{max} of 11.1 MPa $\sqrt{m}$ as a function of temperature show a minimum in growth rate at approximately 250 to 350°C.
(*c*) A frequency effect on FCGR is observed at temperatures greater than approximately 250°C. At 650 and 750°C, crack growth per cycle is found to increase with decreasing frequency, suggesting a contribution from environmentally assisted crack growth. The effect of frequency at elevated temperature in a vacuum environment is similar to that observed in laboratory air, but the growth rates are lower than those obtained in laboratory air. In addition, there appears to be a frequency effect on FCGR at room temperature. Vacuum testing shows growth rates to be sensitive to environment over the entire temperature range from room temperature to 750°C.
(*d*) Hold times of increasing duration are found to decrease and then increase the cyclic crack growth rate of Ti-25Al-25Nb. During small hold times, crack-tip blunting occurs, and the subsequent growth rate per cycle decreases. During large hold times, the crack tip is held open to the environment for a longer period. This appears to degrade the material ahead of the crack tip, resulting in higher growth rates upon subsequent cycling (a resharpening of the crack tip).
(*e*) For the microstructural conditions examined in this study, the fatigue crack growth rate of Ti-25Al-25Nb is slightly higher than that of Ti-24Al-11Nb at room temperature but slightly lower than that of Ti-24Al-11Nb at 650°C. The fatigue crack growth rate of Ti-25Al-25Nb is significantly higher than that of the conventional high-temperature titanium alloy, Ti-1100, at both room temperature and 650°C.

Acknowledgment

This work was supported by the U.S. Air Force under in-house Project 2302P1 and the Wright Laboratory, Materials Directorate.

References

[*1*] Sprague, R. A., "Future Aerospace-Materials Directions," *Advanced Materials and Processes*, Vol. 133, No. 1, 1988, pp. 67–69.
[*2*] Ronald, T. M. F., "Advanced Materials to Fly High in NASP," *Advanced Materials and Processes*, Vol. 29, No. 37, 1989.
[*3*] Blackburn, M. J. and Smith, M. P., "Research to Conduct an Exploratory Experimental and Analytical Investigation of Alloys," AFML-TR-78-18, Air Force Materials Laboratory, Wright-Patterson AFB, OH, March 1978.
[*4*] DeLuca, D. P. et al., "Fatigue and Fracture of Titanium Aluminides," WRDC-TR-89-4136, Wright Research and Development Center, Wright-Patterson AFB, OH, Feb. 1990.
[*5*] Gambone, M. L., "Fatigue and Fracture of Titanium Aluminides," WRDC-TR-89-4145, Vol. II, Wright-Patterson Research and Development Center, Wright-Patterson AFB, OH, Feb. 1990.
[*6*] Blackburn, M. J. and Smith, M. P., "Improved Toughness Alloys Based on Titanium Aluminides," WRDC-TR-89-4095, Wright Research and Development Center, Wright-Patterson AFB, OH, Oct. 1989.

[7] Marquardt, B. J. et al., "Research and Development for Improved Toughness Aluminides," WRDC-TR-89-4133, Wright Research and Development Center, Wright-Patterson AFB, OH, June 1990.

[8] Chesnutt, J. C. et al., "Very High Temperature Titanium Base Materials," Interim Report No. 8, Contract F33615-86-C-5073, GE Aircraft Engines, General Electric, Evansdale, OH, Sept. 1990.

[9] Banerjee, D. et al., "A New Ordered Orthorhombic Phase in a Ti_3Al-Nb Alloy," *Acta Metallurgica*, Vol. 36, 1988, pp. 871–882.

[10] Rowe, R. G., "The Mechanical Properties of Titanium Aluminides Near Ti-25Al-25Nb," *Microstructure/Property Relationships in Titanium Aluminides and Alloys*, Y.-W. Kim, J. A. Hall, and R. R. Boyer, Eds., The Minerals, Metals, and Materials Society, Warrendale, PA, 1991, pp. 387–398.

[11] Smith, P. R. et al., "Interfacial Evaluation in a Ti-25Al-17Nb/SCS-6 Composite," *Interfaces in Metal-Ceramics Composites*, R. Y. Lin, R. J. Arsenault, G. P. Martins, and S. G. Fishman, Eds., The Minerals, Metals, and Materials Society, Warrendale, PA, 1990.

[12] Aswath, P. B. and Suresh, S., "Microstructural Effects on Ambient and Elevated Temperature Fatigue Crack Growth in Titanium Aluminide Intermetallics," *Metallurgical Transactions*, Vol. 22A, 1991, pp. 817–828.

[13] Balsone, S. J. et al., "Environment and Frequency Effects on Crack Growth in a Titanium Aluminide Alloy," *Elevated Temperature Crack Growth*, S. Mall and T. Nicholas, Eds., MD-Vol. 18, American Society of Mechanical Engineers, New York, 1990, pp. 87–91.

[14] Zawada, L. P., unpublished research.

[15] Weerasooriya, T., "Effect of Frequency on Fatigue Crack Growth Rate of Inconel 718 at High Temperature," *Fracture Mechanics: Nineteenth Symposium, ASTM STP 969*, T. A. Cruse, Ed., American Society for Testing and Materials, Philadelphia, 1988, pp. 907–923.

[16] Nicholas, T. and Mall, S., "Thermo-Mechanical Fatigue Crack Growth in Aircraft Engine Materials," *FATIGUE 90*, Vol. III, H. Kitagawa and T. Tanaka, Eds., Materials and Component Engineering Publications Ltd., Birmingham, UK, 1990, pp. 1905–1910.

[17] Mall, S., Staubs, E. A., and Nicholas, T., "Investigation of Creep/Fatigue Interaction on Crack Growth in a Titanium Aluminide Alloy," *ASME Journal of Engineering Materials and Technology*, Vol. 112, 1990, pp. 435–441.

Ralph W. Bush,[1] *Robert J. Bucci,*[1] *Paul E. Magnusen,*[1] *and G. William Kuhlman*[2]

Fatigue Crack Growth Rate Measurements in Aluminum Alloy Forgings: Effects of Residual Stress and Grain Flow

REFERENCE: Bush, R. W., Bucci, R. J., Magnusen, P. E., and Kuhlman, G. W., "**Fatigue Crack Growth Rate Measurements in Aluminum Alloy Forgings: Effects of Residual Stress and Grain Flow,**" *Fracture Mechanics: Twenty-Third Symposium, ASTM STP 1189,* Ravinder Chona, Ed., American Society for Testing and Materials, Philadelphia, 1993, pp. 568–589.

ABSTRACT: An investigation to determine the causes of increased variability in fatigue crack growth (FCG) rate measurement in aerospace aluminum forgings compared to that observed in aluminum flat rolled plate was conducted. Fatigue cracks were grown at constant applied ΔK, consistent with ASTM Test Method for Measurements of Fatigue Crack Growth Rates (E 647-88a), through regions of rapidly changing grain-flow direction within thin 7075-T73 precision forgings and large closed-die 7050-T74 forgings. The local grain flow in each specimen was correlated subsequently with measured crack growth rates so that the contribution of grain-flow variability to the scatter in measured crack growth rates could be determined. These results were found to be comparable to FCG results from 7075-T7351 and 7050-T7451 plate, once residual stress biases were removed by means of closure measurement. Hence, it is concluded that the effects of microstructural features such as grain flow on FCG rate are minimal, and the inherent FCG resistances of aerospace aluminum forgings and plate are comparable. Consequently, the analytical fracture mechanics framework applicable to damage tolerance verification of plate product should extend equally to forging product forms. However, the results indicate that failure to account for residual stress effects in interpretation of forging test results can lead to erroneous conclusions about the material performance.

KEY WORDS: fatigue crack growth, forgings, flat-rolled plate, residual stress, grain flow, damage tolerance, fracture mechanics, fatigue (materials)

Qualification of damage-tolerant critical airframe components requires crack growth analysis. The fracture mechanics tools employed for this purpose have been developed largely for plate, while experience in forgings is more limited. Since plate prototype parts involve shorter lead time and are more cost efficient to initiate than forging prototype parts, initial component testing and damage-tolerant qualification are usually done on parts machined from plate. In certain cases, it may be attractive to consider a forging as an alternative to a part machined from plate, provided that the cost and time required for the forging qualification be relieved with the help of analytical tools largely proven on plate.

One barrier to the qualification of forged parts using plate testing is that data in the literature indicates that variability in fatigue crack growth (FCG) measurements of thick aluminum

[1] Senior engineer, technical consultant, and staff engineer, respectively, Aluminum Company of America, Alcoa Technical Center, Alcoa Center, PA 15069.

[2] Manager of Research and Advanced Technology-Forgings, Alcoa Forging Division, Cleveland, OH 44105.

aerospace forgings is greater than that observed in thick aluminum plate [1–3]. This increased variability has been attributed to large thickness variations within a given forging, variations in process history, unrelieved residual stresses in forgings and the complex and variable nature of the grain flow of forged products. However, there have been no systematic studies that quantify the relative contributions of these factors to the observed variability.

Three of the four potential causes of variability in FCG measurements just mentioned alter the intrinsic properties of the material via changes in microstructure. The single exception is unrelieved residual stresses, whose magnitude and orientation within a forging are extrinsic to the material. Their presence in FCG test specimens results in a significant internal stress system that alters the local crack driving force (ΔK).

Because of the difference in the intrinsic and extrinsic natures of the potential sources of scatter in aluminum forging FCG data, it is important to understand the relative contributions of each factor to the scatter. This is particularly important for fracture critical airframe applications.

The objectives of this paper are threefold. First, it seeks to determine the contributions of grain flow and residual stress to excessive FCG rate variability often encountered in thick aluminum aerospace forgings. Second, it seeks to comment on problems associated with FCG rate measurement in forgings and to suggest methods to generate valid data representative of the material. Lastly, it will briefly comment on the applicability of using plate data for damage tolerance qualification of forged parts.

Background

One can imagine several scenarios by which variable grain flow might introduce scatter into FCG measurement. Among these scenarios would be the grain flow changing direction within a single FCG specimen. Another example might involve removing FCG specimens from the same location within several nominally identical forgings, which in reality do not have identical grain-flow patterns. In both cases, the scatter results from assuming an incorrect specimen orientation with respect to the grain flow. A change in grain-flow orientation in a forging is nominally equivalent to changing the fracture specimen orientation in plate. It has been documented that fracture toughness and fatigue crack growth rates differ with specimen orientation (that is, L-T versus S-L) in plate products [4]. Thus, an estimate of the scatter introduced by uncertainty in grain-flow orientation can be obtained from plate specimens tested in a variety of orientations.

The effects of residual stresses on experimental FCG rate measurement and analytical life prediction for welded structures are well known [5]. However, it is not as widely appreciated that residual stresses due to nonuniform cooling during rapid quenching of thick aerospace forgings may also play a significant role in the FCG behavior of parts fabricated from forgings. Mechanical stress relief by stretching as done for flat rolled plate is not practical for forgings. Hand forgings are stress relieved by compression, which is less effective than stretching, and die forgings generally can not be effectively stress relieved due to their complex shapes. Consequently, forgings possess internal residual stress variations that often exceed those of plate.

Bucci has discussed the distribution of residual stresses produced during quenching and the effects that these residual stresses have on FCG measurements [6]. A short summary of his findings follows. Because the last portion of a part to cool is generally left in residual tension, it follows that the outer surfaces of quenched aluminum products are left in residual compression while the interiors are in residual tension. In nonstress-relieved product forms, the residual stresses can create problems during testing. Residual stress patterns in isolated coupons may show little resemblance to those of the original parent metal. Through-thickness residual stress variations in specimens can cause excessive crack front curvature rendering the test invalid. Residual stresses parallel to the crack plane in compact tension (CT) specimens create clamping or opening moments about the crack starter notch that can retard or accelerate crack growth respectively depending on the position of the specimen within the original piece. During testing, the residual stresses are relieved as the crack grows and their effects on the FCG measurements are reduced as the test progresses. Therefore, crack growth rates measured at short crack lengths and low applied loadings are most adversely affected. The presence of these in-plane residual stresses can be detected by measuring relative displacement across the crack starter notch before and after machining of the notch. Yet another indication of a residual stress bias is a combination of falling closure loads as the test progresses and excessive scatter in duplicate specimens. Finally, the residual stress bias can be removed by measuring crack closure and plotting crack growth rate as a function of effective ΔK.

In addition to the question of the relative significance that each factor contributes to variability in forging FCG measurements, there is the question of how to properly characterize forging FCG behavior, given the complications mentioned earlier. Experimental measurement of FCG behavior in stress-relieved plate, using ASTM Test Method for Measurements of Fatigue Crack Growth Rates (E 647-88a), is relatively straightforward due to well-defined grain flow and relief of residual stresses during the stretching operation. However, while the test method used to measure FCG performance of material from forged products is identical to that employed for plate, sufficient care must be given to specimen placement and design to avoid generation of spurious results. The effects of complex grain flow may be circumvented by removing test coupons from areas with well-behaved grain flow. Through-thickness residual stresses can be minimized by selecting the thickness-to-width ratio of the specimen to be small. Effects of in plane residual stresses acting parallel to the crack growth direction can be minimized by selection of a symmetrical specimen configuration such as the M(T). In some cases where the region of interest does not allow the utilization of one or more of the preceding precautionary measures, it is prudent to check for the effects of grain flow and residual stresses to verify that the data accurately characterize the material FCG performance.

The following investigation documents the relative effects of grain flow direction and residual stresses on experimentally measured FCG rates using CT specimens excised from 7075-T73 thin precision forgings and 7050-T74XX hand and die forgings. These results are then compared to FCG results from stress-relieved 7075-T7351 and 7050-T7451 plate to determine whether the observed differences in FCG results are due to intrinsic material variability, extrinsic residual stress effects, or a mixture of both.

Testing Approach

Thin 7075-T73 Precision Forgings

The thin 7075-T73 precision forging used for this study is illustrated in Fig. 1. Quenching residual stresses in this part were expected to be minimal, providing an opportunity to measure FCG rates in a situation where the influence of residual stress in a forging was minor. The area immediately adjacent to and beneath the ribs of the forging provides a small region of rapid grain-flow direction change that was utilized to quantify effects of grain flow direction on FCG rates. This is illustrated schematically in Fig. 2, which shows the specimen locations with respect to the ribs and the principal grain-flow direction in the starting stock. All specimens were full-thickness CT specimens. The T-L and L-T specimens were taken from open web areas that contained well-defined and constant grain-flow direction. The S-L and S-T orientations were approximated by removing specimens from beneath the ribs. Mixed grain-flow-direction specimens spanned the ribs. Cracks were grown normal to the ribs such that the crack grew initially in either an L-T or T-L orientation, propagated through a region of rapidly changing grain flow and then back through the original orientation.

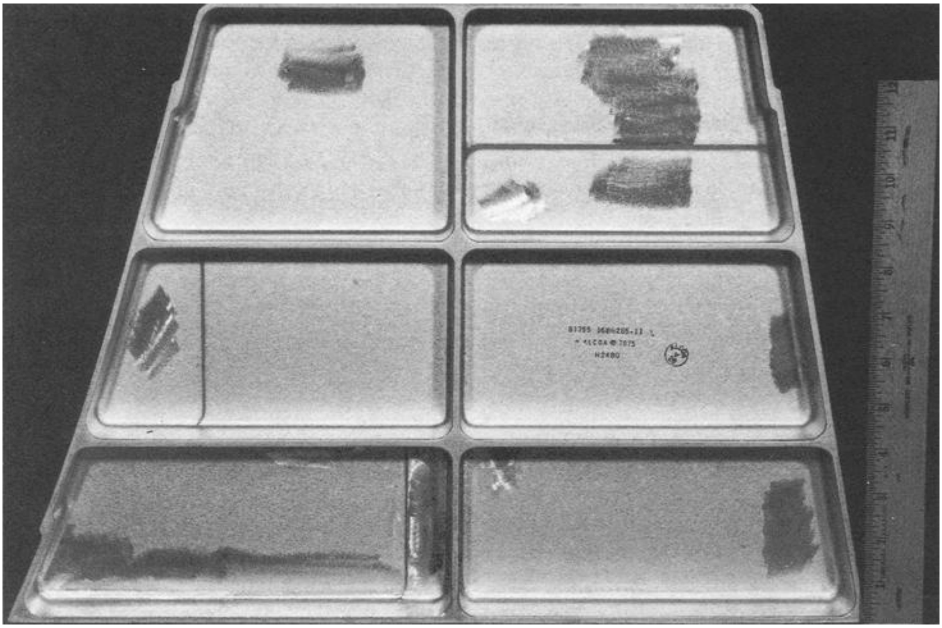

FIG. 1—*7075-T73 precision die forging.*

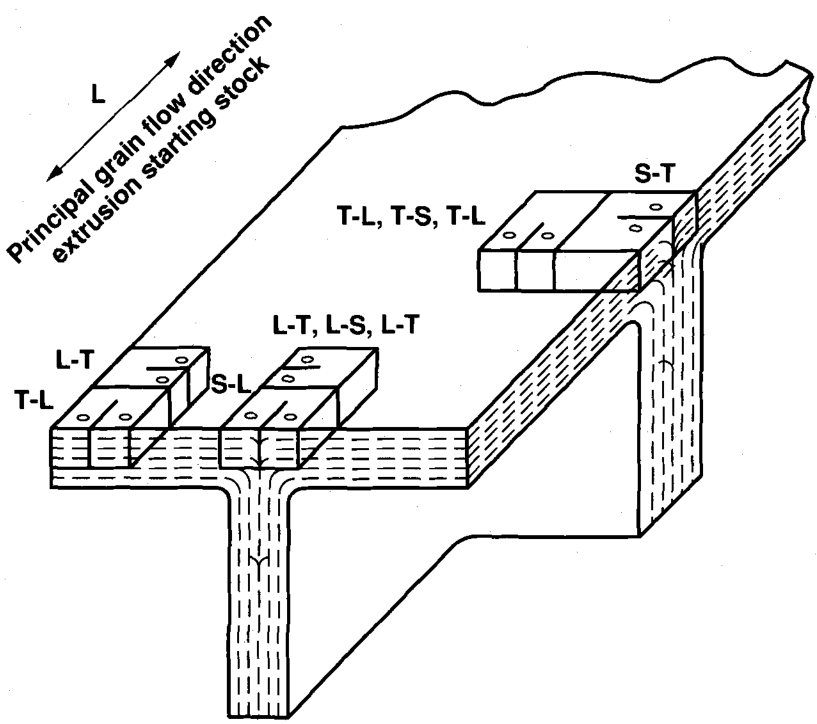

FIG. 2—*7075-T73 thin precision forging test specimen layout.*

Residual stress screening was performed by measuring the relative displacements between reference scribe marks about the crack starter notch before and after machining.

Constant ΔK fatigue crack growth tests were performed in accordance with ASTM E 647-88a at stress intensity ranges of 6.6, 11.0, and 19.8 MPa $\sqrt{m}$. After testing, fractographic examination of the fracture surfaces and macroetching of the specimens to reveal the grain-flow directions were performed. The grain-flow changes were then compared to the crack growth rate results to determine whether any systematic change in growth rates coincided with changes in grain-flow direction.

More traditional, constant-load-amplitude FCG tests were performed using CT specimens from the precision forging and 7075-T7351 plate in the L-T orientation to provide full-range da/dn versus ΔK curves for the two product forms.

7050-T74 Closed-Die Forgings

The thick 7050-T74 closed-die forging evaluated was chosen because it contained areas of rapidly varying grain-flow direction and was expected to contain quenching residual stresses great enough to alter crack growth rates determined by coupon tests. Several nominally S-T orientation CT specimens were removed from regions of constant and rapidly changing grain flow and from areas of different thickness within the forging. Examples of specimen location shown against the grain-flow backdrop are illustrated in Fig. 3. Screening for residual stresses was performed in the same manner as for the specimens from the thin precision forging. These specimens were tested at constant ΔK ranges of 6.6, 11.0, and 19.8 MPa $\sqrt{m}$. Other specimens from the L-T, T-L, S-L, and L-S orientations were tested at a constant ΔK range of 11.0 MPa $\sqrt{m}$, only, for comparison to the S-T results. After testing, the specimens were macroetched to verify the expected grain-flow patterns.

Constant-load-amplitude FCG tests were performed using CT and M(T) specimens in the L-T orientation from a thick section of a 7050-T74 closed-die forging. Macroetching confirmed the well-behaved nature of the grain flow in the region from which the specimens were taken. This data was compared to FCG data of thick 7050-T7452 hand forgings and several thicknesses of 7050-T7451 plate.

All FCG tests were performed in air with a relative humidity of 95% and at a stress ratio of $+1/3$. Crack closure measurements were made during all tests on forgings. The crack opening stress intensity was determined by compliance using a variable offset technique.

Results

Thin Precision Forgings

Constant ΔK *Testing*—Crack growth rate versus crack length results from T-L specimens at three levels of ΔK are presented in Fig. 4. These specimens were from an open web area of the forging and hence the grain flow was well controlled. Variation of the crack growth rates within any one test is on the order of $\pm$ 15%, indicating that the tests were well controlled. The lack of significant residual stresses in the specimens is indicated by the horizontal slopes of the curves. Consequently, the behavior is expected to be comparable to that of 7075-T7351 plate.

The results from a T-L, T-S, T-L specimen (see Fig. 2) cycled at a ΔK range of 6.6 MPa $\sqrt{m}$ are presented in Fig. 5. This figure consists of three parts, which are from top to bottom: (1) a macroetching of the test specimen showing the grain flow, (2) a low magnification photograph of the specimen fracture surface, and (3) the crack growth rate plotted versus crack length. A vertical line drawn at any point in the figure will intersect the macroetching, fracture

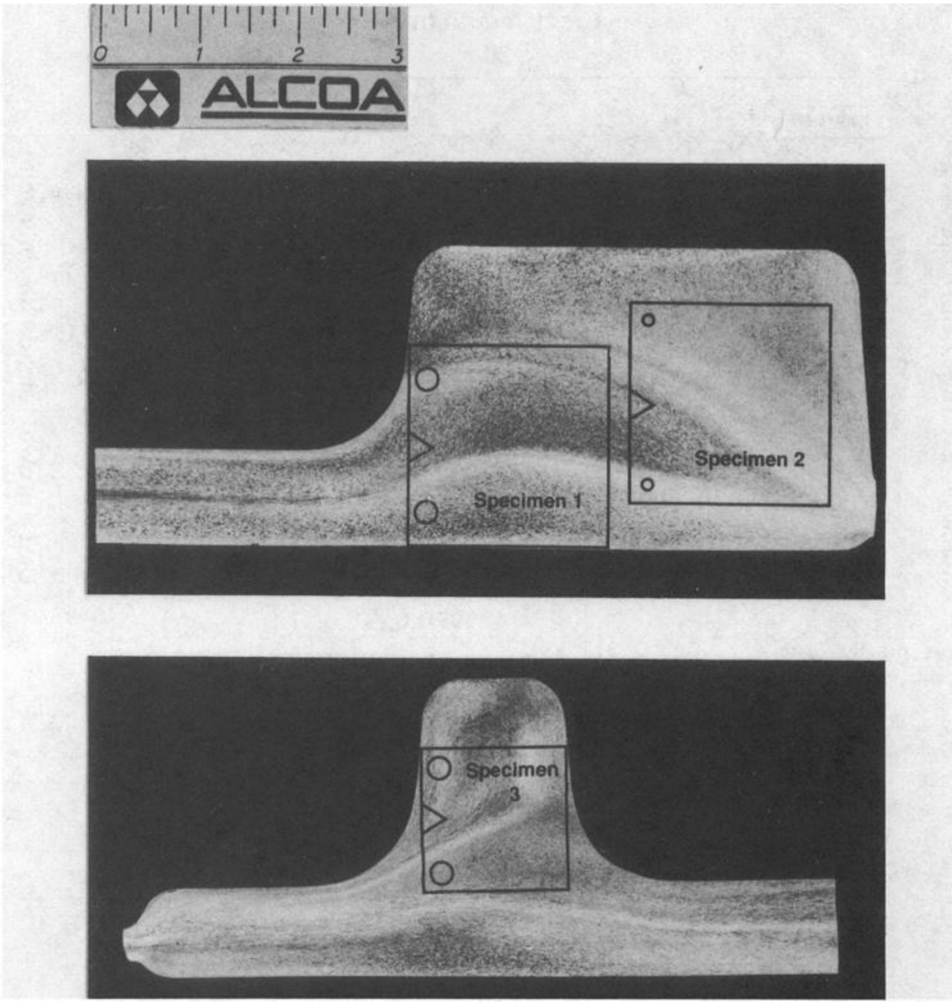

FIG. 3—*Example of fatigue crack growth specimen placement on 7050-T74 closed-die forgings.*

surface, and plot at the same crack length, such that the crack growth rate at any point can be related directly to the corresponding fracture surface features and grain-flow direction. The vertical dashed line denotes the center of the flange. The grain-flow direction is changing most rapidly on either side of this line. However, the crack growth rate curve remains horizontal despite crack growth through changing grain flow. The same general results can also be observed at ΔK values of 11 and 19.8 MPa $\sqrt{m}$ in Figs. 6 and 7.

The results for all six fracture specimen orientations are shown in Figs. 8 and 9, at ΔK ranges of 6.6 and 11 MPa $\sqrt{m}$ using an expanded crack growth rate scale. The center of all traversed flanges are indicated to show the insensitivity of crack growth rate to changes in grain flow. The fatigue crack growth rates are comparable for all six orientations, and the horizontal curves again indicate the absence of residual stress bias in the data.

Despite the lack of any difference in crack growth rates at identical driving forces (ΔK range)

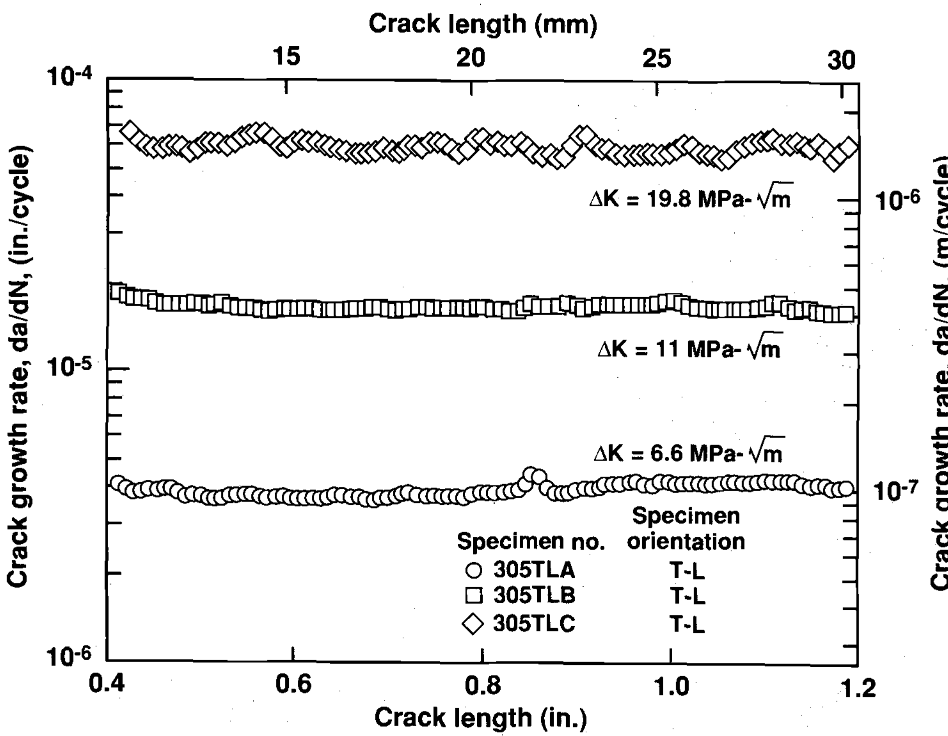

FIG. 4—*7075-T73 thin precision forging crack growth rate versus crack length constant* ΔK *test (*R = *0.33,* f = *25 Hz, high humidity air).*

TABLE 1—*7075-T73 precision forging effect of test orientation on crack propagation path.*

Test Orientation	ΔK, MPa $\sqrt{m}$	Crack Angle, Ω°
T-L	6.6	0.0
T-L	11.0	0.0
T-L	19.8	10.0[a]
S-L	6.6	0.0
S-L	11.0	5.0
S-L	19.8	3.0
T-L, T-S, T-L	6.6	1.0
T-L, T-S, T-L	11.0	3.0
T-L, T-S, T-L	19.8	3.0
L-T	6.6	1.0
L-T	11.0	12.0[b]
L-T	19.8	9.0[a]
S-T	6.6	20.0[b]
S-T	11.0	16.0[b]
S-T	19.8	3.0
L-T, L-S, L-T	6.6	7.0[a]
L-T, L-S, L-T	11.0	10.0[a]
L-T, L-S, L-T	19.8	14.0[b]

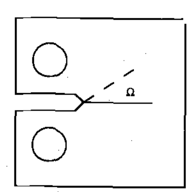

[a] 5° to 10° out-of-plane cracking.
[b] Greater than 10° out-of-plane cracking.

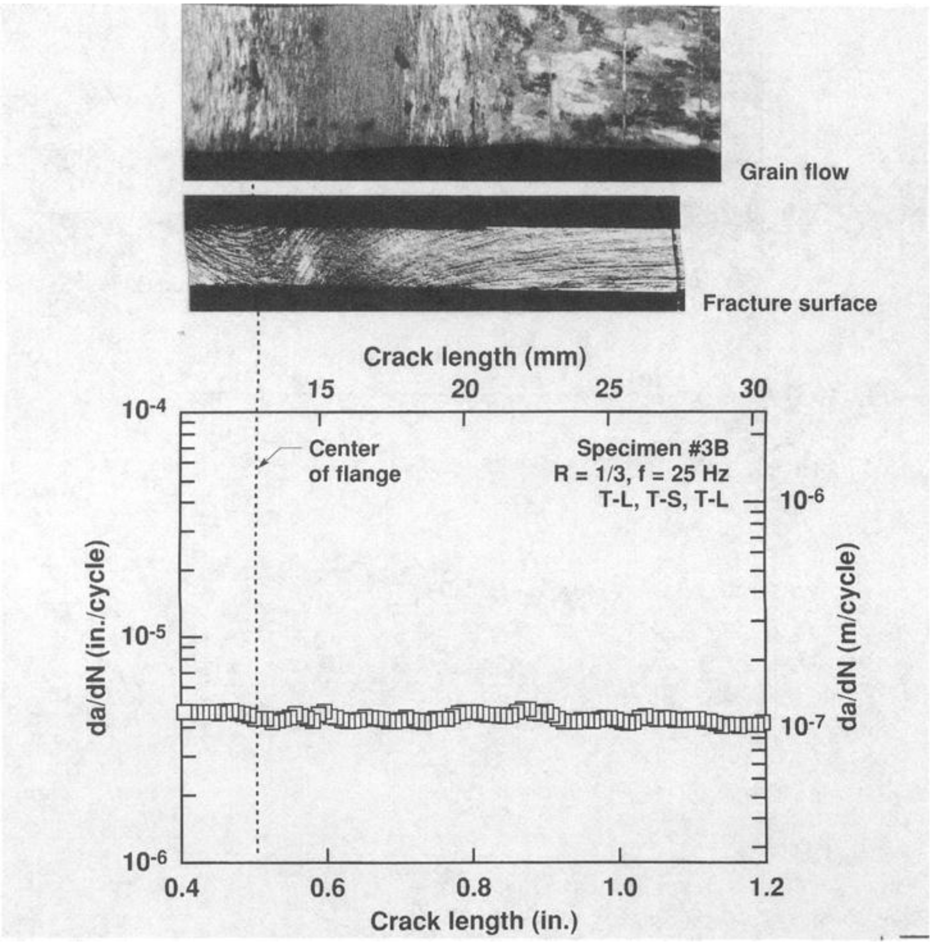

FIG. 5—*Correspondence of fatigue crack growth rate to grain flow and fracture surface in a 7075-T73 precision die forging* ($\Delta K = 6.6\ MPa\sqrt{m}$).

among crack orientations, there was a propensity for cracks propagating in the L direction to remain in the plane of the starting notch and for cracks growing in the T direction to veer out of the notch plane. Supporting data for this observation is presented in Table 1, in which the specimen orientation and the angle that the crack made with the starting notch are tabulated. The second letter of the specimen orientation indicates the intended crack growth direction. The crack remained inside the $\pm 5°$ envelope, specified in ASTM E 647-88a, in eight of nine tests in which the crack growth direction was longitudinal. Whereas in seven of nine specimens in which the crack growth direction was transverse, the crack deviated from the envelope.

This observation is not unique to forgings, but can also be observed in plate. Figure 10 illustrates tested 7050-T7451 CT FCG specimens taken from plate. The specimen orientations are S-L plus 0, 10, 20, and 30°. The test parameters include a constant ΔK of 3.3 MPa $\sqrt{m}$, a stress ratio of 0.7, and an environment of air at a relative humidity of 95%. In all four cases, the crack growth direction is within 4° of the longitudinal direction.

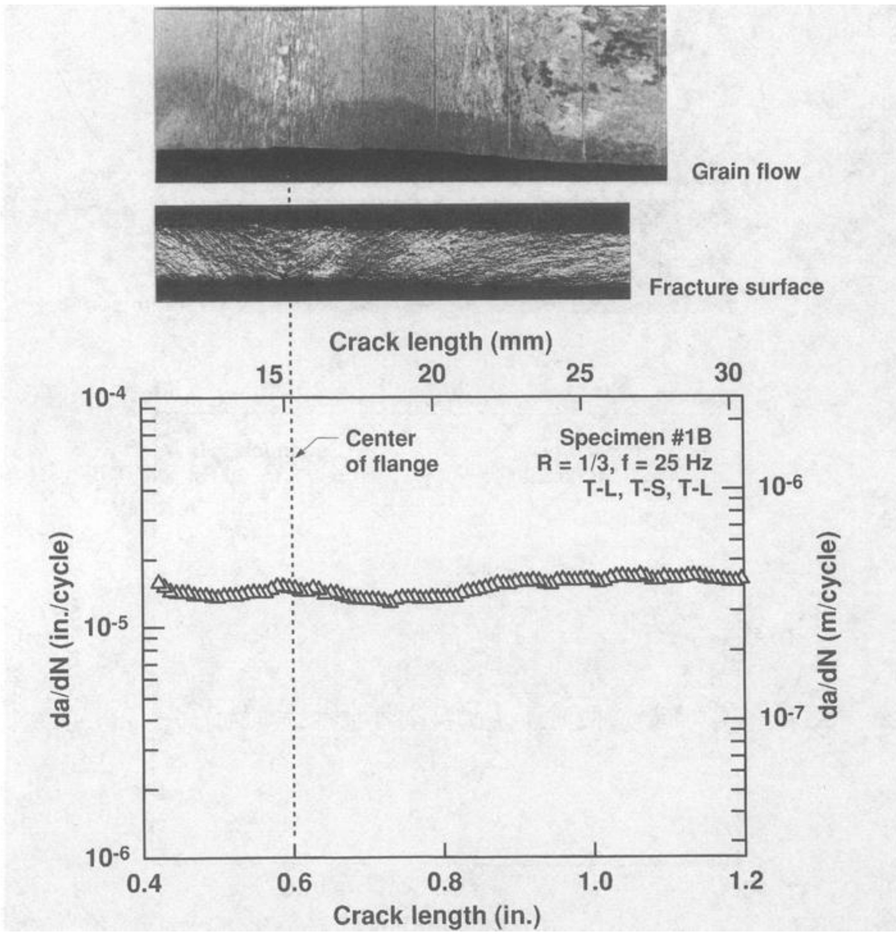

FIG. 6—*Correspondence of fatigue crack growth rate to grain flow and fracture surface in a 7075-T73 precision die forging* ($\Delta K = 11.0$ *MPa* $\sqrt{m}$).

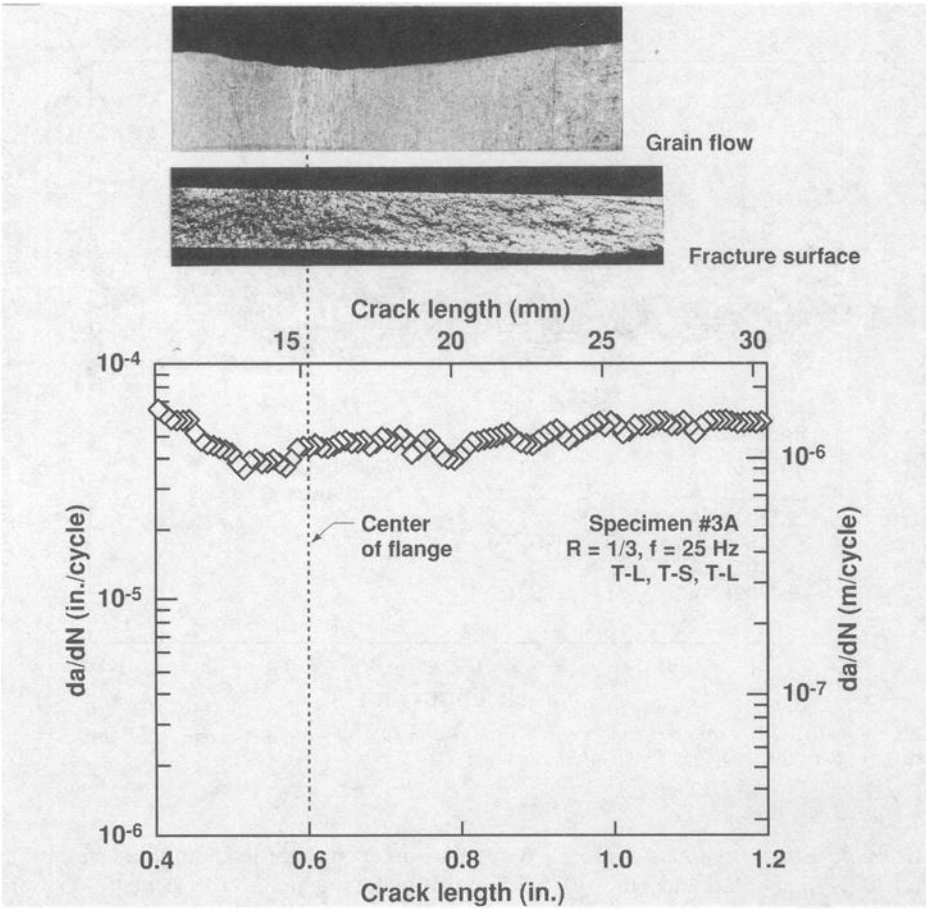

FIG. 7—*Correspondence of fatigue crack growth rate to grain flow and fracture surface in a 7075-T73 precision die forging (ΔK = 19.6 MPa $\sqrt{m}$).*

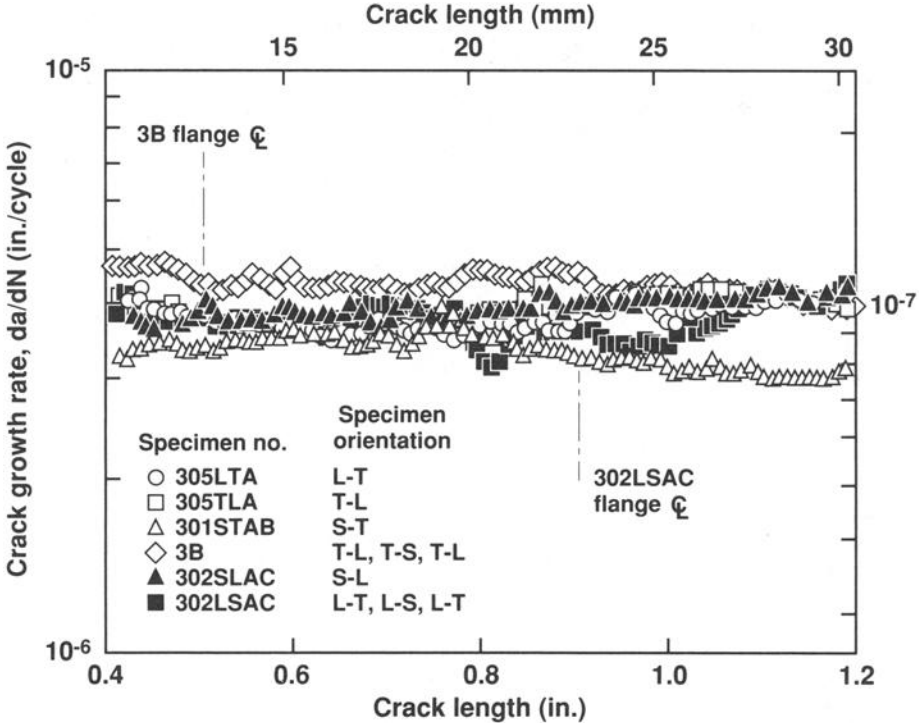

FIG. 8—*7075-T73 thin precision forging, crack growth rate versus crack length, constant* $\Delta K = 6.6$ *MPa* $\sqrt{m}$ *(R = 0.33, f = 25 Hz, high humidity air).*

Constant-Load-Amplitude-Testing—A comparison of constant-load-amplitude test results from 7075-T7351 plate and a thin 7075-T73 precision forging in the L-T orientation is shown in Fig. 11. The plate and thin precision forging show comparable FCG rate response.

Large 7050-T74 Closed-Die Forgings

Constant-Load-Amplitude Testing—Constant-load-amplitude FCG results for various thicknesses of 7050-T7451 stress-relieved plate in the L-T orientation are shown in Fig. 12. This plot represents four lots of material and seven tests on material from 25.4 mm to 152.4 mm thick. The plate data are well behaved and reproducible with the greatest amount of scatter lying in the threshold regime below 4 MPa $\sqrt{m}$. For comparison, Fig. 13 illustrates the FCG behavior of material from a 115-mm-thick rib section of a 7050-T74 closed-die forging plotted against a backdrop of the scatter bands for 7050-T7451 plate and 7050-T7452 152.4 and 190.5-mm-thick hand forgings. Residual stress screening indicated that residual stresses parallel to the fracture plane in the die forging specimens were negligible. Hence, the resulting FCG is well-behaved and reproducible. In contrast, while the FCG measurements of the hand forgings are comparable to those of the plate and die forgings at higher ΔK values, scatter below ΔK values of about 5 MPa $\sqrt{m}$ increases.

Similar behavior can be observed in Fig. 14 that compares FCG results in the S-L orientation of multiple lots of thick 7050-T7451 plate and a single 7050-T7452 hand forging. The

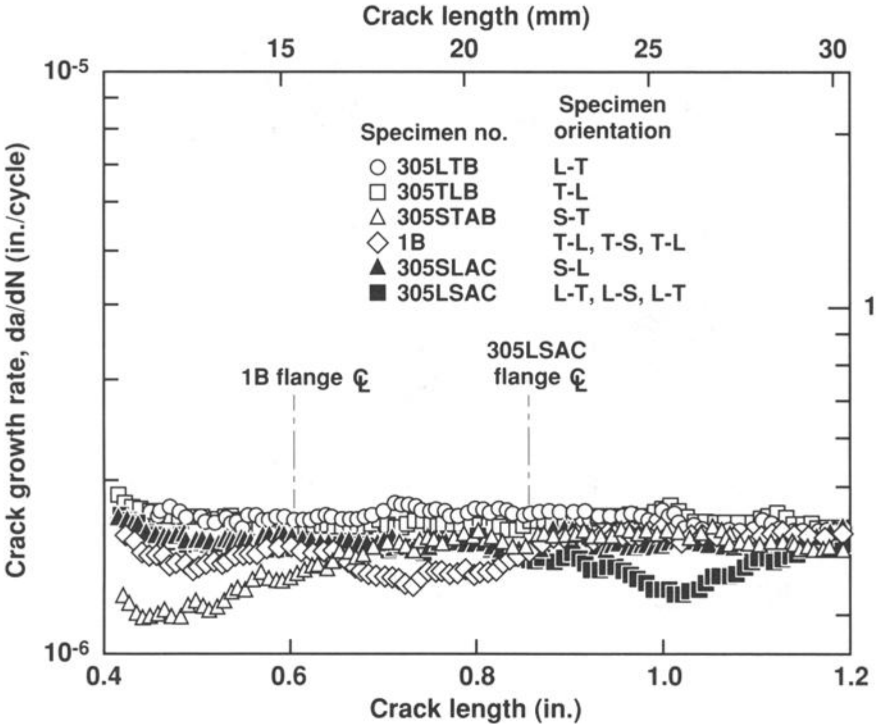

FIG. 9—*7075-T73 thin precision forging, crack growth rate versus crack length, constant* ΔK = *11 MPa* $\sqrt{m}$ *(R = 0.33, f = 25 Hz, high humidity air).*

scatter at low values of ΔK in the hand forging data is much greater than that of the plate data, while at larger values of ΔK the results from both product forms are essentially identical. However, when the data sets of Fig. 14 are corrected for closure and replotted against effective ΔK rather than applied ΔK in Fig. 15, the differences disappear. The wide scatter band of the hand forging data collapses into a narrow scatter band that is indistinguishable from that of the plate results. Thus implying that after closure correction to remove residual stress bias, the intrinsic FCG responses of forgings and plate are revealed to be the same.

Constant ΔK *Test*—Experimentally measured crack growth rates are plotted in Fig. 16 against crack length for seven nominally S-T orientation CT specimens taken from two thick 7050-T74 closed-die aerospace forgings and tested at a constant ΔK of 6.6 MPa $\sqrt{m}$. Due to the increased thickness of these forgings compared to the 7075-T73 precision forgings, it would be expected that the magnitude of the quenching residual stresses would be greater in the thick die forgings. This assumption is supported by the increase in crack growth rates with increasing crack length and by the relative crack mouth displacements that occur during notch preparation, shown in Table 2. Both of these results suggest that residual stresses parallel to the fracture plane are producing clamping moments that in turn are biasing the coupon test results. The scatter in these data is similar to that observed in the hand forging FCG data in Figs. 13 and 14. Likewise, as was the case for the hand forgings, when the constant ΔK data of Fig. 16 are corrected for closure (to remove residual stress bias) and plotted at an effective ΔK of 6.6 MPa $\sqrt{m}$ in Fig. 17, the scatter is greatly reduced and the crack growth rate becomes independent of crack length.

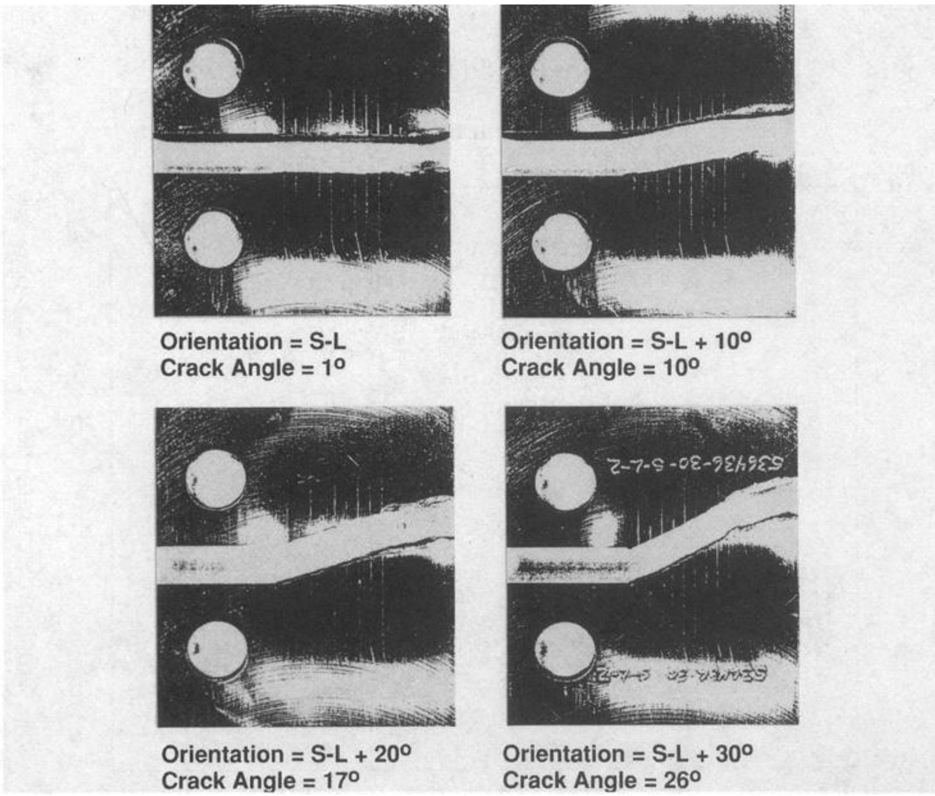

FIG. 10—*Effect of specimen orientation on crack propagation path of 7050-T7451 plate (constant* $\Delta K = 3.3\ MPa\ \sqrt{m}$, $R = 0.7$).

TABLE 2—*7050-T74 die-forging relative displacement measurements for residual stress screening.*

Specimen ID	ΔK, MPa $\sqrt{m}$	Notch Width Difference, mm
2554ST1	6.6	0.065
2554ST2	11.0	0.040
2555ST1	6.6	0.050
2555ST2	11.0	0.000
2536ST1	6.6	0.040
2536ST2	11.0	0.040
2537ST1	6.6	0.040
2537ST2	11.0	0.040
7631ST1	6.6	0.050
7631ST2	11.0	0.050
7632ST1	6.6	0.065
7632ST2	11.0	0.040
7633ST1	6.6	0.025
7633ST2	11.0	0.025

Locations for displacement measurements in CT FCG specimens

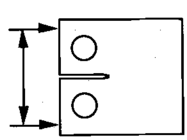

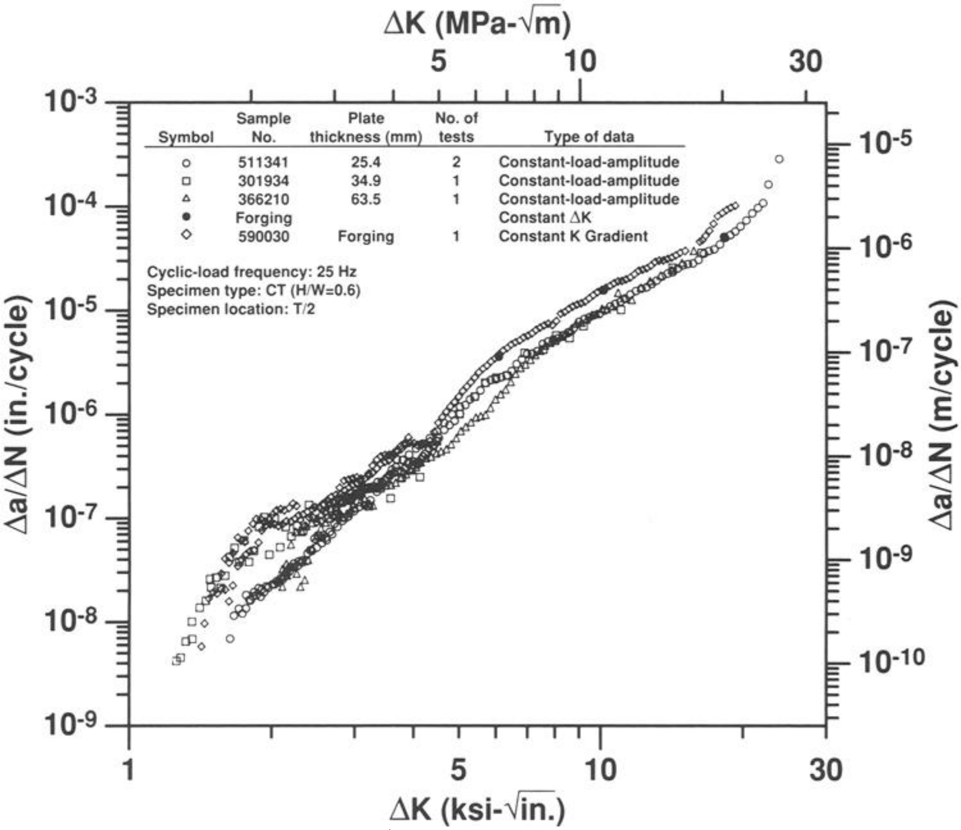

FIG. 11—*Constant-load-amplitude fatigue crack propagation data for 7075-T7351 plate and 7075-T73 precision forging: L-T orientation,* R*-ratio* = +0.33, *high humidity (RH > 90%) air.*

At a larger constant ΔK of 11.0 MPa $\sqrt{m}$, the experimentally measured crack growth rate of seven nominally S-T specimens are tightly grouped and independent of crack length. This is shown in Fig. 18. The crack length independence of the FCG rates implies that in-plane residual stresses have little effect on these measurements. This is consistent with the previous results that showed that the scatter in measured FCG rates diminishes with increasing magnitudes of ΔK.

The data of Fig. 19 reveal that crack growth rates at constant ΔK of 11.0 MPa $\sqrt{m}$ are also insensitive to grain-flow orientation as well. The FCG results from five of the six possible grain-flow orientations are plotted as a function of crack length. All the data fall into a narrow band, thus indicating no major impact of grain-flow orientation on FCG behavior at intermediate levels of ΔK.

Discussion

The initial assertion that the complex grain flow of die forgings may contribute significantly to the greater amount of scatter sometimes observed in the FCG data of die forgings is not supported by the results of this study. In both 7075-T73 and 7050-T74 forgings, changes in

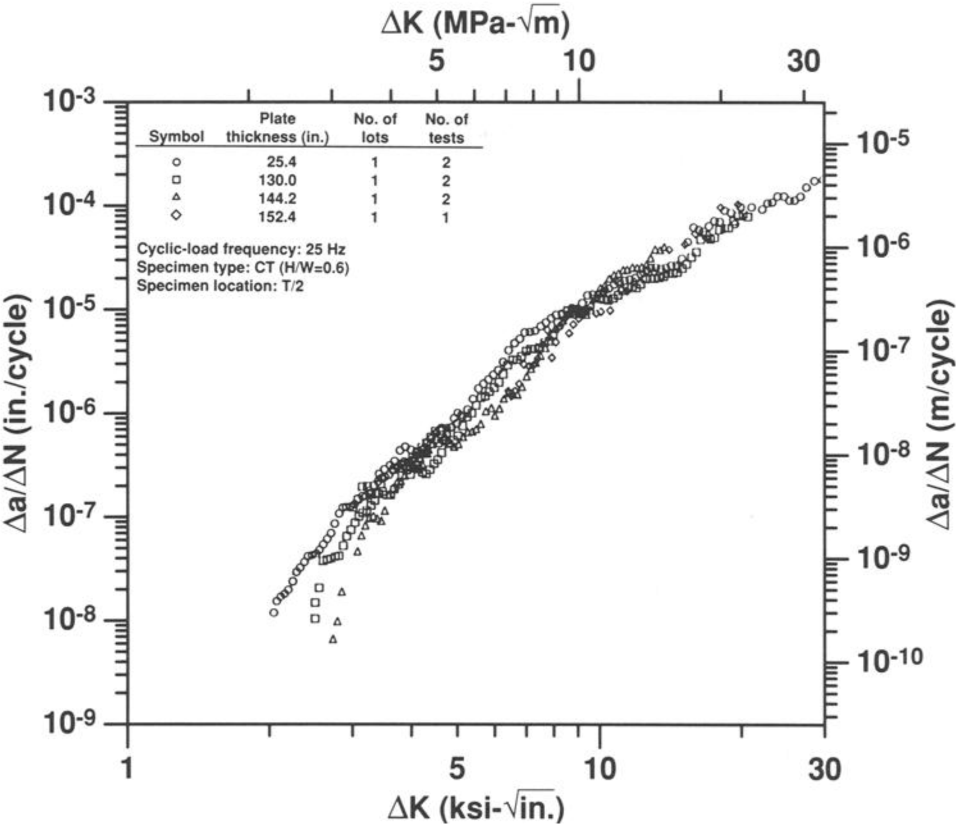

FIG. 12—*Constant-load-amplitude fatigue crack propagation data for various thicknesses of 7050-T7451 plate: L-T orientation,* R*-ratio = +0.33, high humidity (RH > 90%) air.*

crack growth rate as the crack grows through changing grain-flow direction are typical of the variability observed in materials with simple well-behaved grain flow. Therefore, over the ΔK and growth rate ranges studied in this report (predominantly Region II), the grain flow has, at most, only a minor influence on FCG behavior.

The assertion that the scatter in experimentally measured FCG rates of thick aluminum die forgings is an extrinsic effect caused by unrelieved residual stresses is supported by this study. In the absence of significant quenching residual stresses, measured FCG rates of thin (2 to 3 mm) 7075-T73 precision forgings are comparable to those rates obtained from stress-relieved 7075-T7351 plate.

The FCG measurements for 7050-T7452 and T74 hand and die forgings in Figs. 13, 14, and 16 showed all the signs associated with residual stress bias discussed earlier. Scatter in Figs. 13 and 14 is greatest at short crack lengths and low stress intensities, where residual stress bias is accentuated. Similarly, in the constant ΔK tests of Fig. 16, the crack growth rates increase with crack length as the residual stresses (clamping forces) are relieved by crack extension. The group of two tests in Fig. 16 with the lowest crack growth rates came from the two specimens from the center of the thickest portions of the die forgings. Tensile residual stresses would be expected to be at a maximum at those locations. Hence, it is reasonable that these specimens

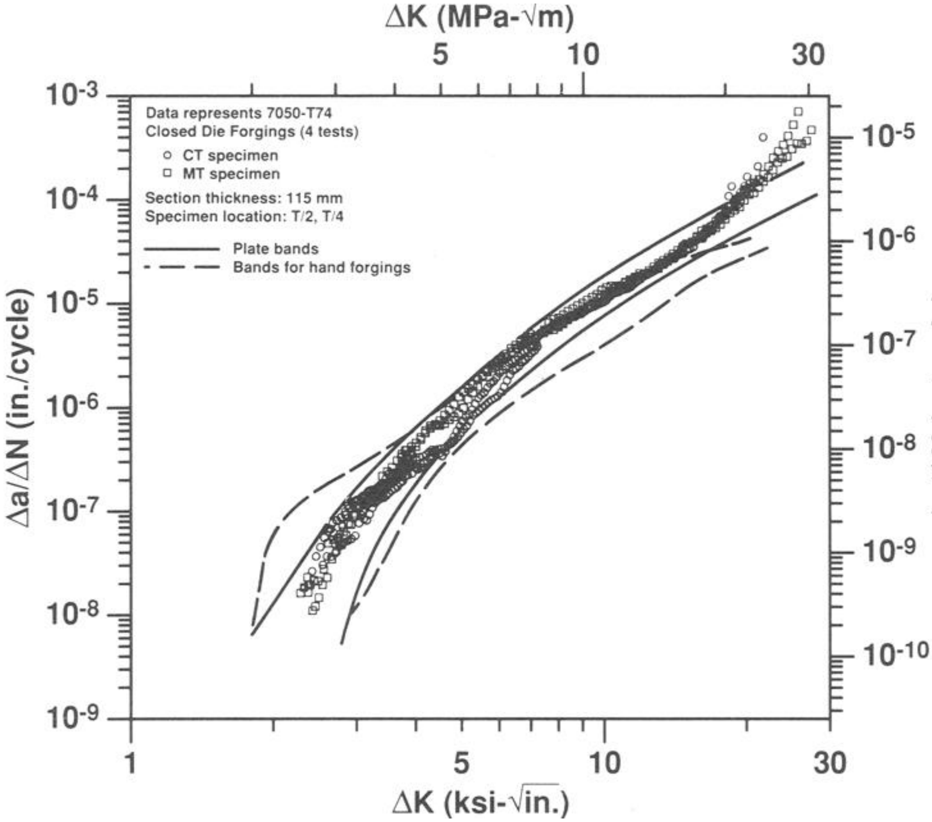

FIG. 13—*Constant* K-*gradient fatigue crack propagation data for thick 7050-T74XX closed-die forgings, hand forgings, and plate: L-T orientation,* R-*ratio = +0.33, high humidity (RH > 90%) air.*

should also have the maximum clamping bending moments tending to retard crack growth. This hypothesis is supported by the data in Table 2 where it is shown that these two specimens also had the largest relative displacements when machining the crack starter notch. Furthermore, when the residual stress bias is removed by means of closure measurement and the crack growth rates are plotted versus ΔK effective in Figs. 15 and 17, the observed scatter is reduced to the level expected in FCG measurements for stress-relieved plate. Once the residual stress bias is removed, the intrinsic crack growth response of the forgings and the plate, as plotted in terms of ΔK effective in Fig. 15, is the same.

It should be emphasized that all the tests performed in this study are valid according to ASTM E 647-88a with the exception that some of the cracks veered out of the $\pm 5°$ envelope about the plane of the crack starter notch. However, there is no correlation between the scatter and out-of-plane cracks. Despite the apparent validity of the tests, the specimens containing excessive residual stresses may not be representative of the material behavior for the following reasons. First, the act of excising the specimen from the forging alters the residual stress state in the specimen material. Hence, the residual stresses in the specimen may not be representative of those in the parent metal or the final part. Second, the characterization of FCG behavior utilizes low loads to propagate long cracks in CT specimens. Under these circumstances,

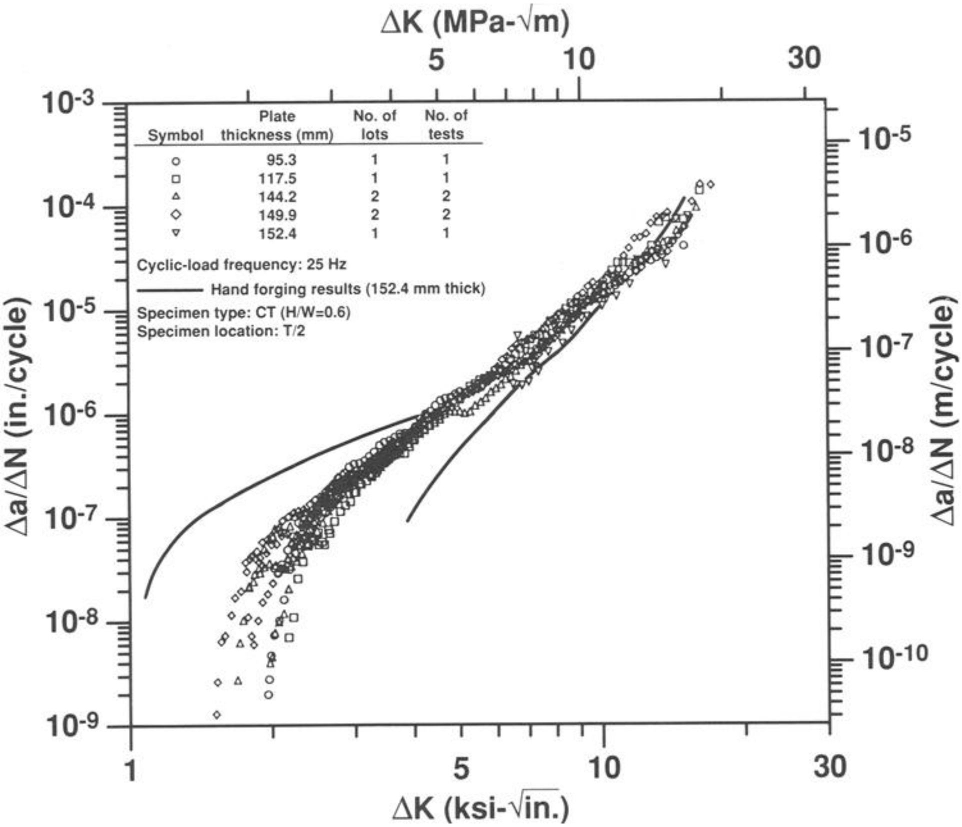

FIG. 14—*Constant-load-amplitude fatigue crack propagation data for various thicknesses of 7050-T7451 plate and 7050-T7452 hand forgings: S-L orientation,* R-*ratio* = +*0.33, high humidity (RH* > *90%) air.*

relatively small residual stresses can have substantial effects on crack growth behavior. In an actual structure, the cracks are more likely to be smaller with respect to the component size and the applied loads are more likely to be higher. This concept can be also expressed in terms of stress intensity as follows. It is more likely that the ratio of residual stress-induced stress intensity to the stress intensity produced by remote loading ($K_{res}/K_{applied}$) is greater in the specimen than in a structural part. Therefore, the residual stresses may have less of an impact on FCG behavior in the structure than in the coupon.

The results of this investigation show that the mean intrinsic FCG performance of forged and flat-rolled plate products are comparable to one another. Residual stresses present in thick aluminum forgings produce increased variability in FCG coupon test data, which may not be representative of actual parent material or part performance and have the potential for producing a flawed FCG data base in the literature. In the absence of significant residual stresses, such as in the case of thin precision and thin die forgings, components fabricated from any of the aforementioned product forms should exhibit comparable FCG behavior. Hence, in these situations qualification of forgings for damage-tolerant critical applications should be no different than for parts machined from plate. When significant residual stresses are present, such

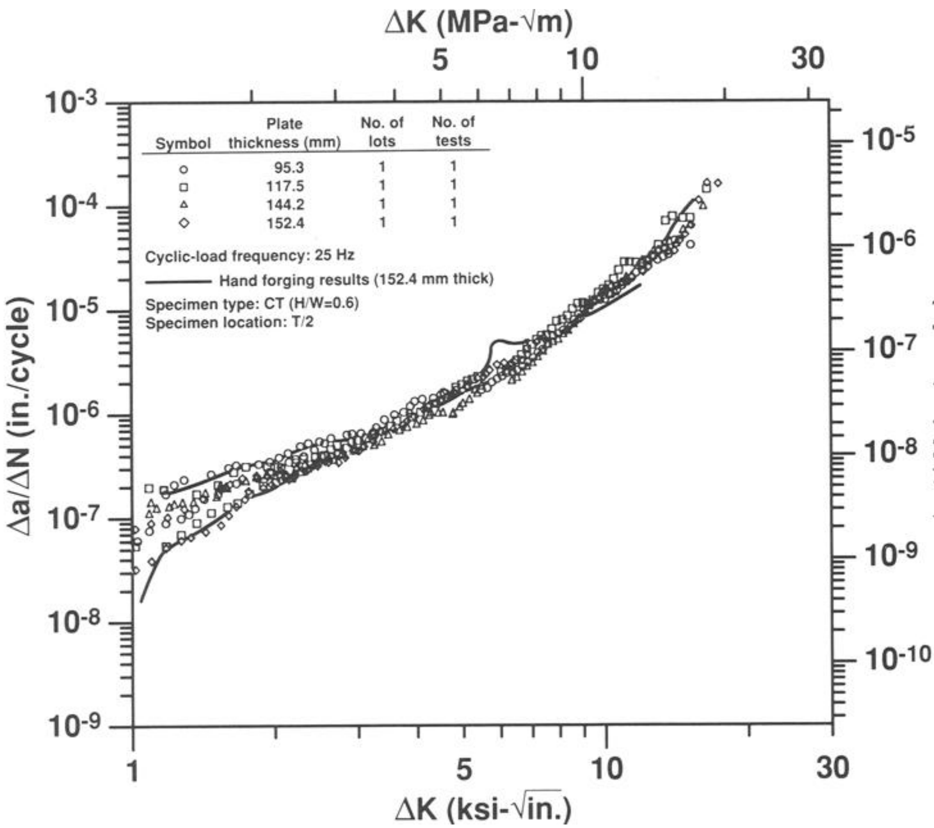

FIG. 15—*Closure-corrected fatigue crack propagation data for various thicknesses of 7050-T7451 plate and 7050-T7452 hand forgings: S-L orientation,* R-*ratio* = +0.33, *high humidity (RH > 90%) air.*

as in the case of thicker closed-die forgings, some method must be used to account for the residual stresses during component qualification. Component testing could be used to estimate the scatter that the residual stresses produce, or knowledge of the behavior of the component in conjunction with an estimate of the residual stresses could be used to analytically assess the damage-tolerant capabilities of a thick forged component.

Conclusions

Based on the results of this study the following conclusions are justified:

1. Grain flow does not contribute significantly to the observed scatter in FCG data of 7075-T73XX or 7050-T74XX aluminum forged or plate products.
2. When specimen residual stress effects are small, such as in the case of the thin forging examined in this study, the FCG rate behaviors of 7075-T73 precision forgings and 7075-T7351 plate are comparable.

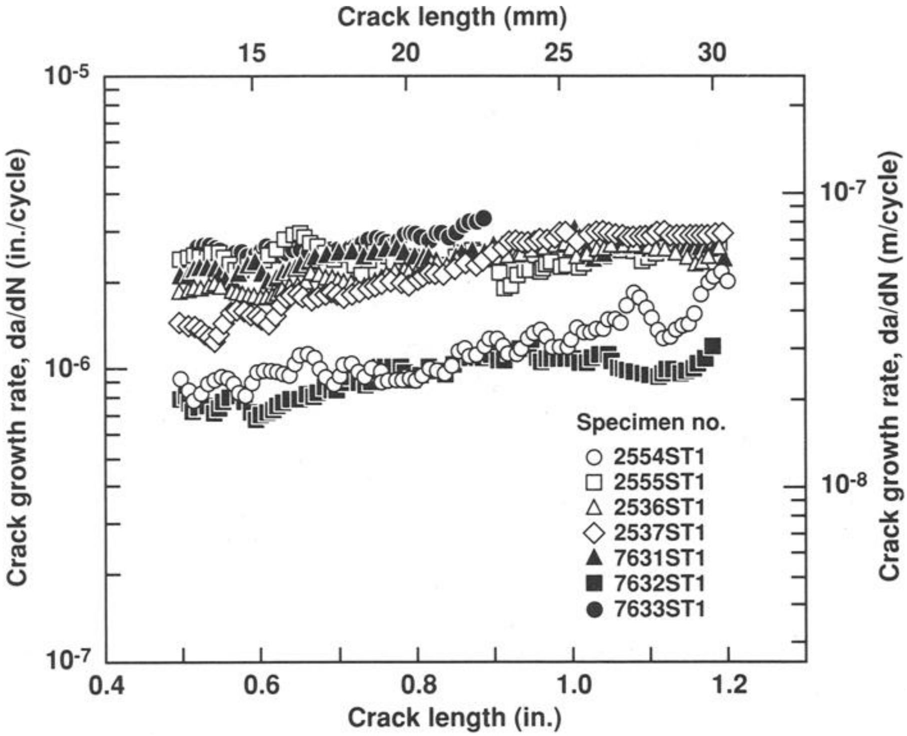

FIG. 16—*7050-T74 closed-die forging crack growth rate versus crack length constant* $\Delta K = 6.6$ *MPa* $\sqrt{m}$ *(S-T orientation,* R = *0.33,* f = *25 Hz, high humidity air).*

3. Quenching residual stresses found in thick nonstress-relieved aluminum die and hand forgings are the primary cause of scatter observed in FCG data from those product forms. However, the mean intrinsic FCG response of thick 7050-T74 closed-die forgings and thick 7050-T7451 plate is comparable.
4. Forgings are amenable to fracture mechanics analysis, but reliable interpretation requires awareness of possible confounding residual stress influences.
5. Crack closure concepts are useful for separating extrinsic testing effects from intrinsic material behavior.

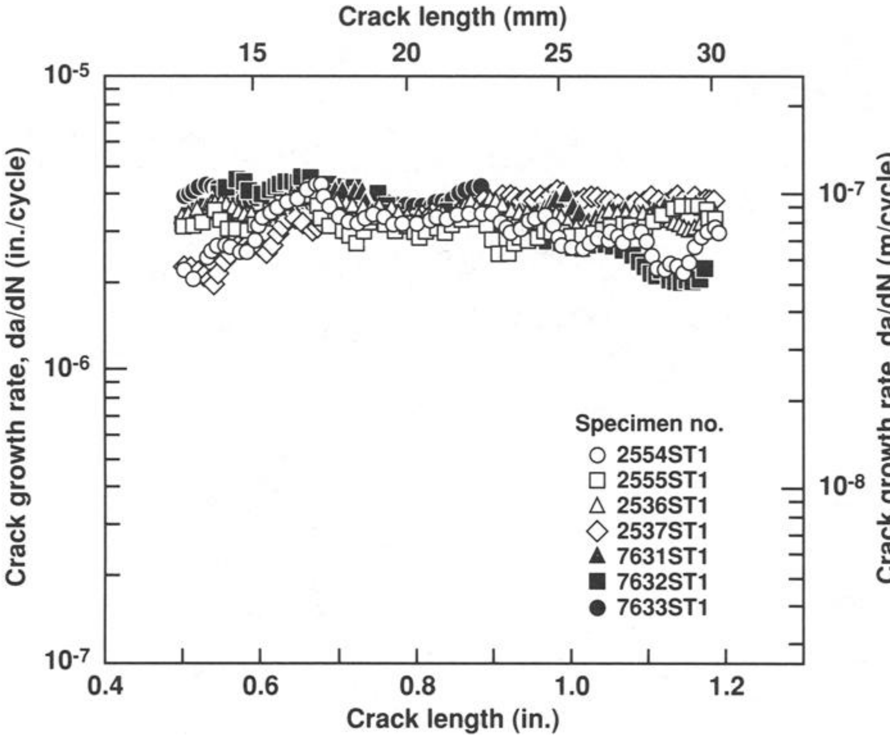

FIG. 17—*7050-T74 closed-die forgings crack growth rate versus crack length closure corrected constant* ΔK_{eff} *= 6.6 MPa* $\sqrt{m}$ *(S-T orientation, R = 0.33, f = 23 Hz, high humidity air).*

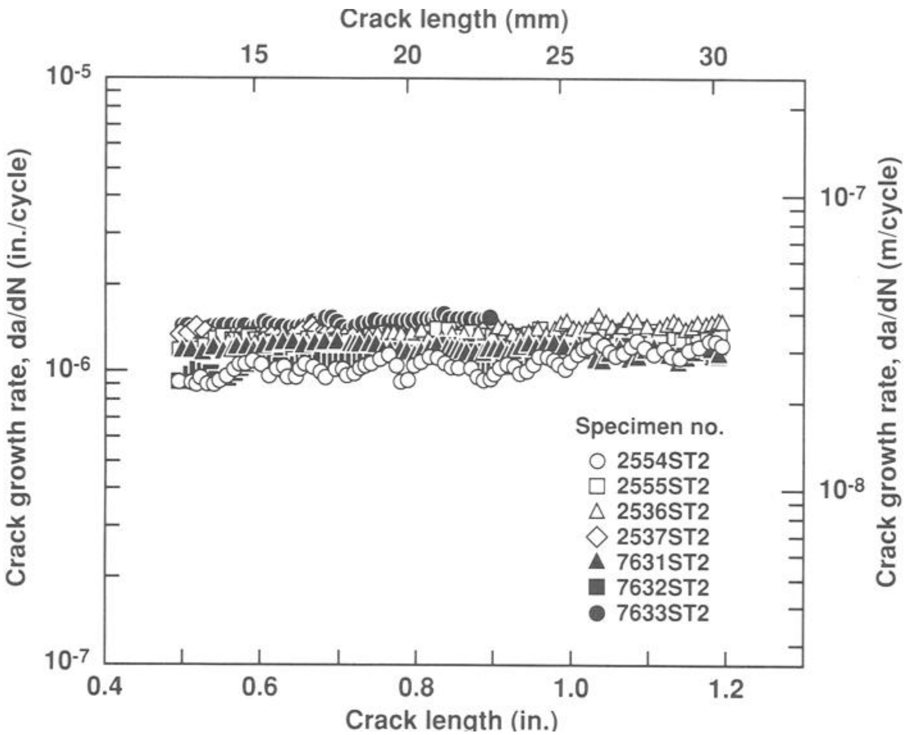

FIG. 18—*7050-T74 closed-die forging, crack growth rate versus crack length constant* ΔK = *11 MPa* $\sqrt{m}$ *(S-T orientation,* R = *0.33,* f = *25 Hz, high humidity air).*

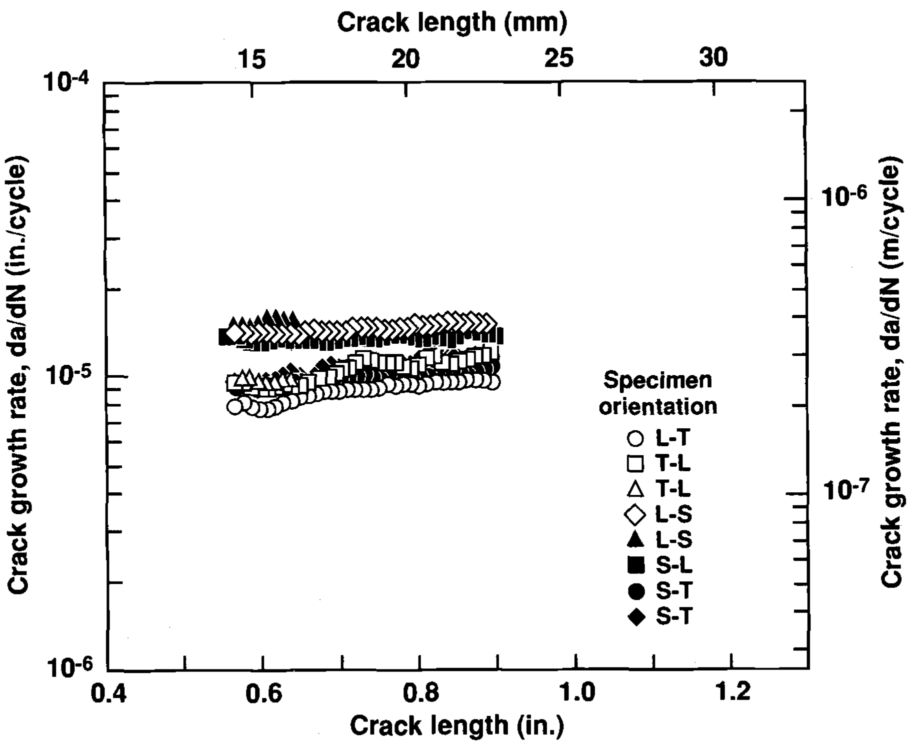

FIG. 19—*7050-T74 closed-die forging, crack growth rate versus crack length constant* ΔK = *11 MPa* $\sqrt{m}$ *(R = 0.33, f = 25 Hz, high humidity air).*

References

[*1*] Schutz, W., "Fracture Behavior of Aluminum Forgings (I)," *Aluminum 58,* Vol. 5, 1982, 263–270.

[*2*] Schutz, W., "Fracture Behavior of Aluminum Forgings (II)," *Aluminum 58,* Vol. 6, 1982, pp. 350–354.

[*3*] "Alcoa Green Letter: Alcoa Aluminum Alloy 7050," Aluminum Company of America, Alcoa Center, PA, 1985.

[*4*] Hertzberg, R. W., *Deformation and Fracture Mechanics of Engineering Materials,* 2nd ed., Wiley, New York, 1983, pp. 415–418, 593–595.

[*5*] Kelsey, R. A. and Nordmark, G. E., "Effect of Residual Stresses on Fatigue Properties of Aluminum Butt Welds," *Aluminum 55,* Vol. 6, 1979, pp. 391–394.

[*6*] Bucci, R. J., "Effect of Residual Stress on Fatigue Crack Growth Rate Measurement," *Fracture Mechanics (Thirteenth Conference), ASTM STP 743,* R. Roberts, Ed., American Society for Testing and Materials, Philadelphia, 1981, pp. 28–47.

Somnath Chattopadhyay[1]

Fatigue Crack Growth Analysis of Structures Exposed to Fluids with Oscillating Temperature Distributions

REFERENCE: Chattopadhyay, S., "**Fatigue Crack Growth Analysis of Structures Exposed to Fluids with Oscillating Temperature Distributions,**" *Fracture Mechanics: Twenty-Third Symposium, ASTM STP 1189,* Ravinder Chona, Ed., American Society for Testing and Materials, Philadelphia, 1993, pp. 590–597.

ABSTRACT: This investigation considers amplitudes and frequencies of the oscillating temperature distribution as parameters for crack propagation studies. The alternating stresses produced by the temperature distribution are used to determine the ranges of stress intensity factors for a particular crack geometry using the principles of linear elastic fracture mechanics. The crack growth is then studied using a crack growth law for the material relating the crack growth per cycle to the number of cycles.

The analysis predicts that the number of cycles required to drive a crack of a specified initial size is dependent on the frequency of temperature cycling. The model also predicts that as the frequency increases, larger amplitudes of temperature variation can be permitted for the same number of cycles to failure. A design curve relating the temperature amplitude with the number of cycles to failure (a specified crack length) is obtained for various frequencies of temperature oscillations.

KEY WORDS: analysis, fatigue crack growth, oscillating temperature, thermal stresses, fracture mechanics, fatigue (materials)

Thermal transients in metal structures exposed to fluid undergoing temperature oscillations are encountered in many fields. The oscillating temperature distribution produces alternating stresses in the structure leading to the possibility of fatigue damage. In Ref *1*, the thermal response of the plates immersed in a fluid with oscillating temperature has been addressed. Oscillatory transients can take place in internal combustion engine cylinder walls, rotary regenerators, and pipelines in which two fluid streams at different temperatures are mixed. In the nuclear industry, such fluid temperatures are encountered. In pressurized water reactor steam generators, the mixing of cold inlet water with hotter water introduces oscillatory temperature distribution in the feedlines. This introduces alternating stress fields leading to the likelihood of propagation of surface cracks in the steam generator feedlines. In boiling water reactor pressure vessels, mixing of the cold inlet stream with hotter water in the vessel can cause oscillatory fluid temperatures at the walls adjacent to the nozzle. This leads to initiation and growth of surface fatigue cracks.

The purpose of this investigation is to develop a model for the assessment of the amplitudes and frequencies of the oscillating temperature distribution on fatigue parameters for crack propagation. The temperature distribution in the metal exposed to the oscillating fluid tem-

[1] Department of Mechanical Engineering, the University of Vermont, Burlington, VT 05405-0156.

perature is determined first. The alternating stresses produced by this temperature variation are used to determine the ranges of stress intensity factor for a particular crack geometry using the principles of linear elastic fracture mechanics. The crack growth is then studied using a crack propagation law for the material relating the crack growth per cycle to the number of cycles. The number of cycles required to extend a crack to a certain depth, as influenced by the temperature amplitude as well as the frequency of the temperature oscillations, can be determined readily by this procedure.

Thermal Response Under Oscillating Fluid Temperatures

Referring to Fig. 1, we assume the fluid temperature adjacent to the metal to vary harmonically, or

$$T_w = \overline{T} + T_a \cos \omega t \tag{1}$$

where

$\overline{T}$ = mean temperature,
T_a = amplitude,
ω = frequency of the temperature variation, and
t = time.

With the assumption of an infinite heat transfer coefficient between the fluid and the adjacent metal, the quasi-steady temperature distribution in a semi-infinite solid occupying the region, $x \geq 0$ (Fig. 1), is given by [2]

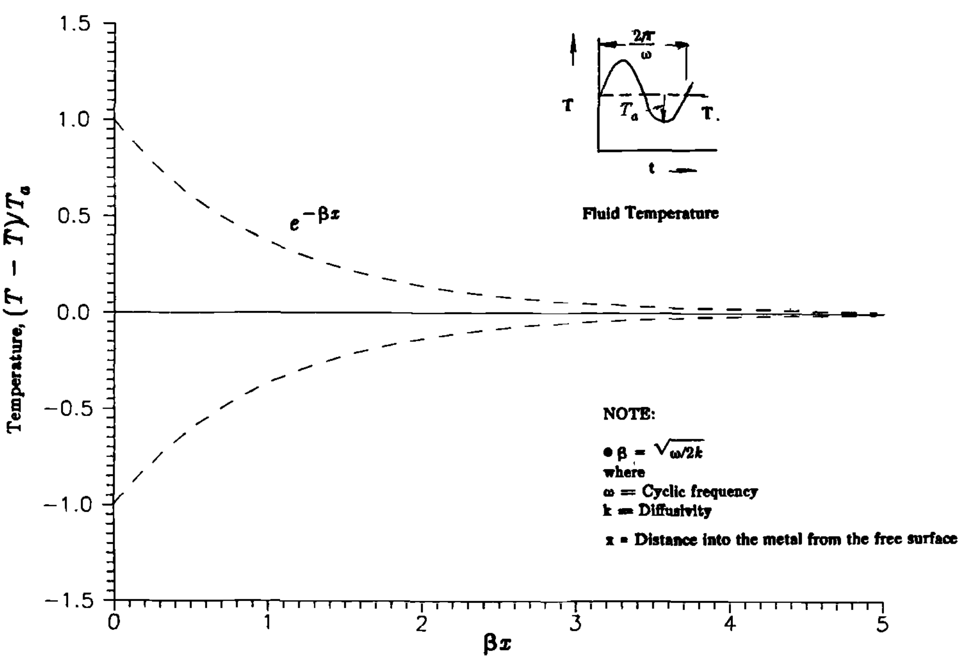

FIG. 1—*Envelope of temperature distribution in an semi-infinite solid.*

$$(T - \overline{T})/T_a = e^{-\beta x} \cos (\omega t - \beta x) \tag{2}$$

where $\beta = \sqrt{\omega/2k}$ and k = thermal diffusivity.

Although the assumption of an infinite film coefficient may not be truly representative of all of the actual conditions in service, the crack propagation characteristics will not be altered significantly. The finite heat transfer coefficient causes a delayed transient response as investigated in Ref *1*. The typical value of heat transfer coefficient in a pressurized water reactor steam generator is about 30 kW/m^2K.

From Eq 2, the limiting values of the temperature response can be written as

$$|T - \overline{T}|/T_{a\max} = e^{-\beta x} \tag{3}$$

The thermal response of the metal adjacent to fluid is thus enveloped by an exponential decay function that gives us an upper bound on the thermal gradient. This temperature gradient will provide us an upper-bound estimate of stresses.

Stress Intensity Factors

As outlined in Ref *3*, the stress intensity factor for a continuous semicircular surface crack in a semi-infinite body is given by

$$K = 2\sqrt{a/\pi} \int_0^a \sigma(x)dx/\sqrt{a^2 - x^2} \tag{4}$$

where a is the crack depth (see Fig. 2) and $\sigma(x)$ is the applied nonuniform stress field.

The stress at a point in the metal is given by

$$\sigma(x) = E\alpha \, \Delta T(x)/(1 - \nu) \tag{5}$$

where

$\Delta T = T - \overline{T}$,
E = elastic modulus,
ν = Poisson's ratio, and
α = coefficient of thermal expansion.

Substituting the maximum value of $\Delta T = T - \overline{T}$ from Eq 3 into Eq 5 and observing from Fig. 1 that $T_a = \Delta T_m/2$, where ΔT_m is the maximum temperature range for thermal oscillations, we obtain the maximum stress range as

$$\Delta\sigma(x)_{\max} = E\alpha \, \Delta T_m e^{-\beta x}/2(1 - \nu) \tag{6}$$

The stress distribution in Eq 6 is highly nonlinear. This is a very unique feature for oscillating temperatures. The stress decays exponentially away from the surface. For high frequencies of fluid temperature oscillations, characterized by high values of β, this decay is very rapid.

Substituting ΔT from Eq 6 into Eq 4, we obtain the maximum range of stress intensity factor as

$$\Delta K = \sqrt{a/\pi} E\alpha \, \Delta T_m/(1 - \nu) \int_0^a e^{-\beta x}/\sqrt{a^2 - x^2} \, dx \tag{7}$$

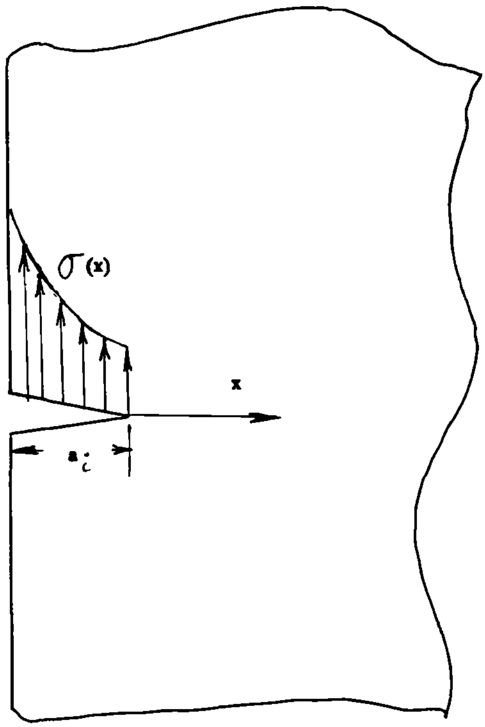

FIG. 2—*Continuous surface crack in semi-infinite body.*

As outlined in the Appendix, Eq 7 may be approximated as

$$\Delta K = E\alpha \, \Delta T_m/(1 - \nu)\sqrt{\pi a}\, e^{-\sqrt{\beta a}} \tag{8}$$

This expression for ΔK will be used for crack growth studies. This expression is based on a simplification of the actual function in the integral to obtain the stress intensity factor range as shown in Fig. 3.

Crack Growth

The growth of a crack per loading cycle is dependent on the range of applied stress intensity factor, ΔK, by the following

$$da/dN = C_0 \, \Delta K^n \tag{9}$$

where da/dN represents the crack growth per cycle and C_0 and n are material parameters. We assume that the temperature excursions are small, thereby validating the use of constant temperature material properties. We also neglect the creep and creep fatigue interactions that can occur in thermal cycling. We then have, when integrating Eq 9

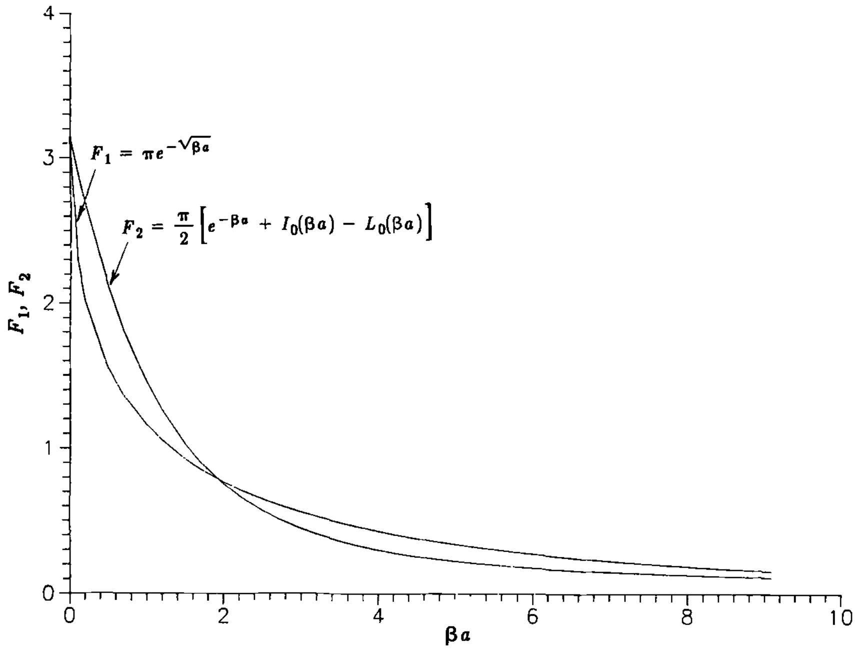

FIG. 3—*Comparison of functions.*

$$N = \int_{a_i}^{a_f} da/[C_0(\Delta K)^n] \tag{10}$$

where a_i and a_f are the initial and final crack sizes, respectively, and N is the number of cycles.

Using the substitution, $x = \sqrt{\beta a}$ and ΔK from Eq 8, Eq 10 takes the following form

$$N = 2a_i/C_0(\Delta K_0)^n](\beta a_i)^{n/2-1} \int_{\sqrt{\beta a_i}}^{\sqrt{\beta a_f}} e^{nx}/x^{n-1}\, dx \tag{11}$$

where

$$\Delta K_0 = E\alpha\, \Delta T_m/(1 - \nu) \sqrt{\pi a_i} \tag{12}$$

Equation 11 gives the number of cycles, N, required to extend a crack of a depth, a_i, to a depth, a_f, as a function of ΔT_m and β, which is related to the frequency of the temperature cycling, ω.

Numerical Results

For the purpose of illustrating the effects of frequency and temperature amplitude, we use typical initial and final flaw sizes. The typical values of a_i and a_f are taken as 2.5 mm and 2.8 mm, respectively.

TABLE 1—*Material properties used in fatigue crack growth analyses.*

Property	Value
Young's modulus, GPA	186
Density, kg/m^3	7750
Thermal conductivity, W/mK	40.45
Specific heat capacity, J/kgK	564.3
Coefficient of thermal expansion, /K	4.0×10^{-5}
Poisson's ratio	0.3

Three different frequencies of oscillating temperature distribution are considered, namely, 1, 5, and 10 Hz. The integral in Eq 11 is evaluated numerically for different limits characterized by β, which is related to the frequency.

Table 1 shows the various material properties used in fatigue crack growth analyses. The properties are for the SA106 Grade B material at 560 K.

Using these properties and noting that a_i = 2.5 mm, we obtain the following numerical relationship from Eq 12

$$0.09635\ \Delta T_m\ \mathrm{MPa}\sqrt{\mathrm{m}} \tag{13}$$

where ΔT_m is the temperature amplitude in K.

Using the crack growth law of the following form [4]

$$da/dN = 0.92 \times 10^{-5}\,(\Delta T_m)^{5.95}\ \mathrm{mm/cycle} \tag{14}$$

we have $C_0 = 1.2 \times 10^{-5}$ and $n = 5.95$.

Using the numerical values in Eq 14 and the expression for K_0 in Eq 13, as well as Eq 11, we have the number of cycles, N, required to propagate a crack from 2.5 mm to 2.8 mm, as

$$N = \begin{array}{ll} 7.053 \times 10^{10}\,(1.8\ \Delta T_m)^{-5.95} & \text{for } f = 1\ \mathrm{Hz} \\ 2.838 \times 10^{12}\,(1.8\ \Delta T_m)^{-5.95} & \text{for } f = 5\ \mathrm{Hz} \\ 2.338 \times 10^{13}\,(1.8\ \Delta T_m)^{-5.95} & \text{for } f = 10\ \mathrm{Hz} \end{array} \tag{15}$$

Figure 4 shows the temperature amplitude, ΔT_m, as a function of the number of cycles for three different frequencies of 1, 5, and 10 Hz. These values have been obtained from Eq 15.

Conclusions

The number of cycles required to propagate a crack exposed to the fluids with oscillating temperatures is predicted to be strongly dependent on the frequency of temperature cycling (Fig. 4). Whether a crack of a particular geometry and under a particular loading condition will grow or not depends on the threshold value of the reference stress intensity factor, ΔK_{th}, that is, of course, a function of the R-ratio and crack size. As long as the stress intensity factor exceeds ΔK_{th} (a material property), the procedure outlined in this work can be applied readily to crack growth studies in structures exposed to fluids with harmonically varying temperatures.

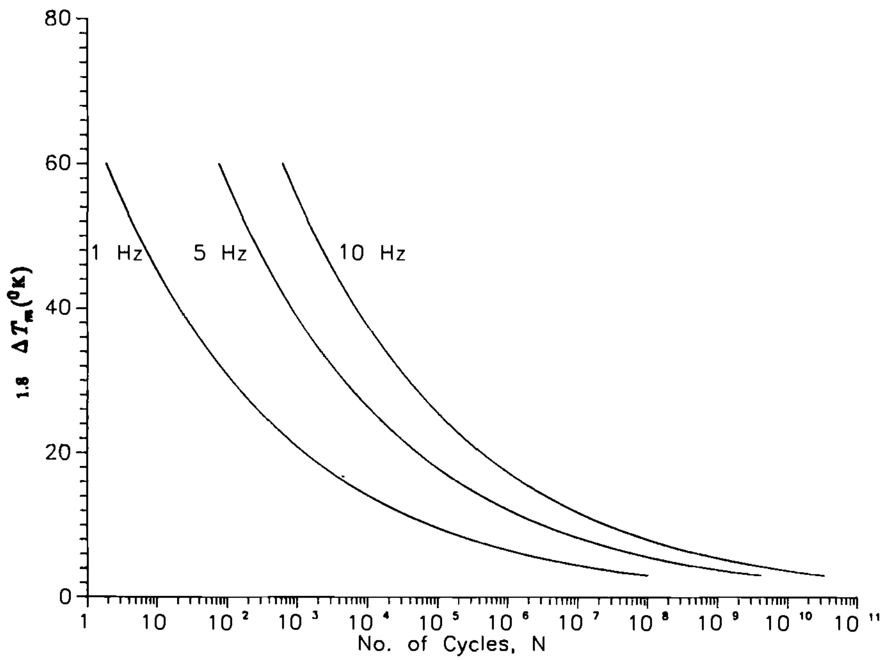

FIG. 4—*Temperature amplitude as a function of number of cycles.*

APPENDIX

Evaluation of the Integral to Determine the Stress Intensity Factor

The integral $\int_0^a (e^{-\beta x}/\sqrt{a^2 - x^2})\, dx$, from Eq 7 can be written as

$$\int_0^a \frac{e^{\beta x}}{\sqrt{a^2 - x^2}}\, dx = e^{-\beta x}\, |\sin^{-1} x/a|_0^a + \beta \int_0^a e^{-\beta x} \sin^{-1} x/a\, dx \tag{16}$$

The integral $\int_0^1 e^{-bz} \sin^{-1} z\, dz$, has been evaluated in Ref 5 and is given by

$$\int_0^1 e^{-bz} \sin^{-1} z\, dz = \pi/2b\, [I_0(b) - L_0(b)]$$

where $I_0(b)$ and $L_0(b)$ are the modified Bessel and Struve functions of zeroth order, respectively.

With the substitutions, $z = x/a$ and $b = a\beta$, Eq 16 gives us the required integral as

$$\int_0^a \frac{e^{-\beta x}}{\sqrt{a^2 - x^2}}\, dx = \pi/2e^{-\beta a} + \pi/2[I_0(\beta a) - L_0(\beta a)] \tag{17}$$

The numerical values on the right-hand side of Eq 17 obtained from Ref *6* are plotted in Fig. 3. Also shown is the plot of a simplified expression, $\pi e^{-\sqrt{\beta a}}$. Because of the closeness of the two functions, for all practical purposes

$$\int_0^a \frac{e^{-\beta x}}{\sqrt{a^2 - x^2}}\, dx \simeq \pi e^{-\sqrt{\beta a}} \tag{18}$$

References

[*1*] Poindexter, A. M., "Thermal Response of a Flat Plate of Finite Thickness Immersed in a Fluid with Oscillating Temperature," *Nuclear Technology,* Vol. 55, 1981, p. 650.
[*2*] *Handbook of Heat Transfer,* W. M. Rohsenow and J. P. Harnett, Eds. McGraw-Hill, New York, 1973.
[*3*] Lloyd, G. J. and Wood, D. W., "Fatigue Crack Initiation and Propagation as a Consequence of Thermal Striping," *International Journal of Pressure Vessels Piping,* Vol. 8, 1980, pp. 255–272.
[*4*] *ASME Boiler and Pressure Vessel Code, Section XI: Rules for Inservice Inspection of Nuclear Power Components,* American Society of Mechanical Engineers, New York, 1989.
[*5*] Ryshik, I. M. and Gradstein, I. S., *Tables of Series, Products and Integrals,* Academic Press, New York, 1964.
[*6*] Abramowitz, M. and Stegun, I. A., *Handbook of Mathematical Functions,* National Bureau of Standards, Washington, DC, 1964.

Frederic R. Deshayes[1] *and William H. Hartt*[1]

Development of a Fatigue Crack Growth Rate Specimen Suitable for a Multiple Specimen Test Configuration

REFERENCE: Deshayes, F. R. and Hartt, W. H., **"Development of a Fatigue Crack Growth Rate Specimen Suitable for a Multiple-Specimen Test Configuration,"** *Fracture Mechanics: Twenty-Third Symposium, ASTM STP 1189*, Ravinder Chona, Ed., American Society for Testing and Materials, Philadelphia, 1993, pp. 598–618.

ABSTRACT: A new experimental approach developed by fatigue crack growth rates can be determined for multiple specimens tested in series. This involves a geometry such that the response to cyclic loading in each specimen is mutually independent. Relationships between the stress intensity factor, compliance, and crack length and between direct-current potential drop and crack length have been analytically evaluated for the proposed specimen geometry. An appropriate side-groove depth that avoided crack deviation from the intended plane of extension was determined experimentally, and an analytical expression that accounted for reduced thickness in the crack plane was verified. Calibration curves between crack length and compliance and between crack length and potential drop were experimentally verified as well, and the stress intensity-crack length characteristics for the specimen were confirmed by comparing da/dN-ΔK_I curves with those for conventional C(T) specimens. A customized, five specimen frame was designed and fabricated in conjunction with a 98-kN MTS actuator and interfaced with a commercially available control system, the hardware and software of which were modified to accommodate multiple-specimen control and data acquisition. The utility of the proposed specimen and test procedure is discussed within the context of threshold and near-threshold crack growth rate determinations where long test times are normally required for data development, particularly for low cyclic frequency applications such as nuclear and offshore.

KEY WORDS: multiple-specimen testing, fatigue crack growth, stress intensity factor, compliance, tapered specimen, elastic analysis, finite element method, direct-current potential drop technique, side grooves, fracture mechanics, fatigue (materials)

The mechanical response characteristics of the compact tension, C(T), specimen, one of the two types recommended by ASTM Test Method for Measurement of Fatigue Crack Growth Rates (E 647-88a) [*1*], have been investigated extensively during the past two decades through analytical, numerical, and experimental analyses. These studies focused on relating the stress intensity factor and the compliance to crack length [*2–5*], three-dimensional determination of the stress and displacement fields in the vicinity of the crack tip [*6–9*], crack closure effects [*10,11*], crack path stability criteria [*12*], and the influence of side grooves on crack growth character [*6,7,9*]. Different stress-strain laws were considered, such as purely elastic, elastic-perfectly plastic, strain-hardening, and time-dependent responses. In addition, within the framework of the direct current potential drop technique (DCPD), whereby the electrical potential drop across the crack plane in association with a constant current flow in the speci-

[1] Graduate research assistant and director of Center for Marine Materials, respectively, Department of Ocean Engineering, Center for Marine Materials, Florida Atlantic University, Boca Raton, FL 33431–0991.

men is measured and related to crack length, relationships between crack length and potential drop for different-current input and potential lead locations have been published [13,14]. Based on the information obtained thus far, it is apparent that the C(T) specimen has evolved as one of the most commonly employed tools for fatigue crack growth rate testing. This has enabled the *da/dN* properties of numerous metallic materials to be characterized in the power-law regime (Region 2). However, data are more limited in Region 1 (near-threshold); and crack growth mechanisms are less understood, particularly in corrosive environments at low frequency. As an example, in a corrosive environment, the influence of frequency in the near-threshold regime remains controversial, whereas it is well established in Region 2 [15]. This is not only due to the complexity of crack growth processes but also to the time consumed by any corrosion fatigue experiment performed at low frequency. For example, at a crack growth rate of 10^{-7} mm/cycle and a cycling frequency of 0.1 Hz, more than three years is required for a crack to extend 1 mm; and this provides only four da/dN-ΔK_I data points according to the minimum crack extension analysis criterion [1].

For this reason a new experimental technique has been developed that involves concurrent fatigue crack-growth-rate testing of multiple specimens in series using a single actuator and frame. This approach is particularly appropriate for low-frequency, near-threshold situations, where determination of a single da/dN-ΔK_I curve might otherwise require a minimum of several months. The use of multiple C(T) specimens for accomplishing this is inappropriate, since the stress intensity factor range increases with increasing crack length (constant load amplitude or range); this dictates load shedding according to the specimen for which crack propagation is most rapid. The stress intensity factor range for the remaining specimens (smaller crack length) consequently decreases to low values and may even fall to below ΔK_{Ith}, such that little or no information is obtained from them. To overcome this difficulty, a specimen geometry, for which the stress intensity factor decreases with increasing crack length at constant load, has been developed. Load shedding is, therefore, not necessarily required to reduce ΔK_I during the test; therefore, the specimens respond to cyclic loading in a manner that is mutually independent. Also, if the crack in one specimen extends to a length exceeding that for the others, its growth rate decreases to a lower value such that stability is maintained. The purpose of the present paper is to present this specimen design and test procedure and to provide experimental data that substantiate the approach.

Specimen Design

Background

The following description addresses only Mode I crack propagation, and, consequently, the index, I, has been omitted. Mostovoy et al. proposed a side-grooved, tapered, double-cantilever-beam specimen geometry of gross thickness, B, and net crack plane thickness, $B_n = 0.8B$, for plane-strain fracture toughness determination [16]. This specimen was reported to have a crack-length-independent stress-intensity factor over a prescribed interval. It was anticipated by the present authors that this geometry could be modified to provide a decreasing stress intensity factor specimen. More specifically, an analysis was performed that focused on the role of different geometric parameters for the tapered specimen on the K-versus-a profile. Figure 1 illustrates these as:

α = taper angle,
l_1 = neck width,
l_2 = taper width, and
W = total width.

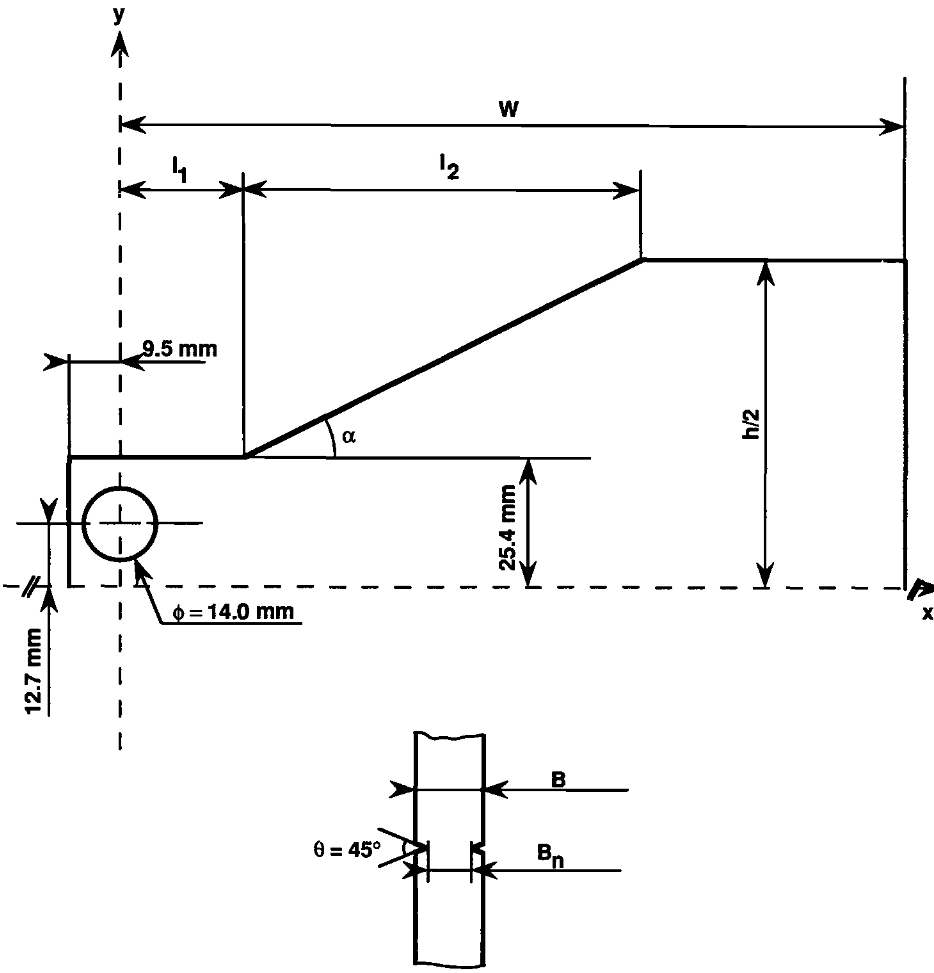

FIG. 1—*Generalized representation of one-half of the proposed specimen.*

The dimensions employed by Mostovoy et al. for their specimen were l_1 = 25.4 mm (1.00 in.), l_2 = 84.6 mm (3.33 in.), W = 139.7 mm (5.50 in.), and a taper angle that varied between 20.4° and 31.0°. For the present analysis, the arm height was 25.4 mm (1.00 in.), and the loading hole diameter was 10% larger than the pins to minimize friction and allow rotation of the specimen during testing. In an initial design, the specimen was ungrooved and B was 12.7 mm (0.50 in.). In a K-versus-a profile determined for a particular set of α, l_1, l_2, and W values and presenting a decreasing region, the highest and lowest stress intensity factors (SIFs) bounding this region were termed SIF_{high} and SIF_{loow} and the corresponding crack lengths, a_{high} and a_{low}. Based on the different tapered specimen geometries that were studied and that provided information on the role of each of the four geometric parameters on the decreasing-K character, a particular set of α, l_1, l_2, and W values were selected such that the load-shedding ratio

$$D(\alpha, l_1, l_2, W) = (\text{SIF}_{\text{high}} - \text{SIF}_{\text{low}})/\text{SIF}_{\text{high}} \tag{1}$$

was at least 0.5, thereby minimizing or eliminating the necessity for externally controlled load reduction during any fatigue crack growth test in the near-threshold regime, and that the crack length range

$$\Delta a(\alpha, l_1, l_2, W) = a_{low} - a_{high} \tag{2}$$

over which K decreased was sufficiently wide to provide an acceptable number of data points. The MARC two-dimensional finite element program was used to determine K (stiffness derivative technique). In the case studied, $B_n = B$. One half of the specimen was modeled by plane-stress second-order isoparametric eight-node elements, and, around the crack tip, triangle-shaped elements with side nodes placed at the one-quarter rather than the midpoints were used to reproduce numerically the $1/\sqrt{r}$ singularity [17]. Young's modulus, E, was taken as 205 GPa and Poisson's ratio, ν was 0.3. To model the undersized pin, a radial load, P, of 1000 N acting uniformly over a 45° arc was applied to the hole faces [3]. Displacement in the y-direction was set to zero along the unbroken ligament. Displacement in the x-direction was taken as zero at the crack tip to avoid a rigid body motion solution in the x-direction.

Results

K was first computed for a specimen with the same l_1, l_2, W, and base height as proposed by Mostovoy et al. (constant taper angle = 24.3°). Subsequently, a smaller taper angle (α = 10°) and four higher angles (30, 40, 55, and 70°) were considered (l_1, l_2, and W unchanged). Figure 2*a* illustrates the effect of taper angle, α, on the KB/P-versus-a profile. Correspondingly, Fig. 2*b* shows the relationship between D and α and Fig. 2*c* between Δa and α. This verifies the constant-K characteristic predicted by Mostovoy et al. with crack lengths between approximately 30 and 50 mm. Comparison of these different curves demonstrates that the value for K and the K-gradient at a given a is dependent sensitively on α when α is small and that the K gradient changes from positive to negative with increasing α. Based upon this, as α of 70° was selected that provided a load-shedding ratio (Eq 1) of about 0.25. Next, the effect of specimen width, W, on the K-versus-a profile was investigated. Figure 3 shows the influence of W on the KB/P-versus-a relationship (l_1 = 25 mm (1.00 in.), l_2 = 85 mm (3.33 in.), and α = 70°). This reveals width to be an important contributor to the decreasing stress intensity character of the specimen. Thus, SIF_{low} varies inversely with W, whereas SIF_{high} is not affected. A value of 216 mm (8.50 in.) was adopted for the total specimen width, which provided a decreasing K between a_{high} = 20 mm and a_{low} = 67 mm, and a load-shedding ratio of about 0.45. However, this value of W, in association with a taper angle of 70° and a taper width of 85 mm (3.33 in.), results in a large specimen size. Consequently, the effect of reduced l_2 on the K gradient was investigated in order to possibly reduce specimen height, h (see Fig. 1). Figure 4 illustrates the significance of l_2 on stress intensity for α = 70°, l_1 = 25 mm (1.00 in.), and W = 216 mm (8.50 in.). This reveals little or no influence of this parameter on K as long as ($l_1 + l_2$) is greater than a_{low} (previously determined for l_2 = 85 mm). Consequently, l_2 was set to 38 mm (1.50 in.) so that a_{low} was approximately equal to ($l_1 + l_2$), and α was increased slightly to 73.3° to adjust the specimen height to 305 mm (12.00 in.).

Figure 5 presents curves of KB/P versus a for different values of l_1 and the influence of l_1 on D and Δa. This reveals higher K-values and steeper K-versus-a gradients as l_1 increases. The D-versus-l_1 graph exhibits a maximum of 0.62 at l_1 = 72 mm (2.80 in.), for which Δa is equal to 46 mm, whereas the Δa-versus-l_1 plot shows a maximum of 48 mm at l_1 = 53 mm (2.10 in.), where D is 0.61. As D for both cases (l_1 = 72 mm and l_1 = 53 mm) was above 0.50 (considered to be the minimum load-shedding ratio necessary for complete determination of

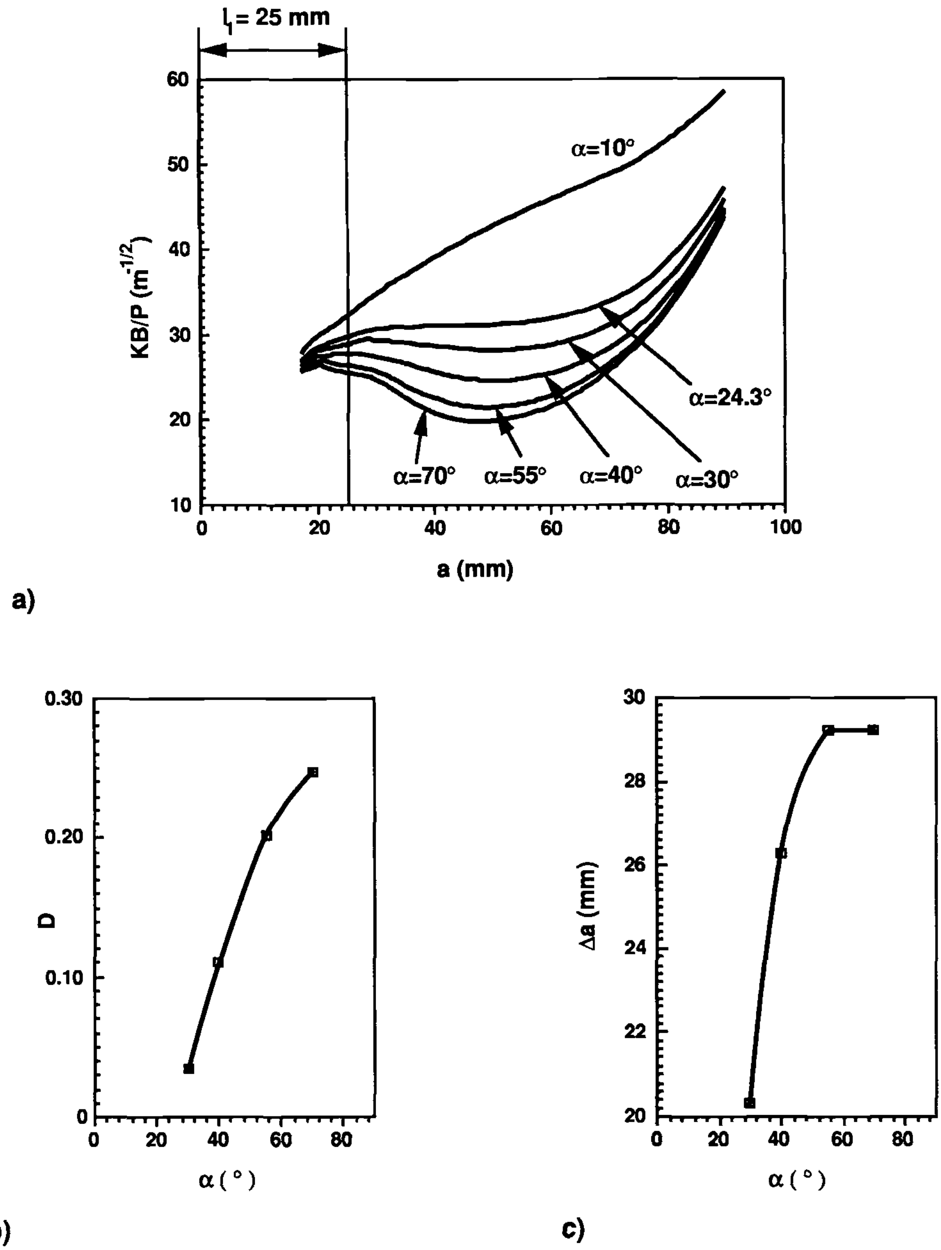

FIG. 2—*Effect of taper angle on* (a) K *versus* a, (b) *load-shedding ratio, and* (c) *crack length range over which* dK/da < 0 *(l_1 = 25 mm, l_2 = 85 mm, and* W = *140 mm).*

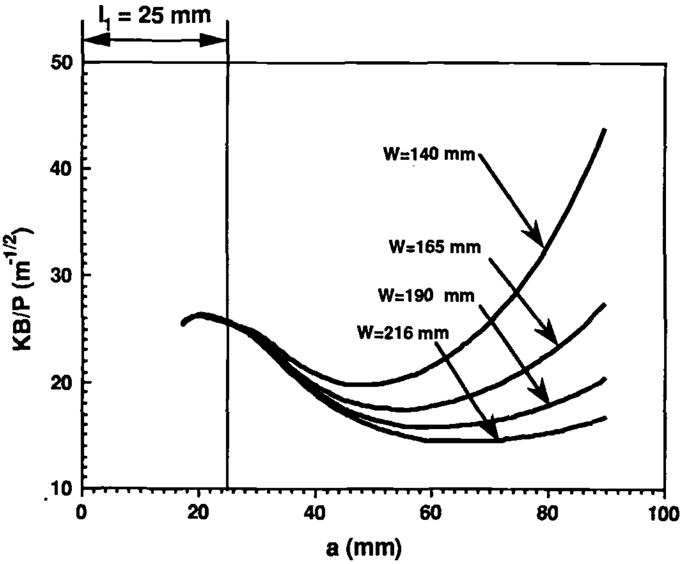

FIG. 3—*Effect of total width on* K *versus* a, *(α = 70°,* l_1 *= 25 mm, and* l_2 *= 85 mm).*

fatigue crack growth rates in the near-threshold regime), the configuration providing the maximum crack length range was adopted; and l_1 was therefore set to 53 mm (2.10 in.).

Based upon these results, a specimen geometry with α = 73.3°, l_1 = 53.3 mm (2.10 in.), l_2 = 38.1 mm (1.50 in.), and W = 215.9 mm (8.50 in.) was chosen. A V-notch was added, and this extended by electro-discharge machining (EDM) using a 0.50-mm-diameter wire to give an initial crack length of 37 mm and a tip radius of approximately 0.25 mm, as recommended

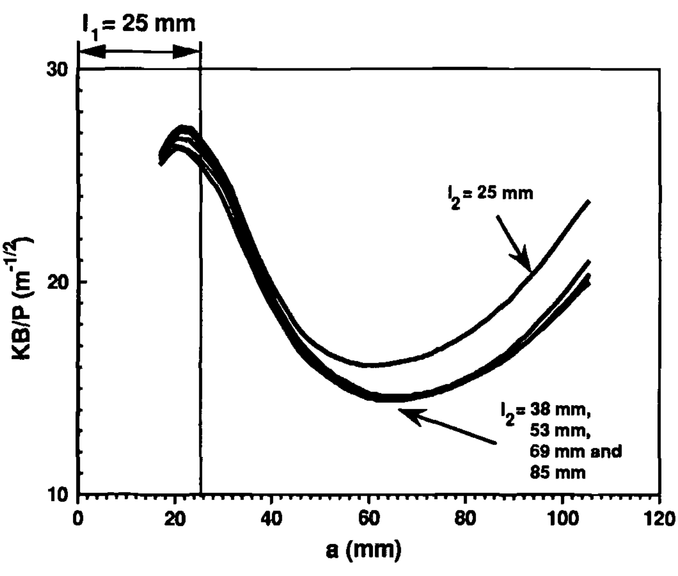

FIG. 4—*Effect of taper width on* K *versus* a, *(α = 70°,* l_1 *= 25 mm, and* W *= 216 mm).*

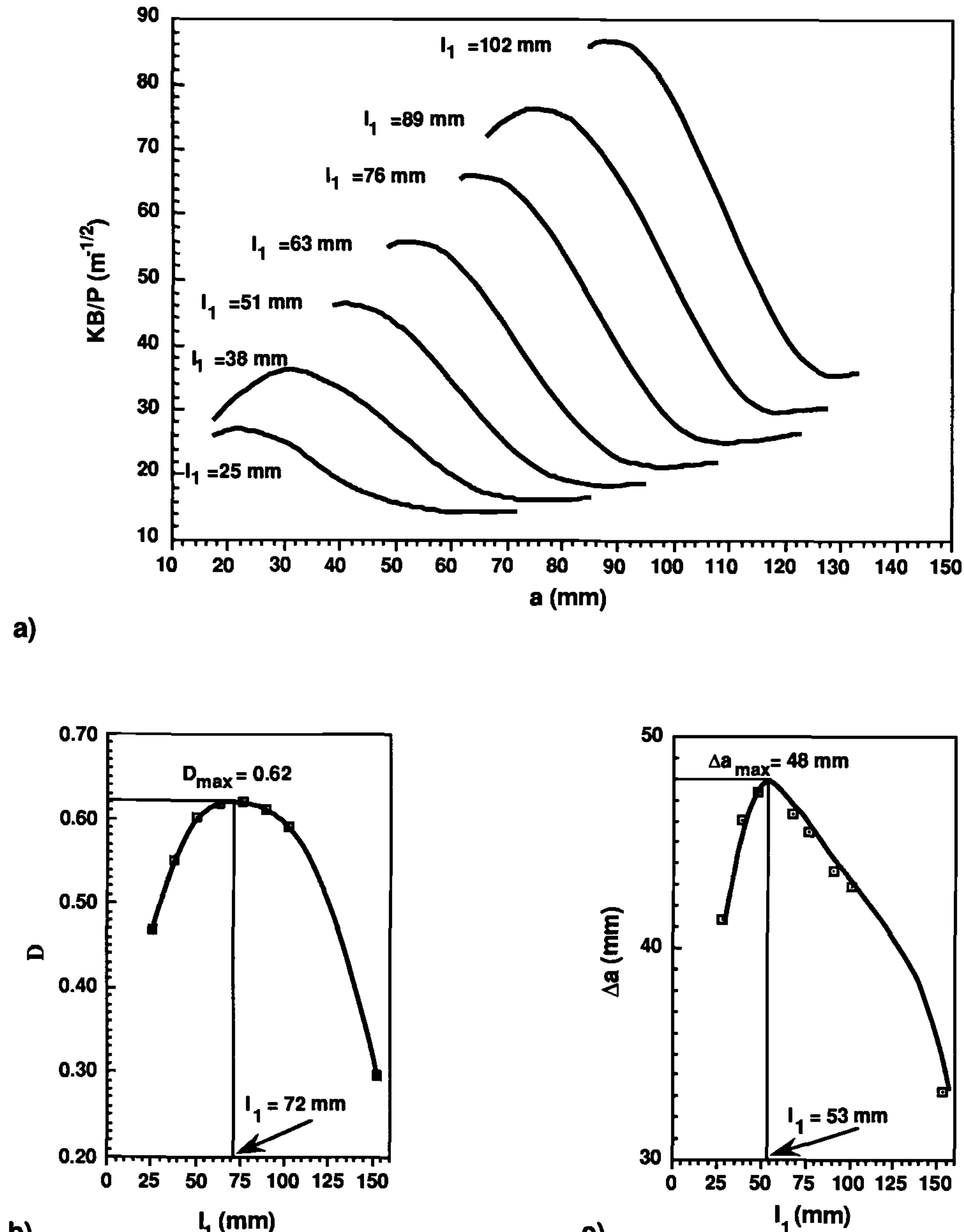

FIG. 5—*Effect of neck width on* (a) K *versus* a, (b) *load-shedding ratio, and* (c) *crack length range over which* dK/da < 0 *(*$\alpha = 73.3°$, $l_2 = 38$ *mm, and* W $= 216$ *mm).*

by ASTM E 647-88a for the particular case of high-strength steels [1]. Figure 6 presents the proposed specimen geometry, and Fig. 7 gives the corresponding relationship between KB/P and a as recomputed considering the presence of the V-notch. No significant difference was found in the K-versus-a relationship when the V-notch was taken into account. A load-shedding ratio of 0.61 between $a_{\text{high}} = 44$ mm and $a_{\text{low}} = 91$ mm is inherent to this geometry, and this was considered sufficient to provide near-threshold da/dN-ΔK information independent of externally imposed load shedding. This is not to preclude, of course, the possibility of

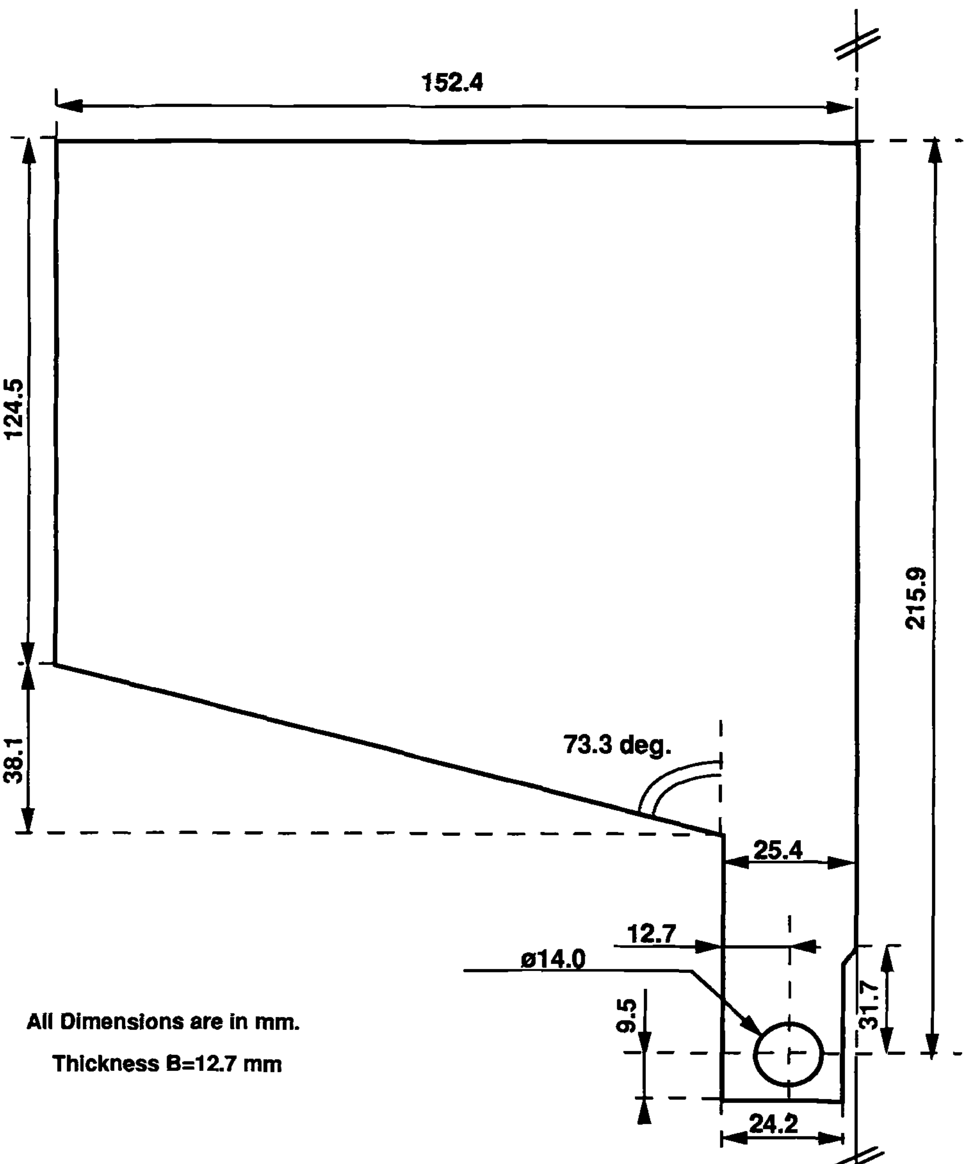

FIG. 6—*Proposed specimen geometry (α = 73.3°, l_1 = 53.3 mm, l_2 = 38.1 mm, and W = 215.9 mm).*

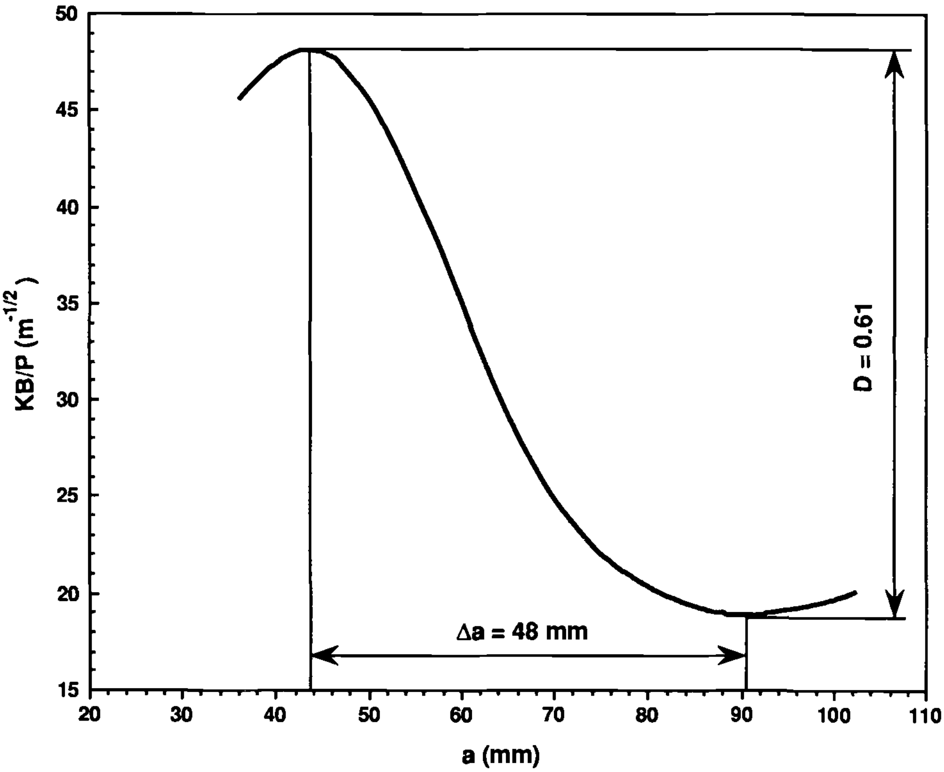

FIG. 7—*Relationship between stress intensity factor and crack length for the proposed specimen geometry.*

including load shedding in a test protocol. While the preceding analysis has not determined the explicit, optimized maximum values for D and Δa, the specimen geometry in Fig. 6 does provide acceptably large values for these parameters in view of other limitations (width, for example).

Side-Groove Effects

Mostovoy et al. reported for the tapered specimen they designed that, in the absence of side grooves, the crack might deviate from the desired plane of extension and fracture one of the specimen arms, but that side-grooves of $B_n = 0.8B$ thickness and included angle, $\theta = 45°$, maintained the crack in the center plane [*16*]. Even if analytical crack stability criteria were developed based on comparisons between nominal bending stresses in the arm and the ligament computed by the beam theory [*12,16,18*], side-groove depth determination is essentially an experimental task. Consequently, one ungrooved specimen and six specimens of various side-groove depths and included angles were fabricated from a 12.7-mm (0.50 in.) thick plate of cold-rolled 1018 steel, according to the dimensions in Fig. 6, and fatigue loaded in air at constant maximum load, P_{max}, and load ratio, R, to determine an appropriate side-groove configuration. The side-groove geometry and test results presented in Table 1 show that crack deviation occurred from the outset for the ungrooved specimen that led to breaking off of one the specimen arms. It was also observed that for relatively shallow side grooves (Specimens 2 to 4) the crack propagated straight, initially, but then deviated from the side-grooved plane at some critical length (see Table 1). However, for the more severe side-groove geometries (Specimens 5 to 7), crack propagation remained straight until a length of at least a_{low} (91 mm). This demonstrated that a normalized side-groove depth, B_n/B, of 0.70 and an included side-groove angle of 45° were adequate to maintain the crack in the intended orientation, and these values were employed in the final specimen design.

Because of the reduction in thickness in the crack plane when side-grooves are present, the stress intensity factor is larger than for an ungrooved specimen. Assuming that specimen compliance is not affected by the presence of side grooves, the stress intensity factors without and with side grooves are expressed, respectively, by

$$K^2 = \frac{E'P^2}{2B}\frac{\partial C_p}{\partial a} \tag{3}$$

and

$$K'^2 = \frac{E'P^2}{2B_n}\frac{\partial C_p}{\partial a} \tag{4}$$

where

K = stress intensity factor at a given crack length for a specimen without side grooves;
K' = stress intensity factor for the same specimen and crack length but with side grooves;
E' = E in-plane stress and $E/(1 - \nu^2)$ in-plane strain;
C_P = specimen compliance measured along the load line, m/N; and
E = Young's modulus, Pa.

K' is then related to K by the relationship

$$K' = \frac{K}{\sqrt{\dfrac{B_n}{B}}} = 1.195K \quad \text{if} \quad \frac{B_n}{B} = 0.7 \tag{5}$$

Experimental results are presented subsequently that confirm the appropriateness of Eq 5, where the main assumption is that the side groove-independent character of the proposed specimen compliance is maintained when $B_n/B = 0.70$.

TABLE 1—*Side-groove depths and included angles, loading conditions, and critical crack lengths.*

Specimen Number	B_n/B, θ	P_{max}, R	Critical Crack Length for Deviation from Groove Plane
1	1.00,/	7 kN, 0.35	no straight crack propagation
2	0.92, 60°	7 kN, 0.35	52 mm
3	0.88, 60°	7 kN, 0.35	60 mm
4	0.80, 60°	8 kN, 0.30	65 mm
5	0.72, 45°	11 kN, 0.50	>91 mm
6	0.64, 45°	11 kN, 0.50	>91 mm
7	0.58, 45°	11 kN, 0.50	>91 mm

Determination of Crack Length by the DCPD Technique

Consistent with historical experimental and analytical approaches [*14*], the crack length of the proposed specimen was evaluated in terms of current leads that were centered along the load line and potential leads across the notch. This arrangement was assumed to provide, as in the case of the standard C(T) specimen, both good reproducibility and sensitivity. A current, I, of 10 A was applied, and material conductivity, k, was assumed to be 0.2 $\mu\Omega \cdot$m, which represents an average value found in the literature for low carbon steel [*19*]. The potential field in the proposed specimen was evaluated in two dimensions by employing the MARC-HEAT finite element heat-flow program. Both heat and current flow conform to the same steady-state equation; and heat-flow programs can, therefore, be used to determine the potential field in a specimen with a current flowing into it. As for the previous analysis, only one half of the proposed specimen was studied and eight-node isoparametric elements were employed. Because of the two-dimensional character of the analysis, side grooves were not considered. Temperature (potential) was set to zero along the unbroken ligament plane, and Current I was applied as a heat flux on the area of the specimen in contact with the current input wire. This area was assumed to be a rectangle of size 10.0 mm $\times$ 12.7 mm.

The initial potential drop corresponding to the EDM machined crack (37 mm) was termed V_0. Figure 8 presents a schematic of the DCPD instrumented specimen with the current and potential lead locations and plots crack length-versus-normalized potential drop, V/V_0, for the proposed specimen along with the published calibration curve for two C(T) specimens, one of total width, $W = 100$ mm, and the other of the same total width as the proposed specimen (216 mm). The calibration curve for the proposed specimen geometry was patterned after Ref *14* and may be approximated by a third-degree polynomial according to

$$\frac{a}{W} = -0.40359 + 1.1115\left(\frac{V}{V_0}\right) - 0.75815\left(\frac{V}{V_0}\right)^2 + 0.22024\left(\frac{V}{V_0}\right)^3 \tag{6}$$

or in reverse notation

$$\frac{V}{V_0} = 2.9572 \cdot 10^{-2} + 6.8032\left(\frac{a}{W}\right) - 6.9683\left(\frac{a}{W}\right)^2 + 1.8274\left(\frac{a}{W}\right)^3 \tag{7}$$

where 37 mm $\leq a \leq$ 102 mm. It is observed from Fig. 8 that the curvature of the a-versus-V/V_0 curve for the proposed specimen is reversed compared to the classic C(T) specimen. Consequently, the sensitivity dependence of the DCPD technique on a is different for the two specimens. If the absolute and relative sensitivities, respectively, for the a-versus-V/V_0 trend are defined by

$$\text{Abs}\,(a) = \frac{\dfrac{\Delta V}{V_0}}{\Delta a} \tag{8}$$

and

$$\text{Rel}\,(a) = \frac{\dfrac{\Delta V}{V}}{\Delta a} \tag{9}$$

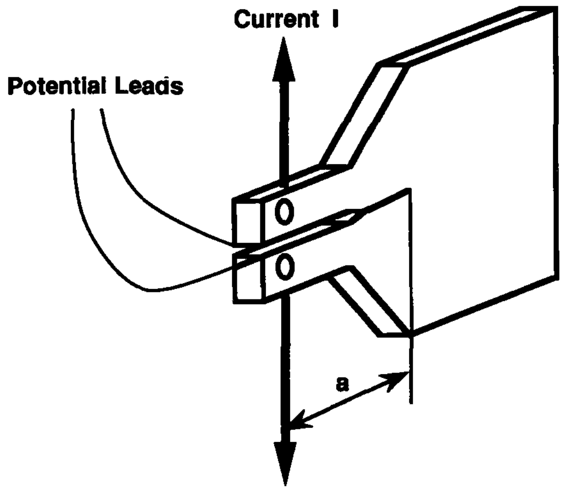

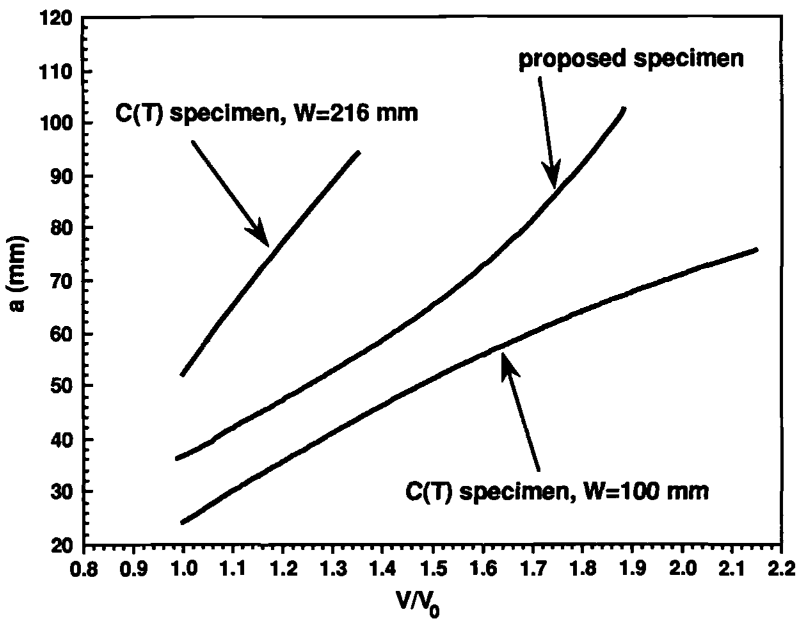

FIG. 8—*Relationship between crack length and normalized potential drop for the proposed specimen and two C(T) specimens.*

where Δa = change in crack length (mm) and ΔV = corresponding change in potential drop (V), then Fig. 9 shows the dependence of Abs and Rel on a for the proposed specimen geometry and the C(T) specimen geometry with two different widths. The general trend is one of better sensitivity for the proposed specimen than for the C(T) specimen having the same width to approximately 90 mm, as far as absolute sensitivity is concerned, and 78 mm for relative sensitivity. This is due to the fact that for small crack lengths the tapered specimen height, h,

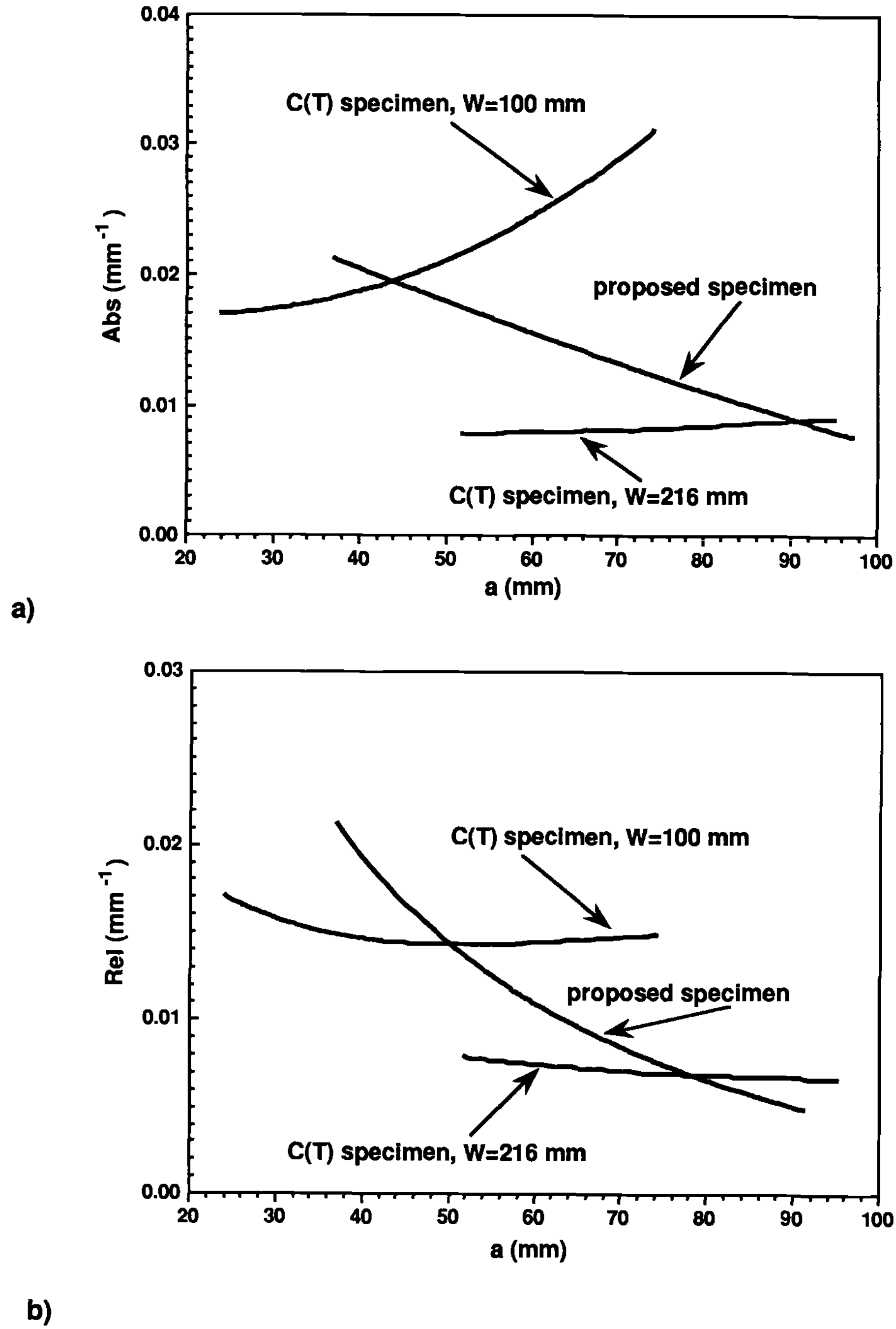

FIG. 9—*Relationship between* (a) *absolute sensitivity and* (b) *relative sensitivity and crack length for the proposed specimen and two C(T) specimens.*

is smaller than the 216-mm-wide C(T) specimen (height $1.2W = 259$ mm), whereas the opposite is true for long cracks. Another effect of the tapered height is that both functions, Abs and Rel, decrease progressively with increasing crack length, whereas Abs increases and Rel first decreases and then increases when C(T) specimens are considered.

Experimental Verification of the Analytical Expressions $C_P = f(a)$, a $= f(V/V_0)$, and $K = f(a)$

To confirm the calculated K-versus-a and V/V_0-versus-a trends, two specimens, one with side grooves ($B_n/B = 0.70$ and $\theta = 45°$) and the other ungrooved, were machined according to the geometry in Fig. 6 from the same cold-rolled steel plate mentioned earlier. These were progressively saw-cut to different crack lengths in 5 mm increments. Maximum and minimum loads were applied in the range 0 to 9 kN, and deflection was measured with a clip gage placed at the front of the specimen arms across the notch. In addition, potential drop was measured as described earlier. In this manner, compliance was measured as a function of crack (actually, saw-cut) length. Potential drop measurements were corrected for temperature variations by using a reference specimen, and measurements were taken while reversing the current flow to account for thermal electromotive forces.

Effect of Side-Grooves on Specimen Compliance

Figure 10 presents compliance data as a function of crack length for both the smooth and side-grooved, tapered specimens along with plane stress compliance obtained through the finite element analysis of the stress intensity factor. A good correlation between predicted and experimental data to about a 70 mm crack length was observed, beyond which compliance determined by the finite element analysis was lower. This difference could be a consequence of the amount of material removed by saw-cutting the specimen, which would lead to a larger arm deflection than expected compared to when an actual crack is present. In addition, the computed curve assumes a plane stress state with a Young's modulus of 205 GPa, which is not necessarily an exact value for the tested steel plate. However, no difference was observed between ungrooved and side-grooved specimen compliances, and so the principle assumption on which Eq 5 is based was verified. As a consequence, valid da/dN-ΔK data can be generated with this side-grooved specimen, as it demonstrated subsequently.

During fatigue crack growth testing with the proposed side-grooved, tapered specimen, crack bowing was observed with the through-thickness curvature of the crack in the direction of propagation. Figure 11 schematically compares this crack curvature with the one usually observed for ungrooved C(T) specimens. This was due to the stress singularity developed by the side-grooves at the outer edges of the crack tip that curved the crack front so that the local stress intensity factor was constant along it [*6–9*]. The crack curvature correction recommended by ASTM E 647-88a was used to account for the larger crack length near the side-grooves than at the specimen center (a difference of about 1 mm was observed for $B_n/B = 0.70$), and K was calculated at this average crack length. A more appropriate procedure may be, however, to base the analysis on the crack length at the midthickness.

Crack Length versus Potential Drop

Figure 12 presents the experimental values for V/V_0 as a function of normalized crack length, a/W, for both the smooth and side-grooved specimens along with the calibration relationship previously presented in Fig. 8. A good correlation of V/V_0 for the finite element analysis compared to the experimental results is apparent with no side-groove influence. However,

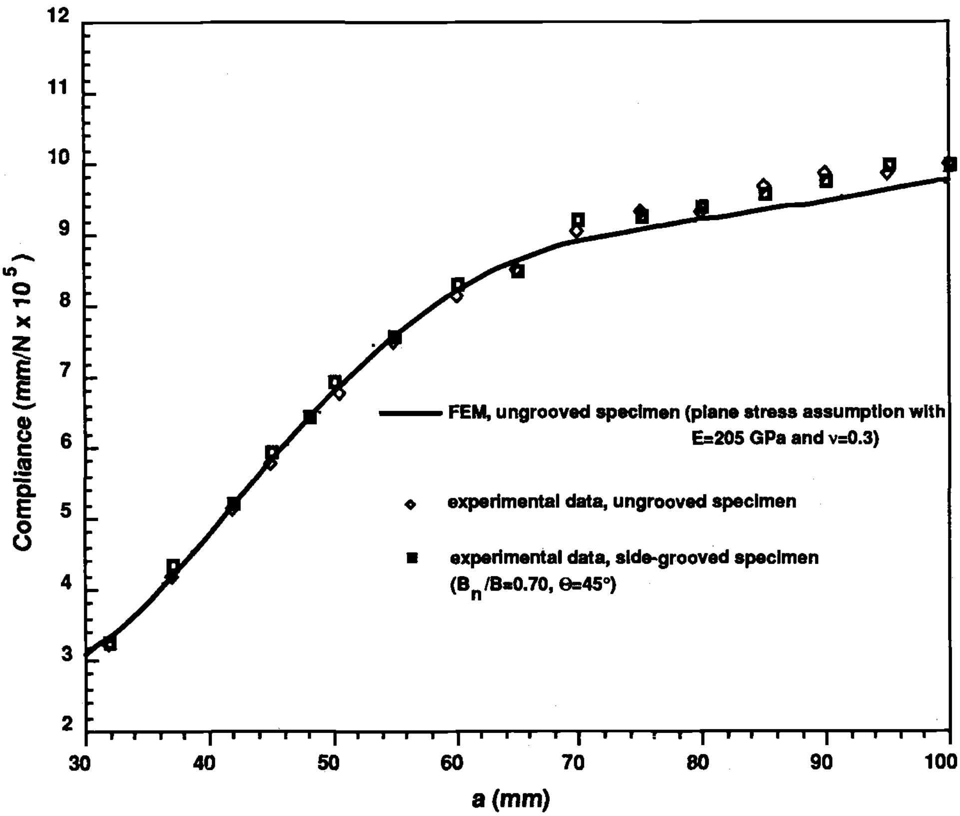

FIG. 10—*Relationship between compliance (numerically and experimentally determined) and crack length for the proposed specimen geometry.*

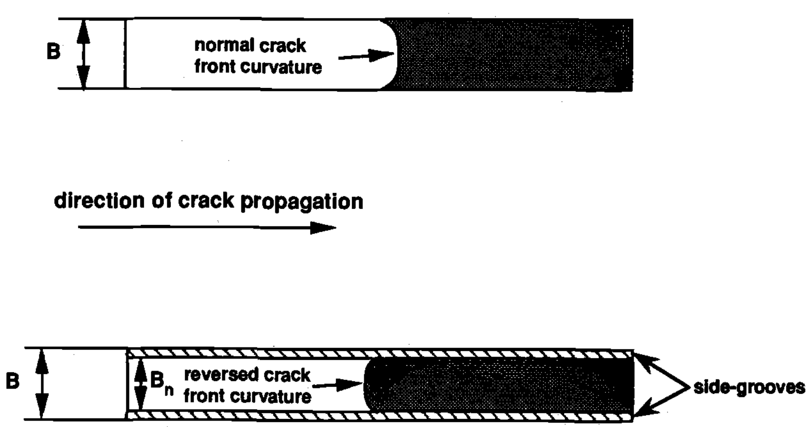

FIG. 11—*Schematic representation of crack bowing for an ungrooved and a side-grooved specimen.*

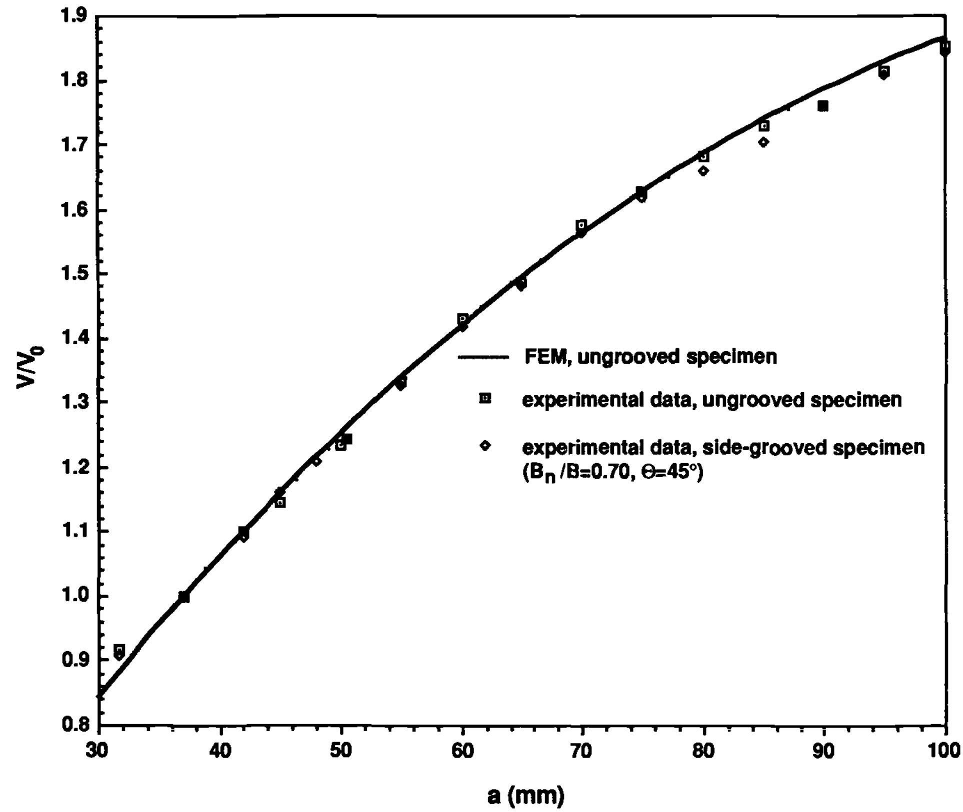

FIG. 12—*Relationship between normalized potential drop (numerically and experimentally determined) and crack length for the proposed specimen geometry.*

because the midplane of the specimens employed for DCPD measurements was saw-cut, the cut surfaces were not in contact. During actual crack propagation, electrical contact occurs between the two crack surfaces, and this may lead to an underestimation of crack length by the DCPD technique. To quantify this shorting effect, beach marks were made during crack growth testing on tapered Specimens 3 to 7 (see Table 1) by decreasing the maximum load during a crack length increment of 1 mm. When the experiments were completed, the crack length (a_{visual}) corresponding to these marks was measured and compared to that determined from the DCPD technique, as shown in Table 2. Underestimation by approximately 0 to 4.6 mm was confirmed depending on crack length, load ratio, and side-groove configuration. A technique involving post-test calibration must, therefore, be included to accurately project crack growth rate as a function of stress intensity factor range. In the present experiments, a classic linear interpolation based upon optical measurements on the crack faces was used to correct DCPD determined crack length, and then the crack growth rate and the stress intensity factor range were calculated from this.

Stress Intensity Factor versus Crack Length

The relationship between the stress intensity factor and the crack length (Fig. 7) and Eq 5 was verified by comparing, under the same loading conditions, crack growth rates obtained

TABLE 2—*Comparison between crack length measured by the DCPD technique during crack propagation and crack length visually observed by marking the crack surface.*

Number	a_{DCPD}, mm	a_{visual}, mm	Error ($a_{visual} - a_{DCPD}$), mm
3	44.9	47.8	2.9
4	48.2	52.8	4.6
5	55.1	57.6	2.5
	58.5	62.2	3.7
	65.8	69.1	3.3
6	59.7	60.6	0.9
	63.3	64.2	0.9
	71.4	71.5	0.1
7	62.2	63.6	1.4
	65.0	66.2	1.2
	73.2	73.5	0.3

from tapered Specimens 5 through 7 and from a conventional C(T) specimen 102 mm wide and fabricated from the same cold-rolled steel plate. Specimens 5 through 7 were simultaneously tested in series. Figure 13*a* plots the shorting effect of uncorrected da/dN-ΔK data for Specimens 5 through 7 compared to those for the C(T) specimen and shows specimen-to-specimen differences at low ΔK. In this figure, ΔK was computed according to Eq 5. Figure 13*b* shows the same data with tapered specimen results corrected for the shorting effect, but without using Eq 5 to take into account the side-groove presence. Relatively large differences are apparent due to stress intensity factor underestimation for the tapered specimens. Finally, Fig. 13*c* shows the same results corrected for the shorting effect and considering the presence of side grooves (Eq 5). On this basis, all data conform to a single band. Comparing of these results, it appears that the linear interpolation, used to correct the DCPD data for the shorting effect, and Eq 5, used to consider the presence of side grooves, provides a satisfactory approach to fatigue crack growth rate testing using the proposed specimen and that valid da/dN-ΔK data can be generated.

Experimental Setup for Multiple Specimen Testing

The experimental approach developed for corrosion fatigue testing of multiple specimens loaded in series is based on a specially configured, multiple-station frame and a DCPD data acquisition system. The frame was operated in conjunction with a 98-kN MTS actuator, closed-loop servo-hydraulic control system, and a DCPD data acquisition system. The control and data acquisition system hardware and software, initially developed by Fracture Technology Associates for three specimens, were modified to test a maximum of six specimens in series by adding a three-channel multiplexer to switch back and forth between two specimens. A schematic of the overall testing system is shown in Fig. 14. This specific system could be expanded to accommodate six additional specimens. A constant current (10 A) supplied by the d-c source passes through six specimens, five of which are under fatigue loading and one is a reference specimen. Current flow is reversed every five cycles to account for thermal electromotive forces, and measurements made on the reference specimen are used to correct the potential drop for temperature fluctuations on the active specimens. Figure 15 shows

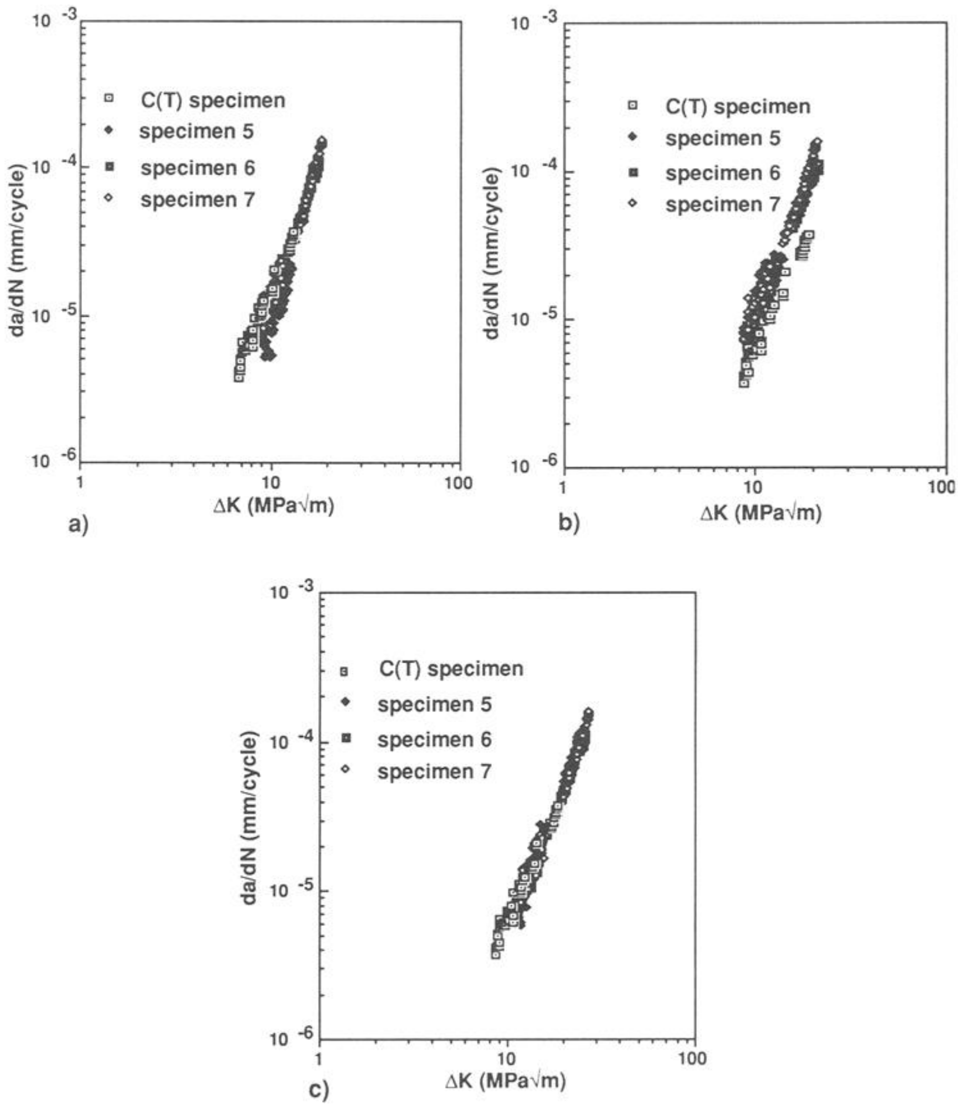

FIG. 13—*Comparison of* da/dN-ΔK *relationships obtained from three tapered specimens and one C(T) specimen* (a) *without shorting effect correction but with considering the side grooves,* (b) *with shorting effect correction but without considering the side grooves, and* (c) *with both corrections.*

five tapered specimens loaded in series for corrosion fatigue crack-growth-rate testing in seawater.

Conclusion

1. Specimen characteristics relevant to crack growth rate testing have been determined for a constant taper, side-grooved, compact-tension geometry designed to present a negative *K*-gradient at constant load over a prescribed crack length interval.

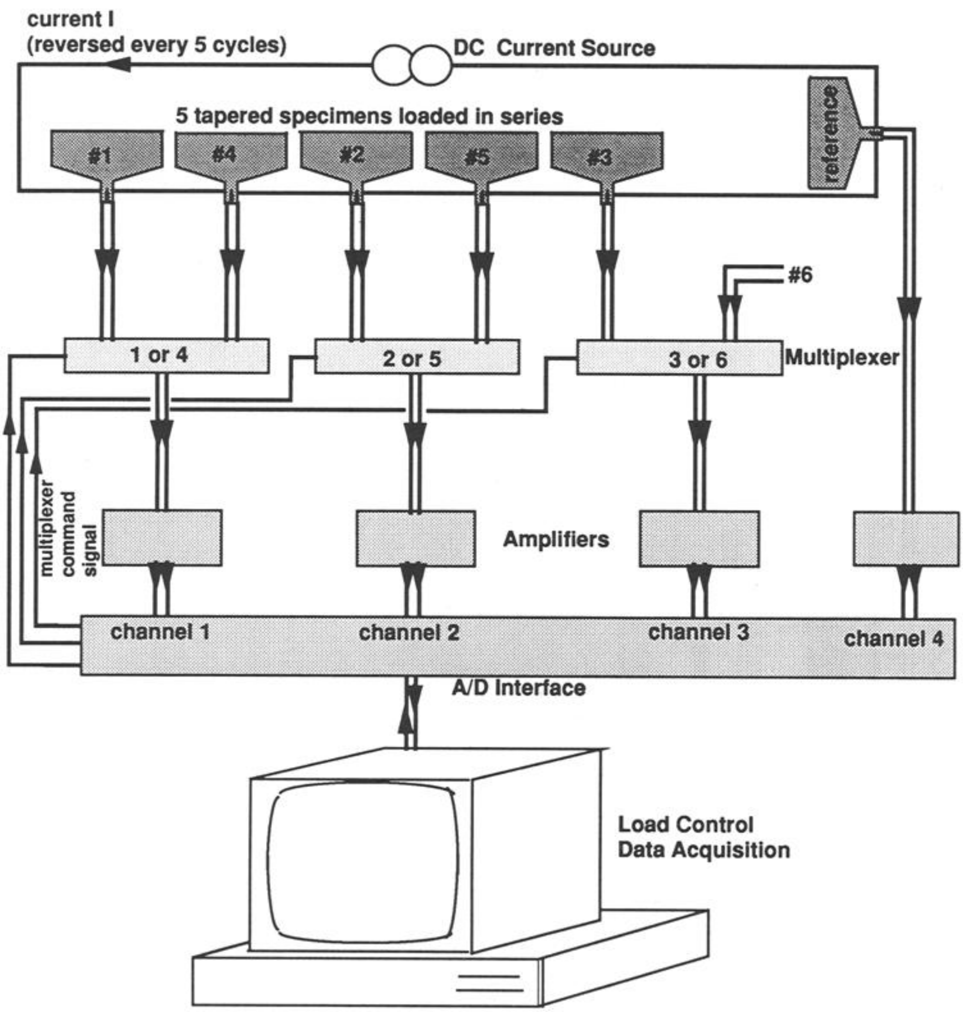

FIG. 14—*Schematic representation of the experimental setup for multiple-specimen testing.*

2. Compliance-crack length, DCPD-crack length, and stress intensity factor-crack length expressions numerically determined by two-dimensional finite element analysis were experimentally verified.
3. The same da/dN-ΔK curve was obtained for the proposed specimen and for a standard C(T) specimen loaded in air under the same conditions after correcting the tapered specimen data for the presence of side grooves and DCPD shorting that occurred due to contact between the crack surfaces.
4. The proposed, tapered-type specimens tested in series (multiple specimen testing) responded to cyclic loading in a manner that was mutually independent. This is particularly advantageous for low-frequency long-life testing, where determination of a single da/dN-ΔK curve might otherwise require a minimum of several months.

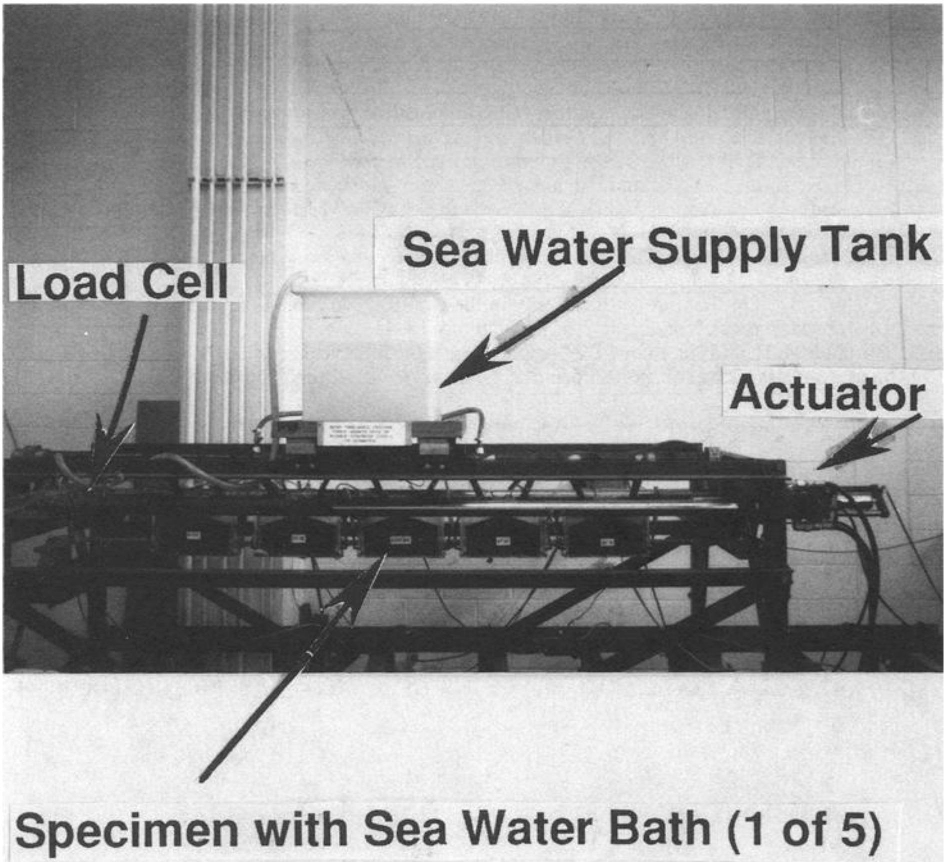

FIG. 15—*General view of the loading frame with five specimens under test.*

References

[1] ASTM Test Method for Measurements of Fatigue Crack Growth Rates, (E 647-88a) *Annual Book of ASTM Standards,* American Society for Testing and Materials, Philadelphia, 1988, pp. 636–654.
[2] Srawley, J. E., "Wide Range Stress Intensity Factor Expressions for ASTM E399 Standard Fracture Toughness Specimens," *International Journal of Fracture Mechanics,* Vol. 12, No. 3, June 1976, pp. 475–494.
[3] Newman, J. C., Jr., "Stress Analysis of the Compact Specimen Including the Effects of Pin Loading," *Fracture Analysis (Eighth Conference), ASTM STP 560,* American Society for Testing and Materials, Philadelphia, 1974, pp. 105–121.
[4] Saxena, A. and Hudak, J. J., "Review and Extension of Compliance Information for Common Crack Growth Specimens," *International Journal of Fracture,* Vol. 14, No. 5, Oct. 1978, pp. 453–468.
[5] Papaspyropoulos, V. and Ahmad, J., "On Modified Compact Tension Test Specimens," *Engineering Fracture Mechanics,* Vol. 14, No. 1, 1980, pp. 227–232.
[6] Riedel, H., *Fracture at High Temperatures,* B. Ilschner and N. J. Grant, Eds., Springer-Verlag, Berlin, 1987.
[7] Delorenzi, H. G. and Shih, C. F., "3-D Elastic-Plastic Investigation of Fracture Parameters in Side-Grooved Compact Specimen," *International Journal of Fracture,* Vol. 21, No. 3, March 1983, pp. 195–220.

[8] Smith, A. P., Towers, O. L., and Smith, I. J., "Variations in Stress Intensity Factor Across Curved Crack Fronts in Compact-Tension Specimens," *Proceedings*, Third International Conference on Numerical Methods in Fracture Mechanics, A. R. Luxmore and D. R. Owen, Eds., Pineridge Press, Swansea, UK, 1984, pp. 205–217.
[9] Kikuchi, M. and Miyamoto, H., "On the Numerical Analysis of the Three Dimensional Crack Growth Problem," *International Conference on Numerical Methods in Fracture Mechanics*, A. R. Luxmore and D. R. J. Owen, Eds., Pineridge Press, Swansea, UK, 1984, pp. 249–260.
[10] Suresh, S., Zamisky, G. F., and Ritchie, R. O., "Oxide-Induced Crack Closure: An Explanation for Near-Threshold Corrosion Fatigue Crack Growth Behavior," *Metallurgical Transactions A*, American Society for Metals, Vol. 12A, Aug. 1981, pp. 1435–1443.
[11] Bachmann, V. and Munz, D., "Fatigue Crack Closure Evaluation with the Potential Method," *Engineering Fracture Mechanics*, Vol. 11, No. 1, 1979, pp. 61–71.
[12] Cotterell, B., "On Fracture Path Stability in the Compact Tension Test," *International Journal of Fracture Mechanics*, Vol. 6, No. 2, June 1970, pp. 189–192.
[13] Schwalbe, K. H. and Hellmann, D., "Application of the Electrical Potential Method to Crack Length Measurements Using Johnson's Formula," *Journal of Testing and Evaluation*, Vol. 9, No. 3, May 1981, pp. 218–221.
[14] Hicks, M. A. and Pickard, A. C., "A Comparison of Theoretical and Empirical Methods of Calibrating the Electrical Potential Drop Technique for Crack Length Determination," *International Journal of Fracture Mechanics*, Vol. 20, No. 2, Oct. 1982, pp. 91–101.
[15] Gangloff, R. P., "Corrosion Fatigue Crack Propagation in Metals," *Environment-Induced Cracking of Metals, Proceedings*, National Association of Corrosion Engineers, Houston, 1989, pp. 55–109.
[16] Mostovoy, S., Crosley, P. B., and Ripling, E. J., "Use of Crack-Line-Loaded Specimens for Measuring Plane-Strain Fracture Toughness," *Journal of Materials*, Vol. 2, No. 3, Sept. 1967, pp. 661–681.
[17] Parks, D. M., "A Stiffness Derivative Finite Element Technique for Determination of Elastic Crack Tip Intensity Factors," *International Journal of Fracture*, Vol. 10, No. 4, Dec. 1974, pp. 487–502.
[18] Mai, Y. W., Atkins, A. G., and Caddell, R. M., "On the Stability of Cracking in Tapered DCB Testpieces," *International Journal of Fracture*, Vol. 11, No. 6, Dec. 1975, pp. 939–953.
[19] *Metals Handbook*, 10th ed., Vol. 1, American Society for Metals, Metals Park, OH, 1990, p. 199.

R. Bruce Thompson,[1] Otto Buck,[2] and David K. Rehbein[3]

Ultrasonic Characterization of Fatigue Crack Closure

REFERENCE: Thompson, R. B., Buck, O., and Rehbein, D. K., "**Ultrasonic Characterization of Fatigue Crack Closure,**" *Fracture Mechanics: Twenty-Third Symposium, ASTM STP 1189,* Ravinder Chona, Ed., American Society for Testing and Materials, Philadelphia, 1993, pp. 619–632.

ABSTRACT: The characterization of fatigue crack closure is an important objective because of its influence on fatigue crack propagation, particularly under conditions of variable amplitude loading. This paper describes a nontraditional technique for characterizing closure, in which ultrasonic scattering measurements are used to obtain estimates of the number density and size of asperities bridging the crack faces, with subsequent estimates of the crack-tip shielding being based on those geometrical parameters. The paper first reviews the experimental configuration and the basic elasto-dynamic theory underlying the technique. It then presents recent results obtained in studies of the influence of block overloads and load shedding on the growth of fatigue cracks in aluminum alloys. In both cases, the change in the closure state after the overload can be seen unambiguously even in the raw data. Moreover, data analysis suggests that it may be possible to predict when the crack will reinitiate based on more subtle changes in the ultrasonically inferred closure state. In the case of load shedding, a massive closure region is observed, whose characteristics appear consistent with the notion that threshold phenomena can be explained in terms of crack closure.

KEY WORDS: asperities, contact topology, crack closure, crack-tip shielding, dynamic crack-opening displacement, fatigue cracks, load shedding, overloads, through transmission, ultrasonic scattering, fracture mechanics, fatigue (materials)

The growth of a fatigue crack is modeled generally in terms of empirical rules such as the Paris law [*1*], which states that $da/dN = \alpha(\Delta K)^m$ where a is the crack length, N is the number of fatigue cycles, ΔK is the stress intensity range, and α and m are material constants. Over the last decade, a mounting body of evidence has established that the full excursion of the applied load does not drive the crack tip forward due to a variety of phenomena that are referred to as crack-tip shielding [*2,3*]. In one class of shielding, contact is assumed to develop along the crack faces at plastically deformed asperities, dislodged oxide particles, or other geometrical features that prevent a perfect mating of the fracture surfaces when the applied load is released. Since these contacts bear load, they modify the stress distribution in the vicinity of the tip, thereby altering the crack growth rate.

Figure 1 schematically sketches such a situation. Compressive internal stresses, σ_0, are created on either side of the partially contacting crack surfaces. In reaction, opening loads, P_i,

[1] Associate director for Science and Technology, Ames Laboratory and professor, Materials Science and Engineering Department and Aerospace Engineering and Engineering Mechanics Department, Iowa State University, Ames, IA 50011.

[2] Program director, Ames Laboratory and professor, Materials Science and Engineering Department, Iowa State University, Ames, IA 50011.

[3] Associate metallurgist, Ames Laboratory, Iowa State University, Ames, IA 50011.

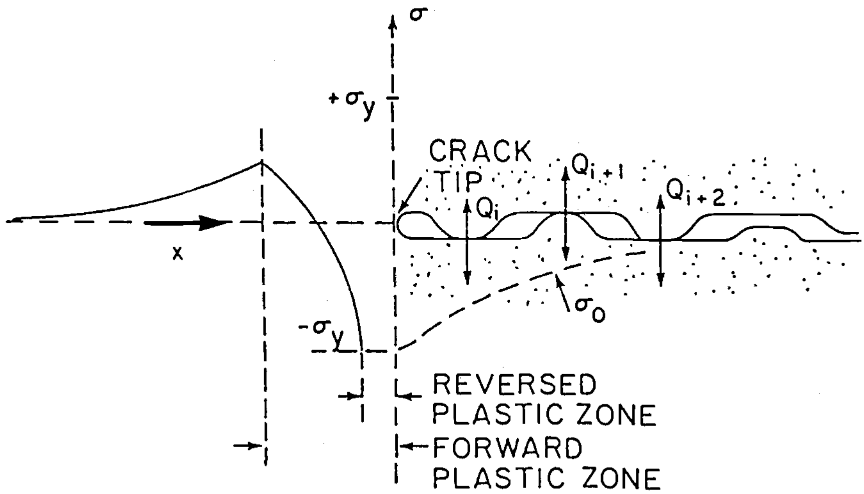

FIG. 1—*The stresses, normal to the crack plane, in the vicinity of the crack tip (schematically).* $+\sigma y$ *and* $-\sigma y$ *are the tensile and compressive yield stresses, respectively.*

arise producing a stress intensity factor, K_{sh}, which shields the crack tip from the variations of the externally applied stress intensity factor, as indicated in Fig. 2. This shielding occurs below a stress intensity factor, K_{cl}, at which the first contact during unloading occurs. Thus, a consequence of asperity contact is that the applied stress intensity range, $\Delta K = K_{Imax} - K_{Imin}$, which is usually considered to provide the driving force for fatigue crack propagation, has to be modified to include the effects of crack-tip shielding. By using information from acoustic transmission and diffraction experiments [*4*], we have succeeded in determining the size and density of contacting asperities in the closure region of a fatigue crack, grown under constant ΔK conditions, as well as an estimate of the shielding stress intensity factor, K_{sh}, due to the contacting asperities. The present paper reports on the extension of our earlier work [*4,5*] in an attempt to determine and quantify the effects of a variable ΔK on fatigue crack propagation by using acoustic experiments. In conclusion, it appears that the acoustic measurements assist in predicting future crack growth rate behavior.

Experimental Configuration

The experimental configuration for the ultrasonic measurements is shown in Fig. 3. A planar fatigue crack, grown in a compact tension specimen, is illuminated by a longitudinal wave incident perpendicular to the crack face and focused in the plane of the crack. The longitudinal wave transmitted directly past the crack can be picked up by a coaxial receiver placed on the opposite side of the specimen. Alternatively, as discussed in detail elsewhere [*5*], by changing the angular orientation of the receiver and translating it so that it is still directed towards the illuminated spot, longitudinal or transverse waves diffracted from the crack tip or contacting asperities can be detected.

By deconvolving these signals with those observed in a reference experiment in which the beam is directly transmitted through the uncracked portion of the specimen, most of the influence of the measurement system, such as the efficiency of the transducers, is eliminated from the data. This deconvolved information is thus characteristic of the crack itself. By spectral

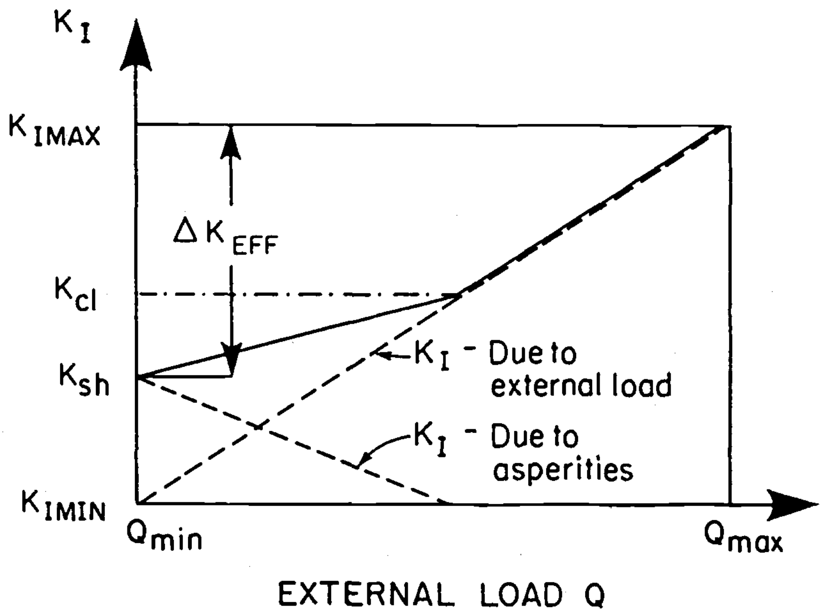

FIG. 2—*The stress intensity factor as a function of external load (schematically).*

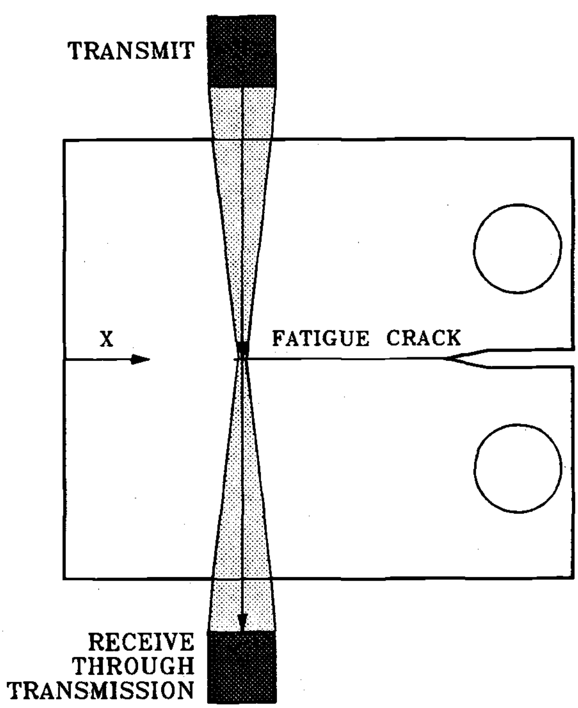

FIG. 3—*Arrangement to determine the effects of closure on acoustic transmission and diffraction.*

analysis, translation of the sample, or rotation of the receiver, one can respectively monitor the frequency and spatial dependence of the crack transmissivity.

Modeling and Evaluation of the Contact Topology

Ultrasonic Scattering-General Formalism

The theory for the scattering of elastic waves from fatigue cracks is based on the electromechanical reciprocity theory of Auld [6] that states that the flaw-induced change in the signal transmitted from an illuminating to a receiving transducer, $\delta\Gamma$, is given by

$$\delta\Gamma = \frac{j\omega}{4P}\int_A (u_i^R\tau_{ij}^T - u_i^T\tau_{ij}^R)n_j dA \tag{1}$$

where u_i^R and τ_{ij}^R are the displacement and stress patterns that would be produced if the receiving transducer irradiated a flaw-free material; u_i^T and τ_{ij}^T are the displacement and stress fields produced when the flaw is irradiated by the transmitting transducer, P is the electrical power incident on the transmitting transducer, and integration is performed over the surface of the scatterer, which has a normal n_j. A time dependence of the form exp $(j\omega t)$ has been assumed. Noting that τ^T, τ^R, and u^R must be continuous in the plane of the crack (assuming the noncontacting regions to have infinitesimal volume), one concludes that

$$\delta\Gamma = \frac{j\omega}{4P}\int_{A+} \Delta u_i^T\tau_{ij}^R n_j^+ \, dA \tag{2}$$

where A^+ is the illuminated face of the crack, n_j^+ is its normal, $\Delta u_i^T = u_i^+ - u_i^-$ is the dynamic crack-opening displacement (DCOD), since u_i^+ and u_i^- are the displacements on either side of the crack.

In an experimental situation, one does not measure $\delta\Gamma$ but rather $\Gamma = \Gamma_R + \delta\Gamma$ where Γ_R is the reference signal that would be observed with no crack present. For the experimental geometry illustrated in Fig. 3, the reference signal may be estimated by applying Eq 2 to a perfect, planar crack (that is, no contacts). In that case, $\delta\Gamma = -\Gamma_R$ and Eq 2 becomes

$$\Gamma_R \cong \frac{j\omega}{4P}\int_{A+} 2u_i^I\tau_{ij}^R n_j^+ \, dA \tag{3}$$

where u_i^I is the displacement field of the incident illumination and it is assumed that the displacement is approximately doubled at the stress-free crack surface during the reflection of a normally incident beam. Combining Eqs 1 through 3 leads to the final result

$$\Gamma = \frac{j\omega}{4P}\int_{A+} (2u_i^I - \Delta u_i^T)\tau_{ij}^R n_j^+ \, dA \tag{4}$$

Computation of the crack scattering now requires three sets of fields to be known. One must know the stress radiation pattern of the receiver, τ_{ij}^R, the displacement radiation pattern of the transmitter, u_i^I, and the DCOD, Δu_i^T. All three fields are schematically shown in Fig. 4. As reported previously, a scalar Gaussian beam approximation [7] has been employed to estimate the radiation fields, τ_{ij}^R and u_i^I. This model includes such effects as diffraction-induced beam spread, but does not include the full tensor character of the elastic fields. For beams whose

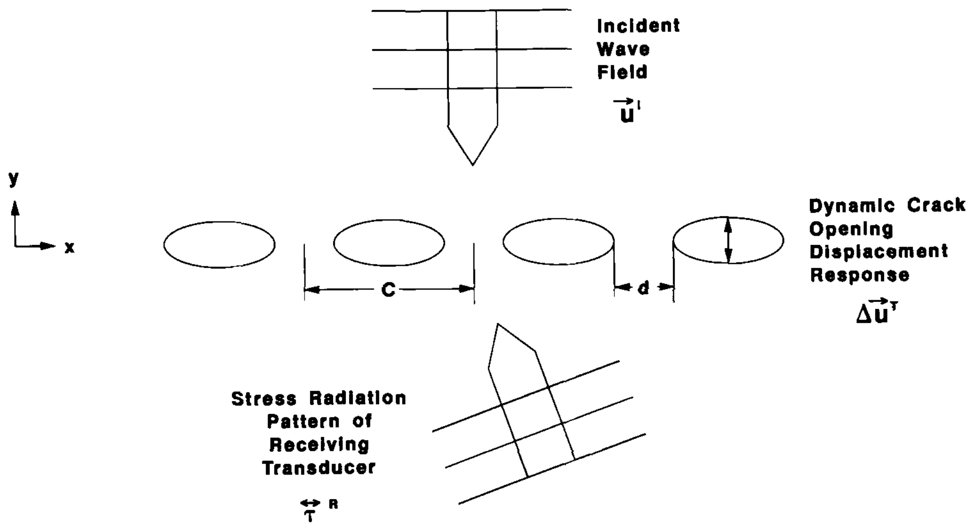

FIG. 4—*The fields, important in acoustic scattering.*

widths are several wavelengths in extent, the scalar approximation should be reasonable since the direction of polarization does not substantially vary over the beam cross section.

The Dynamic Crack-Opening Displacement and Contact Topology

The major problem in evaluating Eq 4 is in selecting an appropriate description of the DCOD Δu_i^T, which depends mainly on asperity contact spacing, c (or areal contact density, N), and the contact diameter, d, or, in other words, on the contact topology. Thus, if Γ in Eq 4 has been determined experimentally, Eq 4 provides the means to determine the information on the contact topology depending on the specific model chosen.

The simplest model to represent a contacting fatigue crack is a spring model [8], in which the partially contacting interface, in the $z = 0$ plane, is represented by the modified boundary condition

$$\sigma_{3i}^+ = \sigma_{3i}^- \tag{5}$$

$$\sigma_{3i}^+ = \kappa_{ij}(u_j^+ - u_j^-) \tag{6}$$

where the superscripts, "+" and "−," refer to the two sides of the interface. The matrix, κ_{ij}, may be thought of as representing a set of massless springs joining the two sides of the interface. For simple interface topographies, this matrix will be diagonal, with κ_{11} and κ_{22} representing the contact-induced resistance to shear and κ_{33} representing the resistance to compression. The properties of the interface are assumed to be linear. This requires that there be resistance to tension as well as compression, which is true when the dynamic stresses of the ultrasonic wave are small with respect to the static stresses associated with the contact. Baik and Thompson [9] have developed a quasi-static model relating κ_{33}, hereafter abbreviated as κ, to solutions of static deformation problems for a variety of crack topologies. κ is found to be a function of both the contact density and dimensions. For sparse, penny-shaped contacts, $\kappa = N\pi E'd/8$, where N is the contact density, d is their diameter, $E' = E/(1 - \nu^2)$, E = static Young's modulus, and ν = Poisson's ratio. In this case, Δu_i^T in Eq 4 is an averaged value $\overline{\Delta u_i^T}$. The model was found to work well for through-transmitted signals. However, this model does not predict strongly diffracted signals observed experimentally [10]. This deficiency has been suggested to be a consequence of the absence of discrete contacts in the model. Several discrete contact models have therefore been developed [10,11], and the general formalisms established. The details are beyond the scope of this paper. It should be mentioned, however, that preliminary evaluation of these formalisms have shown that the areal density of the contacts, N, strongly influences the strength of the diffracted signals [5] with specific details still to be worked out.

Crack-Tip Shielding by Asperity Contact

The acoustically obtained information on the average distance, c, between asperities and their size, d, can now be used to estimate the crack-tip shielding stress intensity factor, K_{sh}, for an unloaded specimen. Consider first a loaded specimen with a fully open crack. The stress intensity factor, K_{max}, is then determined by the externally applied load, Q_{max}, and the crack depth. As the load decreases, the stress intensity factor assumes the value K_{cl} [2] as the first row of asperities (parallel to the crack front) contacts the opposite fracture surface. Assuming that the average distance, c, between contacting asperities does not change on further unloading, the average diameter, d, of the asperities increases as does the load, Q_i, carried by each individual contact. As unloading continues, additional rows of asperities come into contact with the opposite fracture surface so that a shielding stress intensity factor, K_{sh}, builds up, which is determined by Q_i and c. Therefore, K_{sh}, is at a maximum when the external load is fully removed or, in other words, as $K_{min} = 0$. If this shielding effect is taken into account, the "effective" stress intensity range should then be considered as

$$\Delta K_{eff} = K_{max} - K_{sh} \tag{7}$$

rather than

$$\Delta K = K_{max} - K_{min} \tag{8}$$

or, as was suggested by Elber [2]

$$\Delta K = K_{max} - K_{cl} \tag{9}$$

The following paragraphs are devoted to an estimation of K_{sh}. Each individual asperity contact in the wake of the crack carries its individual load, Q_i, and, therefore, produces a stress intensity factor, K_i, given by [12]

$$K_i = \frac{2^{1/2}}{(\pi c)^{3/2}} Q_i \frac{1}{1 + (z/c)^2} \tag{10}$$

where c is the nearest distance between the contact and the crack front and assumed to be equal to the average distance between contacts, and z is the coordinate along the crack front with its origin at the closest point to the contact. Superposition of a series of contact points along the crack front, as shown in Fig. 5, yields the stress intensity factor shielding contributions [5,13]

$$dK_{sh} = \left(\frac{2}{\pi}\right)^{1/2} \frac{\Delta Q}{Bc^{1/2}} \tag{11}$$

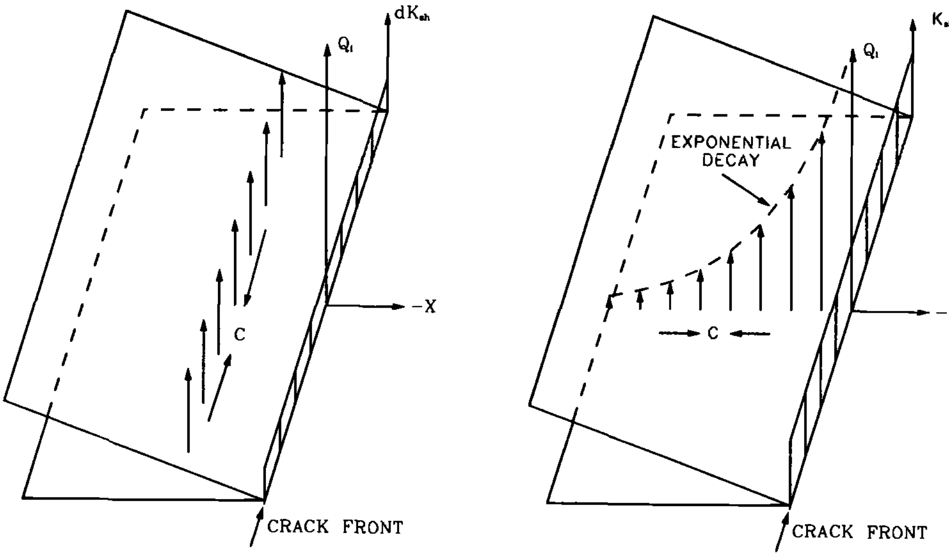

FIG. 5—*Crack-tip shielding by individual contacts.*

where B is the specimen thickness and ΔQ is the load carried by the row of contacts. On average, the load, ΔQ, carried by the contacts can be related to the static stress, σ_0 (an internal stress), across the partially closed crack by

$$\Delta Q = B\sigma_0 dx \tag{12}$$

where x is the coordinate perpendicular to the crack front. Based on earlier work by Haines [*14*] and Thompson et al. [*9,15*], connecting σ_0 to the acoustic transmission coefficient, it has been shown [*16*] that

$$\sigma_0 = \left(\frac{\kappa}{k^*E}\right)^2 \frac{\pi}{N} P_m \tag{13}$$

where κ is the interface stiffness, discussed earlier, $k^* \approx 2$ (depending on the precise shape of the contact). E is the elastic modulus, N is the areal contact density (related to c) and P_m is the "flow pressure" of the material (usually about three times the ultimate tensile strength). Under the assumption that N is a constant, which is determined by factors related to microstructure and the mechanisms producing closure, then all the quantities in Eq 13 are independent of x, except for κ. For a fatigue crack grown at constant ΔK, κ was found to be an exponential of the form

$$\kappa = \kappa_0 \exp(-\beta x) \tag{14}$$

by a best fit analysis of the frequency-dependent transmission data [*5*]. Using Eqs 11 through 13 under the constraint that the separation between the strips is much less than β^{-1}, c can be replaced by x, yielding

$$dK_{sh} = (2\pi)^{1/2} \left(\frac{\kappa_0}{k^*E}\right)^2 \frac{P_m}{N} \frac{\exp(-2\beta x)}{x^{1/2}} dx \tag{15}$$

As indicated in Fig. 5, the total contribution of the closure zone will therefore be

$$\int_0^\infty dK_{sh} = K_{sh} = \pi \left(\frac{\kappa_0}{k^*E}\right)^2 \frac{P_m}{N\beta^{1/2}} \tag{16}$$

with $N \approx c^{-2}$. Thus, the acoustically determined parameters, κ_0, β, and N (requiring two independent measurements), are sufficient to estimate K_{sh}, assuming the "materials parameters" E and P_m are known. Using a compact tension specimen of Al 7075-T651, we found for the unloaded crack, grown under constant ΔK conditions, $K_{sh} \approx 6.8$ MPa m$^{1/2}$ a value that was roughly 40% of K_{max} [5]. In this study, the experimentally observed and deduced values were $\kappa_0 \approx 5.3 \times 10^8$ MPa m^{-1}; $N \approx 2.3 \times 10^8$ m^{-2}; and $\beta \approx 2.5 \times 10^3$ m^{-1}; and furthermore the "materials parameters" $P_m \approx$ three times the ultimate tensile strength $\approx 1.7 \times 10^3$ MPa; $E \approx 7 \times 10^4$ MPa; and $k^* \approx 2$ from Kendall and Tabor's work [17].

Evidence for the validity of this theory may be obtained from an experimental determination of the internal stress, σ_0, in the wake of the crack. Using X-ray diffraction, Welsch et al. [18] determined the internal stress distribution in 4140 steel in the wake of the crack in plane stress. Their data indicate a maximum compressive stress of about 60% of the yield stress, in good agreement with the present calculation, using Eq 13. They also observed a decay of the internal stresses along the closure region, as expected from Eqs 13 and 14. Lastly, one may consider if the acoustically obtained numerical values for the contact topology (c and d) are reasonable. We found, near the crack tip, $d \approx 35$ μm and $c \approx 70$ μm (on the order of the grain size) for Al 7075-T651. Note that d decays exponentially with increasing distance from the crack tip. Independent acoustic measurements on copper-copper diffusion bonds [19,20] provided information on the interface stiffness, and thus on the contact topology that, in this case, can be confirmed by fractography of the bondline. We noted that for medium quality bonds the topology is quite similar to that for the contact in the wake of a crack in Al 7075-T651. We view these observations as additional evidence for the validity of our assumptions.

Effects of a Variable ΔK *on Crack-Tip Shielding*

We have extended earlier work [4,5,21], studying the effects of ΔK-changes on the acoustic transmission signal and its effects on crack-tip shielding. In an experiment [5,21] in which the crack first was grown at a constant $\Delta K = 12.2$ MPa $\sqrt{m}$, an overload block of 21 cycles at a stress intensity range of $2\Delta K = 24.4$ MPa $\sqrt{m}$ was applied to retard the crack. Immediately after the overload block, cycling at the original ΔK continued. Crack growth resumed after a retardation period of about 120 000 cycles. Even after an additional growth of over 4 mm, the growth rate was found to be about 50% slower than before application of the overload. It was noted [5] that this lower growth rate can be quantitatively explained by a strip of contact due to the overload block that produced shielding in addition to that due to the exponentially decaying κ. Quantitatively, K_{sh} increased from 6.8 to 8.0 MPa $\sqrt{m}$. Using Eq 7 therefore reduced the crack growth rate by roughly 50%. We did not succeed, however, in calculating K_{sh} for the crack immediately after the overload.

We therefore repeated the experiment at a constant $\Delta K = 10.0$ MPa $\sqrt{m}$ with an overload block of 10 cycles at $2\Delta K = 20.0$ MPa $\sqrt{m}$. Crack mouth opening results of this experiment on the length of the fatigue crack as a function of fatigue cycles are shown in Fig. 6, using a calibrated clip-on gage. The application of the overload block at A retarded the crack growth for roughly 70 000 cycles. Transmission data were taken at A, immediately after the overload block (B), during the retardation period and after crack growth resumed (C). The interface stiffnesses, κ, at A and B are shown in Fig. 7. The effect of the overload on β is quite obvious.

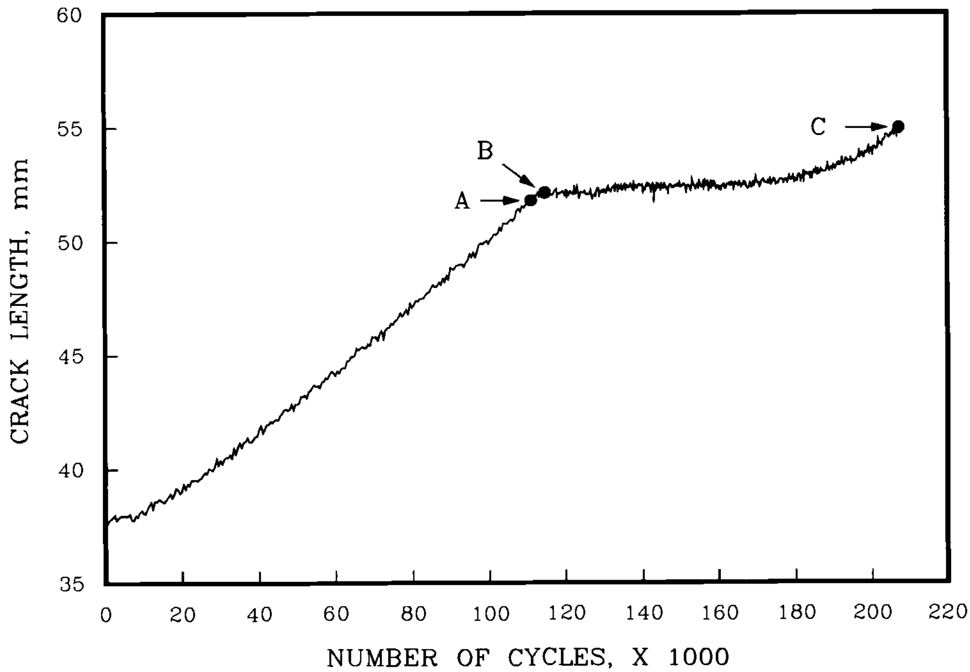

FIG. 6—*Crack length versus number of fatigue cycles in an overload experiment.*

Also plotted in Fig. 7 is the spring stiffness, κ_3, once crack growth resumes (*C*). κ_3 is no longer a simple exponential. As before [*21*], κ_3 can be described basically by the sum of an exponential and a peak as

$$\kappa(x) = \kappa_0 e^{-\beta x} + \frac{\kappa'}{1 + \left[\frac{2(x-\delta)}{\gamma}\right]^4} \tag{17}$$

where δ is the distance of the crack tip to the position where the overload was applied, and γ is the width of the overload region, taken as the width at half the amplitude of the κ-peak. At $x = \delta$, the amplitude of the spring constant due to the overload is κ'.

The change in β as a consequence of the overload block is shown in Fig. 8. We note that β increases by about a factor of four due to the overload. It slowly returns to the level prior to the overload as crack growth resumes, as in the previous experiment [*21*]. Trends in κ_0 are not as clear as the observed changes in β. However, as indicated in the center of Fig. 7, it appears as if κ_0 increases by as much as a factor of ten immediately after the overload. In that case, K_{sh}, as calculated from Eq 16, increases strongly after the overload. Also unclear remains the area contact density, *N*, during the retardation. However, as crack growth resumed, we noted (see Fig. 7) the same strip of contact appearing as before [*21*] at a location slightly ahead of the position of overload application.

Therefore, we are still unable to demonstrate quantitatively the validity of Eq 7 for a retarded crack. We have demonstrated, however, that for a retarded crack the closure region is smaller (due to the larger β) than for the propagating crack. We believe that this observation

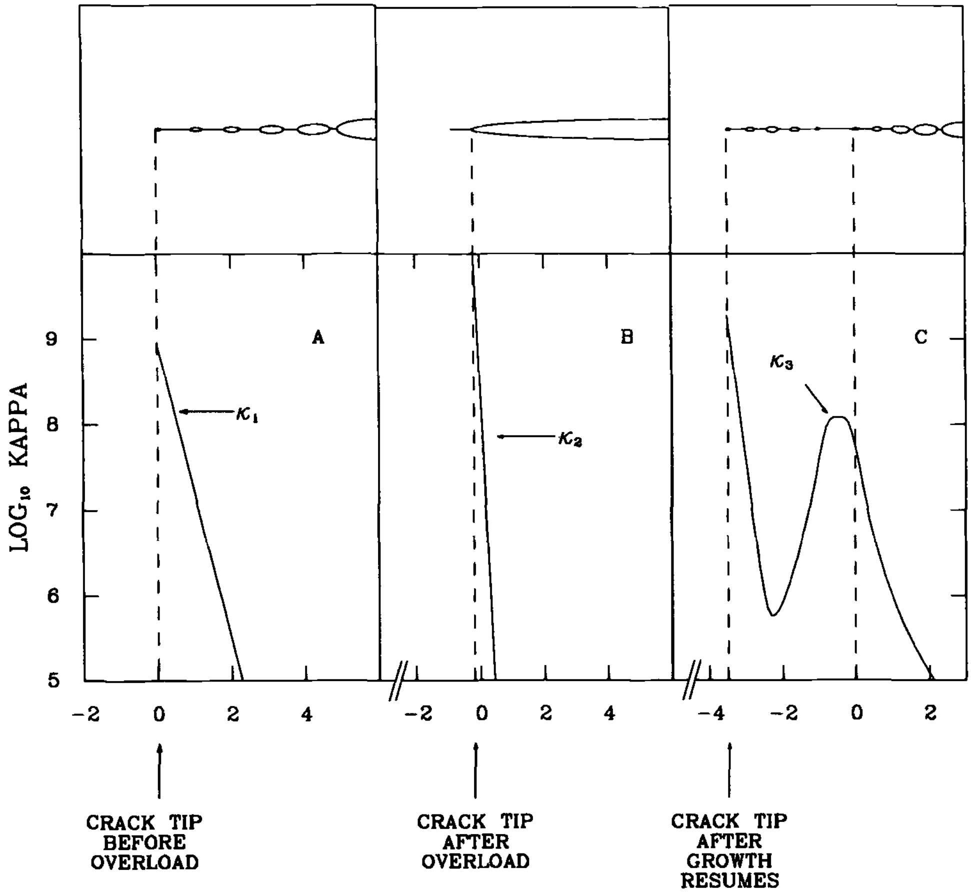

FIG. 7—*Spring constant, κ (quantitatively), and asperity contact (schematically):* (left) *before application of the overload;* (center) *immediately after the overload (retardation);* (right) *after crack growth resumes.*

is of significance to the nondestructive evaluation community that, at the present time, can not distinguish between a retarded and a propagating crack. Further experiments to evaluate the κ_0 and N parameters, important to determine shielding, are in progress.

Results of a second experiment, in which the applied ΔK was dropped continuously, on the resulting crack propagation rate are shown in Fig. 9. The ΔK data (full line) indicate that the growth regime changed from the Paris to the near-threshold regime. Acoustic transmission data at various acoustic frequencies with no load applied to the specimen were taken in both propagation regimes as shown in Fig. 10. The top half of Fig. 10 shows the frequency-dependent transmission data in the Paris regime (D) and the bottom half in the near-threshold regime (E). As before, the dropoff in the transmission data indicates a frequency-independent, exponentially decaying κ with a closure region typical for that of a crack grown under ΔK conditions in the Paris regime. Remarkably different is the spatial variation of the transmission data in the near-threshold regime. As seen in the bottom half of Fig. 10, at large distances away from the crack tip, the transmission coefficient stays at a relatively high and almost constant

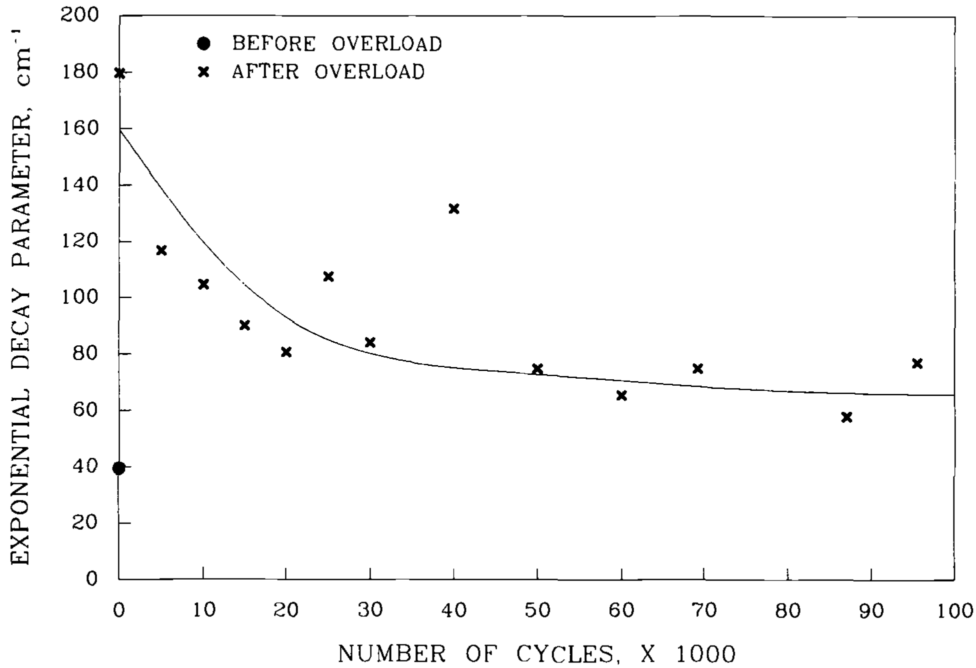

FIG. 8—*The exponential decay parameter, β, as a function of the number of fatigue cycles applied after the afterload.*

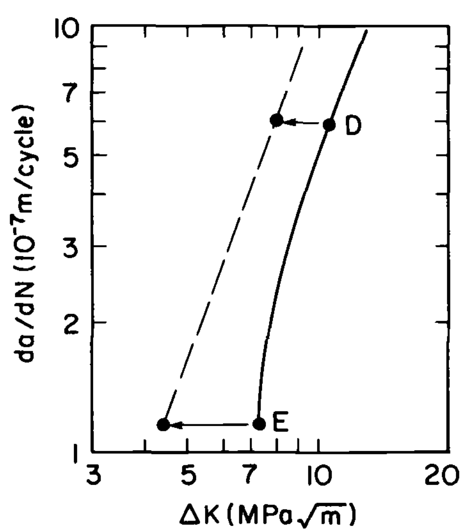

FIG. 9—*Crack growth rate as a function of ΔK in the "threshold" regime.*

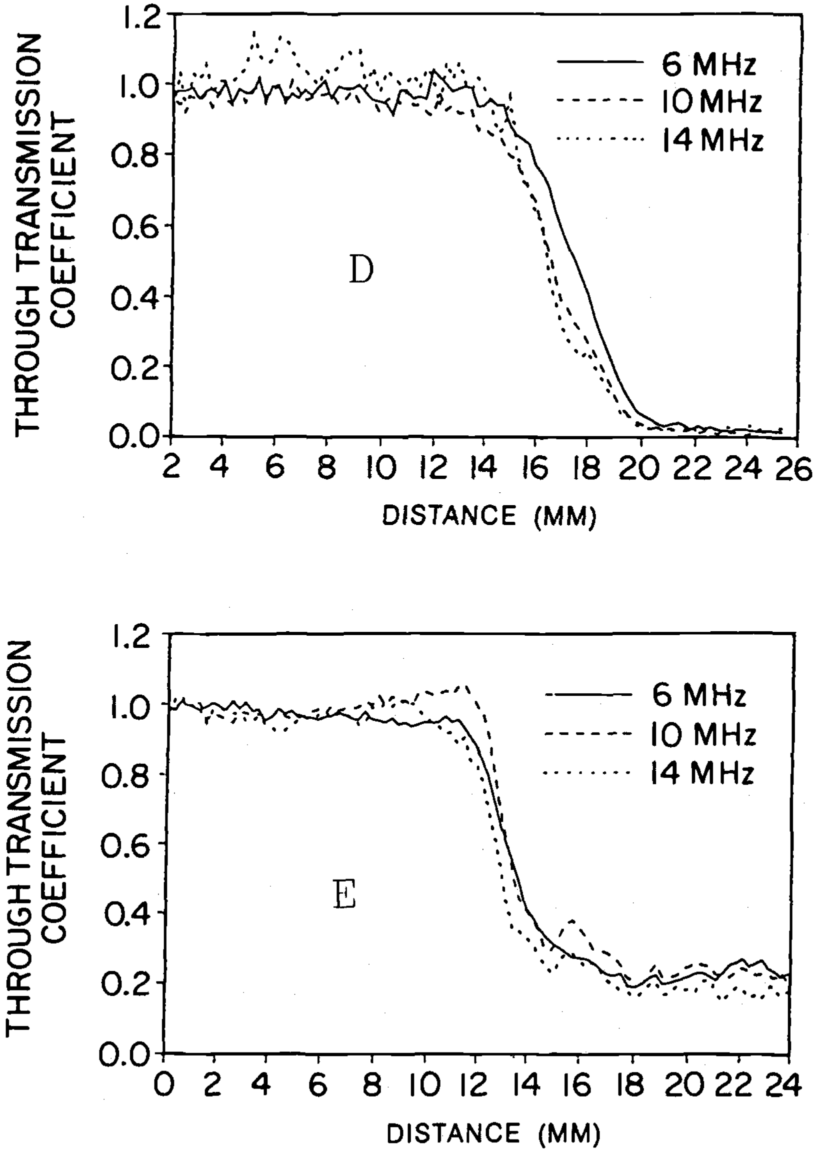

FIG. 10—*Through transmission:* (top) *in the "Paris" regime;* (bottom) *in the "threshold" regime.*

level. This indicates to us that the closure region is extended with respect to that in the Paris regime and the resulting K_{sh} is about 45% larger. A conversion of da/dN versus ΔK in Fig. 9 to da/dN versus ΔK_{eff} (dashed line) then provides a new correlation for the data shown in Fig. 9 that has a slope close to that in the Paris regime. Thus, it appears that the "threshold" behavior, seen in Fig. 9, has been created artificially by the extensive closure, shown in the bottom half of Fig. 10, in agreement with earlier observations [*22*].

Conclusion

Acoustic measurements on fatigue cracks provide some detailed information on the state of the crack due to its past history. Any change in the load spectrum applied to the crack affects the crack face contact and consequently the "shielding" of the crack from the external driving force. Because they can characterize this contact, acoustic measurements indicate that they are able to assist in predicting future crack growth rate changes. Elastodynamic theories of wave scattering play a crucial role in making these interpretations quantitative.

Acknowledgment

Ames Laboratory is operated for the U.S. Department of Energy by Iowa State University under Contract No. W-7405-ENG-82. This work was supported by the Office of Basic Energy Sciences, Division of Materials Sciences.

References

[1] Paris, P. C. and Erdogan, F. J., *Journal of Basic Engineering, Transactions*, American Society of Mechanical Engineers, Vol. D85, 1963, p. 528.
[2] Elber, W., in *Damage Tolerance in Aircraft Structures, ASTM STP 486*, American Society for Testing and Materials, Philadelphia, 1971, p. 230.
[3] Ritchie, R. O., *Materials Science and Engineering*, Vol. A103, 1988, p. 15.
[4] Buck, O., Rehbein, D. K., and Thompson, R. B., *Morris E. Fine Symposium*, P. K. Liaw et al., Eds., The Minerals, Metals, and Materials Society, Warrendale, PA, 1991, p. 349.
[5] Buck, O., Rehbein, D. K., and Thompson, R. B., *Engineering Fracture Mechanics*, Vol. 28, 1987, p. 413.
[6] Auld, B. A., *Wave Motion*, Vol. 1, 1979, p. 3.
[7] Thompson, R. B. and Lopes, E. F., *Journal of Nondestructive Evaluation*, Vol. 4, 1984, p. 107.
[8] Thomspon, R. B. and Fiedler, C. J., *Review of Progress in Quantitative Nondestructive Evaluation*, Vol. 3A, D. O. Thompson and D. E. Chimenti, Eds., Plenum Press, New York and London, 1984, p. 207.
[9] Baik, J.-M. and Thompson, R. B., *Journal of Nondestructive Evaluation*, Vol. 4, 1984, p. 177.
[10] Rehbein, D. K., Thompson, R. B., and Buck, O., *Review of Progress in Quantitative Nondestructive Evaluation*, Vol. 4A, D. O. Thompson and D. E. Chimenti, Eds., Plenum Press, New York and London, 1985, p. 61.
[11] Thompson, R. B., Van Wyk, L., Rehbein, D. K., Tsai, Y.-M., and Buck, O., *Advances in Fracture Research*, K. Salama et al., Eds., Pergamon Press, Oxford, 1989, p. 3165.
[12] Tada, H., Paris, P. C., and Irwin, G. R., *The Stress Analysis of Cracks Handbook*, Del Research Corporation, St. Louis, 1985.
[13] Beevers, C. J., Bell, K., Carlson, A. L., and Starke, E. A., *Engineering Fracture Mechanics*, Vol. 19, 1984, p. 93.
[14] Haines, N. F., "The Theory of Sound Transmission and Reflection at Contacting Surfaces," Report RD/B/N4711, Research Division, Berkeley Nuclear Laboratories, Central Electricity Generating Board, Gloucestershire, UK, 1980.
[15] Thompson, R. B., Skillings, B. J., Zachary, L. W., Schmerr, L. W., and Buck, O., *Review of Progress in Quantitative Nondestructive Evaluation*, Vol. 2A, D. O. Thompson and D. E. Chimenti, Eds., Plenum Press, New York and London, 1983, p. 325.
[16] Buck, O., Thompson, R. B., and Rehbein, D. K., *Journal of Nondestructive Evaluation*, Vol. 4, 1984, p. 203.
[17] Kendall, K. and Tabor, D., *Proceedings*, Royal Society, London, Vol. A232, 1971, p. 321.
[18] Welsch, E., Eifler, D., Scholtes, B., and Macherauch, E., *Residual Stresses in Science and Technology*, E. Macherauch and V. Hauk, Eds., DGM Informationsgesellschaft Verlag, Oberursel, FRG, 1987, p. 785.
[19] Palmer, D. D., Rehbein, D. K., Smith, J. F., and Buck, O., *Journal of Nondestructive Evaluation*, Vol. 7, 1988, p. 153.

[*20*] Palmer, D. D., Rehbein, D. K., Smith, J. F., and Buck, O., *Journal of Nondestructive Evaluation*, Vol. 7, 1988, p. 167.

[*21*] Buck, O., Rehbein, D. K., and Thompson, R. B., *Effects of Load and Thermal Histories on Mechanical Behavior of Materials*, P. K. Liaw and T. Nicholas, Eds., Metallurgical Society of American Institute of Mining, Metallurgical, and Petroleum Engineers, Warrendale, PA, 1987, p. 49.

[*22*] Frandsen, J. D., Inman, R. V., and Buck, O., *International Journal of Fracture*, Vol. 11, 1975, p. 345.

Composites and Nonmetals

Syue-Sinn Leu[1] and James L. Hill[1]

Debonding Force of a Single Fiber from a Composite Body

REFERENCE: Leu, S.-S. and Hill, J. L., "**Debonding Force of a Single Fiber from a Composite Body,**" *Fracture Mechanics: Twenty-Third Symposium, ASTM STP 1189,* Ravinder Chona, Ed., American Society for Testing and Materials, Philadelphia, 1993, pp. 635–648.

ABSTRACT: The force necessary to break the adhesive bond of a single fiber from a multilayer composite is investigated. An important application of this analysis is the determination of the force required to pull the wire-guided fiber from the wound spool of a missile as it deploys the control fiber in flight. Deformations of the pulled fiber include bending, stretching, and torsion. The equilibrium equations are similar to the equation that governs a beam on an elastic foundation except that the three equations are coupled. A closed-form solution to the equilibrium equations is obtained with the constants of integration evaluated by carefully applying the appropriate boundary conditions. Results obtained include the variation of debonding force with the pulling angle, the transition of the governing failure mode of the adhesive layers, and the stress distributions in the adhesive layers. Results obtained for a special case of the double-cantilever beam are in excellent agreement with results in the literature.

KEY WORDS: adhesive, adherend (substrate), adhesive failure, debonding force, debonding angle, singly-bonded zone, doubly-bonded zone, double-cantilever beam, failure condition, maximum failure stress, stress intensity factor, stress energy release rate, fracture mechanics, fatigue (materials)

In this research, the force necessary to debond a fiber from a composite body when pulled at an arbitrary angle is analyzed. Figure 1 shows that a fiber on the top of the body is bonded to its neighboring fiber in the top layer and to the fibers in the layer below it by an adhesive with a long portion of the fiber unbonded. Obviously, the debonding force depends on the strength of adhesives and the mechanisms of failure including adhesive failure and cohesive failure. The analysis of debonding force to break the adhesive bond of a single fiber in a multilayer composite has not appeared in the literature.

Nevertheless, most of the basic studies of adhesive bonding can serve as a very useful background for the research on debonding problems. Two simple models, double-cantilever-beam (DCB) specimens and cracked-lap-shear (CLS) specimens, are commonly used experimentally to obtain properties of the adhesives and to determine the accuracy of theories developed for calculating the stresses in the adhesive joints. ASTM standards, [*1*], such as T-peel test (ASTM Test Method for Peel Resistance of Adhesives (T-Peel Test) (D 1876-72)), pure tensile test (ASTM Recommended Practice for Preparation of Bar and Rod Specimens for Adhesive Tests (D 2094-69)), and pure shear test (ASTM Test Method for Strength Properties of Adhesives in Shear by Tension Loading (Metal-to-Metal) (D 1002-72)), can be consulted for the details of such test methods. The analytical approach and the finite-element method have been employed to determine the stress distribution in many adhesive joints. Of particular interest

[1] Graduate research associate, and professor and head, respectively, Department of Engineering Mechanics, University of Alabama, Tuscaloosa, AL 35487.

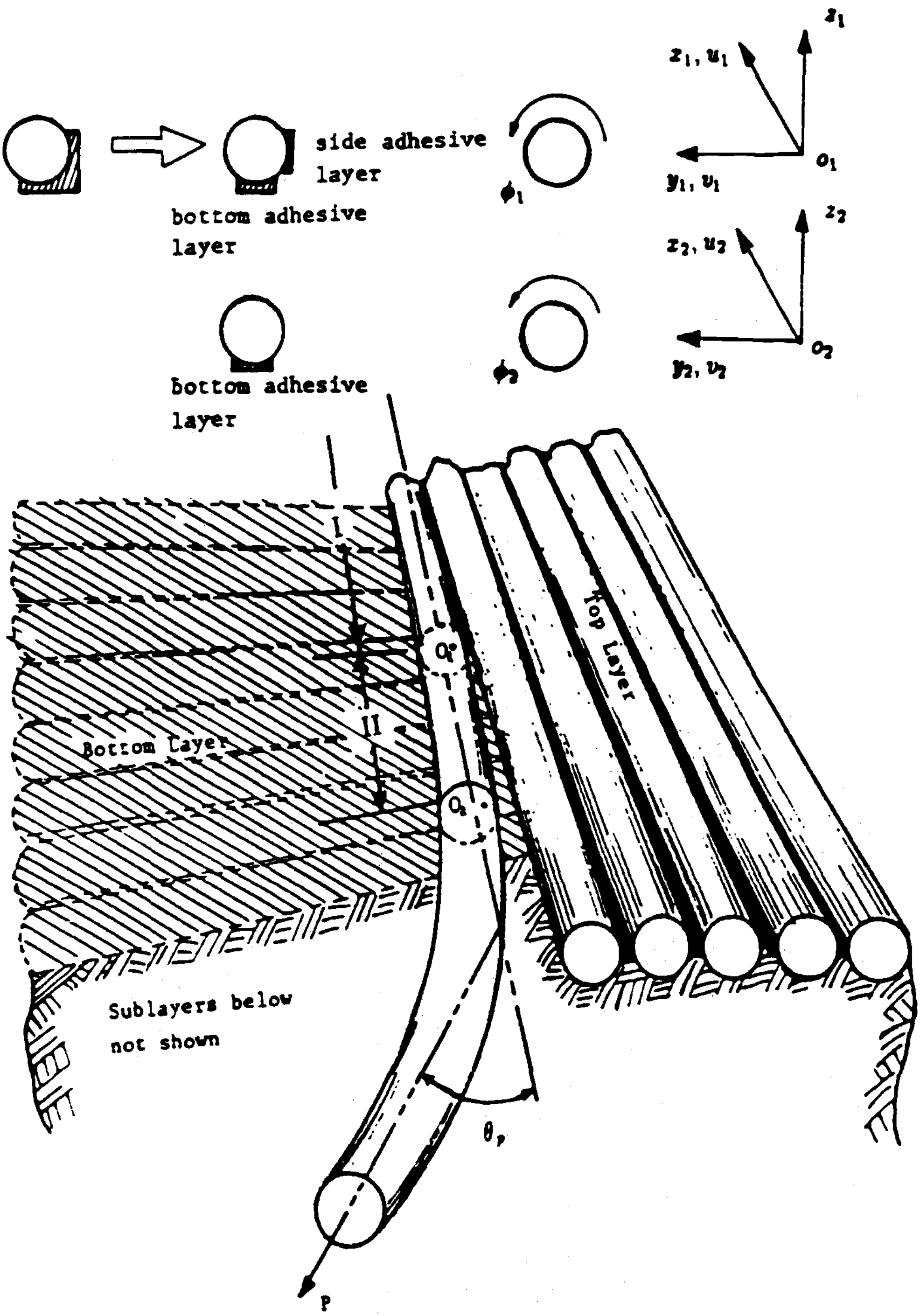

FIG. 1—*Model of the composite body.*

to designers are the magnitude and the distribution of stresses in such joints that can be used to assess their ultimate strength and performance under service conditions. In the works of Malyshev and Salganik [2], Lubkin and Lewis [3], Williams [4], and Roberts [5], analytical approaches of plane stress problems for adhesively bonded joints are studied. Investigations, using the finite-element method, that consider DCB specimens and CLS specimens have been performed by Anderson et al. [6], Bennett et al. [7], Adams and Peppiatt [8], Dattaguru et al. [9], Johnson [10], Yamada [11], and Amijima et al. [12]. Their general idealizations to the analysis of adhesive joints are important in dealing with the formulation of the mathematic model for this debonding problem.

The fracture energy of the adhesives is commonly used to represent the strength of adhesive joints; consequently, the failure criteria have been studied recently for dissimilar composite materials. The dissimilar materials are modeled usually as a beam on an elastic foundation. That approach is found in assessing a stress-intensity factor of Kanninen [13], stress energy release rates of Yamada [11], and peel adhesion of Gardon [14]. This model will be modified as a beam bonded to two elastic foundations, one at its side and another at the bottom, for use in this debonding study of composite body with multiple adhesive layers. If adhesive failure is being considered, the energy balance approach is always adopted as one of failure criteria, from which another criteria, stress intensity factors, can be inferred. Williams [15] has elucidated the similarity of adhesive and cohesive failure from the standpoint of a Griffith energy balance analysis. Also, several researchers show special interest in peel mechanics, whenever debonding problems are discussed. Hellan [16,17] and Williams [18], considering the debonding of an elastic strip from a rigid substrate, assumed that dissipative processes involved in the breaking of adhesive bonds are confined to the geometrical surface of contact between strip and substrate, with Griffith's energy balance governing the separation. However, not a great deal of literature of adhesive failure can be followed as a failure criterion for mixed-mode fracture in this debonding problem. In this research, the criteria of maximum stresses similar to that in the uniaxial material test are used.

The objective of this study is to investigate debonding behavior of a single fiber from a composite body. An example of this is a missile control wire being pulled from a multiple-glued layer spool. Because of the nonhomogeneous nature and the geometrical complexity of the composite model, an exact analysis regarding the debonding force, in general, is complicated even for a linear, elastic material. Under several simplifying assumptions of materials and geometry, this paper investigates the two-dimensional debonding force in a single fiber that is parallel to and adhesive-bonded with other fibers.

Problem Formulation

In the simplest model of a multilayer fiber composite body, a fiber, acted upon by the debonding force, is parallel to and adhesive-bonded with other fibers, on the side and on the bottom, as shown in Fig. 1. The structural response v, u, and ϕ, due to bending, stretching and twisting is considered. In Zone I, the fiber is constrained by layers of adhesives on the side and on the bottom, whereas in Zone II the side layer has been debonded. Zone I is very long while Zone II is just the region between the side layer failure point and the point at which the failure is completely free of the body. Coordinate systems $(o_1\, x_1\, y_1\, z_1)$ and $(o_2\, x_2\, y_2\, z_2)$, are located at the beginning of each of Zone I and Zone II with their respective origins (o_1, o_2) located at the undeflected position of the center of the pulled fiber. The width and thickness of the side and bottom adhesive layers are b_1 and t_{a1} and b_2 and t_{a2}, respectively.

To simplify the analysis, the following assumptions are made: (a) the composite body, consisting of fibers and adhesives, behaves as Hookean body; (b) the fibers considered are sufficiently long and of uniform cross sections; (*c*) except for the pulled fiber and adhesive around it, the rest of the composite body is considered rigid; (*d*) adhesive layers are isotropic, homogeneous and of uniform thickness; (*e*) the diameter of fiber is large compared to the thickness of adhesive; (*f*) static debonding force is independent of debonding rate; (*g*) pure adhesive failure, rather than the cohesive failure, is assumed; (*h*) operating temperature remains constant through-out the entire loading period, and (*i*) body force of the pulled fiber is not important.

Based on the preceding assumptions, a free-body diagram of the pulled fiber element with a length of Δs is shown in Fig. 2. The element is acted upon by axial force, T, bending moment, M, shear force, V, torsional moment, T_{or}, and five stress components that are σ_{1y}, τ_{1x}, and τ_{1r} in the side adhesive layer, and τ_{2x} and τ_{2r} in the bottom adhesive layer. The derivation of the governing differential equations begins with the conditions of static equilibrium. Summing moments about a line parallel to the z-axis through the center of the element yields Eq 1

$$V = M' - \tau_{1x} b_1 r_f \tag{1}$$

where the prime ($'$) indicates differentiation with respect to x, and r_f is the radius of the pulled fiber. Retaining linear terms in the sum of forces in the y-direction yields Eq 2

$$V' + \tau_{2r} b_2 + \sigma_{1y} b_1 = 0 \tag{2}$$

Substitution of Eq 1 into Eq 2 gives

$$M'' - \tau'_{1x} b_1 r_f + \tau_{2r} b_2 + \sigma_{1y} b_1 = 0 \tag{3}$$

Summing forces in the x-direction produces

$$T' - \tau_{2x} b_2 - \tau_{1x} b_1 = 0 \tag{4}$$

Finally, the sum of moments about the x-axis through the center of the element yields

$$T'_{or} + (\tau_{1r} b_1 - \tau_{2r} b_2) r_f = 0 \tag{5}$$

Equations 3, 4, and 5 constitute the differential equations of equilibrium that govern the internal axial force, T, and the internal moments, M and T_{or}.

The internal axial force and moments are related to the displacements u, v, and the rotation, ϕ, by the usual definitions from mechanics of materials as follows

$$T = A_f E_f u' \tag{6}$$

$$M = E_f I_f v'' \tag{7}$$

$$T_{or} = -G_f J_f \phi' \tag{8}$$

where

E_f = Young's modulus of the fiber material,
G_f = shear modulus of the fiber material,
$I_f = \pi r_f^4/4$ = moment of inertia of the fiber cross section,
$J_f = \pi r_f^4/2$ = polar moment of inertia of the fiber cross section,
$A_f = \pi r_f^2$ = area of the fiber cross section, and
Subscript f = pulled fiber.

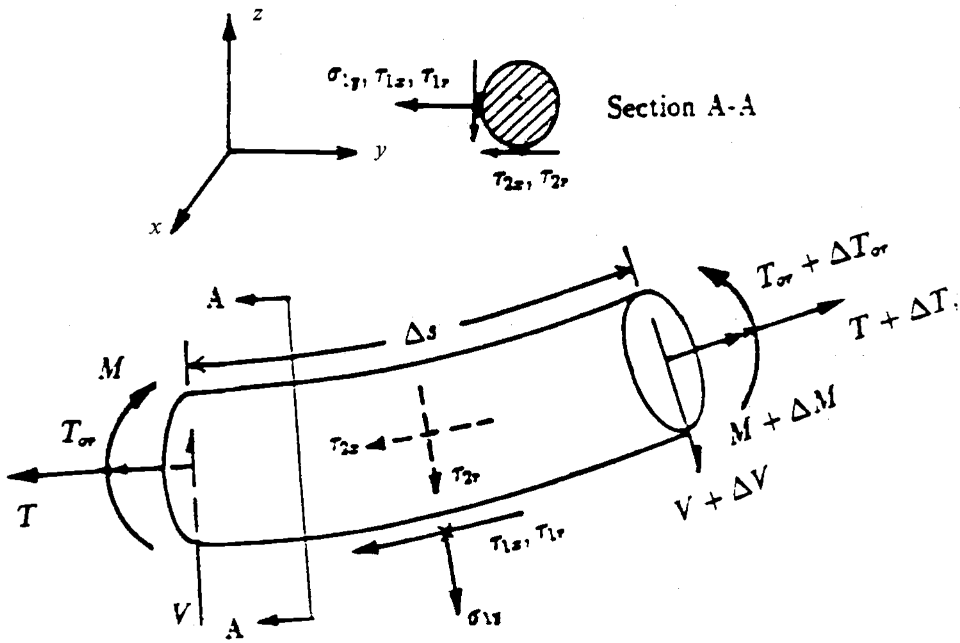

FIG. 2—*Equilibrium of the fiber element.*

The stress components, σ_{1y}, τ_{1z}, τ_{1r}, in the side adhesive layer and τ_{2r}, τ_{2x} in the bottom adhesive layer are related to the displacements u, v, and ϕ by first expressing the strain components in the two layers. In the side adhesive layer, the normal strain, ϵ_{1y}, is assumed to be

$$\epsilon_{1y} = v/t_{a1} \tag{9}$$

The shear strain in the x-direction is

$$\gamma_{1x} = (u + r_f v')/t_{a1} \tag{10}$$

and in the z-direction is

$$\gamma_{1r} = r_f \phi/t_{a1} \tag{11}$$

In the bottom adhesive layer, the shear strain in the x-direction is

$$\gamma_{2x} = u/t_{a2} \tag{12}$$

and the shear strain in the y-direction is given by

$$\gamma_{2r} = (v - r_f \phi)/t_{a2} \tag{13}$$

Hook's law for the assumed linear elastic behavior of the adhesives yields the stresses as follows

$$\sigma_{1y} = E_a \epsilon_{1y} = E_a v/t_{a1} \tag{14}$$

$$\tau_{1x} = G_a\gamma_{1x} = G_a(u + r_f v')/t_{a1} \tag{15}$$

$$\tau_{1r} = G_a\gamma_{1r} = G_a r_f \phi/t_{a1} \tag{16}$$

$$\tau_{2x} = G_a\gamma_{2x} = G_a u/t_{a2} \tag{17}$$

$$\tau_{2r} = G_a\gamma_{2r} = G_a(v - r_f\phi)/t_{a2} \tag{18}$$

where

E_a = Young's modulus of the adhesives,
G_a = shear modulus of the adhesives, and
Subscript a = adhesive materials.

The final equations that govern u, v, and ϕ are obtained by substituting Eqs 6, 7, 8, 14, 15, 16, 17, and 18 into Eqs 3, 4, and 5 and are given here

$$v_i'''' + A_{i1}v_i'' + A_{i2}v_i + A_{i3}u_i' + A_{i4}\phi_i = 0 \tag{19}$$

$$u_i'' + B_{i1}u_i + B_{i2}v_i' = 0 \tag{20}$$

$$\phi_i'' + C_{i1}\phi_i + C_{i2}v_i = 0 \tag{21}$$

The displacements, u and v, and the distance, x, have been nondimensionalized by dividing them by the fiber radius, r_f. A subscript, i, has been added to u, v, and ϕ to indicate that Eqs 19, 20, and 21 must apply in Zone I ($i = 1$) where both the side and bottom adhesive layers are bonded to the fiber and in Zone II ($i = 2$) where the side adhesive layer has been debonded. The physical nondimensionalized constants for Zone I and Zone II are given in the Table 1.

The system of governing equations is linear and homogeneous. The response (deformation) vectors can be expressed in the form of Eq 22. The double subscripts denote quantities related to the j^{th} eigenvalue of the i^{th} coordinate system for singly-bonded zone and doubly-bonded zone referred to in Fig. 1.

$$[v_i, u_i, \phi_i]^T = [a_{ij}, b_{ij}, c_{ij}]^T e^{\alpha_{ij}x_i} \tag{22}$$

where

$[v_i, u_i, \phi_i]^T$ = a response vector,
$[a_{ij}, b_{ij}, c_{ij}]^T$ = a coefficient vector,
α_{ij} = an eigenvalue, and
x_i = a nondimensional spatial coordinate.

Determining the eigenvalues and eigenfunctions give rise to the following solution.

$$\begin{aligned}[v_i, u_i, \phi_i]^T = {} & \sum_{j=1}^{l} K_{i,j}[V_{i,j}]e^{(\alpha_{ij}x_i)} + \sum_{j=l+1}^{l+m} K_{i,j}[V_{i,j}]x_i^{j-l-1} \\ & + \sum_{j=l+m+1}^{l+m+n} \{K_{i,2j-l-m-l}\{[U_{i,2j-l-m-1}]\cos(\omega_{ij}x_i) \\ & + [U_{i,2j-l-m}]\sin(\omega_{ij}x_i)\}e^{(\beta_{ij}x_i)} \\ & + K_{i,2j-l-m}\{[V_{i,2j-l-m-1}]\cos(\omega_{ij}x_i) \\ & + [V_{i,2j-l-m}]\sin(\omega_{ij}x_i)\}e^{(\beta_{ij}x_i)}\}\end{aligned} \tag{23}$$

TABLE 1—*Physical constants of the elastic adhesives.*

Zone I	Zone II
$A_{11} = -(G_a b_1 r_f^4)/(E_f I_f t_{a1})$	$A_{21} = 0$
$A_{12} = (E_a b_1 r_f^4)/E_f I_f t_{a1}) + (G_a b_2 r_f^4)/(E_f I_f t_{a2})$	$A_{22} = (G_a b_2 r_f^4)/E_f I_f t_{a2})$
$A_{13} = -(G_a b_1 r_f^4)/(E_f I_f t_{a1})$	$A_{23} = 0$
$A_{14} = -(G_a b_2 r_f^4)/(E_f I_f t_{a2})$	$A_{24} = A_{14}$
$B_{11} = -(G_a b_1 r_f^2)/A_f E_f t_{a1}) - (G_a b_2 r_f^2)/(A_f E_f t_{a2})$	$B_{21} = -(G_a b_2 r_f^2)/A_f E_f t_{a2})$
$B_{12} = -(G_a b_1 r_f^2)/(A_f E_f t_{a1})$	$B_{22} = 0$
$C_{11} = -(G_a b_1 r_f^4)/(G_f J_f t_{a1}) - (G_a b_2 r_f^4)/(G_f J_f t_{a2})$	$C_{21} = -(G_a b_2 r_f^4)/(G_f J_f t_{a2})$
$C_{12} = (G_a b_2 r_f^4)/(G_f J_f t_{a2})$	$C_{22} = C_{12}$

where the first term represents the l eigenfunctions corresponding to the l real eigenvalues, the second term represents the m eigenfunctions corresponding to the m repeated zero eigenvalues, and the last term represents the $2n$ pairs of eigenfunctions corresponding to n pairs of complex conjugate eigenvalues ($\alpha_{ij} = \beta_{ij} \pm i\omega_{ij}$). The K_{ij} are the eight constants of integration for the i^{th} coordinate system.

Possible Failures

The failure occurs in the side and the bottom adhesive layers of the pulled fiber. The side adhesive layer in Zone I fails by the normal mode for large pulling angles, θ_p, and by the shear mode for small θ_p. The failure of the side layer happens prior to the failure of the bottom layer and creates Zone II of length x_{2l} in which the fiber is bonded only by the bottom layer. Maximum stress criteria are used so that when the normal stress reaches a specified maximum normal stress ($\sigma_{\max}$) the adhesive layer is assumed to fail in the normal mode. Similarly, when the shear stress reaches the maximum stress ($\tau_{\max}$), the layer is assumed to fail in the shear mode. It is assumed that $\sigma_{\max}$ and $\tau_{\max}$ are known material properties of the adhesive.

The first possible failure condition is named Case–NS for large pulling angles. The side adhesive layer fails due to the normal mode but the bottom layer fails due to the shear mode. This condition is expressed as follows

$$\sigma_1 = \sigma_{\max} \tag{24}$$

$$\tau_{c1} = \sqrt{\tau_1^2 + \tau_{1t}^2} < \tau_{\max} \tag{25}$$

$$\tau_{c2} = \sqrt{\tau_{2\theta}^2 + \tau_{2r}^2} = \tau_{\max} \tag{26}$$

For the small pulling angles, the second failure condition is called Case–SS. In this case, both adhesive layers fail in the shear mode. This condition is expressed as follows

$$\tau_{c1} = \sqrt{\tau_1^2 + \tau_{1t}^2} = \tau_{\max} \tag{27}$$

$$\sigma_1 < \sigma_{\max} \tag{28}$$

$$\tau_{c2} = \sqrt{\tau_{2\theta}^2 + \tau_{2r}^2} = \tau_{\max} \tag{29}$$

The combined shear stresses, τ_{c1} and τ_{c2}, are at failure points in the side adhesive layer and bottom layer, respectively.

Boundary Conditions

The length of Zone I is large compared to the diameter of the fiber and is modeled as the semi-infinite region defined by $0 \leq x_1 < \infty$. The solution in Zone I remains finite as x_1 approaches ∞ so the constants of integration, $K_{1,j}$, that are coefficients of the solutions that correspond to eigenvalues with positive real parts must be zero. For reasonable values of the physical parameters, it is found that the characteristic equation for Zone I has two pairs of real roots with opposite signs and two pairs of complex roots with real parts of opposite signs. Thus, four of the eight roots have positive real parts and so the four corresponding constants, $K_{1,j}$, are set to zero. In Zone II, the roots are similarly classified as four real and four complex roots but due to the limited length of Zone II, none of the constants $K_{2,j}$ are required to be zero.

The long free portion of the fiber that has been torn free from the composite body is modeled as an elastica that is pulled at Angle θ_p, far removed from the complete failure point at $x_2 = 0$ by an unknown debonding force, P. The elastica solutions of Gardon [*14*] and Gent and Hamed [*19*] have been modified to give the following relationships

$$\left.\begin{aligned} M_0 &= \sqrt{2PE_fI_f(1 - \cos(\theta_p - \theta_0))} \text{ (bending)} \\ T_0 &= P\cos(\theta_p - \theta_0) \text{ (tension)} \\ V_0 &= P\sin(\theta_p - \theta_0) \text{ (shear)} \\ T_{or0} &= 0 \text{ (torsion)} \end{aligned}\right\} \tag{30}$$

where M_0, T_0, V_0, T_{or}, and θ_0 are values of bending moment, axial force, shear force, torque, and slope at $x_2 = 0$, respectively.

For either failure condition Case–NS or Case–SS, the unknowns are twelve $K_{i,j}$, x_{2l} (length of Zone II), θ_0, and P, for a total of fifteen. Continuity of the solutions in the free length, Zone II, and Zone I requires that the following matching conditions be satisfied.

At $x_2 = 0$

$$\left.\begin{aligned} v_2'(0) &= -\tan\theta_0 \\ \phi_2'(0) &= 0 \\ v_2''(0) &= \sqrt{P^*(1 - \cos(\theta_p - \theta_0))} \\ v_2'''(0) &= 0.5P^*\sin(\theta_p - \theta_0) \\ u_2'(0) &= 0.125P^*\cos(\theta_p - \theta_0) \end{aligned}\right\} \tag{31}$$

where $P^* = 2Pr_f^2/(E_fI_f)$.

At $x_2 = x_{2l}$ or $x_1 = 0$

$$\left.\begin{aligned} v_1(0) &= v_2(x_{2l}) & v_1'(0) &= v_2'(x_{2l}) \\ v_1''(0) &= v_2''(x_{2l}) & v_1'''(0) &= v_2'''(x_{2l}) \\ \phi_1(0) &= \phi_2(x_{2l}) & \phi_1'(0) &= \phi_2'(x_{2l}) \\ u_1(0) &= u_2(x_{2l}) & u_1'(0) &= u_2'(x_{2l}) \end{aligned}\right\} \tag{32}$$

For Case-NS (large θ_p), the normal stress, σ_1, in the side layer at $x_1 = 0$ satisfies

$$\sigma_1 = \sigma_{max} = E_a r_f v_1(0)/t_{a1} \tag{33}$$

For Case-SS (small θ_p), the combined shear stress, τ_{c1}, in the side layer at $x_1 = 0$ satisfies

$$\tau_{c1} = \tau_{max} = (G_a r_f/t_{a1})\sqrt{(u_1 + v_1')^2 + \phi_1^2} \tag{34}$$

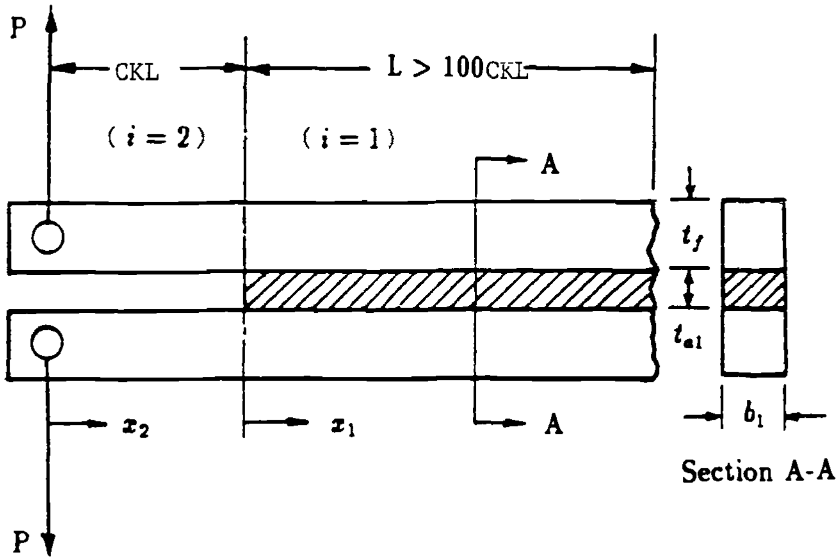

FIG. 3—*Model of the DCB specimen.*

In both cases, the combined shear stress, τ_{c2}, in the bottom layer at $x_2 = 0$ satisfies

$$\tau_{c2} = \tau_{\max} = (G_a r_f / t_{a2})\sqrt{(v_2 - \phi_2)^2 + u_2^2} \tag{35}$$

Numerical Results

To establish the validity of the preceding method, the standard double-cantilever beam (DCB) specimen was analyzed. The DCB specimen as shown in Fig. 3 is one of the most well-defined specimens for evaluating the constitutive behavior and peel properties of the adhesive layer. The specimen consists of two parallel beams joined together with an adhesive layer. The DCB test could be treated as a special case of the doubly-bonded composite body by removing the bottom adhesive layer. Using physical properties and the equation of the free beam in Yamada's [*11*] analysis for modification of an opened crack, the stress energy release rate (SERR) from the present study is found in excellent agreement with Yamada's results on elastic materials. The physical properties are shown in Table 2. For crack lengths (CKL) of 0.76, 1.27, 1.78, and 2.29 cm, the values of the SERR are shown in Figs. 4 and 5 with respect to the applied force and to the load line deflection for two cases: (*a*) assuming the crack is extended

TABLE 2—*Physical properties of DCB specimen.*

DCB	Adhesive	Crack Length, cm
E_f = 117 (GPa)	E_a = 27.6 (GPa)	0.76
t_f = 1.02 (mm)	t_{a1} = 0.254 (mm)	1.27
b_1 = 0.64 (mm)	$\sigma_{\max}$ = 34.5 (MPa)	1.78
I_f = 0.057 (mm^4)		2.29

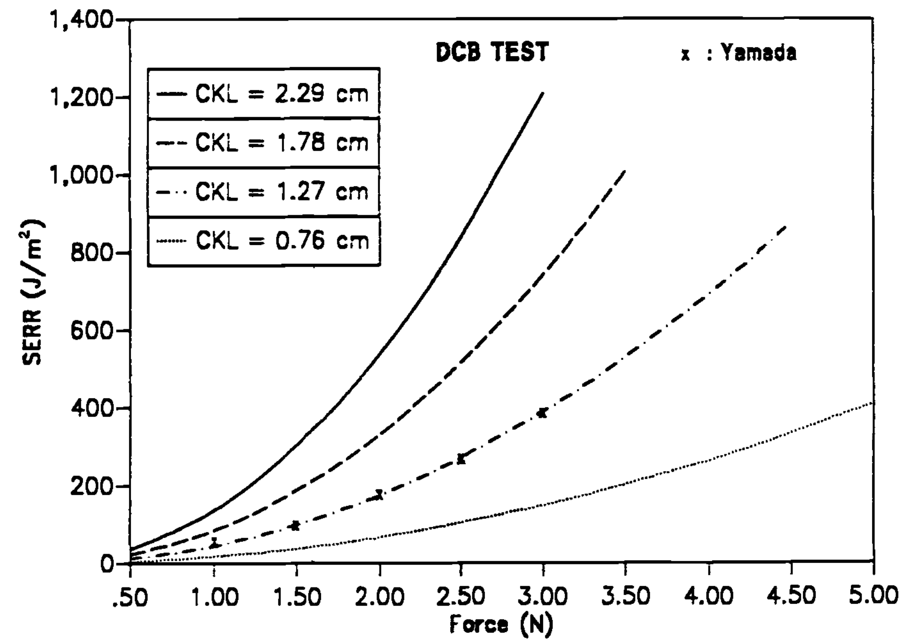

FIG. 4—*SERR versus force relationship.*

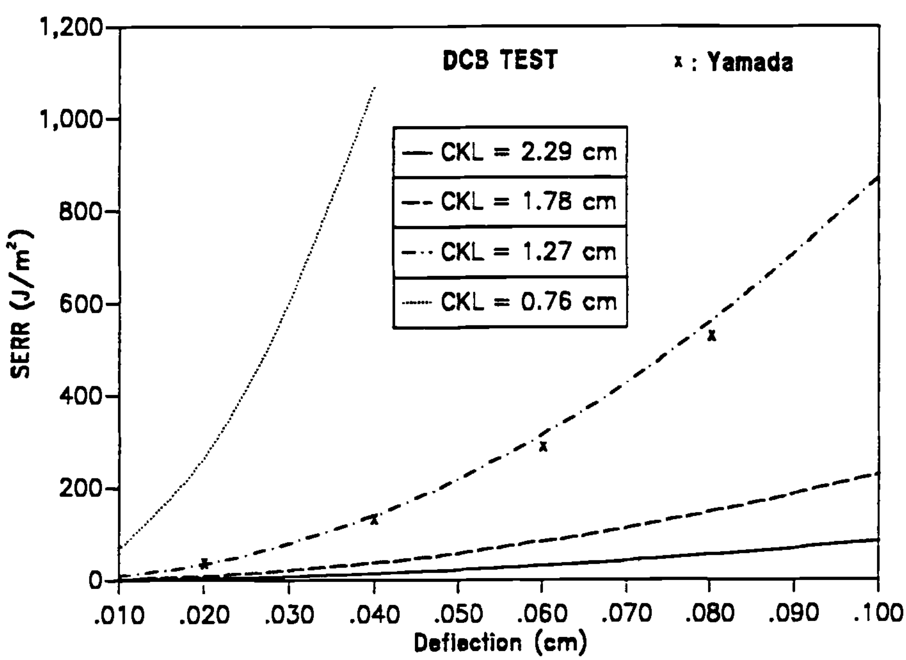

FIG. 5—*SERR versus deflection relationship.*

TABLE 3—*Physical properties of the fiber bonded with two adhesive layers.*

Glass Fiber	Epoxy Adhesive
E_f = 100 (GPa)	E_a = 3 (GPa)
G_f = 33 (GPa)	G_a = 1 (GPa)
r_f = 1.0 (mm)	σ_{max} = 60 (MPa)
I_f = 0.785 (mm^4)	τ_{max} = 20 (MPa)
J_f = 1.571 (mm^4)	$t_{a1} = t_{a2}$ = 0.1 (mm)
	$b_1 = b_2$ = 1.0 (mm)

at constant displacement, and (*b*) assuming the crack is extended at constant load. This is important evidence confirming the validity of this investigation.

For the doubly-bonded fiber, the debonding behavior for an arbitrary pulling angle (θ_p) is the primary objective of this investigation. Numerical results are presented for a glass fiber doubly bonded to the remainder of the composite body with adhesive epoxy. Important physical parameters for the glass fiber and the epoxy adhesive are listed in Table 3. The force necessary to break the bonds of the side and bottom adhesive layers (debonding force, *P*) is shown in Fig. 6 as a function of the pulling angle, θ_p. For small pulling angle (less than about 6°), the pulling angle varies greatly from being more than 100 N for θ_p = 1° down to about 7.8 N at θ_p = 6°. Beyond θ_p = 6°, the debonding force decreases gradually to an asymptotic value of 0.43 N for pulling angle more than 30°. The debonding angle, θ_0, as shown in Fig. 6 is very small (less than 0.2°).

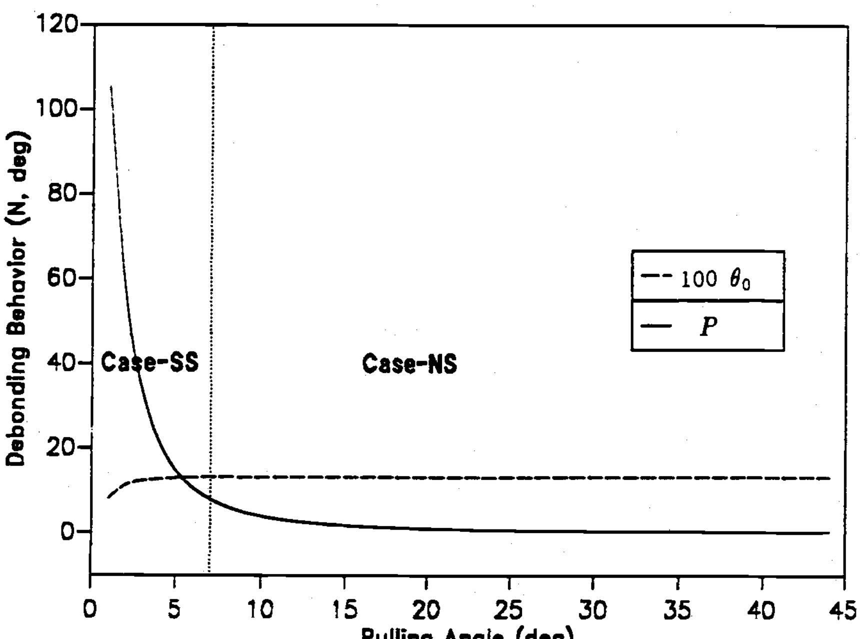

FIG. 6—*Debonding force and debonding angle versus pulling angle.*

The large variation of debonding force for pulling angles between $\theta_p = 1°$ and $\theta_p = 6°$ is due to the transition of the failure mode of the side adhesive layer in Zone II changing from shear mode (Case–SS) for $\theta_p < 6°$ to normal mode (Case–NS) for $\theta_p > 6°$. The length of Zone II, x_{2l}, varies as a function of θ_p as shown in Fig. 7. Figure 7 shows a distinct change in the behavior of x_{2l} with θ_p because the failure mode in the side layer changes from the shear mode to normal mode.

The stress distributions in the adhesive layers are shown in Fig. 8 for $\theta_p = 90°$. Two sets of stresses, σ_{1y}, τ_{1x}, τ_{1r}, and τ_{2x}, τ_{2r}, correspond to stresses in the side and bottom layers, respectively, are shown. Zone I and Zone II are marked to show that there are only two shear stresses in Zone II and all five stresses act on the adhesive layers in Zone I. Note that all components of stress decrease as the distance from the complete failure point (at $x_2 = 0$) increases.

Conclusion

The theory of a beam-on-elastic-foundation was employed to investigate stress distribution, debonding angle, and debonding force in a composite body with multiple adhesive layers. The model was used to consider the DCB specimen and yielded an excellent agreement with Yamada's results.

The criteria of adhesive failure are vital in debonding force calculations. In this paper, simple maximum stress criteria are adopted. Other failure criteria may be more appropriate for the mixed-mode conditions in the debonding of a fiber from a composite body. We found no references reporting experimental research on failure criteria for situations similar to ours. Future work could include such fundamental experimentation and modification of this analysis if alternate failure criteria are more applicable.

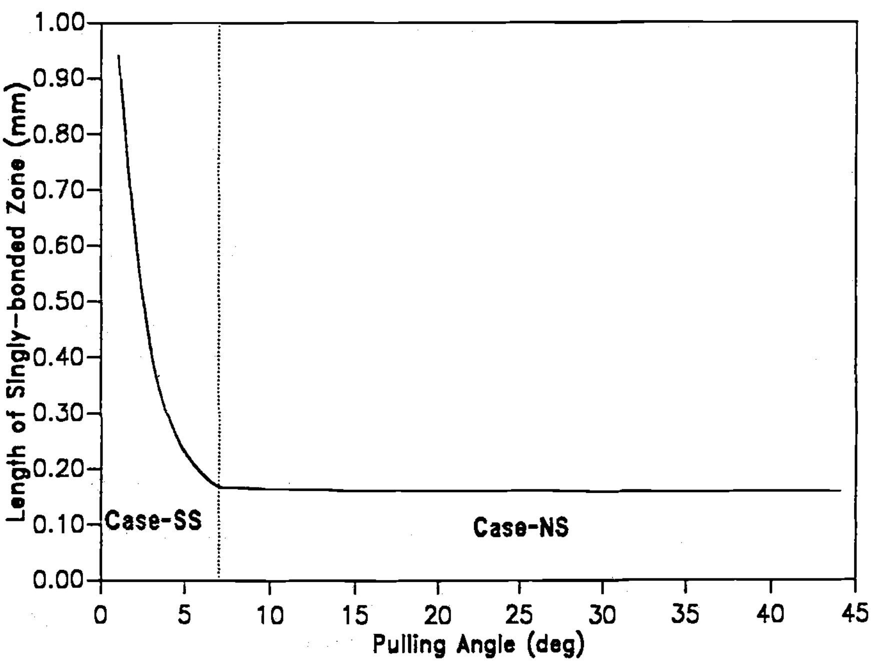

FIG. 7—*Length of the singly-bonded zone* (x_{2l}) *versus pulling angle* (θ_p).

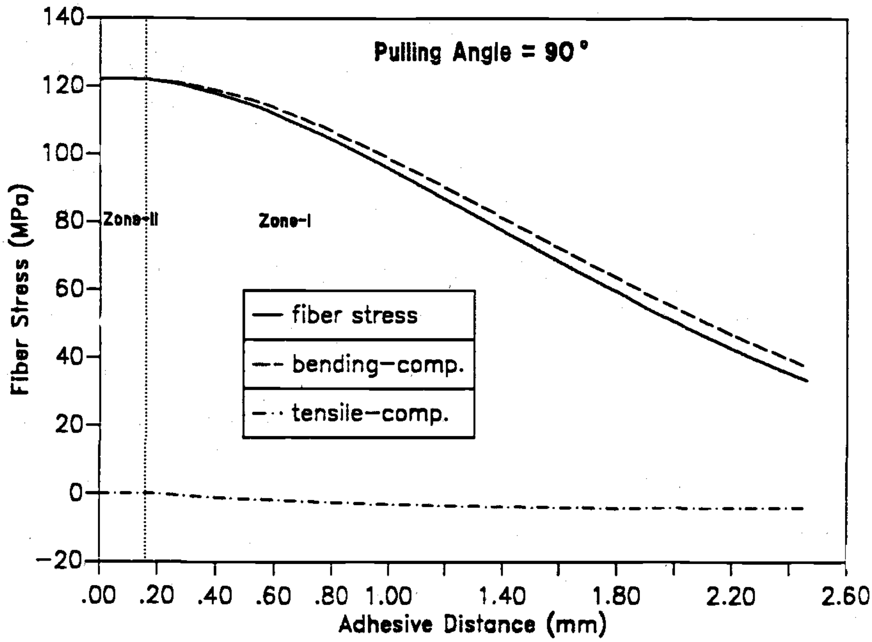

FIG. 8—*Adhesive stress distribution for* $\theta_p = 90°$.

Acknowledgment

Mr. Leu acknowledges the Peter Prater Foundation and the University of Alabama for financial support of his graduate study.

References

[*1*] *Adhesives Technology Handbook,* A. H. Landrock, Ed., Noyes, Park Ridge, NJ, 1986.

[*2*] Malyshev, B. M. and Salganik, R. L. "The Strength of Adhesive Joints Using the Theory of Cracks," *International Journal of Fracture,* Vol. 26, 1984, pp. 261–275.

[*3*] Lubkin, J. L. and Lewis, L. C., "Adhesive Shear Flow for an Axially-Loaded Stringer Bonded to an Infinite Sheet," *Quarterly Journal of Mechanics and Applied Mathematics,* Vol. 22, Pt. 4, 1970, pp. 521–533.

[*4*] Williams, J. H., "Stresses in Adhesive between Dissimilar Adherends," *Journal of Adhesion,* Vol. 7, 1975, pp. 97–107.

[*5*] Roberts, T. M., "Shear and Normal Stresses in Adhesive Joints," *Journal of Engineering Mechanics,* Vol. 115, No. 11, 1989, pp. 2460-2479.

[*6*] Anderson, G. P., Devries, K. L., and Williams M. L., "Finite Element in Adhesive Analysis," *International Journal of Fracture,* Vol. 9, No. 4, 1973, pp. 421–436.

[*7*] Bennett, S. J., Devries, K. L., and Williams, M. L., "Adhesive Fracture Mechanics," *International Journal of Fracture,* Vol. 10, No. 1, 1974, pp. 33–43.

[*8*] Adams, R. D. and Peppiatt, N. A., "Stress Analysis of Adhesive-Bonded Lap Joints," *Journal of Strain Analysis,* Vol. 9, No. 3, 1974, pp. 185–196.

[*9*] Dattaguru, B., Everett, R. A., Whitcomb, J. D., and Johnson, W. S., "Geometrically Nonlinear Analysis of Adhesively Bonded Joints," *Journal of Engineering Materials and Technology, Transactions,* American Society of Mechanical Engineers, Vol. 106, 1984, pp. 59–65.

[*10*] Johnson, W. S., "Stress Analysis of the Cracked-Lap-Shear Specimen: An ASTM Round-Robin," *Journal of Testing and Evaluation,* Vol. 15, No. 6, 1987, pp. 303–324.

[*11*] Yamada, S. E., "Elastic/Plastic Fracture Analysis for Bonded Joints," *Engineering Fracture Mechanics,* Vol. 27, No. 3, 1987, pp. 315–328.

[*12*] Amijima, S., Fujii, T., Ebata, S., and Tanaka, T., "Two Dimensional Stress Analysis on Adhesive Bonded Lap Joints," *Japanese Journal of Adhesive,* Vol. 24, No. 3, 1988, pp. 86–98.
[*13*] Kanninen, M. F., "An Augmented Double Cantilever Beam Model for Studying Crack Propagation and Arrest," *International Journal of Fracture,* Vol. 9, No. 1, 1973, pp. 83–91.
[*14*] Gardon, J. L., "Peel Adhesion. II. A Theoretical Analysis," *Journal of Applied Polymer Science,* Vol. 7, 1963, pp. 643–665.
[*15*] Williams, M. L., *Stress Singularities, Adhesion, and Fracture, Proceedings,* Fifth U.S. National Congress of Applied Mechanics, American Society of Mechanical Engineers, New York, 1966, pp. 451–464.
[*16*] Hellan, K., "Debond Dynamics of an Elastic Strip, I: Timoshenko-Beam Properties and Steady Motion," *International Journal of Fracture,* Vol. 14, No. 1, 1978, pp. 91–100.
[*17*] Hellan, K., "Debond Dynamics of an Elastic Strip, II: Simple Transient Motion," *International Journal of Fracture,* Vol. 14, No. 2, 1978, pp. 173–184.
[*18*] Williams, M. L., "The Continuum Interpretation for Fracture and Adhesion," *Journal of Applied Polymer Science,* Vol. 13, 1969, pp. 29–40.
[*19*] Gent, A. N. and Hamed, G. R., "Peel Mechanics," *Journal of Adhesion,* Vol. 7, 1975, pp. 91–95.

Carlos R. Corleto[1] *and Harry A. Hogan*[1]

A Finite-Element Analysis of Nonlinear Behavior of the End-Loaded Split Laminate Specimen

REFERENCE: Corleto, C. R. and Hogan, H. A., "**A Finite-Element Analysis of Nonlinear Behavior of the End-Loaded Split Laminate Specimen,**" *Fracture Mechanics: Twenty-Third Symposium, ASTM STP 1189,* Ravinder Chona, Ed., American Society for Testing and Materials, Philadelphia, 1993, pp. 649–667.

ABSTRACT: A finite-element analysis has been developed to evaluate the J-integral for the end-loaded split laminate specimen (ELS) used to characterize Mode II delamination fracture toughness of composites. The analysis includes the use of nonlinear beam theory to evaluate the J-integral from typical output data obtained using nonlinear beam elements. The beam elements include large deflections and rotations, midplane straining, and the effect of shear deformations. Several composite laminates going from unidirectional to multidirectional layups have been studied. The path independence of the J-integral using this analysis has been verified except for paths very close to the crack tip where the complex state of stress that develops at the crack tip invalidates beam theory approximations. For all the layups studied, midplane straining from the development of large rotations shows no significant effect on J. Furthermore, J has been found to be independent of shear deformations even when shear deformations are no longer negligible in the load-deflection response of the ELS. The effect of limited inelasticity on J, as is typical of multidirectional layups, has also been studied. This analysis illustrates the feasibility of evaluating the J-integral from simplified finite-element analyses, where global quantities away from the complex state of stress at the crack tip are used instead of local stresses and strains near the crack tip.

KEY WORDS: J-integral, composite materials, nonlinear finite-element analysis, Mode II delamination, shear deformation, inelasticity, damage, fracture mechanics

One of the most commonly used specimens in the study of Mode II delamination behavior of fiber-reinforced composite materials is the end-loaded split laminate specimen (ELS) [*1–5*] depicted in Fig. 1. This specimen configuration was originally proposed by Vanderkley [*3*] assuming linear elastic composite behavior and linear beam theory, with the strain energy release rate, G, as the fracture parameter. A finite-element analysis by Corleto et al. [*6*] also showed that indeed a pure Mode II loading condition develops at the crack tip. An extension to nonlinear beam theory was later done by Williams [*7*]. Recently, Corleto [*8*] and Goetz [*9*] have introduced a J-integral approach for the ELS including a more generalized material and geometric response. Corleto derived equations for J with the ELS under linear beam theory assumptions but with distributed damage developing in the cracked legs of the specimen [*8*]. Goetz extended the theory to nonlinear beam theory with midplane straining and large strains [*9*]. An experimental assessment of these analyses [*9*] has shown the feasibility of using J as a fracture parameter even for composite laminates with limited inelasticity. Limited inelasticity

[1] Research associate and assistant professor, respectively, Department of Mechanical Engineering, Texas A&M University, College Station, TX 77843-3123.

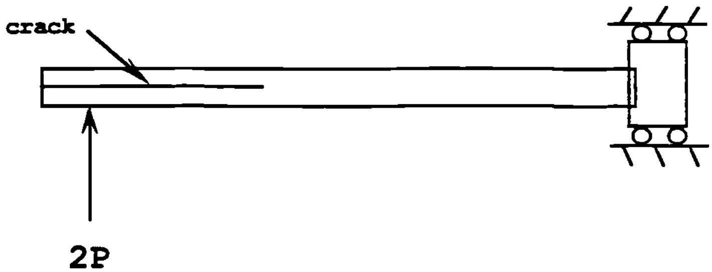

FIG. 1—*End-loaded split laminate (ELS) test used for Mode II delamination fracture characterization of composites.*

refers herein to inelastic effects due to damage in the form of microcrack formation away from the crack tip.

The evaluation of the *J*-integral using finite-element analyses has been done traditionally using continuum elements refined locally to model an explicit crack tip. This approach usually requires a relatively large number of elements, and the *J*-integral is calculated from stresses along paths within the interior of the structure or body in the region near the crack tip. Furthermore, if nonlinear material or geometric behavior is added to the analysis, computing time and storage requirements are increased significantly making the analyses very costly. In the approach presented in Refs *8* and *9*, the integration paths for calculating *J* have been taken to be far away from the complex state of stress at the crack tip. This allows the *J*-integral to be expressed in terms of global quantities. Under these circumstances, the evaluation of *J* using finite-element analysis can become significantly easier, since localized mesh refinement is not needed and simpler element types and mesh configurations can be used.

The purpose of this investigation has been to develop a finite-element analysis to evaluate the *J*-integral of the ELS as proposed in Refs *8* and *9* using standard nonlinear beam elements. The approach includes the use of nonlinear beam theory to evaluate the *J*-integral from typical output data for beam elements. The effects of midplane straining, shear deformation, and distributed damage in the legs of the ELS on *J* have been investigated. Also, the path independence of *J* as proposed in Refs *8* and *9* for the ELS has been assessed. The results illustrate the feasibility of evaluating the *J*-integral from simplified finite-element analyses, where global quantities away from the complex state of stress at the crack tip are used instead of local stresses and strains near the crack tip.

Analysis

The J-Integral Approach for the ELS

The *J* integral expression for the ELS developed by Goetz [*9*] is given by

$$J_{\text{II}} = \frac{2}{B}\int_0^{M_c} K_c^* dM + \frac{2}{B} P \sin\phi_c - \frac{1}{B}\int_0^{M_u} K_u^* dM - \frac{2}{B} P \sin\phi_u \tag{1}$$

In this expression, P is the load applied to each leg (Fig. 2), and B is the width of the ELS. The angles, ϕ_c and ϕ_u, refer to slope angles at the path locations in the cracked and uncracked segments of the ELS, respectively. Similarly, M_c and M_u are moments at these locations, and

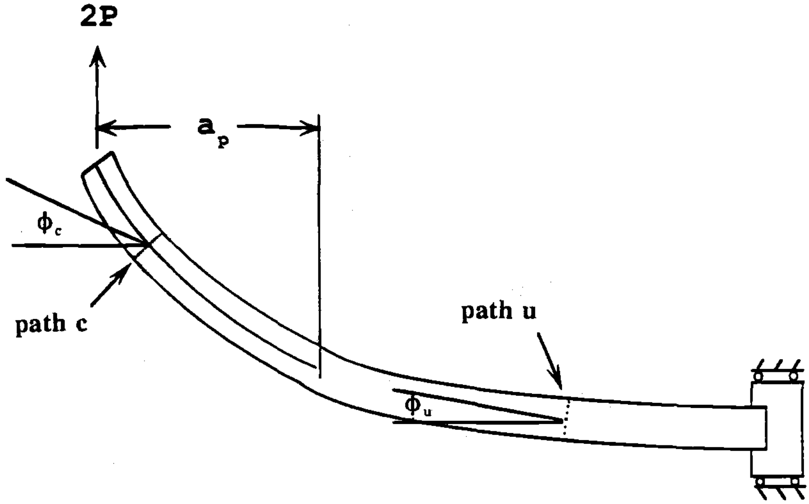

FIG. 2—*ELS specimen under large deformation conditions.*

K_u^* and K_c^* are the curvatures of the planes of zero strain. The relationship between K^* and K, the midplane curvature, is given by

$$K^* = (1 + \epsilon_0)K \tag{2}$$

where ϵ_0 is the midplane strain [9]. Using nonlinear beam theory, it can also be shown that

$$K^* = \frac{\partial\phi}{\partial x} \tag{3}$$

and

$$K = \frac{(\partial\phi/\partial x)}{(\partial u_y^0/\partial x)}\sin\phi \tag{4}$$

where ϕ is the slope angle, x and y are the undeformed configuration coordinates, and u_y^0 is the deflection of the midplane in the y-direction. When no midplane straining occurs, K^* can be replaced by K in Eq 1.

The derivation of Eq 1 assumes negligible effects of shear deformation and friction between the cracked legs. A graphical representation of the moment-curvature relationships in Eq 1 can be seen in Fig. 3. Note that Eq 1 allows for geometric nonlinearities (large deflections and rotations) as well as nonlinear elastic or inelastic (different loading and unloading paths) material behavior. It also accounts for the development of midplane straining through K^*. In addition, if the paths used to evaluate the J-integral are taken very close to the crack tip and linear elastic material behavior is assumed, the moment-curvature relationships can be approximated using beam theory to obtain

$$J_{\mathrm{II}} = \frac{6(M_{\mathrm{tip}}^c)^2}{BE_{11}I_{mu}} = \frac{6P^2a^2}{BE_{11}I_{mu}} \tag{5}$$

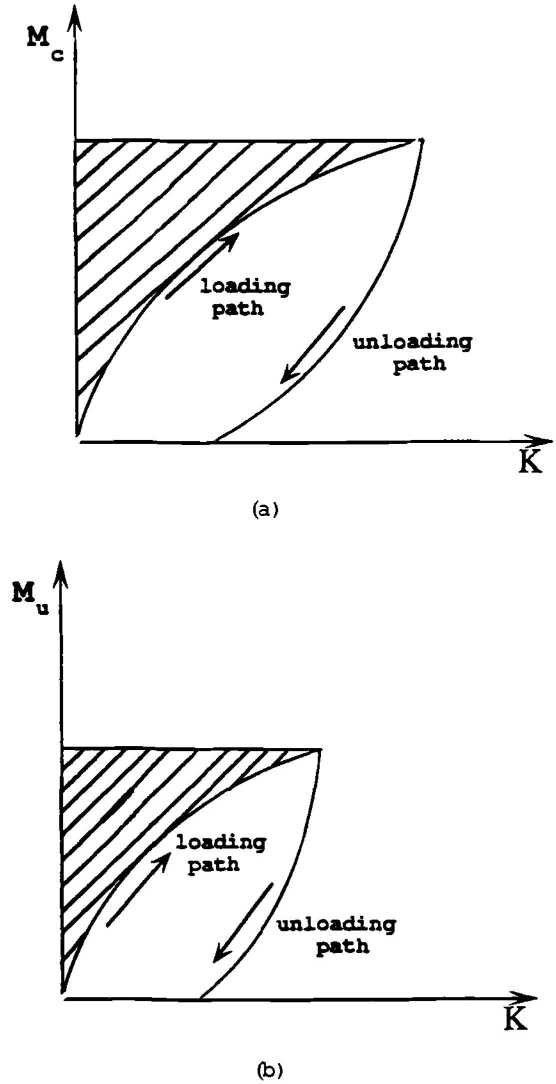

FIG. 3—*Moment curvature relationships for* (a) *cracked and* (b) *uncracked portions of ELS. Note the effect of limited inelasticity.*

where M^c_{tip} is the moment at the crack tip for each cracked leg of the ELS, E_{11} is the elastic modulus in the x-direction, I_{mu} is the moment of inertia of the uncracked portion of the beam, and a is the crack length. This result is the same as that obtained by Vanderkley [3] using the energy release rate approach, G, and linear beam theory, which confirms the equivalence of G and J under linear elastic material conditions. Furthermore, since J_{II} in Eq 5 depends only on the moment at the crack tip, provided shear deformation can be neglected, this expression can be valid for geometric nonlinearities (large deformations and rotations). In this case, the moment arm distance for calculating the crack-tip moment becomes the load-line to crack-tip distance, a_p, instead of the undeformed configuration crack length, a (see Fig. 2). Williams [7] reached the same conclusion with a nonlinear beam theory analysis.

Shear Deformation Effect on J_{II}

In the derivation of the J-integral for the ELS [9], shear deformation effects on J_{II} were assumed to be negligible, since ELS specimens are typically long and slender, making deformations due to bending significantly larger than shear deformation. However, it is not known quantitatively to what extent this assumption is valid. In addition, for orthotropic laminates, the ratio of the tensile modulus to shear modulus also governs the potential significance of shear deformations. Therefore, the effect of shear deformations on J_{II} for the ELS needs to be examined.

Assuming linear elastic material behavior and linear beam theory, Castigliano's Theorem can be used to calculate the deflection at the loaded end of the ELS with shear deformation included. The result is given by

$$\delta = \frac{2P}{3E_{11}I_{mu}}(3a^3 + L^3) + \frac{2PL}{\kappa^2 G_{12}A_u} \tag{6}$$

where A_u is the cross-sectional area of the uncracked segment of the ELS, and κ^2 is a shear correction factor, which is dependent upon the cross-sectional shape. For a rectangular cross-section, κ^2 can be calculated directly from the strain energy term for shear based upon the parabolic distribution of shear stress through the thickness of the beam. In this case, $\kappa^2 = 5/6$. The first term in Eq 6 is the deflection due to bending and the second term contains the contribution due to shear. Equation 6 is given in dimensionless form by

$$\frac{E_{11}I_{mu}\delta}{P(a^3 + L^3)} = \frac{2}{3} + \frac{1}{6\kappa^2}\left(\frac{E_{11}}{G_{12}}\right)\left(\frac{h_u}{L}\right)^2\left(\frac{1}{3(a/L)^3 + 1}\right) \tag{7}$$

where h_u is the thickness of the uncracked beam. From Eq 7, it can be seen that at shorter crack lengths, the thicker the specimen, and the larger the ratio of longitudinal modulus to shear modulus, the greater the effect of shear deformations on δ. Once δ has been determined with shear deformations included, the effect of shear deformations on J_{II} can be assessed using the energy release interpretation of the J-integral. If W is the strain energy and A is the area created by crack extension (where $A = Ba$), then J is given by

$$J = \frac{\partial W}{\partial A} = \frac{1}{B}\frac{\partial W}{\partial a} \tag{8}$$

The strain energy is first expressed in terms of the deflection, δ, and the total load, $2P$, to get

$$W = \frac{1}{2}(2P)(\delta) = \frac{2P^2}{3E_{11}I_{mu}}(3a^3 + L^3) + \frac{2P^2L}{\kappa^2 G_{12}A_u} \tag{9}$$

Finally, substituting Eq 9 into Eq 8 and evaluating the derivative with respect to the crack length, a, yields

$$J_{II} = \frac{6P^2a^2}{BE_{11}I_{mu}} \tag{10}$$

As can be seen, J_{II} is independent of shear deformations even if beam displacements contain significant shear deformation contributions. The significance of this result is that using thick composite laminates to evaluate the J-integral for the ELS will not introduce "error" or require "correction" due to shear effects. The advantage of thick specimens is that they are more likely to maintain geometrically linear behavior that simplifies the measurement of J_{II}. Using finite elements, these findings can be verified and confirmed. A valid finite-element model can also be used to determine if the shear independence of J_{II} holds for large deflections and rotations. In addition, finite-element modeling can be used to address the possible effects of other important factors, such as midplane straining and inelastic material behavior.

Finite-Element Procedures

A finite-element model of the ELS is shown in Fig. 4. The model consists of 63 nodes and 62 elements with a crack-to-length ratio, a/L, of 0.5. However, the number of nodes and elements varied as the a/L ratio was changed from 0.4 to 0.8. The total beam length, L, was 25.4 cm and the height of the beam was 2.54 cm. The beam elements include large deflections and rotations, midplane straining, and shear deformation. Rigid beam elements were used at the crack tip to offset the elements comprising each leg of the cracked portion of the ELS. The ANSYS[2] finite-element package has been used for this investigation. Geometrically nonlinear analysis procedures have been employed throughout in order to model large displacement and large rotation deformation. Material nonlinearity is included as well for the cases studying limited inelasticity in the legs of the ELS specimen. Each problem was therefore solved incrementally with the load applied in load steps (ranging from 15 to 31). A DEC VAX 8650 mainframe computer was used to run the ANSYS finite-element package. Several composite materials with different material properties were modeled in order to create a wide range of composite layups for studying the effect of midplane straining, shear deformation, and limited inelasticity. These material systems are summarized in Table 1.

The J-integral for the ELS was evaluated using the results from the finite-element analysis along with Eqs 1, 3, and 4. Since the finite-element modeling included geometric nonlinearities, the problem was solved incrementally. Moments, slopes, and displacements at each node for each load step were recorded. Next, a particular "path" for evaluating the J-integral was chosen. This simply amounted to selecting a single node in the uncracked portion of the model and a pair of nodes (equidistant from the crack tip) in the cracked portion. Data from the first node was used to evaluate the last two terms in Eq 1 and results from the other two nodes were used to evaluate the first two terms. In order to evaluate the two integral terms in Eq 1, a series of values for K^* were first approximated according to Eq 3. To do this, the slope (ϕ) was plotted versus undeformed location (x) at every node in the model for each load step and a polynomial curve was fit to this data. Next, the resulting curve-fit expression was differentiated at each of the nodes on the path to generate an estimate of K^* for these points for each load step. These curvatures (K^*) were plotted subsequently as a function of corresponding moments (M) and then integrated numerically. With each of the integrals in Eq 1 thus determined, an approximate value for J_{II} was calculated.

Values for J_{II} were also computed using K instead of K^* for the integral terms of Eq 1. In this case, a series of values for K were determined for each load step in a similar manner as for K^*, but using Eq 4. The additional information required was the denominator term in Eq 4, which was estimated by plotting the deflection of the midplane in the y-direction (u_y^0) versus undeformed location (x) for each load step, fitting a polynomial curve, and then differentiating at the nodal locations of interest.

[2] Registered trademark of Swanson Analysis Systems, Inc., Houston, PA.

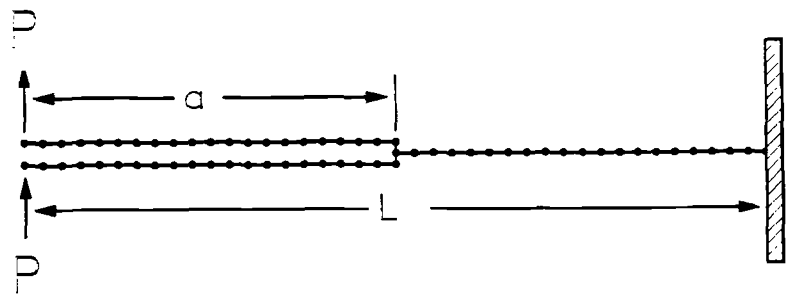

FIG. 4—*Finite-element model of ELS. Model consists of 63 nodes and 62 elements. (Not to scale: vertical offset exaggerated.)*

The results generated from these calculations were summarized by plotting J_{II}, using both K^* and K, as a function of crack-tip moment for the cracked portion of the ELS. For comparison purposes, G_{II} was also calculated using the actual moment at the crack tip from the finite-element nonlinear analysis and in conjunction with the linear expression for G_{II} (Eq 5 or 10). To verify the effect of geometric nonlinearities, G_{II} was also calculated under entirely linear assumptions, that is, using the load, P, and the underformed crack length, a, in Eq 10. In this case, the differences between J_{II} and G_{II} could only be demonstrated by plotting them as a function of the load, P, rather than the crack-tip moment.

The path independence of the proposed J-integral for the ELS was determined by comparing J_{II} evaluated at various path locations along the beam length. The distance from these paths to the crack tip ranged from 0.635 cm to 11.43 cm. The effect of midplane straining was studied by comparing J_{II} using K^* and K in Eq 1. Composites representing a wide range of stiffnesses were examined.

In order to assess the analysis presented in the previous section for J_{II} with shear effects included, several finite-element runs were performed for a/L ratios ranging from 0.4 to 0.8 with and without shear deformation. The resulting load versus δ curves were compared with the theoretical model (Eq 6). The curves were also used to numerically evaluate J_{II} from the fundamental definition presented previously in Eq 8, that is, as the derivative of the strain energy with respect to cracked area. The purpose was to determine whether the predicted independence of J_{II} with shear deformation for the case of linear deformations could be extended to nonlinear deformations. The procedure for calculating J_{II} this way began by selecting a particular load level ($2P$) and then numerically integrating each $2P$ versus δ curve (for each a/L) up to that load to get the strain energy, W. This created a dataset of strain energies and corresponding crack lengths that was curve-fit and then differentiated at each crack length value of interest.

TABLE 1—*Material properties for composites studied.*

Composite	Layup	E_{11}, GPa	G_{12}, GPa
AS4/3502 [*6*] (graphite epoxy)	0°	136	7.1
B(4)/5505 [*10*] (boron/epoxy)	0°	204	5.6
Scotchply [*10*] (glass/epoxy)	0°	38.6	4.1
T300/5208 [*10*] (graphite/epoxy)	±45°	25 (E_x)[a]	46.6 (G_{xy})[a]

[a] Laminate properties with x parallel to the 0° direction.

The effect of limited inelasticity on J_{II}, which typically occurs in multidirectional layups in the form of microcracking, was modeled by using the stress-strain curve shown in Fig. 5 to describe the material response in the finite-element model. This material behavior was assumed for the cracked legs only with the uncracked leg remaining linear elastic. The slope of the linear portion of this stress-strain curve was the same as the axial modulus of the T300/5208 $\pm 45°$ graphite/epoxy composite. The nonlinear portion was generated to simulate theoretically the actual development of inelasticity in the form of damage. The formation of damage in the form of microcracking in the ELS has been observed to occur mainly in the cracked legs for $\pm 45°$ and $\pm 30°$ layups [*8,9*]. The stress-strain curve for the finite-element analysis (Fig. 5) limits the study to monotonic loading with no unloading allowed since a real material would unload along a different path due to permanent damage. However, this is sufficient for the evaluation of J_{II} using Eq 1. It should be pointed out that Eq 1 is actually valid for different loading and unloading paths for "steady state crack growth" [*8*]. The present study was limited to monotonic loading to simplify the computational procedures for demonstrating the effect of limited inelasticity.

Modeling off-axis layups using beam finite elements neglects stretch-twist and bend-twist coupling, and this should be noted as a limitation of the present approach. This case has been included here as a real example of a type of layup for which significant inelasticity develops in the form of microcracking in the cracked legs of the ELS. The practical usefulness of the present analysis is not seriously compromised in many cases. Coupling effects can be minimized using off-axis layups with negligible stretch-twist and bend-twist coupling, or when 0° plies bound the delamination crack plane with the rest of the layup being multidirectional. The critical issue is whether the crack loading remains predominantly Mode II even in the presence of potential coupling. This could be verified experimentally to ensure the applicability of the

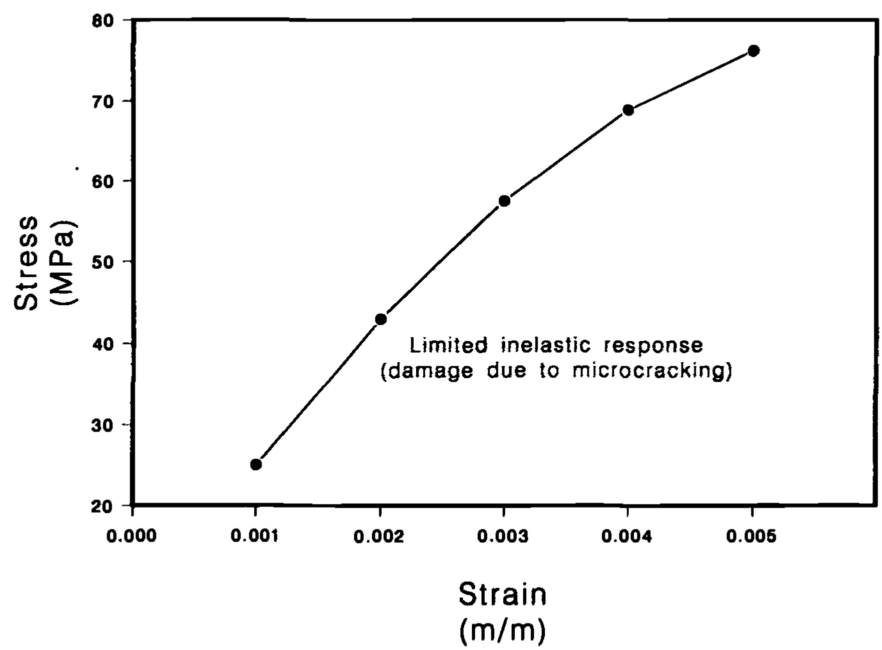

FIG. 5—*Stress-strain curve used to model limited inelastic material response in the cracked legs of ELS specimen.*

current analysis. The motivation for this part of the study was simply to demonstrate the usefulness of the method in including inelastic effects.

Results and Discussion

Verification of the Finite-Element Approach for J_{II}

Figure 6*a* shows J_{II} and G_{II} plotted as a function of M^c_{tip}, the moment at the crack tip for either of the cracked beam portions. The particular specimen modeled was a unidirectional layup of AS4/3502 graphite-epoxy composite with $a/L = 0.5$ and $h_u/L = 0.0125$. J_{II} has been calculated using the proposed method to evaluate the *J*-integral for the ELS (Eq 1). Large deformations and rotations, midplane straining, and elastic material conditions were assumed. Both K^* and K were used in evaluating the integral terms in Eq 1, and the paths were at ± 6.35 cm from the crack tip. G_{II} was calculated from Eq 5 by using the actual moment at the crack tip (M^c_{tip}) directly from the finite-element output data. When calculated this way, G_{II} is valid for nonlinear beam deflections and rotations but not midplane straining. As these results show, the proposed procedure to evaluate J_{II} using the finite-element output coincides with G_{II} in the geometrically linear and geometrically nonlinear range of deformations. Note that J_{II} calculated using K^* and K are the same indicating no significant midplane straining. Thus, G_{II} and J_{II} should be equivalent since linear elastic material behavior has been assumed.

Figure 6*b* shows a comparison of J_{II} with G_{II} calculated from purely linear beam theory assumptions. As mentioned previously, the plots must be presented as a function of the total load, $2P$, rather than the crack-tip moment, M^c_{tip}, in order to show the nonlinear effect. Note from Fig. 6*b* that J_{II} corresponds very well with G_{II} at the lower loads since the response is still in the linear range. As the load increases, however, the two curves deviate substantially with the linear theory greatly overpredicting the fracture energy.

Figure 7 shows the results for J_{II} evaluated at several path locations for the same model analyzed in Fig. 6*a*. The path locations ranged from ± 0.635 to ± 11.43 cm away from the crack tip. Except for the path location very close to the crack tip (Path 1), the curves are nearly identical, thereby confirming the path independence of the J expression for the ELS (Eq 1) calculated using the current procedures. The deviation for the path closest to the crack tip is most likely due to the complex state of stress that develops at the crack tip and for which beam theory approximations are no longer valid. Note again the equivalency of G and J.

These results clearly demonstrate the feasibility of the approach developed to evaluate the *J*-integral for the ELS from simplified finite-element analyses where global quantities away from the complex state of stress at the crack tip are used instead of local stresses and strains near the crack tip.

Effect of Midplane Straining on J_{II}

The results presented previously in Figs. 6*a* and *b* suggest that midplane straining has no significant effect on J_{II}, but this is only for one particular composite material system. In order to more comprehensively study the possible effects of midplane straining on J_{II}, three other composite systems were examined as well. In addition to the AS4/3502 graphite/epoxy of Fig. 6*a*, 0° unidirectional layups of two other materials (boron/epoxy and glass/epoxy) were modeled. The same specimen dimensions were retained ($a/L = 0.5$ and $h_u/L = 0.0125$), and linear elastic material behavior was again assumed. Figure 8*a* shows the results for the unidirectional boron/epoxy material with J_{II} calculated using K^* and K in Eq 1. Once again, no significant midplane straining is observed in J_{II}. This is not unexpected, however, since the axial modulus of this composite is very high (204 GPa compared to 136 GPa for AS4/3502).

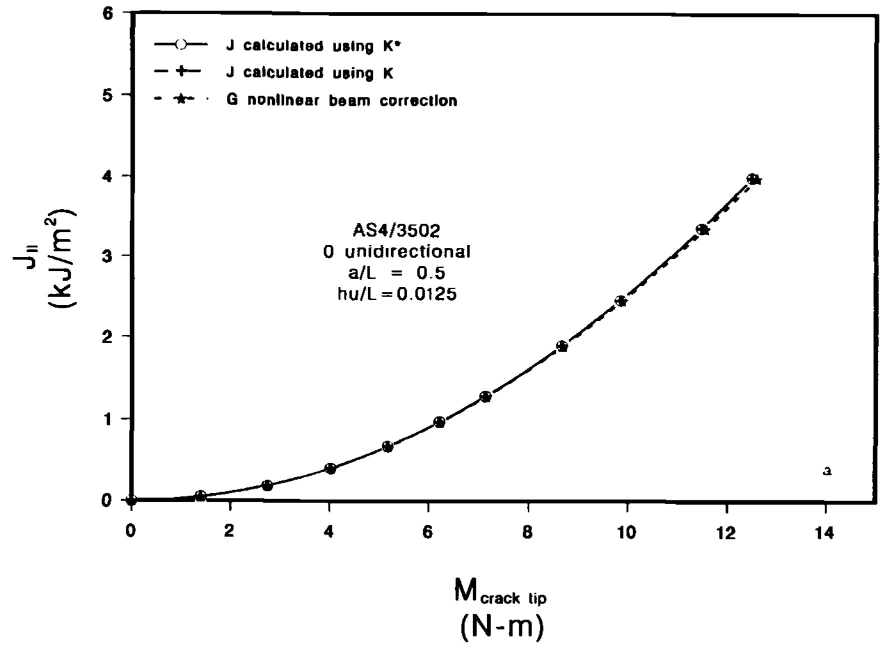

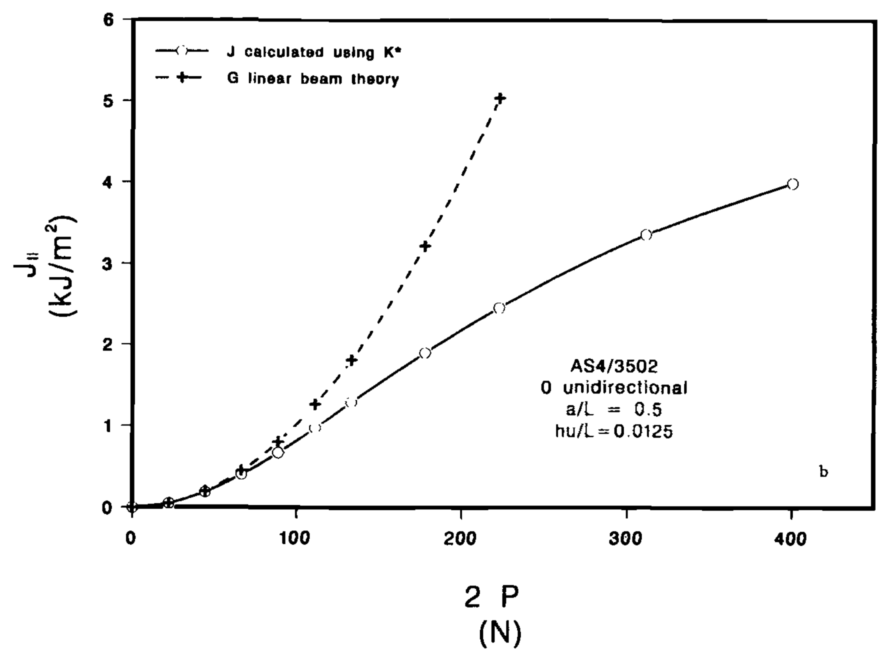

FIG. 6—(a) J_{II} *as a function of crack-tip moment for ELS calculated using* K* *and* K *in Eq 1 and using* G_{II} *(Eq 5) with nonlinear beam correction.* (b) J_{II} *and* G_{II} *as a function of actual load (*2P*) with* G_{II} *computed using linear beam theory (that is, Eq 5 with* P *and the undeformed crack length,* a*).*

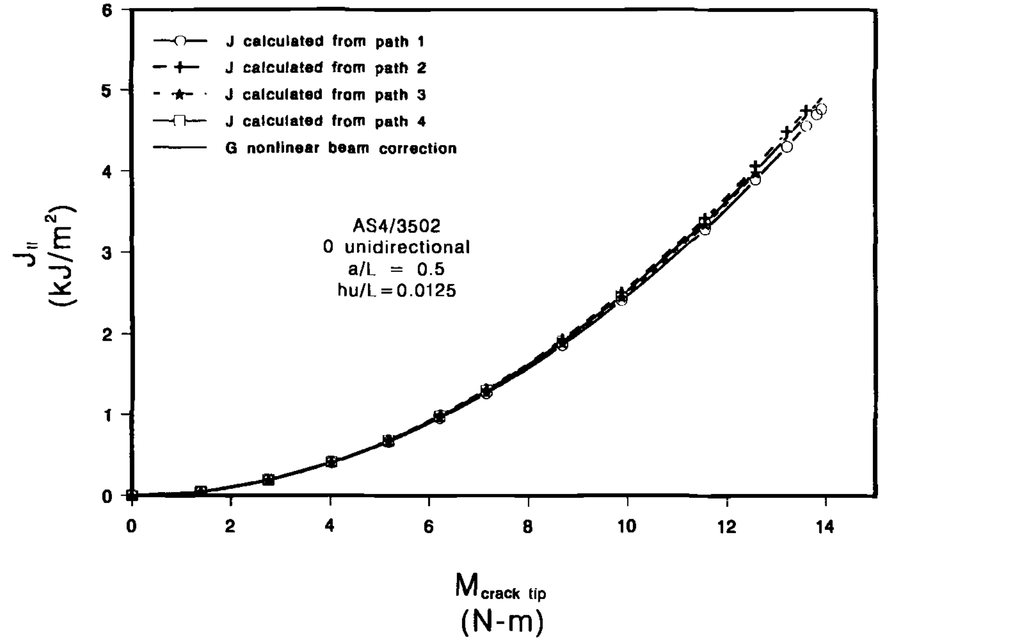

FIG. 7—*Path independence of* J_{II} *as a function of crack-tip moment. Path 1 is located at* ±*0.635 cm from crack tip; Path 2 at* ±*2.54 cm; Path 3 at* ±*6.35 cm; and Path 4 at* ±*11.43 cm.*

Figure 8*b* contains similar results for the 0° unidirectional glass/epoxy material. This material represents the other extreme in axial modulus since its stiffness is much lower (only 38.6 GPa). J_{II} is again seen to be unaffected by midplane straining, however. Taken as a whole, the results of Figs. 6 and 8 seem to suggest that the magnitude of the midplane strains developed from the effect of large rotations (which introduce an axial load component) are significantly smaller than the strains developed due to bending. Therefore, their effect on J_{II} is negligible.

Effect of Shear Deformation on J_{II}

Figure 9 shows a plot of $2P$ as a function of δ for a 0° layup of a boron/epoxy composite. The graph compares the effect of shear deformation on δ using finite element results with and without shear deformations included, and also computed using the linear beam theory analysis derived previously (Eq 6). An a/L ratio of 0.4, a h_u/L ratio of 0.1, and a E_{11}/G_{12} ratio of 36 were used to generate these graphs. With this combination of specimen geometry and material properties, shear effects would be expected to be significant. Indeed, the analysis without shear effects deviates significantly from the other two curves for the entire load range and represents a stiffer response as would be expected. The linear beam theory analysis (with shear deformations included) and the finite-element model (with shear deformations) correspond quite closely at the lower end of the load range. This confirms the accuracy of the linear beam theory analysis in the absence of geometric nonlinearities. For higher loads, the finite-element results deviate from the linear analysis by showing a stiffer response due to geometric nonlinear effects. In addition, a comparison of the actual data revealed that the percent difference between δ due to bending and δ due to shear deformations for the geometrically linear and

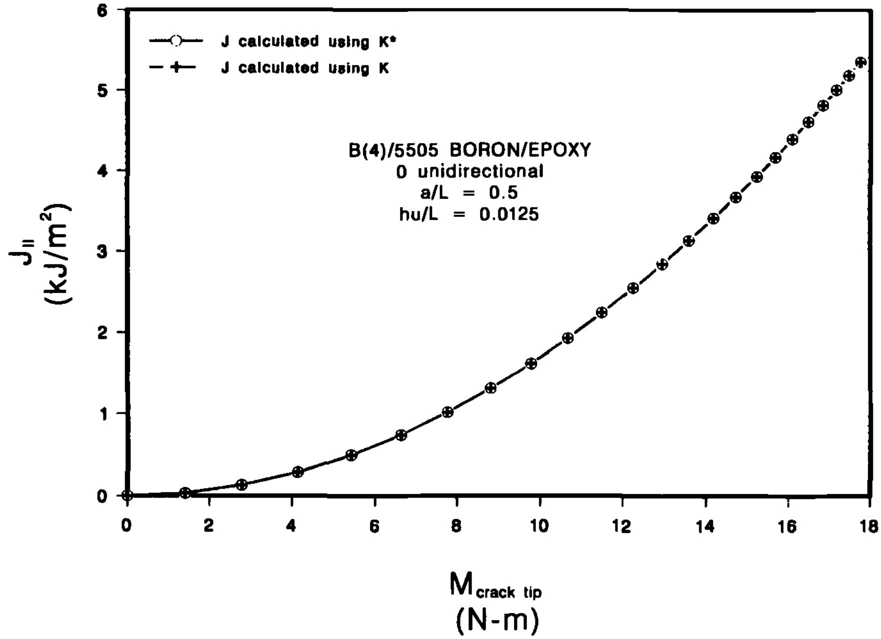

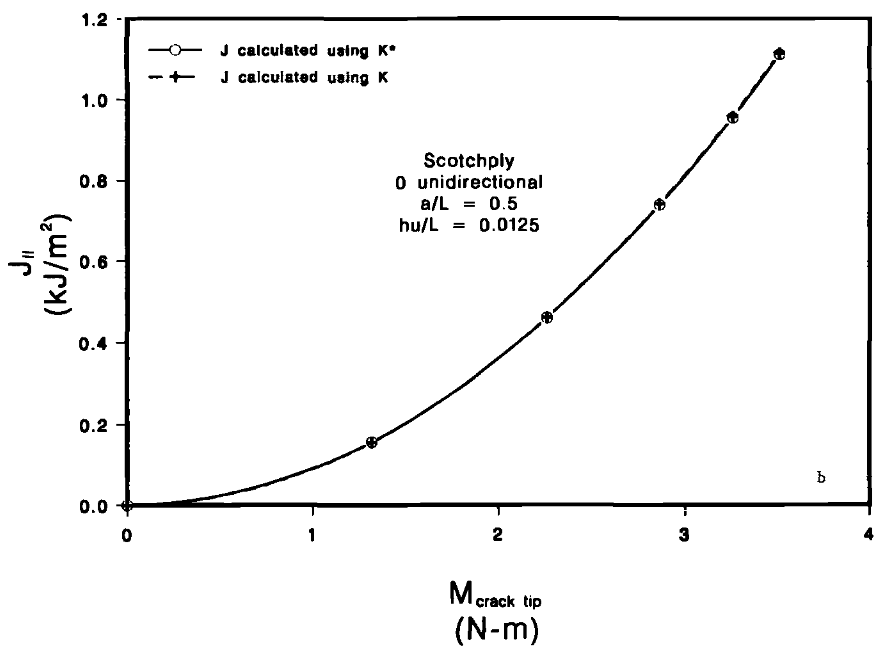

FIG. 8—*Effect of midplane straining* on J_{II} *from large rotations undergone by ELS for:* (a) *a boron/epoxy 0° unidirectional composite, and* (b) *a glass/epoxy 0° unidirectional composite.*

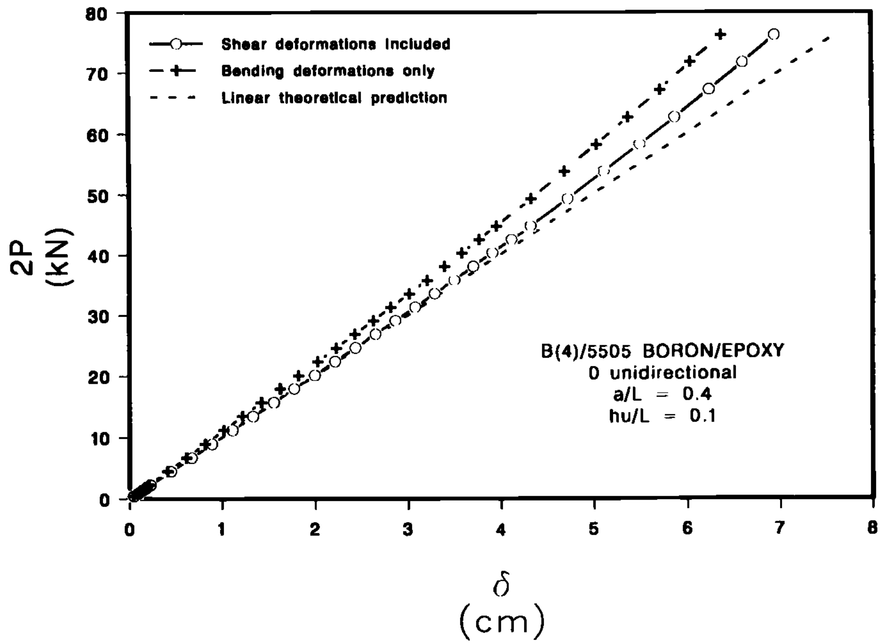

FIG. 9—*2P as a function of δ showing the effect of shear deformations on δ using finite elements and linear theoretical prediction (Eq 6).*

nonlinear range was the same. This indicates the effect of shear deformations is the same for linear and nonlinear deformations, at least for the aspect ratios studied in this paper.

Several $2P$ versus δ curves with and without shear deformation are shown in Fig. 10 for a/L ratios of 0.5, 0.6, 0.7, and 0.8. The h_u/L and E_{11}/G_{12} ratios used for these cases were the same as those used for the results shown in Fig. 9. As can be seen, the effect of shear deformations on the load-deflection response decreases as the crack length increases. This is consistent with the predictions of Eqs 6 and 7. Similar to the case in Fig. 9, the effect of shear deformations for the geometrically linear and nonlinear range for these cases is the same.

Using these load-deflection curves, the effect of shear on J_{II} for the ELS has been determined. Since J is proportional to the change in strain energy with respect to crack length (see Eq 8), the analysis is presented in terms of $\partial W/\partial a$. Figure 11*a* shows a graph of $\partial W/\partial a$ plotted as a function of crack length for a fixed load level. This load level falls in the range of linear deformations. The plots were generated by first integrating the load-deflection curves in Figs. 9 and 10 to obtain plots of W versus a at the chosen load level with and without shear deformations. The derivative of the strain energy with respect to cracked length was then calculated at each crack length. The results in Fig. 11*a* show that $\partial W/\partial a$ is the same whether shear deformation develops or not, despite the fact that shear deformation alters the load-deflection response (Fig. 10). Therefore, using the energy interpretation of the J-integral, Eq 8, it can be concluded that J_{II} is also independent of shear deformation. Note also the agreement between the curves using the load-deflection results from the finite-element analysis and the theoretical prediction. The theoretical results were obtained by differentiating the expression in Eq 9.

Figure 11*b* shows a plot of $\partial W/\partial a$ versus crack length but at a load level within the range of nonlinear deformations (see Fig. 10). Similar to the linear range results, $\partial W/\partial a$ is independent

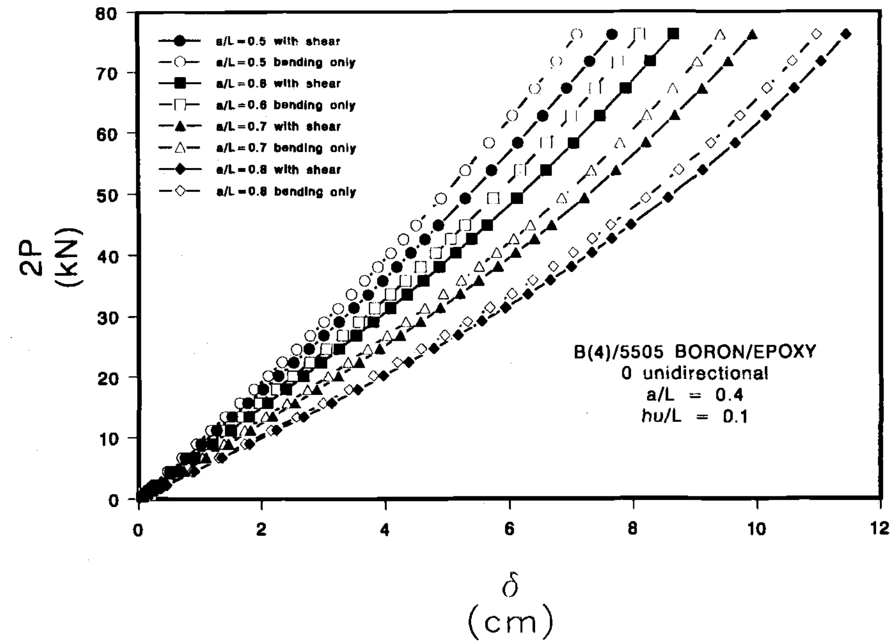

FIG. 10—2P *as a function of* δ *showing the effect of shear deformations on* δ *for different* a/L *ratios.*

of shear deformations. Therefore, J_{II} is independent of shear deformations also under nonlinear beam theory assumptions (that is, large deformations and rotations undergone by the ELS).

Effect of Limited Inelasticity in the Legs of the ELS on J_{II}

The effect of limited inelasticity in the cracked legs of the ELS on J_{II} can be seen in Fig. 12. Recall that the limited inelastic response was obtained by using the stress-strain curve shown in Fig. 5 for the elements of the cracked legs and for linear elastic material behavior for the elements of the uncracked leg. J_{II} has been plotted as a function of crack-tip moment and compared to the case where elastic material behavior is assumed throughout the ELS. At the smaller moments in Fig. 12, J_{II} is the same for both cases. At the higher moments, however, J_{II} becomes significantly higher for the case when inelasticity develops in the cracked legs. Limited inelasticity has been observed experimentally to develop in the cracked portion of the ELS for ±35° and ±45° layups due to the progression of damage in the form of microcracking [*8,9*].

Figures 13 through 15 provide additional insight into the effect of limited inelasticity. Figures 13 and 14 show the moment-curvature response of the uncracked and cracked portions of the ELS for the elastic and limited inelastic cases. Note in Fig. 13 how the moment-curvature response is the same for both cases since it was assumed that the uncracked portion remained elastic even when inelasticity develops in the cracked legs. However, as seen in Fig. 14, the moment-curvature responses are different where damage development makes the specimen more compliant. As a result, the integral of the moment-curvature relationship (the first term in Eq 1) is larger when damage develops compared to the totally elastic response. There-

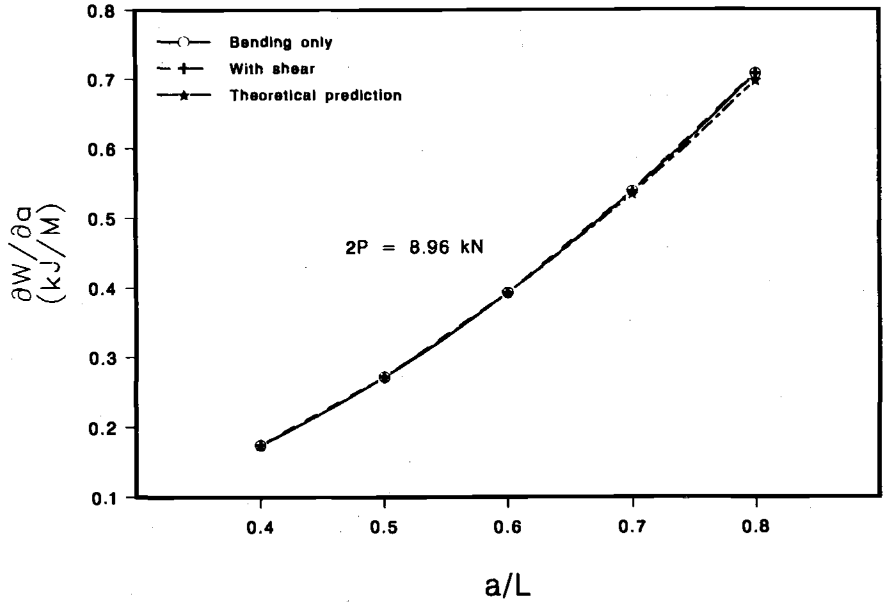

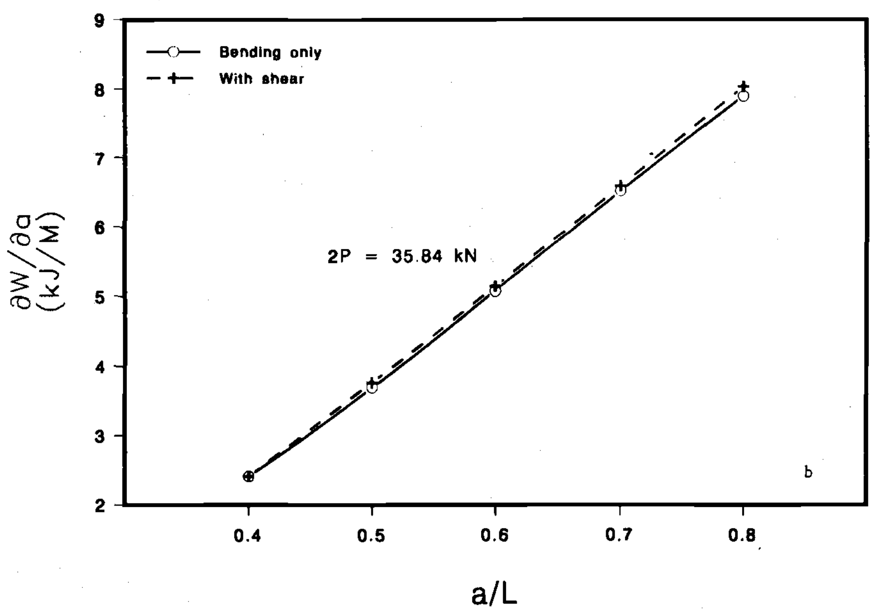

FIG. 11—$\partial W/\partial a$ *as a function of* a/L *using finite elements with and without shear deformations and using theoretical predictions. Load level is in the* (a) *linear range of deformations, and* (b) *nonlinear range of deformations.*

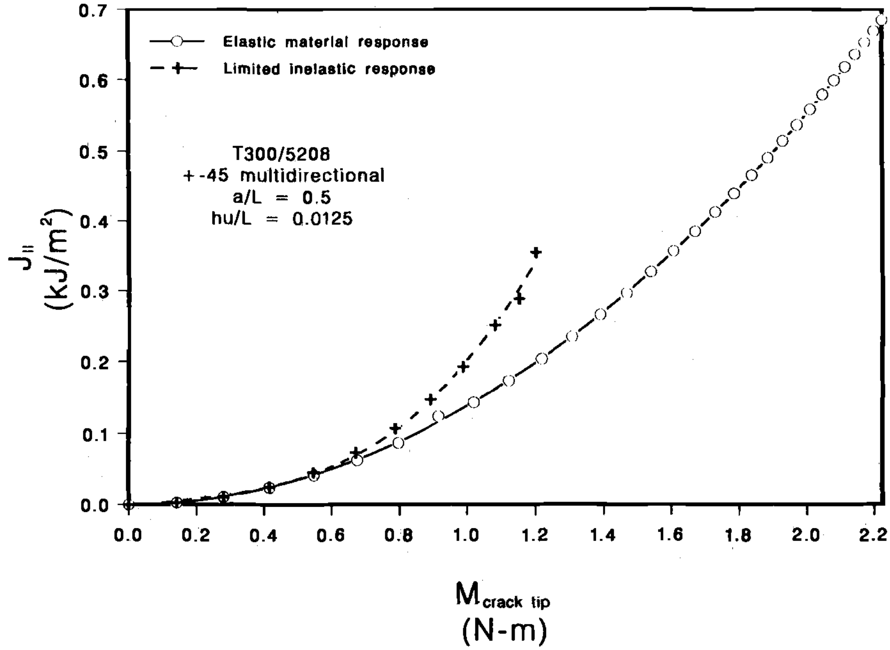

FIG. 12—J_{II} *as a function of crack-tip moment showing the effect of limited inelasticity in the cracked legs of the ELS.*

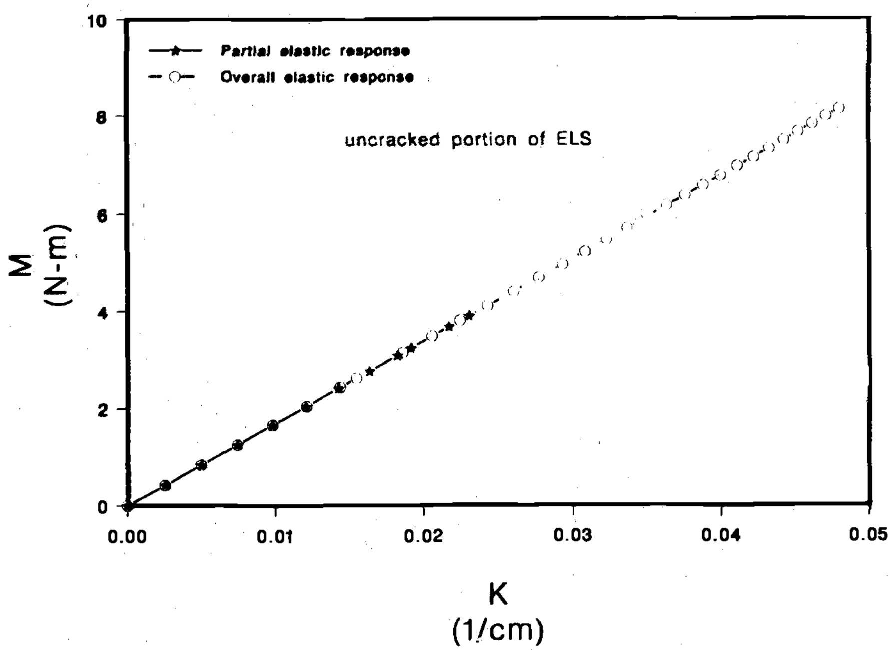

FIG. 13—*Moment-curvature relationship of uncracked portion of ELS.*

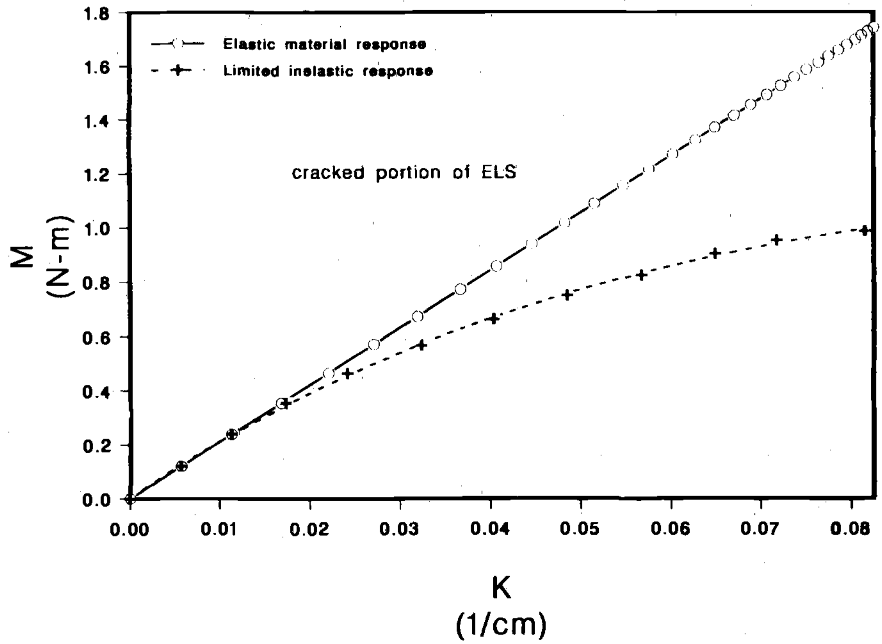

FIG. 14—*Moment-curvature relationship of cracked portion of ELS showing the effect of limited inelasticity.*

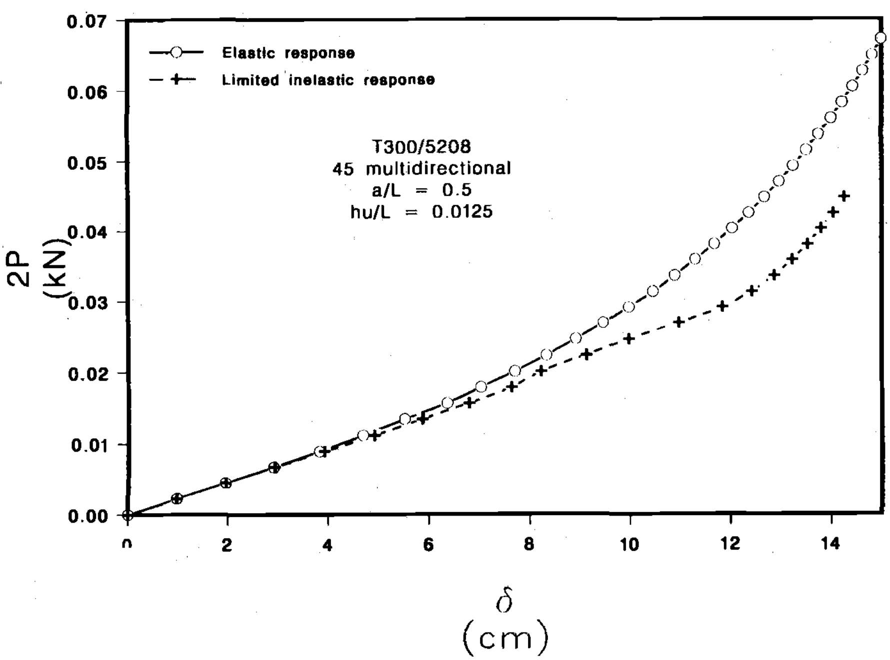

FIG. 15—*2P as a function of δ showing the effect of limited inelasticity and large deformations and rotations in the ELS.*

fore, J_{II} is likewise larger, which confirms the result shown in Fig. 12. Finally, Fig. 15 shows the load-deflection record when damage forms compared to the elastic case. For smaller deflections, both cases are the same. At higher deflections, however, the specimen is more compliant for the inelastic case. Note also the irregularity of the curve at the higher moments as a result of a competing process between the effect of large deformations (which tend to stiffen) and softening due to damage formation.

Conclusions

The major conclusions of this investigation can be summarize as follows:

1. A finite-element procedure has been developed and demonstrated for evaluating the J-integral for the ELS specimen used to study Mode II delamination of composite materials. The procedure uses nonlinear beam theory to evaluate the J-integral from typical output data obtained using nonlinear finite elements. The beam elements used include large deflections, midplane straining, and the effect of shear deformations.
2. The path independence of the J-integral using this approach has been verified except for paths very close to the crack tip where the complex state of stress that develops at the crack tip invalidates beam theory approximations.
3. For all of the layups studied, midplane straining from the development of large rotations shows no significant effect on J_{II}.
4. J_{II} for the ELS has been found to be independent of the effect of shear deformations for the aspect ratios studied under elastic conditions for geometrically linear and nonlinear deformations.
5. J_{II} has been found to be higher when limited inelasticity in the form of damage develops in the ELS compared to the elastic case.
6. Finally, the finite-element approach developed to approximate the J-integral for the ELS illustrates the feasibility of evaluating the J-integral from simplified finite-element analysis where global quantities away from the complex state of stress at the crack tip are used instead of local stresses and strains near the crack tip.

References

[1] Bradley, W. L. and Jordan, W. M., "The Relationship Between Resin Ductility and Composite Delamination Fracture Toughness," *Proceedings*, International Symposium on Composite Materials and Structures, 10–13 June 1986, Beijing, China, pp. 445–450.

[2] Jordan, W. M. and Bradley, W. L., "Micromechanics of Fracture in Toughened Graphite/Epoxy Laminates," *Toughened Composites, ASTM STP 937*, N. J. Johnston, Ed., American Society for Testing and Materials, Philadelphia, 1987, pp. 74–94.

[3] Vanderkley, P. S., "Mode I-Mode II Delamination Fracture Toughness of a Unidirectional Graphite/Epoxy Composite," Master's thesis, Texas A&M University, College Station, TX, 1981.

[4] Hashemi, S., Kinloch, A. J., and Williams, J. G., "The Analysis of Interlaminar Fracture in Uniaxial Fibre-Polymer Composites," *Proceedings of the Royal Society of London*, Vol. A427, 1990, pp. 173–199.

[5] Hashemi, S., Kinloch, A. J., and Williams, J. G., "Interlaminar Fracture of Composite Materials," *Proceedings*, Sixth ICCM and Second ECCM, July 1987, London, UK, Vol. 3, 1987, pp. 3.254–3.255.

[6] Corleto, C., Bradley, W., and Henriksen, M., "Correspondence Between Stress Fields and Damage Zones Ahead of Crack Tip of Composites Under Mode I and Mode II Delamination," *Proceedings*, Sixth ICCM and Second ECCM, July 1987, London, UK, Vol. 3, 1987, pp. 3.378–3.387.

[7] Williams, J. G., "Large Displacement and End Block Effects in the 'DCB' Interlaminar Test in Modes I and II," *Journal of Composite Materials*, Vol. 21, 1987, pp. 330–341.

[8] Corleto, C. R., "Mode II Delamination Fracture Characterization of Fiber Reinforced Composite

Materials," Ph.D. thesis, Department of Mechanical Engineering, Texas A&M University, College Station, TX, 1990.

[9] Goetz, D. P., "Determination of the Mode I Delamination Fracture Toughness of Multidirectional Composite Laminates," Ph.D. thesis, Department of Civil Engineering, Texas A&M University, College Station, TX, 1988.

[10] Tsai, S. W. and Hahn, H. T., *Introduction to Composite Materials*, Western Hemisphere Publishing Co., Lancaster, PA, 1980.

Chi-Tsich Liu[1]

Investigating the Near-Tip Fracture Behavior and Damage Characteristics in a Particulate Composite Material

REFERENCE: Liu, C.-T., "**Investigating the Near-Tip Fracture Behavior and Damage Characteristics in a Particulate Composite Material,**" *Fracture Mechanics: Twenty-Third Symposium, ASTM STP 1189,* Ravinder Chona, Ed., American Society for Testing and Materials, Philadelphia, 1993, pp. 668–679.

ABSTRACT: In this study, the local fracture behavior and damage state near the crack tip in a particulate composite material were investigated through the use of precracked sheet specimens. The specimens were subjected to a simple incremental strain history at room temperature. During the test, a high-energy real-time X-ray system was used to record the X-ray data and the fracture process near the crack-tip region. The experimental data were analyzed and the results are discussed.

KEY WORDS: particulate composites, damage, crack opening, failure process zone, fracture mechanics, fatigue (materials)

In recent years, a considerable amount of work has been done in studying crack growth behavior in highly filled polymeric materials [*1–7*]. The importance of these studies stems from the fact that the crack growth behavior in the material can significantly affect the integrity of the structure made of that material. The basic approach used in characterizing the crack growth behavior in the particulate composite material is based on linear elastic or linear viscoelastic fracture mechanics. According to theories developed by Schapery [*8*] and Knauss [*9*], failure occurs in a small region when the work done on the small region by the surrounding material is equal to the fracture energy of the material. This small region, located at the tip of a crack, is known as the failure process zone. In this zone, the material may be highly nonlinear or suffer extensive damage. The size of the failure process zone strongly influences how a crack grows and is a key parameter in viscoelastic fracture mechanics. Therefore, in order to obtain a fundamental understanding of crack growth behavior in a highly filled polymeric material, a detailed knowledge of the characteristics of damage mechanisms and local fracture behavior near the crack tip is required.

In this study, the local fracture behavior and damage state near the crack tip were investigated through the use of precracked sheet specimens. The specimens were subjected to a simple incremental strain history at room temperature. During the test, Lockheed Research Laboratory's high-energy real time X-ray system was used to record, simultaneously, the X-ray data and the fracture process near the crack-tip region. The recorded X-ray data were processed to create a visual indication of the energy absorbed in the material. A region of high absorption (that is, a high-damaged area) will be shown as a dark area, whereas a region of low absorption will produce a light or white area, with 254 shades of gray in between. The X-ray

[1] Project manager, Phillips Laboratory (AFSC), Edwards Air Force Base, CA 93523-5000.

image at a given applied global strain level was plotted in the form of isointensity contours of the transmitted X-ray energy to enhance the resolution of the damaged field.

In this paper, in addition to investigating the damage characteristics, the local fracture behavior in the immediate neighborhood of the crack tip was also investigated. Experimental data revealed that the material in a small region, known as the failure process zone, in the immediate vicinity of the crack tip was highly damaged. It was found that the crack growth behavior was closely related to the characteristics of the failure process zone that, in turn, was closely related to the microstructure near the crack tip. The results of these analyses were used to explain some of the important phenomena that were observed during the crack propagation test.

Specimen and Testing

In this study, the local fracture behavior and damage state near the crack tip were investigated through the use of edge-cracked and center-cracked sheet specimens. The specimen geometries are shown in Fig. 1. As indicated in Fig. 1, a circular cutout was made at the vertical edges of the center-cracked specimen and the left-side vertical edge of the edge-cracked specimen in order to minimize the stress concentration at the corners of the specimen. During the tests, a special fixture was used to prevent the specimen from rotating, and the specimen was loaded incrementally at intervals of 5% strain at 50.8 mm/min (2 in./min) crosshead speed. Prior to testing, cracks with different crack lengths were cut through the thickness of the specimens with a razor blade. For the edge-cracked specimen, the crack length was 8.13 mm (0.32 in.), whereas for the center cracked specimen, the crack length was 38 mm (1.5 in.). An inert solid propellant, which was a highly filled polymeric material and manufactured by Morton

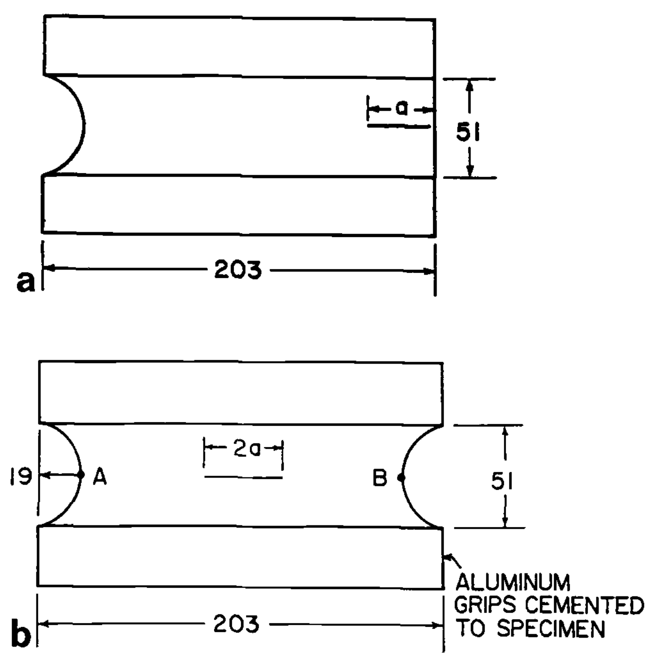

FIG. 1—*Specimen geometry (dimensions in millimetres):* (a) *edge-cracked specimen (*a *= 8.31 mm) and* (b) *center-cracked specimen (2*a *= 38 mm).*

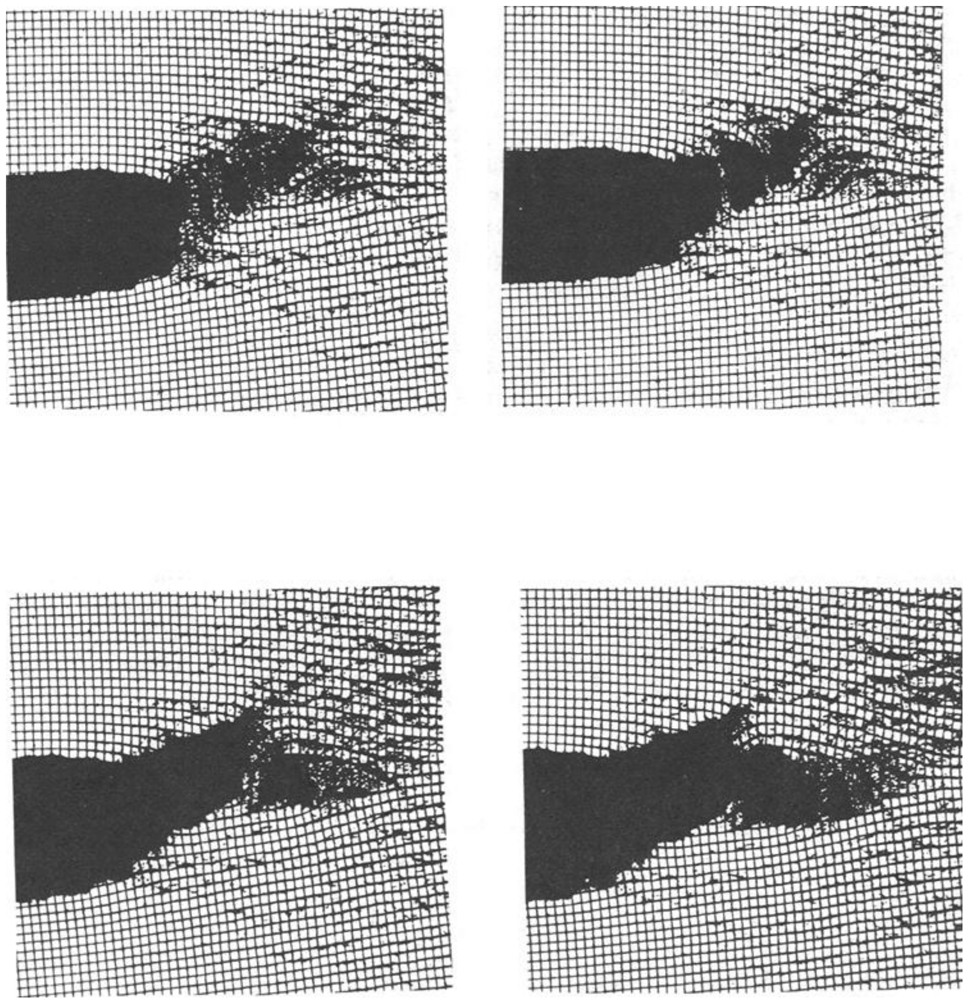

FIG. 2—*Crack opening and growth in the cast specimen.*

Thiokol Inc., was used to fabricate the specimens. The edge-cracked specimen was machined and the center-cracked specimen was cast. The cast specimen had a polymeric rich layer of material on the surface. Therefore, the microstructure of the cast specimen is different from that of the machined specimen.

In this study, the Lockheed Research Laboratory's high-energy real-time system (HERTS) was used to investigate the characteristics of the damage field near the crack tip. During the test, the specimen was placed between the X-ray radiation source and the X-ray camera. The X-ray image exits from the specimen and strikes the screen that is in front of the X-ray camera. The screen converts the X-ray image into a light image. This image is reflected into a low-light-level television camera by a mirror placed at 45° to the beam in the back of the camera. The isocon TV camera then converts the light image into an electronic signal that can be routed into the main monitor and into the video tape recorder. A detailed description of the HERTS can be found in Ref *10*. The recorded X-ray data were processed to create a visual indication of the energy absorbed in the material. A region of high absorption (that is, a high damage area) will be shown as a dark area, whereas a region of low absorption will produce a light or white area, with 254 shades of gray in between. The X-ray image at a given applied global strain level was plotted in the form of isointensity contours of transmitted X-ray energy to enhance the resolution of the damaged field.

Before giving a detailed discussion of the experimental results, I will briefly discuss the basic damage mechanism in highly filled polymeric materials such as solid propellants.

For a highly filled polymeric material that consists of a large number of fine particles, on the microscopic scale, it can be considered nonhomogeneous. When this material is stretched, the different sizes and distribution of the filler particles, the different crosslinking density of polymer chains, and the variation of bond strength between the particles and the binder can produce highly nonhomogeneous local stress and strength fields. Because of the particle's high rigidity relative to the binder material, the magnitude of the local stress is significantly higher than that of the applied stress, especially when the particles are close to each other. Since local stress and strength vary in a random fashion, the failure site in the material also varies randomly and does not necessarily coincide with the maximum stress location. In other words, the location and degree of damage will also vary randomly in the material. The damage may appear in the form of microcrack and microvoid in the binder, or in the form of particle/binder separation known as dewetting. When the particle is dewetted, the local stress will be redistributed. With time, additional particle/binder separation and vacuole formation takes place. This time-dependent process of dewetting nucleation, or damage nucleation, is due to the time-dependent processes of stress redistribution and particle/binder separation. Depending on the formulation of the material and testing conditions, damage growth may take place as material tearing or by successive nucleation and coalescence of the microvoids. These damage initiation and evolution processes are time-dependent, and are the main factor responsible for the time-sensitivity of the strength degradation as well as the fracture behavior of the material.

Having discussed the damage mechanisms in particle-filled polymeric materials, I will now discuss the results of fracture and real-time X-ray tests.

Results and Discussion

Typical sets of photographs showing the crack surface profile and local damage near the tip of a crack in the cast and the machined specimens are shown in Figs. 2 and 3, respectively. From these two figures, we note that the crack-tip-blunting phenomenon is different for the two specimens. For the machined specimen, the magnitude of blunting prior to crack growth is much larger than that after crack growth. For the cast specimen, the magnitude of blunting, during crack growth, varies irregularly with the position of the propagating crack tip. The magnitude of blunting may be smaller or larger than that prior to crack growth. In addition to the different blunting behaviors during crack growth, the local damage mechanisms near the crack tip are different for the two types of specimens. This is discussed in the following paragraphs.

Figures 2 and 3 show the local damage near the tip of the crack in the cast specimen and the machined specimen, respectively. According to Figs. 2 and 3, the highly damaged region, or the failure process zone, at the crack tip has a cusp shape that is consistent with that predicted by Schapery in his study of fracture of viscoelastic materials. Although the shape of the failure process zone is similar for the two different types of specimens, the failure mechanisms inside the failure process zone are different. For the cast specimen, when the local strain reaches a critical value, a small void is generated in the failure process zone. Because of the random nature of the microstructure of the material, the first void is not necessarily formed in the immediate neighborhood of the crack tip. As the applied strain is increased with time, additional voids are generated; both on the surface and in the interior of the specimen. Conse-

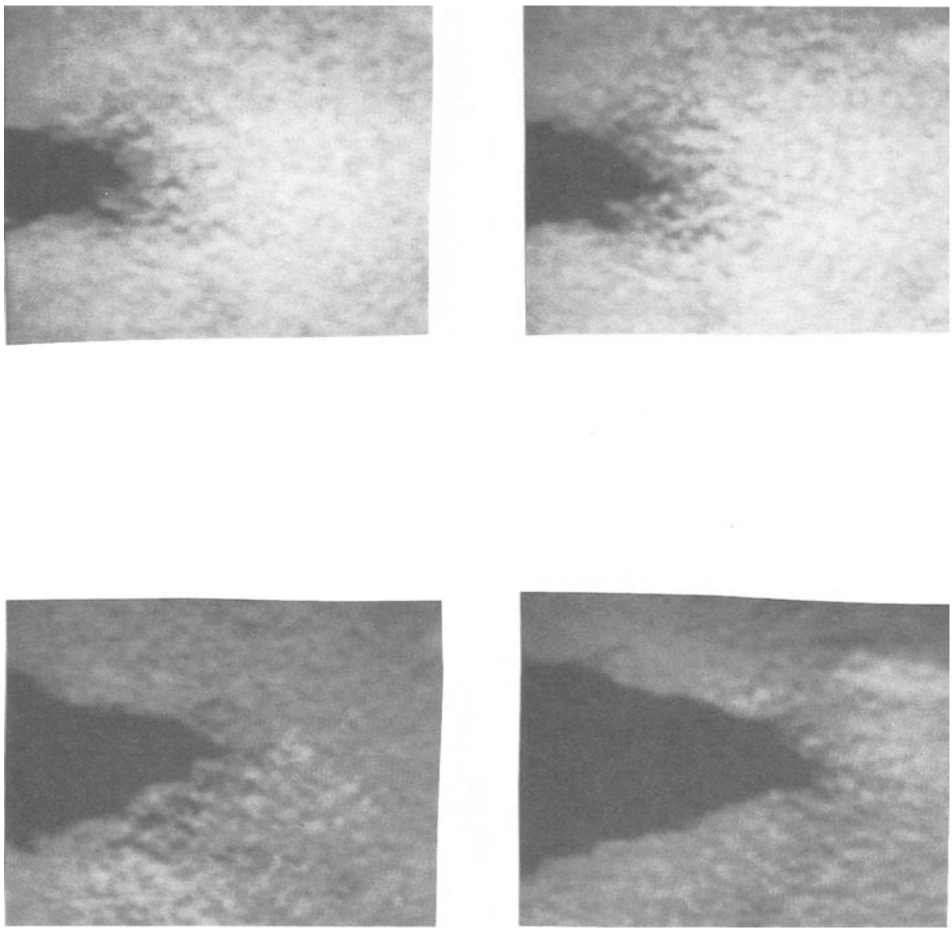

FIG. 3—*Crack opening and growth in the machined specimen.*

quently, there are a large number of strands that separate the voids and are essentially made of the binder material formed inside the failure process zone. The coalescence of the voids in the failure process zone, as well as that of the main crack tip with the large void near the crack tip, leads to crack growth to a distance that is approximately equal to the length of the failure process zone. This kind of time-dependence of the failure mechanisms is one of the contributing factors to the time-sensitivity and discontinuous crack growth behavior in highly filled polymeric materials such as solid propellants.

Experimental findings reveal that the local microstructure affects not only the damage mechanism but also the crack growth direction. For the cast specimen, the direction of the developed process zone shows a relatively large variation. Prior to crack growth, depending upon the local microstructure, the failure process zone can be developed either above, below, or along the crack plane. After crack growth, the successively developed failure process zone at the tip of the propagating crack undulate about the crack plane, resulting in a relatively large zig-zag shape of crack growth as shown in Fig. 2.

The preceding discussion is centered on the damage mechanisms and crack growth behavior in the cast specimen. For the machined specimen, the magnitude of crack-tip blunting, the shape and size of the failure process zone prior to crack growth are compatible with that observed in the cast specimen. However, during crack growth, the size of the failure process zone and the variation of the crack growth direction in the machined specimen are much smaller than that in the cast specimen. However, the basic crack growth behavior (including crack-tip blunting, resharpening, and zig-zag crack growth) in the two different types of specimens is qualitatively the same. But, it should be pointed out that the basic damage mechanisms in the failure process zone in the machined specimen are quite different from the cast specimen. For the machined specimen, experimental data indicate that microcracks are generated in the failure process zone as shown in Fig. 3. The number of microcracks increases with increasing applied strain level. The basic damage evolution process is coalescence of the microcracks. The coalescence of a large microcrack with the main crack tip leads to the growing of the main crack. Depending upon the severity of the damage in the failure process zone, the main crack can grow a short distance in the failure process zone or it can grow a distance that is approximately equal to the failure process zone length.

The preceding paragraphs discuss the basic near-tip damage mechanisms and crack growth behavior in the two types of specimens with different microstructures. In order to determine the damage intensity and the damage fields near the crack tip, real-time X-ray test data are analyzed. The results of the analyses are discussed in the following paragraphs.

To determine the size and the damage intensity in the damage zone, isointensity contours of the transmitted X-ray energy, I_t, were plotted and are shown in Figs. 4 and 5. In Fig. 4, the number between two contour lines is the minimum intensity level of a range of I_t between the minimun intensity level and the next intensity level. The small number indicates that the intensity of the transmitted X-ray energy is low or that the damage level is high. The nonuniform distribution of I_t in the virgin specimen is an indication of the material's nonhomogeneity. A number of factors, such as the existence of a cluster of filler particles in a small region, undercure of the binder material in a local area, and large voids in the material, may contribute to the nonuniform distribution of I_t in the specimen. When the specimen is strained, the high intensity of the stress near the crack tip will induce high damage near the crack tip as shown in Fig. 4. This figure reveals that the size of the damage zone and the intensity of damage in the damage zone increase with increasing applied strain level. It also reveals that the magnitude of blunting at the crack tip prior to crack growth and in the earlier crack growth stage is much larger than that in the later crack growth stage. In addition, during the blunting stage, the damage gradient near the crack tip is very steep. The region that has a steep damage gradient is restricted to a very small area in the immediate neighborhood of the crack tip. When the applied strain level is low, the damage intensity outside the steep damage gradient area is negligible. As the applied strain level is increased, the damage gradient is decreased and the size of the high damage region is increased as shown in Fig. 4. However, the damage intensity outside the high damage region remains small until a critical applied strain level is reached; then the damage intensity outside the highly damaged region also increases with increasing applied strain level. These experimental findings, obtained from real-time X-ray data, are consistent with experimental findings reported by Smith et al. [*11*] and Liu [*12*] in their study of local strain distribution near the tip of a crack in a composite solid propellant. As pointed out by Liu and Smith, the intense strain zone ahead of the crack tip is much smaller and the strain level outside the intense strain zone is approximately equal to the applied strain level. Under this condition, it is expected that if the applied strain level is below a critical value it can be assumed that no damage will develop outside the intense strain zone.

The preceding discussion was centered on damage characteristics near the tip of a crack in

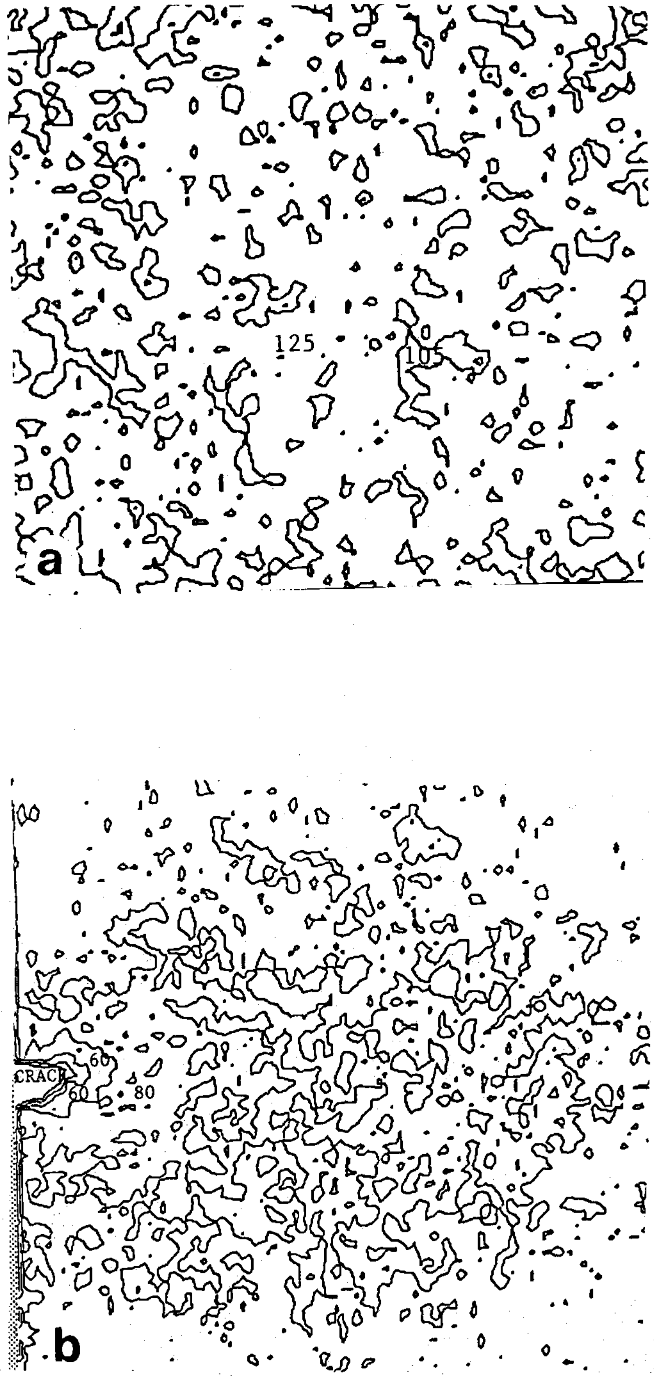

FIG. 4—*Isointensity contour plots of X-ray image near the crack tip of the edge crack (machined specimen):* (a) *0% strain,* (b) *3.7% strain,* (c) *5.9% strain,* (d) *7.8% strain,* (e) *11% strain, and* (f) *14% strain.*

FIG. 4—*Continued.*

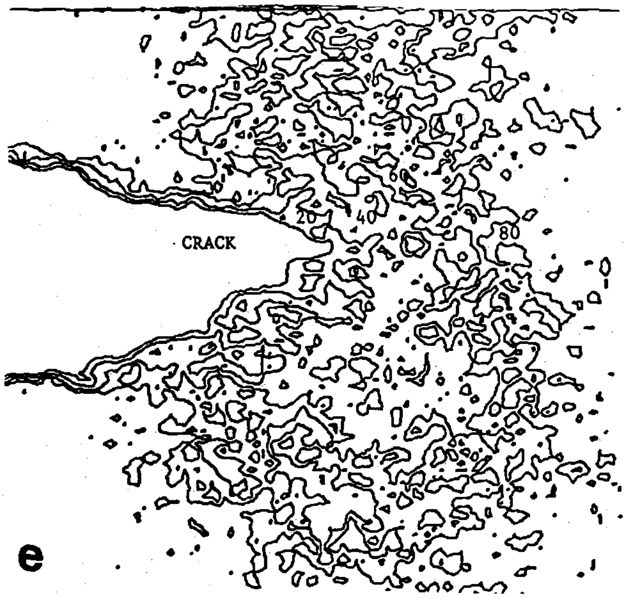

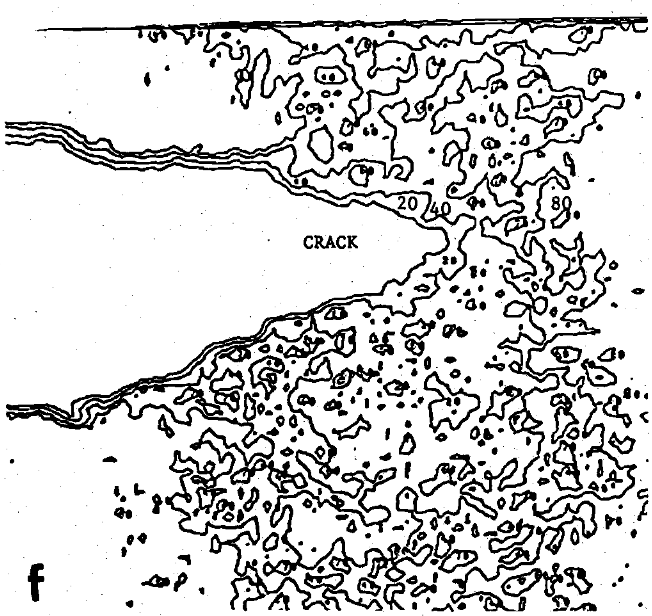

FIG. 4—*Continued.*

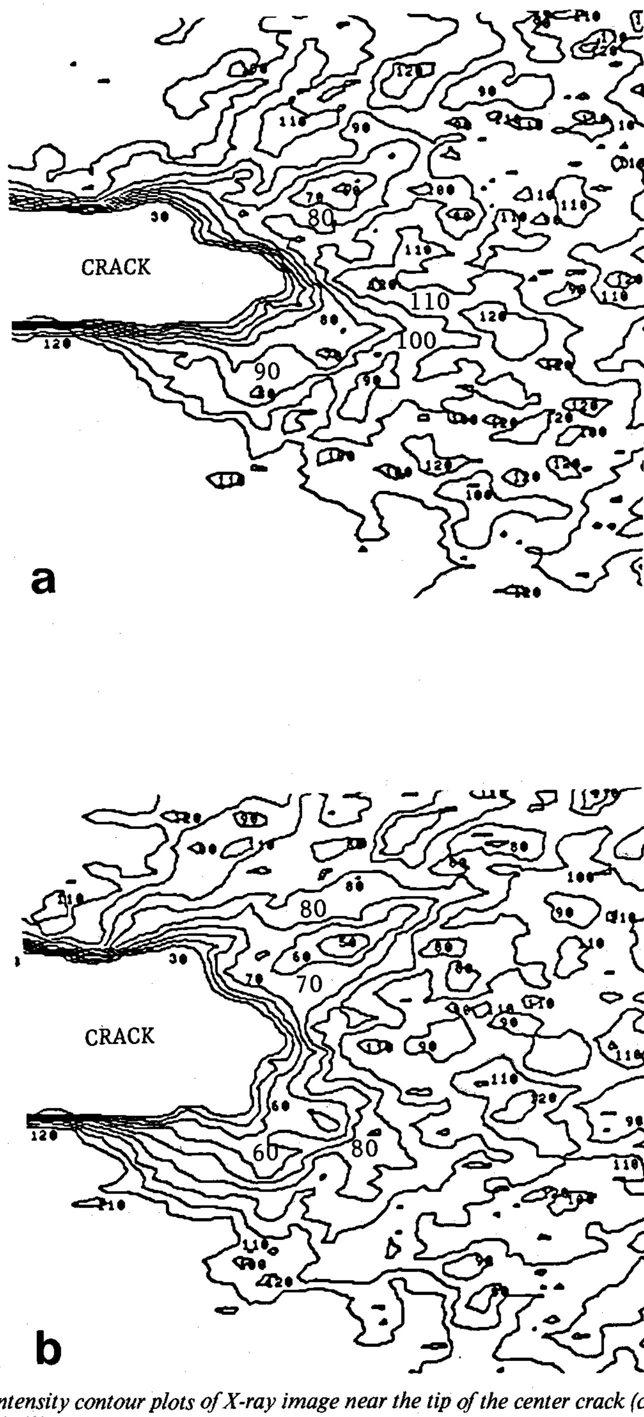

FIG. 5—*Isointensity contour plots of X-ray image near the tip of the center crack (cast specimen):* (a) *3% strain and* (b) *6% strain.*

the machined specimen. In the following paragraph, the results of real-time X-ray data of the cast specimen are discussed.

Figure 5 shows the isointensity contours near the tip of a crack in the cast specimen. From this figure, it can be seen that the crack tip is highly blunted. Under this condition, the high stress region changes from the crack tip to the upper and the lower corners of the blunted crack tip. Consequently, the high damage fields also shift to the two corners of the blunted crack tip as shown in Fig. 5. When the applied strain level is increased from 3 to 6%, two small regions with relatively high damage intensity are developed at small distances away from the corners of the blunted crack tip. With increasing applied strain level, voids are developed in the highly damaged regions. The conclusion from these experimental findings is that the damage initiation and evolution processes are closely related to the crack-tip geometry and the local microstructure.

Conclusions

The local fracture behavior and damage characteristics near the crack tip in the machined and the cast specimens were investigated. Experimental results indicated that the basic crack growth behavior (crack-tip blunting, resharpening, and zig-zag crack growth) in the two different specimens is qualitatively the same. However, due to the different microstructures, the basic damage mechanisms in the failure process zone for the machined specimen are quite different from the cast specimen. In addition, during crack growth, the size of the failure process zone and the variation of crack growth direction in the machined specimen are much smaller than that in the cast specimen.

Acknowledgments

This work was supported by the Air Force Office of Scientific Research, Air Force System Command, under Project 2302M1. The author would like to express his appreciation to Professor C. W. Smith of Virginia Polytech Institute and State University, Dr. B. Betz of Lockheed Research Laboratory for helpful discussions, Miss B. Trang of Lockheed Research Laboratory for processing the X-ray data, and to Ms. L. Woodworth for typing the manuscript.

References

[*1*] Beckwith, S. W. and Wang, D. T., "Crack Propagation in Double-Base Propellants," AIAA Sixteenth Aerospace Science Meeting, AIAA Paper No. 78-170, American Institute of Aeronautics and Astronautics, Washington, DC, 16–18 Jan. 1978.

[*2*] Francis, E. C., Carlton, C. H., and Thompson, R. E., *Predictive Techniques for Failure Mechanisms in Solid Rocket Motors,* AFRPL-TR-79-87, Air Force Rocket Propulsion Laboratories, 1979.

[*3*] Liu, C. T., "Crack Propogation in an HTPB Propellant," *Proceedings,* 1980 JANNAF Structures and Mechanical Behavior Subcommittee Meeting, CPIA Publication 311, Vol. I, Chemical Propulsion Information Agency, Laurel, MD, March 1980.

[*4*] Dengel, D. H., Kornbluth, J. S., and Hunston, D., "Fracture Behavior of Crosslinked Double Base Propellant," *Proceedings,* 1981 JANNAF Structures and Mechanical Behavior Subcommittee Meeting, CPIA Publication 351, Chemical and Information Agency, Laurel, MD, Dec. 1981.

[*5*] Liu, C. T., "Variability in Crack Propagation in a Composite Propellant," *Proceedings,* AIAA/ASME/AHS 24th Structure, Structural Dynamics, and Materials Conference, AIAA Paper No. 83-1015, American Institute of Aeronautics and Astronautics, Washington, DC, May 1983.

[*6*] Liu, C. T., "Crack Growth Behavior in a Composite Solid Propellant with Strain Gradients—Part I," *Proceedings,* AIAA/ASME/SAE Twentieth Joint Propulsion Conference, AIAA Paper No. 84-1294, American Institute of Aeronautics and Astronautics, Washington, DC, June 1984.

[*7*] Liu, C. T., "Crack Growth Behavior in a Composite Solid Propellant with Strain Gradients—Part II," *Proceedings,* AIAA/ASME/ASCE/AHS Twenty Sixth Structure, Structure Dynamics, and

Materials Conference, AIAA Paper 85-0615, American Institute of Aeronautics and Astronautics, Washington, DC, April 1985.

[8] Schapery, R. A., "On a Theory of Crack Growth in Viscoelastic Media," Report MM 2765-73-1, Texas A&M University, College Station, TX, March 1973.

[9] Knauss, W. G., "Delayed Failure—The Griffith Problem for Linearly Viscoelastic Materials," *International Journal of Fracture Mechanics,* Vol. 6, March 1970, pp. 7–20.

[10] Sklensky, A. F. and Buchanan, R. A., "Sensitivity of High-Energy Real-Time Radiography with Digital Integration," *Real-Time Radiologic Imaging: Medical and Industrial Applications, ASTM STP 716,* D. A. Garrett and D. A. Bracker, Eds., American Society for Testing and Materials, Philadelphia, 1980, pp. 315–329.

[11] Smith, C. W. and Liu, C. T., "Effect of Near Tip Behavior of Particulate Composites on Classical Fracture Concepts," *Journal of Composites Engineering,* to be published.

[12] Liu, C. T., "Investigating the Local Behavior Near the Crack Tip in a Composite Solid Propellant," *Proceedings,* 1989 SEM Spring Conference on Experimental Mechanics, The Society for Experimental Mechanics, Inc., Bethel, CT, 29 May–June 1989, pp. 491–496.

David C. Lo,[1] *David H. Allen,*[1] *and Charles E. Harris*[2]

Modeling the Progressive Failure of Laminated Composites with Continuum Damage Mechanics

REFERENCE: Lo, D. C., Allen, D. H., and Harris, C. E., "**Modeling the Progressive Failure of Laminated Composites with Continuum Damage Mechanics,**" *Fracture Mechanics: Twenty-Third Symposium, ASTM STP 1189,* Ravinder Chona, Ed., American Society for Testing and Materials, Philadelphia, 1993, pp. 680–695.

ABSTRACT: A continuum-damage-mechanics-based model is proposed for the analysis of the progressive failure process in laminated composite structures. The laminate's response is determined by nonlinear constitutive equations that account for each type of matrix-dominated damage through strain-like internal state variables. Evolution of these internal state variables is governed by the damage-dependent ply-level stresses. The updated damage state and the ply-level stresses are then employed in the local-global evaluation of component failure. This model is incorporated into a finite-element analysis code to facilitate the examination of structures with spatially varying stress fields. The stress and damage distribution obtained from the analysis at various points in the loading history provide information about the progression of events leading to the failure of the component. The progressive failure of fatigue-loaded rectangular crossply-laminated plates containing a centered circular cutout has been examined with the model. Most of the predicted damage is localized in a region near the cutout. Rather than propagating outward, the damage intensifies in this region until failure occurs. The feasibility of modeling the evolution of each type of subcritical damage is demonstrated with the current framework. This ability to simulate the progressive failure process at this level of detail will assist in the design of safer and more efficient composite structures.

KEY WORDS: laminated composites, progressive failure, matrix damage, continuum damage mechanics, finite-element analysis, damage accumulation, fracture mechanics, fatigue (materials)

The accumulation of subcritical damage in laminated composites is of major concern especially in light of the increased use of these advanced material systems in critical engineering applications. Although in some instances distributed damage can retard the failure process in a component by redistributing load away from the high stress region, it is still the primary contributing factor to the eventual catastrophic failure. While efforts can be made to delay the development of damage by modifying the laminate stacking sequence or the component design, distributed damage is present throughout the life of the component. Even before entering service, damage is inflicted on the component by the manufacturing process.

To produce safe and reliable laminated composite components, it is essential to know how such damage affects the performance and failure of these components. Experimental approaches are not economical due to the large numbers of parameters that can be varied by the designer. Thus, much effort has been placed on the development of analytical methods to

[1] Graduate research assistant and director, respectively, Center for Mechanics of Composites, Aerospace Engineering Department, Texas A&M University, College Station, TX 77843-3141.
[2] Head, Mechanics of Materials Branch, NASA Langley Research Center, Hampton, VA 23665-5225.

supplement the designer's database. To accomplish this task requires a thorough knowledge of the failure characteristics of laminated composites as well as the ability to analytically model this failure process.

The progressive nature of the failure process in laminated composites has been well documented in the published literature [1-4]. This process involves the accumulation of several types of damage. Generally, the first type of damage to appear is matrix cracking in regions of high stress gradients. Along the free edges and at the intersection of matrix cracks from adjacent plies, delaminations are propagated by large intralaminar stresses. The stress redistribution resulting from these two types of damage in turn assist in the development of damage in the surrounding areas. As matrix-dominated damage accumulates, the loads are transferred to the plies with fiber orientation aligned closest to the direction of the applied loads. The bonds between the fibers and matrix are fractured in these plies. This is accompanied by the fracture of the fibers. Since the reinforcing fibers are the primary load-carrying component of the laminate, their fracture signifies the imminent failure of the structure itself. This failure process is in contrast to that observed in conventional homogeneous materials where failure can be traced to the propagation of a single flaw. In composites, each flaw in the laminate will not greatly affect the overall response of the structure; instead, it influences the development of other flaws. It is the cumulative effect of the subcritical damage that results in the failure of the structure. Thus, any attempt to predict the residual strength and life of laminated composite structures must address the damage accumulation process as well as its effect on the response of the material.

Most analyses have not adequately accounted for this history-dependent subcritical damage accumulation process. Some linear elastic fracture mechanics based approaches replace the distributed damage with a single equivalent macrocrack [5,6]. When the stress intensity factor or the strain energy release rate is equal to the fracture toughness, failure occurs. Other approaches calculate the stress field with the assumption of no accumulated damage. To compensate for the stress redistribution, the failure criteria are either evaluated at a distance away from the stress concentrator or are evaluated using the stresses that are averaged within this region [7-9]. A limitation of these approaches lies in the determination of the equivalent macrocrack size or the evaluation zone. Analytical expressions are not provided to relate the distributed damage to the equivalent geometric properties. Instead, these values are selected to correlate with experimental data and thus are restricted to similar geometries and loading histories [10]. Often these values that are supposed to describe the evolving damage state are assumed to be constant throughout the failure process. Furthermore, in light of the increasing inhomogeneity with damage accumulation, these indirect approaches to the accounting of subcritical damage do not provide sufficient information to predict accurately the evolution of the damaged region and the eventual failure of the component.

Ply discount methods have also been used in conjunction with the aforementioned approaches to model the stress redistribution process, but the abrupt loss of stiffness does not reflect the gradual degradation that occurs with subcritical damage accumulation. Recent efforts have explicitly modeled each flaw in the damaged region to capture the conditions leading to failure. Elasticity solutions are available for idealized component geometries and sparse damage states. However, numerical computational approaches such as the finite-element method have to be employed for typical damage configurations [11-16]. To obtain accurate stress fields, each flaw is modeled by a large number of elements. The stress fields are then used in the failure criterions to determine the initiation and propagation of each flaw. It is necessary to update the finite-element model as the damage state evolves. This type of analysis, unfortunately, can rapidly become computationally untenable since a component may accumulate many interacting flaws before failure occurs.

The requirement for information concerning the subcritical damage accumulation and the desire for a tractable analysis scheme have prompted the use of the continuum-damage-mechanics approach in the analysis of progressive failure in laminated composite structures [*17–20*]. The size and distribution of the subcritical damage found in laminated composites enable the selection of a representative volume element (RVE) of material that is small in scale relative to the structure, but is of sufficient size to characterize the damage contained within by statistically averaged quantities. These averaged quantities, known as internal state variables, describe the physical attributes of each mode of damage. The resulting effects of the distributed damage are then reflected in the constitutive relationship through the internal state variables. Therefore, a medium containing a multitude of small internal cracks can be analyzed as a continuum without internal boundaries. Due to the nonlinear nature of the constitutive equations, this type of analysis is approached numerically by methods such as finite elements. This homogenization of the subcritical damage eliminates the task of modeling individual flaws; but since the homogenization is performed at a scale that is small with respect to the structure, the results are of sufficient resolution to provide an indication of the damage accumulation and stress redistribution.

A progressive failure model incorporating the continuum-damage-mechanics approach to model-matrix-dominated damage has been under development by the authors [*21–26*]. The model's capability to predict the development of matrix cracks under tension-tension fatigue loading conditions is used to examine the development of damage in composite laminates. The information obtained is then used to predict the failure of the component.

Progressive Failure Model

The proposed progressive failure model consists of three components. The first is the nonlinear constitutive relationships derived using continuum damage mechanics. Next is the structural analysis algorithm incorporating the aforementioned constitutive relationships, and, finally, failure criteria to indicate the catastrophic failure of the structure. Due to the progressive nature of the failure process, these components are employed in a time-stepping manner to evaluate the stress state and damage evolution throughout the loading history. The results obtained at each step are then used to update the model for the next step in the loading history. The following sections will first present the essential aspects of each component of the progressive failure model. These components will then be assembled in an analysis scheme to form the progressive failure model. More in-depth discussions on these components can be found in the published literature [*21–26*].

Damage-Dependent Constitutive Relationships

The damage-dependent constitutive relationships form the foundation of this progressive failure model. These relationships determine the stress-strain response in the presence of internal damage as represented by the internal state variables. Within the framework of continuum damage mechanics, the rate of change of these internal state variables is calculated from history-dependent damage-evolution laws. Thus, in the course of the analysis, both the changes in the stress state as well as in the damage state are determined. The probable location and mode of failure can then be inferred from these results calculated at sequential points in the loading history. The principles of continuum damage mechanics further require the selection of local volume elements in which homogenization is performed. For matrix cracking, this volume can be specified at the ply level. This selection of the local volume serves as the logical building block in this analysis. The model of a composite laminate can then be formed by assembling these building blocks together. By also developing damage evolution laws and failure functions to be applicable at the ply level, the formulation becomes independent of the lamination geometry. The relative scale and location of occurrence of delamination damage preclude its specification at the ply level; it is instead introduced at the laminate level. To maintain the geometric independence of the model, a set of damage-dependent lamination equations with modifications to accommodate the effects of the delamination damage is employed.

The kinematic effects of the matrix cracks and delaminations are quantified by the internal state variables used in this model. Matrix cracking is measured by the volume averaged dyadic product of the crack face displacement, u_i, and the crack face normal, n_j, as proposed by Vakulenko and Kachanov [27]

$$\alpha_{ij}^{M} = \frac{1}{V_L} \int_{s} u_i n_j dS \tag{1}$$

where α_{ij}^{M} is the second-order tensor internal state variable, V_L is the local representative volume in the deformed state, and S is the crack surface area. This product represents the averaged kinematics of the crack faces and can be interpreted as additional strains incurred by the material as a result of the internal damage. Since the internal state variable is a second-order tensor, it is capable of modeling all three kinematic modes of crack face displacement. From micromechanics, it has been found that the effects of the matrix cracks can be introduced into the ply-level constitutive equations as follows [28]

$$\{\sigma_L\} = [Q]\{\varepsilon_L - \alpha_L^{M}\} \tag{2}$$

where σ_L are the locally averaged components of stress, $[Q]$ is the ply-level transformed stiffness matrix, ε_L are the locally averaged components of strain, and α_L^{M} are the components of the internal state variable for matrix cracking. Since interlaminar delaminations are not statistically homogeneous through the laminate thickness, their effects cannot be homogenized at the ply level like the matrix cracks. The effects of the delamination are modeled instead using an RVE at the laminate level. The presence of interply delaminations in a laminate introduces jump discontinuities in the displacement and rotation of the normal line to the midplane of the plate. The Kirchhoff-Love hypothesis is thus modified to account for these discontinuities at the damage interfaces as shown here [29]

$$u(x,y,z) = u^{o}(x,y) - z\,[\beta^{o} + H(z - z_i)\beta_i^{D}] + H(z - z_i)u_i^{D} \tag{3}$$

$$v(x,y,z) = v^{o}(x,y) - z[\eta^{o} + H(z - z_i)\eta_i^{D}] + H(z - z_i)v_i^{D} \tag{4}$$

$$w(x,y,z) = w^{o}(x,y) + H(z - z_i)w_i^{D} \tag{5}$$

where u^{o}, v^{o}, and w^{o} are the midplane displacements; β^{o} and η^{o} are the ply rotations; u_i^{D}, v_i^{D}, and w_i^{D}, are the ply jump displacement due to delamination; β_i^{D} and η_i^{D} are the ply jump rotations due to delaminations; and $H(z - z_i)$ is the Heavyside step function. These displacement equations are averaged over a local area to produce locally averaged displacements. The results are then used in the calculation of the average strains via the ply level constitutive relationship shown in Eq 2. Integrating these ply stresses through the thickness of the laminate will produce the following damage-dependent lamination equations

$$\begin{aligned}\{N\} = \sum_{k=1}^{\tilde{n}} [Q]_k(z_k - z_{k-1})\{\varepsilon_L^{o}\} - \frac{1}{2}\sum_{k=1}^{\tilde{n}} [Q]_k(z_k^2 - z_{k-1}^2)\{\kappa_L^{o}\} + \sum_{i=1}^{d} [\tilde{Q}_1]_i t_i\{\alpha^{D}\}_i \\ + \sum_{i=1}^{d} [\tilde{Q}_2]_i(z_i - z_{i-1})\{\alpha^{D}\}_i - \sum_{k=1}^{\tilde{n}} [Q]_k(z_k - z_{k-1})\{\alpha^{M}\}_k\end{aligned} \tag{6}$$

$$\{M\} = \frac{1}{2}\sum_{k=1}^{\tilde{n}} [Q]_k(z_k^2 - z_{k-1}^2)\{\varepsilon_L^o\} - \frac{1}{3}\sum_{k=1}^{\tilde{n}} [Q]_k(z_k^3 - z_{k-1}^3)\{\kappa_L^o\} + \sum_{i=1}^{d} [\tilde{Q}_3]_i t_i^2\{\alpha^D\}_i$$
$$+ \sum_{i=1}^{d} [\tilde{Q}_4]_i(z_i^2 - z_{i-1}^2)\{\alpha^D\}_i - \frac{1}{2}\sum_{k=1}^{\tilde{n}} [Q]_k(z_k^2 - z_{k-1}^2)\{\alpha^M\}_k \quad (7)$$

where N is the component of the resultant force per unit length; M is the component of the resultant moments per unit length; $\tilde{n}$ is the number of plies in the laminate; ε_L^o and κ_L^o are components of the midplane strains and curvatures; $[Q]_k$ is the elastic modulus matrix for the k^{th} ply in laminate coordinates; $\{\alpha^M\}_k$ contains the matrix cracking internal state variables for the k^{th} ply; d is the number of delaminated interfaces; and $[\tilde{Q}_j]_i$ are the weight-averaged stiffness matrices of the sublaminate associated with the i^{th} delaminated interface [*26*]. This sublaminate is composed of the ply directly above and below the delaminated interface. t_i is the thickness of this sublaminate. $\{\alpha^D\}_i$ are components of the delamination damage internal state variable, which includes components for crack face displacements and rotations, for the i^{th} delaminated interface. These delamination internal state variables are defined in a similar manner as for matrix cracking. However, the local volume is now specified at the sublaminate level. The effects of the internal damage are accounted for by the last three terms on the right-hand side of Eqs 6 and 7, the first two representing the contribution from delamination and the last term from matrix cracking. These terms can be viewed as "damage induced" forces and moments whose application to the undamaged material will produce midplane strain and curvature contributions equivalent to those resulting from the damage-induced compliance increase. If no damage were present, these equations would reduce to the elastic lamination equations.

The internal state variables for the matrix cracks and delaminations can be determined either from experimental data [*22,28*] or damage evolution equations [*30*]. The former method requires prior knowledge of the damage state in the structure. Since the objective of this research effort is to predict the accumulation of damage and its effect on the structure, damage evolution equations are used in this model. These relationships describe the rate at which the internal state variables are changing in the RVE and are functions of only the current state at each locally averaged material point. The damage state at any point in the loading history is then found by integrating the damage evolutionary laws. For symmetric crossply laminates subjected to uniaxial loading conditions, the predominant type of damage is the Mode I opening intraply matrix crack. It is assumed that all the crack surfaces are oriented perpendicular to the plane formed by the ply. Thus, matrix damage in each ply can be characterized by only one component of the damage tensor. This component, α_{22}^M, is associated with the displacement of the crack face in a direction parallel to the crack face normal. Based on the observation that the accumulation of matrix crack is related to the strain energy release rate, G, in a power law manner [*31*], the authors have proposed the following evolutionary relationship for this component of the damage tensor when the load is applied cyclically [*30*]

$$d\alpha_{22}^M = \frac{d\alpha_{22}^M}{dS}\check{k}G^{\check{n}}dN \quad (8)$$

where the term $d\alpha_{22}^M/dS$ reflects the changes in the internal state variable with respect to changes in the crack surfaces. This term is calculated analytically from a relationship describing the average crack surface displacements in the pure opening mode (Mode I) for a medium containing alternating 0° and 90° plies [*28*]. It has been found that for typical brittle graphite/epoxy material systems $d\alpha_{22}^M/dS$ varied little with damage when subjected to fatigue at constant load levels. Therefore, $d\alpha_{22}^M/dS$ is assumed to be independent of the number of matrix cracks in the ply. This approximation leaves the component of the far-field load normal to the crack surface and the layer thickness as the determining factor for the value of $d\alpha_{22}^M/dS$. G is the strain energy release rate calculated from the ply-level damage-dependent stresses. The material parameters, $\check{k}$ and $\check{n}$, are phenomenological in nature and must be determined from experimental data. For the present model, $\check{k}$ and $\check{n}$ are determined from the damage history of a $[0_2/90_2]_s$ AS4/3502-6 graphite/epoxy laminate fatigue loaded at a maximum stress amplitude of 296.5 MPa and a cycle ratio of 0.1 as reported by Chou et al. [*31*]. The parameters have been found to be

$$\check{k} = 4.42, \qquad \check{n} = 6.39 \tag{9}$$

for this material system. Because $\check{k}$ and $\check{n}$ are assumed to be material parameters, the values determined from one laminate stacking sequence should be valid for other laminates as well. This has been found to be accurate for crossply laminates with varying numbers of transverse plies and stress amplitudes [*32*]. Further investigation of other laminate stacking sequences will be required to determine whether this assumption is valid for noncrossply layups. Since the interactions with the adjacent plies and damage sites are implicitly reflected in the calculation of the ply-level response through the laminate-averaging process, Eq 8 is not restricted to a particular laminate stacking sequence. Thus, both the transverse matrix cracking and axial splits in a crossply laminate subjected to tensile cyclic loading conditions can be modeled with the same equation.

Structural Analysis Algorithm

To incorporate the damage-dependent laminate constitutive relationship into a finite-element formulation, the damage-dependent force and moment resultants, Eqs 6 and 7, are substituted into the plate equilibrium equations. The restriction to symmetric laminate stacking sequence is taken to simplify the formulation. This assumption produces a zero coupling stiffness matrix and results in uncoupled governing differential equations. These governing differential equations are integrated against variations in the displacement components to produce a weak formulation of the damage-dependent laminated plate equilibrium equations. The current algorithm uses a three-node triangular element with five degrees of freedom at each node; this consists of two in-plane displacements, one out-of-plane displacement, and two out-of-plane rotations. This element is formed by combining a constant strain triangular element and a nonconforming plate bending element. Corresponding displacement interpolation functions are substituted into the weak formulation of the plate equilibrium equations to produce the following equilibrium equations in matrix form [*33*]

$$\begin{bmatrix} K^{11} & K^{12} & 0 \\ K^{21} & K^{22} & 0 \\ 0 & 0 & K^{33} \end{bmatrix} \begin{Bmatrix} u \\ v \\ \delta \end{Bmatrix} = \begin{Bmatrix} F_A^1 \\ F_A^2 \\ F_A^3 \end{Bmatrix} + \begin{Bmatrix} F_M^1 \\ F_M^2 \\ F_M^3 \end{Bmatrix} + \begin{Bmatrix} F_D^1 \\ F_D^2 \\ F_D^3 \end{Bmatrix} \tag{10}$$

where $[K]$ is the element stiffness matrix, $\{\delta\}$ contains the out-of-plane displacement and rotations, $\{F_A\}$ is the applied force vector, and $\{F_M\}$ and $\{F_D\}$ are the "damage-induced" force vectors resulting from matrix cracking and delamination, respectively. The effects of the internal damage now appear on the right-hand side of the equilibrium equations as damage-induced force vectors. This representation eliminates the need to recalculate the elemental stiffness matrices each time the damage state evolves, thus saving much computational time.

Failure Criteria

The objective of the failure criteria is to evaluate the structural integrity of the component using the current stress and damage states calculated by the model. This entails the examination of the failure process at both the local material level and the global structural level because the failure at one material point may create stress redistributions that can cause simultaneous failure in the surrounding regions. Typical failure during tensile conditions is signaled by fiber fracture in the principal load carrying plies of a multidirectional laminate. This is evaluated by the following criterion

$$\varepsilon_{11} \geq \varepsilon_{11_f} \tag{11}$$

where ε_{11} is the average ply level strain in the fiber direction and ε_{11_f} is the tensile failure strain measured from a unidirectional laminate. After failure has been declared, the ply no longer can support additional load. The current analysis considers this condition as the failure of component. In situations where the failure process is permitted to progress beyond the first fiber failure, the stability of the failure process is evaluated at the global level. The stress state for the entire structure with the updated damage is recalculated using the current loading condition. Local laminate failure is evaluated once again in the structure. If it has been determined that additional laminate failure has not occurred, then the failure process is stable and the analysis is continued to the next increment of loads. On the other hand, new local laminate failure would indicate an unstable fracture process and signals the initiation of global failure. This local-global procedure forms the failure evaluation of the progress failure model. Other modes of failure can be included in the evaluation by the application of the appropriate criteria at the local level of the analysis.

Progressive Analysis Scheme

The aforementioned components are assembled together as shown in Fig. 1 to form the progressive failure model. In a typical analysis, the applied loads and initial damage state are entered into the damage dependent constitutive relationships to determine the effective damage-induced forces. These resultant damage forces along with the applied forces are used in the structural analysis algorithm to calculate the global structural response. The results are once again sent to the constitutive relationships where the local stress/strain response is obtained. The changes in the damage state are also determined at this stage by the damage evolutionary relationships using the local ply stresses. The failure criteria are evaluated locally with the updated damage state; if failure has occurred, global failure is examined. Next, the entire process is repeated for the next load step. This model is coded into a computational program to facilitate the analysis of engineering structures.

Numerical Results and Discussion

The proposed progressive failure model is employed to examine the residual life of a crossply laminated plate subjected to fatigue loading conditions. A circular cutout is placed at the center of the plate to produce stress gradients that are conducive to the growth of subcritical damage. This configuration is similar to those used to model fastener holes found in many composite structures. Thus, by examining how the stresses are redistributed and damage accumulates near the fastener hole, information can be gathered to determine the merits of a particular design. The dimensions of the rectangular plate used in this study are 25.4 by 50.8 mm. The circular cutout has a diameter of 6.4 mm. A cyclic tensile load is applied at the nar-

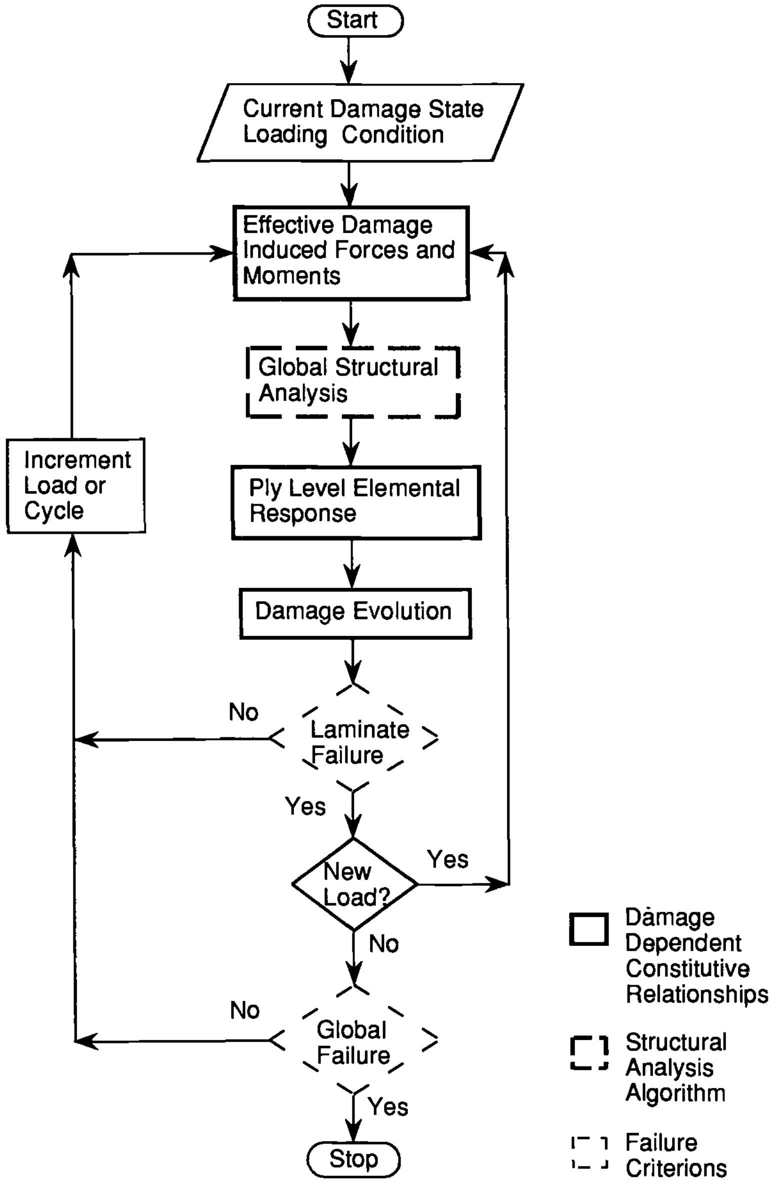

FIG. 1—*Progressive failure analysis methodology.*

row end of the plate. Due to symmetry about the length and width of the plate, the finite-element mesh represents a quarter of the plate. It is discretized into 90 three-node triangular elements, as shown in Fig. 2. The plate has a $[0/90_2]_s$ laminate stacking sequence. The material properties, shown in Table 1, for AS4/3501-6 graphite/epoxy have been used in the calculation. The fatigue load is applied at a cycle ratio of 0.1 and follows the maximum stress history shown in Fig. 3. The first 50 cycles consist of the ramp up to the test load. This is done in part

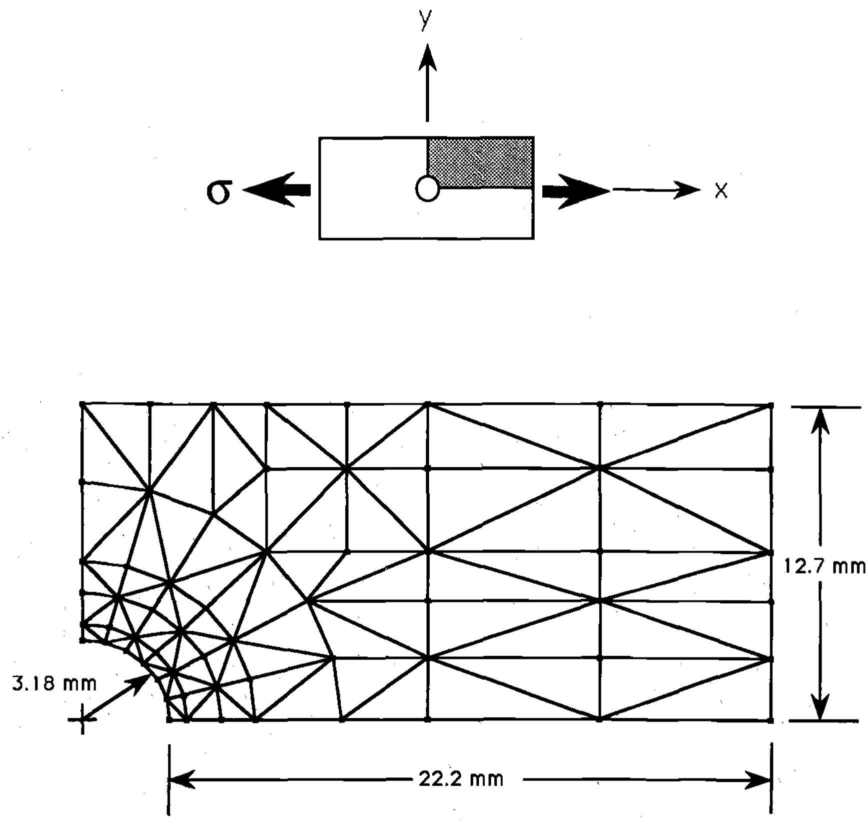

FIG. 2—*Finite-element mesh of plate with circular cutout.*

to control the incremental changes to the damage state during the initial portion of the loading history. In this simulation, matrix cracking is assumed to be the only form of damage mode and because of the crossply stacking sequence, component failure is assumed to occur at the first fiber fracture in the 0° plies.

The predicted accumulation of matrix crack damage in the 90° plies of a panel loaded at a maximum stress of 184.0 MPa is shown in Fig. 4. The amount of damage is expressed in terms

TABLE 1—*Ply-level material properties for AS4/3501-6 used in simulation.*

E_{11}	146.9 GPa
E_{22}	10.4 GPa
G_{12}	4.3 GPa
ν_{12}	0.26
ν_{23}	0.42
t_{ply}	0.128 mm
ε^{f}_{11crit}	15 000 μstrain
GROWTH LAW PARAMETERS	
$\check{k}$	4.42
$\check{n}$	6.39

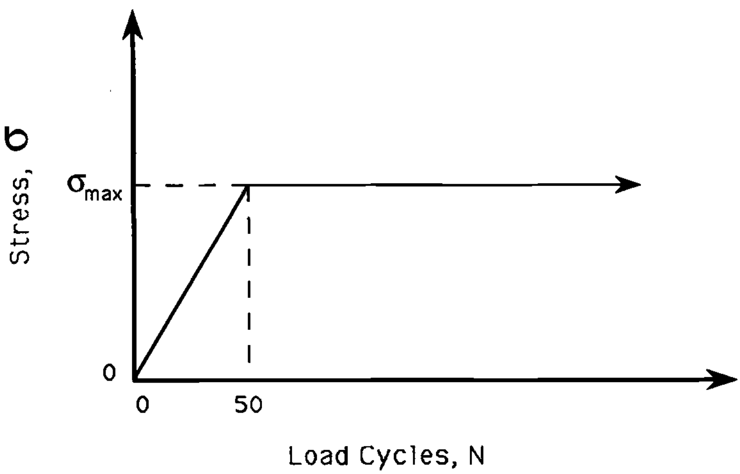

FIG. 3—*Maximum fatigue stress history used in simulation (*R *= 0.1).*

of the volume-averaged crack face displacement as defined by Eq 1. At the end of the load ramp up, matrix damage has developed throughout the plate. The greatest damage being located near the notch. This region of high damage gradient expands outward after 1550 cycles. The amount of damage also increases in the rest of the plate. However, after 7550 cycles, much of the damage evolution emanates from the region adjacent to the notch. This shift in the damage evolution reflects the load redistribution occurring inside the laminate. The corresponding axial stress history for the 0° plies is shown in Fig. 5. The effects of the damage growth that occurs between 50 and 1550 cycles can be seen by the increase in stress near the notch. The interesting changes in the stress distribution beyond this point in the loading history are not discernible from the stress contour plots; but examination of the numerical data indicates load transfer taking place in a confined area adjacent to the notch. This decelerated change in the stress distribution is in part due to the small fraction of the total load initially carried by the 90° plies. Any loss in the load carrying capability in the 90° plies will translate to small changes in the stress state in the 0° plies. The accumulation of damage further reduces the load available for transfer. However, a sufficient amount of load is transferred to the 0° plies to cause fiber fracture and component failure after 7634 cycles. During the life of the plate, the greatest accumulation of matrix damage is located at a region adjacent to the notch. Rather than expanding outward, the damage intensifies in this region until first fiber failure in the 0° plies. This behavior has also been predicted by Chang et al. [*34*] in crossply laminates subjected to monotonically increasing tensile loading conditions.

The predicted cycles to first fiber failure at various maximum fatigue stress levels are shown in Fig. 6. At the higher stresses, the load redistribution progresses rapidly from the formation of the high-damage gradient zone to the failure of the first fiber. This indicates a sufficient amount of energy was available after the formation of this zone to produce this result. At lower applied stresses, a large portion of the available energy is expended during the formation of the damage zone. Therefore, the intensification stage spans over a relatively high number of fatigue cycles. The increase in the number of cycles to failure from decreasing the applied stress at the lower stress levels is large. Decreasing the applied stress from 185.7 to 183.4 MPa increases the cycles to failure by more than 100 000 cycles. A possible cause for this response is related to the amount of load redistribution taking place inside the laminate. Recall that these predictions are based on the assumption that matrix cracking is the only type of matrix-

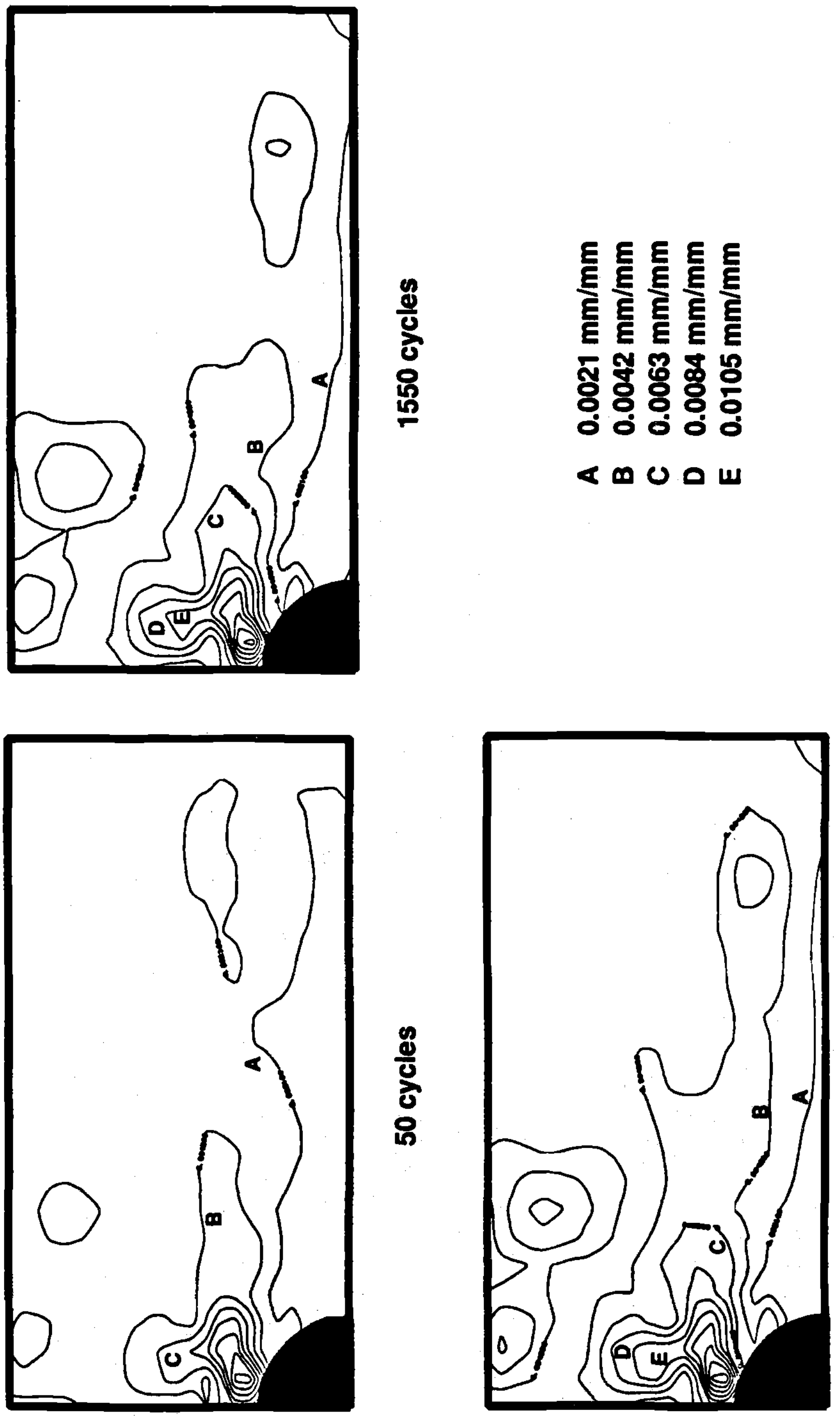

FIG. 4—*Matrix crack damage accumulation in the 90° plies of a plate fatigue loaded at a maximum stress of 184.0 MPa.*

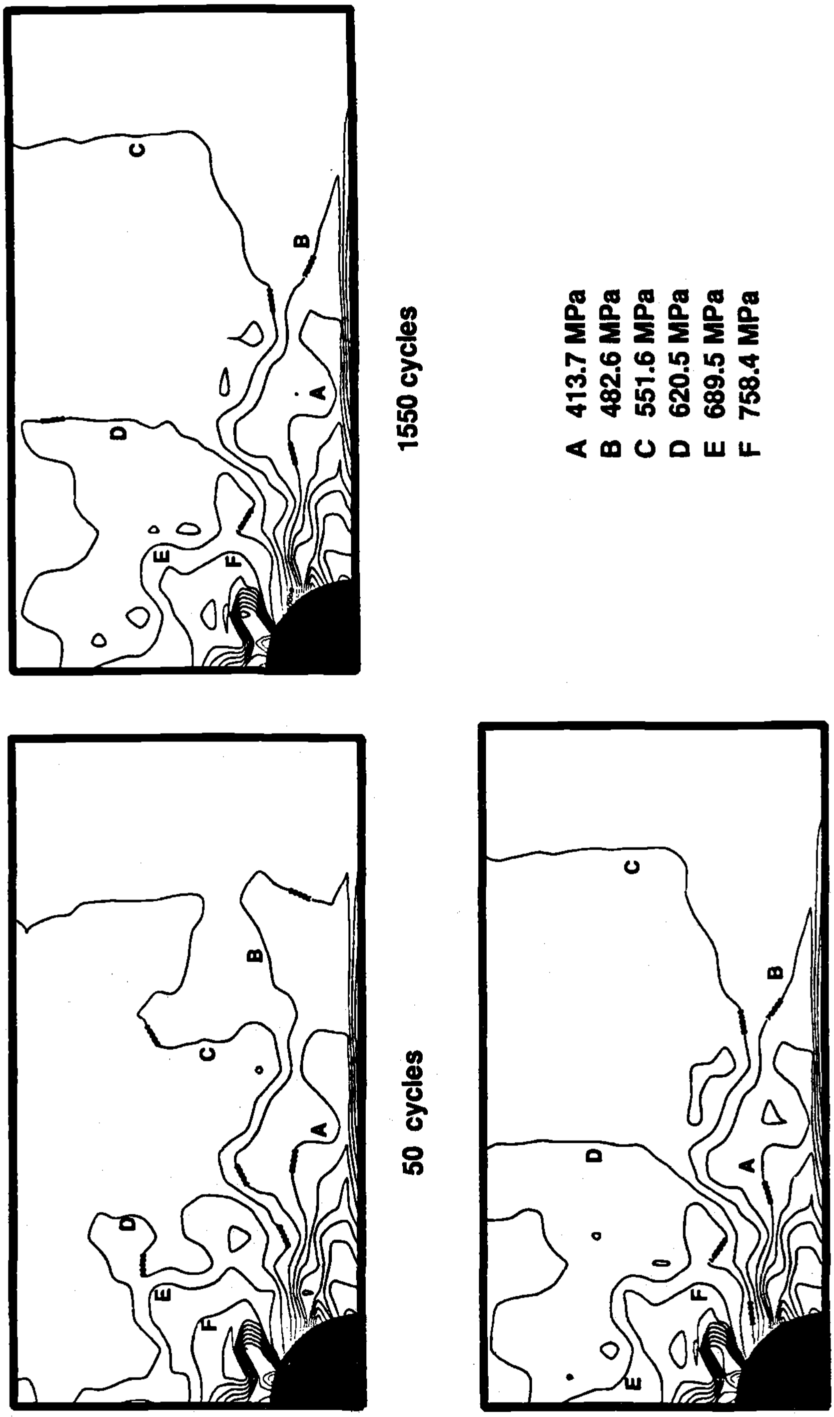

FIG. 5—*Axial stress distribution in the 0° plies of a plate fatigue loaded at a maximum stress of 184.0 MPa.*

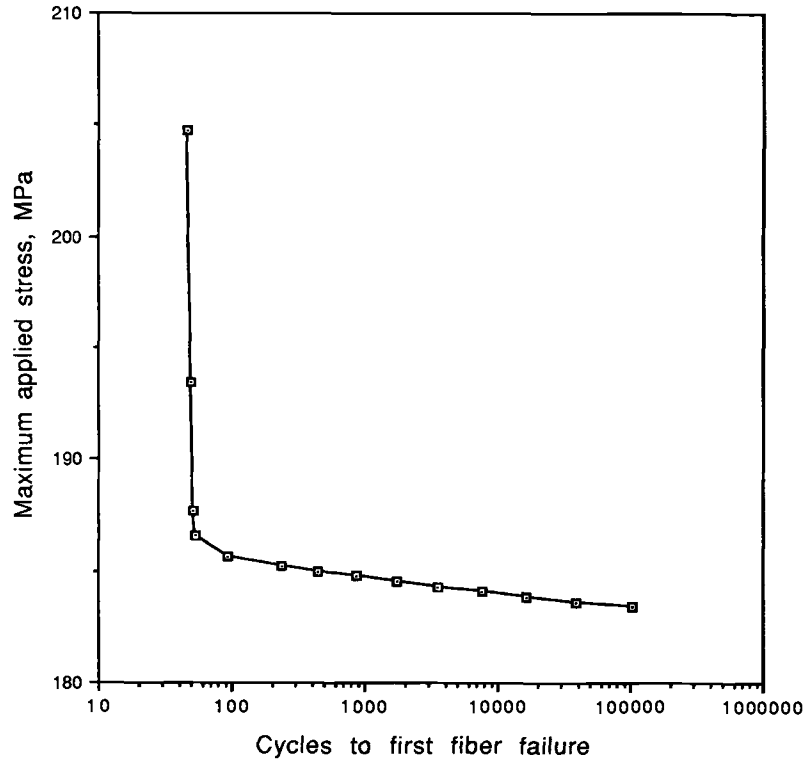

FIG. 6—*Predicted cycles to first fiber failure of fatigue-loaded plate with a circular cutout.*

dominated damage present. The inclusion of delamination damage into the analysis will alter the stress redistribution and damage accumulation. Its effects will be most apparent at the lower stress levels where the delamination damage can initiate and accumulate before fiber failure occurs. The number of fatigue cycles required for first fiber failure at these stress levels will decrease due to the additional source of load redistribution. Since the stress redistribution and damage formation are coupled, additional analysis and experimental verification would be required before any quantitative conclusions can be drawn about effects of including delamination damage. However, it would enable the current progressive failure analysis framework to capture a more complete picture of the complex interactive process and enhance the model predictions.

The type of information obtained from the simulation could be potentially very useful to the designer or analyst. The ability to locate critical regions and to track the evolution of damage in these regions would allow designers to create safer and more efficient components. Alternately, a damaged region detected in a component can be characterized and then entered into the model to determine its effect on the residual responses so that it can be removed from service at the appropriate time. The proposed model demonstrates the feasibility of the continuum-damage-mechanics approach. Further developments are in progress to achieve the capabilities for analyzing more complex damage states.

The current analysis assumes component failure to occur at the first fracture of fibers in the principal load carrying plies. This assumption is valid in narrow specimens where there is not sufficient area to redistribute the tensile loads within these plies. In wider specimens, global fracture can be stable; thus, the progressive failure process extends beyond the first fiber failure. Therefore, the full implementation of the matrix-dominated damage evolution laws and the introduction of fiber fracture internal state variables and growth laws are future objectives of the research effort. This will be followed by the modeling of compressive failure modes.

Conclusion

The use of continuum damage mechanics in the progressive failure model provides an efficient means of modeling distributed damage found in laminated composites. Each type of damage is represented by a set of strain-like internal state variables. The internal state variables evolve with the accumulation of damage at each material point. These values are predicted by damage evolution relationships that are functions of the current state of the material including all the damage present. Since the formulation permits the gradual accumulation of damage and the concurrent growth of different damage types, the analysis reflects the events occurring inside the laminate. The current framework operates in a time-stepping manner where the stress distribution and damage accumulation predicted at each step are employed in the local-global structural integrity evaluation. This ability to simulate the progressive failure process will enhance the design and maintenance of laminated composite structures by reducing the dependence on experimental support.

Even though continuum damage mechanics is suited for the examination of damages that are distributed in nature and fracture mechanics is applicable for the evaluation of well-defined macrocracks, there are situations that require the incorporation of the two approaches. One such case is the existence of a sharp notch in a composite laminate. In this instance, a damage zone containing many distributed microcracks will develop ahead of this notch when load is applied. To account for the stress redistribution in this zone, continuum mechanics can be used to determine the state of the material. These results can then be evaluated on the global scale using fracture mechanics. Thus, rather than choosing one method over the other, they should be viewed as integral units in the failure analysis of laminated composite structures.

Acknowledgment

The support from NASA Langley Research Center under Contracts NGT-50262 and NAG-1-1120 is gratefully appreciated by Mr. Lo and Mr. Allen.

References

[*1*] Stinchcomb, W. W. and Reifsnider, K. L., "Fatigue Damage Mechanisms in Composite Materials: A Review," *Fatigue Mechanisms, ASTM STP 675*, J. J. Fong, Ed., American Society for Testing and Materials, Philadelphia, 1979, pp. 762–787.

[*2*] Stinchcomb, W. W., Reifsnider, K. L., Yeung, P., and Masters, J., "Effect of Ply Constraint on Fatigue Damage Development in Composite Material Laminates," *Fatigue of Fibrous Composite Materials, ASTM STP 723*, K. N. Lauraitis, Ed., American Society for Testing and Materials, Philadelphia, 1981, pp. 65–84.

[*3*] Reifsnider, K. L. and Jamison, R., "Fracture of Fatigue-Loaded Composite Laminates," *International Journal of Fatigue*, Vol. 4, No. 4, Oct. 1982, pp. 187–197.

[*4*] Jamison, R. D., Schulte, K., Reifsnider, K. L., and Stinchcomb, W. W., "Characterization and Analysis of Damage Mechanisms in Tension-Tension Fatigue of Graphite/Epoxy Laminates," *Effects of Defects in Composite Materials, ASTM STP 836*, K. L. Reifsnider, Ed., American Society for Testing and Materials, Philadelphia, 1984, pp. 21–55.

[*5*] Cruse, T. A., "Tensile Strength of Notched Composites," *Journal of Composite Materials*, Vol. 7, April 1973, pp. 218–228.

[*6*] Tirosh, J., "On the Tensile and Compressive Strength of Solids Weakened (Strengthened) by an Inhomogeneity," *Journal of Applied Mechanics*, Vol. 44, No. 3, Sept. 1977, pp. 449–454.

[7] Whitney, J. M. and Nuismer, R. J., "Stress Fracture Criteria for Laminated Composites Containing Stress Concentrations," *Journal of Composite Materials*, Vol. 8, July 1974, pp. 253-265.
[8] Nuismer, R. J. and Labor, J. D., "Application of the Average Stress Failure Criterion: Part I—Tension," *Journal of Composite Materials*, Vol. 12, July 1978, pp. 238-249.
[9] Chang, F. K., Scott, R. A., and Springer, G. S., "Failure Strength of Nonlinearly Elastic Composite Laminates Containing a Pin-Loaded Hole," *Journal of Composite Materials*, Vol. 18, Sept. 1984, pp. 464-477.
[10] Awerbuch, J. and Madhukar, M. S., "Notched Strength of Composite Laminates: Predictions and Experiments—A Review," *Journal of Reinforced Plastics and Composites*, Vol. 4, No. 1, 1985, pp. 3-159.
[11] O'Brien, T. K. and Raju, I. S., "Strain-Energy-Release Rate Analysis of Delamination Around an Open Hole in Composite Laminates," AIAA Paper 84-0961, American Institute of Aeronautics and Astronautics, New York, 1984.
[12] Whitcomb, J. D. and Raju, I. S., "Analysis of Interlaminar Stresses in Thick Composite Laminates With and Without Edge Delamination," *Delamination and Debonding of Materials, ASTM STP 876*, W. S. Johnson, Ed., American Society for Testing and Materials, Philadelphia, 1985, pp. 69-94.
[13] Mahishi, J. M. and Adams, D. F., "Energy Release Rate During Delamination Crack Growth in Notched Composite Laminates," *Delamination and Debonding of Materials, ASTM STP 876*, W. S. Johnson, Ed., American Society for Testing and Materials, Philadelphia, 1985, pp. 95-111.
[14] Whitcomb, J. D., "Instability-Related Delamination Growth of Embedded and Edge Delaminations," NASA TM 100655, National Aeronautics and Space Administration, Hampton, VA, Aug. 1988.
[15] Reddy, E. S., Wang, A. S. D., and Zhong, Y., "Simulation of Matrix Cracks in Composite Laminates Containing a Small Hole," *Journal of Reinforced Plastics and Composites*, Vol. 9, March 1990, pp. 104-117.
[16] Wang, A. S. D., Reddy, E. S., and Zhong, Y., "Three-Dimensional Simulation of Crack Growth in Notched Laminates," *Journal of Reinforced Plastics and Composites*, Vol. 9, March 1990, pp. 134-150.
[17] Harris, C. E., Allen, D. H., and Lo, D. C., "A Mechanics Framework for a Progressive Failure Methodology for Laminated Composites," *Proceedings*, Fourth ASC Conference on Composites, Blacksburg, VA, Oct. 1989.
[18] de Rouvray, A. and Haug, E., "Failure of Brittle and Composite Materials by Numerical Methods," *Structural Failure*, T. Wierzbicki and N. Jones, Eds., Wiley, New York, 1989, pp. 193-254.
[19] Ladeveze, P., Allix, O., and Daudeville, L., "Mesomodeling of Damage for Laminate Composites Application to Delamination," *Proceedings*, IUTAM Symposium on Inelastic Deformation of Composite Materials, Troy, NY, 29 May-1 June 1990.
[20] Allix, O., Daudeville, L., and Ladeveze, P., "Delamination and Damage Mechanics," *International Journal of Fatigue and Fracture of Engineering Materials and Structures*, to be published.
[21] Allen, D. H., Harris, C. E., and Groves, S. E., "A Thermomechanical Constitutive Theory for Elastic Composites with Distributed Damage—Part I: Theoretical Development," *International Journal of Solids and Structures*, Vol. 23, No. 9, 1987, pp. 1301-1318.
[22] Allen, D. H., Harris, C. E., and Groves, S. E., "A Thermomechanical Constitutive Theory for Elastic Composites with Distributed Damage—Part II: Application to Matrix Cracking in Laminated Composites," *International Journal of Solids and Structures*, Vol. 23, No. 9, 1987, pp. 1319-1338.
[23] Allen, D. H., Harris, C. E., Groves, S. E., and Norvell, R. G., "Characterization of Stiffness Loss in Crossply Laminates with Curved Matrix Cracks," *Journal of Composite Materials*, Vol. 22, No. 1, 1988, pp. 71-80.
[24] Harris, C. E., Allen, D. H., and Nottorf, E. W., "Damage Induced Changes in the Poisson's Ratio of Cross-Ply Laminates: An Application of a Continuum Damage Mechanics Model for Laminated Composites," *Damage Mechanics in Composites, AD-Vol. 12*, A. S. D. Wang and G. K. Haritos, Eds., The American Society of Mechanical Engineers, New York, 1987, pp. 17-23.
[25] Harris, C. E., Allen, D. H., and Nottorf, E. W., "Modeling Stiffness Loss in Quasi-Isotropic Laminates Due to Microstructural Damage," *Journal of Engineering Materials and Technology*, Vol. 110, 1988, pp. 128-133.
[26] Allen, D. H., Nottorf, E. W., and Harris, C. E., "Effect of Microstructural Damage on Ply Stresses in Laminated Composites," *Recent Advances in the Macro and Micro-Mechanics of Composite Materials Structures, AD-Vol. 13*, D. Hui and J. R. Vinson, Eds., The American Society of Mechanical Engineers, New York, 1988, pp. 135-145.
[27] Vakulenko, A. A. and Kachanov, M. L., "Continuum Theory of Cracked Media," *Izvestia AN SSR, Mekhanika Tverdogo Tela*, Vol. 6, 1971, p. 159.

[28] Lee, J. W., Allen, D. H., and Harris, C. E., "Internal State Variable Approach for Predicting Stiffness Reductions in Fibrous Laminated Composites with Matrix Cracks," *Journal of Composite Materials*, Vol. 23, 1989, pp. 1273–1291.

[29] Allen, D. H., Groves, S. E. and Harris, C. E., "A Cumulative Damage Model for Continuous Fiber Composite Laminates with Matrix Cracking and Interply Delaminations," *Composite Materials: Testing and Design (Eighth Conference), ASTM STP 972*, J. D. Whitcomb, Ed., American Society for Testing and Materials, Philadelphia, 1988, pp. 57–80.

[30] Lo, D. C., Allen, D. H., and Harris, C. E., "A Continuum Model for Damage Evolution in Laminated Composites," *Proceedings*, IUTAM Symposium on Inelastic Deformation of Composite Materials, Troy, NY, 29 May–1 June 1990.

[31] Chou, P. C., Wang, A. S. D., and Miller, H., "Cumulative Damage Model for Advanced Composite Materials," AFWAL-TR-82-4083, Air Force Wright Aeronautical Laboratories, OH, 1982.

[32] Lo, D. C., "A Matrix Damage Accumulation Model for Laminated Composites," Master's thesis, Texas A&M University, College Station, TX, May 1990.

[33] Buie, K. D., "A Finite Element Model for Laminated Composite Plates with Matrix Cracks and Delaminations," Master's thesis, Texas A&M University, College Station, TX, Dec. 1988.

[34] Chang, K. Y., Liu, S., and Chang, F. K., "Damage Tolerance of Laminated Composites Containing an Open Hole and Subjected to Tensile Loadings," *Journal of Composite Materials*, Vol. 25, 1991, pp. 274–301.

Catherine A. Bigelow[1] *and William S. Johnson*[1]

Effect of Fiber-Matrix Debonding on Notched Strength of Titanium Metal-Matrix Composites

REFERENCE: Bigelow, C. A. and Johnson, W. S., "**Effect of Fiber-Matrix Debonding on Notched Strength of Titanium Metal-Matrix Composites,**" *Fracture Mechanics: Twenty-Third Symposium, ASTM STP 1189,* Ravinder Chona, Ed., American Society for Testing and Materials, Philadelphia, 1993, pp. 696–712.

ABSTRACT: Two specimen configurations of a $[0/90]_{2s}$ SCS-6/Ti-15-3 laminate were tested and analyzed: a center-hole (CH) specimen and a double-edge-notched (DEN) specimen. The two specimen configurations failed at similar stress levels in spite of the large difference in the stress concentration factors for the two geometries. Microscopic examinations of the failure surfaces indicated more fiber-matrix debonding at the notch tip in the DEN specimen than in the CH specimen. Based on the experimental results, it was hypothesized that the radial stresses that developed at the fiber-matrix interface ahead of the notch tip in the DEN specimen caused fiber-matrix debonding in the 0° plies, thus lowering the stress concentration in the DEN specimen to a level comparable to that of the CH specimen.

Two analytical techniques, a three-dimensional finite-element analysis and a macro-micromechanical analysis, were used to predict the overall stress-deformation behavior and the notch-tip fiber-matrix interface stresses in both configurations. The micromechanical analysis predicted radial stresses next to the notch in the DEN configuration that were nearly seven times as large as those predicted for the CH configuration. The overall stress-deformation response of both configurations was predicted accurately when debonding of the 90° plies was included. Predictions of the axial stress in the notch-tip 0° fiber correlated well with the specimen static strength when fiber-matrix debonding of 0° plies was included for the DEN specimen. The results shown indicate that a first fiber failure criteria based on the axial stress in the first intact 0° fiber can predict the static strength of notched specimens when interfacial damage is modeled.

KEY WORDS: micrographs, fracture mechanics, finite element analysis, micromechanics, fiber stress, fatigue (materials)

Fiber-matrix interfaces can play a key role in the mechanical behavior of continuous fiber-reinforced metal-matrix composites (MMCs) [*1*]. Interfaces govern the mode and extent of load transfer between the fiber and matrix. When the interfaces are strong and transmit all loads fully, isolated fiber fractures tend to spread more rapidly to other fibers, and hasten failure [*2*]. Continuous fiber-reinforced composites can often be made more damage tolerant by decoupling fractured fibers from their neighbors through controlled interfacial failure. It may be possible to tailor the strength and toughness of the interface to decouple broken fibers from their surroundings. To accomplish such a feat, it is first necessary to understand interfacial behavior and debonding in MMCs. Early work with boron/aluminum (B/Al) MMCs showed that in this low-yield matrix, the interface was not a critical factor. Instead extensive yielding of the matrix occurred at the notch tips, such that specimens with sharp notches and center holes failed at similar stress levels [*3*]. In brittle polymeric matrix composites, similar notch-insensitive results have been observed for quasi-isotropic laminates [*4*]. However, in poly-

[1] Research engineer and senior scientist, respectively, NASA Langley Research Center, Hampton, VA 23665.

meric composites, the notch insensitivity was caused by extensive matrix cracking and delaminations near the crack tip that significantly reduced the local stress concentration [5]. The fiber-matrix interface can play a particularly significant role in MMCs with a matrix having a high yield strength, such as the SCS-6/Ti-15-3 system currently being investigated. Debonding of the fiber-matrix interface is a primary damage mechanism in SCS-6/Ti-15-3 composites [1]. Proper modeling of interfacial debonding is needed to accurately predict composite fracture behavior. To study the stress state governing fiber-matrix debonding, a micromechanics analysis is required.

The objective of the present work is to predict the static strength of notched SCS-6/Ti-15-3 composites. Two specimen configurations of a $[0/90]_{2s}$ SCS-6/Ti-15-3 laminate were tested and analyzed: a center-hole (CH) specimen and a double-edge-notched (DEN) specimen. Microscopic examinations of the failure surfaces in both configurations were made. Two analytical techniques, a three-dimensional finite-element analysis (PAFAC) and a macro-micromechanical analysis (MMA), were used to analyze the behavior of both the DEN and CH specimens. The MMA was used to analyze the stresses in the notch-tip element in the interior 0° ply in both the DEN and CH specimens to determine the fiber-matrix interface stress state for perfectly bonded fibers. PAFAC was used to predict the global stress-deformation response with interfacial debonding in the 90° plies. PAFAC was also used to predict the fiber axial stresses in the first 0° fiber next to the notch for the two configurations with interfacial debonding in the 90° and 0° plies. The static strengths of each specimen were compared to the predictions of first fiber failure in the 0° plies.

Materials and Test Procedures

Materials and Specimens

The Ti-15-3 alloy, a shortened designation for Ti-15V-3Cr-3Al-3Sn, is a metastable betastrip alloy [6]. The composite laminates were made by hot-pressing Ti-15-3 foils between unidirectional tapes of silicon-carbide fibers held in place with molybdenum wire. The manufacturer's designation for these silicon-carbide fibers is SCS-6. The fiber diameter is 0.14 mm. Two specimen configurations of the SCS-6/Ti-15-3 material were tested: a CH specimen and a DEN specimen. The two specimens were cut from a panel of $[0/90]_{2s}$ material. Each specimen consisted of eight plies and was approximately 1.67 mm thick. The fiber volume fraction was approximately 39% for both specimens.

Each specimen was 19.1 mm wide and 152.4 mm long. One specimen (CH) had a circular hole with a diameter of 6.35 mm cut in the center of the specimen. The other specimen (DEN) had two edge notches cut on the sides of the specimen using electro-discharge machining. Each notch had a length of 3.18 mm with a width of 0.25 mm and a notch tip radius of 0.125 mm. The two specimen configurations are shown in Fig. 1. No surface damage due to the machining of the notches or hole was observed in either specimen. Both specimens were tested in the as-fabricated condition.

Testing Techniques

The tests were conducted on an 89-kN servohydraulic test stand. Load control was used with a quasi-static loading rate of approximately 0.89 kN/s. Both specimens were pulled statically in tension to failure. An extensometer with a 25.4-mm gage length was mounted in the center of each specimen to record the deformation. An *X-Y* recorder was used to record the load-deformation response of the specimen using the load cell and extensometer output. Global strains of the specimens were calculated from the extensometer output.

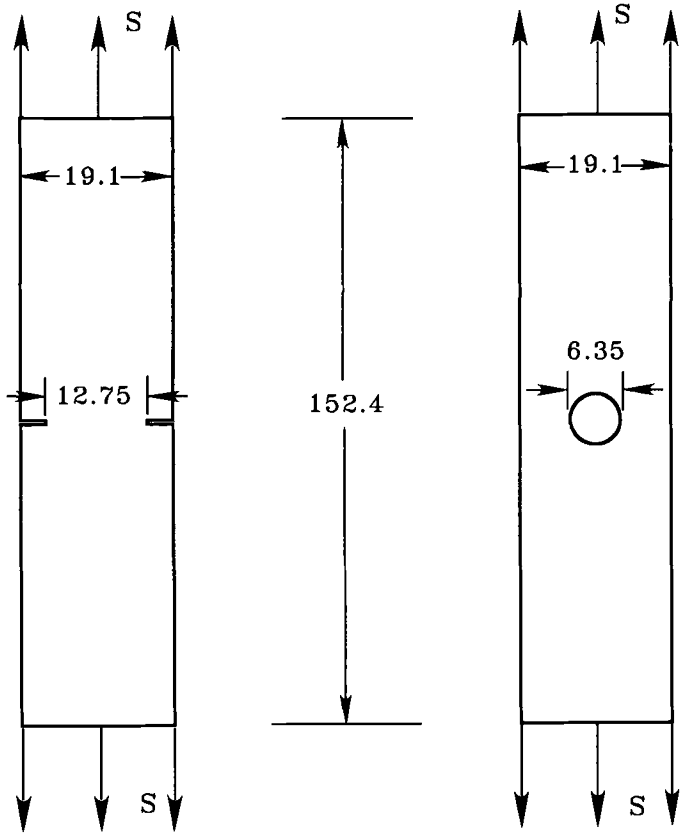

FIG. 1—*Specimen configurations and loading: $[0/90]_{2s}$ SCS-6/Ti-15-3 (all dimensions in millimetres).*

Analytical Techniques

Two analytical techniques were used to model and predict various aspects of the specimen and material behavior. The first, a three-dimensional finite-element analysis (PAFAC [*7*]), was used to analyze the global behavior of both notched SCS-6/Ti-15-3 specimens with interfacial debonding and yielding. The second, a macro-micromechanical analysis (MMA) [*8*], was used to analyze notch-tip stress states in both the DEN and CH specimens with perfectly bonded fibers. Both analytical techniques are based on constituent properties. The fiber and matrix properties [*1*] used in both analyses are given in Table 1. The two techniques will be described in more detail in the following sections.

Three-Dimensional Analysis, PAFAC

The three-dimensional finite-element analysis, Plastic and Failure Analysis of Composites (PAFAC), was used to analyze the overall behavior of both specimens. The analysis uses the vanishing-fiber-diameter material model [*9*] to account for the elastic-plastic behavior of the matrix and the elastic behavior of the fiber. PAFAC uses an eight-noded hexahedral element; each element represents a unidirectional composite material whose fibers are arbitrarily oriented in the structural coordinate system. Using this material model, the analysis calculates

TABLE 1—*Constituent properties for SCS-6/Ti-15-3* [1].

MATRIX (AS-FABRICATED)	
E, Pa	ν
9.239E10	0.36
FIBER	
E, Pa	ν
3.93E11	0.25
MATRIX STRESS-STRAIN CURVES (AS-FABRICATED)	
Strain	Stress, Pa
0.0	0.0
0.0076	6.8948E8
0.0082	7.4119E8
0.0088	7.8428E8
0.0094	8.2737E8
0.0098	8.4461E8
0.0106	8.7908E8
0.0113	8.9632E8
0.0118	9.0494E8
0.0124	9.1356E8
0.0132	9.2217E8
0.0146	9.3079E8
0.0168	9.3941E8
0.0208	9.4803E8

the fiber and laminate stresses and predicts when yielding occurs in each element of the finite-element mesh. The PAFAC analysis does not account for the thermal residual stresses that are present in this material due to the fabrication process.

Figure 2 shows a plan view of each of the finite-element meshes that were used to model the DEN and CH specimens. In both cases, only one-eighth of the specimen was modeled due to symmetry through the thickness, as well as in the plane. The mesh for the DEN specimen contained approximately 2600 nodes and 1600 elements; the notch was modeled as a rectangle. The mesh for the CH specimen contained approximately 1500 nodes and 1040 elements. Each ply of the $[0/90]_{2s}$ laminate was modeled with one layer of elements. Thus, each mesh contained four layers of the elements through the thickness (Z-direction). The smallest elements, located next to the notch, were sized to represent one fiber spacing. This fiber spacing was calculated using the fiber volume fraction (v_f = 39%), the fiber diameter (d_f = 0.14 mm), and the ply thickness (t = 0.209 mm). A uniform stress was applied to the end of each specimen to simulate loading. A convergence study [*3*] was done to evaluate the accuracy of the finite-element models.

Earlier work with unnotched SCS-6/Ti-15-3 laminates [*1*] indicated interfacial debonding in 90° plies at very low load levels. To model this phenomenon, PAFAC was modified to include a failure criterion to approximate interfacial debonding in the 90° plies. Using the discrete fiber-matrix model described in the Appendix, the transverse modulus of a unidirectional laminate with a completely debonded fiber-matrix interface was calculated. When the transverse stress in the elements in the 90° plies reached a specified critical value, the material properties of the 90° plies were modified to represent an isotropic material with an elastic modulus

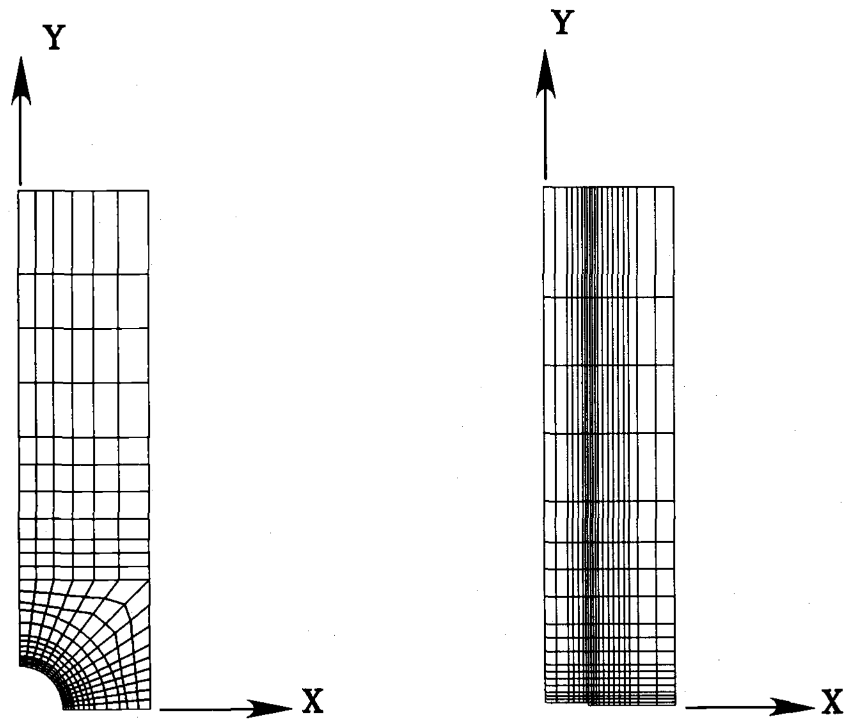

FIG. 2—*Plan view of the finite-element meshes used for the CH and DEN specimens.*

equal to the transverse modulus of a unidirectional laminate with a completely debonded interface. The effect of modeling an orthotropic layer with an isotropic material model was examined and is discussed in the Appendix. The critical transverse stress was chosen to be 155 MPa based on experimental observations of unnotched $[90]_8$ laminates [*1*]. The predicted stress-deformation curves with debonding of the 90° plies will be compared to the experimental data for both the DEN and CH specimens.

The PAFAC analysis was also modified to account for interface debonding in the 0° plies at the notch tip in the DEN specimen; the approximation used is shown schematically in Fig. 3. The original mesh at the notch tip for the DEN model is shown in Fig. 3*a,* where the mesh contains one layer of elements per ply and the elements at the notch tip are one fiber spacing wide. The fibers are shown for reference only; since the material model in PAFAC is homogeneous, it cannot model the fibers discretely. The elements next to the notch tip, which were one fiber spacing wide, were each divided into two elements. Then additional layers of elements were added such that each 0° ply was modeled with three layers of elements, as opposed to one layer used previously. The material properties of the additional elements were specified so that the elements next to the notch and between each layer were isotropic with the material properties of the matrix. The isotropic elements added between the 0° and 90° plies were 0.0345 mm thick. The remaining elements in the 0° plies were modeled as composite elements with appropriately higher fiber volume fractions. Adding the isotropic layers does not affect the overall stress-deformation response of the laminate. To model the effects of fiber-matrix debonding of the 0° fiber next to the notch, the elastic modulus of the isotropic elements in both 0° plies indicated by the shaded areas in Fig. 3*b* was reduced. Poisson's ratio was

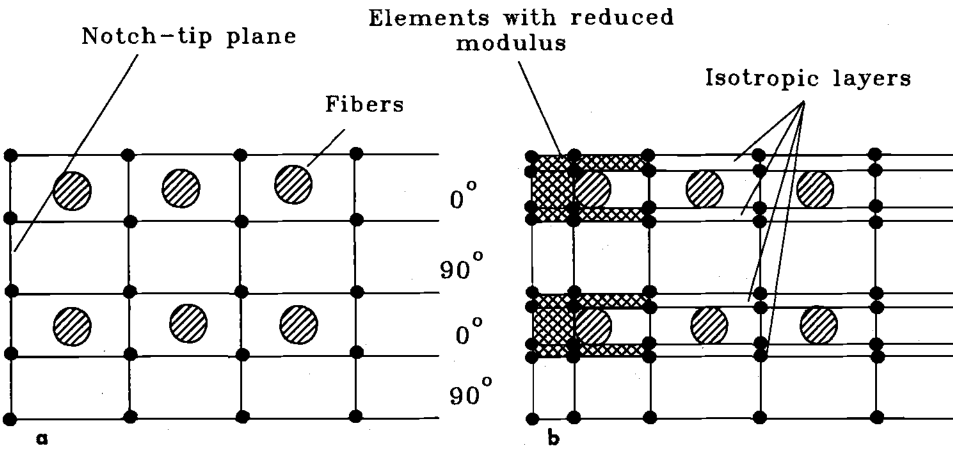

FIG. 3—*Schematic view of approximation used to model notch-tip interfacial debonding of the 0° plies in the* $[0/90]_{2s}$ *DEN specimen: (a) original mesh and (b) modified mesh.*

unchanged. Predictions of the notch-tip 0° fiber stress were made reducing the elastic modulus by a factor of 10, 100, and 1000 to determine the sensitivity of fiber stress to the reduction factor.

In the PAFAC analysis, it was also possible to vary the number of elements with the reduced modulus in the longitudinal direction (parallel to the 0° fibers). The effect on the 0° fiber stress due to varying the number of elements in the longitudinal direction with reduced moduli was also examined. Varying the number of elements in this direction would be equivalent to modeling different debond lengths for the 0° fiber at the notch tip.

Macro-Micromechanical Analysis (MMA)

The second analytical technique, the macro-micromechanical analysis (MMA) developed by Bigelow and Naik [*8*], was used to analyze notch-tip stress states in both the DEN and CH specimens. The MMA combines the three-dimensional homogeneous, orthotropic finite-element analysis (PAFAC) of the notched specimen and a discrete fiber-matrix (DFM) micromechanics model of a single fiber. The MSC-NASTRAN finite-element code [*10*] was used to analyze the DFM model. An eight-noded, hexahedral element was also used in the MMA models. The MMA was used to calculate the stresses in the notch-tip element in the interior 0° ply of the $[0/90]_{2s}$ laminate assuming a perfectly bonded fiber-matrix interface. The interior 0° ply was the location of the highest axial fiber stress predicted by the PAFAC analyses of the specimens. As mentioned, in both specimen configurations, the finite-element mesh was designed so that the dimensions of the elements next to the notch corresponded to a single fiber spacing. A plan view of the finite-element mesh, and its dimensions, that was used to model the notch-tip element for both configurations is shown in Fig. 4. A convergence study of the MMA mesh refinement was done in Ref *8*. A schematic view of the macro-micro interface used in the MMA for the DEN specimen is shown in Fig. 5. Displacement boundary conditions from the macro-level analysis are applied to the micro-level DFM mesh to simulate the stress state next to the notch. A similar concept was used for the CH specimen, where the element next to the hole was defined to be identical to the element used next to the notch in the DEN specimen. The micro-level model shown in Fig. 4 was used for both the DEN and CH configurations. Thermal residual stresses were not included in this analysis.

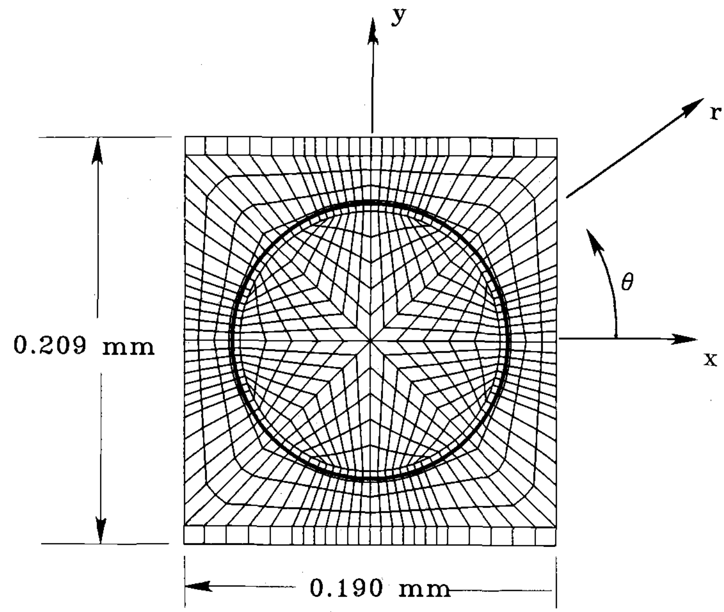

FIG. 4—*Plan view of DFM finite-element mesh used to model notch-tip element:* v_f = *39%.*

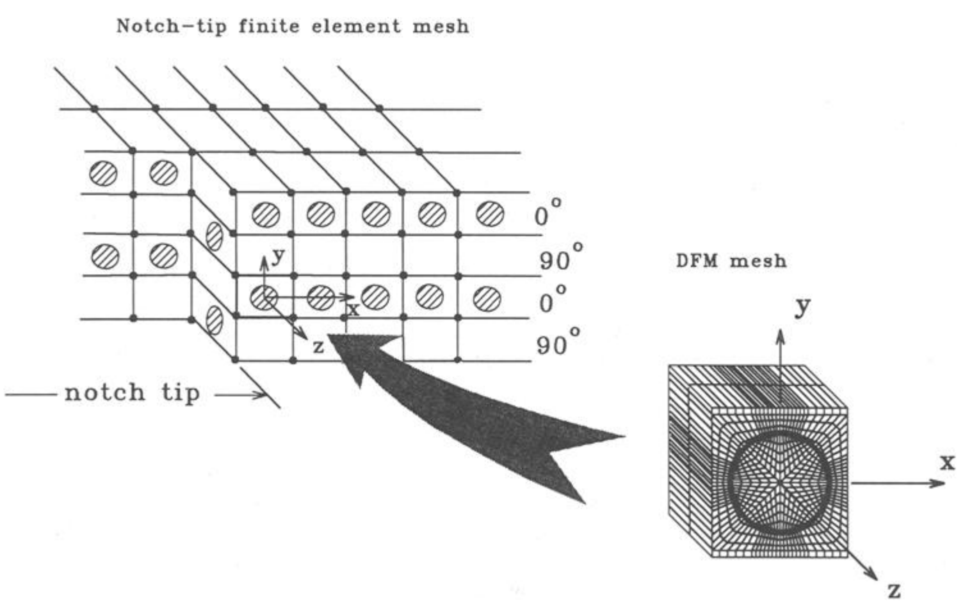

FIG. 5—*Schematic representation of the macro-micromechanical interface for the DEN specimen.*

Results and Discussion

Experimental Observations

The two specimen configurations failed at similar stress levels in spite of large differences in their stress concentration factors. The elastic stress concentrations, K_T, are 3.7 for the CH specimen and 5.7 for the DEN specimen. These values of K_T were calculated, assuming perfectly bonded fiber, at the element centroids using the PAFAC analysis and the meshes shown in Fig. 2. The K_T for the DEN is roughly one and one half times that of the K_T of the CH configuration. The static strength of the DEN specimen was 520 MPa, and was 501 MPa for the CH specimen. These strengths were unexpectedly close given the difference in the K_Ts.

The failure surfaces next to the notch were examined microscopically for both specimen configurations in order to identify the failure mechanisms. The surface of each specimen was polished to reveal the first layer of 0° fibers. Typical photographs for each configuration are shown in Fig. 6. In these photographs, the light-gray area is matrix and the darker-gray areas are fibers. In Fig. 6*a*, the carbon core in the SCS-6 fiber and the molybdenum wire are visible. Figure 6*a* shows the area just ahead of the notch for the DEN specimen. The first fiber ahead of the notch was damaged during the machining of the notch; thus, this fiber probably failed rather early in the loading history. The next fiber failed away from the plane of the notch, exhibiting fiber pullout; this type of behavior would be expected if fiber-matrix debonding had occurred over that length of the fiber. In this case, the fiber-matrix debond length is three to four fiber diameters in length. Figure 6*b* shows an area next to the hole for the CH specimen. Minimal fiber pullout is seen next to the hole, indicating that significant fiber-matrix debonding was not present prior to specimen failure.

Based on the experimental results, it was hypothesized that tensile radial stresses at the fiber-matrix interface ahead of the notch tip in the DEN specimen were large enough to cause extensive fiber-matrix debonding in the 0° plies, thus lowering the stress concentration in the DEN

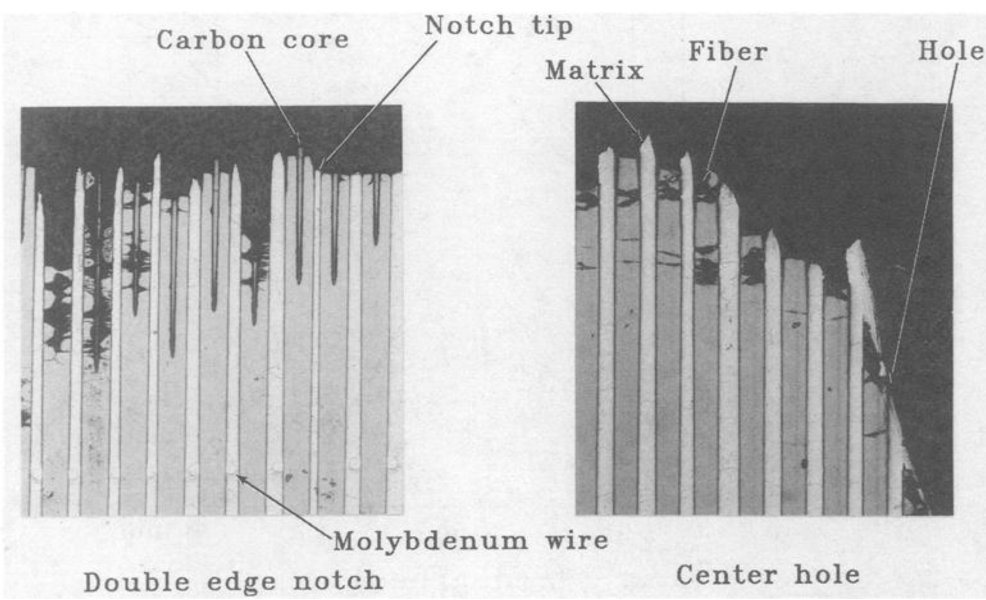

FIG. 6—*Photomicrographs of the failure surface for the DEN and CH* $[0/90]_{2s}$ *SCS-6/Ti-15-3 specimens:* v_f = *39%.*

specimen. Both analytical techniques, PAFAC and the MMA, were used to examine the hypothesis. The MMA was used to analyze the stresses in the notch-tip element in the interior 0° ply in both the DEN and CH specimens to determine the fiber-matrix interface stress state. PAFAC was used for two analyses. First, the global stress-deformation response was predicted including matrix yielding and interfacial debonding in the 90° plies. Second, the fiber axial stresses in the first 0° fiber next to the notch were predicted for the two configurations. The effects of modeling interfacial debonding in the 90° and 0° plies on the axial stress in the notch-tip 0° fiber were examined.

Interface Stresses

For a unit applied stress (S = 1 MPa), the MMA predicted the stresses shown in Figs. 7 and 8 for the DEN and CH specimens, respectively. The stresses shown do not include the thermal residual stresses that would be present due to the fabrication of the composite. The stresses presented are the stresses in the matrix at the fiber-matrix interface calculated at the finite-element nodal points. For comparison, the matrix stresses in the interior 0° ply in an unnotched $[0/90]_{2s}$ specimen due to a unit applied stress are shown in Fig. 9. The stresses are presented with respect to the cylindrical coordinate system shown. Stresses are shown for the plane of symmetry on the XZ plane, that is, through the center line of the notch or hole. Due to symmetry, the shear stresses are zero on this plane; thus, only the three normal stress components will be presented. For the two notched configurations, θ = 180° is the side of the fiber next to the notch.

In all three configurations, the peak values of the normal stresses occur at θ = 180°. In the

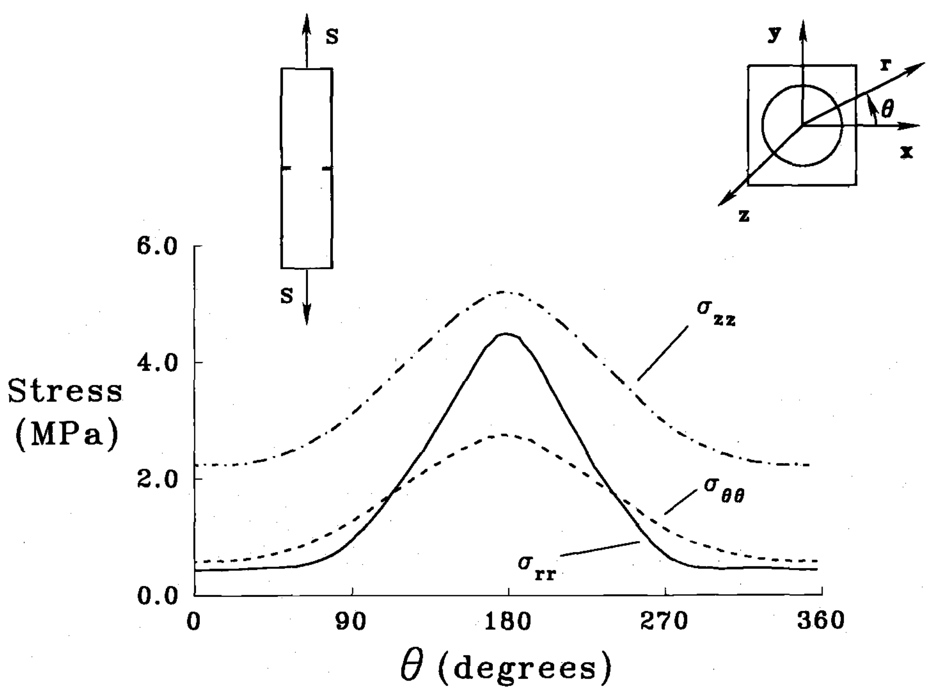

FIG. 7—*Matrix stresses at the fiber-matrix interface in 0° ply next to the notch for the* $[0/90]_{2s}$ *DEN specimen due to unit applied stress (S = 1 MPa): SCS-6/Ti-15-3,* v_f = *39%.*

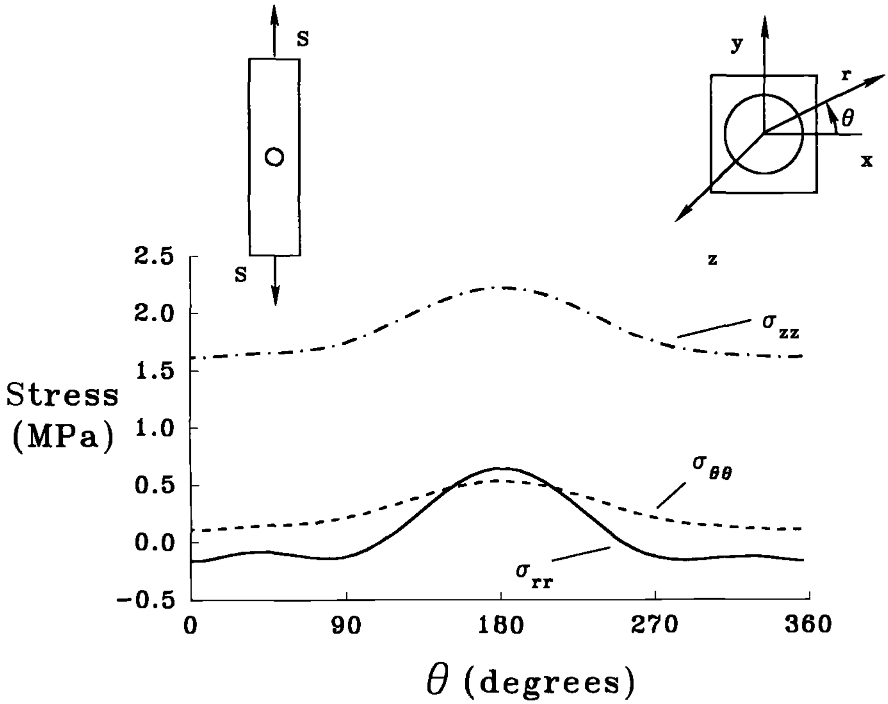

FIG. 8—*Matrix stresses at fiber-matrix interface in 0° ply next to notch for* $[0/90]_{2s}$ *CH specimen due to unit applied stress* (S = *1 MPa*)*: SCS-6/Ti-15-3,* v_f = *39%.*

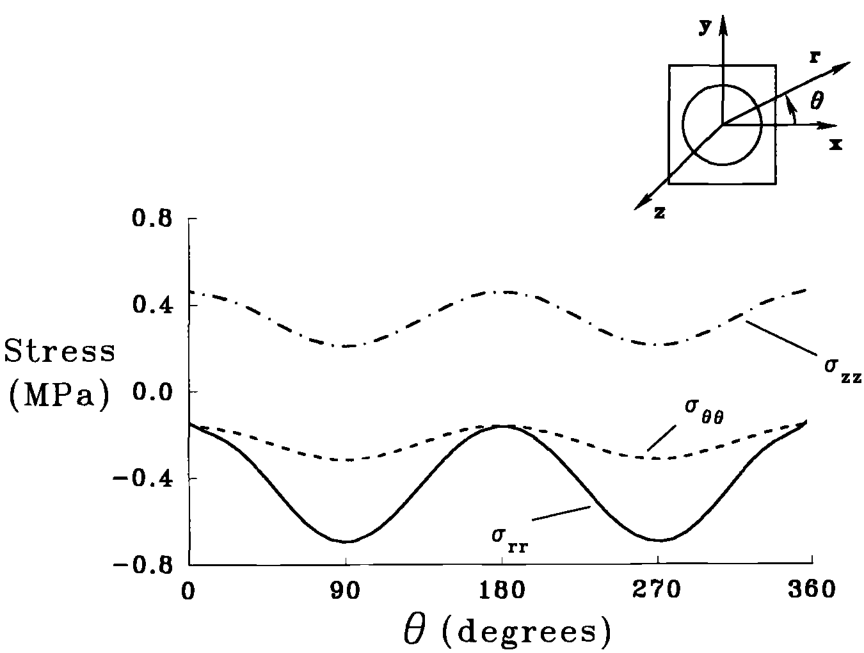

FIG. 9—*Matrix stresses at the fiber-matrix interface in the 0° ply of the unnotched* $[0/90]_{2s}$ *due to the unit applied stress* (S = *1 MPa*)*: SCS-6/Ti-15-3,* v_f = *39%.*

DEN and CH configurations, the stresses are nearly symmetric at about $\theta = 180°$. This is expected since the stresses were calculated for an interior ply. In the unnotched laminate (Fig. 9), the stresses are symmetric at about $\theta = 0°$ and $180°$. In fact, for the unnotched laminate, it was sufficient to model only a quarter of the fiber. However, results are presented for $0° \leq \theta \leq 360°$ for comparison with the notched laminate results in Figs. 7 and 8.

All three stress components shown are the largest for the DEN specimen and the smallest for the unnotched laminate. The gradient in the stress distribution is also much larger for the DEN specimen than the CH specimen. Consider, for example, the axial component. The axial stress in the DEN specimen ranges from a peak value of 5.2 MPa to a minimum of 2.2 MPa, whereas in the CH specimen, the axial stress only ranges from 2.2 to 1.6 MPa. This is due, of course, to the higher stress concentration of the DEN specimen. Likewise, the peak value of the radial stress component is much larger relative to the hoop and axial stress components in the DEN specimen compared to the CH specimen. In the DEN specimen, the maximum radial stress is 1.67 times the hoop stress and 0.87 times the axial stress. In the CH specimen, the maximum radial stress is 1.24 times the hoop stress and only 0.25 times the axial stress. It is also interesting to note that the radial stresses for the DEN configuration (Fig. 7) are tensile for all values of θ, whereas for the CH configurations, the radial stresses are tensile only from approximately 110° to 250° (Fig. 8), and for the unnotched laminate, the radial stresses are compressive for all values of θ (Fig. 9).

For interfacial failure, the stress component of primary concern is the radial stress. The peak values of the radial matrix stresses due to a remote stress of 1 MPa are 4.5 and 0.67 MPa for the DEN and CH specimens, respectively. The peak value of the radial stress for the unnotched laminate is -0.17 MPa. Thus, for a given interfacial strength, the interface in the DEN specimen will debond much earlier in the loading history than in the CH specimen. Conversely, for a given load, the 0° fibers next to the notch in the DEN specimen are more likely to have debonded than in the CH specimen. Since an interfacial strength is not available, it is not possible to predict when the interface will debond. Based on the stresses shown in Figs. 7 and 8 and the evidence of a weak interface in the SCS-6/Ti-15-3 material [*1*], it is likely that much more debonding of the 0° plies occurred in the DEN than in the CH specimen. In fact, based on the micrographics presented in Fig. 6, the 0° plies probably did not debond in the CH specimen.

Calculations with Interface Debonding

The predicted and experimental stress-deformation curves for both specimens are shown in Fig. 10. The PAFAC predictions were made including interfacial debonding in the 90° plies. From the DFM analysis described in the Appendix, the transverse modulus of a unidirectional laminate with a completely debonded interface was found to be 50.1 GPa. As described previously, a simplistic failure criterion was incorporated in the PAFAC analysis to simulate a debonded interface in the 90° plies. After the critical transverse stress (155 MPa) was reached in any finite element with an orientation of 90°, that element was then modeled as an isotropic material with an elastic modulus of 50.1 GPa. By modifying the material properties of the 90° plies to simulate the failed interfaces, the predicted stress-deformation behavior agreed quite well with the experimental results for the CH specimen and reasonably well for the DEN specimen.

The PAFAC analysis was then used to determine the effect of debonding in the 0° plies on the notch-tip fiber stress concentrations. The axial fiber stresses in the element next to the notch in the interior 0° ply were predicted for both the DEN and CH specimens using the modified material properties for the 90° plies (that is, debonded 90° fiber-matrix interfaces) as described earlier. Figure 11 shows the predictions of the 0° fiber stress in the first element next to the notch as a function of applied stress for the DEN and CH specimens assuming no

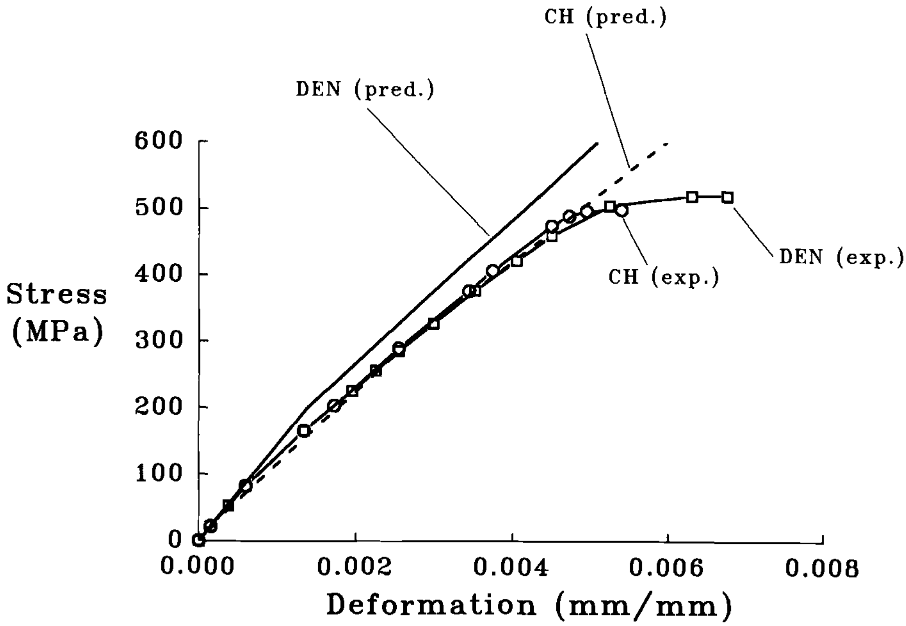

FIG. 10—*Predicted and experimental stress-deformation behavior of the DEN and CH specimens with interface debonding in 90° plies: SCS-6/Ti-15-3* $[0/90]_{2s}$, $v_f = 39\%$.

debonding of the 0° plies. The horizontal dashed line indicates an assumed fiber strength of 4200 MPa, and the two vertical dash-dotted lines show the experimental strengths of the two specimens. The fiber strength was calculated from the strain to failure of an unnotched $[0/90]_{2s}$ coupon ($\epsilon_{ult} = 0.0105$ mm/mm). The solid and dashed lines indicate the predicted 0° fiber stress with no debonding in the 0° plies for the DEN and CH specimens, respectively. If the

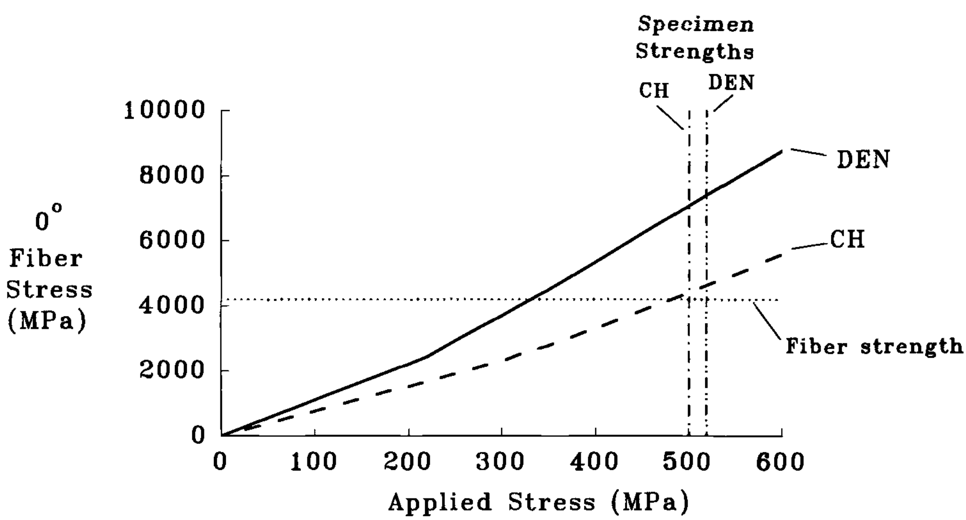

FIG. 11—*Notch-tip 0° axial fiber stress as a function of applied stress for the DEN and CH specimens with interface debonding in the 90° plies: SCS-6/Ti-15-3*$[0/90]_{2s}$, $v_f = 39\%$.

strength of the first 0° fiber is used as a failure criteria, the analysis predicts the strength of the CH specimen quite well. However, the strength of the DEN specimen is significantly underpredicted. Earlier work with boron/aluminum [*3*] indicated that a first 0° fiber failure criteria accurately predicted the static strengths of a variety of notched specimens.

Based on the earlier hypothesis of debonding at the notch tip in the DEN specimen, the approximation shown in Fig. 3 was used to model the effects of debonding in the 0° plies in the DEN configuration. As shown in Fig. 3*b*, the elastic modulus of the elements indicated by the shaded areas was reduced by a factor of 10, 100, and 1000 to approximate the interface debonding of the notch-tip 0° fiber in the DEN specimen. Little difference in the 0° axial fiber stress (less than 1%) was seen whether the modulus was reduced by 10, 100, or 1000, so results are shown for a reduction factor of 1000. The number of elements parallel to the 0° fiber direction with a reduced modulus was varied to represent different debond lengths. This is shown schematically in Fig. 12 for the various numbers of elements modified.

The axial notch-tip 0° fiber stress in the interior 0° ply for both configurations is shown in Fig. 13. The fiber stresses shown in Fig. 13 were calculated with interfacial debonding of the 90° plies. In addition, the calculations for the DEN specimen include the interfacial debonding of the notch-tip elements in the 0° plies. The two solid lines are the predictions made for no debonding of the 0° plies repeated from Fig. 11. Reducing the modulus of only one element (dashed line) reduced the fiber stress in the DEN specimen considerably, as shown in Fig. 13. Reducing the modulus of only two elements caused the 0° fiber stress to drop nearly to the level of the CH configuration. A two-element length is equivalent to a debond length of 3.5 fiber diameters. This debond length is in good agreement with the micrographs showing a

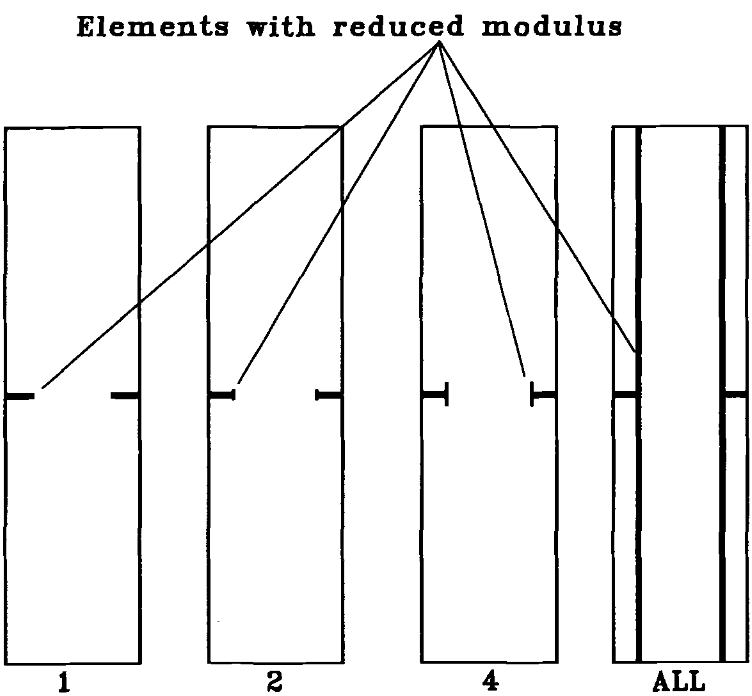

FIG. 12—*Various notch-tip debond lengths simulated with reduced modulus elements in the 0° plies in the DEN predictions:* $[0/90]_{2s}$ *SCS-6/Ti-15-3,* v_f = *39%.*

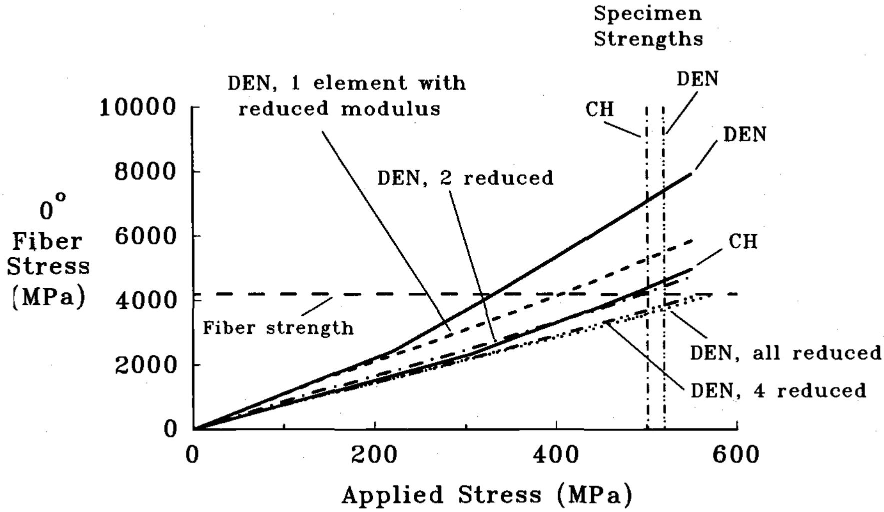

FIG. 13—*Notch-tip 0° fiber stress as a function of applied stress for the CH and DEN specimens with interface debonding in the 90° plies and in the 0° plies at the notch tip of the DEN specimen:* $[0/90]_{2s}$ *SCS-6/Ti-15-3,* $v_f = 39\%$.

debond length of three to four fiber diameters (Fig. 6*a*). By reducing the modulus of four or more elements, the 0° fiber stress in the notch-tip element in DEN specimen was reduced to a level below that of the CH configuration. The results shown in Fig. 13 agree with predictions made using a two-dimensional shear lag model of a unidirectional composite [*11*] showing that any damage will bring the solutions for a notch and a hole closer together. From Fig. 13, a first fiber failure criteria based on the axial stress of the notch tip 0° fiber would predict the strength of the CH specimen to be 490 MPa and the strength of the DEN specimen to be from 320 to 560 MPa, depending on the debond length modeled in the 0° plies of the DEN specimen. For a debond length of 3.5 fibers (two elements) in the 0° plies next to the notch, the PAFAC analysis predicts a strength of 500 MPa for the DEN configuration. The strength prediction correlates reasonably well with the experimental strengths of 520 MPa observed for the DEN specimen. As mentioned earlier, the thermal residual stresses that are present in this material due to the fabrication process were not accounted for in the analyses. A compressive axial stress would be present in the 0° fibers due to the temperature change during the fabrication process. However, the same thermal residual stress state would be present in both the CH and DEN specimens, and in the unnotched specimen used to determine the fiber strength. The results shown indicate that the axial stress in the first intact 0° fiber may dictate the static strength of the specimen, and a first fiber failure criteria would predict specimen strengths when interfacial debonding is modeled.

Concluding Remarks

The static notched strengths of $[0/90]_{2s}$ SCS-6/Ti-15-3 laminates were predicted based on the stress in the notch-tip 0° fiber. Two specimen configurations of a $[0/90]_{2s}$ SCS-6/Ti-15-3 laminate were tested and analyzed: a center-hole (CH) specimen and a double-edge-notch (DEN) specimen. The two specimen configurations failed at similar stress levels in spite of the large difference in the stress concentration factors for the two geometries. Microscopic examinations of the failure surfaces for both configurations showed fiber pullout for the DEN specimen, indicating fiber-matrix debonding had occurred. Minimal fiber pullout was seen in the CH specimen. Based on the experimental results, it was hypothesized that the radial stresses that developed at the fiber-matrix interface ahead of the slit tip in the DEN specimen were large enough to cause fiber-matrix debonding in the 0° plies, thus lowering the stress concentration in the DEN specimen to a level comparable to that of the CH specimen.

Two analytical techniques, a three-dimensional finite-element analysis (PAFAC) and a macro-micromechanical analysis (MMA), were used to predict the overall stress-deformation behavior and the notch-tip fiber-matrix interface stresses in both configurations. The MMA predicted radial stresses next to the notch in the DEN configuration that were nearly seven times as large as those predicted for the CH configuration. Thus, fiber-matrix debonding in the 0° plies will occur much earlier in the loading history for the DEN specimen, and, for a given stress level, more fiber-matrix debonding will occur in the DEN specimen than in the CH specimen. The overall stress-deformation response of both specimens was predicted accurately when interfacial failure of the 90° plies was included in the analysis. The modulus of the 90° ply with failed interfaces was determined using a discrete fiber-matrix (DFM) model containing gap elements. By reducing the modulus of elements at the notch tip to simulate debonding next to the notch in the 0° plies, predictions of notch-tip 0° fiber stress for the DEN configuration were reduced to a level comparable to that of the fiber stress in the CH configuration, indicating that fiber-matrix debonding in the DEN specimen could reduce the notch-tip stress sufficiently so that both configurations would have similar strengths. When the interfacial debonding of the 90° plies and the notch-tip 0° plies (in the DEN specimen) was modeled, the axial stress in the first intact 0° fiber correlated well with the specimen static strength for both specimen configurations. The analyses assumed no significant debonding in the 0° plies in the CH specimen. The analyses also did not account for thermal residual stresses in the material. However, the same thermal residual stress state would be present in both the CH and DEN specimens, and in the unnotched specimen used to determine the fiber strength. The results shown indicate that a first fiber failure criteria based on the axial stress in the first intact 0° fiber can predict the static strength of notched specimens when interfacial damage is modeled.

APPENDIX

Interfacial Debonding of a Unidirectional Laminate

In tests of unnotched laminates of the SCS-6/Ti-15-3 material, a knee was seen in the stress-deformation response. This knee occurred well below the yield strength of the matrix material and was found to be due to debonding of the fiber-matrix interface in the 90° plies [*1*]. A DFM model assuming an infinitely repeating rectangular array of fibers was used to analyze debonding of a unidirectional laminate. MSC/NASTRAN [*10*] was used for the finite-element analysis. The ply thickness (0.194 mm), the fiber volume fraction (32.5%), and the fiber diameter (0.14 mm) were used to calculate the dimensions of the model. The ply thickness, the fiber volume fraction, and the fiber diameter are typical for the SCS-6/Ti-15-3 material tested in Ref *1*. A plan view of the DFM model, composed of eight-noded, hexahedral elements, is shown in Fig. 14. The same mesh refinement was used here as in the MMA shown in Fig. 4. In the DFM model, the debonded interface was modeled using the gap elements available in MSC-NASTRAN. Gap elements are nonlinear elements that may have significant compression and shear forces only if the gap is closed. The gap elements were placed between the fiber and matrix and given a zero length. Upon loading, the gap elements have zero stiffness when the gap opens and the same stiffness as the fibers if the gap remains closed, thus modeling a failed interface. With the completely debonded interface, the modulus of the unidirectional laminate was calculated by loading the DFM model with the gap elements with a uniform stress applied in the transverse direction, as shown in Fig. 14. The modulus was calculated

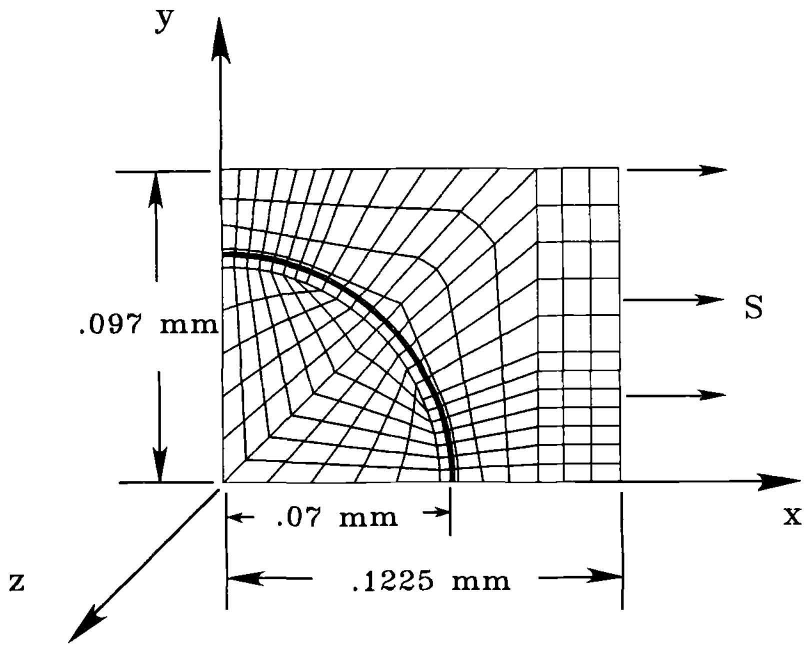

FIG. 14—*Discrete fiber-matrix model used to model the debonded interface in unidirectional laminate,* V_f = *32.5%.*

from the slope of the stress-deformation curve. The stress-deformation curve was nearly linear for the loading range analyzed. The transverse modulus of a unidirectional laminate with a debonded interface was calculated to be 50.1 GPa. This value of the transverse modulus is lower than the experimental value (66 GPa) given in Ref *1*. The discrepancy may have been caused by the effects of the friction between the fiber and matrix when the interface is debonded. The model used assumed a perfectly smooth, frictionless interface between the fiber and matrix, which may not be realistic. Additionally, the analysis assumes that all the fiber-matrix interfaces are completely debonded, whereas, in actuality all the fibers may not be debonded throughout the specimen.

When the transverse stress in the elements in the 90° plies reached a specified critical value, the material properties of the 90° plies were modified to represent an isotropic material with an elastic modulus equal to the transverse modulus of the unidirectional laminate with a completely debonded interface. This, in effect, models the 90° plies with a bilinear stress-strain curve. The critical transverse stress was chosen to be 155 MPa based on experimental observations of unnotched $[90]_8$ laminates [*1*]. Thermal residual stresses, which were present in the experimental observations, were not included in the analyses.

The material model used in PAFAC is based on constituent properties; thus the material properties required are the elastic modulus and Poisson's ratio for the fiber and matrix, and a stress-strain curve for the matrix. It is not possible, for example, to reduce the transverse modulus of one constituent to model interfacial failure. Nor is it possible to reduce the transverse modulus (E_{22}) of an orthotropic material to model interfacial debonding of a 90° ply. Thus, in order to simulate interfacial debonding with the PAFAC analysis, the 90° plies with a debonded interface were modeled as isotropic plies with an elastic modulus equal to the transverse modulus of a unidirectional laminate with a completely debonded interface. This gave the debonded 90° plies in the $[0/90]_{2s}$ laminate an unrealistically low modulus in the axial fiber direction. The effect of this low modulus was found to be negligible (less than 2.5%) on the stress-deformation response of the laminate.

The unnotched laminate data presented in Ref *1* and used in this appendix are for a fiber volume fraction of 32.5%. The notched laminate data presented in the body of the paper are for a fiber volume fraction of 39%. The transverse modulus predicted for the debonded fiber-matrix interface in the v_f = 32.5% laminate is higher than would be predicted for a v_f = 39% laminate. However, it was felt that this discrepancy would not have a significant effect on the predictions.

References

[*1*] Johnson, W. S., Lubowinski, S. J., and Highsmith, A. L., "Mechanical Characterization of Unnotched SCS_6/Ti-15-3 Metal Matrix Composites at Room Temperature," *Thermal and Mechanical Behavior of Metal Matrix and Ceramic Matrix Composites, ASTM STP 1080,* J. M. Kennedy, H. M. Moeller, and W. S. Johnson, Eds., American Society for Testing and Materials, Philadelphia, 1990, pp. 193–218.

[*2*] Naik, R. A., Pollock, W. D., and Johnson, W. S., "Effect of a High Temperature Cycle on the Mechanical Properties of Silicon Carbide/Titanium Metal Matrix Composites," *Journal of Materials Science,* Vol. 26, 1991, pp. 2913–2920.

[*3*] Johnson, W. S., Bigelow, C. A., and Bahei-El-Din, Y. A., "Experimental and Analytical Investigation of the Fracture Processes of Boron/Aluminum Laminates Containing Notches," NASA TP-2187, National Aeronautics and Space Administration, Washington, DC, 1983.

[*4*] Daniel, I. M., "Failure Mechanisms and Fracture of Composite Laminates with Stress Concentrations," *Proceedings,* Seventh International Conference on Experimental Stress Analysis, Haifa, Israel, 23–27 Aug. 1982, pp. 1–20.

[*5*] Harris, C. E. and Morris, D. H., "A Fractographic Investigation of the Influence of Stacking Sequence on the Strength of Notched Laminated Composites," *Fractography of Modern Engineering Materials: Composites and Metals, ASTM STP 948,* J. E. Masters and J. J. Au, Eds., American Society for Testing and Materials, Philadelphia, 1987, pp. 131–153.

[*6*] Rosenberg, H. W., "Ti-15-3: A New Cold-Formable Sheet Titanium Alloy," *Journal of Metals,* Vol. 35, No. 11, Nov. 1986, pp. 30–34.

[*7*] Bigelow, C. A. and Bahei-El-Din, Y. A., "Plastic and Failure Analysis of Composites (PAFAC)," LAR-13183, *COSMIC,* University of Georgia, Athens, GA, 1983.

[*8*] Bigelow, C. A. and Naik, R. A., "A Macro-Micromechanics Analysis of a Notched Metal Matrix Composite," NASA TM-102728, National Aeronautics and Space Administration, Washington, DC, Sept. 1990.

[*9*] Bahei-El-Din, Y. A. and Dvorak, G. J., "Plasticity Analysis of Laminated Composite Plates," *Journal of Applied Mechanics,* American Society of Mechanical Engineers, Vol. 49, 1982, pp. 740–746.

[*10*] MCS/NASTRAN, Version 6.6, MacNeal-Schwendler Corporation, 1991.

[*11*] Goree, J. G., Dharani, L. R., and Jones W. F., "Mathematical Modeling of Damage in Unidirectional Composites," NASA Contractor Report 3453, National Aeronautics and Space Administration, Washington, DC, Aug. 1981.

John G. Bakuckas, Jr.,[1] *Jonathan Awerbuch,*[2] *Tein-Min Tan,*[2] *and Alan C. W. Lau*[2]

Evolution of Notch-Tip Damage in Metal-Matrix Composites During Static Loading

REFERENCE: Bakuckas, J. G., Jr., Awerbuch, J., Tan, T.-M., and Lau, A. C. W., **"Evolution of Notch-Tip Damage in Metal-Matrix Composites During Static Loading,"** *Fracture Mechanics: Twenty-Third Symposium, ASTM STP 1189*, Ravinder Chona, Ed., American Society for Testing and Materials, Philadelphia, 1993, pp. 713–737.

ABSTRACT: The evolution of notch-tip damage during static loading in center-notched unidirectional boron/aluminum and silicon carbide/titanium composites was characterized through a two-prong investigation involving experiments and analysis. The effects of heat treatment on the failure process in boron/aluminum were addressed. In the experimental phase, the notch-tip damage initiation and progression was monitored and recorded in real time through a high-magnification (×150) closed-circuit television system, acoustic emission, and load-deformation responses. Fracture surface morphologies were examined via a scanning electron microscope in order to identify the microfailure mechanisms.

In the analytical phase, a numerical technique was employed to predict the failure process in the materials studied without specifying the crack path a priori. The predictions elucidated the failure mechanisms and their interaction in the evolution of damage ahead of an existing crack. Correlations were made with experimental results in terms of the observed failure process and load-deformation responses. Good agreement was obtained between the observed failure process and predictions. The computational predictions captured the salient features in the observed failure processes.

Notch-tip damage progression was quite different in the various materials studied. A complex state of damage developed in the vicinity of the notch-tip consisting of several dominant failure mechanisms. The various failure mechanisms were identified, and the development of the notch-tip damage zones was determined.

KEY WORDS: damage initiation, damage progression, failure mechanisms, failure process, fracture surface examinations, deformation characteristics, acoustic emission, damage predictions, fracture mechanics, fatigue (materials), metal-matrix composites

Metal-matrix composites (MMCs) reinforced with continuous fibers have excellent potential for use in aerospace and aircraft primary structures [*1–4*]. Metal-matrix composites exhibit superior performance compared with other engineering materials. When compared with resin-matrix composites, MMCs have higher shear modulus and shear strength, larger ranges of operating temperatures, and better resistance to moisture absorption and delamination. In addition, MMCs have higher stiffness-to-weight and strength-to-weight ratios and better fatigue and fracture tolerances compared with conventional metals.

In spite of these advantages, the failure process is of major concern in MMCs. The failure

[1] Graduate research assistant, Department of Mechanical Engineering and Mechanics, Drexel University, Philadelphia, PA 19104; presently, research associate, National Research Council, NASA Langley Research Center, Hampton, VA 23681.

[2] Professor and associate professors, respectively, Department of Mechanical Engineering and Mechanics, Drexel University, Philadelphia, PA 19104.

process is a complicated evolution involving the combination and interaction of several modes of damage. The primary mechanisms of damage in MMCs are fiber breakage, matrix plastic deformation, matrix cracking, and fiber-matrix interface debonding. A thorough understanding of the failure process is warranted before MMCs can be considered for advanced aerospace applications.

Results of a comprehensive experimental and analytical investigation on the failure process in several MMC systems have been reported in Ref *5*. The major objective of that research was to gain a rational understanding of damage initiation and progression in MMCs during quasi-static loading. In this paper, highlights of the results from Ref *5* obtained for two material systems, namely, as-received boron/aluminum (B/Al-AR) $[0]_8$ and silicon carbide/titanium (SCS-6/Ti-6Al-4V) $[0]_4$ are presented. In order to determine the effect of matrix properties on the failure process, solution-treated and aged boron/aluminum (B/Al-T6) $[0]_8$ was studied as well. Experimentally, several techniques have been used to study notch-tip damage growth, including optical observations, laser interferometric displacement gage, acoustic emission, and scanning electron microscopy.

In the analytical phase, detailed numerical predictions were performed to gain a better understanding of the failure process in the materials studied. The procedure formulated in Refs *5* and *6* was employed to numerically predict damage initiation and progression in three representative center-cracked monolayer MMCs. Highlights of these predictions are given here; additional details are reported in Refs *5* and *7*. The numerical predictions were compared with experimental results in terms of the observed failure process, load-deformation characteristics, and notched strength. An excellent qualitative agreement between the optically observed damage and the numerical prediction was established. The salient features observed in the sequential failure process in these composites were captured and reflected in the predictions.

Materials and Test Procedure

Two unidirectional MMC systems have been investigated in this research: (*1*) B/Al-5.6/6061 $[0]_8$ fabricated by D.W.A. Composite Specialties and (*2*) SCS-6/Ti-6Al-4V $[0]_4$ fabricated by AVCO Corp. using hot isostatic pressing (HIPing). The range of fiber volume fractions of the B/Al-5.6/6061 and SCS-6/Ti-6Al-4V were 0.48 to 0.53 and 0.33 to 0.37, respectively. The B/Al-5.6/6061 laminates were studied under two conditions, namely, as-received (B/Al-AR), and solution-treated and aged (B/Al-T6) conditions. All plates were machined using electro-discharge machining (EDM) into parallel-sided coupons having a width of 25.4 mm. Center notches 1.27, 2.54, 5.08, 10.16, and 12.70 mm long by 0.25 mm wide were produced by EDM. All notches were perpendicular to the loading direction. Aluminum end tabs were installed on all specimens following a procedure similar to that used in strain gage bonding so that slippage, tab failure, and unwanted acoustic emission from the tab ends were minimized.

All tests were performed on a closed-loop servohydraulic Instron testing machine (Model 1331). Damage progression was monitored continuously during quasi-static loading conditions under stroke control mode at a rate of 0.05 mm/min. The fixtures used were standard 25.4 mm-wide wedge-action friction grips. The development of notch-tip damage at various stages of static tensile loading were studied and recorded on a high magnification ($\times 150$) closed circuit television system (CCTV). This provided a clear view of the macrofailure modes and processes in the notch-tip region. In addition, notch-tip damage progression was monitored through acoustic emission and load-deformation responses. A laser interferometric displacement gage was used to measure accurately the crack opening displacement (COD) [*8*]. This method is highly sensitive to notch-tip damage, evident from the nonlinearities in the load-COD curves, sudden jumps in COD, and permanent COD upon unloading. In addition, global displacements were measured using an extensometer having a gage length of 25.4 mm. Finally, fracture surface examinations via a scanning electron microscope (SEM) were conducted in order to identify the microfailure mechanisms.

Notch-Tip Damage Progression in Unidirectional MMCs

It was demonstrated [*5,9–11*] that heat treatment and constituent properties significantly affect the failure process, mechanical performance, and the fracture behavior of MMCs. In this study, notch-tip damage in three material systems was investigated in terms of optical observations, fracture surface examinations, acoustic emission signatures, and load-deformation responses as discussed in the following sections.

Optical Observations

Notch-tip damage extension was optically monitored in real time via a CCTV system that allows magnification up to ×150. Primary emphasis was placed on determining the extent of matrix plastic deformation, matrix splitting, fiber-matrix interfacial debonding, and the number of fiber breaks ahead of the notch-tip, all as a function of applied load. The observed notch-tip failure process at various loading stages is shown in the photographs of Figs. 1, 2, and 3 for B/Al-AR, B/Al-T6, and SCS-6/Ti-6Al-4V, respectively. Damage from only one notch tip is shown. The effects of heat treatment and constituents on the observed failure process can be seen clearly in these photographs.

In the B/Al-AR specimens, matrix plastic deformation initiated at the notch tips at a relatively low load level (23% of notched strength) and grew towards the first intact fiber, Fig. 1*a*. Matrix plastic deformation is seen as the white zones emanating from the notch tips. These white zones are the reflection of light from the specimen's surface due to the out-of-plane displacements caused by matrix plastic deformation. As the load level increased, the plastic zones progressed along the fiber direction, Fig. 1*b*. Eventually, the load level became high enough (79% of notched strength) to fracture the first intact fiber as seen from the lateral extension of notch-tip damage, Fig. 1*c*. This lateral damage extension was abruptly arrested in the next matrix bay due to the rapid formation and progression of plastic deformation in the second matrix bay, Fig. 1*d*. At 89% of the static notched strength, the second intact fiber fractured, and the formation and progression of a third matrix plastic zone developed along the next (third) intact fiber, Fig. 1*e*. An additional increment in load was required to fracture the third intact fiber, Fig. 1*f*. As fibers break, the bridging matrix bays fail in a ductile manner transverse to the fibers. In summarizing, a sequential failure process was evident involving matrix plastic deformation, matrix cracking, and fiber breakage. These major modes of damage occurred progressively in that sequence until a state of damage prior to catastrophic fracture was reached as shown in Fig. 1*g*. Here, four matrix bays were plastically deformed and three fibers were broken. In addition, some of the matrix bays fractured in a ductile manner. This is evident from the fractographs of the fracture surface of the aluminum matrix as discussed later.

The characteristics of the notch-tip damage progression in the solution-treated and aged specimens (B/Al-T6) were considerably different than those in the as-received specimens, Fig. 2. In the B/Al-T6, matrix plastic deformation did not initiate until approximately 69% of notched strength (compared with 23% in the B/Al-AR), Fig. 2*a*. As the applied load increased, the plastic zone remained confined to the notch-tip region ahead of the first intact fiber. Matrix cracking occurred at approximately 86% of the notched strength, Fig. 2*b*. At 99% of the static notched strength, the first intact fiber fractured. The damage propagated through the first intact fiber and into the next matrix bay where it became momentarily blunted, Fig. 2*c*. Lateral damage extension then occurred very rapidly leading to catastrophic fracture, where the

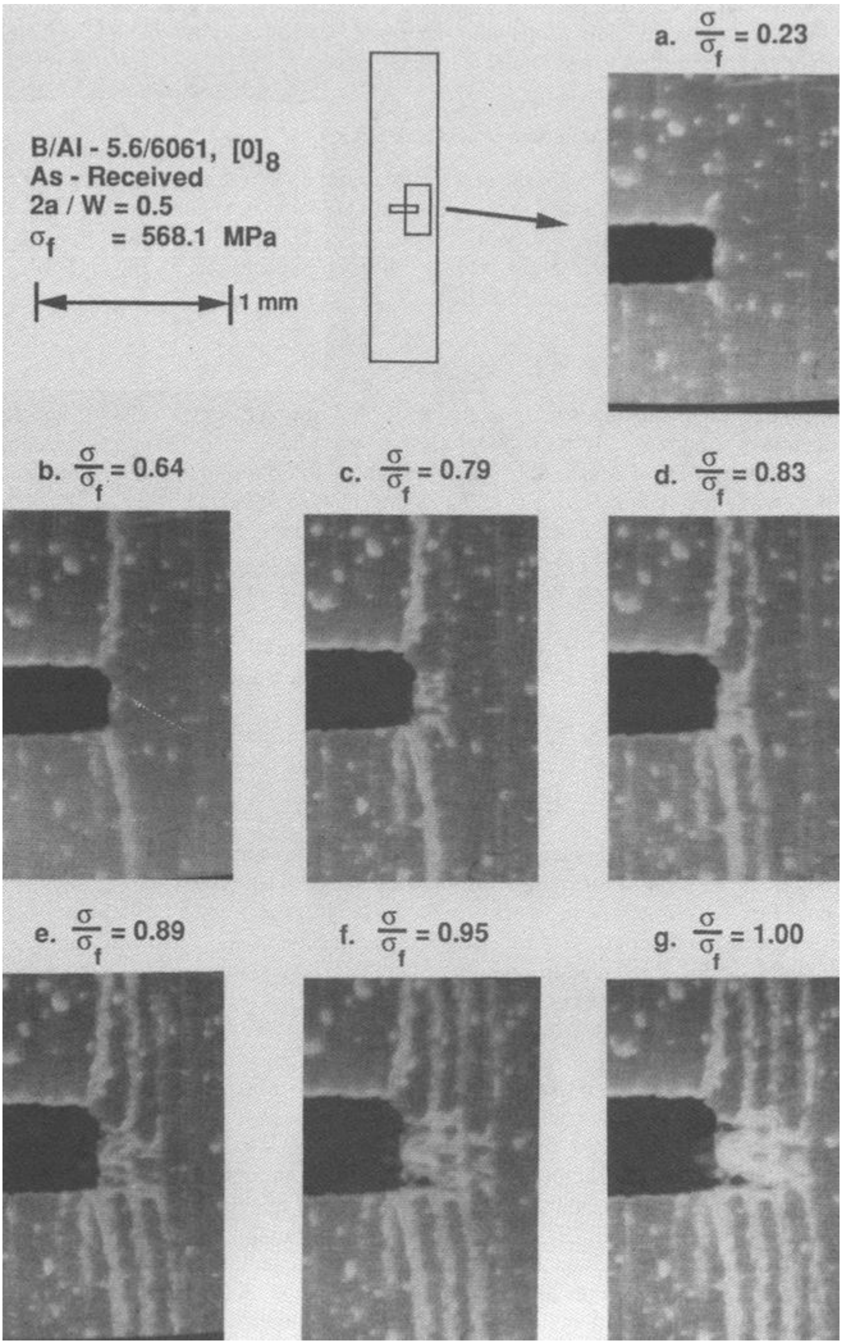

FIG. 1—*Development of notch-tip damage in as-received B/Al-5.6/6061* $[0]_8$ *consisting primarily of longitudinal matrix plastic deformation and fiber breakage. Following each fiber break, a matrix plastic zone is formed along the next intact fiber.*

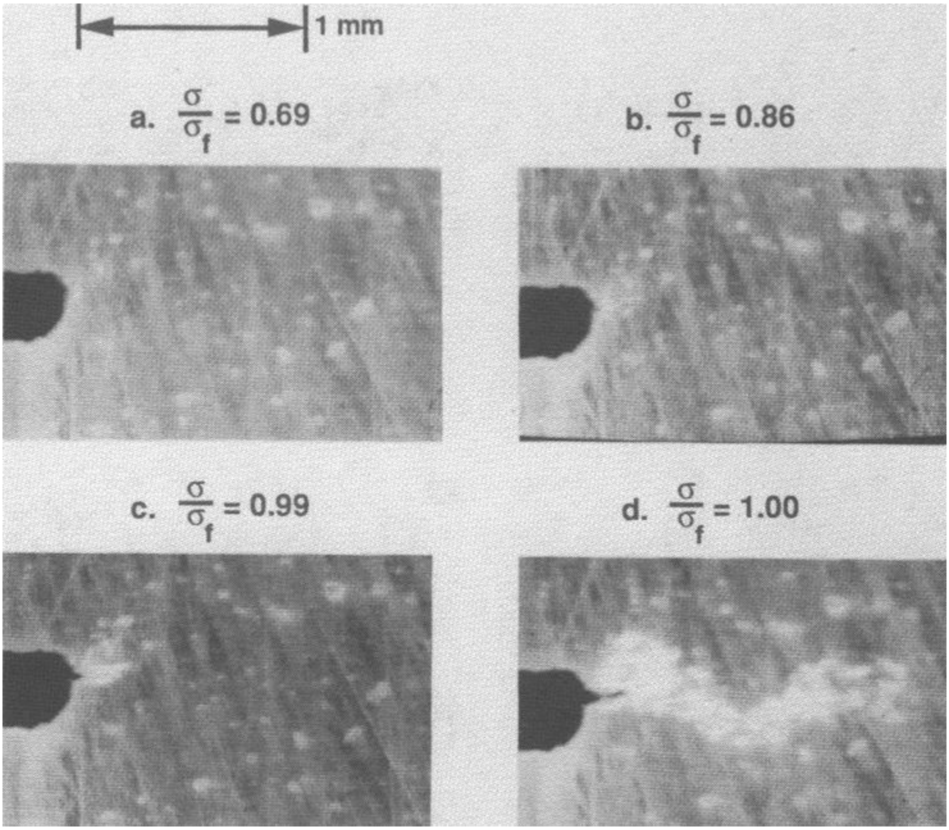

FIG. 2—*Development of notch-tip damage in solution-treated and aged B/Al-5.6/6061* $[0]_8$. *Matrix plastic deformation is confined to the notch centerline resulting in rapid, self-similar damage progression* (2a/W = *0.5*, σ_f = *394.0 MPa).*

notch-tip damage zone remained within a narrow-banded region flanking the plane of the artificial notch, Fig. 2*d*.

The ductile matrix in the B/Al-AR specimens permitted substantial matrix plastic deformation that alleviated the local stress concentrations [*9,10*]. The plastic zones diffused the concentrated stresses requiring an additional increment in load to recommence crack growth. Such cracks may progress in different directions depending upon the local material properties and the existing state of damage. Hence, the lower yield strength and more ductile matrix in the as-received specimens created an effective crack arrest mechanism permitting a slow failure process and a meandering macroscopic crack.

In the higher yield strength matrix specimens (B/Al-T6), damage initiation occurred at a significantly higher load. Following damage initiation, a rapid failure process took place. The higher yield strength 6061-T6 matrix permitted little matrix plastic deformation to relieve the crack-tip stress concentrations [*9,10*]. The concentrated stress field therefore remained within a narrow-banded region about the notch centerline. Eventually, this buildup of energy in the vicinity of the notch tip produced stresses sufficient to fracture fibers along the notch centerline resulting in a self-similar crack extension. The absence of an effective crack arrest mechanism

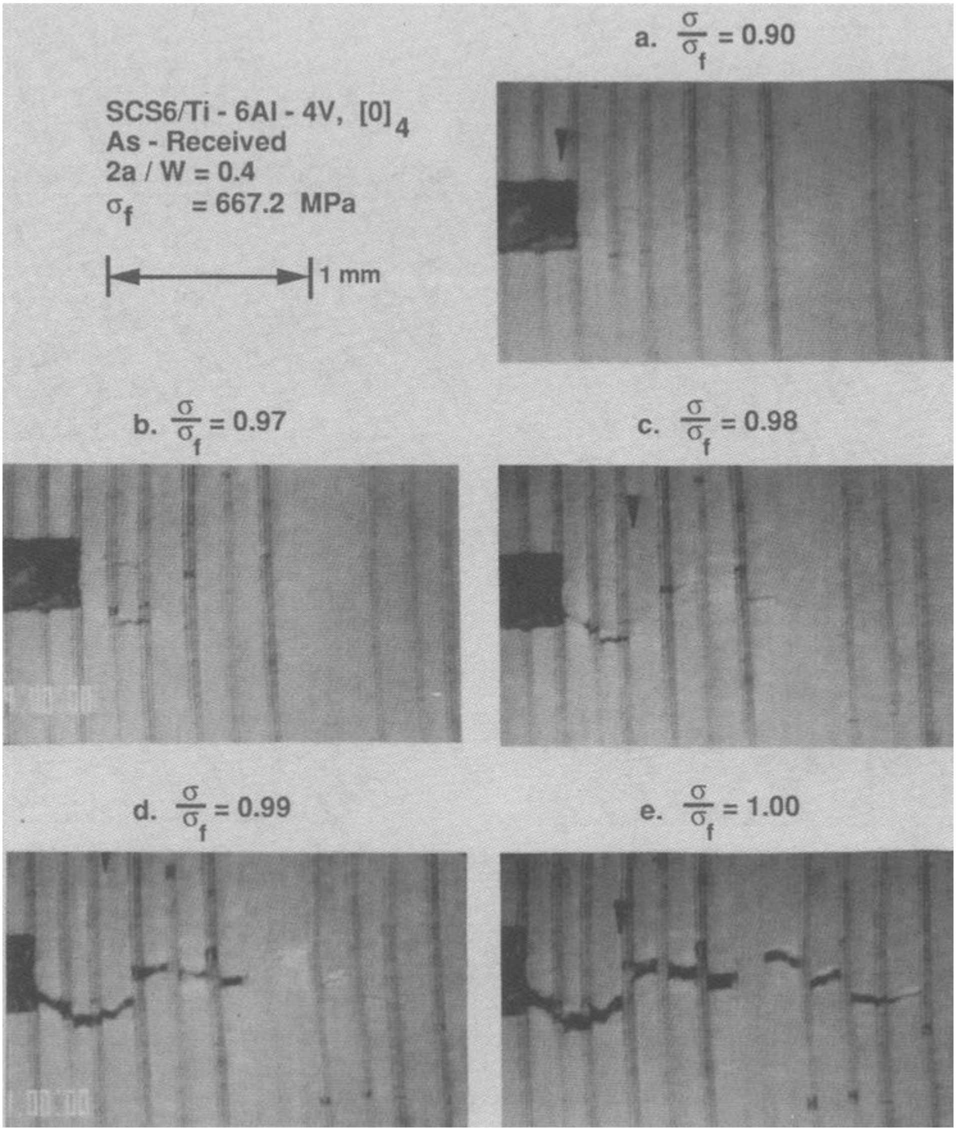

FIG. 3—*Development of notch-tip damage in as-received SCS-6/Ti-6Al-4V* $[0]_4$ *consisting primarily of matrix cracking, fiber breakage, and interfacial debonding. Matrix cracking remains within the notch width.*

(that is, matrix plastic deformation) resulted in a strength reduction when compared with the as-received specimens.

The development of the notch-tip damage progression in the SCS-6/Ti-6Al-4V specimens was completely different than that in the B/Al-5.6/6061 specimens, Fig. 3. The vertical lines in the figure are the fibers that were exposed by partially removing the outer layer of matrix material. Damage initiated at extremely high load levels in the SCS-6/Ti-6Al-4V specimens. At approximately 90% of the static notched strength, fiber breakage occurred, Fig. 3*a*. The subsequent damage progression revealed that as many as 16 fibers ahead of the notch-tip fractured, while the matrix bays remained intact, Fig. 3*b*. Here, five fibers fractured ahead of the notch tip while matrix cracking was observed in the first two matrix bays. In addition, the fibers appeared to fracture at locations above and below the plane of the artificial notch, within a span of 0.5 mm, while the matrix plastic deformation and matrix cracking occurred along the notch centerline, Fig. 3*c*. With increasing applied load, fibers fractured ahead of the matrix cracks. In addition, interfacial debonding was observed to initiate at the ends of the broken fibers, resulting in fiber pullout, Fig. 3*d*. Generally, an intermittent failure sequence was observed. The damaged zone was confined to the plane of the original notch, and thus crack extension could be considered, macroscopically, as self-similar, Fig. 3*e*.

Fracture Surface Morphology

Scanning electron micrographs of the fracture surface in the vicinity of the notch tip where slow damage development transpired are shown in Fig. 4 for the three materials tested. The fracture surface examinations reveal fiber shattering that is indicated by the fragmented wedge-shaped pieces at the fractured fiber ends in the B/Al-AR and B/Al-T6, shown in Figs. 4*a* and *b*, respectively. The appearance of these fragments indicates a good fiber-matrix bonding.

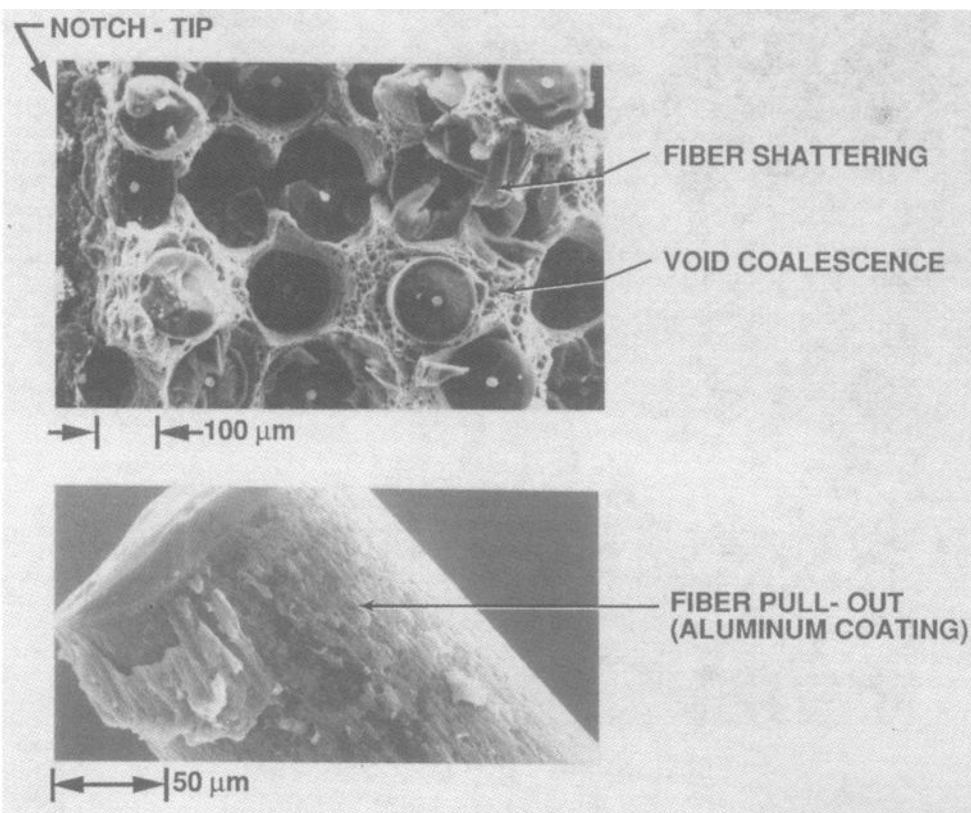

FIG. 4—*Scanning electron micrographs of the fracture surface near the notch tip where stable damage progression took place in the three materials studied.* (a) *B/Al-5.6/6061* $[0]_8$ *as-received.*

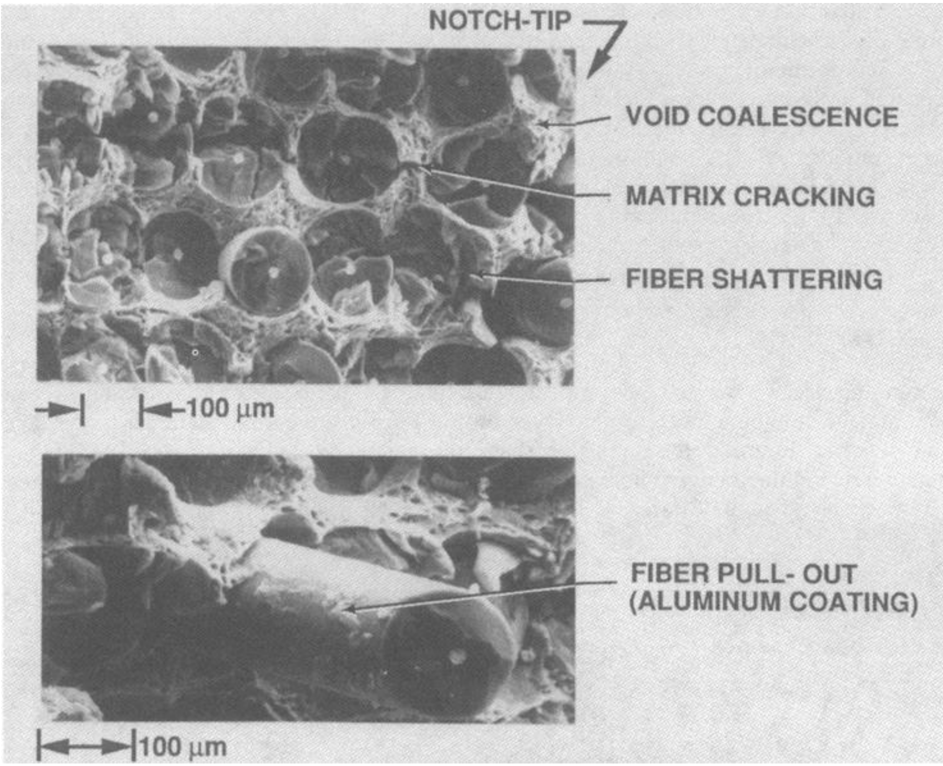

FIG. 4 *(continued)*—(b) *B/Al-5.6/6061,* $[0]_8$ *solution-treated and aged.*

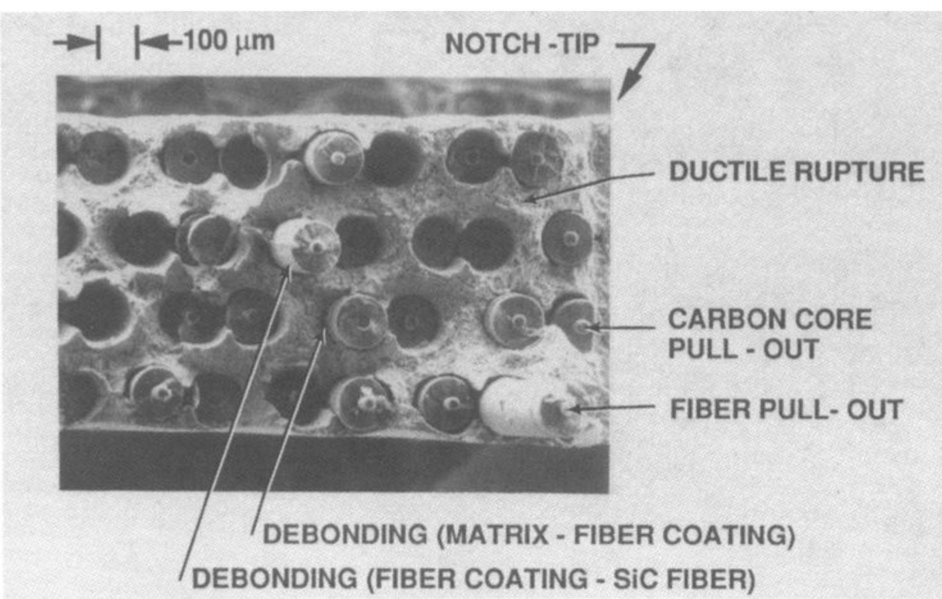

FIG. 4 *(continued)*—(c) *SCS-6/Ti-6Al-4V,* $[0]_4$ *as-received.*

Fiber shattering was less prevalent in the SCS-6/Ti-6Al-4V specimen, in which a significant amount of interfacial debonding occurred, Fig. 4*c*.

Fiber breakage did not necessarily occur on the plane of the fracture surface. As a result, fibers were pulled out of the matrix, evidenced by the cylindrical cavities that previously housed the fibers. Fiber pullout was observed in varying degrees in the three material systems and was more pronounced in the notch-tip vicinity where slow damage progression took place. Only a few fibers were pulled out in the B/Al-5.6/6061 specimens. All pullout fibers in these specimens were coated with a thin layer of aluminum, indicating that the fiber-matrix bond strength was higher than the shear strength of the matrix, Figs. 4*a* and *b*. This aluminum coating exhibited a shear-like dimpled texture resulting from voids coalescing in an elongated manner (due to the shear stresses along the interface). The pullout fibers in the SCS-6/Ti-6Al-4V specimens appeared to be relatively clean of matrix material indicating a weak interface, Fig. 4*c*. This micrograph shows a significant amount of interfacial debonding between the fiber coating (two carbon-rich C/Si layers) and the SiC fiber. Debonding also occurred between the fiber coating and the titanium matrix. In addition, carbon core pullout was observed.

A ductile-type fracture of the aluminum matrix was evident in the B/Al-AR and B/Al-T6 specimens where microvoid coalescence took place, Figs. 4*a* and *b*. Matrix cracking also occurred in the B/Al-T6 specimen. In the SCS-6/Ti-6Al-4V, fracture of the matrix was by ductile rupture, Fig. 4*c*. Additional details of the fracture surface morphology are given in Ref *5*.

Acoustic Emission

The conventional monitoring of damage via optical observations reveal only surface damage. Investigations of internal damage through fracture surface examinations provides key information only after catastrophic fracture has occurred. Although these experimental techniques are vital in the study of damage, they do not provide a means to monitor the accumulation of internal damage in real time. The acoustic emission (AE) technique can serve as an important tool for this purpose.

The application of the AE technique to monitor and identify the major modes of damage in real time has been addressed in Refs *11* and *12* for various MMCs during static tensile loading. The three major modes of damage (namely, fiber breakage, matrix plastic deformation, and fiber-matrix interfacial failure) generate AE events of three different amplitude ranges [*12*]. It was concluded that the high amplitude events (>90 dB) are caused by fiber fracture, the middle range amplitude events (65 to 90 dB) could be caused by matrix plastic deformation, while the low range amplitude events (40 to 65 dB) could be caused by fiber-matrix interfacial failure or matrix shear deformation along the fibers or both.

The major differences in the modes of damage discussed previously for the three materials studied are depicted by the differences in the acoustic emission event amplitude. Figure 5 shows the amplitude distribution histograms (ADH) of all the events accumulated during quasi-static monotonic loading to failure for the three MMC systems studied. In these three-dimensional figures, the number of events having distinct values of amplitude are shown as a function of the applied stress. In B/Al-AR, high-amplitude events associated with fiber breakage were detected already at 20% of ultimate, Fig. 5a; while in the B/Al-T6 specimen, they occurred only at 50% of ultimate, Fig. 5*b*. Optical observations also revealed that fiber breakage occurred at a lower percentage of the notched strength in the B/Al-AR compared with the B/Al-T6. It should be noted that the AE technique is much more sensitive in detecting fiber breakage than are the optical observations mentioned earlier.

The number of high-amplitude events is much greater for the B/Al-AR specimen than for the B/Al-T6 specimen. This agrees with the observations of slow crack growth in the B/Al-AR composite compared to the rapid crack growth in the B/Al-T6 composite. In the latter mate-

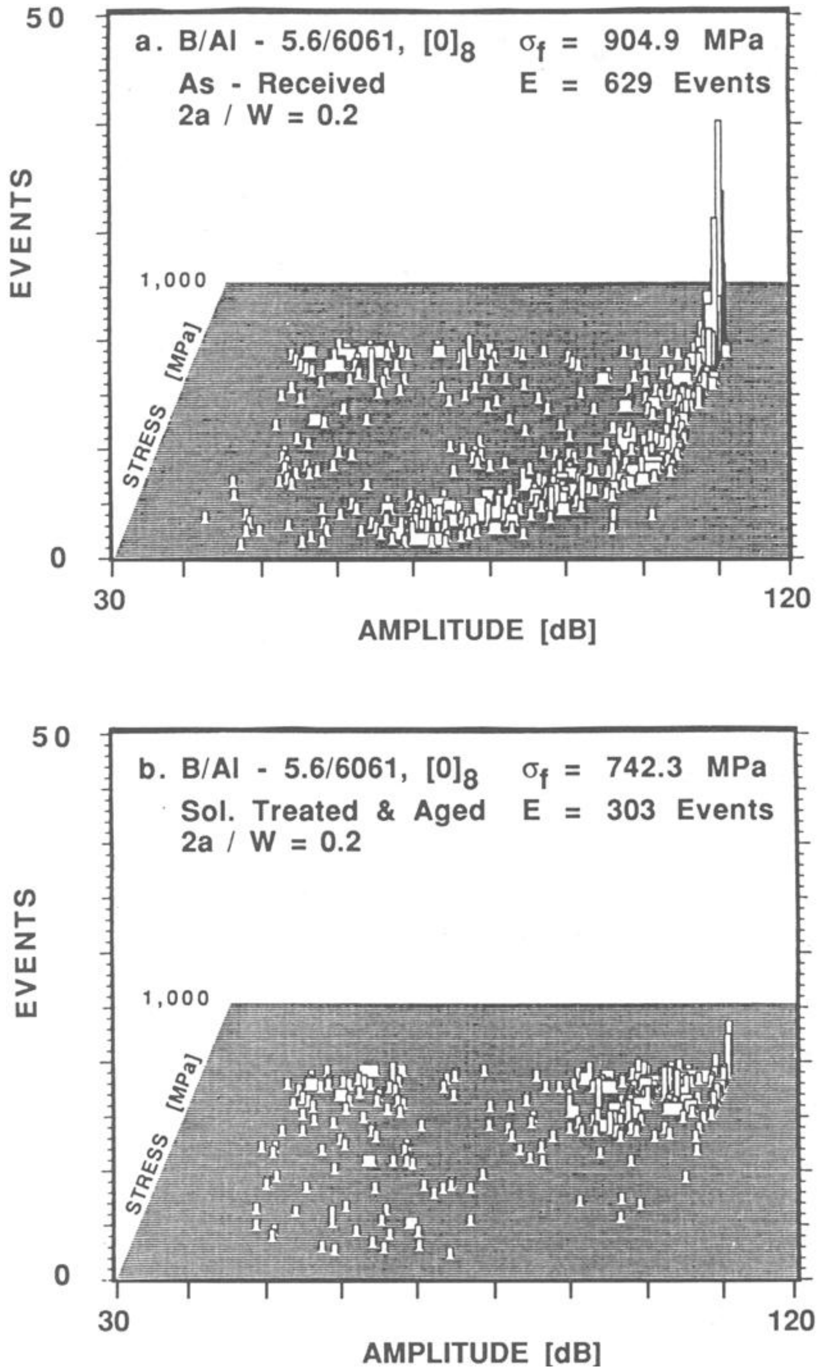

FIG. 5—*Three-dimensional plots of amplitude distribution histograms of events accumulated throughout loading to failure of the three materials studied. The ADH shows the rate of emission within different amplitude ranges associated with the dominant modes of damage.*

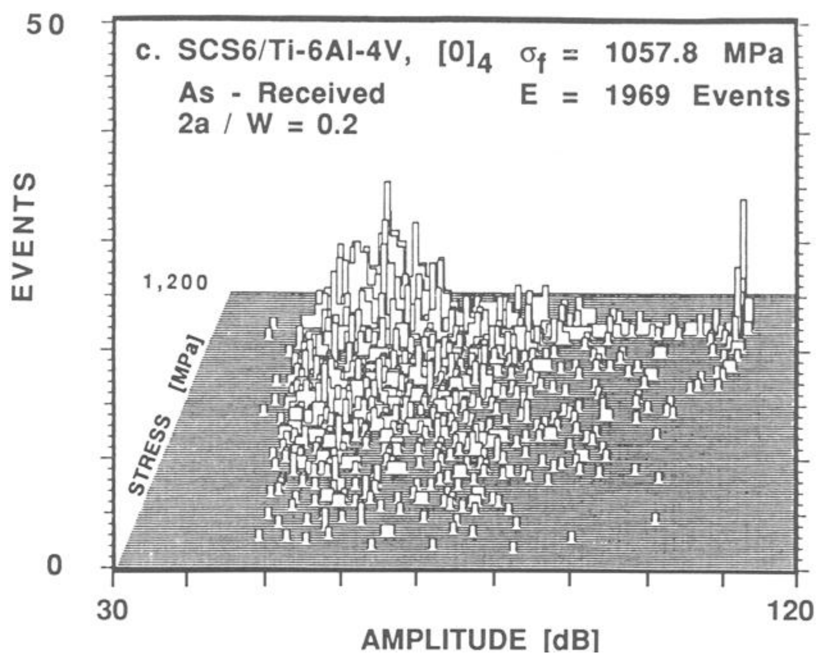

FIG. 5—*Continued.*

rial, catastrophic crack growth occurred soon after the breakage of the first intact fiber ahead of notch tip. In the B/Al-AR composite, the number of middle-range amplitude events, which are associated primarily with matrix plastic deformation, is much greater than in the B/Al-T6 specimen. As shown in Fig. 5*a*, the majority of middle-range amplitude events occur in the B/Al-AR during the initial stages of loading. This corresponds to the observed slow development of the notch-tip matrix plastic zone (in the first matrix bay) prior to the breaking of the first intact fiber, Figs. 1*a* and *b*. Subsequent fiber breaks are accompanied by rapid initiation and progression of matrix plastic deformation in the adjoining matrix bays, Figs. 1*c* to *g*. The AE data acquisition system is not capable of acquiring all the AE events generated during this rapid formation of the matrix plastic zones. Hence, at the higher load levels, the number of events recorded is smaller than that actually occurring.

In the B/Al-T6 specimen, the middle-range amplitude events occurred at a relatively high load range, that is, with the occurrence of fiber breakage (high-amplitude events), Fig. 5*b*. These AE results again correspond very well with the observations where in the B/Al-T6 specimen the plastic deformation was limited primarily to the first matrix bay, was highly localized, and initiated at high load levels, Fig. 2. Furthermore, the notch-tip damage in the B/Al-T6 specimen extended beyond the first matrix bay only when catastrophic fracture was imminent, Fig. 2*d*. Therefore, the amount of the middle- and low-range amplitude events was very limited, Fig. 5*b*.

In the SCS-6/Ti-6Al-4V specimen, the initiation of high-amplitude events occurred at approximately 70% of the static notched strength, Fig. 5*c*. In addition, the relative number of middle-range amplitude events was similar to that generated for the B/Al-AR specimen. Although, in the SCS-6/Ti-6Al-4V specimen, plastic deformation and cracking in the matrix bays are limited to the notch-line region, a much larger number of matrix bays were plastically deformed as compared with the B/Al-AR. Therefore, the relative number of events of middle-range amplitude events can still be large.

The ADH of events also show that a relatively large number of events are of the low-amplitude range (40 to 65 dB). These events could be caused by interfacial failure, fretting among the fracture surfaces, fiber pull-outs, or a combination thereof. The number of low-amplitude events in the B/Al-5.6/6061 specimens were very limited. This agreed with the fact that no matrix splitting and only a relatively small number of fiber pullout appeared; thus, only a limited amount of friction emission was expected. A significant number of low-amplitude events were generated in the SCS-6/Ti-6Al-4V composite, Fig. 5*c*. This is expected since in this material system extensive amounts of matrix cracks, fiber-matrix debonding, and fiber pullout occurred. Thus, emission was generated by the grating among the fracture surfaces along the interface and during fiber pullout. It is of interest to note that in all cases the ADH showed that the majority of low-amplitude events are generated after the occurrence of high-amplitude events (>90 dB), which were caused by fiber breakage. This should be expected since fiber pullout occurs subsequent to fiber breakage.

Deformation Characteristics

Notch-tip damage initiation and propagation is an evolutionary process that is clearly revealed in the deformation characteristics. Divergence of the load-displacement response from linearity signifies damage progression that takes place in the proximity of the notch tip. In this section, notch-tip damage initiation and propagation in the three materials is studied in terms of composite deformation characteristics.

The effect of heat treatment on the load-global displacement response (measured using an extensometer with a 25.4-mm gage length) of center-notched ($2a/W = 0.2$) B/Al-5.6/6061 specimens is shown in Fig. 6. In the B/Al-AR specimen, jumps in global displacement are apparent. These jumps are associated with fiber breakage and indicate a slow failure process with several fibers breaking prior to catastrophic fracture. In the B/Al-T6 specimen, the load-global displacement response was nearly linear up to failure with an ultimate strength approximately 27% less than that recorded for the B/Al-AR specimen. No jumps in global displacement were evident for the B/Al-T6 specimen indicating a rapid failure process with very few fiber breakages prior to catastrophic fracture. The strength reduction in the B/Al-T6 specimen is attributed to the foregoing observed failure process.

The load-crack opening displacement (COD) curves for B/Al-AR and SCS-6/Ti-6Al-4V specimens containing a center notch, $2a/W = 0.3$, are shown in Fig. 7. From this figure, it is clear that the B/Al-AR specimen displays a larger amount of nonlinearity in the load-COD response compared with the SCS-6/Ti-6Al-4V specimen. The damage process zone in the B/Al-AR specimens was wide spread consisting of long longitudinal matrix plastic zones along the fibers that essentially blunt the notch. On the other hand, damage was more confined to the center-line of the notch in the SCS-6/Ti-6Al-4V specimens resulting in less displacement in the longitudinal direction. Consequently, the COD in the B/Al-AR was larger than that in the SCS-6/Ti-6Al-4V specimens.

Numerical Approach

A novel technique to numerically predict the onset and growth of damage in monolayered composites was formulated in Refs *5* and *6* and was used in this research to study the individual failure mechanisms and their interaction in the evolution of the failure process ahead of an existing crack. This numerical scheme is capable of predicting the occurrence and sequence of the major modes of damage that occur in MMCs including fiber breakage, matrix plastic

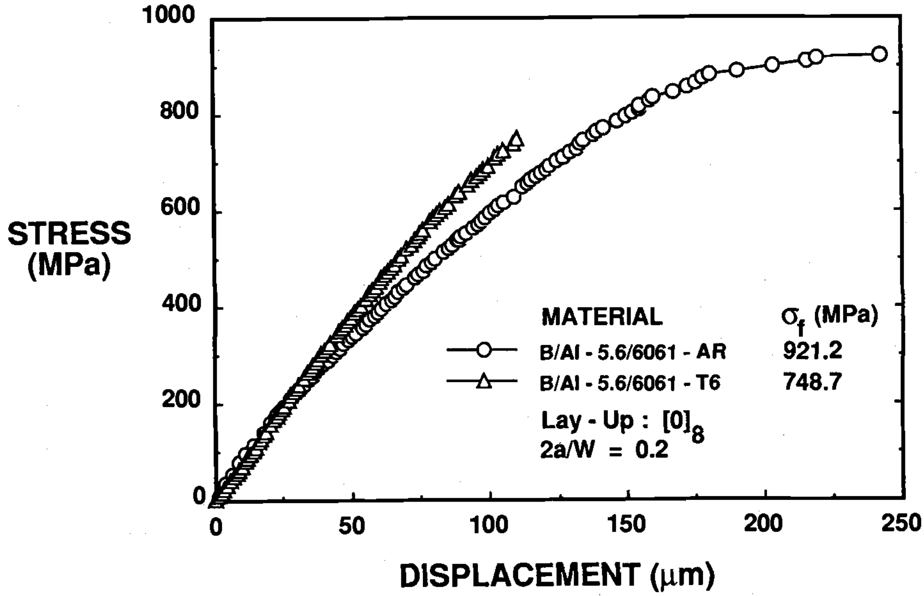

FIG. 6—*Effect of heat treatment on the stress-global displacement response in B/Al-5.6/6061,* $[0]_8$ *containing a center notch of* 2a/W = *0.2. Notched strength and deformation in the solution-treated and aged specimen is lower than that in the as-received specimen.*

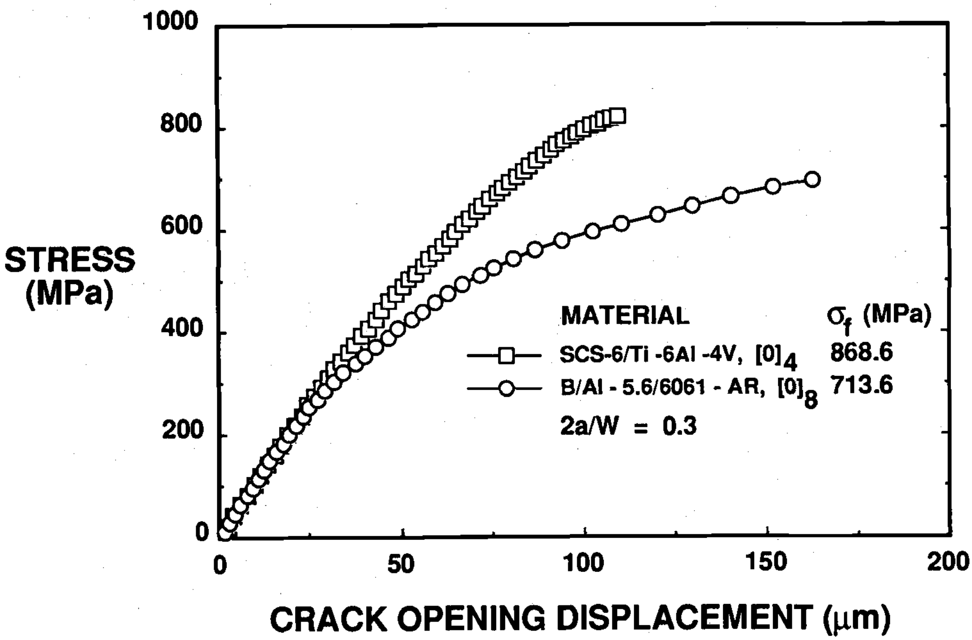

FIG. 7—*Stress-crack opening displacement response in unidirectional as-received B/Al-5.6/6061 and SCS-6/Ti-6Al-4V. The B/Al-5.6/6061 specimen displays more deformation while the SCS-6/Ti-6Al-4V specimen has a higher notched strength.*

deformation, matrix cracking, matrix splitting, and fiber-matrix interfacial debonding. The primary feature of this numerical technique is that the crack path does not have to be selected a priori. Furthermore, any combination of fiber, matrix, and interface constituent properties can be used. A brief description of the major features of the damage growth prediction technique formulated in Refs *5* and *6* is provided here.

This technique employs a displacement-based incremental elastic-plastic finite-element method. A node-splitting and nodal force relaxation algorithm was formulated to create new crack surfaces. The dominant modes of damage that exist in MMCs are incorporated using node-splitting mechanisms in conjunction with appropriate failure criteria. Predictions of fiber breakage, matrix cracking, and fiber-matrix debonding are accomplished by determining the sequence and direction of nodal splitting using the maximum normal and shear strength criteria. For each node, the dominant mechanism and mode of failure are determined. The parameters that dictate local material separation are the normal and shear strength values for the matrix, fiber, and interface. The material properties and critical values for the constituents are listed in Table 1. When the condition for a particular failure mechanism is satisfied at a node, a crack is created by introducing a double node at that location. At that stage, the nodes are reassigned to the appropriate elements, boundary conditions are updated, and the stresses are redistributed. Using the node-splitting and nodal force relaxation algorithm, the failure mechanisms and the crack path can be predicted at each stage of damage evolution without preselecting the crack path.

A hybrid material model was employed in the prediction. A local heterogeneous region is used to model the vicinity of the crack tip that is contained within a homogeneous continuum. The numerical predictions of the failure process are conducted within the heterogeneous region where the fiber and matrix occupy distinct zones. Within this region, the fibers are modeled as elastic, the matrix modeled as elastic-plastic using an incremental J_2 flow theory with isotropic hardening, and the interface is assumed to be well bonded. The outer homogeneous continuum has the actual structural dimensions and geometry to which the external loading is applied. The homogeneous continuum is modeled as an elastic material. The rule of mixtures was used to obtain the effective properties of the homogeneous region where the fiber volume fraction was 0.53.

The specimen geometry, loading conditions, hybrid regions, and finite-element mesh are shown in Fig. 8. The finite-element mesh consisted of 2729 elements and 11 087 nodes. Nine-

TABLE 1—*Constituent properties and critical strengths.*

	Matrix			Fiber	
	6061-AR [*5*]	6061-T6 [*5*]	Ti-6Al-4V [*13*]	Boron	SCS-6
		ELASTIC PROPERTIES			
E_0, GPa	72.1	72.1	125.4	400.0 [*5*]	385 [*5*]
ν	0.33	0.33	0.33	0.21 [*14*]	0.25 [*15*]
		STRENGTHS[a]			
Normal, MPa	160	360	1055	2800 [*16*]	3800 [*17*]
Shear, MPa[b]	107	240	703	NA[c]	NA

[a] Critical values for the interface are assumed to be the same as those of matrix.

[b] Assuming the shear strength is 1.5 times less than normal strength based on typical ratios of normal strength to shear strength for metallic materials given in Ref *18*.

[c] NA = not applicable.

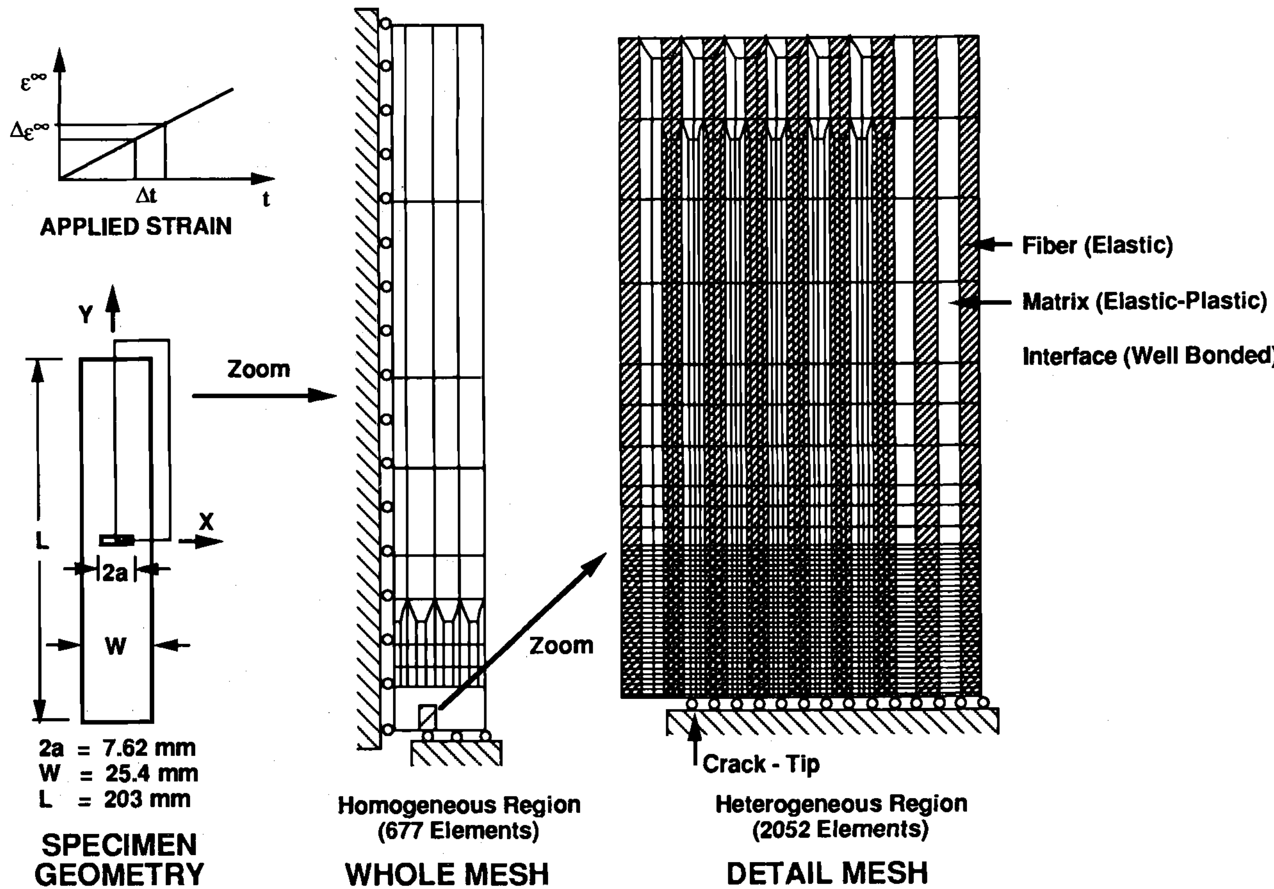

FIG. 8—*Finite-element model showing specimen geometry, loading function, homogeneous region, and heterogeneous region. Predictions of the failure process are conducted within the heterogeneous region.*

noded isoparametric elements with 3 by 3 Gauss numerical integration were used. Note, the finite-element mesh used in the numerical predictions allows four fiber breakages ahead of the notch tip. The damage growth predictions can allow for as many fiber breakages as desired. However, because of the extensive computing time required, only four fiber breakages were considered. The predicted notched strength was assumed to be the far-field stress after the fourth fiber fractured.

Comparisons Between Experiments and Predictions

Predictions of the crack-tip damage process at various stages of quasi-static monotonic loading were conducted in the materials studied. It should be noted here that the fiber volume fractions in the actual B/Al-AR, B/Al-T6, and SCS-6/Ti-6Al-4V laminates ranged between 0.48 to 0.53, 0.48 to 0.53, and 0.33 to 0.37, respectively. For the purpose of comparing among the three material systems, it was decided to use the same fiber volume fraction of 0.53 and the same mesh in the predictions for all three material systems.

The nodal displacements of the mesh within the heterogeneous region were plotted at progressive states of damage in Refs 5 and 7. From the displaced meshes, the failure mechanisms (namely, fiber breakage, matrix plastic deformation, matrix cracking, matrix splitting, and interface debonding) could be easily identified. Matrix plastic deformation was revealed by extreme distortions of the matrix elements and by the numerical values of the equivalent plastic strain. In general, the numerical predictions were in good agreement with the optical observations for the three materials in terms of capturing the occurrence and sequence of the damage modes in the development of a macroscopic crack [5,7]. Highlights of the these findings are presented for the three materials studied.

Boron/Aluminum-5.6/6061-AR

The numerical prediction of the crack-tip damage state at the final stage of quasi-static loading is shown in Fig. 9 for a B/Al-AR monolayer and compared with the optical observation. In this figure, the nodal point displacements of the elements in the vicinity of the crack tip have been magnified ten times. The failure events leading up to the state of damage shown here consisted of: (1) initiation and progression of matrix plastic deformation; (2) sudden fiber breakage leaving behind intact matrix bridges; (3) fiber crack arrest in the next matrix bay; and (4) slow and stable crack growth through the matrix ligaments. This failure cycle was repeated after each fiber break (up to four). This accurately predicted the sequential failure process observed in this material, Fig. 1. The distorted elements in the matrix bays and numerical values of the effective plastic strain (not shown) reveal extreme shear deformation of the matrix bays, Fig. 9. This corresponds quite accurately with the observed longitudinal matrix plastic zones shown in the same figure.

A comparison between the measured and predicted load-COD curves is shown in Fig. 10. Both the predicted and measured load-COD curves are characterized by a nonlinear response followed by jumps in COD. Details of the measured jumps in COD are shown in the figure. The characteristics of the predicted curve are qualitatively similar to the experimental curve.

The predictions and observations show that prior to the breakage of the first intact fiber, matrix damage in the form of plastic deformation (transverse and along the fibers), matrix cracking, and matrix splitting take place in the first matrix bay. In the predictions, these damage events only cause a slight increase in the COD. The load must be continuously increased in order to develop new damage (that is, node splitting). Hence according to the predictions, the initial nonlinear region in the load-COD curve is attributed to these damage modes. This point is further verified by the experiments. According to observations, the first fiber fails at

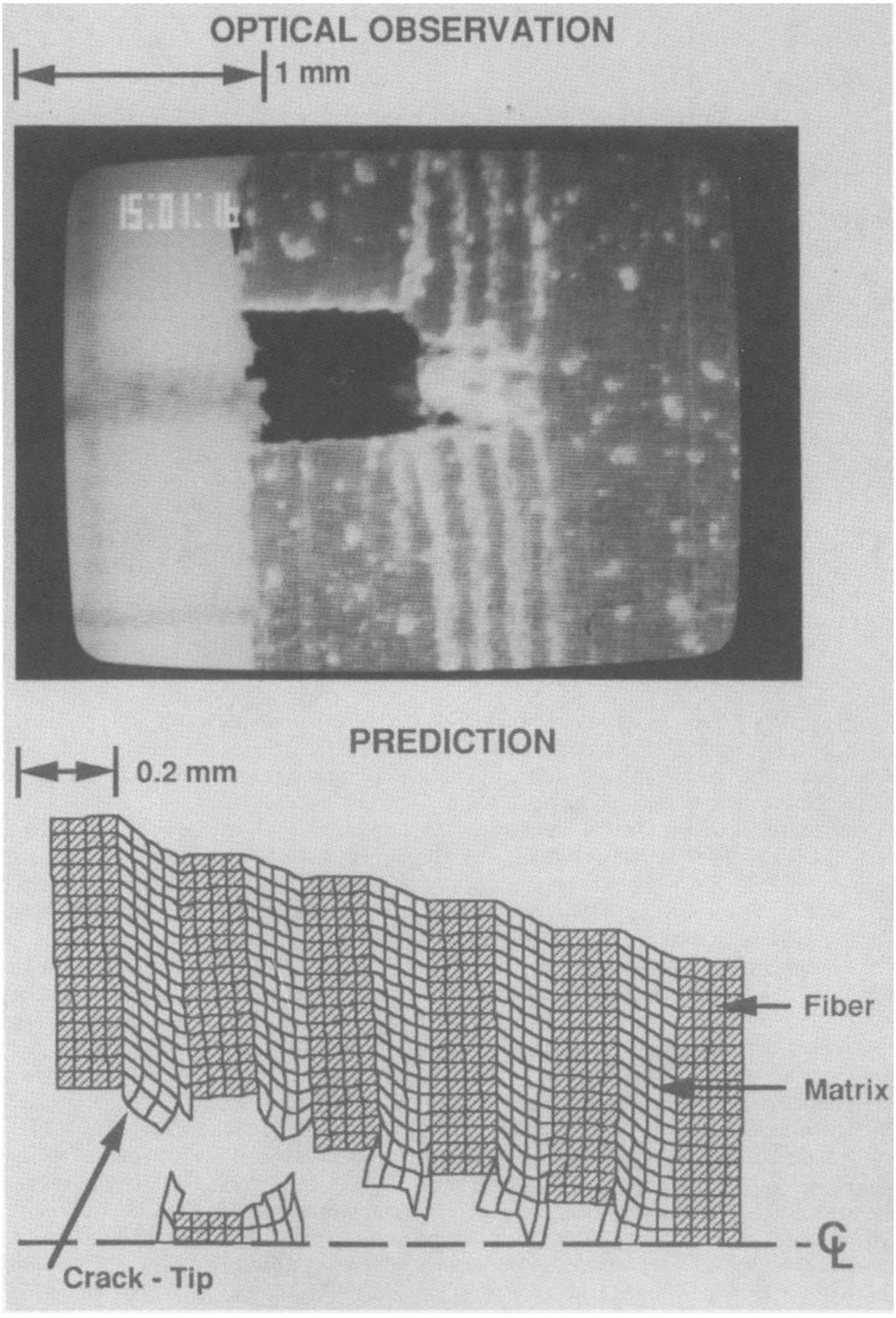

FIG. 9—*Comparison between optical observations and predictions in as-received B/Al-5.6/6061. The deformed mesh in the crack-tip region is shown where the nodal displacements were magnified ten times. The prediction reflects the optically observed modes of damage (2*a/W *= 0.5,* σ_f *= 568.1 MPa).*

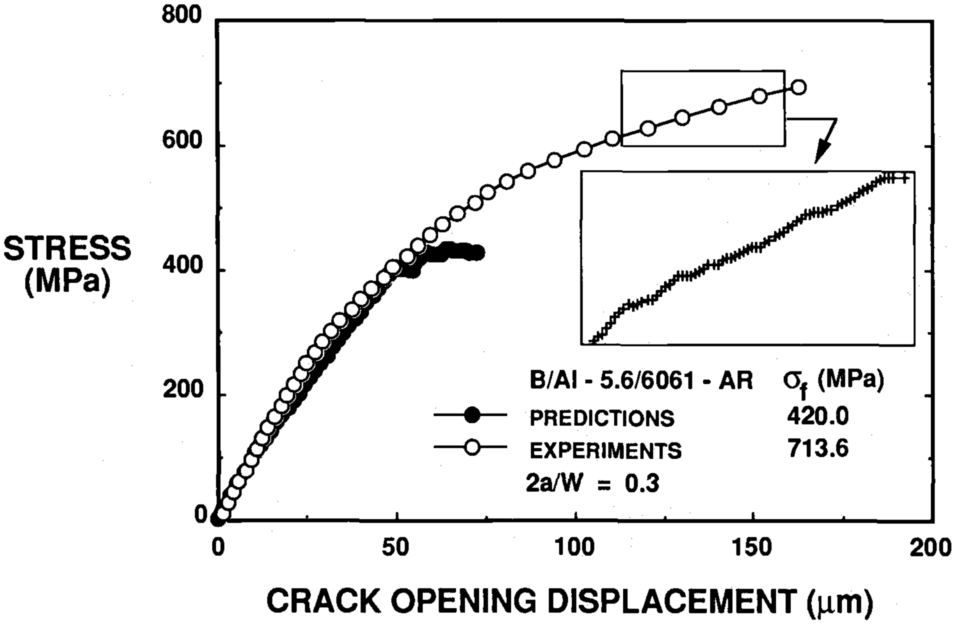

FIG. 10—*Comparison between the measured and predicted stress-crack opening displacement responses in as-received B/Al-5.6/6061. Characteristics of the predicted curve qualitatively agree with those of the measured curve.*

approximately 79% of the ultimate strength, Fig. 1*c*. The experimental load-COD response is typically continuous up to that point. In addition, most of the AE events generated in the initial stages of loading are of the middle-amplitude range that corresponds to the formation of matrix plastic deformation and matrix cracking, Fig. 5*a*.

Both the predictions and experiments verify that the jumps in COD in the load-COD curves, Fig. 10, are associated with fiber breakage. The predictions revealed that there is a substantial increase in COD and a slight reduction in the global stress following each fiber break. The jumps in the experimental COD were typically accompanied by audible levels of acoustic emission and sudden surges in the notch-tip damage (observed via CCTV).

The numerical prediction agreed with the experimental load-COD curves, Fig. 10, in the initial loading range. However, the agreement was not as good in the later stages of loading. In addition, the figure indicates that the predicted notched strength is approximately 60% of that obtained experimentally (the predicted notched strength was the far-field stress after the four-fiber breakage). This difference could be attributed to the difference between the actual in situ fiber strength and that used for the numerical predictions. There is large scatter in the strength of fibers (2 to 4 GPa for boron fibers [*16*]). Clearly, the predictions of the load-COD, and notched strength will depend strongly on the proper selection of fiber strength (2.8 GPa was chosen as the fiber strength in the predictions, Table 1). In addition, the characteristics of the load-COD curve (for example, the loads at which jumps in COD occur, the load range between consecutive jumps in COD, etc.) depend on the actual fiber strength and the distribution of the fiber strength within the specimen, which were not accounted for in the prediction. Also, it should be noted that the experimental load-COD curves were obtained for $[0]_8$ specimens, while the predictions were made for a monolayer. Finally, the predictions were made for a specimen containing a center crack whereas the experiments were performed with a specimen containing a blunted center notch having a width of 0.25 mm.

Boron/Aluminum-5.6/6061-T6

Figure 11 shows the predictions and observations of the final state of damage in B/Al-T6 where the nodal point displacements of the elements in the vicinity of the crack tip have been magnified ten times. The numerical predictions revealed a completely different failure process compared to the B/Al-AR monolayer. In the B/Al-T6, the major modes of damage observed and predicted numerically were limited matrix plastic deformation, matrix cracking, and fiber breakage. These failure modes were repeated following each fiber break. The distortion of the elements in the matrix bays is significantly smaller compared with those in the B/Al-AR, Fig. 9. Damage growth occurred quite rapidly and in a self-similar manner where the notch-tip damage zone remained within a narrow-banded region flanking the plane of the notch as shown in both the predictions and the optical observations, Fig. 11.

Both the experimental observations and the numerical predictions demonstrated the influence and importance of matrix plastic deformation in the failure process in B/Al-5.6/6061. In the B/Al-AR, the ductile matrix undergoes substantial plastic deformation that diffuses and alleviates local stress concentrations. Lateral damage extension (due to fiber fracture) is abruptly arrested by the formation and progression of matrix plastic zones (along the fibers) in the vicinity of the broken fibers. Typically, fibers fracture ahead of the matrix leaving behind connecting "bridges." These ligaments fail in a ductile manner. A continuous increase in the applied load is required to propagate a crack through the matrix. Hence, the lower yield strength and more ductile matrix in the B/Al-AR laminate creates an effective crack arrest mechanism permitting a slow microscopic failure process.

The higher yield strength and less ductile matrix in the B/Al-T6 provided limited matrix plastic deformation to relieve the concentrated stresses and therefore the damage remained confined to the crack-tip vicinity. Eventually, the buildup of stress became high enough to initiate matrix cracking and fiber fracture within the plane of the existing crack resulting in a rapid self-similar crack propagation. Consequently, the ultimate notched strength in the B/Al-T6 was considerably reduced compared to the B/Al-AR.

A comparison of the predicted load-COD curves for the B/Al-AR and the B/Al-T6 is shown in Fig. 12. Similar trends in the predicted load-COD curves are seen when compared to the experimental data of the load-global displacement curves, Fig. 6. That is, B/Al-AR exhibited higher notched strength and underwent substantially larger deformation compared with the B/Al-T6. The predicted and actual notched strengths of the B/Al-AR were approximately 47 and 27% greater than that of the B/Al-T6, respectively.

Silicon Carbide/Titanium-SCS-6/Ti-6Al-4V

The numerical prediction and the optical observation of the crack-tip damage progression in the SCS-6/Ti-6Al-4V prior to catastrophic fracture is shown in Fig. 13. The nodal point displacements of the elements in the vicinity of the crack tip have been magnified ten times. Here, a totally different failure process was predicted compared to the B/Al-5.6/6061 monolayers. The predicted damage progression consisted primarily of matrix cracking and fiber breakage. The optical observations revealed fiber-matrix interfacial failure. Examinations of the fracture surfaces, Fig. 4*c*, also indicated a significant amount of fiber-matrix interfacial debonding. Since the interface strength used in the predictions were higher than the actual values, interface failure could not be predicted. Interfacial failure will cause a deflection in

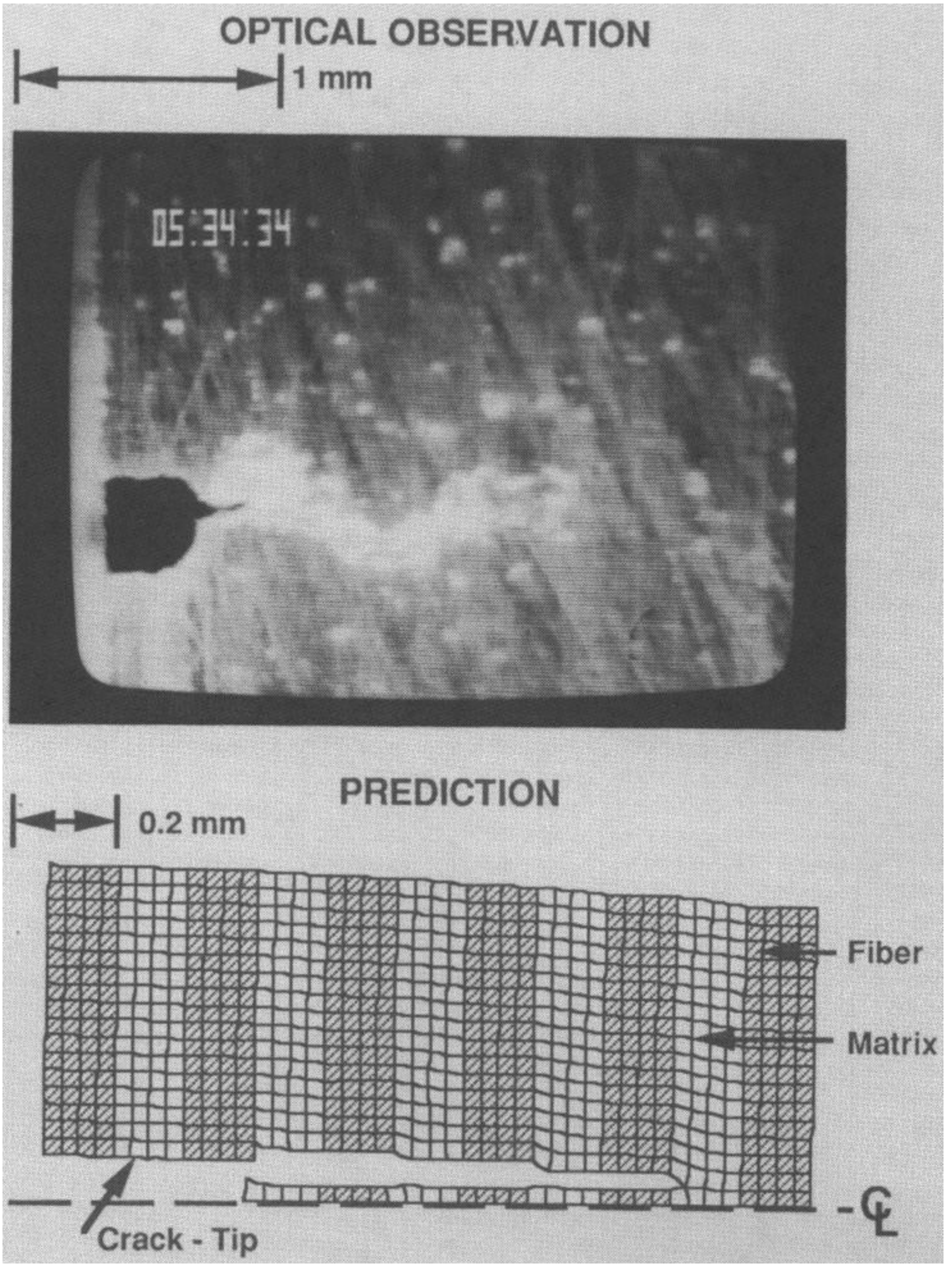

FIG. 11—*Comparison between optical observations and predictions in solution-treated and aged B/Al-5.6/6061. The deformed mesh in the crack-tip region is shown where the nodal displacements were magnified ten times. Both observations and predictions reveal a macroscopically self-similar damage progression* ($2a/W = 0.5$, $\sigma_f = 394.0$ *MPa*).

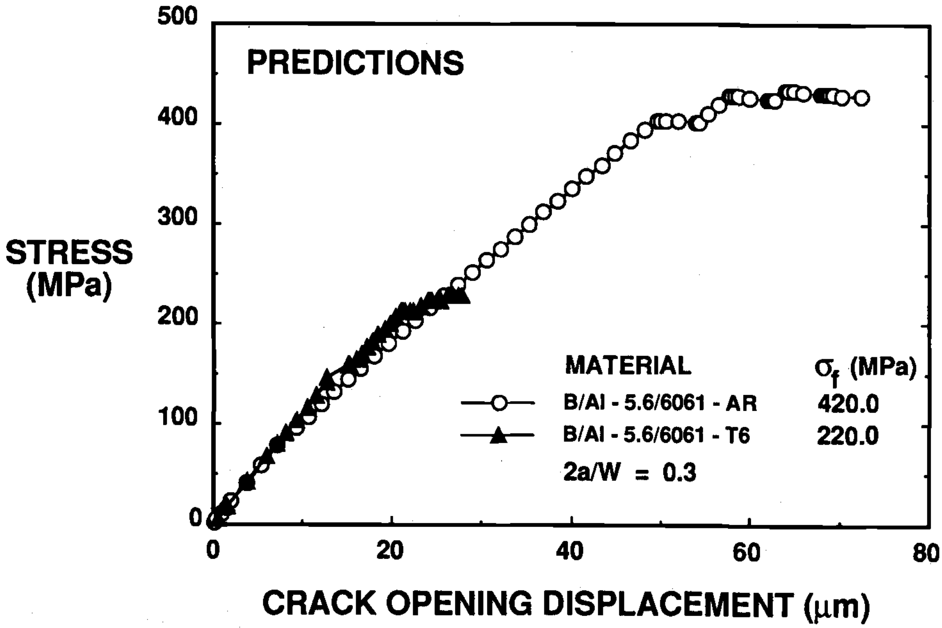

FIG. 12—*Effect of heat treatment on the predicted stress-crack opening displacement curves in B/Al-5.6/6061. Notched strength and deformation in the solution-treated and aged specimen is lower than that in the as-received specimen.*

crack path and appears to be the dominant crack arrest mechanism in SCS-6/Ti-6Al-4V. In the absence of available interfacial strength data, this process could not be accurately quantified in the predictions. Without interfacial failures, the numerical predictions displayed a more unstable and rapid damage progression compared with the experimental observations.

The experimental and predicted load-COD curves are shown in Fig. 14. The numerical simulation accurately predicted the initial stages of the load-COD curves; however, a poor agreement was obtained in the later stages. In addition, the figure indicates that the predicted notched strength is approximately 25% of that obtained experimentally. As discussed previously for the B/Al-AR case study, these differences could be attributed to the following reasons: (1) the difference in actual in situ fiber strength; (2) the distribution of fiber strength within the actual specimen; (3) the thickness effect (that is, monolayer versus $[0]_4$ laminate); and (4) the difference in the geometry of the discontinuity (that is, crack versus notch).

In the SCS-6/Ti-6Al-4V, an additional issue should be considered. It was shown that during quasi-static loading of a SCS-6/Ti-6Al-4V specimen, as many as 16 fibers broke ahead of the notch tip prior to catastrophic fracture, Fig. 13. However, the numerical prediction conducted here accounted for only four fibers ahead of the notch tip. If more fibers were considered in the model, a higher predicted notched strength and a better correspondence with experiments could be anticipated. Note, the numerical predictions can allow for as many fiber breakages as desired; however, because of the extensive computing time required, only four fiber breaks were modeled. The agreement between the predicted and experimental notched strength in the B/Al-AR case was much better than that in the SCS-6/Ti-6Al-4V case, since in the former, three to five fiber breakages occurred prior to catastrophic fracture, Fig. 9.

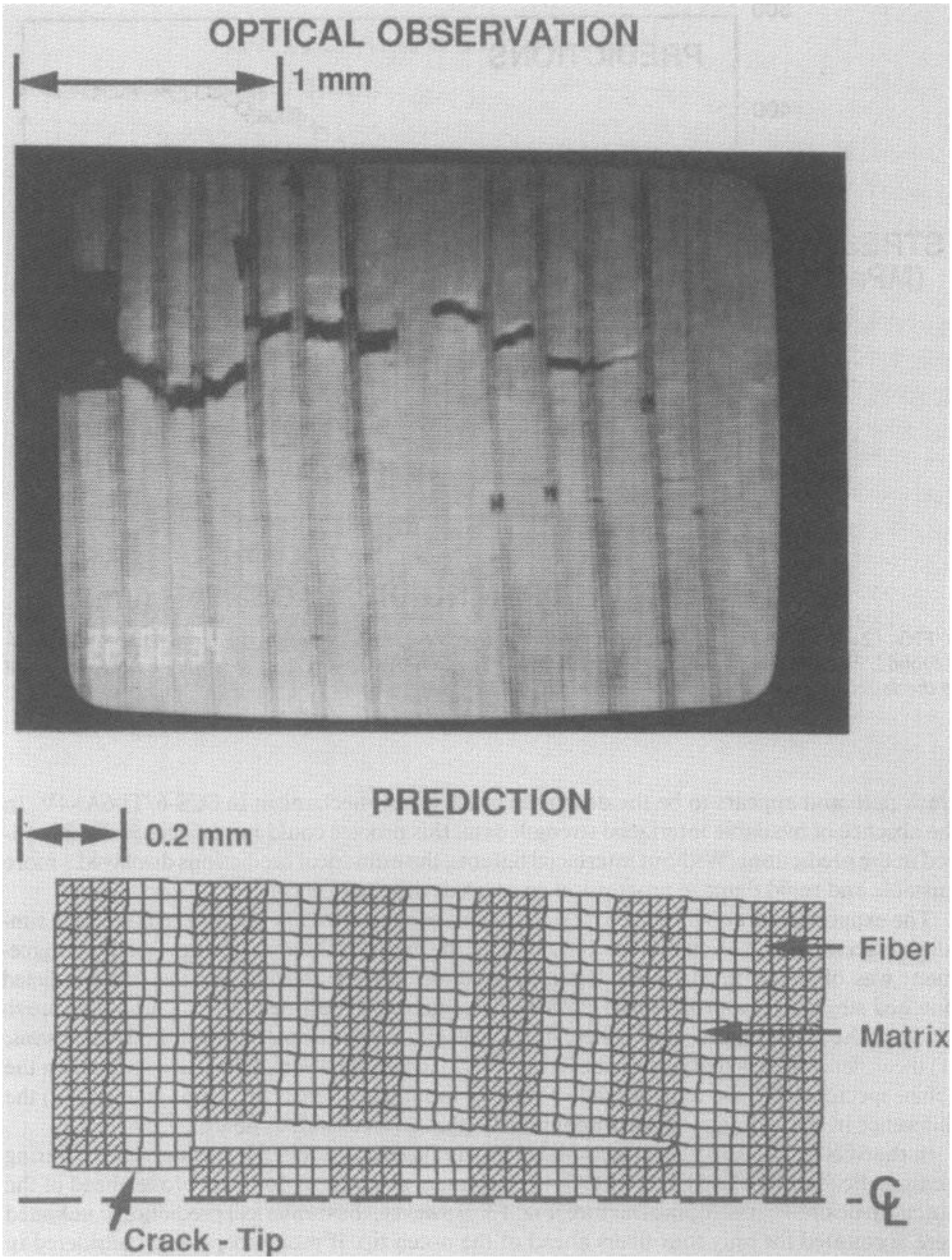

FIG. 13—*Comparison between optical observations and predictions in as-received SCS-6/Ti-6Al-4V. The deformed mesh in the crack-tip region is shown where the nodal displacements were magnified ten times. Both observations and predictions reveal macroscopically, self-similar damage progression* (2a/W $= 0.4$, $\sigma_f = 667.2$ *MPa*).

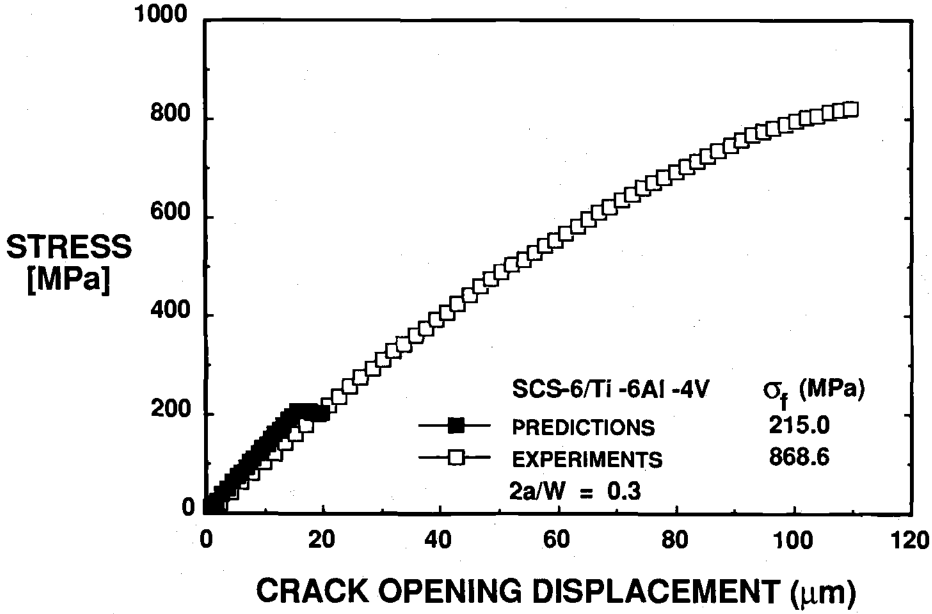

FIG. 14—*Comparison between the measured and predicted stress-crack opening displacement responses in as-received SCS-6/Ti-6Al-4V.*

Summary and Conclusions

Notch-tip damage initiation and progression in unidirectional B/Al-5.6/6061 and SCS-6/Ti-6Al-4V were investigated. Two conditions of B/Al-5.6/6061 were tested, namely, as-received and solution-treated and aged conditions. In the B/Al-AR specimen, notch-tip damage progression was characterized primarily by extensive matrix plastic deformation along the fibers that serve as a crack arrest medium. Instantaneous jumps in the COD were associated with a sudden increase in notch-tip damage extension due to fiber breakage. Subsequent to each fiber break, damage extension abruptly ceased due to the initiation and progression of matrix plastic deformation along the next intact fiber. The matrix plastic deformation alleviated and dispersed the concentrated stresses. Following crack arrest, an additional increment in applied load was required to recommence fiber breakage. As observed optically, and manifested in the load-COD curves, this process was repeated several times resulting in a relatively stable failure process and higher notched strength when compared to the B/Al-T6 specimens.

An effective crack arrest mechanism was not observed in the B/Al-T6 specimens. The high yield strength matrix material in the B/Al-T6 laminate underwent very localized and confined plastic deformation that provided little relief of the stresses at the crack tip. These stresses were high enough to fracture fibers within the plane of the existing notch resulting in rapid and unstable self-similar crack extension. The specimen failed catastrophically shortly after the first fiber fractured as was illustrated in the limited jumps in displacement in the load-global displacement curve.

A completely different failure process was exhibited in SCS-6/Ti-6Al-4V specimens. Experimental observations indicated a relatively large number of fiber breaks prior to catastrophic fracture. These fiber breaks apparently occurred on planes approximately 0.25 mm on either side of the notch centerline. Matrix cracking lagged behind fiber breaks and occurred primarily along the notch centerline. As the matrix cracks progressed, interfacial failures were noticed along the fiber ends associated with fiber pullout. Fiber-matrix debonding appears to be the primary crack arrest mechanism in the SCS-6/Ti-6Al-4V.

Acoustic emission event amplitude ranges were correlated with the failure process in the three material systems. The large number of high-amplitude events (>90 dB) associated with fiber breakage in the B/Al-AR and SCS-6/Ti-6Al-4V agreed with the slow failure process and large number of observed fiber breaks. A significantly smaller number of high-amplitude events were recorded for the B/Al-T6 that corresponds with the rapid and sudden catastrophic fracture.

The occurrence and sequence of the damage events leading to a macroscopic crack were accurately predicted. A qualitative agreement between the observations and the numerical predictions was obtained where the prominent features of the notch-tip damage progression were captured. The analysis combined with experimental data provided a better understanding of the notch-tip damage evolution.

Acknowledgments

The research reported in this manuscript has been partially supported by the Strategic Defense Initiative Office/Innovative Science and Technology under the Solid Mechanics Program, Office of Naval Research (Contract No. N00014-85-K-0628) with Dr. Y. Rajapakse as the program monitor. This research has also been partially sponsored by General Electric Company, Aircraft Engine Business Group, Evandale Plant, Evandale, Ohio, with Dr. K. Wright and Mr. Mark Sensmeier as the contract monitors.

References

[*1*] Baetz, J. G., "Metal Matrix Composites: Their Time Has Come," *Aerospace America*, Nov. 1988.

[*2*] Sprague, R. A., "Future Aerospace—Materials Directions," *Advanced Materials and Processes*, Vol. 133, Issue 1, Jan. 1988.

[*3*] Renton, W. J., *Hybrid and Selected Metal Matrix Composites*, American Institute of Aeronautics and Astronautics, New York, 1977.

[*4*] Johnson, W. S., "Metal Matrix Composites: Their Time to Shine?," *ASTM Standardized News*, Oct. 1987.

[*5*] Bakuckas, J. G., Jr., "Damage Progression During Static and Fatigue Loading in Metal Matrix Composites," Ph. D. thesis, Drexel University, Philadelphia, 1991.

[*6*] Bakuckas, J. G., Tan, T. M., Lau, A. C. W., and Awerbuch, J., "Computational Prediction of Damage Growth in Unidirectional Composites, Part I: Theoretical Formulations and Numerical Implementations," Drexel University Report MEM-CML-9101, Drexel University, Philadelphia, 1991.

[*7*] Bakuckas, J. G., Lau, A. C. W., Tan, T. M., and Awerbuch, J., "Computational Prediction of Damage Growth in Unidirectional Composites, Part II: Case Studies," Drexel University Report MEM-CML-9102, Drexel University, Philadelphia, 1991.

[*8*] Awerbuch, J. and Hahn, H. T., "K-Calibration of Unidirectional Metal Matrix Composites," *Journal of Composite Materials*, Vol. 12, 1978, p. 222.

[*9*] Bakuckas, J. G., Lau, C. W., and Awerbuch, J., "Damage Analysis of Notched Unidirectional Metal Matrix Composites," *Proceedings*, Thirteenth International Symposium for Testing and Failure Analysis, ISTFA/87, Los Angeles, 1987, pp. 43–53.

[*10*] Bakuckas, J. G., Awerbuch, J., and Lau, C. W., "Effect of Heat Treatment on Damage Progression in Center-Notched Boron/Aluminum Composites," *Proceedings*, Fourth Japan–U. S. Conference on Composite Materials, Washington, DC, 1988, pp. 661–672.

[*11*] Awerbuch, J. and Bakuckas, J. G., "On the Applicability of Acoustic Emission for Monitoring Damage Progression in Metal-Matrix Composites," *Metal Matrix Composites: Testing, Analysis, and Failure Modes, ASTM STP 1032*, W. S. Johnson, Ed., American Society for Testing and Materials, Philadelphia, 1989, pp. 68–99.

[*12*] Madhukar, M. S. and Awerbuch, J., "Monitoring Damage Progression in Center–Notched Boron/Aluminum Laminates Through Acoustic Emission," *Composite Materials: Testing and Design (Seventh Conference), ASTM STP 893*, J. M. Whitney, Ed., American Society for Testing and Materials, Philadelphia, 1986, pp. 337–367.

[*13*] Ruff, P. E., Specification of MIL-HDBK-5C, AFWAL-TR-80-4110, Air Force Wright Aeronautical Laboratories, OH, 1980.
[*14*] Tsai, S. W. and Hahn, H. T., *Introduction to Composite Materials*, Technomic Publishing Company, Westport, CT, 1980.
[*15*] Johnson, W. S. and Wallis, R. R., "Fatigue Behavior of Continuous-Fiber Silicon Carbide/Aluminum Composites," *Composite Materials: Fatigue and Fracture, ASTM STP 907*, H. T. Hahn, Ed., American Society for Testing and Materials, Philadelphia, 1986, pp. 161–175.
[*16*] Madhukar, M. S., "Fracture Behavior of Boron/Aluminum Laminates at Room and Elevated Temperatures," Ph. D. thesis, Drexel University, Philadelphia, 1985.
[*17*] Martineau, P., Lahaye, M., Pailler, R. N., Couzi, M., and Cruege, F., "SiC Filament/Titanium Matrix Composites Regarded as Model Composites," *Journal of Materials Science*, Vol. 19, 1984, pp. 2731–2748.
[*18*] *ASM Metals Reference Book*, 2nd ed., American Society for Metals, Metals Park, OH, 1983.

David E. Richardson[1] *and James G. Goree*[2]

Experimental Verification of a New Two-Parameter Fracture Model

REFERENCE: Richardson, D. E. and Goree, J. G., "**Experimental Verification of a New Two-Parameter Fracture Model,**" *Fracture Mechanics: Twenty-Third Symposium, ASTM STP 1189,* Ravinder Chona, Ed., American Society for Testing and Materials, Philadelphia, 1993, pp. 738–750.

ABSTRACT: This paper presents an experimental verification of a new two-parameter fracture model based on the equivalent remote biaxial stresses (ERBS) developed by the authors. A detailed comparison is made between the new theory and the constant, K_{Ic}, approach of linear elastic fracture mechanics (LEFM). Fracture is predicted through a failure curve representing the change in a variable fracture toughness, K_c, with the ERBS ratio, B. The nonsingular term, T, in the series expansion of the near crack-tip transverse stress is included in the model. Experimental results for polymethyl methacrylate (PMMA) show that the theory can account for the effects of geometry on fracture toughness as well as indicate the initiation of crack branching. It is shown that the new criterion predicts failure for PMMA with a 95% confidence zone that is nearly three times smaller than that of the LEFM K_{Ic} approach.

KEY WORDS: fracture (materials), failure criterion, T-stress, biaxial loading, fracture toughness, linear elastic fracture mechanics, fracture mechanics, fatigue (materials)

For many years the concept of a constant fracture toughness (K_{Ic}), from linear elastic fracture mechanics (LEFM), has been used to predict failure in cracked bodies. Recently, however, researchers have pointed out that some of the basic assumptions of LEFM may not be accurate [*1*]. Others have found inconsistencies in predicting fracture for some materials, both isotropic and anisotropic, from test results that satisfy the LEFM requirements for brittle plane-strain behavior [*2,3*]. The purpose of this paper is to present some of the experimental test results from Ref *4* that show the limitations of the constant K_{Ic} failure criterion and support the new equivalent remote biaxial stress (ERBS) fracture model proposed in Ref *4*.

The ERBS concept is based on the fact that the near-crack-tip stresses in any arbitrary coupon subjected to Mode I loading with a load-free crack surface may be equated to those in an infinite biaxially loaded center-cracked panel of the same material and thickness and with a fixed crack length, c^* (Fig. 1). This is done by requiring that the stress intensity factors (K_I) and the constant terms (T) in the series expansion of near-crack-tip stresses for both geometries be equal. For coupons of anisotropic material

$$K_I = \sigma_y^\infty \sqrt{\pi c^*}$$

$$T = \sigma_x^\infty + \sigma_y^\infty\{s_1 s_2\}$$

[1] Principal Engineer, Thiokol Corporation, Space Operations, Brigham City, UT 84302; formerly, Ph.D. student in Engineering Mechanics, Department of Mechanical Engineering, Clemson University.
[2] Clemson University Centennial professor, Department of Mechanical Engineering, Clemson University, Clemson, SC 29634-0921.

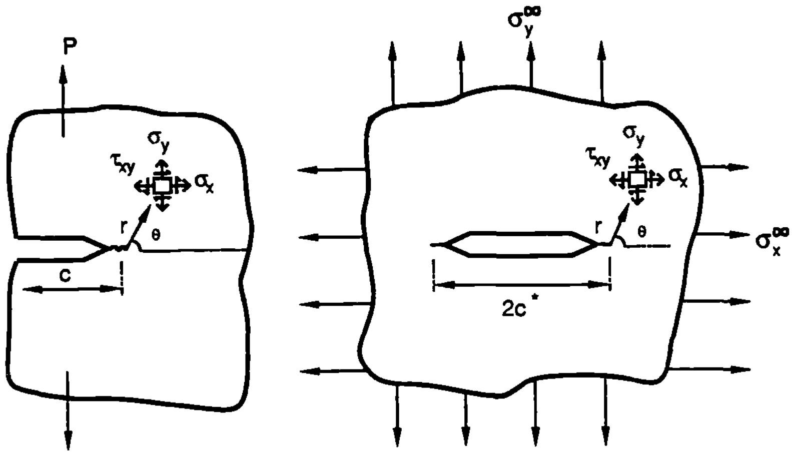

FIG. 1—*Comparison of an arbitrary cracked coupon with an infinite center-cracked panel.*

Solving for σ_x^∞ and σ_y^∞ gives

$$\sigma_x^\infty = \frac{-K_I}{\sqrt{\pi c^*}} Re\{s_1 s_2\} + T$$

$$\sigma_y^\infty = \frac{K_I}{\sqrt{\pi c^*}}$$

From these equivalent remote biaxial stresses (ERBS), the ERBS ratio (B) is defined as

$$B = \frac{\sigma_x^\infty}{\sigma_y^\infty} = \frac{T}{K_I}\sqrt{\pi c^*} - Re\{s_1 s_2\} \tag{1}$$

This ratio plays an integral role in the failure criterion. Here, s_1 and s_2 are the positive roots of the characteristic equation [5]. For an isotropic material, both roots are positive i ($i = \sqrt{-1}$).

The basic assumption of the ERBS fracture model is that failure in any planar arbitrary Mode I coupon with an unloaded crack surface will be the same as that found in an "equivalent" infinite biaxially loaded center-cracked panel of the same material with a fixed crack length, c^*. The failure of the infinite cracked panel with different remote loadings (Fig. 1) is characterized through an ERBS curve, a graph representing the change in fracture toughness, K_c, with the ratio of the remote biaxial stresses, B ($\sigma_x^\infty/\sigma_y^\infty$). K_c is a variable fracture toughness as opposed to the LEFM concept of a constant fracture toughness, K_{Ic}.

To predict fracture in an arbitrary cracked coupon, K_I and T must be found. The ERBS ratio (B) is then determined through Eq 1, and from the ERBS curve, K_c may be obtained for that particular coupon. K_c can be used to predict crack growth initiation just as K_{Ic} in the LEFM approach. Because fracture toughness (K_c) is used in the failure criterion, this theory is applicable for any material that does not exhibit any large amounts of crack-tip anomolies (large plastic zones, extensive fiber pullout, etc.). Since higher order terms are used, the theory is more accurate than the conventional LEFM approach.

Even though the ERBS curve represents failure of an infinite cracked panel, the curve need not be generated by fracture testing very large biaxially loaded cracked panels. Indeed, if this were the case, the theory would have little practical use. The ERBS curve may be generated by testing a variety of relatively simple, but different, coupon geometries (for example, pin-loaded edge-notched coupons) at various crack lengths. Configurations are chosen to vary K_I and T in such a manner as to provide coupons with a wide range of B values (see Eq 1). Each coupon that is tested provides only one point on the failure curve. A curve fit for a series of test results gives a mathematical expression for the shape of the ERBS curve.

Testing

To illustrate the similarities and differences between the LEFM and the ERBS failure criterions, and to demonstrate the accuracy of the ERBS approach, a series of fracture tests were conducted on various coupons of polymethyl methacrylate (PMMA). The 12.7-mm-thick PMMA used in this study meets the plane-strain thickness requirement specified in the ASTM Test Method for Plane-Strain Fracture Toughness of Metallic Materials (E 399-83) that thickness be greater than 2.5 K_{Ic}^2/σ_{ys}^2).

After numerically analyzing a number of geometries [4], four basic coupons were selected to be used for generating an ERBS curves for PMMA. These included the half-dogbone tension coupon (HDT), the elongated compact-tension coupon (76.2 mm CT), the standard compact-tension coupon (CT), and the wide compact-tension coupon (CT-50.8 mm) (Fig. 2). The results of the numerical analysis (seen in Tables 1 through 4) show that testing of these geometries over a wide range of crack lengths can give fracture results that may be used for creating ERBS curves with B values ranging from -1.56 to $+2.81$.

To evaluate the effectiveness of the ERBS curve for predicting failure in arbitrary coupons, various other specimen geometries were tested. These coupons included the single edge-notched coupon (SENT), the elongated compact-tension coupons (44.5 mm CT), and the delta coupons (DT = xx), seen in Fig. 3.

An MTS 880 test machine was used for the testing of all coupons. A clip gage was employed to measure the crack opening displacements (COD), and crack lengths were approximated through compliance equations. The load during precracking was reduced continuously to maintain a constant stress intensity factor, K_I.

In general, the test procedures specified in ASTM E 399-83 were used to find K_c for each geometry. Most coupons were fatigue precracked such that the maximum stress intensity of each cycle was less than 60% of the fracture toughness, K_c, for the last 2.5% of the precrack growth (as specified by ASTM E 399-83). Any test that exceeded this limit significantly was considered invalid. During fatigue precracking, the loading ratio was chosen to be 0.1, and the frequency was typically 30 Hz.

Just as in ASTM E 399-83, the critical stress intensity, K_Q, was calculated for each coupon. If the test results for a particular coupon met the validity requirements, the K_Q value was considered to be the fracture toughness, K_c. All PMMA results met the ASTM E 399-83 requirement that P_M/P_Q should be less than 1.1.

For each coupon, five crack length measurements were made as described in ASTM E 399-83 ($c1$ at the center, $c2$ and $c3$ at the midpoints between the surfaces and the center, and $c4$ and $c5$ on the surfaces). The crack length, c, used for the analysis, was the average of the three inner measurements ($c1$ to $c3$). According to ASTM E 399-83, for valid test results the crack front measurements must satisfy the following length, roundness, and symmetry requirements:

1. $0.45 < c/W < 0.55$,
2. $\max(|c1 - c2|, |c1 - c3|, |c2 - c3|) < 0.1c$,

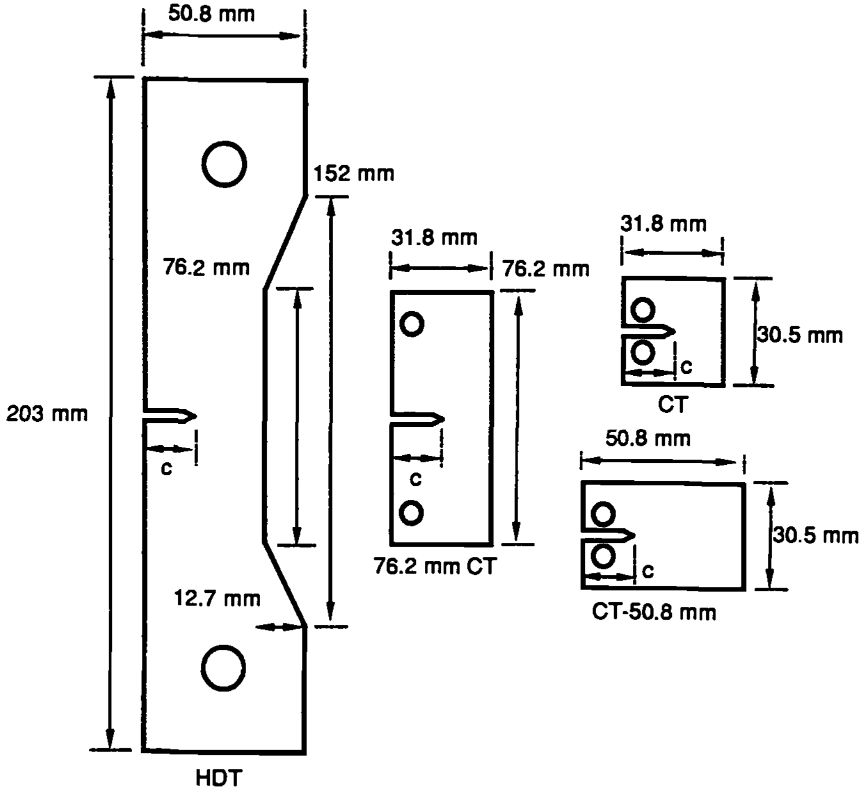

FIG. 2—*The four basic coupon geometries used in the test program (HDT, 76.2 mm CT, CT, and CT-50.8 mm).*

TABLE 1—*Numerical results for the HDT coupon.*

Crack Length, mm	K_I, MPa $\sqrt{m}$	T, MPa	B
5.6444	0.13033	−1.18194	−1.56441
6.3500	0.15825	−1.33618	−1.38765
7.7612	0.22429	−1.64921	−1.07926
9.1722	0.30225	−1.96480	−0.83818
10.5834	0.39867	−2.28238	−0.61883
11.9944	0.51105	−2.58969	−0.43292
12.7000	0.57496	−2.74090	−0.34801
14.8166	0.79819	−3.16687	−0.12190
15.8750	0.93305	−3.35393	−0.01644
16.9334	1.09308	−3.53321	0.08599
17.9916	1.28062	−3.68965	0.18530
19.0500	1.48455	−3.79873	0.27643
21.1666	2.02281	−3.89809	0.45508
22.2250	2.34955	−3.81376	0.54101
23.2834	2.77288	−3.64435	0.62836
24.3416	3.24088	−3.28312	0.71354
25.4000	3.86518	−2.73711	0.79976
26.8112	4.91022	−1.45940	0.91596
28.2222	6.34130	0.76555	1.03414
28.9278	7.23913	2.56218	1.10008

TABLE 2—*Numerical results for the 76.2 mm CT coupon.*

Crack Length, mm	K_I, MPa $\sqrt{m}$	T, MPa	B
9.1722	3.3665	−4.09949	0.65566
10.5834	3.8699	−3.30567	0.75846
11.9944	4.4585	−2.34954	0.85099
12.7000	4.7875	−1.78884	0.89434
13.8544	5.4176	−0.71963	0.96244
15.5865	6.5019	1.35032	1.05873
16.7409	7.4254	3.14419	1.11974
17.8956	8.5501	5.43802	1.17985
19.0500	9.9321	8.41259	1.23951
20.2044	11.6741	12.38811	1.30007
21.9365	15.3615	21.20585	1.39035
23.0909	18.8228	30.45101	1.45746
24.2456	23.6158	44.31368	1.53060
25.4000	30.6717	66.96727	1.61739

TABLE 3—*Numerical results for the CT coupon.*

Crack Length, mm	K_I, MPa $\sqrt{m}$	T, MPa	B
9.1722	3.6579	17.92279	2.38549
10.5834	4.2664	11.97951	1.79399
11.9944	5.0112	9.15973	1.51686
12.7000	5.4073	8.91255	1.46607
13.8544	6.0901	10.82356	1.50255
15.5865	7.3235	16.04473	1.61951
16.7409	8.2298	20.16374	1.69281
17.8956	9.2943	24.42892	1.74322
19.0500	10.5982	28.77470	1.76774
20.2044	12.2550	33.30189	1.76840
21.9365	15.8405	41.45598	1.74003
23.0909	19.3329	49.25306	1.72039
24.2456	24.2719	61.30503	1.71421
25.4000	31.7734	83.52465	1.74333

TABLE 4—*Numerical results for the CT-50.8 mm coupon.*

Crack Length, mm	K_I, MPa $\sqrt{m}$	T, MPa	B
11.9944	4.6684	10.41614	1.63091
12.7000	4.9711	10.41476	1.59242
13.8544	5.4530	12.79540	1.66351
15.5865	6.2254	18.95601	1.86102
16.7409	6.6594	23.86884	2.01351
17.8956	7.0641	28.99782	2.16075
19.0500	7.4497	34.16783	2.29691
20.2044	7.8258	39.20276	2.41652
21.9365	8.4127	46.57400	2.56545
23.0909	8.8217	51.20131	2.64120
24.2456	9.2519	55.64975	2.70085
25.4000	9.6869	59.93216	2.74947
26.9113	10.2874	65.38004	2.79710
28.1686	10.8253	69.60158	2.81808

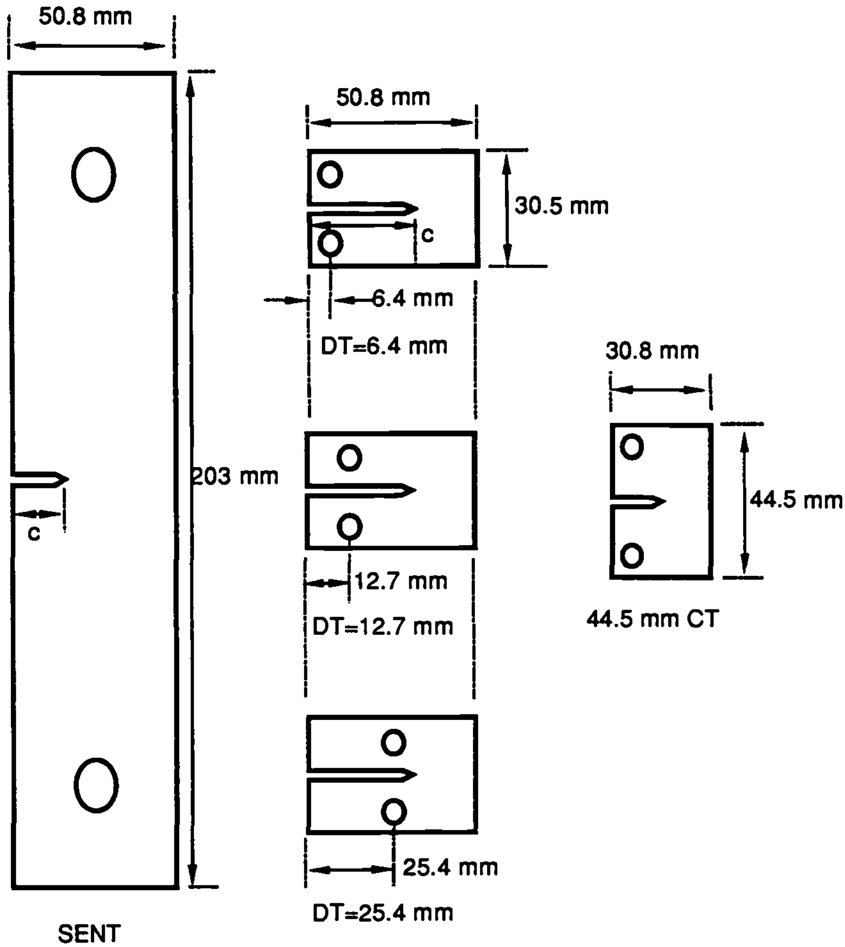

FIG. 3—*The SENT, DT = xx, and 44.5 mm CT coupons.*

3. min ($c1$,$c2$,$c3$,$c4$,$c5$) > (c + 1.3 mm),
4. max ($|c4 - c|$, $|c5 - c|$) < $0.15c$, and
5. $|c4 - c5| < 0.1c$.

where W is the width of the coupon.

For this study, however, to obtain fracture results for a wide range of B values, coupons with crack lengths shorter than $c/W = 0.45$ and longer than $c/W = 0.55$ were tested (contrary to Requirement 1). As can be seen, Guidelines 2, 4, and 5 are based on percentages of the crack length. These requirements are too restrictive for short cracks and too loose for long cracks for coupons of the same geometry. For example, consider Requirement 2 which states that the maximum difference between any two of the inner crack length measurements must be less than 10% of the average crack length. For a short crack, c = 5 mm, the maximum allowable difference would be 0.5 mm, whereas for a long crack, c = 20 mm, this maximum allowable difference would be 2 mm. It is recognized that these requirements are adequate for the restricted crack lengths required by ASTM E 399-83. However, if coupons with longer and shorter cracks are to be tested, it is recommended that the requirements be changed to be based on the fixed width of the coupon and not on the variable crack length. This would make the requirements equal for small and large cracks in coupons of the same geometry. For this study, the test was considered valid if the differences in Guidelines 2, 4, and 5 were less than 0.1 ($W/2$), 0.15 ($W/2$), and 0.1 ($W/2$), respectively.

Because nonstandard crack lengths were used in the test, it was necessary to ensure that the damage zone did not extend to the coupon boundary. The predicted plastic zone size for a plane-stress coupon is approximately 0.3 mm. The remaining ligament size of all test coupons was significantly larger than 0.3 mm.

Both K_I and the constant term, T, for each coupon were calculated using a modification of a numerical code written by Raju and Fichter [*6*]. The accuracy of this code was demonstrated in Ref *4*. From the numerical work, K_c and B were determined for each coupon geometry. In this study, c^* was chosen to be 25.4 mm as described in Ref *4*.

Experimental Results

The results of the experimental test program for PMMA will be presented using two different approaches. First, to demonstrate the limitations of the LEFM theory, the data will be analyzed using the assumption that K_{Ic} is a material constant. Next, the ERBS failure criterion will be presented and analyzed. To illustrate the similarities and differences between both theories, each fracture model will be discussed in detail.

LEFM

Assume that an accurate prediction of fracture toughness is required for the coupon geometries (with a range of crack lengths) seen in Figs. 2 and 3. These coupons, constructed of 12.7-mm-thick PMMA, fulfill the LEFM requirements for brittle plane-strain fracture (as pointed out earlier). Therefore, according to LEFM, failure should be predicted by a constant K_{Ic}, independent of crack length and geometry.

To find K_{Ic}, several tests were conducted using the guidelines specified in ASTM E 399-83. For each test, a critical load, P_Q, was found. This load (and the coupon geometry) was used to determine the critical stress intensity factor, K_Q. If the test conformed to the validity requirements specified in the standard, K_Q was then considered to be an accurate measure of the fracture toughness K_{Ic}. For this study, the fracture toughness of PMMA was found to be 1.018 MPa $\sqrt{m}$ (from fracture tests using CT coupons).

To evaluate the LEFM prediction that all planar PMMA cracked bodies of the same thickness should fail at $K_{Ic} = 1.018$ MPa $\sqrt{m}$, coupons of the geometries in Figs. 2 and 3 were next tested. The results of the tests are plotted in Fig. 4, where the horizontal line represents the predicted fracture toughness (1.018 MPa $\sqrt{m}$). Note the wide amount of scatter in the data. There is over 35% difference between the highest and lowest measured fracture toughness values. Some extreme cases of error in the failure predictions may be seen in the HDT and the SENT coupons. The HDT coupons have errors ranging from 23% below to 13% above the predicted K_{Ic}. The fracture toughness of the SENT coupons is 15% higher than the predicted toughness.

A statistical analysis of the results shows that the standard deviation (or standard error) is $\sigma = 0.110$ MPa $\sqrt{m}$. By using the Student t distribution, it can be shown that the test results have a 95% confidence level within a range of ± 0.181 MPa $\sqrt{m}$ from the predicted value. This means that the LEFM K_{Ic} approach predicts fracture 95% of the time to within $\pm 18\%$ error for this material.

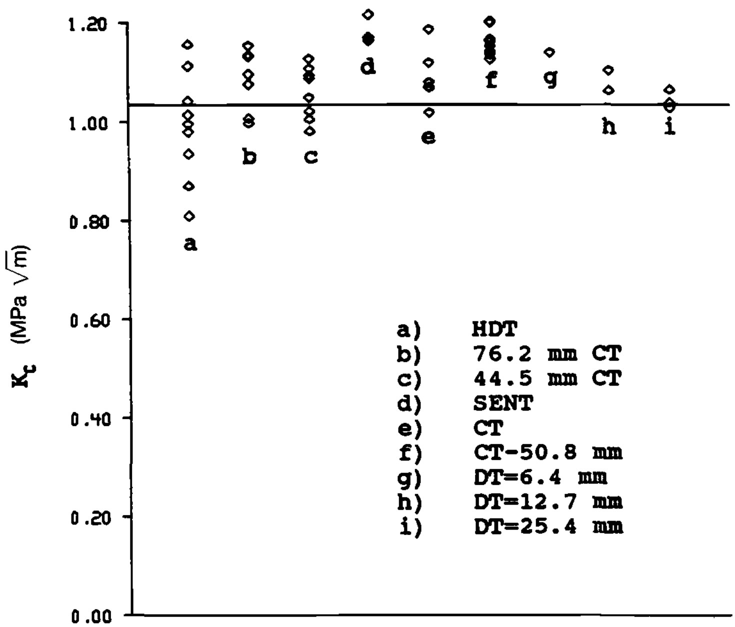

FIG. 4—*Fracture results of the PMMA coupons using the LEFM approach.*

Note that a wide range of crack lengths were tested for each coupon. This explains why there is so much scatter in the data. For the characterization of K_{Ic}, ASTM E 399-83 restricts the crack length to fall with the range $0.45 < c/W < 0.55$. If tests were conducted on the geometries specified earlier with such a limited range of crack lengths, the scatter would not be as large.

It is interesting to note that during fracture of the CT-50.8 mm coupons, the crack initially propagated at a small angle from the horizontal ($0° < \alpha < 5°$, Fig. 5). As fracture progressed in these coupons, the crack continued to turn until arm breakage occurred. This initial small-angle crack turning was also noted in some CT and DT coupons. The arm breakage was, however, found exclusively in the CT-50.8 mm coupons. These differences in crack propagation direction cannot be predicted by the single parameter K_{Ic}.

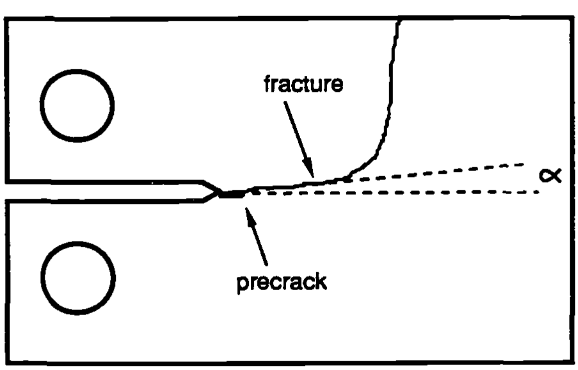

FIG. 5—*Crack turning in CT-50.8 mm coupons.*

ERBS

Now consider the ERBS approach for predicting failure in the PMMA coupons of Fig. 3. To make such predictions, it was necessary to generate the ERBS curve for PMMA. This required the testing of various coupons of different geometry (as opposed to one coupon geometry for LEFM). For this study, the specimens shown in Fig. 2, with a wide range of crack lengths, were chosen for generation of the ERBS curve. Tests of these coupons gave fracture results for $-0.57 < B < 2.81$. Each fracture test represented only one "calibration" point on the ERBS curve. Polynomial curve fits were made to these "calibration" data to give a mathematical expression for the ERBS curve.

The tests were conducted following the procedures specified by ASTM E 399-83 for K_{Ic} determination; however, nonstandard coupons were used, and the crack front validity requirements were altered as discussed in the previous section. From each test, a load-versus-COD curve was obtained, and the critical load, P_Q, was determined. If the results from a particular test were valid, K_Q was considered to be the fracture toughness, K_c, for the ERBS ratio, B, corresponding to the particular coupon geometry.

For clarity, first consider the test results of the HDT and the 76.2 mm CT coupons shown in Fig. 6. This region of the ERBS curve will be called Zone I. As seen in the figure, a second-order polynomial curve fits closely to these "calibration" data. A statistical analysis shows that a polynomial of this order gives the best fit to the data (the standard error, σ, is minimum).

Now consider the fracture results of the CT-50.8 mm coupons shown in Fig. 7. This part of the ERBS curve will be called Zone III. There are two points that seem to indicate that the failure mechanism in Zone III is different from that in Zone I. First, as seen in the figure, the shape of the ERBS curve within Zone I is dramatically different from the shape of the curve

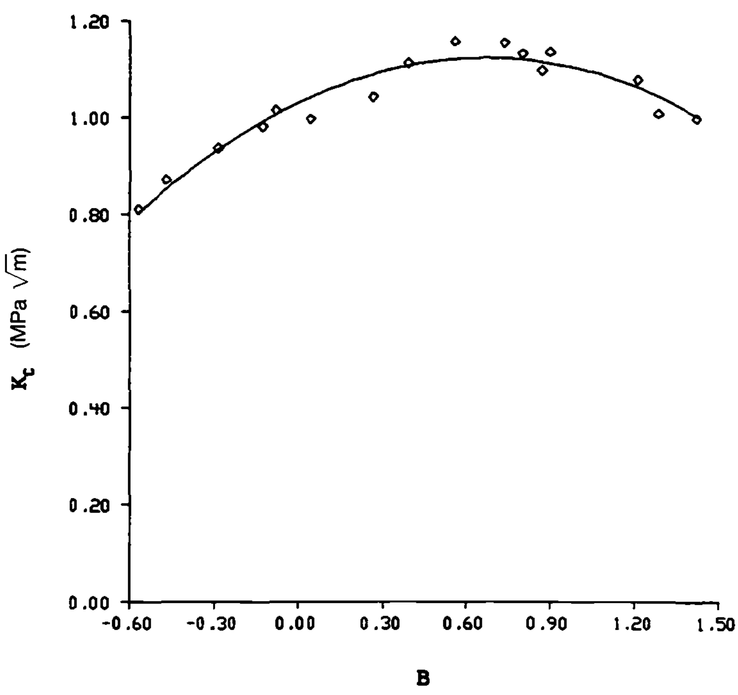

FIG. 6—*The Zone I ERBS curve for PMMA.*

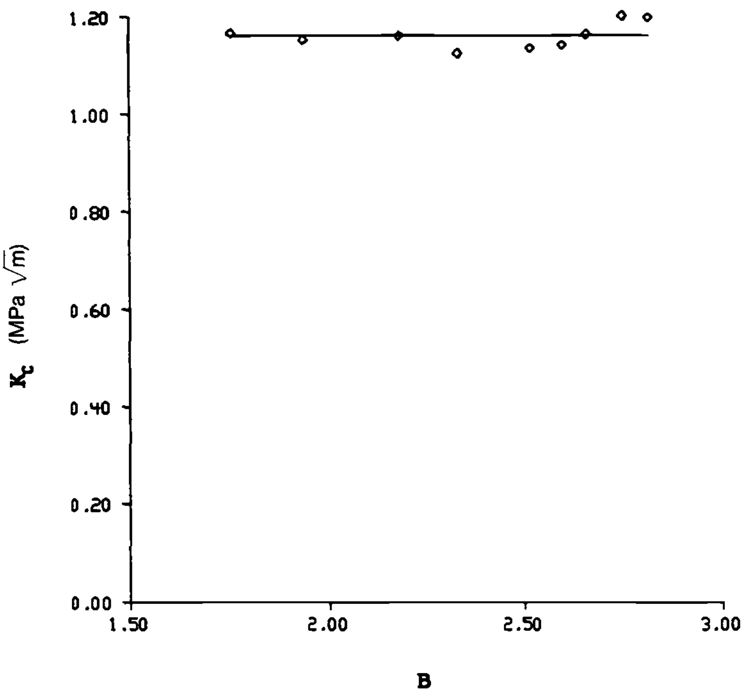

FIG. 7—*The Zone III ERBS curve for PMMA.*

inside Zone III. Second, the crack propagation direction appears to be different. Apparently, a crack-turning fracture mechanism occurs in Zone III, while Zone I exhibits a more stable transverse crack growth mechanism. Within Zone III, the critical stress intensity, K_c (because of crack branching K_c is not referred to as the fracture toughness), appears to be nearly constant (1.160 MPa $\sqrt{m}$). Therefore, an approach similar to that of LEFM for predicting fracture behavior may be used within this zone; however, a proper K_c must be found. Obviously, the fracture results from Zone I may not be used to predict accurately failure in Zone III (compare Figs. 6 and 7).

Zone II is a transitional region between Zone I and Zone III. This region is determined by the fracture results of the standard CT coupon. Within this zone, there is a considerable amount of scatter in the fracture results. It is interesting to note that small amounts of crack turning were seen in some, but not all of these coupons. The failure of coupons within Zone II may be predicted by an average critical stress intensity of 1.100 MPa $\sqrt{m}$.

These results support the conclusions of Betegon and Hancock [7] that J_{Ic} may be influenced by the constant term, within the region, $T < 0$ ($B < 1$). Note that Zone I falls within this region. They also hypothesized that J_{Ic} would be nearly constant for $T > 0$ ($B > 1$). This behavior was seen in Zone III. Betegon and Hancock did not present any experimental work to verify their predictions.

With the characterization of the fracture behavior of PMMA through the ERBS curve, a verification of the failure theory was made by predicting failure in the coupons of Fig. 3. The stress intensity factor, K_I, and the constant term, T, for each coupon geometry were determined numerically. From these parameters, B was calculated using Eq 1. The fracture toughness, K_c, for each B value was read from the ERBS curve. It was predicted that failure, in these coupons, would initiate when K_I reached this critical stress intensity factor, K_c. The major differences between this method for predicting fracture from the LEFM approach is that B is calculated and that the fracture toughness, K_c, is not a constant but changes with B.

When analyzed numerically, it was found that the SENT coupons and the 44.5 mm CT coupons have B values that fall within Zone I. The results of the fracture tests for these coupons are plotted in Fig. 8 along with the ERBS curve for Zone I. Note how closely these "verification" data fit the ERBS curve. The maximum percent error is 7% for one SENT coupon. All other results have error below 5.5%.

A statistical analysis for this zone determined that the standard error for this prediction is $\sigma = 0.0362$ MPa $\sqrt{m}$. This can be interpreted statistically to say that 95% of all Zone I fracture toughness test results will be predicted by the ERBS curve to within 6% error. The region of 95% confidence for the ERBS approach is nearly three times smaller than that for the LEFM method.

The DT = 6.4 mm and DT = 12.7 mm coupons have B values that fall within Zone III (Fig. 9). The maximum percent error is 6%. Statistically, the ERBS theory predicts the critical stress intensity factors within this region with the same amount of accuracy as seen in Zone I. As expected, these coupons exhibit small amounts of crack turning at initiation as did the CT-50.8 mm coupons.

The DT = 25.4 mm coupons fall within Zone II. Because of the scatter in this region, the accuracy of the ERBS theory, within this zone, is little better than that of the LEFM approach. Figure 8 is a plot of the complete ERBS curve along with all the fracture data. This figure clearly shows the transitional zone.

As can be seen from the results presented earlier, through the use of the ERBS curve, one can predict fracture behavior in PMMA more accurately than with the LEFM K_{Ic} approach (except within Zone II where they are nearly equal). Also, it seems that the curve may be used

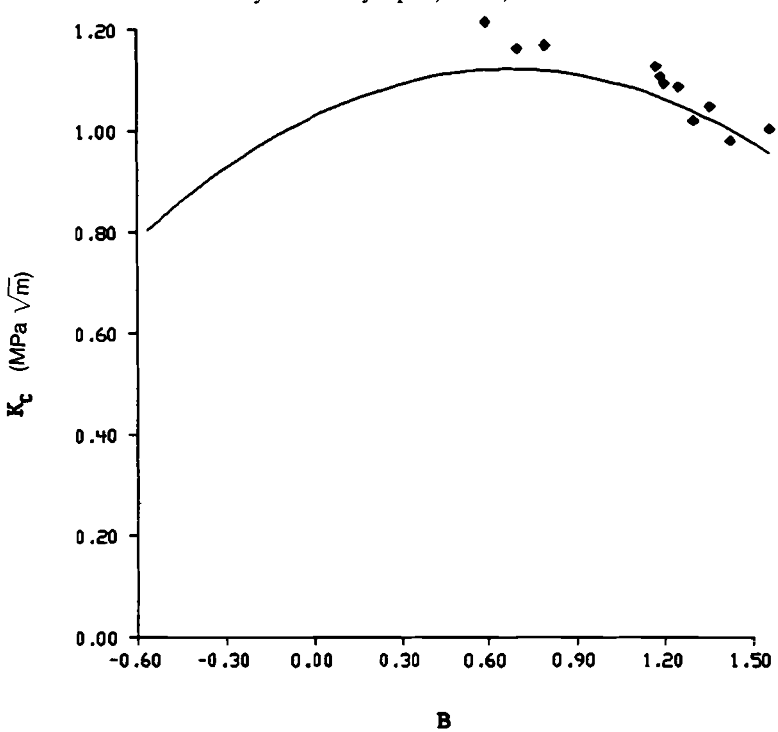

FIG. 8—*Fracture predictions within Zone I for PMMA.*

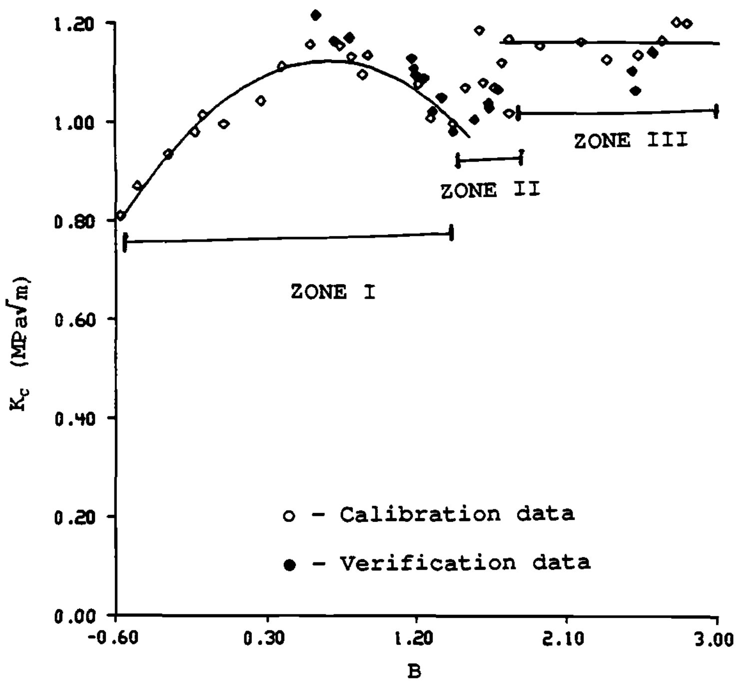

FIG. 9—*The complete ERBS curve and all PMMA fracture results.*

to predict the initiation of crack turning (Zone III). It should be noted that most of the testing procedures and many of the numerical analyses are simple extensions to the current LEFM approach.

It is interesting to note that the crack path stability criterion proposed by Cotterell [8] is not completely accurate for the coupons tested in this study. It is true that for values of $T < 0.0$ ($B < 1.0$) that no branching (Class I fracture) occurs. However, for $T > 0.0$ ($B > 1.0$), branching (Class II fracture) does not always occur. This is illustrated by the fracture behavior of the 76.2 mm CT specimens. These coupons exhibited no branching behavior although, in most cases, B was greater than 1.0 ($T > 0.0$).

Conclusions

It has been demonstrated clearly through the experimental results of this study that the LEFM assumption that fracture toughness is a constant material property may lead to inaccurate predictions of fracture behavior. As seen in the testing results, K_c can be strongly dependent on the geometry of a cracked body. Also, the LEFM approach cannot be used to predict differences in crack propagation direction at initiation.

This study has shown that the ERBS curve predicts fracture initiation with a 95% confidence zone that is nearly three times smaller than that of the LEFM approach. The experimental results also show that the theory does predict changes in fracture behavior due to differences in geometry. The ERBS concept also has the potential to predict crack branching. A major advantage of this theory is that many of the procedures and methods of analysis are the same as those used in the LEFM method.

Because the ERBS theory can account for differences in fracture behavior, these results verify the conclusions of various researchers, summarized by Eftis et al. [*1*], that the *T*-stress plays a significant role in fracture. The experimental results have also shown that the crack path direction stability criterion, suggested by Cotterell [*8*], may not be accurate in all cases.

Acknowledgments

This research was supported by E. I. Du Pont, Dr. E. Chen, monitor, and by NASA under Grant NAG-1-971, Dr. W. S. Johnson Jr., monitor.

References

[*1*] Eftis, J., Jones, D. L., and Liebowitz, H., "Load Biaxiality and Fracture: Synthesis and Summary," *Engineering Fracture Mechanics,* Vol. 36, No. 4, 1990, pp. 537–574.
[*2*] Kibler, J. J. and Roberts, R., "The Effect of Biaxial Stresses on Fatigue and Fracture," *Journal of Engineering for Industry,* Vol. 92, Nov. 1970, pp. 727–734.
[*3*] Albritton, J. R. and Goree, J. G., "Fracture of Silicon Carbide Whisker Reinforced Aluminum," *Proceedings,* Seventh International Conference on Fracture (ICF7), 20–24 March 1989, Pergamon, New York, pp. 889–896.
[*4*] Richardson, D. E., "A New Biaxial Stress Failure Criterion," Ph.D. thesis, Clemson University, Clemson, SC, Aug. 1991.
[*5*] Wu, E. M., "Fracture Mechanics of Anisotropic Plates, *Composite Material Workshop,* Technomic Publishing, Lancaster, PA, 1968, pp. 20–43.
[*6*] Raju, I. S. and Fichter, W. B., "A Finite-Element Alternating Method for Two Dimensional Mode I Crack Configurations," *Engineering Fracture Mechanics,* Vol. 33, No. 4, 1989, pp. 525–540.
[*7*] Betegon, C. and Hancock, J. W., "Two-Parameter Characterization of Elastic-Plastic Crack-Tip Fields," *Journal of Applied Mechanics,* Vol. 58, March 1991, pp. 104–110.
[*8*] Cotterell, B., "Notes on the Paths and Stability of Cracks," *International Journal of Fracture Mechanics,* Vol. 13, 1980, pp. 526–533.

Charles E. Harris[1] *and Don H. Morris*[2]

Translaminate Fracture of Notched Graphite/Epoxy Laminates

REFERENCE: Harris, C. E. and Morris, D. H., "**Translaminate Fracture of Notched Graphite/Epoxy Laminates,**" *Fracture Mechanics: Twenty-Third Symposium, ASTM STP 1189,* Ravinder Chona, Ed., American Society for Testing and Materials, Philadelphia, 1993, pp. 751–774.

ABSTRACT: The strength of three notched graphite/epoxy laminates has been shown experimentally to be a function of laminate thickness. The notched strength of the $[0/\pm45/90]_{ns}$ and $[0/90]_{ns}$ laminates decreased toward asymptotic values with increasing laminate thickness. Conversely, the notched strength of the $[0/\pm45]_{ns}$ laminate increased toward an asymptotic value with increasing laminate thickness. For all three laminate types, the notched strength decreased with increasing notch size, regardless of thickness. The fracture of the thick laminates were essentially uniform and self-similar with the notch. The "universal" value of the general toughness parameter, $Q_c/\epsilon_{tuf} = 1.5\sqrt{\text{mm}}$ $(0.30\sqrt{\text{in.}})$, developed by Poe successfully predicted the notched strength of the thick laminates. The strength of specimens with surface cuts was predicted using a linear elastic, homogeneous, isotropic fracture mechanics solution.

KEY WORDS: notched laminates, fracture, composite materials, thick laminates, fracture toughness, fracture mechanics, fatigue (materials)

Nomenclature

a	Crack half-length in center-cracked specimen; Crack depth in surface-notched specimen (semi-elliptic cut)
a_0	Characteristic distance for average stress model
B	Half width of surface-notched specimen
C	Half of surface crack length of semi-elliptic cut
COD	Crack opening displacement measured at notch centerline
d	Characteristic distance for inherent flaw model
d_0	Characteristic distance for point stress model
E_{11}	Elastic modulus of 0° ply
E_{22}	Elastic modulus of 90° ply
E_x	Laminate engineering modulus in loading (0° fiber) direction
E_y	Laminate engineering modulus in transverse (90° fiber) direction
F	Boundary correction factor for surface-notched specimen (semi-elliptic cut)
G_{12}	In-plane shear modulus of 0° ply
K	Stress intensity factor
K_Q	Stress intensity factor at failure
P	Load at catastrophic failure

[1] Branch head, Mechanics of Materials Branch, NASA Langley Research Center, Hampton, VA 23665-5225.

[2] Professor and assistant head, Department of Engineering Science and Mechanics, Virginia Polytechnic Institute and State University, Blacksburg, VA 24061-0219.

Q Shape factor for an elliptic crack
Q_c General [fracture] toughness parameter
S Far-field uniform tensile stress
t Thickness of laminate and test specimens
W Width of center-cracked specimen
Y Finite width correction factor for center-cracked specimen
α Fiber angle measured from the x-axis (loading direction)
σ_0 Unnotched laminate strength
σ_f Notched laminate strength
ν_{xy} Poisson's ratio of laminate
ν_{12} Poisson's ratio of 0° ply
ϵ_{tuf} Tensile ultimate fiber failing strain
ϕ Elliptic angle for semi-elliptic surface cut

The damage tolerance of laminated composite structures has been the subject of research for many years. A thorough review of notched strength prediction methodology, written by Awerbuch and Madhukar in 1985, is documented in Ref *1*. In spite of this extensive effort by the research community, rigorous mechanics-based damage tolerance prediction methodology still does not exist. Currently, there are extensive research efforts underway to develop finite-element-based progressive failure methodologies. However, the structural designer is still using the empirical notched strength models developed over a decade ago. In 1989, ASTM Committee E24 established a subcommittee on translaminate fracture. The increased emphasis on this topic by ASTM has provided the motivation for this paper.

A large comprehensive experimental program [*2*] was conducted in which the primary objective was the study of the effect of laminate thickness on the strength of notched laminated composites. A machined crack-like slit was selected for study. This notch simulates the damage produced by an engine blade penetrating a composite airframe structure such as the fuselage. The first phase of the research showed that laminate thickness affects both the type of fracture as well as the value of the notched strength.

There are several well-known macromechanical models that predict the strength of a laminate as a function of notch size. The inherent flaw model of Waddoups, Eisenmann, and Kaminski [*3*] and the point stress and average stress models of Whitney and Nuismer [*4,5*] are well known and have received considerable attention in the literature. The usefulness of the models to predict the notched strength of thin laminates with a variety of notch sizes and shapes has been investigated by Yeow, Morris, and Brinson [*6*]. The general toughness parameter model of Poe [*7,8*] was also successful in predicting the notched strength of thin laminates with a variety of laminate stacking sequences and material systems.

The purpose of this paper is to make an assessment of the applicability of several empirical-based failure criteria to predict the notched strength of thick laminates. The emphasis of this paper is not to evaluate the previously mentioned models with regard to predicting the notched strength of thin laminates. Rather, the objective is to utilize the thin laminate test results to determine the material property data required for the models and then use the models to predict the fracture strength of thick laminates. After a brief description of the failure models, the test program will be described along with the pertinent test results. This is followed by the predictions of strength as a function of notch size for both the thin and thick laminates of this study. Finally, a value of fracture toughness for thick laminates along with a linear elastic fracture mechanics approach will be used to predict the strength of a quasi-isotropic laminate with a surface cut. It is to be noted that the models are used only to predict notched strength. No attempt is made to model damage development and growth.

Notched Laminate Failure Models

Model Descriptions

The inherent flaw model [3] and the point and average stress models [4,5] are two parameter models utilizing a characteristic distance and the unnotched laminate strength to predict the notched laminate strength. A schematic of each model is shown in Fig. 1. The inherent flaw model is based on linear elastic fracture mechanics and uses an Irwin-type adjustment to the original crack length. The point stress and average stress models are strength criteria and postulate that fracture occurs when the stress at the characteristic distance from the notch tip equals the unnotched laminate strength. The Irwin-type adjustment (d) and the characteristic distances (d_0 and a_0) are computed from experimental values of notched and unnotched laminate strength as follows (see Refs 3, 4, and 5).

$$d = \frac{a}{\left(\frac{\sigma_0}{Y\sigma_f}\right)^2 - 1} \tag{1}$$

$$d_0 = a\left\{\left[a\left(\frac{Y\sigma_f}{\sigma_0}\right)^2\right]^{-1/2} - 1\right\} \tag{2}$$

$$a_0 = 2a\left\{\frac{\left(\frac{Y\sigma_f}{\sigma_0}\right)^2}{\left[1 - \left(\frac{Y\sigma_f}{\sigma_0}\right)^2\right]}\right\} \tag{3}$$

Equation 1 is for the inherent flaw model, and Eqs 2 and 3 define the point stress and average stress models, respectively. For these equations, a is the crack half-length, σ_f is the far-field uniform stress at failure (notched strength), Y is a finite-width correction factor, and σ_0 is the unnotched laminate strength. The finite-width correction factor is necessary since σ_f is found experimentally for finite-width plates, and the theoretical development of Eqs 1, 2, and 3 is for an infinitely wide plate. Thus, the term $Y\sigma_f$ is for a plate of infinite width. The three equations are for a uniaxially loaded tension specimen with a centrally located through-the-thickness crack that is perpendicular to the applied load.

The general fracture toughness parameter model [7,8] is based on a strain failure criterion. Laminate failure is postulated to occur whenever the fiber strains in the principal load carrying laminae reach a critical value. Using the plane stress, Mode I linear-elastic fracture mechanics expressions for strain in a singular zone at a crack tip of an orthotropic material, and the postulated strain failure criterion, a general fracture toughness parameter, Q_c, was defined as

$$Q_c = \frac{K_Q(\xi_1)_i}{E_x} \tag{4}$$

where K_Q is the stress intensity factor at failure, and for the i^{th} principal load-carrying ply

$$(\xi_1)_i = \left[1 - \nu_{xy}\sqrt{\frac{E_y}{E_x}}\right]\left[\sqrt{\frac{E_y}{E_x}}\sin^2\alpha + \cos^2\alpha\right] \tag{5}$$

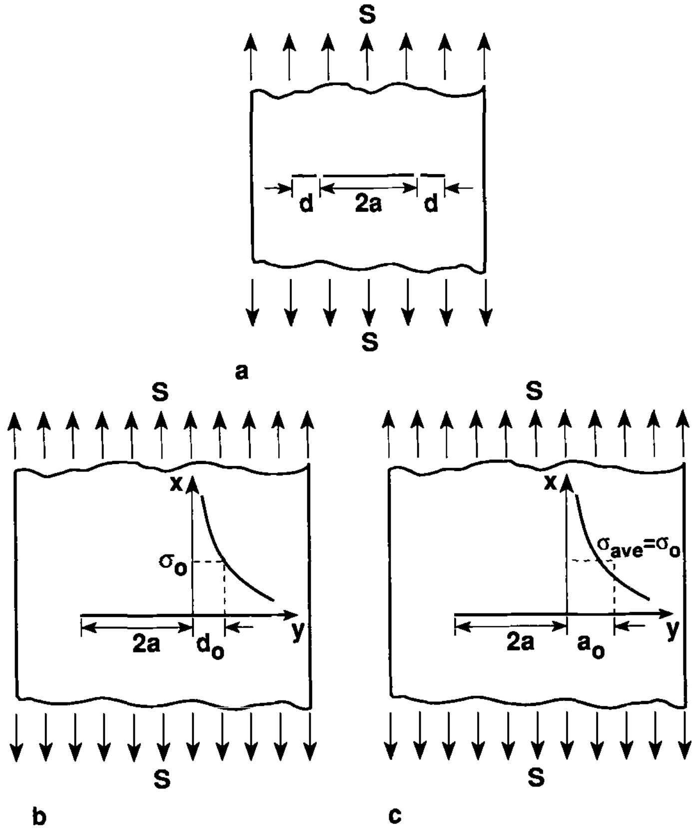

FIG. 1—*Schematic of two-parameter models for predicting notch strength:* (a) *inherent flow model,* (b) *point stress model, and* (c) *average stress model.*

In Eq 5, ν_{xy} is Poisson's ratio; E_x and E_y are the laminate stiffnesses (where x is the loading direction, Fig. 2); and α (measured from the x-axis) locates the fibers of the principal load-carrying laminae. For example, α is zero for a $[0/\pm45/90]_s$ laminate, and α is 45° for a $[\pm45]_s$ laminate. Poe [*7,8*] showed that Q_c is independent of laminate orientation, and when Q_c was divided by the ultimate tensile strain of the fibers, ϵ_{tuf}, the resulting ratio, Q_c/ϵ_{tuf}, was equal to $1.5\sqrt{\text{mm}}$ ($0.30\sqrt{\text{in.}}$). This value of the ratio was based on a statistical analysis of extensive experimental data for laminates of various laminate orientations, types of fibers, and matrix materials. The value, $1.5\sqrt{\text{mm}}$ ($0.30\sqrt{\text{in.}}$), was applicable to all the laminates investigated except those that split extensively at the crack tips or had other deviate failure modes than essentially self-similar crack growth. A more precise value of Q_c/ϵ_{tuf} for a given laminate could be obtained by using Eqs 4 and 5 along with experimentally determined values of K_Q.

Notched Strength

Once the values of the Irwin-type adjustment, the characteristic distances, or the ratio, Q_c/ϵ_{tuf} have been determined, the notched laminate strength for any notch size can be predicted

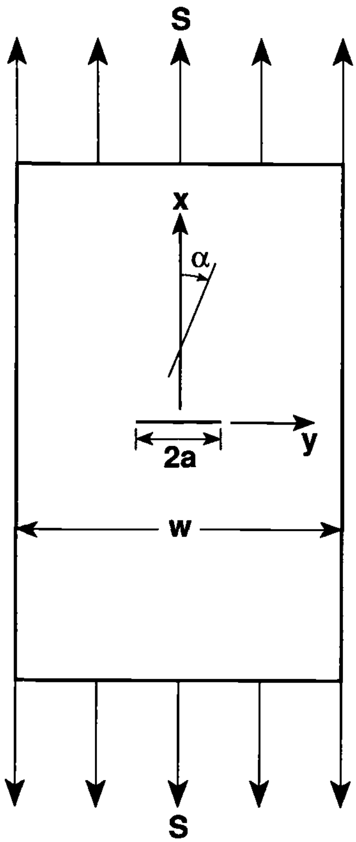

FIG. 2—*Geometry of the center-cracked tension specimen.*

using the following equations for the inherent flaw model, the point stress model, the average stress model, and the general fracture toughness parameter model, respectively.

$$\sigma_f = \frac{\sigma_0}{Y\left[\frac{a}{d} + 1\right]^{1/2}} \tag{6}$$

$$\sigma_f = \frac{\sigma_0}{Y}\left[1 - \left(\frac{a}{a + d_0}\right)^2\right]^{1/2} \tag{7}$$

$$\sigma_f = \frac{\sigma_0}{Y}\left[\frac{a_0}{2a + a_0}\right)^{1/2} \tag{8}$$

$$\sigma_f = \frac{\sigma_0}{Y}\{1 + \pi a[(\xi_1)_i\sigma_0/Q_cE_x]^2\}^{1/2} \tag{9}$$

The determination of the finite-width correction factor will be discussed in a later section.

Notched Strength for Semi-Elliptic Surface Cuts

Fracture toughness behaves much like a material property for the thick laminates [2]. To determine if this fracture toughness could be used to solve a problem of practical significance, a study of the fracture behavior of a thick laminate with a surface cut was undertaken. The specimen geometry is shown in Fig. 3. The quasi-isotropic $[0/\pm 45/90]_{10s}$ laminate with a semi-elliptic surface cut was selected since stress intensity factor solutions exist for an isotropic material with this notch geometry [9].

For finite-geometry plates with semi-elliptic surface cuts, subjected to remote tensile loading (S), the stress intensity factor (K) solution of Newman and Raju [9] is

$$K = S\sqrt{\pi a/Q}\, F(a/c, a/t, c/2B, \phi) \tag{10}$$

where a is the depth of semi-elliptic cut, c is the half of surface crack length, t is the specimen thickness, $2B$ is the specimen width, ϕ is the elliptic angle, Q is the shape factor for an elliptical crack, and F is a boundary correction factor. At failure, the stress intensity factor is the fracture toughness, K_Q, and the remote stress (S) is σ_f, the notched strength. To find the notched strength, Eq 10 is recast in the form

$$\sigma_f = K_Q/F\sqrt{\pi a/Q} \tag{11}$$

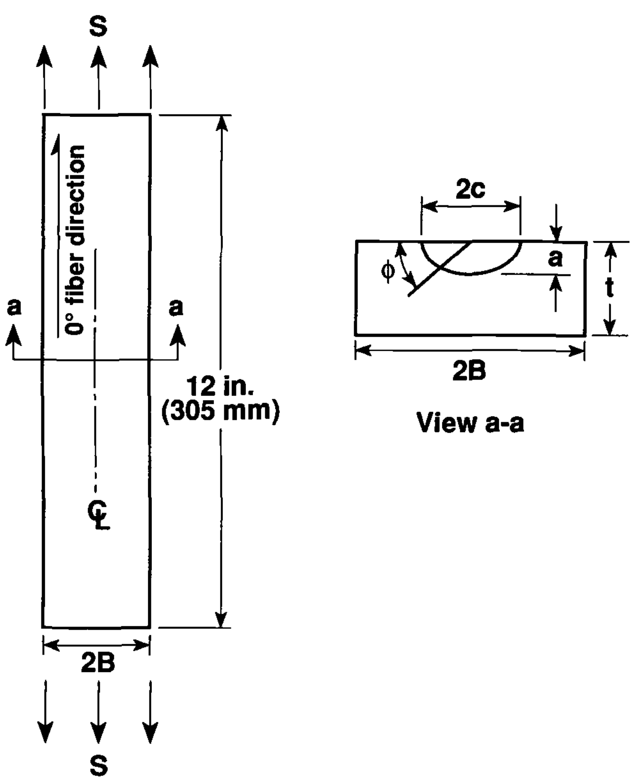

FIG. 3—*Geometry of the surface-notch test specimen.*

The boundary correction factor, F, is a function of ϕ, and thus the stress intensity factor varies along the border of the flaw. The maximum value of F, which occurs at $\phi = 0°$ or $90°$, was used in all calculations when predicting strength, just like in metals. Analytical expressions for Q and F are given by Newman and Raju [9].

Experimental Program

Material Properties

Graphite/epoxy (T300/5208) panels were prepared by a prepreg tape layup and autoclave curing process. The laminate stacking sequences were $[0/\pm45/90]_{ns}$, $[0/\pm45]_{ns}$, and $[0/90]_{ns}$ where ns means multiple layers with the same repeated sequence and is symmetric about the midplane. Laminate properties were computed from basic lamina properties by standard laminate equations [10]. The following basic lamina properties were experimentally measured

$$E_{11} = 20.1 \times 138.6 \text{ GPa } (10^6 \text{ psi})$$

$$E_{22} = 1.56 \times 10.76 \text{ GPa } (10^6 \text{ psi})$$

$$\nu_{12} = 0.318$$

$$G_{12} = 0.867 \times 5.98 \text{ GPa } (10^6 \text{ psi}$$

Subscript 1 refers to the fiber direction and Subscript 2 is the direction perpendicular to the fibers. The laminate stiffness values in the loading direction (0° fiber direction) were computed to be [2]

$[0/\pm45/90]_{ns}$ $E_x = 8.06 \times 55.6$ GPa (10^6 psi)

$[0/\pm45]_{ns}$ $E_x = 8.95 \times 61.7$ GPa (10^6 psi)

$[0/90]_{ns}$ $E_x = 11.07 \times 76.3$ GPa (10^6 psi)

Specimens were not available for determining the unnotched strength of the three laminates. However, since the stress-strain relationship for the laminates is essentially linear to failure, the unnotched laminate strength can be estimated by multiplying the stiffness in the loading direction by the failing strain. For similar laminates, the failing strain was approximately 1.0% [11]. Thus, the unnotched laminate strength (σ_0) values are

$[0/\pm45/90]_{ns}$ $\sigma_0 = 556$ MPa (80.6 ksi)

$[0/\pm45]_{ns}$ $\sigma_0 = 617$ MPa (89.5 ksi)

$[0/90]_{ns}$ $\sigma_0 = 763$ MPa (110.7 ksi)

This approach does not result in precisely determined values of unnotched strength. However, the approach is considered to be acceptable because these values are only used herein in a relative fashion to normalize the notched laminate strength.

The value of fracture toughness to be used in Eq 11 to compute the notched strength of the surface cut specimens was determined to be 1043 MPa $\sqrt{\text{mm}}$ (30 ksi $\sqrt{\text{in.}}$) [2].

Test Matrix

All tests using center-cracked tension specimens (Fig. 2) were 50.8 mm (2 in.) wide and 203 mm (8 in.) long. The center cracks and surfaces cuts were machined slots of width 0.406 mm (0.016 in.) cut by an ultrasonic vibration technique. No attempt was made to sharpen the ends of the slot.

The specimen thickness and crack length-to-width ratio, $2a/W$, were test variables. For the $[0/\pm 45/90]_{ns}$ and $[0/90]_{ns}$ laminates, the thicknesses were 8, 32, 64, 96, and 120 plies. The thicknesses were 6, 30, 60, 90, and 120 plies for the $[0/\pm 45]_{ns}$ laminate. The per-ply thickness was approximately 0.127 mm (0.005 in.). However, the measured thickness was used in all calculations. At the six- or eight-ply thickness for each laminate type the $2a/W$ values were 0.25, 0.375, 0.50, and 0.625. These same values were used for the $[0/\pm 45/90]$ 120-ply laminate, the $[0/90]$ 96-ply laminate, and the $[0/\pm 45]$ 90-ply laminate. Otherwise, the $2a/W$ ratio was 0.50. Four replicate tests were conducted at each test condition.

Fracture Test Procedure

The tests were conducted at a constant crosshead displacement rate of 0.02 mm/s (0.05 in./min). The specimen ends were held in 50.8 mm (2 in.) wide, wedge-action friction grips such that the specimen length between grips was approximately 127 mm (5 in.). End tabs were not used; sandpaper was placed between the grips and specimen. The thin specimens, six or eight plies, were supported with an antibuckling device to prevent out-of-plane displacements. Recorded test data included a plot of the crack-opening displacement (COD) at the crack centerline measured by a split ring gage versus applied load.

Determination of Notched Laminate Strength

In order to compare experimental strength values of notched finite-width specimens to analytically predicted values for infinite-width plates, the effect of the finite width of the specimens must be taken into account. The notched laminate strength is normally expressed as $Y\sigma_f$, where Y is the finite-width correction factor and σ_f is the far-field failure stress for a finite-width specimen. A finite-element stress analysis [2] yielded anisotropic stress intensity factors that did not differ significantly (less than 8%) from the isotropic values. Therefore, the following isotropic expression for Y was used for the center-cracked tension specimen [12]

$$Y = 1 + 0.1282(2a/W) - 0.2881(2a/W)^2 + 1.5254(2a/W)^3 \tag{12}$$

where $2a$ = crack length and W = specimen width.

The failure stress was computed using the equation, $\sigma_f = P/Wt$, where P is the load at catastrophic failure and t is the specimen thickness.

Test Results

The Thickness Effect

The load-COD record of a $[0/\pm 45/90]_s$ specimen is shown in Fig. 4. This record is typical for thin laminates and exhibits several discontinuities. These "COD jumps" correspond to the formation of subcritical crack-tip damage [2]. For example, the X-ray radiograph in Fig. 5

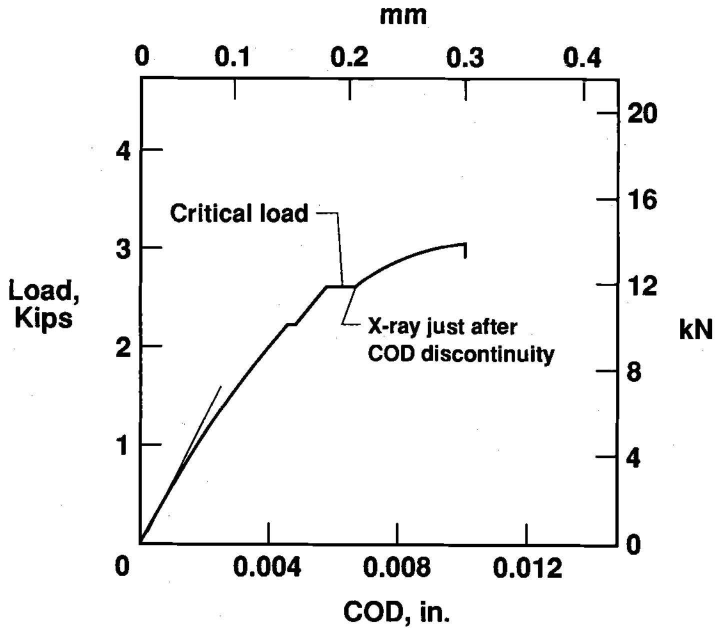

FIG. 4—*Typical load versus COD for a center-cracked tension specimen under stroke control.*

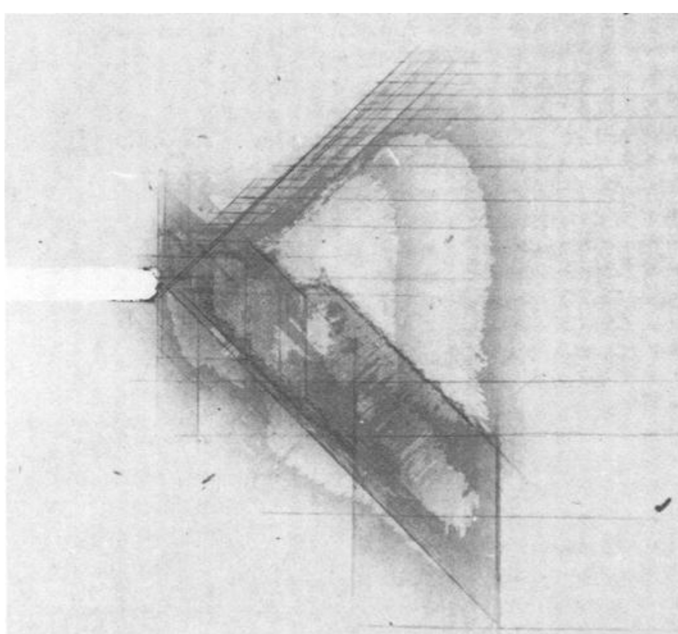

FIG. 5—*X-ray radiograph of the crack-tip damage just after a large COD discontinuity.*

shows the crack-tip damage state associated with the large COD jump shown in Fig. 4. All three laminate types exhibited substantial crack-tip damage prior to fracture. (The nature of the damage was studied using the nondestructive enhanced X-ray technique [*13*] and the destructive deply technique [*14*].)

The crack-tip damage resulted in natural crack-tip blunting and increased the resistance to crack growth. This was especially the case in the $[0/90]_{2s}$ laminate where long axial matrix splits formed in the 0° plies adjacent to the crack tip. These splits, shown in Fig. 6, significantly

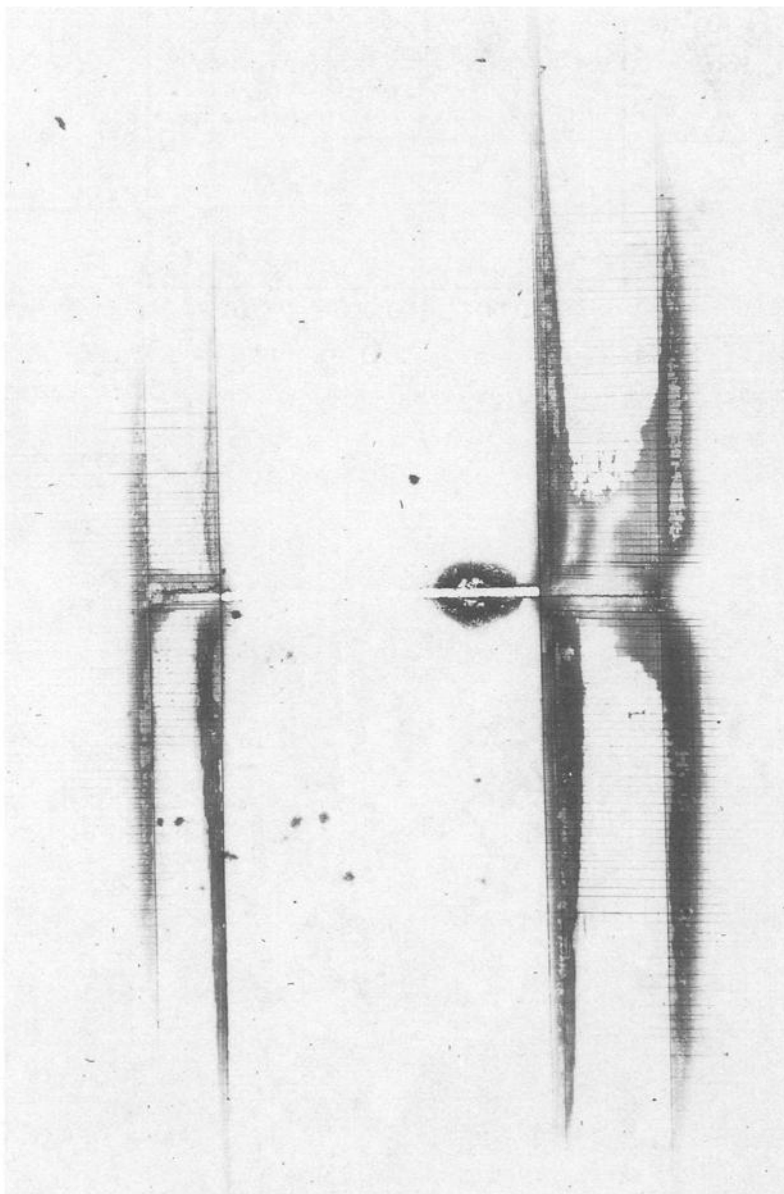

FIG. 6—*Crack-tip damage in the eight-ply* $[0/90]_{2s}$ *specimen at 92% of failing load.*

reduced the strength of the crack-tip singularity and elevated the fracture strength. The final fracture surfaces shown in Figs. 7 through 9 for the $[0/\pm45/90]_s$, $[0/90]_{2s}$, and $[0/\pm45]_s$ laminates, respectively, exhibit the effects of ply uncoupling due to delamination and substantial matrix cracking. This is especially evident in the fracture of the $[0/\pm45]_s$ laminate, Fig. 9. The two interior $-45°$ plies are uncoupled completely from the adjacent $+45°$ plies by delaminations at the $+45°/-45°$ interface. Laminate failure occurred more-or-less simultaneously with the development of sublaminate damage. The 45° plies failed by a matrix crack extending from the notch to the specimen edge. Broken fibers in the outside 0° plies extended in a $+45°$ line from the crack tip parallel to the matrix crack in the adjacent $+45°$ plies.

The effect of laminate thickness on the fracture strength of the three laminate types is illustrated in Fig. 10, for $2a/W = 0.50$. Notched strength is affected by thickness, and exhibits nearly asymptotic behavior with increasing thickness. Because of the thickness direction constraint in the thicker laminates, the substantial delamination and matrix splitting described earlier for the thin laminates were confined to a surface boundary layer in the thick laminates. Deply examinations of the thick laminates [2] confirmed the absence of delaminations and

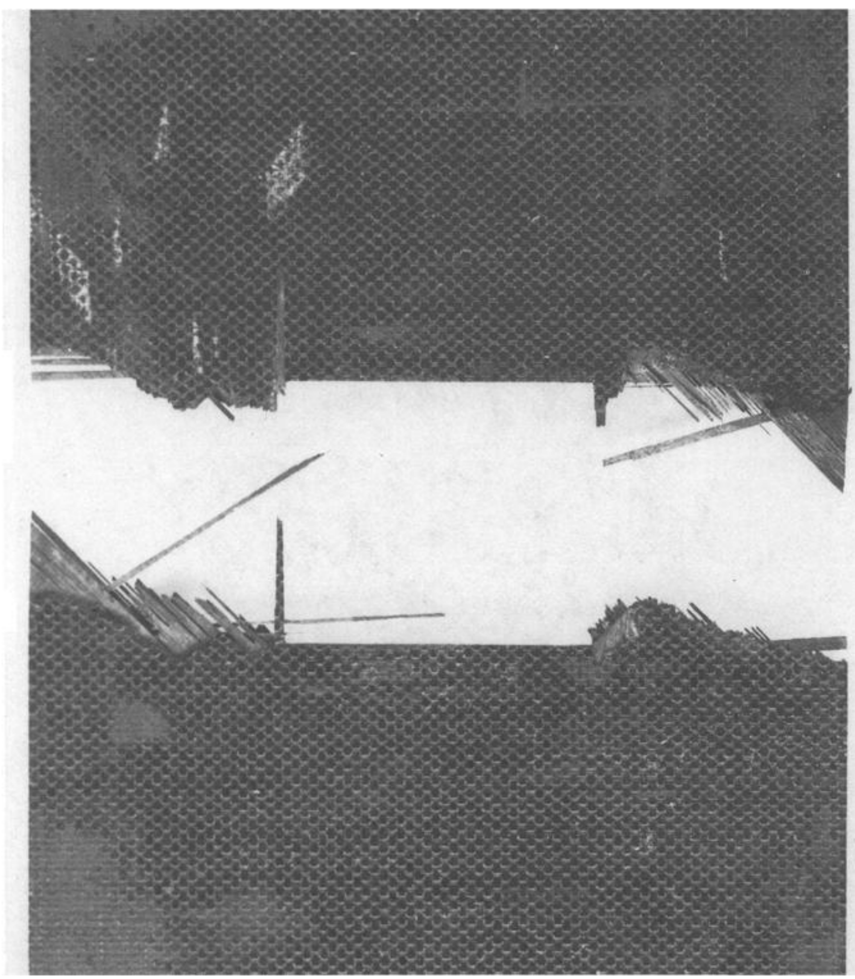

FIG. 7—*Photograph of the fracture surface of an eight-ply* $[0/\pm45/90]_s$ *specimen.*

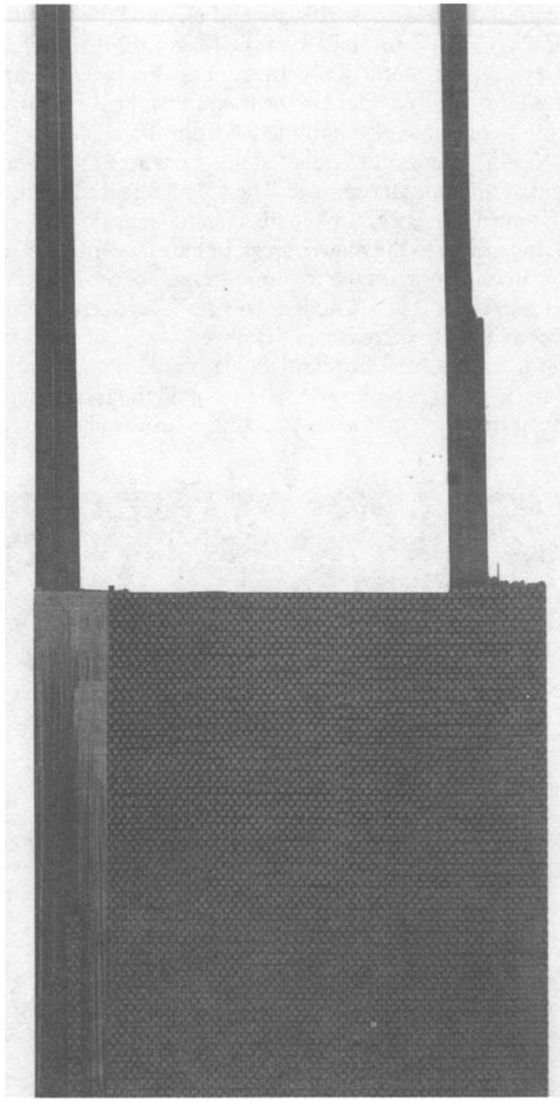

FIG. 8—*Photograph of a fractured eight-ply* $[0/90]_{2s}$ *specimen.*

matrix splitting in the specimen interior that would lead to substantial natural crack tip blunting. The final fracture of the thick laminates, shown in Figs. 11 through 13, is characterized by a fairly uniform fracture in the specimen interior that is practically collinear with the original notch. The surface boundary layer effect is illustrated clearly by the nonself-similar damage at the surfaces.

The notched strength of the quasi-isotropic laminates, $[0/\pm45/90]_{ns}$, decreased with increasing laminate thickness but approached a lower bound asymptotic value. This trend is very similar to the effect of specimen thickness on the fracture of homogeneous metals. Also, both the thin and thick laminates fractured in a self-similar manner as illustrated in Figs. 7

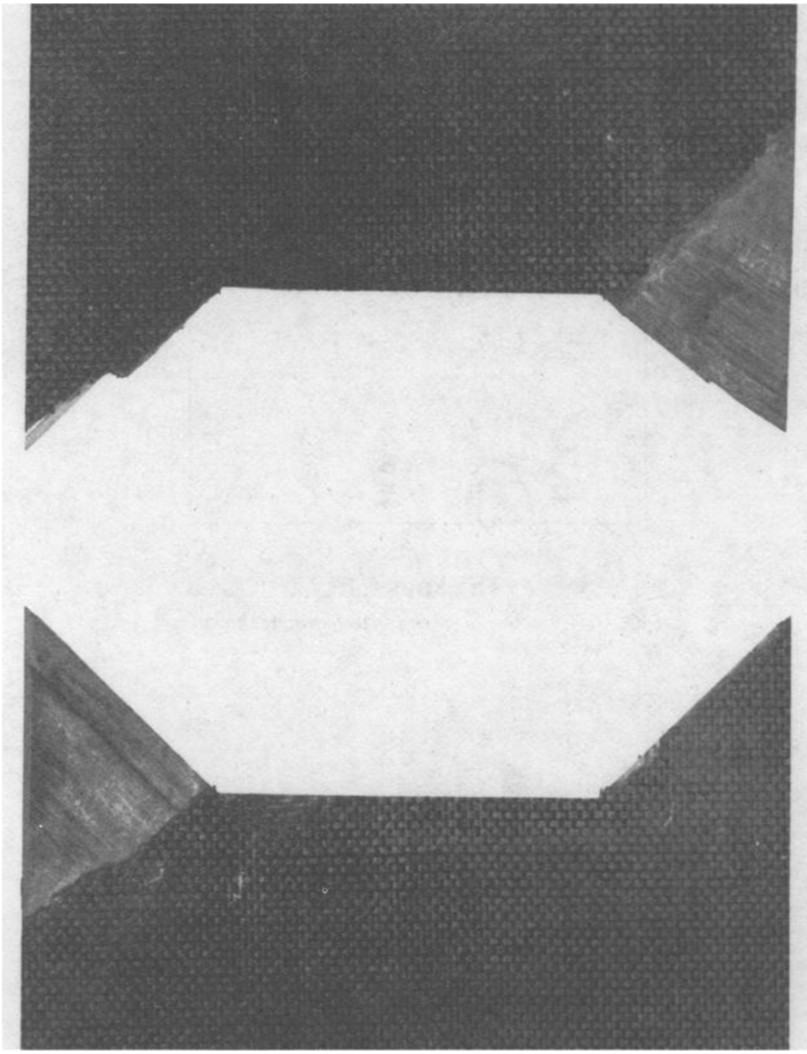

FIG. 9—*Photograph of a fractured six-ply* $[0/\pm 45]_s$ *specimen.*

and 11. This suggests that a fracture mechanics approach may be useful to predict the residual strength of quasi-isotropic laminates.

In the case of the $[0/90]_{ns}$ laminates, Figs. 8 and 12, axial splitting at the crack tip in the 0° plies was confined to the surface ply. These splits had no effect on the fracture of the thick laminates, whereas they dominated the fracture of the thin laminates by diminishing the strength of the crack-tip singularity. This resulted in the dramatic reduction in notched strength with increased thickness shown in Fig. 10.

The thickness constraint in the interior of the $[0/\pm 45]_{ns}$ specimens prevented the delamination and uncoupling mechanism from taking place in the thick specimens, as illustrated in Figs. 9 and 13. Fibers broke in all the plies of the thick specimens rather than just the two 0°

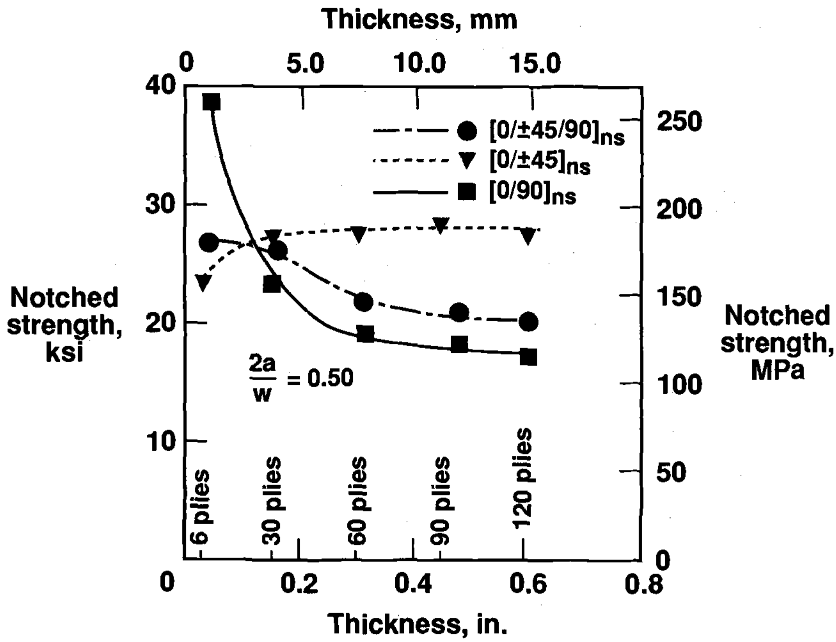

FIG. 10—*Notched strength versus laminate thickness.*

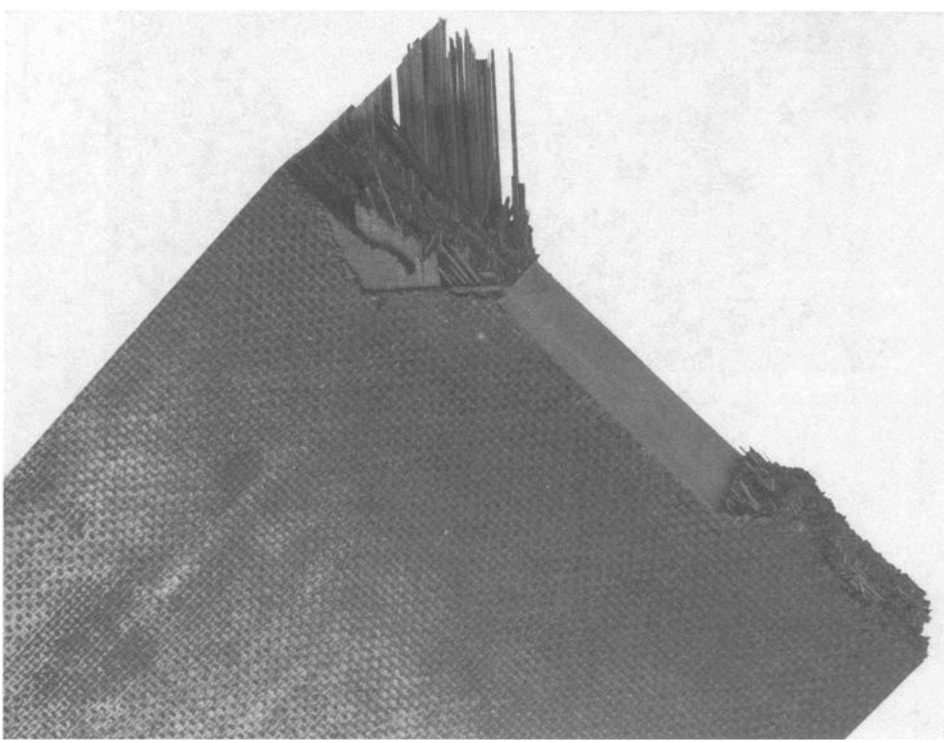

FIG. 11—*Photograph of the final fracture surface of a 120-ply* $[0/\pm 45/90]_{15s}$ *specimen.*

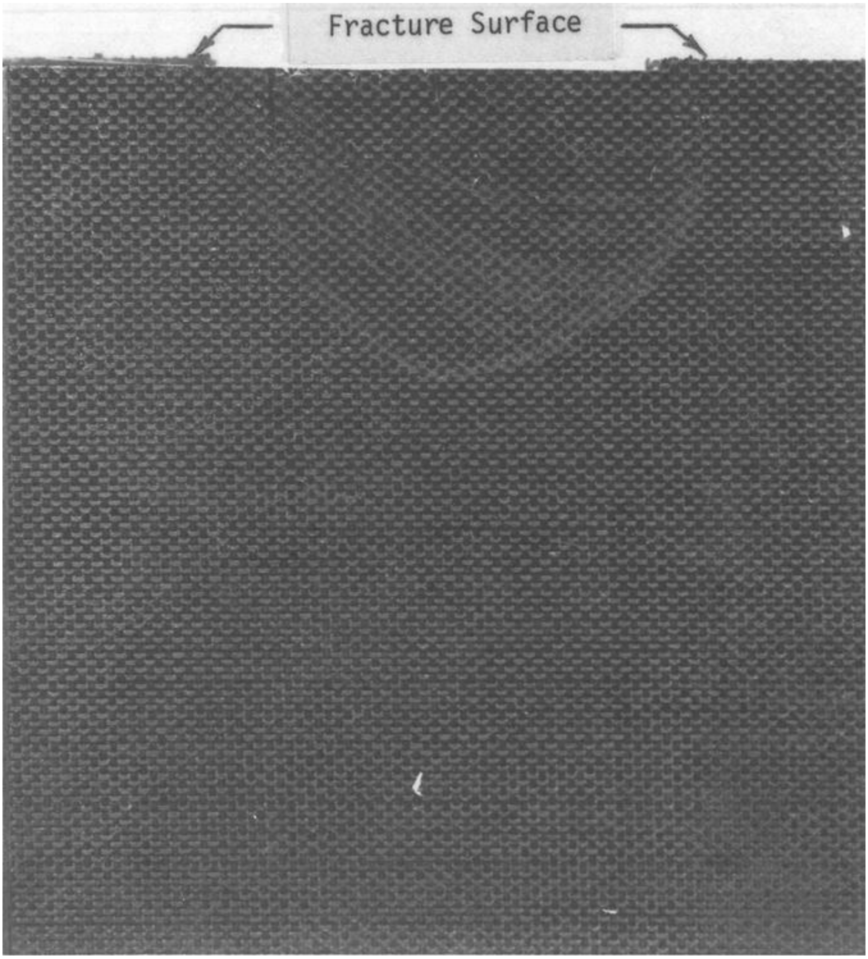

FIG. 12—*Photograph of the fracture surface of a 120-ply* $[0/90]_{30s}$ *specimen.*

surface plies as was the case for the $[0/\pm45]_s$ laminate. This would require greater fracture energy and is believed to be the reason the notched strength initially increased with increasing laminate thickness, as shown in Fig. 10. A more complete description of the laminate thickness effect can be found in Ref *2*.

The Notch-Size Effect

The effect of notch size on laminate strength is shown in Figs. 14 through 16 for the $[0/\pm45/90]_{ns}$, $[0/\pm45]_{ns}$, and $[0/90]_{ns}$ laminates, respectively. The experimental values of the strength were adjusted for finite-width effects and normalized by the unnotched strength, which was assumed independent of thickness. (The strength models shown in these figures will be discussed in the next section.) The reduction in strengths with increasing notch size is similar for the thin and thick laminates of the $[0/\pm45/90]_{ns}$ and $[0/\pm45]_{ns}$ types.

The strength data for the $[0/90]_{2s}$ laminate exhibit the influence of the axial splits that

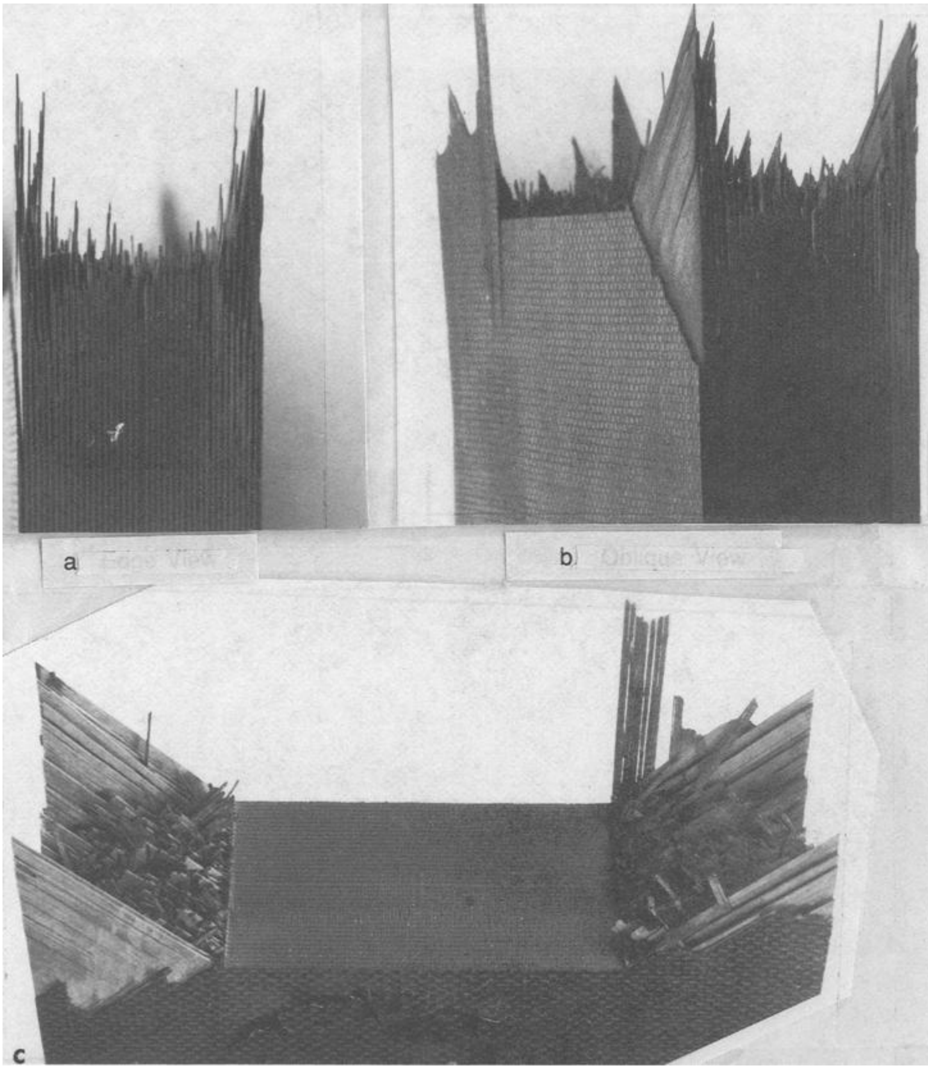

FIG. 13—*Photographs of the fracture surface of several 120-ply* $[0/\pm45]_{20s}$ *specimens:* (a) *edge view,* (b) *oblique view, and* (c) *oblique view.*

formed at the crack tip. Specimens with longer cracks were more susceptible to axial splitting than those with shorter cracks. Therefore, the strength of the laminates with the longer cracks are somewhat more elevated than would otherwise be the case. The influence of the axial splits is easily visualized by comparing the experimental values of strength (shown in Fig. 17) that were computed using the load at the onset of splitting, and the critical load (as shown schematically in Fig. 4) to those of Fig. 16 that were computed using the failing load. (The strength at the onset of splitting was determined from the load at the first COD discontinuity.) By taking out the influence of the axial splits, the strength of the $[0/90]_{2s}$ laminate decreases with increasing crack size just like the other two laminate types.

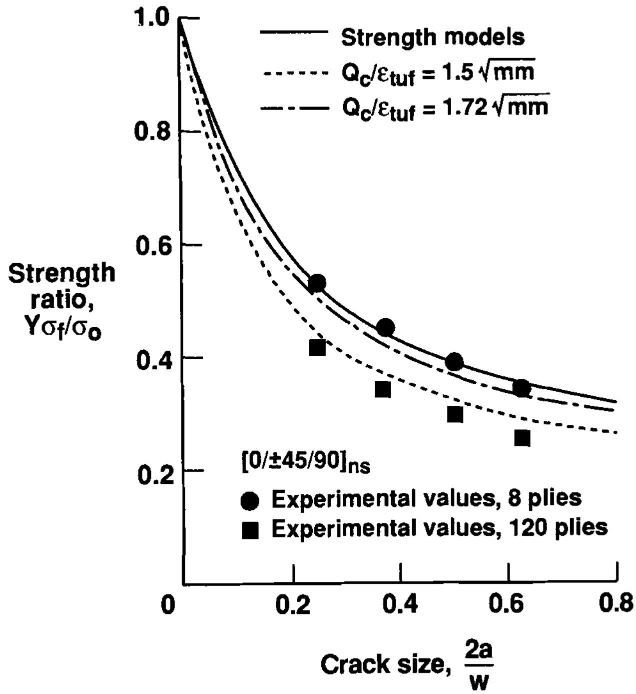

FIG. 14—*Experimental and analytically predicted values of residual strength versus crack size for the* $[0/\pm 45/90]_{ns}$ *laminate.*

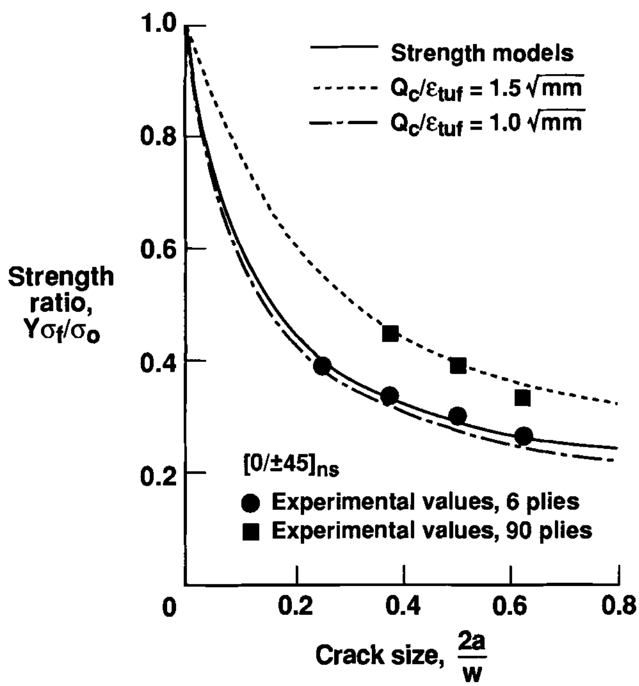

FIG. 15—*Experimental and analytically predicted values of residual strength versus crack size for the* $[0/\pm 45]_{ns}$ *laminate.*

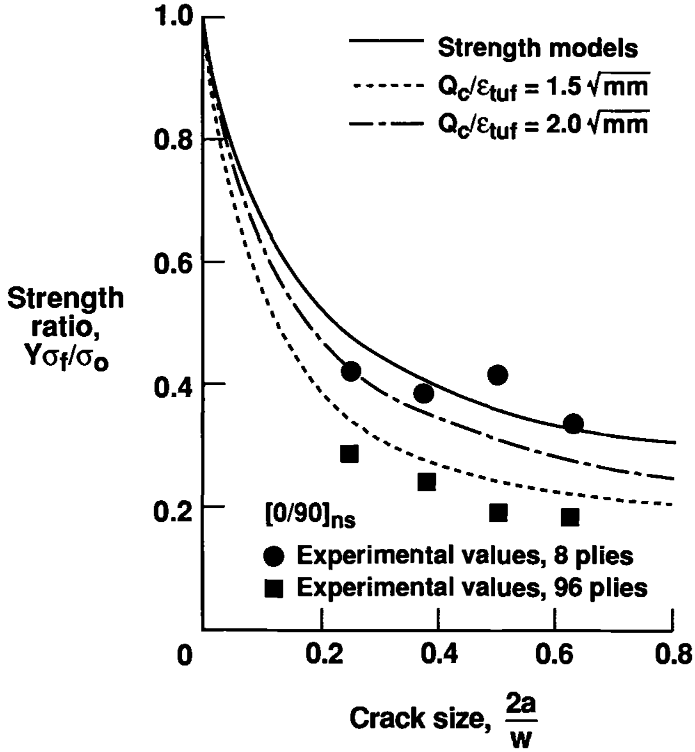

FIG. 16—*Experimental and analytically predicted values of residual strength versus crack size for the* $[0/90]_{ns}$ *laminate at the maximum test load.*

Prediction of Notched Laminate Strength

Predicted Strength of Thin Laminates

The experimental values of the notched strength of thin laminates, along with Eqs 1, 2, and 3, were used to compute the characteristic distances for the inherent flaw, the point stress, and the average stress failure models. Shown in Table 1 are the average values of characteristic distance for the four notch sizes for the thin laminates. Using these values and Eqs 6 through 8, one can determine the strength as a function of notch size.

There was no significant distinction between the prediction curves of the inherent flaw, point stress, and average stress models. Therefore, they are represented by the solid line in Figs. 14 through 16 for the $[0/\pm45/90]_s$, $[0/\pm45]_s$, and $[0/90]_{2s}$ laminates, respectively. (These three models are collectively referred to hereinafter as the "strength models.") The strength models accurately predicted the strength of the eight-ply $[0/\pm45/90]$ and six-ply $[0/\pm45]$ laminates. Because of the influence of axial splitting in the eight-ply [0/90] laminate, the predicted strength is not in good agreement with the experimental values. However, as Fig. 17 illustrates, the strength at the onset of splitting in the $[0/90]_{2s}$ laminate is accurately predicted by the strength models when using the appropriate values of characteristic distance. This distance was determined using Eqs 1 through 3 and the stress, σ_f, at the load at the onset of splitting. It should be noted that the "general toughness parameter" model does not apply to predict the onset of splitting. Therefore, the good agreement shown in Fig. 17 is fortuitous.

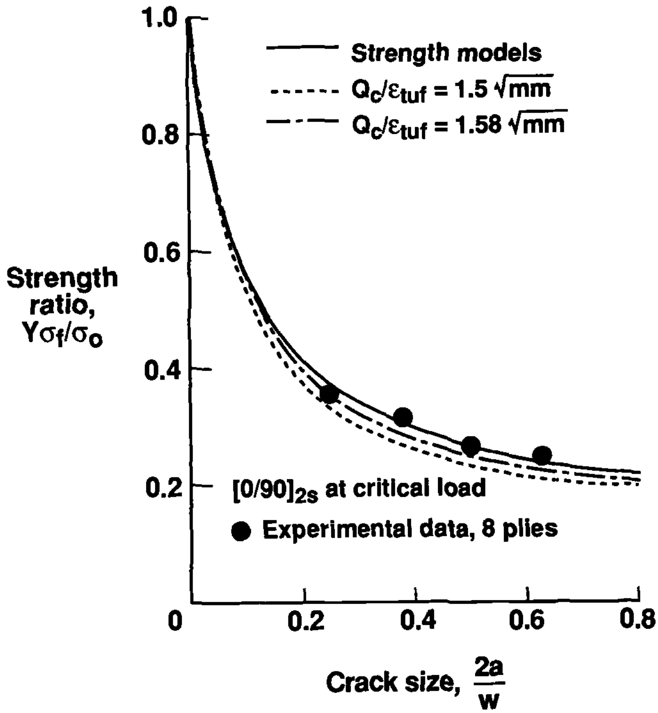

FIG. 17—*Experimental and analytical predictions of the residual strength versus crack size for the* $[0/90]_{ns}$ *laminate at the critical load.*

The thin laminate data were also used to calculate values of the general toughness parameter using Eqs 4 and 5. The average values of Q_c/ϵ_{tuf} computed for the four notch sizes were 1.72, 1.00 and 2.00 $\sqrt{mm}$ (0.341, 0.198, and 0.397 $\sqrt{in.}$) for the $[0/\pm45/90]_s$, $[0/\pm45]_s$, and $[0/90]_{2s}$ laminates, respectively. Strength as a function of notch size was computed using these values of Q_c/ϵ_{tuf} and Eq 9. These predictions are represented by the "dot-dashed" lines in Figs. 14 through 16. Also shown for comparison purposes is the predicted strength using the average general toughness value of 1.5 $\sqrt{mm}$ (0.30 $\sqrt{in.}$) from Ref 7. The average value did not yield

TABLE 1—*Average values of characteristic distances.*

Characteristic Distance	$[0/\pm45/90]_s^a$, mm (in.)	$[0/\pm45]_s^a$, mm (in.)	$[0/90]_{2s}^a$, mm (in.)	$[0/90]_{2s}^b$, mm (in.)
Inherent flaw model, d	2.39 (0.094)	1.20 (0.047)	1.93 (0.076)	1.04 (0.041)
Point stress model, d_0	1.12 (0.044)	0.58 (0.023)	0.91 (0.036)	0.51 (0.020)
Average stress model, a_0	4.75 (0.187)	2.39 (0.094)	3.86 (0.152)	2.06 (0.081)

[a] Evaluated at failing load (total fracture).
[b] Evaluated at onset of splitting.

accurate predictions of strength for the thin laminates. When the average values of Q_c/ϵ_{tuf} determined from the experimental data were used, the general toughness parameter model accurately predicted the strength of the $[0/\pm 45/90]_s$ and $[0/\pm 45]_s$ laminates. The strength of the $[0/90]_{2s}$ laminate was not accurately predicted because of the crack-tip splitting.

Predicted Strength of Thick Laminates

As was stated earlier, the approach employed herein was to determine the parameters of the failure models from the thin laminate data (previous section) and utilize those values to predict the strength of the thick laminates. Because the strength models (inherent flaw, point stress, average stress) are not explicitly a function of laminate thickness, there are no available modifications in form to account for the thickness effect. Furthermore, in the absence of unnotched strength as a function of thickness, it does not seem appropriate to compute characteristic distances from the thick laminate data. Therefore, no modifications to the strength models are available to account for the thickness effect. The experimental strength values for the thick laminates are shown in Figs. 14 through 16. The strength models overestimate the strength of the $[0/\pm 45/90]_{15s}$ and $[0/90]_{30s}$ laminates and underestimate the strength of the $[0/\pm 45]_{15s}$ laminate.

The general toughness parameter model is based on a strain criterion and was developed for a homogeneous, orthotropic laminate in a condition of plane stress. An obvious modification to account for the thickness effect is to modify the form of Eqs 4 and 5 for a plane-strain constitutive relationship. Assuming that plane-strain conditions do exist in the thick laminate, this modification to the value of Q_c/ϵ_{tuf} would be 5.7%, 3.5%, and 9.2% for the $[0/\pm 45/90]_{15s}$, $[0/90]_{24s}$, and $[0/\pm 45]_{15s}$ laminates, respectively. This alone would not account for the total thickness effect. However, a review of the data presented in Figs. 14 through 16 reveals that the "average" value of the general toughness parameter results in an equation that quite closely predicts the strength of the thick laminates. The strengths of the $[0/\pm 45/90]_{ns}$ and $[0/90]_{ns}$ laminates are reduced by the thickness effect toward the 1.5 $\sqrt{\text{mm}}$ (0.30 $\sqrt{\text{in.}}$) prediction curve. The converse is true for the $[0/\pm 45]_{ns}$ laminate. This is not just a fortuitous occurrence. The fracture of the thick laminates of all three laminate types was essentially uniform and self-similar with the notch. Likewise, the average value of Q_c/ϵ_{tuf} = 1.5 $\sqrt{\text{mm}}$ (0.30 $\sqrt{\text{in.}}$) was a statistical mean to a large database [*7*] in which those laminates that fractured in a nearly self-similar manner had values of Q_c/ϵ_{tuf} very close to 1.5 $\sqrt{\text{mm}}$ (0.30 $\sqrt{\text{in.}}$). Those laminates that failed in a deviate manner, such as the $[0/90]_{2s}$ or $[0/\pm 45]_s$ laminates, had values of Q_c/ϵ_{tuf} considerably different from 1.5 $\sqrt{\text{mm}}$ (0.30 $\sqrt{\text{in.}}$). Therefore, the basis for using Q_c/ϵ_{tuf} = 1.5 $\sqrt{\text{mm}}$ (0.30 $\sqrt{\text{in.}}$) is consistent with the fracture mode of the thick laminates.

The self-similar fracture surfaces exhibited by the thick laminates, Figs. 11 through 13, suggests that a fracture mechanics approach for homogeneous materials may be used to predict notched strength. An additional indicator of this approach may be obtained by plotting the notched-to-unnotched strength ratio versus the crack length-to-width ratio on a log-log plot. The data will fall along a line with a slope of −0.5 for a linear elastic material. (This approach was first taken by Mar and Lin [*15*].) The data for the subject study are plotted in Fig. 18. The slope of the line through the thick laminate data is very nearly −0.5 for each stacking sequence. This is obviously not the case for the $[0/90]_{2s}$ and $[0/\pm 45]_s$ thin laminates.

The fracture mechanics approach was more fully investigated by studying the behavior of specimens with semi-elliptic surface notches. A schematic of a surface-notched test specimen is shown in Fig. 3. The specimens were gripped in the same manner as the through-the-thickness test specimens. Figure 19 is a comparison between experimental and predicted values of strength. For a/t greater than about 0.3, the experimental and predicted values are in good agreement. A more detailed discussion of these results may be found in Ref *16*.

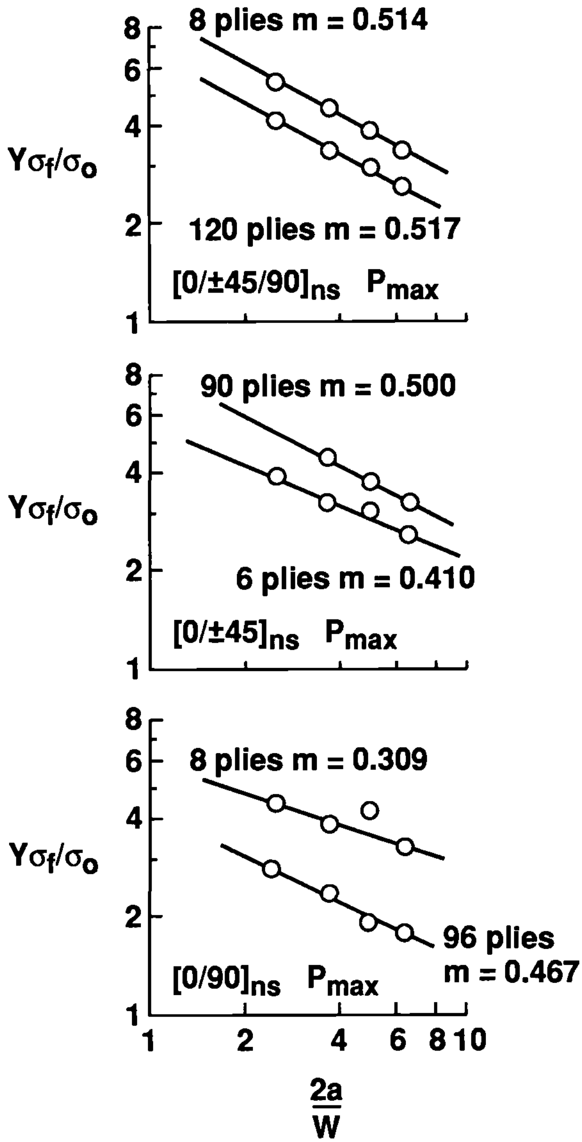

FIG. 18—*Log-log plot of strength versus crack length.*

Discussion of Results

The effect of notch size on residual (or notched) strength can be effectively predicted by the two-parameter strength models when the characteristic distances are determined from experimental data for the exact laminate of interest. However, it is not obvious that the characteristic distance is a material property because it is a strong function of the laminate stacking sequence and thickness. The comparisons given in Figs. 14 through 16 are excellent for the thin laminates but poor for the thick laminates. If the characteristic distances had been determined from the thick laminate data rather than the thin laminate data, the quality of the com-

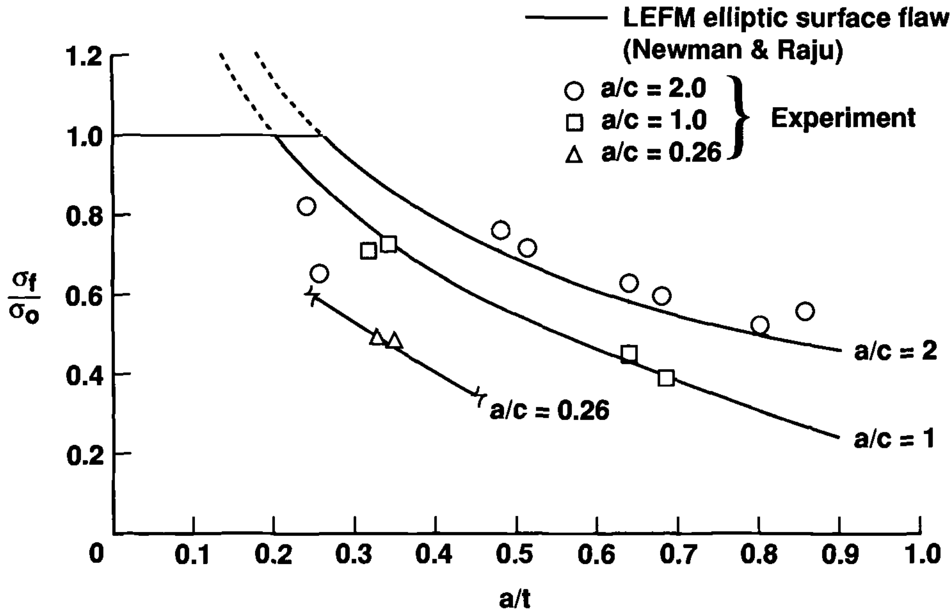

FIG. 19—*Experimental and analytical predictions of the residual strength versus notch depth for the surface notch specimens in the* $[0/\pm 45/90]_{ns}$ *laminate.*

parisons would have been just the opposite. However, the values of the characteristic distances for the thin and thick laminate data sets would be significantly different.

The fracture mechanics approach of Poe is also quite accurate when the value of the general toughness parameter is determined specifically for the laminate of interest. However, the average value, 1.5 $\sqrt{\text{mm}}$, may be used accurately for any laminate and material system that exhibits self-similar fracture. This is why the average value was successful in predicting the fracture of the thick laminates. On the other hand, the average value gave poor results for the $[0/\pm 45]_s$ and $[0/90]_{2s}$ laminates that did not fail in a self-similar manner. It was also obvious from the results of the surface-cut specimens that fracture mechanics can be used to predict the notched strength of thick laminates when the stacking sequence is selected to produce a homogeneous laminate.

Summary and Conclusions

The effect of thickness on the through-the-thickness notched strength of three graphite/epoxy laminates was studied. The $[0/\pm 45/90]_{ns}$ and $[0/90]_{ns}$ laminates had thicknesses of 8, 32, 64, 96, and 120 plies. At 8 and 120 plies, crack length-to-width ratios of 0.25, 0.375, 0.50, and 0.625 were test parameters. For both of these laminates, the fracture strength decreased, but exhibited asymptotic behavior, with increasing thickness. The $[0/\pm 45]_{ns}$ laminate had thicknesses of 6, 30, 60, 90, and 120 plies, with the preceding crack sizes being varied for laminates of 6 and 90 ply thickness. The fracture strength of this laminate increased with increasing thickness, but also exhibited asymptotic behavior.

The $[0/\pm 45/90]_s$ laminate exhibited some delamination but fractured in a more-or-less self-similar manner. Long axial splits developed in the 0° plies of the $[0/90]_{2s}$ laminate at the tip of the crack. These splits reduced the strength of the crack tip singularity and, thereby, elevated the fracture strength. The $[0/\pm 45]_s$ laminate failed by an uncoupling mechanism where the two interior $-45°$ plies completely delaminated from the adjacent $+45°$ plies. The thick laminates of all three laminate types exhibited essentially self-similar fracture that was practically uniform in the interior of the specimen.

Several macromechanical models that predict through-the-thickness notched strength as a function of notch size were evaluated. Only the general toughness parameter model accurately predicted the fracture strength of the thick laminates. The average value of $Q_c/\epsilon_{tuf} = 1.5\ \sqrt{\text{mm}}$ ($0.30\ \sqrt{\text{in.}}$) was equally applicable to all three thick laminates, in spite of the dramatically different notched strength-thickness behavior of these laminates.

The strength of the surface-notched specimens was predicted using an asymptotic value of fracture toughness and a linear elastic, homogeneous, isotropic fracture mechanics solution. The predicted and experimental values were in close agreement when a/t is greater than 0.3.

The macromechanical models were used to predict only strength. No attempt was made to model the damage development in the three laminates.

References

[*1*] Awerbuch, J. and Madhukar, M. S., "Notched Strength of Composite Laminates: Predictions and Experiments—A Review," *Journal of Reinforced Plastics and Composites,* Vol. 4, 1985, pp. 3–159.

[*2*] Harris, C. E. and Morris, D. H., "Fracture Behavior of Thick, Laminated Graphite/Epoxy Composites," NASA Contractor Report 3784, National Aeronautics and Space Administration, Washington, DC, March 1984.

[*3*] Waddoups, M. E., Eisenmann, J. R., and Kaminski, B. E., "Macroscopic Fracture Mechanics of Advanced Composite Materials," *Journal of Composite Materials,* Vol. 5, Oct. 1971, pp. 446–454.

[*4*] Whitney, J. M. and Nuismer, R. J., "Stress Fracture Criteria for Laminated Composites Containing Stress Concentrations," *Journal of Composite Materials,* Vol. 8, July 1974, pp. 253–265.

[*5*] Nuismer, R. J. and Whitney, J. M., "Uniaxial Failure of Composite Laminates Containing Stress Concentrations," *Fracture Mechanics of Composites, ASTM STP 593,* American Society for Testing and Materials, Philadelphia, 1975, pp. 117–142.

[*6*] Yeow, Y. T., Morris, D. H., and Brinson, H. F., "A Correlative Study Between Analysis and Experiment on the Fracture Behavior of Graphite/Epoxy Composites," *Journal of Testing and Evaluation,* Vol. 7, No. 2, 1979, pp. 117–125.

[*7*] Poe, C. C., Jr., "A Unifying Strain Criterion for Fracture of Fibrous Composite Laminates," *Engineering Fracture Mechanics,* Vol. 17, No. 2, 1983, pp. 153–171.

[*8*] Poe, C. C., Jr., "Strain Intensity Factor Approach for Predicting the Strength of Continuously Reinforced Metal Matrix Composites," *Metal Matrix Composites: Testing, Analysis, and Failure Modes, ASTM STP 1032,* W. S. Johnson, Ed., American Society for Testing and Materials, Philadelphia, 1989, pp. 173–193.

[*9*] Newman, J. C., Jr., and Raju, I. S., "Stress-Intensity Factor Equations for Cracks in Three-Dimensional Finite Bodies," *Fracture Mechanics Fourteenth Symposium, Volume I: Theory and Analysis, ASTM STP 791,* J. C. Lewis and G. Sines, Eds., American Society for Testing and Materials, Philadelphia, 1983, pp. I-238–I-265.

[*10*] Jones, R. M., *Mechanics of Composite Materials,* McGraw-Hill, New York, 1975.

[*11*] Garber, D. P., "Tensile Stress-Strain Behavior of Graphite/Epoxy Laminates," NASA Contractor Report 3592, National Aeronautics and Space Administration, Washington, DC, Aug. 1982.

[*12*] Brown, W. F., Jr., and Srawley, J. E., *Plane Strain Crack Toughness Testing of High Strength Metallic Materials, ASTM STP 410,* American Society for Testing and Materials, Philadelphia, 1966.

[*13*] Chang, F. H., Couchman, J. E., Eisenmann, J. R., and Yee, B. G. W., "Application of a Special X-Ray Nondestructive Testing Technique for Monitoring Damage Zone Growth in Composite Laminates," *Composite Reliability, ASTM STP 580,* American Society for Testing and Materials, Philadelphia, 1975, pp. 176–190.

[*14*] Freeman, S. M., "Characterization of Lamina and Interlaminar Damage in Graphite-Epoxy Composites by the Deply Technique," *Composite Materials: Testing and Design (Sixth Conference),*

ASTM STP 787, I. M. Daniel, Ed., American Society for Testing and Materials, Philadelphia, 1982, pp. 50–62.

[*15*] Mar, J. W. and Lin, K. Y., "Fracture of Boron/Aluminum Composites with Discontinuities," *Journal of Composite Materials,* Vol. 11, Oct. 1977, pp. 405–421.

[*16*] Harris, C. E., Morris, D. H., and Nottorf, E. W., "Analytical and Experimental Investigation of the Notched Strength of Thick Laminates with Surface Notches," *Composite Materials: Testing and Design (Eighth Conference), ASTM STP 972,* J. D. Whitcomb, Ed., American Society for Testing and Materials, Philadelphia, 1988, pp. 298–321.

C. Wm. Smith,[1] Lei Wang,[1] Hervé Mouille,[1] and Chi-T. Liu[2]

Near-Tip Behavior of Particulate Composite Material Containing Cracks at Ambient and Elevated Temperatures

REFERENCE: Smith, C. W., Wang, L., Mouille, H., and Liu, C.-T., **"Near-Tip Behavior of Particulate Composite Material Containing Cracks at Ambient and Elevated Temperatures,"** *Fracture Mechanics: Twenty-Third Symposium, ASTM STP 1189*, Ravinder Chona, Ed., American Society for Testing and Materials, Philadelphia, 1993, pp. 775–787.

ABSTRACT: After briefly reviewing the results of a series of constant head rate tests on center-cracked "biaxial" test specimens of a particulate composite at room temperature, a second test series utilizing edge-cracked "biaxial" specimens of a particulate composite with a different particulate gradation at ambient and elevated temperatures and low and moderately high head rates is discussed. Results show different near-tip mechanisms for crack opening and growth for the two materials and, while changes in head rate and temperature produced quantitative differences in near-tip fields of displacement and strain for both materials, they did not affect the basic near-tip mechanisms of each material qualitatively.

KEY WORDS: fracture mechanics, particulate composites, crack opening, crack growth, near-tip fields, dominant eigenvalues, fatigue (materials)

Nomenclature

- x_i Cartesian coordinate axes
- u_2 Displacement component normal to crack plane
- ϵ_2 Normal strain component normal to crack plane
- γ_{12} Shear strain component in x_1x_2 plane
- $\bar{\epsilon}_2$ Global strain normal to crack plane $\bar{\epsilon}_2 = \Delta h/h$ where h is specimen height
- λ_u Dominant displacement eigenvalue

Generally speaking, composite materials may be defined as a combination of two or more materials into a polyphase material wherein each of the constituents retains its separate properties. In recent years, structural analysis of composite materials has been dominated by fiber-reinforced materials and their laminates. It is interesting to note, however, that enormous volumes of particulate composites are used annually. These composites may consist of soft particles in hard matrices, as with a number of metal alloys, or hard particles in soft matrices, as with gaskets, seals, solid propellant, etc. Particulate composite structures may also be subject to failure by fracturing but the processes involved may be complex.

The present paper reports on the extension of a study initiated in 1985 that was directed towards the development of an understanding of the mechanisms involved in the opening and growth of cracks in "biaxial" test specimens and an effort to describe associated crack parameters in terms of a continuum theory.

[1] Alumni professor and graduate research assistants, respectively, Department of Engineering Science and Mechanics, Virginia Polytechnic Institute and State University, Blacksburg, VA 24061.
[2] Program manager, Phillips Laboratory (AFSC), Edwards Air Force Base, CA 93523-5000.

Review of Prior Work

Center-cracked "biaxial" specimens (Fig. 1*a*), so-called because such specimens without cracks exhibited biaxial tension at their center, were made from a particulate composite consisting of polybutadiene rubber embedded with polyhedral particles of potassium chloride ranging in size from 0.01 to 0.50 mm and occupying about 75% of the volume of the specimen material. A specially-prepared coarse cross grating (0.2 by 0.2 mm) of negligible stiffness was deposited on one side of the specimens in the near-tip zone and was photographed at various times during constant head rate tests at ambient temperature. Rigid grips fixed against in-plane rotation were used in all tests.

Typical photographs are shown in Figs. 1*b* through *e* and show that the crack grows by coalescing with large ovalized voids ahead of the crack. Moreover, damage, as reflected by breakdown of the grating is confined to a more or less fan-shaped region emanating from the crack tip. These photographs were then digitized and both displacement and engineering strain fields were obtained in the neighborhood of the crack tip. Typical results for u_2, ϵ_2, and γ_{12} are shown in Fig. 2. Moreover, the displacement field, u_2, was used to estimate the value of the dominant eigenvalue, λ_u (see Appendix) near the crack tip at the free surface using an algorithm based upon Benthem's continuum theory [*1*]. Good agreement was obtained with Benthem's Theory for the early stages of crack opening and growth, suggesting that, despite significant blunting that occurs at the crack tip due to the presence of the hard particles, the process can be considered to be embedded in a singularity-controlled zone, though not with the conventional inverse square root stress singularity at the free surface.

It was concluded that the local blunting process resulted from a stretching of the matrix ahead of the crack tip that moved the larger hard particles above and below the crack tip while ovalized voids with long dimension normal to the crack plane developed in the stretch zone, as described pictorially in Fig. 3. These voids then coalesced to produce crack extension, followed by temporary resharpening of the crack tip. Thus, the growth process proceeded as a blunt-growth-blunt process that appeared highly nonlinear. In tests on the matrix material without particles, the growth process appeared to be smooth and steady without severe blunting.

All of the preceding discussion dealt with observations at the surface of the specimens. In addition to the observations, a black powder was fired into the open cracks for specimens 5.1 and 15.3 mm thick. In both cases, the growing crack front marked by the black powder remained essentially straight for both thicknesses, with no thumbnailing, suggesting an absence of internal transverse constraint. This can be interpreted to mean that voiding in the process zone resulted in fiber bundles of matrix loaded essentially in uniaxial tension with negligible transverse connections, and this interpretation was confirmed by backlighting the cracks during crack growth.

Finally, although varying the head rate by an order of magnitude from 2.5 to 25.4 mm/min did increase the slope of the load versus time curve for the cracked specimens, and quantitatively altered the near-tip displacement and strain fields, it did not produce qualitative differences that would indicate the presence of different local crack opening and growth mechanisms. Results of the studies summarized here are found in Refs *2* and *3*.

The Experiments

The experiments described in the sequel were conducted to quantify the near-tip behavior of a similar particulate composite at elevated temperature, 74°C (165°F). In the present program, edge cracked "biaxial" specimens (Fig. 4) were used, all of which were 2.5 mm thick.

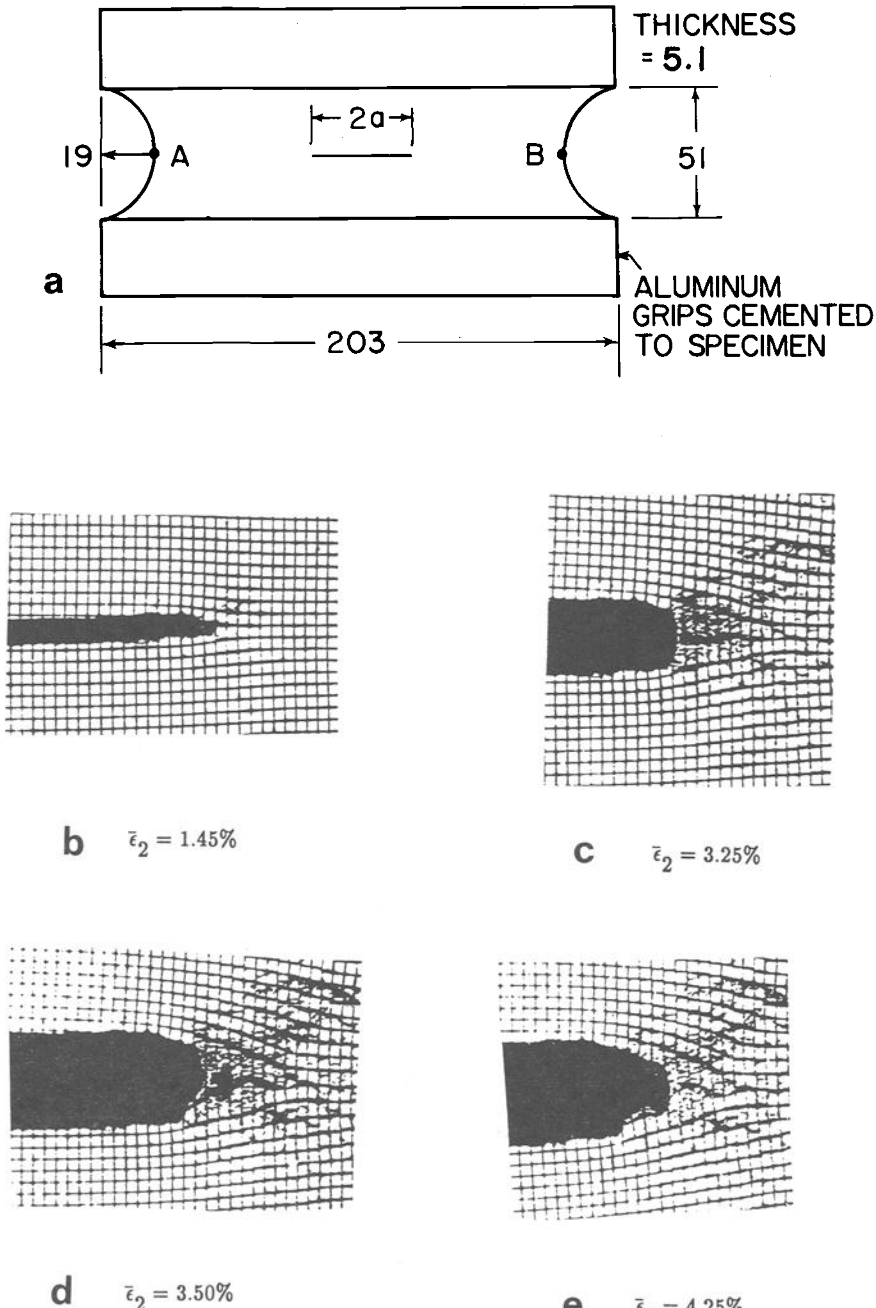

FIG. 1—(a) *Center-cracked biaxial specimen (dimensions in millimetres, initial crack length (2*a*) = 38 mm and specimen thickness = 15.25 mm;* (b) *early stage of crack opening,* (c) *development of stretch zone ahead of crack with tip blunting,* (d) *increased blunting with void formation ahead of crack, and* (e) *Crack extension by void coalescence (resharpening of crack follows).*

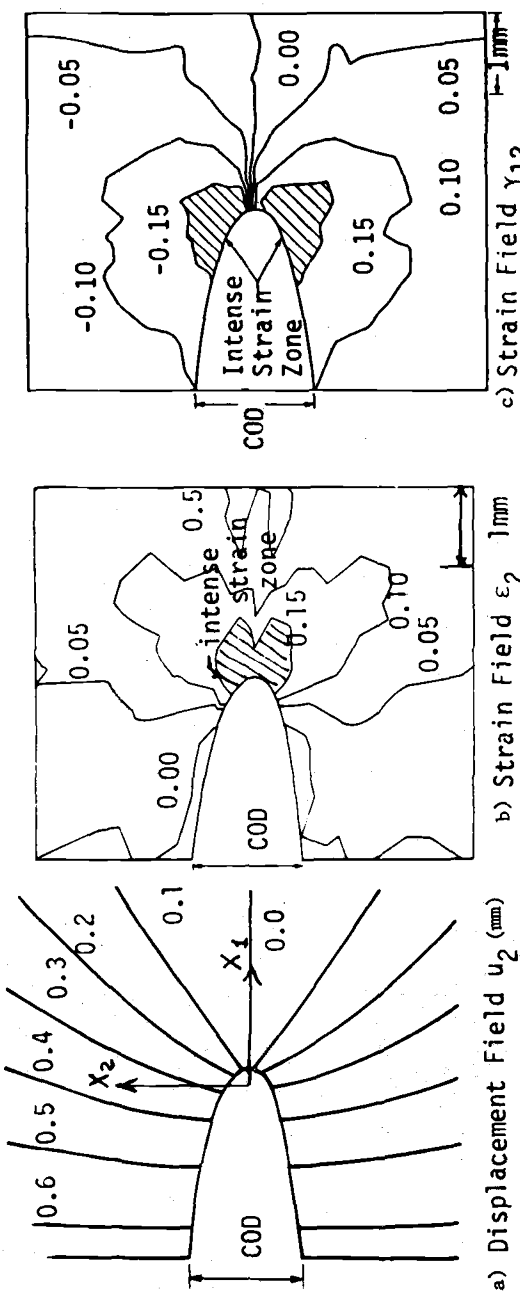

FIG. 2—*Typical set of digitized data from center-cracked tests (COD is crack opening displacement): head rate = 2.5 mm/min and global strain,* $\bar{\epsilon}_2$ = *4.0%.*

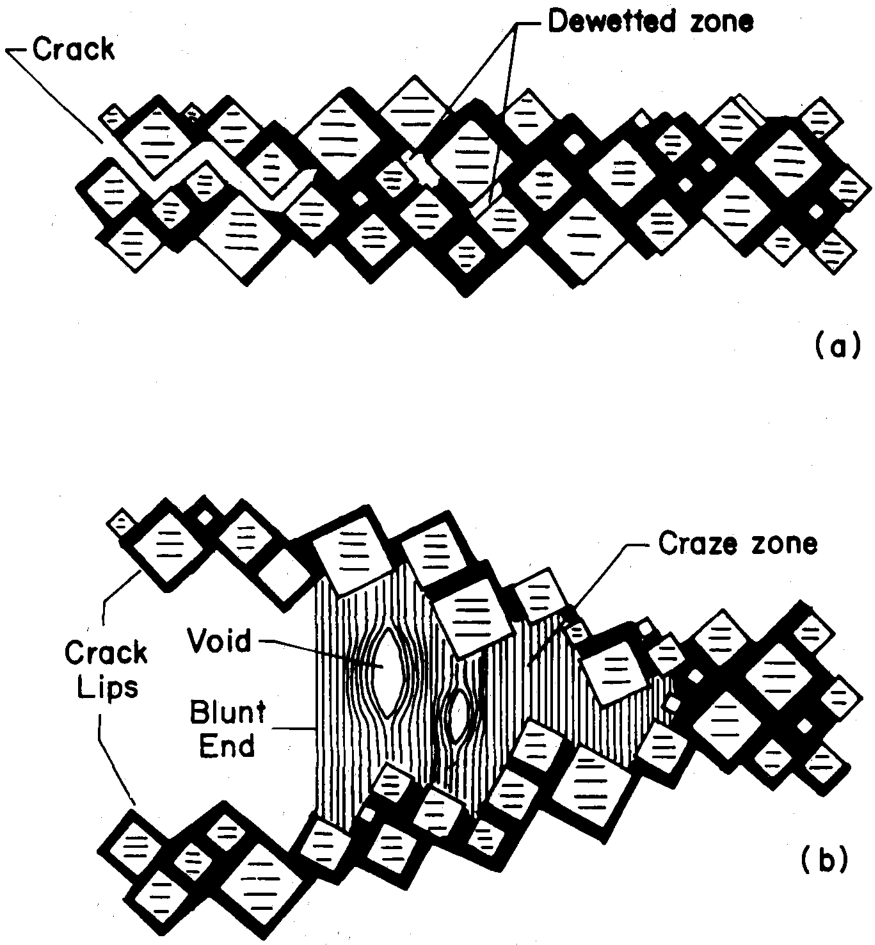

FIG. 3—*Idealized crack-tip blunting.*

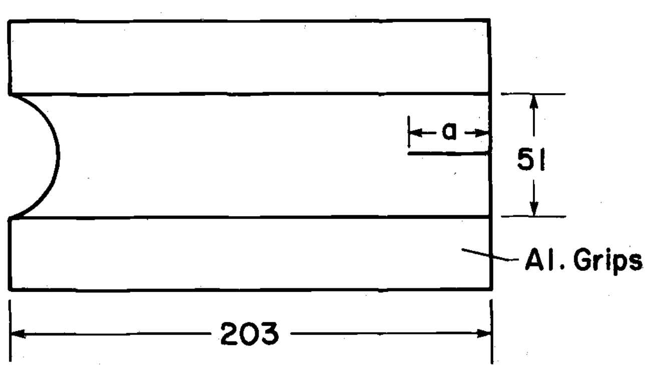

FIG. 4—*Edge-cracked specimen dimensions (dimensions in millimetres,* a = *25.4 mm).*

However, since the near-tip analysis of medium-length edge cracks differs little from center cracks [*4–6*], and prior tests showed no thickness effect, the present approach was deemed comparable to prior work. There were, however, many more fine particles as small as 0.001 mm in the edge-cracked specimens.

The same size of grating was used as before and was applied as follows:

1. Lightly sand surface.
2. Spread black powder evenly over surface.
3. Apply silicone grease mixed with black powder.
4. Embed a screen in the surface.
5. Sprinkle on white powder (titanium oxide).
6. Remove excess powder and then the screen.

The resulting black grating on a white background adhered to the surface but provided negligible stiffness. The matrix modulus was ≈0.78 MPa (112 psi).

Control tests were run at room temperature at head rates of 2.5 and 12.7 mm/min and tests at 74°C (165°F) were conducted at 0.25, 2.5, and 12.7 mm/min. Photographs were again taken at various time intervals during extension, and these photographs were digitized to obtain near-tip displacement and engineering strain contour maps as before.

Figure 5 shows that the global specimen responses at room temperature and at 74°C (165°F) were similar with the load rising faster for the room temperature tests as expected. Figure 6

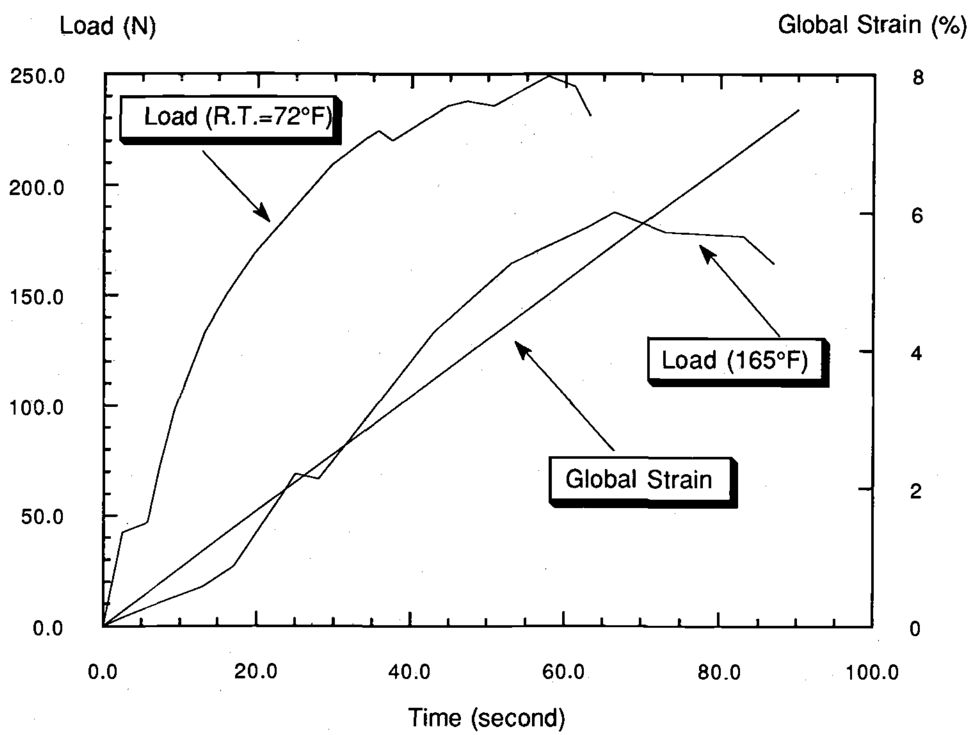

FIG. 5—*Load and global strain versus time at 2.54 mm/min and 22 and 74°C (72 and 165°F).*

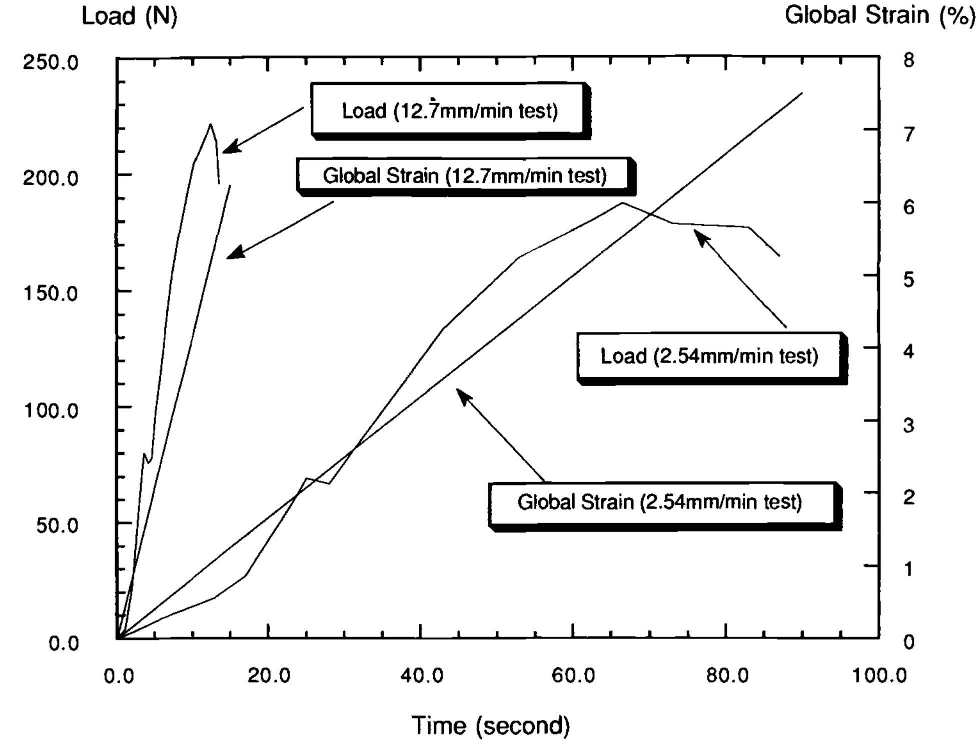

FIG. 6—*Load and global strain versus time at 74°C (165°F).*

compares the elevated temperature responses for two different head rates, again showing expected global effects. Figure 7 shows a sequence of photographs revealing how surface micro-cracks develop ahead of the main crack covering a fan angle of nearly 180° from the crack-tip vertex, some of which coalesce with the main crack to produce irregular growth patterns. Figure 8 shows a typical set of contour maps at elevated temperature that were similar to room temperature patterns qualitatively.

Altogether, a total of 12 edge-cracked biaxial specimen tests were conducted. Three tests were run at 22°C (72°F) and nine at 74°C (165°F). One of the tests at 72°F was run at a head rate of 12.70 mm/min and two tests at 2.54 mm/min. At 74°C (165°F), the following tests were conducted:

1. two tests at 0.25 mm/min,
2. four tests at 2.54 mm/min, and
3. three tests at 12.70 mm/min.

Displacement and strain fields were obtained by digitization of the deformed grating data using a 0.025-mm digitizer. In digitizing the data, no account was taken of the presence of the multiplicity of surface flaws ahead of the main crack. That is, the additional separation between adjacent points due to a microcrack opening in between them was recorded as part of the overall relative displacement.

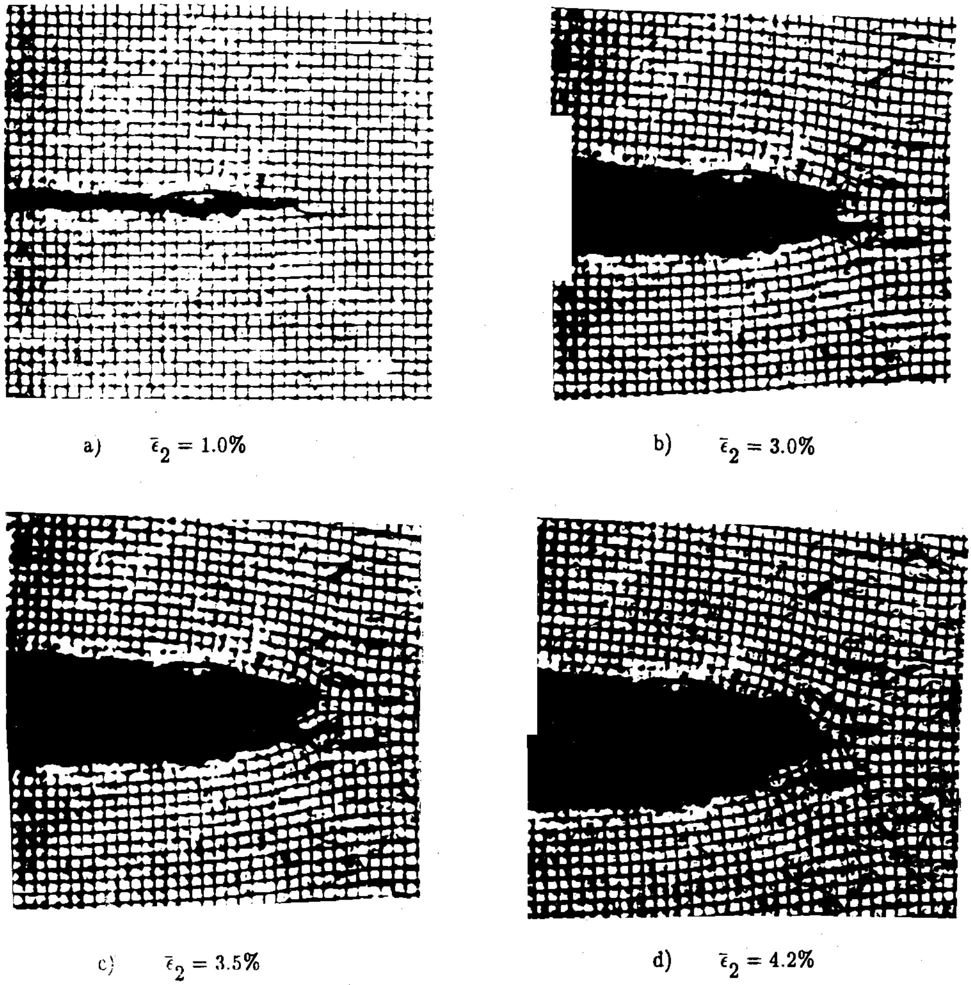

FIG. 7—*Crack opening and growth at 74°C (165°F):* (a) *early stage of crack opening,* (b) *tip blunting and microcrack formation ahead of tip,* (c) *microcrack opening with continued blunting, and* (d) *crack extension and resharpening by coalescence with microcrack.*

Discussion of Results

Globally, at room temperature and at 74°C (165°F), the load-versus-time curves (Figs. 5 and 6) differed in shape from those from prior studies in one particular respect, namely, a plateau of nearly constant load at about 50 to 80 N for several seconds. At this level, a large number of surface microcracks appeared over a large area ahead of the main crack, some of which subsequently intersected the main crack (Figs. 7*b* and *c*). These cracks first appear at the onset of the plateau in Figs. 5 and 6 and there follows a small growth at the specimen surface of the main crack by coalescence with the near-tip surface microcracks. It is conjectured that the opening of these cracks allow continued global specimen extension without increase in load for several seconds. This may also imply that these cracks, likely resulting from separation of matrix from particles, may also be found inside the body but, at this load level, are not connected to one another through the thickness.

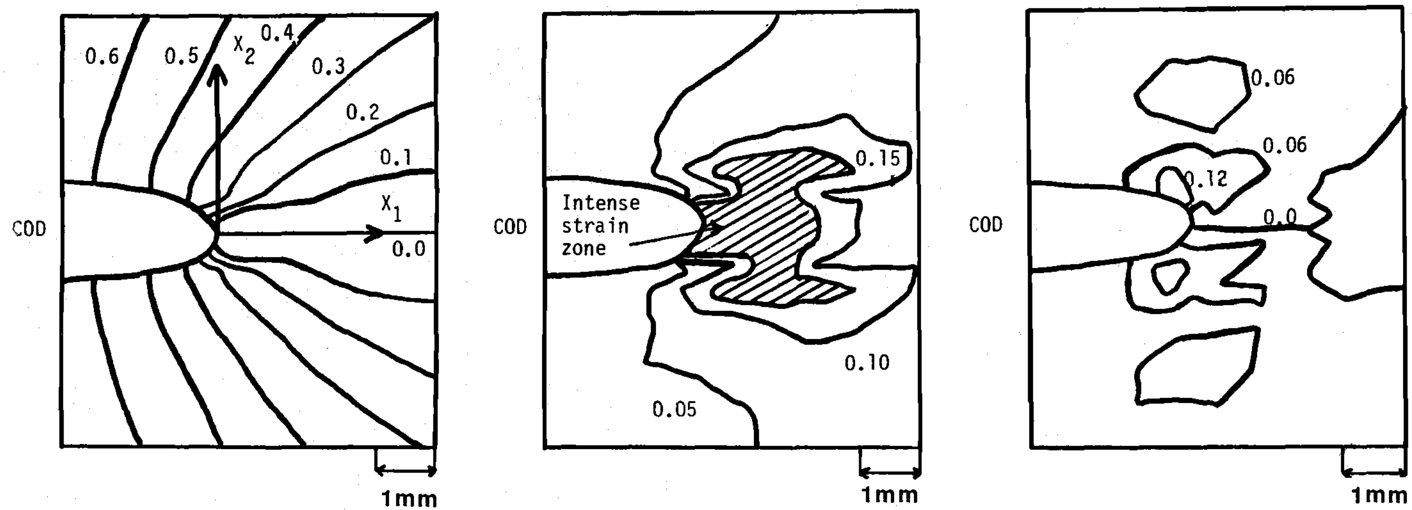

(a) Displacement Field U_2 (mm) (b) Strain Field ε_2 (c) Strain Field γ_{12}

FIG. 8—*Typical set of digitized data from edge-cracked tests at 74°C (165°F): head rate = 12.7 mm/min and global strain,* $\bar{\varepsilon}_2$ = *4.2%.*

As the main crack opened under increasing load, these microcracks proliferated and opened further, and resulted in a "flattened" ϵ_2 contour pattern outside a larger local stretch zone (compare Fig. 2*b* with Fig. 8*b*). However, the γ_{12} contour patterns were of similar shape and slightly lower intensity (compare Fig. 2*c* with Fig. 8*c*). Moreover, the opening of the microcracks apparently eliminated the stretch zone seen ahead of the cracks in previous work and idealized in Fig. 3. Instead, the surface microcracks that are parallel to the main crack coalesce with the main crack and lead to crack extension without significant blunting.

Using the algorithm in the Appendix, ln-ln plots of u_2–u_{20} versus r were plotted by a computer routine and values of the dominant eigenvalue for ambient and elevated temperature were obtained for the various head rates and typical results are found in Table 1 in the Appendix.

The microcracks produced some irregularities in the displacement contours that, in some cases, precluded accurate determination of λ_u (see Appendix). However, for relatively smooth u_2 patterns, λ_u values were obtained, but with more scatter than in Refs *2* and *3*. By identifying common linear zones in specimens with smooth u_2 contour patterns, this scatter was minimized as much as possible. Typical results are found in Table 1 (see Appendix). Their divergence from the Benthem result is attributed directly to the influence of the presence and distribution of multiple surface flaws. Thus, despite the presence of surface microcracking, the continuum algorithm extracted from Benthem's analysis still yields reasonable results where smooth u_2 contour patterns existed or can be used to establish the location of the dominant eigenvalue zone, but not necessarily comparable to the Benthem solution. The authors conjecture that the multiple surface flaws are due to poor gradation at the hard particles.

Comparisons with Prior Studies [*2,3*]

It is clear from the preceding discussion that the near-tip behavior in the present material was somewhat different from that studied in Refs *2* and *3*. The former material developed a matrix-rich stretch zone (Fig. 3) with severe crack-tip blunting, and the crack grew by coalescing with ovalized voids with a start–stop blunt–growth process, resharpening at the beginning of each growth phase. On the other hand, extensive surface (and perhaps internal) microcracking occurred during loading of the edge-cracked specimens and crack opening began at the first plateau in Figs. 5 and 6 and, after further microcracking, began to grow in a start–stop manner by coalescing with sharp near-tip microcracks, meandering about the plane of the initial crack (Fig. 7) without severe blunting. Since auxiliary isotropic analysis [*4–6*] indicates no significant differences between stress intensity factors for the center-cracked and edge-cracked biaxial specimens near the crack tip, and auxiliary tests indicated no thickness effects, one is led to conjecture that the previously noted differences in the crack opening and growth processes described herein are likely related to the differences in particle gradation and to bond characteristics between the matrix and the hard particles in the two materials. Moreover, when comparing test results for the current material at room and at elevated temperature, and at low

TABLE 1—*Test data.*

Test No.	Test Temperature, °C (°F)	Head Rate, mm/min	Global Strain, %	Linear Zone, mm	P_{max} N	Experimental Value of λ_u
1	74 (165)	2.54	3.8	$0.42 < r < 3.40$	178	0.49
6	74 (165)	12.70	4.2	$0.55 < r < 3.00$	231	0.62
12	22 (72)	2.54	4.2	$0.50 < r < 1.94$	249	0.67
13	22 (72)	12.70	4.2	$0.51 < r < 1.54$	300	0.45

and high head rates (Figs. 5 and 6, respectively) together with local displacement and strain fields, only quantitative differences were observed. No qualitative differences suggesting different near-tip mechanisms due to head rate or temperature for either material were observed.

Summary

After reviewing a series of tests on center-cracked biaxial specimens with center cracks at various head rates and ambient temperature, results from a second test series employing edge-cracked specimens of a different material were presented for both ambient and elevated temperature and low and moderately high head rates. Comparison of results from the two programs revealed differences in the near-tip crack opening and growth processes, that the processes for each material were the same for both low and moderately high head rates, and that the current material showed the same qualitative near-tip behavior for both ambient and elevated temperature. Moreover, it was found that the dominant eigenvalue could be extracted in both cases from a continuum-type algorithm, yielding results in reasonable agreement with Benthem's Theory. However, for the current material, multiple surface cracks ahead of the main crack apparently produced irregularities in the u_2 distribution that led to substantial scatter in λ_u values.

Acknowledgments

The authors gratefully acknowledge the support of Phillips Laboratory (AFSC) under Contract No. FO470090M4945 and the staff and facilities of the Department of Engineering Science and Mechanics at Virginia Polytechnic Institute and State University.

APPENDIX

Benthem [1] employed a variables separable series eigenfunction analysis to obtain a three-dimensional solution for a quarter infinite crack in a half space (Fig. 9) for the vertex singularity at the point of intersection of the crack with the free surface of the half space. He assumed that

$$u_i = \sum_{k=1}^{\infty} r^{\lambda_u^k} h_i(\theta,\phi)_k \qquad (1)$$

and a corresponding set of equations for σ_{ij} for an elastic material. Truncating Eq 1 for u_2, one may write for $\phi = \pi/2$, $\theta = \pi/2$ (Fig. 9)

$$u_2 = D_2 r^{\lambda_u} \qquad (2)$$

therefore

$$\ln u_2 = \ln D_2 + \lambda_u \ln r \qquad (3)$$

The crack-tip profiles were sharp when measured during the early stages of opening and growth but were somewhat blunted in between these stages. In order to approximately account for blunting, a blunt height of u_{20} was arbitrarily introduced into Eq 3, yielding

$$\ln (u_2 - u_{20}) = \ln D_2 + \lambda_u \ln r \qquad (4)$$

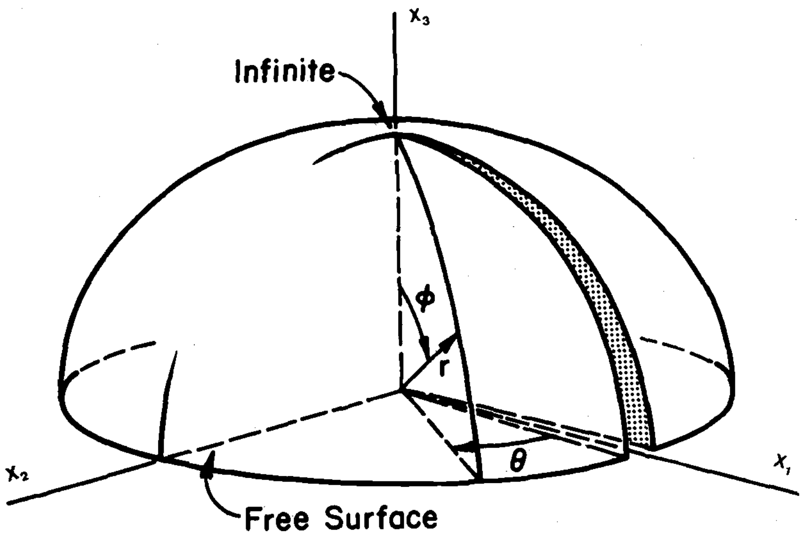

FIG. 9—*Benthem's problem geometry.*

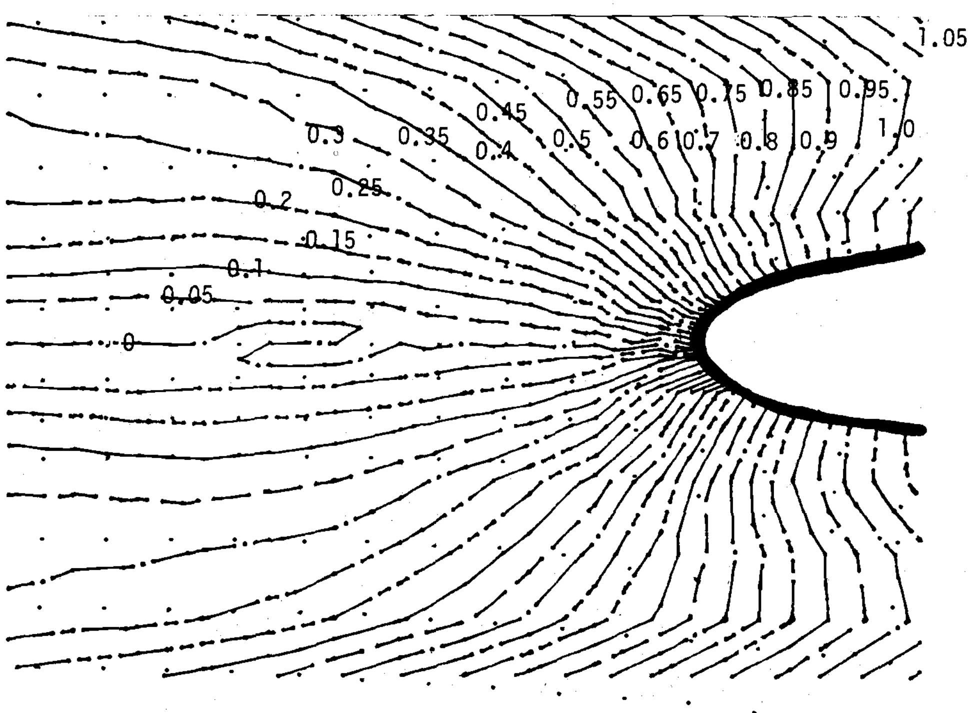

FIG. 10—*Smooth* u_2 *contour map: Specimen 13 (room temperature = 22°C (72°F)),* u_2 *field, head rate = 12.7 mm/min, time elapsed = 10 s, digitizing interval = 0.05 mm, and global strain = 4.2%.*

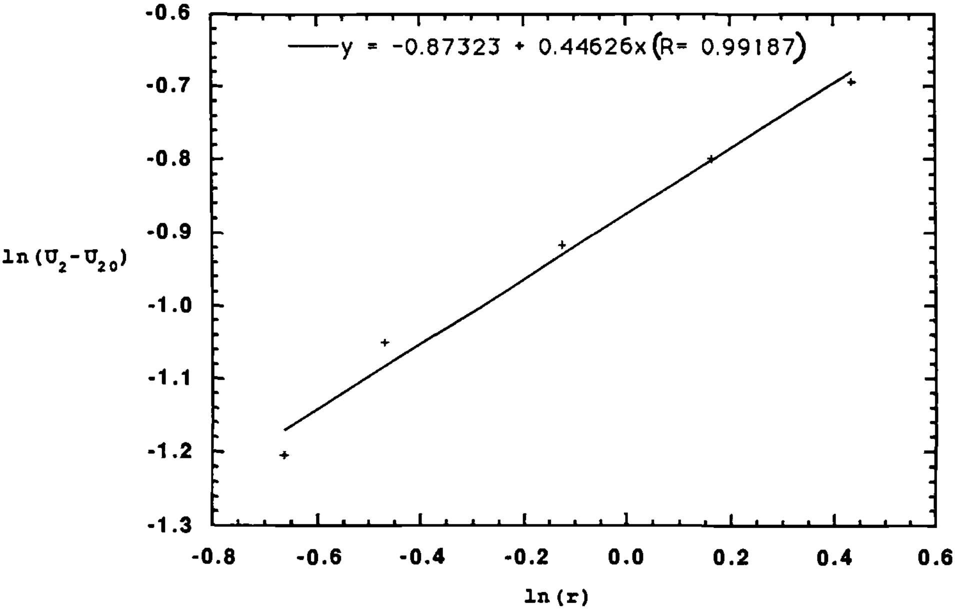

FIG. 11—*Determination of* λ_u*: Specimen 13, linear zone (0.51 < r < 1.54 mm).*

The value of u_{20} was taken to be equal to the grating size of 0.20 mm so as to avoid interpolations within the intense strain zone.

Thus, by plotting ln $(u_2 - u_{20})$ versus ln r along $\theta = \pi/2$, a linear zone should result, the slope of which is λ_u, the dominant displacement eigenvalue. In linear elastic fracture mechanics, $\lambda_u = \frac{1}{2}$, but Benthem's results showed that, for an incompressible material $\lambda_u = 0.67$. Since the matrix of the current material is nearly incompressible, we would expect a similar result. Use of Eq 3 with a set of typical test data for u_2 on the current material (Fig. 10) is illustrated in Fig. 11. In this example, the u_2 displacement contours are not smooth due to microcracking, and λ_u (the coefficient of X in the equation at the top of Fig. 11) is 0.45, which is well below Benthem's value of 0.67. However, when the u_2 contours were smooth, results closer to Benthem's result were obtained as in Tests 6 and 12. By using specimens with the smoothest u_2 contours to locate the zone of the dominant eigenvalue, and then fitting the algorithm to data in that region for less smooth data, typical results are shown in Table 1.

References

[1] Benthem, J. P., "The Quarter Infinite Crack in a Half Space: Alternative and Additional Solutions," *International Journal of Solids and Structures*, Vol. 16, 1980, pp. 119–130.

[2] Smith, C. W., Czarnek, R., and Rezvani, M., "Determination of Continuum Fracture Parameters for a Particulate Composite," *Journal of Engineering Materials and Technology*, Vol. 112, No. 2, April 1990, pp. 247–252.

[3] Smith, C. W. and Liu, C. T., "Effects of Near Tip Behavior of Particulate Composites on Classical Fracture Concepts," *Journal of Composites Engineering*, in press.

[4] Rice, J. R., "Stresses in an Infinite Strip Containing a Semi-Infinite Crack," *Transactions*, American Society of Mechanical Engineers, Series E, *Journal of Applied Mechanics*, Vol. 34, 1967, pp. 248–249.

[5] Isida, M., "Effect of Width and Length on Stress Intensity Factors of Internally Cracked Plates under Various Boundary Conditions," *International Journal of Fracture*, Vol. 7, No. 3, 1971, pp. 301–316.

[6] Torvik, P. J., "On the Determination of Stresses, Displacements, and Stress-Intensity Factors in Edge-Cracked Sheets with Mixed Boundary Conditions," *Transactions*, American Society of Mechanical Engineers, Series E, *Journal of Applied Mechanics*, Vol. 46, 1979, pp. 611–617.

Kai Duan,[1] Brian Cotterell,[1] and Yiu-Wing Mai[1]

Static Fatigue in Dilatant-Zone-Toughened Ceramics

REFERENCE: Duan, K., Cotterell, B., and Mai, Y.-W., "**Static Fatigue in Dilatant-Zone-Toughened Ceramics,**" *Fracture Mechanics: Twenty-Third Symposium, ASTM STP 1189,* Ravinder Chona, Ed., American Society for Testing and Materials, Philadelphia, 1993, pp. 788–796.

ABSTRACT: An approximate model is presented for the effect of crack-tip shielding due to dilatant zone toughening on subcritical crack growth in ceramics. This model relies on estimating the transformed zone from the applied stress intensity factor. Slow crack growth can be predicted with this model in ceramics toughened by the stress-triggered martensitic transformation in zirconia-bearing ceramics, if the slow crack growth data for the same ceramic with the transformation either already completed by thermal aging or suppressed by stabilizers is known.

KEY WORDS: transformation-toughened ceramics, static fatigue, subcritical crack growth, magnesia-stabilized zirconia, zirconia-toughened alumina, fracture mechanics, fatigue (materials)

High-performance ceramics such as partially stabilized zirconia (PSZ) and alumina containing a dispersion of zirconia particles (ZTA) exhibit *R*-curve toughening characteristics due to the shielding of the crack tip [*1–9*]. In these ceramics, the resistance to fracture increases with crack growth, which greatly improves crack tolerance and reliability [*10,11*]. Since environmentally assisted subcritical crack growth depends on the state of stress at the crack tip, shielding in these ceramics also decreases the rate of crack growth [*12–18*].

By comparing the behavior of PSZ as-fired with that for the same material after annealing, so that the tetragonal phase was transformed to monoclinic thus preventing any transformation toughening during crack growth, it has been found that the crack growth rate in the low applied stress intensity factor regime (Region I) is decreased by some six orders of magnitude by the presence of an *R*-curve [*15*]. Other researchers have found similar reductions in the crack growth rates [*16*]. The shielding of the crack tip can also, at higher applied stress intensity factors, produce a pseudo diffusion-limited crack growth regime (Region II) that is actually the result of transformation toughening [*12,13*].

Reductions in crack growth rates in ZTA have also been observed. Two versions of an alumina toughened by 20% zirconia by volume were tested by Becher [*14*]: one containing 1 mol % yttria to partially stabilize the zirconia and the other 3 mol % yttria that completely stabilizes the zirconia and prevents any transformation toughening. In Region I, the crack growth in the alumina with partially stabilized zirconia was some seven orders of magnitude less than that for the completely stabilized ceramic.

There have been few quantitative analyses of the effect of crack shielding on the slow crack growth of ceramics. Our earlier work showed that the results of Becher [*14*] for ZTA could be predicted from the crack growth data for alumina with the completely stabilized zirconia if it

[1] Postgraduate student, reader, and professor, respectively, Centre for Advanced Materials Technology, Department of Mechanical Engineering, University of Sydney, NSW 2006, Australia.

was assumed that the crack growth rate depended solely on the actual stress intensity factor at the crack tip [19]. Dauskardt et al. [20] have suggested that the actual stress intensity factor at the crack tip can be estimated if the transformed zone is assumed to depend on the stress due to the applied or far-field stress intensity factor. Although no experimental confirmation of this approach was given for a creep situation, they did obtain good agreement for the effect of an overload for magnesia-stabilized zirconia (Mg-PSZ) subjected to alternating load by assuming that the crack growth rate was solely a function of the stress intensity factor level, that is, there was no true cyclic fatigue effect. This method, which is similar to the approximate method used by Budiansky and others [21,22] for the analysis of steady-state toughening, overestimates the transformation zone size [23,24]; but at the lower stress intensity factors used in static fatigue, this overestimate is probably not very significant. The algorithm for crack growth, assuming that the transformation zone can be estimated from the applied stress intensity factor, is very simple since no iteration is necessary.

An Approximate Crack Growth Resistance for Transformation-Toughened Ceramics

The crack tip of a transformation-toughened ceramic is shielded by the transformed region that undergoes a dilatant transformation, θ^T. The effect of the dilatation can be obtained by integrating the expression obtained by Hutchinson [25], and for a Mode I crack under plane strain the expression for the actual stress intensity factor at a crack tip, K_{tip}, is given by

$$K_{\text{tip}} = K_a + \frac{E\theta^T}{3\sqrt{2\pi}(1 - \nu)} \int_A\int r^{-\frac{3}{2}} \cos\frac{3}{2}\,\phi dA \tag{1}$$

where K_a is the applied or far-field stress intensity factor, E is Young's modulus, and ν is Poisson's ratio; and the integral is taken over the transformed region. Usually it is assumed that the martensitic transformation occurs when the hydrostatic stress reaches a critical value [2,21], though the maximum principal stress has also been used as a criterion [26]. The hydrostatic stress, assuming the crack tip is in a state of plane strain, is given by

$$\sigma_m^c = \frac{K(1 + \nu)}{3}\left(\frac{2}{\pi R}\right)^{1/2} \cos\phi/2 + \int\int_A F(z,z_0)\, dx_0 dy_0 \tag{2}$$

where $z = (x + iy)$ and

$$F(z, z_0) = \frac{E\theta^T}{18\pi}\left[\frac{1 + \nu}{1 - \nu}\right] \text{Re}\left\{\frac{1}{\sqrt{(zz_0)}[\sqrt{z} + \sqrt{(z_0)}]^2} + \frac{1}{\sqrt{(z\bar{z}_0)}[\sqrt{z} + \sqrt{\bar{z}_0}]^2}\right\} \tag{3}$$

where R and ϕ are defined in Fig. 1, and the integral is taken over the transformed region.

Because Eq 2 does not give the transformed zone explicitly, Budiansky et al. [21,22] have assumed that the hydrostatic stress can be approximated by the first term. This assumption leads to an overestimate of the transformed region as has been shown by their later work that includes the second term [23,24]. However, it is necessary to solve a nonlinear integral equation to determine the "exact" shape of the transformed zone. The R-curve based on the "exact" shape of the zone has been calculated using a multivariable iterative procedure by Stump and Budiansky [24] in Fig. 2 where L is the characteristic length related to the critical hydrostatic stress for transformation, σ_m^c, and the fracture toughness, K_{Ic}^0 by

$$L = \left(\frac{2}{9\pi}\right)\left[\frac{K_{\text{Ic}}^0(1 + \nu)}{\sigma_m^c}\right]^2 \tag{4}$$

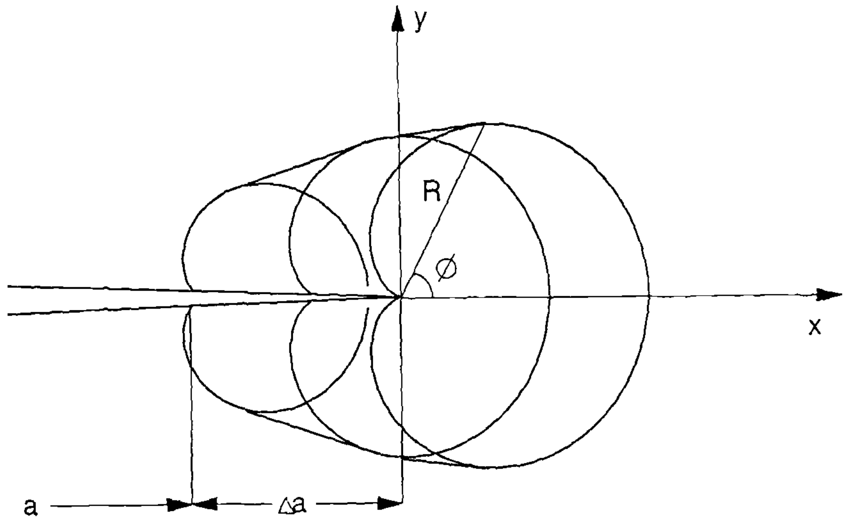

FIG. 1—*The development of the transformation zone at a crack tip.*

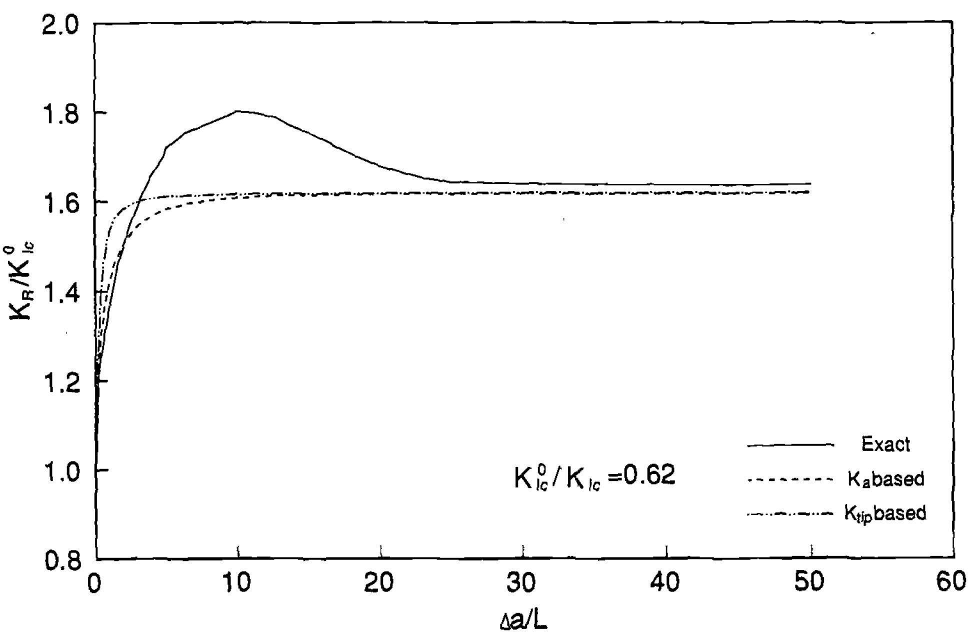

FIG. 2—*Comparison of* R*-curves based on approximate and "exact" theory* (K_{Ic}^0/K_{Ic}^∞ = 0.62).

For applications to static fatigue, it is desirable to have a simpler algorithm. Here we assume that the hydrostatic stress can be approximated simply by the first term in Eq 2 and the transformation zone, $R(\phi)$, may be calculated from either the applied stress intensity factor, K_a, or the crack tip stress intensity factor, K_{tip}, that is

$$R(\phi) = \left(\frac{2}{9\pi}\right)(1 + \nu)^2 \left(\frac{K}{\sigma_m^c}\right)^2 \cos^2(\phi/2) \tag{5}$$

where $K = K_a$ or K_{tip}. The R-curves based on these two K values (K_a and K_{tip}) are also calculated and shown in Fig. 2 along with the "exact" R-curve predicted by including the second term in Eq 2. The approximate R-curves fail to predict the high toughness values above the steady-state toughness, K_{Ic}^{∞} in the range of $\Delta a/L$ values between 2 and 20. However, for $\Delta a/L < 2$, these R-curves are overestimated, although the curve based on K_a in Eq 5 agrees reasonably well with the exact R-curve. Unfortunately, the exact R-curve has not yet been matched with the experimental data. Indeed, the approximate methods give R-curves that are consistent with test results [*9*]. As mentioned in the beginning of this paper, we prefer to analyze slow crack growth in the transformation–toughened ceramics using K_a rather than K_{tip} in estimating $R(\phi)$ from Eq 5. This avoids the iterative calculations that would otherwise be required, and the predicted R-curve is in reasonable agreement with the exact R-curve other than in the region where the toughness values are above the plateau value. For steady-state crack growth in this case, the crack-tip stress intensity factor, K_{tip}, is equal to the fracture toughness, K_{Ic}^0 of the equivalent nontoughened ceramic and the ratio of K_{Ic}^0 to the R-curve plateau value of the stress intensity factor, K_{Ic}^{∞}, can be written as [*21*]

$$K_{Ic}^0/K_{Ic}^{\infty} = 1 - \omega/4\sqrt{3}\,\pi \tag{6}$$

where $\omega = (1 + \nu)E\theta^T/\sigma_m^c(1 - \nu)$ is a nondimensional parameter that defines the transformation toughening process.

Approximate Theory for Slow Crack Growth in Transformation-Toughened Ceramics

It is assumed that the power law

$$\frac{da}{dt} = AK_{tip}^n \tag{7}$$

describes environmental crack growth in the stress-controlled regime (Region I), where da/dt is the crack growth rate, and A and n are constants. The value of the crack-tip stress intensity factor, K_{tip}, depends on the applied stress intensity factor, K_a, and the amount of crack growth, Δa, as given in Eq 1. Hence, the rate of crack growth is not strictly a unique function of the applied stress intensity factor, but apart from the initial period of crack growth at higher crack growth rates before the transformed shielding zone is well established, the dependence of crack growth on the initial starting conditions is slight.

The applied stress intensity factor, K_a, can be expressed in terms of a nondimensional geometrical factor, $Y(a)$, by

$$K_a = \sigma_n Y\sqrt{\pi a} \tag{8}$$

where σ_n is a nominal stress independent of the crack size, a. The crack-tip stress intensity factor, K_{tip}, at first decreases with crack growth due to the shielding of the crack tip. The crack growth can arrest if the applied stress intensity factor is small and shielding reduces the crack-tip stress intensity factor to the threshold value of the stress intensity factor. If $K_{Ic}^0 < K_a^0 < K_{Ic}^{\infty}$, the crack will grow instantaneously until the shielding of the crack tip reduces the crack-tip stress intensity factor to K_{Ic}^0, the crack-tip stress intensity factor will then still further be reduced during the initial slow crack growth. Eventually, the shielding effect will reach a maximum, and thereafter the crack-tip stress intensity factor and the crack growth rate will increase with the applied stress intensity factor.

As a crack grows, the material ahead of the crack tip will be transformed as the hydrostatic stress increases to the critical stress for transformation that is calculated approximately from the applied stress intensity factor, K_a. The crack length is increased incrementally, and the applied stress intensity factor for the new crack length is calculated. The region at the crack tip with a hydrostatic stress greater than the critical value is estimated. Straight lines with common tangents to the new transformed zone and the zone at the previous crack position are found (see Fig. 1). The crack-tip stress intensity factor, K_{tip}, is then calculated from Eq 1. If $K_{tip} > K_{Ic}^0$, the crack growth rate is infinite until the shielding reduces the crack tip stress intensity factor to K_{Ic}^0. When $K_{tip} \leq K_{Ic}^0$, the crack growth rate is given by Eq 7.

Comparison of Theoretical and Experimental Crack Growth Rates

Becher [*15*] has obtained subcritical crack growth data on magnesia (7.2 mol %) partially stabilized zirconia both as-fired and after aging at 1400°C in air for 8 h. After aging, most of the tetragonal zirconia have transformed to monoclinic, and there is very little shielding of the crack tip due to phase transformation. However, in this as-fired PSZ, only a small fraction of the tetragonal zirconia have transformed on cooling and, during crack propagation, the crack tip is shielded significantly by the transformation. Figures 3 and 4 give the slow crack growth

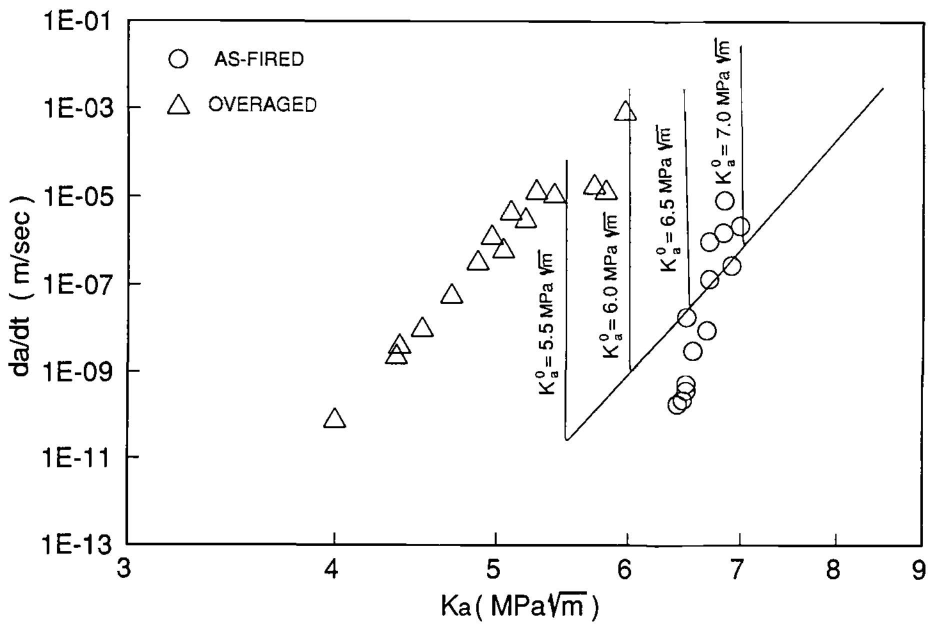

FIG. 3—*Subcritical crack growth in air for Mg-PSZ with 7.2 mol % MgO (experimental results taken from Ref* 15*).*

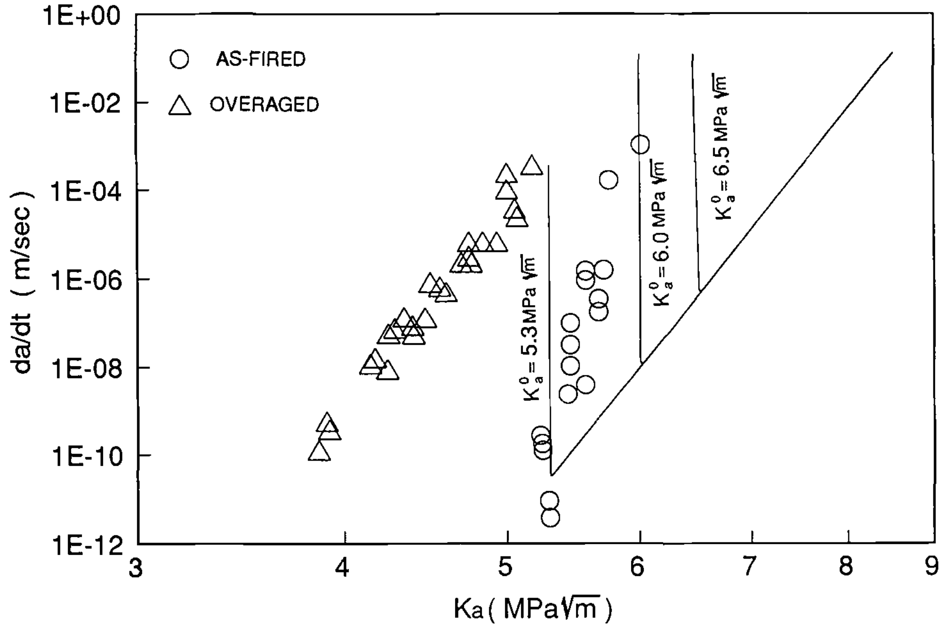

FIG. 4—*Subcritical crack growth in water for Mg-PSZ with 7.2 mol % MgO (experimental results taken from Ref* 15).

behavior of the Mg-PSZ in the two conditions in air and water at 22°C. Linear regression has been used to fit lines to Region I for the curves for the aged PSZ; since there is little shielding of the crack tip in this material, it is assumed that the slope and intercepts of these lines give the crack growth rate as a function of the crack-tip stress intensity factor as defined in Eq 7. The fracture toughness of the aged material, which was 6.0 MPa $\sqrt{m}$, is identified with K_{Ic}^0, and the critical stress intensity factor for the as-fired material (8.5 MPa $\sqrt{m}$) is identified with the plateau fracture toughness, K_{Ic}^{∞}. The shielding parameter, $\omega = 6.4$, has been calculated from Eq 6 using the ratio, K_{Ic}^0/K_{Ic}^{∞}. Using a range of initial values of the applied stress intensity factor, K_a^0, the crack growth rates for the as-fired materials have been calculated as described earlier. The theory initially predicts a period of high decelerating crack growth. However, the crack extension in this region of high crack growth is very small, and it would be difficult to detect. Decelerating crack growth has been reported for very small natural cracks $< 200\ \mu m$ in Mg-PSZ, in these tests the negative slope decreased with the initial value of the stress intensity factor [*17,18*]. The theory predicts approximately the correct shift in K_a for the tests performed in air, though it does not model the increase in the slope of the crack growth data. For the tests performed in water, the shift in K_a is overestimated and the theory again fails to predict the increase in slope.

Swain [*16*] has shown some static fatigue data for a Mg-PSZ (with 9 mol % MgO) ceramic subjected to different heat treatments giving an as-fired (AF) material with a fracture toughness 6.5 MPa $\sqrt{m}$, a maximum strength (MS) grade with a toughness of 10 MPa $\sqrt{m}$, and a thermal shock resistant (TS) grade with a toughness about 13.5 MPa $\sqrt{m}$. These slow crack growth results are shown in Fig. 5. Since the tetragonal zirconia precipitates in this AF material are cooled rapidly, they are smaller than the critical size required for the stress-induced $t \rightarrow m$ transformation. Its higher toughness than the cubic stabilized zirconia is merely caused by the presence of the stable tetragonal zirconia phase, and there is little transformation toughening

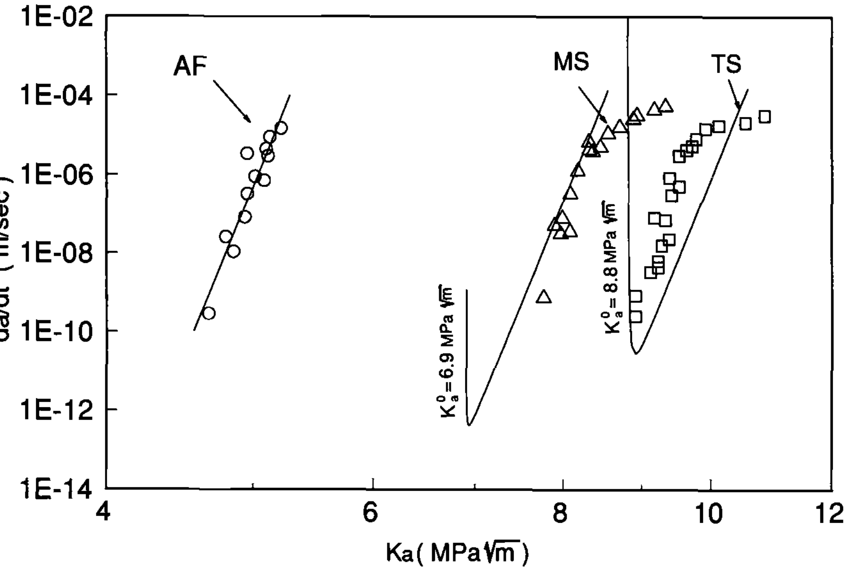

FIG. 5—*Subcritical crack growth in air for Mg-PSZ with 9.4 mol % MgO (experimental results taken from Ref* 16*).*

available. Using the AF material data as the reference curve and the shielding parameter, ω = 8.3 for MS-PSZ and ω = 10.9 for TS-PSZ obtained from Eq 6, we can predict the slow crack growth data for both MS and TS materials as shown in Fig. 5. Quite clearly, the predictions from the proposed model agree quite well with experimental data in Region I where there is little change in the slopes with increased toughness.

Becher [*14*] has also given slow crack data on ZTA. The theory given in this paper cannot be applied strictly to such ceramics because some 30 to 40% of the shielding of this toughened ceramic comes from the reduction in the Young's modulus in the transformed region due to the microcracking [*27*]. Becher tested two alumina ceramics containing 20% by volume zirconia at 22°C and 65% relative humidity: one partially stabilized with 1 mol % of yttria and the other completely stabilized by 3 mol % of yttria (Fig. 6). It is assumed that there is no crack-tip shielding in the stabilized alumina, though there will be some toughening due to microcracking and crack bridging, and its fracture toughness of 4.5 MPa $\sqrt{m}$ can be identified with K_{Ic}^{0}. The plateau value of the stress intensity factor, K_{Ic}^{∞}, for the partially stabilized version is 8.5 MPa $\sqrt{m}$. Ignoring the effect of the reduction in the Young's modulus, we have again used Eq 6 to obtain an estimate of the toughening parameter (ω = 10.2). Having obtained the constants, A and n, in Eq 7 from the crack growth data for the stabilized ceramic, we have estimated the crack growth rates for the partially stabilized ceramic. Although the present theory is not strictly applicable to the ZTAs, it does predict the crack growth data for the toughened ceramic quite well for a range of initial applied stress intensity factor values, K_a^0, as given in Fig. 6.

Conclusions

An approximate theoretical model has been given for predictions of the subcritical crack growth in dilatant-zone-toughened ceramics. By using the stress field due to the applied stress intensity factor to calculate approximately the transformed region, rather than calculating the exact region, iteration is avoided. The theory predicts an initial region where there is a rapid

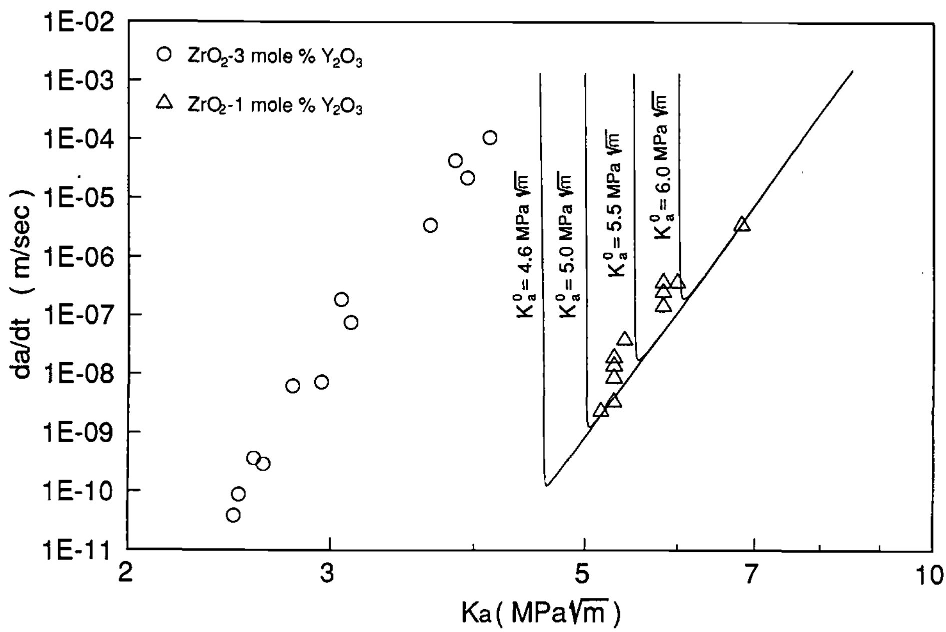

FIG. 6—*Subcritical crack growth in air for Y-ZTA (experimental results taken from Ref* 14).

deceleration in the crack growth. This decelerating crack growth has only been reported for very short cracks [*17,18*]; for the long cracks, the deceleration predicted is so rapid that, if present in the tests, it would not be detected. Apart from this initial crack growth, the crack growth rate is virtually independent of the initial stress intensity factor or specimen geometry. The theory predicts the crack growth curve is shifted to lower growth rates with little change in slope, that is, A of the slow crack growth Eq 7 is substantially reduced but n remains relatively constant. The Mg-PSZ tests of Becher [*15*] do show a reduction in slope as well as a shift. However, his results for ZTA [*14*] and Swain's results for Mg-PSZ [*16*] show no change in the slope; hence these data are reasonably predicted by the approximate theory.

The theory presented does not precisely predict the experimental results, but refinement of the theory to more accurately estimate the transformation zone based on Eq 2 with the second term would not increase the accuracy of the predictions of the crack growth rates. Not all of the toughening observed is due to transformation, and the estimation of the toughening parameter, ω, from the K_R-curve is not precise. The prediction of crack growth from the crack-tip stress intensity factor is reasonably accurate.

Acknowledgments

The authors wish to thank the Australian Research Council for the continuing support of this work. Mr. Kai Duan is supported by a CSIRO/Sydney University Collaborative Research Scholarship.

References

[*1*] Evans, A. G. and Heuer, A. H., "Review—Transformation Toughening in Ceramics: Martensitic Transformation in Crack Tip Stress Fields," *Journal*, American Ceramics Society, Vol. 63, 1980, pp. 241–248.

[2] McMeeking, R. M. and Evans, A. G., "Mechanics of Transformation Toughening in Brittle Materials," *Journal,* American Ceramics Society, Vol. 65, 1982, pp. 242–246.

[3] Evans, A. G. and Faber, K. T., "Crack-Growth Resistance of Microcracking Brittle Materials," *Journal,* American Ceramic Society, Vol. 67, 1984, pp. 255–260.

[4] Evans, A. G. and Cannon, R. M., "Toughening of Brittle Solids by Martensitic Transformations," *Acta Metallurgica et Materiala,* Vol. 34, 1986, pp. 761–800.

[5] Evans, A. G., "Perspective on the Development of High-Toughness Ceramics," *Journal,* American Ceramics Society, Vol. 73, 1990, pp. 187–206.

[6] Claussen, N., "Fracture Toughness of Al_2O_3 with an Unstabilized ZrO_2 Dispersed Phase," *Journal,* American Ceramic Society, Vol. 59, 1976, pp. 49–51.

[7] Claussen, N., "Transformation-Toughened Ceramics (TTC)," *Ceramics in Advanced Energy Technologies,* H. Krockel, M. Merz, and O. Van Der Biest, Eds., D. Reidel Publishing Company, Dordrecht, 1984, pp. 51–86.

[8] Claussen, N., Steeb, J., and Pabst, R. F., "Effect of Induced Microcracking on the Fracture Toughness of Ceramics," *The American Ceramic Society Bulletin,* Vol. 56, 1977, pp. 559–562.

[9] Swain, M. V. and Hannink, R. H. J., "R-Curve Behavior in Zirconia Ceramics," *Advance in Ceramics, 12, Science and Technology of Zirconia II,* N. Claussen, M. Rühle, and A. H. Heuer, Eds., American Ceramic Society, Columbus, OH, 1984, pp. 225–239.

[10] Kendall, K., Alford, N. M., and Birchall, J. D., "Weibull Modulus of Toughened Ceramics," *Advanced Structural Ceramics, MRS 78,* P. F. Becher, M. V. Swain, and S. Sõmiya, Eds., Materials Research Society, Philadelphia, 1987, pp. 189–197.

[11] Kendall, K., Alford, N. M., Tan, S. R., and Birchall, J. D., "Influence of Toughness on Weibull Modulus of Ceramic Bending Strength," *Journal of Materials Research,* Vol. 1, 1986, pp. 120–123.

[12] Li, L.-S. and Pabst, R. F., "Micromechanics of Subcritical Crack Growth of Partially Stabilized Zirconia (PSZ)," *Proceedings,* Third European Colloquium on Fracture, J. C. Radon, Ed., Pergamon, New York, 1980, pp. 251–255.

[13] Lenz, L. K. and Heuer, A. H., "Stress-Induced Transformation during Subcritical Crack Growth in Partially Stabilized Zirconia," *Journal,* American Ceramic Society, Vol. 65, 1982, pp. C192–C194.

[14] Becher, P. F., "Slow Crack Growth Behavior in Transformation-Toughened Al_2O_3–$ZrO_2(Y_2O_3)$ Ceramics," *Journal,* American Ceramics Society, Vol. 66, 1983, pp. 485–488.

[15] Becher, P. F., "Subcritical Crack Growth in Partially Stabilized $ZrO_2(MgO)$," *Journal of Materials Science,* Vol. 21, 1986, pp. 297–300.

[16] Swain, M. V., "Lifetime Prediction of Ceramic Materials," *Materials Forum,* Vol. 9, 1986, pp. 34–44.

[17] Jensen, D. G., Zelizko, V., and Swain, M. V., "Small Flaw Static Fatigue Crack Growth in Mg-PSZ," *Journal of Materials Science Letters,* Vol. 8, 1989, pp. 1154–1157.

[18] Lentz, W., "Fatigue Behaviour and Lifetime of a Magnesia Partially Stabilized Zirconia Containing Micro-Cracks due to Indentation," diplomarbeit thesis, Universität Karlsruhe, Karlsruhe, Germany, 1989.

[19] Mai, Y.-W, "Fracture Resistance and Fracture Mechanisms of Engineering Materials," *Materials Forum,* Vol. 11, 1988, pp. 230–267.

[20] Dauskardt, R. H., Carter, W. C., Veirs, D. K., and Ritchie, R. O., "Transient Subcritical Crack-Growth Behavior in Transformation-Toughened Ceramics," *Acta Metallurgica et Materiala,* Vol. 38, 1990, pp. 2327–2336.

[21] Budiansky, B., Hutchinson, J. W., and Lambropoulos, J. C., "Continuum Theory of Dilatant Transformation Toughening in Ceramics," *International Journal of Solids and Structures,* Vol. 19, 1983, pp. 337–355.

[22] Hutchinson, J. W., "Initial Crack Growth Tearing Resistance in Transformation Toughened Ceramics," *Advanced Materials for Severe Service Applications,* K. Iida, Ed., Elsevier, London, 1987, pp. 77–90.

[23] Amazigo, J. C. and Budiansky, B., "Steady-State Crack Growth in Supercritically Transforming Materials," *International Journal of Solids and Structures,* Vol. 24, 1988, pp. 751–755.

[24] Stump, D. M. and Budiansky, B., "Crack-Growth Resistance Curves in Transformation-Toughened Ceramics," *International Journal of Solids and Structures,* Vol. 25, 1989, pp. 635–646.

[25] Hutchinson, J. W., "On Steady Quasi-Static Crack Growth," Report DEAP S-8, Harvard University, Cambridge, MA, 1974.

[26] Lambropoulos, J. C., "Shear, Shape and Orientation Effects in Transformation Toughening," *International Journal of Solids and Structures,* Vol. 22, 1986, pp. 1083–1106.

[27] Hutchinson, J. W., "Crack Tip Shielding by Micro-Cracking in Brittle Solids," *Acta Metallurgica et Materiala,* Vol. 35, 1987, pp. 1605–1619.

Zhikai Guo,[1] Jung-Heum Yon,[2] Neil M. Hawkins,[2] and Albert S. Kobayashi[1]

Fracture Energy Dissipation Mechanism of Concrete

REFERENCE: Guo, Z. Yon, J.-H., Hawkins, N. M., and Kobayashi, A. S., "**Fracture Energy Dissipation Mechanism of Concrete,**" *Fracture Mechanics: Twenty-Third Symposium, ASTM STP 1189,* Ravinder Chona, Ed., American Society for Testing and Materials, Philadelphia, 1993, pp. 797–805.

ABSTRACT: Moiré interferometry was used to determine the crack opening displacements (COD) along a stably or dynamically propagating crack in three-point-bend concrete specimens. For stable crack growth studies, the measured COD together with applied loading was input to a finite element model of the specimen to determine directly the crack closure stress (CCS) versus COD relationship along the fracture process zone (FPZ) that trailed the crack tip. For dynamic crack growth studies, the COD data together with three strain gage data taken along the crack path were used in an inverse analysis to extract the CCS versus COD relationships using a dynamic finite element model of the fracturing specimen. Variations in energy release and dissipation rates with crack extension were determined and the FPZ was identified as the major energy sink in concrete fracture.

KEY WORDS: concrete fracture, fracture process zone, energy release rate, energy dissipation rate, moiré interferometry, fracture mechanics

The concept of a fracture process zone (FPZ) that trails an advancing crack tip and retards crack opening through aggregate bridging has been attributed generally to Hillerborg [*1*]. Visual inspection of the tortuous fracture surface, which is unique to concrete fracture, has lent credence to the concept of aggregate bridging without experimental quantification at that time. Of the score of papers published after Hillerborg, most involved an inverse analysis with a maximum tensile strength criterion for crack extension. Modeling of the FPZ was considered complete when the computed and measured remote loading parameters, which unfortunately were insensitive to the small changes in the FPZ, coincided. An exception to the preceding is the two-parameter fracture criterion that involved a critical stress intensity factor, K_{Ic}, and a critical crack tip opening displacement, $CTOD_c$, proposed by Shah and his colleagues [*2*]. The existence of a crack-tip singularity in the Jenq-Shah model was later verified from crack opening displacement (COD) studies of concrete specimens using holographic interferometry [*3*].

The authors and their colleagues unknowingly traced this same history in their studies of the fracture process zone in concrete. At the onset of our studies, we matched the experimentally and numerically determined remote loading parameters in concrete fracture specimens using a postulated FPZ, without the crack tip singularity. This FPZ modeling approach, that is, a nonsingular FPZ, was later contradicted by the existence of a parabolic crack tip opening

[1] Predoctoral research associate and professor, respectively, Department of Mechanical Engineering, University of Washington, Seattle, WA 98195.

[2] Postdoctoral research associate and professor/head, respectively, Department of Civil Engineering, University of Illinois, Urbana, IL 61801.

profile that was unambiguously shown by moiré interferometry studies of the COD in concrete fracture specimens [4]. The parabolic crack tip opening profile, according to linear elastic fracture mechanics, implies the existence of a $1/\sqrt{r}$ stress singularity and resulted in the development of an FPZ model that incorporated a stress singularity and was referred to as a singular FPZ model [5]. This model also provided the size effect necessary for using the same linear elastic fracture mechanics analysis for large concrete structures, such as a dam, as well as for small concrete fracture specimens. At one of these two extremes, a fully developed singular FPZ, which is material dependent, would have a negligible effect on the driving force, that is, the stress intensity factor, of a long crack in a large concrete structure. However, the same singular FPZ will reduce the stress intensity factor in a laboratory fracture specimen while retaining the same critical stress intensity factors for stable and unstable crack growths.

In this paper, the singular FPZ model is used to study the fracture energy dissipation mechanism of concrete fracture specimens that are undergoing stable and rapid crack growth.

Procedure

The singular FPZ in a three-point bend, concrete fracture specimen was determined by a hybrid experimental-numerical procedure. The crack opening displacements (COD), determined by moire interferometry, were incorporated into a static/dynamic finite-element model of the fracture specimen, and the various fracture parameters were computed, either directly or by an inverse analysis. Details of the inverse and the direct analyses are found in Refs *6* and *7*, respectively.

Experimental Analysis

Specimens

Figure 1 shows the three-point-bend, concrete fracture specimens used in this study. High early strength portland cement, an aggregate of 6.4 mm maximum size and a local Seattle sand were used in the mix that is shown in Tables 1 and 2. The tensile strengths of the statically loaded concrete specimens were varied by removing each specimen from the constant humidity storage room at different times and then leaving them to cure in the laboratory. For most of the specimens, stable or rapid crack growth was initiated from a saw-cut notch.

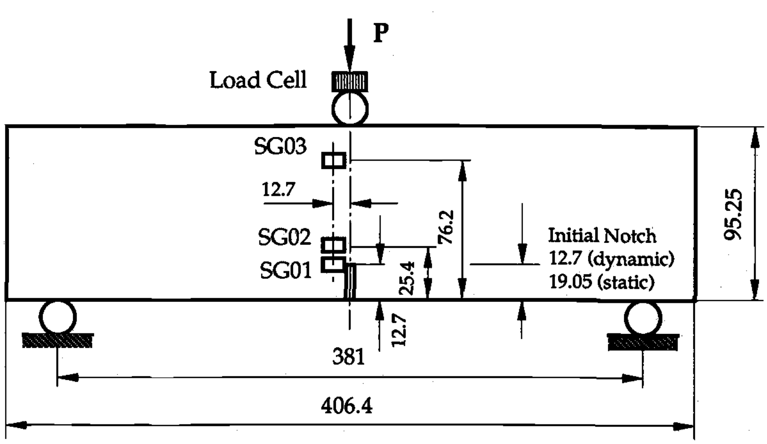

FIG. 1—*Geometry and strain gage locations for three-point-bend specimen.*

TABLE 1—*Static properties.*

	Displacement-Controlled Bend Tests			
	Average of Five Tests	TPB-02	TPB-04	TPB-05
Mix design (by weight)	Cement:Gravel:Sand:Water (1.0:3.4:2.9:0.6)(1.0:2.0:2.5:0.4 to 0.5)			
Static compression strength, MPa	35.4	...	...	...
Elastic modulus tension compression, GPa	29.6 29.6	37.9 ...	40.5 40.5	42.5 42.5
Maximum length of FPZ, mm	96.6	60	45	60

Experimental Procedure

Two-beam moiré interferometry was used to measure the COD of the propagating crack. For the dynamic study, three strain gages were located as shown in Fig. 1, and used to determine the position of the tip of the rapidly extending crack.

The test procedure for stable crack growth study consisted of recording the load and the moiré fringes associated with an incremental increase in applied displacement loading. Fracture was initiated by drop-weight for the dynamic crack propagation study. Four frames of transient moiré fringe patterns were recorded by a specially configured IMACON 790 image converter camera. The strain-gage data and load-line displacement were also recorded using oscilloscopes.

Numerical Analysis

The early portion of the static fracture analysis and all of the dynamic analysis were conducted using an inverse procedure where the assumed crack closure stress (CCS) versus COD relationship was varied to best fit both the measured COD distribution along the stably or rapidly extending crack and other remote loading parameters, such as the load and the load-line displacements. In addition, in the dynamic analysis, the modulus of elasticity and the residual stress due to shrinkage in the vicinity of the notch tip were varied so that the computed and measured time histories for the three strain gages matched [4,5]. In later static analysis, a direct procedure was used where a curve of best fit to the measured COD and applied load data were

TABLE 2—*Dynamic properties.*

	Drop-Weight Bend Test, Average of Four Tests
Mix design (by weight)	Cement:Gravel:Sand:Water (1.0:2.0:2.5:0.4 to 0.5)
Static compression strength, MPa	55.1
Elastic modulus tension, compression, GPa	34.5 41.4
Maximum length of FPZ, mm	50.8

used as input boundary conditions to the finite element model of the fracture specimen [6,7].

For both static and dynamic analyses, energy release rates were computed directly by incrementing the crack tip by one finite element node. The energy dissipation rate was computed from the work rate in the FPZ. The stress intensity factor was computed directly from a calibrated crack tip state of stress.

Results

Experimental Results

Figure 2 shows typical moiré fringe patterns corresponding to the displacement field vertical to the crack. The variations in the measured COD with stable crack growth are shown as unbroken lines for a typical test in Fig. 3. Figure 4, which is a composite figure of the results for four tests, shows the variations in COD with rapid crack extension.

Numerical Results

Figure 5 shows the final CCS versus COD relationships, that is, the relationship that controls the FPZ used in matching the CODs, transient strains, and remote load parameters where applicable, for these three-point-bend, concrete fracture specimens. The four different relationships for the static tests are due to the varying curing conditions to which each specimen was subjected and which therefore affected the shrinkage stresses at the crack tip.

Figure 6 shows the measured and computed strains along the crack path as well as the load history in the specimens fractured by drop weight loading. The experimental results are averages of four test results.

Table 1 shows the static and dynamic mechanical properties gleaned from the numerical analysis. These mechanical properties are categorized in terms of curing conditions, that is, moist air curing, laboratory air curing, and loading conditions. Thus, the mechanical properties for moist air curing are averaged values of several tests while those of laboratory air curing are for single tests for Specimens TPB-02, TPB-04, and TPB-05.

Figure 7 shows the energy released and the energy dissipation rates for the different fracture specimens. This energy dissipation rate relates only to the FPZ and thus does not include those due to other energy sinks, such as microcrackings ahead of the crack tip and aggregate-mortar debonding in the stressed specimen. The energy dissipation rates of the TPB-02 and TPB-04 specimens were omitted in Fig. 7, since they overlapped with those of TPB-05. The energy rates for the earlier displacement-controlled and the present specimens (TPB-02, TPB-04, and TPB-05) differ considerably. The possible difference is attributed to the extreme brittleness of the TPB-02, TPB-04, and TPB-05 specimens as evidenced by their lower energy release rates prior to the onset of unstable crack growth. This brittleness is attributed to the shrinkage stress generated during the extended laboratory air curing process prior to final testing. The parallel but increasing energy rates prior to reaching a fully developed FPZ are attributed to the gradual development of the FPZ with crack extension. After the FPZ is fully developed, the energy rates remain constant during subsequent crack extension. The constant differences between the energy release and the FPZ dissipation rates throughout the entire crack extension is attributed to the energy dissipated at the frontal process zone due to microcracking at the crack tip.

Figure 8 shows the resistance curves in terms of the stress intensity factor for the five groups of tests. As is to be expected, the resistance curves for the specimens with the FPZ remains relatively constant throughout the crack growth.

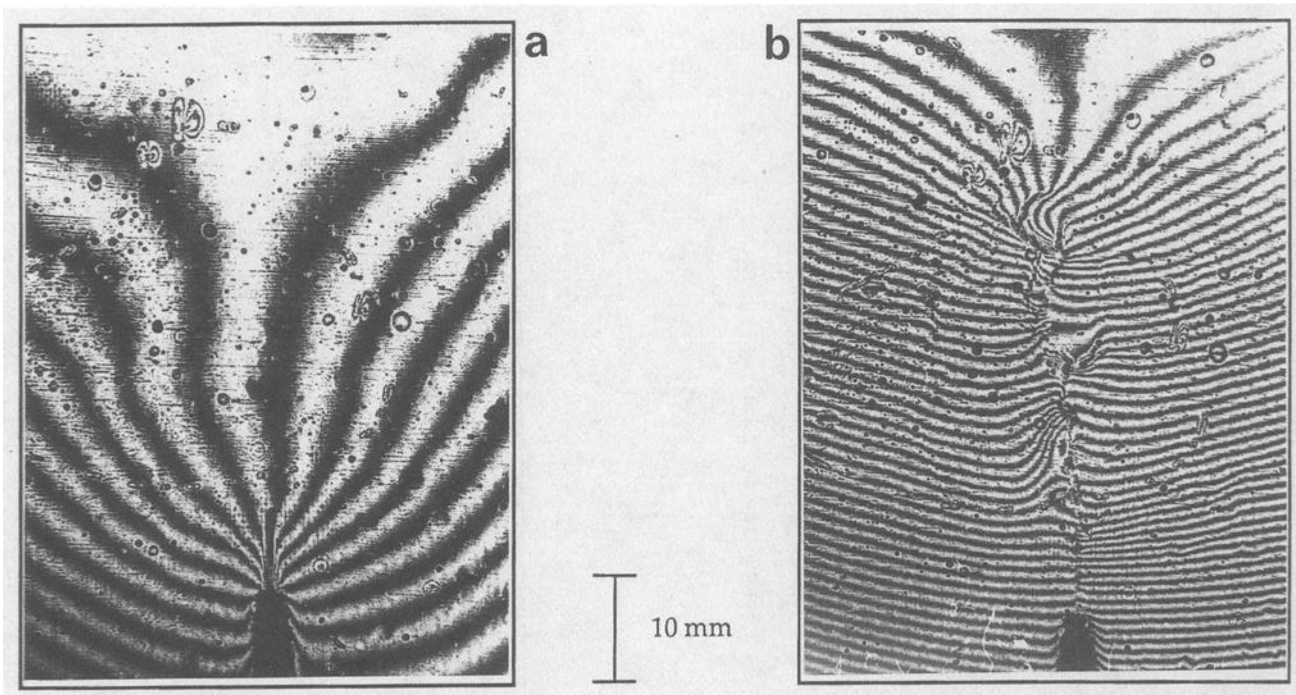

FIG. 2—*Typical moiré interferometry fringes at two stages of loading prior to peak loading for three-point-bend specimen TPB-05;* (a) *load = 1905 N and* (b) *load = 4050 N.*

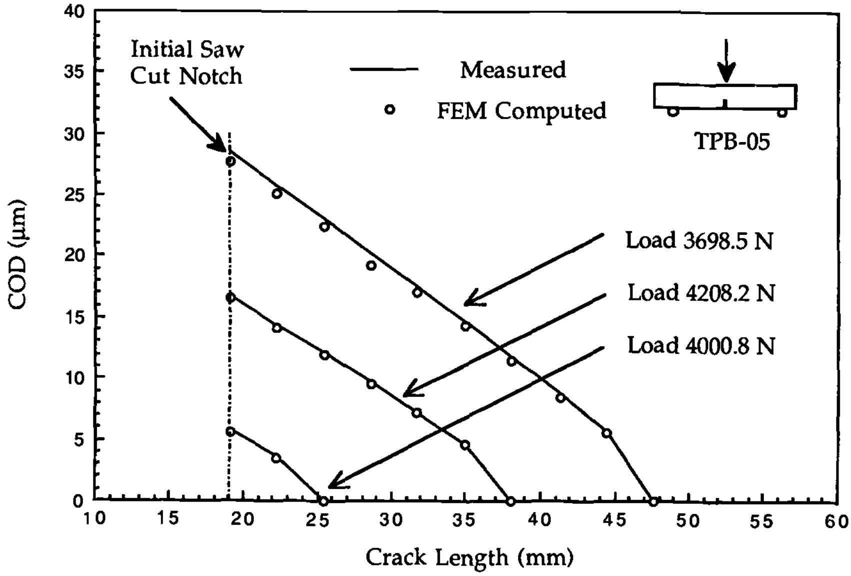

FIG. 3—*COD variations for an extending crack in a statically loaded specimen.*

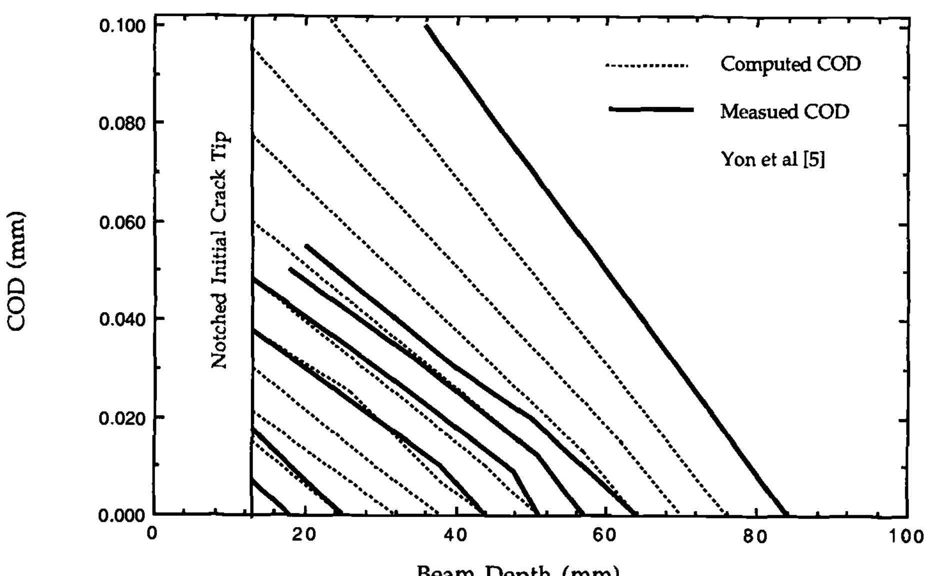

FIG. 4—*COD in dynamically loaded three-point-bend specimen. Composite data of four tests.*

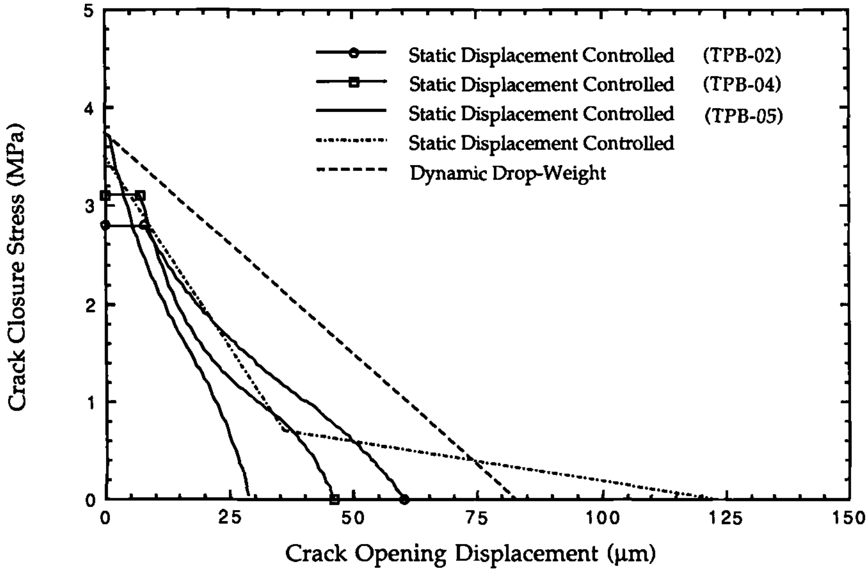

FIG. 5—*Crack closure stress versus crack opening displacement relationships in three-point-bend specimens.*

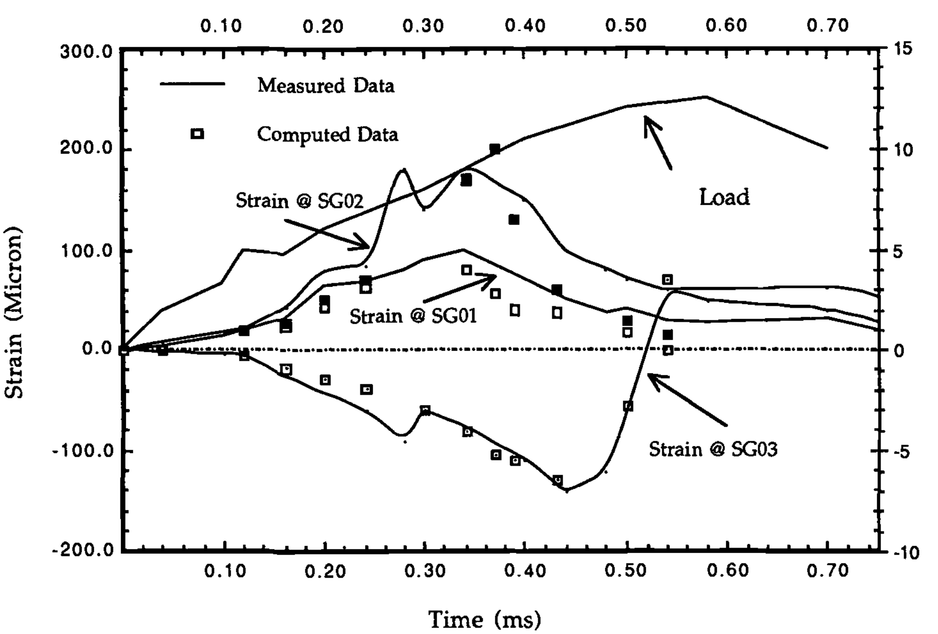

FIG. 6—*Measured and computed strain histories for drop-weight-bend tests. Average of four tests.*

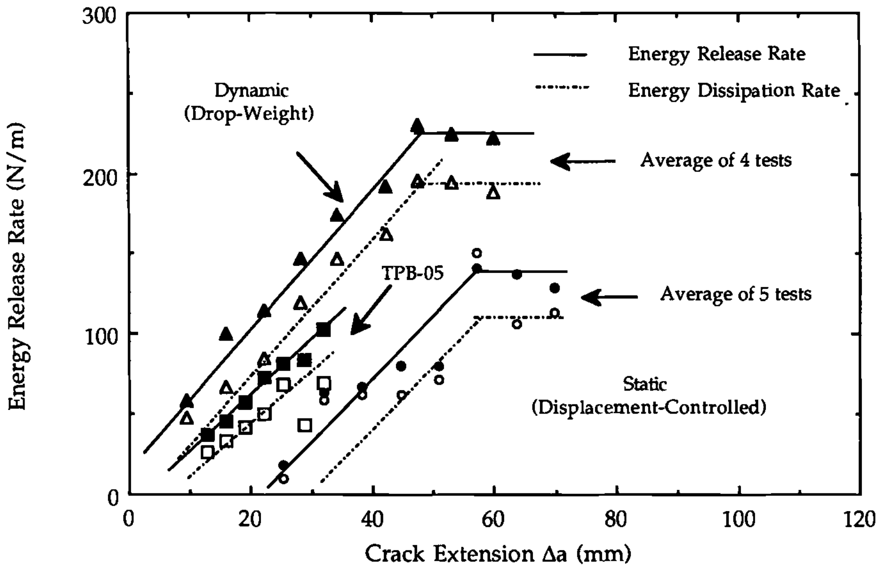

FIG. 7—*Energy release and dissipation rates for three-point-bend fracture specimens.*

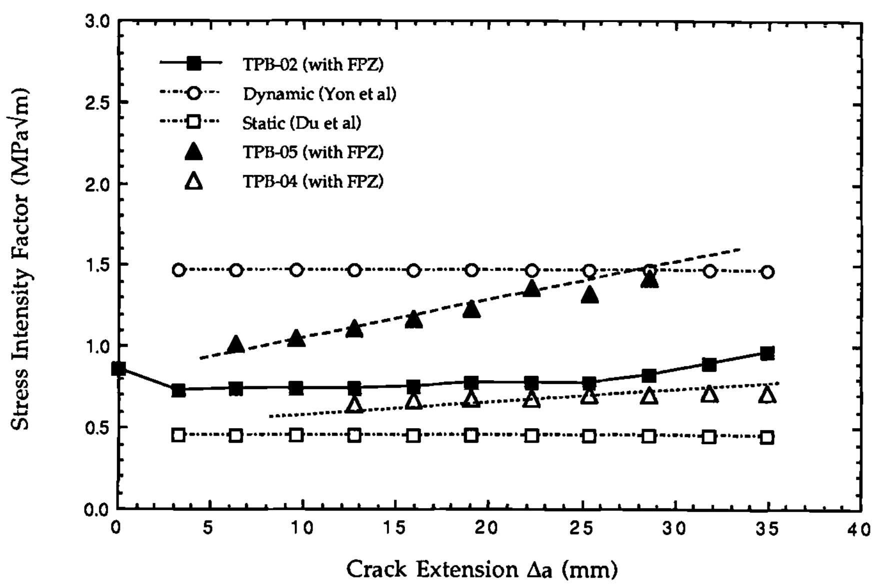

FIG. 8—*Fracture resistance curves.*

Conclusions

1. While CCS versus COD relationship varied with concrete strength and loading condition, it remained invariant throughout crack extension for a given specimen.
2. The singular FPZ model for concrete fracture provides a flat resistance curve, that is, a flat K_R, which is consistent with the behavior for other brittle materials, such as ceramics.
3. The dominant energy dissipation mechanism during concrete fracture is crack bridging in the fracture process zone (FPZ).

Acknowledgment

This research was supported by the U.S. Air Force Office of Scientific Research (AFOSR) Grants AFOSR 86-0204 and 91-0218 and National Science Foundation (NSF) Grant MSM-892287. The authors wish to thank Dr. Spencer Wu, AFOSR, and Dr. Ken Chong, NSF, for their continuing support and encouragement.

References

[1] Hillerborg, A., Modeer, M., and Petersson, P. E., "Analysis of Crack Formation and Crack Growth in Concrete by Means of Fracture Mechanics and Finite Elements," *Cement and Concrete Research*. Vol. 6, 1976, pp. 773–782.

[2] Jenq, Y.-S. and Shah, S. P., "Two Parameter Fracture Model for Concrete," *Journal of Engineering Mechanics*, American Society of Civil Engineers, Vol. 110, 1985, pp. 1227–1241.

[3] Miller, R. A., Shah, S. P., and Bjelkagen, H. I., "Crack Profiles in Mortar Measured by Holographic Interferometry," *Experimental Mechanics*, Vol. 28, No. 4, 1988, pp. 388–394.

[4] Du, J. J., Yon, J.-H., Hawkins, N. M., Arakawa, K., and Kobayashi, A. S., "Fracture Process Zone for Concrete for Dynamic Loading," *Material Journal*, American Concrete Institute, Vol. 89, No. 3, 1992, pp. 252–258.

[5] Yon, J.-H., Hawkins, N. M., and Kobayashi, A. S., "Numerical Simulation of Mode I Dynamic Fracture of Concrete," *Journal of Engineering Mechanics*, American Society of Civil Engineers, Vol. 117, No. 7, July 1991, pp. 1595–1610.

[6] Yon, J.-H., Hawkins, N. M., Guo, Z.-K., and Kobayashi, A. S., "Fracture Process Zone Associated with Concrete Fracture," *Fracture Processes in Concrete, Rock and Ceramics*, J. G. M. van Mier, J. G. Rots, and A. Bakker, Eds., EFN Spon, London, 1991, pp. 485–494.

[7] Guo, Z. K., Kobayashi, A. S., and Hawkins, N. M., "Fracture Process Zone for Mode I Concrete Fracture," *Fracture of Engineering Materials and Structures*, J. H. Teoh and K. H. Lee, Eds., Elsevier Applied Sciences, London and New York, 1991, pp. 332–337.

Probabilistic and Dynamic Issues

Lawrence E. Eiselstein,[1] *David O. Harris,*[1] *T. M. Scoonover,*[2] *and Charles A. Rau*[1]

Probabilistic Fracture Mechanics Evaluation of Local Brittle Zones in HSLA-80 Steel Weldments

REFERENCE: Eiselstein, L. E., Harris, D. O., Scoonover, T. M., and Rau, C. A., **"Probabilistic Fracture Mechanics Evaluation of Local Brittle Zones in HSLA-80 Steel Weldments,"** *Fracture Mechanics: Twenty-Third Symposium, ASTM STP 1189,* Ravinder Chona, Ed., American Society for Testing and Materials, Philadelphia, 1993, pp. 809–825.

ABSTRACT: The engineering significance of local brittle zones in multipass, HSLA-80 steel weldments that might be subjected to large strains (such as the straining that occurs during explosive bulge testing) was evaluated through the use of probabilistic fracture mechanics. The heat-affected zone of HSLA-80 was modeled as containing only two distinct types of material along the fusion line, local brittle zones, and the gaps between them. The local brittle zones have a lower toughness than gap material, and both have toughness properties that are lower than those of the base plate. The model calculated the failure probability of weldments as they are plastically strained to various levels by simulating the growth of preexisting crack-like weld defects that are distributed along the fusion line and within the weld metal. Failure was considered to occur if weld defects link up and grow through the entire plate thickness. The model incorporates the statistical variation of the toughness for the base metal, weld metal, local brittle zones, and gap materials to model the tearing resistance along the fracture path. The probabilistic fracture mechanics modeling of typical HSLA-80 weldments indicates that the distribution and toughness of local brittle zones and gaps have a small effect on the failure probability at large plastic strains typical of explosive bulge tests. The calculated failure probabilities agree with a limited number of actual explosive bulge tests. At the large strain levels considered, the simulations showed that the failure probabilities are nearly equal to the existence probability of welding defects.

KEY WORDS: probabilistic fracture mechanics, welds, heat-affected zones, local brittle zones, HSLA-80 steel, A710 Grade A Class 3 steel, explosive bulge tests, weld defect distributions, elastic-plastic fracture mechanics, ship plate welds, fracture mechanics, fatigue (materials)

Many high-strength low-alloy steel (HSLA) weldments contain a microstructural feature known as local brittle zones (LBZs). These LBZs are contained within the heat-affected zone (HAZ) of the weldment, usually at or near the weld fusion line. These LBZs have been shown to have a much lower toughness than other regions in the weldment. The objective of this paper is to describe a probabilistic fracture mechanics (PFM) model to calculate the increase, if any, in the probability of service failure caused by the presence of local brittle regions in the HAZ of typical HSLA-80 steel multipass weldments.

[1] Managing engineers and vice president, respectively, Failure Analysis Associates, Inc., Menlo Park, CA 94025.
[2] Materials engineer, David Taylor Research Center, Annapolis, MD 21402.

Background

HSLA-80 is the name used to designate ASTM A710 Grade A Class 3 steel that has been modified to a military specification that, along with other requirements, specifies a minimum yield strength of 550 MPa [*1*]. The Navy's certification of HSLA-80 for use in surface ship hull construction occurred in February 1984 and provided shipbuilders with their first new steel since the mid 1950s [*2*]. This steel has been used as a replacement for martensitic HY-80 steel in the construction of U.S. Navy ships beginning with cruisers of the Ticonderoga class [*2–5*]. The low carbon content of HSLA-80 makes it much less sensitive to hydrogen-assisted HAZ cracking, and therefore it is able to be welded without the expensive preheat and process controls required for HY-80 [*2–5*].

During the certification process, the Navy conducted an intensive testing program to characterize HSLA-80 base plate and weldment properties, as well as the appropriate welding parameters [*2,4*]. Research conducted at David Taylor Research Center (DTRC) on HSLA-80 base plate and HAZ microstructures and mechanical properties after the certification program for HSLA-80 had been completed [*3,6,7*] showed that the fracture properties of certain small grain-coarsened regions of the HAZ were much lower than those of the base plate material. This raised the issue of whether these locally brittle zones could significantly increase the probability of fracture of welded plates. Figure 1 shows a macrograph of the material structure near a weld. Weld metal, base metal, and HAZ are shown. The LBZs in the HAZ are indicated. The presence, size, and location of the LBZs vary widely along a weld and from weld to weld. The size and location of LBZs are treated deterministically in this paper.

Large-scale (mostly explosive bulge) tests, conducted by the Navy during and after the certification program, indicated that welded plates with LBZs can withstand considerable mechanical strain before failure [*8*]. However, three weldments made from thick plate failed the explosive bulge test. Of these failures, only one showed a strong tendency for fracture to follow the weldment's HAZ.

The purpose of this paper is to describe a probabilistic fracture mechanics (PFM) analysis that was performed to quantify the influence of LBZs on the reliability of weldments in HSLA-80. In addition to the considerable variability in LBZ location, size, and toughness, other weld defects can be present with wide variability in frequency and size. Figure 2 schematically shows the types of weldments and weld defects considered. The heat-affected zone (HAZ) is considered to consist of local brittle zones and gap material (that is, material in the HAZ that is not LBZ).

In order to quantify the influence of LBZs on weld reliability, while accounting for the considerable scatter in material properties and defect characteristics, a PFM model was constructed and implemented by use of Monte Carlo simulation [*9*]. The computer code for the Monte Carlo simulation was called WREC, an acronym for Weld Reliability Evaluation Code. Figure 3 presents a schematic of the components of the code and their interrelationships.

The PFM model is based on an underlying deterministic fracture mechanics foundation. That is, a conventional deterministic fracture mechanics model of crack behavior is constructed, and then some of the inputs to the model (such as size and location of crack-like defects) are considered to be distributed randomly. Once the statistical distribution of the input random variables is defined, the weld reliability can be evaluated by successive (deterministic) calculations of strain to failure using a set of inputs drawn randomly from their respective distributions.

The remainder of this paper describes the deterministic fracture mechanics model, selection of deterministic inputs and distribution of random inputs, and generation of weld reliability results using the probabilistic model.

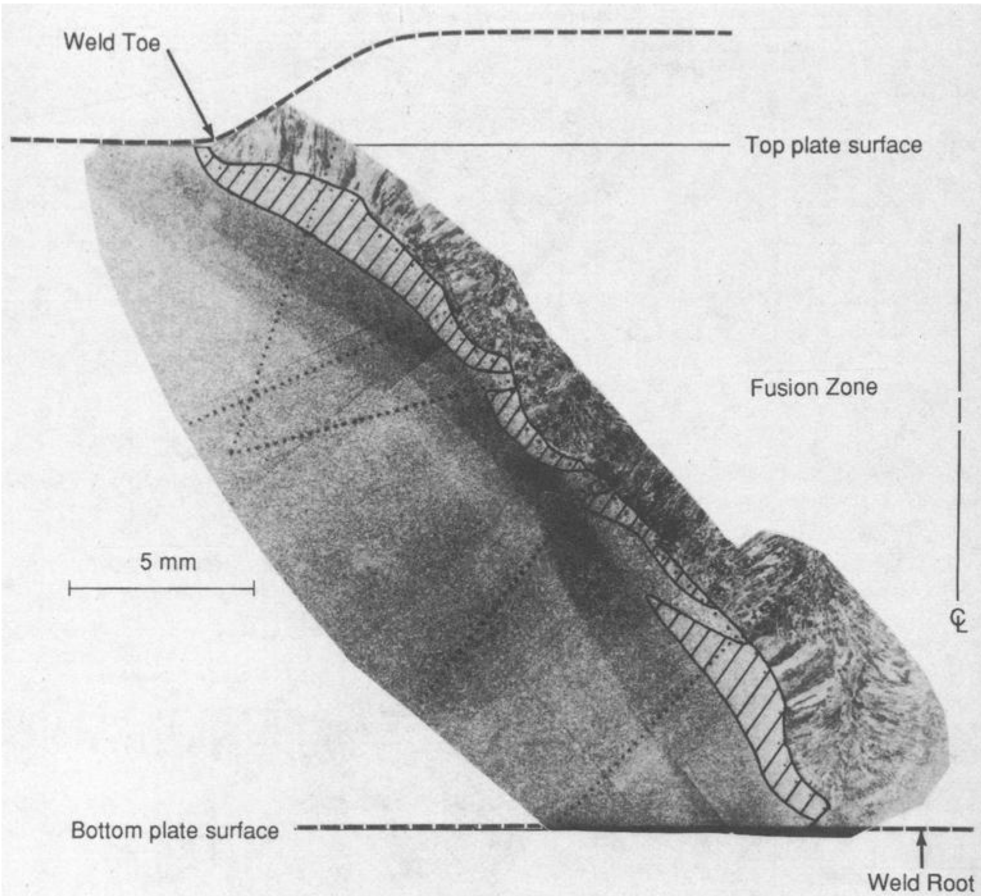

FIG. 1—*Macrostructure of HSLA-80 weldment cross section (weldment: C37, 19-mm thick, single-V, 90° equivalent total included angle). LBZs indicated by cross-hatching.*

Fracture Mechanics Model

The fracture mechanics model for treatment of the growth and arrest of cracks at various locations in the vicinity of a weld is described in this section. Cracks are considered to be either a buried crack in an infinite body or a surface crack in a semi-infinite body. The crack driving force is considered to be described by the value of the J-integral [*10–12*]. For a given crack size (and orientation), the only difference between weld metal, base metal, and the two types of HAZ material (LBZ and gap) is in the fracture toughness, which is described by J_{Ic} [*10*]. If J-applied exceeds the local value of J_{Ic}, the crack is considered to grow unstably. If J-applied subsequently decreases below the local value of J_{Ic}, or the crack grows into a region with a J_{Ic} higher than J-applied, the crack is considered to arrest.

The plane-strain-elastic and fully plastic J-solutions for buried and surface cracks for unbounded media from He and Hutchinson [*11*] are used. The stress-strain relationship is the

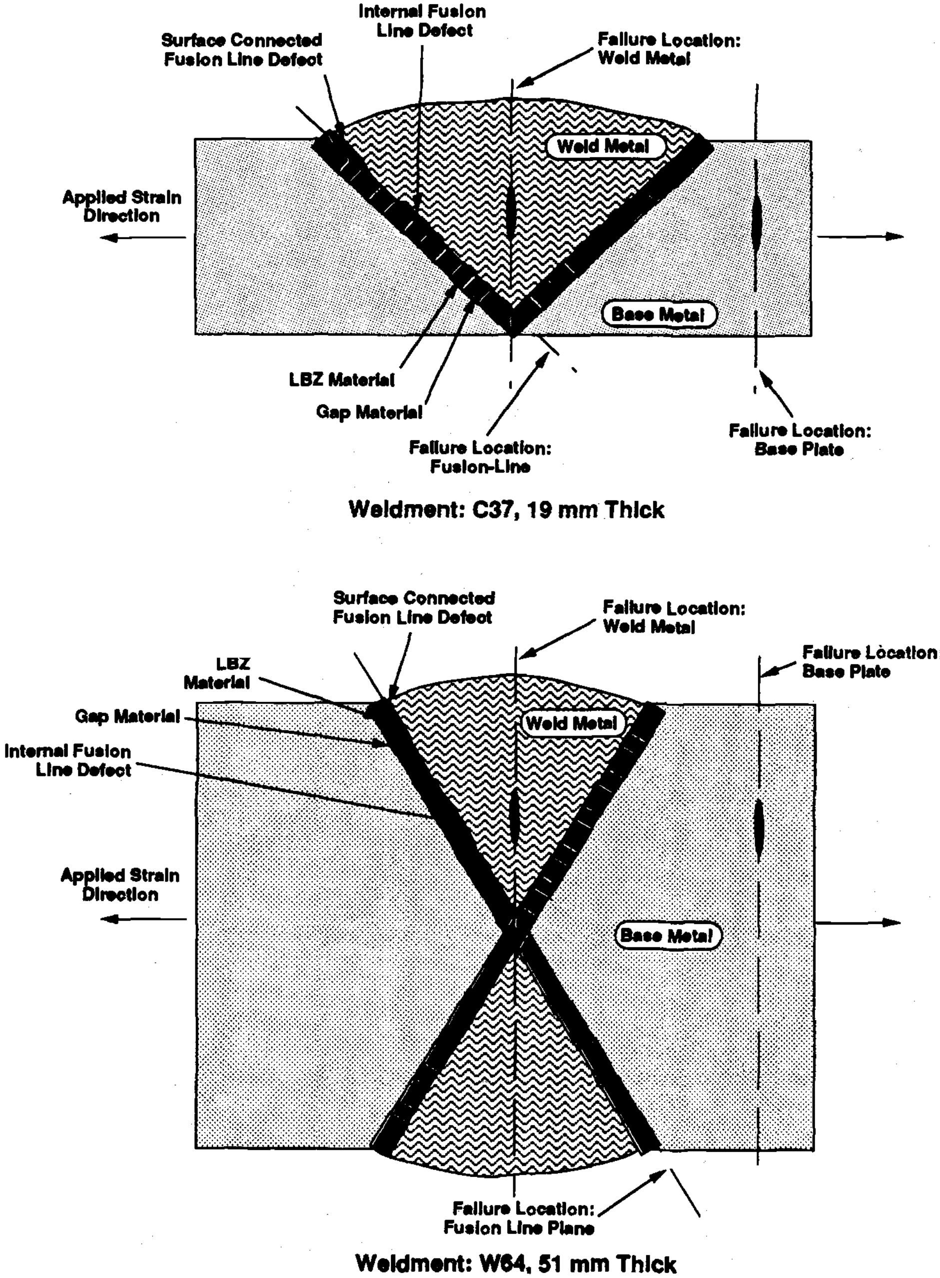

FIG. 2—*Schematic of location of LBZs and gaps and their orientation along the failure planes for the two weldments modeled.*

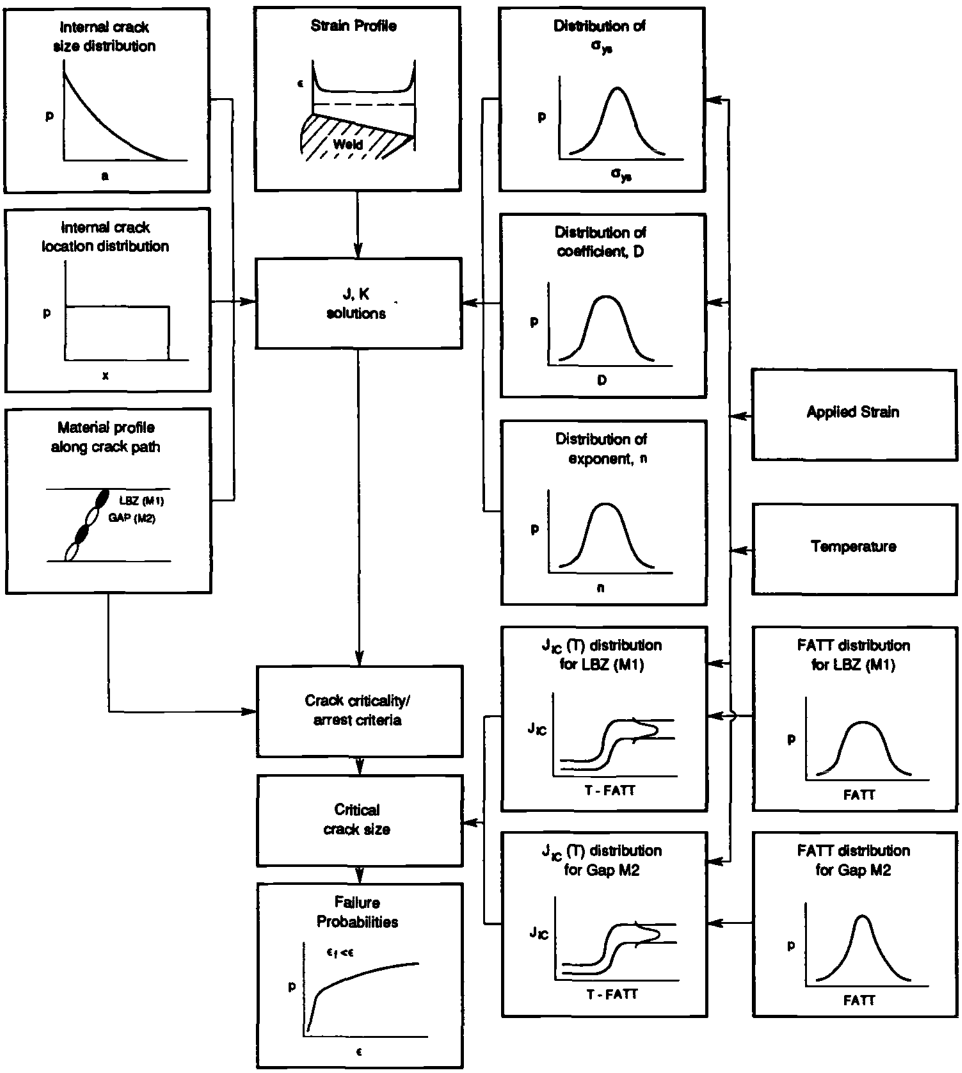

FIG. 3—*Block diagram of components in WREC.*

conventional Ramberg-Osgood, which for uniaxial tension is

$$\epsilon = \epsilon_e + \epsilon_p = \frac{\sigma}{E} + \left(\frac{\sigma}{D}\right)^n \tag{1}$$

The conventional interpolation scheme [*10,12*] for estimation of the elastic-plastic value of J is employed.

This simple treatment has three complicating factors (1) mixed-mode loading for cracks on the weld fusion line; (2) the effects of strain gradients near the weld, which includes undercut effects; and (3) transitioning from subsurface to surface cracks

Cracks on the weld fusion are constrained to grow along the weld fusion line. Such cracks are at an angle to the applied strains, which constitutes mixed-mode loading. Erdogan and Sih's [*13*] linear elastic treatment of the affects of mixed-mode loading on crack stability was used for mixed-mode elastic-plastic loading. This allows the critical value of J_I-applied to be calculated in terms of crack orientation, θ and J_{Ic}.

A rigorous treatment of the effect of strain gradients on applied values of J is beyond the current state of the art of elastic-plastic fracture mechanics. The idealized strain gradient shown in Fig. 4 was used to describe the strains through the thickness of the weld fusion line.

Once K_t, h_t, K_b, and h_b are specified, the value of ϵ_m to preserve net section stresses in the plate is defined. The value of K_t is intended to reflect the effect of the weld crown, but not the undercut. Values of the parameters describing the strain gradient are inputs to the code and are functions of the remotely applied strain. A default table to these parameters was estimated from engineering judgment and incorporated into the code. They are described in Ref *14*.

The value of J-applied was calculated using the local value of the strain at the location of the crack tip (prior to introduction of the crack). Subsurface cracks transition to surface cracks when J-applied exceeds local J_{Ic} and no intervening arrest occurred. The stability of the resulting surface crack is then checked, again using the local value of strain at the crack tip location in the J-solution.

Deterministic Input Variables

Values of the deterministically defined input parameters are defined in this section. The temperature of the weldment is defined by the user and is considered to be fixed. The remotely applied strain is the independent variable, and plate thickness and weld angle are user defined.

The spatial distribution of microstructure zones along a crack path was considered to be fixed and also is defined by the user. In the HAZ, all microstructural zones were modeled as either LBZs (in which thermal cycles to high peak temperatures near the fusion line produced grain-coarsened microstructures) or gaps (in which the thermal cycles caused by subsequent weld passes refined the grain-coarsened microstructures). The gaps and LBZs have different statistical distribution of toughness, each of which are temperature dependent. The location and size of LBZs was determined for two weldments by microstructural examination.

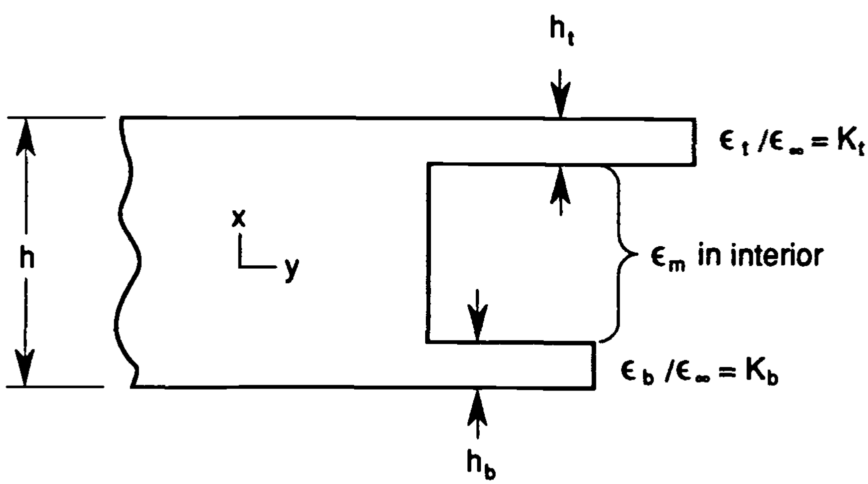

FIG. 4—*Idealized strain gradient.*

Figure 1 shows a low-magnification cross section of a 19-mm-thick, single-V, 90° weld, which is also shown schematically in the upper portion of Fig. 2. The LBZs were identified at ×100, which is required to identify the coarse-grained microstructure. The LBZs were then photographically reduced and superimposed on the lower magnification (×9) composite photomicrograph shown in Fig. 1.

The other HSLA-80 weldment modeled was a 51-mm-thick plate, double-V, 60° total-inclusive angle weld, which is shown schematically in the lower part of Fig. 2. The 19- and 51-mm-thick weldments had 4 and 6 LBZ regions, respectively, distributed along the fusion line representing 89 and 73% of the fusion line strength, respectively. Further details regarding weldment parameters, how the measurements were made, and the results of the LBZ and gap measurements are reported in Ref *7*.

Random Variables

In the model, the initial defect distribution at the fusion line, and the mechanical properties of the base plate, weld metal, and HAZ, are treated as random variables. The following discussion considers only cracks at the fusion line. These cracks can be considered to be a result of lack of fusion, hot tearing, slag inclusions, or weld porosity. Reference *14* includes a more complete treatment that also considers defects in the weld metal and base material.

Defect Distributions—The distribution of initial cracks is one of the key inputs to any PFM analysis. In fact, uncertainties in the initial crack size are often the reason for resorting to probabilistic techniques. Cracks are considered to be very long relative to their depth, so that only the depth, a, is required to describe their size. There are three major aspects to describing the random nature of initial cracks: the probability of cracks existing (crack or undercut existence probability), the size distribution of a crack or undercut, and the location distribution (surface connected crack or distance from plate surface to center of internal cracks).

Distribution of Weld Cracks—The crack size distribution provides the description of the probability of having a crack in a given depth increment (given that a crack exists). Little information exists that completely characterizes the frequency and size distribution of welding defects that are typical of Navy ship fabrication practices.

After an extensive literature search, the results of Bokalrud [*15*] were selected to define the frequency and size distribution of defects in ship weldments. His data are from the results of ultrasonic inspection, and therefore, contain uncertainty due to nondetection of some cracks and errors in sizing of detected cracks. Two depth distributions were therefore developed: (1) a Weibull distribution based on his reported defect data, and (2) an exponential distribution based on his two largest crack depth histogram cells. The treatment leading to the exponential distribution is felt to represent an upper bound on the number and size of weld defects.

The following depth distributions were obtained using Bokalrud's data:

Weibull

$$P(>a) = \exp\left[-(a/\sigma)^{\eta}\right] \tag{2}$$

where $\sigma = 3.90$ mm (0.154 in.) and $\eta = 2.49$.

Exponential

$$P(>a) = \exp\left[-(a/\beta)\right] \tag{3}$$

where $\beta = 0.930$ mm (0.037 in.).

These depth distributions, which are conditional on a crack being present, are considered to be applicable to weld metal and HAZ material. The location through the thickness was taken to be uniformly distributed.

The weld defect existence frequencies were also estimated from the data of Bokalrud [*15*]. As described in Ref *14*, the following estimates were made to go along with the depth distributions discussed earlier. The frequency of weld defects per unit area of fusion surface corresponding to the two preceding crack depth distributions were estimated to be

$$\text{Weibull: } 7.6 \times 10^{-4}/\text{in.}^2 = 1.2 \times 10^{-6}/\text{mm}^2$$
$$\text{Exponential: } 2.1 \times 10^{-2}/\text{in.}^2 = 3.3 \times 10^{-5}/\text{mm}^2$$

These crack existence frequencies combine with the (conditional) crack depth distribution to describe the overall probability of having a crack of a given depth in a weld.

Material Property Distributions

The material properties that enter into the criterion for final failure are random. The scatter in these properties results in a distribution of the critical crack sizes, even when the applied loads and strains are considered to be deterministic. This distribution of critical crack sizes will influence the failure probability, which in homogeneous materials is simply the probability of having a crack of a size larger than the critical size. In this model, the distribution of critical crack sizes gives the probability of crack growth initiation. If the crack is growing in the HAZ, the crack still has the possibility of arresting if it grows into a region with a toughness that is sufficiently high.

In ductile materials, such as HSLA-80 weldments, the crack driving force may be taken to be the J-integral. J-integral solutions depend on the yield strength, strength coefficient, and stress exponent distributions for each weldment region. These values were used as random variables that are a function of temperature.

The material property that enters into the final failure criterion in elastic-plastic fracture analysis is J_{Ic}. For steels, toughness usually undergoes a transition from ductile to brittle fracture at a temperature related to the Charpy fracture appearance transition temperature (FATT). Existing experimental data on HSLA-80 were used to estimate the distributions of FATT values for the base plate, weld metal, LBZs, and gaps. The temperature dependence of J_{Ic} was expressed through the excess temperature (T-FATT), for the weld metal and base plate LBZs, and gaps.

The required mechanical property and fracture toughness data were collected from a wide variety of sources. In the case of base plate data only HSLA-80 or A710 data for Grade A, Class 3 steel and only data for plates with thicknesses between 13 and 33 mm was used. For the weld metal most of the available data was used since plate thickness and welding process were considered to be second order effects for this material. However, the data from flux cored arc welds were excluded since this material appears to have had some problems meeting toughness requirements in the past. All the data on the properties of regions of the HAZ have come from Scoonover's extensive experiments on HSLA-80 steel, which was Gleeble heat-treated to simulate actual welding thermal cycles [*3,7*].

Yield Strength

The average yield strength of the base plate at room temperature was found to be 609 MPa with a standard deviation of 24.5 MPa calculated from data on many heats of HSLA-80 and A710 [*16–19*]. The yield strength at a given temperature was assumed to be distributed normally. The temperature dependence of the average yield strength from tension tests was obtained from Ref *18* and described by

$$\ln(\overline{\sigma}_{ys}(T)) = 64.26\left(\frac{1}{T}\right) + 6.194 \quad \text{for base metal} \tag{4}$$

$$\ln(\overline{\sigma}_{ys}(T)) = 64.26\left(\frac{1}{T}\right) + 6.256 \quad \text{for weld metal} \tag{5}$$

$$\ln(\overline{\sigma}_{ys}(T)) = 64.26\left(\frac{1}{T}\right) + 6.216 \quad \text{for LBZ metal} \tag{6}$$

where

$\overline{\sigma}_{ys}$ = average yield strength (MPa) and
T = temperature (K).

The gap material average yield strength, standard deviation, and temperature dependence of the mean yield strength were taken to be the same as the base plate, since no tensile data were available and since the gap material microhardness was similar to the base plate material [*7*]. The room temperature base metal standard deviation of 24.5 MPa for the yield strength was assumed to be applicable to all materials at all temperatures.

Strain Hardening

The strain hardening response of these materials was modeled as

$$\epsilon_p = \left(\frac{\sigma}{D}\right)^n \tag{7}$$

where

ϵ_p = true plastic strain,
σ = true flow stress,
D = strength parameter, and
n = stress exponent.

The average stress exponent, n, at room temperature for base metal was calculated from data in Refs *3* and *19* and was found to be 8.3 with a standard deviation of 1.21. The stress exponent was assumed to be distributed normally and have a constant standard deviation, of 1.21, over the temperature range of interest (−17 to 20°C). The temperature independence of n over the temperature range of interest was confirmed by reviewing data on similar materials reported in Refs *17* through *19*.

The values of n and D can not be treated independently. The following relationship was developed to describe the variation of the strength parameter (D) with temperature and stress exponent for the base plate metal.

$$\ln[D(T,n)] = 64.26\left(\frac{1}{T}\right) + 4.793 + 6.215\left(\frac{1}{n} - \frac{1}{\overline{n}}\right) \tag{8}$$

where

$D(T,n)$ = temperature and stress exponent dependence of the strength parameter and
$\overline{n}$ = mean stress exponent at room temperature.

Since n is a random variable, so is D.

The strain hardening response of the weld metal was assumed to be the same as that of the base plate since no relevant data could be found for weld material.

The average stress exponent, n, of grain coarsened HSLA-80 (LBZ) was found to be 13.5 with a standard deviation of 1.57 as determined from tension tests on HSLA-80 that had been given an LBZ-producing thermal cycle [3,7]. The stress exponent was assumed to be distributed normally and have a constant standard deviation, of 1.57, over the temperature range of interest. The temperature and stress exponent dependence of the LBZs strength parameter was assumed to have the same form as was determined for the base plate material, with, of course, the appropriate constants.

The strain hardening response of the gap material was taken to be identical to that of the base plate since relevant data could not be found.

Base Plate Toughness Properties

The fracture toughness of a material has an important influence on the critical crack size, and its value must be estimated in order to estimate when a flaw will grow. The value of the fracture toughness in steels is highly temperature-dependent and subject to considerable variation. The temperature dependence is generally expressed through the "excess temperature," which is denoted as T' and is equal to (T-FATT). FATT is the temperature at which the fracture surface of a Charpy specimen exhibits 50% flat fracture (cleavage). FATT was estimated by using the temperature corresponding to the midpoint between the upper and lower CVN energies. The FATT for the base plate (A710 or HSLA-80) data from Refs *7, 16, 18,* and *19* was found to have an average value of -72°C with a standard deviation of 18.6°C. FATT was assumed to be distributed normally and is, by definition, independent of temperature.

For this analysis, J_{Ic} is needed to determine when cracks extend. There were limited J_{Ic} data, and they were used when available. However, when they were not available, CVN or K_{Ic} data were converted to J_{Ic}. When CVN data were used, procedures described by Rolfe and Barson [20] were employed by converting them to J_{Ic}. Figure 5 provides a plot of all of the available J_{Ic} data for base metal as a function of excess temperature.

The statistical distribution of the fracture toughness at a given excess temperature for the data set of Fig. 5 was characterized by use of a maximum likelihood estimation technique [9] to estimate the temperature dependence of the parameters of a shifted Weibull distribution that describes the scatter in the fracture toughness at a given excess temperature. This procedure assumes that at a given excess temperature (T') the probability density function is a one-sided Weibull distribution with parameters that depend on the excess temperature. The parameters of the distribution (J_0, σ, η) are fit to vary as a function of excess temperature (T'), as outlined in Ref *21*.

This assumed temperature variation has a lower plateau at small T', an upper plateau at large T', with a transition of variable location and abruptness. Figure 5 presents plots of the resulting zero, first, tenth, fiftieth, and ninety-ninth percentiles of the distribution of toughness as a function of excess temperature for the base plate.

Weld Metal Toughness

The FATT for the weld metal was found to have an average value of -33.2°C with a standard deviation of 18.8° C [7,18]. The FATT data were estimated from CVN data using the same method described earlier for the base plate.

The same probability distribution function used to describe the temperature dependence of toughness of the base plate was also assumed for the weld metal, but different parameters were determined to describe weld metal toughness distribution.

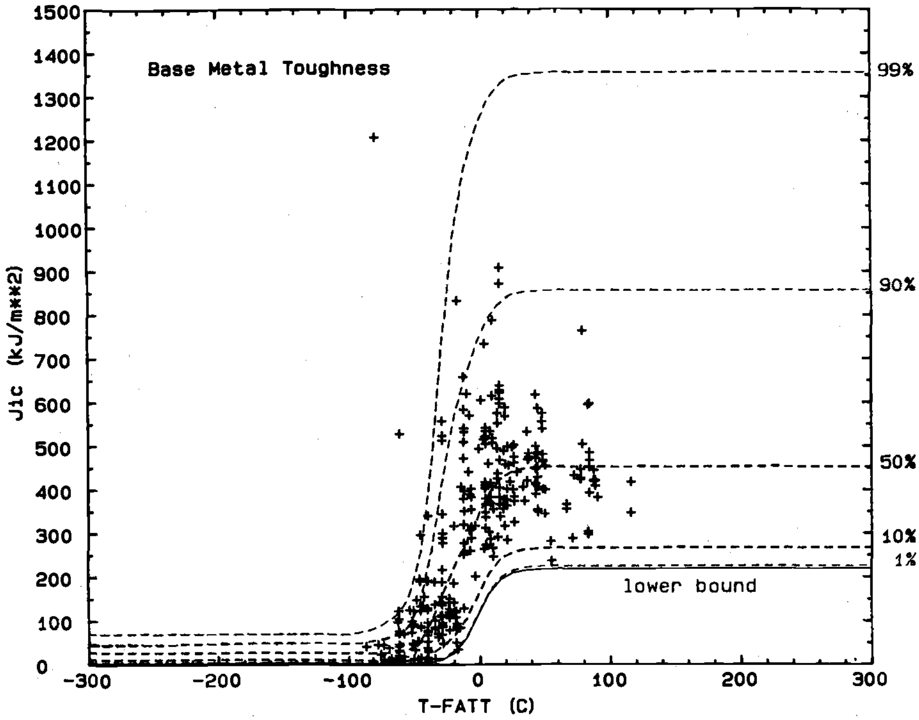

FIG. 5—*Base metal fracture toughness versus excess temperature for HSLA-80 Grade A, Class 3, showing selected percentiles of distribution.*

LBZ Toughness Properties

The FATT for the LBZs was estimated from CVN energy data to have an average value of −6.7°C with a standard deviation of 11°C [7]. The FATT data were estimated from CVN data using the same method described for the base plate.

The same probability distribution function used to describe the temperature dependence of toughness of the base plate was also used for the LBZs. However, the parameters for the LBZ toughness distribution were different. Figure 6 presents plots of the resulting zeroth, first, tenth, fiftieth, and ninety-ninth percentiles of the distribution of LBZ toughness as a function of excess temperature along with data points estimated from CVN values [7].

Gap Toughness Properties

The statistical distribution of gap material toughness for a given excess temperature (T') was assumed to be identical to that of weld metal, since very little gap CVN data are available. Gap metal FATT was found to have an average of −34°C, with a standard deviation of 11°C—based on estimations from CVN data [7].

Results and Discussion

The underlying deterministic elastic-plastic fracture mechanics treatment described here was combined with Monte Carlo simulation using the statistical distributions of random input

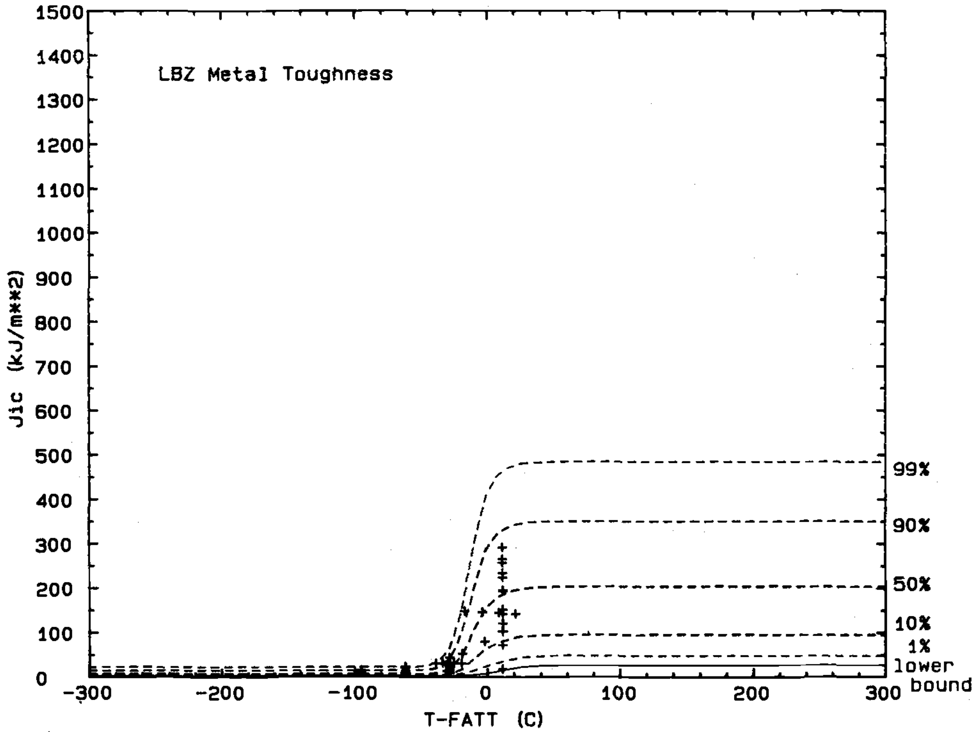

FIG. 6—*LBZ toughness versus excess temperature for HSLA-80 Grade A, Class 3, showing selected percentiles of distribution.*

variables to evaluate the failure probability as a function of strain for a given temperature. Calculations were performed for many sets of inputs and are reported in Ref *14*. Selected results are presented here. Monte Carlo simulation results reported in Ref *14* indicate that the crack depth distribution employed (Weibull or exponential) has a large affect on the calculated failure probabilities. Alternatively, these simulations show the strain concentration has only a small influence at appreciable plastic strain levels. The size and location of LBZs in the two welds considered was deterministically defined, based on microstructural observations of representative welds.

The probabilistic model described in Ref *14* considered inclusions and weld undercuts as additional types of defects. It was found that failure due to inclusions has a very low probability at the strain levels considered, and a distribution of undercut depth and root radius based on data from Bokalrud [*15*] had a minimal influence on predicted weld failure probability. Hence, this paper concentrates on crack-like weld defects. Undercut defects may be more influential in fatigue, but the present discussion is limited to monotonic straining.

Figure 7 presents typical results, which are for the two welds depicted in Fig. 2. Results are presented as a function of applied plastic strain for two different temperatures. (The length of weld fusion line is twice the length of weld.) The Weibull depth distribution of Eq 2 was employed, and results are for a weld fusion line length of 25.4 mm. The exponential depth distribution results are not presented since it represents an upper bound and over predicts failure rates as based on explosive bulge tests.

The results of Fig. 7 can be extended to other lengths of weld by considering each segment

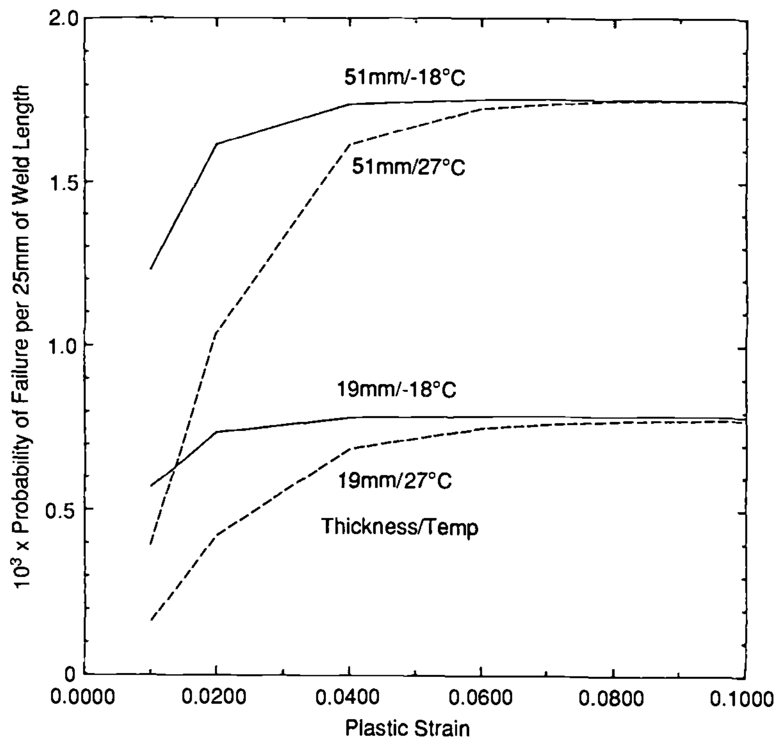

FIG. 7—*Effect of plastic strain on the fusion line failure probabilities of 19- and 51-mm-thick plate with 25.4 mm (1 in.) of weld interface.*

of weld fusion line to be independent. For a length of weld, L_w (which gives $2L_w$ length of fusion line), the failure probability, in terms of the values shown in Fig. 7, are

$$P(L_w) = 1 - (1 - P_{Ref})^{2L_w/L_{Ref}} \tag{9}$$

where P_{Ref} is in Fig. 7, with L_{Ref} being 25.4 mm.

The failure probability in Fig. 7 is higher for the thicker weld, primarily because of the higher probability of having a weld defect in a given length of thicker weld. The failure probabilities "plateau out" independent of temperature at higher plastic strains. This plateau is largely controlled by the probability of having a weld defect.

Figure 8 presents results showing the effect of toughness of HAZ microstructure on the failure probability of the weld fusion line for 19-mm-thick plate subjected to 1% plastic strain. Results were generated using the Weibull crack depth distribution for 25.4 mm of fusion line length. The lines labeled base, gap, and weld consider all the metal on the weld fusion line to have the toughness of base, gap, and weld metal, respectively. Results for gap and weld metal are nearly the same, because the toughness distribution at a given T' is the same for both materials and the distribution of FATT is only slightly different. The detrimental effect of LBZs on weldment performance is shown by including regions of LBZ and base or gap toughness distributed along the fusion line as shown in Fig. 1. This detrimental effect is shown in Fig. 8. The presence of LBZs increase the weld failure probability by a factor of 2 to 10, depending on the temperature.

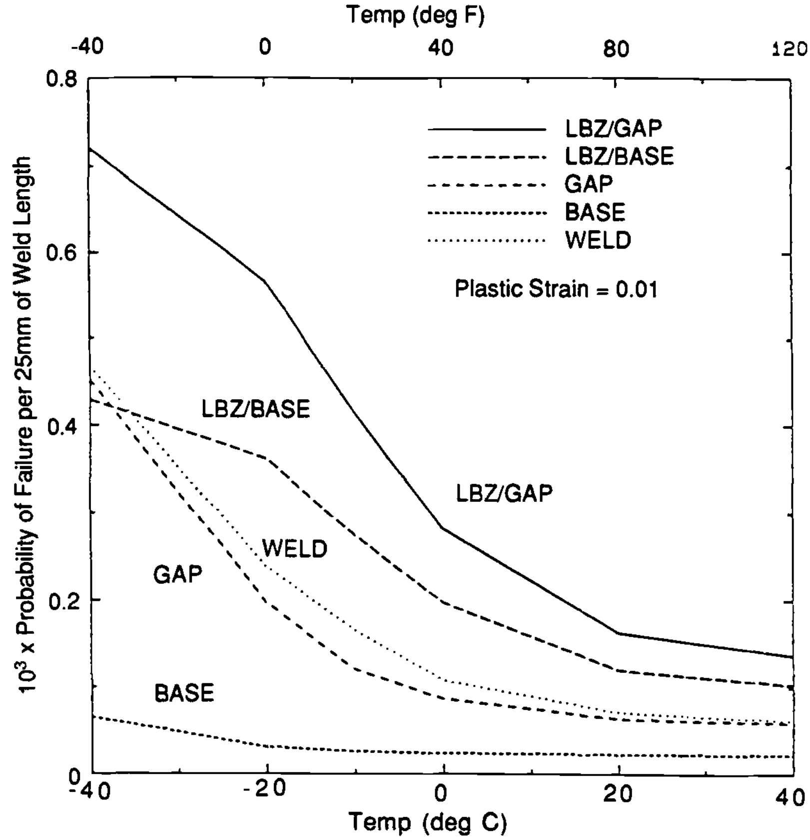

FIG. 8—*Effect of HAZ toughness properties on the fusion line failure probabilities in 25.4 mm of weld interface of 19-mm-thick plate strained 1%.*

Comparison with Explosive Bulge Test Results

The accuracy of predictions made of the influence of LBZs on weldment failure can be checked qualitatively by comparing these predictions with the results of explosive bulge tests. These tests were developed around 1950 to investigate the factors that determine the performance of weldments in large structures [*22*], and consist of either an explosive crack starter or explosive bulge test.

Table 1 summarizes the results of some explosive bulge tests on HSLA-80 steel. The results are for a standard 254 mm (10 in.) length of weld (508 mm of weld fusion line) subjected to about 10% strain at −17°C. The results show zero failures out of ten specimens of 19 mm thickness and two failures out of two specimens for 51 mm thickness. Table 2 summarizes the observations and predicted failure probability at the weld fusion line calculated by use of Eq 9 and information from Fig. 7. Also included in Table 2 are corresponding predicted failure probabilities in the weld metal based on results from Ref *14*. The thicker plate is predicted to have a higher failure probability, which agrees with the observations. Also, the failure probability in the weld metal is predicted to be higher than at the weld fusion line, which points out the minimal effect of LBZs on weld reliability. The number of samples is very small, so no quantitative comparison can be made.

TABLE 1—*Summary of results of explosive bulge tests (≈10% strain at −17°C, 254 mm of weld length).*

Producer	Weld Type	Heat Input, kJ/cm	Inclusion Control	Thickness, mm	Test Type	Number of Tests	Number of Failures
Phoenix	GMAPW	18	yes	19	starter	2	0
					bulge	2	0
Lukens	SAW	...	...	19	starter	2	0
					bulge	4	0
Phoenix	GMAW	22	yes	51	starter	1	1
					bulge	1	1
Armco	GMAW	22	yes	33	starter	1	0
		33			bulge	1	1

Results for 33-mm-thick plate included in Table 1 show a failure at higher heat input. This is consistent with observations of thicker and more continuously distributed LBZs when higher weld heat inputs are used.

Conclusions

Probabilistic fracture mechanics modeling of HSLA-80 steel weldments has shown:

1. The failure probabilities of these weldments are dominated by the distribution of weld metal defects.
2. The Weibull representation of defect distributions appears to give failure probabilities that are in reasonable qualitative agreement with large-scale tests performed by the Navy.
3. The effect of size, distribution, and toughness of LBZs and gaps in the HAZ on failure probabilities at the 10% strain level is small because failure is mainly controlled by the presence of defects. At lower strain levels, the failure probabilities are more sensitive to these HAZ characteristics and show a greater temperature dependence, but this effect is not large. On this basis, one concludes that the measured HAZ characteristics do not

TABLE 2—*Summary of observed failure during explosive bulge tests and corresponding predicted failure probabilities.*

Thickness, mm	19	51
Samples	10	2
Failures in fusion line	0	0
Failures in weld metal	0	2
P_{Ref}, fusion line[a]	8.0×10^{-4}	1.75×10^{-3}
P_{Ref}, weld[b]	3.3×10^{-3}	8.80×10^{-3}
P_{test}, fusion line[c]	1.6×10^{-2}	3.4×10^{-2}
P_{test}, weld[d]	3.3×10^{-2}	8.4×10^{-2}

[a] From Fig. 7.
[b] From Ref *14*, Table 6.
[c] $P_{test} = 1 - (1 - P_{Ref})^{2L_w/L_{Ref}}$ where $L_{Ref} = 25.4$ m, $L_w =$ 254 mm.
[d] $P_{test} = 1 - (1 - P_{Ref})^{L_w/L_{Ref}}$ where weld results are per unit length.

have a significant influence on large strain failure probabilities. For high-cycle fatigue failures, where strains are in the elastic region and concentrated at the toe and root of the fusion line, HAZ characteristics may have a greater significance.

4. The model predicts that thick plates will have higher failure rates, primarily due to the increased probability of weld defects. However, metallurgical factors can also cause the toughness to be lower in thick plates, and this may be one cause of the explosive test failures of the two weldments made from 51-mm-thick plate.
5. Since predicted failure probabilities are higher in the weld metal than in the HAZ, the presence of LBZs in the HAZs of HSLA-80 steel weldments should not significantly increase the probability of weldment failure under conditions of large plastic strains. However, this conclusion is not valid for very high heat-input, single-pass weldments where LBZs form a more continuous path along the fusion line.

References

[1] "Steel Plate, Sheet or Coil, Age-Hardening Alloy, Structural, High Yield Strength (HSLA-80)," Military Standard Mil-S-24645, 1984.

[2] Montemarano, T. W., Sack, B. P., Gudas, J. P., Vassilaros, M. G., and Vandervelt, H. H., "High Strength, Low Alloy Steel in Naval Construction," *Journal of Ship Production,* Vol. 2, 1986, pp. 145–162.

[3] Scoonover, T. M., "Heat-Affected Zone Toughness and Tensile Properties in ASTM A710 Steel Weldments," ASME Paper No. OMAE-88-909, American Society of Mechanical Engineers, Houston, TX, Feb. 1988.

[4] Kvidahl, L. G., "An Improved High Yield Strength Steel for Shipbuilding," *Welding Journal,* Vol. 64, 1985, pp. 42–48.

[5] Irving, R. R., "A Cost Effective Replacement for HY-80," *Iron Age,* 16 May 1986, pp. 53–55.

[6] Scoonover, T. M., Lukens, W. E., and Pande, C. S., "Correlation of Heat Affected Zone Microstructure With Peak Heating Temperature in HSLA-80 Steel Weldments," *Unusual Techniques and New Applications of Metallography,* Vol. 2, R. J. Gray and L. R. Cornwell, Eds., American Society for Metals, Metals Park, OH, 1986, pp. 91–104.

[7] Scoonover, T. M., "Evaluation of Local Brittle Zones in HSLA-80 Weldments," *Proceedings,* International Conference on The Metallurgy Welding and Qualifications of Microalloyed (HSLA) Steel Weldments, American Welding Society, Miami, FL, 1990.

[8] Czyryca, E. J., unpublished data, David Taylor Research Center, 1985 and 1988.

[9] Ang, A. H.-S. and Tang, W. H., *Probability Concepts in Engineering Planning and Design, Vol. II: Decision, Risk, and Reliability,* Wiley, New York, 1984.

[10] Kanninen, M. F. and Popelar, C. H., *Advanced Fracture Mechanics,* Oxford University Press, New York, 1985.

[11] He, M. Y. and Hutchinson, J. W., "Bounds for Fully Plastic Crack Problems for Infinite Bodies," *Elastic-Plastic Fracture, Vol. I—Inelastic Crack Analysis, ASTM STP 803,* C. F. Shih and J. P. Gudas, Eds., American Society for Testing and Materials, Philadelphia, 1983, pp. I-277–I-290.

[12] Kumar, V., German, M. D., and Shih, C. F., "An Engineering Approach for Elastic-Plastic Fracture Analysis," Electric Power Research Institute Report NP-1931, Palo Alto, CA, 1981.

[13] Erdogan, F. and Sih, G., "On Crack Extension in Plates Under Plane Loading and Transverse Shear," *Journal of Basic Engineering,* Dec. 1963, pp. 519–525.

[14] Eiselstein, L. E., Harris, D. O., Rau, C. A., et al., "Probabilistic Fracture Mechanics Evaluation of Local Brittle Zones In HSLA-80 Steel Weldments," report prepared for Department of Navy, David Taylor Research Center, Annapolis, MD, Contract N6153389M1103, DTRC/SME-CR-05-90, Dec. 1989.

[15] Bokalrud, T. and Karlsen, A., "Control of Fatigue Failure in Ship Hulls by Ultrasonic Inspection," *Norwegian Maritime Research,* Vol. 10, No. 1, 1982, pp. 9–15.

[16] Gudas, J. P., "Micromechanisms of Fracture and Crack Arrest in Two High Strength Steels," Ph.D. thesis, Johns Hopkins University, Baltimore, MD, 1985.

[17] Natishan, M. E., "Mechanisms of Strength and Toughness in a Microalloyed Precipitation Hardened Steel," DTRC/SME-88-81, Department of Navy, David Taylor Research Center, Annapolis, MD, 1988.

[18] *Structural Alloys Handbook,* Battelle Columbus, Columbus, OH, 1987.

[19] Kirk, M. T., unpublished data, David Taylor Research Center, 1987.
[20] Rolfe, S. T. and Barson, J. M., *Fracture and Fatigue Control in Structures—Application of Fracture Mechanics,* Prentice-Hall, Inc., Edgewood Cliffs, NJ, 1977.
[21] Rau, S. A., Harris, D. O., and Wells, C. H., "Improved SAFER Code," Electric Power Research Institute Report-EPRI RP-2785-1, Palo Alto, CA, 1987.
[22] "Standard Procedures for Explosion Testing Ferrous and Non-Ferrous Metallic Materials and Weldments," Military Standard MIL-STD-2149(SH), 1983.

Patrick S. Leevers,[1] Paşa Yayla,[1] and Marcus A. Wheel[1]

Rapid Crack Propagation in Polyethylene Pipes: The Role of Charpy and Dynamic Fracture Testing

REFERENCE: Leevers, P. S., Yayla, P., and Wheel, M. A., "**Rapid Crack Propagation in Polyethylene Pipes: The Role of Charpy and Dynamic Fracture Testing,**" *Fracture Mechanics: Twenty-Third Symposium, ASTM STP 1189,* Ravinder Chona, Ed., American Society for Testing and Materials, Philadelphia, 1993, pp. 826–839.

ABSTRACT: Pressurized pipelines of extruded ductile polyethylenes can, under severe conditions, fail by brittle rapid crack propagation (RCP). Critical pressures, below which RCP always arrests, have been measured for grades of medium-density (MDPE) and modified high-density polyethylene (HDPE) pipe, using a small-scale test. For 180- to 250-mm-diameter pipe of 11- to 24-mm wall thickness, HDPE performs much better than MDPE; but both materials show temperature, crack velocity, and thickness-promoted ductile-brittle transitions, beyond which their behaviors converge. Instrumented Charpy impact tests reflect the transitions, but only qualitatively. High-speed double-torsion tests for dynamic crack resistance across a spectrum of crack velocities yield only plane-strain data, even at 0°C and for specimens only 6 mm thick. They therefore do not help to locate the thickness-dependent fracture transition, but more efficiently characterize the worst case of a highly constrained crack in a thick pipe.

KEY WORDS: rapid crack propagation, polyethylene, pipelines, crack arrest, brittle fracture, Charpy test, dynamic crack resistance, fracture mechanics, fatigue (materials)

Full-scale field tests on pressurized plastic pipelines have shown that above a critical pressure, p_c, a crack initiated at sufficient velocity in the axial direction can continue to propagate indefinitely. Rapid crack propagation (RCP) is characterized by speeds of about 100 to 350 ms^{-1}, and by the brittle response of materials that may be very ductile under quasi-static conditions. The critical pressure falls with increasing diameter and decreasing temperature, and is strongly material dependent [*1*].

Similar experiments show that for gas pressurization, p_c is much lower than for water [*2*]. For reasons that are not obvious, the threat that RCP could pose to the gas distribution industry is perceived differently in the United States and in Europe. In the United States, RCP was investigated in depth following early failures in gas-pressurized steel pipelines in the early 1960s; a more recent overview of research is provided by papers in *ASTM STP 711* [*3,4*]. The Charpy test proved to provide an effective pass-fail index for ductility in pipeline steels, and service failures became rare. The problem regained attention when unplasticized polyvinyl chloride and polyethylene grades entered widespread use for local distribution networks and, despite some research effort [*5*], has not been satisfactorily solved; nor has it been pushed further up the agenda by the occurrence of service failures.

Within Europe, pipe sizes are larger and RCP is more widely acknowledged as a critical fail-

[1] DuPont lecturer and postdoctoral research associates, respectively, Mechanical Engineering Department, Imperial College of Science, Technology and Medicine, London SW7 2BX, UK.

ure mode. Individual national standards have been set, notably by British Gas (which certifies pipe for service only up to a proportion of the full-scale test critical pressure) and in Belgium, within which the small-scale test developed by Vancrombrugge has been standardized. It has now been proposed to an International Standards Organization (ISO) Subcommittee that following the forthcoming revision of ISO 4437 [6], a small-scale RCP test on pipe should become mandatory. Forthcoming European standards, too, will include an RCP test.

Full-scale tests must serve as the ultimate reference, but they are extremely expensive. In work at Imperial College, we have sought a p_c prediction methodology that can minimize the need for them. To be reliable and economically feasible—for material developers as well as for gas utilities and pipe manufacturers—this methodology must embody several interlocking elements.

First, we will discuss reference data for critical pressure, p_c, from full-scale tests. We regard the British Gas full-scale test method [1,7] as definitive, and a systematic correlation with our results is currently being pursued via a collaborative project.

Second, a "model" of RCP in pipelines, which can relate p_c to pipe dimensions and material properties and to the properties of the contained fluid (for example, gas or water), will be covered. The simplest model, assuming that crack propagation completely and instantaneously releases strain energy stored in the pipe wall, leads to the Irwin-Corten equation

$$p_c = \frac{t}{D}\sqrt{\frac{8EG_D}{\pi D}} \tag{1}$$

where D and t are the pipe diameter and thickness (often related by a standard dimensional ratio, SDR $= D/t$), and E and G_D are the dynamic tensile modulus and dynamic crack resistance of the pipe material, respectively. This equation serves a useful normalizing role, but the model neglects the influences of crack velocity, of the properties of the contained fluid, and of decompression ahead of the crack tip. More sophisticated modeling is discussed later.

Third, we will investigate small-scale laboratory "material tests" for geometry-independent properties that, according to the model, control p_c. For the Irwin-Corten model underlying Eq 1, these are E and G_D. This paper reviews the use of Charpy and of high-speed double-torsion tests [8] for generating G_D data relevant to RCP.

Finally, a "small-scale pipe test" for RCP is needed. This must be abstract enough to model, so that correlations with the full-scale test are feasible; but realistic enough to reflect the fact that extruded pipe is not simply a set of dimensions enfolding an isotropic and homogeneous material, but records (for example, as residual stress and crystallinity profiles) its production history. We have developed the small-scale steady-state (S4) test [9,10] that has already shown encouraging correlation with full-scale test results [7,11].

Full-Scale and Small-Scale Pipe Tests: Material Dependence

Crack Propagation and Arrest in Pressurized Pipes

Medium-density polyethylene (MDPE) is currently the most widely used material for gas and water distribution systems. Most MDPE grades yield broadly similar p_c results in full-scale tests. For MDPE-1, a typical resin, the critical pressure for 250-mm-diameter SDR 17.6 pipe is 6.1 bar at 0°C. Recently introduced "third-generation" grades based on high-density polyethylene (HDPE) perform much better, with RCP effectively unobtainable in full-scale tests at any statically sustainable pressure at 0°C.

These results are reflected by the S4 test [8,9] whose standardization has been recommended to the International Standards Organization. This method tests a seven-diameter-long specimen of as-extruded pipe (Fig. 1). An axial crack is initiated near one end in wedge opening by radial impact from a chisel-ended projectile. This crack runs into a second, isolated "gage section," within which, depending on the controlled pressure, it either arrests promptly or settles into steady propagation at a uniform velocity.

The transition from arrest to propagation at the critical pressure, termed p_{cS4}, defined within the draft standard as crack propagation to a length of less than one diameter from the end of the gage section, is very sharp. Figure 2 compares p_{cS4} results for 180-mm pipe of MDPE-1 and HDPE-2 (a third-generation gas pipe grade) over a range of temperatures. To promote rapid settling to steady-state crack propagation in the S4 test, internal baffles throttle flow along the pipe and thus retard transient decompression of the specimen during fracture. In a full-scale test, however, flaring of the separated flaps allows free exhaust of the pressurizing gas, greatly extending the length of axial crack propagation required for settling to a steady state. One-dimensional modeling has shown [*12*] that the minimum possible pressure at a fixed point in a long air-filled pipe freely and steadily exhausting by choked axial outflow is 28% of the upstream value. Thus, while the crack-tip region in an S4 test is maintained at almost the full initial pressure, in a full-scale test it may have been unloaded to 28% of this level but no less. Results for similar materials tend to confirm that the S4 test identifies a critical pressure, p_{cS4}, that is only 28% of the full-scale p_c value.

The Ductile-Brittle Transition: Minimum Crack Speed

In fracture mechanics terms, crack arrest can be explained as an inequality between the generalized force driving a crack, G, and the frictional force, G_D, with which the material resists it. Crack arrest does not necessarily reflect a transition in the response of the material, but may result from an insufficient energy release rate. Fracture surfaces from full-scale and S4 tests, however, do suggest that crack arrest in polyethylene (PE) is associated with a ductile-brittle transition (DBT).

Figure 3 shows that as the S4 test pressure is reduced from an initial value well above p_{cS4}, the average axial crack velocity through the gage section also falls. Stress whitened "tear lips"

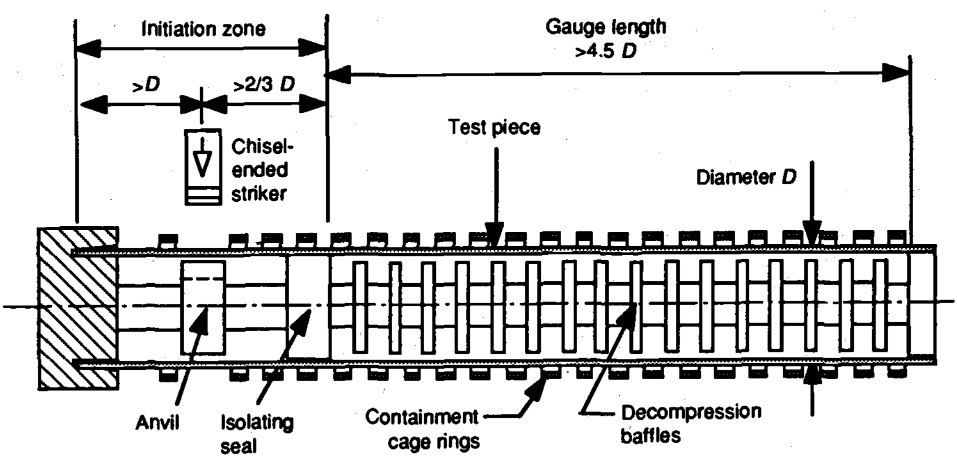

FIG. 1—*Schematic diagram of the small-scale steady-state (S4) test for rapid crack propagation resistance of pipe.*

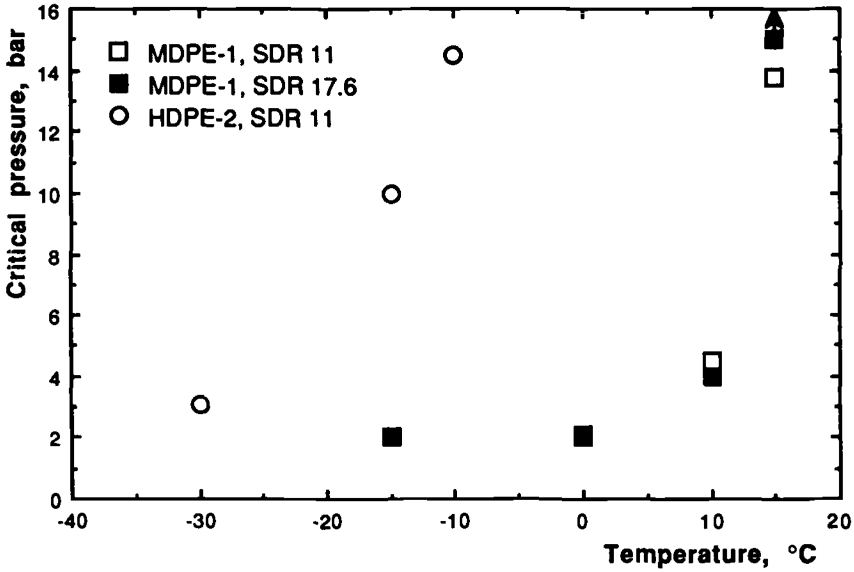

FIG. 2—*Critical pressure for 180-mm polyethylene pipes measured using the S4 test.*

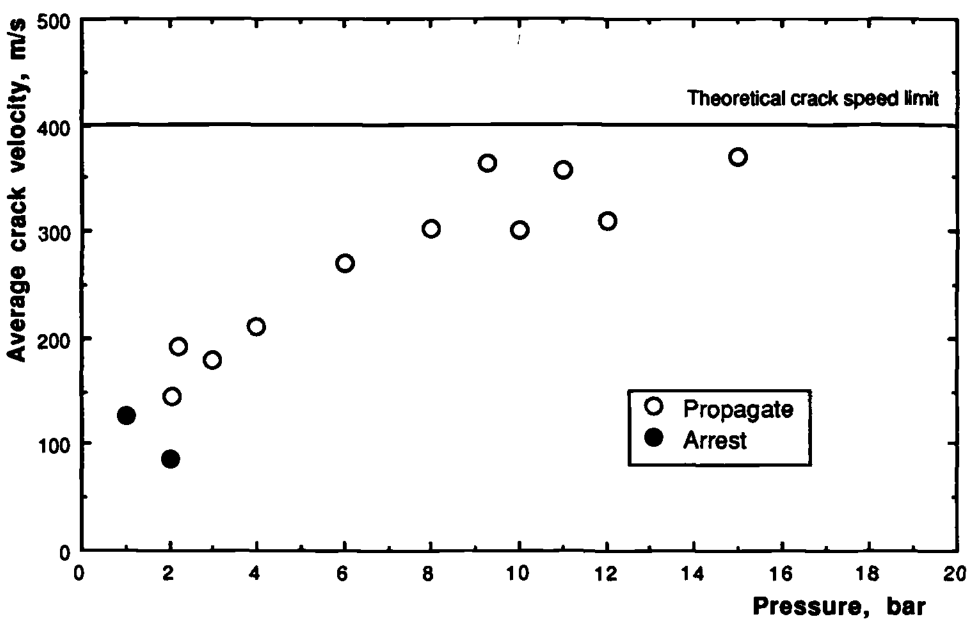

FIG. 3—*Variation of crack velocity with pressure in 180-mm SDR 17.6 MDPE-1 pipe at −15°C.*

at the free boundaries of the fracture surface grow in width, the overall fracture surface roughness increases, and arrest is associated with a minimum sustainable crack velocity of about 150 ms^{-1} at $-15°C$. At 0°C, the minimum crack speed is lower: about 70 ms^{-1}.

Although arrest clearly follows a rate effect on the material resistance, crack driving force is also crack speed dependent. The velocity independent crack driving force implied by Eq 1,

$$G_0 = \frac{\pi}{8E}\frac{D^3}{t^2}p^2 \tag{2}$$

originates in strain energy released from the pipe wall by circumferential relaxation. Kanninen [*13*] has shown that this deformation mode has a propagation velocity

$$C_0 = \frac{3}{4}C_l\sqrt{\frac{2t}{D}} \tag{3}$$

where C_l is the longitudinal wave velocity

$$C_l = \sqrt{\frac{E}{\rho}} \tag{4}$$

in a pipe material of density, ρ. At high crack speeds—approaching C_0—the deforming pipe walls acquire significant kinetic energy, which must be deducted from the energy release rate, G_0, to the crack tip; thus, as for waveguide-type systems in general, G may have the form

$$G = G_0\left[1 - \left(\frac{\dot{a}}{C_0}\right)^2\right] \tag{5}$$

Above C_0, no energy can flow to the crack tip. For MDPE-1 of dynamic modulus, $E = 2.32$ GPa, and density, $\rho = 940$ kgm^{-3}, this implies a limiting crack velocity of 400 ms^{-1}, which is well supported by the data.

At low crack speeds, decompression by axial backflow and radial outflow becomes significant even in the S4 test, due to leakage around each baffle. As a result, as Kanninen [*14*] has demonstrated using a coupled elastodynamic/fluid-dynamic numerical model of a freely decompressing pipeline, the crack driving force, G, has the general form shown in Fig. 4. The peak crack driving force, at intermediate crack velocities, may be several times greater than G_0 as predicted by Eq 2. The additional crack driving force is applied directly, by gas expansion against the released pipe walls, as they flare behind the crack front.

Superimposed on Fig. 4 is an assumed $G_D(\dot{a})$ characteristic for PE, in which the observed brittle-ductile transition is reflected in inverse rate dependence at low crack speeds. Points at which the curves intersect on the stable branch

$$\frac{d}{d\dot{a}}(G - G_D) < 0 \tag{6}$$

represent stable rapid crack propagation conditions and are therefore limited, as shown, by a minimum sustainable velocity "independent" of the ductile-brittle transition (DBT).

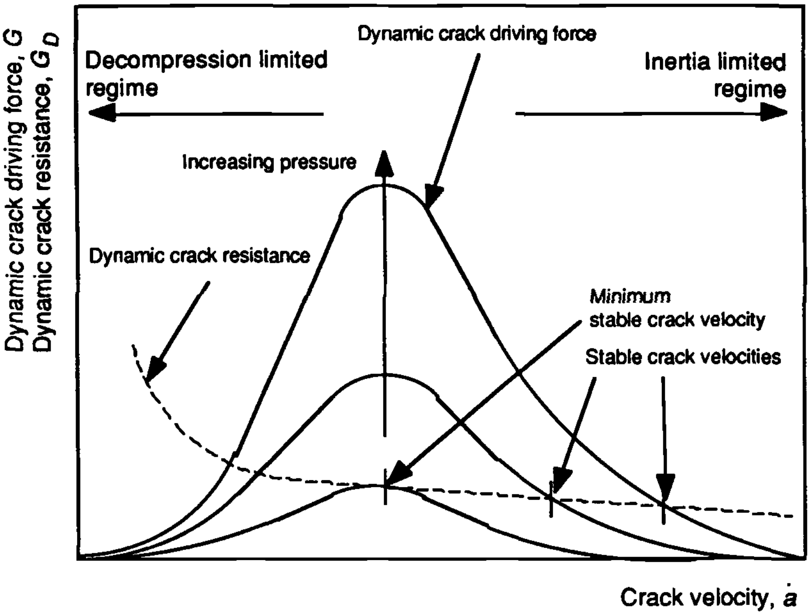

FIG. 4—*Schematic of driving force and resistance for rapid crack propagation in a pressurized pipeline.*

The Ductile-Brittle Transition: Temperature Effects on Critical Pressure

S4 pipe testing at varying temperatures, highlights ductile-brittle transitions in MDPE-1 and HDPE-2 (Fig. 2), emphasizing that these materials differ less in their RCP resistance on the lower plateau than in their DBT temperatures: around −5°C for MDPE-1 and −30°C for HDPE-2. There is insufficient data to quantify the difference in lower-shelf p_{cS4}, but it is clearly less than 50%.

A significant feature of Fig. 2 is the lack of thickness effects in MDPE on the ascent from the lower shelf: SDR 11 and SDR17.6 pipes show similar p_{cS4} values despite their 60% thickness difference. According to Eq 1, this would imply that a thicker wall exhibits lower dynamic toughness, for a material in which a lower temperature has the same effect. This equivalence of decreasing temperature and increasing thickness in their effect on the DBT is common in polymers. The data here are incomplete: tests are needed to show that Eq 1 yields formally correct predictions for the dependence of lower-shelf p_{cS4} on geometrical parameters. Data from British Gas full-scale tests [7] suggest that it will.

Thus, two parameters seem to be crucial to characterizing pipe performance: the lower-shelf critical pressure and the characteristic temperature of the DBT. We have considered two candidates for material property tests that could be used to index the distinction between MDPE and HDPE in a geometry-independent way:

1. The notched Charpy "impact" test—This widely accepted classical test can be used to identify a DBT temperature or, using fracture mechanics analysis, to estimate crack initiation resistance.
2. The high-speed double-torsion (HSDT) test—This has been developed at Imperial College over the last few years as a method for determining dynamic fracture toughness, G_D, as a function of crack speed.

Charpy Impact Tests

Notched Charpy impact tests were carried out, over a range of temperatures, using a CEAST instrumented pendulum machine. The 5-mm-wide by 10-mm-deep by 40-mm-span specimens were machined from the pipe wall, with the notch running parallel to the pipe axis and the crack initiation direction oriented radially outwards. For most temperatures, the initial razor-notch depth was 2 mm in all tests, but at three temperatures (−15°C, 0°C, and 23°C) in each material, tests were carried out using notch depths of 2, 4, and 6 mm. Tests were carried out at 1.6 ms^{-1}.

The fracture surfaces (Fig. 5), arrayed according to test temperature, manifest the DBT as a "nil-ductility temperature:" stress whitening in the least constrained areas appears above about −5°C in MDPE-1 and −55°C in HDPE-2.

Figures 6 and 7 show impact energy release rate results from a fracture mechanics analysis [*15*] of both peak load and total energy data. Each individual data point represents the average for three or four tests. Plotting both peak-load and total-energy results on the same graph shows, for each material, the temperature at which the "tail" of the force-time trace begins to absorb substantial energy. As expected, this point corresponds closely to the phenomenological DBT.

The energy release rate calculated from peak load during impact, G_{ci}, can be interpreted as a dynamic crack initiation resistance. The lower shelf G_{ci} value for HDPE-2 is very well defined at 11.5 kJ m^{-2}; but for MDPE-1, G_{ci} is still apparently falling with temperature even at −60°C, at which it is 3.8 kJ m^{-2}. Unfortunately, increased scatter with decreasing toughness is to be expected from Charpy data analyzed from the $BD\Phi$ method, since G_{ci} is evaluated as a small difference between larger energy release rates subject to random and dynamic errors [*15*].

High-Speed Double-Torsion Tests

While the Charpy impact test measures the resistance of a material to crack "initiation" under rapidly increasing load, the high-speed double-torsion (HSDT) test [*4*] is a dynamic fracture test: it provides data for resistance to steady dynamic crack "propagation," G_D, as a function of crack velocity. The HSDT specimen resembles a wide-span (100-mm) and extremely broad (200-mm) Charpy specimen, four-point loaded by impact of a projectile opposite one end of the V-notch. Having initiated in impact, however, the crack continues to run along the length of the specimen, guided by the V-notch, at an almost constant velocity controlled by that of the projectile. Behind the crack front, the specimen deforms in torsion. Although the specimen is only 6 to 10 mm thick, and the crack path even narrower, the torsional deformation mode makes the crack front long and curved [*16*], providing high constraint. Any possibility of ductile tearing and hinging at the free surface opposite the V-notch is suppressed by cutting a second, shallow, very sharp sidegroove.

A maximum crack velocity is imposed by that of the torsional wave that propagates along the specimen from the initiating impact, and the torsional wave velocity is a fraction, determined by specimen thickness and span, of the material shear wave speed. This provides a direct method for measuring an appropriate dynamic shear modulus for the material. An HSDT test is carried out on a specimen that has already been separated along its crack path, and rejoined only at the end furthest from impact. In such a test, the specimen exerts a resisting force induced by inertial "dynamic impedance" alone [*17*], from which the dynamic modulus, *E*, can be measured at appropriate shear strains.

Figures 8 and 9 show dynamic crack propagation resistance as a function of crack velocity for MDPE-1 and HDPE-2. Although these materials are known to be very resistant to low-speed tearing, the data show remarkably low- and velocity-independent crack resistance above some characteristic velocity. Below this velocity (about 160 ms^{-1} for MDPE-1 and 130 ms^{-1}

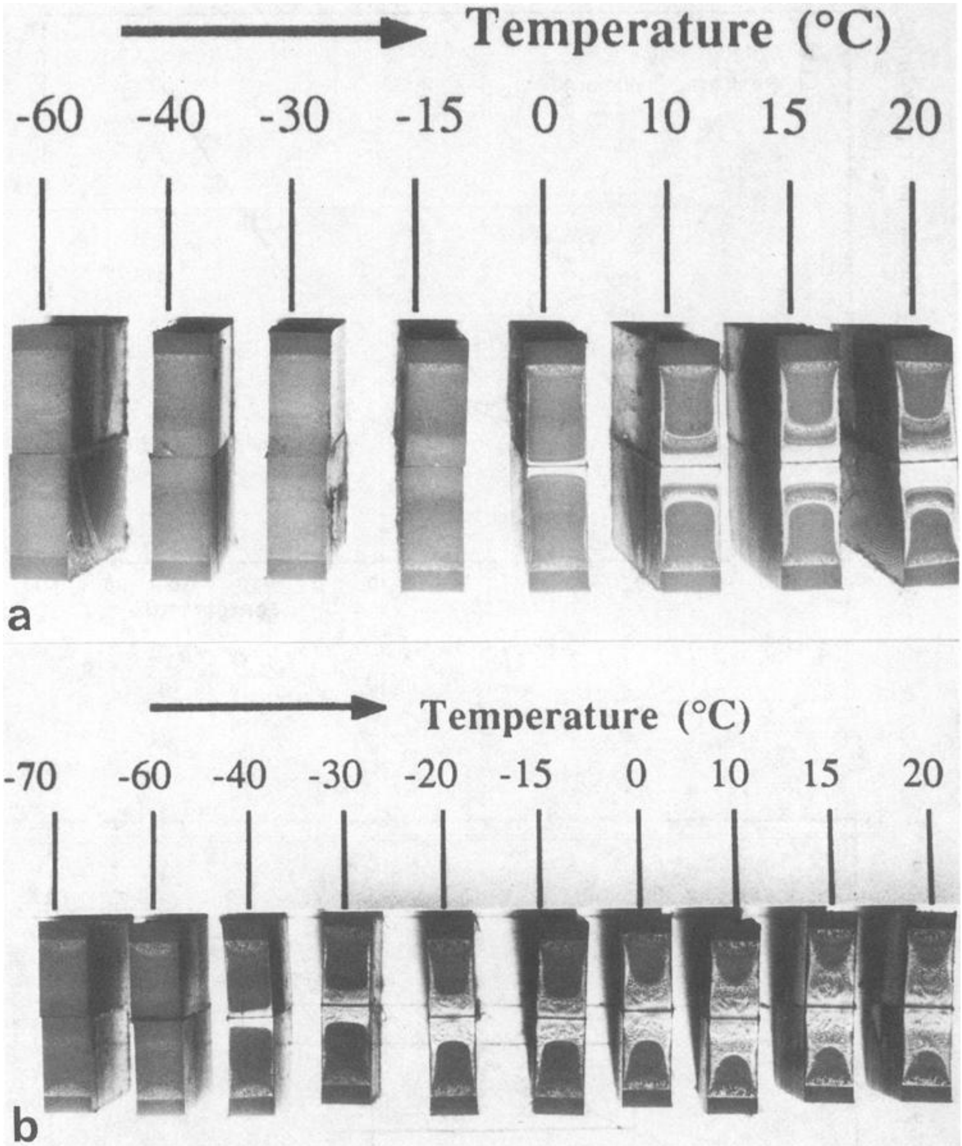

FIG. 5—*Notched Charpy impact test specimens showing well-defined ductile-brittle transitions in* (a) *MDPE-1 and* (b) *HDPE-2. Each specimen cross-section is 5 by 10 mm.*

for HDPE-2), stick-slip crack growth occurs, indicating an inverse velocity dependence, G_D, that may reflect the DBT. A minimum viable crack speed is also observed in pipe tests, but in both tests it is too poorly defined to serve as a measurable characterizing parameter. The maximum observable crack velocity in the HSDT test corresponds closely to the torsional wave speed, underpinning the analysis used to compute G_D from displacement data using a one-dimensional torsional wave model [*17*].

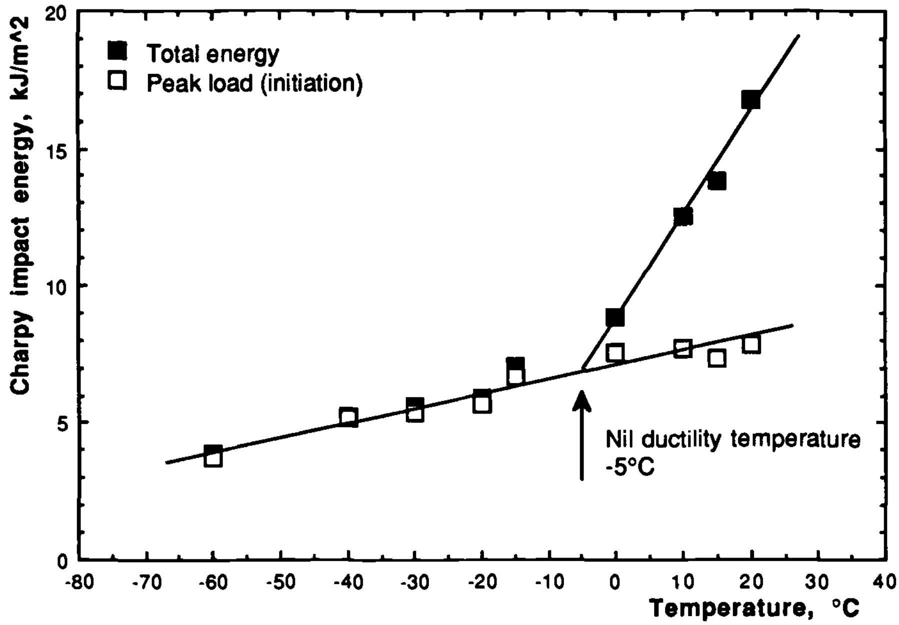

FIG. 6—*Charpy impact energy release rate versus temperature for MDPE-1.*

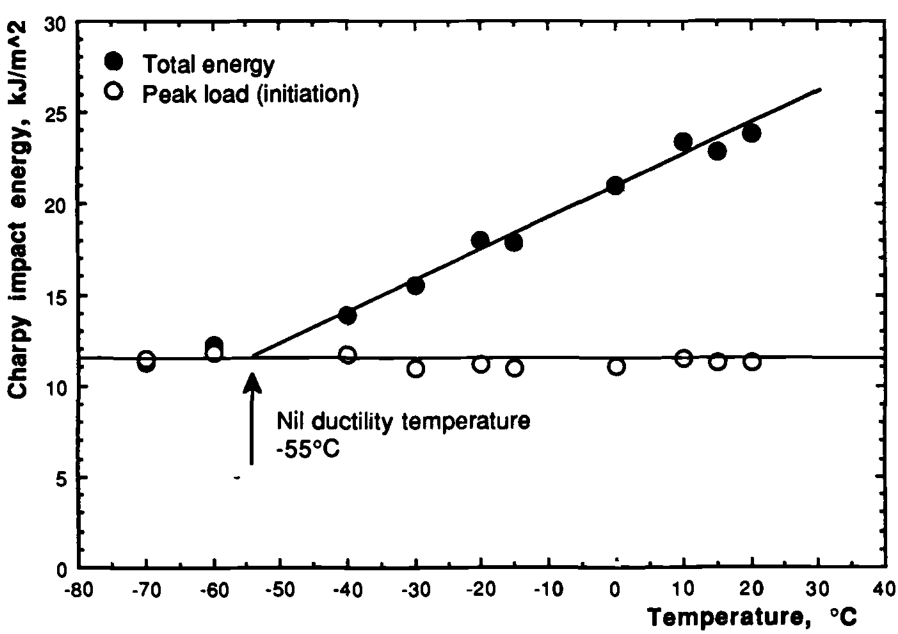

FIG. 7—*Charpy impact energy release rate versus temperature for HDPE-2.*

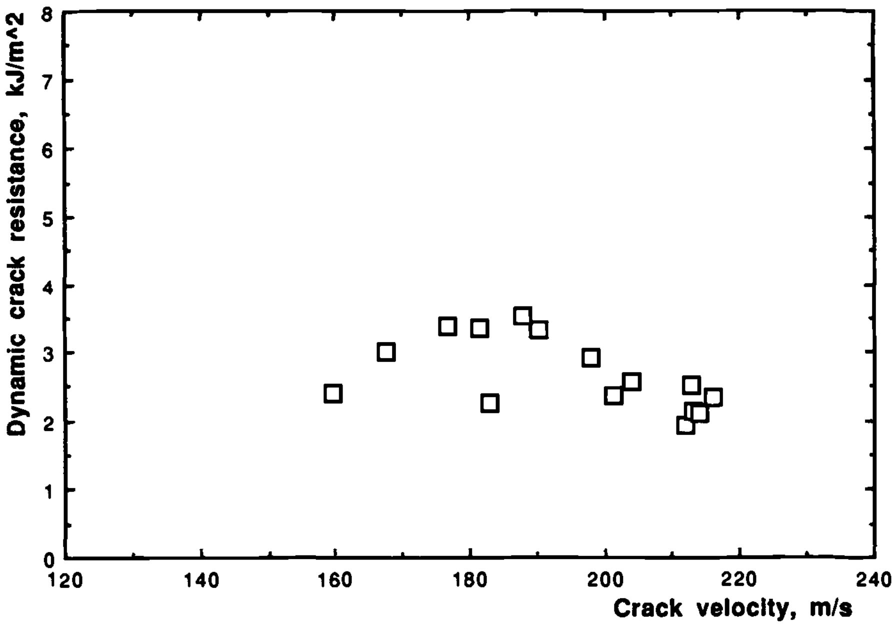

FIG. 8—*Dynamic crack propagation resistance of MDPE-1 at 0°C; high-speed double-torsion test data.*

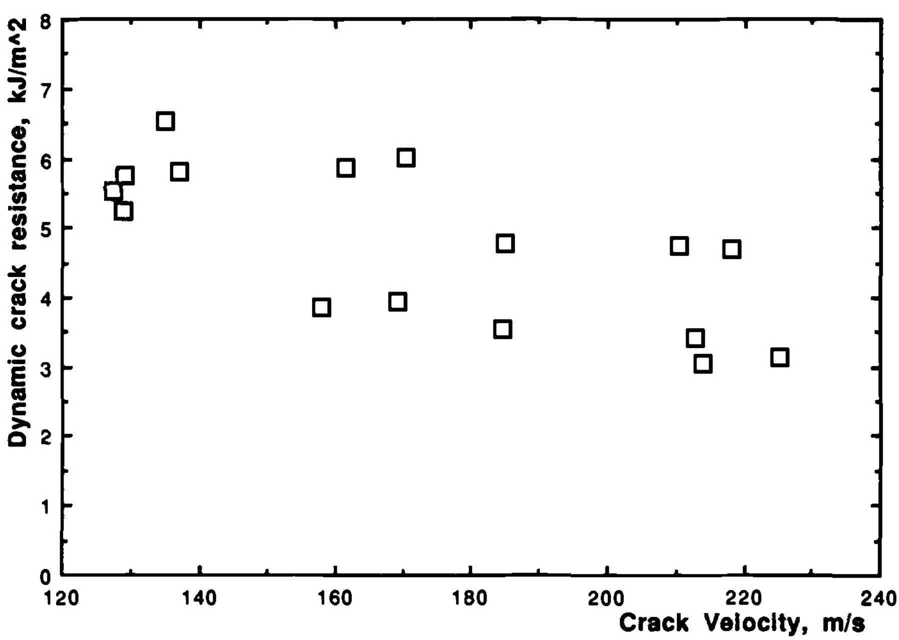

FIG. 9—*Dynamic crack propagation resistance of HDPE-2 at 0°C; high-speed double-torsion test data.*

The G_D data show some scatter (less significant when it is used in Eq 1, due to the square root). Since the focus of interest is low velocities, reflecting proximity to the DBT, the two materials could be characterized by the average G_D (3 kJ m^{-2}) for MDPE-1 and a minimum velocity "intercept" value of 6 kJ m^{-2} for HDPE-2, whose gently falling characteristic is not so well characterized by its average.

Figure 10 shows data for another MDPE grade, in which tests were conducted on specimens of two thicknesses, both with and without an upper razor-cut sidegroove. All of the data fall on a single characteristic, confirming the absence of intrinsic thickness effects and suggesting that the ductile layer near the upper plate free surface has relatively minor influence on measured G_D.

Thickness Effects in the S4 Test

RCP Behavior of Notched Pipes

The low values and crack-speed independence of G_D data generated using the HSDT test suggest that if the crack front in a pipe were highly constrained, either by low temperature or by a very thick pipe wall, the performance of MDPE-1 and HDPE-2 would be more similar than the 180-mm S4 pipe test data for SDR 11 and 17.6 (Fig. 2) suggest. In particular, we would expect to see RCP in HDPE-2 at 0°C.

Fracture surfaces created by RCP in PE pipe normally show more ductility at the bore than at the outside diameter. To suppress this, S4 tests were carried out on 180-mm SDR11 specimens of MDPE-1 and HDPE-2 modified by a 1-mm-deep axial razor cut along the entire length of the bore. The intention was to generate RCP in the minimum toughness state.

These specimens showed remarkably low critical pressures. For MDPE-1 p_{cS4} at 20°C dropped to 1.0 bar; while for HDPE-2, in which RCP had been previously impossible even at

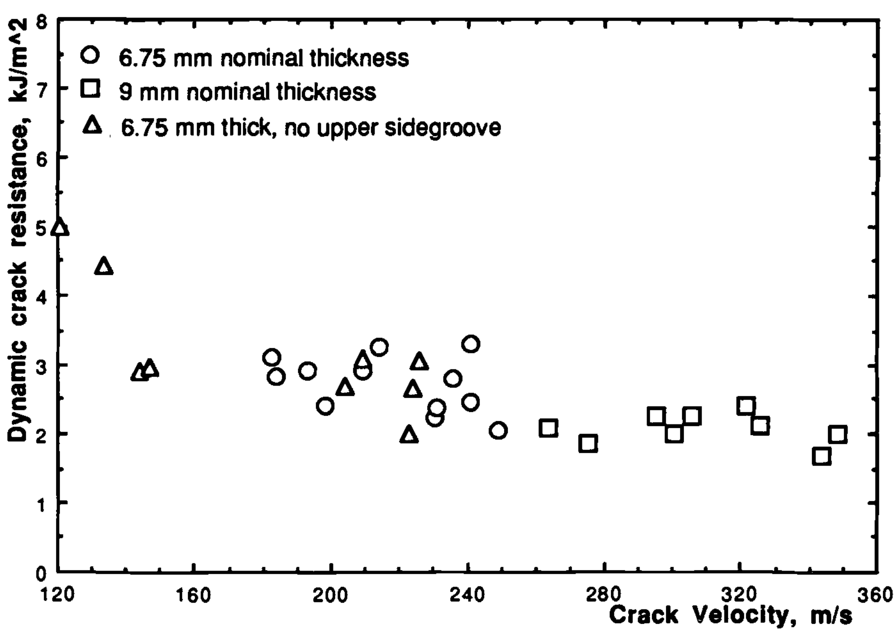

FIG. 10—*Dynamic crack propagation resistance of MDPE-3 at 0°C; high-speed double-torsion test data.*

0°C, p_{cS4} at 20°C was just 1.5 bar. Fracture surfaces bore a striking resemblance to those in HSDT specimens: glassy throughout the full thickness, showing only quasi-brittle surface features. For HDPE-2, p_{cS4} continued to fall at lower temperatures (0.8 bar at 0°C, 0.75 bar at −15°C), while MDPE pipes fragmented, making tests impossible.

Table 1 compares these measured S4 critical pressures to those predicted by the Irwin-Corten analysis (Eq 1, using E and G_D data from the HSDT test). For conditions under which the underlying theory should be most realistic (that is, minimal reduction of the driving force by decompression, increase of the driving force by flaring, or increase of the crack resistance by surface plane-strain deformation), the critical pressures predicted from the strain-energy release theory are an order of magnitude too high: that is, the driving force due to strain energy (Eq 2) is two orders of magnitude too small to pay for the crack.

It is interesting to estimate the radial distance by which the pressurized fluid would need to expand at the critical pressure to provide all of the work absorbed by the fracture surface

$$r_e = \frac{G_D}{p_c}\frac{t}{\pi D} \tag{7}$$

This is just 0.87 mm for MDPE-1 and 1.16 mm for HDPE-2, which is considerably less than even the limited pipe wall flaring allowed by the S4 test. These results lead to the overall conclusion that crack arrest in a gas-pressurized polyethylene pipeline is little affected by the release rate of elastic strain energy from the pipe wall. It is primarily determined by the point at which a crack driving force generated primarily by pipe wall flaring, and thus depleted by gas decompression at low crack speeds, is overwhelmed by the increased crack resistance of the material at its DBT.

RCP Behavior of Thin-Walled Pipes

The way in which decreasing thickness affects the DBT was studied more closely by reducing the wall thickness of S4 specimens in a series of one-diameter-long steps. A fast crack was generated in the usual way, penetrating the gage section at full wall thickness. Crack propagation velocity measurements showed that each subsequent reduction in thickness quickly (within $0.2D$) decelerated the crack to a new steady velocity. Finally, the crack reached its minimum viable speed and arrested.

There seem to be two (possibly synergistic) effects at work here: at each reduction in thickness, the level of constraint falls and the fracture surface shows a concomitant increase in stress whitening. Perhaps as a result of local softening (decreasing E) compounded by reduction of the limiting wave speed with thickness (Eq 3), the crack decelerates, reducing strain rates and further promoting flow. This precipitates an instability by which ductility arrests the crack. A number of experiments have indicated that instability is expressed as an effectively constant "critical thickness" below which RCP is not viable at any pressure.

TABLE 1—*Comparison of HSDT test crack resistance data with pipe performance.*

				S4 Test Critical Pressure p_{cS4} for 180-mm SDR 11 Pipe, bar			
Material	Modulus, E (GPa)	Dynamic Crack Resistance at 0°C, G_D	$\sqrt{EG_D}$, MPa m$^{1/2}$	0°C, Eq 1	−15°C, Unnotched	0°C, Unnotched	20°C, Notched
MDPE-1	2.32	3.0	2.64	9.02	2.05	2.25	1.0
HDPE-2	3.19	6.0	4.37	14.9	10.0	very high	1.5

Experiments on 180-mm pipe have shown that for MDPE-1 at 0°C the critical thickness, t_c, is about 6 mm; while for HDPE-2, it exceeds the thickness of SDR 11 pipe (17.6 mm). Figure 11 presents the results of a series of S4 tests designed to estimate t_c for HDPE-2 by extrapolation from data at lower temperatures. Starting at −30°C, the critical thickness was measured by testing a sequence of specimens tapered in successively finer steps. Increasing the temperature to introduce ductility in a controlled way showed that simple linear extrapolation to 0°C yields a satisfactory (and almost certainly conservative) estimate for t_c of 20 mm.

Of equal interest here is the temperature at which t_c for HDPE-2 falls to 6 mm, that of MDPE-1 at 0°C. This is about −35°C, reflecting the difference in DBT temperatures seen in S4 test data for full thickness pipe (Fig. 2). However, this correspondence does not carry over into the Charpy data, which, for specimens of similar thickness, would have indicated a DBT temperature of −55°C for HDPE-2 (Fig. 7).

Conclusions

S4 pipe tests on as-received pipe highlight the distinction between conventional MDPE and high-performance HDPE grades, both in terms of a critical pressure at 0°C and as a transition temperature from a lower plateau. Charpy tests on small specimens at varying temperatures reflect qualitatively, but not quantitatively, differences in S4 test transition temperature. Lower-shelf crack initiation resistance values for HDPE are three times higher than for MDPE.

High-speed double-torsion tests show that G_D varies little with crack velocity, above a minimum velocity below which continuous RCP cannot be sustained. G_D data represent a thickness-independent lower plateau value and are still twice as high for HDPE as for MDPE. S4 tests on pipe specimens internally notched to give maximum constraint yield very low critical

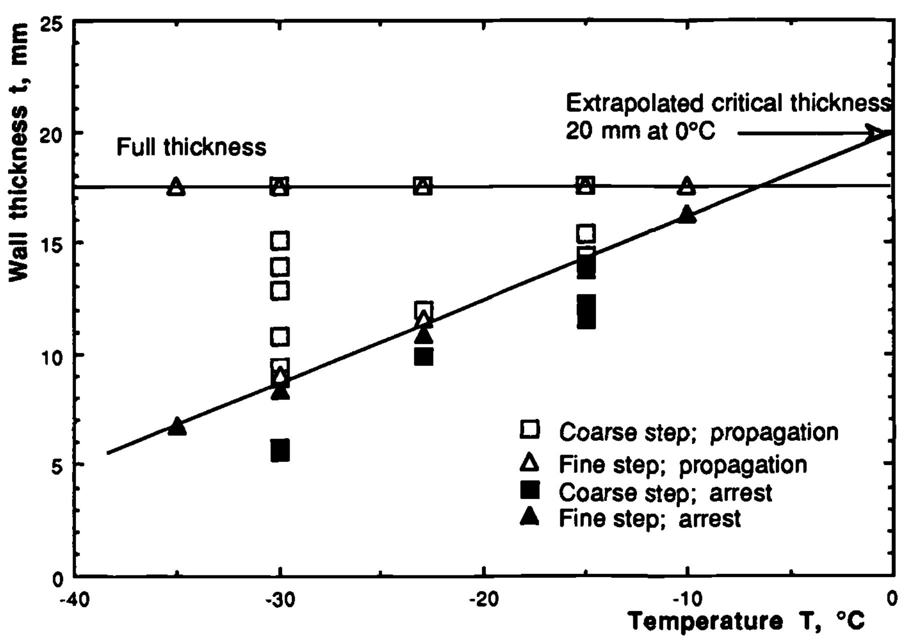

FIG. 11—*Variation of critical thickness with temperature, from S4 tests on 180-mm HDPE-2 pipes with step-tapered wall thickness.*

pressures, proportional, as expected, to $\sqrt{EG_D}$ measured from the HSDT test. Practical characterization of pipe-grade polyethylenes can most usefully focus on predicting the temperature-dependent minimum thickness below which RCP is effectively impossible.

Acknowledgments

This project has been funded by the Science and Engineering Research Council grant, supported by British Gas, Water Research Centre, BP Chemicals, Stewart and Lloyds, and Du Pont (UK). Dr. Yayla wishes to express particular appreciation for support by Du Pont (UK) and by Yildiz University, İstanbul, Turkey. The results presented in Fig. 11 were obtained by Gregory Venizelos and are presented by agreement with WRc (Swindon).

References

[1] Greig, J. M., "Fracture Arrest Conditions in Polyethylene (PE) Gas Pipes," *Plastics Pipes 6, Proceedings,* Sixth International Conference on Plastic Pipes, York, UK, 26–28 March 1986, Plastics and Rubber Institute, London, pp. 20.1–20.8.

[2] Greig, J. M., "Rapid Crack Propagation in Hydrostatically Pressurized 250 mm Polyethylene Pipe," *Plastics Pipes 7, Proceedings,* Seventh International Conference on Plastic Pipes, Bath, UK, 19–22 Sept. 1988, Plastics and Rubber Institute, London, pp. 12.1–12.7.

[3] Freund, L. B. and Parks, D. M., "Analytical Interpretation of Running Ductile Fracture Experiments in Gas-Pressurized Linepipe," *Crack Arrest Methodology and Applications, ASTM STP 711,* G. T. Hahn and M. F. Kanninen, Eds., American Society for Testing and Materials, Philadelphia, 1980, pp. 359–378.

[4] McGuire, P. A., Sampath, S. G., Poelar, C. H., and Kanninen, M. F., "A Theoretical Model for Crack Propagation and Crack Arrest in Pressurized Pipelines," *Crack Arrest Methodology and Applications, ASTM STP 711,* G.T. Hahn and M. F. Kanninen, Eds., American Society for Testing and Materials, Philadelphia, 1980, pp. 341–358.

[5] Krishnaswamy, P., Maxey, W., Leis, B., and Hulbert, L., "A Design Procedure and Test Method to Prevent Rapid Crack Propagation in Polyethylene Gas Pipe," Battelle Columbus Division report to the Gas Research Institute, Columbus, OH, Oct. 1986.

[6] Buried Polyethylene (PE) Pipes for the Supply of Gaseous Fuels—Metric Series—Specification," International Standard ISO 4437: 1988 (E), International Standards Organization, 1988.

[7] Greig, J. M., Leevers, P. S., and Yayla, P., "Rapid Crack Propagation in Pressurized Plastic Pipe. I: Full Scale and Small Scale RCP Testing," *Engineering Fracture Mechanics,* Vol. 42, 1992, pp. 663–673.

[8] Leevers, P. S. and Williams, J. G., "Double Torsion Testing of High Velocity Crack Resistance," *Journal of Material Science,* Vol. 22, 1987, pp. 1097–1107.

[9] Yayla, P. and Leevers, P. S., "A New Small-Scale Pipe Test for Rapid Crack Propagation," *Proceedings,* 11th Plastic Fuel Gas Pipe Symposium, San Francisco, CA, 3–5 Oct. 1989, American Gas Association, Arlington, VA.

[10] Yayla, P., "Rapid Crack Propagation in Polyethylene Gas Pipes," PhD thesis, University of London, Imperial College, UK, 1991.

[11] Yayla, P. and Leevers, P. S., "Rapid Crack Propagation in Pressurized Plastic Pipe. II: Critical Pressures for Polyethylene Pipe," *Engineering Fracture Mechanics,* Vol. 42, 1992, pp. 675–682.

[12] Eiber, R. J., "Fracture Propagation," *Proceedings,* Fourth Symposium on Line Pipe Research, American Gas Association, Dallas, TX, 1969.

[13] Kanninen, M. F., "Research in Progress on Unstable Crack Propagation in Pressure Vessels and Pipelines," *International Journal of Fracture Mechanics,* Vol. 6, 1970, pp. 94–95.

[14] Leung, C. P., Couque, H. R., Grigory, S. C., Popelar, C. F., Kanninen, M. F., O'Donoghue, P. E., and Mamoun, M. M., "The Development and Validation of a Fracture Mechanics Methodology for Rapid Crack Propagation in PE Gas Distribution Pipes," *Proceedings,* Twelfth Plastic Fuel Gas Pipe Symposium, Boston, 24–26 Sept. 1991, American Gas Association, Arlington, VA.

[15] Williams, J. G., *Fracture Mechanics of Polymers,* Ellis Horwood, London, 1984, pp. 237–289.

[16] Leevers, P. S. and Williams, J. G., "Material and Geometry Effects on Crack Shape in Double Torsion Testing," *Journal of Material Science,* Vol. 20. 1985, pp. 77–84.

[17] Wheel, M. A. and Leevers, P. S., "High Speed Double Torsion Testing of Pipe Grade Polyethylenes," *Proceedings,* Eighth European Conference on Fracture, Torino, Italy, 1–5 Oct. 1990.

Richard Salzbrenner[1] *and Thomas B. Crenshaw*[1]

Effects of Sample Size and Loading Rate on the Transition Behavior of a Ductile Iron (DI) Alloy

REFERENCE: Salzbrenner, R. and Crenshaw, T. B., **"Effects of Sample Size and Loading Rate on the Transition Behavior of a Ductile Iron (DI) Alloy,"** *Fracture Mechanics: Twenty-Third Symposium, ASTM STP 1189,* Ravinder Chona, Ed., American Society for Testing and Materials, Philadelphia, 1993, pp. 840–857.

ABSTRACT: The measurement and understanding of the fracture toughness of ductile irons (DI) are critical to the analysis of nuclear transportation casks made from these alloys. Cask containment must be assured for all loading events from normal handling to accidents during which high loads can be delivered at elevated rates. Cask walls are commonly in the range of 20 to 50 cm thick (or greater) in order to provide requisite nuclear shielding, and this requires that associated mechanical constraint effects must be considered. At elevated temperatures (that is, in the vicinity of ambient), DI behaves in an elastic-plastic manner, even for large section sizes (thickness > 20 cm) and moderately high loading rates. However, as the temperature is lowered or the loading rate is increased, ferritic DI alloys exhibit a relatively sharp transition to linear elastic behavior, with a significant decrease in the fracture toughness.

The fracture toughness of a DI alloy has been measured using linear elastic and elastic-plastic experimental techniques. Measurements have been made as a function of temperature, loading rate, and section size. The loading rates span the range that a cask could experience during normal transport and handling, as well as accident events. Specifically, the stress intensity rate, $\dot{K}$, was varied between 10^{-3} to $>10^{+5}$ MPa $m^{1/2}$/s. The range in section size that was examined was restricted to moderate thicknesses (~ 1 to ~ 4 cm) because of the limitations of available hydraulic test frames. For static testing rates, it was found that increasing specimen thickness appears to shift the transition behavior to slightly higher temperatures. The effect of increased specimen thickness during elevated rate testing was more pronounced. As the thickness was increased from ~ 1 to ~ 2 cm, the fracture toughness was decreased by roughly 25% at 25°C, and 40% at −29°C (the fracture toughnesses of both thicknesses were the same at −50°C where fracture was essentially all cleavage). Initial fractographic results show that the amount of brittle cleavage (at initiation) was larger for the thicker specimens in the ductile-brittle transition region. The decrease in fracture toughness with increasing section size (in the transition region) occurred even though all specimens met the size criteria of the ASTM Test Method for J_{Ic}, A Measure of Fracture Toughness (E 813-87). Measurements also showed that the temperature range of the transition region for this DI alloy increased with increasing loading rate and extended up to room temperature. A consistent explanation for the measured behavior seems to be that increased constraint (from increased specimen thickness) can cause an increase in cleavage if the test temperature (for a specific loading rate) is close to the transition region. The extent of this effect has an obvious impact on the analysis of the fracture resistance of transportation containers.

KEY WORDS: fracture (materials), *J*-integral, elastic-plastic behavior, linear-elastic behavior, ductile-to-brittle transition, specimen size, loading rate, transition temperature, fracture toughness, fracture mechanics fatigue (materials)

[1] Senior member of the Technical Staff and senior technical associate, respectively, Packaging and Structural Metallurgy Division, Sandia National Laboratories, Albuquerque, NM 87185.

Ferritic ductile iron (DI) alloys are being considered for use in nuclear transportation casks that have wall thicknesses of 40 cm or more and a total mass of 100 metric tons or more. The primary concern in using DI alloys for this application is the safety issue of the resistance of the cask to brittle fracture during all normal and accident conditions. Alloys of this type can exhibit a shift from ductile tearing behavior to a brittle mode of fracture. This transition occurs with a change in fracture appearance (from ductile tearing to cleavage) and a decrease in the energy required to initiate cracking from a preexisting flaw. Under certain conditions, this initiation energy can be measured as an intrinsic materials property known as fracture toughness. The fracture toughness can be used to quantify the resistance of the cask to fracture under a range of loading conditions [*1*]. From an engineering standpoint, it is the decrease in the measured fracture toughness in the ductile-to-brittle transition that is of major importance.

A transportation cask that carries high-level radioactive material must be able to survive the series of hypothetical accident conditions that are specified in the Code of Federal Regulations (10 CFR 71) [*2*]. In terms of the potential for failure by fracture, the primary event that must be considered is the requirement that the cask survive a 9 m (30 ft) drop onto an unyielding target. This drop test must be conducted at a temperature of −29°C (−20°F). This test, which combines the effects of high loading rate and low temperature, is intended to determine whether a specific alloy (such as DI) in a particular cask geometry can be driven to fail by fracture. However, even if a prototype cask successfully passes the drop test (and the other tests required in 10 CFR 71), a proper method has heretofore not been specified by international regulatory authorities that will guarantee that all other casks of nominally the same design and material will behave similarly. Such a guarantee depends on a rigorous fracture mechanics assessment. The behavior of each serial cask is related to the results of the prototype cask drop test through fracture toughness measurement. Determination of the fracture toughness (either by direct measurement or assessment of a suitably related property or feature) is the essential basis for the quality assurance plan necessary to guarantee adequate resistance to fracture.

A research program at Sandia has been developed to demonstrate how a fracture mechanics approach can be used to quantify the fracture resistance of transportation casks. One portion of the overall program is an effort to establish laboratory methods (specifically for high rate loading) for measuring the fracture toughness values used in the fracture mechanics assessment. The influence of temperature, loading rate, and size on fracture toughness is of obvious importance in assessing transportation casks, since such casks are massive and must withstand elevated rate loadings at low temperatures (during accident conditions). The laboratory testing described in this report is part of an on-going effort to obtain a fundamental understanding of the effects of temperature, loading rate, and size on the fracture toughness of DI. This understanding will allow the properly conservative evaluation of specific transportation casks (that is, particular design and material combinations).

Experimental Methods

Material

The material used in this study is a fully ferritic DI alloy that has been described previously [*3–5*]. The composition of this material is reported in Table 1, and the mechanical properties are listed in Table 2. Microstructural measurements pertaining to this alloy are presented in Table 3. All of the testing was conducted on as-cast material; that is, no heat treatment was conducted on the DI alloy.

TABLE 1—*Composition (percent by weight) of the ductile iron used in this study.*

C	Si	Ni	S	Cu	Cr	Mn	Fe
3.60	1.91	0.03	0.006	0.05	0.07	0.24	bal.

TABLE 2—*Mechanical properties (at room temperature) of the ferritic ductile iron used in this study.*

Static Yield Strength, MPa	Static Ultimate Strength, MPa	Static Tensile Elongation, %	Static Reduction in Area, %	Young's Modulus, MPa	$\dot{\varepsilon} = 10^2$ Yield Strength, MPa	$\dot{\varepsilon} = 10^2$ Ultimate Strength, MPa
239	369	21	23	1.83×10^5	348	419

Static Rate Fracture Toughness Measurements

Standard test methods exist that can be applied to the measurement of the fracture toughness in two regimes. Materials that exhibit a limited amount of plastic deformation prior to crack extension (from a pre-existing crack) can ordinarily be measured by following the methods covered in ASTM Test Method for Plane-Strain Fracture Toughness of Metallic Materials (E 399-81). The fracture toughness of alloys that display extensive plastic deformation prior to crack extension, and stable crack extension with ductile tearing can be determined by the methods described in ASTM Test Method for J_{Ic}, A Measure of Fracture Toughness (E 813-87). There is substantial commonality between the data required to determine the fracture toughness by either of the two standard methods. An essential requirement for both methods is a load-displacement record that can be generated from the same type of precracked specimen. The elastic-plastic testing requires additional information concerning the crack length at various points during the test. The commonality of required data between the two methods can be used to advantage by presuming that a sample will behave as an elastic-plastic material. If the sample does indeed behave in an elastic-plastic fashion, the data (load, load line displacement, and intermediate crack length measurements) can be used to determine the elastic-plastic fracture toughness. On the other hand, if the sample behaves in a linear elastic manner (as evidenced by a linear load-displacement test record), the linear elastic fracture toughness can be determined directly from the load-displacement record. The two types of fracture toughness measurements can be related through the equation

$$J_{Ic} = K_{Ic}^2/E \tag{1}$$

where J_{Ic} is the elastic-plastic fracture toughness, K_{Ic} is the linear elastic fracture toughness, and E is the Young's modulus. Great care must be exercised if Eq 1 is used to generate fracture

TABLE 3—*Microstructural measurements for the ferritic ductile iron used in this study.*

Nodule Count, Number/mm^2	Nodule Spacing, mm	Nodule Type	Ferrite Grain Size, mm	Graphite Volume Fraction, %	Pearlite Volume Fraction, %
105.0	0.049	100% Type I [*4*]	0.042	13.2	<1

TABLE 4—*Important dimensions of the compact specimens (with side grooves) used in this study.*

Nominal Thickness, cm	Gross Thickness, B_g (mm)	Net Thickness, B_n (mm)	Width, mm	a_0/W
1	11.4	10.3	25.4	~0.605
2	21.6	19.4	50.8	~0.605
4	43.2	38.9	101.6	~0.605

toughness values used in engineering calculations (Refs *1* and *6* provide some guidance and caveats in this regard). Equation 1 is nonetheless very useful for providing a means of directly comparing fracture toughness values from the ductile regime (upper shelf) to those of the more brittle region (lower shelf).

Since the data requirements for linear elastic testing can be considered to be a subset of those required for elastic-plastic testing, all static rate testing was based on a single-specimen J_{Ic} technique that complies with the standard test method for determining the fracture toughness of elastic-plastic alloys. Testing was conducted on compact specimens that allow direct measurement of the displacement along the load line. All specimens were grooved on each side, so that the net specimen thickness was 90% of the gross thickness (note that ASTM E 399-81 does not specifically allow specimens with side grooves for linear elastic testing). Three different specimen sizes were used and are nominally referred to as having thicknesses, B, of 1, 2, and 4 cm. The exact sample dimensions are listed in Table 4. Precracking was performed in accord with the requirements in ASTM E 813-87, and the precracking stress intensity was maintained below 20 MPa $m^{1/2}$ for all specimens (tested at either static or elevated rates). Testing was performed on a computer-controlled servohydraulic load frame. The loading rate (measured at the load line of the sample) for the static testing was held constant for each sample size at 5×10^{-4} cm/s. A detailed description of the test technique can be found elsewhere [*3*]. A chamber that controls temperature to ± 1°C was used for testing over the range of -150 to $+30$°C. Specimens that exhibited extensive plastic deformation prior to crack extension were analyzed according to elastic-plastic procedures [*3,4,7*]. Those specimens that displayed a suitably linear elastic test record were analyzed according to the methods of ASTM E 399-81, and the values were converted into elastic-plastic fracture toughness units according to Eq 1. Specimens that behaved in a linear elastic fashion in general did not meet the sample size requirements for a valid plane-strain result, but always met requirements concerning linearity, and the critical load used to calculate the fracture toughness was always within 10% of the maximum load.

An intermediate region between these two types of behavior is not covered by either standard. When crack extension in the intermediate regime is accompanied by too much plastic deformation, a direct measurement of fracture toughness under the guidance of ASTM E 399-81 is not possible.[2] The methods of ASTM E 813-87 are limited strictly to alloys that exhibit only stable tearing, and this usually does not occur in the transition region. Thus, an alloy (in the transition region) may exhibit too much plasticity to be evaluated by linear elastic methods, and yet failure by unstable crack extension precludes meeting essential requirements of elastic-plastic methods.

[2] The progression to larger and larger specimens in order to increase the constraint and limit the extent of the plastic deformation can require such massive specimens that testing is difficult to perform and interpret. Specimens of greater than 25 cm in thickness are indicated (from ASTM E 399-83 methods) as being required for testing of ferritic ductile iron in the upper transition region. Such a large specimen would have a significant microstructural variation, and since the ductile fracture has been shown previously [*4*] to depend on the nodule spacing, the interpretation of test results would be extremely difficult.

Although an alloy in the transition region can display a behavior that does not comply with either linear elastic or elastic-plastic standard test methods, the data can be dealt with in a straight-forward manner. Most of the ferritic DI alloy specimens used in this research, when tested in the transition region, did not exhibit stable crack tension. However, the test records showed that significant amounts of plastic deformation preceded the catastrophic extension of the crack. Under such conditions the energy related to the initiation of crack extension (for that specific specimen) is appropriately calculated by applying the methods of ASTM E 813-87. This method is reported elsewhere [*3*,*7*], and the fracture toughness values calculated in this manner are generally called J_C (C for cleavage). Values of J_C are reported as initiation toughness values for those cases where essentially no ductile tearing occurred prior to cleavage. The point at which cleavage crack extension occurs is distinctly evident on the test record, and the associated area under the load-displacement curve is used in the ASTM E 813-87 equations to calculate the J_C value. Even though there is little or no ambiguity in the determination of the energy associated with the cleavage crack extension, it must be emphasized that the value determined "may not be independent of sample size." The importance of this will become evident following the presentation of the data.

Elevated-Rate Fracture Toughness Testing

When the effect of elevated loading rate on the fracture toughness is to be investigated, only the behavior at or near the lower shelf (that is, brittle fracture) is covered by the currently approved standards. The standard for elastic-plastic fracture toughness does not allow for testing beyond slow loading rates. Thus, the potential for reporting data that fully complies with recognized standard test methods for determining the fracture toughness for elevated loading rates is even more limited than for static rate testing.

An approach for high loading rate testing of alloys that displays elastic-plastic behavior has been reported on elsewhere [*5*,*8*]. A multiple-specimen method is employed in which four to five specimens are used to generate the J-Δa record (where Δa is crack extension). This test technique complies with all of the measurement requirements listed in the standard static rate method with the exception that testing is performed at higher-than-recommended loading rates. A special set of fixtures is used to control precisely both the amount of displacement and the time duration of the loading to a precracked specimen. The intercept between the specimen J-Δa curve and an offset line (parallel to the blunting line) defines the initiation fracture toughness in a manner analogous to the procedure described in ASTM E 813-87.

As with static rate testing, there is a transition region behavior at elevated loading rate that is not covered by either linear elastic or elastic-plastic testing methods. The data (in the transition region) are treated similarly to the static rate data: the energy to cleavage (for a specific specimen thickness) is calculated as an ASTM E 813 J value. At even lower temperatures, the material can behave in a completely linear elastic manner. Linear elastic behavior is captured by the same test configuration. The load-displacement record needed to calculate the K_{Ic} fracture toughness is automatically captured during the multiple-specimen sequence used to generate the crack growth resistance curve (R-curve) for elastic-plastic behavior. All experiments were set up with the presumption that the material would behave in an elastic-plastic manner but, if a specimen failed by unstable crack extension, the load-displacement record was used to calculate either the linear elastic fracture toughness or the J-value at cleavage. The additional specimens that would have been required to determine the R-curve are not required. This test practice is similar to that described previously for the static rate tests in which the data required to calculate linear elastic toughness or the J-value at cleavage (load-displacement plus other requirements) can be considered a subset of that needed to determine the elastic-plastic toughness (load-displacement plus instantaneous crack length plus other requirements).

A high-rate servohydraulic test system (MTS Frame 318.25 and Controller 458.20) was used for the high loading rate tests (see Refs *5*, *8*, and *9* for more experimental details). The actuator rate was approximately 63 cm/s, which (in linear elastic units) translated into a stress intensity loading rate of greater than 3×10^5 MPa $m^{1/2}$/s for each specimen. Actuator rates below 100 cm/s do not introduce significant inertial effects, and thus static J formulations were used [*7*, *10*]. The capacity of the machine (as well as the availability of material) limited the testing to the specimens with the nominal thicknesses of 1 and 2 cm (see Table 4 for complete specimen dimensions). All other aspects of specimen geometry and preparation were identical to those described for the static rate testing.

Experimental Results

Static-Rate Fracture Toughness Measurements

As a function of temperature, the load-load line displacement (P-LLD) records showed that the DI alloy can act as an elastic-plastic material, a linear elastic material, or as an intermediate material that displays some aspects of both behaviors. The P-LLD curves displaying the full range of transition behavior for the 2-cm-thick specimen are shown in Fig. 1. The sample tested at -120°C had a linear elastic behavior that was reflected in both the P-LLD record and in the fracture surface that exhibited 100% cleavage. When the temperature was raised to -100°C, the sample had a significant increase in plasticity prior to failure by cleavage (the fracture surface was still essentially 100% cleavage). As the temperature was raised to -90°C, the material exhibited stable tearing for a significant amount of displacement, before failing by unstable crack propagation (that is, cleavage). However, even during the portion of the test that was predominated by stable tearing, there was some evidence of instability (see the "pop-in" events at displacements of $\sim$5 and 8.5 mm). The fracture surface for this sample showed a mixed-mode fracture (ductile fracture with $\sim$10 to 20% cleavage) occurred prior to a shift to 100% cleavage at the end of the test. As the testing temperature was raised still further (to -80°C or higher), the specimens that were tested displayed only stable (100%) ductile tearing throughout the entire loading sequence. All fracture surfaces for specimens (with B = 2 cm) tested at or above -80°C showed no evidence of cleavage.

The specimens that were different in thickness (B = 1 or 4 cm) were tested in the same fashion and displayed a similar transition behavior. The B = 1 cm specimens matched the behavior of the B = 2 cm specimens quite closely. At -90°C, for example, the 1-cm-thick sample showed a similar instability at the end of the test, in which the sample failed unstably by cleavage. At lower temperatures, the crack extension was predominated by cleavage, while for all temperatures above -80°C, crack extension resulted from ductile tearing. Thus, there seemed to be no measurable effect of size between B = 1 and B = 2 cm specimens. However, the larger (B = 4 cm) specimens seemed to promote brittle behavior at higher temperatures. At -90°C, for example, very little deviation from linear elastic behavior was seen prior to the onset of unstable tearing (Fig. 2*a*), for the B = 4 cm specimen compared to the substantial plastic deformation displayed by the thinner specimens. When the temperature was raised to -80°C (Fig. 2*b*), the P-LLD record showed significant deviation from linear elastic behavior, but the specimen failed in a brittle manner when a displacement of $\sim$0.8 mm was reached. The B = 1 and 2 cm samples (at -80°C) showed no evidence of cleavage or pop-in events. The fracture surface for the B = 4 cm specimen tested at -80°C, demonstrated that the crack extension occurred by cleavage. The test conducted at -60°C for the B = 4 cm specimen

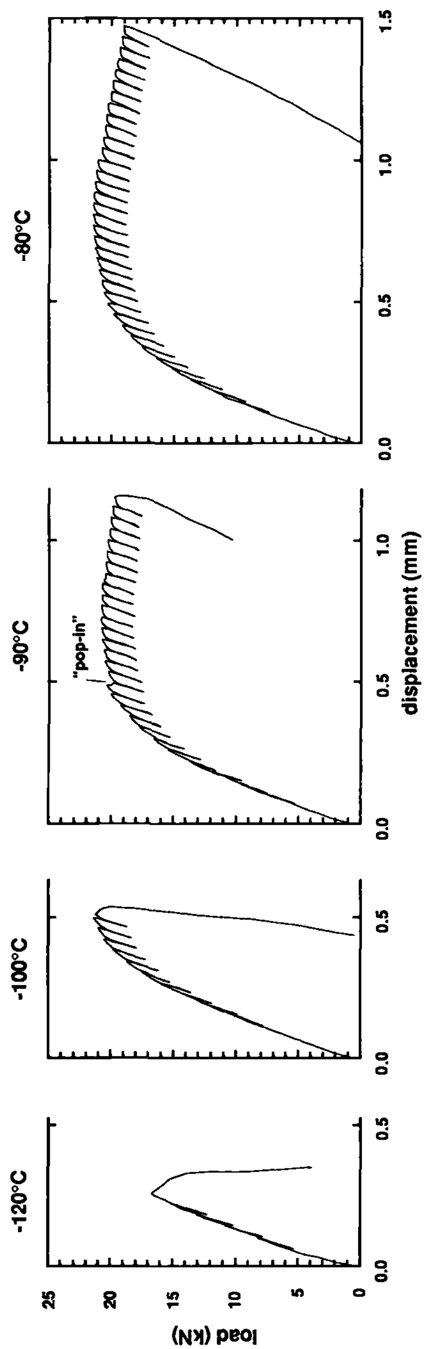

FIG. 1—*The load-displacement records for the compact specimens (B = 2 cm, W = 5 cm) of ferritic ductile iron at temperatures near the transition region for quasi-static rates.*

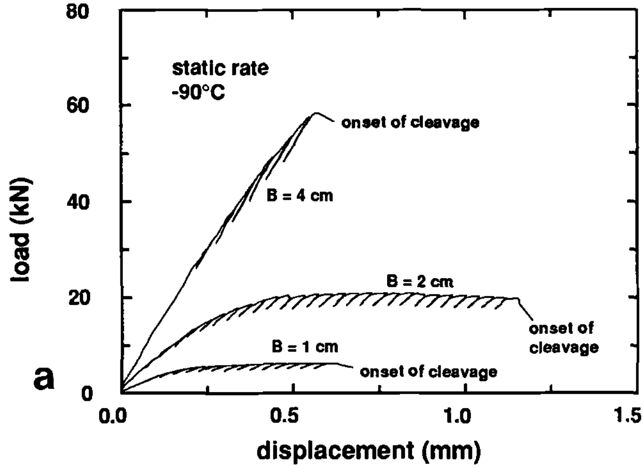

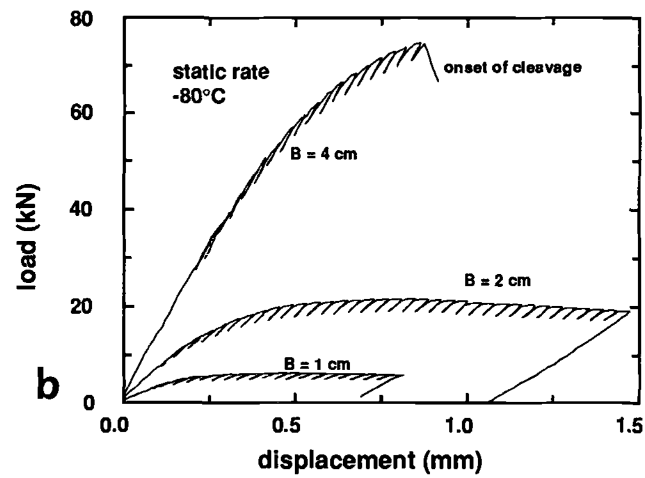

FIG. 2—*Static loading rate load-displacement records for compact specimens (*B = *1, 2, and 4 cm) at:* (a) *−90°C, and* (b) *−80°C.*

showed fully plastic behavior, despite the fact that the initiation fracture toughness remained approximately constant for the tests at −80 and −60°C (that is, J_C at −80 is approximately equal to J_{Ic} at −60°C). Recall that J_C is termed "initiation" toughness if the stable tearing that preceded cleavage was negligible.

The initiation fracture toughness values for all of the specimens tested at static loading rates are shown in Fig. 3. A dashed line has been drawn through the data to estimate the transition behavior for the B = 1 and 2 cm specimens. The data from the thicker specimens (that is, B = 4 cm) suggests a shift in the transition behavior to somewhat higher temperatures.

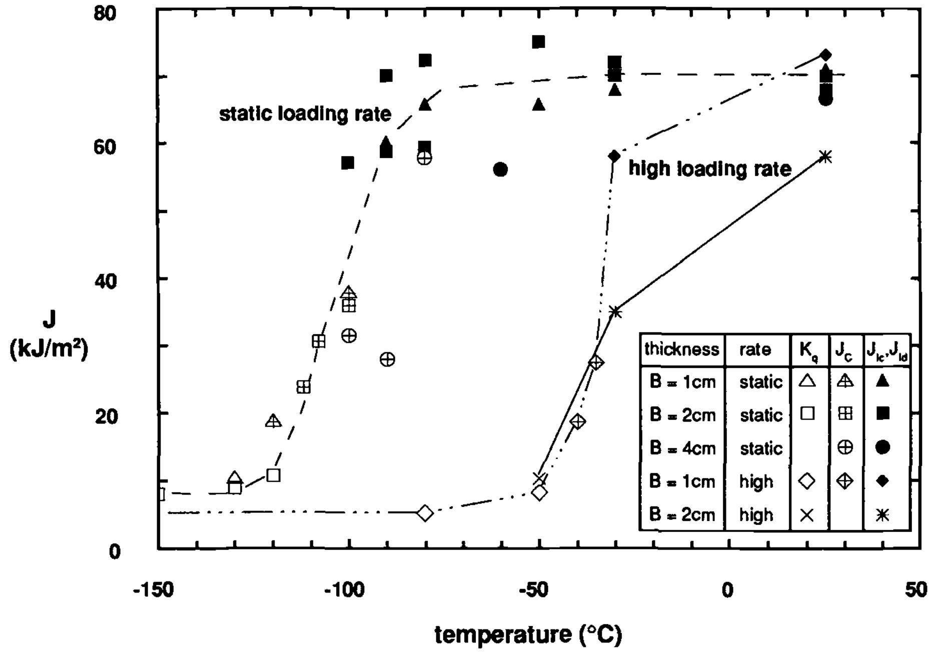

FIG. 3—*The measured fracture toughness behavior of a ferritic ductile iron alloy as a function of temperature (loading rate and specimen thickness are noted in the legend).*

Elevated-Rate Fracture Toughness Measurements

The multiple-specimen testing at elevated loading rate produced material behavior that ranged from linear elastic to fully plastic. Figure 4 shows the P-LLD records for B = 2 cm specimens at temperatures of −50, −29, and +25°C. At −50°C, the 2-cm-thick specimen behaved in a linear elastic fashion; this was corroborated by the fracture surface that was 100% cleavage. At a temperature of −29°C, the B = 2 cm specimens behaved as elastic-plastic material and displayed a mixed-mode fracture surface. Figure 5*a* is a fractograph that shows the fracture surface in the vicinity of the precrack for a specimen tested at −29°C. The fracture initiated in cleavage, but then shifted to ductile tearing, which allowed some stable crack growth to occur. It should be noted however, that the P-LLD record at −29°C did not indicate any pop-in behavior. The B = 2 cm specimens tested at room temperature displayed essentially full elastic-plastic behavior as shown by the fracture surface (Fig. 5*b*) in which greater than 95% of the fracture from the high rate loading was ductile tearing.

The behavior of the thinner specimens (B = 1 cm) was similar, in that the samples tested at −29°C exhibited stable tearing. The fracture surface showed that there was cleavage during initial crack extension that then shifted to ductile tearing. Pop-in behavior (associated with the early cleavage) was not indicated by the P-LLD record at −29°C. The B = 1 cm specimens tested at 25°C displayed fracture surfaces in which crack extension occurred only by ductile tearing; there was no evidence of cleavage.

Although the specimens of two different thicknesses were nominally similar (that is, based on the appearance of the fracture surfaces as well as the P-LLD behavior), the multiple-specimen analysis [5] used to produce a J-Δa plot revealed a significant difference between the two

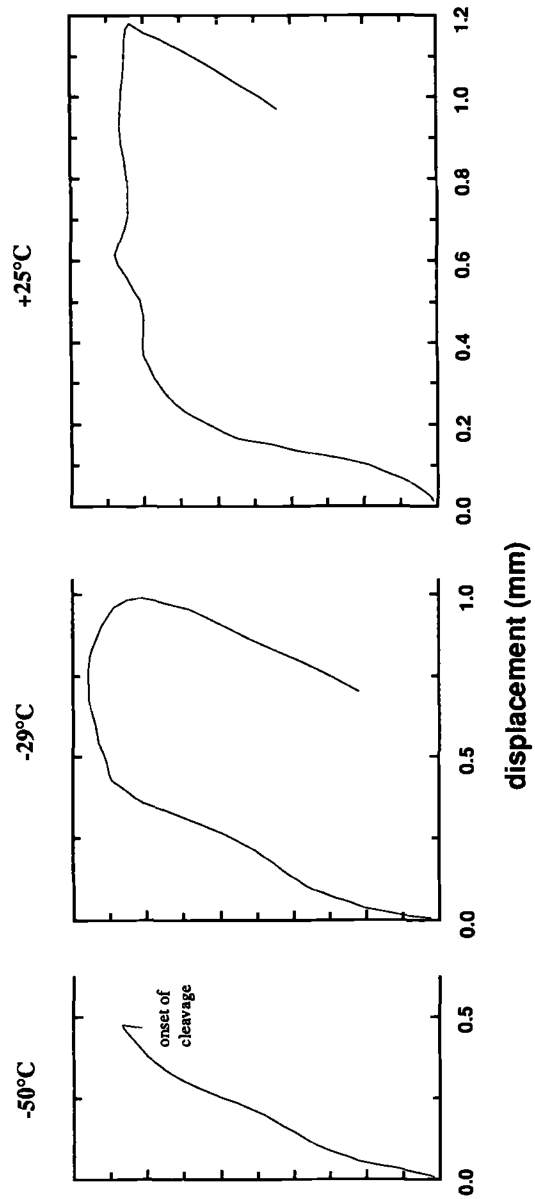

FIG. 4—*The load-displacement records for the compact specimens* (B = 2 *cm*, W = 5 *cm*) *of ferritic ductile iron at temperatures at various points in the transition behavior for high loading rates* ($\dot{K} \sim 4 \times 10^{+5}$ *MPa* $m^{1/2}$/*s*).

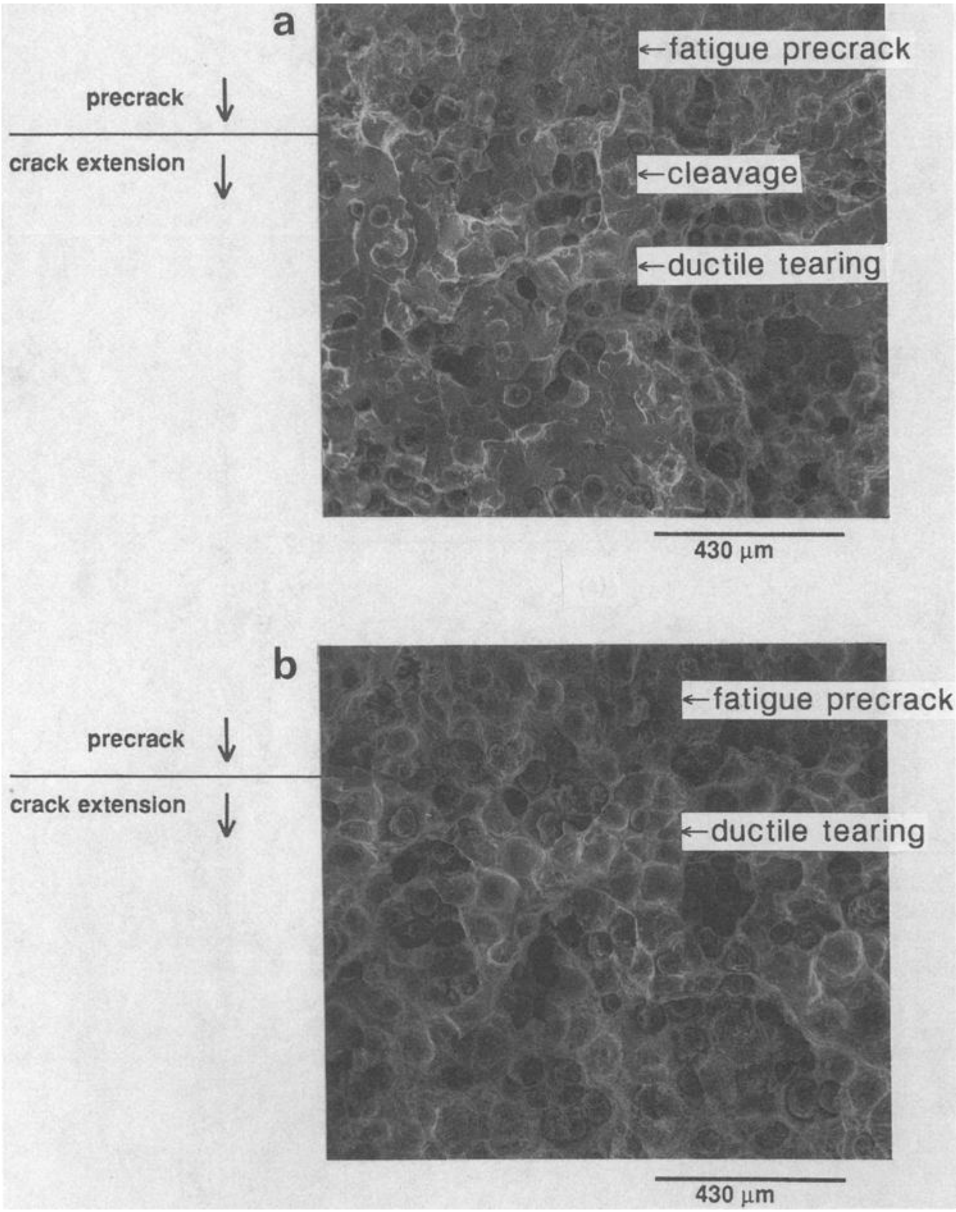

FIG. 5—*Fracture surface of specimen (*B *= 2 cm) tested at elevated loading rate* (a) *at −29°C and* (b) *at +25°C.*

thicknesses. Figure 6 displays the J-Δa (or JR) curves for the B = 1 and 2 cm specimens at temperatures of −29 and +25°C. The intersection of the power law fit through each set of data and the 0.15-mm offset line (as shown in Fig. 6) defines the initiation fracture toughness. Not only are the initiation values different for each on these specimen thickness-temperature combinations, but there is a difference in the "slope" of the data taken at +25°C versus that

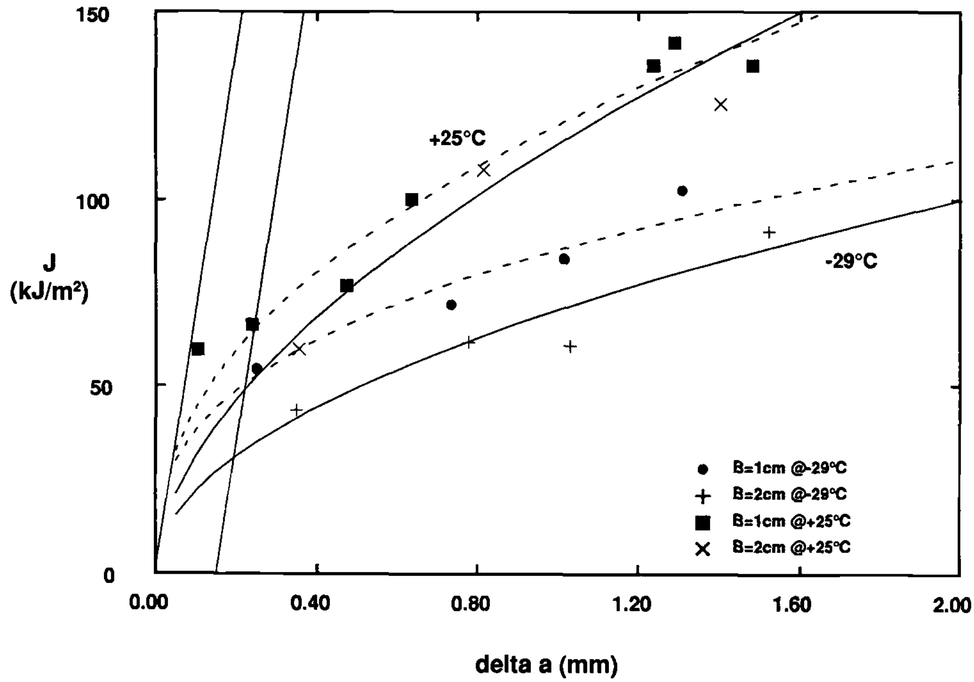

FIG. 6—*The measured* J-Δa *behavior of a ferritic ductile iron alloy at high loading rate* ($\dot{K} \sim 4 \times 10^{+5}$ *MPa* $m^{1/2}/s$) *is shown for two temperatures and two specimen thicknesses.*

taken at $-29°C$. The initiation fracture toughness and the "level" of the *JR* curve seem to be dependent on the specimen thickness even though both specimens exceed the minimum dimension requirements specified by the ASTM E 813-87 (for static rate testing). The influence of specimen thickness seems to be more pronounced at the lower (that is, $-29°C$) temperature than it does for the room temperature testing. However, on the "lower shelf" where the fracture occurred in an entirely linear elastic manner, the $B = 1$ and 2 cm specimens yielded the same value of initiation fracture toughness (as defined by ASTM E 399). There was no measurable effect of increasing the specimen thickness from 1 to 2 cm when the fracture was entirely brittle cleavage. The transition behavior for the $B = 1$ and 2 cm specimens is shown in Fig. 3. The points for the specimens at $-29°C$ and above are developed from multiple-specimen tests in which several individual samples are used to produce the single initiation fracture toughness value (see Fig. 6).

The fracture surfaces from 1- and 2-cm-thick specimens tested at $-29°C$ were examined in more detail to characterize any differences that in turn might explain the change in measured initiation fracture toughness. Complete montages of the fracture surface in the vicinity of the end of the fatigue precrack, across the thickness of $B = 1$ and 2 cm specimens were assembled. This is shown schematically in Fig. 7. Cleavage was found predominantly at the beginning of initiation (that is, immediately adjacent to the end of the fatigue precracked region) and the average length of this initial cleavage region was established. The measurements to date indicate that the thicker specimen has a longer length of initial cleavage crack growth region than does the thinner specimen (for example, the average initiation cleavage length in the $B = 2$ cm specimen is ~0.27 mm, compared to ~0.20 mm for the $B = 1$ cm specimen). The average length of the ductile tearing region depends on the total amount of crack growth (which varies

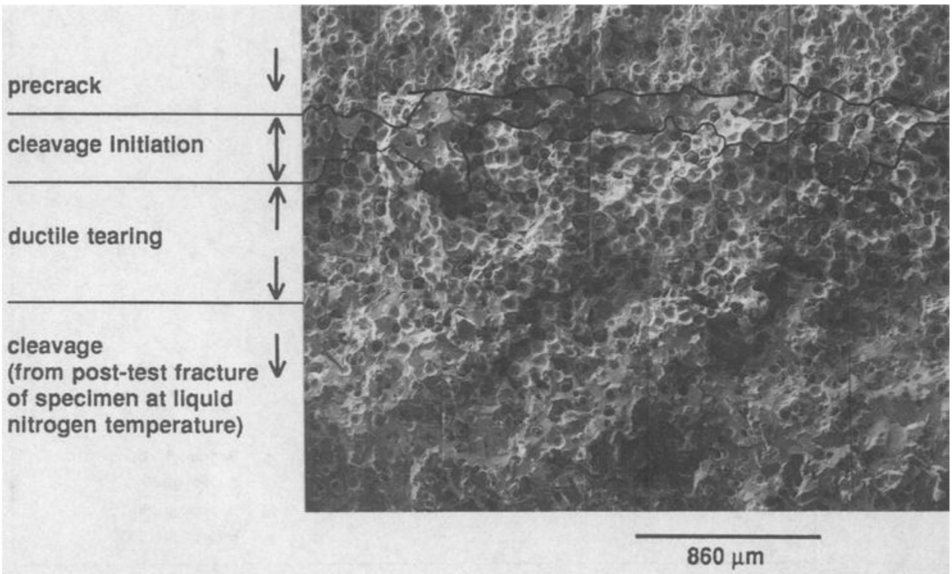

FIG. 7—*Montage of fracture surface of* B = *2 cm specimen tested at elevated rate at* −*29°C. Fracture initiated in cleavage then changed to ductile tearing.*

from sample to sample in a multiple-specimen test). These are preliminary results based on detailed measurements of selected specimens. These measurements must be extended to all of the specimens tested at −29°C to determine whether this difference (that is, different amount of cleavage at initiation) is always present.

Discussion

The experiments reported in the previous section demonstrate a clear effect of temperature and loading rate on the initiation fracture toughness. In addition, there seems to be an effect of size on the fracture toughness behavior in the vicinity of the transition region.

The effects of temperature and loading rate are clearly shown in Fig. 3. Considering first only a single loading rate (and constant specimen size), there is a narrow temperature range through which the initiation fracture toughness undergoes a significant decrease with decreasing temperature. This decrease in toughness is accompanied by a change in fracture mechanism from ductile tearing to (brittle) cleavage. For the slow loading rate tests, the transition between high and low toughness takes place in the −90 to −120°C range (Fig. 3). For the high rate testing, the change occurs over the range of >25 to −40°C (Fig. 3). Comparing curves for static loading rates with the high loading rate curves indicates that the major effect of increased loading rate is to cause the ductile-brittle transition range to occur at higher temperatures. The increase in loading rate may also broaden the temperature range between fully ductile and fully brittle behavior. The effect of loading rate on the level of fracture toughness on either the upper- or lower-"shelf" regimes seems to be minimal. There was no measurable effect on the toughness level of the lower shelf, while there may be a slight enhancement in the upper-shelf toughness (for the high loading rate) once fully ductile tearing is attained (see for example, the data for the 1-cm-thick specimen at +25°C). The small increase in toughness with increased loading rate may be expected because of an increase in yield strength as the loading rate is raised. The effects of temperature and loading rate on the fracture toughness of this ferritic DI alloy are similar to those that have been commonly observed in other iron-based alloys [*11*].

The observations associated with sample size that are reported in this paper are not as straight forward to describe as the rate and temperature effects. In static rate testing, the B = 1 and 2 cm specimens show that transition behavior takes place in the −90 to −120°C range. There is no evidence of cleavage instability (from the load displacement record) at −80°C. However, as the specimen thickness is increased to 4 cm (at −80°C), the sample exhibited considerable plastic deformation, but failed by cleavage. This significant change in behavior took place despite only a minimal decrease in initiation fracture toughness. At a somewhat lower temperature (−90°C), the 1- and 2-cm-thick specimen showed plasticity and (semi-)stable crack extension that was accompanied by some instability (that is, small "pop-ins" that were arrested) in the P-LLD record. After a limited amount of crack extension, these specimens ultimately became unstable and failed by cleavage at the end of the test. The fracture surface showed that ductile tearing preceded cleavage failure. In contrast, at a specimen thickness of 4 cm, just a minor amount of plastic deformation was seen at −90°C (in the P-LLD record) before unstable crack initiation. Only cleavage was noted on the fracture surface of the B = 4 cm specimen at −90°C. Although the number of measurements is small, the effect of size does not seem to be caused by the "statistical effect" reported elsewhere [*12,13*]. If statistically occurring weak links dominate the fracture toughness behavior, small specimens should show a large variation in toughness from sample-to-sample. Large specimens on the other hand would be more likely to exhibit a lower toughness since "weak links" are more likely to be present. However, in the current experiments, smaller specimens (B = 1 and 2 cm) did not display the scatter in toughness behavior that would be expected if the statistical appearance of microstructural weak links was a dominant factor. Further, the presence of some cleavage (for example, pop-in instabilities) indicates that there were sufficient initiation sites or "weak links," but insufficient constraint to propagate a cleavage failure [*14*]. The data are thus consistent with the contention that the apparent size effect is caused by an increased constraint that in turn increases the stored energy that can extend the crack once it has initiated. Additional experiments will need to be performed to determine whether or not "constraint" can be proven conclusively as the cause of the size effects observed during toughness testing of DI in the transition region.

At elevated loading rates, there is an effect of size between the B = 1 and 2 cm specimens at −29 and +25°C. The B = 1 cm specimens exhibit a higher initiation toughness as well as higher overall J-Δa curves. At −29°C both the B = 1 and 2 cm specimens initiate in cleavage, but then shift into stable ductile tearing. The reason for the shift into ductile tearing is not presently understood. The displacement versus time records do not show any decrease (until the displacement limiter is contacted) that might be associated with a decrease in the loading rate caused either by the capacity of the load frame or some aspect of the experimental setup. Additional experimental work is required to determine if any aspects of experimental technique (for example, specifics of the precracking procedure) may cause the specimen to initiate in cleavage, while retaining the capability to revert to ductile tearing (after, for example, the crack has extended beyond a "zone" damaged during precracking). The samples tested at −29°C seemed to show a slightly different amount of cleavage, which might explain the lower initiation toughness for the B = 2 cm specimen compared to the B = 1 cm specimen. An additional set of detailed measurements will be required to determine whether a statistically meaningful difference in the amount of cleavage between the two specimens is, in fact, present. For the specimens tested at room temperature, there was a minor amount of cleavage noted in the B = 2 specimen, while none was found in the B = 1 cm specimen. Again, additional testing will be required to determine if the small difference in cleavage can consistently be observed between the two different-sized specimens.

The J-Δa curves (for the $B = 1$ and 2 cm specimens) were each the result of measuring several specimens at $-29°C$. Each individual specimen behaved in a consistent manner, and thus the data (taken as a whole) strongly suggest that the differences shown in Fig. 3 (for high rate tests of different specimen thicknesses) are not due to experimental error, but are reproducible changes in the way each type of specimen behaves.

A recently published paper by Anderson and Dodds [15] describes suggested size criteria for size independent results for specimens in the transition region where the specimen fails by cleavage, but also exhibits enough plasticity to make measurement by linear elastic techniques essentially impractical. The size criteria that they developed (using finite-element modeling) is

$$B,\ b,\ a > 200(J_C/\sigma_y) \tag{2}$$

where B, b, and a are specimen-specific dimensions reflecting the specimen thickness, the length of the remaining ligament, and the (initial) crack length, respectively. The flow strength, σ_y, of the alloy is equal to ½ (yield strength plus ultimate strength). The value of J at unstable crack extension (cleavage), J_C, is calculated as described previously. The 200 multiplier used in Eq 2 compares to a value of 25 required to meet the criteria set in ASTM E 813-87 for testing fully plastic alloys. For linear elastic testing, the relevant equation is

$$B,\ b,\ a > 2.5(K_{Ic}/\sigma_{ys})^2 \tag{3}$$

where K_{Ic} is the linear elastic fracture toughness and σ_{ys} is the yield strength of the alloy. For the current alloy, the different size criteria (at room temperature, quasi-static loading rates, and using the highest values of J_{Ic} measured for the $B = 1$ and 2 cm specimens) are: (1) for a direct measure of the linear elastic fracture toughness (that is, if large-specimen dimensions alone could cause the material to behave in a linear elastic manner), $B, b, a > 51$ cm; (2) for a specimen size independent measure of J_C (Eq 2), $B, b, a > 4.7$ cm; and (3) for a fully elastic-plastic alloy, $B, b, a > 0.59$ cm (the specimen size requirements in (1), (2), and (3) are calculated for descriptive purposes only—more exact values should be calculated using the toughness values (K_{Ic}, J_C, or J_{Ic}) and the σ_{ys} or σ_y measured at the appropriate temperature and loading rate).

Using the criteria of Eq 2 and noting that the specimen failed by cleavage, the $B = 4$ cm specimen meets the validity requirement for J_C measurements at $-80°C$ (and lower temperatures). If the arguments promulgated in Ref *15* are applicable to the ferritic DI alloy tested here, the $B = 4$ cm specimen should be sufficient to measure the size independent fracture toughness at temperatures that cover a large portion of the transition region. Increasing the specimen dimensions will not appreciably lower the initiation fracture toughness, nor will there be any further change in the fracture mechanism (since the specimens failed by cleavage). The results for the $B = 4$ cm specimens that were tested at -60 and $+25°C$ also met the requirements of Eq 2, even though these specimens did not exhibit any cleavage crack growth. An extension of the arguments presented by Anderson and Dodds [15] suggest that testing even larger specimens is not likely to induce a cleavage-type failure.

Equation 2 can also be applied to the high rate measurements. The $B = 1$ cm specimen should provide a valid J_C for values of ~ 19.5 kJ/m^2 and below, while the $B = 2$ cm specimen can be used to measure directly J_C values up to ~ 37 kJ/m^2 (these values were calculated using the actual values for B_{net} (Table 4) and strength values measured from high rate tension tests (Table 2)). The results from the $B = 1$ cm specimens at $-40°C$ and below should thus provide valid J_C, while the larger specimen ($B = 2$ cm) should allow the valid J_C measurement at $-29°C$. Experiments should be conducted, however, to verify that increased size will not cause the toughness to be lowered further even though the size criteria of Eq 2 were met. Results from the $B = 1$ cm specimen at -29°C, and the $B = 1$ and 2 cm specimens at $+25$°C do not meet the validity requirements of Eq 2. Using the results from the $B = 2$ cm specimen at $+25$°C, Eq 2 suggests that a specimen of $B = 3.0$ cm should be tested to determine whether cleavage failure (at $+25$°C) can be induced in this alloy by the effects of increased constraint.

Using the validity guidelines presented by Eq 2, the data presented in Fig. 3 can be used to begin to provide a rational basis for selecting an appropriate value of fracture toughness for fracture mechanics assessments of very heavy-walled DI nuclear transportation casks. The lowest temperature that must be considered for accident conditions is -20°F (-29°C), which is very conservative considering the heat loading provided by contents such as spent nuclear fuel. The loading rate applied during the high-rate fracture toughness tests surpassed that measured during actual drop tests conducted without impact limiters [*16,17*]. For example, the time to peak load in the high-rate laboratory tests was ~0.75 ms, while the time to peak load during an actual drop test [*16*] was ~1.4 ms. The effects of loading rate on the increase in the ductile-to-brittle transition behavior should be captured conservatively by the laboratory measurements (assuming verification of the lack of further size effects as discussed previously). The high rate toughness at -29°C (with suitable error bars that should be provided by additional testing) can thus be used as a conservative estimate for the minimum toughness to assess cask safety from a fracture mechanics perspective. The initiation J-value at -29°C from Fig. 3 is 35.2 kJ/m^2 and compares well to previous high rate measurements [*9*] for similar samples from other ferritic DI alloys (at -29°C) that range from 32.9 to 34.5 kJ/m^2 (in every case, the specimen dimensions exceeded those required by Eq 2). It is also important to note that each reported initiation fracture toughness value was determined from a multiple-specimen technique, and that of the total of 18 specimens that have been tested (at -29°C), none have failed at an unexpectedly low toughness value (thus, specimen dimensions seem to be adequate to ensure that the lowest fracture toughness behavior will be measured).

In comparing the values of high-rate fracture toughness of DI as determined by others, it is important to note the broad range of techniques used. The precracked Charpy techniques generally provide a loading rate that is comparable to the loading rate used in this study (that is, $\dot{K} \sim 10^5$ MPa m$^{1/2}$/s). The upper-shelf dynamic fracture toughness values determined from such studies [*18,19,20*] are generally lower (that is, they range from 12 to 25 kJ/m^2) than the values determined by the technique used for this work. Other high rate methods that use precracked specimens that are larger than the standard Charpy [*19,20,21*] have produced estimates of fracture toughness that range from 37 to 53 kJ/m^2. This level of toughness is in general agreement with the measurements reported in this paper. It is emphasized, however, that these other methods generally do not directly control or measure the crack extension.

Conclusions

1. The effects of temperature and loading rate on the fracture toughness of ductile iron are generally consistent with the behavior observed in many ferritic steels. Namely, as the temperature is lowered, the alloy can undergo a transition from (high toughness) ductile tearing to (low toughness) cleavage failure. Increasing the loading rate causes the ductile-to-brittle transition temperature range to be shifted to higher temperatures.

2. Even though all specimens that were tested exceeded the specimen size requirements with respect to elastic-plastic testing, there appears to be an effect of specimen size (that is, thickness) near the transition temperature range for a specific loading rate. Static rate testing demonstrated that increasing the specimen dimensions caused the fracture mechanism to change. The change in fracture mechanism could be accompanied by either a minimal change in ini-

tiation toughness (at −80°C) or a quite significant decrease (at −90°C). For specimens that were tested at high loading rate, an increase in size caused a decrease in initiation toughness. This occurred without a dramatic change in the fracture appearance.

3. The results of all tests were examined with respect to size criteria suggested by Anderson and Dodds [*14*]. The results from the largest specimens tested at static loading rate should be sufficient to establish the size-independent fracture toughness of the material. Similarly, the largest specimen tested −29°C for the high loading rate, should be large enough to provide a valid toughness value (that is, an increase in specimen dimensions should not cause a change in fracture mechanism, nor a dramatic decrease in the level of toughness).

4. If the fracture toughness measured at high loading rate at −29°C is, in fact, size independent (as suggested by the Anderson and Dodds criteria), this value can be used in the fracture mechanics based evaluation of the fracture resistance of heavy-walled nuclear transport casks. The high loading rate tests were performed at a rate that exceeds that applied during regulatory (9 m) drop tests and in that respect can be considered conservative. Additional testing is required to verify the size independence.

Acknowledgments

This work was performed at Sandia National Laboratories, Albuquerque, New Mexico, supported by the U.S. Department of Energy under Contract Number DE-AC04-76DP00789.

References

[*1*] Salzbrenner, R., Sorenson, K. B., and Wellman, G. W., "Application of LEFM Design to Nuclear Material Transport Casks," *International Journal of Radioactive Materials Transport*, Vol. 1, 1990, pp. 33–40.

[*2*] *Code of Federal Regulations, Title 10, Part 71*, "Packaging for Transportation of Radioactive Material," Aug. 1983.

[*3*] Salzbrenner, R., Van Den Avyle, J. A., Lutz, T. J., and Bradley, W. L. "Fracture Toughness Testing of Ductile Cast Irons," *Fracture Mechanics: Sixteenth Symposium, ASTM STP 868*, M. F. Kanninen and A. T. Hopper, Eds., American Society for Testing and Materials, Philadelphia, 1985, pp. 328–344.

[*4*] Salzbrenner, R., "Fracture Toughness Behavior of Ferritic Ductile Cast Iron," *Journal of Materials Science*, Vol. 22, 1987, pp. 2135–2147.

[*5*] Salzbrenner, R. and Crenshaw, T. B., "Multiple Specimen J-integral Testing at Intermediate Rates," *Experimental Mechanics*, Sept. 1990, pp. 217–223.

[*6*] Kanninen, M. F. and Popelar, C. F., *Advanced Fracture Mechanics*, Oxford University Press, New York, 1985, pp. 281–391.

[*7*] Joyce, J. A. and Hackett, E. M., "Transition Range Drop Tower J-R Curve Testing of A106 Steel," *Experimental Mechanics*, Sept. 1989, pp. 274–278.

[*8*] Salzbrenner, R. and Sorenson, K. B., "Dynamic Fracture Toughness Measurements of Ferritic Ductile Cast Iron," *Proceedings*, PATRAM '89, The 9th International Symposium on the Packaging and Transportation of Radioactive Materials, 11–16 June 1989, Washington, DC, Oak Ridge National Laboratory, Oak Ridge, TN, 1989, pp. 728–735.

[*9*] Salzbrenner, R. and Crenshaw, T. B., "Mechanical Property Mapping of the Ductile Cast Iron MOSAIK Cask," Sandia Report SAND90-0776, UC-512, Sandia National Laboratories, Albuquerque, NM, Aug. 1990.

[*10*] Nakamura, T., Shih, C. F., and Freund, L. B., "Three Dimensional Simulation of a Dynamically Loaded Three-Point-Bend Ductile Fracture Specimen," *Proceedings*, Third International Conference on Nonlinear Fracture Mechanics, American Society for Testing and Materials, Knoxville, TN, 6–8 Oct. 1986.

[*11*] Barsom, J. M. and Rolfe, S. T., *Fracture & Fatigue Control in Structures: Applications of Fracture Mechanics, Second Edition*, Prentice-Hall, Inc., Englewood Cliffs, NJ, 1987, pp. 109–158.

[*12*] Landes, J. D. and Shaffer, D. H., "Statistical Characterization of Fracture in the Transition Region," *Fracture Mechanics (12th Conference), ASTM STP 700*, American Society for Testing and Materials, Philadelphia, 1980, pp. 368–382.

[*13*] Bates, R. C., "Micromechanical Modeling for Prediction of Lower Shelf, Transition Region, and Upper Shelf Fracture Properties," *Fracture Mechanics: Microstructure and Micromechanisms*, S. V. Nair, J. K. Tien, R. C. Bates, and O. Buck, Eds., American Society for Metals International, Metals Park, OH, 1989, pp. 131-168.

[*14*] Anderson, T. L. and Williams, S., "Assessing the Dominant Mechanism for Size Effects on CTOD Values in the Ductile-to-Brittle Region," *Fracture Mechanics: Seventeenth Volume, ASTM STP 905*, J. H. Underwood, R. Chait, C. W. Smith, D. P. Wilhem, W. A. Andrews, and J. C. Newman, Eds., American Society for Testing and Materials, Philadelphia, 1986, pp. 715–740.

[*15*] Anderson, T. L. and Dodds, R. H., Jr., "Specimen Size Requirements for Fracture Toughness Testing in the Ductile-Brittle Transition Region," *Journal of Testing and Evaluation*, Vol. 19, 1991, pp. 123-134.

[*16*] Sorenson, K. B., Salzbrenner, R., Wellman, G., Uncapher, W., and Bobbe, J., "Results of the First Thirty Foot Drop Test of the MOSAIK KfK Cask," presented at Waste Management '91, American Society of Mechanical Engineers, New York, Tucson, AZ, 24–28 Feb. 1991.

[*17*] Gunther, B. and Frenz, H., "Ductile Cast Iron (DCI)—Progress on Research Activities on Fracture Mechanics," *Proceedings*, PATRAM '89, The Ninth International Symposium on the Packaging and Transportation of Radioactive Materials, 11-16 June 1989, Washington, DC, Oak Ridge National Laboratory, Oak Ridge, TN, 1989, pp. 736-742.

[*18*] Kobayashi, T., Yamamoto, H., and Matsuo, K., "Evaluation of Dynamic Fracture Toughness on Heavy Wall Ductile Cast Iron for Container," *Engineering Fracture Mechanics*, Vol. 30, No. 3, 1988, pp. 397–407.

[*19*] McConnell, P. and Sheckherd, B., "High Loading Rate Fracture Toughness of Nodular Ductile Cast Iron," FCC 84-12-3R, Fracture Control Corporation, Goleta, CA, 1984.

[*20*] Tanner, G. M. and Bradley, W. L., "Evaluation of the Fracture Toughness of Ductile Iron Using Fatigue Precracked Charpy, Dynamic Tear, and Compact Tension Specimens," *Fracture Mechanics: Eighteenth Symposium, ASTM STP 945*, D. T. Read and R. P. Reed, Eds., American Society for Testing and Materials, Philadelphia, 1988, pp. 405–418.

[*21*] Krasowsky, A. J., Kramarenko, I. V., and Kalaida, V. V., "Fracture Toughness of Nodular Graphite Cast Irons Under Static, Impact, and Cyclic Loading," *Fatigue and Fracture of Engineering Materials and Structures*, Vol. 10, No. 3, 1987, pp. 223–237.

Author Index

Subject Index

N

O

P

Q

R

S

T

U, V, W

Z

ISBN 0-8031-1867-8